

26TH CONGRESS OF THE EUROPEAN SOCIETY OF BIOMECHANICS

BOOK OF ABSTRACTS

ORGANIZED BY
POLITECNICO MILANO 1863

The 26th Congress of the European Society of Biomechanics took place on July 11-14, 2021 with on online edition. The organization was in charge to Politecnico di Milano.

CONGRESS CHAIRS

Francesco Migliavacca, Congress Chair
Gabriele Dubini, Congress Co-Chair
Manuela Galli, Congress Co-Chair
Alberto Redaelli, Congress Co-Chair
Pasquale Vena, Scientific Program Chair
Dario Gastaldi, Scientific dissemination Chair, Website and Virtual Conference management
Giulia Luraghi, Conference-portal management
Francesca Berti, Sponsorship and Exhibitor management
Matteo Zago, Member of the ESB Education and Student Committee, Students activities Chair
Michele Marino, President of the ESB-ITA Board, Poster Session Chair
Simona Celi, Member of the ESB-ITA Board
Claudio Chiastra, Member of the ESB-ITA Board
Enrico Dall'Ara, ESB Council representative

LOCAL ORGANISING COMMITTEE

Boschetti Federica
Cimolin Veronica
Costantino Maria Laura
Contro Roberto
Fiore Beniamino
Frigo Carlo Albino
Mantero Sara
Pandolfi Anna
Pennati Giancarlo
Petrini Lorenza
Pietrabissa Riccardo
Rasponi Marco
Rodriguez Matas José Félix
Soncini Monica
Villa Tomaso
Votta Emiliano

INTERNATIONAL SCIENTIFIC COMMITTEE

Aliverti	Andrea	Italy
Ariza Gracia	Miguel Ángel	Switzerland
Avril	Stéphane	France
Barakat	Abdul	France
Barros	Ricardo	Brasil
Bastien	Christophe	United Kingdom
Bluestein	Danny	USA
Bourauel	Christoph	Germany
Brunner	Reinald	Switzerland
Burriesci	Gaetano	United Kingdom
Capelli	Claudio	United Kingdom
Carniel	Emanuele	Italy
Cereatti	Andrea	Italy
Checa	Sara	Germany
Ciardelli	Gianluca	Italy
Conti	Michele	Italy
Costi	John	Australia
Cristofolini	Luca	Italy
Dall'Ara	Enrico	United Kingdom
Della Croce	Ugo	Italy
Deriu	Marco	Italy
Di Giancamillo	Alessia	Italy
Di Martino	Elena	Canada
Dickinson	Alex	United Kingdom
Dörsam	Istabrak	Germany
Farè	Silvia	Italy
Edelman	Elazer	United States
Ferguson	Stephen	Switzerland
Fernandes	Paulo	Portugal

Flamini	Vittoria	USA
Fotiadis	Dimitrios	Greece
Franz	Thomas	South Africa
Furlong	Laura-Anne	United Kingdom
Galbusera	Fabio	Italy
García-Aznar	José Manuel	Spain
Gasser	Christian	Sweden
Gerbau	Frederic	France
Geris	Liesbet	Belgium
Gijsen	Frank	The Netherlands
Gill	Richie	United Kingdom
Heller	Markus	United Kingdom
Hellevik	Leif Rune	Norway
Hellmich	Christian	Austria
Ho-Ba-Tho	Marie Christine	France
Hoekstra	Alfons	The Netherlands
Hsu	Ming-Chen	USA
Ignatius	Anita	Germany
Innocenti	Bernardo	Belgium
Isaksson	Hanna	Sweden
ito	Keita	The Netherlands
Jonkers	Ilse	Belgium
Kamenskiy	Alexey	USA
Kaufman	Kenton	USA
Kazakidi	Asimina	United Kingdom
Kelly	Daniel	Ireland
Klisch	Stephen	USA
La Barbera	Luigi	Canada
LaDisa	John	USA

PERSPECTIVE TALKS

Prospective authors were invited to submit their latest research for a podium or a poster presentation. Those selected for the 2020 edition were re-invited for this edition.

CONGRESS TOPIC and TRACKS

The congress chairs invited distinguished colleagues to act as track chairs for the individual congress topics/tracks. The track chairs helped in announcing the call for abstracts, reviewed the submitted abstracts, arranged the order of the talks within the assigned sessions, and assigned chairs to the individual sessions. The topics grouped a few tracks on the same theme and act to coordinate the whole program. The topics were also used as title sessions for the poster presentations and for the poster awards.

CARDIOVASCULAR

Topic Coordinators: José Felix Rodriguez Matas, Emiliano Votta

TR01: Cardiovascular mechanics

Track chairs: Giulia LURAGHI (Politecnico di Milano, Italy), Frank GIJSEN (Erasmus University Medical Center, Rotterdam, The Netherlands)

TR02: Implants and devices for cardiovascular applications

Track chairs: Zhao LIGUO (Loughborough University, UK), Elisa LIEHN (Aachen University Hospital, Germany)

TR03: Imaging for cardiovascular applications

Track chairs: Henk MARQUERING (Academisch Medisch Centrum Universiteit, Amsterdam, The Netherlands), Patrick SEGERS (Gent University, Belgium)

TR04: Computational methods for cardiovascular applications

Track chairs: Frans VAN DE VOSSE (Technical University Eindhoven, The Netherlands), Irene VIGNON-CLEMENTEL (INRIA, France)

CELL AND MOLECULAR

Topic Coordinators: Marco Rasponi, Monica Soncini

TR05: Cellular and molecular biomechanics

Track chairs: Gwendolen REILLY (University of Sheffield, UK), Laoise McNAMARA (NUI Galway, Ireland), Marco DERIU (Politecnico di Torino, Italy)

TR06: Mechanobiology

Track chairs: Jose Manuel GARCIA-AZNAR (University of Zaragoza, Spain), Liesbet GERIS (Univeristy of Liege, Belgium)

TR07: Tissue engineering

Track chairs: Matteo MORETTI (Galeazzi Hospital, Milan, Italy), Andrea REMUZZI (Università di Bergamo, Italy)

MUSCOLOSKELETAL AND ORTHOPAEDICS

Topic Coordinators: Carlo Frigo, Manuela Galli

TR08: Musculoskeletal biomechanics

Track chairs: Claudia MAZZÀ (University of Sheffield, UK), Massimo SARTORI (University of Twente, The Netherlands)

TR09: Spine

Track chairs: Luigi LA BARBERA (Polytechnique Montreal, Canada), Fabio GALBUSERA (IRCCS Galeazzi Milano, Italy)

TR10: Imaging for muscoloskeletal applications

Track chairs: Luca CRISTOFOLINI (University of Bologna, Italy), Zimi SAWACHA (University of Padova, Italy)
(endorsed by International Society of Biomechanics)

TR11: Implants and devices for orthopaedic applications

Track chairs: Bernardo INNOCENTI (Université Libre de Bruxelles, Belgium), Nico VERDONSCHOT (University of Twente, The Netherlands), Luca CRISTOFOLINI (University of Bologna, Italy)

TR12: Impact/injury biomechanics

Track chairs: Peter ZIOUPOS (Cranfield University, UK), Christophe BASTIEN (Coventry University, UK)

TR13: Computational methods for orthopaedic applications

Track chairs: Ilse JONKERS (KU Leuven Belgium), Luca MODENESE (Imperial College London, UK)

TISSUE MECHANICS

Topic Coordinators: Pasquale Vena, Dario Gastaldi

TR14: Hard tissue biomechanics

Track chairs: Enrico DALL'ARA (University of Sheffield UK), Uwe WOLFRAM (Heriot Watt University, Edinburgh, UK), Jérôme NOAILLY (Universitat Pompeu Fabra, Barcelona, Spain)

TR15: Soft tissue mechanics

Track chairs: Rosaire MONGRAIN (McGill University, Montreal, Canada), Marie Christine HO-BA THO (University of Technology Compiegne, France)

TR16: Computational methods in tissue mechanics

Track chairs: Javier MARTINEZ REINA (Univesidad Sevilla, Spain), Peter PIVONKA (Queensland University of Technology Brisbane, Australia)

LOCOMOTION AND REHABILITATION

Topic Coordinators: Veronica Cimolin, Manuela Galli

TR17: Human movement

Track chairs: Reinald BRUNNER (University of Basel, Switzerland), Manuela GALLI (Politecnico di Milano, Italy)

TR18: Orthotics & prosthetics

Track chairs: Jaap HARLAAR (Delft University of Technology, The Netherlands), Alberto LEARDINI (IRCCS Istituto Ortopedico Rizzoli, Bologna, Italy)

TR19: Sport biomechanics

Track chairs: Laura-Anne FURLONG (Loughborough University, UK), Amanda SILVATTI (Universidade Federal de Viçosa, Brazil)
(endorsed by International Society of Biomechanics in Sports)

TR20: Ergonomics/Occupational biomechanics/Rehabilitation

Track chairs: Ugo DELLA CROCE (Università degli studi di Sassari, Italy), Andrea CEREATTI (Università degli studi di Sassari, Italy)
(endorsed by International Society of Biomechanics)

EMERGING TOPICS IN BIOMECHANICS

Topic Coordinators: Tomaso Villa, Sara Mantero

TR21: In silico trials and clinical biomechanics

Track chairs: Marco VICECONTI (University of Bologna, Italy), Richie GILL (University of Bath, UK)
(endorsed by VPH Institute)

TR22: Verification, validation and uncertainties quantification

Track chairs: Leif HELLEVIK (Norwegian University of Science and Technology, Trondheim, Norway), Keefe MANNING (The Pennsylvania State University, USA)

TR23: Computational biology

Track chairs: Alfons HOEKSTRA (University of Amsterdam), Paul WATTON (University of Sheffield, UK)

TR24: Additive manufacturing for biomedical applications and bioprinting

Track chairs: Claudio CAPELLI (University College of London, UK), Michele CONTI (University of Pavia, Italy)

OTHER TOPICS IN BIOMECHANICS

Topic Coordinators: Federica Boschetti, Giancarlo Pennati

TR25: Animal and plant biomechanics

Track chairs: Mauro MALVÉ (Public University of Navarra, Spain), Alessia DI GIANCAMILLO (Università degli Studi di Milano, Italy)

TR26: Biofluid and respiratory mechanics

Track chairs: Sean McGINTY (University of Glasgow, UK), Abdul BARAKAT (Ecole Polytechnique, Paris, France), Andrea Aliverti (Politecnico di Milano, Italy)

TR27: Biomaterials

Track chairs: Silvia FARE' (Politecnico di Milano, Italy), Guangyin YUAN (Shanghai Jiao Tong University, P.R. China)
(endorsed by the European Society for Biomaterials)

TR28: Dental biomechanics

Track chairs: Christoph BOURAUEL (University of Bonn, Germany), Istabrak DÖRSAM (University of Bonn, Germany)

TR29: Ocular biomechanics

Track chairs: Anna PANDOLFI (Politecnico di Milano, Italy), Miguel Ángel ARIZA GRACIA (University of Bern, Switzerland)

TR30: Reproductive biomechanics

Track chairs: Séverine LE GAC (MESA+ Institute for Nanotechnology, TechMed Center, The Netherlands), Renato NATAL JORGE (University of Porto, Portugal)

KEYNOTE LECTURES

COMPUTER MODELS SIMULATING THE MUSCULOSKELETAL SYSTEM OF THE LOWER EXTREMITY

MICROFLUIDICS, ELECTRIC FIELDS AND MACHINE LEARNING: THE PERFECT MATCH FOR SINGLE-CELL ANALYSIS

“TURBULENCE” IN BLOOD: EVERYTHING OLD IS NEW AGAIN



Prof. Dr. ir. Nico Verdonschot

Orthopaedic Research Laboratory of the Radboud University Medical Centre, Nijmegen, The Netherlands

Technical Medical Centre, Twente University, Enschede, The Netherlands

Dr. Verdonschot is an expert on computer modeling in the field of orthopaedic-biomechanics. He obtained a mechanical engineering degree at Twente University after which he worked at the orthopaedic department of the Radboud Medical Centre. Currently, he also works as the scientific director of the Technical Medical Centre of Twente University, thereby representing 400 researchers in the biomedical field. He is co-author of over 325 peer reviewed papers. He got an ERC advanced grant on the topic of Biomechanical diagnostic, pre-planning and outcome tools to improve musculoskeletal surgery. Furthermore, he is visiting professor of the Politecnico di Milano and has an honorary doctorate of the University of Aalborg.



Prof. Federica Caselli

University of Rome Tor Vergata Department of Civil Engineering and Computer Science Rome, Italy

Federica Caselli is Associate Professor in Biomedical Engineering at University of Rome Tor Vergata. She graduated in Medical Engineering, in Mathematics, and obtained her Ph.D. in advanced computational methods in biomechanics. Dr. Caselli’s research deals with the development of lab-on-a-chip devices for diagnostics and life science, with a special focus on microfluidic impedance cytometry for single-cell biophysical phenotyping. She has published about a hundred contributions in journals, conference proceedings and book chapters, including over thirty journal articles. She was awarded a grant from the “Scientific Independence of Young Researchers Programme” and she has been nominated in the “Women in Microfluidics & BioMEMS” list.



Prof. Dr. David Steinman

University of Toronto Mechanical & Industrial Engineering and Biomedical Engineering

David Steinman is recognized as a pioneer in the integration of medical imaging and computational modelling, and their use in the study of cardiovascular disease development, diagnosis and treatment. His current research focuses on improving rupture risk prediction for cerebral aneurysms; elucidating the nature of turbulence in blood flow; and developing ‘art-inspired’ data visualization and sonification techniques. Dr. Steinman co-founded the widely-used Vascular Modelling ToolKit, and spearheaded the International Aneurysm CFD Challenge series. He has been the recipient of numerous prestigious salary awards from the Heart & Stroke Foundation of Canada and is a Fellow of the American Society of Mechanical Engineers.

HUISKES MEDAL



Marco Viceconti
Alma Mater Studiorum - University of Bologna, Italy

Marco Viceconti is full professor of Computational Biomechanics in the department of Industrial Engineering of the Alma Mater Studiorum – University of Bologna, and Director of the Medical Technology Lab of the Rizzoli Orthopaedic Institute. He started his career as researcher in biomechanics in 1989 at the University of Florida – Madison, under the supervision of Prof Alì Seireg. Over the years he worked on various topics related to neuromusculoskeletal biomechanics, but in the last 20 years he focused primarily on In Silico medicine, where patient-specific physics-based computer models are used as clinical decision support systems. He served two full mandates in the Council of the European Society of Biomechanics, including a term as President. He is currently one of 25 members of the World Council of Biomechanics. According to SCOPUS he published 351 papers (H-index = 50). In 2018 he became Fellow of the Royal Academy of Engineering.

BEST PhD THESIS AWARD



Guillaume Durandau
University of Twente, Enschede, the Netherlands
Thesis title:
Towards the next Generation in Human-machine interfacing: Controlling Wearable Robots via Neuromusculoskeletal Modelling

Guillaume Durandau obtained his engineering diploma at ISEN-Toulon, France, and his master's degrees at the University of Sherbrooke, Canada. During his master's, he spent four months at the CINESTAV, Mexico. He also obtained during his master, the Mitacs Globalink Research Award. In 2016, he started his PhD at the Institute of Neurorehabilitation Systems, UMG, Gottingen, Germany, under the supervision of Prof. Dario Farina and Dr Massimo Sartori and then moved in 2017 to the University of Twente, Enschede, the Netherlands to continue his PhD under the supervision of Prof. Herman van der Kooij and Assoc. Prof. Massimo Sartori. During his PhD, he won the Best Demo Award in 2018 at the 7th IEEE International Conference on Biomedical Robotics and Biomechatronic and Best paper Published by IEEE-EMBS in 2017-18, 3rd place at the 7th Dutch Bio-medical Engineering Conference. He is currently a Postdoc researcher at the Department of Biomechanical Engineering at the University of Twente, Enschede, the Netherlands.

STUDENT AWARD FINALISTS

Katia Capellini
AN IMAGE-BASED CFD AND RBF MESH MORPHING APPROACH: AN ALTERNATIVE FOR STANDARD FSI TECHNIQUE

Gabriele Nasello
MECHANO-DRIVEN REGENERATION PREDICTS BONE INGROWTH IN LARGE ANIMAL MODEL BASED ON SCAFFOLD IMPLANTATION SITE

Karol Calò
IN VIVO AORTIC HEMODYNAMICS ANALYSIS COMBINING COMPLEX NETWORKS THEORY AND 4D FLOW MRI

Anna Corti
A FINITE ELEMENT – AGENT-BASED COUPLED MODEL OF RESTENOSIS: LINKING TISSUE DAMAGE TO CELLULAR DYNAMICS

WORKSHOP SESSIONS

Below the organised workshops.

Date: Monday, 12/July/2021	
EXEMPLAR - DASSAULT SYSTEMES.1	Workshop: "EXEMPLAR - Simulia workflow for life science applications"
PARAMETRIC DESIGN - ANSYS.1	Workshop: "How ANSYS transforms the cardiovascular activity: from Research to Medical Innovation, from Regulatory to Clinical Applications"
QUALISYS	Workshop: "Streamline your research with QUALISYS motion capture"

Date: Tuesday, 13/July/2021	
CERENOVUS	Workshop: "Endovascular Stroke treatment and career paths in the biomedical industry"
EXEMPLAR - DASSAULT SYSTEMES.2	Workshop: "EPYGON - Towards the implementation of ASME V&V 40-2018 for the structural assessment of EPYGON transcatheter mitral valve"
PARAMETRIC DESIGN - ANSYS.2	Workshop: "How ANSYS transforms the orthopedic activity: from research to medical Innovation, from regulatory to clinical applications"
ZEISS	Workshop: "X-ray computed tomography and digital volume correlation in musculoskeletal research"

Date: Wednesday, 14/July/2021	
EXEMPLAR - DASSAULT SYSTEMES.3	Workshop: "INSILICO TRIALS - A new in silico tool for TAVI standard tests available on InSilicoTrials.com, the first cloud-based platform"
MATERIALISE	Workshop: "Automating musculoskeletal modeling workflows: challenges and solutions"
PARAMETRIC DESIGN - ANSYS.3	Workshop: "ANSYS overview and PARAMETRIC DESIGN researches in the respiratory field"

SPONSORING & EXHIBITION

PROJECTS CORNER

Contents

KEYNOTE LECTURES **12**

ESB Student Award **15**

PERSPECTIVE TALKS **19**

SCIENTIFIC TRACKS **52**

TR01: Cardiovascular mechanics . . . 52
TR02: Implants and devices for cardiovascular applications . . . 98
TR03: Imaging for cardiovascular applications . . . 135
TR04: Computational methods for cardiovascular applications . . . 146
TR05: Cellular and molecular biomechanics . . . 189
TR06: Mechanobiology . . . 215
TR07: Tissue engineering . . . 247
TR08: Musculoskeletal biomechanics . . . 265
TR09: Spine . . . 305
TR10: Imaging for muscoloskeletal applications . . . 349
TR11: Implants and devices for orthopaedic applications . . . 366
TR12: Impact/injury biomechanics . . . 396
TR13: Computational methods for orthopaedic applications . . . 408
TR14: Hard tissue biomechanics . . . 448
TR15: Soft tissue mechanics . . . 488
TR16: Computational methods in tissue mechanics . . . 513
TR17: Human movement . . . 537
TR18: Orthotics and prosthetics . . . 552
TR19: Sport biomechanics . . . 562
TR20: Ergonomics/Occupational biomechanics/Rehabilitation . . . 572
TR21: In silico trials and clinical biomechanics . . . 586
TR22: Verification, validation and uncertainties quantification . . . 604
TR23: Computational biology . . . 614
TR24: Additive manufacturing for biomedical applications and bioprinting . . . 622
TR25: Animal and plant biomechanics . . . 643
TR26: Biofluid and respiratory mechanics . . . 649
TR27: Biomaterials . . . 661
TR28: Dental biomechanics . . . 676
TR29: Ocular biomechanics . . . 687
TR30: Reproductive biomechanics . . . 700

COMPUTER MODELS SIMULATING THE MUSCULOSKELETAL SYSTEM OF THE LOWER EXTREMITY

Nico Verdonschot

Radboud University Medical Center, Radboud Institute for Health Sciences, Orthopaedic Research Laboratory, Nijmegen, The Netherlands
University of Twente, Department of Biomechanical Engineering, Enschede, The Netherlands
Nico.Verdonschot@radboudumc.nl

Introduction

Musculoskeletal disorders are causing the highest burden of disease in the western world, and this will continue to rise due to aging of population.
A solution for musculoskeletal diseases that is proposed is a personalized approach. 'Personalized Medicine' originates from the genomics methodology, hinting that a disease has a molecular basis. However, the term 'personalized medicine' has received a bigger context and includes also the specific anatomical and biomechanical analysis of the musculoskeletal system. Hence, none-standardized, personalized surgical plans are being executed to enable optimal recovery with the least complications leading, ultimately, to better quality of live and lower healthcare costs.
Another solution to assess musculoskeletal diseases is to generate models of a population which is expected to include the variation within a patient cohort and which can be utilized to assess potential outliers that respond unexpectedly to a certain treatment.

Personalized Models

Biomechanical engineers are working together with imaging experts to develop fast and accurate tools to capture the essential aspects of the musculoskeletal system that is related to the pathology. Multi-modal (dynamic) imaging such as ultrasound, MRI and CT scanning are generating important information to develop personalized biomechanical models (see Figure). To feed the models with appropriate mechanical properties is complex as it is difficult to obtain reliable information about all tissues that might affect the behaviour of the joint which is analysed.

Population based models

Ideally, these types of models include the variations seen in cohorts of patients. Different anatomical geometries are included, typically using statistical shape models. Variations in mechanical properties are obtained from literature and entered into the population to analyse the sensitivities to these variations. These models are highly useful for orthopaedic companies to enhance the robustness of their implants.

Acknowledgements

This research was generated by the collaborative efforts of many researchers and clinicians at Radboudumc and the University of Twente.

Dr. Verdonschot is an expert on computer modeling in the field of orthopaedic-biomechanics. He obtained a mechanical engineering degree at Twente University after which he worked at the orthopaedic department of the Radboud Medical Centre. Currently, he also works as the scientific director of the Technical Medical Centre of Twente University, thereby representing 400 researchers in the biomedical field. He is co-author of over 325 peer reviewed papers. He got an ERC advanced grant on the topic of Biomechanical diagnostic, pre-planning and outcome tools to improve musculoskeletal surgery. Furthermore, he is visiting professor of the Politecnico di Milano and has an honorary doctorate of the University of Aalborg.

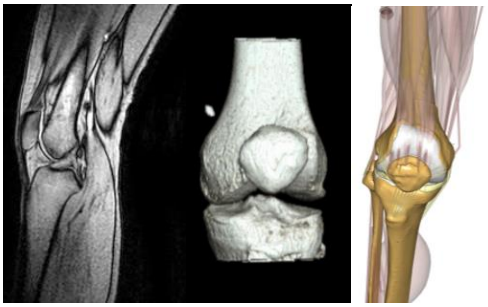

Figure showing how dynamic MRI (left), dynamic CT (middle) can help building a personalized musculoskeletal model of the knee joint (right).

Future directions

In the future we may see that artificial intelligence (AI) methods applied to large cohorts of patients replace the biomechanical (mechanistic) models. Optimally, mechanistic models are combined with AI methods to allow for faster development. Generating personalized models will remain highly challenging for the next decade as the mechanical properties are still difficult to assess. Imaging modalities such as ultrasound elastography might help to partly solve this issue, but more methods are required to perform in-situ quantification of the mechanical properties. Furthermore, loading conditions are variable amongst patients; methods to quantify these differences in loads are required.
Finally, the societal relevance of the modelling tools as described must be demonstrated more explicitly in order to remain of great value in the views of funding agencies such as the EC and NIH and regulatory bodies.

MICROFLUIDICS, ELECTRIC FIELDS AND MACHINE LEARNING: THE PERFECT MATCH FOR SINGLE-CELL ANALYSIS

Federica Caselli

Department of Civil Engineering and Computer Science, University of Rome Tor Vergata, Rome, Italy

Background

Cell is the fundamental unit of life. Accordingly, understanding of cell function in health and disease is critical to diagnosis and treatment. Moreover, modern approaches towards personalized and precision medicine highlight the potential of cell analysis and manipulation for the development of novel therapeutic solutions to tackle, e.g., cancer and infectious disease. This raises the need to develop technological tools to assist biologists and clinicians in their mission to improve healthcare. In this scenario, microfluidics, electric fields and machine learning represent three key players. Microfluidics matches well with the size of typical biological cells and has potential for high reproducibility, large parallelization, easy operability and low-cost. Electric fields offer tremendous opportunities for analysis and manipulation of biological cells, by means of versatile, effective and yet simple sensing and actuation features, which can be integrated into a multifunctional microfluidic system. Machine learning enables to equip such a system with a *brain* that provides real-time monitoring and automatic control, by deciding tasks based upon its perception of the microenvironment.

Intelligent microfluidic impedance cytometry

After an introduction on the emerging synergy of microfluidics, electric fields, and machine learning for single-cell analysis and manipulation, I will present the great opportunities provided within this landscape by Microfluidic Impedance Cytometry (MIC). MIC is a label-free and high-throughput technique that uses electric fields to stratify the heterogeneity of cellular systems based on their biophysical properties (i.e., electrical and mechanical properties). Emerging applications range from fundamental life science and drug assessment research to point-of-care diagnostics and precision medicine. Recently, novel chip designs and data analytics strategies are laying the foundation for multiparametric cell characterization and subpopulation distinction, which are essential to understand biological function, follow disease progression, and monitor cell behaviour in microsystems. Moreover, neural networks are showing their potential for real-time processing of high-content cell electrical fingerprints, paving the way for impedance-based sorting of target cell subpopulations. Further emerging directions include the development of automated, multifunctional, all-electrical platforms as well as hybrid platforms that couple MIC with other microfluidic approaches. Overall, these research efforts are expected to advance single-cell analysis to the next level in the coming years.

Federica Caselli is Associate Professor of Biomedical Engineering at University of Rome Tor Vergata. She graduated in Medical Engineering, in Mathematics, and obtained her Ph.D. in advanced computational methods in Biomechanics. She was awarded a grant from the "Scientific Independence of Young Researchers Programme" and she has published about a hundred contributions in journals, conference proceedings, and book chapters. Dr. Caselli's research deals with the development of lab-on-a-chip devices for diagnostics and life science, with a special focus on microfluidic impedance cytometry. She seeks novel solutions for single-cell biophysical phenotyping and manipulation, by using model-based device design, signal processing and data analytics.



Figure 1: Cover page image from Ref. [1], giving a suggestion of the synergistic convergence of microfluidics, electric fields and machine learning towards single-cell analysis and manipulation.

References

1. Honrado et al., Lab Chip, 21:22-54, 2021.
2. Hayes and Caselli, Anal. Bioanal. Chem., 412:3799–3800, 2020.
3. Honrado et al., Anal. Bioanal. Chem., 412:3835–45, 2020.
4. De Ninno et al., Biosens. Bioelectron., 150:111887, 2020.
5. Reale et al., Lab Chip, 19:1818–27, 2019.
6. Nodargi et al., Comput. Methods Appl. Mech. Eng., 338:392-411, 2018.

Acknowledgements

I would like to thank all the collaborators who participated in these studies, in particular A. De Ninno, R. Reale, N. Nodargi, P. Bisegna, and N. Swami's group at University of Virginia. Financial support from the Italian Ministry of University and Research is gratefully acknowledged (Grant RBSI14TX20).

“TURBULENCE” IN BLOOD: EVERYTHING OLD IS NEW AGAIN

David A. Steinman, PhD

University of Toronto, Canada

Background

Textbooks tell us that blood flow is normally laminar, with “turbulence” typically only expected in pathological conditions such as stenoses or distal to heart valves. Such flows have been subject of much research for the past 50 years. Beginning in the 1970s, the groups of Young [1] and of Giddens [2] (stenosis), and Stein and Sabbah [3] (heart murmurs), among many others, made great strides in understanding the nature of physiological turbulence, and its potential impact on vessel walls and blood. The group of Margot Roach (whom I had the good fortune to know and work with at the University of Western Ontario before she retired) also performed pioneering investigations into hemodynamic sources of bruits and hums in the cerebrovasculature [4].

Beginning around a decade ago, high-fidelity computational modelling began to reveal high-frequency flow instabilities where smooth, laminar flows were presumed to be present [5]. Our work in particular has tried to highlight the perils of this self-fulfilling prophecy, in that modelling decisions are inevitably informed by presumptions about the flow regimes [6]. For want of a better word we refer to these energetic flows as “turbulent-like”, encompassing laminar vortex-shedding, transition, relaminarization, and non-isotropic turbulence.

Recent Advances

Turbulent-like flows are of keen interest for predicting hemolysis caused by medical devices, of course, but also now aneurysm rupture and cardiac energetics [7], among other applications. CFD Challenges have highlighted the, er, challenges of replicating these flows, especially when it comes to comparing against experiments [8]. Osborne Reynolds himself acknowledged that “utmost care [was required] to reduce the external disturbances” in his pioneering experiments [9], which raises new questions about artificially “clean” numerical and experimental studies in light of messy physiological realities. And while CFD can now resolve these flows down to the scale of red blood cells [10], theoretical arguments [11] and experimental studies [12] are there to remind us that, at those scales, the biorheology of blood may be more like that of a slurry than a simple fluid.

The renewed interest in turbulent-like flows has also reinvigorated interest in understanding and modelling flow-induced vessel wall vibration [13]. High-fidelity fluid-structure-interaction (FSI) solvers are now coming online to help elucidate how the different turbulent-like flow “phenotypes” may drive flow-induced vibrations [14]. Advances in data visualization (and sonification) are also helping us to start to make sense of these highly complex flows in non-trivial geometries [15].

David Steinman is a Professor of Mechanical and Biomedical Engineering at the University of Toronto. He obtained his PhD in Computational Hemodynamics at U. Toronto in 1993 and did a post-doctoral fellowship in Radiology at the University of Western Ontario from 1993-1996. His research focuses on image-based computational modelling of cardiovascular disease, at the interface of engineering, medicine and the arts. He is an author of nearly 150 peer-reviewed journal articles, including leadership on the International Aneurysm CFD Challenge series, and co-development of the Vascular Modelling ToolKit (VMTK). In 2012 he was elected Fellow of the American Society of Mechanical Engineers.

Future directions

Setting aside the theoretical and computational complexity of these flows, the presence of high-frequency wall shear stress (WSS) and pressure fluctuations raises questions about the mechanobiology that have yet to be addressed. Does the endothelium glycocalyx anyway damp high frequency WSS fluctuations? Can extracellular membranes and smooth muscle cells sense and/or respond to high-frequency vibrations?

And what of the clinical implications? With increasingly small and sensitive transducers and machine learning, we may be able to better pinpoint and distinguish murmurs, bruits and hums, perhaps returning auscultation to the clinician’s armamentarium after being arguably displaced by advances in medical imaging over the past 50 years. But (how) will we be able to connect these with any specificity or sensitivity if we (still) cannot make out an individual’s vessel wall structure and properties? These and other questions should keep us biomechanical engineers busy for the next decade (and more!).

References

1. Forrester JH, et al. J Biomech 1970;3(3):307-16.
2. Giddens DP, et al. Circ Res 1976;39(1):112-9.
3. Stein PD, et al. Circ Res 1976;39(1):58-65.
4. Roach MR, et al. Stroke 1972;3(3):255-67.
5. Valen-Sendstad K, et al. J Biomech 2011;44(16):2826-32.
6. Khan MO, et al. Am J Neuroradiol 2015;36(7):1310-6.
7. Chnafa C, et al. Ann Biomed Eng 2016;44(11):3346-3358.
8. Zmijanovic V, et al. Int J Numer Method Biomed Eng 2017;33(1).
9. Rott N. Annu Rev Fluid Mech 1990;22:1-11.
10. Jain K, et al. Computers & Fluids 2016;127:36-46.
11. Antiga L, et al. Biorheology 2009;46(2):77-81.
12. Biswas D, et al. J Biomech Eng 2016;138(7).
13. Mancini V, et al. J Biomech Eng 2020;142(9):091007.
14. Bergersen AW, et al. JOSS 2020;5(50):2089.
15. Pereira VM, et al. J Neurointerv Surg 2020.

MECHANO-DRIVEN REGENERATION PREDICTS BONE INGROWTH IN LARGE ANIMAL MODEL BASED ON SCAFFOLD IMPLANTATION SITE

Gabriele Nasello (1,2), Maria Ángeles Pérez (1), José Manuel García-Aznar (1)

1. University of Zaragoza, Spain; 2. KU Leuven, Belgium

Introduction

Three-dimensional (3D) printed scaffolds offer patient-specific porous surfaces that enhance the biological engraft with the surrounding bone tissue [1], thus they are moving orthopedic implants from inert materials to bioactive scaffolds guiding the bone regeneration process. Tuning the scaffold mechanical properties is appropriate for encouraging bone ingrowth into porous materials, although the host sensitivity to mechanical stimulus has a critical impact on bone regeneration [2]. Therefore, patient-specific porous scaffolds should consider the variability in the host response. We developed a computational model of mechano-driven bone regeneration where the local environment and the regenerative potential of an individual host regulate the bone ingrowth within a porous scaffold. We calibrated the model by means of *in vivo* animal data of bone ingrowth in 3D printed scaffolds inserted in distinctive implantation sites and in different recipients [3].

Materials and methods

The computational model consisted of three parts: the scaffold, the granulation tissue filling the scaffold pores and the surrounding bone. It was assumed that bone regeneration could be reduced to a simultaneous process of cell invasion and bone formation regulated by the mechanical stimulus [3]. Bone ingrowth in porous titanium scaffolds was simulated for 12 weeks in the distal femur and proximal tibia of three goats. Numerical outputs were compared to results of an *in vivo* study conducted by Materialise NV (Belgium), where bone ingrowth was quantified in the medullary, middle and periosteal subregions of the scaffold.

Results

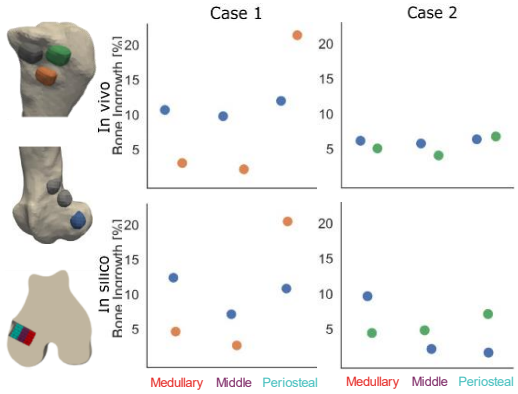

Figure 1: In vivo and in silico bone ingrowth outcomes. Scaffolds were inserted into epiphyseal (blue, green) and diaphyseal (orange) locations.

Bone ingrowth shifted from a homogeneous distribution pattern, when scaffolds were in contact with trabecular bone (max local ingrowth 12.47%), to a localized bone ingrowth when scaffolds were implanted in a diaphyseal location (max local ingrowth 20.64%) (Figure 1). Bone formation mostly occurred in the outer pores of the scaffold throughout the numerical analysis, as observed *in vivo* (Figure 2). After calibrating the model, we identified one animal with higher sensitivity to mechanical stimulation. Moreover, we found that the stimulus initiating bone formation was higher in the femur than in the tibia for all individuals [3].

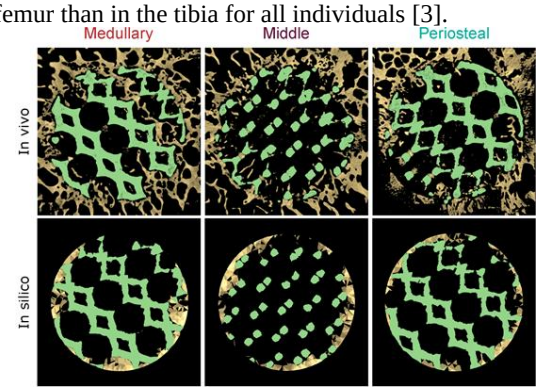

Figure 2: In vivo and in silico microCT slices of the medullary, middle and periosteal subregions where bone is labeled in yellow and scaffold in green.

Discussion

The computational model revealed that a regenerative process purely based on mechanical stimulation predicts the bone ingrowth distributions, penetration depths and the bone formation dynamics observed *in vivo* when scaffolds were implanted in different recipients and implantation sites. Calibration enlightened differences in mechano-sensitivity between recipients, showing that osteointegration cannot depend on scaffold mechanical properties alone. Overall, the dependence of the osteogenic response on the host biomechanics means that the regenerative potential depends on both the scaffold and the host environment.

References

1. Pobloth, A.M. et al., Sci Transl Med, 10, eaam8828, 2018.
2. Reznikov, N. et al., Biomaterials, 194, 183–194, 2019.
3. Nasello, G. et al., Bone, 144, p.115769, 2021.

Acknowledgements

Authors have received funding from the EU Horizon2020 project No. 722535 and SMEC DPI2017-84780-C2-1R.

IN VIVO AORTIC HEMODYNAMICS ANALYSIS COMBINING COMPLEX NETWORKS THEORY AND 4D FLOW MRI

Karol Calò (1), Andrea Guala (2), Diego Gallo (1), Jose Rodriguez-Palomares (2), Stefania Scarsoglio (1), Luca Ridolfi (1), Umberto Morbiducci (1)

1. PolitoBIOMed Lab, Department of Mechanical and Aerospace Engineering, Politecnico di Torino, Italy;
2. Hospital Universitari Vall d'Hebron, Department of Cardiology, CIBER-CV, Vall d'Hebron Institut de Recerca (VHIR), Universitat Autonoma de Barcelona, Barcelona, Spain

Introduction

In the progression of the ascending aorta (AAo) dilation a relevant role is played by local adverse hemodynamics, which in turn stimulates adverse biological reactions ultimately leading to fatal events such as aneurysms rupture. In this study, the spatiotemporal heterogeneity of large-scale aortic flow features is investigated *in vivo* for the first time applying the Complex Networks (CNs) theory [2] to 4D flow MRI data of ten patients, five of them presenting with AAo dilation [1]. Technically the acquired time-resolved phase velocity data were used to build correlation-based CNs. Then, the anatomical and functional length of persistence of the correlation of velocity time histories were quantified and their association with *in vivo* measurable hemodynamic quantities as well as AAo dilation was explored.

Methods

Study methods are summarized in **Fig.1**. The study population comprises five patients presenting with AAo dilation and five with no AAo dilation. Full details on 4D flow MRI acquisition protocol are exhaustively reported elsewhere [1]. For each patient, the thoracic aorta lumen geometry was reconstructed and three CNs were built on the time-resolved waveforms obtained from *in vivo* data of: velocity magnitude |V|; (through-plane) axial velocity component V_{ax} [3]; (in-plane) secondary velocity component V_{sc} [3]. Each node of the CNs was defined by the voxel where the velocity-based time history is acquired. Two nodes were connected by a topological link if the Pearson correlation coefficient R_{ij} between the time histories at nodes i and j was greater than a threshold $\hat{R}$ (**Fig. 1**). For each CN an adjacency matrix A_{ij} was built and three metrics were computed [2] (**Fig. 1**): (1) the *degree centrality* (DC_i) of node *i*, measuring the homogeneity/heterogeneity of the time history in *i* with respect to the whole fluid domain; (2) the *normalized average Euclidean distance* (AED_i) between node *i* and all its nearest neighbours, and (3) the *average shortest path length* ($ASPL$). AED_i and $ASPL$ quantify the anatomical and topological length of persistence of the correlation between velocity time histories in the aorta, respectively [2].

Results

DC volume maps, displayed in **Fig.1**, show that |V| and V_{ax} CNs are scarcely connected (low DC), reflecting from very poor to moderate homogeneity of velocity time history shapes. The CNs of V_{sc} time histories presented patterns of connections between nodes denser than |V| and V_{ax}. Notably, AED was negatively associated with AAo maximum diameter D_{max}, whereas $ASPL$ was positively associated with D_{max} only in |V| CNs, indicating that, in general, high D_{max} values reduce the anatomical extension of the correlations among velocity waveforms and increase voxels topological separation. No links emerged between CNs metrics and kinetic energy and flow eccentricity.

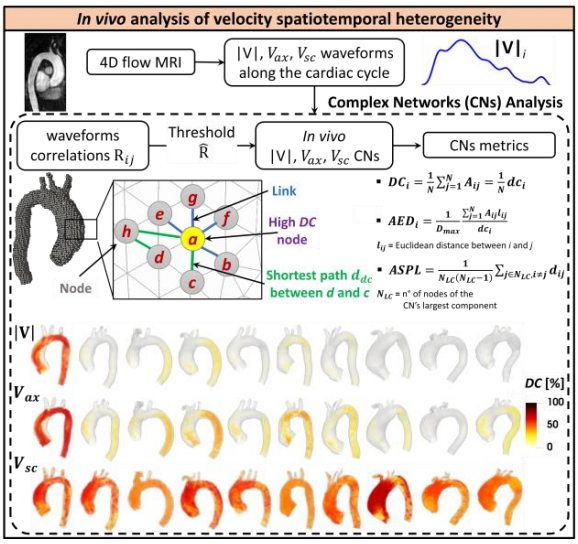

Figure 1: Schematics of the study design and DC maps.

Discussion

The CNs-based analysis of 4D flow MRI aortic data suggests that AAo dilation plays a major role in disrupting spatiotemporal similarity in velocity waveforms, causing a marked reduction of the physiological Euclidean and topological length of correlation persistence in patients with larger maximum AAo diameter. Apart of basic knowledge of the aortic hemodynamics, our findings suggest that *in vivo* measurable CNs distance metrics may contribute to a finer risk stratification of AAo disease.

References

1. Dux-Santoy et al., Eur Hear J-Cardiovasc Imaging,34:1-11,2019.
2. Calò et al., IEEE Trans Biomed Eng, 67:1841-53, 2020.
3. Morbiducci et al., J Biomech, 48.6:899-906, 2015.

AN IMAGE-BASED CFD AND RBF MESH MORPHING APPROACH: AN ALTERNATIVE FOR STANDARD FSI TECHNIQUE

Katia Capellini (1,2), Emanuele Gasparotti (1,2), Emanuele Vignali (1), Benigno Marco Fanni (1,2), Ubaldo Cella (3), Emiliano Costa (4), Marco Evangelos Biancolini (3), Simona Celi (1)

1. BioCardioLab, Fondazione Toscana G. Monasterio, Italy; 2. Dept. of Information Engineering, University of Pisa, Italy; 3. Dept. of Enterprise Engineering, University of Rome Tor Vergata, Italy; 4. RINA Consulting Spa, Italy

Introduction

Computational fluid dynamic (CFD) simulations for thoracic aorta turned out to be an effective strategy to assess the hemodynamics even though the rigid wall assumption implicates a non-negligible limitation. Fluid structure interaction (FSI) simulations, that are quite diffused in literature [1,2], overcome this aspect but introduce some additional assumptions, such as the material properties definition, that are difficult to be extracted in-vivo. Radial Basis Functions (RBF) mesh morphing technique, together with numerical simulations, was already established in cardiovascular field [3], given its capability to cope vessel deformation by modifying geometrical properties of computational models in a meshless way.
This work aims to compare the fluid dynamic effects resulted from the integration of biomedical imaging, CFD and RBF mesh morphing technique (CFD_{RBF}) with those obtaining by performing transient CFD or FSI simulations.

Methods

Starting from ten volumetric CT datasets synchronized with patient ECG, 3D models of thoracic aorta were reconstructed by segmentation for each cardiac phase. RBF mesh morphing technique was applied to each model and the RBF incremental solutions were activated sequentially during the transient simulation in function of time, to automatically synchronize the actual movement of the vessel with the pulsating fluid flow [4]. In addition to the implemented strategy, standard CFD simulations for the aorta models at minimum and maximum deformation stages (0% phase ($CFD_{0\%}$) and 40% ($CFD_{40\%}$) phase of cardiac cycle) were performed. Moreover, a 2-way FSI simulation was also carried out. The results of these simulations were compared in terms of fluid velocity, helicity, flow eccentricity, blood pressure, wall shear stress, and vessels deformations. Regarding the boundary conditions, an aortic flow velocity profile was imposed at inlet and pressure outlet conditions were applied at the four outlets (supra-aortic vessels and descending aorta) by implementing a 3-elements Windkessel model. The CFD solver Ansys® Fluent® was used for all simulations, for the morphing process the RBF Morph software was used.

Results

A significant displacement for the aorta was detected at the ascending portion by analysing 3D models, therefore, the RBF mesh morphing technique was applied only in this region and it turned out to be effective without loss of accuracy in mesh quality. Regarding the hemodynamics, differences were found by comparing the extracted indices of interest for all implemented simulation strategies. The results in terms of WSS and pressure maps in ascending region at deceleration phase of cardiac cycle are reported in Figure 1. In particular, the WSS map for the CFD_{RBF} strategy (Fig 1b) shows a high difference with respect to other cases in terms of spatial distribution and the difference in terms of maximum value is about 40%. Regarding the pressure the 2-way FSI map (Fig 1d) shows a reduction of about 4% compared to CFD and CFD_{RBF} simulations.

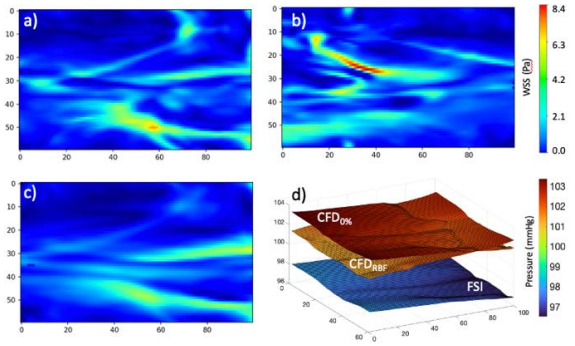

Figure 1: WSS maps along ascending aorta for $CFD_{0\%}$ (a), CFD_{RBF} (b) and FSI simulations (c); blood pressure maps along ascending aorta for $CFD_{0\%}$, CFD_{RBF} and FSI simulations.

Discussion

The obtained results suggest how effects of the aortic deformation on hemodynamics during cardiac phases are not negligible. The combined application of RBF mesh morphing technique and CFD transient simulation allowed to investigate the effects of ascending aortic geometry changes on the fluid dynamics without the material properties definition needed for the FSI. Moreover, CFD_{RBF} is characterized by a much lower computational time than that 2-way FSI simulation. A further analysis may include a comparison with a patient 4D-flow MRI dataset to assess the accuracy of CFD_{RBF} strategy.

References

1. R. Campobasso et al, Card Eng. Tech, 9(4):707-722, 2018.
2. A. Boccadifuoco et al, Card Eng Tech, 9(4):688-706, 2018.
3. K. Capellini et al, J Biomech Eng, 140(11), 2018
4. K. Capellini et al, Med Eng Phys, 2020

A FINITE ELEMENT – AGENT-BASED COUPLED MODEL OF RESTENOSIS: LINKING TISSUE DAMAGE TO CELLULAR DYNAMICS

Anna Corti (1), Monika Colombo (1), Federica Colombo (1), Scott A. Berceli (2, 3), Francesco Migliavacca (1), Jose F. Rodriguez Matas (1), Claudio Chiastra (1,4)

1. LaBS, Dept. of Chemistry, Materials and Chemical Engineering "Giulio Natta", Politecnico di Milano, Italy; 2. Dept. of Surgery, University of Florida, FL, USA; 3. Malcom Randall VAMC, FL, USA; 4. PoliTo^{BIO}Med Lab, Dept. of Mechanical and Aerospace Engineering, Politecnico di Torino, Italy

Introduction

Percutaneous transluminal angioplasty (PTA) is an established procedure for the treatment of peripheral artery disease (PAD). However, the high incidence of restenosis remains a serious complication compromising the long-term success of the intervention. Among the different factors contributing to restenosis, the arterial wall damage provoked by balloon expansion plays a major role. Indeed, the activated inflammatory response may result in a maladaptive healing process, consisting in excessive cellular proliferative and synthetic activities, ultimately leading to lumen re-narrowing [1].

In this context, multiscale computational modeling is deemed to deepen the understanding of the underlying mechanobiological processes of restenosis. Accordingly, we present a novel multiscale framework that links the PTA-induced damage at the tissue scale with the inflammatory driven cellular dynamics, through a finite element method (FEM) – agent-based model (ABM) coupling.

Methods

The workflow of the developed FEM-ABM framework is shown in Fig. 1.

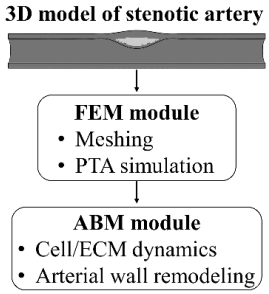

Figure 1: FEM-ABM framework.

The framework was applied to an idealized three-dimensional (3D) femoral artery geometry with an eccentric stenosis. The material properties of the healthy media and adventitia layers were derived from uniaxial tensile tests of human femoral artery samples. For the intima, the material properties of a heavily calcified plaque were used in the stenotic region, including a fully calcification area [2]. A damage model was adopted to describe the softening behavior of the material under stretch [3]. The PTA simulation was performed in Abaqus/Explicit (Dassault Systèmes Simulia Corp., USA), using a properly calibrated model of the Armada balloon (Abbott Vascular, USA).

As preliminary study, a two-dimensional (2D) ABM was implemented in Matlab (MathWorks, USA) for the arterial cross-section with minimum lumen area [4]. The 2D ABM was filled with extracellular matrix (ECM), vascular cell and plaque agents. The FEM-computed damage was assigned to each cell/ECM agent. Probabilistic behavioral rules were adopted to describe cell mitosis and apoptosis, and ECM production and degradation. While constant activities were set in the media and adventitia, cell mitosis and ECM production in the intima depended on the FEM-computed damage.

Results

After the PTA, a lumen area gain of ~50% of the studied cross-section was observed (Fig. 2). The computed mechanical damage in the intima was used to initialize the 2D ABM, which replicated arterial wall remodeling in response to the PTA-induced injury and provided results resembling clinical expectations [5].

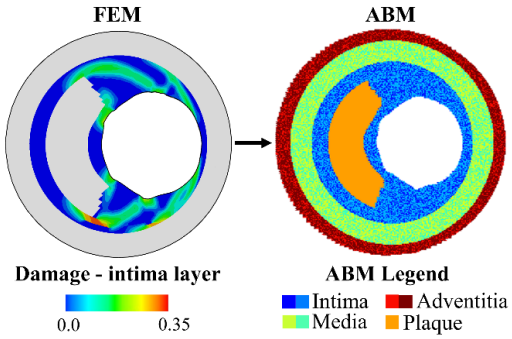

Figure 2: Results of the FEM-ABM framework.

Discussion and conclusions

In this work, a novel multiscale FEM-ABM framework was developed, which, by integrating tissue damage with cellular dynamics, allowed investigating the arterial response to PTA. In the near future, the response to different plaque dimension and composition will be evaluated and several cross-sections will be analyzed.

References

1. DeSart K. et al. *J Vasc Surg* 64: 766-778.e5, 2016.
2. Cunnane E. M. et al. *Acta Biomater.* 11: 295–303, 2015.
3. Rodríguez J.F. et al. *J Mech Phys Solids* 54: 864-886, 2006.
4. Corti A. et al. *Comput. Biol. Med.* 118: 103623, 2020.
5. Schillinger M. et al. *J. Endovasc. Ther.* 8: 477–483, 2001.

Acknowledgements

The work has been supported by Fondazione Cariplo, Italy (Grant number 2017-0792, TIME).

TOWARDS EVIDENCE-BASED PROSTHETIC SOCKET DESIGN: MODELLING AND OPTIMISATION TOOLS TO SUPPORT PROSTHETISTS

Alex Dickinson

Mechanical Engineering Dept., University of Southampton, United Kingdom

Background

Rehabilitation after lower limb amputation presents a major and growing socioeconomic challenge. Research previously focused on advanced prosthetic knees and ankles, but patient outcomes depend ultimately on the human-prosthesis interface, commonly a personalised socket which is produced through plaster casting and 'rectification' by skilled prosthetists. This process is iterative, and rehabilitation is uncomfortable and slow, as the residual limb tissues must heal and functionally adapt to their dramatically-altered loadbearing role. Socket rectifications give a varying field of press-fit and clearance over the residuum's relatively load tolerant and intolerant regions, to balance functional limb-prosthesis coupling and acceptable pressure. Despite developments in CAD/CAM socket design beside 3D scanning and CNC fabrication, this remains a skill and experience-based process. A proposed design support tool is Finite Element Analysis (FEA), which we reviewed in 2017 [1]. This paper describes subsequent work to address the lack of available quantitative design tools, which limit patient satisfaction and cost clinics by preventing highly evidence-based socket design.

Recent Advances

Our review uncovered key challenges in applying loads to these highly nonlinear models (both stance and gait loads, and intrinsic loads from socket donning), and perpetuated errors through unrepresentatively stiff linear elastic soft tissue material models. We developed best-practice recommendations for modellers, and to assist clinicians in appraising FE literature.

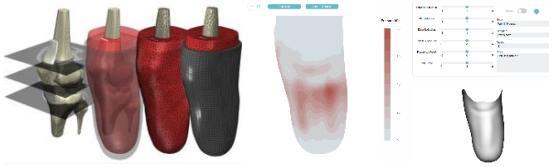

Figure 1: FE model generation from MR imaging, and web-app environment providing real-time predictions of how socket design changes affect interface pressure.

We addressed technical barriers to clinical use of FEA (software cost, pre-processing and computation time, and training) by developing and verifying a Kriging surrogate model for parameterised residual limb population anatomy and socket design [2]. A PCA-Kriging 'Statistical Output Model' was then used to provide 10^6 x faster results visualisation vs. full simulation (2 ms vs. >30 mins), on a laptop computer, allowing prosthetists to inspect the effects of socket design changes in real-time, with <3 kPa interface pressure error prediction (<5%).

Alex is an Associate Professor at the Mechanical Engineering Department, University of Southampton, where he obtained his PhD in 2010. After post-doctoral research with Fraunhofer IPA he held a prestigious RAEng Research Fellowship (2015-20) *'Designing, Testing and Fitting the Next Generation of Prosthetic Limbs'* and now leads a team working on prosthetic biomechanics. He is an IMechE Biomedical Engineering Division board member and Associate Editor (Reviews) for *Medical Engineering & Physics*. He has authored over 20 journal papers.

Our review also highlighted challenges in interpreting model predictions, as there is little knowledge of safe residuum loads and durations. The second aspect of this paper presents physiology and imaging measures to assess tissue composition and damage precursors (ischemia, inflammation and deformation) *in vivo* [3], showing quantitative evidence of soft tissue functional adaptation between intact and amputated limbs.

Future directions

We have begun to explore the parametric socket design paradigm further by applying multi-objective Genetic Algorithm (GA) optimisation [4]. By adjusting the weighting of proximal (patella tendon, fibula head) and distal (residuum tip) loadbearing objective functions, we obtained quantitative candidate socket designs which corresponded with two of the main judgement-based approaches used by prosthetists.

We might continue to enhance our models' biofidelity but our community's greater challenges are human: user experience (UX) research will be essential. We must consider how to balance a model's advice with the prosthetist's expertise, to develop and validate clinically useful tools, which are acceptable to patients. With close clinical collaboration we can adapt our developments to their needs, rather than force them to adapt. Ideally these tools will improve quantitative design consistency, but also free prosthetists from time-consuming gross design and let them focus their effort and skill on the detailed, patient-facing task of enhancing comfort.

References

1. Dickinson, Steer & Worsley 2017, ME&P.
2. Steer, Worsley, Browne & Dickinson 2019, BMMB
3. Bramley, Worsley, Bostan, Bader & Dickinson 2019, POI
4. Steer, Grudniewski, Sobey et al 2019, BMMB.

Acknowledgements

The author is very grateful to colleagues at University of Southampton, in particular Dr Joshua Steer, Jennifer Bramley and Dr Peter Worsley. Funding: RAEng (RF/130), EPSRC (EP/M508147/1, EP/M000303/1) and the EU (E! 9396).

COLLECTIVE CELL MIGRATION AND RESIDUAL STRESS ACCUMULATIONBS

Ivana Pajic-Lijakovic

Faculty of Technology and Metallurgy, University of Belgrade, Serbia

Abstract

Stress generation during collective cell migration represents one of the key factors which influence the configuration of migrating cells, viscoelasticity of multicellular systems and their inter-relation. Local generation of stress (normal and shear) is significant even in 2D (up to ~100-150 Pa). Compressive stress is primarily accumulated (1) within a core region of migrating cell clusters during their movement through the dense environment and (2) during the collisions of migrating cell clusters caused by uncorrelated motility. Shear stress could be significant within perturbed boundary layers around migrating clusters. Cells are more sensitive to the action of shear stress compared with compressive stress. Shear stress of a few Pa significantly influences cell state. Deeper insight into cell strategy to minimize undesirable shear stress is a priority in order to understand various biological processes such as morphogenesis, wound healing and cancer invasion. We pointed out to cause-consequence relations of these complex phenomena based on rheological modeling consideration in order to stimulate further experimental work.

Background

Collective cell migration induces a local generation of stress (normal and shear) significant even in 2D (up to *100-150 Pa*). Cells well tolerate compressive stress up to a few *kPa*. However, shear stress of a few Pa can induce severe damage to vimentin and keratin intermediate filament networks during *1 h*, while shear stress of *~60 Pa* influences gene expression which can cause the inflammation in epithelial cells during *5.5 h*. Cell strategy to minimize undesirable shear stress generation was discussed based on rheological consideration.

Recent Advances

Various aspects of viscoelasticity of multicellular systems caused by collective cell migration have been considered such as: (1) residual stress accumulation and its influence to configuration of migrating cells [1-3], (2) migrating-to-resting cell state transition and jamming state transition [3,4], (3) formulation of constitutive model at various time scales [5,6]. New book (the edited collection of chapters) titled: "Viscoelasticity and Collective Cell Migration: An interdisciplinary perspective across levels of organization" will be published in June 2020 supported by Elsevier.

Ivana Pajic-Lijakovic is currently Scientific Advisor at the Department of Biochemical Engineering, University of Belgrade. She obtained her PhD in Biorheology at the University of Belgrade in 2002. She is a Subject Editor for Facets (Canadian Science Publishin) and a Guest Editor for Seminars in Cell and Developmental Biology, Special Issue Viscoelasticity of multicellular systems. Her present research mainly focuses on multiscale modeling of viscoelasticity of multicellular systems. She is an author of more than 80 publications in peer-reviewed journals and several chapter books.

Future directions

Additional experiments are necessary to determine stress distribution during 3D collective cell migration and its change and correlate: (1) the stiffness inhomogeneity per single migrating cluster with the type and distribution of adheren junctions (AJs) and tight junctions (TJs), and (2) slip effects within perturbed boundary layers around the migrating cluster with the type and distribution of AJs and TJs within them.

Figures

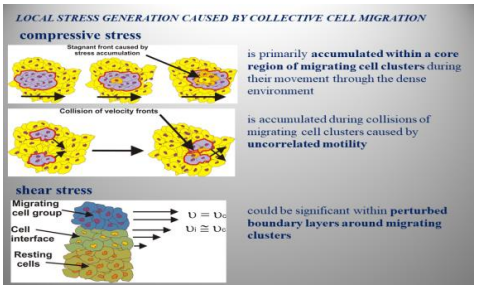

Figure 1: Residual stress accumulation caused by collective cell migration

References

1. Pajic-Lijakovic I et al. Sem. Cell Dev. Biol. 93:87-96, 2019.
2. Pajic-Lijakovic I et al. Appl. Bionics Biomech. doi.org/10.1155/2019/4892709, 2019.
3. Pajic-Lijakovic I et al. J. Biol. Phys. 43:197-209, 2019.
4. Pajic-Lijakovic I et al. J. Biol. Eng. 13(73):1-12, 2017.
5. Pajic-Lijakovic I et al. J. Biomech. 60:1-8, 2017.
6. Pajic-Lijakovic I Sem. Cell Dev. Biol. 93:1, 2019.

Acknowledgements

The authors gratefully acknowledge funding support of the Ministry of Education, Science and Technological Development of the Republic Serbia grant III 46001.

MODELLING STROKE AND STROKE TREATMENT, PAVING THE WAY FOR IN-SILICO STROKE TRIALS

Charles Majoie (1) and Alfons Hoekstra (2) on behalf of the INSIST collaboration

(1) Amsterdam University Medical Centers, location AMC, Amsterdam, the Netherlands, c.b.majoie@amsterdamumc.nl

(2) Computational Science Laboratory, Institute for Informatics, Faculty of Science, University of Amsterdam, the Netherlands, a.g.hoekstra@uva.nl

A revolution in Stroke treatment

In 2015 the MRCLEAN trial demonstrated for the first time that Endovascular thrombectomy (EVT) is very effective in treating proximal large vessel occlusion in acute ischemic stroke. Currently EVT is standard care for these patients. However, despite very successful recanalization, only 33-50% recovers after EVT. This requires deeper understanding of the underlying processes, and further research into improving treatment options. To proceed, both animal experimentation and new clinical trials are underway. However, an alternative would be to develop an In Silico Trial for stroke treatments.

In Silico Trials

Quoting the Avicenna roadmap, an In Silico Trial (IST) is "the use of individualised computer simulation in the development of regulatory evaluation of a medicinal product or medical device/medical intervention". ISTs have many potential usage scenarios, among others in preclinical settings to reduce, refine, and (partly) replace animal experimentation or to help in the design of clinical trials in different stages of the regulatory process, or to even partly replace clinical trials.

In Silico Stroke Trials

The INSIST Project (www.insist-h2020.eu) is a European collaboration aiming at ISTs for treatment options for acute ischemic strokes. Leveraging on available clinical data collected in the MRCLEAN trial and other stroke treatment trials, the INSIST project is creating a collection of models that together capture both the pathophysiological processes in relation to stroke and the acute ischemic brain, as well as treatment with EVT or intra venous thrombolysis (IVT). Moreover, a virtual population model, which is a statistical description of the distribution of relevant medical and clinical parameters (such as e.g. age, sex, or clot location and volume, clot composition, vessel geometries) and their correlations, as observed in patients that were included in the trials, is being developed. Finally, a statistical model is under development that correlates the final predicted infarcted brain tissue to a clinical endpoint (such as the 24 h NIHSS score or the 3 months follow up MRS score).

Charles Majoie is full professor in Neuroradiology at the Amsterdam University Medical Centers, location AMC, Amsterdam. His main interest is diagnosis and endovascular treatment of neurovascular diseases, with focus on acute stroke. He was Co-PI of the MRCLEAN trial, showing for the first time that endovascular treatment really improves outcome of patients with acute ischemic stroke.

Alfons Hoekstra is full professor in Computational Science and Engineering at the University of Amsterdam, where he leads the Computational Science laboratory. His main interest is in modelling human health and disease, multiscale modelling and simulation, reproducible and actionable simulation based science, and high performance computing.

Recent Advances

A first validated version of the virtual population model has been delivered, including data on clot composition based on histology of retrieved clots after EVT, clot location, and vasculature. Multiscale models for brain tissue perfusion are developed. Detailed models of the thrombectomy procedure, including mechanical properties of the clot and clot vessel-wall interaction, have been developed and are being validated based on a range of datasets, from benchtop experiments to clinical data. Also, models are underway for the thrombolysis and first results have been reported.

Future directions

Next steps will be to integrate all models into an IST for acute stroke. The paradigm that we adopt will be that a of discrete event model, and the event handling consists of, most likely, surrogate models that mimic the most relevant processes. The IST will be validated against retrospective trial data. Finally, three prospective ISTs will be performed, to provide a proof of concept for the in silico stroke trials.

Acknowledgements

We acknowledge collaboration with all members of the INSIST consortium. (www.insist-h2020.eu). We acknowledge funding from the European Union's Horizon 2020 research and innovation programme under grant agreement No 777072 (INSIST project).

PERSPECTIVES ON MUSCLE ELASTOGRAPHY: FORCES, FIBERS, FRACTALS AND FRACTIONAL CALCULUS

Thomas J. Royston, PhD

University of Illinois at Chicago, USA

Summary

Dynamic elastography imaging, whether based on magnetic resonance, ultrasound or optical modalities, attempts to reconstruct quantitative maps of the viscoelastic properties of biological tissue, properties that are altered by disease and injury. Reconstruction often assumes isotropy and homogeneity and neglects boundary conditions. Skeletal muscle violates all these assumptions, posing challenges and opportunities for developing better imaging biomarkers. These challenges and novel methods to address them are reviewed.

Background

In striated muscle, anisotropy and inhomogeneity are so prevalent that ignoring them leads to significant estimation error in the elastography reconstruction problem. Muscle also poses additional challenges due to its fractal-like fiber structure and variation in properties under passive and activated conditions. Muscle fibers present a multiscale fractal-like heterogeneous geometry. Depending on the length scales of interest and wavelengths generated in the elastography measurement, it may be possible to "homogenize" this aspect of muscle heterogeneity [1-2]. Also influenced by this fractal structure, muscle elastography measurements have identified dispersive rheological behaviour best described by fractional calculus models of viscoelasticity [3] that are linked to fractal structure.

Muscle activation and varying tensile loads can also influence measurement interpretation. For bulk shear waves in an isotropic viscoelastic material without boundary conditions the measured wavelength correlates with the square root of the tissue's shear elastic modulus and viscosity, important rheological parameters. But, under significant tensile loading, which may increase with muscle activation, the measured transverse wavelength can correlate more with the tensile load, than the muscle's inherent rheological properties. The governing equation transforms to that of a string, with transverse waves only depending on the tensile (boundary) load and material density.

Anisotropy in muscle also poses challenges in elastography. Due to aligned fibers, muscle possesses transversely isotropic properties; waves propagating along the fiber experience a "stiffer" material than waves propagating across fibers, leading to an elliptic or super-elliptic wave field emanating from a wave source.

Recent Advances

Recent animal and human subject experimental studies have quantified the significant effect of tensile loading [4] and the activation state of muscle [5] on its rheological properties, as assessed by the frequency-dependent wave phase speed and attenuation. Novel elastography reconstruction strategies that account for anisotropy have also recently been formulated. One such method, Transformation Elastography, involves distorting space in order to make the anisotropic problem become isotropic [6]. This has been demonstrated in 2D studies of transversely isotropic material with slow and fast shear waves [7-8].

Thomas J. Royston, PhD, Professor and Head of Bioengineering at the University of Illinois at Chicago (UIC), earned his PhD in Mechanical Engineering from the Ohio State University in 1995. His NIH and NSF-supported research in mechanical wave motion and imaging in soft tissue-like materials, and acoustics applied to medical diagnostics and therapy has been recognized with the NSF Career Award, the NIH NIBIB Nagy Award and the Acoustical Society of America Lindsay Award. He is a Fellow of the American Society of Mechanical Engineers and American Institute for Medical and Biological Engineering, and has authored >85 peer-reviewed journal articles.

Future directions

While the Transformation Elastography concept shows promise, future studies are needed to assess the new strategy in the case of more complex geometries and mechanical wave patterns, including extension to heterogeneous and three-dimensional problems under preloaded conditions, with experimental noise levels typically found in in vivo elastography measurements.

References

1. Guidetti M et al., J Mech Beh Biom Mat, **89**:199-208, 2018.
2. Palnitkar H et al. J Mech Beh Biom Mat, **98**:108-120, 2019.
3. Klatt et al., Phys Med Biol **55**: 6445–6459, 2010.
4. Bernabei et al., J Appl Phys. In Press, 2019.
5. Wang et al., J Biomech, **94**:115-122, 2019.
6. Guidetti M et al., J Acous Soc Am, **144**: 2312–23, 2018.
7. Guidetti M et al., J Acous Soc Am, **145**: EL59–65, 2019.
8. Guidetti M et al., J Acous Soc Am, In Press, 2019.

Acknowledgements

The following contributed to the presented research: M Bernabai, D Caratelli, J Crutison, M Guidetti, M Hammersly, D Klatt, SSM Lee, P Lewis, G Lorgna, S Majumdar, H Palnitkar, EJ Perreault, RO Reiter, TG Sandercock, RN Shah, P Vena, AB Wang. Grant support: NSF #1852691 (PI: Royston); NIH #AR071162 (PI: Perreault).

WHY WILL VISCOSITY AND NONLINEARITY BIOMARKERS RECAST ELASTOGRAPHIC DIAGNOSIS?

Guillermo Rus

Ultrasonics Lab, Dept. Structural Mechanics, University of Granada + Biosanitary Research Institute, Spain.

Background

Ultrasonic characterization and understanding of soft tissue has been developed as a clinical diagnostic tool over the last two decades [1] and evolved through different technologies: quasi-static, dynamic elastography, based acoustic radiation force: ARFI, vibroacoustography or pSWE, or on direct excitation: sonoelastography and our emerging torsional wave principle [2]. New elastography sensor technologies to characterize soft tissue biomechanics, are bound to endow a new class of biomarkers that quantify the mechanical functionality and abnormalities in the structural architecture of soft tissues are intimately linked to a broad range of pathologies including tumors, atherosclerosis, brain ageing, gestational disorders, liver fibrosis or osteoarticular syndromes, to name a few. These higher order mechanical parameters may become key discriminating biomarkers since: (1) the physics of wave propagation is explaining how dispersion is a compound expression of the rheological, poroelastic, and microstructural scattering phenomena governed by the complex fibrous multiscale microarchitecture of the stroma, which undergoes characteristic changes during pathologies [3]; and (2) the extreme hyperelasticity that soft tissue exhibits clearly manifests as quantifiable harmonic generation, hypothesized to strongly depend on the unfolding of its collagen fibres, which again controls the tissue's mechanical functionality.

Recent Advances

Existing ultrasonic techniques are restricted to map first order tissue stiffness. In contrast, recent advances covering:

a) new mechanical wave-based sensing technologies ranging magnetic resonance elastography, ultrasonic shear wave elastography or torsional wave elastography (that propagate in quasifluids radially and in depth in a curled geometry),

b) wave propagation models and multiscale interaction with michroarchitectural changes, and

c) patient testing, are allowing to quantify the mechanical functionality through relevant parameters beyond linear: dispersive and nonlinear.

Future directions

d) To understand how structural architecture of soft tissue is intimately linked and controls a broad range of pathologies, which underpins the foundation of a new diagnostic technology.

Guillermo Rus [Professor at UGR] is the Head and founder of the NDE Lab and Ultrasonics Group. He specialized in ultrasonics as a Fulbright Postdoc at MIT, and later as visiting scientist at UCL (UK), NASA (US), Paris 6 (FR), Linköping IT, Chalmers (SE) and TUHH (DE). He actively collaborates with Caltech, Boston University, Rochester IT (US), Kings College, UCL (UK) and Karolinska (SE). He has authored 100+ JCR publications (90% Q1, 1000+ cites, h-index 20), 20+ invited seminars, and reviews/edits 60+ journals. His career has been awarded by the Prognosis Health Management Society (2014), UGR (2001), Juan Carlos Simó (2007), and Wessex Institute of Technology (2005).

e) To develop new sensor technologies capable of effectively sensing tissue elasticity, and yield simple and robust diagnostic tests and instruments.

f) To ground a new generation of biomarkers of physical nature based on the mechanical micro-architecture and properties of the tissue.

The unexplored nature and applicability span of viscous and nonlinear mechanical biomarkers and torsional waves endows a foundational diagnostic technology.

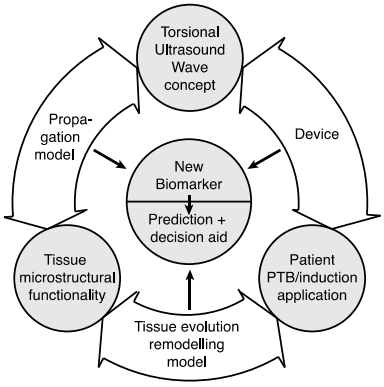

Figure 1: Dimensions of the problems to be addressed to generate a solid scientific backgound.

References

1. Barr R. G., et al. 2012. *Ultrasound Quarterly* 28 13-20.
2. Melchor J and Rus G. Ultrasonics, 54(2014): 1950-1962.
3. Peralta L., et al. 2015. *J. of Biomechanics* 48 1557-1565.

Acknowledgements

This research was also performed by Juan Melchor, Antonio Callejas, Antonio Gómez, Inas Faris, Jorge Torres, Francisca Molina, Olga Ocón, Beatriz Blanco, and supported by the Spanish Ministry of Education DPI2017-85359-R, DPI2014-51870-R, EQC2018-004508 and UNGR15-CE-3664 projects.

MODELLING HUMAN LOCOMOTION FOR PERSONALIZED EXERCISE PRESCRIPTION FOR OSTEOPOROSIS

Saulo Martelli

College of Science and Engineering, Flinders University, Adelaide SA, Australia

Background

Reduced bone mass and compromised bone strength in osteoporosis is a major socio-economic burden. Physical exercise has long been proposed as a means for reducing the risk of fragility fracture by promoting bone accrual and improving motor function. However, the modest and variable bone response to exercise in adult people complicates prescribing the type and amount of exercise for optimal bone health [1]. Modern digital technology can complement exercise prescription for osteoporosis by providing information about skeletal mechanics during locomotion.

Recent Advances

The superior neck is a common location for hip fracture and a relevant exercise target for osteoporosis. Exercise can stimulate anabolic response in the neck by either offsetting habitual strain levels or by bending of the neck for inducing localized tension in the superior cortex. Current studies showed that fast walking and stair ambulation, but not necessarily running, optimally load the femoral neck and therefore theoretically would mitigate the natural age-related bone decline, being easily integrated into routine daily activity [2]. High intensity jumps and hopping have been shown to promote anabolic response by inducing high strain in the superior-anterior neck. Multidirectional exercises may cause beneficial non-habitual strain patterns across the entire femoral neck[3]. Resistance knee flexion and hip extension exercises induce high strain in the superior neck, provided adequate muscle strength for inducing above normal strain levels to the hip[4]. The hamstring muscles and the gluteus maximus have the highest potential for generating tension in the superior neck, hence providing a target for the design of exercise regimen for osteoporosis.

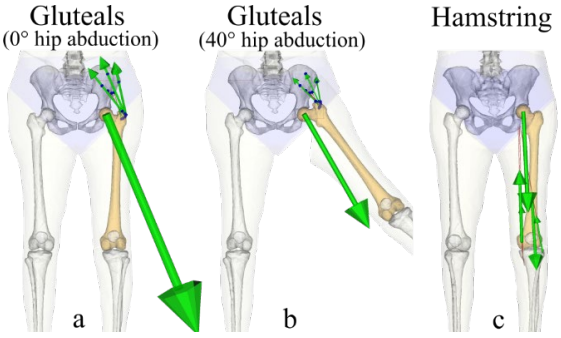

Figure 1: Changes in orientation of the hip force potentially generated by the gluteals at 0° and 40° hip abduction (a,b) and the hamstring muscles (c).

Saulo is currently Senior lecturer at the College of Science and Engineering, Flinders University. He obtained his PhD in Biomehanics at the University of Bologna in 2008. He was a post-doctoral fellow at the Rizzoli Orthopaedic Institute in 2008-2011 and at the University of Melbourne in 2012-2013. He is a member of the Australian and New Zealand Orthopaedic Research Society. His present research mainly focuses on hip and knee biomechanics. He is an author of 35 publications in peer-reviewed journals, book chapters and more than 100 Contributions to Conferences.

Future directions

Personalized exercise prescription requires discerning individual features of the hip response to exercise caused by complex interaction between anatomy, muscle function, bone distribution and metabolism. Significant progress has been made toward a fast, reliable and personalized physics-based models of human physiology. Current technologies can incorporate anatomical, mechanical, physiological, and neurological features in each individual. The body anatomy in the model can be informed by medical imaging or extracted from population databases. Real-time or near real-time numerical methods have been developed to predict muscle and joint force, bone strains and strength[5]. Recent evolutions of the mechanostat model, can determine the amount of bone deposited, or resorbed, as function of exercise, individual metabolism, diet and pharmacological treatment [6]. Incorporation of models of hip metabolism and mechanics during exercise is a current focus of the bone research community. High-performance computing, efficient algorithms and open-source databases have reduced the burden of modelling. Retrospective and longitudinal exercise interventions can allow identification of the appropriate technology for personalized exercise prescription for osteoporosis.

References

1. Beck et al., J Sci. and Med. in Sport, 20:438–445, 2017.
2. Kersh et al., J Bone & Min. Res., 33:1999–2006, 2018.
3. Martelli, Comp. Math. Meth. Med., 2873789, 2017
4. Martelli et al., J Biomech., 47:1784–91, 2014.
5. Pizzolato et al., Frontiers Comp. Neurosc., 11:96, 2017
6. Lerebours et al., Biom. Mod. Mechanob., 15:43–67, 2016.

Acknowledgements

Australian Research Council (DP180103146, FT180100338). Co-workers: B. Beck, M. Taylor, D. Lloyd, D. Saxby, P. Pivonka.

CHALLENGES AND SOLUTIONS FOR ADDITIVE MANUFACTURING OF BIODEGRADABLE MAGNESIUM IMPLANTS

Yinchuan Wang, Guangyin Yuan*
**E-mail: gyyuan@sjtu.edu.cn (G.Yuan)*
National Engineering Research Center of Light Alloys Net Forming and State Key Laboratory of Metal Matrix Composite, Shanghai Jiao Tong University, Shanghai 200240, China

Background

Additive manufacturing (AM) techniques, due to their capability of fabricating geometrically complex structures, have provided unprecedented opportunities to produce biodegradable Mg implants. However, due to the inherent properties of low vapor temperature, high vapor pressure and high tendency to oxidize of Mg alloys, there are many challenges hindering the fabrication of AM-processed Mg implants, such as the difficulty of Mg powder preparation, powder splash and crack formation during AM process. Recently AM-processed WE43 scaffold with diamond structure was fabricated for the first time and meet the functional requirements for bone substitutes [1]. However, bare WE43 scaffold was not suitable for cell adhesion due to its relative fast degradation rate in physiological environment, and the architecture of porous Mg scaffold also needs to be improved. In the present work, the solutions regarding the challenges for additive manufacturing of biodegradable Mg alloys were analysed. AM-processed Mg scaffolds with preferable structures were introduced. Moreover, further surface treatment of AM-processed scaffolds was performed.

Recent Advances

The novel-developed Mg-Nd-Zn-Zr alloy (JDBM) powder with smooth surface and good roundness was firstly synthesized successfully using gas atomization method. And the AM parameters for Mg-based alloys were optimized by lowering the specific energy input for prevent of potential powder splash and cracks appearance. Then based on the optimized parameters, porous JDBM scaffolds with three different architectures (biomimetic, diamond and gyroid-shape) were fabricated by selective laser melting (SLM). The CAD design models and the micro-CT reconstructed structures of the scaffolds after chemical polishing are presented in Fig.1. The as-polished scaffolds have fully interconnected structures consistent with the as-designed models. The gyroid-shape scaffold has best combination of mechanical performance and degradation behaviour, with yield strength of 16.25 ± 0.86MPa and Young's modulus of 0.76 ± 0.02GPa, however, still displaying a relatively low corrosion resistance. Therefore, the gyroid-shape scaffold was selected for DCPD coating treatment so that the degradation rate was suppressed greatly and the cytocompatibility was increased significantly, indicating a promising prospect of clinical applications as bone tissue engineering scaffolds.

Dr. Guangyin Yuan is a tenured professor in the School of Materials Science and Engineering at Shanghai Jiao Tong University, China. He received his Ph.D. in Materials Science and Engineering from Southeast University, China in 1999. He then worked as a JSPS researcher from 2002 to 2004 in Tohoku University, Japan. He is the standing committee member of the Chinese Biomaterials Society Medical Metal Branch and vice President of the Chinese Medical Magnesium Alloy Industry Technology Innovation Strategic Alliance. His research focused on the development of novel biodegradable magnesium-based alloys for medical applications. He has published over 100 research papers which have been cited over 3500 times.

Future directions

In vivo animal study will be conducted to characterize the degradation behavior of the DCPD-coated gyroid-shape scaffold, along with its influence on the new bone formation. Meanwhile, taking the advantage of the AM techniques for the fabrication of geometrically complex structures, personalized Mg implants will be investigated.

Figures

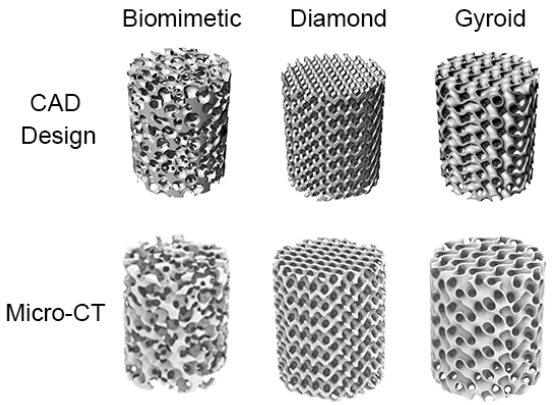

Figure 1: CAD design models and micro-CT reconstructed structures of three different scaffolds: biomimetic, diamond, and gyroid-shape.

References

1. Y. Li, J. Zhou et al., Acta Biomater, 77:380-393, 2018.

Acknowledgements

This work was supported by the National Natural Science Foundation of China (No. 51571143).

MECHANO-MEDICINE: DECIPHERING MECHANO-SIGNALLING TO ELICIT CONTROL OVER PERIVASCULAR STEM CELL FATES

Justin Cooper-White

School of Chemical Engineering and the Australian Institute for Bioengineering and Nanotechnology, The University of Queensland, Brisbane, Australia

Background

Crucial to their survival and function as reparative cells within all human tissues, perivascular-derived stem cells (PvSCs (pericytes, mesenchymal stromal cells)) actively sense and respond to variations in extracellular matrix (ECM) composition and changes in the mechanics of their local microenvironment. However, the underlying mechanisms defining how such fates are temporally modulated remains to be better elucidated.

Recent Advances

Through the construction of hydrogel- and self-assembling block copolymer-based substrates tailored for defined cellular interactions, we have probed the interplay of substrate stiffness and ligand type [1], the impacts of substrate viscoelasticity (effecting creep and stress relaxation) [2,3], and ligand redundancy, lateral spacing and type [4-7] on PvSC fate choice. These studies have shown that ligand-integrin interactions (in type and number) represent the permissive, necessary cues for cells sensing and responding to variations in the mechanics of their local environment. Most recently, we have turned to studying the dynamics of PvSC adhesion, mechano-sensing and -transduction at high spatial and temporal resolution on nanopatterned substrates, using a range of real-time fluorescent location and FRET-based biosensors over timeframes of 2 hours to 14 days [8]. These studies have revealed that changes in lateral spacing of adhesion motifs from 30 to 60 nm affect the temporal recruitment and activation of critical focal adhesion proteins and mechanotransduction signalling pathway modulators (including RhoGTPases and YAP/TAZ), which ultimately leads to the observed bias in cell fate commitment through the regulation of well-known morphogenic determinants. Smaller nanospacings bias upregulation of the Rac 1/ myosin IIA / YAP-TAZ / RUNX 2 pathway, confirming that observed switches in osteo- versus adipo-genic fate commitment are the result of (early) differences in tension force at focal adhesions of a little as 5pN! We know, however, that in response to differences in matrix mechanics or ligand presentation, hMSCs produce a range of other regulatory molecules, besides proteins. Could these pathway modulators offer a solution to overcoming the impacts of 'perturbed' ECM microenvironments on hMSC behaviour and function to effect functional tissue repair? To address this question, we have also recently identified differentially expressed mechanosensitive microRNAs (mechano-miRs) produced by PvSCs (or their progeny) in response to varying matrix stiffness and RhoA activity [9], or post activation in an injury site. Thereafter, using hydrogels and self-assembling nanoparticles, we have shown that modulating these mechano-miRs can overcome *in vitro* local 'soft' mechanical cues to drive commitment to stiffer tissues (e.g. bone)[9], or suppress the creation of 'stiff' fibrotic tissue within an injured 'soft' tissue in a small animal model of fibrosis.

Justin is currently is Professor of Bioengineering (School of Chemical Engineering), and Senior Group Leader (with the AIBN) at the University of Queensland (UQ), Co-Director of the UQ Centre in Stem Cell Ageing and Regenerative Engineering, CSO of Scaled Biolabs Inc., and Editor-in-Chief of APL Bioengineering. He obtained his PhD in Biopolymer Physics from UQ in 2000. After a short post-doctoral fellow at the University of Melbourne (UMelb, 2000-2002), he gained tenure at UMelb in 2003. After being recruited back to UQ in 2004, he was promoted to Full Professor in 2007. His research focuses on Mechanobiology, Stem Cell and Niche Ageing, and Regenerative Engineering. He has over 200 journal papers and 6 Worldwide patents awarded in USA, Europe, Asia and Australia.

Future directions

The outcomes of these recent studies provide new understanding of the complex mechanisms regulating mechanosensing, mechanotransduction and differentiation, but also provide us with novel strategies with which to manipulate *mechano-driven* stem and progenitor cell fate and significantly impact tissue engineering and regenerative medicine applications that focus on their exogenous use or endogenous manipulation.

References

1. Rowlands et al., Am J Physiol Cell Physiol, 295(4):C1037-44, 2008.
2. Cameron et al., Biomaterials, 32(26):5979-93, 2011.
3. Cameron et al., Biomaterials, 35(6):1857-68, 2014.
4. Frith et al., J Cell Sci, 125:317-27, 2012.
5. Frith et al., Stem Cells Dev, 21(13):2442-56, 2012.
6. Li et al., Biomater Sci, 2(11):1693-705, 2014.
7. Li et al., Biomacromolecules, 15(1):43-52, 2014.
8. Han et al., ACS Nano, 13(10):11129-43, 2019.
9. Frith et al., Nature Comm., 9:257, 2018.

Acknowledgements

I would like to acknowledge all of the co-authors of the work presented that are listed in the references, and for our unpublished work, Dr Li-Yen Wong, Dr Joan Li, and Ms Bo van Seters.

TOWARDS PERSONALIZED BIOMECHANICAL SIMULATIONS TO OPTIMIZE REFRACTIVE INTERVENTIONS

Philippe Büchler

ARTORG Center for Biomedical Engineering Research, University of Bern, Switzerland

Background

Degradation or loss of vision greatly impacts quality of life. Almost 250 million people worldwide are visually impaired, which has an estimated economic impact of $268.8B per year.

The cornea is responsible for about 80% of the refractive power of the eye. As a consequence, minimal alterations of its shape – by only a few micrometers – have a large impact on the vision of the patients. Surgical interventions and pathologies alter corneal biomechanics, which in turn modifies corneal shape and compromises visual acuity.

Clinically, the surgical intervention is planned using nomogram tables that are based on statistical data. Unfortunately, the change of corneal power is frequently underestimated due to the lack of personalization of the current clinical approach. Therefore, we believe that biomechanical models and patient-specific simulations can be powerful tools to help clinicians optimizing the visual outcome for each individual patient.

Recent Advances

Corneal tissue is anisotropic and exhibits a non-linear mechanical behaviour that can be accurately modelled by an hyperelastic formulation accounting for the tissue microstructure. Based on this formulation, we identified the mechanical parameters of the corneas from donors of different age groups [1].

We also developed a software platform to automate the generation of patient-specific models from clinical data. This tool allows clinicians to predict the outcomes of any sets of treatment parameters that he wants to evaluate for his patient (Optimeyes, OptimoMedical AG). The personalized predictions have been validated on patients undergoing routine cataract surgery and relaxing keratotomy [2,3].

This simulation framework has been combined with numerical optimization routines to directly propose a set of parameters that will provide the best optical outcome for each patient [3]. Evaluation on more than 600 patients' datasets showed that the optimization approach improves the final astigmatism for the patient but, most importantly, reduces the number of overcorrections / outliers compared to the existing clinical approach based on nomograms (Fig. 1).

The large number of patient-specific simulations conducted on our database of patients, allowed us to build surrogate models of the intervention using machine learning techniques, providing reliable estimates of the surgical outcomes instantaneously, without requiring additional finite element calculations.

Philippe Büchler is currently Associate Professor at the ARTORG Center for Biomedical Engineering Research of the University of Bern. He obtained his PhD in Physics at the Ecole Polytechnique Fédérale de Lausanne in 2002. His present research mainly focuses on the development of patient-specific biomechanical models, combined with the in-vivo characterization of the mechanical behavior of soft tissues. His close collaboration with clinical and industrial partners results in research activities oriented towards practical applications. He is an author of ~60 publications in peer- reviewed journals, several chapter books and regularly contributions to international and national conferences.

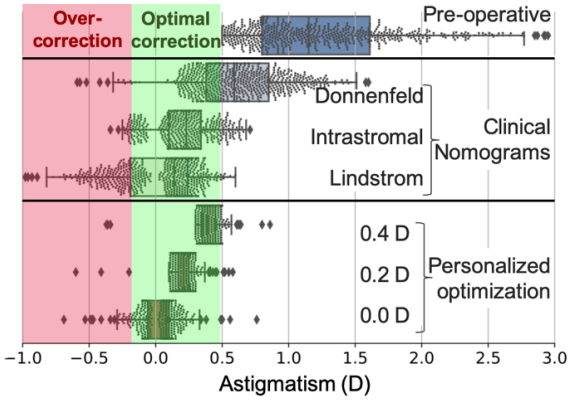

Figure 1: Pre- and postoperative astigmatism using different approaches to plan arcuate keratotomy surgery on 600 patients. Personalized optimizations enable us to control post-surgical astigmatism

Future directions

The current personalization of the patient-specific simulations is limited to anatomical features. This limitation is not critical when modelling healthy tissues but prevents inclusion of pathologies. Our future research in this field focuses on developing methods able to identify corneal biomechanics in-vivo, such as non-contact tonometry or Brillouin scattering.

References

1. Studer et al., J Biomech, 43:836-42, 2010.
2. Studer et al., J Biomech, 46: 751-758, 2013
3. Truffer et al., J Cataract Refract Surg, 45:1084-1091, 2019

Acknowledgements

The author thanks all the present and past group members and collaborators who contributed to this work, in particular X. Larrea, H. Studer, O. Truffer, M.A. Ariza-Gracia

MULTI-SCALE, MULTIDISCIPLINARY RESEARCH INTO BONE MECHANOBIOLOGY DURING OSTEOPOROSIS

Laoise McNamara

National University of Ireland, Galway, Ireland

Background

Biophysical stimuli are as crucial as genes and biochemical signalling for bone development and function [1, 2]. Bone cells continually monitor their mechanical environment and regulate bone formation and resorption to maintain the mechanical function of bone throughout life. During osteoporosis, the levels of estrogen circulating in the blood are deficient, which is accompanied by bone loss, ultimately leading to bone fracture. Despite evidence that bone composition [3-5] and osteoblast biology [6-8] are altered in osteoporosis, conventional drugs target bone resorbing osteoclasts, but only reduce osteoporosis fractures by 50% [9].

Recent Advances

Our studies have revealed that the effects of estrogen deficiency are not restricted to bone loss, but that important changes in bone tissue mineral distribution also occur. Specifically, bone tissue mineral is more heterogeneous during estrogen deficiency in rat and ovine models, which is due to changes in mineral content at specific anatomical regions [10, 11]. These changes are undetectable by conventional diagnostic techniques (DEXA) but may play an important role in bone fracture. These changes occur in early stage estrogen deficiency but are restored in the longer term. Moreover, using novel experimental and computational models, we reported that the mechanical environment of bone cells is altered during early-stage osteoporosis, but is restored in the later stages of estrogen deficiency [12]. Thus bone tissue mineral heterogeneity may arise due to a mechanobiological response to restore homeostasis in the mechanical environment after initial bone loss. Our recent studies are unravelling the time sequence of changes in bone microarchitecture, mechanical environment and mineral distribution. We have discovered that osteoblast and osteocyte mechanotransduction are fundamentally altered during estrogen deficiency (Fig. 1), which is associated with altered production of paracrine factors that govern osteoclast resorption [13-17].

Future directions

We are developing 3D ex-vivo models of human osteoporotic bone, which incorporate critical mechanical cues and multicellular signalling. Such models will provide an advanced understanding of underlying mechanisms leading to bone loss and fracture susceptibility after estrogen withdrawal. We are investigating the potential of Sclerostin inhibition for modulating these mechanobiological responses and associated bone mineralisation and paracrine signalling.

Laoise McNamara is a Professor in Biomedical Engineering at the National University of Ireland, Galway. She holds a PhD from Trinity College Dublin, completed Postdoctoral training at Mount Sinai School of Medicine (USA) and has been a Lecturer at NUI Galway and the University of Southampton (UK). She has dedicated her research career to enhancing mechanistic understanding of bone mechanobiology and osteoporosis. She is an author of more than 80 publications, several chapter books and more than 150 Contributions to International and National Conferences.

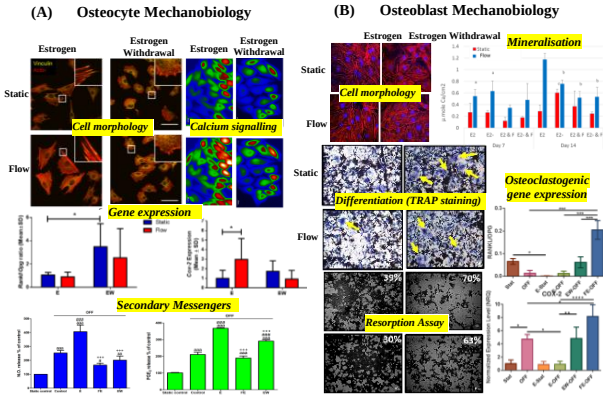

Figure 1: (a) Osteoblast and (b) osteocyte mechanosensation and mechanotransduction are altered in estrogen deficiency, which are associated with pro-osteoclasteogenic paracrine-signalling

References

1. Carter et al., Clin Orthop Relat Res, 1987(219): 237-50
2. Ingber, Ann Med, 2003. 35(8): p. 564-77
3. Bailey et al., Connect Tissue Res, 1993. 29(2): 119-32
4. Gadeleta et al., Bone, 2000. 27(4): p. 541-50
5. McCreadie et al., Bone, 2006. 39(6): p. 1190-5.
6. Neidlinger-Wilk et al., J Biomech, 1995. 28(12): 1411-8.
7. Sterck et al., Am J Physiol, 1998. 274(6 Pt 1): E1113-20.
8. Bakker et al., Osteoporos Int, 2005. 16(8): p. 983-9
9. Randell et al., J Bone Miner Res, 2002. 17(3): 528-33.
10. Brennan et al., Eur Cell Mater, 2011. 21: p. 396-406.
11. Brennan et al., JMBBM, 2014. 29: 161-70.
12. Verbruggen et al., Biophys J, 2015. 108(7): 1587-98.
13. Deepak et al. FASEB J, 2017.
14. Allison, McNamara, Am J Physiol, 2019. 317(5): C969
15. Geoghegan et al, Sci Rep, 2019. 9(1): 4654

Acknowledgements

European Research Council Grant 258992 (BONEMECHBIO), Science Foundation Ireland (SFI) Investigators Award co-funded under the European Regional Development fund under grant number 14/IA/2884, Irish Research Council (IRC) Laureate.

MULTISCALE TRABECULAR AND COMPACT BONE MECHANICS

Philippe K. Zysset

ARTORG Center, University of Bern, Switzerland

Background

Bone loss and metabolic diseases lead to fractures, loosening of implants and compromise our health and well-being. Understanding the hierarchical organisation of bone and the respective role of the various organic/inorganic constituents on its biomechanical properties are therefore of key interest. A few years ago, Stephen Cowin and John Currey left us, but left us with a rich and inspiring heritage of knowledge on bone mechanics. This perspective talk aims at reporting two advances in the mechanics of trabecular and compact bone respectively, that developed along their visions.

Recent Advances

A first advance based on Steve Cowin's concept of fabric in trabecular bone mechanics consists of the establishment of simplified, strong fabric-elasticity and fabric-strength relationships using computational homogenization.

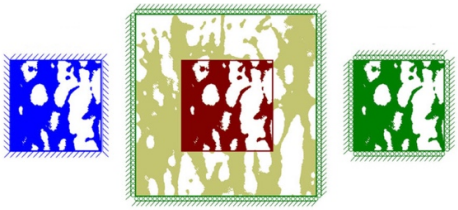

Figure 1: Boundary conditions for trabecular bone homogenization have a profound effect on apparent elastic and yield properties.

In these relationships, no differences were found among anatomical locations and no differences were found in specific diseases such as hypoparathyroidism. No further improvements in the predictions of stiffness or strength were achieved by adding further morphological variables. Finally, the critical role of boundary conditions in this homogenization process was quantified and the intrinsic limitation of a representative volume element for trabecular bone was recognized [1].
A second progress emerging from John Currey's ongoing interest in cracks developing in compact bone consists in applying continuum damage mechanics at multiple scales to quantify the biomechanical implications of these cracks. Micromechanical testing demonstrated conservation of the elastic modulus across the scales and a major scale effect for the post-yield properties. Rheological models representing compressive and tensile crack families allowed to explain the scale effect and to reproduce the accumulation of damage in compact bone at the macroscopic level [2]. A unit cell finite element model of the mineralized collagen fibre was also developed to calculate the axial and transverse elastic properties.

Philippe Zysset is Professor of Biomechanics at the ARTORG Center for Biomedical Engineering Research of the University of Bern. He was a research fellow at Harvard Medical School in 1989-1990 and obtained his PhD in Biomechanics at EPFL in 1994. He was a post-doctoral fellow at the University of Michigan in 1995-1997, assistant professor at EPFL in 1997-2003 and professor at TU-Wien in 2003-2011. His research mainly focuses on multiscale structure-function relationships of musculoskeletal tissues. He is an author of more than 200 articles in peer-reviewed journals, proceedings and books. Next to his teaching of biomechanics, he is leading a master's program in biomedical engineering.

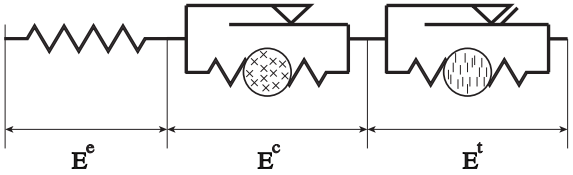

Figure 2: Rheological model of bone extracellular matrix with compressive and tensile cracks.

Future directions

The improved knowledge gained on the mechanical properties of bone helps us to better address the issues of osteoporosis-related bone fragility. Clinical imaging tools such as DXA, HR-pQCT or QCT provide areal or volumetric bone mineral densities, that are limited surrogates of bone strength and fracture risk. These images must therefore be properly interpreted in the light of the above homogenization procedure in order to build finite element models and deliver better estimates of bone strength in a personalized fashion.
Moreover, the gained knowledge also allows to better understand the interaction of bone with dental or orthopedic implants. Progressive damage and densification during implant insertion and frictional contact between bone and implant surface are the key ingredients to model primary stability and the initial conditions for bone healing.

References

1. Wili et al., Biomech Model Mechanobiol, 16:1925-1936, 2017.
2. Zysset et al., J Mech Behav Biomed Mater, 74:448-462, 2017.

Acknowledgements

I thank my PhD mentor, Alain Curnier, as well as my supporting research team and collaborators. SNF grants no 165510 and 183584 are gratefully acknowledged.

OCULAR BIOMECHANICS AND MECHANOBIOLOGY

C. Ross Ethier

Wallace H. Coulter Department of Biomedical Engineering, Georgia Tech/Emory, Atlanta, USA

Background

The eye is s surprisingly biomechanically-active organ, subjected to both external (e.g. extraocular muscles, optic nerve sheath tension, cerebrospinal fluid pressure) and internal (blood pressure, intraocular pressure [IOP]) loads. Further, mechanobiology plays an important role in multiple ocular pathologies, including glaucoma, myopia, keratoconus, and idiopathic intracranial hypertension, to name only a few. Here I describe a selection of intriguing, unsolved ocular biomechanical problems.

Myopia (Near-Sightedness)

Severe myopia is a risk factor for sight-threatening ocular pathologies, including retinal detachment and glaucoma. The incidence of myopia continues to increase, with > 90% of adolescents being affected in some countries. In almost all cases, myopia occurs because the eye is "too long" for its optical power, which in turn is due to abnormal growth of the sclera, the white part of the eye. Thus, there are long-standing interests in scleral biomechanics during myopia [1,2]. We are using a mouse model to study scleral remodelling in myopia, specifically characterizing scleral biomechanical properties using unconfined compression data interpreted using the Biphasic Conewise Linear Elastic Model [3]. We find that induction of form deprivation myopia in C57BL/6 mice leads to a time-dependent increase in scleral hydraulic permeability and a decrease of in-plane scleral stiffness. The signalling pathways leading to this remodelling remain unknown and represent an important therapeutic target for myopia.

Genetics of Scleral Stiffness

The sclera, in addition to its importance in myopia, is biomechanically important in other conditions [5]. Since scleral stiffness varies substantially between subjects, we used QTL analysis in the BXD recombinant inbred mouse set [6] to identify genes controlling scleral stiffness (Fig. 1). We identified *Smarce1* and *Tns4* as two genes associating with ocular compliance, an indirect measure of scleral stiffness, that are expressed at significant levels in the cornea and sclera. The protein product of *Tns4* is Tensin4, and the tensins are known to interact with actin filaments and β-integrins in focal adhesions, suggesting *Tns4* as an excellent candidate gene to modulate scleral biomechanical properties.

Glaucoma

Glaucoma is the leading cause of irreversible blindness. Elevated IOP is a major risk factor for glaucoma, and is the only treatable risk factor. IOP is largely controlled by the trabecular meshwork (TM), a porous tissue in the anterior eye that continually drains the aqueous humor from the eye, and thus there is significant interest in measuring and understanding TM function. We and others have shown an association between TM stiffness and TM hydrodynamic flow resistance, indicating that TM stiffness can provide information about TM function. We have thus developed a non-invasive technique to measure TM stiffness, coupling optical coherence tomographic imaging with an inverse FEM approach. We can detect increased TM stiffness in a clinically relevant mouse model of steroid glaucoma, and can further detect a return to normal TM stiffness after ocular delivery of a rho-kinase inhibitor, a clinically-approved anti-glaucoma medication [4]. This non-invasive stiffness measuring approach shows great promise for clinical translation as a tool to evaluate TM function.

C. Ross Ethier is the Gellerstedt Chair in Bioengineering and a Georgia Research Alliance Eminent Scholar in the Coulter Department of Biomedical Engineering at Georgia Tech/Emory. He obtained his PhD from MIT in 1986. His research is in the biomechanics of cells and whole organs, with specific emphasis on ocular biomechanics. He works on developing treatments for glaucoma, myopia and SANS, a syndrome affecting astronauts that is a major NASA health concern. He is an author of c. 185 papers in peer-reviewed journals and two books. He has held multiple academic leadership positions in biomechanics.

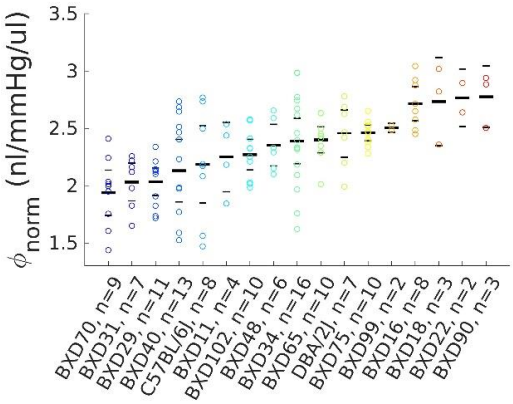

Figure 1: Ocular compliance (normalized by ocular volume), measured in 129 eyes of 17 BXD recombinant inbred mouse strains.

References

1 Grytz & Siegwart, *Invest Ophth Vis Sci*, 2015, **56**, 2065.
2 Siegwart & Norton, *Vision Res.*, 1999, **39**, 387–407.
3 Soltz & Ateshian, *J. Biomech. Eng.*, 2000, **122**, 576–586.
4 Li et al., *PNAS*, 2019, **116**, 1714–1722.
5 Ethier et al., *Ann. Rev. Biomed. Eng.*, 2004, **6**, 249.
6 Geisert et al., *Mol. Vis.*, 2009, **15**, 1730–63.

Acknowledgements

I thank the following collaborators/trainees: Dillon Brown and Machelle Pardue (myopia); Guorong Li, Chanyoung Lee, Ke Wang and Dan Stamer (TM stiffness); and Liz Boazak, Darryl Overby, Joseph Sherwood and Eldon Geisert (scleral stiffness). Funding support: NIH and Georgia Research Alliance.

COMPUTATIONAL METHODS FOR CARDIOVASCULAR APPLICATIONS: ACHIEVEMENTS AND FUTURE PERSPECTIVES

Peter E. McHugh

Biomedical Engineering, School of Engineering, National University of Ireland Galway, Galway, Ireland

Background

Computational methods have revolutionized engineering analysis and design across essentially all disciplines, and have come so much to the fore in recent years due to the huge advances in computational power, that make highly complex simulations practical for use in both fundamental and applied research, and in direct engineering design and performance assessment. Computational modelling has become very extensively multi-scale (from sub-nano to macro) and very extensively multi-physics, combining hitherto relatively disparate domains (structural, thermal, fluidic, chemical, etc.) to quite accurately simulate complex and multi-component physical environments and problems. It could be argued that the enormous development of biomedical engineering/bioengineering internationally over the last twenty five years has directly fueled these computational modelling advances; a key aspect of this is that biomedical engineering, and the development of medical implant and device technology in particular, has necessitated the application of computational modelling directly within the biological arena (to address topics within cell and tissue mechanics and mechanobiology for example) to a much greater extent than heretofore, thereby significantly broadening the multi-physical scope of computational modelling. Cardiovascular biomechanics and cardiovascular medical device mechanics (within biomedical engineering) is no exception to the above, and computational modelling has enabled huge advances to be made in (i) gaining a fundamental understanding of cardiovascular tissue and fluid mechanics, and in (ii) analysis, design and performance assessment of cardiovascular medical implants and devices. Additionally, computational modelling has become an important part of the medical device (FDA) regulatory approval process.

Recent Advances

Arguably, cardiovascular computational modelling was initially primarily concerned with coronary artery mechanics and stent angioplasty [1], utilizing solid or fluid continuum mechanics. While stent angioplasty modelling has continued apace, due to rapid evolution in technology (drug coated stents, bifurcation stenting, biodegradable stents, etc. [2]), computational modelling has become increasingly applied in structural heart applications (heart valve, heart wall, etc. [3]) and in vascular applications more generally (including abdominal, thoracic, peripheral and cerebral vasculature, etc. [4]). Consistent with this, constitutive models continue to be developed and calibrated for an ever-broader range of healthy and diseased cardiovascular tissue types, including inhomogeneous atherosclerotic plaque and thrombus [5]; there has been more extensive use of fluid-structure interaction (FSI) methods, and the expansion of the multi-physics approach to incorporate aspects of biomaterial science and pharmacology (in relation to drug carriers and delivery, etc.); and in relation to high resolution imaging technology, appropriate for model generation and validation, 4D MRI is showing huge promise.

Peter McHugh is Established Professor of Biomedical Engineering, and Head of School of Engineering, at NUI Galway, Ireland. Following his primary degree in mechanical engineering (NUI Galway, 1987) he obtained his PhD in mechanics of solids from Brown University, USA (1992). His research is focused on applying computational and experimental methods to investigate the mechanics of medical devices and tissue, particularly in the cardiovascular domain. He has a very distinguished publication and research funding record, with 160 peer-reviewed journal papers, over 350 conference papers, over €13m in funding, and 50 research student graduates (PhD/MSc). He has received numerous awards, including membership of the Irish Academy of Engineering (2019), Royal Irish Academy (2011), and the Alexander von Humboldt Fellowship (1995).

Future directions

Arguably the next major "disruptive" technological change on the horizon for the cardiovascular domain is the "convergence" of "traditional" cardiovascular devices with the domains of electricity, electronics, and data analytics, to generate "smart" cardiovascular devices, with enhanced sensing, actuation and self-powering features. Such technologies will include implantable sensors, robotic angioplasty catheters, electrical stimulation and denervation devices, and soft robotic devices. Computational modelling has a huge role to play here in terms of both fundamental studies (e.g. tissue electro-mechanics, building on recent studies [6]) and in applied implant and device analysis, design and performance assessment.

References

1. Conway et al., Cardiovasc. Eng. Technol. 3:1–14, 2012.
2. Boland et al. Int J Numer Meth Biomed Engng. 35:e3247, 2019.
3. Shirazi et al. Adv. Healthcare Mater. 8:1900228, 2019.
4. Johnson et al., Ann. Biomed. Eng., 45:2494–250, 2017.
5. Weafer et al., J NeuroIntervent Surg. 11:891–897, 2019.
6. Cinelli et al., IEEE Trans Biomed Eng 65:1373-1381, 2018.

Acknowledgements

The author acknowledges excellent collaborations with research students, postdocs, and academic, industry and clinical colleagues.

BIOMECHANICS OF THE TISSUES OF THE EYE WALL AND APPLICATIONS TO GLAUCOMA

Thao (Vicky) Nguyen

Department of Mechanical Engineering, Johns Hopkins University, Baltimore, MD, 21218, USA.

Background

The sclera and optic nerve head, along with the cornea, are connective tissues that form the outer wall of the eye in humans. These stiff and tough tissues serve to mechanically support the delicate retinal and neural tissues of the eye while maintaining an optimal shape for refraction. The mechanical properties of the cornea arise from the fiber-reinforced microstructure of the extracellular matrix, which is composed mainly of collagen and elastin fibers arranged in a proteoglycan-rich matrix. The extracelullar matrix structure in the human optic nerve head is called the lamina cribrosa for its fenestrated appearance. The lamina cribrosa is composed of a stack of perforated plates that resemble a collagen beam network structure when viewed *en face*. The collagen beams support a network astrocytes and axons of the retinal ganglion cells as they exit the eye. Variations in the mechanical properties of the lamina cribrosa, sclera and cornea may contribute to the susceptibility and progression of glaucoma.

In this presentation, I will describe our efforts to understand the structure-properties relationship of the sclera and optic nerve head tissues of human and mouse eyes using an integrated experimental and computational method. To measure the mechanical behavior of the tissues under physiological conditions, we have developed ex-vivo inflation tests with optical imaging and 3D digital image correlation (3D-DIC). We also developed methods to measure the anisotropy of the collagen microstructure of the sclera and the beam network microstructure of the lamina tissue of our inflation tested specimens. This has allowed us to develop specimen specific computational models to study the structure-properties relationship of these tissues and extract their anisotropic nonlinear elastic properties using inverse analysis.

Recent Advances

Recent studies have focused on the mechanical behaviour of the tissues of the optic nerve head. We have developed ex vivo inflation tests that use a laser scanning nonlinear optic microscope to image the 3D volume of the optic nerve head tissues, digital volume correlation (DVC) to calculate the 3D strain field from controlled pressurization in the imaged volume, and morphological characterization methods that quantitatively characterize the network structure of the human and mouse optic nerve head tissues. The outcomes of these studies have elucidated the relationship between the collagen structure and the mechanical behaviour of the tissues under inflation. Moreover, they reveal significant effects of age and glaucoma on the mechanical behaviour and properties of the sclera and optic nerve head, and suggest that strains and stiffness are factors determining the susceptibility to glaucoma axon damage.

Thao (Vicky) Nguyen received her S.B. from MIT in 1998, and M.S. and Ph.D. from Stanford in 2004, in Mechanical Engineering. She was a research scientist at Sandia National Laboratories from 2004-2007 before joining Johns Hopkins University, where she is currently a Professor and The Marlin U. Zimmerman Faculty Scholar in Mechanical Engineering. She has received numerous awards, including the 2008 Presidential Early Career Award in Science and Engineering and the 2013 National Science Foundation CAREER Award. She currently serves as an Associate Editor for the Journal of Biomechanical Engineering and is the 2020 President of the Society of Engineering Science.

Future directions

The cross-sectional *ex vivo* experimental studies have show significant differences between the mechanical behavior of the sclera and optic nerve head of normal and glaucoma eyes. However, the differences may be baseline differences that increase the susceptibility to glaucoma damage or the result of remodeling induced by glaucoma. To study the remodeling of the tissues of the optic nerve head, we are developing methods that use optical coherence tomography (OCT) and DVC to measure *in vivo* the strain response of the optic nerve head to changes in the intraocular pressure (Fig. 1). We are also developing patient-specific models to analyze the DVC measured strains for the mechanical properties of the optic nerve head tissues. The in vivo studies may reveal biomechanical markers that predict the susceptibility to glaucomatous axon loss and the effectiveness of pressure-lowering therapies in glaucoma patients.

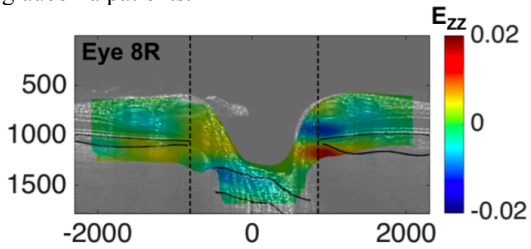

Figure 1: *Contour of the out-of-plane strain E_{zz} in the inferior-superior section of the optic nerve head obtained from DVC analysis of in vivo radial OCT scans of subjects experiencing an increase in the intraocular pressure (IOP). An increase in IOP caused compressive E_{zz} in the lamina cribrosa*

A Computational Perspective on Virtual Liver Design: Fluid Flow, Zonation, Fibrosis and Mechanics

Jack A. Tuszynski

DIMEAS, Politecnico di Torino, Turin, Italy and Dept. of Physics, University of Alberta, Edmonton, Canada

Abstract

This talk will focus on two critical issues for the 3D liver tissue engineering development: (a) fluid flow, zonation, and drug screening; and (b) biomechanics, tissue stiffness and fibrosis. Following a general overview of liver bioreactor designs, computer simulations of flow, reactive transport and biomechanics at the liver lobule and liver tissue scale will be discussed. The fundamental issues of tortuosity and upscaling include disease and fibrosis effects. Idealized simulations of the effects of fibrosis on lobule drug transport and mechanics responses will be presented. We will conclude with an outline of practical applications of tissue engineering showing how efficient computational upscaling techniques such as dual continuum modeling might quantify the transition of bioreactor results to the full liver scale.

Jack Tuszynski is currently Allard Research Professor of Oncology and Professor of Physics Pat the University of Alberta and Professore Ordinario at DIMEAS, Politecnico di Torino. He obtained a PhD in Theoretical Physics at the University of Calgary in 1983. He held visiting professor appointments at the Univ. of Duesseldorf, University of Giessen, Catholic University of Leuven, Ecole Normale Superieur in Lyon and Nankai Univeristy in Tianjin, China. He is an author of over 500 publications in peer- reviewed journals, 12 books, 27 book chapters and has given more than 200 invited and 200 contributed talks at national and international conferences and seminars on all six continents.

Background

Tissue engineering, with the goal to repair or replace damaged tissue and organs, continues to make dramatic science-based multi-disciplinary advances since its origins in the late 1980's/ early 1990's. Excellent monographs provide a general overview and historical perspective of the field [1,2]. Two topics critical for the liver tissue engineering that computational simulations recently focus on are: (a) fluid flow, zonation, and drug screening; as well as (b) biomechanics, tissue stiffness and fibrosis, all within the context of 3D structures.

Recent Advances

In addition to the role of fluid flow for the maintenance of healthy liver tissue activity, appropriate tissue matrix stiffness contributes to normal liver cell function [3]. Cell mechanosensors and mechanotransduction imply that these two factors are coupled. Various liver diseases (steatosis, fibrosis, cirrhosis, and cancer) represent altered states of tissue stiffness that have been modeled extensively by various groups [4]. Computational models provide quantitative representations of the *in-vivo* state and the effects of possible parameter variations. Here, we focus on the liver lobule as the "gold standard" for tissue engineering constructs to mimic. Numerous research groups have explored aspects of the liver lobule using computational methods. Since hepatocytes vary in enzyme expression and function depending on their spatial location in the lobule (zonation), models of cellular and drug metabolism must account for this. We furthermore focus on the impact of fibrosis on the lobule fluid flow and mechanical response Such samples exhibit biphasic creep and stress relaxation responses due to coupled elastic solid and fluid flow phenomena. To simulate the mechanical response of tissues dynamically, we will couple fluid flow simulation with a continuum finite element simulator. As such, the competition between stiffness (Young's modulus) and flow (hydraulic permeability) is paramount. Most commonly, averaged single continuum models are used for upscaled fluid flow or mechanics simulations. Implicitly, such models are appropriate only at later timescales when mass transfer between regions has come to pseudo equilibrium.

Future directions

A computationally efficient algorithm to upscale lobule-level results to the tissue scale, and ultimately to the full organ scale is needed. Such an algorithm, termed dual continuum modeling, should represent each averaged spatial location property by one averaged tissue property value, and one averaged sinusoid property value. This holds for both static properties such as porosity, permeability as well as dynamic properties such as component concentrations.

References

1. Lanza, R, Langer, R, Vacanti, J, "Principles of Tissue Engineering", 2nd ed., Academic Press, New York, 2000
2. Sharma, K, "Transport Phenomena in Biomedical Engineering: Artificial Organ Design and Development, and Tissue Engineering", McGraw-Hill, New York, 2010
3. Rani, et al. J. Biomech, 39: 551-63, 2006,
4. Wells, R, Hepatology, 47, 1394-400, 2008
5. Wells, R, Biochim. Biophys. Acta.1832, 884-90, 2013.

Acknowledgements

This presentation represents a joint research project with my collaborators and co-authors of this abstract: Prof. Vahid Rezania, Dept. of Physical Sciences, MacEwan University, Edmonton, Canada and Dr. Dennis Coombe, Computer Modelling Group Ltd, Calgary, AB T2L 2A6, Canada

REDUCING THROMBOEMBOLIC EVENTS IN BLOOD VESSELS AND ARTIFICIAL PUMPS.

Lisa Prahl Wittberg
FLOW, Dept. of Engineering Mechanics, Royal Institute of Technology (KTH), Stockholm, Sweden

Background

Cardiovascular diseases are the most common cause of death in the western world, where heart failure (HF) has been stated a global pandemic by Savarese and Lund [1], affecting approximately 26 million people worldwide. Heart transplant (HTX) is the final treatment for severe HF where mechanical circulatory support (MCS) devices have been developed for temporary or long-term support cardiac support due to shortage of available organs. Despite anticoagulation therapy, both thromboembolism and bleedings remain major issues and limiting factors in using MCS. Thrombi formation with or without embolism is also found in atherosclerosis. The close connection between endothelial activation and the activation of the inflammatory and coagulation systems is well established. Hence, similar models were commonly applied for activation of endothelial cells, platelets and leukocytes. Nevertheless, most current activation models are of phenomenological character and do not reflect the underlying processes.

Recent Advances

An important issue related to all in-vitro studies is the sources and levels of uncertainties of the results relative to the clinical situation. In MCS, our result indicates that the platelets experience varying stress in space and time that may significantly differ from the stress character in the calibrating experiments for available platelet activation models [2]. These models were found to suffer from high sensitivity due to model formulation deficiency, being unable to reflect known facts about platelet activation [3, 4]. Moreover, common indicators for atherosclerosis were found to identify common sites of stenosis but could not be used for prognostic purposes [5]. One reason was due to the indicators heavily relying on the scalar form of the wall shear stress (WSS), not reflecting the tensorial character of the stress.

Blood flow simulations require an adequate description of the geometry and appropriate boundary conditions. Our recent results indicate the sensitivity of the results to boundary conditions and the uncertainties in anatomical data [6]. In fact, the available clinical data is not only sparse, but also with low spatial and temporal resolution. Thus, a consistency verification of the computed flow field with the underlying assumptions of the BC that generated the flow has to be carried out. The sensitivity to temporal and spatial variations in the inlet conditions is strong even when expressed in terms of averaged variables such as commonly used wall shear stress (WSS) indicators.

Dr. Lisa Prahl Wittberg is currently Associate Professor and Head of the Division of Fluid Mechanics and Acoustics at the Department of Engineering Mechanics, Royal Institute of Technology (KTH), Stockholm. She obtained her PhD in Fluid Mechanics in Lund University in 2007. She joined KTH 2008 as a post-doctoral researcher and worked at the University of Cincinnati/Cincinnati Children's Hospital in 2012 as a visiting researcher. Her research interest focuses on complex fluids, in particular blood, using both detailed numerical simulations and experiments to study the physics of blood flow linked to clinical applications. The research is carried out in close collaboration with ECMO Centre Karolinska, Karolinska University Hospital. She is an author of 27 publications in peer-reviewed journals, and more than 25 contributions to international and national conferences.

Future directions

Peak femoral loading varied between 1.49 kN and 5.97 kN depending on impact condition. The average peak femoral forces in anterior, lateral, and posterior fall direction were 4.79kN, 5.51 kN, 3.14 kN, respectively. Impact posture affected peak femur forces more in posterior falls compared to anterior and lateral falls.

References

1. Savarese & Lund, Card Fail Rev 3(1):7-11, 2017.
2. Berg et al., Flow Turb Comb 102:469-483 2019.
3. Fuchs et al., Sci Rep 8:13985, 2018.
4. Fuchs et al. Sci Rep 9:8809, 2019.
5. Fuchs et al. Fluids 4(1):26, 2019.
6. Berg et al. Flow Turb Comb 102:27-41, 2019.

Acknowledgements

The author gratefully acknowledges N Berg, A Fuchs, J Lemétayer, F Rorro & F Fiusco at the *Royal Institute of Technology (KTH)*, G Fuchs at *Sundsvall Hospital* and L Mikael Broman at *ECMO Centre Karolinska, Karolinska University Hospital*.

This work was supported by Region Stockholm (HMT2017) and the Swedish Heart – Lung Foundation. Computational resources were provided by the Swedish National Infrastructure for Computing (SNIC).

BONE FRACTURE TOUGHNESS: LESSONS LEARNT FROM BRITTLE BONES

Alessandra Carriero

The City College of New York, USA

Background

Bone is the major structural component of the human body, operating as its protective load-bearing framework. While performing its primary function, this dynamic organ is constantly remodeling (self-repairing) and adapting its shape to the forces that are daily applied upon it. Composition and structure of the bone over many length-scales are responsible for its strength, toughness, and ability to adapt to mechanical loads. Aging and disease alter bone composition, disrupt its hierarchical structure and change the loads acting on it, therefore affecting bone's mechanical and biological properties, increasing its vulnerability to fractures and deformities. Thus, it is of extreme importance to examine bone multi-scale mechanics and mechano-adaptation in growth, aging and disease to comprehensively understand bone fractures and deformities, and aid in the development of new treatments for skeletal pathologies.

Recent Advances

Bone achieves its unique material properties of strength and toughness from its highly organized hierarchical structure, made primarily of collagen and hydroxyapatite arranged on multiple length scales. While bone strength well correlates with bone mineral density, toughness is still not well characterized. In these recent years, we have examined composition, structure, and mechanics of bone, and developed a novel multidisciplinary approach for investigating multi-scale mechanics and mechanisms of fracture in bone. Using models of osteogenesis imperfecta (OI or brittle bone disease) with genetic defects of the collagen, and knockout models (such as TIMP3 deficient mice), we revealed how small length scale abnormalities ramify at larger length scales, causing whole bone fragility. At the whole bone level, we have determined the fracture toughness, and examined the initiation and crack-growth toughness, and the extent of the stable crack growth, using in-situ investigations and R-curves [1, 2]. Brittle bones have lower initiation and crack-growth toughness and shorter stable crack-growth than healthy controls [1]. To determine mechanisms of crack growth toughness at the tissue level, we examined the influence of porosity in crack initiation and growth toughness using synchrotron CT combined with finite element modelling. We have further determined the lamellar structure and tissue composition using FTIR spectroscopy. At equal vascular porosity, higher canal density and branching increase the risk of fracture and reduces fracture resistance during crack propagation [1, 3]. Similarly, rounder lacunae increase the tissue fragility around them [4]. Tissue heterogeneity, instead, increases fracture resistance [3]. At the collagen/mineral level we have examined X-ray scattering simultaneous to mechanical loading and observed less stiff mineralized fibril contributing to bone fragility [1, 4]. At the molecular level, we analysed the collagen crosslinks using spectroscopy and molecular fluorescence. Brittle bones have abnormal collagen crosslinks, which affect the deformation mechanisms of mineralized fibrils [1].

Dr. Carriero is Assistant Professor at the Department of Biomedical Engineering, The City College of New York. She obtained her MSc from Politecnico di Milano and her PhD from Imperial College London. She was post-doctoral fellow at ETH, at Lawrence Berkeley National Laboratory, and at Imperial College. She received several international recognitions for her innovative and outstanding research in the field of biomedical engineering, including the Sir George Macfarlane Award from The Royal Academy of Engineering in 2012, the John Haddad and the Harold Frost Awards from the American Society of Bone and Mineral Research in 2016, and a CAREER Award from National Science Foundation in 2017.

Future directions

Future work will use this multi-scale pipeline to better understand factors at each length scale that are critical to bone fracture resistance. Further improving the translation of research from mice to humans, this whole body of research will offer insights to what needs to be targeted in bone for more effective treatment strategies for bone frailty.

References

1. Carriero et al., JBMR, 29:1392-1401, 2014
2. Carriero et al., JMBBM, 39:38-47, 2014
3. Carriero et al., Bone, 61:116-124, 2014
4. De Paolis, et al., ESB Vienna 2019
5. Miller et al., Calc Tiss Int, 100:631-640, 2017
6. Poulet B, et al., Plos Biol, 21:11(12), 2016

Acknowledgements

I would like to acknowledge my collaborators: Sandra Shefelbine, Robert Ritchie, Adele Boskey, Ralph Muller, Andrew Pitsillides, George Bou-Gharios, Elizabeth Zimmerman, Bjorn Busse, Simon Tang and my postdoc and students that contributed to this work: Annalisa De Paolis, Micheal Vogt, Simone Castagno, Brendyn Miller and Anxhela Docaj.

HUMAN IN SILICO DRUG TRIALS WITH MULTISCALE MODELS OF CARDIAC ELECTROMECHANICS

Elisa Passini

Department of Computer Science, University of Oxford, United Kingdom

Background

In silico trials in medicine refer to the evaluation of a medical therapy using computer modeling and simulations. Already established in engineering applications (such as aeronautics), *in silico* trials are now starting to be adopted in medicine, with a broad impact in academia, industry and regulatory bodies [1]. Potential applications include drug safety and efficacy testing. Cardiotoxicity is still one of the main causes of failure during drug development, and most of the experiments are still performed using animal models. This raises ethical questions, and the translation of the results to humans is limited, mainly due to inter-species differences.

Recent Advances

In my talk, I will describe the recent progress made by our group in computational modelling and simulations of the human heart, towards the realisation of *in silico* trials for cardiac pharmacology and medicine.

I will showcase how populations of human multiscale models, from ionic currents to whole-organ dynamics, are able to capture the biological variability observed experimentally, both in control and diseased conditions.

I will present our recent simulation results on human *in silico* drug trials in populations of single cell models, where we were able to predict drug-induced pro-arrhythmic risk with 90% accuracy, thus outperforming preclinical animal studies [2-3], based on simulated action potential and calcium biomarkers.

I will introduce our framework for multiscale simulations, which integrates the electrophysiology with patient-specific anatomical information from clinical images. This allows to simulate the electrocardiogram, validated based on experimental and clinical datasets, and also to investigate how perturbation of heart orientation and pose within the torso affect the electrophysiology [4]. The functional and structural consequences of disease conditions such as myocardial ischemia and cardiomyopathies are also implemented in the 3D framework, to characterise how the arrhythmic risk is modulated by both disease and drugs [5].

I will present our latest results about the development and validation of a multiscale *in silico* model of cardiac electro-mechanics, integrating biophysically detailed models of cardiac electrophysiology and contractility. This model allows to investigate changes in cardiac contraction from single cell to the whole-organ level, and derive biomarkers such as ejection fraction and left ventricular pressure, which can be directly compared with clinical measurements from patients.

Elisa Passini is currently a Senior Research Associate at the Department of Computer Science, University of Oxford (UK). She obtained her PhD in Bioengineering at the University of Bologna in 2015, and she joined the Computational Cardiovascular Science group in 2013. Her research focuses on the development of human-based computer model of the heart to predict drug safety and efficacy. Elisa was awarded the 2017 International 3Rs prize for the contribution of her research to the Replacement, Refinement and Reduction of Animals in Research, showing how computer models can predict drug safety and efficacy with higher accuracy than animal experiments.

I will finally illustrate how we have developed this research program into human *in silico* trials in partnership with collaborators across academia, industry and regulatory agencies [6].

Future directions

I will highlight the next steps in our research program, including the extension of human *in silico* drug trials to simulations of drug-induced effect on both cardiac electrophysiology and contractility. This will allow for a more comprehensive evaluation of drug safety and efficacy, both in control and diseased conditions.

References

1. Pappalardo F et al., Brief Bioinform, bby043, 2018
2. Passini E et al., Front Physiol, 8:668, 2017.
3. Passini E et al., Br J Pharmacol, 176(19):3819-3833, 2019.
4. Minchole A et al. Front Physiol, 10:1103, 2019.
5. Martinez-Navarro H et al. Sci Rep, 9(1):16803, 2019.
6. Rodriguez B et al., Europace, 18(9):1287-98, 2016.

Acknowledgements

The research presented in this talk is work conducted within the Computational Cardiovascular Science team, led by B Rodriguez and A Bueno-Orovio (www.cs.ox.ac.uk/ccs), with financial support by a NC3Rs Infrastructure for Impact award (NC/P001076/1), a Wellcome Trust Senior Research Fellowship in Basic Biomedical Sciences (100246/Z/12/Z and 214290/Z/18/Z), the Oxford BHF Centre of Research Excellence (RE/08/004/23915 and RE/13/1/30181), an Engineering and Physical Sciences Research Council Impact Acceleration Award (EP/K503769/1), the CompBioMed project (European Commission grant agreement No 675451), and the TransQST project (Innovative Medicines Initiative 2 Joint Undertaking under grant agreement 116030, receiving support from the European Union's Horizon 2020 research and innovation programme and EFPIA).

CUSTOM-MADE DESIGN AND MANUFACTURING OF PROSTHESES AND ORTHOTICS

Alberto Leardini, Claudio Belvedere, Paolo Caravaggi

IRCCS, Istituto Ortopedico Rizzoli Bologna, Italy

Background

Additive-manufacturing technology now allows each medical device to be fabricated layer-by-layer according to a computer model: this finally enables the design of the device to be personalized, i.e. according to the anatomy, dimensions, status, and demand of each single patient. It is fundamental to quantify advantages and possible drawbacks of these novel procedures for custom-made additive-manufacturing in orthopaedics, particularly to understand whether their introduction is feasible and cost-effective, for both implantable and non-implantable products. A careful assessment and comparison of the instruments and tools, software and hardware, are also now necessary.

Recent Advances

Historically, first areas were patient-specific instrumentation, particularly for total knee replacement [1], and clinical and biomechanical investigations on special custom complex talonavicular replacements [2,3]. Custom Total Ankle Replacement has been largely investigated recently, likely because of the poor/fair clinical outcomes and of the smaller indication. In this area, original overall procedures [4], the effect of imaging modalities [5], anatomical modelling from biomedical imaging [6,7], experimental based validations of new designs [8,9] and even technological and biological assessments [10-12] have been developed. Possible customization procedures also for insoles [13] and Ankle-Foot Orthosis on joint kinematics base [14] were analysed. In the Institute, also the following custom-made additive-manufacturing have been experienced, with either SLM or EBM technology: massive musculo-skeletal reconstructions for bone tumours in the spine, thorax, pelvis and upper and lower limbs; tools for coronoid reconstruction with osteochondral radial head autograft; open-wedge high tibial osteotomy for surgical correction of valgus knee. A recent experience in support to another hospital has resulted in a biomodel in ABS, FDM technology, used for the pre-op planning and optimal positioning of the fixation rods and screws, and demonstrated to be fundamental before operation for instruments preparation, and during surgery for visibility enhancement: this has resulted in patient safety and surgical time reduction.

Future directions

Today it is the time to deploy the introduction of these techniques in the routine clinical practice. But to obtain all this, additional analyses (imaging, modelling, designing, prototyping) are necessary, which involves multidisciplinary competences and resources. On the other hand we are confident that custom-made implants will reduce industrial costs, minimise instrumentation, simplify hospital and surgical arrangements, and optimize final performances of the devices, resulting therefore in cost-effective overall solutions for health-care systems. Future education and training programmes shall address this area in medicine and biomechanics.

Alberto Leardini is Director of the Movement Analysis Laboratory and Responsible for the Line of Research "Innovative and Prosthetic Surgery" at Istituto Ortopedico Rizzoli. He has been the President of the Italian Digital Biomanufacturing Network, and now President-Elect of the International Society of Biomechanics. His research mainly focuses on Motion Analysis, Joint Biomechanics and Orthopaedics Implants; more recently on Prosthesis Design and Additive Manufacturing. He is author of 195 publications in peer- reviewed journals, 47 book chapters, more than 890 Contributions to National and International Conferences, and 4 patents.

References

1. Ensini et al, Knee Surg Sports Traumatol Arthrosc, 22(3):621-9, 2014.
2. Giannini et al, J Foot Ankle Surg, 55(6):1271-1275, 2016.
3. Belvedere et al, J Foot Ankle Surg, 56(4):836-844, 2017.
4. Belvedere et al, J Orthop Res, 37(3):760-768, 2019.
5. Durastanti et al, Quant Imaging Med Surg, 9(8):1368-1382, 2019.
6. Matsiushevich et al, J Biomech, 84:247-251, 2019.
7. Leardini et al, Semin Musc Radiol, 23(6):643-656, 2019.
8. Belvedere et al, J Biomech, 53:97-104, 2017.
9. Belvedere et al, J Biomech, 75:159-163, 2018.
10. Liverani et al, Materials & Design, 106:60-68, 2016.
11. Liverani et al, Procedia CIRP, 65:25-31, 2017.
12. Caravaggi et al, J Biomed Mater Res B Appl Biomater, 107(7):2343-2353, 2019.
13. Caravaggi et al, Gait Posture, 50:232-238, 2016.
14. Ferraresi et al, Proc Inst Mech Eng H, 231(9):831-838, 2017.

Acknowledgements

Many bioengineers, radiologist and orthopaedic surgeons have participated to the developments of these devices, within and outside Istituto Ortopedico Rizzoli: I really want to acknowledge them all.

MATRIX AGEING AND THE LINK TO CONNECTIVE TISSUE DISEASE

Jess G. Snedeker

University and ETH Zurich, Switzerland

SUMMARY

We present our past efforts (and recent unpublished successes) to understand the connections between age-related oxidative damage within the collagen matrix and related biophysical effects at the molecular, cellular and tissue levels. This work directly links matrix ageing to diminished cellular mechano-transduction. From this base, we present ongoing work exposing how these age-related changes in cell-matrix interactions may derail tissue homeostasis and potentially drive tissue disease.

Background

Concurrent with a progressive loss of regenerative capacity, connective tissue aging is characterized by a progressive accumulation of Advanced Glycation End-products (AGEs). These products occur as a result of unregulated oxidative reactions between systemic glucose and long-lived proteins such as collagen. Although AGEs are associated with a wide range of clinical disorders, the mechanisms by which AGEs contribute to connective tissue disease in aging and diabetes are still poorly understood.

Recent Advances

Our work harnesses multiscale imaging techniques to characterize in vitro models of sugar induced collagen aging. We have benchmarked these data against experiments on native human tissues from donors of different age, including the very old. These efforts have yielded unprecedented insight into the mechanical changes in collagen tissues across hierarchical scales from molecule, to fibre, to tissue. Our studies show that AGEs reduce tissue viscoelasticity by severely limiting fibre–fibre and fibril–fibril sliding [1,2].

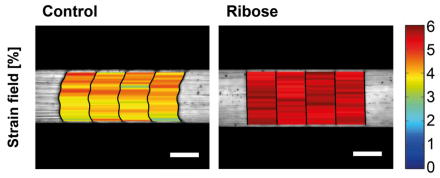

Figure 1. Collagen glycation induced by ribose (as a model sugar) dramatically reduces fibre-fibre sliding within the collagen matrix of tendon [2]. bar=100μM

Our most recent work exploits in situ calcium imaging to directly expose mechano-transduction events. We have isolated collagen fibre-fibre sliding as an essential biophysical stimulus that triggers cellular signalling. We have very recently demonstrated that these stimuli and downstream signalling consequences are heavily suppressed in aged tendons (of mice). These data confirm our long-standing hypothesis that cellular mechanosensitivity within the aged collagen matrix is strongly diminished. We have also begun work to examine how this lost mechano-sensitivity may underlie connective tissue disease.

Trained as a mechanical engineer (BSc Lehigh University 1996), Jess first worked in industrial product design and manufacturing process engineering (1996-1998). He began applying engineering approaches to the study of human physiology in his graduate work (MSc Penn State 2000, PhD ETH Zurich 2004). He has led an independent research group in Zurich since 2006 with dual faculty appointments at the University of Zurich (Medical Faculty, D-Orthopedics) and ETH Zurich (Institute for Biomechanics). He heads the Swiss Center for Orthopedic Innovation at the Balgrist Campus, designated and funded as a "research infrastructure of national importance" since 2016.

Future directions

We enjoy a scientific era marked by revolutionary advances in molecular biology and imaging tools. These tools have opened the floodgates for targeted study of basic mechanisms of cell-matrix interaction and cellular mechano-transduction. In the very near future our field will identify and localize the specific molecular sensors that regulate tissue adaptation to exercise and cellular response to matrix damage. As a community we will soon be confronted by the challenges of unwinding the daunting complexity downstream of these stimuli and their cellular sensors. The approaching research horizon will involve challenging work that employs biomedical engineering approaches to disentangle cell-system cross-talk in connective tissue patho-physiology. We suspect that this work will continue to expose age-related alterations of cell-matrix interaction as a central player in many human ailments and their clinical treatment.

References

1. Li et al., Matrix Biology, 32:169-177, 2013.
2. Gautieri et al., Matrix Biology, 59:985-108, 2017.

Acknowledgements

The body of work we will present includes key contributions from Mr. Fabian Passini (ETH), Dr. Alfonso Gautieri (Polimi), Dr. Yufei Li (ETH), and Mr. Patrick Jaeger (ETH). The majority of work was funded by the Swiss National Science Foundation, with complementary and essential funding contributions generously provided by the Cariplo Foundation and ETH Foundation.

BIOMECHANICS OF EARLY HUMAN LIFE

David Elad

Department of Biomedical Engineering, Tel Aviv University, Tel Aviv, ISRAEL

Background

Human reproduction is the outcome of a series of complex events that act in concert to produce a living offspring. The detached ovum is sucked into the fallopian tube and the spermatozoa are transported to the fallopian tube where fertilization may occur. The newly born embryo (zygote) is driven to the uterine cavity, and then, it is conveyed to its implantation site in the uterine wall. The placenta is developed to provide the fetus efficient exchange of materials via the maternal blood circulation. The fetus is developed in a dynamic physical environment within the amniotic sac, and at term, uterine contractions push out the baby. These events are driven by synchronized molecular activity and biochemical procedures which are integrated with physical forces and transport phenomena from cell to organ levels.

Early human life is the period of about 10 days that starts with the onset of fertilization and ends when the embryo implants into the uterine wall, where the placenta starts to develop. It is well established that the sperm transverse the uterus and fallopian tube within minutes, but according to flagellar propulsion theories it would take at least an order of magnitude longer; what is the mechanism that accelerates sperm motion to meet the ovum? And, is there a physical mechanism that directs the sperm towards the ovulated side where the ovum is waiting? Fertilization is the outcome of sperm and oocyte merging, however, what are the physical mechanisms that generate the forces requires for merging? Following entrance to the uterine cavity, the embryo is waiting 3-5 days for the window of implantation; what is resisting gravity to keep it available in the fundal region? Embryo Implantation is known as invasion of the embryo into the endometrium, however, maybe the endometrium is swallowing the embryo?

Recent Advances

The dynamic intra-uterine physical environment may include structural, mechanical, chemical and electrical components at all levels. The cascade of process during reproduction may be described if a flow chart as shown in Fig. 1. Recent advances include studies on the biomechanics of non-pregnant uterine peristalsis[1], intra-uterine pre-implantation embryo transport[1], transport of glucose and other components across a tissue-engineered multi-layer placental barrier model[2], tissue engineering models of the receptive uterine wall, and more of speculations about mechanobiology during fertilization and implantation[3].

David Elad is currently emeritus professor of biomedical engineering at Tel Aviv University. He received his DSc in biomedical engineering from the Technion (1982). His research activities include experimental and computational problems in the respiratory and reproductive systems from cell to organ levels: Transport in the nasal cavity, shear stress and mucus secretion in cultured nasal epithelial cells, uterine peristalsis, transport across a tissue-engineered placental barrier, mechanobiology of a uterine wall model and biomechanics of infant feeding. He was a member of the World Council for Biomechanics and presently he is a fellow of AIMBE, BMES-USA, IAMBE and EAMBES.

Future directions

Embryo implantation is a major cause for the low rate of success in natural and assisted conception. However, studies of human reproduction, including biomechanical factors are limited due to ethical and accessibility issues, as well as differences between mammalian species. Tissue engineered models that mimic the anatomical structure and physiological functions of *in vivo* organs, as well as computational models, may further advance the knowledge of molecular and biomechanical mechanisms of physiological processes in early human reproduction.

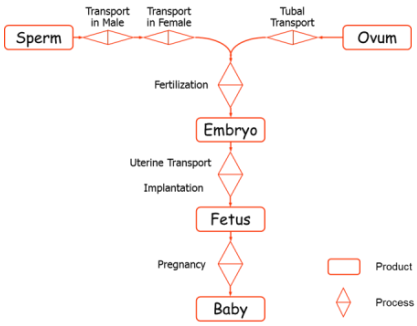

Figure 1: Flow chart of the cascade of events during human reproduction.

References

1. Myers & Elad. *WIREs*, 9: e1388, 2017
2. Levkovitz et al., *Placenta*, 34: 699-715, 2013.
3. Elad et al., Physiology, to appear Feb. 2020.

Acknowledgements

The research was conducted in collaboration with Jaffa Ariel & Grisaru Dan from Tel Aviv Medical Centre, Zhang Ying & Duan Enkui from Chinese Academy of Science and graduate students at Tel Aviv University.

NOVEL DEVELOPMENTS IN EXPERIMENTAL MICROMECHANICS AND THEIR APPLICATION TO MINERALIZED TISSUES

Jakob Schwiedrzik

Empa Swiss Federal Laboratories for Materials Science and Technology, Switzerland

Background

Bone is a mineralized tissue featuring a hierarchical architecture that combines properties like stiffness, toughness and strength with a low specific weight. To better understand the mechanisms leading to this advantageous combination of attributes, its mechanical properties have to be investigated at all length scales. At the macroscale, bone mechanics has been studied for more than a century. However, challenges remain due to intra- and inter-subject, disease or age-related variation. Considering bone as a hierarchical material and investigating its properties on several length scales is of high relevance, as bone's inelastic behaviour at lower levels of tissue organisation influences the mechanical response of the whole organ. One of the most common micromechanical testing techniques for bone is microindentation [1]. However, it is very difficult to uniquely interpret indentation curves in terms of nonlinear material behaviour [2]. Therefore, there is a need for novel experimental methods assessing the microscale strength and fracture properties of bone.

Recent Advances

The development of focused ion beam technology has provided a tool for preparing micromechanics specimens at a high spatial resolution. Novel testing techniques, such as micropillar compression [3] or microtensile testing [4] allow measuring mechanical properties at the length scale of micrometers. At the Laboratory for Mechanics of Materials and Nanostructures, we develop instrumentation and methods for performing experiments under controlled environmental conditions (in physiological solution or at controlled relative humidity and temperature). Furthermore, novel sensor concepts have been engineered that allow probing materials not only under quasistatic loading, but also at high strain rates representative of an impact or fracture (1-1000s^{-1}) [5] and at high frequencies (0.01-10kHz). Additionally, we have developed specimen geometries and experimental methods for probing properties such as fracture toughness [6] or viscoelasticity (in both frequency and time domain) at the microscale.

The development of novel instruments and methods makes a careful characterization and validation necessary to achieve a high level of accuracy and reliability. We tackle this problem with detailed finite element modelling of the experimental setup as well as calibration and validation experiments on well-characterized materials. This allows us to significantly push the boundaries of what can be assessed experimentally on the microscale while retaining a high level of confidence in the results. Application of these methods to osteonal bone has demonstrated a significant scale effect [3] and allowed us insights into microscale deformation mechanisms, anisotropy, tension-compression asymmetry, hydration [7], as well as viscoelastic and viscoplastic effects.

Jakob is currently heading a research team at Empa Swiss Federal Laboratories for Materials Science and Technology. He studied Mechanical Engineering at TU Vienna and obtained his PhD in Biomedical Engineering at the University of Bern in 2014 on the topic of analytical, computational, and experimental micromechanics of bone. He was a postdoctoral fellow at Empa from 2014 to 2017. His present research focuses on instrument and method development in experimental micromechanics as well as multiscale mechanics of hierarchical materials. He authored 40 publications in peer reviewed journals and more than 25 contributions to international conferences as presenting author.

Future directions

Significant problems in experimental micromechanics of mineralized tissues are the long time needed for the production of each specimen, the natural variation in the underlying microstructure, and the resulting scatter that complicates the identification of significant trends in the data. Therefore, efforts are undertaken to considerably speed up the specimen preparation, standardize and automate experimental protocols and data analysis, and combine mechanical experiments with site-matched microstructural analysis to identify microscale structure-property relationships, which can be used to develop and validate multiscale models of bone fracture.

References

1. Oliver & Pharr, J Mat Res 7(6), 1992
2. Chen et al., J Mech Phys Solids 55(8), 2007
3. Schwiedrzik et al., Nat Mat 13, 2014
4. Casari et al., J Mat Res 34(14), 2019
5. Ramachandramoorthy et al., Nano Letters 19(4), 2019
6. Schwiedrzik et al., Fat & Fract Eng Mat Struc 41(5), 2018
7. Schwiedrzik et al, Acta Biomaterialia 60, 2017.

Acknowledgements

The contributions of D. Casari, C. Peruzzi, and T. Kochetkova, as well as collaborations with R. Ramachandramoorthy, J. Ast, J.-M. Breguet, U. Wolfram, P. Vena, P. Zysset, E. Mazza, and J. Michler are gratefully acknowledged.

NEW TRENDS IN STOCHASTIC CARDIOVASCULAR MODELING

Daniele E. Schiavazzi

Department of Applied and Computational Mathematics and Statistics, University of Notre Dame, US

Background

Deterministic cardiovascular modeling has seen tramendous progress in the ability to simulate complex multiphysics phenomena [1]. However, this improved realism may not necessarily lead to greater accuracy for situations where uncertainty/ignorance permeates the segmented anatomy, patient-specific boundary conditions or vascular material properties. I will argue that, for such situations, a stochastic approach where both outputs and model parameters share the same probabilistic formalism, is essential for a correct interpretation of the results.

Recent Advances

Uncertainty Quantification (UQ) in cardiovascular (CV) modeling has done giant steps in the past decade (see, e.g.,[2]), with recent advances able to achieve dramatic computational savings, making UQ increasingly appealing for clinical diagnosis and device design. Here, we focus on three complementary new trends. First, non-intrusive uncertainty quantification invariably relies on the solution of a large number of high-fidelity models, one for each realization of their random parameters. Thus ***ensemble simulation*** with explicit-in-time numerical integration appears as a promising new paradigm enabling simulatenous GPGPU solution of multiple models. Second, CV models are increasingly used for personalized predictions, requiring their parameters to be trained from a sparse collection of electronic health records [3]. In this context, I will discuss recent advances in Bayesian techniques for ***data assimilation***. Third, computationally inexpensive, low-fidelity 0D and 1D hemodynamic models can be automatically created as a by-product of the model generation process for 3D high-fidelity CV models. Recent advances in ***multi-fidelity Monte Carlo estimators*** combine all these formulations to compute 3D model statistics, achieving substantial computational savings [4].

Future directions

A number of exciting future directions have been proposed to facilitate the transition of stochastic cardiovascular modeling from academia to industry/health providers. Two align with our current research. The first consists in the ability to re-use the solution of expensive cardiovascular models through "active" repositories, made possible by novel Monte Carlo estimators, but a significant challenge to overcome is how to generate maps across models of the same anatomical region but from different patients. I will also discuss about new approaches to unify the solution of forward and inverse problems in UQ, using networks for probabilitstic resoning, designed to provide clinically relevant, probabilistic answers combining expert opinion, data and numerical models.

Daniele is currently an Assistant Professor in the Department of Applied and Computational Mathematics and Statistics at the University of Notre Dame, US. He obtained his Ph.D. in Applied Mathematics at Universita' degli Studi di Padova in 2013. He was a post-doctoral fellow at the University of California , San Diego in 2013-2015 and at Stanford University in 2015-2016. His research interests include stochastic analysis, uncertainty quantification, numerical modeling, data assimilation and use of computational models to inform clinical decisions under uncertainty. He has received a postdoctoral fellowship from AHA in 2015 and a DARPA Young Faculty Award in 2018.

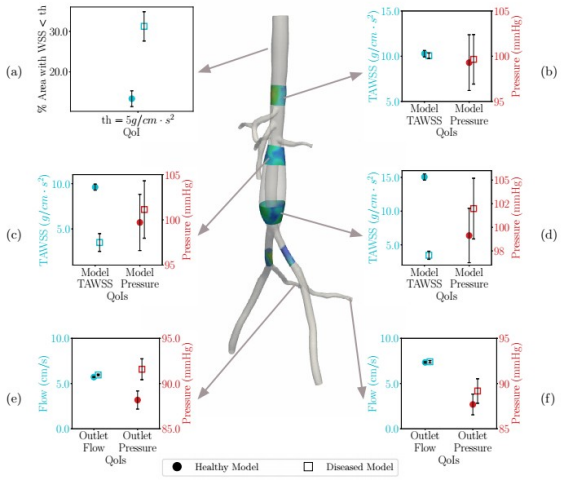

Figure 1: Multi-fidelity estimators and their confidence for pressure, flow and wall shear stress results in healthy/diseased abdominal aortic model.

References

1. Takizawa, K. et al., Math. Models Methods Appl. Sci., 24(12):2437-2486,2014.
2. Tran, J. et al. , CMAME, 345:402-428, 2019.
3. Schiavazzi, D.E. et al., IJNMBE, 33(3):e02799,2017.
4. Fleeter, C. et al., arXiv preprint arXiv:1908.04875, 2019.

Acknowledgments

The contributions of Xue Li (ensemble cardiovascular solver) and of Casey Fleeter, Gianluca Geraci and Alison Marsden (multi-fidelity Monte Carlo estimators) are gratefully acknowledged.

MECHANOSENSATION AND FIBROSIS IN THE CARDIOVASCULAR SYSTEM: TOWARD A MECHANICAL FRAMEWORK OF AGING PROCESS

Maurizio Pesce

Centro Cardiologico Monzino, IRCCS, Italy

Background

The common trait of several cardiovascular pathologies is the progressive deterioration of the homeostatic cell functions that provide adequate renewal of the matricellular components necessary to fulfill tissues mechanical functions. In the cardiac valves, the activation of the 'interstitial' cells and their differentiation into mineralized matrix depositing cells is the hallmark of stenotic pathology. In the myocardium, cellular stress conditions such as ischemia or dysmetabolism, determine activation and proliferation of myofibroblasts with a consequent extracellular matrix stiffening and maladaptive ventricular remodeling resulting into heart failure. In arteries, finally, phenotype changes in resident cells (fibroblasts, smooth muscle cells) modify wall compliance causing stiffening, calcification and intima hyperplasia. Being strictly connected to aging, these pathologies have been so far treated as an outcome of cumulative risk conditions affecting the self-renewal ability of the tissues.

Recent advances

Mechanosensation is the ability of the cells to 'sense' the physical properties of the surrounding 3D environment, e.g. stiffness, geometrical arrangement of extracellular matrix components, traction forces. This occurs by bi-directional signal transduction pathways generated by the cytoskeleton, controlling gene expression (outside-in effects) and phenotypic adaptive changes (inside-out effects) affecting tissue architecture, composition and renewal [1-3]. Decryption of these pathways has been impossible until recently for the lack of suitable tools to assess the behavior of cells under conditions reproducing the tissue physical environment and investigate these responses in the context of classical cell stressors and risk conditions. In an effort to create a systematic framework of cardiovascular fibrosis, my research Group has endeavored research project with the aim at understanding the relationships between physical sensing the paracrine control of pro-fibrotic stromal cells differentiation. In three different projects, we have found that exposure of patient-derived fibroblasts from valves, myocardium and vessels to environments with defined mechanical characteristics and/or cyclic mechanical stimulation elicits common molecular responses, highlighting the contribution of pathways so far validated only in other pathology models (e.g. cancer) [4 – 5]. These findings are unraveling an outstanding conservation of the fundamental mechanisms governing cellular physical perception and point to intracellular transduction of mechanical cues as one of the 'core' signaling mechanisms connected to chronic fibrotic progression. Moreover, since our unpublished data show cause-effect relationships between response of pathologic cells to mechanical cues and epigenetic modifications promoting cellular senescence, we hypothesize that pathologic physical perception of the 3D environment may also establish mechanical 'memories' associated to imbalanced tissue renewal.

Maurizio Pesce is since 2011 the Group Leader of the Cardiovascular Tissue Engineering Research Unit at Centro Cardiologico Monzino, IRCCS, in Milano. He has a MSc in Biology and a PhD in Embryology. He made his postdoctoral training at the Gene Expression Programme of the European Molecular Biology Laboratory (EMBL) in Heidelberg (Germany) on transcriptional regulation of stem cells pluripotency, and worked for ten years as a Senior Researcher in cardiovascular regenerative medicine before becoming independent. His research focuses on decryption of mechano-paracrine pathways in fibrotic diseases of the cardiovascular system and on engineering of living replacements for cardiovascular therapy. He is Author of 88 publications, 30 peer-reviewed abstract presentations, 8 book chapters and 3 patents.

Future directions

Our effort consists of defining mechanosensation in cardiovascular stromal cells using, as a model system, cells directly derived from patients with cardiovascular diseases. One of the advantages of this approach is that, by rigorous subject selections, it is possible to analyze mechanical perception of the cells directly in relationship with the typology of the risk conditions. Another advantage is that it is possible to test the effects of pharmacological and/or genetic interfering with the downstream molecular targets of mechanosensation. In our opinion, this will open the way to strategies to 'desensitize' cells to the effects of risk-dependent pro-fibrotic signaling, and will be crucial to reduce the burden of the aging process in the cardiovascular system.

References

1. Santoro and Pesce, Pharmacol Ther, 2017, 171:75-82
2. Ferrari and Pesce, Int J Mol Sci. 2019 Dec 19;21. E28
3. Garoffolo and Pesce, Cells, 2019 Dec 11;8. E1607
4. Santoro et al., Biomaterials, 181:268-279
5. Garoffolo et al., Theranostics, 2020, 10(6): 2597-2611

COMPUTATIONAL MODELING OF PRIMARY FIXATION OF TOTAL KNEE ARTHROPLASTY

Dennis Janssen

Radboud university medical center, Nijmegen, the Netherlands

Background

Total knee arthroplasty is one of the most successful orthopaedic interventions, with about one million operations annually in Europe alone [1]. This number is only expected to increase, particularly since patients increasingly are being treated at a young age. Although successful, TKA does not provide a life-long solution, particularly for younger patients, due to their longer life expectancy and more active lifestyle. The leading cause for revision is aseptic loosening, which is why biomechanical analyses primarily have focused on fixation mechanisms, and analyses of critical parameters that affect primary stability.

Recent Advances

Primary stability of uncemented implants relies on a press-fit fixation that is achieved during surgery by impacting slightly undersized implants onto the prepared bone surfaces. The combination of the frictional properties of the implant-bone interface and the generated compressive stresses provide the mechanical stability that is required to achieve long-term fixation through in- and ongrowth of bone.

Recent advances in computational models of primary stability recently have been focused on improving the prediction of the bone material response near the interface, on providing more realistic contact surfaces, and on improving frictional models of the implant-bone interface.

Traditionally, linear elastic material models have been used to represent the bone. However, implantations of TKA devices onto cadaveric femurs clearly show that permanent deformation and abrasion leave significant imprints into the bone, with bone being compacted and scraped off by the implantation process. [2] MicroCT analyses of these specimens demonstrated a very localized permanent bone deformation, with a depth of 1 to 2 mm [3]. Interestingly, a similar permanent deformation has been shown in hip replacement [4].

Since these phenomena obviously affect the primary stability, efforts have been made to provide a more realistic bone material behavior, by using material models that capture post-yield behavior of bone. Simulations reproducing femoral TKA experiments showed that models including plasticity indeed provide a better prediction of the implant-bone interface micromotions [5].

Another limitation of traditional simulations is the assumption of an idealized implant-bone contact surface. From analyses of actual implantations it is known that only a fraction of the implant surface is actually in contact with the bone, both in hip and knee replacements. Detailed geometries of the prepared bone cuts through optical surface scanning has recently been used to more realistically represent the actual interface conditions.

Finally, from high-resolution frictional experiments of the implant-bone interface can provide us with accurate representations of the contact mechanics, including the relative proportion of elastic deformation and actual relative displacements at the interface.

Dennis Janssen is the Head of Experimental Research of the Orthopaedic Research Lab of Radboud university medical center. He spent part of his PhD at SUNY Upstate Medical University in Syracuse, NY, obtained his degree in 2009. His research focuses on the analysis of fixation of orthopaedic implants, from fundamental mechanics of the implant-bone interface to population-based modelling and analysis of implant, patient, and surgery-related variations on implant fixation and peri-prosthetic bone adaptation. He is an author of 70+ peer-reviewed publications.

Future directions

The next step is to use the recently developed advanced techniques in larger cohorts of simulations that are required to investigate the effects of different sources of variability on the primary fixation, such as patient related factors (e.g. anatomy bone quality, BMI, activity level), implant variables (design, material, interference fit), and surgical variation (impaction, alignment, accuracy). Such population-based analyses are essential to produce robust results that are required to achieve significant improvements in TKA procedures.

Eventually, the ultimate step is to prove the value of these models against clinical data, radiological evaluations, and large implant registry studies.



References

1. OECD, “Health at a glance: Europe 2016,” Report, OECD Publishing, 2016.
2. Berahmani et al. Clin Biomech 51:1-9; 2017.
3. Rapagna et al., J Mech Behav Biomed Mater 97:278-287, 2019.
4. Bishop et al., J Biomech 47(6):1472-8, 2014.
5. Berahmani et al. J Biomech 61:137-143, 2017.

Acknowledgements

This work is based on past and current PhD projects of Sanaz Berahmani, Thomas Anijs, Esther Sanchez, and Corine Post.

PREDICTING TRAUMATIC BRAIN INJURY AT THE CUTTING-EDGE INTERSECTION BETWEEN ENGINEERING AND MEDICINE

Mazdak Ghajari

Design Engineering, Imperial College London, UK

Background

Traumatic Brain Injury (TBI) is the leading cause of death and disability in young adults and in the UK alone it has an estimated economic cost of £15b/year. TBI is a mechanical insult in nature. Head exposure to mechanical forces during sporting collisions, road traffic accidents, falls, assaults and in a military context can damage axons, neurons and blood vessels. Despite several decades of research on mechanisms of TBI and great progresses in the field, there is still limited understanding of the relationship between mechanical forces, brain injury and its progressive effects. One key challenge is predicting the distribution and intensity of forces during head loading and determining their link to the distribution and severity of pathology. Advances in computational modelling, imaging and histopathology now allow us to address this problem in new ways.

Recent Advances

We recently developed a high fidelity Finite Element (FE) model of TBI in human and used it to predict the distribution of maximal strains across the brain in three TBI cases, an American Football impact, a fall and a motorcycle accident [1]. Recent research has shown the prevalence of a dementia type disease in American Football players, called Chronic Traumatic Encephalopathy (CTE) [2]. CTE pathology is defined by the accumulation of tau proteins in depths of sulci. Our model predicted maximal strains in sulcal regions and we found converging evidence from Diffusion Imaging data of nearly 100 TBI patients of the distribution of white matter abnormality in sulci. We extended this work by simulating 148 American Football head collisions, which also confirmed that strains were significantly larger in sulci than gyri [3].

We have recently validated our computational approach using controlled cortical impacts (CCI) in a rat model of TBI [4]. Two weeks post-injury, we performed multi-shell high-field MRI and quantitative histopathology to determine white matter abnormalities in corpus callosum. We also performed high fidelity FE modelling of the injuries. We found a clear relationship between the predicted strains in Corpus Callosum and changes in diffusion (Fractional Anisotropy, Neurite Density) and histopathology measures (astrocytes and microglia).

Vascular injury is a key facet of acute TBI management. We have incorporated detailed anatomy of vessels, with a nearly 5 microns resolution, in our rat model of TBI to test whether we can predict patterns of vascular injury seen in SWI images of injured animals and determine the role of vascular anatomy in producing pathology [5]. We are extending this approach to incorporate detailed anatomy of vessels in a human model of TBI [6].

Mazdak Ghajari is an associate professor in Design Engineering, Imperial College London. He obtained his PhD from Imperil College in 2011 and secured an Imperial College research fellowship to establish the TBI biomechanics area at Imperial College, bringing together engineers, neuroscientists, biologists and designers. He is a member of the Centre for Blast Injury Studies and British Standardization Committee for head protection. His work brought him the young researcher award of the International Research Council of Biomechanics of Injury (IRCOBI), where he currently is a member of the scientific review committee.

TBI management can be improved if we can predict risk of TBI from sensor data. We are currently using a UK-based in-depth road collisions database to map out the severity of TBI in victims and test whether collision characteristics measured by vehicle installed sensors, such as delta-V, can predict TBI severity [7].

Future directions

Understanding TBI and addressing its prevention, diagnosis, prognosis and treatment, require an interdisciplinary approach. We had a unique opportunity to establish strong collaboration between faculties of engineering and medicine, and we will build on this to develop prevention systems using modelling and new materials and to understand progressive effects of TBI, which are associated with dementia.

References

1. Ghajari et al, Brain, 7;140(2), 2017.
2. McKee et al, Neuropath and Exp Neurology. 68, 2009.
3. Kim et al, ESB 2020.
4. Donat et al, Brain, Submitted.
5. Khosroshahi et al, ESB 2020.
6. Duckworth et al, ESB 2020.
7. Baker et al, ESB 2020.

Acknowledgements

I would like to acknowledge the key input from colleagues in Department of Brain Sciences, Prof David Sharp, Dr Magdalena Sastre and Prof Steve Gentleman, the members of the HEAD lab (https://www.imperial.ac.uk/human-experience-analysis-design/) and support from Transport Research Laboratory, Centre for Blast Injury Studies, Wellcome Trust, EPSRC and Royal Society.

NUCLEAR PORE COMPLEX MECHANOBIOLOGY

Mohammad R. K. Mofrad

Departments of Bioengineering and Mechanical Engineering, University of California Berkeley

Background

The nuclear pore complex (NPC) is a vital nanomachinery that resides in the nuclear envelope (Figure 1) and functions as the primary gateway for nucleocytoplasmic transport in eukaryotic cells [1]. The building blocks of the NPC are a family of proteins called nucleoporins (nups). Nearly one-third of nups contain the hydrophobic, natively unfolded phenylalanine-glycine (FG)-repeat motifs, which are believed to play the key role in the transport of cargos through the NPC. Despite the high throughput of ~1000 translocations per NPC per second, the NPC strictly controls and regulates the bi-directional passage of individual cargos. While cargos smaller than ~5–9 nm can passively diffuse through the NPC, larger cargos up to ~39–40 nm actively transport through the pore, which only occurs if they are bound to a nuclear transport receptor (NTR). Inert cargos that are not small enough to passively diffuse, and lack NTRs to actively transport, are prohibited by the NPC from entering the nucleus. Despite the vital importance of the NPC and nucleocytoplasmic transport in cell biology, little is known about the mechanics and dynamics of the NPC and nucleocytoplasmic transport.

Recent Advances

The mechanism of nucleocytoplasmic transport is an active topic of debate and has led to the suggestion of several hypotheses to explain the rapid, yet selective, nature of the transport processes. The complex, yet delicate, geometry of the NPC and the fine spatiotemporal resolution at which the nucleocytoplasmic transport takes place have so far hindered the direct, experimental investigation of this exquisite nanopore. Computational models offer a strong platform for capturing the nanosecond-scale interactions between cargo and FG-repeats in a nanometer spatial resolution to shed light on the details of transport phenomena through the nuclear pore.

Using a hybrid of computational modeling approaches, ranging from finite element [2] to coarse-grained Brownian dynamics [3] to molecular dynamics techniques [4] to new agent-based modeling methods [5-7], we study the structure and function of the nuclear pore complex and the dynamics of nucleocytoplasmic traffic.

Future directions

Understanding the biomechanics of the nuclear pore complex and nucleocytoplasmic transport will broadly impact our understanding of viral diseases and may revolutionize therapeutic approaches (e.g. gene therapy) and open the door to many industrial applications of biomimetic artificial nanopores.

Mohammad R. K. Mofrad is a professor of Bioengineering and Mechanical Engineering at the University of California Berkeley. His research program (http://mechano.bio) combines the state-of-the-art molecular and multiscale biomechanics, computational biology and bioinformatics, and statistical learning approaches toward understanding and diagnosis of human diseases. Prof. Mofrad is a Fellow of the American Institute for Medical and Biological Engineering (AIMBE).

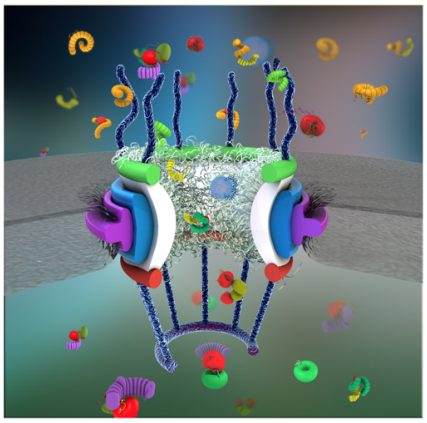

Figure 1: A schematic representation of the NPC structure with the cargo-complex indicated as an NTR-bound blue sphere inside the central channel. [1].

References

1. Jamali T, Jamali Y, Mehrbod M, Mofrad MRK. "Nuclear Pore Complex: Biochemistry and Biophysics of Nucleocytoplasmic Transport in Health and Disease." Int. Rev. Cell and Molecular Biology, 2011; 287: 233-286.
2. Wolf CB, Mofrad MR. "On the octagonal structure of the nuclear pore complex: insights from coarse-grained models." Biophysical Journal. 2008; 195(4):2073-2085.
3. Moussavi-Baygi R, Mofrad MRK. "Rapid Brownian Motion Primes Ultrafast Reconstruction of Intrinsically Disordered Phe-Gly-Repeats Inside the Nuclear Pore Complex." Scientific Reports, 2016, 6: 29991.
4. Zhao C, Mahboobi SH, Moussavi-Baygi R, Mofrad MRK. "The Interaction of CRM1 and the Nuclear Pore Protein Tpr." PLoS One, 2014; 9(4):e93709.
5. Azimi M, Bulat E, Weis K, Mofrad MRK. "An agent-based model for mRNA export through the nuclear pore complex." Molecular Biology of the Cell, 2014; 25(22):3643-53.
6. Soheilypour M, Mofrad MRK. "Agent-based Modeling in Molecular Systems Biology". BioEssays, 2018 Jul;40(7):e1800020.
7. Soheilypour M, Mofrad MRK. "Quality Control of mRNAs at the Entry of the Nuclear Pore: Cooperation in a Complex Molecular System". Nucleus, 9(1):202-211, 2018

BIOFABRICATION OF FUNCTIONAL LIVING TISSUES: THE CROSSROAD OF TWO RESEARCH SOCIETIES

Miguel Castilho [1,2,3]

[1] *Department of Orthopaedics, University Medical Center Utrecht, Utrecht, The Netherlands*
[2] *Department of Biomedical Engineering, Eindhoven University of Technology, Eindhoven, The Netherlands*
[3] *Regenerative Medicine Center Utrecht, Utrecht, The Netherlands*

Background

Every day, approximately 18 people die in Europe alone due to a shortage of available human donor organs. To overcome this, great efforts have been devoted to Regenerative Medicine (RM) strategies that could potentially restore tissues and organs. Since its first appearance regenerative strategies have come a long way from the first stem-cell transplantation to the three-dimensional (3D) biofabrication of artificial tissue-like structures today [1]. Biofabrication allow the *in vitro* fabrication of biological constructs with precise combinations of cells and biomaterials, while digital manufacturing enables biological structures to be shaped into the geometry of the target tissue or organ. Biofabrication comprises a large toolbox of a wide range of fabrication strategies of which the most established are droplet, extrusion, laser- and light- assisted bioprinting. Each of these strategies has a different working principle, which has its own associated advantages and drawbacks with regards to cell processing, resolution and material selection. Up to now, researchers have mostly been adopting a single fabrication strategy and conventional computer aided design (CAD) tools based on the target tissue composition and/or size. However, none of these fabrication strategies, or design tools, taken individually have been able to recreate biological structures with the functional richness, multiscale structure and size of a living tissue.

Recent Advances

Recent evidence suggests that the simultaneous use of complementary fabrication processes can take us closer to the heterogenous composition and complex multiscale organization of living tissues. In addition, advanced digital design technologies, including topology optimization and soft computing techniques, have opened new avenues to the design and manufacture of biological systems. This presentation will provide a comprehensive overview of the recent advances in 3D biofabrication technologies and digital design technologies, with the aim to fabricate more functional tissue structures. The main topics that will be covered are,

(1) use of single deposition biofabrication methods for living tissue fabrication: mimicking tissue shape but not function

(2) recapitulate functionality of native tissues by combining complementary manufacturing technologies into a single biofabrication platform. Particular focus will be given to the extrusion of thermoplastic supports and cell-laden hydrogels for bone and cartilage tissue repair [2,3]

(3) use of multi-objective and topology optimization design tools coupled with (bio) fabrication to create materials with locally tuned structures and properties that can better resemble biological materials [3].

Miguel Castilho is currently an Assistant Professor in (Bio)fabrication at the Department of Orthopedics, University Medical Center Utrecht and a guest researcher at the Department of Biomedical Engineering, Eindhoven University of Technology. He obtained his PhD in Biomedical Engineering at the University of Lisbon in 2015 and from 2015-2018 performed his postdoctoral studies at University Medical Center Utrecht. His research focus lies on combining 3D printing technologies and multi-scale modelling to design and fabricate bio-inspired materials along all different length scales. He is an author of > 24 publications in peer- reviewed journals, and several contributions to International Conferences.

Future directions

The last part of the presentation discusses an even more enticing feature in biological materials fabrication which is the integration of advanced digital design and artificial intelligence-powered real-time monitoring tools with multi-technology bioprinting to allow for high-throughput biofabrication of functional living tissues. With this presentation I expect to steer the biomechanical community to the scientific challenges in the (recent) bio fabrication field and promote bridges between the two societies.

References

1. Moroni et al. Nature Reviews Materials, 2018.
2. de Ruijter et al., Adv Healt Mat, 8, 1800418, 2019
3. Castilho et al., Acta Biomaterialia, 95, 297 - 306
4. Castilho et al., J Mech Behav Biomed, 65:344-355, 2017.
5. Villette et al. Biomech. Model. Mechanobiol. 16: 2077-2091, 2017

Acknowledgements

The author acknowledge the support from the strategic alliance University Medical Center Utrecht – Utrecht University – Eindhoven University of Technology and the contribution of Claire Villete, Stephen Beirne, Keita Ito and Jos Malda

MARKERS OF WALL VULNERABILITY IN AORTIC ANEURYSMS

Elena S. Di Martino

Department of Civil Engineering, Centre for Bioengineering Research and Education, Libin Cardiovascualr Institute, University of Calgary, Canada

Background

As the aorta ages, the balance of synthesis and degradation of extracellular matrix (ECM) results in modified constituents ratios with less and more degraded elastin. These changes are reflected in macroscopic changes, increased stiffness and energy loss. As elastin fails the load is increasingly transferred to collagen, further stiffening the artery's structure (1). Low grade pro-inflammation has recently been linked to arterial aging and elastin loss (2). Aortic aneurysms share many of the hallmarks of vascular aging, including elastin fragmentation and loss, newly deposited collagen, cell death and inflammation, although these adverse changes often occur prematurely and affect the aorta in a very heterogeneous manner.
The natural history of an aneurysm is progressive weakening of the wall; when left untreated the end result is rupture or dissection often with fatal consequences for the patient. The only proxy for an aneurysm's rupture potential currently in use is the repeated assessment of key geometric indices, such as the maximum diameter; however, this approach has failed at accurately representing individualized risk (3).

Recent Advances

At a young age, the mechanical properties of the aorta in the physiologic range are almost linear. As the artery ages, the stress-strain response shows increased anisotropy as well as a distinct 'stiffening' represented by a higher effective modulus of elasticity. An essential limitation of computational simulations for biomechanics assessments of arteries is the assignment of material properties based on population-average material parameters that do not account for patient-to-patient and intra-patient local variability. To this end we developed methods to compute the mechanical deformation of the vascular wall in vivo from dynamic CT or MR images (4).
The second important ingredient was establishing a mechanistic link between the mechanical milieu of the aorta and progressive wall weakening (5). In brief, we hypothesize that the aorta remodels locally following a cascade of factors that involve altered hemodynamics and aberrant remodelling of the medial layer, including loss of elastin and proteoglycans and poorly organized collagen fibres. Combining hemodynamic descriptors and non-invasive in-vivo strain analysis performed on ECG-gated dynamic CT images, we defined a novel index, the Regional Rupture Potential, that provides a surrogate measure of aortic weakening and rupture risk for individual aortas (6). The index correlates significantly with mechanical weakening and upregulation in genes related to ECM degradation.

Elena Di Martino is currently Professor at the Department of Civil Engineering and Director of the Centre for Bioengineering Research and Education, University of Calgary, Canada. She obtained her PhD in Cardiovascular Pathophysiology at the University of Milano in 1999. She was a post-doctoral fellow at Politecnico of Milano in 2000 and at the University of Pittsburgh 2001-2003. She is a member of the Libin Cardiovascular Institute of Alberta. Her present research mainly focuses on Cardiovascular Tissue Mechanics. She is an author of 48 publications in peer- reviewed journals, several chapter books, three patent applications, and more than 100 contributions to National and International Conferences.

Future directions

Future directions include in-situ functional imaging on a custom made device and the assessment of RNA expression from the patient's blood as a mean to increase sensitivity of the RRP.

Figures

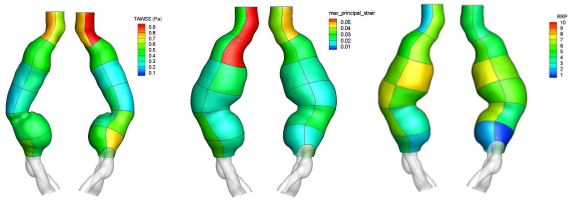

Figure 1: Wall Shear Stress (at the lumen), Maximum Principal Strain and Regional Rupture Potential (RRP) index computed on patches on the aortic wall surface for a AAA case example.

References

1. Akhtar et al., J Mech Behavior Biom Mat, 64:10-7, 2016.
2. Wang et al. J Vasc Res, 55(4):210-23, 2018.
3. Kuivaniemi et al. Expert Rev Cardiov Ther. 13(9):975–987, 2015.
4. Satriano et al, J Biomech, 48(2):354-60, 2015.
5. Martufi et al., Frontiers Cardiov Med, 5 82, 2018.
6. Forneris et al. J Vasc Surg: Cases and Innovative Techniques, in press.

Acknowledgements

Acknowledgements go to the Biological Tissue Mechanics Laboratory (Dr. A. Forneris, M. Nightingale, R. Beddoes, L. Gomez, Dr. T. Sigaeva), Dr. Rinker, Mr. Kennard, Dr. Fedak, Dr. Flores, and Dr. White at the University of Calgary.

PREDICTING FLOW AND PRESSURE IN THE CIRCULATION USING STRUCTURED–TREE MODELS

Nicholas A. Hill

School of Mathematics and Statistics, University of Glasgow, Scotland, U.K.

Background

To quote Thomas Young FRS (1773-1829), who first developed the theory of wave propagation in elastic tubes, ` … the enquiry, in what manner, and in what degree, the circulation of the blood depends on the muscular and elastic powers of the heart and of the arteries, supposing the nature of those powers be known, must become simply a question belonging to the most refined departments of the theory of hydraulics.' This is as true today as it was in 1809, since the range of scales from centimetres to micrometres, the number of vessels (~10^8), the nonlinear viscoelasticity of the blood vessel walls, the non-Newtonian rheology of the blood, and physiological control mechanisms, all pose major computational challenges. Consequently, sophisticated mathematical modelling is being developed to understand the key principles on which the circulatory system works, and also to meet the clinical need for patient-specific solutions to predict outcomes following strokes, heart attacks, and vascular dissections and aneurysms.

It is currently too time-consuming to compute pulsatile 3D blood flow in more than a few elastic blood vessels and bifurcations, so the most useful approach is to solve for the cross-sectional averaged '1D' flow and pressure in 100+ of the largest vessels. The boundary conditions at the end of the tree of large vessels are often approximated by windkessels (small networks of 3 or 4 compliances and resistances), the parameters of which are tuned using *ad hoc* methods to obtain realistic flows. While useful in many applications, these models cannot capture the details of flows and disease in the smaller vessels. Important progress was made in 2000, when Olufsen [1] introduced structured trees to approximate the geometry and material properties in the smaller arteries of the vascular beds of the systemic circulation. They used the small vessel radius to linearize the governing equations and encapsulate the fluid dynamics by computing the impedance of each structured tree.

Recent Advances

In collaboration with Olufsen, my group has developed the theory and application of structured trees to calculate flow and pressure in the vascular beds [2], simulate the pulmonary circulation and study wave intensity [3,4], and couple the left ventricle to the systemic arteries [5]. Most recently, we have applied Bayesian statistical parameter estimation to study pulmonary hypertension in a mouse model of the disease [6,7].

Nicholas Hill FIMA is Simson Professor of Mathematics at the University of Glasgow, and Executive Director of the SofTMech Centre which specializes in Mathematical and Computational Modelling of Soft Tissue Mechanics. He obtained his PhD in Applied Mathematics at Imperial College, London in 1985. His research interests include physiological fluid mechanics and the circulation, the mechanobiology of the large arteries including dissection, discrete-to-continuum upscaling from cells to tissue, and bioconvection. He is an author of 75+ publications in peer-reviewed journals, and is on the Editorial Boards of the Journal of Mathematical Biology, and Mathematical Medicine & Biology.

Future directions

The objective of this research is to complete a full multiscale simulation of the full cardiovascular system, and the next key steps that I will present are constructing a model for the flow in the capillaries surrounding the alveoli, and the perfusion of the cardiac wall in the beating heart.

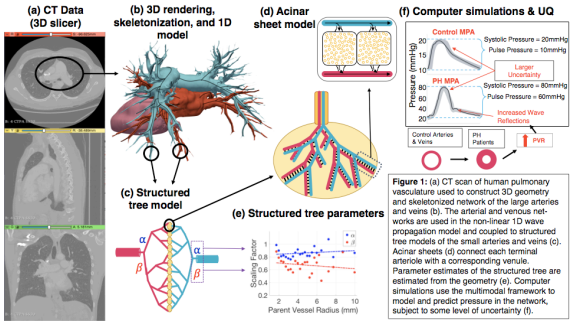

Figure 1. Diagram illustrating the key steps in constructing a model of the pulmonary circulation.

References

1. Olufsen MS *et al*. Ann Biomed Eng, 28:1281-1299, 2000.
2. Olufsen MS *et al*. J Fluid Mech, 705:280-305, 2012.
3. Qureshi MU *et al*. BMMB, 13: 1137-1154, 2014.
4. Qureshi MU & Hill NA, J Math Biol, 71:1525-1549, 2015.
5. Chen WW *et al*. J Biomech, 49:2445-2454, 2016.
6. Paun LM *et al*. Stat Neerlandica, 72:306-338, 2018.
7. Qureshi MU *et al*. BMMB, 18:219-243, 2019.

Acknowledgements

Profs Mette Olufsen & Mansoor Haider, Mitchel Colebank NCSU. Umar Quereshi, Kitware. Profs Dirk Husmeier & Xiaoyu Luo, Hao Gao, Mihaela Paun, Jay Mackenzie, Gareth Vaughan, Weiwei Chen, University of Glasgow. Drs Christopher Sainsbury & Martin Johnson, NHS Scotland. EPSRC.

ON THE THERMODYNAMICS OF CELL SPREADING AND CONTRACTILITY

Patrick McGarry

National University of Ireland Galway, Ireland

Background

Our early computational models of cell-substrate interactions revealed that the effective stiffness of the cell and strength of its adhesion actively evolves with increased spreading [1]. Subsequent active models of stress fibre evolution and contractility were shown to provide accurate predictions of experimentally measured active force generated by cells on micro-pillars [2] and cells subjected to compression [3]. Our models were then extended to incorporate dynamic contractility [4] providing accurate predictions of cell forces induced by dynamic AFM loading [5]. Our thermodynamic model of actin-myosin cross-bridge cycling in stress fibres provides a physiological explanation for empirically observed "fading memory" effects in dynamically loaded cells [6]. In our first study of free energy as a driver of cell spreading we identified low (or minimum) free energy spread states within a limited phase space of axisymmetric configurations [7]. This approach provides a reasonable prediction of the trend of increased cell spreading and cytoskeletal formation on stiffer substrates, as observed experimentally by Engler et al. [8], in addition to accurate predictions of stress fibre alignment on "V" shaped ligand patches (Fig.1a).

Recent Advances

Cells never attain an equilibrium minimum free energy state while alive. Thermodynamically motivated statistical mechanics modelling of cell spreading recognizes the non-deterministic nature of cell spread states and predicts the statistics of biological observables (e.g. cell area, aspect ratio etc.) under the constraint that the cell maintains a homeostatic state [9,10]. This framework predicts an ensemble of cell spread states as a function of the surrounding physical environment (Fig.1b). The emergence of an energetic competition (between reducing free energy due to stress fibre contractility and increasing elastic free energy due to passive cytoplasm stretching) within the statistical mechanics framework of the homeostatic ensemble provides a significant advance in current understanding of the influence of ligand density and substrate stiffness on cell spreading.

Future directions

The thermodynamically motivated statistical mechanics framework is currently being extended to predict the distribution of spatial positions and spread morphologies of cells in three dimensional tissue scaffolds. Such an approach will guide the fabrication of synthetic tissue by uncovering the thermodynamic mechanism by which cells actively respond to the application of multiaxial mechanical loading to tissue constructs.

Dr Patrick McGarry's research focuses on cell and tissue biomechanics. He has published over 75 journal papers and over 100 conference abstracts/proceedings. He has been awarded five major research grants by Science Foundation Ireland in the areas of cell, artery and cardiac biomechanics. His research group has graduated 16 PhD students and has been awarded ten major international research prizes. In 2017 he was appointed as Visiting Professor at the Technical University of Graz and as Faculty Fellow at the University of Texas at Austin. He held a visiting faculty position at the University of Cambridge in 2018.

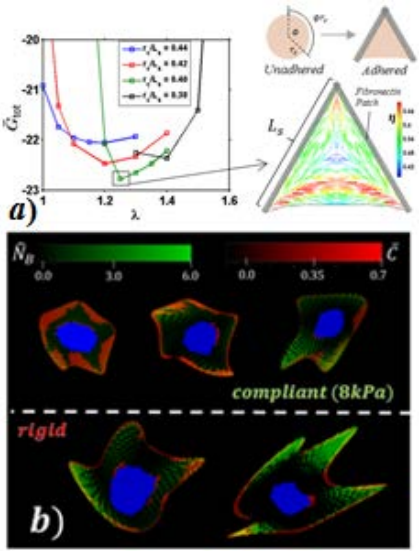

Figure 1: a) Minimum free energy prediction of spread cell on a "V" ligand patch [7]; b) statistical mechanics predictions of cells on compliant/rigid substrates [10].

References:

1. Mcgarry et al, JMPS, 56(4): 1554-1565, 2008.
2. McGarry et al, Phil. Trans. R. Soc., 367:3477–3497, 2009
3. Weafer et al, Bull Math Biol 75:1284, 2013.
4. Reynolds, McGarry, Acta Biomat, 27: 251–263, 2015.
5. Weafer et al, Acta Biomat, 27: 236–250, 2015.
6. McEvoy et al, BMMB, 18: 921–937, 2019.
7. McEvoy et al, JMBBM,74: 283-295, 2017.
8. Engler et al, Eur. Cells Mater. 6: 7–8, 2003.
9. Shishvan et al, BMMB, 17: 1631, 2018.
10. McEvoy et al, Biophys J, 115(12): 2451-2460, 2018.

Acknowledgements: Science Foundation Ireland (18/ERCD/5481)

IMAGE-BASED SHEAR STRESS ANALYSES IN HUMAN CORONARY ARTERIES: WHERE ARE WE?

Frank Gijsen, PhD

Biomedical Engineering, department of Cardiology, Erasmus MC, Rotterdam, The Netherlands

Background

Wall shear stress (WSS) is sensed by endothelial cells via various cell components, which (de)activate intra-cellular pathways leading to regulation of gene and protein expression. This force-induced regulatory process plays a continuous role in the development, growth, and remodelling of the vascular system. Endothelial cells exposed to high, unidirectional WSS assume a quiescent state, while endothelial cells exposed to low and/or oscillating WSS are activated, displaying a pro-inflammatory state. As such, WSS is of eminent importance for the initiation and progression of atherosclerosis and development of in-stent restenosis in human coronary arteries. To determine WSS patterns in these arteries accurately, we rely on image-based computational fluid dynamics (CFD). This combination of techniques provides us with insights into the role of WSS in human coronary artery disease[1].

Recent Advances

In vitro and *in vivo* studies in animals demonstrate that WSS influences the development of atherosclerosis. As such, the major clinical interest in WSS arises from its ability to identify patients at risk for future cardiovascular events or complications after stent placement. Although several clinical CFD studies seem to reflect the observations of *in vitro* and *in vivo* animal experiments, findings in human patients are far from unanimous or clear-cut. Both low and high WSS have been associated with aspects of plaque progression and vulnerability in clinical imaging studies, but the precise relationships remain unclear and studies are sometimes contradictory. Low WSS has been associated with future angiographically-driven revascularization and non-culprit cardiovascular events. High wall shear stress has been associated with future myocardial infarctions.

Dr. Gijsen obtained his PhD on cardiovascular flow modelling from the Eindhoven University of Technology. He moved to the Erasmus MC in 2001 to apply engineering tools, mainly focusing on image-based biomechanical modeling, in a clinical setting. Dr. Gijsen is an Associate Editor of the Journal of Biomechanics, co-founder and organizer of the yearly symposium on 'Cardiovascular Biomechanics in Vascular Biology and Cardiovascular Disease', (co-) author of more than 100 scientific papers with over 6000 citations.

In stented coronary arteries, it was demonstrated that low WSS after stent implantation was associated with neointimal hyperplasia formation. After bioresorbable scaffold implantation, low WSS also promotes neointimal hyperplasia and contributes to scaffold healing with normalisation of wall shear stress[1].

Future directions

We can use WSS analyses in stent design, to optimize strut thickness and shape for the local hemodynamic forces. We also envision application of WSS metrics in native arteries by generating WSS maps, subdivide them into different regions, and use these maps to predict location of plaque progression and plaque rupture.

References

1. Gijsen et al., European Heart Journal, 40 (41), 2019.

Acknowledgements

I would like to acknowledge all students, clinical partners, and national and international collaborators who contributed to this work. I specifically want to acknowledge Jolanda Wentzel, Anton van der Steen and Patrick Serruys.

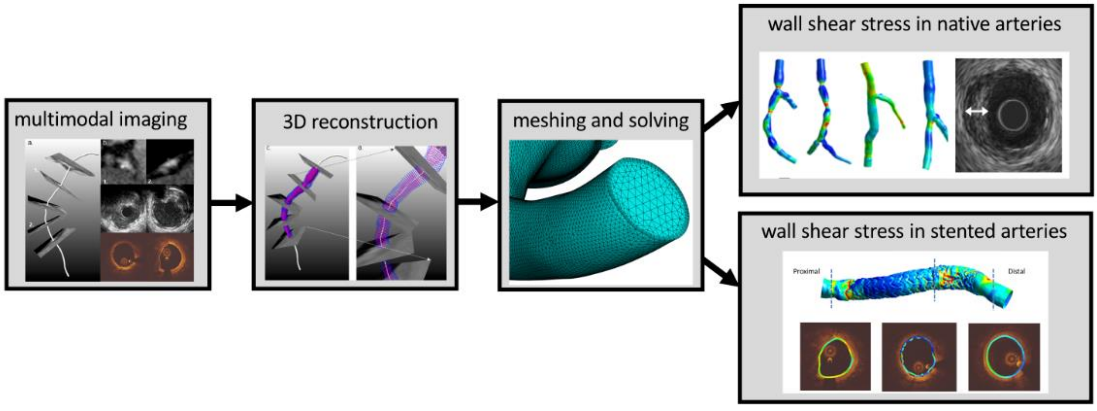

Figure 1: WSS analysis in human coronary arteries: going from imaging to prediction.

MULTISCALE MODELING OF VEIN GRAFT ADAPTATION: A PREDICTIVE TOOL TO IDENTIFY TARGETS FOR IMPROVED CLINICAL OUTCOMES

Scott Berceli, M.D, Ph.D

University of Florida, U.S.A.

Background

Arterial occlusions, manifested through myocardial, cerebrovascular, and lower extremity ischemia, accounted for 26% of all worldwide deaths in 2016. Although vein bypass grafting can provide immediate improvements in perfusion, the half-life of these treatments is measured in months. Excised from the venous system and implanted into the arterial tree, the acute change in hemodynamic forces induces an injury-response, which promotes progressive thickening of the wall, narrowing of the lumen, and graft occlusion.

In an effort to identify novel therapeutic strategies, researchers have applied a wide variety of approaches to mitigate this response. Despite incremental progress, no durable treatments have become a clinical reality.

Strategies to date have focused largely on reductionist strategies and static models to describe the physical and biological components of the disease. Embracing the complexity of the problem, our multidisciplinary team has developed the experimental and multiscale modeling tools that are required to predict the dynamics of vein graft adaptation as it responds to the local environment, essential components to modulating the trajectory of the vein graft response and identifying opportunities to improve long-term durability.

Recent Advances

Over the past decade, we have developed a multiscale model of vein graft adaptation that uses molecular-level genomic information to provide cellular-level predictions of proliferation and matrix synthesis that yield tissue-level estimations of the graft architecture. Progression through these various scales is accomplished through the iterative process of module development and experimental validation, with each subsequent level of complexity built on modules fuelled by *in vivo* experimental results. Upon compilation, the final model utilizes an iterative loop, employing hemodynamic, gene regulatory, and cell kinetic modules that are interfaced through an agent-based model to predict changes in tissue architecture.[1-3]

Using our novel rabbit vein graft model, samples were collected at times ranging from 2 hours to 28 days for mRNA transcriptional profiling and histologic analysis. Stochastic optimization and clustering algorithms were used to examine the 9,792 unique genes and identify the subset of genes (n=283) that map to the core biologic processes of graft wall thickening.[4-6] Through a systematic evaluation of the gene regulatory network, we identified those key hub genes in which early inhibition or augmentation lead to significant reductions in wall thickening and enhancement in lumen preservation. Focusing on the 71 upstream signaling genes as opportunities to influence the network at multiple locations, 23 of these genes were identified to have a significant impact on graft architecture 1 month after implantation. Notably, TRIM24 is predicted to induce the largest lumen radius and has thus been identified as the potential best candidate. Six have been selected to move forward into the in-vitro testing phase, four genes predicted to have a positive impact (TRIM24, CSF2, FGF2, and NOTCH1), and two genes are predicted to have a negative effect on the system (TP53 and COL4A3).

Scott Berceli is currently the Vice-Chair of Research and the Axline Basic Science Professor of Surgery and Bioengineering at the University of Florida. He also serves as the Chief of Vascular Surgery at the Malcom Randall VAMC. He received his M.D. and Ph.D. in Chemical Engineering from the University of Pittsburgh, followed by surgical training at Harvard University and the University of Washington. His research focuses on the role of physical forces in modulating physiologic and maladaptive vascular adaptation. He has authored 131 peer-reviewed publications and 16 book chapters. He has been funded by the NIH, NSF, VA, and several private foundations over the last 20 years.

Future directions

Employing a high-throughput cell culture system and siRNA gene silencing/AAV augmentation strategies, we will investigate the impact of key hub gene modulation on cell proliferation, apoptosis, matrix production, matrix degradation, and cell motility. Examining these vectors both in isolation and in combination, the most promising gene sets will move forward into a large animal validation model for ultimate translation to a therapeutic tool to improve vein graft survival.

References

1. Casarin et al., PLoS One, 12:e0187606-e0187606, 2017.
2. Garbey, et al., J Theor Biol, 429:149-163, 2017.
3. Garbey,et al., Biomech Model Mechanobiol 18:29-44, 2019.
4. Berceli, S. A., et al., Vascular 17:2-9, 2009
5. Wang, J. et al. Nucleic Acids Res 41:e97-e97, 2013.
6. Wang, Y. et al., Brief Bioinform, 13, 162-174, 2011.

Acknowledgements

Dr. Marc Garbey, Dr. Stefano Casarin, and Jared Rozowsky were integral to this work. Support received from NIH Grants 1R01HL095508 and 1U01HL119178.

3D STRETCH AND STRESS DISTRIBUTIONS OF HUMAN ARTERIES BASED ON TWO-LAYER MODEL CONSIDERING RESIDUAL STRESSES

Keiichi Takamizawa

4-17-10-811 Fuda, Chofu, Tokyo 182-0024, Japan

Introduction

There exist detailed data for the mechanical properties of human arteries [1,2], but the stretches and stresses in the arterial wall have not been analysed in detail. The author analysed the distributions of stretch ratios and stresses in human carotid arteries with considering circumferential and axial residual strains based on the two-layer model. It was found that the stress distributions in the human arteries have been significantly different from those of animal arteries even under physiological conditions. Those were also analysed under supraphysiological conditions.

Method

The author analysed the distributions of stretches and stresses accounting for the circumferential and axial residual deformations, and the morphological and mechanical data in published literature [1,2]. The stress-free configurations are the arterial rings opened by radial cut and axial strips curing for the adventitia and media separated from the intact arterial segments. For human arteries, the separation of two layers is relatively easy compared to animal arteries. Therefore, we can analyse the distributions of stretches and stresses based on two-layer model. The author used a strain energy function as follows [3]:

$$W = \frac{\mu}{2}(I-3) + \frac{k_1}{k_2}(\exp\{k_2[(1-\varsigma)(I-3)^2+\varsigma(K-1)^2]\}-1) \quad (1)$$

where μ and k_1 denote constants with energy density dimension, respectively. I and K are the invariants:

$$I=\lambda_\theta^2+\lambda_z^2+\lambda_r^2, \quad K=\lambda_\theta^2\cos^2\varphi+\lambda_z^2\sin^2\varphi \quad (2)$$

where λ_θ, λ_z, and λ_r are stretch ratios of circumferential, axial, and radial directions with reference to the stress-free configuration, respectively. The material parameters of k_2 and $\varsigma\in[0,1]$ are nondimensional values. The angle of φ represents mean fibre angle against the circumferential direction with a bimodal fibre distribution although this angle was not determined a histological observation. The parameter ς represents the weight of the fibre component in the arterial wall. The principal stresses are determined as follows:

$$\sigma_{ii}=-p+\lambda_i\frac{\partial W}{\partial\lambda_i} \quad (\text{not sum with } i) \quad (3)$$

where p represents undetermined Lagrange multiplier due to the incompressibility of the arterial wall and i denotes θ, z, or r.

Results

The author used the mean material parameters in the strain energy function in the published paper [2] as the values for the human common carotid artery. The intraluminal pressure vs outer radius relationships and the intraluminal pressure vs axial stretch ratio relationships maintaining the axial force were calculated before the stress analysis. Figure 1 shows the calculated results of the stress distributions in the arterial wall.

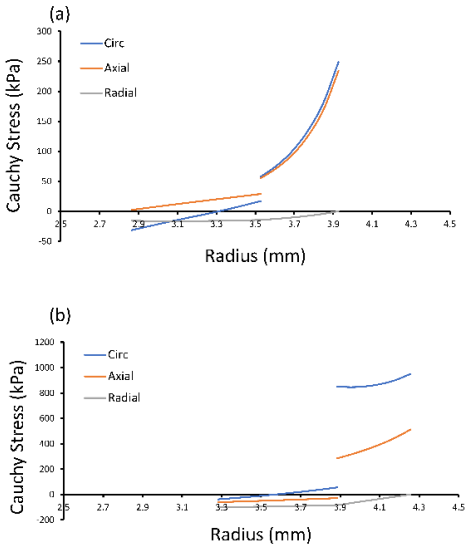

Fig. 1: The stress distributions at the intraluminal pressures of 16 kPa (a) and 100 kPa (b). The axial stretch ratio is 1.1 with reference to the intact unloaded state.

Conclusions

The circumferential and axial stresses at the intraluminal pressures of 16 and 100 kPa were high in the adventitia compared to the media and increased from the inner surface to the outer surface.

References

1. Sommer G et al, Am J Physiol Heart Circ Physiol, 298: H898-H912, 2010.
2. Sommer G and Holzapfel G A, J Mech Behav Biomed Mater, 5:116-128, 2012.
3. Holzapfel G A et al, Am J Physiol Heart Circ Physiol, 289:H2048-H2058, 2005.

3D CHARACTERIZATION OF CRACK PROPAGATION DURING THE ONSET OF A DISSECTION USING X-RAY MICROTOMOGRAPHY ON PRESSURIZED AORTIC SEGMENTS

Joseph Brunet (1), Baptiste Pierrat (1), Éric Maire (2), Jérôme Adrien (2), Nicolas Curt (1), Brooks Lane (1), Pierre Badel (1)

1. Mines Saint-Etienne, Univ Lyon, Univ Jean Monnet, INSERM, U 1059 Sainbiose, Centre CIS, F - 42023, Saint-Etienne, France; 2. INSA-Lyon, Université de Lyon, MATEIS CNRS UMR5510, Villeurbanne, France

Introduction

Aortic dissection is a life-threatening disease with a high mortality rate involving multiple mechanisms. The dissection process being intramural and dynamic, its observation is particularly complex. Various experimental studies investigated this phenomenon [1]; however, most of these studies are distant from in vivo conditions. In the present study, the objective was to describe and quantify the mechanisms leading to the initiation and propagation of a dissection by performing an *in situ* tension-inflation test with X-ray tomography.

Materials and methods

The descending aorta of n=6 rabbits was carefully excised few hours after death. The branches were sutured with silk wire and the specimens were immersed during 12 hours in sodium polytungstate to ensure a good contrast on the X-ray images. A tension-inflation device fitting inside an X-ray tomography setup was developed. The specimens were turned inside out and a notch was created in the circumferential (n=4) and longitudinal orientations (n=2). The specimens were attached to the device and a pre-stretch of 1.3 was applied to them. A syringe pump infused PBS into the aortic segments to increase the pressure and a proportional–integral–derivative controller maintained the pressure constant. A scan was taken every 100 mmHg until dissection of the sample occurred. The acquisition time of a scan was 180 seconds and the resolution was 7 x 7 x 7 μm^3. Radiographic images were also taken during the dissection process at 0.2 images per second to observe in real time the failure of the sample.

Results

The notches propagated in the antegrade and retrograde directions at critical pressures ranging from 291 to 902 mmHg. No re-entry tear was identified. As observed in clinics, a rupture of the false lumen often occurred to reduce the pressure after the dissection. Positive correlations were found between the different morphological dimensions of the tear and the critical pressure. The diameter and the thickness of the sample were measured all along the pressurization and showed a non-linear behavior as often observed with arterial tissues. A bulge was observed at the tip of the notch before and after dissection of the specimen (Figure 1). The formation of this bulge is explained by the change of morphology of the aorta in order to maintain the pressure equilibrium. An elastic recoil of the flap between 5.3% and 12.3% was measured on the X-ray images. The real-time images showed that the sample dissected in less than a second.

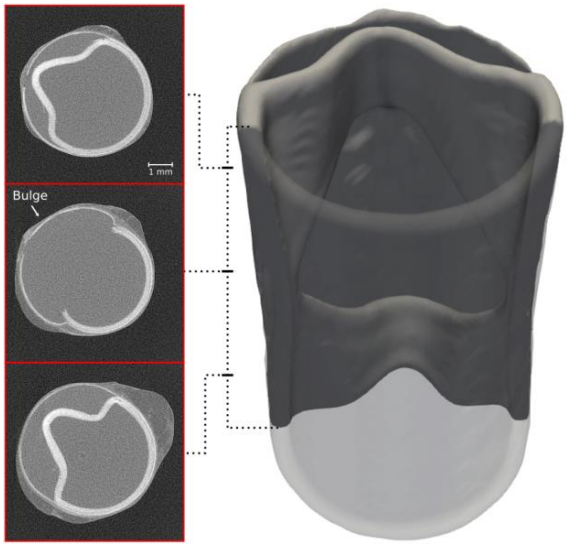

Figure 1: 3D segmentation of a representative aortic sample with a circumferential notch after propagation of the dissection. Three cross-sections are displayed at different heights of the specimen. A bulge of the outer wall can be observed.

Conclusion

To conclude, different mechanisms of aortic dissection were described in this study. To the knowledge of the authors, this is the first study to observe the 3D morphology of the aorta during the delamination process. The morphological data presented herein could fill the lack in the literature and serve to the validation of numerical models [3]. Furthermore, the findings of this study could help in the diagnosis of patients or in the development of new treatments for aortic dissection.

References

1. Roberts et al., Am Heart J, 101.2:195-214, 1981
2. Sherifova, et al., Acta Biomater, 99:1-17, 2019
3. Gültekin et al., Biomech Model.Mechanobiol, 18.6:1607-1628, 2019

CALCIFICATION CHARACTERISTICS AND ABDOMINAL AORTIC ANEURYSM WALL STRESS

Stewart McLennan (1), Zinan He (1), Rosaire Mongrain (1), Gilles Soulez (2)

1. Department of Mechanical Engineering, McGill University, Canada; 2. Centre de recherche du centre hospitalier de l'Université de Montréal, Canada

Introduction

The one year mortality rate for hospitalized abdominal aortic aneurysm (AAA) patients is approximately 40% [1]. While it has been established that calcification (Ca) changes aorta tissue mechanical properties and alters the distribution of wall stress [2], there is debate over whether this change leads to an increase or decrease in the risk of rupture. In the present paper, a numerical simulation study is performed to evaluate which, if any, Ca characteristics influence aorta wall stress for patients undergoing endovascular aorta aneurysm repair (EVAR) and whether Ca characteristics can be used to assess rupture risk of AAAs.

Methods

The impact of percent relative Ca presence (Ca Volume/Aorta Wall Volume × 100) and spacing between individual Ca pieces (mean Euclidian distance between Ca centres) was assessed for ten patients (mean age, 77; range, 66-88 years) during EVAR using patient-specific finite element analysis (FEA) simulations (Fig. 1). The impact of Ca shape variation was assessed using idealized FEA simulations for 3 typical calcification geometries, both idealized and real. (Fig. 2).

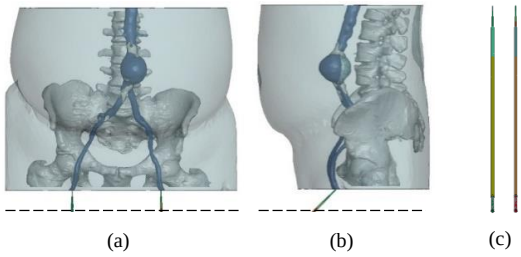

Figure 1: FEA model: (a) Patient front view (b) Patient left side view (c) Ipsilateral/contralateral guidewires and delivery devices.

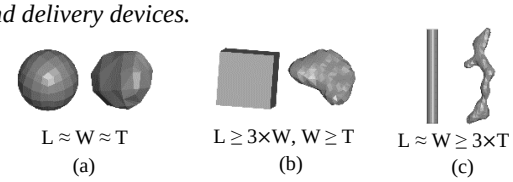

Figure 2: Ca shapes (Left - idealized; Right - real): (a) Stone (b) Flake (c) Strip.

Results

The results show that greater relative Ca presence leads to a greater increase in the average von Mises stress (VMS) wall stress (14.24±8.27%). A positive correlation was found between the Ca spacing and the stress increase (R=0.663, p<0.05, N=10). The risk of wall failure is always the highest with Ca flakes and generally lowest with Ca stones.

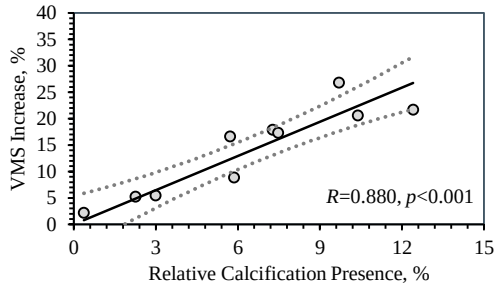

Figure 3: Average wall VMS increase and percent relative Ca presence relationship (EVAR simulation). Solid line indicates least squares linear regression; dashed lines, 95% confidence interval of the regression.

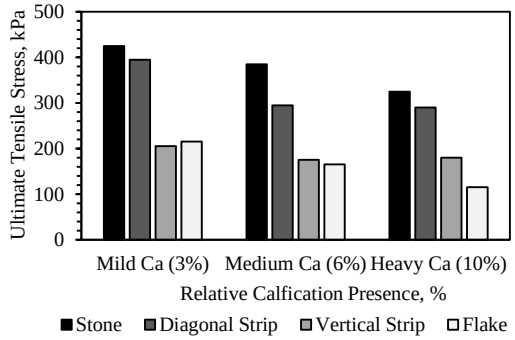

Figure 4: Peak wall stress for different Ca geometries (idealized simulation).

Discussion

Relative presence of calcification was found to be the best indicator of the studied calcification characteristics for patient rupture risk. Variation in Ca shapes appears to have a significant impact on rupture risk, suggesting the importance of considering calcification geometry in clinical evaluations.

References

1. Sweeting et al, Eur J Vasc Endovasc Surg, 50:297-302, 2015.
2. O'Leary et al, J Mech Behav Biomed, 42:154-167, 2015.

Acknowledgements

This work was supported by the Nature Sciences and Engineering Research Council of Canada (NSERC) and Siemens Healthcare GmbH.

EFFECTS OF CARDIAC GEOMETRIC REMODELING DURING HEART FAILURE ON CARDIAC FUNCTION

Yu Zheng (1), Wei Xuan Chan (1), Choon Hwai Yap (2)

1. Department of Biomedical Engineering, National University of Singapore, Singapore; 2. Department of Bioengineering, Imperial College London, UK

Introduction

Heart failure with preserved ejection fraction (HFpEF, EF ≥ 50%) and heart failure with reduced ejection fraction (HFrEF, EF ≤ 40%) are two main types of heart failure (HF) with similar prevalence. 88% of HFpEF [1] and 80% of HFrEF [2] undergo cardiac remodeling. Here we investigate whether these geometric changes benefit or impede heart function.

Currently, the diagnosis of HFpEF remains clinically challenging due to the preservation of EF and clinical heterogeneity. The inability of EF to indicate disease in HFpEF, and reports that EF can be skewed by cardiac geometric changes [3, 4] demonstrate its ineffectiveness as an indicator of function, but it is not clear why. Here, we develop a myocardial numerical model to explain why EF is ineffective, and propose a new corrected EF measure to improve it.

Methods

CMRI of 5 HFpEF porcine animal models, 10 HFrEF porcine animal models, and 6 sham/healthy are obtained before intervention (baseline) and at the 28th or 42nd day time point (ending). Cardiac anatomic parameters and endo- and epicardial longitudinal and circumferential strains are measured. A numerical model of the LV is reconstructed based on MRI images, as a discretized, idealized prolate shape. It can undergo specific magnitudes of spatially uniform and incompressible strains, and allow the calculation of the consequent stroke volume.

Results

HFpEF and sham EF are above 50%, while HFrEF EF is less than 40%. HFpEF likely experiences a concentric hypertrophy (higher LVM and wall thickness), while HFrEF likely has an eccentric hypertrophy with dilation (decreased SI and unchanged RWT). Both HF models has decreased strains.

With the numerical LV model, increasing wall thickness (Fig. 1A) was found to increase EF but not SV, suggesting that wall thickness changes artificially increased EF when there is no change to flow function. Increasing dilation (Fig. 1B) was found to increase SV, but decrease EF, suggesting that dilation enhances flow function, but EF is not a successful indicator of this. Interestingly, wall thickening is found to increase the epi-to-endo spatial variability, while dilation reduces the difference.

Due to radial strain, the epi- and endo- surfaces have different strains from the mid-wall layer. The epi- and endo- surfaces are thus not good locations for quantifying strain or volumetric flow function. We thus propose a novel marker, the corrected ejection fraction (CEF), which is calculated using the mid-wall layer rather than the endocardial layer:

$$CEF = SV/Vol_{ED,mid} = \alpha \times EF \quad (1)$$

$$\alpha = Vol_{ED,endo}/(Vol_{ED,endo} + LVM/2\rho_{LV}) \quad (2)$$

When applied to the porcine data, CEF can successfully differentiate between healthy and HFpEF hearts, while EF cannot (Fig. 2), and is shown to be free of biases due to geometric changes to the heart.

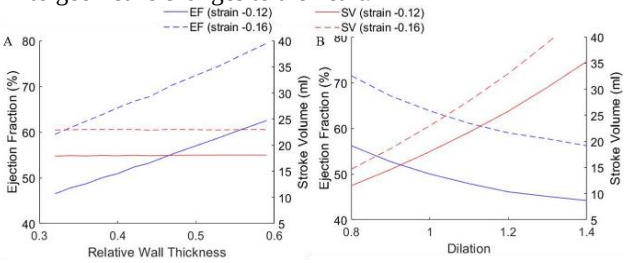

Figure 1: The dependence of EF and SV on (A) relative wall thickness and (B) dilation.

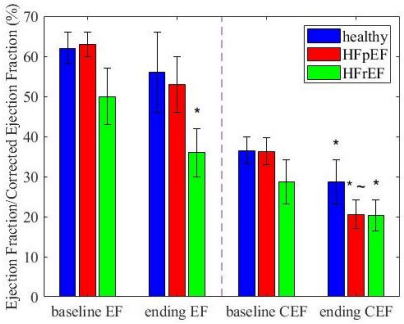

*Figure 2. EF and CEF of healthy, HFpEF and HFrEF porcines hearts at baseline and ending time points. * $p<0.05$ with baseline. ~ $p<0.05$ with healthy ending.*

Conclusions

From our modeling, we find that dilation to be advantageous to cardiac flow function, but not wall thickening. We further find that EF is an imperfect indication of function because it can be modulated by the cardiac geometry changes and cannot distinguish some HF phenotypes from normal because of its reliance on measurements on the endocardial boundary rather than the mid-wall layer. We proposed a corrected EF measure, the CEF, which we show can remove this geometric dependency and enable a better representation of cardiac contractile function.

References

1. Katz et al., *Am J Cardiol*, 112, 1158-1164, 2013.
2. Nauta et al., *Eur J Heart Fail*, 22, 1147-1155, 2020.
3. MacIver et al., *Int J Cardiol Heart Vasc*, 7, 113-118, 2015.
4. Stokke et al., *J Am Coll Cardiol*, 70, 942-954, 2017.

Acknowledgements

Funding by National University of Singapore Research Scholarship, and Imperial College startup.

HAEMODYNAMICS IN PATIENT-SPECIFIC AORTAE OF TURNER SYNDROME CHILDREN WITH MRI-OBTAINED AORTIC INFLOW

Lauren Johnston (1), Ruth Allen (2), Pauline Hall-Barrientos (2), Avril Mason (2) and Asimina Kazakidi (1)

1. University of Strathclyde, UK; 2. Royal Hospital for Children, Queen Elizabeth University Hospital, UK

Background

Girls with Turner syndrome (TS), a chromosomal condition in which a female has complete or partial absence of the second sex chromosome, present a unique group of patients, with an increased risk of cardiovascular disease. Congenital heart abnormalities occur in up to 50% of TS individuals and mortality rates are three times higher compared with the general population, with the most common cause of death being from cardiovascular disease [1-2]. We hypothesise that patients with TS present a greater variance in aortic arch morphology and haemodynamics than their healthy counterparts, because each TS patient is regarded as a unique anatomical and physiological case study.

Methodology

Three-dimensional patient-specific geometries of the aortic arch were reconstructed from retrospectively-obtained MRI/CT images (Figure 1a shows segmentation, surface reconstruction, and mesh generation processes). Numerical simulations were performed within a validated finite volume framework of the open-source software OpenFOAM®. Patient-specific MRI-obtained boundary inflow conditions were applied at the inlets. Velocity streamlines and time-dependent haemodynamic metrics, such as the time-averaged wall shear stress (TAWSS) and oscillatory shear index (OSI), were computed for all models. Particular attention was paid to regions of extreme (very low and very high) wall shear stresses (WSS) for association with subclinical atherosclerosis and damage to the arterial vascular endothelium.

Results

Numerical simulations of blood flow in patient-specific geometries of TS patients were achieved based on retrospective MRI/CT medical images (Figure 1b). The results have shown morphological aortic differences between patients to have a strong effect on the haemodynamic environment. Velocity streamlines indicated regions of secondary flow and recirculation. In addition, WSS (commonly used as an indicator of atherosclerotic predisposition) varied considerably throughout each model.

Figure

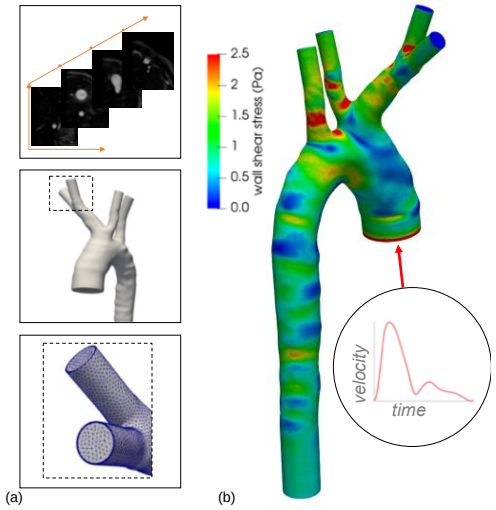

Figure 1. (a) Workflow of 3D model generation from (top) image segmentation of MRI/CT data, (middle) surface reconstruction, (bottom) mesh generation. (b) WSS distribution in the aortic arch of a TS patient.

Conclusion

In this investigation, we present a computational fluid dynamic analysis of blood flow in unique geometries of the aortic arch of TS children with patient-specific physiologically realistic haemodynamic inflow conditions. Future work will take into account peripheral arterial compliance and resistance through the use of a Windkessel model at the outlet boundaries. We also aim to expand the study cohort to adult turner syndrome patients.

References

1. M Silberbach et al., Circ Genom Precis Med. 11: pages, 2018.
2. C. Gravholt, Am J Cardiovasc Drugs 2:pages, 2002.

Acknowledgements

This work is supported in part from the University of Strathclyde Research Studentship Scheme (SRSS) Student Excellence Awards (SEA) Project No1619, and the European Union's Horizon 2020 research and innovation programme under the Marie Sklodowska-Curie grant agreement No 749185.

MRI-BASED FLUID-STRUCTURE INTERACTION ANALYSIS OF THE BICUSPID AORTIC VALVE BIOMECHANICS

Francesco Sturla (1,2), Monica Emendi (2,3), Ram P. Ghosh (3), Matteo Bianchi (3)
Filippo Piatti (1), Francesca R. Pluchinotta (1,2), Daniel Giese (4), Massimo Lombardi (1)
Alberto Redaelli (2), Danny Bluestein (3)

1. IRCCS Policlinico San Donato, San Donato Milanese, Italy; 2. Politecnico di Milano, Milano, Italy;
3. Stony Brook University, Stony Brook, NY, USA; 4. Siemens Healthcare GmbH, Erlangen, Germany

Introduction

Bicuspid aortic valve (BAV) is the fusion of two out of the three aortic leaflets, with up to 2% worldwide incidence [1]; BAV hemodynamics can alter mechanical and flow shear stresses on the leaflets, playing a role in the onset of calcific aortic valve disease [2]. We developed a fluid-structure interaction (FSI) patient-specific BAV model from magnetic resonance imaging (MRI) to quantify the biomechanical impact of BAV hemodynamics on the valve leaflets.

Methods

A 26-year-old female patient, with type-1 BAV fusion, was acquired on a MAGNETOM Aera 1.5 T clinical scanner (Siemens Healthcare, Erlangen, Germany); we reconstructed the aortic root geometry (Fig. 1) from 18 long axis *cine* MRI planes [3] in Matlab (MathWorks, Inc., Natick, MA, USA). The distal ascending aorta was included from magnetic resonance angiography (MRA) using Mimics (Materialise, Leuven, Belgium). Sub-grid geometry resolution (SGGR) 2-way FSI analysis was performed in FlowVision 3.10 (Capvidia NV, Leuven, Belgium), coupling BAV hemodynamics with the structural biomechanics solved in Abaqus 6.14 (Simulia, Dassault Systèmes, Providence, RI, USA).

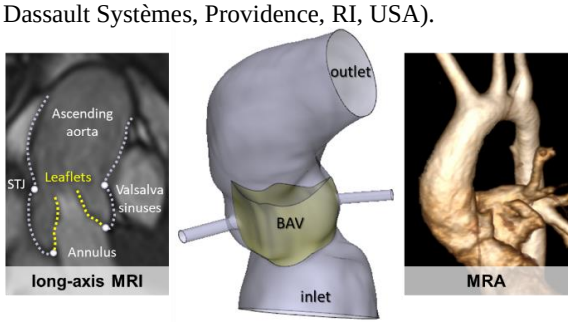

Figure 1: MRI-based reconstruction of BAV anatomy.

BAV leaflets, with a uniform thickness of 0.6mm, were discretized in hexahedral elements and modeled as isotropic and hyperelastic with a 3rd-order Ogden strain energy function; aortic wall was assumed rigid. Blood was treated as a Newtonian and incompressible fluid. Physiological pressure boundary conditions, adapted to the patient heart rate, were imposed at the inlet and outlet; paradigmatic flow rate curves were prescribed for the coronary arteries. FSI results were compared against 3D time-resolved velocity-encoded phase-contrast MRI (4D Flow), acquired on a thoracic oblique-sagittal volume with prospective ECG-gating [4].

Results

FSI aortic bulk flow well compared against 4D Flow (Fig. 2): the systolic flow jet, originating from an elliptical 1.6 cm^2 orifice, reached a peak velocity of 252.2 cm/s, 0.6% lower than 4D Flow, progressively impinging on the ascending aorta convexity. The FSI peak flow rate was equal to 22.4 l/min, 6.7% higher than 4D Flow.

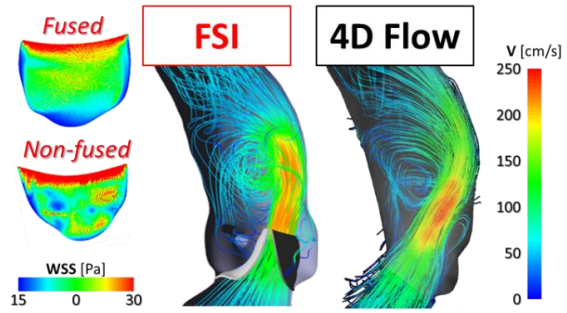

Figure 2: Systolic FSI bulk flow vs. 4D Flow and average WSS on ventricular surface of BAV leaflets

At systole, the ventricular side of the non-fused leaflet revealed the highest wall shear stress (WSS) average magnitude, up to 14.6 Pa along the free margin, with WSS progressively decreasing towards the leaflet belly. During diastole, the aortic side of the fused leaflet exhibited the highest diastolic maximum principal stress, up to 322 kPa within the leaflet attachment region.

Discussion

Non-invasive MRI can improve the patient-specific FSI reproduction of native BAV hemodynamics in order to deepen the fluid-mediated stimuli acting on BAV leaflets and their potential role in the pathogenesis of BAV calcific degeneration.

References

1. Sievers *et al*, J Thorac Cadiovasc Surg, 133:1226-33, 2007
2. Sun *et al*, PloS ONE, 8(12):e84433, 2013
3. Votta *et al*. Int J Numer Meth Biomed Engng, e2849, 2016
4. Piatti *et al*. Front Physiol, 8:441, 2017

Acknowledgements

This project was supported by NIH-NIBIB-BRPU01EB026414 (DB). IRCCS Policlinico San Donato is a clinical research hospital partially funded by the Italian Ministry of Health.

BIOMECHANICS OF THE HUMAN FETAL HEART WITH CRITICAL AORTIC STENOSIS AND EVOLVING HLHS

Chi Wei Ong (1), Meifeng Ren (2), Hadi Wiputra (2), Joy Mojumder (3), Wei Xuan Chan (2), Andreas Tulzer (4), Gerald Tulzer (4), Martin Buist (2), Citra Nurfarah Zaini Mattar (5), Lik Chuan Lee (3), Choon Hwai Yap (6)

*1. Institute of High Performance Computing, A*STAR, Singapore; 2. Dept of Biomedical Engineering, National University of Singapore, Singapore; 3. Dept of Mechanical Engineering, Michigan State University, USA; 4. Children's Heart Center Linz, Dept of Pediatric Cardiology, Kepler University Hospital, Austria; 5. Dept of Obstetrics and Gynecology, National University of Singapore, Singapore; 6. Dept of Bioengineering, Imperial College London, UK*

Introduction

Some cases of Hypoplastic Left Heart Syndrome (HLHS) develop due to abnormalities during mid-gestation. Fetal critical aortic stenosis (AS) is an example. The stenosis causes drastic alteration to the biomechanical environment, including reduction of contractile deformation and stroke volume, increase in left ventricular (LV) blood pressure, and occurrence of mitral regurgitation (MR). Consequently, the normally growth LV develops poorly going forward, and becomes HLHS at birth. Such cases are thus evolving HLHS cases. In these case, fetal aortic valvuloplasty (FAV) has been shown to be able to relieve LV outflow obstruction to restore normative biomechanics, resulting in a promising number of cases avoiding HLHS at birth. Since both AS and FAV involves drastic changes to the LV biomechanics, and the heart is known to grow and remodel according to biomechanical stimuli, it is important to study and understand diseased and post-interventional biomechanics, which is the motivation of the current study.

Methods

4D (STIC) and Doppler ultrasound measurements of 3 normal human fetal hearts, and 2D and Doppler ultrasound measurements of a further 32 fetuses with critical AS were obtained, with IRB and consent. A validated cardiac motion estimation algorithm was used to track LV motion. A previous Finite Element (FE) model of the heart was adapted for fetal heart studies, featuring Guccione active tension model, transversely isotropic Fung passive stiffness, spatially varying fiber orientations, and a simplified Windkessel model, and was solved with FEniCS. The healthy fetal heart FE model was used to model various disease features to understand their effects, including (1) AS, (2) AS and MR, (3) myocardial wall thickening, (4) myocardial fibrosis, (5) cardiomyopathy.

Results and Discussion

FE modeling produced LV geometries with a good match to reconstructions from images, with an average surface distance error of about 1% of the heart's diameter. With AS alone, LV pressures were elevated by 10-20mmHg, and stroke volume could be drastically reduced, depending on severity. When MR was included, these abnormalities were reduced. AS was found to increase systolic duration to about 70% of cardiac cycle, corroborating with Doppler images.

Modelling shows that AS and MR causes elevated valve flow velocities, but by themselves, could not reach clinically measured MR velocities of 3.4±0.9 m/s. This was only possible when wall thickening is modelled, suggesting that typical fetal AS should be associated with wall hypertrophy. Indeed, measurements in our diseased cohort found an average of 105% increase in LV wall thickness. However, such an extent of thickening in our model showed excessive LV blood pressures, much higher than invasive clinical measurements, which suggest that typical diseased cases should have some cardiomyopathy.

Increased myocardial stiffness caused only modest changes to biomechanics, suggesting that endocardial fibroelastosis found in some cases was merely a byproduct of disease, rather than a factor impeding function, contrary to current clinical opinion.

Conclusions

Image-based FE modeling can be a good way to enhance our understanding of fetal heart disease physiology. In future, we hope to extend our studies to understand the effects of intervention, and to build tools for predicting outcomes. This will enable us to more accurately select patients for FAV, reducing unnecessary procedural risks, and extending benefits to more patients.

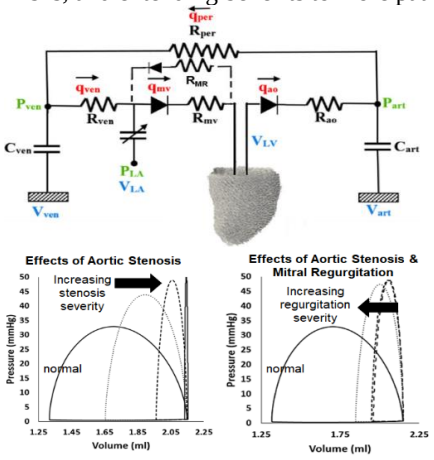

Figure 1: (Top) Schematic of FE and Windkessel model. (Bottom) Sample results, pressure-volume loops of fetal AS and MR.

Acknowledgements

Funding is provided by Singapore Ministry of Education Grant number MOE-T2-1-003, and Imperial College Startup grant.

LOCAL EX-VIVO EVALUATION OF THE BIOMECHANICAL PROPERTIES OF THE ASCENDING AORTIC ANEURYSMS

Siyu Lin[(1)], Marie-Catherine Morgant[(1,2)], Alexandre Cochet[(1,2)], Alain Lalande[(1,2)], Olivier Bouchot[(1,2)]
1. ImViA laboratory, University of Burgundy, Dijon, France; 2. University Hospital of Dijon, Dijon, France

Introduction

An aneurysm of the ascending aorta (AsAA) can progressively evolve over years and can provocate an aortic dissection and/or rupture. Currently, treatment recommendations are based on the maximum diameter of the ascending aorta and valve type given by European cardiac guideline[1].Understanding the biomechanical properties of the aorta could lead to develop biomechanical criteria, and then to be more accurate in predicting the development of aortic aneurysm. In this framework, the aim of this work is to study the local patient specific elastic modulus distribution of the AsAA from biaxial tensile test.

Methods

Pathologic ascending aortic tissue samples (n = 65) were obtained from patients undergoing elective surgical repair of AsAA (**NCT03746964**). The samples were grouped by the type of valve (tricuspid aortic valve (TAV) and bicuspid aortic valve (BAV)) (Table.1).

Type of valve	Number of patients	Maximum diameter of aorta (mm)	Median age	Number of female
TAV	39	50 ± 7.4	69	26
BAV	26	50 ± 6.4	64	20
Total	65	50 ± 7.0	68	46

Table 1: Patient characteristics.

The biaxial tensile tests were performed within two hours of the resection of AsAA. All the aortic wall samples were partitioned related to medial (MED), posterior (POST), lateral (LAT), and anterior (ANT) quadrants. Each AsAA sample was cut in square size (15 mm x 15 mm) with marking the circumferential (CIR) and longitudinal (LON) directions. An average thickness was measured, using an electronic micrometer (Litematic VL-50, Mitutoyo®). The experiments were carried out by a biaxial tensile test machine (ElectroForce®). Each specimen was stretched 10 times of 10% preconditioning and 10 mm/min till rupture.
The maximum elastic modulus (MEM) was obtained from each stress-strain curve of Young Modulus which is a parameter of stiffness[2,3].

Results

The longitudinal (LON) direction of the aorta allows less strain than the circumferential (CIR) direction ($p<0.05$), except the LAT of BAV group showing the opposite result. There is no significant difference between tissue types in neither longitudinal (LON) nor circumferential (CIR) direction for the maximum elastic modulus. The LAT shows a higher stiffness, roughly the double value of the MED. (Figure 1.a)
The thickness of TAV and BAV AsAA shows a similar behavior based on quadrants: higher value in the medial than the rest three quadrants ($p<0.001$) (Fig. 1.b).
Figure 1: a. The MEM for the longitudinal and circumferential directions for TAV and BAV samples for each quadrant. b. The thickness of TAV and BAV tissues did not show significant difference in the four regions of the AsAA wall.

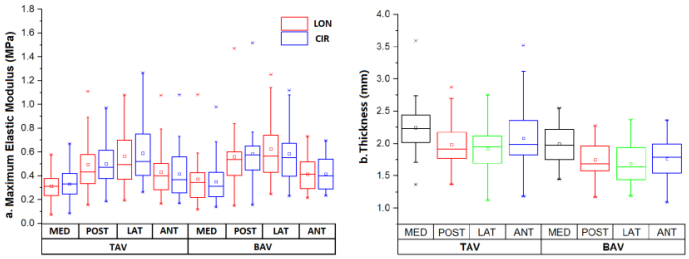

Among the 65 AsAA tissues, there was no correlation between the regional thickness and mechanical properties (E_M) of the expanded samples, neither TAV nor BAV.

Discussion

As the patient ages, blood flow will impact on the lateral quadrant (outer curvature), which evolves stronger elasticity. Due to the narrower opending of BAV, the blood flow passage speed is faster, so the impact force on LAT can be stronger. As a result, the performance of this part of LON and CIR is different from the performance of the remaining groups[4].

Concussion

Heterogeneity of the elasticity can be observed according to the quadrant.

References

1. R. Erbel et al. Eur Heart J., 1;35(41):2873-926, 2014
2. A.Duprey et al. Acta Biomaterialia, 42:273–285,2010
3. A.Duprey et al. European Journal of Vascular and Endovascular Surgery, 39:700-707, 2010.
4. N.Choudhury et al, Cardiovascular Pathology, 18(2)83-91,2009

Acknowledgements

We thank the association of “Bourgogne Coeur” for the financial support in the experiments.

FLOW THROUGH A MALAPPOSED FLEXIBLE STENT WITHIN AN ARTERIOVENOUS FISTULA

Sanjiv Gunasekera (1), Olivia Ng (1), Shannon Thomas (2), Ramon Varcoe (2), Charitha de Silva (1), Tracie Barber (1)

1. School of Mechanical and Manufacturing Engineering, The University of New South Wales, N. S. W. 2052, Australia; 2. Prince of Wales Hospital, N. S. W. 2031, Australia

Introduction

An arteriovenous fistula (AVF) is a surgical connection between the radial artery and cephalic vein of an end-stage renal disease patient. This vascular structure enables easy and efficient haemodialysis however, the AVF is prone to many diseases of which the most common is stenosis in the juxta-anastomotic (JXA) region caused by intimal hyperplasia (IH). It is well known that an adverse haemodynamic environment in the AVF is a factor in the onset of IH. The clinical success of the treatment involving the implantation of a flexible stent [1] has motivated this study to understand the impact of the stent on the dynamics of bulk flow within the AVF.

Methodology

A phantom model of a patient-specific arteriovenous fistula was obtained using a freehand ultrasound scanning methodology. Subsequently, an Abbott Vascular Supera stent, the same size that was implanted in the patient, was deployed in the phantom model. A micro-CT (micro–Computed Tomography) scan of the stented phantom model was used to segment the vessel lumen and the stent features in the same coordinates [2].

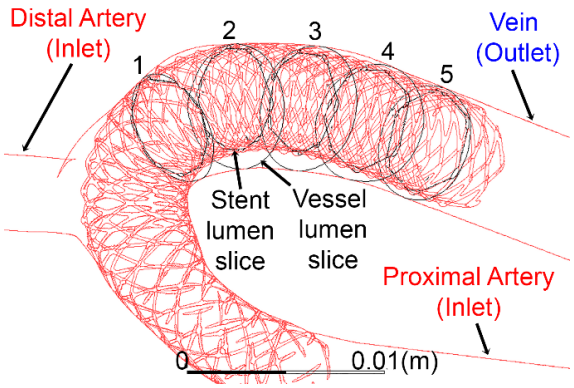

Figure 1: The patient-specific stented arteriovenous fistula geometry with the locations of the cross sectional slices.

To understand the unsteady fluid effects of the stent implantation, a transient Reynolds Averaged Navier-Stokes simulation was run within the vessel lumen with and without the presence of the stent (here-forth referred to as the 'stented' and 'unstented' geometries respectively) [2]. Five cross-sectional slices were created in the vessel lumen. Due to the presence of malapposition in this region of the vein, only a subset of these slice areas were encapsulated by the stent. The stent lumen slices (located within the vessel lumen slices) were created by manually defining locations representing the stent incident coordinates on each slice as illustrated in figure 1. These slices (of the stent and vessel lumen) were defined in both 'stented' and 'unstented' geometries.

Results

The flowrates captured across the stent lumen slices were compared with the corresponding flowrates across the relevant vessel lumen slices to measure the ratio of flow that was held in the stent encapsulated region. The level of malapposition was also calculated using the area ratio between the stent and vessel lumen slices.

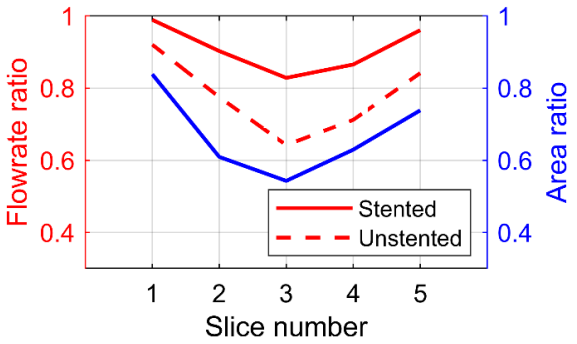

Figure 2: The variation of the flowrate ratio and area ratio across the slices in the vein.

The variation of the area ratios (as seen in figure 2) show that the maximum amount of malapposition occurs at slice number three. The flowrate ratio patterns show a minimum at this slice. However, the most important feature is the significantly higher flow rate ratio in the stented geometry as opposed to the unstented geometry. This pattern is consistent across the other slices as well.

Discussion

The variation of flowrate ratios above, clearly shows the funneling of the venous blood flow through the stent encapsulated region. This feature, when coupled with malapposition at the JXA region, could lead to lower recirculating flow and weaker turbulent fluctuations close to the vessel wall regions prone to disease.

References

1. Thomas et al, J Endovasc Ther, 26(3):394-401, 2019
2. Gunasekera et al, Proceedings of the 22nd AFMC, 2020

ULTRASOUND-BASED FLUID-STRUCTURE INTERACTION MODELING OF ABDOMINAL AORTIC ANEURYSMS INCORPORATING PRE-STRESS

Judith Fonken (1,2), Esther Maas (1,2), Arjet Nievergeld (1,2), Marc van Sambeek (1,2), Frans van de Vosse (1), Richard Lopata (1)

1. Eindhoven University of Technology, the Netherlands; 2. Catharina Hospital Eindhoven, the Netherlands

Introduction

An abdominal aortic aneurysm (AAA), a dilation of the abdominal aorta, can lead to a fatal bleeding when rupture occurs. Current clinical guidelines rely on diameter measurements and population statistics. Biomechanical models using patient-specific geometries have shown to provide better markers of rupture risk. However, frequent follow-up, as well as studies on AAA development, require the use of a non-invasive imaging modality. Recently, AAA modeling based on time-resolved 3-dimensional ultrasound (3D+t US) was demonstrated, which also allows for simultaneous estimation of wall stresses and stiffness.

The modeling framework needs to be further advanced to fluid-structure interaction (FSI) modeling, to incorporate the influence of hemodynamics on wall mechanics, and vice versa. So far, US has not been used for FSI, due to its limitations in contrast and field-of-view with respect to the golden standard, CT [1].

In addition, previous studies did not account for the pre-stress that is present in the measured geometry, which has shown to influence the wall mechanics [2]. Thus, incorporating the pre-stress in FSI models is necessary.

In this study, a framework to execute FSI models of AAAs based on 3D+t US data was created and the effect of incorporating the pre-stress was evaluated.

Methods

The established framework (Fig. 1) uses the patient-specific AAA geometry and brachial blood pressure (BP) as input to generate FSI models. The geometry can be derived from either a 3D+t US or CT segmentation. Based on this framework, the segmentation was elongated and converted into a lumen surface mesh. The solid mesh was obtained by extruding the lumen surface mesh with a wall thickness of 2 mm. The pre-stress in the solid geometry was estimated using the Backward Incremental Method (BIM) [2], using the mean arterial pressure (MAP), which was derived from the brachial pressure. The AAA wall was modeled using a Neo-Hookean model, whereas blood was modeled using a Carreau model. A time-varying flow profile was prescribed at the inlet and a 3-element Windkessel model was used to prescribe the outlet pressure [3].

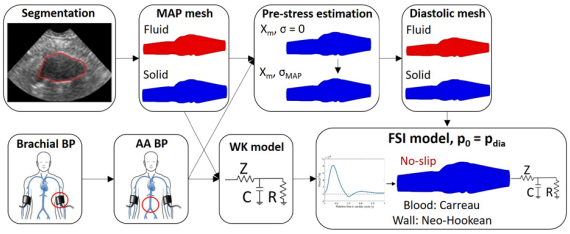

Figure 1: FSI framework using 3D+t US or CT based segmentations and brachial blood pressure (BP, diastolic: DBP, systolic: SBP) as patient-specific input.

In the FSI model, the fluid and solid model interact in a partitioned approach. The FSI model was initialized with the diastolic BP, multiple cardiac cycles were simulated and the results were evaluated on the last cardiac cycle.

Results

FSI simulations without and with pre-stress estimation were carried out using the same 3D+t US data. Fig. 2 visualizes the wall displacement, wall stress, pressure and wall shear stress (WSS) of the two models at systole.

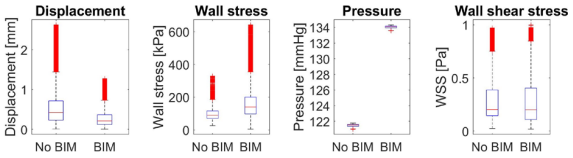

Figure 2: wall displacement, wall stress, pressure and wall shear stress at systole for a FSI model without ('No BIM') and with ('BIM') pre-stress estimation.

Discussion

AAA FSI models based on 3D+t US data were executed successfully and the effect of including the pre-stress was evaluated. An overestimation of displacement and underestimation of wall stress and pressure is observed when the pre-stress is omitted. Furthermore, the peak WSS is slightly underestimated. These results underline the importance of incorporating the pre-stress.

In a future study, the framework will be employed on a dataset consisting of 58 patients with both 3D+t US and CT data, to compare the imaging modalities.

The obtained framework for FSI models using 3D+t US data paves the way for future longitudinal studies on AAA development, growth and rupture risk.

References

1. Salman et al, Front. Bioeng. Biotechnol., 7:111, 2019.
2. De Putter et al, J. Biomech, 40(5):1081-1090, 2007.
3. Bessems et al. J. Fluid Mech., 580:145-168, 2007.

Acknowledgements

This work was supported by the Dutch Research Council (NWO) and received funding from the NWO talent program VIDI. This work was carried out on the Dutch national e-infrastructure with the support of SURF Cooperative. We want to thank ANSYS Inc for their valuable technical support.

EX-VIVO TENSILE TESTING, NANO-INDENTATION AND DIGITAL IMAGE CORRELATION BASED PLAQUE RUPTURE ANALYSIS

Su Guvenir (1), Pablo de Miguel (1,2), Ali C. Akyildiz (1,2)

1. Department of Biomedical Engineering, Erasmus Medical Center, Rotterdam, the Netherlands
2. Department of Biomechanical Engineering, Delft University of Technology, Delft, the Netherlands

Introduction

Atherosclerotic plaque rupture occurs when local stress levels are higher than the strength of the plaque tissue [1]. For patient-specific rupture risk prediction, assessment of local plaque deformation and local elastic and fracture properties are essential. In this work, we aimed at extracting local tissue fracture properties of human carotid plaques using uni-axial tensile testing, digital image correlation (DIC) and nano-indentation techniques.

Methods

Human carotid artery endarterectomy (CAE) samples (n=30) were collected at the Erasmus Medical Center. As preliminary work, three rectangular plaque tissue strips (from common (n=2) and internal (n=1) carotid artery regions) were used for the uniaxial tensile testing in the circumferential direction and DIC. Following the mechanical testing, engineering stress and gauge length-based average Green-Lagrange strain were calculated. Furthermore, DIC (by using the Ncorr software (version 1.2)) was performed to obtain local deformation measures. To measure the local stiffness of the strips, the Piuma nano-indenter (Optics11 Life) with a 263 microns tip and 0.64 N/m stiff cantilever was used. 10 to 15 indentations were performed per strip and the Hertz model was fit the force-indentation displacement curves.

Results

Three plaque strips were successfully tested, and four ruptures were observed during the uniaxial mechanical testing. The engineering stress and gauge length-based average Green-Lagrange strain at the initial rupture timepoint were calculated as; 1st strip: 0.24 MPa and 26%, 2nd strip: 0.20 MPa and 24%, 3rd strip: 0.07MPa and 16%. Then, the DIC-based strain measurements (circumferential (E_{yy}) and absolute shear (E_{xy})) were obtained (Fig.1). The maximum and mean values in the tensile direction were; 1st strip: 84% and 21%, 2nd strip: 59% and 20%, 3rd strip: 53% and 13%. Although the DIC-based overall mean values were in line with the gauge length-based measurements, the maximum local measurements were higher than the averaged gauge-length based measurements (65.3% vs 22% on average). Two of the rupture sites (1st sample and 3rd sample, upper left region rupture) were observed at high local tensile strain zones of approximately 84% and 35%. On contrary, the other two ruptures (2nd sample and 3rd sample, lower right region) were observed at high shear strain regions of approximately 25% and 55%, respectively. The local Effective Young's modulus values of the strips from the nanoindentation tests were; 1st strip: 274.8 Pa to 41.8kPa, 2nd strip: 550.9Pa to 53.1kPa, 3rd strip: 968.4Pa to 22.3kPa, and they showed quite a large variation. The stiffest locations were all observed close to the rupture sites.

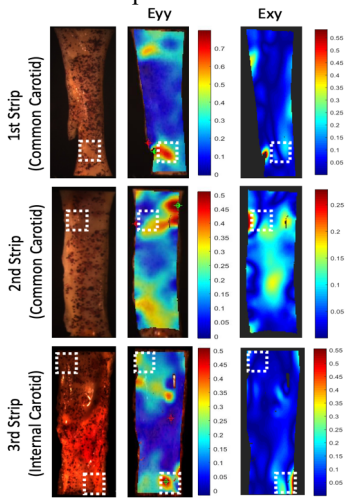

Figure 1: DIC-derived local E_{yy} and E_{xy} strains of three tissue strips. Dashed lines cover rupture initiation sites.

Discussion

In this work, we have performed a preliminary investigation of local elastic and failure properties of the heterogenous plaque tissue using human CAE samples. Based on our observations, the gauge length-derived measurements (assuming homogeneity) underestimate the local (heterogeneous) tissue rupture strains. Moreover, the correlation of the rupture sites with the DIC-based high tensile and/or shear strain locations indicate a possibility of different failure mechanism due to microstructural organization. As future work, we will perform histology to obtain microstructural information, and investigate its correlation with local mechanical properties. A possible link between the local mechanical and structural properties holds great potential to provide insights for the failure mechanisms involved in rupture.

Acknowledgements

This project has received funding from the European Commission's Horizon 2020 research and innovation program under the Marie Skłodowska-Curie grant agreement # 749283.

References

1. Cheng et al., Circulation, 87.4: 1179-1187, 1993.

FIRST PATIENT-SPECIFIC IN SILICO THROMBECTOMY PROCEDURE

G. Luraghi (1), S. Bridio (1), J.F Rodriguez Matas (1), N. Boodt (2), F.J.H. Gijsen (2,3), A. van der Lugt (2), B. Fereidoonnezhad (4), K. Moerman (4), P. McGarry (4), P. Konduri (5), N. Arrarte Terreros (5), H.A. Marquering (5), C.B.L.M. Majoie (5), F. Migliavacca (1)

1. Politecnico di Milano, Italy; 2. Erasmus MC, Netherlands; 3. Delft University of Technology, Netherlands; 4. National University of Ireland Galway, Ireland; 5. Amsterdam UMC, location AMC, Netherlands.

Introduction

An acute ischemic stroke (AIS) arises when an acute large vessel occlusion caused by a thromboembolus (clot) prevents blood supply to the brain tissues. The main innovative stroke treatment is intra-arterial thrombectomy, a minimally invasive procedure based on stent-retriever technology [1]. Despite the promising and encouraging results, complications may occur, such as thrombus fragmentation [2]. This study presents for the first time a patient-specific thrombectomy procedure through finite element analysis.

Methods

CTA images of a 64-year-old male patient with AIS in the right middle cerebral artery were segmented [3-4] to reconstruct the geometry of the cerebral arteries and discretized [5] with quadrilateral shell elements (Fig.2a). The thrombus was generated and positioned according to the available clinical and imaging data, meshed with tetrahedral elements and modeled as a hyperelastic compressible material. The thrombectomy procedure involved two attempts (Fig.1) with TREVO XP 4-20 mm stent (Stryker, US), which was modeled with beam elements and super-elastic shape memory alloy material (Fig.2b). The thrombectomy procedure was replicated with simulations performed in LS-DYNA (ANSYS, USA). This consisted of three steps [6]: (i) the guide microcatheter is positioned in the vessel, while the stent is crimped; (ii) the crimped stent is positioned and then deployed by unsheathing the catheter; (iii) the stent and the trapped thrombus are retrieved along the vessel. Furthermore, the stress field was used to predict the fragmentation of the thrombus during the procedure.

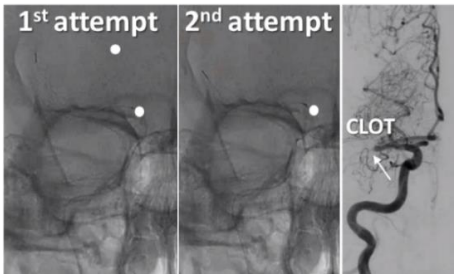

Figure 1: X-ray images: in the first attempt the stent was placed thoroughly distal (to the clot), while in the second and successful attempt only two-thirds of the stent was placed distal to the clot. White dots define the stent ends. The clot was detected at the same location before each attempt.

Results

The results of the thrombectomy procedure during both the attempts are depicted in Fig. 2c-d. As in the real situation, the in silico model showed that two attempts were necessary to remove the clot. Furthermore, the stress results indicated that clot fragmentation did not occur because the clot that turned out to be loaded mainly in compression which prevents the clot cracks from propagating.

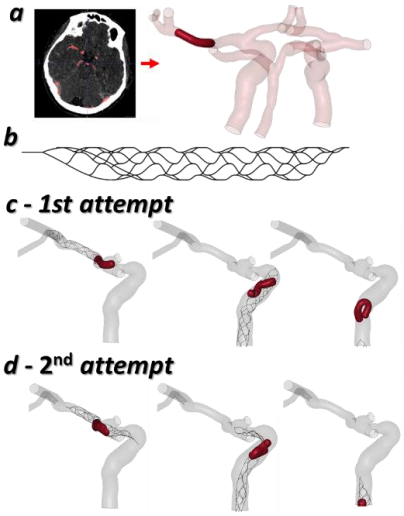

Figure 2: (a) patient-specific domain; (b)stent-retriever model; (c) thrombectomy results from the 1st (unsuccessful) and 2nd (successful) attempt.

Discussion

The development of realistic and accurate in silico thrombectomy models can be used to improve the mechanical thrombectomy procedure itself, to design and optimize new devices and to help in clinical decisions and intervention planning.

References

1. Berkhemer et al, New Eng J Med, 372 (1):11-20, 2015.
2. Kühn et al, J Cereb Blood F&M, 40 (12): 2350-2365, 2020.
3. Barros et al, J Neurointerv Surg, 12: 848–852, 2020.
4. Chen et al, Magn Reson Med, 79(6): 3229–3238, 2018.
5. Moerman et al, J Open Source Softw, 3: 506, 2018.
6. Luraghi et al, Interface Focus, 11(1):20190123, 2021.

Acknowledgements

This project has received funding from the European Union's Horizon 2020 research and innovation programme under grant agreement No 777072.

COMPUTATION OF BLOOD FLOW IN PATIENT-SPECIFIC MODELS OF TETRALOGY OF FALLOT WITH MRI-OBTAINED INFLOW CONDITIONS

Maria Boumpouli (1), Emilie Sauvage (2), Claudio Capelli (2), Silvia Schievano (2), Asimina Kazakidi (1)

1. Department of Biomedical Engineering, University of Strathclyde, Glasgow, UK; 2. University College London, Institute of Cardiovascular Science & Great Ormond Street Hospital for Children, London UK

Introduction

Tetralogy of Fallot (TOF) is the most common cyanotic congenital heart disease with a prevalence of 1 in 3000 live births [1]. Adults with repaired TOF are at risk of chronic complications including branch pulmonary stenosis and regurgitation, which may lead to dysfunction of the right ventricle and the pulmonary valve [2]. It is therefore important to improve our understanding of the haemodynamic environment in the pulmonary bifurcation of these patients for better evaluation of the disease and treatment. The focus of this study was to computationally investigate the blood flow in patient-specific geometries of the TOF pulmonary bifurcation, using inflow velocities derived from phase-contrast magnetic resonance imaging (PC-MRI).

Methods

Three-dimensional models of the pulmonary junction were reconstructed from MRI images of seven patients with TOF. Flow data of the same patients were also retrospectively acquired with phase-contrast MRI (PC-MRI) and used at the inlet boundaries of the models [3] (Fig. 1a). The walls were assumed rigid, assigned with the no-slip boundary condition. Averaged boundary conditions derived from the seven patients of this study were used to better understand the effect of geometry in flow development. Wall shear stress (WSS) values around the pulmonary junction were evaluated. An investigation of the effect of smoothing the geometries without losing the details of the curvature and angle of the branches was also conducted. All simulations were performed using a validated finite volume scheme in OpenFOAM®.

Results

There was great variation in the morphology of the pulmonary bifurcation among the TOF patients, and blood flow development was highly dependent on such characteristics. Time averaged WSS (TAWSS) values were calculated with the through-plane 3D inlet velocity profile, obtained from patient-specific PC-MRI data (Fig. 1b). The TAWSS distribution shared qualitatively similar characteristics with the TAWSS pattern obtained with a uniform inlet velocity profile, based on the averaged pulsatile waveform (Fig. 1c).

Discussion

Patient-specificity is deemed necessary to better diagnose and treat patients with tetralogy of Fallot. Nevertheless, in the absence of flow data, a uniform velocity at the inlet can still capture TAWSS and velocity distribution at the pulmonary junction of the models. Smoothing does not seem to affect the wall distribution of the haemodynamic parameters investigated, provided that the morphological variations are preserved. To confirm these findings, future work will include a larger cohort of patients and possibly the correlation of the flow results with clinical outcomes.

Figure

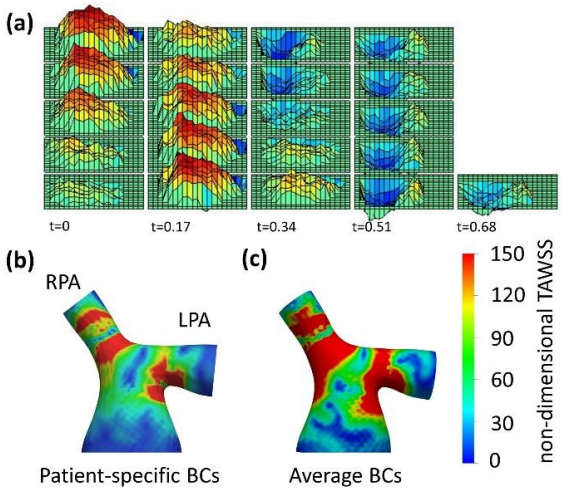

Figure 1: (a) Patient-specific 3D-velocity profiles over a cardiac cycle, extracted from PC-MRI data. (b-c) Non-dimensional time averaged wall shear stress distribution (TAWSS) (b) with patient-specific, and (c) averaged boundary conditions.

References

1. Rao B.N.S et al, Am Heart Journal, 81:361-371, 1971.
2. Zhang W et al, Int CardVasc and Thorac Surg, 23:519-525, 2016.
3. Van Doormaal M., Kazakidi A. et al., J. R. Soc. Interface 9:2834-2844, 2012.

Acknowledgements

This work is supported in part by the University of Strathclyde Research Studentship Scheme (SRSS) Research Excellence Awards (REA), Project No 1208 and the European Union's Horizon 2020 research and innovation programme, under the Marie Skłodowska-Curie grant agreement No 749185. The work in University College London was conducted thanks to the UKNF SRV funding. Results were obtained using the ARCHIE-WeSt High Performance Computer (www.archie-west.ac.uk) based at the University of Strathclyde.

HEMODYNAMIC IMPACT OF STENT DESIGN AND OVERLAPPING IN SUPERFICIAL FEMORAL ARTERIES

Monika Colombo (1), Anna Corti (1), Andrea Colombo (1), Giacomo Antognoli (1), Luca Antonini (1), Martina Bernini (2), Ciara McKenna (2), Scott Berceli (3,4), Ted Vaughan (2), Francesco Migliavacca (1), Claudio Chiastra (1,5)

1. LaBS, Dept. Chemistry, Materials and Chemical Engineering "Giulio Natta", Politecnico di Milano, Italy; 2. Biomechanics Research Centre (BioMEC), National University of Ireland Galway, Ireland; 3. Dept. Surgery, University of Florida, Gainesville, FL, USA; 4. Malcom Randall VAMC, Gainesville, FL, USA 5. PoliTo^{BIO}Med Lab, Dept. Mechanical and Aerospace Engineering, Politecnico di Torino, Italy

Introduction

In-stent restenosis (ISR) widely affects superficial femoral arteries (SFAs) treated with self-expanding stents, especially in the presence of long lesions (>150mm) and multiple overlapping devices [1]. The role of hemodynamics on ISR onset and development is still debated. In this work, the impact of stent design and interventional procedure, in particular of different stent overlapping configurations, on the hemodynamics of patient-specific SFA models is analyzed.

Methods

The SFA geometry of two patients treated with EverFlex self-expanding stents at the Malcom Randall VAMC (Florida, USA) was reconstructed from computed tomography (CT) at the immediate post-operative follow-up (Cases A and B) [1,2]. Since the low CT resolution did not allow to detect the stent struts, an *ad hoc* developed morphing technique was applied to virtually implant the stent models within the vessels to obtain the final stented SFA geometries. The stent location within the vessel was verified by CT visual inspection. The stented SFA geometries were used for computational fluid dynamics (CFD) analyses, performed imposing a patient-specific inflow velocity profile derived from Doppler ultrasound images [2].
The impact of stent design on hemodynamics was evaluated by considering, in addition to the EverFlex stent, three devices (i.e. Zilver Flex, Cordis, and braided stents), virtually implanted in Case A at the same location of the reference EverFlex. The impact of stent overlapping was studied by comparing two scenarios (Fig. 1), adopted in clinical practice: normal procedure, with distal stent implanted first (called "step-down"); reversed procedure, with the proximal stent implanted first ("step-up"). Case B was used because it presented two overlapping devices. The hemodynamics was investigated by analyzing the wall shear stress (WSS) vector field along the stented region.

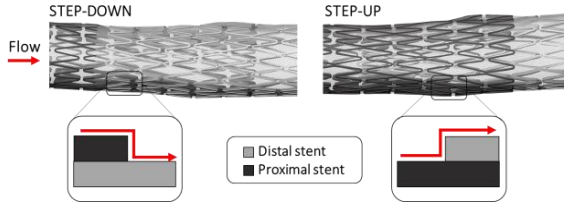

Fig. 1: Stent overlapping configurations.

Results

Regarding the impact of stent design, higher values of mean WSS were found in the case of braided and Zilver Flex stents (0.38 and 0.34 Pa, respectively) as compared to the other devices (EverFlex: 0.27 Pa, Cordis: 0.27 Pa). Considering the percentage of lumen surface subjected to low WSS (<0.2 Pa, median of the pooled distribution in the stented region), the lowest value (21.0%) was found for the braided stent, followed by Zilver Flex (30.8%), EverFlex (43.5%) and Cordis (43.6%) stents.
Regarding the implantation procedure, the results revealed that the bulk and the near-wall hemodynamics were maximally impacted by the "step-up" stent overlapping configuration.

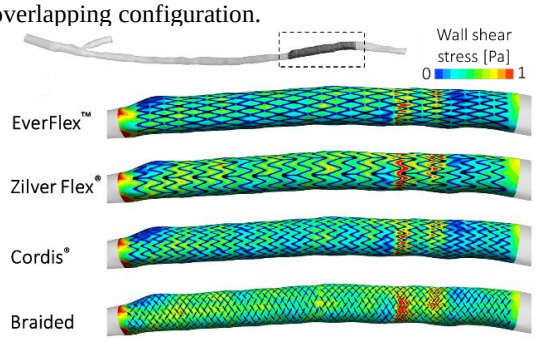

Fig. 2: Wall shear stress distributions induced by the four different stent designs implanted in case A.

Discussion and conclusions

Compared to other vascular regions (e.g. coronary arteries), the implantation of long (>100mm) and multiple stents is very common in the SFA. Here, CFD analyses were performed to study the altered hemodynamics induced by either different stent designs or stent overlapping configurations in image-based SFA models. The braided and Zilver Flex stent designs, as well as the "step-down" overlapping configuration, presented the best hemodynamic results, with associated lower risk of ISR. The study confirms that CFD is a valuable tool for the design of endovascular devices and the analysis of different interventional procedures.

References

1. Colombo M et al., Sci Rep, 11: 1-13, 2021.
2. Colombo M et al., Med Eng & Phys, 75: 23-35, 2020.

Acknowledgements

This work has been supported by Fondazione Cariplo, Italy (Grant number 2017-0792, TIME).

FUNCTIONAL MITRAL REGURGITATION EX-VIVO MODEL IN DEER HEARTS FOR APPLICATION IN PRECLINICAL RESEARCH

M. Jaworek (1,2), E. Maroncelli (1), E. Salurso (1,2), F. Perico (1,2), C. Romagnoni (2,3), G. Gelpi (1,2,3), R. Rosa (2,3), A. Mangini (2,3), G.B. Fiore (1,2) and R. Vismara (1,2)

1. Department of Electronics, Information and Bioengineering, Politecnico di Milano, Milan, Italy;
2. ForcardioLab – Fondazione per la Ricerca in Cardiochirurgia ONLUS, Milan, Italy;
3. Cardiovascular Surgery Department, ASST Fatebenefratelli Luigi Sacco University Hospital, Milan, Italy

Introduction

Functional mitral regurgitation (FMR) is secondary to cardiac ischemia and is characterized by mitral annulus and left ventricular dilation. Surgery is denied to >50% of potential candidates. Emerging transcatheter approaches could offer a therapeutic option for the patients with high surgical risks [1]. Ex-vivo FMR reproduction in healthy porcine hearts, the most common animal model in cardiovascular preclinical research, is challenging. There is a need for an alternative that could enable realistic preclinical assessment of new FMR therapies.
The aim of this work was to assess the applicability of deer hearts for ex-vivo FMR reproduction.

Material and methods

6 frozen deer hearts were housed in a pulsatile flow mock circulation loop [2] and tested in the following conditions: heart rate of 60 bpm, stroke volume of 120 ml and mean aortic pressure at baseline of 100 mmHg. At baseline, the deer mitral valve had physiological coaptation in systole. The pathological state was induced by 60-minutes preconditioning under constant intraventricular pressurization at 150 mmHg. Valve competency could be restored by tensioning two adjustable bands placed externally to myocardium, at the level of the annulus and the papillary muscles. The hemodynamic and echocardiography-based assessment was performed at baseline, FMR and restored physiological conditions.

Results

In FMR condition mitral valve coaptation was lost; leaflets tethering and restricted motion was observed (Figure 1). Quantitatively (Table 1), preconditioning caused statistically significant decrease of cardiac output and increase of mitral annulus and left ventricular dimensions. Application of the adjustable bands allowed to restore the baseline conditions at hemodynamic and geometrical level. Overall low cardiac output was related to elevated compliance of the deer hearts.

Conclusions

Deer left hearts dilatation by intraventricular pressurization allowed to replicate typical mechanistic features of FMR when housed in pulsatile mock loop. Indeed, annular and ventricular dilation, lack of coaptation, and leaflets tethering were observed. This level of realism was not possible to be obtained using porcine hearts up to date. Deer hearts have potential to be used for realistic preclinical testing of novel mitral valve transcatheter therapies.

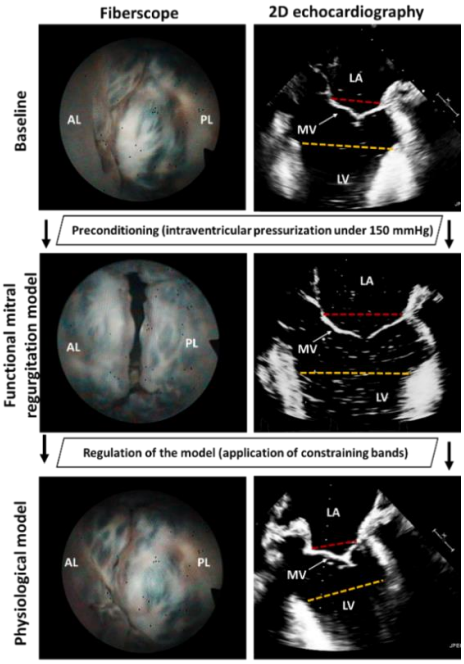

Figure 1: Fiberscope (atrial view) and 2D echocardiographic (antero-posterior plane) images of mitral valve (MV) in peak systole at baseline, pathological and physiological model conditions. AL=anterior leaflet; PL=posterior leaflet; LA=left atrium; LV=left ventricle. Red line – antero-posterior diameter, orange line – left ventricular diameter.

	Baseline	FMR model	Physiological model
Cardiac Output, l/min	1.7±0.8*	0.9±1.0	1.8±0.8*
Antero-posterior diameter, mm	32±6*	40±6	30±7*
Left ventricular diameter, mm	70±6*	79±7	67±5*

*Table 1: Hemodynamic and echocardiographic assessment of baseline, FMR and physiological model. * - statistical significance vs. FMR model ($p<0.05$).*

References

1. Herrmann et al., Circulation, 130:1712-22, 2014
2. Leopaldi et al., J. Biomech., 45:1133-39, 2012

INVESTIGATING THE POTENTIAL OF *IN-VIVO* MRI STRAIN MEASUREMENTS TO IDENTIFY CAROTID PLAQUES AT RISK OF RUPTURE.

Johnston, R.[1,2], Gaul, R. [1,2], Ghasemi, M.[1,2], Tornifoglio, B.[1,2], Lally, C. [1,2,3]
[1] Trinity Centre for Biomedical Engineering, Trinity College Dublin, Dublin 2, Ireland
[2] Department of Mechanical, Manufacturing Engineering & Biomedical Engineering, School of Engineering, Trinity College Dublin, Dublin 2, Ireland
[3] Advanced Materials and Bioengineering Research Centre (AMBER), Trinity College Dublin, Dublin, Ireland.

INTRODUCTION

The development and rupture of atherosclerotic plaques at the carotid bifurcation are known contributors to ischemic stroke cases [1]. Knowing that rupture is a mechanical process, whereby the stress exerted on the plaque exceeds its mechanical strength, a diagnostic indicator should include some quantification of plaques' mechanical integrity [3]. Despite this, the current gold standard for diagnosis is percent vessel stenosis, even though rupture of plaques often occurs below the critical threshold of 50% stenosis [4].

The aim of this present study is to better understand the mechanisms behind plaque rupture and develop a sensitive mechanical rupture risk indicator that can be readily translated to *in-vivo* imaging measurements. To achieve this goal, we (i) image diseased vessels *in-vivo* and determine the circumferential strain across the plaque, (ii) experimentally test atherosclerotic plaque caps, the location at highest risk of rupture, and determine their ultimate tensile strength and stiffness with respect to collagen fibre orientation, and (iii) develop patient specific computational models that use the obtained mechanical data to further understand the stress-strain environment of the plaque and how *in-vivo* magnetic resonance imaging (MRI) strain measurements may offer a diagnostic measure of plaques at greatest risk of rupture.

MATERIALS AND METHODS

In-vivo MRI: T2 weighted MRI scans of the carotid arteries were obtained from patients (n=9) undergoing a carotid endarterectomy procedure. Images were acquired at both diastolic and systolic phases in the cardiac cycle enabling circumferential vessel strains to be calculated for both contralateral and ipsilateral sides.

Experimental Methods: Excised carotid plaques (n=20) were taken from endarterectomy procedures and plaque cap samples delineated from the tissue in the circumferential direction. Small angle light scattering (SALS) was performed on samples before testing, allowing each sample to be characterized by its fibre orientation, that is a predominantly axial (F_A) or predominately circumferential (F_C) fibre orientation. A speckle pattern was applied to the samples for digital image correlation (DIC) to be used to track local displacements of the tissue. Uniaxial tensile tests were then performed to failure to determine the ultimate tensile strength, strain and stiffness of the plaque caps.

Computational Model: Patient specific finite element models were created from the *in-vivo* MRI images using in-house developed protocols [5]. Implemented via a UMAT user subroutine, the arterial and plaque tissue were modelled as anisotropic hyperelastic materials [5]. Two separate simulations were performed with fibres being set in the (i) axial and (ii) circumferential direction.

RESULTS

Testing revealed that collagen fibre direction, as opposed to collagen content, plays the most significant role in determining the ultimate tensile strength and stiffness of atherosclerotic plaque caps (Fig.1(A-C)). Samples with predominately circumferential fibres sustained higher stress and lower strain before failure, with the opposite observed for axially aligned fibres.

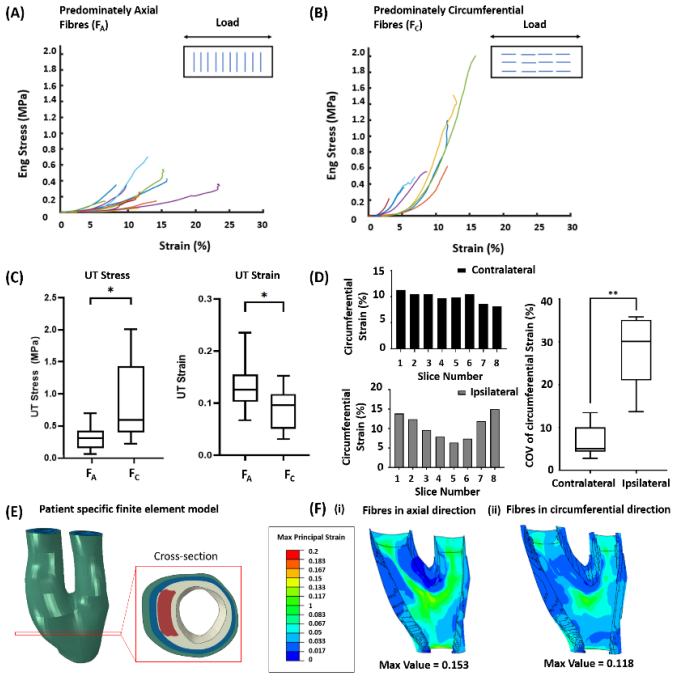

Figure 1: Engineering stress versus strain for (A) predominately axial (n=12) and (B) predominately circumferential fibre (n=8) plaque caps. (C) Ultimate tensile stress and strain grouped according to dominant fibre direction, (D) Coefficient of variation of in-vivo circumferential strain across the bifurcation for contralateral and ipsilateral sides, (E) Computational model of patient specific atherosclerotic artery geometry, (F) Strain in plaque tissue where fibres were defined in the (i) axial and (ii) circumferential direction.

DISCUSSION

In-vivo MRI measurements of the circumferential strain show that the contralateral side experiences a more consistent strain range when compared with the ipsilateral side, see Fig.1D. This is observed across all datasets, with the coefficient of variation of circumferential strain being significantly different from ipsilateral and contralateral sides, see Fig.1D. Insights from the plaque cap testing suggest that axial fibre orientation may give rise to higher strains on the ipsilateral side and a corresponding higher risk of rupture. The computational models confirm these findings, where plaques experience higher strains when fibres are aligned in the axial direction, see Fig.1E-F. Consequently, noninvasively characterising plaque strains using MRI may offer a critical biomarker of plaques at greatest risk of rupture.

REFERENCES

[1] M. Hollander *et al.*, *Circulation*, vol. 105, no. 24, pp. 2872–2877, 2002.
[2] Z. Teng *et al.*, *Acta Biomater.*, vol. 10, no. 12, pp. 5055–5063, 2014.
[3] C. Huang *et al.*, *Ultrasound Med. Biol.*, vol. 42, no. 2, pp. 365–377, 2016.
[4] B. A. Wasserman, *et al.*, *Stroke*, vol. 36, no. 11, pp. 2504–2513, 2005.
[5] M. Ghasemi, PhD Thesis, Trinity College Dublin, www.tara.tcd.ie/handle/2262/86675 , 2019.

ACKNOWLEDGEMENTS

This project has received funding from the European Research Council (ERC) under the European Union's Horizon 2020 research and innovation programme (grant agreement No. 637674)

PERMANENT STRAIN ACCUMULATION IN BOVINE PERICARDIUM: ROLE OF COLLAGEN FIBRE CRIMP

Alix Whelan (1, 2, 3, 4), Gordon O'Brien (2), David O'Reilly (4), Caitríona Lally (1, 2, 3)

1. *Trinity Centre for Biomedical Engineering, Trinity College Dublin, Ireland;* ***2.*** *Department of Mechanical, Manufacturing & Biomedical Engineering, Trinity College Dublin, Ireland; Ireland;* ***3.*** *Advanced Materials and Bioengineering Research Centre (AMBER), Trinity College Dublin, Ireland;* ***4.*** *Structural Heart Division, Boston Scientific Corporation, Ireland*

Introduction

Pericardial leaflets in bioprosthetic heart valves (BHVs) are long associated with inadequate durability *in vivo* [1]. Importantly, it is known that all tissue changes up to 50 million cycles at physiological loads are due to a permanent strain accumulation in the pericardial matrix (~ 1 year *in vivo*, [1]). Yet, the role of the mechanically significant collagen fibres in this matrix-permanent strain accumulation is unknown. Improved understanding of this phenomenon, which dominates the early-stage response of BHV leaflets *in vivo*, will aid in improving the performance of pericardial leaflets. This will help identify optimal leaflet fibre patterns that minimize the progression of permanent strain accumulation.

Materials & Methods

Circular specimens of commercial-grade glutaraldehyde-fixed bovine pericardium (GLBP, Ø 20 mm) were non-destructively pre-sorted with Small Angle Light Scattering [2], according to collagen fibre alignment, as highly dispersed (HD, n=10) or highly aligned fibres (HA, n=10). In a novel testing system, bidirectional cyclic bulge loading was conducted at a hypertensive pressure of 150 mmHg, where tissue deformation and permanent strain were measured at several time points up to 60 million cycles. Using material parameters calibrated to uniaxial tensile tests for HD and HA cases, a finite element simulation of the mechanical testing was conducted to elucidate the individual roles of the pericardial matrix and fibres in the fatigue study. Finally, collagen fibre crimp was measured via post-processing of second harmonic generation imaging analysis (SHG) in ImageJ (San Diego, California, see Fig 1(c)).

Results

HD samples demonstrated increased deformation under 150 mmHg compared to HA samples (3.10 $\pm$ 0.61 mm vs 2.34 $\pm$ 0.63 mm, see Fig. 1(a)), and consequently had significantly higher permanent strain at all time points (Fig. 1(b)). Computational analysis revealed that the experimental deformation could only be simulated for the HD case when the fibre contribution to load bearing was removed from the material model. SHG analysis revealed that collagen fibre crimp in HD tissue was significantly greater than that in HA ($p = 0.0005$, Fig. 1 (d)). As such, this prevented the fibres from load bearing in the HD group, which resulted in the more compliant matrix taking up the applied load; eliciting increased tissue deformation and matrix-driven permanent strain.

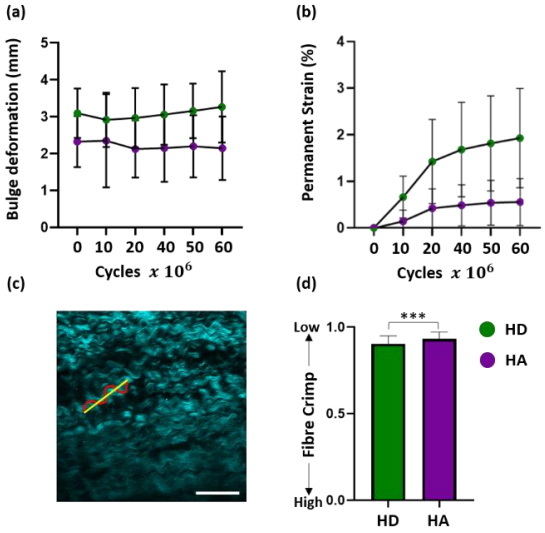

Fig. 1: HD/HA (a) deformation under 150 mmHg (n=6), (b) permanent strain (n=10), (c) SHG analysis with fibre crimp measure (yellow/red), scale bar = 100 μm, (d) fibre crimp, 15 measurements per sample, n=4, p = 0.0005.

Discussion

Although HD GLBP was previously found to have significantly increased collagen content in comparison to HA GLBP [3], in the current study increased HD deformation was observed under low-strain cyclic bulge loading. Furthermore, a computational model revealed that the greater HD deformation was due to an absence of load-bearing fibres. Post-processing of SHG analysis explained this behaviour; where fibres in HD GLBP were significantly more crimped than in HA GLBP (Fig. 1(d)). As collagen fibres must be in tension to load-bear, the highly crimped HD fibres were protected from load-bearing under 150 mmHg. Fundamentally, this increased the mechanical burden on the matrix, and thus increased matrix permanent strain (Fig. 1(b)).

These results have important implications for BHV leaflets, whereby the lack of leaflet pre-screening as per ISO-5840 could result in the use of leaflets with prohibitively high collagen fibre crimp. This would lead to excessive permanent strain-induced geometry changes in the first year *in vivo* and negatively affect the long-term durability of BHVs in patients.

References

1. Zhang and Sacks, *J. Mech. Behav. Biomed. Matr, 75, 2017*.
2. Gaul et al., *J. Mech. Behav. Biomed. Matr, 75, 2017*.
3. Whelan et al., *Ann. Biomed. Eng. 2020*

Acknowledgements This research was funded by the Irish Research Council and Boston Scientific Corporation (EBPPG/2016/353).

ANALYSIS OF A TRANSCATHETER AORTIC VALVE TURBULENT WAKE WITH TOMOGRAPHIC PARTICLE IMAGE VELOCIMETRY

Leonardo Pietrasanta (1), Dominik Obrist (1)

1. ARTORG Center for Biomedical Engineering Research, University of Bern, Bern, Switzerland

Introduction

An increasing number of transcatheter aortic valves (TAVs) is implanted in intermediate-risk aortic stenosis patients with longer life expectancy [1]. Turbulent flow downstream of the TAV increases the transvalvular pressure gradient and over time can cause aorta remodelling, thrombus formation or leaflet damage due to unphysiological stress loads. This study analyses the characteristics of turbulent flow in the aortic root downstream of a self-expanding TAV.

Methods

In-vitro measurement of the three-dimensional flow field in the aortic root was performed in a pulse replicator using a multi-view imaging system for tomographic particle image velocimetry [2]. A self-expanding TAV was inserted in a silicone phantom mimicking the aortic root. The turbulent flow field was measured and statistically analysed. The mean flow field was used to characterize the flow topology while turbulent fluctuations were analysed to assess turbulent kinetic energy (TKE), Reynolds stresses and energy dissipation rate. Turbulent energy density spectra were obtained from the Fourier transform of the autocorrelation function of the turbulent fluctuations.

Results

Turbulent flow was structured in three lobes organized according to the orientation of the valve commissures (Figure 1 A-B-C). Close to the leaflet tips, turbulence was found in the shear layer between the central systolic jet and slower regions of backflow in the vicinity of the aortic wall. One diameter downstream the turbulent field attaches to the aortic wall. TKE was 16.8% of the mean kinetic energy in the aortic root. The turbulent energy spectrum (Figure 1 D) shows an inertial range with slope -5/3. Reynolds stresses reach levels beyond 100 Pa.

Discussion

During systole a Reynolds number (based on peak velocity and valve diameter) of about 5000 is reached in the aortic root and turbulent flow develops. The turbulent flow field is organized along the internal shear layers around the systolic jet and in the vicinity of the aortic wall such that it may contribute to the activation of thrombocytes and the aorta remodeling. The measured energy spectrum is limited by the experimental resolution (around 0.5mm) but shows classical turbulent characteristics.

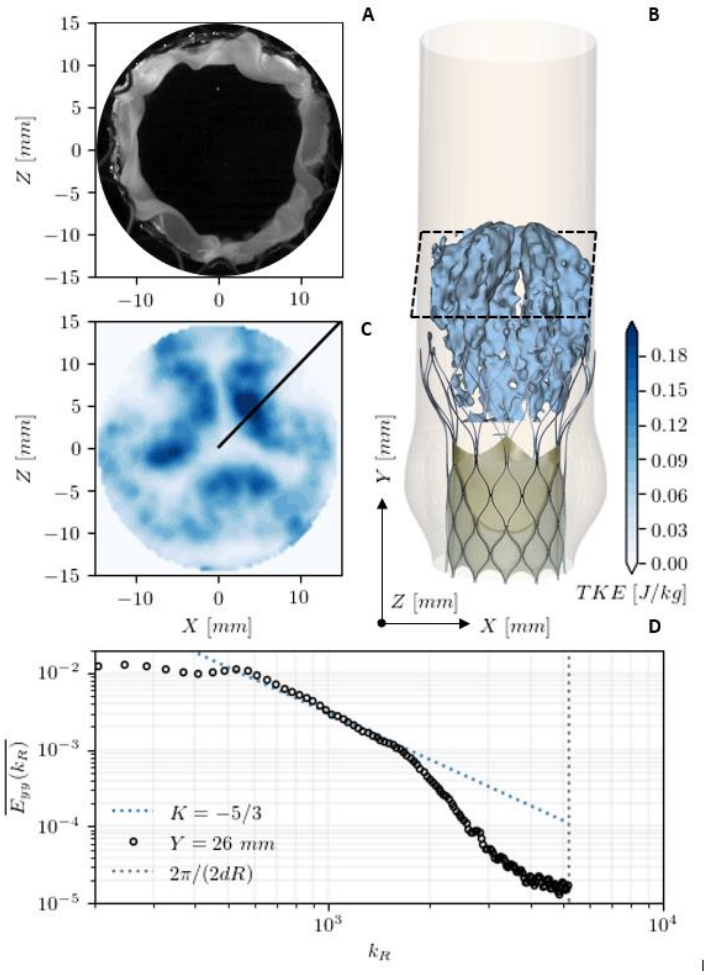

Figure 1: Top axial view of the TAV at peak systole(A). TKE iso-contours(B). TKE density in the aortic root in a slice at 26 mm distance from the sinotubular junction(C). Turbulent energy spectrum $E_{YY}(K_R)$ along the radial wavenumber $K_R(D)$.

References

1. A. Chakos et al., "Long term outcomes of transcatheter aortic valve implantation (TAVI): a systematic review of 5-year survival and beyond," Ann Cardiothorac Surg, vol. 6, no. 5, pp. 432–443, 2017.
2. D. Hasler, A. Landolt, and D. Obrist, "Tomographic PIV behind a prosthetic heart valve," Exp. Fluids, vol. 57, no. 5, pp. 1–13, 2016.

A HYBRID ACTIVE CONTRACTION FOR MYOCARDIUM

Hao Gao, Debao Guan, Xiaoyu Luo

School of Mathematics & Statistics, University of Glasgow, UK

Introduction

The classical Hill model [1] has been widely used for modelling the electro-active response of living tissue, such as myocardium [2]. Due to the complexity of heart wall at different scales, the modelling of myocardium is still challenging, several issues are far from being solved thoroughly, i.e. the strong coupling of electromechanics [2]. In this study, we present a hybrid multiscale active contraction model according to the micro and macro structures of myocardium, both the active stress and active strain approaches are incorporated into a three-element Hill model, see Figure 1.

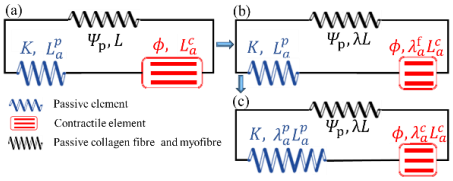

Figure 1: The Hill model of the basic unit of myocardium from the resting state (a) to the passive elongation (b) and to the active contraction (c).

Methods

As shown in Figure 1 for a basic unit of myocardium for describing its mechanical response (here mainly considering sarcomere and collagen), the upper branch characterizes the passive response of myocytes (the titin) and collagen fibres, which can be characterized by a strain energy function $\Psi_{\mathrm{P}}(\mathbf{F})$, $\mathbf{F}$ is the deformation gradient. The lower branch consists of a passive element (i.e. z-disc, costamere complex) and a contractile element (cross-bridges) in series. The contractile element, the region occupied by the thin and thick filaments which can form cross-bridges, is responsible for active contraction further governed by the calcium transient ([Ca]) through action potential. The active tension is transmitted through the passive element to additively contributes to the total stress $\boldsymbol{\sigma}$, that is

$$\boldsymbol{\sigma}=\frac{1}{\det(\boldsymbol{F})}\mathbf{F}\frac{\partial\Psi_{\mathrm{P}}}{\partial\boldsymbol{F}}+K\left(\lambda_a^p-1\right)\hat{\mathbf{f}}\otimes\hat{\mathbf{f}}, \tag{1}$$

where $\hat{\mathbf{f}}$ is the unit myofibre direction, K is the stiffness of the passive element in the active branch, and λ_a^p is the stretch derived from

$$\lambda_{\mathrm{a}}^{\mathrm{p}}L_{\mathrm{a}}^{\mathrm{p}}+\lambda_{\mathrm{a}}^{\mathrm{c}}L_{\mathrm{a}}^{\mathrm{c}}=\lambda L, \tag{2}$$

where $L_{\mathrm{a}}^{\mathrm{p}}$, $L_{\mathrm{a}}^{\mathrm{c}}$, and L are stress-free lengths of the passive element, the contractile element, and the basic unit, λ is the overall fibre stretch, and $\lambda_{\mathrm{a}}^{\mathrm{c}}=\lambda_{\mathrm{a}}^{\mathrm{e}}\,\lambda_{\mathrm{a}}^{\mathrm{f}}$ is the actual stretch of the contractile element with a multiplicative decomposition, a fictious elongation ($\lambda_{\mathrm{a}}^{\mathrm{f}}$) is followed by an electrically activated contraction ($\lambda_{\mathrm{a}}^{\mathrm{e}}$) following the active strain approach, as shown in Figures 1(b) to 1(c). $\lambda_{\mathrm{a}}^{\mathrm{e}}$ further incorporates the length-tension and force-velocity (*f-v*) relationships as follows,

$$\lambda_{\mathrm{a}}^{\mathrm{e}}=\frac{1}{1+\left(1+\frac{\pi}{2}\operatorname{atan}(\beta\ln[Ca])\right)\left(1/\lambda_a^{\min}-1\right)}, \tag{3}$$

$$\lambda_a^{\min}=\left(\kappa_1\lambda^2+\kappa_2\lambda+\kappa_3\right)\frac{1+\kappa_4}{1+\kappa_4 e^{\kappa_5\dot{\lambda}}}, \tag{4}$$

where $\kappa_1 \backsim \kappa_5, \beta$ are constants, $\dot{\lambda}$ is the contracting velocity, [Ca] is the calcium transient.

Results

This new hybrid active contraction model is firstly fitted to the measured experimental active and passive stresses by Hawkins et al [3] as shown in Figure 2(a). Both the active and passive stresses are described very well with this new model at different stretch ratios, and the maximum active tension occurs at $\lambda \approx 1.2$, corresponding to the experimentally reported optimal length of the sarcomere, that is around 2.2 μm. Secondly, an image-derived human LV model is simulated using this active contraction model with fitted parameters from [3] except K. Figure 2(b) shows the modelled end-systolic shapes coloured by myofibre stress, case 1 without *f-v* which has an >50% ejection fraction (EF), case 2 with *f-v* which has a reduced EF (26%), and case 3 with increased K and *f-v* to achieve the same EF as case 1. It can be found that the force-velocity relationship can significantly affect contraction, i.e. more homogeneous stress distribution and wall thickening.

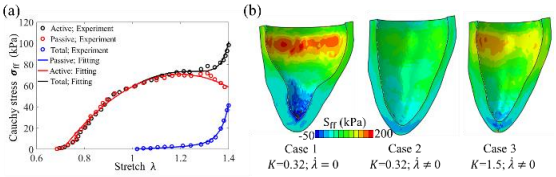

Figure 1: (a) Fitting results to the ref [2]; (b) the Human LV model at end-systole with different K and f-v.

Discussion

A multiscale hybrid active contraction model for myocardium is developed based on the three-element Hill model. It has been successfully fitted to experimental data at different stretches under isometric contraction. We also demonstrate that this model is capable of simulating patient-specific human heart dynamics, and further find that the force-velocity relationship can have a significant effect on the heart pump function.

References

1. Hill et al, Proc. R. Soc. B, 126: 136–195, 1938.
2. Goktepe et al, J Mech Phys Solids, 72: 20 – 39, 2014
3. Hawkins et al, J Biomech, 116: 51-55, 1994.

Acknowledgements

Supported by the UK EPSRC (EP/N014642/1), Chinese CSC scholarship and the fee waiver from the University of Glasgow.

HEMODYNAMIC AND MOLECULAR PROFILES OF STABLE AND UNSTABLE HUMAN CORONARY PLAQUES

Maurizio Lodi Rizzini (1), Giulio Russo (2), Daniela Pedicino (2), Ramona Vinci (2), Diego Gallo (1), Lorenzo Genuardi (2), Francesco Migliavacca (3), Francesco Burzotta (2), Umberto Morbiducci (1), Filippo Crea (2), Giovanna Liuzzo (2), Claudio Chiastra (1)

1. Dept. of Mechanical and Aerospace Engineering, Politecnico di Torino, Italy; 2. Catholic University of the Sacred Heart, Rome; 3. Dept. of Chemistry, Materials and Chemical Engineering, Politecnico di Milano, Italy

Introduction

Coronary atherosclerotic plaques might evolve to different phenotypes (i.e. smooth, eroded, or ruptured plaques) presenting with distinct morphology as well as different molecular patterns [1]. To complete the picture, local hemodynamics, and in particular wall shear stress (WSS), has been identified as a main contributor in plaque erosion due to its biomechanical action on endothelial cells [2]. The interplay among plaque morphology, molecular expression and WSS has been mostly investigated *in vitro* or on animal models, until now. Here we explore the hemodynamic and molecular profiles of stable and unstable (ruptured and eroded) coronary artery plaques in humans combining *in vivo* medical imaging, biological analysis, and computational fluid dynamics (CFD).

Methods

Two groups of patients were enrolled: (1) patients with stable angina (SA) and angiographically confirmed coronary artery disease (n=24); (2) unstable patients presenting with Non-ST Elevation Myocardial Infarction (n=25). Unstable patients were sub-grouped into intact fibrous cap (IFC, n=11) and ruptured fibrous cap (RFC, n=14) based on optical coherence tomography (OCT) analysis. For all patients, peripheral blood mononuclear cells (PBMCs) were isolated from venous blood samples, which were extracted from patients within 24 hours from the symptom onset. The relative gene expression of 17 molecules previously identified as affected by WSS were evaluated using the real time polymerase chain reaction (RT-PCR). Nine cases (3 for each group) were selected for the hemodynamic analysis. Angiographic and OCT images were combined using a previously developed algorithm [3] to obtain three-dimensional models with a high geometrical accuracy. Patient-specific steady-state CFD simulations were performed on the discretized models using the finite volume-based software Fluent (Ansys Inc., Canonsburg, PA, USA). Hemodynamics of the lesion was characterized in term of WSS magnitude and area exposed to high WSS (i.e., >90th percentile of the pooled WSS distribution).

Results

A significant difference was observed between SA, IFC, and RFC groups in 4 out of 17 investigated molecules. As reported in Table 1, IFC group compared to SA and RFC showed a significantly higher levels of genes LGALS8 ($p<0.001$ and $p=0.032$ for SA and RFC, respectively) and EDN1 ($p=0.002$ and $p=0.05$ for SA and RFC, respectively). Levels of gene ADAMTS13 in RFC group were significantly higher than in SA ($p<0.001$) and IFC ($p=0.04$), while levels of gene TNFα in RFC group were significantly lower than in SA ($p=0.016$) and IFC ($p=0.05$).

Gene	SA	IFC	RFC
LGALS8	2.0 (1.2)	17.6(29.2)	6.0(8.7)
EDN1	6.2(5.1)	6.6(3.0)	4.4(2.8)
ADAMTS13	0.9(0.4)	1.0(1.1)	3.1(2.9)
TNFα	22.2(22.6)	26.2(37.1)	2.3(2.9)

Table 1: Median (IQR) of relative gene expression for genes with statistically significant differences between SA, IFC and RFC groups.

RFC plaques presented higher and more heterogeneously distributed WSS values than SA and IFC groups, as a consequence of the higher surface roughness as depicted in the explanatory examples in Figure 1. To confirm WSS visualizations in Figure 1, the RFC group presented with the highest median and interquartile range (IQR) (3.3(7.6) Pa *vs* 1.9(2.4) Pa and 2.5(3.0) Pa for SA and IFC respectively). Moreover, the RFC group presented the largest percentage surface area exposed to high WSS (22.4%), against 10.3% for SA and 5.5% for IFC.

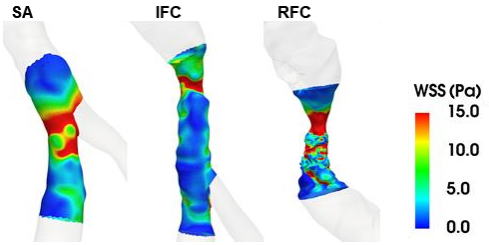

Figure 1: Explanatory examples of WSS luminal distribution in one patient for each investigated group.

Discussion and conclusion

The results obtained in this study confirm that different phenotypes of coronary plaques present different molecular and hemodynamic patterns. Interestingly, the gene ADAMTS13 overexpressed in RFC patients, where WSS was observed to be high, while genes LGALS8, EDN1 and TNFα overexpressed in IFC patients, where WSS was observed to be low. This suggests the existence of a link between gene expression and hemodynamics for the first time *in vivo* in human coronary arteries, which deserves future investigations.

References

1. Pedicino D et al., J Am Coll Cardiol,72(13):1490-503, 2018.
2. Franck G et a., Circ Res, 121:31-42, 2017.
3. Migliori S et al., Med Phys Eng, 78:74-81, 2020.

Numerical and experimental hemodynamic study in an in-vitro 3D printed patient-specific carotid artery bifurcation.

Mahesh S. Nagargoje and Raghvendra Gupta*
Department of Chemical Engineering, Indian Institute of Technology Guwahati, Assam-781039, India.
*Corresponding author: guptar@iitg.ac.in

Abstract

Modeling and simulation of cardiovascular flows contributes to the personalized medicine, surgical planning, and medical device design. The 3D models constructed from the patient's clinical images provide accurate information to plan intervention. Flow patterns in the patient-specific arterial vessels can help in prediction of the probable sites of atherosclerosis formation. Arteries supplying blood to brain are more vulnerable to cardiovascular diseases. Carotid artery is the major cause of atherosclerosis occurance due to presence of sinus. Analysis of hemodynamics in the carotid artery bifurcation shows the flow patterns, identifying and treating the stenosed vessels.

In this work, CFD simulations are performed for three-dimensional patient-specific carotid artery bifurcation to show the probable areas of atherosclerosis formation. Numerical results show that low time-averaged wall shear stress (TAWSS) is observed at the outer wall of the sinus. Similarly, high oscillatory shear index (OSI), and larger relative residence time are observed near the outer wall of the sinus. The low TAWSS, high OSI, and RRT are the indicators of probable sites of atherosclerosis. The particle image velocimetry (PIV) technique is used for the validation of numerical results. The refractive index of the working fluid is matched with the 3D printed patient-specific carotid artery model to avoid an optical error. The flow is seeded with tracer particles and illuminated using the laser. The images are captured using a high-speed camera and cross-correlated to get velocity distribution in a vessel.

Methods

The geometry of the 3D carotid artery model is constructed from CT scan images, which is available online on GrabCAD community.

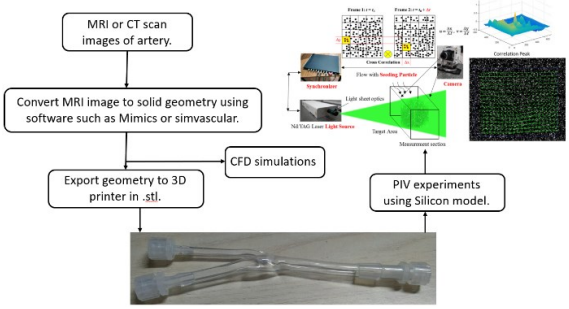

Fig. 1 Schematic diagram of experimental procedure.

Procedure for creating 3D model and silicon phantom of clinical images is shown in Fig. 1. The silicon phantom is further used for PIV experiments. PIV is an optical measurement technique which measures the velocity field in an entire region of interest. PIV consists of laser source, and high-speed cameras for illuminating the tracer particle and aquire images, respectively. In numerical approach, the flow equations are solved with appropriate boundary conditions.

Equation of Continuity:

$$\nabla . \boldsymbol{u} = 0 \quad (1)$$

Equation of momentum conservation:

$$\rho\left(\frac{\partial \boldsymbol{u}}{\partial t} + (\boldsymbol{u}.\nabla)\boldsymbol{u}\right) = -\nabla P + \mu\nabla^2\boldsymbol{u} \quad (2)$$

Results

We have matched the refractive index of blood mimicking fluid (BMF) with flow phantom, as shown in Fig. 2. The properties of BMF are equivalent to blood properties at higher shear rates.

Experimentally validated CFD simulations are carried out for identifying the probable areas of atherosclerosis. The study shows that the sinus has a complex flow patters and outer wall of sinus has a low WSS and high OSI, RRT. Therefore, outer wall of sinus is more vulnerable to atherosclerosis formation.

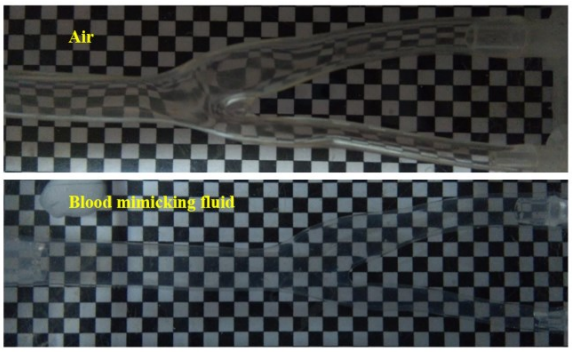

Fig. 2 Refractive index matching of patient-specific carotid artery silicon model with BMF.

Discussion

The procedure for creating silicon phantom is a low cost technique and has a vital role in hemodynamic studies. We are working on the further PIV experiemnts for carotid artery model. Numerical simulations have been carried out with the experimental validation.

References

[1] S. Gunasekera, O. Ng, S. Thomas, R. Varcoe, C. de Silva, and T. Barber, Exp. Fluids **61**, 1 (2020).
[2] W.H. Ho, I.J. Tshimanga, M.N. Ngoepe, M.C. Jermy, and P.H. Geoghegan, Cardiovasc. Eng. Technol. **11**, 14 (2020).
[3] M. Nagargoje and R. Gupta, Comput. Methods Biomech. Biomed. Engin. **23**, 232 (2020).
[4] M. Nagargoje and R. Gupta, Comput. Methods Programs Biomed. **192**, 105440 (2020).

A COMPACT IN VITRO TEST BENCH FOR CARDIOVASCULAR FLOW ANALYSIS FOR SPACE APPLICATION: FEASIBILITY STUDY

Elena Torta (1), Giuseppe Carlo Alp Caridi (1), Stefano Gabetti (1), Claudio Chiastra (1), Diego Gallo (1), Matthieu Compin (2), Umberto Morbiducci (1)

1. PoliTo^{BIO}Med Lab, Dept. of Mechanical and Aerospace Engineering, Politecnico di Torino, Turin, Italy; 2. ISAE-SUPAERO, Université de Toulouse, France

Introduction

The growing interest in the advancement of human deep-space exploration requires a substantial understanding of the associated risks for health. In fact, long-term exposure to microgravity and cosmic radiation pose serious health problems, concerning also the cardiovascular system [1]. For these reasons, the Artery in Microgravity (AIM) project was devised, aiming at investigating how the space environment could impact on coronary artery disease (CAD) development and its common treatments (e.g. the implantation of a coronary stent). In this context, here we propose a compact experimental set-up for the investigation of the local hemodynamics in stenosed and stented left circumflex (LCX) coronary arteries, designed to be used in space flights.

Methods

An experiment cube will fly on board the International Space Station (ISS) within the first "*Orbit Your Thesis!*" Programme of ESA Academy. Technically, a compact in vitro test bench was designed to fit inside a 2U experiment cube (225x100x100mm^3) plugged into the ICE Cubes Facility on board the ISS. An on-board minimal system for Particle Image Velocimetry (PIV) and Flow Visualization (FV) will allow to test if microgravity interferes with blood flow causing flow disturbances that, in turn, lead to CAD or stent failure. Additionally, a pH probe will monitor the concentration of ions released due to the interaction between cosmic radiation and stent metallic alloy. For these purposes, two 3D printed silicone coronary phantoms were obtained from angiographic images, the first representing a stenotic LCX artery, the second reproducing post-stent implantation. Once in orbit, experiments will be remotely controlled by a ground station.

Preliminary FVs were performed to demonstrate the feasibility of the compact and inexpensive optical imaging system applied to the realistic LCX models. Measurements were conducted at a constant pressure head of 8.9 mmHg monitoring flow rates (in the range 40-100 ml/min) and pressure loss (Δp) through the coronaries. A 12 MP ISOCELL 2L3 (pixel size 1.4µm) camera was embedded in the system for time-resolved frames (190x730 pixel at 960Hz) acquisition. The coronary phantoms were illuminated using a white continuous LED. A blood-mimicking fluid (glycerol-water, 33:67) was seeded with polyamide particles (ρ=1.1 g/cm^3, diameter=100µm) ensuring adequate light scattering as shown in Figure 1.

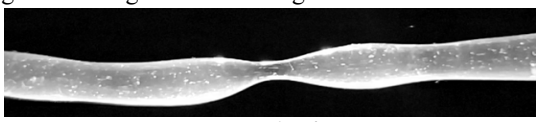

Figure 1: Example of raw image.

Results

The velocity field, obtained with the open-source code PIVlab [2], had a spatial resolution of 0.36 mm (Figure 2), sufficient to capture the main flow features and to estimate Reynolds stresses at different flow conditions. The results also highlighted the expected presence of high spatial velocity gradients in correspondence of the stenosis. The onset of low turbulence structures emerged at higher flow regimes. The presence of an expected recirculation region of extension depending on the investigated flow regime emerged by tracking particles from the time-resolved raw images.

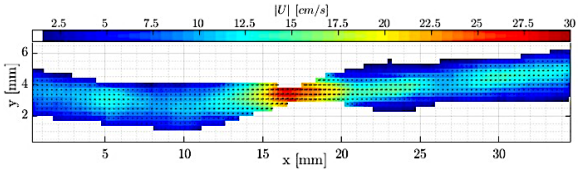

Figure 2: 2D contour plot of the mean absolute velocity field. The fluid flows from the left to the right at 78 ml/min.

Discussion

The findings of this analysis support the feasibility of velocimetry measurements in a very compact test bench for experiments on cardiovascular phantoms in deep space for the first time. The results from on-heart tests will be compared with the planned flight tests in microgravity conditions. Notably, the compact and inexpensive time-resolved imaging system presented in this study candidates to be a reliable low-cost instrument for qualitative and quantitative flow diagnostics for the evaluation of the hemodynamic performance of implantable cardiovascular devices.

References

1. Hughson R.L. et al., *Nat Rev Cardiol*, 15: 167-180, 2018
2. Thielicke W. PIVlab. particle image velocimetry (PIV) tool with GUI, GitHub. Retrieved January 27, 2021.

Acknowledgements

This work was supported by ESA Academy of ESA Education, Fondation ISAE-SUPAERO, Alvimedica, Elastrat, AIRBUS, University Space Centre of Toulouse (CSUT), Space Application Services, ISAE-SUPAERO and Politecnico di Torino.

IMPACT OF NON-NEWTONIAN BLOOD BEHAVIOR ON LEFT VENTRICLE 4D FLOW ENERGETICS

Alessandra Riva (1,2), Francesco Sturla (2,1), Alessandro Caimi (1), Silvia Pica (2), Daniel Giese (3), Paolo Milani (4), Giovanni Palladini (4), Massimo Lombardi (2), Alberto Redaelli (1), Emiliano Votta (1,2)

1. Politecnico di Milano, Milano, Italy; 2. IRCCS Policlinico San Donato, San Donato Milanese, Italy; 3. Siemens Healthcare GmbH, Erlangen, Germany; 4. Fondazione IRCCS Policlinico San Matteo and University of Pavia, Pavia, Italy

Introduction

Blood is a non-Newtonian fluid, whose viscosity (μ) depends on hematocrit level (Hct) and shear rate ($\dot{\gamma}$). However, it is generally modeled as a Newtonian fluid with a constant viscosity. This assumption could be inappropriate for left ventricle (LV) highly pulsatile and recirculating intracavitary flow [1]. We exploited 3D time-resolved velocity-encoded phase-contrast MRI (4D Flow) to assess the impact of different viscosity models on the patient-specific quantification of LV energetics.

Methods

4D Flow, acquired using a prototype sequence on a 1.5T MAGNETOM Aera (Siemens Healthcare, Erlangen, Germany) was analyzed on two small cohorts of controls (n = 5) and patients with cardiac light-chain amyloidosis (AL-CA, n = 5), the latter enrolled due to the relevance of non-Newtonian properties in AL-CA pathology. We investigated the effect of three viscosity models on the 4D Flow–derived LV energetics:

1. Newtonian with standard viscosity, i.e., 3.7 cP [2];
2. Newtonian with subject-specific Hct-dependent viscosity [3];
3. Non-Newtonian, accounting for both Hct and $\dot{\gamma}$ effects, according to the Quemada formula [4]:

$$\mu = \frac{\mu_{plasma}}{\left(1 - \frac{Hct \cdot k_{eq}(\dot{\gamma})}{2}\right)^2} \qquad (1)$$

Specifically, we quantified viscous energy loss (EL), the blood kinetic energy irreversibly lost due to frictional viscous forces, over the cardiac cycle and normalized it by LV end-diastolic volume (EDV), i.e., EL_{EDV}.

Results

If compared to the standard value of 3.7 cP, μ mildly deviated in Model 2, ranging between 3.0 cP (-19%) and 4.3 cP (+16%). In Model 3, μ markedly increased up to 6.0 cP in the intracavitary LV regions at low shear rate ($\dot{\gamma}$ < 100 s^{-1}, **Figure 1**). If compared to Model 2, Model 3 exhibited a Bland-Altman bias equal to +1.4 cP for controls and +0.9 cP for AL-CA patients.

This effect reflected on EL (**Figure 2**), with Model 3 yielding markedly higher EL values or markedly lower when Hct was higher than 39.5% or lower than 30%, respectively. Indeed, EL_{EDV} (**Figure 2**) increased up to 4.73 J/m^3 in subject C_3 (+40% than Model 1) and decreased from 4.73 J/m^3 to 3.73 J/m^3 (-21.2%) in subject A_1.

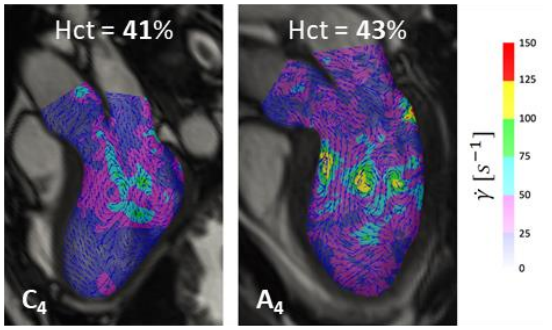

Figure 1: $\dot{\gamma}$ at mid-diastole in datasets C_4 and A_4.

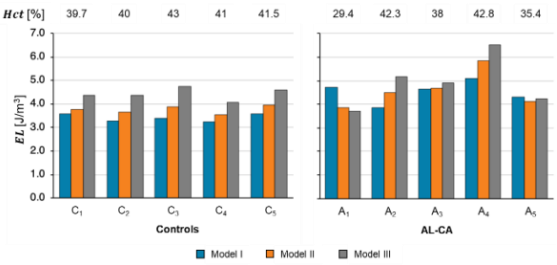

Figure 2: EL_{EDV}, from each dataset for both Newtonian Model 1 (blue) and Model 2 (orange), and non-Newtonian Model 3 (dark-grey).

Discussion

4D Flow characterization of LV blood energetics can be affected by the chosen viscosity model. A more detailed description, accounting for Hct and $\dot{\gamma}$ effects, impacted computations especially in regions characterized by recirculating or low velocity flows. Hence, taking non-Newtonian blood behavior into account on a patient-specific basis may enhance the accuracy of intracardiac non-invasive 4D Flow energetics.

References

1. Caballero *et al.*, Cardiovasc Eng Technol, 4:103-130, 2013
2. Frauenfelder et al, Biomed Eng Online, 6: 1-13, 2007
3. Guyton and Hall, Textbook of Mecial Physiology, 2006
4. Quemada, Rheol. Acta, 17: 643-653, 1978

Acknowledgements

IRCCS Policlinico San Donato is a clinical research hospital partially funded by the Italian Ministry of Health.

REGIONAL DIFFERENCES IN AORTIC FUNCTION: TRI-LAYERED MODELLING OF THE PIG AORTA

Alessandro Giudici (1), Bart Spronck (2,3), Ashraf W Khir (1)

1. Biomedical engineering theme, Brunel University London, Uxbridge, UK; 2. Department of Biomedical Engineering, Yale University, New Haven, CT, USA; 3. Department of Biomedical Engineering, Maastricht University, Maastricht, The Netherlands

Introduction

The micro- and macro-structures of the three-layered arterial wall determine its macroscopic mechanical properties. Despite providing valuable insight into the layer-specific mechanics, uniaxial testing of isolated layers (intima, media, and adventitia) does not adequately mimic the in vivo loading state. On the other hand, by accounting for the layer-specific residual deformations, tri-layered wall modelling allows simulating native physiologic loading conditions. Using this approach, this study aimed to investigate differences in the response of the pig ascending and descending thoracic aorta to both physiological and pathological loading conditions.

Methods

N=5 pig (age 6-12 months) aortae were obtained from a local abattoir and stored at -20ºC. Segments from the ascending aorta (AA) and lower thoracic aorta (LTA) were isolated from each artery, and their circumference measured using a digital calliper. Circumferentially and axially oriented strips were excised from each segment and subjected to uniaxial tensile testing (MFS Stage with 20N load cell, Linkam Scientific Ltd., UK). After testing, each arterial strip was separated into the intima, media and adventitia by peeling, and each layer was tested separately.

The mechanical behaviour of each layer was fitted using a hyperelastic strain energy function [1]. Then, the three layers were computationally assembled into a single flat-walled sample, and the layer-specific residual strains were tuned so that the three-layered model response would match the mechanical response of the intact wall to uniaxial extension. Finally, the flat-walled model was deformed into a cylindrical vessel and physiologically pressurised and axially elongated.

Results

Inner diameter (*D*) and wall thickness (*h*) differed significantly between AA (22.14±1.40 and 2.66±0.14 mm) and LTA (12.88±0.57 and 1.47±0.14 mm) (both $p<0.001$), as did the layers relative thicknesses: 11±1:65±4:24±3% (intima:media:adventitia, AA) and 16±2:46±5:38±4% (LTA, $p<0.001$ for all).

At 100 mmHg of intraluminal pressure, circumferential Cauchy stress was 87±16 and 74±6 kPa at the AA and LTA, respectively. At both locations, the media bore most of the circumferential load (72±8% and 61±7%), with a relatively small contribution of the adventitia (23±7% and 28±7%) and negligible role of the intima. Conversely, when pressure was increased to 160 mmHg, the shift in load-bearing from the media to the adventitia was markedly higher at the LTA (-8±1% for the media and +9±2% for the adventitia) than at the AA (-2±1% and +2±1%, respectively). This shift was driven by the stiffening of the adventitia over the 60 mmHg pressure increase, much higher at the LTA (+226%) than at the AA (+135%, $p<0.001$).

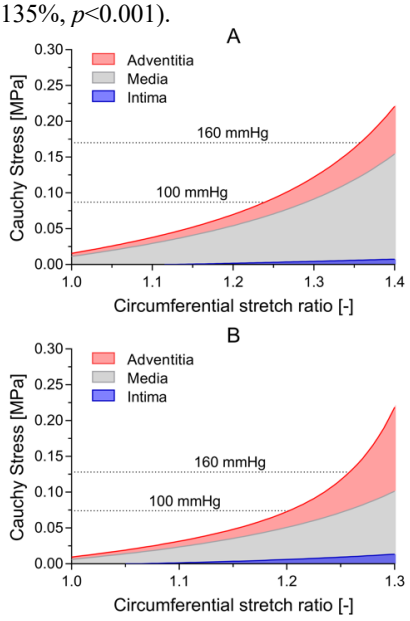

Figure 1: Stress-stretch relationships with load partitioning between layers of one of the studied ascending (A) and lower thoracic (B) aortae.

Discussion

Tri-layered modelling of the arterial wall allowed characterising the pig thoracic aorta's multiscale mechanical behaviour, highlighting marked functional differences between proximal and distal regions. At the AA, the media bears most of the circumferential stress independently of the considered pressure range, thus conferring the highly compliant function to the wall. Conversely, at the LTA the fast recruitment of the adventitia provides protection against high pressures.

References

1. Holzapfel et al, Am J Physiol Heart Circ Physiol, 289:H2048-H2058, 2005.

Acknowledgements

We thank Jay D. Humphrey for his support and valuable advice. This work was supported by the ARTERY society.

ANALYSIS OF THE INFLUENCE OF DIFFERENT MECHANICAL STIMULI IN ATHEROMA PLAQUES IN PATIENT-SPECIFIC CAROTIDS

Patricia Hernández (1), Myriam Cilla (1, 2, 3), Miguel Ángel martínez (1, 3), Estefanía Peña (1, 3)

1. *Aragón Institute of Engineering Research (I3A). University of Zaragoza, Zaragoza, Spain*
2. *Centro Universitario de la Defensa. Academia General Militar, Zaragoza, Spain*
3. *Biomedical Research Networking Center in Bioengineering, Biomaterials and Nanomedicine (CIBER-BBN), Spain*

Introduction

Consequences derived from atherosclerosis –a disease that causes a narrowing of the lumen area of arteries by developing atheroma plaques in the arterial wall- are one of the most important causes of mortality in developed countries. It can result, among others, in ischemia or heart attacks. For all of this, it is important to understand the process of formation of atheroma plaques and the places of the arteries in which they occur, to prevent the development and consequences of the disease. Several authors have studied Wall Shear Stress (WSS) as the main mechanical stimulus to develop atheroma plaques but, recently, some studies have shown that the cardiac cycle has influence on the developed plaques and so, other mechanical stimuli can have influence on it.

Methods

We propose a mathematical model to predict the areas of the arteries susceptible of developing atheroma plaques by using some patient-specific pathological images of carotid arteries bifurcations with presence of plaques. We repair these pathological images by removing atheroma plaques, and finally we reconstruct the wall of the arteries with variable thickness [1].

We study different hemodynamical stimuli to determine which one is the most important to predict the location of plaques. In particular, we use Time Average Wall Shear Stress (TAWSS), Oscillatory Shear Index (OSI) and a new variable that we propose as a combination of them based on pseudo-experimental data [2].

In the mathematical model [3], we use Navier-Stokes equations to model transient blood flow along the lumen [4] and we model the flow of plasma and substances through the endothelium with the model of three pores [5], Darcy's Law and Kedem-Katchalsky equations. Finally, we use convection-diffusion-reaction equations for all the substances in the arterial wall and compute the growth of plaques for a total time of 30 years. We also compute a healthy geometry to validate that it do not develop plaques.

The model considers several substances, that are LDL, oxidized LDL, monocytes, macrophages, cytokines, foam cells, contractile and synthetic smooth muscle cells and collagen fibbers, and includes terms of proliferation, degradation, oxidation, apoptosis and differentiation of the substances.

Results

Results show that the new variable that we propose as combination of TAWSS and OSI predicts better both location and growth of plaques than only use one of them. They also show that TAWSS predicts better the growth of plaques than OSI, but it predicts some plaques that are not in the real patients, while OSI locate in a more precise way the plaques.

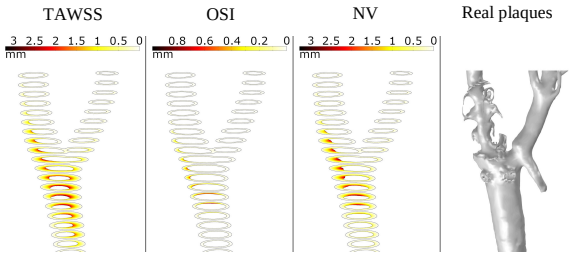

Figure 1: Growth of plaques after 30 years in one of the geometries with the different mechanical stimuli studied and the real plaques of the patient.

Discussion

A computational model capable of predict atheroma plaque apparition in arteries has been developed and validated with different geometries. The model concludes that it is better to consider a combination of TAWSS and OSI to improve the accuracy of plaques prediction, rather than only one of them.

References

1. G. Sommer et al. Am. J. Physiol. - Heart Circ. Physiol. 298(3):898-912, 2010.
2. P. Sáez et al. J. Math. Biol. 67, 1765-1793.
3. M. Cilla et al. J. R. Soc. Interf. 11:201308661, 2014.
4. M. Malvè et al. Comp. Meth. Biomec. Biomed. Eng. 17(11):1248-1260, 2014.
5. U. Olgac et al. Am. J. Physiol. - Heart Circ. Physiol. 294(2)909-919, 2008.

Acknowledgements

Support from the Spanish Ministry of Economy and Competitiveness through the research project DPI2016-76630-C2-1-R and the grant BES-2017-080239.

A COMPUTATIONAL STUDY OF INTERSTITIAL FLOW ON SMOOTH MUSCLE CELLS IN HUMAN COMMON CAROTID ARTERY: THREE-LAYER MODEL

Sercan Altundemir (1), S. Samaneh Lashkarinia (2), Kerem Pekkan (2), A. Kerem Uguz (1)

1. Department of Chemical Engineering, Bogazici University, Istanbul, Turkey
2. Department of Mechanical Engineering, Koc University, Istanbul, Turkey

Introduction

Endothelial cells (ECs) of an artery sense directly the shear stress originating from the blood pressure. The intracellular signals transduced from the alterations in shear stress are transmitted to vascular smooth muscle cells (SMCs) to regulate the function of the artery [1]. In case of an endothelial damage, SMCs are also exposed to shear stress resulted in an increase in the intensity of interstitial fluid flux. These alterations in shear stress lead to phenotype changes in SMCs which are associated with neointima formation and possible flow-initiated atherosclerosis [2].

Understanding interstitial flow and interstitial flow-mediated shear stress on SMCs is critical in determining strategies to prevent the plaque formation. To obtain a viable model to describe the interstitial fluid behaviour of artery, it is necessary to account for both the solid and fluid components of the tissue since the deformational behaviour of artery directly affects the hydraulic permeability.

In this work, a three-layer biphasic model for common carotid artery (CCA) which includes the flow of the interstitial fluid as well as the deformation of the solid phase of the artery is developed and numerical methods were used to compute water flux through the media under lumen blood pressure in FEBio [3]. For each layer of artery, biphasic material consists of hyperelastic solid material and Darcy fluid with a strain dependent permeability model.

Methods

The meshed representation of longitudinal section of FEM model introduced in this paper is shown in Figure 1. A symmetric thick-walled concentric cylindrical model is employed. Each different colored layer represents the real layers in human CCA. The wall of the artery consists of very thin inner (intimal) layer, a medial layer, and an adventitial layer 33% thinner than the medial one at inner zero fluid pressure load configuration.

The biphasic configuration of each layer is initially defined as 37% fluid-filled pores and 63% incompressible solid.

Results

Figure 2 illustrates how interstitial fluid flow changes with increasing transmural pressure difference in physiological range.

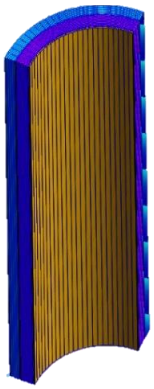

Figure 1: The meshed geometry of the human CCA model.

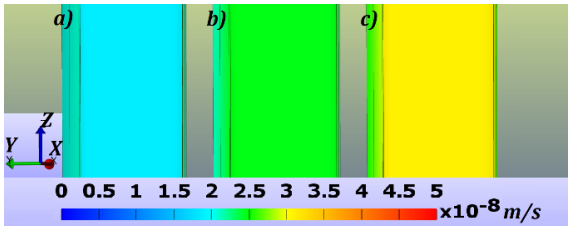

Figure 2: Steady-state interstitial fluid flow in radial direction at a)70 mmHg b)90 mmHg and c)110 mmHg

Discussion

By the alteration of transmural pressure, we are able obtain load-dependent change in interstitial fluid flow and hydraulic permeability for the investigation of shear stress on the smooth muscle cells. Since the thickness of the layers are compressed in radial direction while the diameter of the artery is increased, it is observed that the change in pore volume and hydraulic permeability of the cylindrical configuration show different behaviour than that of an axial and longitudinal stress-free rectangular block model [4]. In this geometry, the dependence of permeability of each layer on the nonlinear deformation is defined in more realistic way.

References

1. Orr et al, J Vasc Res, 47:168–180, 2010
2. Shi et al, Ann Biomed Eng, 39:1608-19, 2011.
3. Maas et al, J Biomech Eng, 134:011005-011005, 2012.
4. Chooi et al, J R Soc Interface, 13: 20160234, 2016.

A COMPUTATIONAL FRAMEWORK FOR MICROSTRUCTURAL REMODELLING INDUCED BY HEMODYNAMIC ALTERATIONS

Daniele Bianchi (1), Elisabetta Monaldo (2), Giuseppe Vairo (3), Michele Marino (3)

1.DICAr, University of Pavia, Italy; 2. Department of Engineering, Roma Tre University, Italy
3. DICII, University of Rome "Tor Vergata", Italy

Introduction

Investigation of arterial physiopathology needs the introduction of multi-field mechanisms, driven by the complex interplay between mechanics and cell-cell signaling pathways [1]. In this framework, a challenging open issue in biomechanics is to model the effects of physio-pathological mechanisms on the macroscale functional response of cardiovascular structures, starting down from their biological onset. With the aiming of understanding physiological and pathological processes to improve diagnosis and therapy, a computational model, instructed with time-varying histological and biochemical information, is developed.
This study addresses the coupling between hemodynamic alterations in wall shear stress (WSS) and in tissue mechanical response by introducing remodelling processes acting on tissue microstructure.

Methods

Pulsatile blood flow is simulated by coupling a 3D computational fluid dynamics (CFD) description within the vessel segment with a 0D treatment of boundary conditions based on a Windkessel model [2]. The fluid-pressure loading is applied as loading condition in the structural problem. The mechanical problem accounts for the nonlinearly elastic anisotropic behaviour of arterial tissues. The constitutive response of aortic tissues is modelled via a recently proposed multiscale structural approach [3]. By describing non-linear mechanics of crimped collagen fibers and accounting for tissue lamellar structure, a multi-step homogenization procedure allows to couple non-linear behavior of tissue substructures at different scales. Following clinical evidence [4], hemodynamic alterations are integrated in a remodeling rationale involving the constituents and the microstructure of the arterial tissues.

Results

Referring to ascending thoracic aortic aneurysm, parametric analyses are performed by comparing different idealized geometries and remodeling laws. Useful indications on localization mechanisms induced by altered flow conditions are obtained. In particular, dysregulations in WSS based index (Topological Shear Variation Index) distributions activate significant changes in wall microstructural features through different scales (from nano to macro). The obtained remodeling induces in turn regional heterogeneities in tissue stiffness (see Fig. 1), in agreement with recent evidence [4].

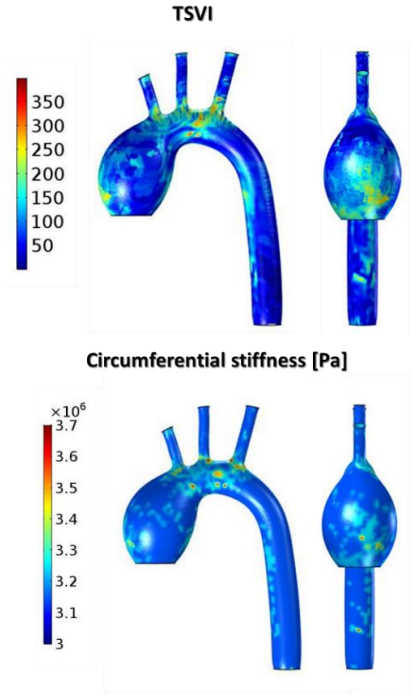

Figure 1: Spatial distribution of: Topological Shear Variation Index (i.e., WSS based index) [4] (top) and circumferential stiffness (bottom).

Discussion

This work investigates vascular pathologies via a multiscale and multiphysics rationale. The proposed condensed remodelling strategy is able to furnish a first insight on the causality coupling hemodynamic alterations and tissue mechanical response as induced by remodelling processes acting on tissue microstructure.

References

1. Michel, J.B. et al., "Topological Determinants and Consequences of Adventitial Responses to Arterial Wall Injury". Arterioscler. Thromb. Vasc. Biol. 27, 1259–1268 (2007).
2. Bianchi, D, et al. "A FSI computational framework for vascular physiopathology: a novel flow-tissue multiscale strategy." Med. Eng. Phys. 47 (2017): 25-37.
3. Bianchi, D, et al. "An integrated computational approach for aortic mechanics including geometric, histological and chemico-physical data." J. Biomech. 49.12(2016):2331-40.
4. De Nisco, G. et al. "Deciphering ascending thoracic aortic aneurysm hemodynamics in relation to biomechanical properties." Med. Eng. Phys. 82 (2020): 119-129.

MECHANICS OF THE POTENTIAL BLOOD FLOW GENERATION ON THE CONCAVE SURFACE OF THE LEFT ATRIUM

E. Talygin, A. Gorodkov
A.N. Bakulev National Medical Research Center of Cardiovascular Surgery

Introduction

The easily disturbed hemostatic blood balance in conjunction with the fragility of the endothelium suggest that swirling blood flow in the heart and great vessels is potential. A-priori there are no local vortex disturbances that spawn separation and stagnant zones that cause a risk of spontaneous thrombus formation. In contrast to other flow regimes, the potential flow regime allows the blood flow to maintain its structure without noticeable changes sought in sufficiently extended sections of the arterial vascular network. Another crucial factor of the hemostatic balance maintaining is the requirement of the blood constant movement along the entire path of the swirling flow. However, obtaining analytical expressions describing the potential flow of an arbitrary structure is fraught with significant theoretical and computational difficulties. Thus, the mechanics of the stable potential flow occurrence in the arbitrary viscous medium has not yet been described. The main problem is that it has not yet been proven whether smooth solutions of the Navier-Stocks equation always exist in three dimensions. So, there are only a few exact solutions for relatively simple special cases [1]. In the previous works, we studied a swirling flow described by one of such exact solutions [2]. This solution assumed that sought flow is potential. However, the mechanics of such potential swirling flow generation remained unclear. It was only experimentally established that a necessary condition for their formation is the presence of a streamlined concave surface [3].

Methods

For this work we used images of the left atrial cavity obtained for 10 moments of the cardiac cycle by MSCT. Then 10 sections of the left atrium dome were derived at different angles for each image. These sections were approximated by some mean generatrix, which was compared with the generatrix obtained from the exact solutions using the least square method. The resulting generatrix was used to construct a surface of revolution, which was considered as a streamlined surface. Further, in accordance with the principles of continuum mechanics, the forces acting on the flow falling in the obtained concave surface were derived.

Results

It has been shown that the streamlined surface of the left atrium is always concave relative to the incoming blood flow. The left atrium dome surface can be approximated by concavity derived from exact solutions with high accuracy. This concavity geometry corresponds to conditions of the potential swirling jet generation. The resultant forces (including centripetal and Magnus forces) are maintained in this concavity, which ensures the formation of a stable swirling jet. When the mitral valve opens and the pressure gradient between the left atrium and the left ventricle appears, the swirling stream of blood is injected along certain streamlines without mixing. Resulting swirling flow is consistent with known transmitral blood flow characteristics both in size, volume, and velocity. Thus, it has been proved that the necessary conditions for the stable potential flow generation are maintained in the left atrium throughout the entire cardiac cycle. In addition, theoretical expressions and related physical mechanisms were obtained for deriving a swirling potential jet of a given structure. It is this flow regime that provides the opportunity to formally describe the known complex of the blood flow characteristics in a single model.

Discussion

The curvature of the left atrium dome corresponds to the necessary and sufficient conditions for the generation and evolution of the flow during the entire cardiac cycle. Incomplete mathematical model can be derived on the mechanics of swirling flow formation on the curved surface of the left atrium. That model can be significantly improved later, considering the systole of the left atrial appendage, which supports constant maintenance of the swirling potential blood flow structure throughout the entire cardiac cycle. This flow regime allows to formally describe the known complex of the blood flow characteristics in a single model.

References

1. C.Y.Wang., Annual Review Of Fluid Mechanics, Vol.23:159-177, 1991.
2. E.A.Talygin, G.I.Kiknadze, A.Yu.Gorodkov et al, ASME IMECE 2019
3. G.I.Kiknadze, I.A.Gachechiladze, A.Yu.Gorodkov, ASME 2009 Heat Transfer Conference

MECHANICAL IN SILICO MODEL OF WELL-ORGANIZED FIBROUS SCAFFOLDS FOR CARDIAC REGENERATION

Nicolás Laita (1), Miguel Ángel Martínez (1,2), Miguel Castilho (3,4), Manuel Doblaré (1,2), Estefanía Peña (1,2)

1. Aragón Institute of Engineering Research (I3A), University of Zaragoza, Zaragoza, Spain

2. Biomedical Research Networking Center in Bioengineering, Biomaterials and Nanomedicine (CIBER-BBN), Spain

3. University Medical Center Utrecht, Utrecht, Netherlands

4. Eindhoven University of Technology, Eindhoven, The Netherlands

Introduction

Myocardium infarction (MI) provokes the necrosis of an area of cardiac muscular tissue. It is mostly caused by the blockage of the coronary artery, which generates hypoxia and subsequent tissue death. This cardiac episode results in a reduction of myocardium mechanical and electrical properties and a consequent significant loss of pumping capacity. One of the most standardized treatments after MI is the application of a ventricular assistant device (VAD) which supplements the pumping function of the pathologic heart. However, these devices do not constitute a long lasting solution due to haemostatic events and infection. Alternative strategies have been proposed in the last years involving new technologies such as cell therapy and tissue engineering [1-2]. One recent promising approach consists on the development of a Biologic VAD (BioVAD) that can restore the myocardium pumping capacity. This device consists of a polycaprolactone (PCL) fibrous scaffold, printed by Melt Electrowritting (MEW), that is then filled with a cell laden hydrogel. In this work, we focused on the design process of the BioVAD scaffold, aiming to optimize its mechanical response regarding the physiological requirements that will withstand once implanted.

Methods

PCL hexagonal-shaped-fibrous scaffold samples were fabricated by MEW as previously described [3]. Uniaxial tensile tests were performed for the validation of the computational models following a testing protocol described elsewhere [3]. An elastoplastic constitutive material model was selected, after looking at the loading-unloading behavior of the tested scaffolds. A specific finite element computational model was created and a parametric analysis was performed to determine the optimal geometrical configuration for the scaffold. The influence of several aspects such as pore size, pore alignment, scaffold thickness or PCL wall thickness was evaluated, and alternative geometries, such as an auxetic one, were also considered. The geometrical configuration was optimized in order to improve its behavior at physiological strains, which was considered to be about 15-25% of strain for the epicardium, where the BioVAD will be implanted.

Results

Our results compare the experimental and simulated mechanical response. Great adjustment was observed until 30% strain (Figure 1b). Greater stiffness was shown as scaffold thickness or pore alignment increased and as pore size decreased. Scaffold + hydrogel in silico models were also created and it was observed that the obtained stiffness also increased significantly.

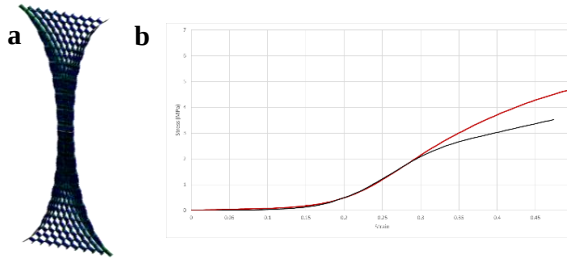

Figure 1: (a) 50% strain Numerical results obtained for a monotonic uniaxial test, (b) Experimental (red) and numerical (black) uniaxial tensile curve comparison

Discussion

A parametric computational model of a BioVAD-specific PCL scaffold was created and validated. A parametric analysis has been performed to study the influence of several geometrical aspects on the mechanical response such as cell alignment, cell size or scaffold thickness. Relevant differences were observed in the mechanical response for each of these parameters, which gives plenty of opportunities to optimize the scaffold design and its performance.

References

1. Mathur, A., et al. *European heart journal*, 2017. 38(39): p. 2930-2935.
2. Weinberger, F., et al. *Circulation research*, 2017. 120(9): p. 1487-1500.
3. Castilho, M., et al. *Advanced Functional Materials*, 2018. 28(40): p. 1803151.

Acknowledgements

Funding provided by the European Economic Community through project BRAV3, C1-BHC-07-2019, H2020 and the Spanish Ministry of Economy and Competitiveness through research project DPI2016-76630-C2-1-R

HETEROGENOUS MATERIAL CHARACTERIZATION OF ATHEROSCLEROTIC HUMAN CAROTID ARTERIES

Su Guvenir (1), Hakki M. Torun (2), Hendrik H.G. Hansen (3), Ali C. Akyildiz (1,4)

1. Department of Biomedical Engineering, Erasmus Medical Center, The Netherlands
2. School of Electrical and Computer Engineering, Georgia Institute of Technology, USA
3. Department of Radiology and Nuclear Medicine, Radboud Medical Center, Nijmegen, The Netherlands
4. Department of Biomechanical Engineering, Delft University of Technology, The Netherlands

Introduction

The knowledge on the heterogenous plaque properties of atherosclerotic human carotids is limited since it is mostly provided as averaged homogenous properties obtained by non-physiological loading conditions [1]. In this work, we developed a numerical-experimental inverse finite element modelling (iFEM) pipeline to characterize heterogeneous atherosclerotic human carotid artery properties. The iFEM comprises an ex-vivo inflation testing, a high resolution pre-clinical imaging and a machine-learning-based optimization.

Methods

Five atherosclerotic human carotids were tested in inflation testing setup with quasi-static pressures of 10 mmHg up to 120 mmHg. At each pressure, arteries were scanned with a high frequency ultrasound (US) (Vevo 2100) and the acquired radiofrequency data were processed by a cross-correlation technique for full-field plaque deformation [2]. After tests, multicomponent atherosclerotic artery compositions were obtained with a high field (7 Tesla) pre-clinical MRI. The plaque components (fibrous intima, lipid core, arterial wall and calcification) of 13 plaque cross sections were segmented on US registered MR images, to create multi-component, 2-D, plane strain FE models (ABAQUS, ver. 2016) as Yeoh solids. Then, these models were used in the iFEM (Fig.1), where the fibrous intima and arterial wall Yeoh constants were iteratively predicted by the Deep Partitioning Tree Bayesian Optimization (DPTBO) [3], by minimizing the difference between the computed and experimentally measured plaque displacements. At the end of the iFEM, a trained Gaussian Process (GP) model, which dramatically reduces the number of optimization iterations [3], was obtained per each cross section. The GPs were then inverted to assess the uniqueness of the iFEM-derived parameters.

Results

For all samples, ex-vivo inflation tests, high-resolution (45x55μm) US data acquisition and high-resolution MRI (50x50μm) were performed successfully. In 13 cross section, a convergence was achieved with average of 3.8 ± 2.2 normalized mean square errors. The material properties achieved by the iFEM approach (Fig.2 (A)) and the GP model (Fig.2 (B)) for a combination of 13 cross sections were demonstrated in Figure 2, and there was no significant difference observed qualitatively between the graphs. Thus, the solutions were concluded to be unique.

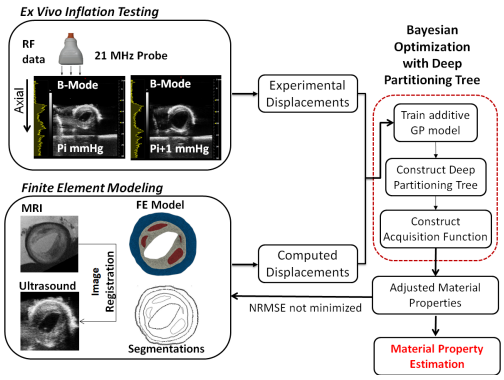

Figure 1: The developed iFEM framework.

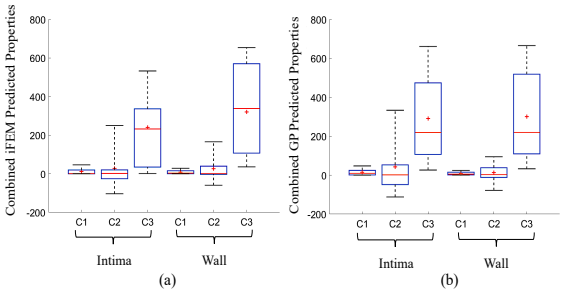

Figure 2: iFEM predicted (a) and GP model predicted (b) Yeoh material constants for 13 cross sections.

Discussion

In this study, we have developed a pipeline, namely the iFEM approach, successfully obtained the component-wise heterogeneous properties of atherosclerotic human carotid arteries by using in-vivo-like inflation testing, pre-clinical US and MRI, and a highly efficient DPTBO. The uniqueness of solutions was qualitatively checked by using the advantage of the trained GP model within the DPTBO system, and the qualitative assessments shown unique results for the cross sections used for this work. The investigation on the use of the clinical versions of the imaging techniques used in this study holds the great potential for the application of the iFEM on in-vivo clinical applications.

References

1. Akyildiz et al., J Biomech, 47.4:773-783, 2014.
2. Hansen et al., IEEE Trans. Med Im., 28.6:872-880, 2009.
3. Torun et al., IEEE Trans. Microw. Theory, 67:2128, 2019.

GARMENTS' INFLUENCES ON BLOOD PERFUSION TO FOOT MICROCIRCULATION DURING INTERMITTENT PNEUMATIC COMPRESSION

Bitian Wang (1), Zhujun Sun(1), Weiyan Ren(2), Yawei Wang (1)*, Yubo Fan (1)*

1. Beijing Advanced Innovation Centre for Biomedical Engineering, School of Biological Science and Medical Engineering, Beihang University, Beijing, China; 2. National Research Center for Rehabilitation Technical Aids, Ministry of Civil Affairs of the PRC, Beijing, China.

Introduction

Intermittent pneumatic compression (IPC) has been used for treating peripheral artery disease for several decades, and there were usually some requirements for the dressing of patients' lower limb in such treatments [1]. However, the reasons for such dressing requirements were not clearly explained, except considerations on comfort. Aimed at gaining some insights into the hemodynamics aspects of these requirements, an experiment and simulation study was carried out for evaluating influences of tight trousers on blood perfusion to foot microcirculation during intermittent pneumatic compression.

Method

The experiment protocol is shown in Figure 1. A total of 14 subjects(23.79 ± 1.63 years old, 7 males, 7 females) participated in the foot microcirculation blood perfusion assessment during IPC compression. The foot blood flow volume was recorded using a laser Doppler flowmeter. The compression pressure curve, P_{comp}, was recored using the custom made IPC device (DF-IPC) developed by Beihang University. The traditional IPC mode rise the air bag pressure up to 20 kPa in 1sec, hold the pressure for 4 secs, then release the pressure to <5kPa in 1 sec, and wait 16 secs until next compression. The rapid IPC mode release the pressure after charging immediately, and will wait for only 2 secs before next charging. The assessment procedure was managed in a way that IPC modes and lower leg garment species were factor controlled and compared correspondingly.

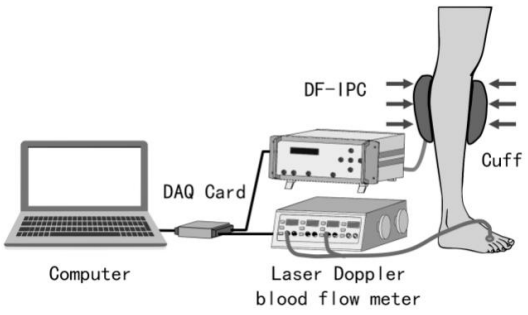

Figure 1: The experiment protocol of the foot microcirculation blood perfusion assessment of two IPC compression modes.

The simulation protocol is shown in Figure 2, the model contains compartments for arteries, arterioles, capillaries, venules and veins in the calf and foot of adult subjects. We used a general tube law reported by Kozlovsky et al. [2] to simulate high-nonlinear collapse behavior of vessels represented by capacitors C_1, C_3 and C_6. Equations are combined into a group of one-order differential equations, which was solved using the 'odeint' function in Scipy packages of Python.

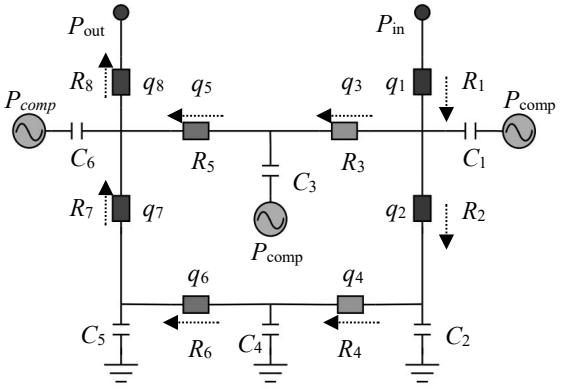

Figure 2: lumped parameter model of the peripheral vessels in the calves and feet.

Results

During compression section of both traditional and rapid IPC modes, the time-averaged blood flow volume augmentation was significantly higher (paired T test, $p < 0.05$) while keeping the lower limb bared comparing with wearing tight garments. In addition, the time-averaged blood flow volume value of the rapid IPC mode was significantly higher (paired T test, $p < 0.001$) than the traditional IPC modes in both garment species groups.

References

1. Sheldon, R. D., B. T. Roseguini, et al. New insights into the physiologic basis for intermittent pneumatic limb compression as a therapeutic strategy for peripheral artery disease. J. Vascul. Surg. 2013, 58(6): 1688-1696.
2. Kozlovsky P, Zaretsky U, Jaffa AJ, Elad D. General tube law for collapsible thin and tick-wall tubes. J. Biomech., 2014, 47: 2378-84.

Acknowledgments

This work was supported by the National Natural Science Foundation of China (12072018, 11421202, 11602013).

PATIENT-SPECIFIC MODELLING OF BLOOD FLOW IN CORONARY ARTERIES OF INDIAN SUBJECTS

***Mudrika Singhal, Raghvendra Gupta**

Department of Chemical Engineering, Indian Institute of Technology Guwahati, Assam, India
**Corresponding Author: msinghal@iitg.ac.in*

Introduction

Heart is a highly oxidative organ and the arteries supplying oxygenated blood to the heart are termed as coronary arteries. Coronary Artery Disease (CAD) is the leading cause of death globally. It is primarily characterized by the deposition of plaque on the inner lining of the arteries, termed as Atherosclerosis and with due course of time results in stenosis formation. This leads to reduced blood supply to the heart and can cause heart attack. Low and oscillating wall shear stresses have been found to be closely associated with the atherosclerosis in coronary arteries [1]. The major factors contributing towards low wall shear stresses are flow separation and recirculation regions. Thus, early detection of CAD becomes important for proper functioning of the heart. Computational modelling and simulation serve as a suitable option for analyzing the factors responsible for the progression, diagnosis and treatment of CAD. As the geometry of coronary artery depends on the age, gender, race, a large variation is observed in the geometry of coronary artery of different patients. In such a scenario, patient-specific modelling can offer the advantage of precisely modelling patient-specific data, analyzing the physiological changes taking place and making right clinical decisions. In this work, we propose a methodology for patient-specific modelling and analyse the flow behaviour in the arteries of Indian subjects.

Methods

The work aims at creation of a 3D model from DICOM images of patients and performing Computational Fluid Dynamics (CFD) simulations to study the hemodynamic behaviour. From the DICOM image, identification of aorta is carried out and position along the axial plane is varied, followed by the identification of left and right coronary arteries. Further, path creation, segmentation is done and finally 3D lofted model is constructed constituting of the origin from the aorta and further bifurcation into the left and the right coronary artery.



Figure 1: Schematic of the working methodology

The 3D model is discretized via creating an unstructured mesh having tetrahedron elements. Inflation layer is created at the boundaries.

Blood is considered to be an incompressible, Newtonian fluid having a constant viscosity for the CFD simulations.

Equations governing the CFD simulations are as follows,

Continuity equation:

$$\nabla . \boldsymbol{V} = 0$$

Momentum conservation equation:

$$\rho\left(\frac{\partial \boldsymbol{V}}{\partial t} + u\frac{\partial \boldsymbol{V}}{\partial x} + v\frac{\partial \boldsymbol{V}}{\partial y} + w\frac{\partial \boldsymbol{V}}{\partial z}\right) = \rho \boldsymbol{g} - \nabla p + \mu\nabla^2 \boldsymbol{V}$$

Pulsatile boundary condition is applied at the inlet and resistance boundary condition is applied at the outlet. The resistance parameter (R) accounts for the resistance offered by the arteries to the blood flow [3] and can be expressed by the mathematical formula,

$$P = RQ$$

Where Q is the flow rate and P is the pressure at the outlet face and is taken constant over the entire face.

Resistance boundary condition is advantageous over the constant pressure boundary condition as it gives a more realistic picture of the pressure waveforms at the outlet. Also, it accounts for the wave reflections which are neglected in the constant pressure condition [2].

Results and Discussion

We aim to study the geometry of three different patients. The differences in the geometrical features of the three arteries would be investigated. The effect of change in geometry on the flow would be investigated.

References

1. Myers, J. G., Moore, J.A., Ojha, M., Johnson, K.W. & Ethier, C.R. Factors influencing blood flow patterns in the human right coronary artery. Annals of Biomedical Engineering. 2001. 29:109-120.
2. Moon, J.Y., Suh, D.C., Lee, Y.S., Kim, Y.W., & Lee, J.S. Considerations of blood properties, outlet boundary conditions and energy loss approaches in Computational Fluid Dynamics Modelling. *Neurointervention.*2014. 9:1-8.
3. Madhavan, S. & Kemmerling E. The effect of inlet and outlet boundary conditions in image-based CFD modelling of aortic flow. Biomedical Engineering Online. 2018.

TUNABLE MAGNETIC HYDROGEL FOR CARDIOMYOCYTES TRAINING

Baptiste Le Roi (1), Ben Maoz (1)

1. Maoz Laboratory, Department of Biomedical Engineering, Sagol School of Neuroscience, The Center for Nanoscience and Nanotechnology, Tel Aviv University, Israel

General context

Heart failure is a major cause of death in Europe as 2% of the European population die from it every year. Heart failure naturally comes with the age but also with the regular consumption of toxics such as tobacco or alcohol. The main cause of heart failure is called cardiomyopathy and corresponds to a permanent loss of contraction strength of cardiac cells. Current treatment are palliative and do not target cardiac cells but arteries which become more compliant.

The contractile force generated by cardiomyocytes (CMs), a key indication of heart functionality, is dependent in part on the levels of external pressure to which the CMs are exposed before and during contraction (preload and afterload, respectively). Yet, current *in vitro* methods are unable to mimic the conditions that create such pressure. Consequently, these methods cannot provide sufficient information regarding CM functionality and drug response. The proposed work aims to create an *in vitro* platform that overcomes this limitation, thereby revolutionizing current cardiac *in vitro* paradigms. The presented platform, involves **the use of magnetic fields to apply dynamic forces to CM tissue, thereby mimicking *in vivo* conditions.**

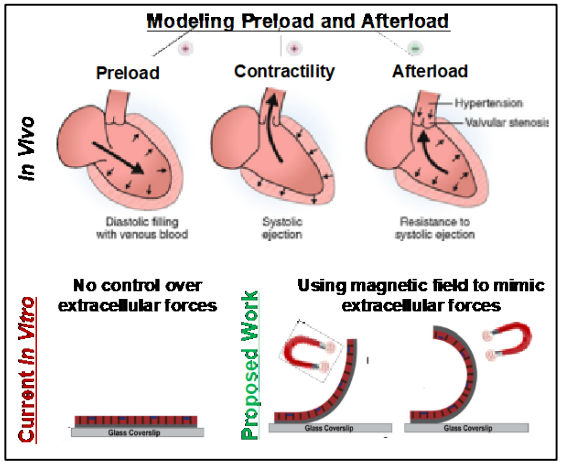

Figure 1 Currently, there is not in vitro system that can emulate the forces applied on the heart

Concept and aims

In the presented work, we aim to to overcome limitations of current *in vitro* cardiac models by creating a human-relevant *in vitro* model of the cardiovascular system that mimics the dynamic environmental pressures to which CMs are subjected *in vivo*. In this work, we were able to:

- *Develop a magnetically controllable soft substrate that uses magnetic fields to mimic preload and afterload pressures.*
- *Integrate CM into the magnetic substrate and identify their response to the substrate.*
- *Assess CM functionality under various preload/afterload conditions, and compare it to known PV loops.*

Preliminary results

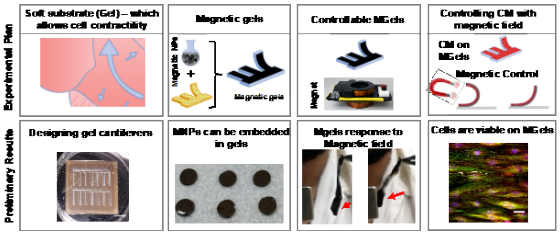

Figure 2 (Top) The experimental design that will culminate in the establishment of a new in vitro platform for cardiac research. (Bottom) Preliminary results which demonstrate a proof of concept.

We have achieved a proof of concept for some of the key elements of the proposed platform (**Fig. 2**). Specifically, we have successfully synthesized MNPs and embedded them in biocompatible gels (gelatin) [1]. In addition, a permanent magnet was used to demonstrate the gels' response to a magnetic field [2]. Then we applied an Ogden model of second order on uniaxial compression test led on gels, we determined that gels present a stiffness of 3.7 kPa which is coherent with values found in literature [3] and that MNP do not act as stiffener. Finally demonstrated that Mgels are not toxic to CM and are optimizing the growth of CMs (up to 14 days currently). Building on these promising preliminary results, we proceed to carry out the remaining steps of our research plan, including: characterising CM functionality in the Mgels and identifying how MNPs affect CM properties, developing magnetic and electric controls, and most importantly, developing an *in vitro–in vivo* extrapolation methodology.

References

1. Shoval. *J. Nanophotonics* 2016; **10**: 036007.
2. McCain. *Biomaterials* 2014; **35**: 5462-5471.
3. Mirsky. *Prog. Cardiovasc. Dis.* 1976; **18**: 277-308.

ADDING MYOCARDIAL MECHANICS IN A 3D FLUID-STRUCTURE INTERACTION MODEL OF THE LEFT CORONARY BIFURCATION

Itziar Ríos-Ruiz (1), Miguel Ángel Martínez (1,2), Estefanía Peña (1,2)

1. Aragón Institute of Engineering Research (I3A), University of Zaragoza, Spain; 2. CIBER-BBN: Centro de Investigación Biomédica en Red en Bioingeniería, Biomateriales y Nanomedicina, Spain

Introduction

Many cardiovascular diseases are highly location specific, such as atherosclerosis or aneurysms. Therefore, the study of the local haemodynamic and mechanical environment of the vessels has become of interest in the past years, as it is a possible trigger for these diseases. Added to this, the use of patient-specific geometries of vessels is valued as it implies more physiologically realistic results and can lead to more accurate simulations.

In this line, fluid-structure interaction (FSI) models, which fully couple the effect of the fluid and the mechanics, have started to be developed. Regarding coronary arteries in particular, which are prone to develop an atheroma plaque at specific sites, FSI models to date have centred on the simulation of real straight parts of the vessel, not including bifurcations, and a single-layered approximation of the vessel wall [1,2,3].

In this study, we propose an FSI model, based on a patient-specific geometry of the bifurcation of the left main (LM), the left circumflex (LCX) and the left anterior descending (LAD). The model includes the mechanical stimuli present in these vessels, i.e., the cyclic bending and axial stretching, as well as the myocardial compression. With this model, we intend to shed light on the mechanisms that trigger atherosclerosis.

Methods

An MRI image of a healthy coronary artery was segmented and processed. The thickness of the vessel wall was extruded and the whole geometry was smoothed and exported to a 3D model.

The mechanical part, i.e., the vessel wall, is split into two layers, the media and adventitia, as the intimal layer is assumed to not contribute to the mechanical behaviour of the vessel, see Figure 1. Both layers are modelled by an anisotropic hyperelastic model, the GHO model [4], which considers the effect of the collagen fibres of the wall.

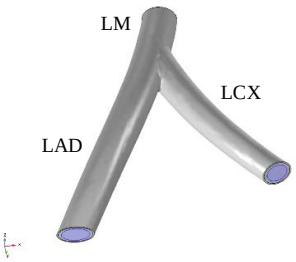

Figure 1: Geometry of the coronary bifurcation. Fluid domain is shown in blue.

The different mechanical stimuli, as well as the blood flow conditions, were obtained from literature [2,3,5].

Results

The 3D model of the coronary bifurcation is shown in Figure 1.

Figure 2 shows some preliminary results of the study. Figure 2.a displays the values of wall shear stress (WSS) that blood flow causes in the vessel wall. Figure 2.b shows the deformation of the vessel wall due to blood flow.

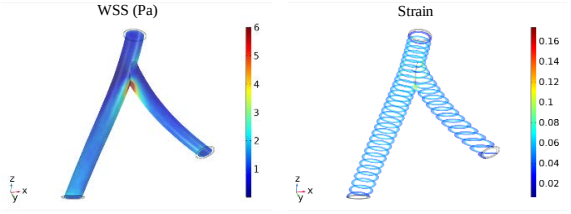

a) *b)*

Figure 2: a) WSS (Pa) produced by blood flow. b) Strain (-) of the vessel wall induced by blood flow.

Discussion

This study adds up to current developments and is the first FSI model of a coronary artery that includes a real patient geometry of a bifurcation, a two layered, anisotropic modelling of the vessel walls, stretching and bending motions and the effect of myocardial compression on the vessel.

The effect of each stimulus in blood flow patterns can bring light to the causes of the apparition of cardiovascular diseases like atherosclerosis.

References

1. Tang et al, J Biomech Eng, 131(6):061010, 2009.
2. Torii et al, Commun Numer Meth Engng, 25:565-580, 2009.
3. Meza et al, J Biomech Eng, 140(12):121006, 2018.
4. Gasser et al, J R Soc Interface, 3:15-35, 2006.
5. Ohayon et al, Am J Physiol Heart Circ Physiol, 301:H1097-H1106, 2011.

Acknowledgements

This work is supported by the Spanish Ministry of Economy and Competitiveness through research project PID2019-107517RB-I00 and by Gobierno de Aragón through grant IIU/1408/2018.

MICRO-BEADS DECREASE THE RUPTURE THRESHOLD ON AN ATHEROMA CAP LABORATORY MODEL

Andrea Corti (1), Annalisa De Paolis, PhD (1), Tariq Shameen (1), Sheldon Weinbaum, PhD (1), Luis Cardoso, PhD (1)

[1]Department of Biomedical Engineering, The City College of New York, New York, USA

Introduction

Approximately half of all cardiovascular deaths associated with acute coronary syndrome occur when the atherosclerotic fibrous cap tissue in a coronary vessel breaks under the action of high blood pressure. Recent studies showed that the plaque's mechanical stability is compromised by the presence of micro-calcifications μCalcs inside the fibrous cap, as μCalcs (D = 5-65μm) act as tissue stress concentrators [1-3]. In this context, we designed a silicone-based laboratory model to investigate changes on the rupture threshold caused by μBeads embedded in a hyperelastic material mimicking arterial tissues.

Methods

We created silicone-based (Sylgard 184, PDMS, Dow Corning) dumbbell-shaped laboratory models (ASTM D412 standard geometries) of arterial tissues. Models were scaled down to 20% of original ASTM dimensions to correspond to those of human fibroatheroma caps. Samples were manufactured using 10:1 pre-polymer to cross-linking agent ratio into two groups, with (n=8) and without (n=8) μBeads. For samples containing μBeads, we added a 1% volume of glass beads (18μm diameter, 3M) to the mixture. The PDMS was thoroughly mixed, degassed for about 30 minutes, poured into sample molds cured at 30°C for two days, removed from the molds and then cured again at 100°C for one hour [4]. After curing, we tested the samples using a custom made micro material testing system equipped with real-time control and acquisition software (LabVIEW, v. 2018, National Instruments). Each sample was tested using a ramp waveform under displacement control at constant strain rate (1.5mm/s) up to rupture. Throughout the test, the reaction force was measured and the rupture recorded using a high resolution camera. The force-displacement curves were converted into engineering stress vs stretch curves, and the ultimate stress to rupture was determined. To obtain a constitutive material description of the samples, we carried out a material evaluation analysis in Abaqus/CAE 6.14-3.

Results

Samples with and without μBeads exhibited a distinct hyperelastic behaviour **(Figure1)**. The constitutive model that most closely represented the data was Ogden third order [5], where the strain energy function depends on the hyperelastic constants μ_i, α_i (**Table 1**) that describe shear moduli and power law coefficients. The ultimate stress (stress at rupture) in the PDMS with μBeads group was much lower than the PDMS only group. Comparison of the mean ultimate stress between these two groups was performed using a two tailed T-test, which demonstrated a significant effect (p=2.06E-5) of μBeads on the rupture threshold of this atheroma cap laboratory model **(Figure 1, top left).**

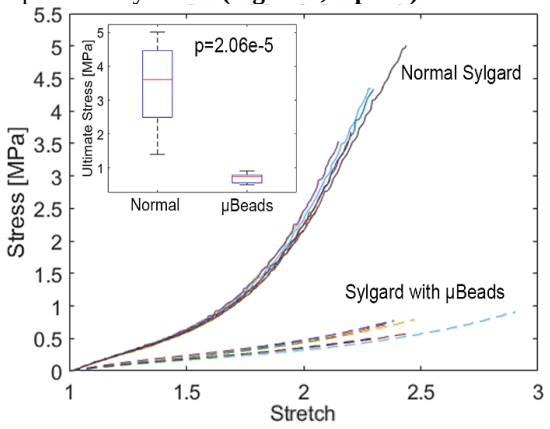

Figure 1: Stress vs stretch ratio for normal samples and samples with μBeads. Top left, Box Plot of the ultimate stresses for the two groups.

Group	μ_1	μ_2	μ_3	α_1	α_2	α_3	D
Norm.	-4.8	4.7	0.7	16.3	16.3	-16.5	0
μBeads	0.2	8.9	-7.4	14.8	14.7	0.9	0

Table 1: Constitutive coefficients values for the two samples groups. μ_i is reported in MPa.

Discussion

Our results clearly capture the influence of μBeads on the hyperelastic behavior and rupture threshold of a vascular tissue mimicking material, as samples with μBeads display significantly lower ultimate stresses. The plausible explanation for the observed change in rupture threshold is the increase in stress concentration around spherical μBeads, which we have previously shown in analytical and numerical studies [1-3] can range from 2 to 5 times the background stress in the material. These experimental observations support our previous studies suggesting that μCalcs located within the fibroatheroma cap may be responsible for significantly increasing the risk of cap rupture that precedes the formation of a thrombus, myocardial infarction and sudden death.

References

1. Vengrenyuk et al, PNAS, 103 (40) 14678-14683, 2006.
2. Kelly Arnold et al., PNAS110 (26) 10741-10746, 2013.
3. Cardoso et al, Ann Biomed Eng, 42(2):415-431, 2015.
4. Johnston et al, J Micromech Microeng, 24 035017, 2014.
5. Ogden, Proc R Soc Lond A, 326:565-584, 1972.

Acknowledgements

NSF grants CMMI-1662970 & MRI-2018485

ATHEROMA CAP RUPTURE DUE TO MICRO-CALCIFICATIONS

Andrea Corti (1); Annalisa De Paolis, PhD (1); Elena Aikawa, PhD (2); Sheldon Weinbaum, PhD (1); Luis Cardoso, PhD (1)

[1]Department of Biomedical Engineering, The City College of New York, New York, USA
[2]Department of Medicine, Brigham and Women's Hospital, Harvard Medical School, Boston, MA, USA

Introduction

The mechanical stability of an atheroma fibrous cap is a crucial factor for the risk of heart attack or stroke in asymptomatic vulnerable plaques. Common determinants of plaque vulnerability are the core size, cap thickness, and the presence of micro-calcifications (μCalcs). Higher local stresses have been linked to thin caps and thick necrotic cores. More recently, our lab demonstrated how μCalcs can potentially initiate cap rupture [1-3]. When combined, these factors can compromise to a greater extent the stability of the plaque. On this basis, we quantitatively analysed both individual and combined effects of key determinants of plaque rupture using a tissue damage model.

Methods

We performed 10 finite element simulations on three-dimensional multi-layered idealized atherosclerotic geometries presenting 70% stenosis and 1.6 remodelling index. We considered three values for the fibroatheroma (FA) cap thickness (200, 100 and 50μm), three relative core thicknesses in the case of the 100μm cap (25%, 50% and 75%), and two μCalc scenarios (no μCalc and one spherical μCalc, D=18μm). Each artery was expanded by a ramp pressure up to 120mmHg. To replicate the rupture of the fibrous cap, we implemented a custom-made user subroutine coded in FORTRAN based on the hyperelastic failure description proposed by Volokh et al. [4]. We considered a max. principal stress for rupture of 300kPa[5]. The arterial layers were described by the Ogden 3rd order constitutive model (**Table 1**). The lipid core and the μCalc were considered as elastic materials (E_{core} = 5kPa, ν_{core} = 0.49; $E_{\mu Calc}$= 18,000 kPa, $\nu_{\mu Calc}$=0.3).

	μ_1	μ_2	μ_3	α_1	α_2	α_3
Int	0.015	2e-5	0.042	4.9	19.2	-1.9
Med	0.002	1e-5	0.0011	6.3	15.3	0.5
Adv	0.0014	1e-6	0.015	8.5	25	-0.8

Table 1: Layer-specific values for the Ogden 3rd model.

Results

To obtain a detailed analysis of the cap stresses, a sub-modeling approach was implemented using ABAQUS (V. 2019 Simulia, Providence, RI) (**Fig. 1A**). The μCalc was introduced into the center of the cap in the third submodel. The stresses and strains reported for each model represent the average value of 200 nodes selected either along the central cap thickness (no μCalc) or around the μCalc tensile poles. Our results confirm that thinner caps and thicker cores induce higher cap stresses. However, no model without μCalc reached the threshold stress for rupture (**Fig. 1B**). On the other hand, when the μCalc was embedded into the tissue, the models with fibrous cap thickness of 50 and 100μm, and with a relative core thickness of 50 and 75% ruptured acutely. In the models with large cap thickness and small core size, the cap rupture didn't occur, although the stresses around the μCalc were significantly higher than the corresponding models without μCalcs. The stress concentration factor (SCF) - ratio between the maximum stress at the tensile poles of the μCalc and the background stress in the tissue - exhibited a SCF of about 2.2. - 2.5.

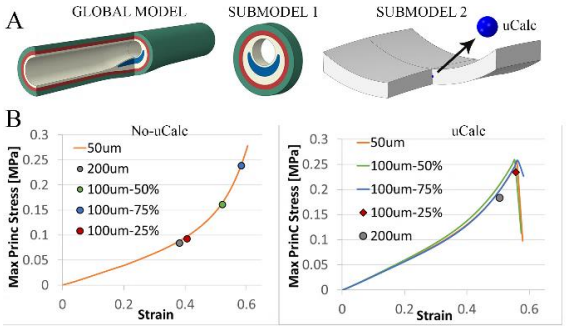

Figure1: (A) Illustration of the sub-modeling approach, from the global model to the portion of the cap. (B) Max Princ. Stress vs Strain for the models without μCalc (left) and with μCalc (right). Cap rupture only occurred when a μCalc was present in a cap ≤ 100μm thick and with a core ≥ 50% thick.

Discussion

Our results clearly show the multifactorial nature of plaque vulnerability and the significance of micro-calcifications on the cap mechanical stability. The presence of a μCalc strongly amplifies the stresses in the surrounding tissue, which when combined with other factors such as the cap and core thicknesses, it can exceed the ultimate strength of the material. The novel implementation of the tissue damage description that we are presenting allows one to quantitatively analyze the individual and combined contribution of key determinants of cap rupture, which precedes the formation of a thrombus, myocardial infarction and sudden death.

References

1. Vengrenyuk et al, PNAS, 103 (40) 14678-14683, 2006.
2. Kelly Arnold et al, PNAS110 (26) 10741-10746, 2013.
3. Kawakami et al, ATVB, 40(8):1838-1853, 2020.
4. Volokh et al, J. Biomech., 41(2), 447–453, 2008.
5. Cheng et al, Circulation, 87(4), 1179–1187, 1993.

Acknowledgements

NIH grants 1R01HL136431, NSF grants CMMI-1662970, MRI-2018485.

A NEW CONSTITUTIVE MODEL FOR PERMANENT DEFORMATION OF BLOOD CLOTS DURING CYCLIC PRESSURE ASPIRATION

Behrooz Fereidoonnezhad (1), Patrick McGarry (1)

1. National University of Ireland, Galway, Ireland

Introduction

Acute ischemic stroke (AIS), the result of embolic occlusion of a cerebral artery, is responsible for 87% of the 6.5 million stroke-related deaths each year. Intra-arterial aspiration thrombectomy is a minimally invasive procedure in which the obstructing thrombus is removed by application of a suction pressure on the clot through an aspiration catheter. Clinical evidence demonstrates that a cyclically fluctuating aspiration pressure results in higher recanalization in comparison to the static aspiration [1]. However, the mechanism that result in improved outcomes for cyclic aspiration have not yet been uncovered.

Methods

In the current study we develope a novel constitutive model which accounts for permanent set in blood clots. Some physical features such as cross-links formation and dissociation in the fibrin network are incorporated into the constitutive model as the underlying mechanism for permanent deformation in blood clots.

The formulation is implemented in a finite element framework via a UMAT subroutine in Abaqus. The model is compared to the experimental data of whole blood clot subjected to cyclic uniaxial tension [2]. Cyclic and static pressure aspiration thrombectomy are then simulated (Figure 2A).

Results

It is demonstrated that the developed model accurately reproduces experimentally observed nominal stress-strain behaviour of whole blood clot subjected to cyclic uniaxial tension (Figure 1). The results of aspiration simulation reveal that a higher level of aspiration is computed under cyclic applied pressure compared to static applied pressure (Figure 2B), as observed clinically.

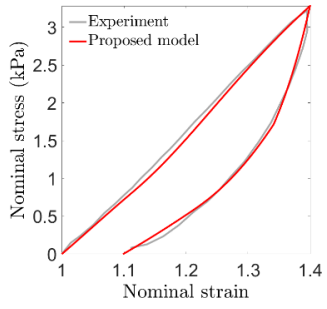

Figure 1: The capability of the proposed model to reproduce the stress-strain experimental data of the cyclic uniaxial tension of whole blood clot [2].

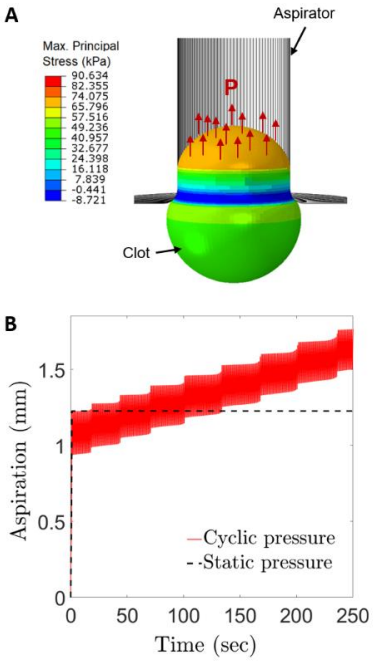

Figure 2: (A) Finite element simulation of cyclic and static pressure aspiration using the developed constitutive model for blood clot, (B) clot aspiration during cyclic and static pressure aspiration thrombectomy.

Discussion

The model developed in this study provides a better characterisation of the mechanical behaviour of thrombus by incorporating the permanent deformation which is crucial to get reliable results from computational simulation of thrombectomy. This model provides a basis for design and assessment of novel aspiration catheter design to improve the first-pass revascularization rate for acute stroke thrombectomy.

References

1. Simon, et al., Journal of neurointerventional surgery, 6(9): 677-683, 2014.
2. Sugerman et al, DOI: 10.1101/2020.07.19.210765, biorxive, 2020.

Acknowledgements

This work has received funding from the European Union's Horizon 2020 research and innovation programme under grant agreement No 777072.

BIOMECHANICAL PROPERTIES OF HUMAN DILATED ASCENDING AORTA DEPENDING ON AORTIC VALVE TYPE

Ivars Brecs (1,3), Peteris Stradins (1,3), Martins Kalejs (1,2), Uldis Strazdins (1), Eva Strike (1,3), Iveta Ozolanta (2), Vladimir Kasyanov (2)

1. Department of Cardiac Surgery, Pauls Stradins Clinical University Hospital, Latvia; 2. Laboratory of Biomechanics, Riga Stradins University, Latvia; 3. Riga Stradins University, Latvia

Introduction

Aneurysms of ascending aorta are dilatation of the first part of the human aorta. Commonly showing no clinical symptoms, but increases the risk of aorta dissection, which is a life-threatening condition [1, 2]. Normally humans have tricuspid aortic valve (TAV), but one of the most frequent congenital malformation is bicuspid aortic valve (BAV). BAV is one of the risk factors associated with aortic dilatation and dissection [3]. In this study we try to elucidate the changes in the biomechanical properties, which occur in the dilated human ascending aorta depending on aortic valve type.

Methods

Twenty-four patients undergoing elective ascending aorta surgery were selected for this study. Two specimens from each ascending aorta anterior region were cut in the longitudinal and circumferential directions. The sample length was 30 - 35 mm, and their width was 5 mm. Specimens were divided in two groups depending on valve type: BAV (n=13), TAV (n=11). Specimens were investigated under a uniaxial tensile test. Tensile test equipment Zwick/Roell (Germany) BDO-FB0.5TS was used. Before the testing of the samples their thickness was measured. The samples were stretched until rupture of the sample occurred. The obtained experimental data were processed using testXpert 2 software, to determine maximal stress, maximal strain and the tangential modulus of elasticity in the linear part of the stress-strain curve.

Results

We observed that there is statistically significant difference in both groups (BAV p = 0.023, TAV p = 0.011) between the maximal stress for the samples of the aortic wall in both directions. In BAV group maximal stress in the longitudinal direction was *Md* = 0.57 MPa (0.41 – 0.63) and in the circumferential direction was *Md* = 0.84 MPa (0.63 – 1.05). In TAV group maximal stress in the longitudinal direction was *Md* = 0.42 MPa (0.30 – 0.52) and in the circumferential direction was *Md* = 0.59 MPa (0.48 – 0.70). There were no statistically significant differences between groups.

There were no statistically significant differences between the maximal strain of the samples in both directions in both groups (BAV p = 0.84, TAV p = 0.80). But there were statistically significant differences between the groups (Figure 1). The maximal strain in the longitudinal direction in the BAV group was *Md* = 62.86 % (58.00 – 67.71) and in the TAV group was *Md* = 48.46 % (43.01 – 53.92), respectively (p = 0.0005). The maximal strain in the circumferential direction in the BAV group was *Md* = 61.02 % (55.20 – 66.85) and in the TAV group was *Md* = 45.33 % (37.88 – 52.79), respectively (p = 0.002).

Tangential modulus of elasticity in both groups in the longitudinal direction for BAV *Md* = 2.08 MPa (1.59 - 2.58) and for TAV *Md* = 1.91 MPa (1.19 - 2.62) was significantly lower (BAV p = 0.0059, TAV p = 0.013) than the elastic modulus of the samples in the circumferential direction for BAV *Md* = 3.43 MPa (2.62 - 4.24) and for TAV *Md* = 3.20 MPa (2.41 - 3.99).

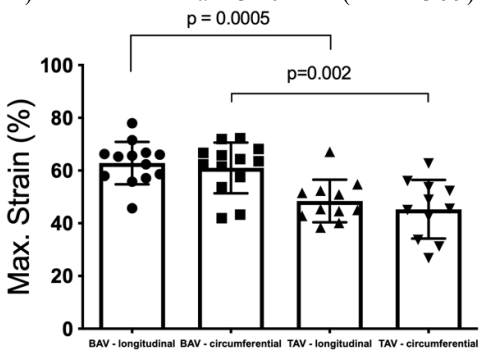

Figure 1: Maximal strain for the samples in the longitudinal and in the circumferential directions in both groups.

Discussion

The obtained results showed a remarkable anisotropy of the ascending aorta tissue. We found higher strength of the tissue in the circumferential direction than in the longitudinal direction in both groups. There were no statistically significant differences between the strains of the samples in both groups, but there were statistically significant differences between the groups. Patients with BAV have greater deformation of ascending aorta wall. Tangential modulus of elasticity showed that tissue in the circumferential direction is stiffer than in the longitudinal direction. Results are consistent with studies available in the literature [4, 5, 6].

References

1. Evangelista, J Heart, 96:979–985, 2010.
2. Lavall et al, J Dtsch Arzteblatt Int, 109:227–233, 2012.
3. Januzzi et al, J Am Coll Cardiol, 43:665-9, 2004.
4. Duprey et al, J Vasc Endovasc Surg, 39:700–707, 2010.
5. Pham et al, J Acta Biomater, 9:7927–7936, 2013.
6. Ferrara et al, J Mech Behav Biomed Mater, 53:257–271, 2016.

HEMODYNAMIC EVALUATION OF RECONSTRUCTED ARCH GEOMETRY AFTER NORWOOD PROCEDURE VS A NON-OPERATED CONTROL

Aloma Blanch-Granada (1), Margaret M. Samyn (2), Joseph R. Cava (2), Stephanie S. Handler (2), Jennifer F Gerardin (2,4), Benjamin Goot (2), Viktor Hraška (3), John F. LaDisa Jr. (1,4)

Departments of [1]Biomedical Engineering, Marquette University and Medical College of Wisconsin; [2]Pediatrics-Division of Cardiology, [3]Surgery - Division of Pediatric Cardiothoracic Surgery, and [4]Medicine - Division of Cardiovascular Medicine at the Medical College of Wisconsin, Herma Heart Institute, and Children's Wisconsin; Milwaukee, WI, USA

Introduction

Hypoplastic left heart syndrome (HLHS) is a congenital cardiovascular defect where the left side of the heart and related structures cannot support systemic cardiac output. The Norwood procedure, performed in the first days of life, creates a neo-aorta along with arch reconstruction to provide unobstructed systemic output from the well-developed right ventricle. To better understand patient outcomes, we aim to characterize hemodynamics within the reconstructed arch, brachiocephalic artery, pulmonary arteries, and BT shunt. Prior studies have studied reconstructed arch geometry [1], but the current project adds more complexity to increase realism relative to patient outcomes, by adding more vessels within the area that can impact local hemodynamics.

Methods

After Institutional Review Board (IRB) approval, patients diagnosed with HLHS or similar left-sided anomalies with prior Norwood operation (n=3) underwent MR angiography (MRA) before Glenn intervention. A control patient was modeled for comparison. The control patient had a single ventricle with a native aortic arch and normal aortic valve, such that the aorta arose unobstructed from the systemic single ventricle. Geometry and boundary conditions were extracted from MRA and phase-contrast data, respectively. Patient-specific models were created in SimVascular (simvascular.github.io). The time dependent Navier-Stokes equations were solved within the 3D model domain. coupled with 3-element Windkessel outlet boundary conditions for the patient specific geometry and an electrical analogue of the heart implemented via closed-loop lumped parameter network (LPN) [2] for a forthcoming virtual reconstructed geometry. These approaches allowed quantification of wall shear stress (WSS) indices and cardiac function for later comparison. Low time-averaged WSS (TAWSS), and elevated oscillatory shear index (OSI) have previously been associated with atherosclerosis [3,4].

Results and Discussion

TAWSS, normalized to body surface area (BSA), was quantified via 5 mm bands in the ascending aorta (AscAo), transverse arch (TA), descending aorta (DAo), and middle of the descending aorta (mDAo) as shown in Figure 1 and Table 1 for models completed to date. When compared with the control subject, patients 1 & 2 exhibited lower TAWSS and higher OSI values upstream of the DAo and mDAo regions, suggesting the AscAo and TA may be the hemodynamically critical regions that need surgical optimization; through virtual reconstruction of the arch as part of that forthcoming work. Patient 3 had a less concave reconstructed arch and closer age to the control, registering similar numbers and alike values to prior controls [5]. Age also seems to play a role in WSS indices revealed in the aortas of HLHS patients.

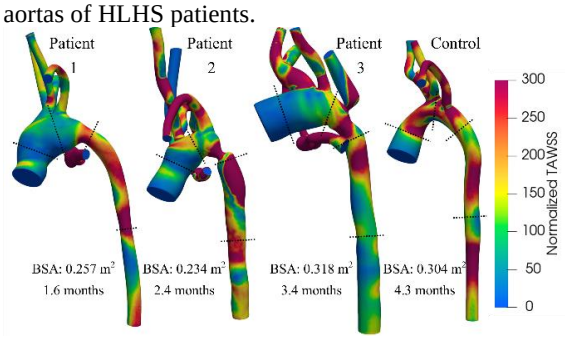

Figure 1: Normalized Time Average Wall Shear Stress

Table 1. Indices of vascular biomechanics.

	Normalized TAWSS $[dyne/cm^2m^2]$				OSI			
	AscAo	TA	DAo	mDAo	AscAo	TA	DAo	mDAo
Patient 1	29	65	226	364	0.29	0.22	0.16	0.14
Patient 2	45	160	479	236	0.22	0.10	0.11	0.07
Patient 3	51	196	158	135	0.24	0.11	0.07	0.04
Control	144	184	122	132	0.11	0.12	0.14	0.15

Motivated by AscAo and TA results above, a closed loop configuration with the coupled behaviour of the 3D and 0D domains [6,7] is now being implemented to further optimize reconstructed aortic arch geometry. Additional information from this future virtual reconstruction work, such as cardiac workload from pressure-volume loops, should provide more valuable details to optimize the arch reconstruction approach.

Acknowledgements

This work is supported by the Fulbright Scholars Program (ABG) and S. Bert Litwin Family Fund (JFL). The authors thank Nicholas Peterson and William K. Johnson.

References

1. Itatani, K. et al, JTCVS 144, 130–138, 2012.
2. Arthurs, C. J. et al, Front Pediatr, 5, 2017.
3. Caro, C. G. et al, Proc. Royal Soc. B, 177, 1971.
4. Wentzel, J. J. et al, J Am Coll Cardiol 45:846–854, 2005.
5. Wendell, D. C. et al, J Biomech Eng, 138.9, 2016.
6. Migliavacca, F. et al, AJP - Heart, 280, H2076-2086, 2001.
7. Moghadam, M. E. et al, J Biomech Eng, 134, 2012.

A MULTISCALE HAEMODYNAMIC SIMULATION ENVIRONMENT FOR ACUTE ISCHAEMIC STROKE MODELLING

Raymond Padmos (1), Tamás Józsa (2), Wahbi K. El-Bouri (2,3), Gábor Závodszky (1), Stephen Payne (2), Alfons Hoekstra (1)

1. Computational Science Laboratory, Informatics Institute, Faculty of Science, University of Amsterdam, the Netherlands; 2. Institute of Biomedical Engineering, Department of Engineering Science, University of Oxford, UK; 3. Liverpool Centre for Cardiovascular Science, Department of Cardiovascular and Metabolic Medicine, University of Liverpool, UK

Introduction

The INSIST project[1] aims to develop computational models to improve treatments of ischaemic stroke, one of the global leading causes of death. Accurately predicting brain tissue perfusion in patients is a key element of the envisaged pipeline. The present work aims to evaluate a multi-scale haemodynamic simulation environment which can fulfil this task.

Model

The coupled model consists of a 1D and a 3D blood flow (BF) model governing large arteries and microvessels, respectively[2]. In the 1D model large arteries are modelled as thin elastic tubes BF is described using a 1D hydraulic network model with pressure-dependent resistance segments. It is assumed that microvessels are rigid and flow inside them is captured using a multi-compartmental porous medium approach[3]. Blood is modelled as an incompressible Newtonian fluid and the primary variable is steady state blood pressure in both models.

The 1D and 3D models are coupled through the pial surface, where the pressure drop between the models is bridged with additional hydraulic resistors symbolising unresolved blood vessels. The linear equation sets corresponding to the 1D and 3D models are solved indirectly at every coupling iteration within which a nonlinear optimisation minimises the residuals defined based on the pressure and volumetric flow rate differences at the interface of the two models.

Results

The coupled model predicts arterial blood flow and tissue perfusion during an acute ischaemic stroke. Here a right middle cerebral artery (RMCA) occlusion is considered. Figure 1a-c and b-d show results corresponding to the uncoupled and coupled cases, respectively Two-way coupling allows for feedback between the models, thereby capturing retrograde flow and leading to a less significant perfusion drop in the occluded scenario. In the coupled case, perfusion gradient is smaller in the brain emphasising how collateral pathways might counteract major vessel occlusions. The coupled model can capture crucial but previously neglected effects, such as blood flow rerouting through mirovessels after an arterial occlusion.

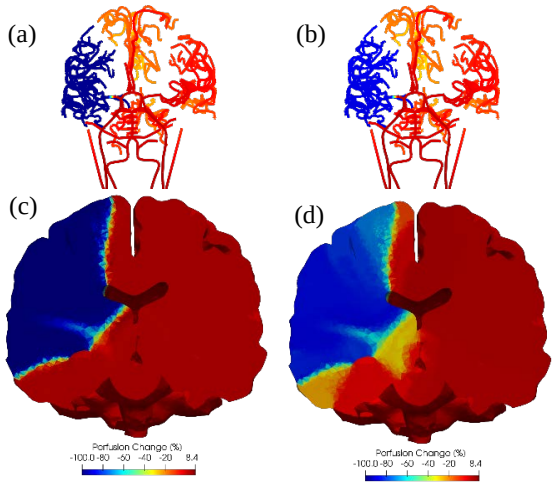

Figure 1: RMCA occlusion simulation: blood pressure in the 1D BF model in uncoupled (a) and coupled (b) cases. Perfusion change compared to the healthy scenario predicted by the 3D model in uncoupled (c) and coupled (d) cases.

Conclusion

Accurately predicting infarct volume after an acute ischaemic stroke requires two-way coupling of models describing arterial blood flow and tissue perfusion. The predicted perfusion maps provide sufficient input for a tissue health model which could estimate Infarction progression as a function of space and time. Therefore, the coupled model paves the way for a thorough validation based on medical imaging data.

References

1 Konduri, P. R. *et al. Front. Neurol.* 11, (2020). doi:10.3389/fneur.2020.558125

2 Padmos, R. M. *et al. Interface Focus* 11, 20190125 (2021). doi:10.1098/rsfs.2019.0125

3 Józsa, T. I. *et al. Interface Focus* 11, 20190127 (2021). doi:10.1098/rsfs.2019.0127

Acknowledgements

This project (INSIST) has received funding from the European Union's Horizon 2020 research and innovation programme under grant agreement No 777072.

PRELIMINARY DESIGN, THEORETICAL ANALYSIS AND EXPERIMENTAL EVALUATION OF A RIGHT VENTRICULAR ASSIST DEVICE

De Gaetano F (1), Giussani A (1), Guidetti I (1), Vandenberghe S (2), Demertzis S (2), Costantino ML (1).

1. Department of Chemistry, Material and Chemical Engineering, Politecnico di Milano, Milan, Italy; 2. Cardiocentro Ticino – Cardiac Surgery, Switzerland

Introduction

Heart failure (HF) is a complex syndrome in which the heart loses the ability to fulfil tissue metabolic requirements with blood flow. HF is strongly associated with aging, its incidence reach 3:100 after 85 years old [1]. Worldwide, HF affects 26 million people. Nowadays, the gold standard to treat HF is heart transplantation but in the future, the demand is going to exceed the supply availability [2]. This pathology mainly charges the left ventricle due to the high mechanical work. The left ventricular assist devices (LVADs) implantation is nowadays a routine procedure, however, LVADs implantation often causes secondary right heart failure that is treated by the implantation of a second standard LVAD connected to the right ventricle. In this project, we prototyped a ventricular assist device specific for the right ventricle (RVAD).

Methods

Five centrifugal pumps RVAD were designed and CFD simulations were performed. The one displaying the best hydraulic performances (based on the characteristic H-Q curves) was manufactured by a resin 3D printer. In order to properly evaluate the support efficiency of the RVAD in different pathological conditions, a hybrid simulator was used. The prototype was tested in three different modalities: continuous flow, and pulsatile flow either in co- or counter-pulsation mode.

Results

RVAD prototype experimental H-Q curves at different rotational speeds and afterloads showed to be more effective for right heart support compared to the standard LVADs (Figure 1), due to the lower pressure generation at the same flow rates. Moreover, the CFD simulations allowed identifying some critical regions inside the RVAD (Figure 2).

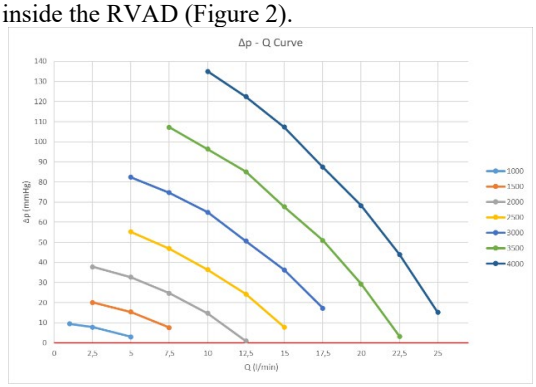

Figure 1: Characteristic curve of the pump obtained from the computational simulations for different rotational velocity of the impeller.

Discussion

The experimental results obtained from the tests on the hybrid simulator proved that our RVAD prototype provides adequate support both in the continuous and pulsatile mode (co-pulsation or counter-pulsation).
We successfully designed a working prototype of a right ventricular assist device, which demonstrated to properly support hemodynamics in a failing right heart.

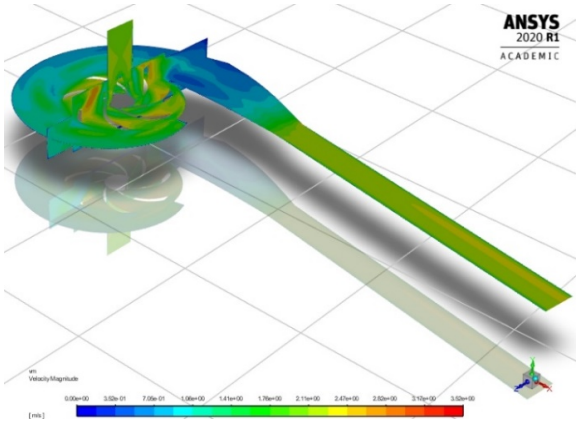

Figure 2: Velocity magnitude of the selected centrifugal pump.

References

1. B. M. Massie, “Heart Failure,” in Goldman’s Cecil Medicine, 2012, pp. 295–303..
2. R. G. Smith and J. G. Copeland, “Mechanical circulatory support devices,” in Cardiopulmonary Bypass: Principles and Practice: Third Edition, Wolters Kluwer Health Adis (ESP), 2012, pp. 128–139.

Acknowledgements

This work was supported by institutional funding of Cardiocentro Ticino and by the Fondazione per la ricerca sulla trasfusione e sui trapianti, Lugano, Switzerland.

A HARDWARE-IN-THE-LOOP STRATEGY FOR FLUID DYNAMIC CHARACTERIZATION OF CARDIOVASCULAR SYSTEMS

Francesco Bardi (1,2), Emanuele Gasparotti (1,3), Emanuele Vignali (1), Miquel Aguirre (2), Stéphane Avril (2), Simona Celi (1)

1. BioCardioLab, Fondazione Toscana Gabriele Monasterio, Italy; 2. Mines Saint-Etienne, Université de Lyon, France; 3. Dept. of Information Engineering University of Pisa, Italy

Introduction

Mock Circulatory Loops serve as a platform to characterize the fluid dynamics of the human circulatory system and to test cardiovascular devices. In a typical setup, a pump imposes a patient's specific flow rate at the inlet of an anatomical model, and passive components, such as compliance chambers and pinch valves, are used to set physiological pressures at its outlets. The passive components, however, require an extensive calibration and cannot be used to replicate complex dynamics. To overcome these drawbacks, a Hardware-in-the-Loop (HIL) strategy was implemented [1]. The aim of the study is to develop a system based on dynamic pressure regulation at the outlet sections of the model, according to the real-time results of a numerical simulator.

Methods

The developed system represents an upgrade to the Mock Circulatory Loop described in [2]. Each passive component was replaced with a pressure-controlled chamber in series with an adjustable resistance, which ensures a constant water level during its operation. The pressure inside each chamber is regulated with a PID controller, whose setpoint is updated via the integration of a Windkessel model, according to the latest flow-rate measurement. The software is programmed with LabVIEW and deployed on the FPGA module of a CompactRIO controller. The new setup, assembled to test a model with a single outlet, is shown in Figure 1.

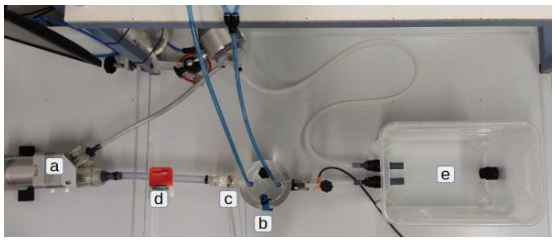

Figure 1: Single outlet configuration: a) piston pump, b) pressure-controlled chamber c) valve housing d) flow-meter and e) reservoir.

In order to validate the new system a bileaflet mechanical aortic valve was tested (St. Jude Medical), by imposing 12 different flow profiles. A transparent housing for the valve, with two orifices to measure the ventricular and the aortic pressure, was designed and manufactured with additive technique. The heart rate was kept constant at 70 bpm, and both the systole to diastole time ratio (α), and the Cardiac Output (CO) were varied. For each condition, the parameters of the numerical simulator were tuned to achieve a pressure range of 80-120 mmHg.

Results

The developed system successfully served as a platform to test the performances of a mechanical heart valve. For each flow profile the mean absolute difference between the setpoint pressure and the measured one was always less than 5 mmHg. A comparison between the setpoint and the pressure inside the chamber, under the most challenging condition (CO=7[l/min] and α=0.5[s/s]), is shown in Figure 2.

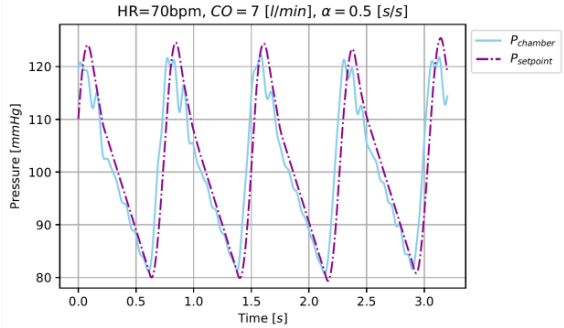

Figure 2: Comparison between the setpoint pressure and the measured pressure inside the chamber.

We then computed the relevant valve metrics, obtaining comparable results with the ones found in literature [3].

Discussion

We have presented a HIL approach that allows to overcome the major drawbacks of a typical Mock Circulatory Loop system. The effectiveness and flexibility of the new system were proven. The setup is under constant development; future works will include testing of anatomical models with multiple outputs and implementation of more sophisticated control algorithms.

References

1 Ochsner et al, IEEE trans bio eng, 60,2 : 507-16, 2013
2 Vignali et al, XXIV AIMETA Conf, 10.1007, 2019.
3 Knott et al, J Thor Card Surg, 96:952-61, 1988.

Acknowledgements

This project has received funding from the Marie Skłodowska-Curie grant agreement Meditate project No 859836.

DECIPHERING THE EFFECT OF THROMBOLYSIS ON CLOT MECHANICAL PROPERTIES AND ITS MICROSTRUCTURE

Anushree Dwivedi (1), John Burke (2), Michael Gilvarry (1) Ray McCarthy (1)

1. Cerenovus, Neuro Technology center, Galway, Ireland; 2. National University of Ireland, Galway, Ireland;

Introduction: Ischemic stroke is one of the major causes of disability and mortality in our society. Rapid recanalization of arteries occluded with thrombi employing a medical and/or endovascular approaches have been shown to be effective treatments. The medical recanalization route involves treating patients with recombinant-tissue plasminogen activator (rtPA). It is critical to understand how the clot structure, histology and occlusion haemodynamics effect thrombolysis. Initially, we examined the effect of thrombolysis on clot mechanical properties in a static model using ovine clot analogues. In this present study, we set out to develop an in vitro thrombolysis AIS occlusion model with an aim to understand the mechanism of action of rtPA under physiological pulsed flow and pressure control. This work is intended to provide outputs to support computational model generation as part of the in silico trials for treatment of Acute Ischemic Stroke (INSIST[1]) to precisely understand thrombolysis.

Methods: In the static model, ovine clot analogues with different red blood cell, fibrin and platelet composition were prepared and exposed to different levels of compaction to simulate arterial blood pressure conditions. The clots were then treated with rtPA in an open container with full immersion of the clots, using different doses of rtPA and for different time durations. After thrombolysis, unconfined compression testing was performed to measure tangent modulus and energy dissipation ratio to assess clot deformation and viscoelasticity respectively.

A dynamic model was then developed to examine the effect of diffusion of rtPA through stagnant and fully-flowing blood vessels proximal and distal to the clots. Diffusion through the clots under different pressure gradients was also examined. Measurement of the rate of change in clot size and changes in the microstructure at different locations on the clot were captured using video-capture and scanning electron microscopy respectively.

Results: In the static model, clot analogues that were exposed to rtPA showed a reduction in tangent modulus ($p < 0.05$) and showed significant reduction in energy dissipation ratio ($p < 0.05$).

In the dynamic model, composition and pressure gradient significantly affect the size of the clot at the occlusion site, thereby resulting in differences in clot compaction. The flow dynamics at the distal and proximal faces of the clot effect the access of rtPA to the clot, which allowed assessment of the impact of diffusion on rtPA effectiveness. SEM images of clot samples showed cleavage of fibrin fibres and exposure of the internal microstructure of the partially lysed clots.

Conclusion: A static and pulsatile in-vitro flow model of thrombolysis incorporating different pressure gradients was developed to study the role of clot composition, pressure and stagnant flow on the mechanism of thrombolysis. Clot composition, platelet contraction and duration of clot exposure to rtPA significantly affects clot mechanical properties.

Figure and Tables

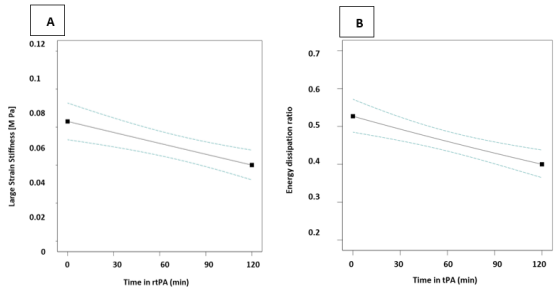

Figure 1: (A) Increasing duration of exposure to rtPA as significant factors affecting clot tangent modulus at large strain (B) and also significantly impacts energy dissipation ratio

References

1. H. C. Alves *et al.*, "Thrombus Migration Paradox in Patients With Acute Ischemic Stroke," *Stroke*, vol. 50, no. 11, pp. 3156–3163, Nov. 2019, doi: 10.1161/STROKEAHA.119.026107.

Acknowledgements

This project has received funding from the European Union's Horizon 2020 research and innovation program under grant agreement No 777072

MECHANICAL CHARACTERIZATION OF THROMBI RETRIEVED WITH ENDOVASCULAR THROMBECTOMY IN PATIENTS WITH ACUTE ISCHEMIC STROKE

Nikki Boodt[1], MD; Philip R. W. Snouckaert van Schauburg[2], MSc; Hajo M. Hund[1], MD; Behrooz Fereidoonnezhad[3], MSc, PhD; J. Patrick McGarry[3], MSc, PhD; Ali C. Akyildiz, MSc, PhD[1,2]; Adriaan C. G. M. van Es[1], MD, PhD; Simon F. De Meyer[4], MSc, PhD; Diederik W.J. Dippel[1], MD, PhD; Hester F. Lingsma[1], MSc, PhD; Heleen M. M. van Beusekom[1], MSc, PhD; Aad van der Lugt[1], MD, PhD and Frank J. H. Gijsen[1,2], MSc, PhD

1. Erasmus MC, Rotterdam, The Netherlands
2. Delft University of Technology, Delft, The Netherlands
3. National University of Galway, Galway, Ireland
4. KU Leuven, Kortrijk, Belgium

Introduction

Mechanical properties of thromboemboli play an important role in the efficacy of endovascular thrombectomy (EVT) for acute ischemic stroke. However, very limited data on mechanical properties of human stroke thrombi is available. We aimed to mechanically characterize thrombi retrieved with EVT, and to assess the relationship between thrombus composition and thrombus stiffness.

Methods

Forty-one thrombi from nineteen acute stroke patients who underwent EVT between July and October 2019 were mechanically analyzed, directly after EVT. We performed unconfined compression experiments and determined tangent modulus at 75% strain (Et75) as a measure for thrombus stiffness. Thrombi were histologically analyzed for fibrin/platelets, erythrocytes, leukocytes and platelets, and we assessed the relationship between histological components and Et75 with univariable and multivariable linear mixed regression.

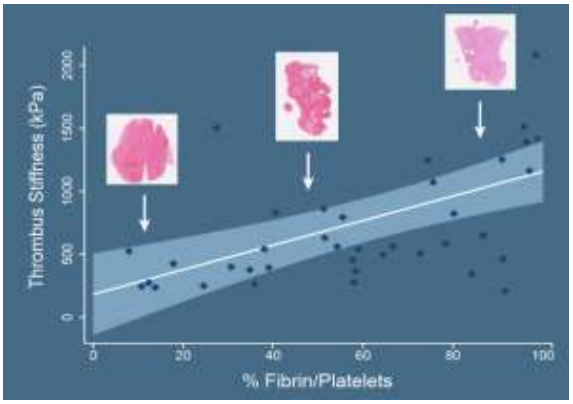

Figure 1: Scatterplot showing the relationship between composition and stiffness of the thrombus.

Results

Median Et75 was 560 (IQR 393-1161) kPa. In the multivariable analysis, fibrin/platelets were associated with increased Et75 (aβ, 9 [95% CI 5-13]) kPa, erythrocytes were associated with decreased Et75% (aβ, -9 [95% CI -5 to -13]) kPa. We found no association between leukocytes and Et75. High platelet values were strongly associated with increased Et75 (aβ, 56 [95% CI 38-73]).

Conclusions

Fibrin/platelet content of thrombi retrieved with EVT for acute ischemic stroke, is strongly associated with increased thrombus stiffness. For thrombi with high platelet values, there was a very strong relationship with thrombus stiffness. Our data provide a basis for future research on the development of next-generation EVT devices tailored to thrombus composition.

A REVIEW ON THE ASSOCIATION OF THROMBUS COMPOSITION WITH CLINICAL IMAGING AND MECHANICAL CHARACTERISTICS

Rachel Cahalane (1), Nikki Boodt (2,3), Ali Akyildiz (1,4), Jo-anne Giezen (4), Manouk Mondeel (4), Aad van der Lugt (2), Henk Marquering (5,6) and Frank Gijsen (1,4)

1. Department of Biomedical Engineering, Erasmus Medical Center (MC), Netherlands 2. Department of Radiology and Nuclear Medicine, Erasmus MC, Netherlands 3. Department of Neurology, Erasmus MC, Netherlands 4. Department of Biomechanical Engineering, Delft University of Technology, Netherlands 5. Department of Radiology and Nuclear Medicine, Amsterdam University Medical Centre (UMC), Netherlands 6. Department of Biomedical Engineering and Physics, Amsterdam UMC, Netherlands

Introduction

A wide variation exists in the histological properties of thrombi retrieved from acute ischemic stroke patients [1]. Thrombus composition significantly impacts the outcomes of thrombolytic therapy and thrombectomy procedures. If the clinical imaging modalities that are currently used in the acute ischemic stroke setting (computed tomography (CT) and magnetic resonance imaging (MRI)) can be leveraged to understand thrombus composition then the treatment can be individualized based on each thrombus. Mechanical retrieval also imposes a wide variation of forces on the occluding thrombus including compressive, tensile, shear and friction. The mechanical properties of an occluding thrombus can dictate the device-tissue interaction and subsequent success of clot retrieval procedures. Here, we present a scoping review detailing associations between thrombus composition, clinical imaging and mechanical characteristics.

Methods

We conducted a scoping literature review.

Results

A positive hyperdense artery sign on CT or susceptibility vessel sign on MRI images are associated with red blood cell (RBC)-rich and mixed thrombi [2]. Eleven studies confirmed a positive association between the RBC content or RBC-rich thrombi and the quantitative density values acquired from non-contrast CT scans [3]. R2* values derived from gradient-echo sequence MRI are also positively correlated to the RBC and iron concentration of thrombus analogs [4]. Contrastingly, thrombus perviousness (a proxy for permeability) on contrast-enhanced CT scans is positively associated with the fibrin/platelet content [5].

Tangent stiffness at 45% tensile strain has a strong positive correlation with fibrin concentration ($r = 0.613$, $p < 0.001$) [6]. Fibrin concentration was found to contribute to the compressive tangential stiffness at three different strain values ($E_{10\%}$, $E_{50\%}$ and $E_{80\%}$ in the order of 1kPa, 10kPa and 100kPa, respectively) [7]. In agreement with this, thrombus analogs with higher RBC content experienced greater maximum indentation depths (due to lower stiffness) in an stent strut indentation experiment [8]. As shown in Fig.1 there is a wide range in the properties reported from compression tests. Fibrin-rich clots have significantly higher coefficients of friction than clots higher RBC content (0.496 for 0% RBC vs 0.203 for 40% RBC) [9]. Data from tensile tests to failure of ex vivo thrombi and thrombus analogs suggest that RBC-rich clots are more prone to fracture and embolization [6,10].

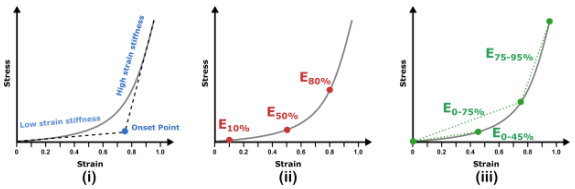

Figure 1: Range of compressive properties reported: (i) low and high strain stiffness and onset points, (ii) tangent stiffness at 10%, 50% and 80% strain, (iii) secant stiffness at 0-45%, 0-75% and 75%-95% strain.

Discussion

The use of multiple MRI sequences has produced promising results in the discrimination of lipid and calcific thrombus components. However, these quantitative MRI results must be validated in an in vivo cohort. Both the tensile and compressive behaviour of thrombi are largely dictated by the fibrin or RBC content. Thrombus analogs exhibit much lower (low-strain) stiffness than retrieved human thrombi. This may be explained by the absence of dynamic thrombus analog protocols, or pre-conditioning in the experimental set-up. To conclude, the use of non-invasive pre-treatment imaging to characterize thrombus composition and subsequent mechanical properties has the potential to inform decision-making in the treatment of acute ischemic stroke.

References

1. Staessens and De Meyer, Platelets, 1-9, 2020
2. Liebeskind et al., Stroke, 42: 1237–1243, 2011
3. Fitzgerald et al., PLoS One, 14:1-14, 2019
4. Bretzner et al., Journal of Neuroradiology, 2020
5. Patel et al., American Journal of Neuroradiology, 2020
6. Liu et al., JoSCD, 29, 2020a
7. Johnson et al., Annals of Biomedical Engineering, 2020
8. Weafer et al., JoNIS, 11:891-897, 2019
9. Gunning et al., JoNIS, 10:34-38, 2018
10. Liu et al., JoSCD, 29, 2020b

MODELING ACUTE ISCHEMIC STROKE RECANALIZATION THROUGH CYCLIC ASPIRATION

Oyekola Oyekloe (1), Francesco Costanzo (1,2), Scott Simon (3), Keefe Manning (1,4)

1. Biomedical Engineering, Penn State University, University Park, PA, USA
2. Engineering Science & Mechanics, Penn State University, University Park, PA, USA
3. Department of Neurosurgery, Penn State Hershey Medical Center, Hershey, PA, USA
4. Department of Surgery, Penn State Hershey Medical Center, Hershey, PA, USA

Introduction

Acute ischemic stroke (AIS), the result of embolic occlusion of a cerebral artery, is responsible for 87% of the 6.5 million stroke-related deaths each year. Despite improvements from first-generation thrombectomy devices for treating AIS, 80% of eligible stroke patients will either die or suffer a major disability. These data provide a strong motivation to improve current technologies for AIS therapies to achieve complete reperfusion on the first pass. To this end, our group embarked on a study on the use of cyclic aspiration in mechanical thrombectomy.

Methods

Our initial computational model [1] consisted of two compartments (Fig. 1): (i) a large-deformation viscoelastic thrombus, and (ii) an interface binding the thrombus to a cerebral artery, which was assumed to be rigid. The interface was modeled as a nonlinear viscoelastic cohesive zone (CZ) subject to a failure mechanism triggered by damage accumulation due to fibril pullout. In this work, we continue our investigation, this time accounting for the arterial deformation by modeling the artery as a hyperelastic solid. Using a geometry and physical properties relevant to AIS, we aim at answering some basic questions concerning the relative importance of arterial deformability in relation to the viscoelastic properties of the thrombus, the constitutive response of the CZ, and the details of how the cyclic aspiration is applied to the thrombus.

Results

Our new results show that, depending on the details of the load application, the thrombus's motion toward the aspirating catheter might be impeded by the artery deformability. Additional considerations pertain to the frequency of cyclic aspiration in relation to the relaxation times of the thrombus and of the CZ as higher aspiration frequencies result in increased viscoelastic stress responses of both the clot and the CZ.

Conclusions

These results suggest that the thrombus adhesion to the endothelium may play a significant role in the use of cyclic aspiration and understanding the force and behavior of clot removal.

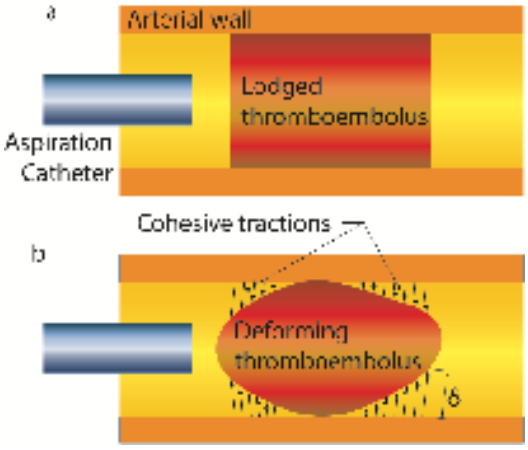

Figure 1: (a) Model with a lodged thromboembolus in a cerebral artery exposed to cyclic aspiration from an upstream catheter. (b) Diagram of the CZ model as the thromboembolus is pulled away from the arterial wall.

References

1. B. C. Good, et al.,Biomechanics and Modeling in Mechanobiology, 19: 761–778, 2020

Acknowledgements

This work was supported by the US National Institutes of Health (NHLBI) through Grant HL146921.

THICKNESS-REDUCED PERICARDIAL TISSUE FOR CATHETER-BASED AORTIC HEART VALVE PROSTHESES

Christine Müller, Alexander Rzany, Bernhard Hensel

Max-Schaldach-Stiftungsprofessur für Biomedizinische Technik, Centre for Medical Physics and Technology, Friedrich-Alexander University of Erlangen-Nuremberg, Erlangen, Germany

Introduction

Aortic stenosis is one of the most common degenerative heart valve defects. The valve becomes constricted, making a replacement necessary in severe cases. [1] When a traditional heart valve surgery cannot be performed, a catheter-based aortic valve implantation (TAVI) represents a modern alternative, provided the patient meets the requirements for that procedure [2]. Such an implant typically consists of a metallic stent with leaflets and skirt made from pericardial tissue. This prosthesis takes up the function of the malfunctioning native valve. [1,2]

To make the TAVI implants available to a broader range of patients, the size of the catheter needs to be as small as possible. To achieve this, research is done on reducing the thickness of the pericardial tissue used for leaflets and skirt of the valve prosthesis. A procedure is established and the properties of the adjusted tissue are examined.

Material and Methods

The used material is porcine pericardium, which is processed until the compound of fibrous pericardium and parietal layer of serous pericardium are free of other adherent tissues. After rinsing in physiological saline solution, water is extracted from the tissue under controlled conditions to reach a thickness-reduced state. Afterwards, the tissue needs to be fixated by cross-linking it with a 0.5% glutaraldehyde solution. To conserve this condition during crosslinking, pressure is applied to the tissue, while at the same time ensuring a permanent inflow of glutaraldehyde solution into the crosslinking assembly. Crosslinking is performed at least for a week.

The thickness and the water content are measured, as well as the mechanical properties using a uniaxial tensile apparatus. The grade of crosslinking is determined by a ninhydrine assay and differential scanning calorimetry. To test the suitability of this material for a valve prosthesis, prototypes were produced and their correct function examined.

Results

The tissue obtained by the above process has altered properties in comparison to standard pericardium. The tissue is significantly thinner (fig.1 top), the appearance becomes transparent and the water content decreases with thickness (fig.1 bottom). The tissue also becomes stiffer and has been shown to be adequately cross-linked for application in medical devices. It has been possible to sew prototype valve prostheses from the thickness-reduced tissue with correct function (see fig.2).

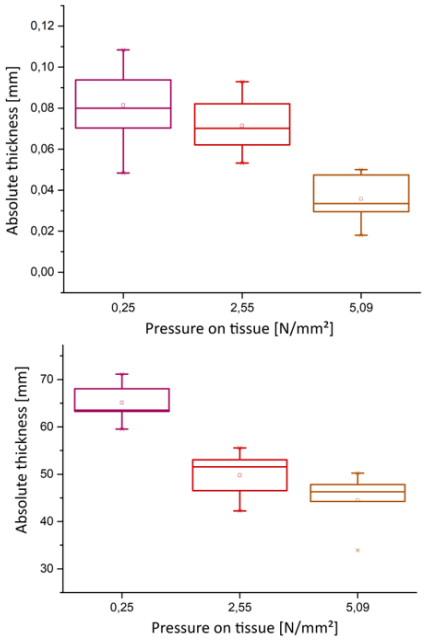

Figure 1: Box plot representation of thickness and water content of thickness-reduced pericardial tissue in dependence of the amount of pressure on the tissue used to remove water.

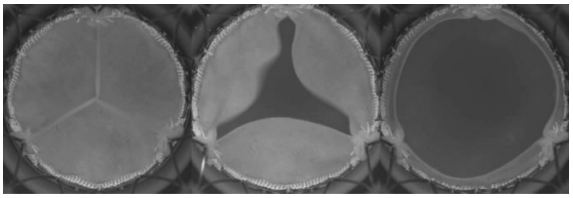

Figure 2: Correct functioning valve prosthesis in the function test system.

Discussion

The presented method produces thickness-reduced pericardial tissue in a reliable way. Furthermore, prototype aortic valves were made of thickness-reduced pericardial tissue with correct function. The altered mechanical properties in comparison to standard pericardium need to be further investigated.

References

1. Ibrahim et al, Kardiologie up2date, 8: 266-272, 2012.
2. Leon et al, N Engl J of Med, 374,17: 1597-1607, 2010.

PREDICTION OF IN-STENT RESTENOSIS BY MODELLING TISSUE DAMAGE AND GROWTH

Ran He and Liguo Zhao

Wolfson School of Mechanical, Electrical, and Manufacturing Engineering, Loughborough University, Epinal Way, Loughborough, LE11 3TU, UK

Introduction

In-stent restenosis (ISR) is one of the major issues for percutaneous coronary intervention, and defined as a decrease of luminal diameter by more than 50% after stent implantation [1]. The correlation between stenting-induced vessel injury and the rate of ISR has been investigated in literature, but the findings relied only on empirical data. The aim of this paper is to investigate the contribution of tissue damage in the media layer to ISR after stent deployment, with a focus on predicting the development of ISR with time. In the current study, a tissue-growth model, associated with vessel damage, was introduced to predict the growth of the media layer, a major contributor to ISR. Systematic finite element (FE) simulations were carried out to analyze the stenting procedure, quantify the tissue damage caused by stenting and predict the subsequent evolution of ISR over a defined time.

Methods

FE simulations were performed by using an Abaqus explicit solver. A two-layer coronary artery with a plaque was built for modelling the deployments of XIENCE Sierra, Endeavor and ABSORB stents. Both ends of the artery were fully fixed throughout the simulations. Stent expansion in the diseased artery consisted of two steps: inflation and deflation. In the subsequent balloon-removal step, contact of the balloon with the stent and artery was removed. In the final tissue-growth step (6 months), the media began to grow based on the damage caused by the stent deployment.
The first-order Ogden model with Mullins effect was adopted to describe the mechanical behaviour of the plaque. The modified HGO-C model with damage was employed to describe the mechanical behaviours of the arterial layers. A growth model [2] was applied to the media to describe the tissue growth.

Results

After 6 months of stent implantation, the mean lumen diameter reduced to 2.39 mm, 2.20 mm and 1.83 mm for the XIENCE Sierra, Endeavor and ABSORB stents, respectively (see Fig. 1). The lumen diameter during the tissue growth was plotted in Fig. 2 as a function of both the maximum lumen dimeter and the growth time, showing a direct correlation of the ISR with the maximum lumen diameter over the time after stent implantation. The diagram represents a 3D surface plot of ISR as a function of peak lumen diameter and time, which can be used directly to predict ISR for a given peak lumen diameter and time point.

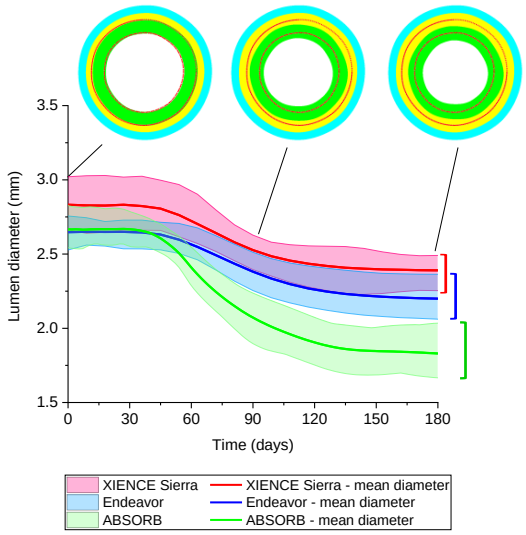

Figure 1: Evolutions of lumen diameter during tissue growth with cross-sectional views of artery.

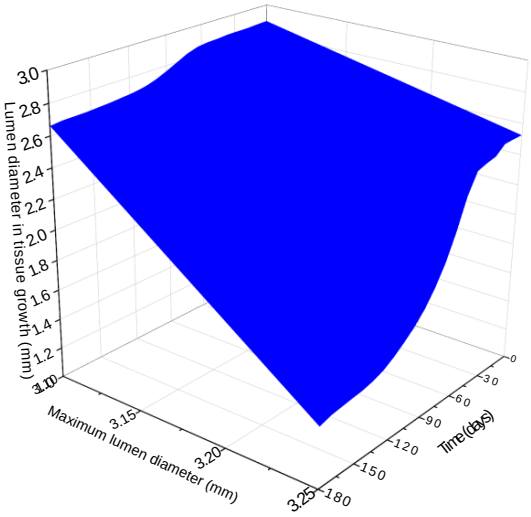

Figure 2: Correlation of in-stent restenosis with the maximum lumen diameter and time.

References

1. Hamid et al, McGrill J Med, 10:105-111, 2007.
2. Fereidoonnezhad et al, J Mech Phys Solids, 101:311-327, 2017.

Acknowledgements

We acknowledge the support from the EPSRC (EP/R001650/1), the British Heart Foundation (FS/15/21/31424) and the Royal Society of the UK (IE160066).

EFFECT OF BRANCHED ENDOGRAFTS ON LOCAL FLOW PATTERNS IN THE AORTIC ARCH IN COMPLEX AORTIC ARCH REPAIR

Sampad Sengupta (1), Yu Zhu (1), Mohamad Hamady (2), Xiao Yun Xu (1)

1. Imperial College London, United Kingdom; 2. Department of Interventional Radiology, St Mary's Hospital, Imperial College London, United Kingdom

Introduction

The evolution of aortic arch repair has equipped clinicians with a wide range of methods to tackle diseases arising in the ascending aorta and arch. Unlike conventional surgical procedures, modern methods such as thoracic endovascular aortic repair (TEVAR) provide a minimally invasive treatment which reduces risks and improves the outcome and speed of recovery [1]. Endografts used in TEVAR vary depending on the procedure and application with branched endografts used to maintain perfusion of blood to the supra-aortic vessels and are the focus of this study. Implantation of a branched endograft alters the geometry of the aorta, which has a profound influence on local flow patterns and haemodynamic parameters, such as velocity, pressure, and wall shear stress [1, 2]. Changes in these parameters can be determined by computational modelling and here we present a detailed computational fluid dynamics (CFD) analysis of the effects of branched endografts on blood flow in the arch.

Methods

The complex anatomical features of the aorta are unique to every individual. CT images acquired from patients who underwent branched endograft implantation were used to generate accurate 3D geometries (Figure 1). CFD simulations were then performed under physiologically realistic boundary conditions; applying the 3-element Windkessel model at all outlets and a representative inflow waveform at the inlet [3].

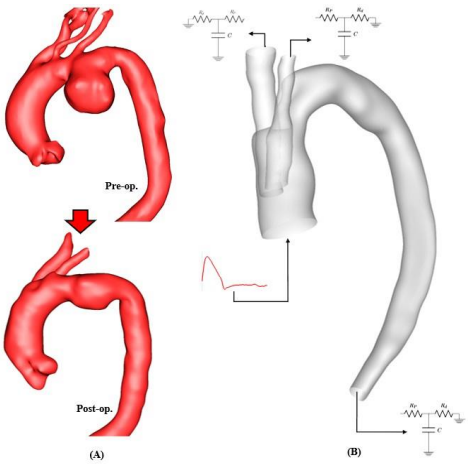

Figure 1: (A) Aortic arch aneurysm treated with TEVAR, before (top) and after (bottom) device implantation. (B) Type A aortic dissection post-TEVAR showing the boundary conditions imposed at outlets.

Results

The effect of branched endografts on flow in the aortic arch of two patients is illustrated in Figure 2. Implantation of the endograft results in accelerated flow in the arch, with higher velocity streams arising in the internal tunnel branch, leading into the supra-aortic branches. It is interesting to note the difference in flow patterns between the two cases, even though the same device with same tunnel branch diameter (12 mm) was used. Whilst the presence of inner tunnels helps guide the flow into the arch vessels, it also causes significant changes in the local flow patterns in the innominate and left common carotid arteries and in the arch region.

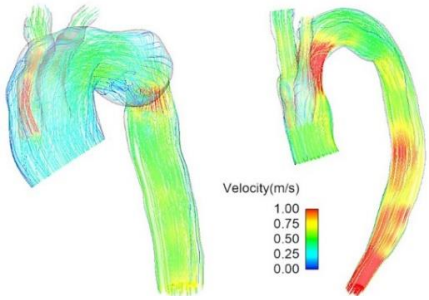

Figure 2: Velocity streamlines recorded at peak systole showing the flow patterns in the regions of interest for an aortic arch aneurysm (left) and dissection (right), both treated with the same branched endograft.

Discussion

Branched endografts have a significant influence on local flow patterns in the arch and stented supra-aortic branches. This is largely dictated by the geometric alterations brought about by the device. Through detailed analysis of haemodynamic parameters, including helical flow index, wall shear stress and its related indices, patient-specific modelling will help evaluate the risk of possible device migration, endoleaks, or device-induced thrombosis in the branches.

References

1. van Bakel, T. M., et al, *Annals of Cardiothoracic Surgery, 7*, 406-413, 2018
2. Zhu, Y., et al, *Medicine in Novel Technology and Devices, 4*, 2019.
3. Pirola, S., et al, *Journal of Biomechanics, 60*, 15-21, 2017.

Acknowledgements

This work is funded by the Doctoral Training Programme studentship from the Engineering and Physical Sciences Research Council, UK.

EFFECT OF STENT OVERLAP ON LUMEN GAIN AND TISSUE DAMAGE

Ran He (1), Liguo Zhao (1), Vadim V. Silberschmidt (1), Yang Liu (1), Felix Vogt (2)

1. Wolfson School of Mechanical, Electrical and Manufacturing Engineering, Loughborough University, Epinal Way, Loughborough, LE11 3TU, UK; 2. Medical Clinic I, University Hospital Aachen, Pauwelsstrasse 30, 52074 Aachen, Germany

Introduction

Placement of multiple overlapping stents is frequently required for patients with a long or angulated lesion, which cannot be treated properly with a single stent. However, stent overlap was not well studied *in silico*, especially its effect on lumen gain and tissue damage. In this study, stent deployment in a patient-specific coronary artery was modelled, considering a layered structure of a diseased artery and their hyperelastic properties. Finite-element simulations were carried out for deployment of three stents with and without overlap. The simulated lumen gain was compared with the clinical results and linked with tissue damage.

Methods

Finite-element simulations were performed by using an Abaqus explicit solver. The artery-plaque model was developed by using Mimics and had an overall length of 30 mm. The vessel was built based on optical coherence tomography (OCT) imaging of a specific patient's right coronary artery. Deployment of three stents, with and without overlap, was simulated and compared. Both ends of the artery were fixed in the longitudinal and circumferential directions throughout the simulations. The interactions and stenting process used in this study were the same as those in [1].

The first-order Ogden model with Mullins effect was adopted to describe the mechanical behaviour of the plaque. The modified HGO-C model with damage was employed to describe the mechanical behaviours of the arterial layers.

Results

The simulated outcomes for three stents with and without overlap are presented in Fig. 1, in comparison with clinical outcomes. The overall lumen area achieved with the non-overlapping stents was smaller than that achieved with the overlapping ones. The dissipation energy in the media layer is plotted in Fig. 2, which represents tissue damage caused by stenting. The maximum damage in the media layer for three non-overlapping stents was higher than that for the three overlapping stents.

Discussion

In this study, the non-overlapping stents resulted in a smaller lumen gain, as well as more severe damage to the media layer, when compared to the overlapping stents. Therefore, if multiple stents are required to treat a long lesion, they should be deployed with a minimal overlap in order to achieve a desired lumen gain as well as to reduce the stenting-induced tissue damage.

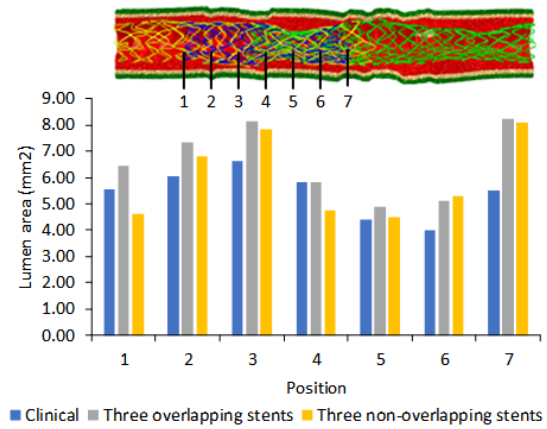

Figure 1: Lumen area after stenting: clinical outcomes vs. simulated results for three stents with and without overlap.

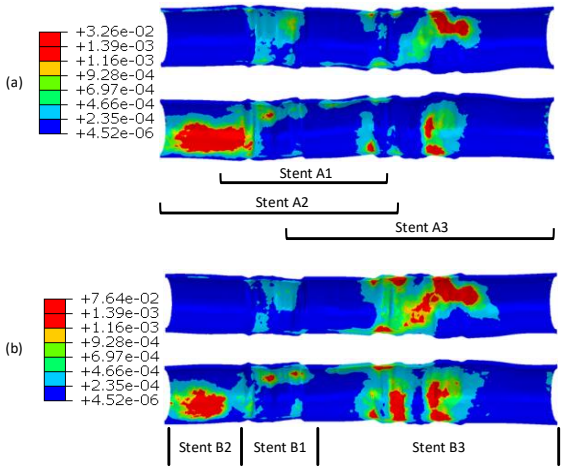

Figure 2: Contour plots of dissipation energy (mJ/mm^3) in media layer after stenting: (a) three overlapping stents and (b) three non-overlapping stents.

References

1. He et al, Biomech Model Mechan, 19: 47-60, 2020.

Acknowledgements

We acknowledge the support from the EPSRC (EP/R001650/1), the British Heart Foundation (FS/15/21/31424) and the Royal Society of the UK (IE160066).

4D XCT OF SYNTHETIC ARTERIAL GRAFTS: TOWARDS AN IMPROVED DESIGN

Alice Coirbay (1,2), Grzegorz Pyka (1,2), Greet Kerckhofs (1,2,3,4)

1. Institute of Mechanics, Materials, and Civil Engineering, UCLouvain, Belgium; 2. Institute of Experimental and Clinical Research, UCLouvain, Belgium; 3. Dept. Materials Science and Engineering, KU Leuven, Belgium; 4. Prometheus, Division of Skeletal Tissue Engineering, KU Leuven, Belgium

Introduction

A common treatment of atherosclerosis, one of the most common cardiovascular diseases, involves the placement of a bypass made of synthetic grafts, such as Dacron or Gore-Tex [1]. However, an important mismatch in the mechanical properties between the native tissue and the graft can result in complications, especially for small-diameter vessels (<6mm) [2]. Therefore, detailed analysis of the global and local mechanical properties of synthetic graft materials, in comparison to native tissue, is essential to further improve vascular graft properties and reducing the risk of graft failure.

Methods

In this study, we applied 4D X-ray microfocus computed tomography (4D XCT) to a Dacron graft. In-situ experiments were performed using a Phoenix Nanotom M XCT system combined with a Deben CT5000 mechanical loading stage. 3D image data was generated at consecutive tensile deformation steps (both in the longitudinal and circumferential direction of the graft) with a maximal displacement of 0.2 mm. Avizo software was used to calculate the local strain maps based on conventional Digital Volume Correlation (DVC). Three different methods of incremental DVC were compared: the "fixed reference image" conventional DVC, using the same fixed reference image volume, the "sequential" incremental DVC, updating the reference volume image at each steps, and the "preconditioned" incremental DVC, updating the reference volume once severe decorrelation occurs.

Results and discussion

A stiffness of 5.75 MPa and 13.65 MPa, calculated in longitudinal and circumferential orientation respectively, highlighted an anisotropy in mechanical properties of Dacron, which was already identified in the literature [3]. The characterization of the graft microstructure was further studied using incremental DVC. From the three incremental DVC methods, the "fixed reference image" conventional DVC enabled a reliable visualization of the evolution of the strain maps until a maximal displacement of 0.6 mm. In the longitudinal direction, the maximum strains for an elongation of 0.6 mm were ranging from -0.8% to 12%. Local strain maps superimposed on the microstructure (Fig. 1A) showed that the highest tensile strain was mainly located at the front and backwards folds within the selected region of interest (ROI), highlighting potential failure location. In the circumferential direction, the region of maximal tensile strain (9.04%) was mostly situated in between the longitudinally warp knitted yarns (Fig.1B). This region potentially became thinner and therefore weaker during the tensile elongation of the sample.

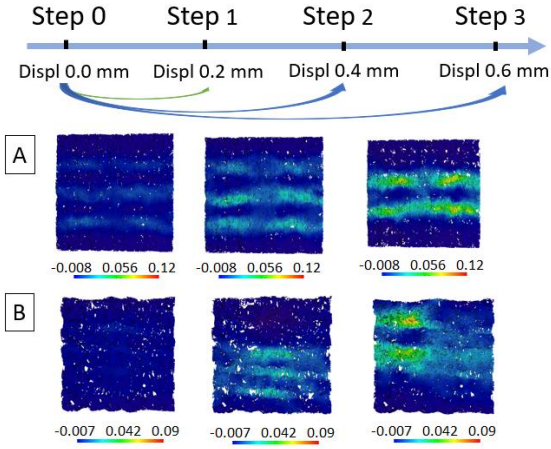

Figure 1: Visualization of the volumetric strains map, generated from the extracted ROI of Dacron loaded in the (A) longitudinal direction and (B) circumferential direction.

Conclusion

Performing 4D XCT on synthetic arterial graft, namely Dacron, as well as a DVC analysis on the resulting scans, enabled to highlight intrinsic mechanical properties of the material and to identify the region of highest deformation and possible failure in its microstructure. This preliminary work also points areas of improvements in the 4D XCT protocol of arterial synthetic grafts. Furthermore, it paved the way to ongoing similar experiments on native tissue using 4D contrast-enhanced XCT (4D CE-CT). Understanding the native tissue microstructure and its changes under mechanical loading will allow to enhance the properties and design of the current grafts.

References

1. J. Chlupác et al, Physiological research, 2009.
2. H. J. Salacinski et al, J. of B iomaterials applications, 2001.
3. D. Tremblay et al., The Annals of thoracic surgery, 2009.

PATIENT-SPECIFIC CFD ANALYSIS OF TRANSCATHETER AORTIC ROOT REPLACEMENT WITH CHIMNEY CORONARY GRAFTS

Rodrigo M. Romarowski (1), Anna Ferrarini (1), Matteo Stochino (1), Ferdinando Auricchio (1), Simone Morganti (1), Ludwig Karl von Segesser (2), Enrico Ferrari (3,4), Michele Conti (1)

1. University of Pavia, Italy; 2. University of Lausanne, Switzerland; 3. University of Zurich, Switzerland; 4. Cardiocentro Ticino, Switzerland

Introduction

Transcatheter aortic root repair (TARR) consists of the simultaneous endovascular replacement of the aortic valve, the root, and the proximal ascending aorta. The aim of the study is to set-up a computational model of TARR based on a previously developed in-vitro model of our group [1], in order to explore the impact of the endovascular procedure on the coronary circulation supported by chimney grafts.

Methods

Computed tomography angiography (CTA) of a patient with dilated ascending aorta was segmented to obtain a 3D representation of the proximal thoracic aorta, including aortic root and supra-aortic branches. Computed assisted design (CAD) tools were used to modify the geometry in order to create the post-procedural TARR configuration featuring the main aortic endograft integrated with two chimney grafts for coronary circulation (Fig. 1). Computational Fluid Dynamics (CFD) simulations were ran using the software SimVascular [2] in both pre- and post-procedural configurations using a pulsatile inflow and lumped parameter models at the outflows to simulate peripheral aortic and coronary circulation. Differences in coronary flow and pressure along the cardiac cycle were evaluated together with the velocity field in the zones of interest.

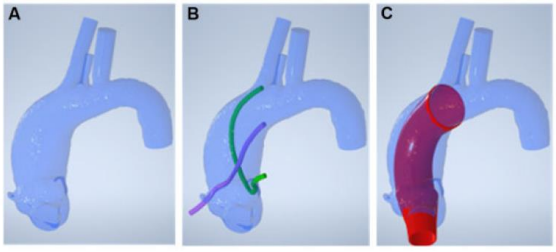

Figure 1: Creation of the virtual post-TARR geometry. A. 3D reconstruction of the CTA of a patient with ascending aorta dilation; B. virtual nsertion of the coronary grafts; C. virtual insertion of the main body of the TARR device.

Results

After the virtual implant of TARR device with coronary grafts, flow became more organized and less recirculation was seen in the ascending aorta (Fig. 2). Coronary perfusion was guaranteed with negligible flow differences between pre- and post-procedural configurations. However, despite being well perfused by chimney grafts, the procedure induces an increase of the pressure drop between the coronary ostia and the ascending aorta of 8mmHg.

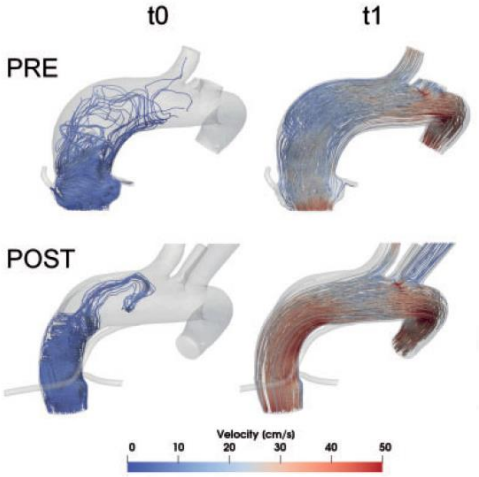

Figure 2: Velocity streamlines at the beginning of the systole (t0) and maximum systolic acceleration (t1).

Discussion

Our simulation results show that there is a negligible difference between pre-procedural and post-procedural coronary perfusion, encouraging further analysis of the proposed TARR procedure towards its clinical implementation. However, at the same time, there was an increase of the pressure drop between the coronary ostia and the aortic inflow section; we can attribute such an increase to the hydraulic resistance induced by the long chimney graft used in the post-procedural TARR configuration, in concomitance with the pressure increase at the aortic inlet, due to the reshaping of the aortic root and ascending aorta determined by the presence of the main endograft. The increase in pressure can be interpreted as a downside of the intervention that has already been described as increasing post-procedural afterload in patients undergoing thoracic endovascular aortic repair [3].

References

1. Ferrari et al, Interact Cardiovasc Thorac Surg, 31 :121-128, 2020.
2. Updegrove et al, Ann Biom Eng, 45:525-541, 2017.
3. Kim et al, Ann Biom Eng, 38:3195-3209, 2010.

RESTENOSIS IN HUMAN STENTED SUPERFICIAL FEMORAL ARTERY: REMODELING TRAJECTORY AND ROLE OF HEMODYNAMICS

Monika Colombo(1), Yong He(2), Anna Corti(1), Diego Gallo(3), Federica Ninno(1,4), Stefano Casarin(5), Jared M Rozowsky(2), Francesco Migliavacca(1), Scott Berceli(2,6), Claudio Chiastra(1,3)

1. LaBS, Dept. Chemistry, Materials and Chemical Engineering "Giulio Natta", Politecnico di Milano, Italy; 2. Dept. Surgery, University of Florida, Gainesville, FL, USA; 3. PoliTo^{BIO}Med Lab, Dept. Mechanical and Aerospace Engineering, Politecnico di Torino, Italy; 4. Dept. Medical Physics and Biomedical Engineering, University College of London, UK; 5. Dept. Surgery, Houston Methodist Hospital, Houston, TX, USA; 6. Malcom Randall VAMC, Gainesville, FL, USA

Introduction

Superficial femoral arteries (SFAs) treated with self-expandable stents are widely affected by in-stent restenosis (ISR). The process of ISR initiation and progression as well as the role of hemodynamics as ISR promoting factor is poorly understood in this vascular region. Accordingly, the aim of this work is to investigate (i) the ISR progression in human SFAs by quantifying the lumen remodeling trajectory in the months after stent implantation and (ii) the impact of hemodynamics on ISR development by performing computational fluid dynamics (CFD) analyses at multiple post-procedural follow-ups.

Methods

The geometrical models of 10 stented lesions from 7 patients were obtained from computed tomography (CT) through a validated reconstruction method [1]. Four follow-ups after stent implantation were considered, namely 1-week (1W), 1-month (1M), 6-months (6M) and 1-year (1Y). By using the reconstructed anatomies and the inlet velocity profile derived from patients' Doppler ultrasound data [1], transient CFD simulations were conducted for the first 3 follow-ups.

The lumen remodeling was quantified in terms of lumen area change (ΔA), the hemodynamics in terms of wall shear stress (WSS) based descriptors [2]. Besides the common WSS-based descriptors (i.e. time-averaged WSS, TAWSS; oscillatory shear index, OSI; relative residence time, RRT), descriptors considering the WSS multidirectionality (e.g. cross flow index, CFI; cycle-averaged ratio of the secondary and axial WSS components, WSSratio) were also introduced. The lumen area was computed every 1-mm along the vessel length at each follow-up. The hemodynamic data were analyzed in two-dimensional maps, averaged circumferentially and every 1-mm axially to match the morphological data, and then subjected to a spatial decorrelation analysis to consider them as spatially independent [2].

Kruskal-Wallis and Mann-Whitney U tests were used to compare the morphological data at consecutive follow-ups and time-intervals (first, 1W-1M; intermediate 1M-6M; last, 6M-1Y). To test the association direction and strength between the WSS-based descriptors and the morphological remodelling, the Spearman's correlation was computed. Statistical significance was assumed for p-value <0.05.

Results

The first time interval was the most dynamic in terms of lumen remodeling, with significant differences between the lumen area at 1W and 1M (p~0.05), and at 1W and 1Y (p<0.05) (Fig. 1A). While the intermediate time interval showed negligible lumen remodeling, in the last time interval portions of the lesions were characterized by severe, focal lumen reduction. The link between hemodynamics and ISR progression was confirmed by the significant correlations in the first and last time intervals (Fig. 1B). Moreover, the direction of the correlations (ρ<0 for TAWSS, ρ>0 for the other descriptors) remained constant along the follow-ups.

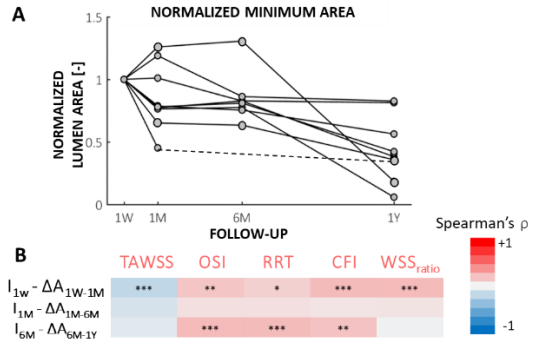

*Figure 1: A) Normalized minimum lumen area; B) Spearman's correlations between lumen area change (ΔA) and the WSS-based descriptors (I). *: p<0.05; **: p<0.01; ***: p<0.001.*

Discussion

The post-intervention lumen remodeling trajectory and the impact of hemodynamics on ISR progression were quantified. The longitudinal nature of this study provided more quantitative morphological and hemodynamic data than previous investigations [2], suggesting that low and multidirectional WSS are important biomechanical factors involved in the ISR process, especially in the time interval 6M-1Y, subjected to focal re-narrowing.

References

1. Colombo M et al., Med Eng & Phys, 75: 23-35, 2020.
2. Colombo M et al., Sci Rep, 11: 1-13, 2021.

Acknowledgements

This work has been supported by Fondazione Cariplo, Italy (Grant number 2017-0792, TIME).

ENDOVASCULAR TARGETED DRUG DELIVERY IN MYOCARDIAL MICROVASCULAR OBSTRUCTION (MVO)

Yannick Rösch (1), Mirunalini Thirugnanasambandam (1), Sabrina Frey (2), David Eggenberger (3), Yves Kuster (3), Cornelia Nef (3), Lino Widmer (1), Jens Ulmer (3), Dominik Obrist (1)

1. ARTORG Center for Biomedical Engineering Research, University of Bern, Switzerland; 2. CorFlow Therapeutics AG, Baar, Switzerland; 3. OST, University of Applied Sciences, Buchs SG, Switzerland

Introduction

MVO occurs in as many as 56.9% of all heart attack (STEMI) patients [1]. MVO may come from residual particles of the primary thrombus, tissue swelling or collapsed vessels. Affected vessels are small in diameter (< 0.2 mm) and inaccessible for catheters. Some-times thrombolytic drugs are injected directly into the aorta or the coronary arteries - with limited success.
To overcome these limitations, we study new methods for catheter-based targeted drug delivery to MVO.

Materials and Methods

A flow loop, representing the left heart circulation, is connected to a model of the coronary arterial tree comprising resistors and compliances to mimic the dynamics of the coronary circulation. This system is filled with deionized water and matched to in-vivo data obtained in a porcine MVO model.
A microfluidic chip made with selective laser etching (SLE) contains a microvascular tree representing the myocardial microcirculation [2] distal to the primary obstruction. This chip is used to study the drug distribution in healthy and in obstructed branches: An occlusion-infusion balloon catheter is used to infuse medication (dye) distally to the inflated balloon (15 ml in 30 s) and block proximal blood flow for further 60 seconds. Reference experiments only infuse the drug without proximal balloon occlusion.
A camera records the intensity of the transmitted light through the chip. Based on previous calibration, the drug concentration c[drug] can be calculated for each pixel (Fig. 1) and is then evaluated in defined regions of interest (ROI) (Fig. 1 and 2).

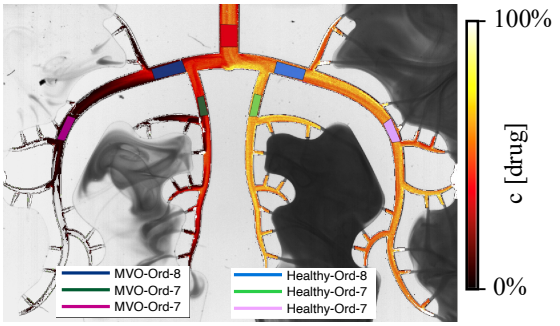

Fig. 1: The arterial tree chip with overlayed concentration map during drug infusion with the balloon catheter. Left: MVO (blocked outlets), right: healthy.

Results

With inflated balloon, 2.5x higher maximal drug concentrations are reached than without balloon (Fig. 2).

The concentration curves integrated over time (cumulated drug dose (CDD)) are significantly higher with the inflated balloon (Two-sample *t*-test; $t(25) = 6.73$, $p < 0.01$).
The ratio *Balloon/NoBalloon* of the CDD can be seen as a measure for drug delivery efficacy to channels affected by MVO, if the balloon is inflated (Fig. 3). Over all MVO-ROIs, the CDD-Ratio is 4.5.

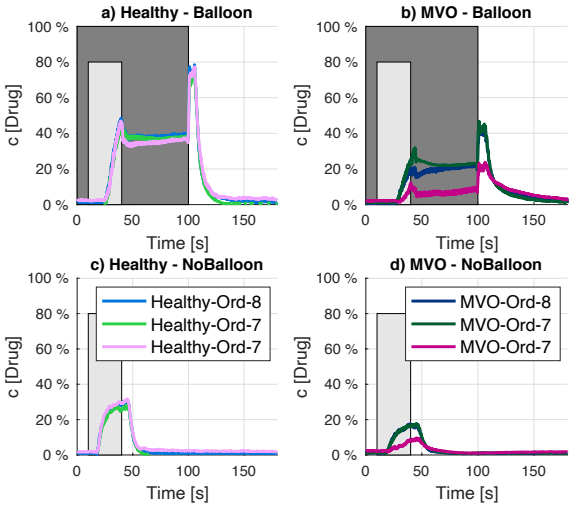

Fig. 2: Drug concentration over time. Light grey: Dye infusion. Dark grey: Balloon inflated.

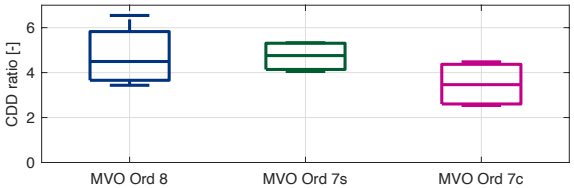

Fig. 3: Box plot of CDD ratio Balloon/NoBalloon per channel order.

Discussion

The results show that infusion with proximal balloon occlusion leads to significant higher CDD. Further experiments must take into account blood mimicking fluid and different treatment protocols.

References

1. de Waha et al, Eur Heart J. 2017 Dec 14; 38(47): 3502-10.
2. Fung, Biomechanics, Springer, 1993

Acknowledgements

This work is financially supported by grant 31010.1 from the Swiss Innovation Agency - InnoSuisse.

CHARACTERIZATION OF AN EX-VIVO PORCINE MODEL OF FUNCTIONAL TRICUSPID REGURGITATION

E. Salurso (1, 2), M. Jaworek (1, 2), F. Perico (1,2), G. Gelpi (1,2,3), C. Romagnoni (2,3), R. Rosa (2,3), M. Contino (2,3), G. B. Fiore (1,2), R. Vismara (1,2)

1. Department of Electronics, Information and Bioengineering, Politecnico di Milano, Milan, Italy;
2. ForcardioLab – Fondazione per la Ricerca in Cardiochirurgia ONLUS, Milan, Italy;
3. Cardiovascular Surgery Department, ASST Fatebenefratelli Luigi Sacco University Hospital, Milan, Italy

Introduction

The emerging treatments for Tricuspid Valve (TV) pathologies leads to the need for realistic pathological models of TV, aimed at studying these new approaches. The most common TV pathology is Functional Tricuspid Regurgitation (FTR) where annulus and right ventricle dilation leads to valve incontinence. Defrosted porcine hearts were used in pulsatile mock loops as an experimental model of FTR [1], but a systematic characterization of the experimental model is lacking. In this work we compared the TV geometrical morphology in fresh and defrosted porcine hearts to assess the porcine heart as an ex-vivo model of FTR.

Methods

Five porcine hearts were collected from a local abattoir. Pulmonary valves were sealed, the ventricles were pressurized at 15 mmHg, and the backflow through the TV was measured. To assess the TV morphology the hearts were connected to a pulsatile mock loop [1] (working parameter were 60 bpm, 70ml of stroke volume, and 15 mmHg of mean pulmonary pressure). 3D-volumetric echocardiographic and endoscopic images of the TV were acquired. The hearts were then kept frozen (–18°C) for 14 days, defrosted, and tested again with the same test protocol. Based on echocardiography, 3D anatomies of the TV in peak systole were segmented and reconstructed by a custom semi-automatic software [2]. The following parameters were obtained: tenting volume, maximum diameter, perimeter, and area of TV annulus.

Results

Figure 1 represents endoscopic views of the TV both in fresh and defrosted hearts. Table1 reports the overall results (mean ± standard deviation). Sample freezing induced significant ($p<0.05$) increase in annulus size (10% and 5% of annulus area and perimeter, respectively). The treatment induced right ventricle dilation, as highlighted by 114% increase in tenting volume. The morphologic alterations were reflected in the significant 7-fold increase of backflow.

Discussion

Fresh hearts can be used to replicate the physiological behavior of the valve, while defrosted porcine TV can be considered a realistic ex-vivo model to reproduce FTR pathology.

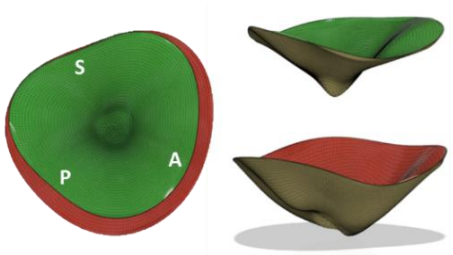

Figure 2: 3D reconstruction of the valve profile during peak systole. Fresh valve in green, defrosted valve in red. A: anterior leaflet, P: posterior leaflet; S: septal leaflet.

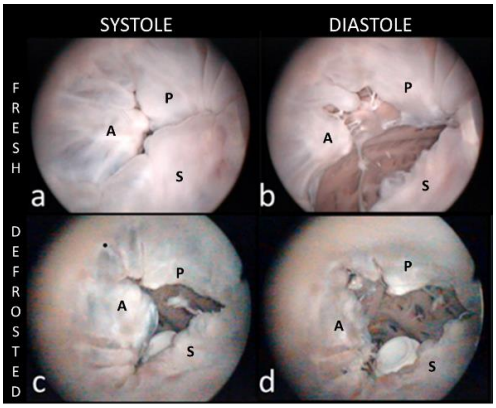

Figure 1: Endoscopic views of the TV:(a) fresh heart in systole;(b) fresh heart in diastole; (c) defrosted heart in systole; (d)defrosted heart in diastole. A: anterior leaflet, P: posterior leaflet; S: septal leaflet.

Parameter	Fresh Hearts	Defrosted Hearts	p-value
Backflow [l/min]	0.3 ± 0.02	2.3 ± 0.8	0.002
Maximum diameter [mm]	48.9 ± 4.5	51.0 ± 2.8	0.01
Annulus perimeter [mm]	144.9 ± 1.2	151.0 ± 8.7	0.02
Annulus area [mm^2]	1617 ± 231	1784 ± 217	0.006
Tenting volume [ml]	6.2 ± 0.9	13.3 ± 3.6	0.005

Table 1: Characteristic parameters evaluated on fresh and defrosted hearts. Paired t-test was performed.

References

1. Jaworek et al., ASAIO J, 63(4):438-444, 2017
2. Pappalardo et al., J Cardiovasc Comput Tomogr, 14:520-523,2020

PHENOMENOLOGICAL APPROACH TO MODELLING THERMOPLASTIC POLYMERS FOR STENT APPLICATION

Kerstin Schümann (1), Wolfram Schmidt (1), Christoph Brandt-Wunderlich (2), Daniela Arbeiter (1), Klaus-Peter Schmitz (1, 2), Niels Grabow (1)

1. Institute for Biomedical Engineering, Rostock University Medical Center, Rostock, Germany; 2. Institute for ImplantTechnology and Biomaterials, Rostock, Germany

Introduction

Biodegradable stents offer the potential to overcome long-term side effects of permanent metallic stents. Besides magnesium, polymeric materials, especially poly(L-lactic acid) (PLLA), play an important role in current research [1].

For the prediction and optimization of the mechanical behavior of polymeric stents an adequate constitutive model is essential to simulate the specific material characteristics of thermoplastic polymers. A phenomenological model considering typical characteristics of thermoplastic polymers is SAMP-1 (Semi-Analytical Model for Polymers), implemented in LS-DYNA (Livermore, USA), which is applied in this study to analyze mechanical properties of polymeric stents made of a PLLA-based blend. Results were compared to data of in vitro tests of stent prototypes.

Methods

Typical characteristics considered in SAMP-1 are the different behavior depending on the load type implemented by a quadratic or Drucker-Prager yield surface (depending on input test data), local necking in tensile testing and strain rate dependency [2].

As input into the constitutive model, Cauchy ("true") stress-strain data from tensile and compression tests were obtained under consideration of non-isochoric plasticity according to [3]. Additionally, a plastic Poisson's ratio as function of plastic strain was determined in tension and compression. Finite element analyses (FEA) applying the material model SAMP-1 in conjunction with said material data were performed with LS-DYNA to simulate the expansion and collapse behavior (*Figure 1*) of four different stent designs. Boundary conditions according to designated in vitro experiments were implemented.

Stent prototypes were fabricated by femtosecond laser cutting of solution casted tubes (ID = 1.4 mm, WT = 150 µm), according to [4, 5]. Following [6], the stent prototypes were analyzed regarding expandability to 3 mm, recoil and collapse pressure. The comparison to numerically determined results enables an evaluation of the applicability of the constitutive model.

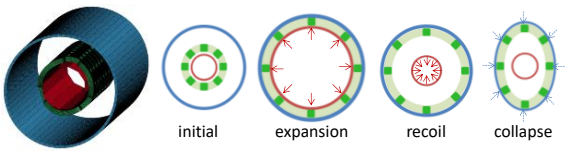

Figure 1: Representative finite element stent model and schematic illustration of analyzed load cases

Results

In *Figure 2* the expanded stents after elastic recoil from FEA and in vitro tests are compared. All designs could be expanded to 3 mm and show similar deformations. The resulting values for the elastic recoil after expansion and collapse pressure under radial loading are shown in *Figure 3*. While basically good results can be achieved with the simulations, both values tend to be overestimated by FEA.

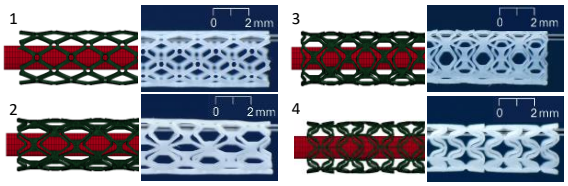

Figure 2: Investigated stent designs 1–4 after expansion (FEA and in vitro)

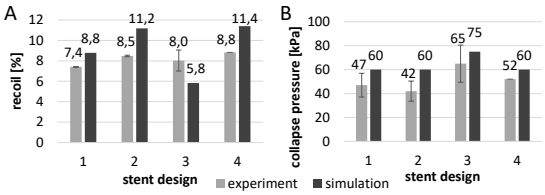

Figure 3: Elastic recoil (A) and collapse pressure (B) for stent designs 1–4 from FEA and in vitro testing

Discussion

The used constitutive model in conjunction with applied material data allows FEA for evaluation and comparison of different stent designs. In the current analysis differences in tension and compression were considered, but no quadratic yield surface was applied. Rate effects were not considered. The model SAMP-1 offers more opportunities to refine the model by additional material test data.

References

1. Arbeiter et al., Polymers, 13,2:292, 2021
2. Kolling et al., 4. LS-DYNA Anwenderforum, 2005
3. Schümann et al., Curr Dir Biomed Eng, 2,1:649-652, 2016
4. Grabow et al., Biomed Tech, 58,5:429-437, 2013
5. Schümann et al., Curr Dir Biomed Eng, 6,3:213-216, 2020
6. Schmidt et al., Eur J Med Res, 23,2, 2018

Acknowledgements

We thank Prof. Dr.-Ing. Udo Röhr for his counselling and advice. This work was partially funded by the BMBF within the project RESPONSE "Partnership for Innovation in Implant Technology".

MANUFACTURING, CHARACTERIZATION AND TESTING OF ADDITIVELY MANUFACTURED 316L STAINLESS STEEL STENTS

Enzoh Langi (1), Parastoo Jamshidi (2), Moataz Attallah (2), Vadim V. Silberschmidt (1), Helen Willcock (3), Felix Vogt (4), Liguo Zhao (1)

1. Wolfson School of Mechanical, Electrical and Manufacturing Engineering & 3. Department of Materials, Loughborough University, Epinal Way, Loughborough, LE11 3TU, UK; 2. School of Metallurgy and Materials, University of Birmingham, Edgbaston, Birmingham, B15 2TT, UK; 4. Medical Clinic I, RWTH University Hospital Aachen, Pauwelsstrasse 30, 52074 Aachen, Germany

Introduction

Stenosis results in partial or complete blockage of arteries due to the accumulation of fatty deposits on the inner surface of the vessel wall, which can be effectively treated with stents. The current stent manufacturing methods produce stents with uniform geometries, in terms of stent diameter, cell design and strut size. These stents have almost the same mechanical properties along either circumferential or longitudinal directions. However, the distribution severity of stenosis varies significantly in patients, for which the use of current stents is not ideal. So, there is a need to develop lesion-specific stents, with varied diameter, design and strut size, for much improved clinical outcomes, which can be achieved via additive manufacturing [1]. The aim of this work was to study the microstructures and mechanical behaviour of additively manufactured 316L stainless-steel (SS) stents.

Methods

Samples of SLMed and commercial 316L SS stents were used in this study. The commercial stent was a Multi-Link RX UltraTM stent produced by Abbott; with a strut size of 100 µm. It was produced by laser micromachining of a thin-walled tube. 316L SS stents were produced using selective laser melting (SLM). Specimens were prepared for microstructural study through sectioning, mounting, grinding and metallurgical polishing procedures. Microstructures were examined using a JEOL 7100F scanning electron microscope, with simultaneous elemental and orientation analyses and electron backscatter diffraction. To quantify the mechanical behaviour, nanoindentation tests were conducted using NanoTest Platform 3 equipment.

Results

The average roughness Ra, root mean square roughness Rq and mean roughness depth Rz for SLMed stent were 8.39, 10.55 and 56.07 µm, respectively. In the same vein, the roughness parameters for the stent were 0.18, 0.26 and 1.23 µm, respectively. The as-built stent was fully austenitic, and no traces of a second phase was recorded. In contrast, the XRD pattern of the commercial stent showed traces of the second phases such as δ-ferrite and α phase. The as-built stent consisted of fine grains towards the wall edges and coarse grains at the middle strut. The coarse grains, with a size of hundreds of microns, were elongated in the longitudinal direction. While the commercial stent had equiaxed, fine grains and presence of twins. The hardness and elastic modulus for the printed stent was higher than commercial stent.

Discussion

In this study, results showed that the microstructures and mechanical properties were affected by the SLM process. The grain microstructure of SLMed stent will need to be optimised, for instance through heat treatment, to further improve the mechanical properties required for stents (e.g. both strength and ductility). It is also necessary to further reduce the strut size during SLM process in future research, to match the thin strut structure of commercial stents [2].

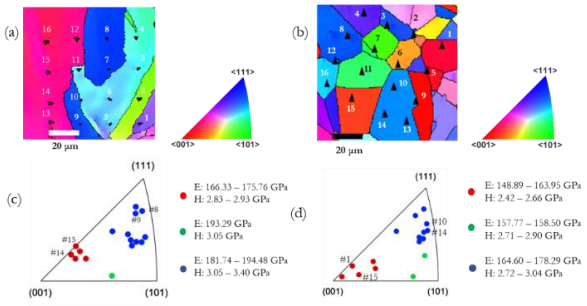

Figure 1: EBSD map & Effect of orientation on hardness and Young's modulus for SLMed ((a) and (c)) and commercial ((b) and (d)) 316L SS stents.

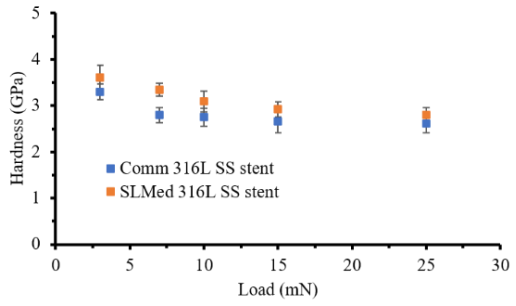

Figure 2: Hardness for SLMed and commercial 316L SS stents at different indentation depth measured with Berkovich indenter tip.

References

[1] Moore, S. et al., *Annals of Biomedical Engineering*, 497–507; DOI: 10.1007/s10439-015-1471-8.
[2] Langi, E. et al., *Journal of Materials Engineering and Performance*, DOI: 10.1007/s11665-020-05366-9

Acknowledgements

We acknowledge the support from the EPSRC of the UK (grant number: EP/R001650/1).

LASER SURFACE TEXTURING OF 316 STAINLESS STEEL FOR STENT APPLICATIONS

Jialin Dong, Priyanka Ghosh, Manuela Pacella, Liguo Zhao

Wolfson School of Mechanical, Electrical, and Manufacturing Engineering, Loughborough University, Loughborough, LE11 3TU, UK

Introduction

Laser surface texturing is preferable surface engineering technic for stents with precise, tailorable, fast and clean modification ability. Existing literatures investigated the mechanical and biological performance of laser textured stainless steel, but the relationship between the laser processing parameters and surface condition is still unclear. Geometrical control of laser-textured surface morphology is important since geometry of texture could affect endothelia cells response [1]. The aim of this research is to investigate the relationship between different laser processing parameters and textured surface morphology. Different laser parameters were applied to fabricate grooves of different aspect ratio on 316 stainless steel. Optical microscope (OM) and InfiniteFocusG5 plus™ profilometer were used for the surface morphology characterization. Results showed clear correlations between laser parameters and textured surface conditions and is helpful for parameters selection and refinement during laser texturing of stents.

Methods

An Innolas MMS - SPI redENERGY G4 pulsed fibre laser (wavelength, 1060 nm; pulse width, ns; output power, 70W) was used for the laser surface texturing of 316 stainless steel (RS components, UK). The samples are 0.5mm-thick plate and all cut into 10mm×10mm pieces by guillotine with as-received surface. Different laser parameters including fluence per pulse, frequency (20, 100, 500kHz), feed speed (300, 500, 1000mm/s) and pulse width (16, 26, 46ns), defocused distance (0, +1, +2, +3mm) with 0.08mm pitch were used in several combinations to investigate the influence of certain laser parameters on the surface condition. All processed samples were characterized by OM and profilometer to obtain the surface morphology data and were compared to a benchmark unprocessed specimen.

Results

The influence of process parameters was clearly demonstrated. The groove width and depth are mainly influenced by fluence per pulse and pulse width (Fig. 1a, 1b) by changing energy transfer and less laser-plasma interaction during laser process [2], defocused distance also contributed to the variation of the groove dimensions (Fig.1c) by changing energy distribution [3]. It is also noticeable that the increasing feed speed resulted in deeper grooves with similar width (Fig. 1d). Heating effect is great at high fluence, long pulse width, high frequency and low feed speed due to the high fluence per pulse (high fluence and long pulse width) and irradiance (high frequency and low feed speed) (Fig. 2). Additionally, increased defocused distance involved less heat effect and smoother surface because of the increased energy distribution and decreased energy concentration. These preliminary experiments show that a full control of surface roughness and textures can be achieved via tuning of laser processing parameters. These results will help the control of laser texturing on stent-related materials.

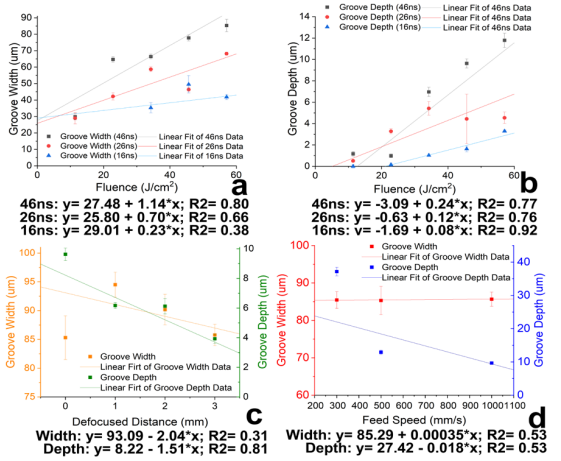

Figure 1: The change of groove width(a) and groove depth(b) with different fluence and pulse width; (c) The change of groove width and depth with different defocused length(c) and feed speed (d).

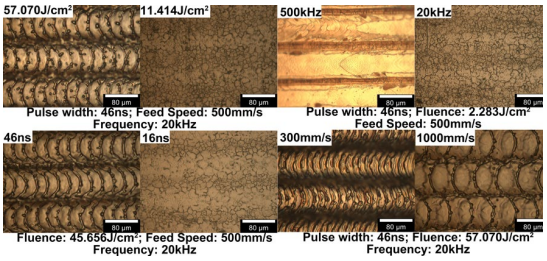

Figure 2: Comparison of samples with different fluence, pulse width, feed speeds and frequency.

References

1. Lu, J. et al, Acta Biomaterialia, 4(1):192-201, 2008.
2. Hamad, A. H., High Energy and Short Pulse Lasers, Chapter 12, 305-325, 2016.
3. Saadlaoui Y et al, Crystals, 10(4):246, 2020

Acknowledgements

We acknowledge the support from Loughborough Materials Characterization Centre at Loughborough University for characterization and also the support of Dr. Mark Caper and Mr. David Britton for laser processing.

A COMPUTATIONAL FRAMEWORK INVESTIGATING THE MECHANICS OF BARE-METAL AND POLYMER-COVERED WIRE BRAIDED STENTS

Ciara McKenna (1), Ted Vaughan (1)
1. Biomedical Engineering, School of Engineering, National University of Ireland Galway

Introduction

Self-expanding wire braided stents have been used in a wide range of medical implant applications due to the distinct flexibility offered by their tunable design parameters. Recently, there has been increasing attention on developing covered stent systems in endovascular repair, whereby the stent frame is wrapped with a graft or textile material, which acts as a mechanical barrier to tissue in-growth/restenosis [1]. However, the addition of a polymeric cover to a wire braided stent fundamentally changes its deformation mechanism(s) and there is lack of understanding on how the functional performance of these systems compares to their bare-metal counterparts [2]. In this study, a combined experimental-computational investigation was carried out to evaluate the functional performance of bare and covered self-expanding wire braided stents.

Materials and Methods

Experimental: Nitinol self-expanding braided stents were manufactured with a one-over-one wire pattern for three separate braid angles (α=30°, α=45°, α=60°) (see Fig 1a). Devices were subsequently dip-coated in a polycarbonate-based silicone polymer to produce cover thicknesses of t=25μm and t=100μm (Aran Biomedical, Galway). The functional biomechanical performance of each bare and covered stent configuration was evaluated through *in vitro* bending, radial and axial compression tests. Results were also compared to a commercially-available Precise Pro laser-cut stent (Cordis, FL).

Computational: Braided stent geometries were created using the python-based software *PyFormex* [3] and imported into the Abaqus finite element software as an orphan mesh of Timoshenko beam elements (Fig 1a). The stent covering process was simulated by applying a small pressure to the outer surface of a hollow cylinder, which wrapped the cover over the stent frame (Fig 1a). Radial compression, axial compression and bending deformations were simulated using Abaqus/Explicit for bare and covered configurations and compared to experimental responses (Fig 1b,c). The validated computational framework was then used to provide detailed insight into covered stent mechanics, by evaluating the role of a multitude of geometrical features (e.g. wire diameter, wire density, braid angle, cover thickness) on covered braided stent mechanics. Next, bare-metal and covered stents were deployed into an idealised stenosed artery and subjected to bending deformations in the physiological range experienced in the femoropopliteal artery. Arterial tissue and plaques were described with isotropic non-linear hyperelastic material models[4-5]. The predicted in-vivo performance was compared to a commercial laser-cut Precise Pro (Cordis, FL) stent (Fig 1e).

Results

It was found that the computational model correctly predicted the radial (Fig 1b), bending (Fig 1c) and axial responses for both bare and covered braided stents. Both computational and experimental results showed substantially stiffer responses with the addition of a cover, as it limited sliding/rotation between wires. At small crimp diameters, there were large increases in radial force as the cover folds and self-contacts (Fig 1b). Braid angle was identified as a key parameter, where low braid angles with circumferentially aligned wires provides greater structural resistance to radial compression (Fig 1d). Under bending, devices were more likely to kink with thick and/or stiff coverings (Fig 1c). Stent deployment and physiological bending showed that bare-metal braided stents were able to accommodate larger external deformations, but were less effective in providing appropriate lumen gains, when compared to polymer covered braided stents and existing commercial laser-cut stents (Fig 1e).

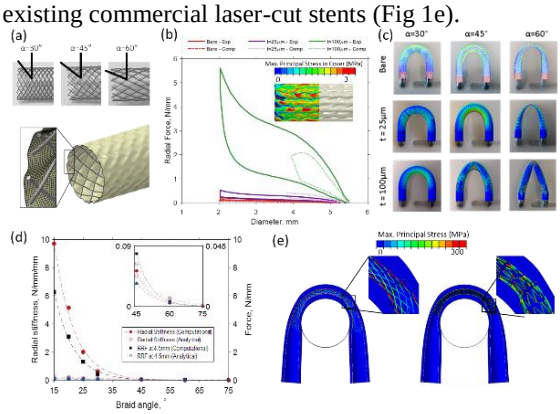

Fig 1 *(a) Bare and covered braided stent geometries. Experimental and computational results for bare and covered braided stents under (b) radial loading and (c) bending. (d) Effect of braid angle on the radial response. (e) Bending behavior of implanted braided and laser-cut stents.*

Discussion

This study developed an experimentally-validated computational model that has provided novel insight into the mechanics of bare-metal and polymer-covered wire braided stents. While the addition of a polymeric cover fundamentally alters the deformation mechanisms associated with wire braided stents, substantial improvements in radial stiffness and kink resistance can be attained when low braid angles were used in combination with thin and compliant covers.

References

1. Lammer et al., J. Am. Coll. Cardiol, 2013.
2. McKenna et al., JMBBM, 2020.
3. Verhegghe, 2019.
4. Prendergast et al., J. Biomech. Eng. 2003.
5. Cunnane et al., Biomed. Eng. Online, 2015.

PROPERTIES OF ISOTROPIC PYROLYTIC CARBON: A MULTISCALE APPROACH

Gianpaolo Serino (1,2), Mattia Gusmini (1), Alberto Audenino (1,2), Giovanni Bergamasco (3), Ornella Ieropoli (3), Cristina Bignardi (1,2)

1. Department of Mechanical and Aerospace Engineering (DIMEAS), Politecnico di Torino,Italy; 2. Polito^{BIO}Med Lab, Politecnico di Torino, Italy; 3. LivaNova (Sorin Group Italia s.r.l.);

Introduction

Pyrolytic carbon (PyC), due to its high mechanical properties and hemocompatibility is the main material used for mechanical heart valves (MHV) fabrication [1]. Mechanical characterization of the PyC used for biomedical application played a crucial role in the development of MHVs production. Here a multiscale approach was adopted, performing three points bending tests and nanoindentation tests.

Methods

Isotropic PyC was deposited on the graphite substrates following two different deposition processes. Three sizes of substrate were used. Obtained specimens were properly cut and polished to be tested through the three-point bending technique (figure 1a) and nanoindentation technique (figure 1b).

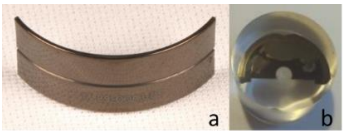

Figure 1. (a) Specimen used for three-point bending tests; (b) Specimen used for nanoindentation tests

A total of 78 specimens (13 for each size) were tested. Three-point bending tests were performed following the ASTM F 417 – 78. Due to arch geometry of the specimens, the maximum flexural stress was calculated according to eq. 1 [2]:

$$\sigma_{MAX} = P_{MAX}\frac{\tan\alpha}{2}\left[\frac{1}{A} - \frac{R}{I}y_e\right] \qquad (1)$$

The Young's modulus was calculated through the principle of the virtual work.

Indentation tests were performed with the Nanoindenter XP (MTS system Corporation, USA) equipped with a Berkovich indenter, previously calibrated on a standard silica specimen. For each specimen, a matrix of 30 indentations was generated. Specifically, the indentations were performed normally to the direction of the PyC deposition. Tests were performed in displacement control, setting the indentation depth to 800 nm. The Oliver & Pharr method [3] was applied to obtain the nanoindentation modulus and the nanoindentation hardness (data here not shown).

Results

Young's modulus and Fracture stress mean values obtained from three-point bending tests were reported respectively in figure 2a and figure 2b. Whereas fracture stress values were found to be slightly lower than that reported in literature [4], probably due to the different geometry of the specimens, measured Young's modulus were consistent with those reported in similar works [4].

The statistical analysis has revealed no significant difference ($p > 0.05$) between the two deposition processes at the macroscopic level.

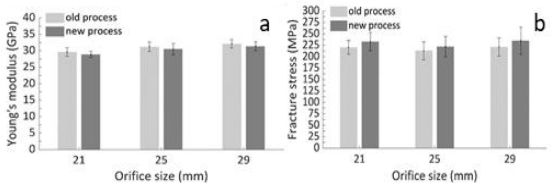

Figure 2. (a) Mean values of Young's Modulus; (b) Mean values of Fracture stress

The mean values of the Nanoindentation modulus (Figure 3) and of the Nanoindentation hardness also agree with those found in literature [5].

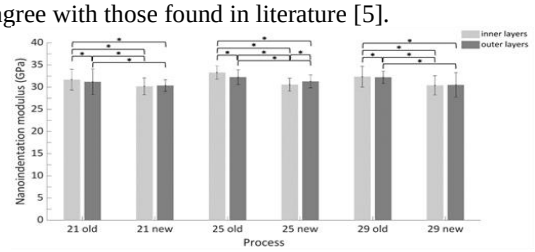

Figure 3. Mean values of nanoindentation modulus

In general, through the new deposition process, a significant reduction of the difference of the nanomechanical properties between the inner and outer layers was registered.

Discussion

Results obtained through three-point bending tests characterize the deposited PyC as bulk material. Since the bulk PyC is a layered material, possible changes due to a change in deposition process are difficult to detect at this scale. As matter of fact, the results of the three-point bending tests indicate that the two deposition processes lead to a PyC with comparable mechanical properties. On the other hands, the mechanical properties obtained at the microscale significatively change with the indentation site and the deposition process. It can be speculated, indeed, that through the nanoindentation approach is possible characterize a single layer of deposited PyC. Thus, information at the submicron scale reveals the effectiveness of settings variation of the deposition process on the layer's mechanical properties.

References

1. F. Oveissi et al, Materials Today Bio 5:1-20, 2020
2. Beer, F. P. Beer, New York: McGraw-Hill Higher Education, 2009
3. Oliver W.C. et al, J. Mater. Res. 7:1564-1583,1992
4. Kaae J.L. et al, Carbon N.Y. 9:291-299, 1971
5. Hofman G. et al, Carbon N.Y. 38: 645-653, 2000

PATIENT-SPECIFIC COMPUTATIONAL FLUID DYNAMICS OF FEMORO-POPLITEAL STENT-GRAFT IN STRAIGHT AND BENT-LEG POSITION

Michele Conti (1), Anna Ferrarini (1), Alice Finotello (2), Giancarlo Salsano (3), Ferdinando Auricchio (1), Domenico Palombo (4), Giovanni Spinella (4), Bianca Pane (4)

1. DICAr, University of Pavia, Italy; 2. DIMES, University of Genoa, Italy; 3. Department of Radiology, Ospedale Policlinico San Martino, Genoa, Italy; 4. Ospedale Policlinico San Martino, University of Genoa, Italy.

Introduction

Intra-stent thrombosis is one of the major failure modes of popliteal aneurysm endovascular repair, especially inside overlapping stent-grafts used to cover long lesions and having different nominal diameters to accommodate the native arterial tapering.

However, the interplay between stent-sizing, post-operative arterial morphology, local hemodynamics, and thrombosis onset is not elucidated, yet.

Given such motivations, the present study deals with a case study (77-year-old, male) of a popliteal artery aneurysm (PAA), treated with endovascular deployment of two overlapped stent-grafts, showing intra-stent thrombosis at one-year follow-up examination. Patient-specific computational fluid-dynamics (CFD) analyses, including straight- and bent-leg position, were performed.

Methods

Starting from Computed Tomography Angiography (CTA), segmentation of the femoro-popliteal artery (FPA) segment, leg bones, intra-stent thrombosis, and implanted stent-grafts was performed VMTK (v1.3). Two 3D models were considered for the CFD simulations: femoro-popliteal artery in straight-leg position and femoro-popliteal artery in bent-leg position. Following mesh convergence analysis, uniform meshes were generated with 651635 total number of elements for the straight-leg model with thrombosis and with 569817 total number of elements for the bent-leg model [2]. Simulations were run in Intel Xeon W-2123 computing workstation (3.6GHz, 32GB RAM) with the commercial CFD software package ANSYS Fluent (*ANSYS Academic Research [Fluent], release 19.2*). We performed transient simulations, in which viscosity was set to 0.004 Kg m^{-1} s^{-1} and blood density to 1060 kg/m^3. In each simulation we prescribed the no-slip condition on the wall of the artery, an outflow condition (Dirichlet boundary condition) enforcing the flow in the anterior tibial artery to be 25% of the inflow, and traction-free condition in the other outlets. For transient simulations, the inflow velocity curve is derived from literature [1], [3]. We selected a laminar model (*ANSYS Academic Research [Fluent], release 19.2*) for all the simulations because the peak Reynolds number at the inlet is 284.

Results

The computational fluid-dynamics analysis showed that the overlapping zone of the stent-grafts induces a severe discontinuity of lumen, dividing the landing site in two regions: the proximal part, where the thrombosis is located, is characterized by larger diameter, low tortuosity, low flow velocity, low helicity, and low wall shear stress; the distal part presents higher tortuosity and smaller lumen diameter promoting higher flow velocity, higher helicity, and higher wall shear stress. Leg bending reduces the flow velocity promoting furtherly atherogenic wall shear stress.

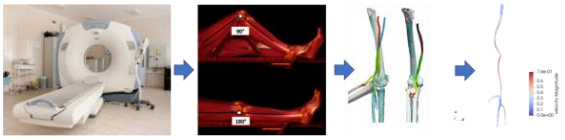

Figure 1: Simulation pipeline. From medical image analysis to patient-specific CFD analysis of both straight- and bent-leg configuration; velocity magnitude is reported in m/s.

Discussion

At the best of our knowledge, the present study is the first reporting patient-specific CFD analysis of both straight- and bent-leg femoro-popliteal models derived from CTA.

Our analyses support the key idea that leg bending induces dramatic biomechanical changes of femoro-popliteal artery; such changes should be taken into account during procedure planning and design of novel devices.

The next step will be to collect and study a large database of patients with similar characteristics, in order to withdraw statistically significant and clinically relevant results.

References

1. A. Desyatova et al, Biomechanics and modeling in mechanobiology,17.1:181-189, 2018.
2. P. Xu et al, Scientific Reports, 6:39225, 2016.
3. D. J. Patel, J Appl Physiol, 20:459-463, 1965.

Acknowledgements

This work is partially funded by the Ministry of Education, University and Research through the Ricerca Finalizzata Project no. RF-2018-12368376 entitled “Impact of peripheral endovascular repair on femoral-popliteal artery kinematic: from clinical experience to in vivo biomechanical modeling (PERFEKT study)”.

WALL SHEAR STRESS TOPOLOGICAL SKELETON FEATURES IN HEMODYNAMIC MODELS OF STENTED CORONARY ARTERIES

Valentina Mazzi (1), Claudio Chiastra (1), Diego Gallo (1), Umberto Morbiducci (1)

1. Polito^{BIO}Med Lab, Department of Mechanical and Aerospace Engineering, Politecnico di Torino, Italy

Introduction

There is ample evidence that flow disturbances are massively involved in in-stent restenosis affecting stented coronary arteries [1]. However, it is still not fully understood which local hemodynamic features and in particular which Wall Shear Stress (WSS) phenotype impact on mechanisms leading to in-stent restenosis. Aiming at bridging this gap of knowledge, recently the WSS Topological Skeleton (TS) is receiving increasing interest, because of its link with flow features (flow separation, recirculation) that have been associated with vascular dysfunction [2][3]. Briefly, the WSS TS is composed by fixed points, where the WSS vanishes, and unstable/stable manifolds connecting them, representing WSS contraction/expansion regions [2]. Here we investigate the possible involvement of WSS topological skeleton features in the in-stent restenosis process using realistic computational hemodynamics models of stented coronary arteries.

Methods

Two cases (A and B) of pathologic left anterior descending coronary artery were considered. A Xience Prime stent by Abbott Vascular was implanted in CASE A and two Endeavor Resolute stents by Medtronic were implanted in CASE B. Exhaustive details on geometry reconstruction and computational hemodynamics simulations are provided elsewhere [4]. A recently proposed Eulerian method was here considered to analyse the WSS TS [2]. Based on this method, the divergence of the normalized WSS vector, defined as:

$$DIV_W = \nabla \cdot \left(\frac{\boldsymbol{\tau}}{\|\boldsymbol{\tau}\|_2}\right) = \nabla \cdot (\boldsymbol{\tau}_u) \qquad (1)$$

where $\boldsymbol{\tau}_u$ is the WSS unit vector, was used to localize contraction/expansion regions, a template of unstable/stable manifolds. According to [2], WSS fixed points were identified and classified by computing Poincaré index and eigenvalues of the Jacobian matrix, respectively. To measure the amount of variation in WSS contraction/expansion action, the Topological Shear Variation Index (*TSVI*) [5]:

$$TSVI = \left\{\frac{1}{\mathrm{T}}\int_0^{\mathrm{T}}\left[\nabla \cdot (\boldsymbol{\tau}_u) - \overline{\nabla \cdot (\boldsymbol{\tau}_u)}\right]^2 dt\right\}^{1/2} \qquad (2)$$

where T is the cardiac cycle period, was computed.

Results

The cycle-average WSS topological skeleton and the $TSVI$ distribution on the luminal surface for CASE A and B are presented in Figure 1. In both cases, WSS fixed points were mostly located at the luminal surface in correspondence with stent peaks, close to all strut connectors in CASE A and in the overlapping region of the two stents in CASE B. WSS contraction regions (negative DIV_W) were located upstream from the struts and WSS expansions regions (positive DIV_W) were located downstream from the struts, with opposite DIV_W distribution in the stent malapposition region for CASE A and in the overlapping zone for CASE B. High $TSVI$ values were located at stent peaks and close to the struts in both models, in the stent malapposition region and close to stent connectors for CASE A and at the stents overlapping region for CASE B (Figure 1B).

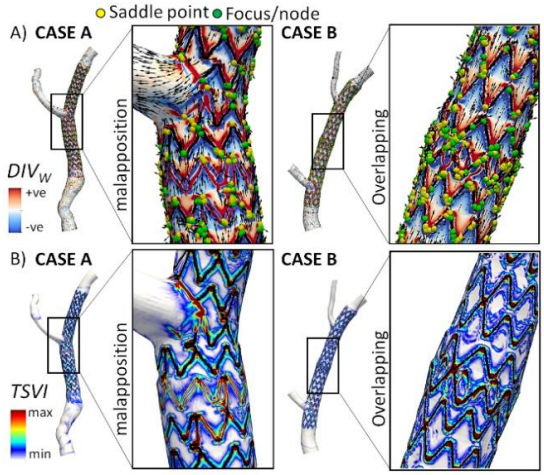

Figure 1: A) Cycle-average WSS topological skeleton and B) TSVI distribution for CASE A and B.

Discussion

Cycle-average WSS contraction and expansion regions, a template of near-wall transport [3], co-localize with endothelial cells migration and accumulation processes upstream and downstream of stent struts, respectively, as experimentally observed [6]. Moreover, the exposure to high variability in the WSS contraction and expansion action could induce a recurring variation in intracellular and intercellular tension [7], impacting on the endothelium in terms of impaired permeability and inflammatory response. Thus, the role of WSS TS features in coronary in-stent restenosis development, in addition to low WSS, deserves further investigation.

References

1. Ng, J. et al., Arterioscler Thromb Vasc Biol, 37:2231-2242, 2017.
2. Mazzi, V. et al., Biomech Model Mechanobiol, 19:1403-1423, 2020.
3. Arzani, A. et al., J Biomech, 73: 145-152, 2018.
4. Chiastra, C. et al., J R Soc Interface, 10: 20130193, 2013.
5. De Nisco, G. et al., Med Eng Phys, 82:119-129, 2020.
6. Hsiao, T.S. et al., Cardiovasc Res., 3:689-701, 2016
7. Melchior, B. et al., Am. J. Physiol. Cell Physiol., 299, 2010

USE OF BIOHYBRID SILKOTHANE® FOR THE DEVELOPMENT OF VASCULAR GRAFTS WITH TUNEABLE MECHANICAL PROPERTIES

Alice Caldiroli (1), Elia Pederzani (2), Sara Cappelletti (2), Alessandro Caimi (2), Emiliano Votta (2), Gianfranco B. Fiore (2), Matteo Tironi (3), Fabio Sangalli (3), Marina Figliuzzi (3), Nadia Azzollini (3), Sonia Fiori (3), Francesco G. Greco (1), Andrea Remuzzi (4), Monica Soncini (2), Stefania A. Riboldi (1), Alberto C.L. Redaelli (2)

1. Bioengineering Laboratories S.r.l., Italy; 2. Department of Electronics, Information and Bioengineering, Politecnico di Milano, Italy; 3. IRCCS Istituto di Ricerche Farmacologiche Mario Negri, Italy; 4. Università degli Studi di Bergamo, Italy

Introduction

One of the major reasons of failure of synthetic vascular grafts and arteriovenous grafts (e.g. vascular accesses for hemodialysis) is known to be the mismatch in mechanical properties between the prosthesis and the adjacent native vessel(s) [1]. To address this issue, in our previous work we developed a technological platform potentially enabling the generation of vascular grafts with adjustable mechanical properties. Such technology relies on the use of a natural, biodegradable protein (regenerated silk fibroin, SF) and a synthetic polymer (polyurethane, PU), blended in the registered material Silkothane® and processed by electrospinning, to realize scaffolds suitable for an *in situ* tissue engineering approach [2,3]. In this work, we characterized the radial compliance of Silkothane® grafts upon modulation of the respective ratios of SF and PU as compared to commercial grafts.

Methods

Tubular constructs were fabricated by electrospinning, according to previously described protocols [2,3], using regenerated Bombyx mori silk fibroin (Innovhub Stazioni Sperimentali per l'Industria, Italy) and the aromatic polycarbonate-urethane Carbothane™ (Lubrizol, USA). They are characterized by a three-layered structure with inner and outer layers of SF, and a core of Silkothane® of varying formulations (SF25PU75, SF50PU50, SF75PU25, $\Phi_{internal}$=6mm). The scaffolds were characterized in terms of diameter and thickness by means of a projector (Taylor Hobson, UK), and a digital micrometer (Mitutoyo, Japan), respectively. To evaluate the radial compliance of both Silkothane® and commercial grafts, Flixene™ (Maquet, USA) and Gore® Acuseal (Gore Medical, USA), a customized dynamic system was developed. Accordingly to Standard ISO 7198, such setup pressurizes the sample reproducing hypo-, normo-, and hyper-tension conditions (P) and estimates the consequent variation in diameter (D) of the sample. Radial compliance (C) is derived as follows:

$$C = \frac{(D_{max} - D_{min})/D_{min}}{P_{max} - P_{min}} \cdot 10^4 \qquad (1)$$

Results

Silkothane® grafts display a mono-tone trend with increasing radial compliance (in the interval of 1-2 %·10^{-2}·$mmHg^{-1}$, Fig. 1) in all the considered pressure ranges (50-90 mmHg, 80-120 mmHg, 110-150 mmHg), according to higher content of PU in the middle layer. This result confirms the tuneability of the mechanical properties of Silkothane® grafts when acting on SF/PU ratio. As expected, both commercial grafts are generally less compliant than these hybrid products, even though a relevant discrepancy is appreciable mainly in comparison with SF25PU75.

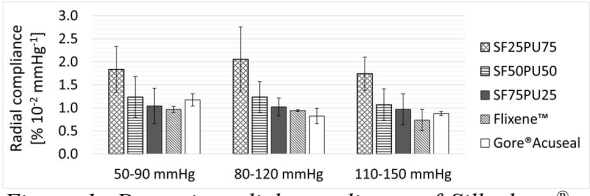

Figure 1: Dynamic radial compliance of Silkothane® and commercial grafts.

Discussion

This study confirmed Silkothane® as a platform for the electrospinning of scaffolds compatible with vascular applications. Despite the matching with brachial artery and basilic vein was not achieved (compliance estimated around 25 and 70 %·10^{-2}·$mmHg^{-1}$, unpublished data) increased performances compared to commercial grafts were assessed. The final aim is the manufacturing of tubular matrices with tunable - potentially patient-specific - mechanical properties. Further work is needed to improve the manufacturing process to optimize the mechanical behaviour of these constructs and their reproducibility.

References

1. Salacinski HJ, J Biomater Appl, 15: 241-78, 2001
2. Van Uden S et al, J Biomed Mater Res B Appl Biomater 107:807-817, 2019.
3. Van Uden S et al, Biomed Mater 14:25007, 2019.

Acknowledgements

This work was supported by the SILKELASTOGRAFT grant #2018-1777 funded by Fondazione Cariplo and Regione Lombardia. The authors would like to thank Prof. Silvia Faré for her assistance with mechanical sampling.

A PULSATILE FLOW SIMULATOR FOR THE EXPERIMENTAL INVESTIGATION OF CARDIOVASCULAR TISSUES AND STRUCTURES

Daniele Bianchi (1), Daniele Bissacco (2), Maurizio Domanin (2), Santi Trimarchi (2), Rodrigo Romarowski (1), Stefania Marconi (1), Ferdinando Auricchio (1), Michele Conti (1)

1. DICAr Department, University of Pavia, Italy; 2. IRCCS Ca' Grande Ospedale Maggiore Policlinico Milano, Italy

Introduction

In-vitro experiments are used as the first step for the validation of numerous medical device (e.g., stent-graft) [1-3]. In the biomechanical analysis of the cardiovascular devices, the replication of the working conditions that the device has to manage represents a key aspect for the reliability of the in vitro test results. Aiming at investigation of cardiovascular structures and devices in a wide range of both physiological and pathological conditions, a pulsatile mock loop system was optimized. Present work shows the capability of the developed system in experimental investigation of aortic biomechanics.

Methods

A custom-made pulsatile mock loop system, based on the system proposed by Lanzarone et al [4], was developed and optimized. The mock loop consists of two main blocks: the pumping system (a piston pump that is driven by an automated-control brushless motor) integrating the ventricular chamber/valve holder and the simulator of the hydraulic input impedance. These blocks are connected with hydraulic conduits in a closed loop, including an atrial reservoir (Fig.1). In detail, the pumping system replicates the left ventricle, and it consists of a low-inertia brushless motor driven by an electronic controller. For the design of the pumping system, the pressure in the ventricular chamber (P_{chamb}) and the supplied flow (Q), were converted into force (F) and speed (v) of the piston, respectively with:

$$F = P_{chamb} \cdot A \quad (1)$$

$$v = Q/A \quad (2)$$

where A is the area of the piston section. The valve holder was fitted with the ventricular chamber including two one-way valves. The inlet conduit is connected to an atrial reservoir, and the outlet conduit is connected to the systemic impedance simulator. The latter replicates the input impedance of the systemic circulation.

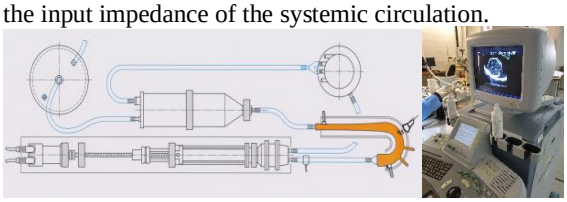

Figure 1: Main components o of the pulsatile mock loop system.

Results

As one of the numerous possible applications, results were obtained evaluating the impact of Thoracic Endovascular Repair (TEVAR) on aortic biomechanics. In particular, a specimen of porcine aorta (segment between the aortic root and the renal arteries) was connected to the developed pulsatile mock loop system. Intraluminal pressure was recorded in order to measure pulse wave velocity (PWV) before and after the stent graft deployment. Figure 2 shows the aortic specimen and the corresponding pressure measurement during cardiac cycle.

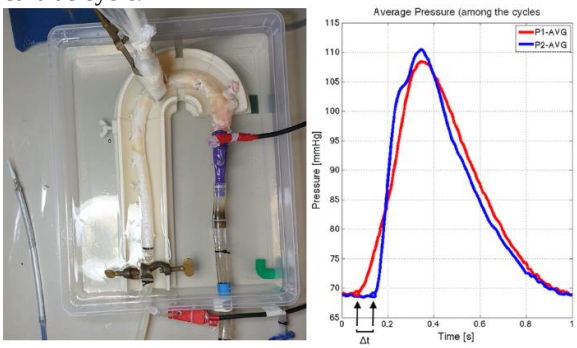

Figure 2: The aortic specimen is placed in the 3D printed guide having a candy-cane shape (left); Measurement of inflow pressure (red) and outflow pressure (blue) during the cardiac cycle (right).

Discussion

The device proved to be a reliable lab apparatus for in-vitro tests, and it was able to replicate the behavior of the human left ventricle in a wide range of physiological and pathological conditions, in terms of flow and pressure curves.

References

1. Ritchie J, …& Yoganathan AP. The material properties of the native porcine mitral valve chordae tendineae: an in vitro investigation. J Biomech 2006; 39:1129-35.
2. de Beaufort, H. W. L., Nauta, F. J. H., Conti, M., Cellitti, E., Trentin, C., Faggiano, E., ... & Auricchio, F. (2017). Extensibility and Distensibility of the Thoracic Aorta in Patients with Aneurysm. European Journal of Vascular and Endovascular Surgery, 53(2), 199-205.
3. de Beaufort, H. W., Conti, M., Kamman, A. V., Nauta, F. J., Lanzarone, E., Moll, F. L., ... & Trimarchi, S. (2017). Stent-Graft Deployment Increases Aortic Stiffness in an Ex Vivo Porcine Model. *Annals of Vascular Surgery*.
4. Lanzarone E, Vismara R, Fiore GB. A new pulsatile volumetric device with biomorphic valves for the in vitro study of the cardiovascular system. Artificial organs 2009; 33:1048-62.

A COMPARATIVE STUDY OF THE MECHANICAL PERFORMANCE OF NITI AND BIORESORBABLE PLLA BRAIDED STENTS

Agnese Lucchetti (1), Ted J. Vaughan (2), Thomas Gries (1)

1. Institut für Textiltechnik, RWTH Aachen University, Aachen, Germany; 2. Biomechanics Research Centre (BMEC), School of Engineering, National University of Ireland Galway, Ireland

Introduction

Despite advances in stent development over the past decades, issues such as thrombosis, in-stent restenosis and vessel remodeling impairment are still associated with permanent metallic stents [1]. Bioresorbable scaffolds (BRSs) have the potential to overcome these drawbacks, staying in the patient just for the time needed. Braiding is a well-established technology in the stent manufacturing and brings advantages especially in terms of a superior device flexibility and a major conformability to the anatomic shape of the lesion [2]. In this study, a comparison of the performance of a Nitinol (NiTi) and bioresorbable Poly-L-Lactic Acid (PLLA) braided stents was carried out by means of *in vitro* bench testing with the aim to have a clear understanding of how the performance of the polymeric devices differ from the one of their metallic counterpart.

Materials and Methods

The PLLA stents were manufactured in-house using a Steeger Braiding Machine (Körting Nachfolger Wilhelm Steeger GmbH & Co., Wuppertal, Germany). Firstly, five devices resembling the same geometrical features of the NiTi stent characterized by McKenna et al. [3] were produced. More specifically, the stents were composed of 24 monofilaments with a 100-µm diameter (ϑ), braided in a 1:1-1 pattern (labeled as PLLA/100/24). The diameter and the length of the stents were 5 mm and 20 mm, respectively. Then, two others configurations were manufactured using a 150-µm filament (PLLA/150/24) and increasing the wire count to 48 (PLLA/100/48). The braiding angle (α), defined as the angle formed by the filament with the longitudinal axis of the stent, was set at 45°, 60° and 70°. For the 150-µm filament stent, the highest braiding angle was not producible due to process limitations. The proper heat set conditions to fix the structure were found to be 140 °C and 10 min. The stents were characterized by means of a radial force test, performed according to DIN EN ISO standard 25539-2-2012. More specifically, all the stents were tested at a constant temperature of 37 °C and crimped to 50% of their initial diameter.

Results

Figure 1 shows that the radial behavior of the stents with lower braiding angle is far from the one of the NiTi stent. However, the gap is narrowed for an increased braid angle, a bigger filament diameter and a higher number of wires. As reported in Table 1, the PLLA stents show for three configurations higher values of initial radial stiffness (RS), radial resistive force (RRF) and chronic outward force (COF) in comparison with the NiTi device.

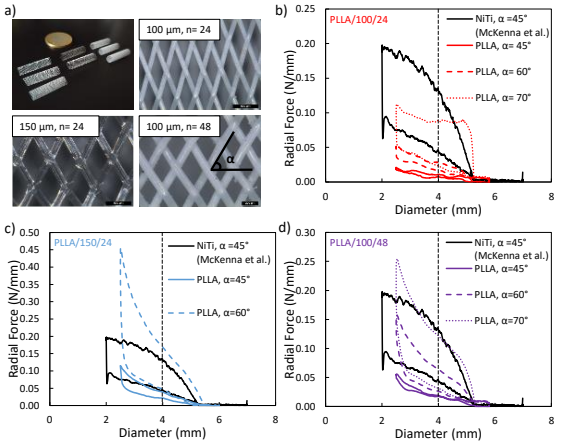

Figure 1: (a) Example of manufactured stents and detail of the braiding patterns. Comparison of NiTi and PLLA performance from the radial test for an increasing braiding angle: (b) PLLA/100/24; (c) PLLA/150/24; (d) PLLA/100/48.

Stent	RS (N/mm²)	RRF (N/mm)	COF (N/mm)
NiTi	0.12	0.13	0.044
PLLA/100/24/70	0.55	0.09	0.024
PLLA/150/24/60	0.14	0.17	0.047
PLLA/100/48/70	0.14	0.12	0.031

Table 1: Radial stiffness (RS), radial resistive force (RRF) and chronic outward force (COF) of the three most meaningful PLLA cases in comparison to NiTi.

Discussion

This study showed that the mechanical performance of PLLA braided devices subdued to a radial load is in a similar range to the one of the NiTi stent for specific braided configurations. Further mechanical testing (i.e. tensile test and bending test) will be carried out with the aim of gaining a comprehensive insight into polymeric braided stents deformation modes. The ultimate aim is the *ad hoc* optimization of the device (e.g. by finding the right combination of braiding parameters and pattern) to further bridge the gap between permanent and bioresorbable devices.

References

1. He et al, Intervent Neurol, 3(2): 67–77, 2015.
2. Zou et al, Results in Physics, 6: 440–6, 2016.
3. McKenna et al, 103: 103549, 2020.
4.

Acknowledgements

This project has received funding from the European Union's Horizon 2020 research and innovation programme under grant agreement No 813869. This publication reflects only the author's view and the REA is not responsible for any use that may be made of the information it contains. The authors would like also to thank Boston Scientific Ltd., Co. Galway, Ireland for their support and collaboration on this work.

INVESTIGATING 3D PRINTED POLYMER RESIN FOR BIOMIMETIC POLYMER AORTIC VALVE LEAFLETS

Celia Hughes (1,2,3), Alix Whelan (1,2,3,4) , Larisa Florea (4,5), David O'Reilly (3), Evelyn Campbell (3), Caitríona Lally (1,2,4)

1. *Trinity Centre for Biomedical Engineering, Trinity Biomedical Sciences Institute, Trinity College Dublin, Dublin 2, Ireland;* ***2.*** *Department of Mechanical, Manufacturing, and Biomedical Engineering, School of Engineering, Trinity College Dublin, Dublin 2, Ireland;* ***3.*** *Structural Heart Division, Boston Scientific Corporation, Galway, Ireland;* ***4.*** *Advanced Materials and Bioengineering Research Centre (AMBER), Trinity College Dublin, Dublin 2, Ireland;* ***5.*** *School of Chemistry, Trinity College Dublin, Dublin 2, Ireland*

Introduction

Aortic stenosis is a debilitating disease with a 50% mortality rate without intervention, affecting almost 8% of patients over the age of 65 in the US[1,2]. Current methods of treatment include mechanical heart valves (MHVs) which have long durability but poor hemodynamics, and bioprosthetic heart valves (BHVs), which have poor durability but superior hemodynamics[3,4]. A proposed solution to this problem is polymer heart valves (PHVs) which could have the greater durability of MHVs while maintaining the superior hemodynamics of BHVs by utilizing an easily manufacturable, customizable, and biomimetic leaflet architecture (Figure 1(a)). The aim of this work is to assess the mechanical properties of a 3D printed polymer resin in comparison to native valve leaflet tissue and the current most common replacement leaflet material, glutaraldehyde-fixed bovine pericardium (GLBP)[5].

Methods

Eighteen (n=18) Formlabs™ Elastic Resin dogbone specimens were obtained from 3D printed sheets using Formlabs™ Form 2 SLA printer and subject to uniaxial tensile testing to failure on Zwick Twin Column Universal Testing Machine. The specimens were subjected to 5 preconditioning cycles between 0.1 and 1MPa, and then loaded to failure at 20 mm/min. Failure was defined as a load drop to 80% of the maximum load reached. Initial stiffness was calculated as the slope of the initial region between 1 and 25% strain, and final stiffness was calculated as the slope of the final 20% of the curve. All statistics were calculated using GraphPad Prism 9.0.0.

Results

The stress-strain curve of the material shows a nonlinear response (Figure 1(e)), with an initial stiffness almost one third of the final stiffness, at an average value of 3.64 ± 0.12 MPa compared to 10.55 ± 2.56 MPa for the final region (P <0.001) (Figure 1(d)). The ultimate tensile strength of the material is 4.78 ± 1.28 MPa (Figure 1(b)), while the ultimate tensile strain is 70.36 ± 7.69% (Figure 1(c)).

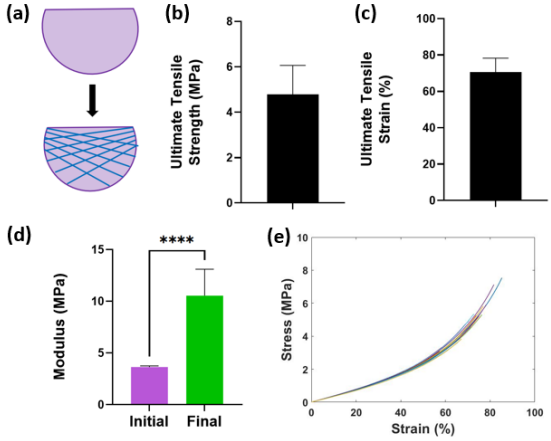

Figure 1: (a) Example of a uniform 3D printed leaflet, top and a leaflet with bioinspired fibre additions, bottom, (b) Ultimate tensile strength, (c) Ultimate tensile strain, (d) Initial and final elastic moduli, and (e) Stress-strain curve of the material.

Discussion

In comparison to the most common replacement leaflet tissue, GLBP, the Formlabs™ Elastic resin material shows promise and more similarity to native tissue due to its lower stiffness and greater failure strain[5,6,7]. Additionally, due to its customizable anisotropy to mimic that of a native leaflet, this material and manufacturing technique is more suitable for valve replacements compared to the non-adaptable GLBP. A recent study has shown similar promising valves and materials; however, the manufacturing techniques are not as adaptable and accessible as the more affordable SLA system[7]. Future directions of this work include carrying out native leaflet analysis for comparison and geometrical analysis and employing finite element techniques to design and verify an optimized valve structure.

References

1. Otto, *Heart*, 84, 2000.
2. Nkomo, et al., *Lancet*, 368, 2006.
3. Yoganathan, et al., *Circulation*, 58, 1978.
4. Bourguignon, et al., *Ann. Thorac. Surg.*, 99, 2015.
5. Rotman, et al., *Expert Review of Med. Devices*, 2018
6. Whelan, et al., *J. Mech. Behav. Biomed. Matr*., 90, 2019.
7. Balguid, et al., *Tissue Eng*.,15, 2007
8. Coulter, et al., *Matter*, 1, 2019.

Acknowledgements

This research is funded by the Irish Research Council and Boston Scientific Corporation (EBPPG/2020/200)

A LUMPED PARAMETER DESIGN TOOL FOR FONTAN TURBINE-PUMP COUPLE: IATVA

Canberk Yildirim (1), Ibrahim Basar Aka (1), Riza Turkoz (2), Hakan Erturk (3), Kerem Pekkan (4)

1. Istanbul Bilgi University, Turkey; 2. Acibadem University, Turkey; 3. Bogazici University, Turkey; 4. Koc University, Turkey

Introduction

Ventricle assist devices (VADs) have been widely used to ease the elevated systemic venous pressure in Fontan circulation failure. However, VADs require an external power to drive the pump, which causes driveline infections. Therefore, Pekkan *et. al* [1] developed a novel device (iATVA) using the minimal amount of systemic flow to drive an aortic turbine, which generates the energy required for pump. In this study, a mathematical model has been established to simulate additional implantation configurations of iATVA. Our previously developed lumped parameter model (LPM) [2] was modified as a typical Fontan circulation and integrated with a turbine-pump couple. Therefore, turbine and pump dimensions and configuration can be patient-specifically determined by the hemodynamic parameters in LPM to achieve a best efficiency point for the patient.

Methods

Euler's turbomachinery equation was used to model turbine and pump sides:

$$Q=\frac{4\pi^2 b_1 b_2.[(w.r_2)^2-\frac{\Delta P}{\rho}-(w.r_1)^2]}{2\pi b_1.w.\cot(\beta_2)+2\pi b_2.w.\cot(\beta_1)} \qquad (1)$$

where Q is the flow rate, 1 is the inlet and 2 is the outlet of the associated turbomachine, as shown in Table 1.

Component	Blade angle – β (1-2)	Impeller radius – r (1-2)	Impeller width – b (1-2)
Pump	59º-40º	3-16 mm	8.5-10 mm
Turbine	14º-10º	7-19 mm	4.5-5 mm

Table 1. Inlet (1) and outlet (2) dimensions.

To determine the common rotational velocity (w) for pump and turbine which also matches with the cardiovascular system operation, following procedure was executed, where T represents the torque:

i. Choose a common w for turbine and pump
ii. Calculate $Q_{turbine}$ and Q_{pump} through Equation 1
iii. Evaluate $\Delta P_{turbine}$ and ΔP_{pump}, match them with physiology
iv. Calculate $T_{turbine}$ and T_{pump}
v. Repeat the previous steps by changing the w until $T_{turbine} = T_{pump}$

Results

Table 2 shows the determined operation conditions of iATVA for various implantation configurations.

Conf.	Turbine	Pump	w (rpm)
No iATVA	n/a	n/a	n/a
1	AO to CA	IVC to PA	1080
2	AO to PA	IVC to PA	1134
3	AO to CA	IVC and SVC to PA	1063
4	AO to ScA	IVC to PA	1145

Table 2. w for different implantations. AO: aorta, CA: common atrium, PA: pulmonary artery, ScA: subclavian artery, I(S)VC: inferior (superior) vena cava

Table 3 demonstrates the simulated hemodynamic parameters through the introduced configurations.

Pars.	No iATVA	1	2	3	4
Q_{tur}	n/a	0.95	0.95	0.95	0.65
Q_{sys}	3.5	4.1	4.1	3.8	4.05
P_{AO}	87	98	98	93	99
P_{IVC}	14.5	10	9.5	13	9
P_{SVC}	15	18	20	13	19
P_{PA}	12	15	17	14.5	15

Table 3. Flows (l/min) and pressures (mmHg) simulated through the model. sys: systemic and tur: turbine

Discussion

In conf 4., a lower aortic steal (Q_{tur}) of 0.3 l/min increases the pump flow and provides a better operation point leading to the decrease in P_{IVC} up to 5.5 mmHg. Conf. 2 has the P_{PA} of 17 mmHg but also the highest P_{SVC} as 20 mmHg. In conf. 3, a Y-branch was used to ease both P_{IVC} and P_{SVC} up to 2 mmHg. iATVA increases the P_{AO} and Q_{sys} to a maximum of 13% and 17%, respectively in all confs. Although conf. 1 and conf. 4 has nearly same outcomes, conf. 1 is considered as the optimal case due to the lower increase level of 1 mmHg in P_{SVC}.

References

1. Pekkan K, Aka IB, Tutsak E, et al. *J Thorac Cardiovasc Surg.* 2018;156:292-301 e297.
2. Yigit B, Tutsak E, Yildirim C, Hutchon D, Pekkan K. *Matern Health Neonatol Perinatol.* 2019;5:5.

Acknowledgement

We acknowledge support of ERC-PoC 966765 BloodTurbine and Tubitak 2247a research grants.

AN EXPERIMENTAL INVESTIGATION OF THE DEGRADATION BEHAVIOUR OF A BIORESORBABLE POLYMER VASCULAR SCAFFOLD

Constantino Fiuza, Katarzyna Polak-Krasna, William Ronan, Ted J. Vaughan.

Biomechanics Research Centre, School of Engineering, National University of Ireland Galway, Galway, Ireland

Introduction

Bioabsorbable vascular scaffolds (BVS) have the potential to form the next generation of vascular stents following on from the current gold-standard, drug eluting stents (DES). Unlike DES, BVS consist of materials that are fully absorbed by the body. BVS are intended to overcome the remaining limitations of DES such as late-stent thrombosis and strut fracture induced restenosis [1, 2]. Challenges facing polymer BVS include understanding physical degradation processes and predicting the long-term implant behaviour once deployed. Most research thus far has focussed on material-level degradation mechanisms of the polymer and/or short-term scaffold performance, with few studies investigating the long-term effects degradation has on the implanted device [3]. Another difficulty in assessing the long-term behaviour of polymers is the long degradation scales involved, typically ~2 years. In this study, an accelerated degradation test protocol [4] was used to evaluate physical and mechanical degradation behaviour of the Reva Medical Fantom Encore, a polymer-based vascular scaffold.

Materials and Methods

Reva Medical Fantom Encore stents [5] were subjected to an accelerated degradation study as per ISO 13781 [4]. Samples were immersed in phosphate buffered saline (PBS) for 112 days at 50°C, solution pH was maintained at 7.4±0.1. Immersion at 50°C equates to an approximate four-fold acceleration in degradation time for PLLA [6]. Physical and mechanical characterisation of the scaffolds was carried out at eleven time points over the 112-day study. The stents were subjected to radial compression testing, whereby the stents were crimped from their deployed diameter of 3.5mm to 2mm, held for 25 seconds and released. Differential scanning calorimetry (DSC) and gel permeation chromatography (GPC) analysis was performed to capture the evolution in thermal properties and molecular weight, respectively. Visual examination was performed by scanning electron microscopy (SEM).

Results

Radial compression tests showed an increase of 30% in radial strength to day 21 followed by a decline, see Figure 1(a). After day 49, the scaffolds underwent brittle fracture. The Fantom Encore retained radial stiffness over radial strength over the course of one year assuming a four-fold increase in immersion time, Figure 1(b). Brittle fracture was confirmed through SEM images at later time points. GPC analysis showed a decrease in molecular weight, DSC showed an increase in crystallinity, with little change observed in the glass transition and melting temperatures (data not shown).

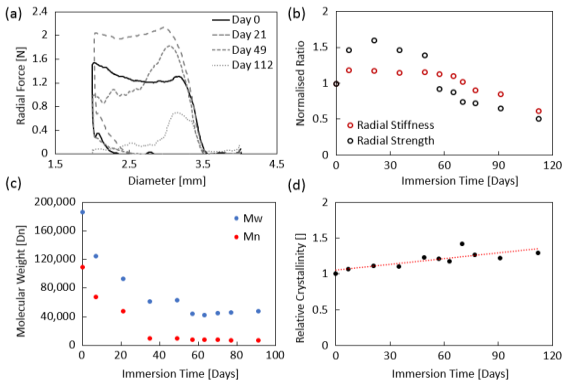

Figure 1: (a) Normalised radial response, (b) Evolution in radial strength and stiffness, (c) Molecular weight evolution, (d). Evolution in relative crystallinity.

Discussion

Degradation of the Reva Medical Fantom Encore stent resulted in a reduction in strain-to-failure of the device, with overall radial strength and stiffness maintained to day 49. This is presented in Figure 1(a) where a sharp decrease in the load bearing capacity of the scaffold is evident. Radial testing also showed a decrease in scaffold stiffness after day 49, Figure 1(b). The radial compression results also suggest an evolution in the yield stress for the stent material. GPC results show a loss of molecular weight over the course of the study. It is interesting how despite losing almost 50% molecular weight by day 21 the scaffold can maintain a higher radial strength compared with day 0. DSC shows, an increase in crystallinity throughout the study, this could explain the initial increase in radial strength however as molecular weight is lost this increased strength is lost.

References

1. Garg et al, Nat. Rev. Cardio., 10:248–60, 2013.
2. Serruys et al, The Lancet, 373:897-910, 2009.
3. Qiu et al, J. Mech. B. Biomed. Mats, 78:254-65, 2018.
4. ISO, B., BS ISO 13781:2017.
5. Reva Medical, San Diego, CA.
6. Weir et al. Proc. Instn Mech. Engrs. 218:321-30, 2004.

Acknowledgements

This project received funding from the European Union's Horizon 2020 research and innovation programme under grant agreement No 777119. The authors would also like to thank CURAM for providing GPC expertise.

IN-SILICO AND IN-VITRO MULTI-AXIAL FATIGUE STRENGTH ASSESSMENT OF NI-TI STENTS WITH POST-FAILURE ANALYSIS

Francesca Berti (1), Luca Patriarca (2), Lorenza Petrini (3)

1. Department of Chemistry, Materials and Chemical Engineering "G. Natta", Politecnico of Milano (Italy); 2. Department of Mechanical Engineering, Politecnico di Milano (Italy); 3. Department of Civil and Environmental Engineering, Politecnico di Milano (Italy)

Introduction

Ni-Ti peripheral stents are subjected to multiple applied loads that affect their long-term fatigue behavior. Recent works [1-2] highlighted the importance of a validated coupled in-silico in-vitro approach for the multi-axial fatigue assessment of peripheral stents. The current literature lacks knowledge on the Ni-Ti local damage mechanisms produced by the cyclic loads which promote crack nucleation and lead to failure of the stents. Accordingly, a detailed post-mortem analysis of the fracture surfaces is of fundamental importance to support the definition of proper multi-axial criteria [3]. The aim of this work is to enhance the predictive capability of a coupled in-silico in-vitro approach by performing post-failure analysis over a range of Ni-Ti specimens and devices tested, respectively, under uni-axial and multi-axial conditions.

Methods

Multi-wires specimens, undergone the same thermo-mechanical treatment of the stents, were tested under different strain levels in order to define the fatigue properties according to a life-constant diagram where the run-out condition was set to 10^6 cycles [4]. Two stents, resembling commercial geometries, were tested using a customized fixture which converted machine axial motion into multi-axial proportional loads, resembling the in-vivo environment. An in-silico validated model was prepared for assessing the local stress/strain fields. Different fatigue criteria available for standard metals (von Mises and critical-plane based Fatemi-Socie, Brown-Miller and Smith-Watson-Topper) were implemented for the fatigue assessment and the identification of the most critical area for fracture. Different remote load magnitudes mimicking the experiments were investigated in order to validate and identify the most accurate fatigue approach. The fracture surfaces of both the uni-axial and multi-axial specimens were successively analyzed by means of the Scanning Electron microscope (SEM) to investigate the crack initiation sites.

Results

The coupled in-silico in-vitro approach successfully predicted the most critical area for failure in both the stent geometries. The von Mises approach, commonly used for interpreting Ni-Ti alloys fatigue performances, was proven to be over-conservative for the loading scenario investigated. On the other hand, critical plane-based criteria were observed to be more representative of the experimental outcomes regardless of stent design. Among them, the BM and SWT gave the most accurate predictions.

Discussion

Through the comparative study of multi-axial in-silico and in-vitro tests, enriched by post-failure analysis, critical plane criteria were demonstrated as reliable predictive tools in the fatigue assessment of Ni-Ti peripheral stents.

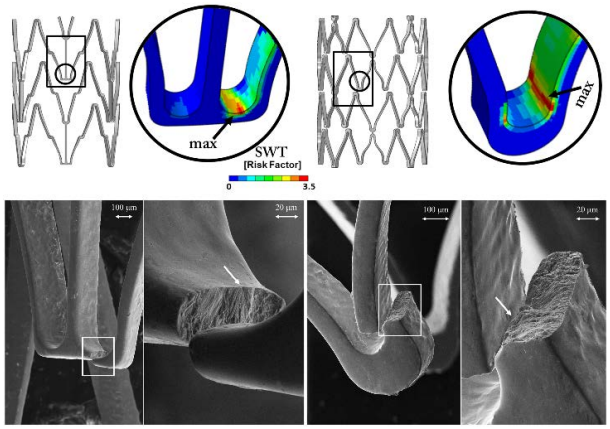

Figure 1: Results of the coupled in-silico in-vitro study according to SWT criterion. The FE analyses allowed the identification of the most critical area for fatigue failure which corresponded with the location of the stent fractures.

References

[1] Berti et al., (2021), J Mech Behav Biomed Mater

[2] Berti et al., (2019), Eng Fract Mech

[3] Robertson et al., (2012), Int Mater Rev

[4] Bonsignore C., (2017), Theor Appl Fract Mech

DIGITAL TWIN OF CARDIOBAND® PROCEDURE FOR MITRAL VALVE REGURGITATION: IN SILICO APPROACH AND VALIDATION

Emanuele Gasparotti (1,2), Emanuele Vignali (1), Elisa Cerone (3), Sergio Berti (3), Simona Celi (1)

1. BioCardioLab, Fondazione Toscana G. Monasterio, Italy; 2. Dept. of Information Engineering, University of Pisa, Italy; 3. Adult Cardiology Unit, Fondazione Toscana Gabriele Monasterio, Italy

Introduction

Mitral valve regurgitation disease is one of the most common heart valve pathology [1]. Cardioband® (Edwards, Irvine) system is a surgical-like direct annuloplasty adjustable device, implanted via transcatheter on beating heart [2]. This procedure is based on the fixing of the device polyester sleeve (PS) around the mitral annulus through insertion of metal anchors. The annulus is contracted by pulling a guidewire (GW) sewed at sew points (SWP) on the PS (changing phase). Currently, the implant size (anchors number) and the anchors position are defined on the basis of the CT dataset by analyzing the site of access and the annulus commissure to commissure distance.

In this study, an in-silico tool for clinical planning of Cardioband® procedure was presented, based on conventional medical images techniques and the Finite Element (FE) method. The accuracy of the tool was evaluated via simulation of five different patients who underwent Cardioband® procedure.

Methods

The computational analysis was performed by developing a specific FE environment in Matlab®, implementing a nonlinear equations system able to describe the behavior of the Cardioband device, the left heart structures and their interactions.

The surrounding left heart structures, reconstructed from 3D CT pre-procedural datasets and meshed, were modeled through FE equations. The compatibility equations were implemented to describe the loads exchanged between annulus and the Cardioband® device. The Cardioband® was modeled through an equation system to reproduce the physical interactions between the PS, the anchors and the GW, which were simplified as follows. In particular, the GW was modeled as a piecewise link composed by ideal cable (no flexural/torsional rigidity, only traction and point loaded) sections interconnecting the SWP. The sections of the PS, instead, are assumed as triangular ideal cable connections between the SWPs and the corresponding anchors. Another feature of this schematization is that the GW can slide through PS at the SP during the cinching phase. Five different patients were simulated. To evaluate the accuracy of the developed routine, the results of simulations were compared with the procedure outputs. The initial anchors and SWP positions were selected from pre-procedure 2D X-ray angiographic images. The resulting positions were compared with the corresponding ones found in the post procedure images.

Results

An example of pre-procedure registration (a), post-procedure comparison (b) and heart radial displacements (c) for an analysed patient case are depicted in Fig. 1. Regarding the post-procedure, it is possible to observe a good overlapping between the clinical procedure and the corresponding simulation in terms of the anchor positions and wire curves.

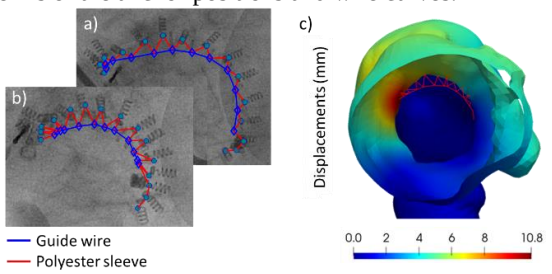

Figure 1: Pre-procedure setup (a) post-procedure comparison (b) and heart radial displacements (c)

Table 1 summarizes the assessment of the accuracy by showing for each case, the position error evaluated as the absolute distance between the simulated and actual final position of the anchor and the SWPs. These values are reported as the average ± standard deviation. The average value error is less than 2 mm both anchor and sew positions.

Error	#1	#2	#3	#4	#5
Anch.	1.6±0.9	1.9±1.3	1.8±0.6	1.7±0.5	2±0.8
SWP	1.9±0.7	1.7±0.9	1.9±1.1	2±0.9	1.7±0.8

Table 1: Position error (mm) estimation for the validation

Discussion

The work presented here confirms that the developed tool for the Cardioband® procedure can simulate the clinical procedures with a good accuracy. It is worth to point out that, the error committed by the FE routine to predict the anchor and sew positions, is mainly affected by the intrinsic errors of the segmentation and by the identification of the anchors in the X-ray projection.

References

1. Fiorilli at al, Annual Rev of Med, 2020.
2. Nickenig et al, JACC: Cardiov Interv, 2016.

Acknowledgements

This work was supported by 3D Virtual Baby Heart (GR-2016-02365072) project.

COUPLED EXPERIMENTAL-NUMERICAL STRATEGY FOR DIGITAL TWIN DEVELOPMENT OF A POLIMERIC CORONARY STENT

Luca Antonini (1), Benedetta Isella (1), Dipok Hossain (1), Francesca Berti (1), Gianluca Poletti (1), Gabriele Dubini (1), Lorenza Petrini (2), Giancarlo Pennati (1)

1. LaBS – Dept. of Chemistry, Materials and Chemical Engineering, Politecnico di Milano, Milan, Italy;
2. Dept. of Civil and Environmental Engineering, Politecnico di Milano, Milan, Italy

Introduction

Finite element simulations are a valuable tool for improving devices and clinical procedures provided they are able to replicate with sufficient accuracy the reality of interest [1]. With regard to coronary stents, the literature is rich in works concerning models of metallic stents [2,3], while there are more scarce studies on the characterization of bioresorbable polymeric stents. The development of a reliable model of a Bioresorbable Vascular Scaffold (BVS) represents a considerable challenge, especially when no information on the polymer of which it is composed is available in the literature. In this perspective, the present work aims to develop a digital twin of a commercial BVS based exclusively on information obtained from the direct investigation of real devices. The adopted strategy couples computational analysis with experimental activities on a small number of delivery systems specifically purchased to investigate the complex mechanical behavior of the polymer.

Methods

Four samples of the Fantom® Encore polymeric stent (REVA Medical) composed of Tyrocore™, have been subjected to mechanical tests easily reproducible in any mechanical laboratory (free expansion and tension testing, the latter carried out with different protocols specifically designed to enhance the viscous characteristics of the polymer) and optically analyzed to reconstruct the geometry. Given the complexity of the behavior experimentally observed, it was decided to describe the Tyrocore™ with the Parallel Rehological Framework material model. The calibration of the material has been performed by reproducing in-silico the tension testing of the stent by varying the value of the model parameters. In order to minimize the computational cost, a single repetitive unit of the stent was used in these simulations neglecting the residual stresses generated by the previous crimping and expansion phases. The reliability of the material model thus obtained was evaluated by considering the in-silico performance of the whole stent subjected to free expansion and tension testing compared with the experimental data.

Results

Figure 1 shows the comparison between computational and experimental performance of the delivery system: on the top the results obtained with respect to the free expansion in terms of central diameter-pressure curve are reported; while bottom shows the force-displacement curves of the stent subjected to tension testing at two different test speeds (“fast” and “slow”).

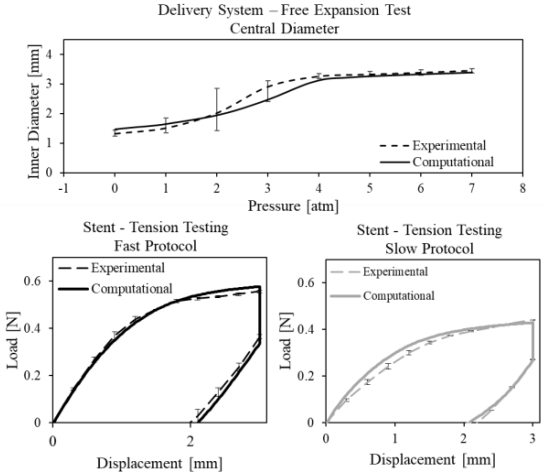

Figure 1: Comparison of numerical and experimental results: (top) stent free expansions; (bottom) tension testing at different velocities.

Discussion

The choice to perform the calibration of the model parameters though a high number of simulations considering only the repetitive unit of the stent allowed to significantly reduce the computational cost without compromising the accuracy of the model. The developed digital twin is able to replicate the behavior of the real device with percentage errors measured on the quantities of interest always below 10%. Hence the experimental-computational strategy has proven effective and potentially usable whenever dealing with a stent whose design is based on repetitive units.

References

1. Debusschere et al, J of Biomech, 48:2012-2018, 2015.
2. Gastaldi et al, Biomech Model Mechanobiol., 9(5):551–61, 2010;
3. Morlacchi et al, Med Eng Phys., 35(9):1272–81, 2013.

Acknowledgements

This project has received funding from the European Union’s Horizon 2020 research and innovation programme under grant agreement no 777119.
This article reflects only the authors’ view and the Commission is not responsible for any use that may be made of the information it contains.

COMPLIANCE MEASUREMENTS OF SMALL VESSELS AND BIOHYBRID VASCULAR GRAFTS FOR HEMODIALYSIS TREATMENT

Monica Soncini(1), Elia Pederzani(1), Alice Caldiroli(3), Marco Pezzotta(1), Alessandro Caimi(1), Emiliano Votta(1), Gianfranco B. Fiore(1), Matteo Tironi(2), Fabio Sangalli(2), Marina Figliuzzi(2), Nadia Azzollini(2), Sonia Fiori (2) Francesco G. Greco(3), Andrea Remuzzi(4), Stefania A. Riboldi(3), Alberto Redaelli(1)

1. Department of Electronics, Information and Bioengineering, Politecnico di Milano;
2. Istituto di Ricerche Farmacologiche Mario Negri IRCCS;
3. Bioengineering Laboratories S.r.l., Italy; 4. Università degli Studi di Bergamo.

Introduction

Patients undergoing chronic haemodialysis need a vascular access to connect the vascular system to an external dialysis equipment. However, clinically available options for long-term haemodialysis access suffer from several drawbacks and are associated to high failure rates. One of the major causes of failure of synthetic grafts is the compliance mismatch between the synthetic graft and the native vessel. Innovative biohybrid arteriovenous grafts have been fabricated with tuneable compliance to approach deformability observed *in vivo*. The grafts are three-layered tubular structures composed by inner and outer layers of electrospun silk fibroin and a core layer of Silkothane®, a blend of silk fibroin and polyurethane [1]. In this work, we developed stationary and dynamic systems to test native arterial and venous vessels and biohybrid grafts deformability following the specifications required by the standards. With the perspective of performing in vivo experiments in a small animal model (rat) to verify the influence of compliance mismatch in graft's failure, biohybrid grafts of small calibre were fabricated. Due to the lack of data available in literature for rat's abdominal aorta and vena cava, we performed a compliance analysis also on native rat vessels.

Methods

We designed and prototyped an *ad hoc* versatile and compact device for stationary compliance measurements able to host native rat vessels and synthetic grafts of small calibre (Figure 1). The entire system is compatible with microscope and micro-CT experiments and compliant with the standards required for vascular grafts tests (temperature control, pressure accuracy, image acquisition).
Native tissue samples (abdominal aorta and vena cava) were harvested from 8-10 weeks Lewis rats of 250 g.
Biohybrid grafts of small calibre were fabricated optimizing the electrospinning parameters and protocols in order to obtain grafts of very small diameters around to 1.5mm and wall thickness of 0.15-0.3 mm. Compliance measurements were performed under a stereo microscope (Nikon SMZ1000) equipped with a digital camera (Fire-I, UniBrain) for the external diameter measurements. Experiments were carried out at 37°C, the samples were pressurized from 0 to 150 mmHg (50 mmHg for venous vessels) with 10 mmHg increments. After 5 cycles of preconditioning, a digital image for each pressure value was acquired in both loading and unloading phase. An automatic tool was developed and used for images post processing.

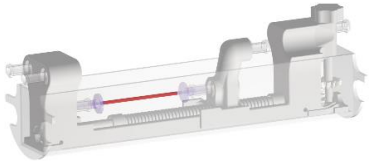

Figure 1 Device developed for the compliance measurements.

Results and discussion

Several tests were carried out on native rat vessels (Figure 2). Abdominal aortas (n=9) from rats showed compliance values of 30.2±4.9, 14.7±1.5, 7.4±1.5%1/100 mmHg in hypo- normo- and hyper-tension ranges, respectively. Vena cava (n=7) showed compliance values of 54.5±33.3 and 32.9±16.9% 1/100 mmHg in 20-30 and 30-40 mmHg ranges. Biohybrid grafts, evaluated up to 150 mmHg, showed compliance values of about 2%, significantly lower than native tissues, but higher than traditional synthetic grafts.

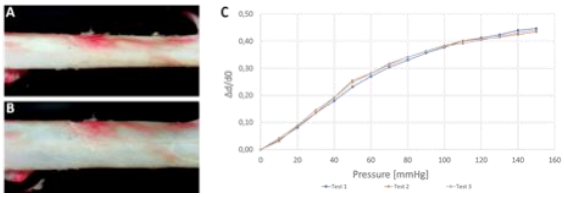

Figure 2 (A) abdominal aorta at 0 mmHg; (B) aorta at 150 mmHg; (C) example of normalized deformation vs pressure.

An *in vivo* study is on going to evaluate the behaviour of Silkothane® grafts. Two implantation sites (abdominal aorta and arterio-venous shunt) and two explant time points (30 and 90 days) are being investigated; up to now, all the implanted rats survived the surgery with blood flow inside the graft, observed by means of echo-doppler analysis. Neointima formation and endothelialization is under evaluation via histological analysis.

References

1. Van Uden S. et al, Biomed Mater 14:25007, 2019

Acknowledgements

SILKELASTOGRAFT grant #2018-1777 funded by Fondazione Cariplo and Regione Lombardia.

ENDOVASCULAR DRUG DELIVERY: STENTS VERSUS BALLOONS

Javier Escuer (1), Estefanía Peña (1,2), Miguel Á. Martínez (1,2), Sean McGinty (3)

1. University of Zaragoza, Zaragoza, Spain 2. CIBER of Bioengineering, Biomaterials and Nanomedicine (CIBER-BBN), Zaragoza, Spain, 3. University of Glasgow, UK

Introduction

Drug-coated balloons (DCB) have emerged as an attractive alternative to drug-eluting stents (DES) for the interventional treatment of coronary artery disease in certain anatomical conditions [1]. While DCB typically transfer drug rapidly to the arterial wall during a short inflation period of the order of 1 minute, DES usually offer sustained drug release over a period of weeks or months. Interestingly, most commercial DES nowadays elute limus compounds, while currently approved DCB elute paclitaxel. The main aim of this work is to investigate theoretically if there are potential benefits of using balloons versus stents and whether or not this depends on the drug used.

Methods

We consider two different 2D-axisymmetric geometries corresponding to idealised straight segments of coronary arteries where either a DES with non-erodible polymeric coating is implanted or a DCB is deployed. Blood flow is modelled using Navier-Stokes equations in the arterial lumen. The arterial wall is considered as a three-layered porous structure including intima, media and adventitia, with Darcy's law used to calculate the pressure and velocity fields through the porous layers. A drug influx is prescribed at the balloon-wall interface to approximate the drug delivered from the DCB during inflation [2], while drug release from the DES is modelled through a diffusion equation [3]. Advection-diffusion equations are used to model drug dynamics through the different layers of the tissue. The endothelium, internal and external elastic laminae are considered as semipermeable membranes and the flux across them is governed by Kedem-Katchalsky equations. In the media, a nonlinear saturable reversible reaction model describes binding of drug to components of the arterial tissue (receptors and general extracellular matrix sites) [4]. We compare three different values of initial mass of drug in the stent coating (M_0) and three balloon inflation times (t_0). We also study the influence of two drugs in the simulations: paclitaxel and sirolimus.

Results

Fig. 1 demonstrates, for the variety of cases considered, that the total drug content (DC) in the arterial wall increases with (i) increasing DCB inflation time and (ii) increasing DES initial drug loading. Interestingly, the peak DC is always higher for the stent. However, by 7 days, the DC is approximately the same, regardless of whether the drug was delivered by the DES or DCB. Similar trends are observed for the case of non-specific bound drug (Fig. 2, left). When we compare specific binding site saturation (Fig. 2, right), again we observe that longer DCB inflation times and higher DES initial drug loading lead to higher values. It is notable, however, that across a period of 30 days, the DES consistently achieves higher values of this marker than the DCB.

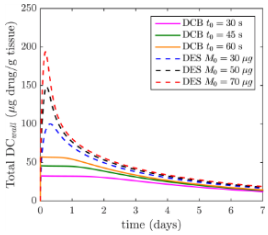

Figure 1: Total DC in the wall. Drug: sirolimus.

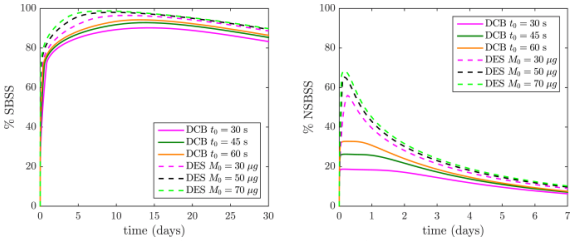

Figure 2: Specific and non-specific binding sites % saturation in the media. Drug: sirolimus.

Discussion

Specific binding site saturation (SBSS) has been linked to efficacy of endovascular drug devices [5]. In this study we have shown, at least for the configurations and drug considered that DCB can achieve lower but similar levels of SBSS compared with DES, despite the drastic difference in drug-elution kinetics. Since the permanence of DES is disadvantageous, our results indicate that it may be preferable, at least in some cases, to utilise a DCB rather a DES.

References

1. Jeger et al, JACC: Cardiovascular Interventions, 13(12): 1391-1402, 2020.
2. Kolachalama et al, Circulation 127:2047-2055, 2013.
3. Escuer et al, J Mech Behav Biomed Mater 104, 103610, 2020.
4. McGinty et al, J Math Chem 54:967–76, 2016.
5. Tzafriri et al, J of Control Release 161(3):918-926, 2012.

Acknowledgements

Funding provided by the Spanish Ministry of Economy, Industry and Competitiveness through project PID2019-107517RB-I00. Dr. McGinty acknowledges funding provided by EPSRC (Grant no. EP/S030875/1).

FREQUENCY EFFECTS ON TAVR TURBULENT FLUID MECHANICS WITHIN AN ACCELERATED ENVIRONMENT

Sailahari V. Ponnaluri (1), Michael S. Sacks (2), Keefe B. Manning (1,3)

1. Department of Biomedical Engineering, The Pennsylvania State University, University Park, PA, USA

2. Willerson Center, Institute for Computational and Engineering Sciences, Department of Biomedical Engineering, University of Texas, Austin, TX, USA

3. Department of Surgery, Penn State Hershey Medical Center, Hershey, PA, USA

Introduction

As of 2017, an estimated 138,400 patients died annually from heart valve disease (HVD) worldwide [1]. The primary treatment option is either a mechanical or bioprosthetic heart valve replacement. However, 30% of HVD patients are unable to receive surgical valves due to comorbidities and/or age [2]. Transcatheter aortic valve replacements (TAVRs) are a novel, minimally invasive approach for HVD. Yet, despite increased interest, TAVR long-term durability is unknown. Durability testing is performed by an accelerated wear tester (AWT) in accordance with ISO:5840. This standard specifies a cycle number and delta pressure maintained across a closed valve for 5% of the cycle, but no testing frequency, contributing to differences between *in vivo* and AWT cycling [3]. With an increase in frequency, porcine heart valve tissue demonstrates decreased leaflet stress relaxation, producing a higher *in vitro* preload [4]. A higher preload could either produce a harsher environment with high stresses sustained over the cycle or a reduced range of stresses, under or over-estimating the durability, respectively. Therefore, this study aims to understand frequency's effect on TAVR turbulent fluid mechanics using high-speed particle image velocimetry (HSPIV).

Methods

A TAVR was cycled in an Electroforce® Durapulse™ AWT composed of a proximal and distal chamber, valve holder, and pressure transducers at each chambers' base (Fig. 1). The TAVR was cycled at three frequencies (10, 15, and 20 Hz) compliant with ISO:5840 in a Newtonian glycerin and saline solution ($\rho = 1.13$ g/ml, $\mu = 3.99$ cP). The TAVR stent was trimmed to create windows to quantify the near valve fluid mechanics.

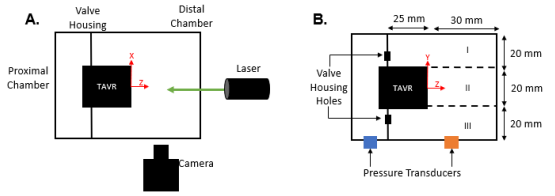

Figure 1: A. AWT HSPIV set-up. B. Side view of regions of interest, pressure transducers, and valve housing fluid recirculation holes indicated.

The geometric orifice area (GOA) was calculated using a custom MATLAB script from enface images to quantify valve motion every 9% of the cycle. HSPIV quantified three regions (above, center, below) downstream of the TAVR (Fig. 1B). Two HSPIV data sets were captured: an averaged set to compare between frequencies every 9% of the cycle and an instantaneous set to visualize eddy formation. Reynolds normal and shear stresses (RNS, RSS respectively) were calculated.

Results

At all frequencies, a jet emerged from the TAVR during systole and achieved a maximum velocity, turbulent stresses downstream of the valve opening, and GOA at 36% of the cycle. During diastole, a large recirculation region appeared at the base of the valve and dissipated downstream until the next cycle. Despite these similarities, there was a decrease velocity, turbulent stresses, jet dissipation, and coaptation with increasing frequency (Table 1).

Frequency (Hz)	GOA (cm^2)	Jet Velocity (m/s)	RNS (Pa)	RSS (Pa)
10	1.54	0.90	867.64	412.66
15	1.10	0.66	581.73	278.67
20	0.91	0.47	337.75	162.87

Table 1: Summary of maximum GOA, jet velocity, and turbulent stresses at 36% of the cycle and period in which the valve is closed and fully loaded.

Discussion

The AWT fluid mechanics demonstrated a clear dependence on frequency. With increasing frequency, the TAVR GOA, maximum jet velocity, and turbulent stresses decreased, all factors that influence TAVR fatigue. Therefore, AWT testing frequency will influence the *in vitro* observed valve life span.

References

1. Yagdir, S., *et al., Circulation*, 141:1670-1680, 2020.
2. Leon M.B., *et al*., *N Engl J Med*, 363:1597-1607.
3. International Standards Organization:5840:3, 2013.
4. Vesely, I., *et al*., *Ann Thorac Surg*, 60:379-383, 1995.

Acknowledgements

Research supported by NIH HL129077 and the Penn State Center for Biodevices Leighton Riess Graduate Fellowship in Engineering.

THE USE OF ETCHING TO OVERCOME DESIGN RESTRICTIONS OF THE SLM TECHNIQUE WHEN 3D PRINTING TITANIUM STENTS

Orla M. McGee (1,2)†, Sam Geraghty (1,2,5)†, Parastoo Jamshidi (3), Damien P. Kenny (4), Moataz M. Attallah (3), Caitríona Lally (1,2,5)

1. Trinity Centre for Biomedical Engineering, Trinity Biomedical Sciences Institute, Trinity College Dublin, Dublin, Ireland; 2. Department of Mechanical, Manufacturing & Biomedical Engineering, School of Engineering, Trinity College Dublin, Dublin, Ireland; 3. School of Metallurgy & Materials, University of Birmingham, Birmingham, B15 2TT, United Kingdom; 4. Children's Health Ireland at Crumlin, Dublin, Ireland.; 5. Advanced Materials and Bioengineering Research Centre (AMBER), Royal College of Surgeons in Ireland and Trinity College Dublin, Dublin, Ireland

† These authors contributed equally

Introduction

Additive manufacturing of metallic stents has the potential to eliminate challenges in both production of stents and treatment of patients, paving the way for the development of bespoke patient specific 3D printed stent designs. A recent study by Demir & Previtali [1] investigated SLM (Selective Laser Melting) of cobalt-chromium stents for cardiovascular stenting. That study outlined the need for a SLM stent to be self-supporting and also suggested rules on creating such a stent geometry to ensure no unnecessary damage is incurred in removing supports post-printing. However, these design rules lead to restrictions in the design of stents available through additive manufacturing. The objective of this study is to investigate using etching as a post-processing tool to improve the development of SLM printed stents.

Methods

Stent Design and Processing: Two different stent designs were developed based on design criteria for additive manufacturing from [5]; a Simple Honeycomb (SH) and a Novel Design (ND) stent. These stents were then printed using the ReaLizer SLM printer (Realizer GmbH) using titanium powder (Ti-6Al-4V ELI). After printing, some of the stents were etched by immersing the samples into etching solution containing hydrofluoric and nitric acid ((HF: HNO3: H2O = 1:2:3) for approximately 12 minutes and then transferred into distilled water for 5 minutes and rinsed with ethanol. Three SH and three ND designs were etched (Figure 1).

Experimental Crush Test: Once printed, these stents underwent an experimental crush test using an Instron 3366 (Instron., MA, USA).

FE Crush Test: Prior to the experimental crush test, measurements of the strut width and thickness of each stent were taken using a stereoscopic microscope. Based on these 'as etched' and 'as printed' measurements the stents were created in Solidworks (Dassault Systemes Solidworks Corp, MA, USA). Stents were then meshed using Ansys Spaceclaim (2019 ANSYS. Inc) and ANSA BETA (BETA CAE Systems, Switzerland). A Finite Element (FE) model was created in ABAQUS and used to replicate the experimental crush test. Using an inverse FE approach the material properties of the printed and etched stents were calibrated.

Surface Roughness Analysis: White light interferometry and scanning electron microscopy (SEM) were used to assess stent surface roughness pre- and post-etching. Arithmetical average roughness, R_a, was measured along the length of 8 individual stent struts for 3 samples of each design.

Results

Etching stents was found to reduce the stent strut width and thickness. Alongside this, stent surface finish was improved post-etching. Furthermore, it was found that combining novel designs with etching allows for open stent designs to be printed without the need for additional supports, see Figure 1. Such techniques can allow for a greater range of 3D printed stent designs to treat specific patient needs. Calibration of the stent material properties found that non-etched stents had lower Young's moduli. This is attributed to the fact that increased surface roughness in the 'as printed' stents led to an overestimation in the stent width and thickness from the stereoscopic measurements, leading to an overestimation in the stent's stiffness in the FE model.

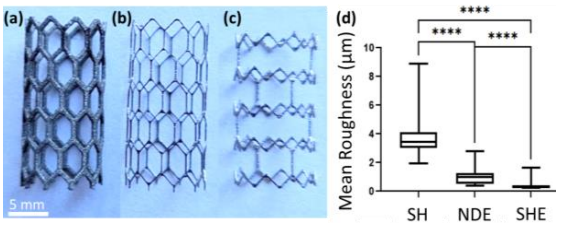

Figure 1: SLM printed stents; (a) Simple Honeycomb (SH) (b) Simple Honeycomb Etched (SHE) and (c) the Novel Design Etched (NDE). (d) Mean surface roughness measurements from the three stent designs.

Discussion

This study demonstrates the benefits of etching as a post processing technique for SLM printed stents. In particular, it shows how etching can enable significant flexibility in SLM stent designs for patient specific applications.

References

1. Demir & Previtali. Mater Design. 119:338-350. 2017

Acknowledgements

This study was funded National Children's Research Centre, Crumlin (Grant No. G/19/3), an Irish Research Council Government of Ireland Postdoctoral Fellowship 2019 (GOIPD/2019/222) and from research supported in part by a research grant from Science Foundation Ireland (SFI) under the grant number 12/RC/2278_2.

IN-SILICO MODELING OF THE LEFT ATRIAL APPENDAGE OCCLUSION: DEFINITION OF A VALIDATION PATH

Francesca Danielli (1), Alissa Zaccaria (1,2), Elisabetta Stretti (1), Maria Francesca Zaccone (1), Emanuele Gasparotti (3,4), Benigno Marco Fanni (3,4), Katia Capellini (3,4), Simona Celi (3), Giancarlo Pennati (1), Lorenza Petrini (5)

1. LaBS, Dept. of Chemistry, Materials and Chemical Engineering, Politecnico di Milano, Italy; 2. Intellimech, Italy; 3. BioCardioLab, Fondazione Toscana Gabriele Monasterio, Italy; 4. Dept. of Information Engineering, University of Pisa, Italy; 5. Dept. of Civil and Environmental Engineering, Politecnico di Milano, Italy

Introduction

Left Atrial Appendage (LAA) is the primary source of thromboembolism (approximately 91%) in patients affected by atrial fibrillation. If anticoagulants cannot be safely administrated, LAA Occlusion (LAAO) with self-expandable Nitinol devices is an appealing alternative [1]. However, LAA complex morphologies hinder the implant procedure, requiring skilled operators and an ad-hoc device sizing and positioning. Like most percutaneous structural heart procedures, strategies to access the anatomical site need to be investigated, including the constraints of the surrounding structures [2]. Focusing on the LAA, the transeptal puncture is crucial in identifying a suitable landing zone [3]. In this scenario, LAAO in-silico modeling is a potential tool for physicians training and planning. In literature, the works on LAAO [4,5] define the optimal device positioning without providing evidence about any possible influence of the nearby anatomical constraints, a key issue for a clinician to assess the implant feasibility. Furthermore, Finite Element (FE) models of the devices are used in complex patient-specific simulations without any preliminary validation. Credibility assessment of a computational model is an unavoidable task if it is intended to support clinical decisions [6,7].
This work aims to build a validated FE model of LAAO, involving the development of digital twins of both an occluder, the Watchman device (Boston Scientific), and patient-specific LAAs. Then, the influence of several transeptal punctures is preliminarily studied.

Methods

The pipeline of the project foresees three main tasks.
i) Device model. CT images of a device sample were used to ensure a high-fidelity geometry reconstruction. The CAD model was discretized with 1D-elements (Fig. 1a). Ad-hoc designed in-vitro tests were performed on the device for characterizing the thermo-mechanical behavior of the Nitinol frame and validate the FE model.
ii) LAA model. 3D geometries of patient-specific LAAs and half Left Atriums (LA) were reconstructed using CT images. On one side, 3D-printed anatomies were manufactured with Elastic50A Resin material and used to perform in-vitro deployments under fluoroscopy (Fig. 1b, left). On the other side, FE models were developed using tetrahedron elements (Fig. 1b, right).
iii) LAAO simulations. The in-vitro tests (ii) were used to validate the device FE model (i) interacting with patient-specific anatomies. Once the validation was assessed, the model was used to evaluate the impact of several transeptal punctures on the occluder positioning.

Results

Nitinol calibration and the device FE model validation were assessed quantitively, comparing in-vitro and in-silico force-displacement curves (errors <7% on the maximum force) and device configurations (Fig. 1c). The comparison of the device positioning between the in-silico deployment and the in-vitro one established a good capability of the model to describe the Watchman deployment (Fig. 1d), allowing the use of the computational tool for studying the influence of the procedural variability on the final device positioning.

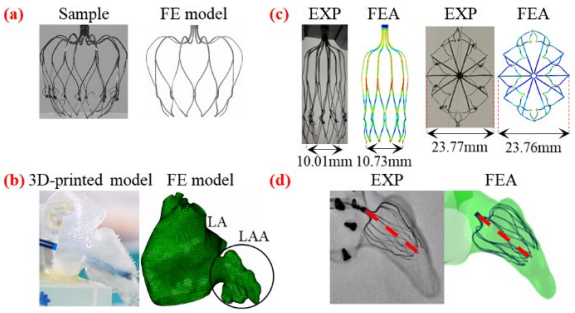

Figure 1: Workflow of the project.

Discussion

The proposed approach allowed to develop an in-silico model of an LAA occluder validated through in-vitro tests. Hence, the validation with in-vivo data should be addressed, involving the comparison with pre and postoperative images. Once the credibility of the computational model is assessed, the virtual twin of the procedure will act as a predictive tool, optimizing the operative planning and increasing the probability of successful outcomes.

References

1. H.M. Pacha et al, World J Cardiol, 57-70, 2019.
2. F.R. Pluchinotta et al, Int J Cardiol, 33-39, 2020.
3. S.C. Harb et al, Circ Cardiovasc Imaging, 1-11, 2019.
4. A.M. Bavo et al, J Cardiovasc Comput Tomogr, 149-154, 2020.
5. A.M. Aguado et al, Front Physiol, 1-13, 2019.
6. ASME Standard, V&V 40, 2018.
7. A. Zaccaria et al, Med Eng Phys, 104-118, 2020.

HOW DO VESSEL CURVATURE AND PLAQUE COMPOSITION AFFECT THE DISTRIBUTION IN TISSUE OF DRUG ELUTED FROM STENTS?

Javier Escuer (1), Irene Aznar(1), Christopher McCormick (3), Estefania Peña (1,2), Sean McGinty (4), Miguel Angel Martinez (1,2)

1. University of Zaragoza, Spain; 2. CIBER of Bioengineering, Biomaterials and Nanomedicine (CIBER-BBN), Spain; 3. University of Strathclyde, UK; 4. University of Glasgow, UK.

Introduction

Atherosclerotic cardiovascular disease is the cause of millions of sudden deaths annually. Coronary artery disease (CAD) is one of the most relevant cardiovascular pathologies. An important advance in the treatment of CAD is the development of Drug Eluting Stents (DES). However one of the main drawbacks is restenosis development after stent implantation. The controlled delivery of anti-proliferative drugs limits restenosis, avoiding the migration and proliferation of smooth muscle cells (SMC) from the media to the intima. Key to the success of DES is the correct release of the drug, i.e. maintaining a therapeutic concentration of drug within the artery but avoiding toxic levels that limits re-endothelialization. The level of drug concentration in the tissue depends on several factors, with the geometry of the artery one of them [1,2]. The objective of this contribution is to analyse the influence of the vessel curvature and plaque heterogeneity on drug transport in the blood flow and in the arterial wall.

Methods

Several 2D computational models corresponding to idealized longitudinal sections of segments of coronary arteries have been considered in this work as a first step to analyze the influence of arterial curvature and plaque composition on drug transport within the arterial wall. In particular, six different geometries of coronary artery, with and without plaque, containing a DES have been considered: one corresponding to a straight segment and the remaining five corresponding to curved segments of varying curvature ratio (κ). The plaque is composed of two different domains: fibrous cap and core. The length of the plaque (approximately 6 mm) and the percentage of diameter stenosis (20 %) correspond to values within the range found in the literature. The arterial wall includes three different layers: subendothelial space, media and adventitia. Endothelium, internal and external elastic laminae are considered as semipermeable membranes. The device is represented by ten circular struts half-embedded in the tissue. Blood flow is modelled using Navier-Stokes equations in the arterial lumen domain, while Darcy's law is used to calculate filtration velocity through porous layers. Drug transport within the arterial wall is modelled using advection-diffusion-reaction equations [3]. Kedem-Katchalsky equations are used to model fluid and solute flux through the membranes [4].

Results

As an example of the obtained results, in Fig. 1 we show a comparison of the normalized drug concentration within the inner wall of the artery at 10 min, 1 h and 4 h after stent implantation for two different curved vessels.

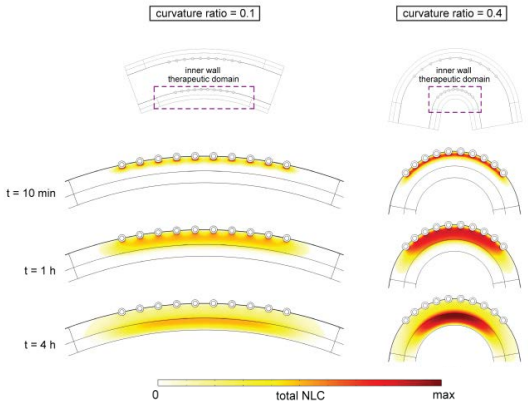

Figure 1: Normalized drug concentration in the inner wall of the artery for two curvature ratios (κ=0.1 and κ=0.4) at different time points after stent implantation.

Discussion

Our results show that the arterial curvature affects the drug transport within the tissue few hours after stent implantation, increasing the levels of drug concentration within the inner wall of the vessel and decreasing within the outer one. Plaque induces a delay in the NMC profiles of both layers: NMC peaks under pathological conditions are reached approximately 3-4 hours later than under healthy conditions. These results suggest that the plaque, especially when calcified acts as a physical barrier preventing the penetration of the drug.

References

1. Hossain, SS. et al., Comput. Mech, 49(2):213-242, 2012.
2. Lu, S. & Zang, S. Biorheology. 56(4):253-263, 2019.
3. McGinty et al, J Math Chem 54:967–76, 2016.
4. Escuer, J. et al, J. Mech Behav Biomed Mater 104, 103610, 2020.

Acknowledgements

Funding provided by the Spanish Ministry of Economy, Industry and Competitiveness through project PID2019-107517RB-I00. Dr McGinty acknowledges funding provided by EPSRC (Grant no. EP/S030875/1).

EXPERIMENTAL ASSESSMENT OF A MOCK CALCIFIED ABDOMINAL AORTIC ANEURYSM

Philippe Mahbeer (1,2), Gilles Soulez (2), Rosaire Mongrain (3)

1. Department of Biological and Biomedical Engineering, McGill University, Montreal, Canada;
2. Centre de recherche du Centre hospitalier de l'Université de Montréal, Université de Montréal, Canada;
3. Department of Mechanical Engineering, McGill University, Montreal, Canada

Introduction

This work focuses on the development of anatomically and biomechanically correct phantoms of an abdominal aortic aneurysm, a large dilatation of the arterial wall, with the presence of small calcium deposits within the wall of the phantom to simulate the calcification of the arterial wall. Analysis of mean strain seem to indicate that a larger surface area of calcifications strongly impacts stress concentration in smaller samples, but has a reduced impact in larger phantoms.

Methods

The phantoms are produced using polyvinyl alcohol (PVA) to mimic the hyper-elastic properties of the abdominal artery. PVA (P1763, Sigma) is prepared as a 10% W/V mix with deionized water [1]. PVA's mechanical properties can be tailored through a series of freezing and thawing cycles (freezing: -0.17°C/min until -20°C; thawing: 0.33°C/min until 10°C) with a freezer [2]. Calcifications are produced by mixing PVA with calcium carbonate powder (115% W/W CaCO3/PVA) beforehand to create a stiffer sample moulded in various observed clinical shapes (flake, stone, strips) [3]. The PVA is initially poured in a 3D printed mould of the artery, then the aneurysm and a large surface area of calcifications (1-2cm^2) are introduced to the mock artery after three freezing-thawing cycles, after which the entire phantom is subjected to an additional five freezing-thawing cycles.

Results

Analysis of elastic modulus was done by uniaxial tensile testing, while mean strain was studied by transverse ultrasound imaging of the phantoms.

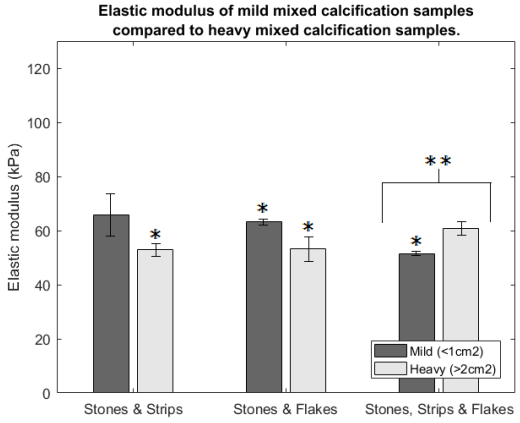

Figure 1: Elastic modulus of PVA samples with various clinical cases of calcifications of different degrees (mild calcification (dark grey) : <1cm^2; heavy calcification (light grey) : >2cm^2) at 15% strain following uniaxial tensile test. One asterisk means the sample has an elastic modulus which is clearly different from blank PVA (101.22 ± 16.94 kPa) ($p < 0.05$); two asterisks means the mild and heavy calcification samples are clearly different ($p < 0.05$). N=3.

Phantoms	Mean strain (%)	p value
Blank	8.723 ± 2.362	-
Flakes & stones	7.353 ± 2.637	0.6391
Strips & stones	10.463 ± 2.282	0.5318
Flakes, strips & stones	7.169 ± 3.752	0.6692

Table 1: Mean strain in arterial phantom with and without calcifications, and two-tailed p-value from paired Student t-test when compared to the blank (no calcifications) phantom (N = 2).

Discussion

Among the factors tested in uniaxial tensile tests, only surface area demonstrates a statistically significant stress accumulation in the arterial wall, whereas depth of calcifications shows no strong correlation to an increase in stress. Regarding strain analysis, a paired Student t-test of 40 different points of the inner arterial wall over two pulsatile flow cycles shows no statistically significant difference when compared to the entire arterial wall of the abdominal aortic aneurysm without calcifications, though it remains unclear whether the presence of calcifications in the phantom's wall has an increasing or decreasing effect on strain and stress accumulation locally.

References

1. Pazos V et al. Polyvinyl alcohol cryogel: Optimizing the parameters of cryogenic treatment using hyperelastic models, J Mech Behav Mat, 2(5):542-549, 2009.
2. He Z, Mongrain R, Chayer B, Cloutier G, Soulez G, Anthropomorphic and biomechanical mockup for abdominal aortic aneurysm, Med Eng Phys. 77:60-68, 2020.
3. Youssef, S.., Mongrain, R. Experimental analysis of a mock atherosclerotic calcified coronary artery. 2012. Thesis, Université de Montréal.

Assessment of Friction for Catheters Design Interacting with Soft Viscoelastic Vascular Tissue

Rosaire Mongrain (1), Zinan He (1), Richard Leask (2), Gilles Soulez (3)

1. Mechanical Engineering, McGill, Canada; 2. Chemical Engineering, McGill, Canada; 3. Department of Radiology, University of Montreal

Abstract

In this work, we present the assessment of catheter friction with soft synthetic materials and vascular tissue for identifying functional (navigation and deployment) design parameters. It is reported that the frictional forces are dependent on the catheter advancement speed. The results are reported with Stribeck curves and it is shown that the frictional forces are highly dependent on the wetness of the interface. The impact of the results are discussed in terms of translation to phantoms and catheters design.

Introduction

Catheters and guidewires are frequently used for cardiovascular procedures for diagnoses (injecting and retrieving fluids) and therapeutic interventions (stenting, drainage, ablation) [1]. The practitioner experiences significant resistance when navigating and positioning the catheter. This resistance is due to friction between the catheter body material and the endothelial surface of the vessel (or cavity). This directly affects the precision of the positioning which is critical for the success of the procedure (ablation or deployment sites). It can also be responsible for vessel wall damage (desquamation, perforation) that can lead to detrimental and lethal consequences. The industry is developing new catheter designs with new materials and coatings to alleviate this friction. However, there is limited development about friction models for studying the interaction between the catheter polymeric material and the soft vascular wall surface. Such model would also be useful for the numerical modeling of catheter navigation and related virtual surgical planning [2].

Methods

Generally, friction is made of three main contributions: adhesion (van der Waals type), lubricating fluid shearing and surface asperities deformation. Given the lubricated nature of the contact, a Stribeck friction model was selected. However, the model is underdetermined for zero sliding speed [3] and requires a dry contact model. In addition, in the case of elastomeric material it was shown that the friction can increase for increasing sliding speed [4].

A MACH Bio-momentum Testing equipment was used with moving speeds between 0.5-50 mm/s and masses (loads) between 10g and 300 g. Rectangular catheter samples of 20 X 20 mm are cut from commercial EVAR catheters (Cook, Medtronic) and affixed to an applicator which is put in contact to slide against excised vascular aortic strips, hydrogel specimens and silicone surfaces. The chosen applied loads are selected to cover the force and torque ranges used in catheter navigation (4N, 18 Nm) [5].

Results

In Figure 1, we illustrate the results for the coefficients of friction for the various surfaces interfacing the catheter material. As it can be noticed, the PVA exhibits the closest properties whereas elastomeric materials have much higher friction.

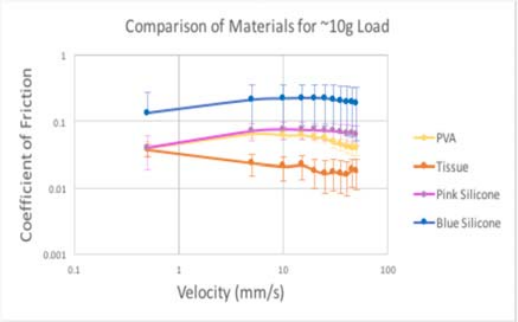

Figure 1: Coefficients of friction of soft surfaces interfacing with the catheter material

Discussion

The results provide information on the reasons why it may be difficult to navigate catheters in situation where the moving speeds are low or from initial (static contact) situations. It also helps for selecting the proper material when fabricating vascular mock-ups. A substance with low coefficient of friction (PVA) would provide more realistic testing conditions for catheter assessment than elastomeric based mock-ups. It can also guide in selecting materials for catheters design and developing coating technologies to decrease the friction coefficients associated with catheters.

References

1. Jin Z & Dowson D, Friction, 1(2):100-113, 2013
2. Roy D et al., Int J Numer Method Biomed Eng, 32(12), 2016
3. Andersson S et al., Tribol Intern 40(4):580-587, 2007
4. Grosch KA, Proc Royal Soc London. Series A, Math Phys Sci, 274(1356): 21-39, 1963
5. Thakur Y et al, IEEE Trans Biomed Eng 56(7):1901-8, 2009

Acknowledgements

This work was supported by a NSERC grant.

INHIBITION OF THE ADHESIVE BEHAVIOR OF VON WILLEBRAND FACTOR DUE TO ENZYMATIC CLEAVAGE

Connor T. Watson (1), Stefano A. Rizzo (2), Shane C. Ward (1), Alberto Redaelli, PhD (2), Keefe B. Manning, PhD (1,3)

(1) Department of Biomedical Engineering, The Pennsylvania State University (2) Department of Biomedical Engineering, Politecnico di Milano (3) Department of Surgery, Penn State Hershey Medical Center

Introduction

The coagulation cascade has a number of biochemical species that mediate thrombosis along both chemical and mechanical pathways. One of these is the von Willebrand Factor (vWF), a bloodborne glycoprotein that functions by connecting platelets in the freestream to the subendothelial matrix in high shear flows. Left ventricular assist devices (LVADs) apply pathological shear rates significantly higher than physiological conditions. Adhesion efficacy may be significantly altered by ADAMTS13, a cleaving enzyme within the blood. The primary goal of this study is to observe the adhesive behavior and thrombogenic contribution of vWF on biomaterials, as well as the modulating effect of ADAMTS13 on adhesion, leading to novel strategies to reduce thrombosis mediated by implanted devices.

Methods

A series of PDMS microfluidic channels was used to create a low volume system of adjustable shear, with easily observable deposition under immunofluorescent microscopy. Velocity profiles were determined using a micro-PIV system (TSI Inc., Shoreview, MN). Channels were coated with bovine type I collagen (100 µg/mL) to provide a base layer for vWF adhesion. Human vWF diluted to 12 µg/mL (Haematologic Technologies, Essex VT) was driven through the channel at adjustable flow rates to achieve the desired shear. Primary and secondary antibodies (Abcam, Cambridge UK) with Alexa Fluor 488 were applied in sequence. Images were acquired with a 4MP CCD camera and colored with pseudocolor.

Results

Within the shear rate range (200-1000 s^{-1}) applied in the microfluidic channel, there was a clear observable difference between mean coverage of vWF alone and the vWF-ADAMTS13 (V-A) solution **(Fig 1)**.

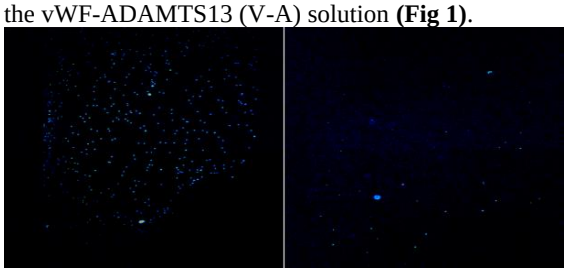

Figure 1: vWF Adhesion depicted in medium BFS channel (300/600 µm), shown (left) vWF after 50 µL/min flow (right) vWF +ADAMTS13 solution after 50 µL/min flow.

Two distinct trends emerged, the direct relationship between increasing shear and adhesion of vWF, and the plateau of V-A. Within the BFS channel, vWF adhered at higher rates within the inlet of the channel, similar rates at the step, and lower rates within the outlet, supporting a relationship between high shear and increased deposition. The same relationship was observed within the straight channels with small variation at low shear (**Fig 2).**

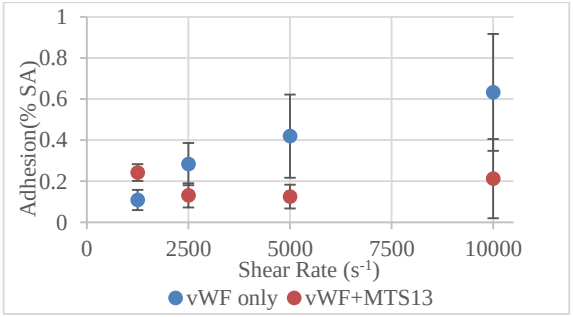

Figure 2: vWF adhesion to collagen coated microchannels (n=6) as a function of shear. Enzymatic cleavage plays a role, demonstrated by the difference between vWF alone and vWF-ADAMTS13. Shear rates range from healthy venous (200 s^{-1}) to pathological stenotic shear (10000 s^{-1}).

Conclusions

This study is a first step towards understanding the behavior of vWF under physiological conditions. There is an observable difference in behavior in vWF dependent on the presence of ADAMTS13, a proteolytic enzyme that generates smaller, inert multimers that effectively stifle the coagulation cascade. Further investigation should explore deposition rates on implanted material surfaces and additional biological materials. Shear rate is shown to have a direct effect on deposition of vWF multimers or mechanically cleaved monomers, while having little effect on the chemically fragmented subdomains generated by ADAMTS13. It is important to determine how the cleaving behavior of ADAMTS13 is affected by both higher shear and additional coagulation factors. This relationship is a factor of interest in further exploring vWF adhesive behavior in the exorbitantly high shear applied by mechanical circulatory devices.

Acknowledgements

This work is supported, in part, by NIH HL136369.

IN VITRO STUDY OF EFFECTS OF ECMO ON PATIENT SPECIFIC AORTA UNDER CARDIOGENIC SHOCK CONDITIONS

Emanuele Gasparotti (1,2), Emanuele Vignali (1), Massimo Scolaro (3), Paolo Del Sarto (3), Simona Celi (1), Dorela Haxhiademi (3)

1. BioCardioLab, Fondazione Toscana Gabriele Monasterio, Italy; 2. Dept. of Information Engineering, University of Pisa, Italy; 3. Intensive Care Unit, Fondazione Toscana Gabriele Monasterio, Italy

Introduction

Venoarterial Extracorporeal Membrane Oxygenation (v-a ECMO) is a form of temporary mechanical circulatory support. It is used to support the cardiac function of patients with severe heart failure in different configurations. In the femoro-femoral (femoral vein - femoral artery) configuration, the fluid-mechanical interactions between ECMO and the patient's circulation can increase the left ventricular afterload, impeding the heart recovery and causing pulmonary congestion [1]. The complex interaction between ECMO and native heart function is poorly investigated. The use of in-vitro simulations can help to measure fluid-mechanical parameters that are fundamental for the patient specific adjustment of ECMO support and that cannot be completely evaluated at bedside.
The aim of this study is to develop a patient specific Mock Circulatory Loop to evaluate the modifications of heart work and flow distribution in the aorta, with different levels of ECMO retrograde support in cardiogenic shock.

Methods

The mock loop is composed of a thoracic aorta phantom, two active components and a series of passive components to model the systemic resistances and compliances at each branch. The phantom was 3D-printed in Clear rigid resin (Form2, Formlabs®). The model was designed with a single inlet at aortic root level and 4 outlets corresponding to the three epiaortic vessels (EV) and the descending aorta (DE) that is connected with iliac bifurcation (IL). The first active component is a speed-controlled piston pump to impose a flow profile at the inlet [2]. The pump profile was set to reproduce the heart function during both healthy and failure condition. The failure condition is modeled with a reduction of 70% in stroke volume with respect to the healthy condition (70 ml) of the patient [3]. The second active element is a centrifugal pump, connected with aorta below the iliac bifurcation, and responsible for the ECMO support. The passive components are adopted to set the pressure waveforms inside the aortic phantom, and they consist in pinch valves and air-filled chambers. The air level and the pinch rod height values were tuned to obtain the patient aortic pressure (82-125 mmHg) during healthy heart functionality. Five different centrifugal pump speeds of extracorporeal support (v_1=1000 rpm, v_2=1500 rpm, v_3=2000 rpm, v_4=2500 rpm, v_5=3000 rpm) were imposed during the experiments at heart failure (hf) conditions. EV, DE at the isthmic level and below IL flows were evaluated with flow transducers and compared with the healthy conditions (ht) as well as the left ventricle work (Lw) and the pressure at the level of the ascending aorta (Ap).

Results

The heart failure test conditions were characterized by a reduction of left ventricle work (-95%) related to a flow (-50%) in aorta outlets and pressure decrease (-70%), as reported in Table 1. The increase of centrifugal pump speed leads to two different phenomena:
1. flow reversal at the isthmic region of DE, at low ECMO flows ($v_1 - v_2$), denoting the establishment of the watershed zone [4] at this level.
2. Flows restoration at healthy values in the EV and IL, when the ECMO support increases ($v_3 - v_4$).
ECMO speeds are also related to a linear increase in left ventricle afterload (Ap). The work requested by left ventricle increases linearly until the ECMO speed is less than 2000 rpm. Beyond this value, the work increase becomes highly non-linear.

	ht	hf	v_1	v_2	v_3	v_4	v_5
EV	4.7	2.5	3.4	4.2	4.6	5.6	6.6
DE	4.2	2	0.1	-1.9	-3.5	-4.7	-6
IL	4.2	2	2.5	3	4	5.7	7
Lw	1.1	0.06	0.07	0.09	0.1	0.3	0.6
Ap	100	30	55	80	102	130	150

Table 1: Experiment results: Br, Des and Il flows (l/min), Lw (W) and AP (mmHg) at healthy, failure and ECMO conditions.

Discussion

With this study, the effectiveness of the in vitro approach for ECMO-patient fluid dynamic interaction modeling with a mock loop was demonstrated with success. The results confirmed the effectiveness of ECMO in the restoration of blood flows. Nevertheless, it was also demonstrated that high ECMO speeds produce a left ventricle overload and work augmentation, interfering with the process of heart recovery

References

1. Abrams et al, J Am Coll Cardiol 2014
2. Vignali et al, Proc. of AIMETA Congress, 2019.
3. Boccadifuoco et al, Cardiov Eng Tech 2018.
4. Hoeper et al, Circ 2014

Acknowledgements

This work was supported by 3D Virtual baby heart from the Italian Ministry of Health funding.

PATIENT-SPECIFIC RECONSTRUCTION OF CORONARY ARTERY STENTS WITH LUMENS BASED ON OPTICAL COHERENCE TOMOGRAPHY

W. Wu[1], B. Khan[1], M. Sharzehee[1], S. Zhao[1], S. Samant[1], A. Panagopoulos[1], J. Makadia[1], F. Muhammad[1], F. Migliavacca[2], G. A. Dubini[2], C. Chiastra[3], I. S. Chatzizisis[1]

1. Cardiovasclar Biology and Biomechanics Laboratory, Cardiovascular Division, University of Nebraska Medical Center, Omaha, Nebraska, USA; 2. LaBS, Dept. Chemistry, Materials and Chemical Engineering "Giulio Natta", Politecnico di Milano, Italy; 3. PoliTo^{BIO}Med Lab, Dept. Mechanical and Aerospace Engineering, Politecnico di Torino, Italy

Introduction

The structural morphology of stents (e.g. expansion, lumen scaffolding, strut apposition), and the local hemodynamic environment after stent deployment in coronary arteries are key determinants of procedural success and subsequent clinical outcomes. High-resolution intracoronary imaging has the potential to enable the geometrically correct 3D reconstruction of coronary stents. The aim of this work was to present a novel algorithm for 3D stent reconstruction of coronary artery stents by OCT and angiography, and test experimentally its accuracy, reproducibility, clinical feasibility and ability to perform CFD studies.

Methods

Our method has the following steps: creation of patient-specific silicon vessel models and stenting, lumen reconstruction by OCT and angiography (Fig.1), stent strut segmentation on OCT images, packaging, rotation and straightening of the segmented struts, and planar unrolling of the segmented struts, planar stent wireframe reconstruction, rolling back of the planar stent wireframe to the 3D reconstructed lumen, and stent volume reconstruction. We tested the accuracy and reproducibility of our method in stented silicone models using micro computed tomography and stereoscopy as reference. The clinical feasibility and CFD studies were performed in clinically stented coronary bifurcations.

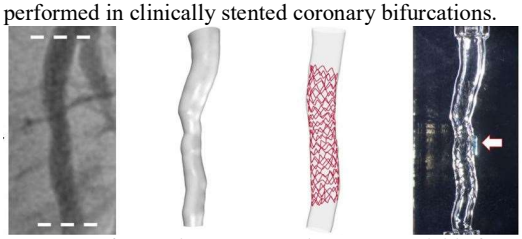

Fig. 1: Left to right: angiography, CAD model before stenting, OCT-reconstructed lumen after stenting and stereoscopy images of the final stented models.

Results

Our experimental and clinical studies showed that our proposed algorithm can reproduce the complex stent configuration in space with high precision and reproducibility (Fig.2). Furthermore, our studies showed that the algorithm is feasible in clinical cases with stents deployed in diseased, bifurcated coronary arteries, enabling CFD studies (e.g. time averaged wall shear stress, TAWSS,) to assess the hemodynamic environment (Fig. 3).

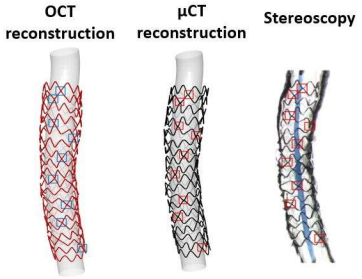

Fig.2: Qualitative experimental validation of stent reconstruction method against μCT and stereoscopy.

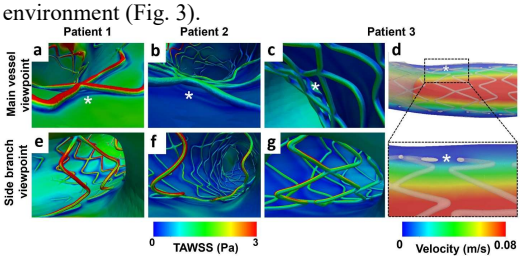

Fig. 3:Three patient cases: (a-c) TAWSS around stent struts, (b-c) the shear stress distribution around malapoposed struts. In (d) longitudinal section showing the low velocity between the lumen and malapposed struts (white asterisks). (e-g) TAWSS distribution at the ostium of the side branch.

Discussion and conclusions

By applying 2D stent wireframe reconstruction and combining the validated lumen reconstruction method, this work overcomes several limitations of previous studies in the field and advances the current state-of-the-art. Notably, the high accuracy of our algorithm was consistent across different stent designs and diameters. We propose a new method that enables accurate, reproducible, time-efficient and clinically feasible 3D reconstruction of coronary artery stents. Our method coupled with patient-specific CFD studies can facilitate stenting optimization, training in stenting techniques, and stent research and development.

Acknowledgements

The study was funded by the National Institutes of Health (R01 HL144690) and Dr. Vincent Miscia Cardiovascular Research Fund.

EFFECT OF MULTIPLE PLAQUES ON THE HAEMODYNAMICS PERFORMANCE IN PERIPHERAL ARTERY

Jiling Feng, Danyang Wang

Department of Engineering, Manchester Metropolitan University, UK

Introduction

Peripheral artery disease (PAD) strikes 202 million men and women worldwide, and its prevalence has a significant growth with the increase of age (Benjamin et al. (2019)). Atherosclerotic plaques build-up inside the arterial wall that diminishes the blood supply to lower extremities is the leading cause of lower limb PAD. Two significant clinical symptoms of lower limb PAD are claudication and critical limb ischemia, which may even lead to ulceration and gangrene of the toes or feet. Besides, patients diagnosed with PAD have an increased risk of cardiovascular morbidity and mortality compared with those without PAD.

Several experimental studies showed that the components of femoral plaques and carotid plaques are different, femoral plaques demonstrate higher calcium and lesser cholesterol concentrations than carotid plaques. Computational studies analysis of the mechanism of atherosclerotic plaques,, including Computer fluid dynamics (CFD) modelling and Finite element (FE) simulations, indicate that changes in the geometry and material property of a model could affect its mechanical behaviour.

The anatomic geometries of atherosclerotic plaques influence the hemodynamic features of the blood flow, which in turn affects the mechanical behaviour of the plaques. Recent studies of 3D FSI simulations, which couples computational fluid dynamics with structure mechanics, have been implemented for coronary, carotid and femoral atherosclerotic artery models.

To the best of author's knowledge, FSI simulations concerning multiple plaques in a realistic model were not reported for human femoral arteries. In this paper, we aim to discuss biomechanical characteristics for an atherosclerotic femoral artery in three models: blood coupling with artery wall and calcified plaque; blood coupling with artery wall and lipid plaque; blood coupling with artery wall, calcified and lipid plaques. Appropriate hyperelastic material parameters obtained from experimental studies are adopted to the femoral arterial wall and plaques. A one-way FSI coupling is employed for patient-specific stenosed femoral artery models. Pulsatile boundary conditions are used in this study.

Methods

A 45 mm-long left femoral artery model is reconstructed based on these CT scans, two types of plaque are identified, shown in Fig. 1. Three dimensional fluid-structure geometry, including lumen, lipid plaque, calcified plaque and arterial wall were constructed for the fluid-structure interaction modelling. The femoral artery wall is assumed to be nonlinear, homogenous and hyperelastic material. The strain energy function W of Mooney–Rivlin constitutive model is employed.

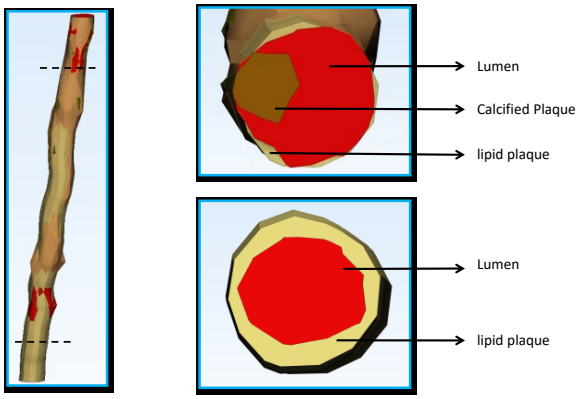

Figure 1 Two types of plaques, lipid and calcified plaques, were identified based on CT scan from a diseased peripheral artery.

Results

It was observed from the simulation results that oscillation of WSS is occurring in the healthy downstream region in the lipid-only model. The pressure around the plaques in the two-plaque model is lower than that in the corresponding one-plaque models due to the reduction of blood flow domain, which consequently diminishes the loading forces on both plaques. Therefore, we found that stress acting on the plaques in the two-plaque model is lower than that in the corresponding one-plaque models.

Discussions

The results from the simulation indicated that new plaque might be further accumulated around the calcified plaque compared with the lipid plaque, while initiation of new plaques may happen in the healthy area behind the lipid plaque. The structure analyses indicate that maximal stress principally sits in the plaque shoulder, where it is commonly accepted as the plaque rupture location.

References

1. Benjamin EJ, Muntner P, Bittencourt MS, American Heart Association. Circulation 139 (10):e56– e528, 2019.

Acknowledgements

This work is supported by EPSRC grant (EP/R001901/1).

3D VARIATIONAL DATA ASSIMILATION OF 4D FLOW MRI IN COMPUTATIONAL HEMODYNAMICS OF INTRACRANIAL ANEURYSM

Riccardo Munafò (1), Simone Saitta (1), Alessandro Caimi (1), Augusto Sanches (2), Thomas Liebig (2), Alberto Redaelli (1)

1. Department of Electronics Information and Bioengineering, Politecnico di Milano Milan, Italy; 2. Institute of Neuroradiology, University Hospital LMU Munich, Germany.

Introduction

Intracranial aneurysm (IA) rupture is the most common cause of subarachnoid hemorrhage (SAH), a life-threatening neurovascular emergency with significant mortality [1]. Accurate hemodynamic analysis may improve IA risk assessment and treatment-planning [2]; here we propose a novel approach combining computational fluid dynamics (CFD), which has been proved valuable for simulating flow in IA [2], and 4D flow magnetic resonance imaging (MRI), a noninvasive technique that enables measurements of blood flow [3]. Both techniques still have limitations. In this study, we implemented and evaluated a data assimilation (DA) approach to combine CFD with 4D flow MRI, enabling super-resolution and noise reduction in 4D flow measurements.

Methods

A 3D variational data assimilation (3DVar) algorithm was developed in *Fenics* through the *dolphin-adjoint* library [4]. A finite elements framework was used to simulate blood flow in an internal carotid artery saccular aneurysm model, obtained from 4D MRI data. Velocity profiles extracted from 4D flow at the peak flow rate and pressure zero were applied as inlet and outlet boundary conditions (BCs), respectively. The weak form of Navier-Stokes model was modified by adding a source term g which acts as control parameter for the DA. This source is multiplied by a function χ, which maps spatially the velocity measurements on the computational mesh (1).

$$\left(\frac{\delta u}{\delta t}, v\right)_\Omega + \left((u\nabla)u, v\right)_\Omega - (p, \nabla v)_\Omega + (\nu\nabla u, \nabla v)_\Omega = (\chi g, v)_\Omega$$
$$(\nabla u, q)_\Omega = 0 \qquad (1)$$

with v and q being suitable test functions and Ω the domain. The source g is calibrated iteratively (via a gradient descent algorithm) such that it minimizes a loss function J (2) which represents the mismatch between the model results (u, velocity) and the measurements (u_{obs}) extracted from 4D MRI data.

$$J = \|\boldsymbol{u} - \boldsymbol{u}_{obs}\|_{L_2(\Omega)} \qquad (2)$$

For comparison, a 4D flow guided-CFD simulation was performed in *Simvascular* [5] on a finer mesh. Prior to 3DVar, 4D flow data were denoised following the approach described in [6].

Results

In *fig. 2* a comparison of velocity magnitudes obtained with 4D flow, High-resolution CFD and 3DVar is reported. In 3DVar, a good similarity can be appreciated with respect to the measurements, in particular in the high velocity flow region, where the SNR in 4D flow data is higher. The Mean Squared Error (MSE) of velocity reported in the figure confirmed the accuracy improvement of 3DVar with respect to the High-resolution CFD.

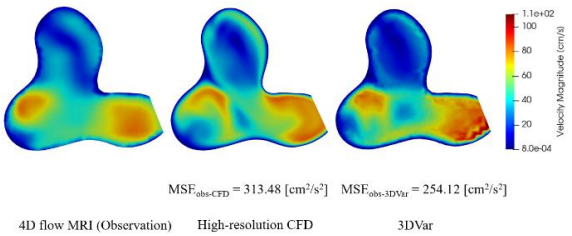

Figure 1: Velocity magnitude colour maps on a transversal plane within the aneurysm. MSE of velocity between Observation and High-resolution CFD and between Observation and 3DVar is showed.

Discussion

The novelty of this study lies in the formulation of the data assimilation algorithm. Contrastingly from previous work [7], the assimilation of the 4D flow measurements was carried out across the whole volume where observations were available, controlling a fictitious source term g added to the Navier-Stokes formulation. This approach allowed us to obtain a good matching between 4D flow data and 3DVar within the region of interest even on a coarse mesh. Data assimilation has proved to be a valid method to increase the CFD accuracy in the assessment of blood flow in IA.

References

[1] T. Steiner *et al., Cerebrovasc. Dis.*, 2013.
[2] K. Valen-Sendstad *et al., Am. J. Neuroradiol.*, 2014.
[3] M. Markl *et al., J. Magn. Reson. Imaging*, 2012.
[4] S. K. Mitusch *et al., J. of Open Source Software*, 2019.
[5] A. Updegrove *et al., Ann. of Biomedical Engineering*, 2017.
[6] V. M. Pereira *et al., J. Neurointerv. Surg.*, 2015.
[7] S. W. Funke *et al., Int J Numer Meth Biomed Engng*, 2019.

3D DIRECTIONAL FILTERS TO IMPROVE COLLAGEN SECOND HARMONIC GENERATED IMAGES

Zeineb Nejim (1), Laurent Navarro (1), Pierre Badel (1), Claire Morin (1)

1 Mines Saint-Étienne, Univ Lyon, Univ Jean Monnet, INSERM, U1059 SAINBIOSE, Centre CIS, 42023 Saint-Étienne, France

Introduction

Quantification of the aortic wall architecture, and especially, in Ascending Thoracic Aortic Aneurysms (ATAA) has been in the center of many cardiovascular researches. Those studies (e.g. [1]) aim to understand the behavior of the aortic microstructure composed mainly of collagen and elastin fibers. In the literature, researchers succeeded in extracting some in-plane, hence 2D, information (orientation and waviness) of the collagen fibers but the third dimension is still overlooked. To deal with this issue, the most widely used imaging modality is multiphoton microscopy, which allows capturing a stack of 2D Second Harmonic Generated (SHG) images of the collagen fibers to form one in 3D. However, those acquisitions may present some artifacts such as shadows and even some black regions due to dust or air, and the quality of the signal in the out-of-plane direction is very poor compared to in-plane, making 3D analysis a challenge. In the present study, we propose a method to correct those artifacts and improve the third dimensional component.

Methodology

We disposed of many stacks of SHG images capturing collagen fibers of the adventitia layer of human aortic wall [2]. In order to deal with the artifacts appearing in our images, a morphological method was proposed, based on directional filters inspired from the *MorphoLibJ* plugin in ImageJ. The proposed method consists in building a filter bank. Each filter consists in a segment of length L and value 1 oriented in a direction d, (figure 1). As a start, we applied these filters in 2D (i.e. successively to every image of our stack), (figure 2). A pixel in the output image takes the maximum value of the pixels at same coordinates in all images resulting from the application of the filter bank.

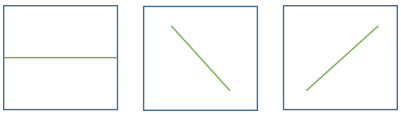

Figure 1: Example of a filter bank with 3 filters (d=3).

Then, in order to improve the entire stack, we proposed to extend this directional filter in 3D. We introduced 3D filters which are tilted with respect to the image plan. We fixed the tilt angles to be 1.5°, 3° and 4.5°. Then the steps are the same as in 2D.
The dimension of the filter in the image plan may vary with respect to the artifacts on the image. The bigger the black region is, the wider the filter is. Regarding the depth of the 3D filter, it is determined by the segment length and the maximum chosen tilt angle.

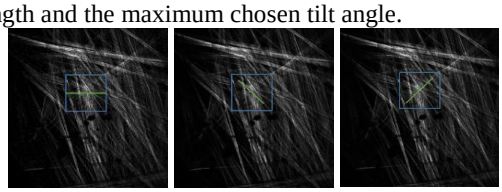

Figure 2: The filter is placed on a sub-image and the mean of their product is computed.

Results and discussion

The proposed methods showed good results to correct the artifacts as can be seen in figure 3, where obvious continuity of fibers is recovered. The choice of the length of the filter is very important to reconstruct the fibers in the presence of big black spots.

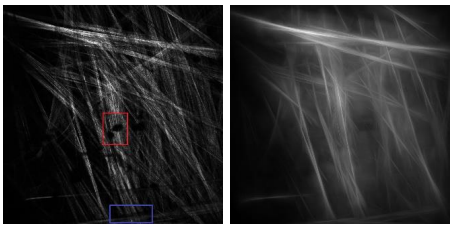

Figure 3: Result of the planar filtering where the black spot (in red) and the shadows (in blue) disappeared.

Besides, the 3D filtering has a good contribution to the improvement of analysis in the third dimension, with visualisation of out-of-plane fiber direction, (figure 4).

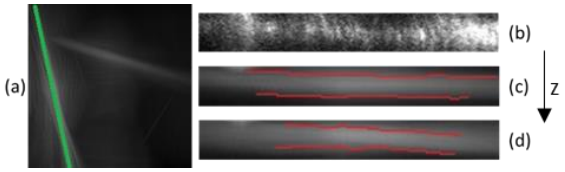

Figure 4: (a): portion of an image where a focus is put on the green fiber. (b): original noisy image. (c): results after a 2D filtering where we cannot tell if the fiber is tilted. (d): result after a 3D filtering where we can tell that the fiber is tilted.

Future work will focus on improving even more those images by deleting the blur introduced by the directional filters and by the used microscope.

References

1. Rezakhaniha et al, J Biomech Model Mechanobiol, 11:461-473, 2012.
2. Cavinato et al, J Mech Behav Biomed Mater, 74:488-498, 2017.

CHARACTERISATION OF HEALTHY AND DISEASED HUMAN CAROTID ARTERIES USING DIFFUSION TENSOR MAGNETIC RESONANCE IMAGING

Brooke Tornifoglio (1,2), Alan J. Stone (1,2), Christian Kerskens (1,3), Caitríona Lally (1,2,4)

1. Trinity Centre for Biomedical Engineering, Trinity Biomedical Sciences Institute, Trinity College Dublin, Ireland; 2. Department of Mechanical, Manufacturing and Biomedical Engineering, School of Engineering, Trinity College Dublin, Ireland; 3. Trinity College Institute of Neuroscience, Trinity College Dublin, Ireland; 4. Advanced Materials and Bioengineering Research Centre (AMBER), Royal College of Surgeons in Ireland and Trinity College Dublin, Ireland

Introduction

Changes in the arterial vessel microstructure are implicated in the progression of atherosclerosis [1] and ultimately plaque rupture – one of the leading causes of ischemic stroke [2]. The formation of specific atherosclerotic plaque features is believed to be indicative of plaque stability [1]. Diffusion tensor imaging (DTI) is commonly used to evaluate various tissue microstructures and has previously been shown to be sensitive to specific microstructural changes in arterial tissue [3,4]. This study investigates this sensitivity within human arteries with an aim to non-invasively characterise healthy and diseased regions.

Methods

Whole carotid artery sections (including the bifurcation and proximal sections of the common, internal and external) were isolated from embalmed cadavers; cardiovascular disease was not implicated as the cause of death in any subjects (aged 70-103). All samples (n=8) were cleaned of connective tissue and scanned in a 7T Bruker BioSpec system with a 3D DTI sequence with the following parameters: TE/TR: 17.682/1000 ms; image size: 96 x 96 x 96, field of view: 30 x 30 x 30 mm, isotropic resolution 312.5 x 312.5 x 312.5 um, b-values: 0, 800 s/mm^2, 10 b-directions, gradient duration: 3.8 ms, gradient separation: 8.802 ms, and acquisition time: 28 hours and 9 minutes. Imaging data was denoised and Gibbs ringing correction performed prior to the calculation of fractional anisotropy (FA) and mean diffusivity (MD) maps. Histology was used to inform the definition of healthy and diseased regions on b=0 s/mm^2 images of all subjects; any region that differed from healthy arterial wall was classified as a diseased region. Mean FA and MD values were extracted for each region. Regions of low SNR were excluded from regional analysis.

Results

Figure 1 (a, c) shows the mean FA and MD values for healthy tissue in the common, bifurcation, internal and external arteries in all subjects (n=8); no significant differences were found. The mean FA in healthy and diseased regions are presented in Figure 1 (b); the FA of healthy tissue, 0.0993 ± 0.018, is significantly (p=0.0405) lower than that of diseased tissue, 0.1088 ± 0.015. Additionally, the mean MD of healthy tissue is significantly higher (p=0.0002) than the MD in diseased regions across all samples, 0.001232 ± 0.0001 and 0.001121 ± 0.00009 mm^2/s, respectively.

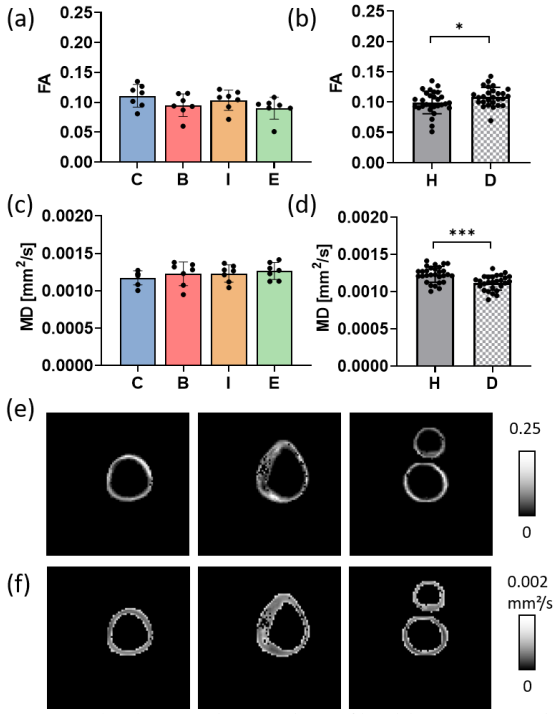

Figure 1: (a, c) FA and MD values of healthy regions in the common (C), bifurcation (B), internal (I) and external (E) arteries. (b, d) FA and MD values of healthy and diseased regions, (p=0.0405, ***p=0.0002). (e, f) FA and MD maps for various cross sections highlighting variations in values regionally.*

Discussion

This study investigates the sensitivity of DTI to arterial tissue microstructure in human carotid arteries. Across eight specimens, no significant differences were seen in FA or MD between healthy anatomical regions. When comparing healthy to diseased regions, there were significant differences in both FA and MD. Future work will focus on histological categorisation of these diseased regions to gain further insight into the ability of DTI metrics to stratify atherosclerotic disease.

References

1. Holm et al, J Intern Med, 287:493-513, 2020
2. Hyun Joh, Cho, Lancet, 8(5):E625-E626, 2020
3. Shahid et al, Phys Med Biol, 62:8850-8868, 2017
4. Tornifoglio et al, Sci Rep, 10:20718:1-12, 2020.

Acknowledgements

We thank the Department of Anatomy at the Royal College of Surgeons for the cadaveric tissue used in this study. This work was funded by the European Research Council under the European Union's Horizon 2020 research and innovation programme (grant agreement No. 637674).

A NOVEL TOOL FOR THE ASSESSMENT OF ENDOCARDIAL DEFORMATION STARTING FROM 3D ECHOCARDIOGRAPHY

Matteo Frigelli (1,2), Francesco Sturla (1,2), Michele Citarella (1), Lorenzo Menicanti (1), Serenella Castelvecchio (1), Emiliano Votta (2,1)

1. IRCCS Policlinico San Donato, San Donato Milanese, Italy; 2. Politecnico di Milano, Milan, Italy

Introduction

3D echocardiography was recently exploited to assess left ventricle (LV) function *in vivo*, including regional longitudinal and circumferential strains of the LV endocardium as quantifiable through 3D speckle-tracking (3DSTE) [1]. However, their entity directly depends on the LV longitudinal axis, which is manually defined by the operator. Minimum principal strain (ε_{min}) analysis has emerged as a valid alternative to overcome these limitations, given its independence from the reference frame [2]. We exploited this novel strategy to investigate local endocardial LV strains in five healthy subjects and in five post-ischemic patients submitted to LV surgical ventricular reshaping (SVR) [3], analyzed before SVR and at 6-month follow-up.

Methods

3D full volume LV echocardiography was acquired and processed off-line in 4D LV TomTec software (TomTec Imaging Systems GmbH, Germany). The endocardium was automatically tracked over the cardiac cycle and extracted as a dynamic triangulated mesh. LV structural simulation was run in Abaqus/Explicit (SIMULIA, Dassault Systémes, USA), imposing at each node the kinematics exported from 3DSTE. The value of ε_{min}, and the principal direction associated to ε_{min} were stored at end systole for each triangle. Based on principal directions, we quantified the angle of contraction α [4], ranging between 0° (circumferential contraction) and 90° (longitudinal contraction), as in Figure 1. Endocardial LV surface was divided into basal, mid and apical segment [1], exploiting papillary muscles position in the 3D dataset as anatomical landmarks. ε_{min} and α distributions were analyzed based on whether the corresponding triangular element fell in the basal, mid, or apical region.

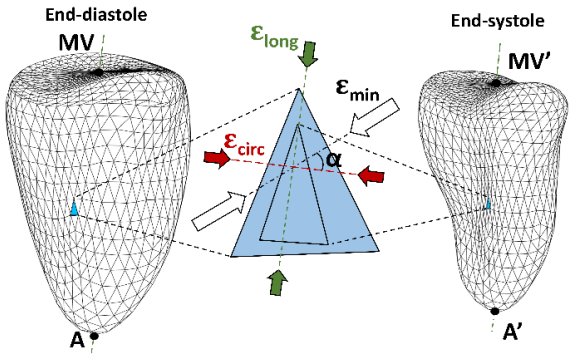

Figure 1: ε_{min} and α computed for a single triangle.

Results

Before SVR, post-ischemic patients showed a global ε_{min} impairment (median values -13% vs -34%, p=0.008) if compared to the control group, paralleled by increased α value, in particular in the mid-apical region (54° vs 16°, p=0.016), as shown in Figure 2. Six months after SVR, LV global ε_{min} improved up to -20%, in particular in the basal region, with ε_{min} changing from -17% (pre-SVR) to -22% (post-SVR). The angle of contraction α slightly decreased to 35°.

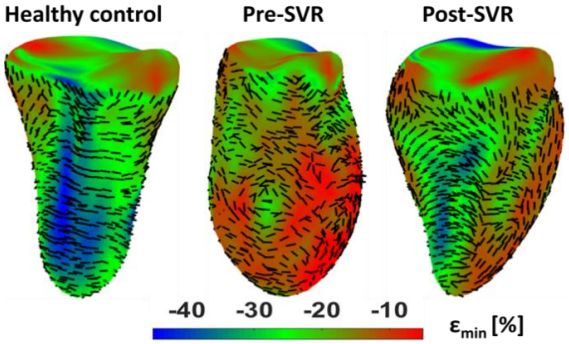

Figure 2: ε_{min} magnitude and directions at end-systole.

Discussion

By complementing the standard off-line analysis with a conceptually simple and very time efficient finite element simulation (approximate time expense 3-4 min), we obtain major extra information: i) a localized, i.e., pointwise, quantification of LV deformation, which allows to deepen the entity of endocardial contractility within the single LV sector; ii) extraction of both LV minimum principal strain and directions, with the latter potentially mimicking the local myofibers orientation [2]. This analysis can be useful, in the single clinical scenario, to pinpoint the severity of post-ischemic dysfunction and to support prognosis in patient that underwent surgical intervention.

References

1. Lang RM et al, J Am Soc Echocardiogr, 28:1-39, 2015.
2. Satriano et al, Int J Cardiovasc Imaging, 33:1970-1992, 2017.
3. McConnell et al, Coronary Artery Disease, 15:91-98, 2004.
4. Satriano et al, J Am Soc Echocardiogr, 3:385-393, 2019.

Acknowledgements

IRCCS Policlinico San Donato is a clinical research hospital partially funded by the Italian Ministry of Health.

CARDIAC CINE-MRI PROCESSING: FROM 3D SHAPE AND MOTION RECONSTRUCTION TO COMPUTATIONAL HEMODYNAMICS

Marco Fedele(1), Ivan Fumagalli(1), Giorgia Pase(2), Christian Vergara(3), Luca Dede'(1), Sonia Ippolito(4), Roberto Scrofani(5), Alfio Quarteroni(1,6)

1. MOX – Dipartimento di Matematica, Politecnico di Milano, Italy; 2. Bernoulli Instituut, Rijksuniversiteit Groningen, Netherlands; 3. LaBS – Dipartimento di Chimica, Materiali e Ingegneria Chimica "Giulio Natta", Politecnico di Milano, Italy; 4. Radiology Unit, L. Sacco Hospital, Milan, Italy; 5. Cardiac Surgery Unit, L. Sacco Hospital, Milan, Italy; 6. Institute of Mathematics, École Polytechnique Fédérale de Lausanne Switzerland (Professor Emeritus)

Introduction

Cardiac MRI is nowadays the gold-standard image acquisition procedure to assess the cardiac function and, in particular, the left ventricle function. In this context, cine-MRI is characterized by a very accurate time resolution that well captures the motion of the ventricle. On the contrary, concerning the spatial resolution, the sole 3D data available is the so-called short-axis (SA) view, that lacks accuracy along the left ventricle long-axis. On the contrary, long-axis (LA) views are usually acquired only for few 2D slices. In order to accurately reconstruct the 3D left ventricle shape and motion, information of the various views should be in some way mixed. However, in clinical practice, 3D measures (e.g. volumes) and their temporal evolution are usually computed only from SA view by using mathematical formula based on simplified assumption on the ventricular shape.

In this work, we first propose a way to create artificial images mixing information from all the cine-MRI views. Then, starting from these images, we propose a complete pipeline to accurately reconstruct the 3D left ventricle shape and motion. Finally, we exploit these geometric and functional data to perform patient-specific computational hemodynamics simulations able to enrich the standard clinical outputs of an MRI exam.

Methods

The pipeline to reconstruct the shape and motion of the left ventricle consists, briefly, in the following steps:

1. create a richer 3D artificial image with a homogeneous resolution in each direction, interpolating the cine-MRI data from SA and LA views.
2. segment the endocardium at each temporal instant using a semi-automatic segmentation algorithm [1].
3. reconstruct the motion of the ventricle by registering the end-systolic reference surface to all the other instants [2].

In order to perform numerical simulations, we extend the reconstructed geometry and motion to the left atrium and the ascending aorta by taking advantages of a template geometry that includes the cardiac valves. In particular, the motion is extended to the template geometry properly solving a Laplace-Beltrami problem in order to recover a realistic motion of the atrium [3,4]. Then, hemodynamics simulations are performed solving with the finite element method the Navier-Stokes equations in an Arbitrary Lagrangian Eulerian (ALE) framework, where the motion of the computational domain is the one recovered from the artificial cine-MRI and the valves are treated using a resistive approach [4,5].

Results

The proposed methods are applied to a set of patients enrolled by "Ospedale L. Sacco" in Milan, including both healthy and pathological cases. Results show the importance of using all the available cine-MRI views to improve the accuracy of the reconstruction and, consequently, to enrich the classical clinical outputs by providing more accurate geometric measures (e.g., volumes, myocardial thickness) and hemodynamics indicators coming from image-based patient-specific simulations.

Discussion

We propose a complete pipeline to perform image-based hemodynamics simulations of the left-ventricle in healthy and pathological scenarios. The accuracy of the shape and motion reconstruction and the possible hemodynamics indicators measurable from numerical simulations are of promising interest for clinical applications, like the study of myocardial pathologies (e.g., hypertrophic or dilated cardiomyopathy) or mitral valve pathologies.

References

1. A. Fetzer et al, Proc MICCAI IMIC Interact Med Image Comput, 1:11, 2014.
2. S. Klein et al, IEEE Transactions on Medical Imaging, 29(1):196–205, 2009.
3. Fedele et al, Int J Numer Meth Biomed Engng, e3435, 2021.
4. I. Fumagalli et al, Comp Biol Med, 123:103922, 2020.
5. M. Fedele et al, Biomech Model Mechan, 16(5):1779–1803, 2017.

Acknowledgements

This project has received funding from the European Research Council (ERC) under the European Union's Horizon 2020 research and innovation programme (grant agreement No 740132, IHEART 2017-2022, P.I. A. Quarteroni).

TOWARDS INCLUDING THE INTRALUMINAL THROMBUS IN PATIENT-SPECIFIC MODELS OF AAAS BASED ON 4-D ULTRASOUND

Arjet Nievergeld (1,2,3), Esther Maas (2,3), Joerik de Ruijter (3), Frans van de Vosse (1,3), Marc van Sambeek (2), Richard Lopata (3)

1.Eindhoven MedTech Innovation Center, the Netherlands; 2. Catharina hospital Eindhoven, the Netherlands; 3. Eindhoven University of Technology, the Netherlands

Introduction

An abdominal aortic aneurysm (AAA) is a localized dilatation of the aorta, which in case of rupture has a mortality rate of 80%. Current clinical guidelines of intervention are based on AAA diameter, which has been proven to be an inadequate criterion. Biomechanical models can improve the prediction of rupture risk in a more patient-specific way, using e.g. CT or ultrasound (US) imaging [1, 2]. US is safer compared to CT and adds temporal information for mechanical characterization of the AAA. It is hypothesized that intraluminal thrombus (ILT) lowers the peak wall stress [3]. Therefore, it is needed to characterize the ILT and include it in patient-specific models. US imaging of the ILT is challenging considering the low contrast. The objective of this study is to determine the patient-specific geometry of the AAA wall, ILT and lumen in 4-D US images for future finite element modelling.

Methods

4-D US images of 30 AAA patients, known to have an ILT, were segmented using an automatic segmentation method. The inner vessel wall was segmented using a slice by slice star-Kalman algorithm [4]. The lumen-thrombus interface (LTI) was determined combining the Star-Kalman algorithm with a 3D-snake [5]. The resulting US-based geometries were compared with CT, calculating the similarity index (SI) and the median Hausdorff distance (HD) per slice [1,6]. 6 automatically segmented AAA geometries were also compared with manual segmentations of 2 observers.

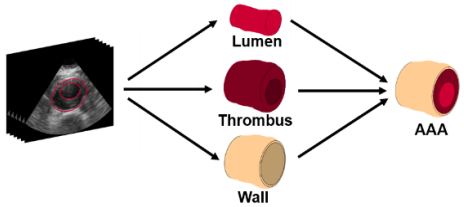

Figure 1: Obtaining 3-D AAA geometry by segmenting lumen, thrombus and wall from 4-D ultrasound

Results

Figure 2 shows the SI and HD, comparing the US-based geometries with CT-based geometries. The inner vessel wall (vessel) and LTI (lumen) have a median SI of 0.91 and 0.78 respectively. The median HD of the inner vessel wall is 4.6 mm and 6.6 mm for the LTI. As can be seen in Figure 3, the median SI for the automatically segmented geometry is 0.87, compared to 0.89 and 0.85 for observers 1 and 2. The median HD is 4.6 mm compared to 4.0 mm and 6.2 mm for the observers.

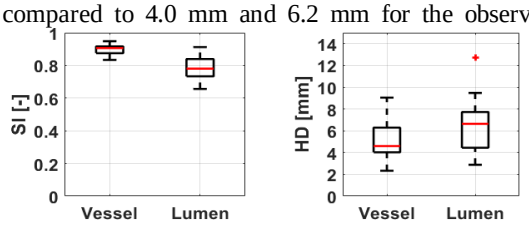

Figure 2: SI and median HD for proposed automatic segmentation method compared with CT

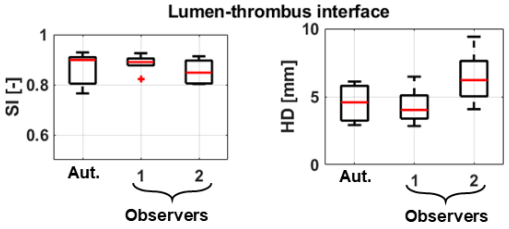

Figure 3: SI and median HD of the LTI comparing the proposed automatic segmentation method (Aut.) and manually segmented LTI with CT-based geometry

Discussion

Despite the low imaging contrast, an automatic segmentation algorithm was developed to successfully extract the geometry of the AAA including the lumen, thrombus and vessel wall. It was also shown that the HD of the automatically segmented geometries were lower compared to the ones manually segmented by observer 2. Future developments in US and improvements in image quality would further improve the success-rate of the segmentation algorithm. The obtained geometry will be used in combination with blood pressure and speckle tracking [1], to determine the mechanical properties of the thrombus and to create a patient-specific mesh of the AAA. This will allow to evaluate the effect of thrombus on stress distribution in the aortic wall and to assess the rupture risk in a patient-specific way.

References

1. Van Disseldorp et al, Eur J Vasc Endovasc Surg, 59: 81-91, 2020
2. Kok et al, J Vasc Surg 61: 1175-1185, 2015
3. Inzoli et al, Eur J Vasc Surg, 7:667-674, 1993
4. Abolmaesumi et al, IEEE Trans Robot, 18: 11-23, 2002
5. Kass et al,. Int J Comput Vis, 1:321–331, 1988.
6. Rote et al, Inform Process Lett, 38: 123-127, 1991

OPTIMIZATION OF MICROCT AND CONTRAST-ENHANCED MICROCT FOR CARDIOVASCULAR APPLICATIONS

Lisa Leyssens (1,2), Maïté Pétré (1,2,3), Greet Kerckhofs (1,2,4,5)

1.iMMC, UCLouvain, Belgium; 2. IREC, UCLouvain, Belgium; 3. Dept. Mechanical Engineering, KU Leuven, Belgium; 4. MTM, KU Leuven, Belgium; 5. Prometheus, Division of Skeletal TE, KU Leuven, Belgium

Introduction

Atherosclerosis is a leading cause of death. To better understand and treat this disease, it is important to evaluate the changes in blood vessel wall microstructure during disease development and to link these structural changes to changes in mechanical properties. Microfocus X-ray computed tomography (microCT) is a powerful technique for assessing, in a non-invasive way, the 3D microstructure of complex materials. To achieve sufficient X-ray attenuation in soft tissues, contrast-enhancing staining agents (CESAs) containing high atomic number molecules are combined with microCT. This technique is referred to as contrast-enhanced microCT (CE-CT). Monolacunary and Hafnium-substituted Wells-Dawson polyoxometalate (Mono-WD and Hf-WD POM respectively) have shown their potential for non-destructive staining of kidney and soft skeletal tissues [1]. Additionally, we have shown with planar biaxial testing that these POMs have a negligible effect on the mechanical properties of the tissue. In this study, both CESAs were evaluated and compared for their staining potential of the porcine aorta. Other types of blood vessels were imaged to show the ability of CE-CT to highlight the vessel wall microstructure, including the different wall layers and their content in elastin and collagen. The novelty of this study lies in the high-detailed comparison of the microstructure of different types of blood vessels (healthy and diseased) in a non-invasive way.

Materials, methods and results

Samples of 1x1cm of porcine aorta were fixed. A control scan and scans at different time points after staining with Mono-WD POM or Hf-WD POM were performed. The grayscale value was measured at different locations inside the tissue (x). This data was then fit to an exponential decay equation [2]:

$$I = I_0 + (I_{max} - I_0)\left(1 - e^{-kt}\right) \qquad (1)$$

where I_0 is the grayvalue of the control sample, I_{max} is the grayvalue after complete staining, and t is the staining time. From this experiment, we concluded that Hf-WD POM stains with much higher intensity and allows a better contrast between the different vessel wall layers while Mono-WD POM stains less bright and more homogeneously but diffuses much faster than Hf-WD POM (Fig. 1).

The optimized staining parameters were then applied to other types of porcine blood vessels (elastic artery, muscular artery, and vein) and allowed to observe the differences in the 3D microstructure of the vessel wall in these tissues. We also showed important species-related (porcine, rat, human) differences in the vessel wall microstructure of the aorta, which can be related to changes in functional behavior. From the data mentioned above, 3D morphometrical parameters can be obtained without altering the native structure of the tissue. Fig. 2 shows a CE-CT based region of interest of a segmented rat aorta from which the elastin volume fraction and elastic fiber waviness and separation can be determined. Finally, healthy and atherosclerotic human femoral arteries were compared. Plaques and onsets of calcifications can be identified and parameters such as calcification volume fraction can be quantified.

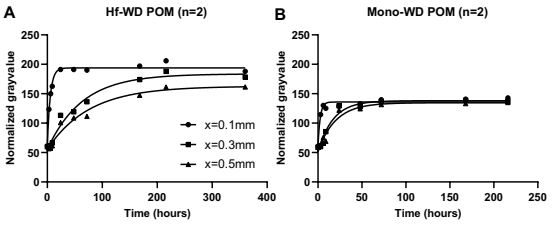

Fig. 1: Normalized grayvalue in function of time for different locations inside the tissue and fitted with the curve from equation 1 for (A) Hf-WD PM and (B) Mono-WD POM.

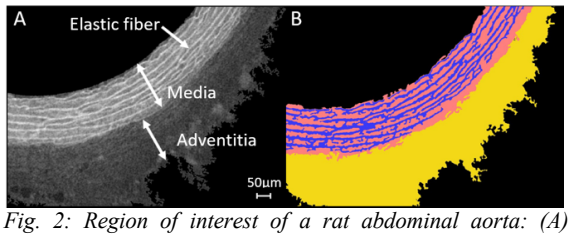

Fig. 2: Region of interest of a rat abdominal aorta: (A) original grayscale slice and (B) segmentation of the different substructures of the aortic wall. Yellow = adventitia, blue = elastic fibers, pink = smooth muscle cells and collagen matrix

Conclusion

CE-CT has shown its potential for high-resolution analysis of the vessel wall layers and their composition. In order to better understand the blood vessel mechanical properties, CE-CT can be combined with *in situ* mechanical testing (4D CE-CT). In the future, this data can then be used as input to obtain more accurate 3D computational models which help to understand the effect of changes in microstructure on functional behavior.

References

[1] de Bournonville et al, Acta Biomater., 105:253-62, 2020
[2] Balint et al, PloS One, 11(4):e0153552, 2016

ON THE POTENTIAL OF STRAIN MEASUREMENTS TO SEGMENT ATHEROSCLEROTIC PLAQUES BASED ON IVUS IMAGES

Álvaro Tomás Latorre (1), Myriam Cilla (1,2,3), Miguel Ángel Martínez (1,2), Jacques Ohayon (4,5) , Estefanía Peña (1,2)

1. *Aragón Institute of Engineering Research (I3A). University of Zaragoza, Zaragoza, Spain.*
2. *Biomedical Research Networking Center in Bioengineering, Biomaterials and Nanomedicine (CIBER-BBN), Spain*
3. *Centro Universitario de la Defensa, Academia General Militar, Zaragoza, Spain*
4. *Laboratory TIMC-IMAG/Biomeca, UGA, CNRS UMR 5525, Grenoble, France*
5. *University of Savoie Mont-Blanc, Polytech Annecy-Chambery, Le Bourget du Lac, France*

Introduction

Cardiovascular diseases are the leading cause of death worldwide and the majority were caused by atherosclerotic plaque rupture, so the characterization of the plaque is an important step in order to get an early diagnosis. Coronary plaque can be detected by intravascular ultrasound (IVUS) that allows us to see the cross section of the artery and gives information of the wall strains. There are many approaches to get the plaque segmented by computing the elasticity properties of the tissue from the IVUS [1,2]. The aim of this work is to segment the lipid core and fibrotic tissue and measure the thickness of the fibrous cap (fibrotic tissue between the lipid core and the lumen) using variables related with the strain map.

Methods

First, a 3D idealized model of a coronary artery with an atheroma plaque with three different fibrous cap thickness: 300, 150 and 65 µm has been created. The materials have been defined by an anisotropic and incompressible hyperelastic model which strain energy function is defined by Gasser et al. [3]. All the finite element computations have been done in the software Abaqus CAE with an internal pressure of 140 mmHg.
The displacement of two consecutive images from an IVUS were taken where a 5 mmHg of pressure increment are applied [1,2]. We use only the data from the finite element model in the maximum stenosis section with the assumption of plain strain to reproduce the IVUS acquisition. Next, we compute different strains measures such as principal strains or equivalent strains and the modulus of their gradients. Moreover, the variable dW proposed by Le Floc'h et al. [2,4] has been calculated to consider the elastic gradient. Finally, the segmentation process consists of joining the maps of two variables and the watershed segmentation process was applied. Furthermore, we have also performed the segmentation process using a 3D slice in order to consider the full strain tensor to check the accuracy of the plain strain model when only radial, circumferential and shear strains are considered.

Results

After the process described before, we obtain the lipid core and the lumen segmented, and we can compute the fibrous cap thickness and the area of the lipid core with an error lower than 10% (Figure 1). In addition, using a combination of variables, we are able to segment other tissues such as calcifications or healthy tissue. Finally, we have applied this methodology in an IVUS geometry where good results have been obtained (Figure 2).

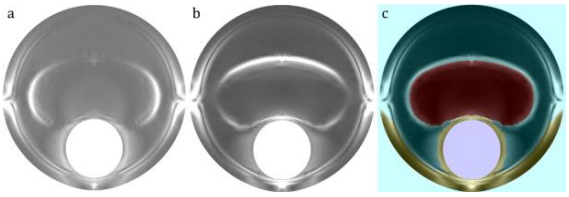

Figure 1: Segmentation results on an idealized geometry with fibrous cap thickness of 150µm, a)$|\nabla \boldsymbol{\varepsilon_x}|$, b)$|\nabla \boldsymbol{\varepsilon_y}|$, c) join of previous variables with the lipid segmented (red) and lumen (purple).

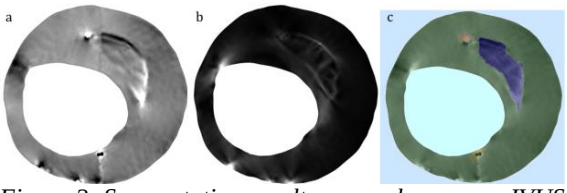

Figure 2: Segmentation results o a real coronary IVUS geometry, a) dW, b)$|\nabla \boldsymbol{\varepsilon_x}|$, c) join of previous variables with the lipid segmented (dark blue) and lumen (light blue).

Discussion

A new methodology for automatic segmentation has been presented by using the strain maps computed from an IVUS. After segmentation, it is possible to measure the thickness of the fibrous cap and some other important clinical data in order to detect a vulnerable plaque.

References

1. 1. Gomez, A. et al. Ultrasound in Medicine & Biology. 45(1):35-49, 2019.
2. 2. Le Floc'h, S. et al. IEEE Transactions on Medical Imaging. 28(7):1126-1137, 2009.
3. 3. Gasser, TC et al. Journal of the Royal Society. 3: 15-35, 2006.
4. 4. Le Floc'h, S. et al. Ultrasound in Medicine & Biology. 38 (12): 2084-2097, 2012.

DEEP LEARNING METHODS FOR PLAQUE TYPE CLASSIFICATION BASED ON THE US IMAGES OF CAROTID ARTERY

Branko Arsic[1,2], Smiljana Djorovic[2,3], Milos Anic[2,3], Igor Saveljic[2,4], Igor Koncar[5], Nenad Filipovic[2,3]

1. Faculty of Science, University of Kragujevac, Serbia; 2. Bioengineering Research and Development Center (BioIRC), Kragujevac, Serbia; 3. Faculty of Engineering, University of Kragujevac, Serbia; 4. Institute of Information Technologies, Kragujevac, Serbia; 5. Faculty of Medicine, University of Belgrade, Serbia

Introduction

Carotid atherosclerotic plaque deposition leads to arterial stenosis and severe catastrophic events over time (stroke and Transitional Ischemic Attack (TIA)). It is well established that the tissue composition plays a central role for the stability and vulnerability of atherosclerotic plaques. Identification of atherosclerotic plaque components is essential to pre-estimate the risk of cardiovascular disease and stratify them as a high/low risk. The main aim of this study was to identify the plaque types such as lipid, fibrous and calcified tissue, by applying the deep learning methods on US images.

Methodology

US Computer-Aided Diagnosis (CAD) system for vulnerable plaque classification can be divided into four phases: image pre-processing, segmentation, feature extraction, and lesion classification [1]. Comparing with traditional CAD systems where feature selection and extraction are important steps, deep learning replaces generic imaging features with processing layers that are more complex and more specific to the data, leading to an optimal use of information and improved prediction power.

In this study, the U-Net, SegNet, and Pyramid Scene Parsing Network (PSPNet) architectures for multi-class image segmentation task have been applied. These architectures found many important applications in segmentation of medical images, especially it holds for U-Net [2, 3]. Although these architectures work well in combination with data augmentation, the results were not satisfactory, because the small regions such as lipid and calcified plaques cannot be detected. That is why only the original and annotated US images were used for model training and testing.

Here, the problem of atherosclerotic plaque components segmentation is defined as multiclass segmentation model, where four classes should be detected in images (input image size is 512x512 pixels): background (black area outside the atherosclerotic ring, pixel map "0"), fibrous (yellow color, pixel map "1"), lipid (blue color, pixel map "2") and calcified (green color, pixel map "3") areas of annotated plaque components.

For the training phase we performed 100 epochs, with batch size 2. For the optimizers *Adadelta*, *Adam*, *RMSprop* were tested, but the results were pretty much the same. In order to handle highly imbalanced classes, we tested different loss functions, but the highest accuracy was achieved by using weighted categorical cross entropy loss function with manually selected weights for each class. At the end a combination of class weights of [0.2, 2, 3, 3] were used for the model training.

Results and Conclusions

Metric which was recorded during the training phase is *mean IoU* (Intersection over Union). PSPNet showed a good accuracy in prediction of lipid, fibrous and calcified carotid plaque types based on US images, a bit better than other two architectures.

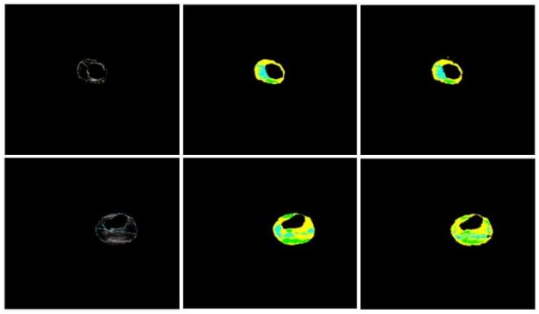

Figure 1: Atherosclerotic plaque zones. The 1st, 2nd and 3rd columns represent the original, manually labelled images, and multi-class prediction results, respectively.

The $mean\ IoU$ value on test set was equal to 0.47753240176078554, while $class\ wise\ IoU$ values for the background, fibrous, lipid and calcified plaques were 0.99153125, 0.58382048, 0.01689708, and 0.31788079, respectively.

The risk stratification of carotid atherosclerotic patients remains challenging due to complexity of the tissue and additional risk factors. The study will be extended on identification of parameters such as Grey Scale Median (GSM), plaque volume area, presence of carotid plaque ulceration and intraplaque hemorrhage.

References

1. Qinghua Huang et al, BioMed Research International, Article ID 5137904, 2018.
2. Olaf Ronneberger et al, MICCAI Conference, 2015.
3. Karim Lekadir et al, IEEE J Biomed Health Inform. 1(1): 48-55, 2017.

Acknowledgements

This paper is supported by the TAXINOMISIS project that has received funding from the European Union's Horizon 2020 research and innovation programme under grant agreement No 755320. This article reflects only the author's view. The Commission is not responsible for any use that may be made of the information it contains.

AUTOMATED GEOMETRIC ANALYSIS OF PULMONARY ARTERIES FROM COMPUTED TOMOGRAPHY PULMONARY ANGIOGRAPHY

Jeff Clark (1), Jennifer Rossdale (2), Pia Charters (2), Rob Mackenzie Ross (2), Jay Suntharalingam (1, 2), Jonathan Rodrigues (2), Andrew Cookson (1)

1. University of Bath, UK; 2. Royal United Hospitals Bath, UK

Introduction

Pulmonary hypertension (PH) is a rare but serious condition, which if left untreated has an average time to mortality of 2 years, 6 months. Initial symptoms are not specific and even if the patient undergoes a CT scan of their chest the diagnosis can be missed by general radiologists. Consequently, the mean time to diagnosis is 2 years, 2 months. The aim of this study is to develop a machine-learning algorithm and software tool that can screen for pulmonary hypertension from routinely acquired computed tomography pulmonary angiography (CTPA) images, using clinically validated geometric measures such as maximum main pulmonary artery diameter [1]. The availability of such a tool could drastically shorten the time-to-diagnosis for many patients by ensuring they are referred to a specialist PH clinical service in a timely manner. This would lead to, earlier and more effective intervention, lower treatment cost and improved quality of life.

Methods

Ground-truth labels were created by two expert clinicians by segmenting the pulmonary artery from CTPA image stacks (n = 44) using ITK-SNAP. The data covered a range of PH disease severity, as verified by the gold-standard diagnosis of pressure catheter measurements. A convolutional neural network (CNN) utilising the U-Net architecture [2] was implemented with the Medical Open Network for AI (MONAI) [3] framework in PyTorch. The model was trained against the ground-truth labels using 26 datasets, totalling 8630 CTPA slices. The model was validated against a further 9 datasets using the Dice score to compare the network-generated predictions to the clinician-segmented ground-truths. When provided with a CTPA stack the trained neural network outputted a segmented, binarised volume of the pulmonary artery, which was smoothed using a Laplacian filter. Vessel centrelines were extracted via the principle of maximum inscribed sphere [4], allowing the maximum arterial diameter to be identified.

Results

Figure 1(a) shows a sample image slice, ground truth segmentation, CNN segmentation and overlay, showing very good visual agreement. Comparison of the segmented volumes shown in Figure 1(b) and the ground-truth data found Dice scores (0.85 ± 0.05) similar to the variation between clinician-segmented volumes (0.88 ± 0.04). Furthermore, the values of the maximum pulmonary artery diameter extracted from these geometries were within 5.4% (1.5mm) of the ground-truth measurements provided by a specialist pulmonary radiologist from images with 1mm voxels.

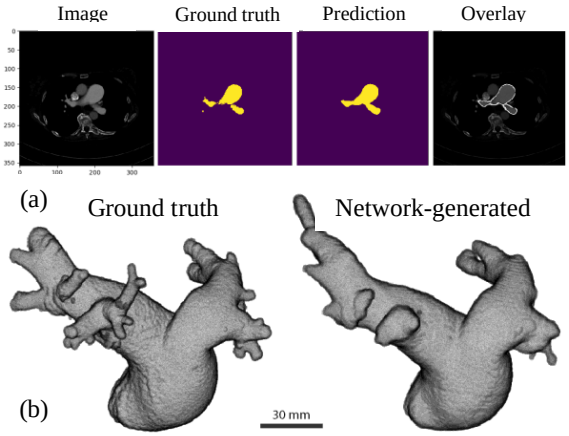

Figure 1: (a). Representative CTPA scan slice from an anonymised patient diagnosed with moderate PH. Left to right: CT scan image (in mm), ground-truth clinician segmentation, network generated segmentation, overlaid comparison on scan data. (b) Segmented volumes of the pulmonary artery. Left: ground-truth segmentation, right: network-generated segmentation.

Discussion

The results demonstrate the feasibility of automatically segmenting the pulmonary vasculature from CTPA images with an accuracy comparable to clinicians. Excellent agreement is observed for maximum diameter measurements. Clinically, this is a 2D measure extracted from one image slice. The approach demonstrated here, a 3D method, may therefore give a more physiological characterisation of the geometry, improving the accuracy of maximum diameter as a screening metric. Future work will train and validate this method on a larger dataset as the next step toward clinical translation.

References

1. Shen, Y., et al, Medicine, 93(27): e256, 2014
2. Kerfoot, E., et al, STACOM 2018, 371-380, 2019
3. The MONAI Consortium, Project MONAI. Zenodo. http://doi.org/10.5281/zenodo.4323059, 2020
4. Piccinelli, M., et al, IEEE Transactions on Medical Imaging, 28(8):1141-55, 2009.

Acknowledgements

This work was supported by a Research Capability Fund grant from the Royal United Hospitals Bath and a University Impact Fund award from the University of Bath.

NON-INVASIVE QUANTITATVE VIRTUAL 3D HISTOLOGY OF THE HEART

Camille Pestiaux (1,2), Greet Kerkchofs (1,2,3,4)

1.Institute of Mechanics, Materials, and Civil Engineering, UCLouvain, Belgium; 2. Institute of Experimental and Clinical Research, UCLouvain, Belgium; 3. Dept. Materials Science and Engineering, KU Leuven, Belgium; 4. Prometheus, Division of Skeletal Tissue Engineering, KU Leuven, Belgium

Introduction: The heart is a highly heterogeneous organ. It is composed of a dense muscle network, cavities, vessels and fibrous tissues made of collagen and elastin. Its contraction rate is prescribed by the complex organization of the cardiomyocytes. A 3D and non-destructive imaging protocol is thus crucial to render its complexity and allow further analysis. Structural analysis such as the position of the heart valves, connection of the chambers, organization of the muscle fibers and main vessels should be accurately performed to provide a better knowledge of the heart and it proper functioning, as well as the effect of diseases on this functioning. This additional knowledge will help to improve the treatment strategies and increase the fidelity of computational models of heart activation. *Ex vivo* microfocus X-ray computed tomography (microCT) is already known as a powerful technique to image biological tissues [1]. Nevertheless, imaging soft tissues requires the addition of a contrast-enhancing staining agent (CESA) to increase the X-ray attenuation of the soft tissues; further referred to as contrast-enhanced microCT (CE-CT) [2]. Currently, Lugol's iodine is the most popular CESA to image the heart and its substituents with CE-CT. However, it is known to induce substantial tissue shrinkage [3]. In this study, we evaluated the potential of an emerging CESA, Hafnium-substituted Wells-Dawson polyoxometalate (Hf-WD POM), to image the heart and we compared it to Lugol's iodine. Moreover, we introduced a new contrasting method allowing to measure the 3D orientation of the muscle fibers in the ventricle. This study is the first to present an alternative to Lugol's iodine to reveal the native anatomy of the heart including organization of the muscle fibers in a non-invasive way based on CE-CT.

Materials, methods and results: A mouse heart was extracted after death, was fixed overnight and stained in 3.5% (wt/v) Hf-WD POM/PBS solution for 10 days at room temperature. It was scanned with a voxel size of 2.4 µm. It was rinsed for 10 days in PBS at room temperature and then stained in homemade isotonic Lugol's iodine for 4 days at room temperature. Then, it was scanned again with the same parameters as previously, and it was prepared for histology.

The anatomical features of the heart, such as the atria and ventricles, the heart valves and the main vessels could be distinguished on both CE-CT datasets allowing the verification of the heart integrity (Fig.1). Both stains allowed segmenting the heart valves from the rest of the heart, enabling assessment of alterations in valve configuration or shape (Fig.1A and 1Ee). Nevertheless, after staining with Lugol's iodine the thickness of the ventricle wall was strongly reduced and the volume of the chambers was increased, indicating an important shrinkage of the tissue. Hf-WD POM respects better the native anatomy of the heart, thus providing a new insight into the native properties of the heart. The muscle fibre bundles can be distinguished after Lugol's iodine staining, but not with Hf-WD POM. For this reason, a new contrasting method was developed that allowed to evaluate the orientation of the muscle fibres in the ventricle in a non-invasive way.

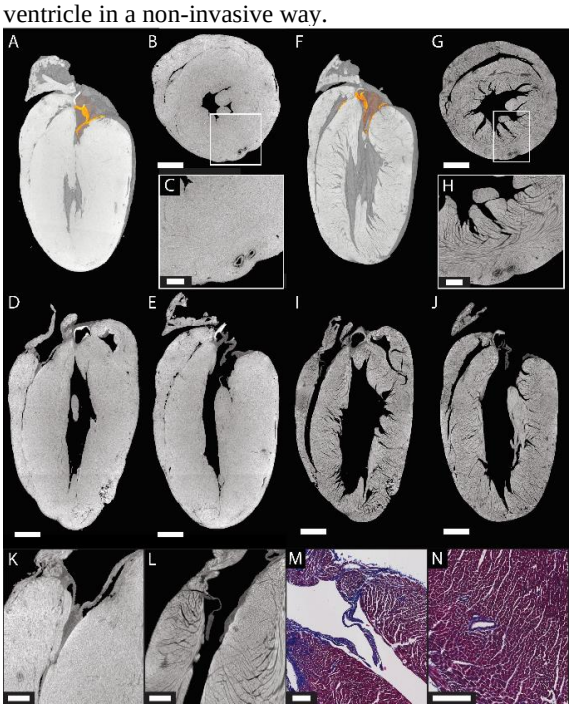

Fig.1: Typical CE-CT images of a mouse heart after Hf-WD POM staining (A-D and K) and isotonic Lugol's iodine staining (F-J and L). A and F are 3D renderings with the heart valves in orange, B-E and G-J are orthogonal slices. K and L are a zoom on the heart valves after Hf-WD POM and isotonic Lugol's iodine staining respectively. Scale bars are 1mm for A-J, 0.3mm for K-L and 0.2mm for M-N.

Conclusion : We applied Hf-WD POM staining for the first time on mouse hearts to perform CE-CT, and compared it to the standard Lugol's iodine staining. We demonstrated that Hf-WD POM respects better the native anatomy of the heart and, combined with a new non-invasive contrasting method, it allows the distinction of the anatomical features.

References: 1. Rawson, S.D. et al., BMC Biol, 18:21, 2020; 2. De Bournonville, S. et al., Contrast Media Mol Imaging, 2019, 3. Degenhardt, K. et al., Circ Cardiovasc Imaging, 3:314-322, 2010

CFD-DERIVED RESISTANCE AS A CLINICAL INDICATOR FOR PROBLEMATIC AVF

Olivia Ng (1), Sanjiv Gunasekera (1), Shannon Thomas (2,3), Ramon Varcoe (2,3), Tracie Barber (1)

1. School of Mechanical and Manufacturing Engineering, University of New South Wales, NSW Australia
2. School of Medicine, University of New South Wales, NSW, Australia
3. Prince of Wales Hospital, NSW Australia

Introduction

The arteriovenous fistula (AVF), a surgically made vasculature that connects the artery and vein, is essential for patients requiring hemodialysis, yet has frequent problems. The formation of intimal hyperplasia (IH), resulting in a narrowing of the blood vessel (stenosis) is most commonly seen, requiring surgical intervention of either stent deployment or balloon angioplasty to salvage the AVF. Complex blood flow in an AVF is a major factor attributed to AVF failure. Pressure drop within an AVF associates with the overall resistance and flow instabilities especially around the anastomotic region of the AVF. Hydraulic resistance shows promising correlation as a possible indicator for problematic AVFs, outlined here by comparing patient trends for pre and post-surgical intervention.

Methods

The radial-cephalic AVF of a 74 year old patient was obtained with an in-house portable scanning system, at two different times [1]. The first scan (pre-intervention) was obtained 4.5 months post-creation, and the second scan (post-intervention) was obtained 6 months post-creation and 43 days after intervention. Flow profiles, which serve as the boundary condition for the CFD model, was measured at each vessel. Once patient scans were processed with Simpleware SCANIP segmentation software (Synopsys Inc., CA, USA), meshes were generated using Ansys ICEM (Ansys ICEM CFD, Release 18.1) before performing CFD simulations using FLUENT software (Fluent, Inc. Lebanon, NH) (Table 1) [2]. Resistance, R (Eq. 1) was calculated after the fourth cycle of each simulation.

$$R = \Delta P / Q \quad (1)$$

ΔP = Pressure drop from the anastomosis to 75mm of the vessel; Q = flow rate of respective vessel

Parameters	Description
Governing Equation	Reynolds-averaged Navier Stokes equation
Element type	Polyhedral volume mesh, 12 prism layers (~8 million cells)
Blood density	1060 kg/m³
Blood viscosity	Non-Newtonian: Carreau model
Boundary conditions	PA and DA: Velocity inlets PV: Zero-pressure outlet
Timesteps	0.001s

Table 1: Summary for the numerical simulation

Results and Discussion

A juxta-anastomotic stent was deployed 15 days after the first scan as the AVF had insufficient flow. R decreases at both vessels post intervention, with an average of 24% decrease at the PA and 98% decrease at the PV (Figure 1). Variation in R along the vessel at 1mm intervals enabled the identification of the stenosis region (Figure 2). The narrowed segment of PV located at about 30mm from the anastomosis coincides with the maximum R change value of 8mmHg/l/min (Figure 2).

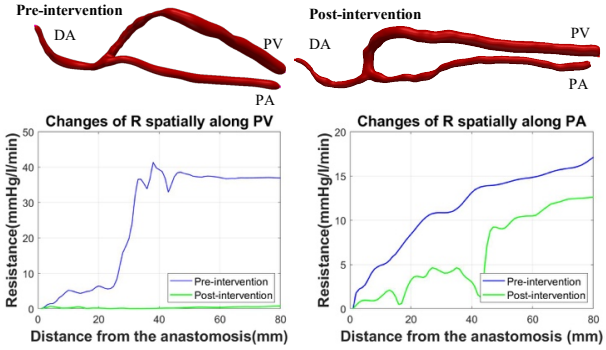

*Figure 1: **(top left)** Pre-intervention geometry **(top right)** post intervention geometry **(bottom left)** Changes of R spatially along the PV and **(bottom right)** the PA*

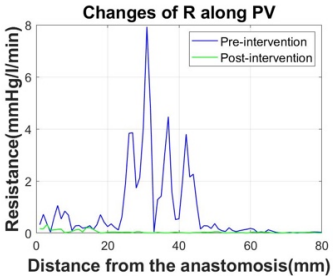

Figure 2: Changes of R at 1mm interval along the PV pre- and post-intervention scans

Based on our patient database, we see a promising trend for CFD-derived resistance for AVF failure prediction.

References

1. E. Colley, J. Carroll, S. Thomas, R. L. Varcoe, A. Simmons, and T. J. Barber, "A Methodology for Non-Invasive 3D Surveillance of Arteriovenous Fistulae Using Freehand Ultrasound," IEEE Trans. Biomed. Eng., vol. 65, no. 8, pp. 1885–1891, 2018.
2. O. Ng, S. Gunasekera, S. Thomas, R. Varcoe, and T. Barber, "A clinical predictive indicator for arteriovenous fistula (AVF) failure," Proc. 22nd Australas. Fluid Mech. Conf. AFMC2020, no. December, pp. 7–10, 2020.

NUMERICAL BIOMECHANICS MODELING OF TREATMENTS FOR MITRAL REGURGITATION

Adi White Zeira (1), Lee Galili (1), Ehud Raanani (2), Gil Marom (1)

1. School of Mechanical Engineering, Tel Aviv University, Israel; 2. Leviev Cardiothoracic and Vascular Center, Chaim Sheba Medical Center, Tel Hashomer, Israel

Introduction

Mitral valve regurgitation (MR) is a disorder of improper valve closure. MR is the most common valvular disease, with estimated five million incidence worldwide, but it has limited available treatments [1,2]. MR can be classified as primary or secondary. Primary MR (PMR) is caused by valve prolapse due to degenerative abnormalities of the valve. Secondary MR, is caused by left ventricular dysfunction [3]. Available treatments include medical management, surgical repair or replacement, and percutaneous repair [4]. The surgical repair, which is the gold standard treatment, includes annuloplasty sawing of a ring that reduces the annular perimeter in open-heart surgery, but it is prohibited for inoperable patients [5]. Therefore, there is a need for alternative minimally invasive treatments such as indirect mitral annuloplasty (IMA) [6]. This study aims to numerically represent PMR and to model annuloplasty surgery and IMA repair in beating heart.

Methods

We used the living heart human model (LHHM; Simulia, Dassault Systèmes), an electro-mechanically coupled heart simulator of the entire heart with the electrophysiology and fibrous architecture of the myocardium [7]. We changed the anatomy to model the MR. By using virtual thermal expansion, we enlarged the tissue of the leaflets and extended the chordae. The annulus was enlarged by applying pressure to inflate the left atrium. We examined two types of annuloplasty treatments, surgery and IMA. For the surgical model, we built flexible band (open ring) and tied it to the pathological annulus. To model the IMA we built a generic device from two anchors and a bridge between them. The IMA device was implanted in the coronary sinus, and by changing the distance between the anchors, the mitral annulus was reduced. All the anatomic changes and the implantations were done in 70% diastolic position. It was followed by models of the beating heart and the closed systolic position was identified. To quantify the blood leakage, we used simplified smoothed particle hydrodynamics (SPH) [8]. We considered only the flow in the left side of the heart, seeded particles in the ventricle, and modeled the ventricular volume reduction by a piston motion.

Results

In the PMR model the chordae were extended by 30%, the tissue enlarged by 24% and the annulus perimeter by 10%. A leakage and a leaflet prolapse were found in the 70% systolic position of the PMR, as expected. In the surgery we reduced the annulus by 33% and in the IMA we reduced the distance between the anchors by 23 mm. The top row of Figure 1 presents the peak systolic position of the mitral valve with and without repairs. The leakage percentage is defined as the number of the particles in the atrium (Figure 1, bottom row) relative to the total number of particles that left the ventricle, including those that left to the aorta. The mitral valve was completely closed post-surgery, while the IMA only reduced the leakage.

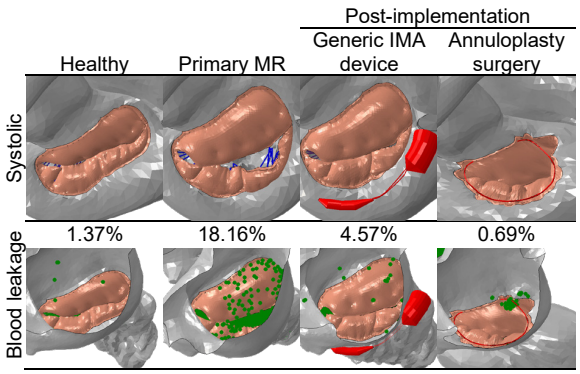

Figure 1: Mitral valve configurations in systolic position (top) and blood leakage illustration with percentage of particles in the atrium (bottom)

Discussion

In this research we presented PMR numerical model by changing the anatomy of the valve. We modeled two types of treatments. In the surgical treatment we showed that the leakage was negligible without shortening the chordae or leaflets resection. With the generic IMA device there was a slight leakage. Since this device is aimed for secondary MR, it was expected that the mitral valve could not get completely closed in PMR. We are currently also modelling surgical and IMA treatments of secondary MR to test if IMA can perform as expected.

References

1. Benjamin et al., Circulation, 139:e56-e528, 2019.
2. Trochu et al., Arch Cardiovasc Dis, 108:88-96, 2015.
3. Asgar et al., J Am Coll Cardiol, 65:1231-1248, 2015.
4. Feldman et al., J Am Coll Cardiol, 54:686-694, 2009.
5. Kheradvar et al., Ann Biomed Eng, 43:858-870, 2015.
6. Patterson et al., Front Cardiovasc Med, 6:1-8, 2019
7. Baillargeon et al., Eur J Mech A/Solids, 48:38-47, 2014.
8. Toma et al., J Numer Method Biomed Eng, 33:e2815,2017.

Acknowledgements

We thank Prof. Ehud Schwammenthal and Dr. Eilon Ram from Sheba medical center for their assistance.

IMPACT OF LEG MOVEMENT ON THE LOCAL HEMODYNAMICS OF FEMOROPOPLITEAL ARTERIES

Ludovica Cestariolo (1), Monika Colombo (1), Giulia Luraghi (1), Maddalena Ravasi (1), Anna Airoldi (1), Claudio Chiastra (1,2), Giancarlo Pennati (1)

1. LaBS, Dept. of Chemistry, Materials and Chemical Engineering "Giulio Natta", Politecnico di Milano, Italy; 2. PoliTo^{BIO} Med Lab, Dept. of Mechanical and Aerospace Engineering, Politecnico di Torino, Italy.

Introduction

The Femoropopliteal Artery (FPA) is a vascular region subjected to a broad spectrum of complex solicitations, mainly determined by the leg movement [1]. The FPA is often affected by atherosclerotic plaque development, presumably favored by the biomechanics of surrounding tissues. Although abnormal hemodynamics in FPA appears to be an important factor in driving plaque development, until now, it has been investigated only in few studies, in which the leg was modeled in either fixed straight [2] or bent configurations [3]. Hence, the current work investigates the impact that the leg movement and the different configurations assumed by the lower limb have on the hemodynamics of femoropopliteal arteries.

Methods

An idealized model of FPA, featured by human-based dimensions, was created to perform moving-boundary Computational Fluid Dynamics (CFD) analyses (Fig. 1) using the ICFD solver (LS-DYNA, LSTC, USA). The vessel geometry, divided into three parts (Superficial Femoral Artery, SFA; Popliteal Artery, PA; Tibial Artery, TA), was subjected to three movements, namely (1) knee flection, (2) hip rotation, and (3) complete gait cycle. The gait configurations of the leg and, thus, the spatial displacement were implemented using sensor-based coordinates. A flat velocity profile, based on a typical femoral artery triphasic waveform with a period of 1 s, was applied at the inlet, while zero-pressure and no-slip conditions were applied at the outlet and the wall, respectively. The moving-boundary models were compared with corresponding cases with fixed walls to evaluate the impact of leg movement on hemodynamics. The results were analyzed by computing hemodynamic descriptors derived from Wall Shear Stress (WSS) (e.g., Time Averaged WSS (TAWSS)).

Results

Figure 1 shows a comparison in terms of velocity at cardiac systole and TAWSS between the fixed and the moving configuration in one configuration of the complete gait cycle. When comparing the fixed- and moving-boundary analyses, the main differences were found in the PA and TA portions. In the hip rotation model, the hemodynamics descriptors were constant along the whole model. In the knee flection movement, the SFA region presented the same results as the fixed-boundary configuration. Instead, the PA and TA regions were highly affected by movement (differences in TAWSS up to ~24 % in the PA region). Compared to the reference walking configurations at different angles, changes in the flow-rate amplitude had the highest impact on hemodynamics. Similarly, TAWSS was highly affected by the bending period (~15%) [4].

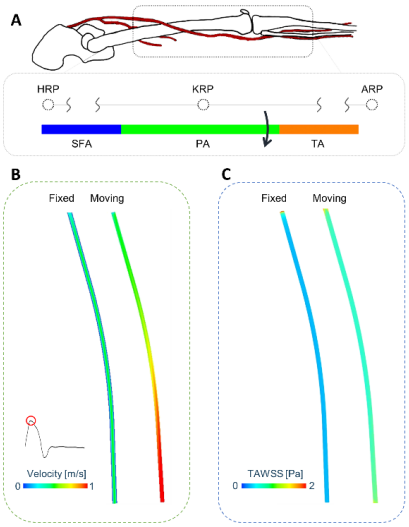

Figure 1: A) Idealized model of an FPA, subjected to rotations around the hip, knee, and ankle reference points (HRP, KRP, and ARP). B) Comparison of velocity at the systole in the fixed and moving models. C) Comparison of TAWSS, plotted in a bent leg configuration, between the fixed and moving models.

Discussion

The current numerical approach highlights the importance of accounting for leg movement to analyze FPA hemodynamics, especially in the PA and TA portions. Indeed, the hemodynamics in the arterial portions under the knee is widely affected by leg movement and should be studied in a moving-boundary configuration.

References

1. A. J. Klein et al., Cardiovasc Interv, 74: 787-798, 2009.
2. M. Colombo et al., Med Eng & Phys, 75: 23-35, 2020.
3. Gökgöl C. et al., Biomech Model Mechanobiol, 18(6): 1883-1893, 2019.
4. M. Colombo and G. Luraghi et al., Med Eng & Phys, 81: 105-117, 2020.

Acknowledgments

This work has been supported by Fondazione Cariplo, Italy (Grant number 2017-0792, TIME). We thank Prof. Manuela Galli (Politecnico di Milano) for providing us gait analysis data.

AORTIC HEMODYNAMICS ASSESSMENT PRE AND POST VSR SURGERY: A PATIENT SPECIFIC 4D FLOW-BASED FSI MODEL

Guido Nannini [1], Alessandro Caimi [1], Maria C. Palumbo [1], Simone Saitta [1], Leonard Girardi [2], Mario Gaudino [2], Jonathan W. Weinsaft [2], Alberto Redaelli [1]

1. Department of Electronics Information and Bioengineering, Politecnico di Milano, Italia;
2. Department of Medicine (Cardiology), Weill Cornell College, New York, NY, USA

Introduction

Ascending thoracic aortic aneurysm (ATAA) is a life-threatening cardiovascular disease, consisting in the focal dilatation of the proximal aorta, due to structural alteration of the arterial wall [1]. Surgical valve-sparing reconstruction (VSR) is a well-established procedure, recommended by consensus guidelines when the ATAA diameter exceeds 50 mm [2], however, the risk of post-surgical complications persists in the non-grafted area. This has been suggested to be related to the alteration in the hemodynamics observed, especially in descending aorta (DAo) [3].

Herein, we present a patient specific fluid-structure interaction (FSI) protocol, based on 4D phase contrast magnetic resonance imaging (PC-MRI/4D flow) data to comprehensively investigate the pre- and post-VSR surgery conditions. We assessed *i)* the impact of the numerical modeling technique comparing FSI results against computational fluid dynamics (CFD) and *in-vivo* 4D flow-measured data; *ii)* the impact of the surgery in aortic hemodynamics and biomechanics, focusing on the shear stress experienced by DAo and the variation in aortic wall distensibility.

Methods

Pre- and post-VSR cardiac MR scans (3TGE SIGNA™) were segmented in MeVisLab 2.7.1 (MeVis Medical Solutions, Munich, DE) and refined in Meshmixer (Autodesk Inc, San Rafael, USA). The aortic wall was obtained extruding the fluid domain in normal direction by 2 mm. Patient specific three-dimensional inlet velocity profile extracted from 4D flow data and pressure-outlet three-elements Windkessel model (3WKM) were assigned as boundary conditions (Fig.1). FSI and CFD simulations were run in ANSYS 17.2 (ANSYS Inc, Canonsburg, USA).

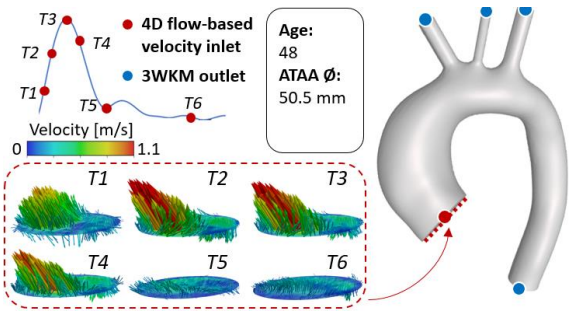

Figure 1: 3D inlet velocity profile at different instants of cardiac cycle applied at patient-specific pre-VSR model.

Results

The velocity pattern computed with our FSI model well matched the 4D flow measurements at systolic peak, while CFD overestimated velocity, especially in DAo. The disagreement between CFD and 4D flow was less pronounced in the post-VSR model (Fig.2b). In general, after VSR an increase in wall shear stress and a decrease in the oscillatory shear index were assessed. DAo distensibility resulted 43% higher after surgery.

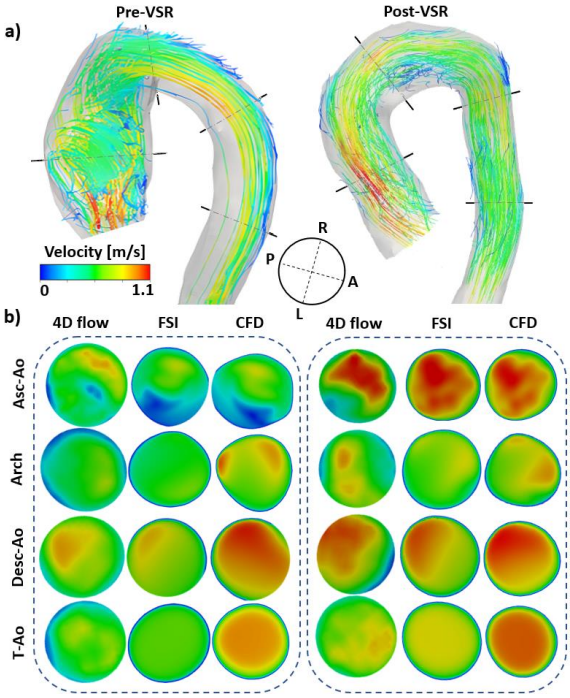

Figure 2: Systolic peak streamlines from 4D flow (a) and velocity contours on four planes along the aorta obtained from 4D flow, FSI and CFD results (b).

Discussion

Our FSI protocol was able to reliably reproduce aortic hemodynamics pre- and post-VSR and deepen the shear stress state experienced by DAo after surgery. Velocity comparisons showed that CFD is an oversimplified approach and FSI is necessary for a reliable model of the aortic hemodynamic and biomechanics.

References

1. Humphrey et al, Biomech Soft Tissue, 1:1-14, 2003.
2. Chau et al, Progr Cardiovasc Dis, 56:74-80, 2013.
3. Gaudino et al, J Thorac Card Surg, 150:1120-1129, 2015.

LARGE-EDDY SIMULATION OF A PATIENT-SPECIFIC AORTA WITH AORTIC STENOSIS: AN INVESTIGATION INTO TURBULENCE EFFECTS

Emily Manchester (1), Selene Pirola (1), Mohammad Yousuf Salmasi (2), Declan O'Regan (3), Thanos Athanasiou (2), Xiao Yun Xu (1)

1. Department of Chemical Engineering, Imperial College London, UK; 2. Department of Surgery and Cancer, St Mary's Hospital, Imperial College London, UK; 3. MRC London Institute of Medical Sciences Imperial College London, Hammersmith Hospital, London, UK

Introduction

Aortic valve stenosis (AVS) is a cardiovascular disease which limits the function of the aortic valve, producing highly complex flow features which may induce laminar to turbulence transition [1]. Disturbed near wall flows are known to promote inflammation and may increase particle transit times, both of which correlate to arterial wall disease [2]. Most computational studies assume laminar flow meaning the effects of transitional and turbulence features are not well understood. This work conducts large-eddy simulations (LES) of a patient-specific aorta with severe aortic stenosis to investigate the effects of turbulence on hemodynamic parameters, especially wall shear stress (WSS) which is examined by considering both mean and turbulent contributions.

Methods

Large-eddy simulations are a numerical method capable of modelling laminar, transitional and turbulent flows. 4D flow MRI from a patient with severe aortic stenosis was used to generate the patient-specific aortic geometry and boundary conditions. At the model inlet time-varying 3D velocity profiles were imposed and the pressure based 3-element Windkessel model was applied at the arch branch outlets and the descending thoracic aorta outlet. The structured mesh consists of 7.4 million elements. The LES methodology was previously validated against experimental data [3] and results were validated against the patient's 4D MRI data using statistical correlation methods. Presented results were phase-averaged over 30 cardiac cycles, ensuring convergence of turbulence parameters. Wall shear stress was decomposed into phase-averaged (mean, $\langle WSS \rangle$) and turbulent (WSS') components as follows:

$$WSS = \langle WSS \rangle + WSS' \qquad (1)$$

$$WSS' = \sqrt{(WSS - \langle WSS \rangle)^2} \qquad (2)$$

Results

Disturbances are present throughout the cardiac cycle, which are more pronounced at peak systole and during systolic deceleration. Figure 1a shows the mean and turbulent WSS components at three time points. Regions of elevated WSS are observed in the ascending aorta, with peak values occurring at peak systole. Figure 1b shows the mean, turbulent and total wall shear stresses spatially averaged over the ascending aorta plotted over a cardiac cycle.

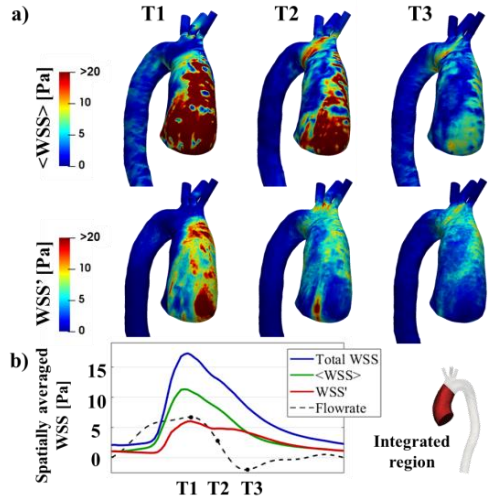

Figure 1. a) mean WSS (top row) and turbulent WSS (bottom) at peak systole (T1), max deceleration (T2) and end systole (T3). b) WSS components spatially averaged over the ascending aorta, plotted over a cardiac cycle.

Discussion

At peak systole both mean and turbulent kinetic energies are high, with turbulent WSS contributing 35% to the total WSS. During systolic deceleration mean kinetic energies are low with mean WSS decreasing rapidly. Turbulent WSS is relatively constant throughout deceleration owing to the additional time it takes for turbulence features to dissipate. Neglecting turbulence effects would underpredict the time-averaged total WSS by 40%, demonstrating that turbulence in AVS can be of considerable magnitude and duration to significantly impact near-wall hemodynamic parameters. Further turbulence-based results will be presented at the conference including kinetic energies and irreversible energy losses which quantify turbulence production against left ventricular load in AVS.

References

1. Sotiropoulos F, et al, Annu. Rev. Fluid Mech, 48:259-283, 2016.
2. Cunningham KS, et al, Nature: Lab Invest, 85:9-23, 2005.
3. Manchester E, et al, Int J Numer Meth Bio, 36:e3389, 2020.

Acknowledgements

This research was supported by an EPSRC DTP studentship. This work used the Cirrus UK National Tier-2 HPC Service at EPCC (EP/P020267/1).

THE EFFECT OF LUMPED PARAMETER BOUNDARY CONDITIONS IN IMAGE-BASED MODELLING OF THE THORACIC AORTA THROUGH CFD

Scott Black (1), Pauline Hall-Barrientos (2) Konstantinos Ritos (3), Craig Maclean (4) Alex Boukis (4), Robbie Brodie (4), Asimina Kazakidi (1)

1. Department of Biomedical Engineering, University of Strathclyde, Glasgow, UK; 2. NHS Greater Glasgow and Clyde, Glasgow, UK; 3. Department of Mechanical and Aerospace Engineering, University of Strathclyde Glasgow, UK; 4. Research and Development, Terumo Aortic, Glasgow, UK

Introduction

Regions of the aortic arch affected by an aneurysm or dissection may require surgical intervention using vascular stent-grafts, which require a means of re-perfusing the supra-aortic branch vessels. For long-term success, the chosen graft configuration must promote physiological perfusion distribution and in-stent haemodynamics. For example, abnormal wall shear stresses can induce thrombosis and graft limb occlusion, and post-dissection aneurysm formation [1]. It is clear, therefore, that enhanced understanding of perfusion in patient-specific cases is critical to improving clinical practice and patient outcomes. The aim of this study was to determine appropriate boundary conditions (BCs) for a computational fluid dynamics (CFD) model which enable the prediction of perfusion distribution and arterial haemodynamics in patient-specific cases.

Methods

A healthy patient-specific aortic arch geometry was reconstructed via a novel 4-dimensional magnetic resonance imaging (4D-MRI) approach. Additionally, a diseased geometry incorporating a dissection was reconstructed from CT images. To generate patient-specific BCs, the arterial geometry was reduced to a one-dimensional (1D) model. Thereafter, the terminal branches were coupled to zero-dimensional (0D) 3-element Windkessel models (3EWM), which are representative of downstream vasculature [2]. In this 0D-1D numerical framework, the 3EWM parameters were changed iteratively to generate branch flow waveforms which minimized the error between computed and *in*-vivo data. These BCs were coupled to terminal branches of the 3D models, and velocity profile extracted from 4D Flow-MRI at the ascending aorta was prescribed at the inlet of the CFD domain. Thus, blood flow was investigated in a fully patient-specific 0D-3D numerical framework. By tailoring the 3EWM parameters thereafter, simulation of a range of healthy and pathological distal vascular conditions was possible.

Results

From 4D Flow-MRI and CFD simulations, clinically relevant haemodynamic parameters including branch flow rate, time averaged wall shear stress (TAWSS) and oscillatory shear index (OSI) were extracted (Figure 1). Results indicate the 3EWM BCs significantly effect branch perfusion, TAWSS, and OSI distribution.

Discussion & Conclusions

The proposed methodology permits prediction of blood flow throughout the thoracic aorta. This capability can in future be used for estimation of post-surgical peripheral organ perfusion, to minimize the long-term risk of neurologic and cardiac events. Generation of patient-specific 3EWM BCs is a vital component in the generation of a CFD model for such clinical applications. This study clearly shows one should not extract arbitrary 3EWM parameters from literature but must generate each BC on a case-by-case basis prior to 0D-3D coupling. It should also be noted that 0D-1D is sufficient to estimate flow throughout the geometry, but 0D-3D coupling is required to extract parameters such as TAWSS and OSI. Moreover, it was evident that the combination of 4D Flow-MRI, CT, and CFD grants unparalleled visualization and quantification of arterial blood flow. In future work, multiple stent-graft configurations will be included within the CFD model to estimate post-surgical haemodynamics.

Figures

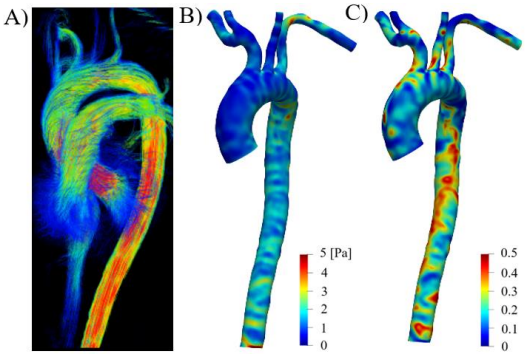

Figure 1: A) Velocity streamlines of a healthy thoracic aorta obtained via 4D Flow-MRI. The aortic geometry was reconstructed to create a 3D computational fluid dynamics model, coupled with 0D, patient-specific 3EWM BCs to quantify B) TAWSS and C) OSI

Acknowledgements

This work is supported by the EPSRC CDT in Medical Devices and Health Technologies, University of Strathclyde, and Terumo Aortic.

References

1. C. Celestin et al, Paediatric Cardiology 36:600-615, 2015.
2. C. Konoura et al, Int J Artif Organs 16:157-163, 2013.

LUMPED MODELS AND COMPUTATIONAL FLUID DYNAMICS TO STUDY HEMODYNAMICS WITHIN THE LEFT ATRIAL APPENDAGE

Jorge Dueñas-Pamplona*(1), Javier García(1), José Sierra-Pallares(2), César Méndez(2), Jorge Muñoz Paniagua(1), Javier Goicolea(3), Francisco Castro(2)

1. Departamento Ingeniería Energética. ETSII Universidad Politécnica de Madrid, Spain

2. Departamento Ingeniería Energética y Fluidomecánica. EII Universidad de Valladolid, Spain

3. Hospital Universitario Puerta de Hierro Majadahonda (Spain)

Introduction

Atrial fibrillation (AF) is one of the most common types of arrhythmia. Although it can appear concomitantly with other diseases like hypertension and heart failure, it is also considered an independent risk factor for stroke. It is known that AF increases the risk of developing thrombus within the left atrial appendage (LAA), a protuberance in the left atrium (LA). The study of AF effects is very complex since, in addition to appearing in conjunction with other diseases, the concomitant incidence of electro-physiological disorder, structural remodeling and flow changes occur. One interesting approach to study the isolated influence of each of the AF effects is mathematical modelling: the combination of lumped modelling and computational fluid dynamics (CFD) has been proved as a very interesting technique to explore the effects of AF [1], where different scales are present. In this work, a lumped model covering the pulmonary veins, the left heart and systemic circulation will be employed, in conjunction with a patient-specific healthy atrium model obtained from 4D CT. The main consequences of AF will be studied, employing the outputs obtained from the lumped model as boundary conditions for the CFD simulations. The changes on hemodynamics indices within the LAA will be studied.

Methods

Atrial CT images of a healthy patient without a prior history of stroke or AF obtained during sinus rhythm have been employed. The images were reconstructed for a total of 10 cardiac phases, allowing us to extract the atrial wall motion in healthy conditions. The Coherent Point Drift (CPD) algorithm has been employed for this purpose.

The lumped parameter model is based in the one proposed by Casas [2], being in this case simplified to cover only the main arteries and veins accordingly to the needs of the present work. It is based in the well-stablished time-varying elastance model and consists of four main compartments: the pulmonary venous system, the left atrium, the left ventricle and the systemic circulation.

Non-linear optimization was used to adjust the literature values to patient-specific values by minimizing the sum squared error between the volume variation waveforms calculated from the segmented geometries and those generated by the model. This was done using the Levenberg-Marquadt algorithm, which is an iterative, nonlinear least-squares optimization method.

Four main consequences of AF have been considered for the parametrical study: lack of atrial kick (AK), left atrial remodeling (LAR), left ventricular systolic dysfunction (LVSD) and high frequency fibrillation (HFF) [1].

A tetrahedral volumetric mesh has been created with the commercial software ANSYS Fluent, employing the output of the lumped-model as boundary conditions to perform a parametric study.

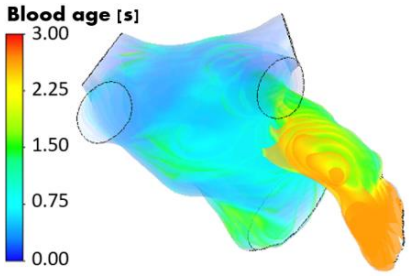

Figure 1: Blood age calculated within the LA and LAA obtained by employing the output of the lumped model as boundary conditions of the CFD model.

Conclusion

In this work, a framework to study the effects of AF in the LAA hemodynamics is proposed. The combined use of lumped parameter models and CFD simulations allows to capture the AF impact both on the cardiovascular system and on the flow patterns within the LA and LAA. It also opens the door to study separately the main effects that AF produces on hemodynamics indices within the LAA, both with rigid and flexible models. This could provide important insights to understand the mechanism of the disease, becoming computational modelling and simulation a crucial tool to improve both diagnose and treatment of AF.

References

1. A. Deyranlou et al, Annals of Biom Eng, 48:4, 2020.
2. B. Casas et al, Scientific Reports, 7:1-15, 2017

Acknowledgements

This work was supported by Ministerio de Ciencia, Innovación y Universidades of Spain under contract **DPI2017-83911-R** and by the regional government of Castilla y León under contract **VA081G18**. We want to show our gratitude to the "Programa Propio - Universidad Politécnica de Madrid".

AN INVERSE ELASTOSTATIC ALGORITHM WITH EXACT LINEARIZATION TO DETERMINE UNLOADED VASCULAR GEOMETRY IN ANISOTROPIC VACULAR TISSUE

Benedetta Fantaci* (1), Carlo Franceschelli* (1), Giulia Luraghi (1), Jose F Rodriguez Matas (1)
Chemistry, Materials and Chemical engineering Department "Giulia Natta", Politecnico di Milano, Italy
**authors contributed equally*

Introduction

Biomechanical studies of the cardiovascular system require a patient specific geometry. However, patient-specific models are generated from gated medical images in which the vascular tissue is under pressure, that is, the imaged tissue is in a prestressed state. Therefore, identification of the zero-pressure geometry would allow for a more accurate estimate of the device performance or risk assessment. A number of iterative methodologies have been developed to solve this problem [1,2]. More recently, a direct methodology based on inverse elastostatics (IE) applicable to anisotropic tissue has been proposed [3]. This work implements the IE approach presented in [3] incorporating exact linearization of the governing equations to improve numerical efficiency. The accuracy and convergence properties of the implementation are demonstrated in a 1element-cube and in an idealized arterial tube.

Methods

In the classical elastostatic problem, the motion $\boldsymbol{\phi}(\boldsymbol{X})$ maps any particle with a known position $\boldsymbol{X}$ in the reference configuration $\mathcal{B}_0$ to the position $\boldsymbol{x} = \boldsymbol{\phi}(\boldsymbol{X})$ in the deformed configuration $\mathcal{B}$, such that $\boldsymbol{x} = \boldsymbol{X} + \boldsymbol{u}$, with $\boldsymbol{u}$ the displacement. The motion $\boldsymbol{\phi}(\boldsymbol{X})$ is computed as the solution of the following equilibrium problem

$$\begin{aligned} \int_V \boldsymbol{\sigma}:\delta\boldsymbol{\varepsilon} dV = \int_V \delta\boldsymbol{u}\cdot\boldsymbol{b} dS + \int_{\partial V} \delta\boldsymbol{u}\cdot\hat{\boldsymbol{t}} dS\,, \\ \boldsymbol{\sigma}\cdot\boldsymbol{n} = \hat{\boldsymbol{t}} \qquad on\ \partial V_t, \\ \boldsymbol{\phi}(x) = \hat{\boldsymbol{\phi}}(x) \quad on\ \partial V_u, \end{aligned} \tag{1}$$

where ∂V_t and ∂V_u are partitions of the boundary surface, $\partial V = \partial V_t \cup \partial V_u$, where surface traction and displacements are applied, $\boldsymbol{b}$ are the body forces, and $\boldsymbol{\sigma}$ is the Cauchy stress tensor that depends on the deformation gradient $\boldsymbol{F} = \partial\boldsymbol{\phi}(\boldsymbol{X})/\partial\boldsymbol{X}$, i.e. $\boldsymbol{\sigma} = \boldsymbol{\sigma}(\boldsymbol{F})$. On the contrary, in inverse elasticity the position $\boldsymbol{x}$ is known and we want to compute $\boldsymbol{X}$. This problem can be solved by a simple re-parametrization of problem (1) in terms of the inverse motion $\boldsymbol{X} = \boldsymbol{\varphi}(\boldsymbol{x})$ and the inverse deformation gradient, $\boldsymbol{f} = \partial\boldsymbol{\varphi}(\boldsymbol{x})/\partial\boldsymbol{x} = \boldsymbol{F}^{-1}$, for which $\boldsymbol{\sigma} = \boldsymbol{\sigma}(\boldsymbol{f}^{-1})$[4]. In this work, the principle of virtual work is solved by means of the Newton-Rapson method where exact linearization of the first integral is carried out, considering that V is a known domain, instead of using a finite difference approximation as in [3]. The methodology, implemented in Matlab R2019a, was validated by comparing its results with results from Abaqus finite element solver.

Results

The algorithm has been tested in (fig. a) a 1 element parallelepiped and (fig. b) an idealized arterial tube discretized with 40 hexahedral elements. Both the models were loaded with a uniform lateral Cauchy traction of 10 kPa. The material was assumed as neo-hookean isotropic with initial shear modulus $\mu = 25$ kPa and Poisson's ratio of 0.48. The IE approach converged in both the geometries quadratically (fig. c). Results from the implemented IE algorithm are compared with results from the commercial software in terms of final unloaded geometry configuration mismatching (fig. d-e).

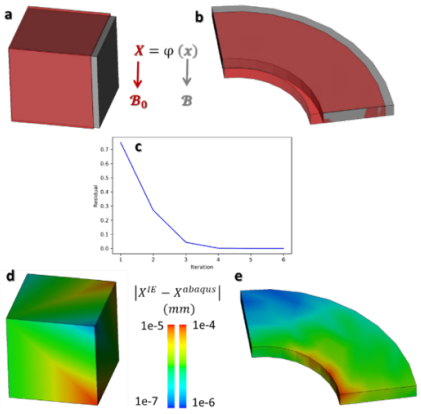

Discussion

The importance of considering the pre-stress state for patient specific simulations has been demonstrated in a number of applications. In [1,2] it is demonstrated that no considering the in-vivo stress state leads to an underestimation of the risk in abdominal aortic aneurysms (AAA). Compared to previous work, the methodology implemented in this work avoids the systematic derivation of the Eulerian equations as proposed in [5] which significantly facilitates the implementation. On the contrary, our work extends the work in [3] by incorporating exact linearization of the governing equations increasing efficiency and accuracy of the algorithm.

References

1. De Putter et al. J. Biomech, 40, 1081-1090, 2007.
2. Riveros et al, Ann. Biomed. Eng, 41:694-708, 2013.
3. Peirlinck et al, J Mech Behav Biomed Mat, 85:124-133, 2018.
4. Mihalic and Govindjee. Comput Methods Appl. Mech. Engrg 136: 47-57, 1996
5. Lu et al. Int. J. Numer. Methods Eng. 69, 1239–1261.

ANALYSES OF BLOOD FLOW THROUGH MECHANICAL TRILEAFLET AND BILEAFLET AORTIC VALVES

Anna Nieroda (1), Marek Pawlikowski (1)

1. Institute of Mechanics and Printing, Warsaw University of Technology, Poland

Introduction

Abnormal functioning of the aortic valve contributes to improper cardiovascular and a significant load on the heart muscle. Often the only and effective solution is an artificial aortic valve transplant. The simulation of blood flow through an artificial aortic heart valve using the finite element method (FEM) is the main subject of the research. The studies aim to verify the performance of mechanical aortic valves of two types, i.e., bileaflet (BIL) and trileaflet (TRI) valves (Figure 1). The construction of the BIL valve is based on commercially used aortic valves.

Methods

The numerical model of the system consisted of the left ventricle, valve, and aortic fragment. We analysed the blood flow at four positions of the valves' leaflets defined through an angle concerning the vertical plane (passing through the symmetry axis of the valve) 60◦ (fully closed valve), 40◦, 20◦, and 0◦ (fully opened valve).

The blood flow was defined in a way reflecting the actual, pulsatile nature of the flow. The correlation of the flow velocity and the time opening of the leaflets was determined utilising the Doppler ultrasound examination in an adult human being [1]. Blood flow through the valve includes both the movement of the fluid and the movement of the valve leaflets. The dynamics of blood circulation were determined using ANSYS 2019 R2 software. The use of three modules made it possible to analyze flow characteristics and determine the influence of structural response on cyclic fluid movement.

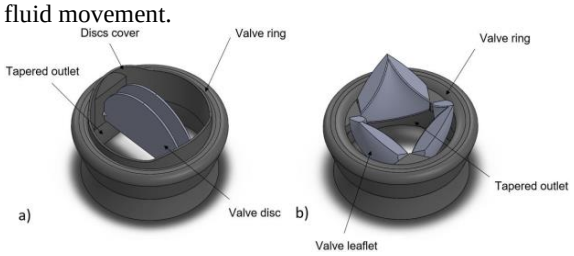

Figure 1: Geometrical models of a) bileaflet and b) trileaflet valves.

Results

The performance of the considered valves was assessed through reduced stress in the valves resulting from the interaction of the flowing blood and the leaflets, shear stress in the aorta wall, and an effective orifice area. Mounting of the leaflets in the valve ring was also analysed. The obtained results give new insights into the strength performance of the design of the leaflet fixation in the annular rings.

Stress distribution in the leaflets of the BIL and TRI valves was calculated as well as the flow through it was characterised. Figure 2 shows the blood velocity distributions during flow through the valve. Besides, the flow velocity profile was analyzed to verify symmetry of the flow.

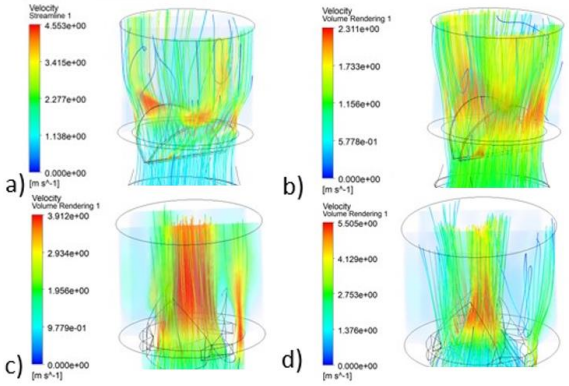

Figure 2: The flow velocity through the valve, with the angle of the opening of the discs, BIL: a) 20◦, b) 40◦, TRI: c) 20◦, d) 40◦.

Discussion

The blood flow velocity is higher in the case of the TRI valve, which results from Bernoulli's law. Interestingly, the lower values of blood flow velocity through the partially and fully opened BIL valve correspond to those for the natural trileaflet aortic valve [2]. The maximal stress concentrations were observed in the hinges. Similar results were also obtained by other investigators [3].

The shear stress affects the behavior of blood cells during flow. Regions of high shear stress can cause a thrombotic response, specifically through haemolysis and shear-induced platelet activation. From the obtained results, we conclude that none of the considered mechanical valves will cause haemolysis.

The paper presents an easy-to-implement methodology of flow modelling and defines liquid-structure interaction. Haemodynamic analysis of an artificial aortic valve is a crucial element of the study and improvement of its construction.

References

1. Amindari A et al, Inf in Medicine Unlocked, 9:191, 2017.
2. Sundström E et al, International Journal for Numerical Methods in Biomedical Engineering, 36(7):1–14, 2020.
3. Kwon YJ, Journal of Mechanical Science and Technology, 24(2):461–469, 2010.

DEEP LEARNING TO ESTIMATE THE ARTERIAL STRAIGHTENING INDUCED BY STIFF GUIDEWIRES DURING EVAR

Alice Fantazzini (1)(2)(3), Michele Conti (2), Curzio Basso (3), Giovanni Spinella (4)

1. Department of Experimental Medicine, University of Genoa, Italy; 2. Department of Civil Engineering and Architecture, University of Pavia, Italy; 3. Camelot Biomedical Systems S.r.l, Italy; 4. Vascular and Endovascular Surgery Unit, University of Genoa, Italy

Introduction

Endovascular aneurysm repair (EVAR) is a minimally invasive procedure emerging as the primary technique to treat patients with intermediate and high operative risks [1]. During the intervention, one or more stent grafts are guided to the aneurysm site using real-time 2D fluoroscopy imaging. In recent workflows, preoperative images are aligned with intraoperative fluoroscopy to get a 3D patient-specific vascular roadmap and reduce the need for contrast agent and radiation dose [2]. However, the insertion of stiff endovascular tools during the intervention may deform the vessel anatomies, degrading the image fusion accuracy [3]. Recently, several studies have focused on finite element analysis (FEA) to estimate the intraoperative tool-tissue interactions [4, 5]. However, computational methods have high cost in terms of computational requirements, which prevents the inclusion of FEA in the clinical workflow. In the last few years, some studies have proposed deep neural networks as FEA surrogate to address the need for real-time predictions [6, 7].
In this study, we investigate the feasibility of using deep learning to predict the arterial straightening induced by stiff guidewires during EVAR. The intraoperative aortic configuration predicted by the deep learning model can be registered to the fluoroscopic images allowing coherent navigation and overcoming the limitations of FEA in terms of computational times.

Methods

Computed Tomography Angiography (CTAs) of 40 patients affected by abdominal aortic aneurysms have been provided by IRCCS San Martino University Hospital (Genoa, Italy). The patient-specific anatomies have been extracted from the CTAs following [8]. To reduce the complexity of the problem, each mesh has been represented with centerline and radius. Given the limited set of 3D aortic models, a Statistical Shape Model was built to increase the dataset: from 40 patient-specific anatomies, a set of 4349 virtual geometries has been generated. These models have been submitted to a FEA simulation in order to estimate the intraoperative straightening caused by stiff guidewires. Finally, a Convolutional Neural Network has been designed to model the non-linear relationships between the preoperative aortic configurations and the corresponding intraoperative state provided by FEA. A grid-search strategy has been adopted to tune the model hyper-parameters and find the optimal hyper-parameters configuration.

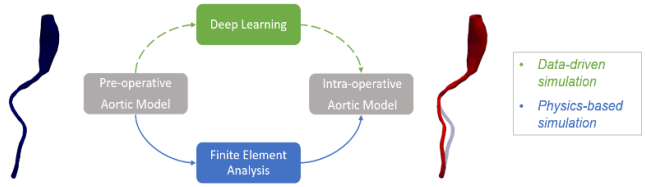

Figure 1: Flowchart of the proposed method.

Results

The performance of the deep learning model has been evaluated in terms of the mean distance between the predicted intraoperative configuration and the ground truth obtained with FEA. The distance has been computed separately for centerline points and the associated radius.
A centerline error of 0.29 ± 0.04 mm, 1.65 ± 0.94 mm, and 1.69 ± 1.06 mm has been computed for the training, validation, and test set, respectively. A mean radius error of 0.0011 ± 0.0007 mm, 0.0054 ± 0.0083 mm, and 0.0050 ± 0.0062 mm has been obtained for the above mentioned sets. The trained method takes around 0.053± 0.028 ms to run a prediction on a single model.

Discussion

A convolutional neural network has been proposed to predict the intraoperative aortic deformations caused by tools-tissue interaction. The proposed approach shows high accuracy on the training data and generalizes quite well on the validation and test data. The promising preliminary results suggest the ability of the network to estimate the intraoperative aortic deformations. Moreover, the deep learning model enables fast prediction in the inference phase, making this surrogate model suitable for clinical workflows.

References

1. H. Rafii-Tari et al, Ann Biomed Eng, 42: 697–715, 2014.
2. C. Kauffmann et al, J Vasc Interv Radiol, 26: 544-551, 2015.
3. A. Duménil et al, IEEE Trans Biomed Eng, 60: 1353–1362, 2013.
4. J. Gindre et al, Int J Numer Methods Biomed Eng, 31:e02716, 2015.
5. H. Mohammadi et al, Ann Biomed Eng, 46: 2148–2161, 2018.
6. L. Liang et al, J R Soc Interface, 15: 20170844, 2018.
7. L. Liang et al, Int J Numer Methods Biomed Eng, 34: e3103, 2018.
8. A. Fantazzini et al, Cardiovasc Eng Technol, 11: 576-586, 2020.

FINITE ELEMENT ANALYSIS OF A NOVEL PROCEDURE FOR THE MITRAL VALVE REPLACEMENT IN PEDIATRIC PATIENTS

Alessandro Caimi (1), Marcello Arcangeli (1), Matteo Frigelli (2), Francesca Pluchinotta (2-1), Francesco Sturla (2-1), Serenella Castelvecchio (2), Peter Hammer (3), Alberto Redaelli (1), Pedro Del Nido (3), Emiliano Votta (1)

1 Politecnico di Milano, Milano, Italy; 2 IRCCS Policlinico San Donato, San Donato Milanese, Italy; 3 Children's Hospital Boston, Boston, United States;

Introduction

Mitral stenosis (MS) is a frequent congenital condition characterized by structural defects of the valve leaflets leading to dangerous complications such as pulmonary hypertension and pulmonary edema [1]. In pediatric patients, the standard treatment consists in the replacement of the pathologic valve with mechanical and bioprosthetic devices or with pulmonary autograft; however, re-replacement is inevitable due to patient somatic grow [2]. Hence, the surgical implant of an oversized stent-mounted Melody™ valve (Medtronic, Minneapolis USA), which can be percutaneously expanded after surgery, was proposed [3]. Even though this procedure seems to be promising in the treatment of young patients, implant durability can be hampered by prosthetic leaflet damage [4]. We exploited finite element (FE) analysis to assess, at off label device implantation, the biomechanical impact of both device shrinking and LV *in vivo* motion on the prosthetic leaflets.

Methods

The FE model consisted in two main parts: the left ventricle (LV) and the Melody™ valve (Figure 1). LV endocardial surface geometry, of a normal patient, and motion were yielded by off-line processing of 3D ultrasound data of a normal subject through TomTec (TomTec Imaging System) and subsequently downsized to achieve LV characteristics of a pediatric patient. The Melody™ valve model included each relevant component: bovine jugular vein, i.e., wall and valve leaflets, and the CP-Stent™ [5]. LV motion was imposed through nodal time-dependent kinematic constraints. Leaflet strains and stresses at peak pressure were comparted vs. those yielded by two auxiliary models, where the valve was implanted in two static cylinders with 22mm diameter, i.e., the nominal working dimension of the valve, and 15mm diameter, i.e., the size of the annulus in the LV model. All simulations were performed in ABAQUS/Explicit (SIMULIA, Dassault Systèmes)

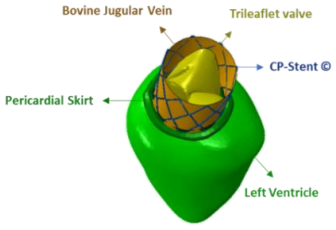

Figure 1: FE model of the Melody™ valve implanted in the LV

Results

When the valve diameter was shrunk to 15mm, two effects were evident: a massive increase in leaflet shear strains and relevant pinwheeling of the free margin, the latter being further exacerbated when the implant in the dynamic LV was simulated (Figure 2). Both effects are consistent with the typical locations of observed leaflet damages.

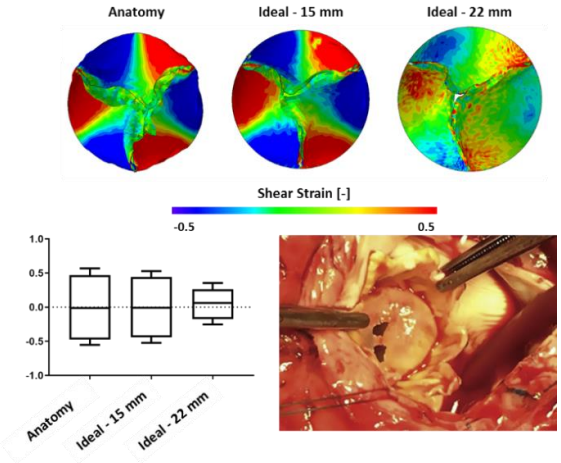

Figure 2: Contour maps and box-plots of shear strain distribution on Melody leaflets in the different tested scenarios; in vivo appearance of localized rupture on the implanted device [6].

Discussion

Our FE framework proved able to couple a realistic numerical model of the Melody™ valve with the kinematics of the LV during the cardiac cycle, elucidating the effect of the procedure on the implanted device. Our results suggest that valve undersizing dominates over annular dynamics in inducing biomechanically driven leaflet damage. If further tested and validated, this approach may support the improvement of the surgical procedure.

References

1. Shahbudin H.R. et al., *Circ*, 2002; 106: 1183-88
2. Brown J.W. et al., *ATS, 2012; 93: 626-33*
3. Emani S.M. et al., *OTTCS*, 2014; 19: 454-463
4. Schneider H. et al., *Int J Cardiol*, 2015; 189: 124-31
5. Caimi A. et al, *J Biomech* 2018; 79: 135-146
6. Grandinetti M. et al, *ATS* 2018, 105: 169-170

A NOVEL METHODOLOGY FOR COMPLIANT, PERSONALISED AORTIC FLOW SIMULATIONS INFORMED BY MULTIMODAL MRI DATA FUSION

Catriona Stokes (1), Mirko Bonfanti (1), Zeyan Li (2), Jiang Xiong (3), Duanduan Chen (2), Stavroula Balabani (1), Vanessa Díaz-Zuccarini (1)

1. University College London, UK; 2. Beijing Institute of Technology, China; 3. Chinese PLA General Hospital, China

Introduction

Four-dimensional Flow Magnetic Resonance Imaging (4D-Flow MRI) is a medical imaging technique that measures time-resolved, three-dimensional and three-component fluid velocity fields *in-vivo*. As its spatial and temporal resolution are limited, some clinically relevant flow features cannot be accurately measured [1]. Computational Fluid Dynamics (CFD) can simulate the flow with higher resolution than MRI. However, accuracy and patient-specificity are challenging to achieve and of critical importance. CFD informed by MRI data can effectively enhance the resolution of MRI images, providing haemodynamic data with higher accuracy and consistency than an individual data source could provide. Despite the widespread use of rigid-wall simulations, arterial wall compliance has been shown to affect accuracy in aortic CFD simulations. Compliance is typically modelled using Fluid-Structure Interaction (FSI), a costly technique that cannot be personalised directly as the structural properties of the aortic wall cannot be measured *in-vivo*. In recent work to inform an aortic FSI model using 4D-Flow MRI data, wall movement was not accurately simulated [2]. This work presents a novel CFD methodology to produce patient-specific compliant aortic flow simulations using multimodal MRI data alone, based on a previously developed Moving Boundary Method (MBM) to circumvent the limitations of FSI [3].

Methods

This work was ethically approved by the Institutional Review Board of the Chinese PLA General Hospital (S201703601). Black Blood MR Angiography (BBMRA), 2D Cine-MRI and 4D-Flow MRI sequences of the thoracic aorta of a healthy volunteer were acquired, in addition to heart rate and non-invasive brachial blood pressure measurements. A data fusion process was employed to address discrepancies in MRI data. The fluid domain was then segmented from BBMRA images, and 2D-Cine MRI images were used to calibrate wall movement. 4D-Flow MRI data provided an inlet flow rate waveform and facilitated the calibration of patient-specific three-element Windkessel outlet boundary conditions. The unsteady Reynolds-Averaged Navier-Stokes equations were solved using ANSYS CFX 19.0 (ANSYS Inc.) using the *k-ω* SST turbulence closure model and a Carreau-Yasuda non-Newtonian viscosity model. CFD results were validated against 2D Cine-MRI and 4D-Flow MRI data, and pressure measurements.

Results

CFD predicted systolic and diastolic pressures within 1% of target values, and mean outlet flow rates within 2%. Flow rate waveforms matched 4D-Flow MRI with a mean percentage error of 6-8% throughout the aorta. Wall movement, quantified as luminal cross-sectional area, closely matched 2D-Cine MRI waveforms, with a mean percentage error of 0.4-2%. Excellent agreement was observed in velocity distributions between 4D-Flow MRI and CFD. The close agreement between CFD and MRI is shown in Fig. 1. Due to its limited spatial resolution, 4D-Flow MRI could not accurately resolve the fluid boundary layer, with a mean thickness of ~5 mm, more than six times the expected thickness of 0.75 mm that was captured by CFD.

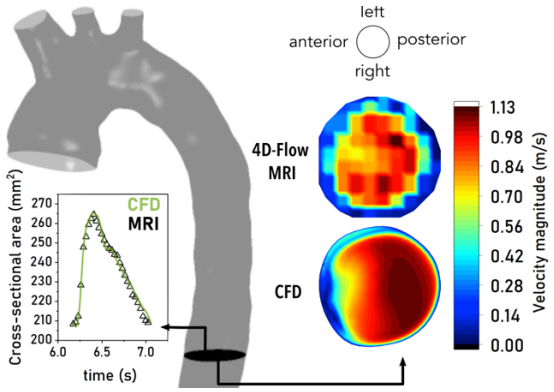

Figure 1: Cross-sectional area comparison between CFD and 2D Cine-MRI (L), and comparison of velocity magnitude contours from 4D-Flow MRI and (R), at a plane in the descending thoracic aorta.

Discussion

Excellent agreement was observed between CFD and MRI, highlighting the effectiveness and accuracy of this novel workflow and its robustness to inconsistencies in MRI data. This technique offers clear benefits in computational efficiency and patient-specificity over MRI-based rigid or FSI simulation techniques and could be generalized to simulate other types of cardiovascular flows.

References

1. Mazzi et. al., *Biomech. Model. Mechanobiol.*, 19:1403-1423, 2019.
2. Boccadifuoco et. al., *Cardiovasc. Eng. Technol.*, 9:688-706, 2018.
3. Bonfanti et. al., *J. R. Soc. Interface*, 14(136), 2017.

BLOOD FLOW SIMULATIONS OF MOVING SINGLE RIGHT VENTRICLES IN PEDIATRIC PATIENTS

Anna Grünwald[1], Jana Korte[1], Nadja Wilmanns[1], Christian Winkler[2], Katharina Linden[2], Ulrike Herberg[2], Sascha Groß-Hardt[1], Ulrich Steinseifer[1], Michael Neidlin[1]

1. Department of Cardiovascular Engineering, Institute of Applied Medical Engineering, Helmholtz Institute, Medical Faculty, RWTH Aachen University, Germany

2. Department of Pediatric Cardiology, University Hospital of Bonn, Germany

Introduction

The treatment of congenital heart defects, such as the univentricular heart, represents a major challenge in cardiovascular research. The univentricular heart (UVH) occurs with a frequency of 0.04 - 0.5% in newborns [1] and is treated using a Fontan procedure. Although quality of life and life expectancy is greatly improved by this treatment, the possibility of death or cardiac transplantation in a 20-year-old patient is between 13-18% [2, 3]. A deeper understanding of physiology and function in UVH is necessary, to improve future treatments and therapies. Computational Fluid Dynamics (CFD) models of blood flow in the single right ventricle, is an option to investigate the hemodynamics in patient-specific geometries. Particularly, the intriguing interaction between the complex three-dimensional ventricular movement and the developing flow features can be analyzed with this technique.

CFD simulation of the pathological single right ventricle in contrast to the healthy left ventricle is the research object of the present work. The aim is the numerical comparison of the intraventricular flow within the ventricles.

Methods

Patient-specific measurements of ventricles from three-dimensional real-time echocardiographic images served as the basis for the simulations with five single right ventricle (SRV) patients and two subjects with healthy left hearts (LV). Interpolation of these data reproduced the shape and continuous motion of the heart during a cardiac cycle. This motion was implemented into a CFD model with a moving mesh methodology. For comparison of the ventricles, the vortex formation as well as the occurring turbulent kinetic energy (TKE) and washout were evaluated. Vortex formation was assessed using the dimensionless vortex formation time (VFT).

Results

The results show significantly lower values for the VFT and the TKE in SRV patients than for the LV patients. Furthermore, diastolic vortex structures exhibit tremendous differences between the two groups, most strikingly the vortex formation does not propagate towards the apex in SRV patients (Figure 1). These findings were confirmed by a significantly lower washout in SRV patients.

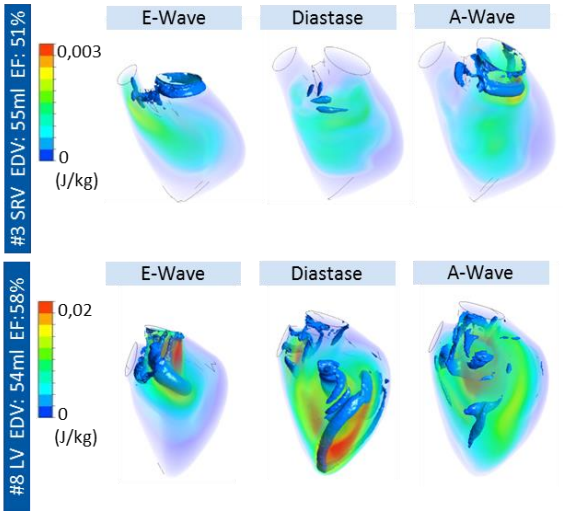

Figure 1: Turbulent kinetic Energy (J/kg) and vortex structure formation with Q-value 6000 (1/s) for subject #3 (SRV) and subject #7 (LV) during diastole

Discussion

Flow simulation within the moving ventricle provides the possibility of more detailed analysis of the ventricular function. Simulation results show altered vortex formation and reduced washout of SRV in comparison to healthy LV. These flow features seem to provide important information on ventricular function and might be useful as a surrogate marker for the planning and treatment of Fontan patients.

References

1. Hoffman et al, Journal of the American College of Cardiology 39, 12:1890-1900, 2002.
2. Ono et al, European journal of cardio-thoracic surgery 30, 6:923-929, 2006
3. Khairy et al, Circulation 117, 1:85-92, 2008

Acknowledgements

This study was funded by Fördergemeinschaft Deutsche Kinderherzen e.V. – PN: W-BN-011/2017 KH BN.

AN INITIAL EXPERIENCE OF CONSTRAINED MIXTURE BASED CARDIAC GROWTH AND REMODELLING

Debao Guan, Xiaoyu Luo, Hao Gao

School of Mathematics & Statistics, University of Glasgow, UK

Introduction

Heart disease is the leading killer worldwide, responsible for about 30% of all deaths each year. The incidence of heart failure, such as after a heart attack, has remained persistently high due to the maladaptive growth and remodeling (G&R). Mathematical modelling of cardiac growth has potential for providing effective, reliable, and consistent risk-stratification to patients. Volumetric growth has been widely used in modelling cardiac G&R, while it has limitations to link with the pathological adaptation of different constituents. To overcome this, we adopt the constrained mixture theory framework for modelling cardiac G&R by treating myocyte and collagen separately in a beating human heart under various physiological and pathological conditions. The updated reference framework [1] is further adapted for simplifying the numerical implementation.

Methods

According to [2], the homogenized constrain mixture theorem assumes all constituents share the same total deformation gradient tensor ($\boldsymbol{F}$) from one configuration to another grown configuration, that is

$$\boldsymbol{F}=\boldsymbol{F}_{\mathrm{e}}^{i}\boldsymbol{F}_{\mathrm{r}}^{i}\boldsymbol{F}_{\mathrm{g}}^{i}, \quad (1)$$

where i is the ith constituent, $\boldsymbol{F}_{\mathrm{g}}^{i}$ is the growth tensor which can be either stress-driven or strain-driven or both, $\boldsymbol{F}_{\mathrm{r}}^{i}$ is the remodeling tensor to ensure geometrical compatibility after G&R (no-overlap, no gap, etc.), and $\boldsymbol{F}_{\mathrm{e}}^{i}$ is the elastic deformation tensor to ensure the constraint requirements. Growth tensors for collagen fibre ($\boldsymbol{F}_{\mathrm{g}}^{\mathrm{c}}$) and myofiber ($\boldsymbol{F}_{\mathrm{g}}^{\mathrm{m}}$) are expressed as

$$\boldsymbol{F}_{\mathrm{g}}^{i}=\vartheta_{\mathrm{f}}^{k}\,\mathbf{f}_0\otimes\mathbf{f}_0+\vartheta_{\mathrm{s}}^{k}\,\mathbf{s}_0\otimes\mathbf{s}_0+\mathbf{n}_0\otimes\mathbf{n}_0,\ \ k=\mathrm{m,c} \quad (2)$$

where $\mathbf{f}_0$, $\mathbf{s}_0$, and $\mathbf{n}_0$ are fibre, sheet, and sheet normal directions at reference configuration, $\vartheta_{\mathrm{f}}^{k}$ and $\vartheta_{\mathrm{s}}^{k}$ are orientational growth multipliers, governed by specific growth laws [3], in specific

$$\dot{\vartheta}=\frac{1}{\tau}\left[\frac{\vartheta^{\max}-\vartheta}{\vartheta^{\max}-1}\right]^{\gamma}\langle\kappa^{e}-\kappa^{\mathrm{crit}}\rangle, \quad (3)$$

where κ^{crit} is the threshold value, and $\kappa=\lambda$ is for eccentric growth driven by stretch, and $\kappa=p$ is for concentric growth driven by stress, in which stretch λ and stress p are mechanical clues from cardiac dynamics. κ, γ, and $\vartheta^{\max}$ are constant parameters. We can further consider a special case, if assuming no growth in collagen, then collagen has to remodel itself to provide support for grown myocytes, that is $\vartheta_{\mathrm{f}}^{\mathrm{c}}=\vartheta_{\mathrm{s}}^{\mathrm{c}}=1$ and

$$\boldsymbol{F}_{\mathrm{r}}^{\mathrm{c}}=\vartheta_{\mathrm{f}}^{\mathrm{m}}\,\mathbf{f}_0\otimes\mathbf{f}_0+\vartheta_{\mathrm{s}}^{\mathrm{m}}\,\mathbf{s}_0\otimes\mathbf{s}_0+\frac{1}{\vartheta_{\mathrm{f}}^{\mathrm{m}}\vartheta_{\mathrm{s}}^{\mathrm{m}}}\mathbf{n}_0\otimes\mathbf{n}_0. \quad (4)$$

$\boldsymbol{F}_{\mathrm{r}}^{\mathrm{c}}$ can be either elastic or inelastic (no force induced).

Results

Figure 1 shows the two cases by considering myocyte G&R with only remodeled collagen network as in Eq. (4), one is strain driven (eccentric growth) and the other one is stress driven (concentric growth). With time, the growth rates are slowed down because of the physiological limitations and reduced strain/stress levels towards a more balanced biomechanical homeostasis. It can be found that heart wall remodeling mainly occurs in the endocardium.

In eccentric growth only with growth along myofibres, if the collagen network is treated to be inelastic remodeling, then it will allow the myocardial mass to be increased by 24% but softer after remodeling because of less collagen volume fraction. In contrast, if $\boldsymbol{F}_{\mathrm{r}}^{\mathrm{c}}$ is elastic, then there is only 8% increment in myocardial mass which can be partially explained by the limitation of the very stiff pre-stretched collagen network. On the contrary, in concentric growth with only cross-fibre growth, myocardium volume increases by 39% with elastic collagen remodelling, larger than the case with the inelastic collagen remodelling (34%).

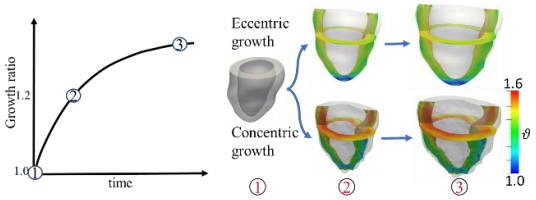

Figure 1: Simulated G&R in a human left ventricle

Conclusion

We have developed a constraint mixture based cardiac G&R framework which can provide critical information in terms of different biological constituents' adaptation under pathological conditions. The interplays of these individual G&R processes in myocytes and collagen have the potential to shed light on the biomechanical mechanism which is responsible for the transition from the compensation stage (myocyte G&R mainly) to the decompensation stage (excessive collagen G&R), and eventually guide us to predict the onset of heart failure.

References

1. Lee et al, Biomech Model Mechanobiol, 15:791-803, 2016.
2. Cyron et al, Biomech Model Mechanobiol, 15:1389-1403, 2016
3. Göktepe et al, J Theor Biol, 265:433-442, 2010

Acknowledgements

Supported by the UK EPSRC (EP/N014642/1), Chinese CSC scholarship and the fee waiver from the UofG.

ASSESSING THE DISTURBED FLOW AND THE TRANSITION TO TURBULENCE IN THE ARTERIOVENOUS FISTULA

Christian Vergara (1), Simone Stella (2), Luca Giovannacci (3), Alfio Quarteroni (4), Giorgio Prouse (3)

1. LABS, Dipartimento di Chimica, Materiali e Ingegneria Chimica, Politecnico di Milano, Italy; 2. MOX, Dipartimento di Matematica, Politecnico di Milano, Italy; 3. EOC-Ente Ospedaliero Cantonale, Lugano, Switzerland; MOX, Dipartimento di Matematica, Politecnico di Milano, Italy& EPFL, Lausanne, Switzerland

Introduction

The arteriovenous fistula (AVF) is the principal vascular access to perform hemodialysis. Its maintenance is very challenging, since it could fail as a consequence of intimal hyperplasia (IH), leading to stenosis. The aim of this work is twofold: (i) to perform a computational study for the comparison of blood flow in different geometric configurations of AVF and (ii) to assess the amount disturbed flow by means of quantifying the transition to turbulence developed as a consequence of sudden change of direction of the flow.

Methods

We reconstructed realistic three-dimensional (3D) geometries of two patients with a side-to-end AVF, by echo-color Doppler (ECD) performed at the EOC-Ente Ospedaliero Cantonale, Lugano, Switzerland. Starting from these two geometries, we built other three virtual AVF configurations obtained by varying the incidence angle. In particular, we consider one smaller and one larger angle with respect to the real one, and a fourth angle greater than 90 degrees to investigate also a smooth loop anastomosis technique.
Computational meshes were then built, with a characteristic mesh size equal to 0.05 cm.
We considered the approximation by Finite Elements of the incompressible Navier–Stokes equations assuming blood as an incompressible and Newtonian fluid. Large eddy simulations (LES) models were introduced to capture the transition to turbulence experienced at the anastomosis. Boundary conditions were obtained from echo-color Doppler (ECD) measurements.

Results and Discussion

To assess and compare the disturbed flow, we considered hemodynamic quantities such as the velocity field, the pressure distribution, and quantities derived from WSS such as OSI. To quantify the transition to turbulence, we computed the turbulent kinetic energy and the standard deviation of the velocity field among different heartbeats in order to assess the variation of the solution.
Results on the velocity field show a very disturbed flow for all the configurations at the anastomosis, see Figure 1. We found also that increasing the angle of incidence of the fistula, if this is less than 90 degrees, the area with high values of OSI, which should be more prone to hyperplasia development, decreases. Moreover, regions with high OSI, are greater and progressively shift toward the anastomosis area and the proximal vein segment with the decrease of the inner angle of anastomosis.

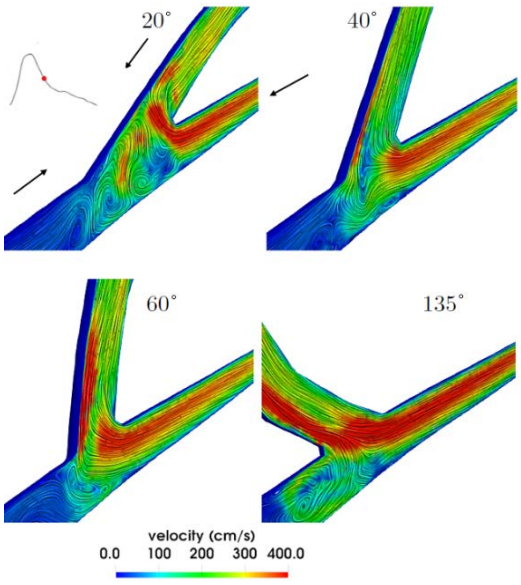

Figure 1: Velocity for the different angle configurations at mid-deceleration. The arrows depict the dominant direction of flow.

Regarding turbulence, we notice that the presence of transitional effects in the fistula is significant at the anastomosis, for any angle of incidence. Indeed, we found large values of the standard deviation of the velocity field (about 40% of the velocity magnitude). This means that high fluctuations of blood flow are present at the anastomosis and are responsible for the transition to turbulence.

References

1. Stella S., Vergara C., Giovannacci L., Quarteroni A., Prouse G., Assessing the disturbed flow and the transition to turbulence in the arteriovenous fistula. Journal of Biomechanical Engineering , 141(10), 101010, 2019
2. Prouse G., Stella S., Vergara C., Quarteroni A., Engelberger S., Canevascini R., Giovannacci L., Computational Analysis of Turbulent Hemodynamics in Radiocephalic Arteriovenous Fistulas to Determine the Best Anastomotic Angles. Ann Vasc Surg, 68,451–9,2020

Acknowledgements

This work has been supported by the Scientific Research Advisory Board of EOC-Ente Ospedaliero Cantonale, Lugano, Switzerland (ABREOC).

LARGE EDDY SIMULATION MODELS FOR PATIENT-SPECIFIC AORTIC HEMODYNAMICS

Anna Ferrarini (1), Michele Conti (1), Alessandro Veneziani (2), Ferdinando Auricchio (1)

1. Department of Civil Engineering and Architecture, University of Pavia, Italy;
2. Department of Mathematics, Department of Computer Science, Emory University, Atlanta, GA, USA.

Introduction

Aortic diseases, such as aneurysms, dissections, and coarctations, are calling for biomechanical assessment of their onset and developments. In particular, detailed comprehension of local hemodynamic change, of the effects of vascular walls modification on the flow pattern, of the gradual adaptation of the global system as a result of surgery, is possible with computational fluid dynamic (CFD) simulations. Proper boundary conditions and turbulent flow modeling should be considered in CFD simulations to get reliable results. As for the treatment of boundary conditions, the main problem is the occurrence of backflow numerical instabilities when prescribing Neumann conditions. Moreover, blood flow in aorta is difficult to simulate and assess due to large Reynolds number at the systolic peak, and complex geometry for aortic diseases [1]. Both these factors may trigger a disturbed or even turbulent flow. In this scenario, Direct Numerical Simulations (DNS) to solve the small significant scales of the flow may require high computational costs, not compatible with a large number of patients, like in a Computer-Aided Clinical Trial. The Reynolds-Averaged Navier-Stokes (RANS) models are not the ideal choice to adopt [2] for the range of Reynolds number of this problem. We are focusing on Large Eddy Simulation (LES) models, which are proved to be more suitable on describing the disturbed flow [3], and, in particular, on the Smagorinsky-Lilly model. This work aims to prove numerically that the Smagorinsky-Lilly model is able to both treat flow disturbances and suppress the occurence of the backflow instability with a proper selection of the Smagorinsky-Lilly constant, C_S.

Methods

We consider three geometries of patient-specific aorta with aneurysm in the vicinity of aortic arch, retrieved from the iCardioCloud Project [4]. We use Netgen [5] for generating the meshes. We perform transient simulations using the commercial software ANSYS (ANSYS Academic Research [Fluent], release 19.2). We prescribe the no-slip condition on the wall of the domain, three-elements Windkessel model [6] at the outlets, and patient-specific flow, as extracted from PC-MRI of each patient, at the inlet. Simulations run for six heart-beats to reach periodicity with a constant time-step set to 0.001 s. We perform both a qualitative and quantitative analysis comparing the results obtained from the LES model with those given by the DNS, running with the software ANSYS Fluent.

Results

We compute the velocity streamlines, the vectors of velocity magnitude and the velocity profiles at the outlets, the time-averaged wall shear stress (TAWSS), the oscillatory shear index (OSI), the local normalized helicity, and the helicity intensity index (h_2 index), defined as in Morbiducci et al. [7]. Figure 1 shows the comparison of OSI results in patient 1 computed from the DNS and the LES model. In particular, we use three meshes to perform LES simulations, ranging from 169124 (coarse mesh) to 1962122 (fine mesh) elements.

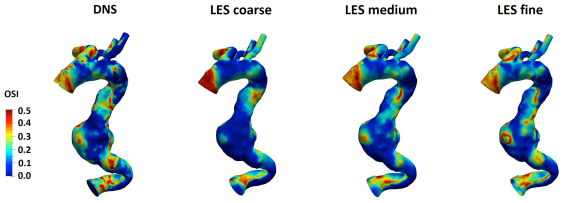

Figure 1: OSI in patient 1 computed from DNS and LES model. Three different meshes (i.e. coarse, medium, and fine) have been involved in the LES results.

Discussion

Our preliminary results prove that the Smagorinsky-Lilly model well controls both flow disturbances and the numerical backflow instability, by tuning the value of C_S. In particular, the latter value is dependent on the mesh size, the Reynolds number, and the shape of the filter of the LES model. In this first study we empirically estimate the value of C_S; however, a future development consists in finding the relation which links the models parameters of the LES together with the mesh size and the Reynolds number.

References

1. H. Xu et al, Annals of Biomedical Engineering, 46:927-939, 2018.
2. Yoganathan et al, Annals of Biomedical Engineering, 33:1689-1694, 2005.
3. J. Lantz et al, Journal of Biomechanics, 46:1851-1858, 2013.
4. R. M. Romarowski et al, Int J Numer Meth Biomed Engng, 34:e314, 2018.
5. J. Schöberl, Comput Visual Sci, 1:41-52, 1997.
6. L. Formaggia et al, Springer Science & Business Media, 2010.
7. U. Morbiducci et al, Journal of Biomechanics, 46:102-109, 2013.

COMPUTATIONAL STUDY TO ASSESS SILICON AORTA MODELS IN PREDICTING CATHETER BIOMECHANICAL PERFORMANCE IN-VIVO

David Symes[1], Patrick King[2], Barry O'Connell[2], Declan Costello[2], Laoise McNamara[1], Claire Conway[3]

1. National University of Ireland Galway, Ireland; 2. Medtronic plc, Ireland; 3. Royal College of Surgeons in Ireland, Ireland.

Introduction

Aortic stenosis develops from the build-up of calcium deposits on the aortic valve. Often, treatment requires intervention via non-invasive transcatheter aortic valve replacement (TAVR). Intermediate-risk patients have a 2% chance of a stroke occurring post-TAVR, which can be caused by catheter delivery forces damaging the vessel or atherosclerotic plaques during intervention [1, 2]. During catheter design and development, the delivery forces are evaluated using in-vitro Delrin benchtop anatomies. However, these in-vitro models are unable to predict plaque rupture and stroke risk. The objective of this research is to develop a patient-specific framework to predict the risk of a cerebrovascular accident occurring post-TAVR. A sub-objective of this research is to implement a finite element (FE) analysis on both an idealized aorta geometry and patient-specific anatomies to investigate the variance between in-vitro testing of catheters and in-vivo mechanical conditions.

Methods

A FE model (**Fig. 1A**) simulating catheter tracking in a 3D idealized deformable aortic arch model was developed using the commercial FE Abaqus/Explicit solver (DS SIMULIA). This model is created as an in-vivo comparison to an in-vitro (benchtop) model in the laboratory. All materials were assumed to be linear elastic and isotropic in terms of finite deformation stress and strain measures. A Poisson's Ratio (PR) of 0.3 was assigned to the catheter and aorta models. The model's moduli were varied from 10 MPa to 2,300 MPa (Delrin). The catheter had a regionally varying modulus (250-950 MPa). An 8-node hexahedral, reduced integration, hourglass control mesh was implemented for all components. The aorta was fixed in the y-direction. A 140mm displacement (z-direction) was applied to the catheter base to simulate tracking around the arch. Surface-to-surface contact was implemented between catheter and aorta wall with a coefficient of friction of 0.15 and employing 'hard' contact behaviour. In **Fig. 1C**, 3D geometries of the aortic arch were created from patient CT scans pre-TAVR (MIMICs, Materialise). Catheter tracking forces in patient-specific anatomies are currently being examined.

Results

Reaction force (RF) predictions were compared to in-vitro RF data obtained in the laboratory (**Fig. 1B**). The RF data predicted in the deformable (10 MPa) model aligns well with RF data obtained in the lab. Peak forces differ between the computational model (35 N at 75 mm of tracking) and the in-vitro test data (20 N at initial contact, 10 mm). It was predicted at lower moduli (10-50 MPa), there was an increase in maximum deflection (0.75-2.5 mm) and a decrease in maximum von Mises stress (1.4–1.6 MPa) in the arch when compared to higher moduli (1000 – 2300 MPa) where the maximum deflections and von Mises stresses ranged between 0.04 – 0.045mm and 1.8 – 1.85 MPa, respectively.

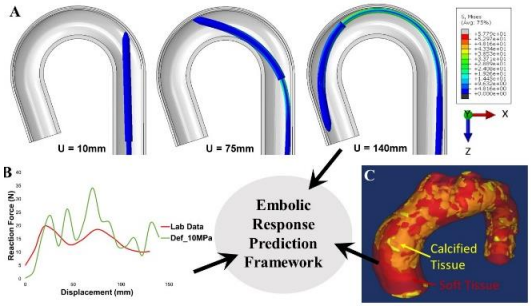

Figure 1: (A) FE catheter model tracking in an idealized aortic arch; (B) RF predictions for the deformable model (green) against in-vitro data (red), and (C) Reconstructed patient-specific aortic arch.

Discussion

This study examined and compared catheter tracking forces obtained from computational predictions simulating in-vivo mechanical conditions to in-vitro test data. The higher peak forces experienced in the deformable model could be contributed to the simplicity of the material model employed. Despite the higher peak forces, the reaction force predictions align closely to the in-vitro data. As such, these preliminary predictions suggest that in-vitro testing provides a reasonable estimate of the forces experienced during in-vivo tracking. The predictions reported here reveal that varying the aortic wall stiffness results in greater maximum deflection at lower moduli and greater maximum von Mises stress at higher moduli in the aortic arch. This mechanical response was expected and further validates the predictions obtained in these simulations. Further research will incorporate XFEM simulations with patient-specific anatomies to predict rupture risk leading to an embolic response post-TAVR. This current study provides the basis to develop a much-needed patient-specific framework to predict the risk of a cerebrovascular accident occurring post-TAVR.

References

1. Thourani *et al.* 2016. The Lancet. 387:2218-25.
2. Finn, Morris. 2016. J Eng Med. 230(2):153-65.

Acknowledgements

Irish Research Council Enterprise Partnership Scheme, Grant Number: EPSPG/2019/508;

TOWARDS A BETTER UNDERSTANDING OF THE FLOW BEHAVIORS IN FEMORO-POPLITEAL ARTERIES THROUGH OCT-BASED CFD MODELS

Can Gökgöl (1), Yasushi Ueki (2), Daniel Abler (1), Nicolas Diehm (3), Rolf Engelberger (4), Tatsuhiko Otsuka (2), Lorenz Räber (2) & Philippe Büchler (1)

1. ARTORG Center for Biomedical Engineering Research, University of Bern, Switzerland; 2. Department of Cardiology, Inselspital, Bern University Hospital, Switzerland; 3. Vascular Institute Central Switzerland, Switzerland; 4. Department of Angiology, HFR Freiburg – Kantonsspital, Switzerland.

Introduction

Selecting the correct endovascular treatment approach for patients with Peripheral Arterial Disease (PAD) is crucial to avoid restenosis in femoro-popliteal (FP) arteries. To reduce potential problems associated with stent implantation, clinicians are frequently performing Percutaneous Transluminal Angioplasty (PTA) in arterial segments affected by leg flexion. However, the impact of different treatment methods on the flow behaviors of FP arteries are poorly understood, as the imaging methodologies used in existing works are unable to accurately represent the post-treatment arterial geometries [1, 2]. The main objective of this study was to develop a framework to build personalized models of FP arteries based on intra-arterial imaging, which allows modeling the arterial dissections that occur following PTA. Our hypothesis is that this increased accuracy enables a detailed analysis of the hemodynamic behaviors of the artery prior to and at different time-points of endovascular therapy.

Methods

8 patients diagnosed with PAD were recruited for the study. Half of the patients were only treated with PTA, while the rest were implanted with Nitinol stents. Before and immediately after endovascular treatment, Optical Coherence Tomography (OCT) and 2D angiographic imaging were utilized to segment the lumen contour and the 3D arterial centerline, respectively. A label image containing the arterial lumen was generated and warped onto the X-ray centerline using a dense displacement field computed between the OCT-based and X-ray centerlines for all the voxels identified from the OCT dataset. The warped label image was used to create a surface mesh of the arterial lumen, which was transferred to LS-DYNA for Computational Fluid Dynamics (CFD) analyses. A volumetric flow profile obtained from the ultrasound measurements of 24 patients was applied at the inlet; while at the outlet, a two-parameter (RC) Windkessel model was defined. Blood flow was simulated over three cardiac cycles and adverse hemodynamic behaviors were evaluated as the regions with low time-averaged Wall Shear Stress (TAWSS) (< 0.5 Pa) and high TAWSS (> 7 Pa).

Results

Prior to endovascular therapy, the mean area affected by low TAWSS was found to be 0.95 cm^2 ± 0.59 cm^2. Balloon angioplasty was found to significantly increase this baseline value, as the affected areas following PTA were computed to be 2.10 cm^2 ± 1.09 cm^2 (p = 0.048). In arteries with dissections, 88% of the surfaces covering the false lumens exhibited low TAWSS and, for three patients, 65% of the affected areas was concentrated at these locations. Similarly, the areas affected by low TAWSS in stented arteries were significantly higher than the pre-PTA configuration (3.10 cm^2 ± 0.98 cm^2, p = 0.013). Compared to PTA, the affected areas were more homogenously distributed along the length of the stented segments.

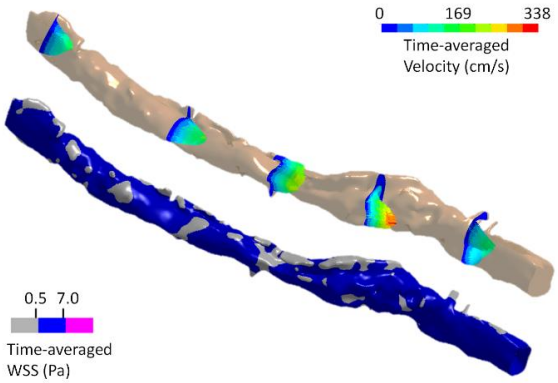

Figure 1: The development of time-averaged flow velocity and distribution of TAWSS in an artery following PTA.

Discussion

While no significant differences were found in adverse flow conditions between Nitinol stent implantation and a PTA-only approach, the presence of false lumens was found to contribute to an increase in the surfaces affected by low TAWSS, which can compromise the decision to leave-nothing-behind. These observations show that the use of OCT-based numerical models has the potential to reveal the long-term effects of endovascular therapy in FP arteries and inform clinicians regarding the optimal treatment approach.

References

1. Gökgöl et al, Biomech M Mechanobiol, 18:1883-93, 2019.
2. Colombo et al, Med Eng Phys, 75 :23-35, 2020.

Acknowledgements

This work was supported by the Swiss National Science Foundation (grant 320030_173130) and Swiss Heart Foundation (grant FF19116).

BENEFITS OF OCT-BASED CFD ANALYSES OF FEM-POP ARTERIES: ARE INTRA-ARTERIAL IMAGING MODALITIES NECESSARY?

Can Gökgöl (1), Yasushi Ueki (2), Daniel Abler (1), Nicolas Diehm (3), Rolf Engelberger (4), Tatsuhiko Otsuka (2), Lorenz Räber (2) & Philippe Büchler (1)

1. ARTORG Center for Biomedical Engineering Research, University of Bern, Switzerland; 2. Department of Cardiology, Inselspital, Bern University Hospital, Switzerland; 3. Vascular Institute Central Switzerland, Switzerland; 4. Department of Angiology, HFR Freiburg – Kantonsspital, Switzerland.

Introduction

Numerical simulations of femoro-popliteal (FP) arteries not only aim at understanding the high restenosis rates afflicting this arterial vasculature, but are also being used to perform virtual testing of different balloon and stent designs. The arterial geometries that form the basis of these analyses are obtained from different clinical imaging modalities and, as such, represent the patient-specific data in varying level of details [1, 2]. However, it is not entirely clear whether models built from more complex modalities, which are usually not part of the clinical routine, produce improved indications within a numerical framework. To determine the necessity of using these additional techniques, we have performed Computational Fluid Dynamics (CFD) analyses on models based only on X-ray angiography or based on a combination of angiographic and intra-arterial imaging.

Methods

12 patients diagnosed with Peripheral Arterial Disease were recruited for the study. 8 patients were only treated with Percutaneous Transluminal Angioplasty (PTA), while the rest were implanted with Nitinol stents. Before and immediately after endovascular treatment, Optical Coherence Tomography (OCT) and 2D angiographic imaging were utilized to segment the lumen contour and the 3D arterial centerline, respectively. The angiography-based 3D models of the arterial lumen were generated from multiple X-ray images using a custom-built 2D/3D reconstruction software. For the OCT-based models, a label image containing the arterial lumen was generated and warped onto the X-ray centerline using a dense displacement field computed between the OCT-based and X-ray centerlines for all the voxels identified from the OCT dataset. This warped label image was used to create the surface mesh of the arterial lumen. Both models were transferred to LS-DYNA for CFD analyses. A volumetric flow profile obtained from the ultrasound measurements of 24 patients was applied at the inlet; while at the outlet, a two-parameter Windkessel model was defined. Blood flow was simulated over three cardiac cycles and adverse hemodynamic behaviors were evaluated as the regions with low time-averaged Wall Shear Stress (TAWSS) (< 0.5 Pa) and high TAWSS (> 7 Pa).

Results

For the pre- and post-PTA timepoints, the mean percentage (%) of the areas affected by low TAWSS were similar for both models (X-ray pre-PTA: 16.33% ± 10.99% & X-ray post-PTA: 22.29% ± 15.94%; OCT pre-PTA: 14.99% ± 12.00% & OCT post-PTA: 23.98% ± 12.60%). For the post-stent group, the models based on the X-ray predicted a slightly higher mean % of affected areas (37.77% ± 26.29) compared to the OCT-based models (29.40 ± 7.91). An individual analysis of the hemodynamics for each patient did not reveal a clear trend regarding the differences between the two imaging modalities, with X-ray models underestimating the adverse hemodynamics for some cases, and overestimating for others based on the corresponding flow rates computed at the inlet.

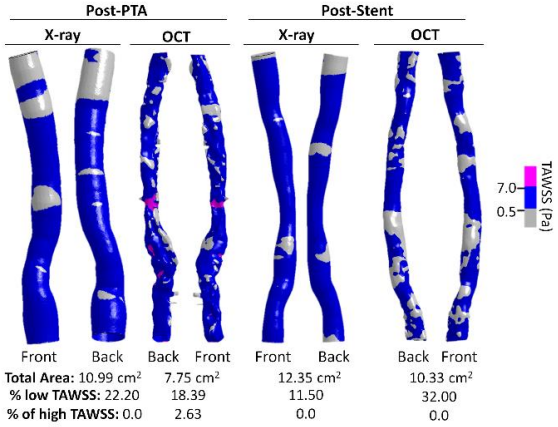

Figure 1: The distribution of TAWSS in X-ray- and OCT-based models for different treatment timepoints.

Discussion

While the mean % of the areas affected by low TAWSS were comparable, the distribution of the TAWSS along the length of the artery showed that X-ray models could not capture the localized flow behaviors, especially around the vicinity of the false lumens created by arterial dissections. As such, the utilization of OCT as the basis of CFD models is important to accurately predict the hemodynamic conditions in FP arteries.

References

1. Gökgöl et al, Biomech M Mechanobiol, 18:1883-93, 2019.
2. Conti et al, Med Eng Phys, 86:57-64, 2020.

Acknowledgements

This work was supported by the Swiss National Science Foundation (grant 320030_173130) and Swiss Heart Foundation (grant FF19116).

IMPACT OF COMPUTATIONAL MODELING STRATEGIES ON PATIENT-SPECIFIC TAVI SIMULATIONS

Anisia Lauditi (1), Alessandro Caimi (1), Francesco Sturla (2,1), Federico De Marco (2), Francesco Bedogni (2), Nedy Brambilla (2), Luca Testa (2), Emiliano Votta (1), Alberto Redaelli (1)

1 Politecnico di Milano, Milano, Italy; 2 IRCCS Policlinico San Donato, San Donato Milanese, Italy;

Introduction

Transcatheter Aortic Valve Implantation (TAVI) is a widely used mini-invasive procedure for the treatment of calcified aortic valve stenosis. TAVI has already proved effective in patients at higher risk for surgery; nonetheless, periprocedural complications may occur, such as ParaValvular Leakage (PVL) and conduction disturbances like the Left Bundle Branch Block (LBBB) [1]. Patient-specific Finite Element Analysis (FEA) can reliably reproduce TAVI procedures and support the prediction of peri-procedural complications. However, FEA is too time-consuming to be included in the decision-making process. Here we search for a trade-off between time-efficiency and reliability, and we assess the impact of modeling simplifications aimed to speeding up simulations.

Methods

The numerical model consisted in a simplified version of self-expandable 26mm CoreValve (Medtronic Inc., USA) modelled with beam elements, and a the patient-specific anatomy based on pre-operative CT imaging. Via segmentation in ITK-SNAP (www.itksnap.org) and *in-house* tools, the aortic root (AR) was reproduced, including calcification spots and aortic valve (AV) leaflets. CoreValve crimping, insertion and deployment into the AR were simulated in Abaqus/Explicit (Dassault Systèmes, France) using five model variants: in variant A, all tissues are modeled as linear elastic; the complexity of their mechanical response is gradually increased in models B-E (Table 1).

Models	Elasto-plastic calcifications	Hyperelastic AV leaflets	AR wall pre-stress [2]
B	✔	-	-
C	-	✔	-
D	-	-	✔
E	✔	✔	✔

Table 1: Mechanical features associated to each model.

Results and discussion

For all model variants, the simulated configuration of the deployed stent well agreed with *in vivo* post-operative CT data, reporting a maximum error below 2 mm, i.e., no more than twice CT image resolution (Figure 1a). Contact pressure (peak value and CPI, evaluated in the target zone between non-coronary sinus and right sinus [3]) and gaps between stent and AR were used to estimate the risk of conduction abnormalities onset and PVL, respectively. Computed values were minimally affected by model complexity and agreed with follow-up data, which reported the absence of LBBB and trace of PVL (Figure 1b-c). Nonetheless, modeling strategies differently impacted on FEA computational cost, which markedly increased when including AV hyper-elastic leaflets (model C, +23% vs. model B) and aortic wall pre-stress (model D, +14% vs. model C), respectively (Table 2).

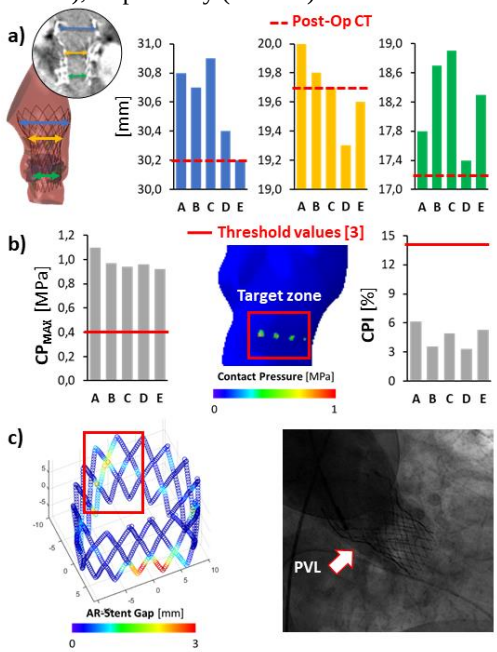

Figure 1: Comparison between post-operative data and FE models predictions.

Models				
A	B	C	D	E
516	550	675	771	756
(-)	(+7%)	(+31%)	(+49%)	(+47%)

Table 2: Computational time expressed in minutes (Intel Core i7-3770 Processor, 16 CPUs).

Conclusions

This work suggests that the use of more sophisticated constitutive models for AR native tissues does not have a major impact on FEA-based predictions on stent-AR wall interaction in patient-specific geometries. Yet, such constitutive models increase the computational cost by up to 45%. This evidence will be further tested on a reasonably large cohort of TAVI candidates.

References

1. Howard et al, *J.Cardiac Surgery*, vol. 34, pp. 1–14, (2019)
2. Votta et al, *Int J Num Methods in Bio Eng*, vol. 33, (2016).
3. Rocatello et al, *C. Interventions*, vol. 11, (2018).

NITINOL STENT OVERSIZING IN PATIENT-SPECIFIC FEMORAL ARTERIES: AN EXPERIMENTAL AND FINITE ELEMENT STUDY

Bernini M.[1,3], Colombo M.[2], Antonini L.[2], Dunlop C.[3], Hellmuth R.[3], Chiastra C.[2,4], Ronan W.[1], Vaughan T. J.[1]

1. Biomechanics Research Centre (BMEC), School of Engineering and Informatics, National University of Ireland Galway (Ireland).
2. LaBS, Dept. Chem., Materials and Chem. Eng., Politecnico di Milano (Italy).
3. Vascular Flow Technologies, Dundee (UK). 4. PoliTo^{BIO}Med Lab, Dept. Mechanical and Aerospace Engineering, Politecnico di Torino (Italy)

Introduction

In endovascular stenting, self-expanding Nitinol stents must be over-sized compared to the vessel diameter to ensure adequate levels of lumen gain and apposition to the arterial wall. However, there is a risk of damage into the vessel wall that might trigger undesired clinical outcomes (e.g. restenosis) [1]. While the common practice is to deploy a stent that is 1-mm larger than the lumen diameter, stent sizing is not always driven by objective criteria but relies on the intuition of clinicians and is influenced by the patient-specific anatomy [2]. Given the controversial outcomes of mis-sizing, a combined experimental-computational investigation is conducted to assess the effects of oversizing of a commercial self-expanding Nitinol stent for femoral applications.

Materials and Methods

Experimental: Axial tension and radial compression tests performed at 37°C were carried out on the Zilver Flex (Cook Medical, USA) to determine its mechanical properties. *In vitro* tests of stent deployments in straight silicon vessel were performed and numerically modelled to assess the interaction among the device and the vessel wall to ensure the robustness of the computational model.
Computational: Finite element analysis (FEA) of the deployment of the self-expanding Nitinol stent into a patient-specific vessel was performed with Abaqus/Explicit 6.14 (SIMULIA, Dassault Systèmes). The stent was modelled in different sizes (6.0x60mm, 7.0x70mm and 9.0x60mm) and assigned the VUMAT super-elastic material model, whose parameters were calibrated through the experiments above mentioned. Two patient-specific human superficial femoral arteries (SFAs), namely patient A and B [4], featured with a low-curvature and high-curvature respectively, were modelled. The non-linear behaviour of SFA was described with an isotropic hyperelastic constitutive law [3]. In both scenarios, a FEA of crimping and deployment was performed. A comparison of the impact of stent sizes was provided.

Results

The configuration of the device deployed into the patients A and B is shown in Figure 1 and the summary of key parameters are in Table 1.

Table 1. Key parameters of deployment structural analysis are compared for different stent sizes in both scenarios.

	Patient A			Patient B		
	6x60mm	7x60mm	9x60mm	6x60mm	7x60mm	9x60mm
LG, %	56.5%	63.0%	62.4%	11.3%	24.1%	23.3%
d_{MAL}, mm	0.63	0.22	0.37	3.03	0.94	0.59

The lumen gain (LG) defined as the increase in the lumen area with respect to the initial cross-section was similar regardless of the stent size in patient A. Contrastingly, in patient B, LG showed a two-fold increase between the 6.0x60mm and 7.0x60mm/9.0x60mm devices. For malapposition, the maximum distance (d_{MAL}) between the stent strut and the arterial wall was reported for the 6x60mm size (0.63mm and 3.03mm in A and B); a consistent improvement was found for 7.0mm and 9.0mm sizes in both patients, although, a critical malapposition (≫0.2mm) was still present in B regardless stent diameter. Additionally, the distribution of maximum principal stress (SMax) in the arterial wall showed lower values induced by the 6.0x60mm, while higher but substantially similar values were reported for 7.0x60mm and 9.0x60mm stents.

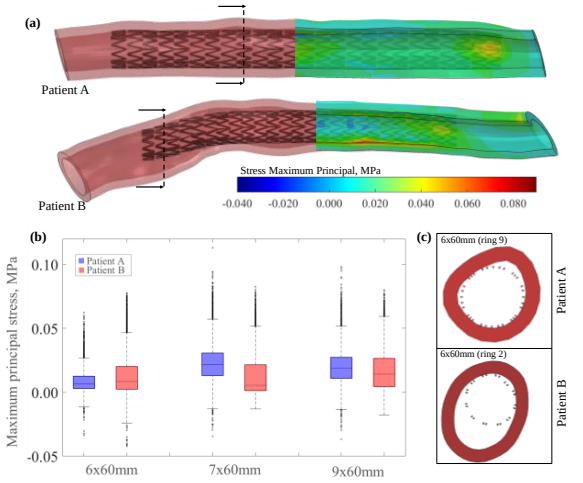

Figure 1. (a) Configuration of stent deployed in patient A and B; (b) boxplot of maximum principal stress values; (c) cut views of the malapposition detachment induced in the most representative rings.

Discussion

In this study, a computational patient-specific analysis to predict the effects of stent oversizing was performed. The relation between the key parameters (luminal gain, mal-apposition detachment, maximum principal stress) with stent diameter showed varying behaviour in both scenarios. For patient A, higher oversizing ratios caused increased arterial stresses, with low additional lumen gain. For patient B, as the oversizing increase, a substantial lumen gain was observed associated with lower malapposition detachment and only modest increases in arterial stress. Results suggest that the choice of oversizing is case-specific; thus, *in silico* tools might provide a clinical support to select the best practice. Next, experimental deployment in 3D-printed patient-specific vessels will be performed to confirm the computational outcomes.

References

[1] Gökgöl et al., *Ann. Biomed. Eng.*, 43, 2868–2880, 2015.
[2] Saguner et al., *Cardiovasc. Intervent. Radiol.*, 35, 906–913, 2012.
[3] Prendergast et al., *J. Biomech. Eng.*, 125, 692–699, 2003.
[4] Colombo et al., *Sci. Rep*, 11: 1-13, 2021.

Acknowledgements

This project has received funding from the European Union's Horizon 2020 research and innovation programme under grant agreement No 813869. M.Colombo, L.Antonini and C.Chiastra have been supported by Fondazione Cariplo, Italy (No. 2017-0792, TIME). This publication reflects only the author's view and the REA is not responsible for any use that may be made of the information it contains.

NEW FULLY AUTOMATED TOOL FOR THE GEOMETRIC ANALYSIS OF THE AORTIC ARCH

Nadia Brambilla (1), Simone Saitta (1), Francesco Sturla (2,1), Emiliano Votta (1,2), Alberto Redaelli (1), Massimiliano Marrocco-Trischitta (2)

1. Politecnico di Milano, Milan, Italy;
2. IRCCS Policlinico San Donato, San Donato Milanese, Italy;

Introduction

Thoracic endovascular aortic repair (TEVAR) is a well-established treatment for aortic arch disease, despite a non-negligible rate of post-operative clinical failure [1]. Accordingly, pre-TEVAR planning is crucial to identify adequate proximal landing zones (PLZ) for endograft deployment according to arch-specific features [2], as in the "bovine" aortic arch variant (CILCA), i.e., with a common origin of the innominate and left carotid artery. CILCA is highly prevalent among TEVAR candidates being recognized as a risk factor for the development of thoracic aortic disease [3].
A systematic geometry-based TEVAR planning is lacking; current practice largely relies on manual, highly operator-dependent and time-consuming operations. We propose a fully automated framework for TEVAR planning, with systematic and comprehensive assessment of aortic arch features, relevant to PLZ identification.

Methods

Aortic arch anatomies of standard (n=23) and CILCA (n=18) configurations were retrieved from previously segmented computed tomography (CT) scans. The workflow automatically provides aortic arch centerline and computational operations for global and regional analysis of aortic arch features (Fig. 1).

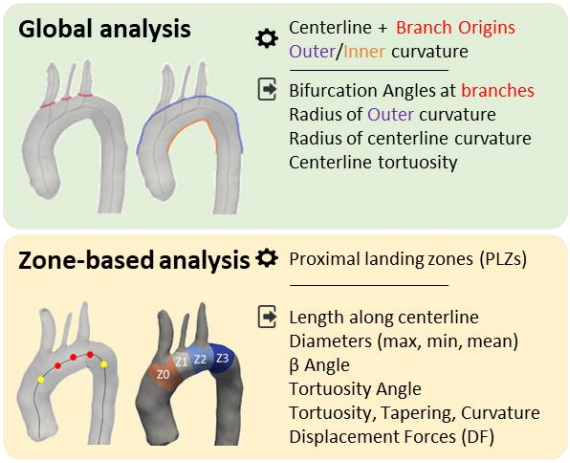

Figure 1: Automatic workflow for TEVAR planning.

PLZs were systematically classified according to the Modified Arch Landing Areas Nomenclature (MALAN) [4]. The analysis also included bifurcation angles and a simplified appraisal to estimate hemodynamic displacement forces (DFs) [5].

Results

All the datasets were successfully analyzed, with no significant differences (P>0.62) between standard and CILCA arch in global metrics. Mean diameters decreased from proximal to distal PLZs (P<0.001) but were higher in the standard arch (P=0.03). Aortic tapering, i.e., the reduction of aortic cross-section along PLZs, was more marked in CILCA (P=0.02), which also reported greater radius of curvature in all PLZs (P=0.04). No difference was observed in terms of tortuosity (Fig. 2).

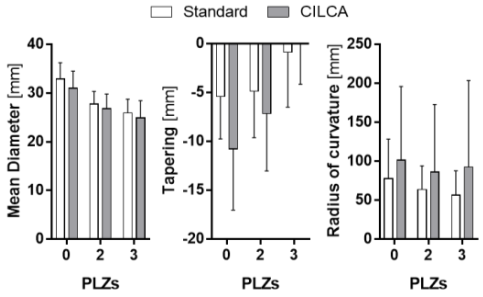

Figure 2: Mean diameter, tapering and radius of curvatures in PLZs of standard and CILCA arch.

PLZ 3 revealed a remarkably higher DF with respect to PLZ 2 (Fig. 3), in particular in CILCA configuration.

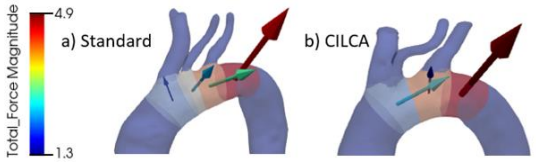

Figure 3: DFs [N] in a standard (a) and CILCA (b) arch.

Discussion

We developed and successfully tested a fully automated and clinical-friendly tool for TEVAR pre-procedural planning and aortic arch analysis, which provides repeatable and objective measurements that would be manually unfeasible. Analysis of a single dataset is compatible with the TEVAR decision-making process, requiring 2 to 3 minutes on a laptop with 32 GB RAM.

References

1. Böckler D. *et al.*, EJVES 2016
2. Grabenwoger et al. Eur Heart J 2012
3. Marrocco-Trischitta *et al.*, EJCTS 2020
4. Marrocco-Trischitta *et al.*, JVS 2017
5. Figueroa et al., JET 2009

PATIENT-SPECIFIC LINEARIZATION OF ANISOTROPIC HYPERELASTIC MODELS FOR FSI ANALYSES OF AORTIC ANEURYSMS

Emanuele Vignali (1), Stéphane Avril (2), Simona Celi (1)

1. BioCardioLab, Fondazione Toscana Gabriele Monasterio, Italy; 2. Mines Saint-Etienne, Université de Lyon, INSERM, U 1059 SAINBIOSE, France

Introduction

In recent years, different computational techniques have been adopted for blood flow simulations in both large and small vessels. In this context, the Fluid-Structure Interaction (FSI) remains the most reliable technique, nevertheless drawbacks and limitations are still present, like the computational cost which is non negligible. Additionally, intrinsic material non linearities and anisotropies, which are key features of vessels, make the calculation even more onerous. For this reason, the isotropic linear elastic material approximation is usually assumed for the aortic vessel [1]. However, this process is often inaccurate and totally neglects the anisotropic and hyperelastic behavior of the vessel. Finally, patient specific data should be used to have a more realistic simulation of the structure.
This work aim is the development of a computational framework for the implementation of the Small On Large [2] linearization approach for an ascending thoracic aortic aneurysm (aTAA) model. Patient specific geometry and material properties, obtained from ex-vivo samples, were included. A two-way FSI simulation with heterogeneous material properties was performed.

Materials and Methods

A patient specific geometry of an aTAA case was reconstructed from CT data. Tissue samples were characterized through biaxial tests. The data were fitted to a state of the art hyperelastic anisotropic model accounting for collagen fiber dispersion [3]. The model was implemented in the ANSYS software, which was used for all the computations. The 0-pressure configuration was obtained starting from the diastolic phase through a reverse displacement algorithm [4]. Then, the simulation was split in two phases: a first large deformation (LD) and a second small deformation (SD) phase. The LD phase was defined as the passage from the 0-pressure to the diastolic configuration with a static simulation by using the implemented hyperelastic material model. Subsequently, the SD phase was defined as the passage from the diastolic to the systolic configuration through a two-way FSI simulation in which the stiffness map (C^0), calculated at the first step, was imposed. The tangential stiffness matrix was modified at each mesh element to maintain the local tissue anisotropy. Results are presented in terms of stiffness ($C^0_{\theta\theta\theta\theta}$, C^0_{zzzz}) values from the LD step. Additionally, circumferential ($\sigma_{\theta\theta}$) and longitudinal (σ_{zz}) stresses from the final SD two-way FSI step were reported.

Results

The presented workflow of aTAA analysis was successfully implemented. The maps of circumferential and longitudinal local stiffness calculated from the LD step are reported in Figure 1 a-b. The $\sigma_{\theta\theta}$ and σ_{zz} at the systolic pressure peak from the SD FSI step are presented as well in Figure 1 c-d.

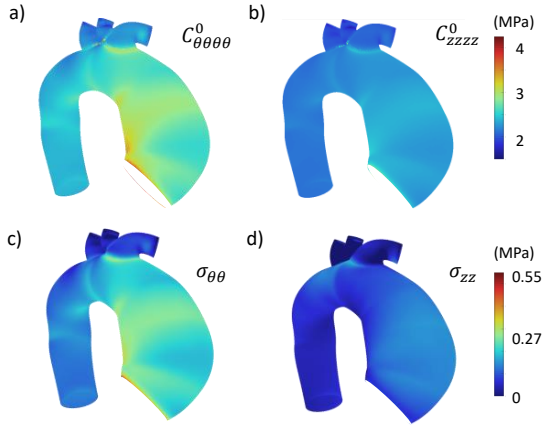

Figure 1: Results for the aTAA simulation: local stiffness maps for the circumferential (a) and longitudinal (b) direction. Stress value maps for the two-way FSI step in terms of $\sigma_{\theta\theta}$ (c) and σ_{zz} (d) at peak systolic pressure.

The results demonstrate the significance of anisotropy. The tissue appears to be significantly stiffer along the circumferential direction, inside the inner curvature of the aTAA. The same trend emerges from the stress distribution from the SD FSI step. This shows that significant heterogeneities of tangent stiffness are expected, even if a homogeneous hyperelastic material model is assumed in the aTAA analysis.

Discussion

A workflow for the computational analysis of a patient-specific aTAA case with Small On Large linearization to obtain a two-way FSI analysis with heterogeneous local stiffness is presented. The results revealed regional variations and anisotropy of tangent stiffness properties, with a significant stiffening in the inner aTAA section.

References

1. Lantz et al, Int J Appl Mech, 3.04: 759-778, 2011.
2. Ramachandra et al, J Biomech, 84: 18-26, 2019.
3. Niestrawska et al, Acta biomaterialia, 88: 149-161, 2019.
4. Raghavan et al, Ann Biomed Eng, 34(9): 1414-19, 2006.

VALIDATION OF PATIENT-SPECIFIC COMPUTATIONAL MODELLING OF TYPE B AORTIC DISSECTION

Chlöe H Armour (1), Simone Saitta (1,2), Selene Pirola (1), Yifan Liu (3), Baolei Guo (3), Zhihui Dong (3), Xiao Yun Xu (1)

1. Department of Chemical Engineering, Imperial College London, London, SW7 2AZ; 2. Department of Electronics, Information and Bioengineering, Politecnico di Milano, Milan, Italy; 3. Department of Vascular Surgery, Zhongshan Hospital, Institute of vascular Surgery, Fudan University, Shanghai, China

Introduction

Computational fluid dynamics (CFD) simulations of TBAD have been developed to study dissection hemodynamics and gain mechanistic understandings of critical anatomical features that have been linked to various disease progressions. For these simulations to provide useful insights, results must be physiologically accurate. Model parameters including geometry, and inlet and outlet boundary conditions should be derived from patient-specific data where possible; the use of 3D inlet velocity profiles (IVPs) [1] and 3-element Windkessel (3EWK) outlet models [2] have been shown to produce the most physiologically accurate results in TBAD simulations. This study aimed to evaluate and validate patient-specific simulations of TBAD through qualitative and quantitative comparisons with in vivo data acquired using 4D flow magnetic resonance imaging (MRI).

Methods

Five TBAD patients (P1-P5) were included in this study. For all patients, diagnostic CT scans, 4D flow MRI and Doppler-wire (DW) pressure measurements were available. DW pressures were taken at the start of each interventional treatment before the stent-graft was deployed. Patient-specific geometries were segmented from diagnostic CT scans, and all geometric models extended from the ascending aorta to the aortic bifurcation and included all major side branches. For each patient, 3D IVPs were derived from 4D flow MRI data using an in-house MATLAB code [3]. 3-element Windkessel models were tuned for each model outlet, based on average flows derived from MRI flow data and DW pressure measurements. Blood was simulated as a non-Newtonian fluid using the Quemada model. All models were meshed in ICEM (v19.2), simulated in Ansys CFX (v15.0) and post processed in Ansys EnSight (v10.2). 4D flow MRI data were processed using in-house MATLAB codes to output velocity fields, which were analyzed in EnSight and used as a gold standard for comparison with CFD results.

Results

Figure 1 shows the peak systolic velocity patterns obtained from CFD and 4D MRI for 2 selected cases, and good qualitative agreements were achieved for all patients. Comparisons of peak systolic maximum velocities through the primary entry tear are reported in Table 1. It can be seen that CFD tends to underpredict the maximum velocity compared to 4D-MRI, in line with previous findings [1,2], with a maximum difference of 0.29 m/s. Attempts were also made to compare DW measurements with CFD predicted pressures. It was found that average pressures, evaluated in the true and false lumen at multiple locations throughout the dissection in each patient, differed by less than 13%. Quantitative differences between CFD results and in vivo measurements are expected, considering the rigid wall assumption in the CFD model, and the 4D-MRI and CT scans were not performed on the same day the DW measurements were taken.

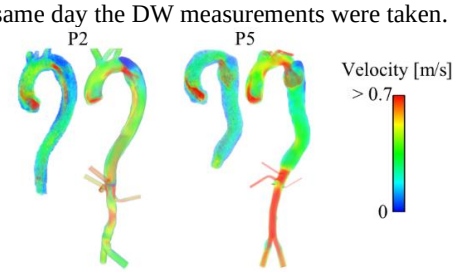

Figure 1: Peak systolic velocity fields. For each patient, 4D-MRI results are shown on the left, alongside the CFD results on the right.

	Maximum Velocity [m/s]				
	P1	P2	P3	P4	P5
4D-MRI	1.8	1.2	0.9	1.7	1.2
CFD	1.6	0.9	0.6	1.6	1.1

Table 1: 4D-MRI derived and CFD simulated maximum peak systolic velocity within the primary entry tear.

Discussion

This study presents a workflow for patient-specific TBAD simulations, incorporating the maximum amount of anatomical and flow data that can be acquired in vivo. Validations against in vivo measurements demonstrate good overall agreement. Future work includes incorporating fluid-structure interaction (FSI) models, which will allow us to make a thorough comparison between rigid CFD, FSI and in vivo data.

References

1. CH Armour et al, Biomech Model Mechan, 2020.
2. S Pirola et al, J Biomech, 60:15-21, 2017.
3. S Pirola et al, IEEE , 66:3411-3419, 2019.

Acknowledgements

CHA is funded by a PhD scholarship award through EPSRC DTP to Imperial College London.

EULERIAN-BASED WALL SHEAR STRESS TOPOLOGICAL SKELETON AS A TEMPLATE OF NEAR-WALL MASS TRANSPORT IN ARTERIES

Giuseppe De Nisco (1), Valentina Mazzi (1), Karol Calò (1), Maurizio Lodi Rizzini (1), Claudio Chiastra (1), Jolanda J. Wentzel (2), David A. Steinman (3), Diego Gallo (1), Umberto Morbiducci (1)

1. PoliTo^{BIO}Med Lab, DIMEAS, Politecnico di Torino, Italy; 2. Department of Cardiology, Biomedical Engineering, Erasmus MC, Netherlands; 3. Biomedical Simulation Laboratory, University of Toronto, Canada

Introduction

Several studies have suggested that mass transfer and transport (e.g., of high plasma levels of low-density lipoproteins, LDL) are involved in the atherosclerosis process [1]. In the last decade, computational fluid dynamics has been largely adopted to elucidate how flow disturbances, mass transport and atherogenesis are linked in human arteries [2]. However, modelling mass transfer in cardiovascular flows requires high computational costs [3]. To overcome this limitation, a marked interest has recently emerged on the Lagrangian-based features of the wall shear stress (WSS) topological skeleton (TS), able to provide a template for near-wall transport [4]. Briefly, the WSS TS is composed by fixed points, points where WSS vanishes, and stable/unstable manifolds, identifying WSS expansion/contraction regions. Here, a recently proposed Eulerian-based method for WSS TS analysis [5] is used to provide a reliable template of near-wall mass transport in patient-specific computational hemodynamic models of three distinct vascular regions. The capability of the proposed approach to depict an affordable picture of the near-wall mass transport is tested against LDL polarization distributions simulated solving the coupled Navier-Stokes (NS) and advection-diffusion (AD) equations.

Methods

The 3D geometries of a human thoracic aorta, a carotid bifurcation, and a right coronary artery were reconstructed from medical images. The finite volume method was applied to solve the coupled NS and AD equations on high-quality mesh-grids [3]. Subject-specific flow measurements were prescribed as boundary conditions. LDL boundary conditions, in particular blood-to-wall transfer were modelled as proposed elsewhere [3]. A recently proposed Eulerian-based WSS TS analysis [5] was here considered. Based on theory and according to [5], the divergence of the WSS unit vector field $\boldsymbol{\tau}_u$, defined as:

$$DIV_W = \nabla \cdot \left(\frac{\boldsymbol{\tau}}{\|\boldsymbol{\tau}\|_2}\right) = \nabla \cdot \boldsymbol{\tau}_u \qquad (1)$$

represents a template of the WSS vector field manifolds, identifying WSS expansion/contraction regions. The Poincarè index and the Jacobian analysis were then used to identify and classify fixed points [5]. In addition, the canonical descriptors of flow disturbances, i.e., *TAWSS*, *OSI*, and *RRT*, were evaluated. The surface areas (SAs) exposed to high local LDL uptake (LDL90), WSS contraction regions (DIV10), and disturbed hemodynamics (TAWSS10, OSI90, RRT90) were identified, and their co-localization was quantified [3].

Results

DIV_W and LDL luminal distributions are provided in Fig. 1. WSS contraction/expansion regions are coloured in blue/red (negative/positive DIV_W, Fig. 1A). A marked co-occurrence of WSS contraction regions and LDL concentration polarization on the vessels wall clearly emerges. These observations are confirmed by quantitative analysis (Fig. 1C), reporting that WSS contraction regions co-localize with high LDL concentration regions at least the 40% more than canonical WSS-based descriptors.

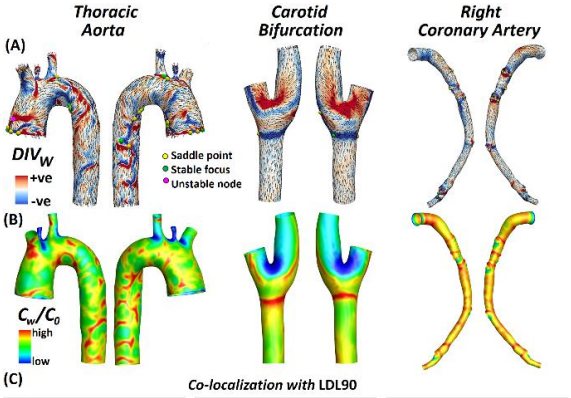

Figure 1: A) Cycle-average WSS TS. B) LDL wall concentration. C) SAs co-localization.

Discussion

Our findings clearly indicate that the Eulerian-based method for analysing the WSS TS [5] provides an effective template of WSS manifolds, which in turn co-localize with LDL polarization areas at the luminal surface. This means that the DIV10-based approach: (1) identifies high LDL polarization areas at the luminal surface better than canonical WSS-based descriptors; (2) reduces computational costs and methodological complexity with respect to classical mass transport simulations.

References

1. Nielsen et al., Atherosclerosis, 123: 1-15, 1996.
2. Lantz et al., J Biomech, 45: 537-542, 2012.
3. De Nisco et al., J Biomech, 68:33-42, 2018.
4. Arzani et al., Biomech Model Mechanobiol,16(3), 2017.
5. Mazzi et al., Biomech Model Mechanobiol,19, 2020.

PATIENT-SPECIFIC PROSTHETIC AORTIC VALVE: A HIGH-FIDELITY APPROACH TO REDUCE SIMULATION TIME

Leonardo Geronzi (1,2), Emanuele Gasparotti (1,2), Corrado Groth (3), Ubaldo Cella (3), Marco Evangelos Biancolini (3), Simona Celi (1)

1. BioCardioLab, Bioengineering Unit, Fondazione Toscana "G. Monasterio", Heart Hospital, Massa, Italy;
2. Department of Information Engineering, University of Pisa, Pisa, Italy;
3. Department of Enterprise Engineering, University of Rome Tor Vergata, Roma, Italy

Introduction

The understanding of the behaviour of prosthetic devices is a key step to improve surgical outcomes of patient-specific valves implantation. In clinical environment, numerical simulation represents a powerful tool to evaluate the features of the blood flow and the performances of a prosthetic device [1]; in particular, a fluid-structure interaction (FSI) analysis could allow to refine the design of valvular prostheses and to assess the onset of the haemolytic/thrombotic process. Despite all the advances in numerical simulation, its application in a clinical environment is limited due to the computational cost and the fidelity of the results. Recently, the use of advanced mesh morphing technique has been demonstrated to be a useful tool to reduce time, avoiding uncertainties of the material behaviour [2].
The purpose of this work is to present a novel numerical approach for the study of prosthetic aortic valves able to reduce computational time preserving high fidelity.

Methods

A parametric model of prosthetic aortic valve is realised using the software SpaceClaim. One-way FSI simulations are performed in Ansys Workbench environment first using remeshing and then with a meshless technique. A Young's modulus of 3 MPa and a Poisson's ratio of 0.4 are assigned to the valve; blood is set as incompressible, viscous-laminar with a viscosity of 4 cP. For the structural simulations, time-varying ventricular and aortic pressures are applied to the leaflets of the prosthesis. The Radial Basis Functions (RBF) mesh morphing technique is chosen for the meshless approach. To set the synchronous deformation of the blood domain with the leaflet deformation at each time step, the RBF-Morph software [3] is employed. For the fluid domain, velocity inlet (Figure 1(a)) and pressure outlet time-varying boundary conditions are used. The results of the analysed methods are then compared in terms of flow velocities and solution time.

Results

Five different valvular states are shown in Figure 1(a). The von Mises stress distributions at the systolic peak and when the valve is completely closed are reported in Figure 1(b). The maximum value detected, located near the junction between the cusps and the circular ring of the open valve, is 1.06 MPa. Concerning the comparison of the FSI analyses, Figure 2 depicts the flow velocity values reached along a selected longitudinal section plane at the systolic peak of cardiac cycle.

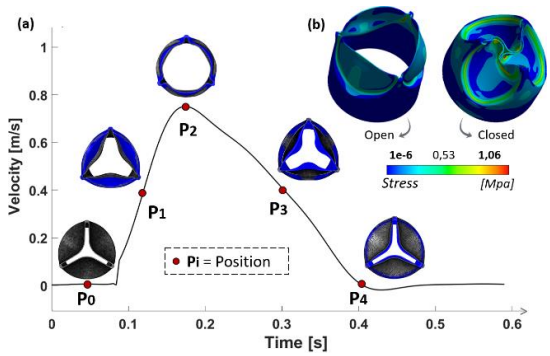

Figure 1: Five different valvular configurations during the opening phase (a) and von Mises equivalent stress distributions for the open and closed valve (b).

Maximum and mean velocities detected with remeshing methods are respectively 1.41 m/s and 0.76 m/s while using meshless approach are 1.48 m/s (difference of 4.96%) and 0.77 m/s (difference of 1.32%).
The solution time required using morphing is 16 time less than that of the remeshing algorithm.

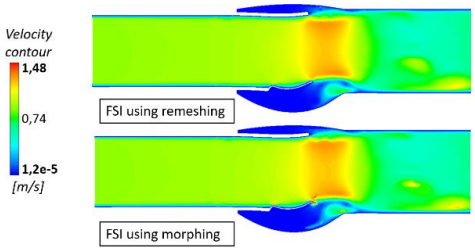

Figure 2: Comparison between remeshing and morphing.

Discussions

The combination of a parametric valvular model and morphing techniques could represent a useful approach to test patient-specific devices, tearing down in this way the time required to obtain relevant clinical results.

References

1. Sigüenza et al, Int J Num Meth Biomed Eng, 34(4), 2018.
2. Capellini et al, J of Biomech Eng, 140(11), 2018.
3. Biancolini, Fast Radial Basis Functions for Engineering Applications. 1st edn. Springer-Verlag, New York, 2017.

TOWARDS ACCURATE AND EFFICIENT SIMULATIONS OF POSITIVE DISPLACEMENT ARTIFICIAL HEARTS

Joe Bornoff (1), Nimesh Singh (1), Maria Carnarius (1), Richie Gill (1), Azad Najar (2), Ina Laura Pieper (2), Andrew Cookson (1), Katharine Fraser (1)

1. University of Bath, UK; 2. Scandinavian Real Heart AB, Sweden

Introduction/Motivation

For those suffering from biventricular heart failure, where a heart transplant is not viable, a total artificial heart is a feasible alternative. The Realheart®, developed by Scandinavian Real Heart, mimics the mechanics of the native heart by vertical translation of an atrioventricular (AV) plane. Previous numerical models of the Realheart® were not flow driven but relied on prescribed motion of AV and semilunar (SL) valves. This tended to overestimate device output and limited the operating conditions that could be simulated. This study's objective was to develop a new modelling strategy, combining computational fluid dynamics and fluid-structure interactions, that generalised the pumping mechanics of the Realheart®. Initially, only the essential and most challenging features will be modelled before proceeding to whole device simulation.

Methods

Fluent (Ansys Inc, Canonsburg Pennsylvania, USA, Version 2020 R2) was used to model a fluid cylinder containing two bileaflet mechanical heart valves aligned in series, representing the AV (upstream) and SL (downstream) valves (figure 1a). Symmetry conditions were imposed such that a 1/4 model was considered. Constant pressures of 15 and 70 mmHg were applied on the inlet and outlet respectively. A 5 mm diameter restriction (figure 1b) represented the resistance of the downstream vasculature. The Navier-Stokes equations were solved assuming Newtonian rheology. Overset meshing allowed for a refined mesh around the boundary of the leaflet valves (figure 1c). The 6 degrees of freedom solver computed the leaflets' rotation using the forces and moments exerted by the fluid. A vertical sinusoidal translation of period 0.6 s and amplitude 12.5 mm was applied to the AV overset zone, achieving both rotational and translational motion of the AV valve. A custom variable time-stepping scheme was used to reduce computation time but maintain accurate capture of leaflet motion.

Results

Variable time stepping was only slightly less accurate than a small, fixed time step, but at 25% of the computation time required (table 1). The SL valve opened at 0.15 s as fluid was pushed through the domain by the AV valve, and closed again at 0.43 s, due to backflow through the outlet (figure 2). Instability and fluttering in SL valve motion was seen upon opening, due to high pressures caused by downward AV motion. At the point that the SL valve fully opened, fluid followed the motion of the leaflets, and was drawn from the edge of the fluid cylinder towards the centre to form a faster flowing central region (figure 1 d).

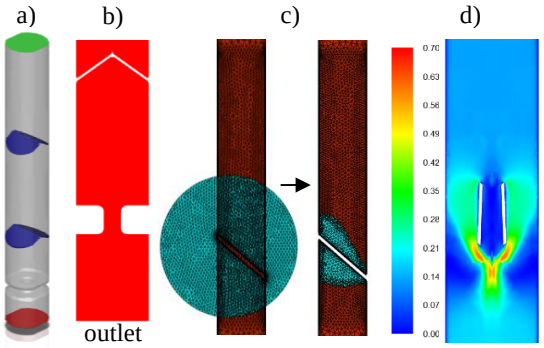

*Figure 1 **(a)** Computational domain: inlet (green), outlet (red), two valves (blue), fluid domain (light grey). **(b)** 2D view of 5 mm diameter restriction placed upstream of outlet. **(c)** Overset meshing: background fluid (red), overset leaflet region (blue). **(d)** Velocity magnitude (m/s) contour plot of SL valve at 0.2 s.*

Time Step Size	1e-3s	Variable	5e-3s	1e-2s
Error (%)	-	5.5	21.0	41.0
Time Steps	600	150	120	60

Table 1 A measure of accuracy and computation time for a 2D, single translating and rotating valve test case. Error defined as percentage difference between leaflet angles at period end for each case compared to 1e-3 s.

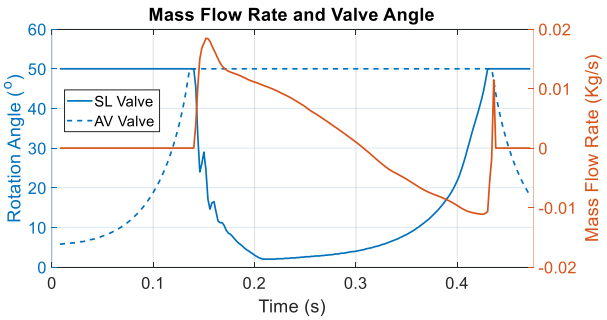

Figure 2 Outlet mass flow rate and valve angles. 0° is open, 50° is closed. Positive mass flow rate is out of the domain.

Conclusions

A modelling strategy has been successfully developed that defines AV plane translation and AV/SL valve rotation, producing pumping characteristics similar to that of the Realheart®. Further work will replace the constriction with a Windkessel model to capture physiological conditions and improve modelling flexibility. Additional studies will be used to understand the interplay between stroke parameters, and efficiency and valve leakage.

A PARAMETRIC EQUATION FOR THE NON-INVASIVE ESTIMATION OF THE ELASTIC PROPERTIES OF MATERIALS

Benigno Marco Fanni (1-2), Emilie Sauvage (3), Silvia Schievano (3), Vincenzo Positano (1), Claudio Capelli (3), Simona Celi (1)

1. BioCardioLab, Fondazione Toscana G. Monasterio, Italy; 2. Dept. of Information Engineering, University of Pisa, Italy; 3. Institute of Cardiovascular Science, University College of London, United Kingdom

Introduction

Patient-specific numerical models represent a promising tool for clinical planning of cardiovascular procedures. While the patient's anatomy of interest can be accurately reconstructed from imaging, the in-vivo patient-specific mechanical characterization of vessels still represents the major uncertainty [1]. In this work we present a novel formulation for the non-invasive estimation of material properties in terms of Young's modulus (E), starting from Phase Contrast Magnetic Resonance Imaging (PC MRI). The flow-area (QA) method was used to infer the E value starting from a standard formula. The equation was tested in a controlled in-silico environment and opportunely modified according to the simulations' results. The formulation was then tested in-vitro using PC MRI of a 3D printed model.

Methods

The QA method is used in clinics to estimate the pulse wave velocity (PWV) using PC MRI or echo data. A literature equation [2] was used to compute the E value from PWV:

$$E = \rho\, PWV^2\, [3\,(1+A_0 / WCSA)] \qquad (1)$$

where ρ is the density of blood, A_0 is the cross-sectional area of vessel's internal lumen and WCSA is the wall cross-sectional area. Eq. (1) was tested in-silico using fluid-structure interaction to assess its capability to infer the E values (ranging from 0.5 to 8 MPa) of different implemented vessels' models, including pipe models and patient-specific anatomies, subjected to a cardiac-like pulsatile regime. Given the non-linearity between the E input and the E from Eq. (1), a corrective factor was included, namely K, defined as:

$$K = RAC\,\gamma \qquad (2)$$

where RAC was the relative area change along the cardiac cycle and γ was a parameter depending on the vessel geometry, flow and pressure. In order to fully parametrize γ, several FSI simulations were run in two main pressure conditions (typical aortic and pulmonary pressure, i.e. 80-120 and 10-20 mmHg), by varying vessel diameter (1-5 cm) and flow peak (100-500 ml/s). The huge amount of simulations was handled making the entire process semi-automatic, from the set-up of the single simulation to its post-processing. The new equation including K was blindly tested in-vitro, on a vessel phantom 3D printed with a deformable material (i.e. Tango+) [3]. The phantom was inserted in an ad-hoc mock-loop circuit under pulsatile conditions. PC MRI of the phantom was acquired and processed to get the E value of Tango+, which was compared to the tensile tests of the material.

Results

Figure 1 shows the results from a patient-specific aorta simulation, with comparison, for five different cross-sections of the vessel, between E values as computed from non-corrected and corrected formula, in respect to the assigned E reference. The effectiveness of the proposed correction factor K was also demonstrated in-vitro, resulting in a percentage error of 2% between the image-based inferred E value (E_K = 0.51±0.04 MPa) and the tensile tests assessment of Tango+ (E_T = 0.50±0.02 MPa), in respect with the 62% difference resulted from the standard Eq. (1) (E_1 = 0.22±0.03 MPa).

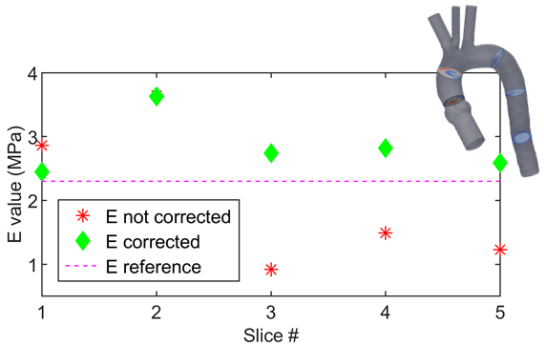

Figure 1: E values as computed from non-corrected (red asterisks) and corrected (green diamonds) formulation.

Discussion

A novel parametric equation requiring only imaging information was here presented. This study relied on the correction of a known literature equation, which was tested and quantified in-silico, then verified in-vitro. A further refinement of the described methodology can potentially lead to a novel tool to quantify the in-vivo mechanical properties of large vessels in a non-invasive way based on solely PC MRI data.

References

1. Huberts et al, J Comput Sci, 1(24):68–84, 2018.
2. Laurent et al, Heart J, 27(21):2588–605, 2006.
3. Fanni et al, CVET, 11(5), pp. 532–543, 2020.

Acknowledgements

Work funded by the IMeC project (SG-2019-12370350).

VIRTUAL THORACIC ENDOVASCULAR AORTIC REPAIR (TEVAR): A FLUID-STRUCTURE INTERACTION STUDY

Anna Ramella (1)*, Elena Redaelli (1)*, Giulia Luraghi (1), Michele Conti (2), Santi Trimarchi (3), Francesco Migliavacca (1)

*1. Politecnico di Milano, Italy; 2. Università degli Studi di Pavia, Italy; 3. Università degli Studi di Milano, Italy *Authors contributed equally*

Introduction

Thoracic Endovascular Aortic Repair (TEVAR) is a minimally invasive technique to treat thoracic aortic pathologies like aneurysms and dissections. A stent-graft is crimped and deployed into the diseased aorta to restore the correct blood fluid-dynamics. Despite its increasing use, some device-related (device migration, endoleaks) and fluid-dynamic (compliance mismatch) complications can occur [1]. From a modeling perspective, the best numerical approach to reproduce the procedure is the fluid-structure interaction (FSI) modelling [2]. This work presents a numerical workflow to virtually implant the stent-graft and to reproduce the pre- and post-TEVAR hemodynamics in an idealized aorta through fully coupled FSI simulations.

Methods

In the first part of the study, the explicit Finite Element solver LS-DYNA (ANSYS) is employed to carry out the device deployment. A commercial stent-graft model (fig.1a) is virtually crimped, morphed and deployed into an idealized aorta with physiological anatomy (fig.2a) [3]. The stent and the graft are made of nickel-titanium alloy and polyethylene, respectively; the aorta is modeled with an isotropic hyperelastic material.
In the second part, strongly coupled, 2-way and boundary fitted FSI simulations are performed with the implicit ICFD solver in LS-DYNA (ANSYS). A physiological velocity waveform is imposed on the ascending aorta as inlet boundary condition [4]. 3-elements Windkessel circuits are assigned to each outlet (three supra-aortic branches and descending aorta) to account for the downstream resistances [5].

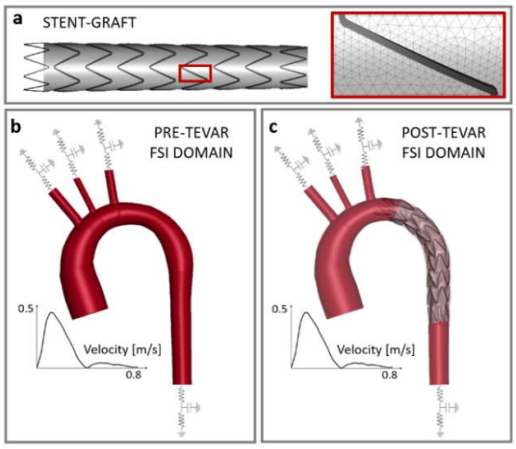

Figure 1: (a) stent-graft model; (b) pre-TEVAR FSI domain; (c) post-TEVAR FSI domain.

The developed FSI simulations are used to model both the pre-TEVAR (fig.1b) and post-TEVAR scenario (fig.1c).

Results

The pre-TEVAR velocity contour at the systolic peak is depicted in fig.2b. The pressure curves are characterized by a diastolic exponential decay and a time delay moving along the aorta. In the post-TEVAR, the systolic velocity field (fig.2c) reaches higher values because of the device with presence of endoleaks between the aortic wall and the stent-graft. Moreover stress field on the stent-graft is shown in fig. 2c.

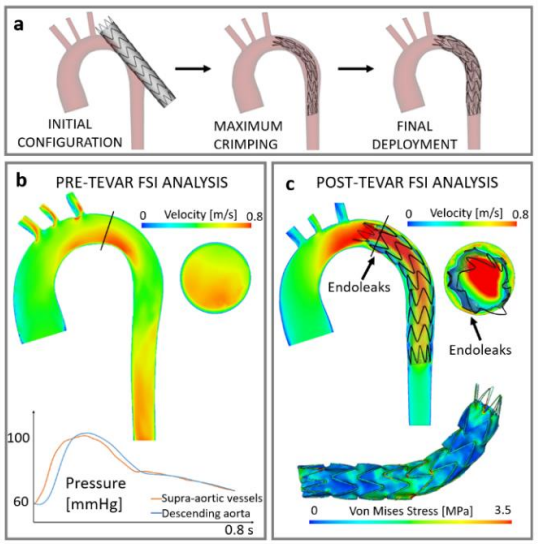

Figure 2: (a) deployment steps; (b) pre-TEVAR and (c) post-TEVAR FSI analysis at systolic peak.

Discussion

The development of a strong FSI tool amenable to model coupled structures and fluid can be useful to improve the TEVAR procedure, to design and optimize new devices and to help in clinical decisions and intervention planning. The presence of the Windkessel boundary conditions and the completeness of the simulations make the model versatile and customizable for future patient-specific in silico analyses.

References

1. Daye et al, Cardio Diagn & Ther, 8:S138, 2018.
2. Luraghi et al, J Biomech, 28: 45-51, 2017.
3. Marconi et al, Med Eng & Phys, 59:21-29, 2018.
4. Burk et al, J Cardiovasc Magn Reson, 14:1-11, 2012.
5. Pirola et al, J Biomech, 60:15-21, 2017.

A SIMULATION FRAMEWORK TO ASSESS POST-STENTING CAROTID HEMODYNAMICS THROUGH IMMERSED APPROACH

Giovanni Maria Formato (1), Michele Conti (1)

DICAr, University of Pavia, Italy

Introduction

Modeling the presence of a stent deployed in a stenotic carotid artery is essential to estimate the post-treatment hemodynamics through computational fluid dynamic (CFD) simulations, but the creation of a suitable computational grid conforming to the complex shape of the endovascular device is often time-consuming and error-prone [1]. We present a framework for the CFD analysis of the post-stenting carotid hemodynamics exploiting the "immersed method" to model the presence of the device in the blood flow field [2]. The framework is validated towards simple numerical benchmarks and then applied in a proof-of-concept study comparing the hemodynamics in a patient-specific carotid artery treated with four different commercial stents.

Materials and Methods

The framework involves two steps (Figure 1). The first is the semi-automatic generation of an unstructured grid of the carotid domain locally refined around the surface of the immersed stent. The inputs are the STL of the carotid lumen and of the deployed stent: the former represents the boundary of the blood domain; the last indicates where to perform the local mesh refinement by centering at each vertex overlapping spheres prescribing the local size of the tetrahedra [3]. The second step involves the transient CFD simulation exploiting the "immersed solid method" implemented in Ansys CFX (ANSYS Academic Research [CFX], release 2020 R1). First, mesh size and simulation parameters were calibrated by comparing velocity and wall shear stress (WSS) fields with those obtained in body-fitted meshes using an idealized model of stent strut immersed in a cylindrical artery. Then, we tested the hemodynamic impact of four different stent designs (closed, open and hybrid cells) implanted in a stenosed carotid bifurcation (24% NASCET method). We prescribed transient parabolic velocity profile at the common carotid artery (CCA), 65% of the inflow at the internal carotid artery (ICA) outlet, a traction-free condition at the external carotid artery (ECA) outlet, a no-slip condition at the wall [4]. Blood was modelled as incompressible Newtonian fluid with density of 1 g/cm^3 and a dynamic viscosity of 0.04 P. Following time-step sensitivity analysis, we chose a time-step size of 2 ms, and results were collected during the second cardiac cycle to describe flow pattern, ICA and ECA resistances, and WSS distribution in each investigated model.

Results

A good solution accuracy was achieved with element size of 25 µm around the stent strut, 0.03 cm in the unrefined region, and a growth with rate of 1.2 between the two zones. The application of the framework on the patient-specific geometry showed that stenting did not significantly alter carotid bulk flow dynamics, increased ECA resistance (particularly closed-cell stent designs), and induced the formation of low time-averaged WSS areas at the carotid sinus and near the stent struts without clear association with stent design.

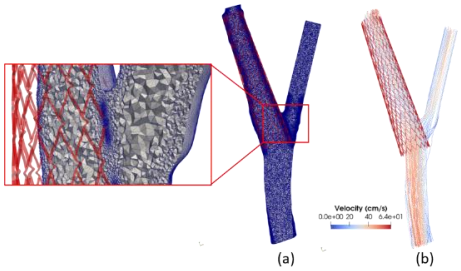

Figure 1: Local mesh refinement and CFD simulation of a stented carotid bifurcation. a) The immersed stent guides the generation of an unstructured grid refined around its surface to achieve a good local accuracy of the solution; b) the "immersed solid approach" is used to compute the velocity field, showing effectiveness to capture the flow disturbances induced by the thin stent struts. The stent is superimposed to the model only for visualization.

Discussion

This study presents a novel pipeline that facilitates the set-up and execution of the CFD simulation modelling the endovascular device immersed in the blood domain. Preliminary results from a proof-of-concept study showed the applicability of the framework to rapidly evaluate the hemodynamic impact of different stent implants, overcoming the difficulties associated with the generation of body-conforming grids. Future studies involving more complex modelling assumptions as well as the validation of the performance of the method on a more numerous cohort of datasets are demanded to withdraw robust and clinically relevant results.

References

1. De santis et al., Comp. Meth. Biomech. Biomed. Eng., 16(6):648–659, 2013
2. Conti et al., Computers & Fluids, 141:62–74, 2016
3. Geuzaine et al., Int. J. numerical methods in eng., 79(11):1309–1331, 2009
4. Morbiducci et al., Annals of Biomed. Eng., 38(12):3688–3705, 2010

APPROACHES TO THE VIRTUAL FLOW-DIVERTER DEVICE DEPLOYMENT AND THE FORECASTING ITS POSSIBLE COMPLICATIONS

Denis Tikhvinskii (1), Iuliia Kuianova (2), Dmitrii Kislitsyn (3), Kirill Orlov (3), Daniil Parshin (2)

1. Novosibirsk State University, Russia; 2. Lavrentyev Institute of Hydrodynamics, Novosibirsk, Russia; 3. Meshalkin Research Centre of Circulation Pathology, Novosibirsk, Russia

Introduction

Cerebral aneurysm is a quite common disease that occurs in an average of 1 person per 50. The main danger of cerebral aneurysms lies in the possibility of their rupture and cerebral hemorrhage. Currently, the endovascular treatment is frequently used among neurosurgeons. In particular, flow-diverter device deployment has proven itself well as a method of occluding cerebral aneurysms. Notwithstanding, up to 10% of all endovascular interventions for the treatment of cerebral aneurysms result in recanalization and reoperation or abnormal endothelialisation of the flow-redirecting device. At this moment, many studies are devoted specifically to determining the risk of rupture of aneurysms, while much less attention is paid to finding the causes of a flow-diverter device deployment. The aim of our study is to find the criteria which is able to show the possible risks of stent deployment in preoperative modelling in the patient-specific cases.

Methods

The 4 real patient-specific 3-D geometry of the cerebral vessels was reconstructed using DICOM-images set. The ANSYS-CFX package was used for the numerical calculation in obtained configuration. Recently, we have compared Newtonian and Non-Newtonian Casson fluid models and found out, that using non-Newtonian fluid in 3-D modelling makes sense only with low velocities [1]. For this reason, we supposed fluid to be Newtonian in the area of a vessel and to be Casson model fluid in the aneurysm dome and its neck.

The flow-diverter device was modeled in 3 different ways: as a layer of porous medium and the tube of porous medium with isotropic and non-isotropic tensor of energy dissipation Fig.1 [2].

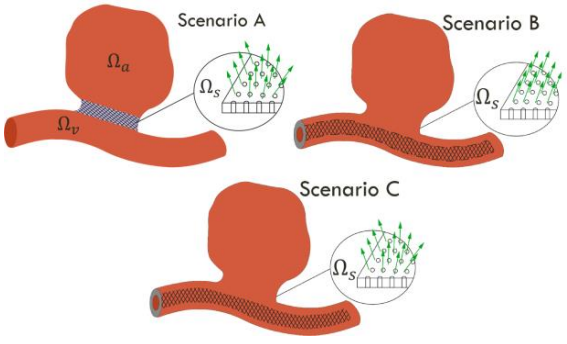

Figure 1: Schematic representation of approaches to stent deployment in Patients. Scenario A: the stent is a porous plug in the neck of the aneurysm; Scenario B: the stent is a porous tube along the vessel wall (the model is not isotropic); Scenario C: the stent is a porous tube along the vessel wall (isotropic model)

Results

The wall shear stress (WSS) values were obtained after numerical calculations in configurations before and after surgery with different flow-diverter device models in all 4 patient-specific cases. All obtained data was analyzed and results presented at Fig.2.



$1.23 < \max \text{WSS value} < 1.68$

Figure 2: Outcome forecasting

Discussion

This study shows that a successful operation to install a flow-diverting device leads to an increase in WSS values in the aneurysm neck area, regardless of the geometric implementation of the stent. In addition, we suppose, that WSS can be an appropriate criterion for forecasting the surgery outcomes.

References

1. D.V. Parshin et al, J. Appl. Mech. Tech. Phys, 59(6): 963-970, 2018.
2. M. Raschi et al, Intern. J. Numer. Meth. Biomed. Engng, 30(9): 909-925, 2014.

Acknowledgements

This work was carried out with the financial support of the Russian Science Foundation, project No20-71-10034.

INVESTIGATING THE SWELLING MECHANISM OF SELF-ADHERENT MICRONEEDLES FOR DRUG DELIVERY TO CARDIAC TISSUE

Ruth Tarpey (1), Shahrin Islam (2), Bruno Bernardo (2), Ellen Roche (1,2), William Ronan (1)

1. Biomedical Engineering, School of Engineering, NUI Galway, Ireland;

2. Department of Mechanical Engineering, Massachusetts Institute of Technology, Cambridge, MA, USA.

Introduction

Myocardial infarction (MI) is the necrosis of the myocardium due to inadequate blood supply. Current treatments of MI aim to restore blood flow but fail to mend the scarred tissue[1]. Localised drug delivery devices, such as the *Therepi* implantable reservoir [2], can rejuvenate the necrotic tissue by delivering the desired concentration of the regenerative therapy to the target site.

Currently, devices such as *Therepi* are attached via sutures [2]; however, sutures are fraught with limitations (Fig. 1a). Alternative adhesion mechanisms such as parasitic-like swellable microneedle (MN) tips [3], could provide both device fixation and drug transportation (Fig. 1b). These MNs have the ability to mechanically interlock with tissue due to their swellable tips and have shown their capabilities in transdermal applications [3].

Here, Finite Element (FE) analysis is used to investigate the shape of the swelling tips of these MN's. These analyses are then used to determine the optimal MN geometry and material to enhance swelling, and subsequently improve their interlocking abilities.

Methods

An axisymmetric FE model (element type CAX4) of a single MN was simulated using Abaqus 2017. The MN consisted of a rectangular backing (with modulus E_b) attached to a cone (with modulus E_c) at the axis of symmetry and coated with a swellable hyperelastic hydrogel layer (with modulus E_h). A uniform layer of this hydrogel material was attached to the backing, to act as a reinforcement and counteract the curvature of the backing as the MN swells (Fig. 1c). To capture the swelling process, an analogous thermal pre-strain was applied to the MN and the periphery of the backing was constrained in the vertical direction. To optimize the MN design for swelling, the material and geometric parameters of the MN, backing, and reinforcement layer were varied

Results

Fig. 1d. illustrates the influence the expansion coefficient α_h, has on the swollen profile of the MN; representing different amount of swelling which can be calibrated to experimental data (not shown). Fig 1e. emphasises the importance of the reinforcement layer in dictating the curvature of the backing. In the absence of the reinforcement layer (i), the backing has a concave curvature which could decrease the MNs adhesion performance, whereas when the reinforcement layer is thicker than the hydrogel layer which coats the MN (iii), the backing has a convex profile which would favour conformability to the tissue topography.

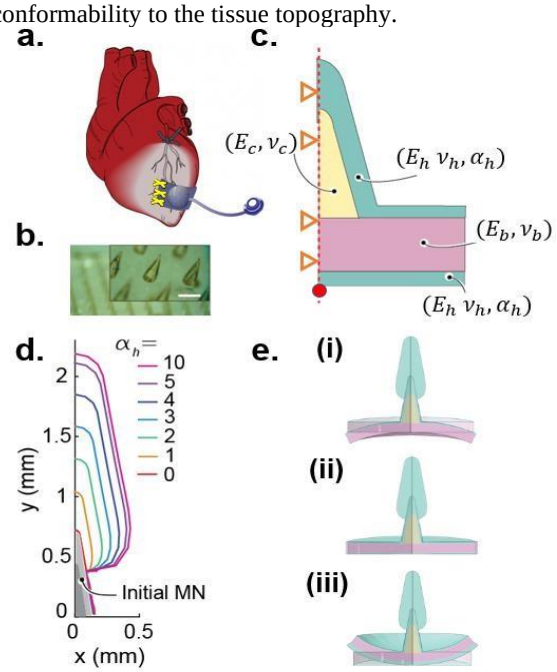

Fig. 1. a. *Therepi reservoir sutured to the heart* [2], ***b.*** *Fabricated MN array* [3], ***c.*** *Schematic of MN swelling FE model,* ***d.*** *MN swelling profiles for different values of* α_h ***e.*** *Material contour plot of MN when* ***(i)*** *there is no reinforcement layer,* ***(ii)*** *the reinforcement layer and MN hydrogel layer are equal thickness and* ***(iii)*** *the reinforcement layer is twice as thick as the MN hydrogel layer.*

Discussion

The introduction of the backing layer prevents the needles from curling away from the tissue; in an array of needles, such curling led to unwanted detachment of a prototype device in an animal study. The simulations here are guiding future iterations of this device. This study also includes modelling of the mechanical interlocking, including an anisotropic material definition of the myocardium.

References

1. Hastings et al, *Advanced Drug Delivery Reviews*, 84: 85106, 2015.
2. Whyte et al, *Nature Biomed Engineering*, 2:416-28, 2018.
3. Yang et al, *Nature Communications*, 4:1702, 2013.

STABILIZATION FOR SEGREGATED ALGORITHMS IN CARDIAC ACTIVE MECHANICS

Francesco Regazzoni (1), Alfio Quarteroni (1,2)
1. MOX - Dipartimento di Matematica, Politecnico di Milano, Italy
2. Mathematics Institute, École Polytechnique Fédérale de Lausanne, Switzerland (Professor Emeritus)

Introduction

In this work we address an unresolved problem in the numerical modeling of cardiac electromechanics, that is the onset of numerical oscillations due to the dependence of force generation models on the fibers shortening velocity [1,2]. A way to avoid numerical oscillations is to use monolithic schemes for the solution of the coupled problem of active-passive mechanics. However, staggered strategies, which foresee the sequential solution of the models of force generation and of tissue mechanics, are preferable, due to their reduced computational cost and low implementation effort. In light of this motivation, in this work we propose a new numerical scheme, that is numerically stable and accurate, yet within a fully partitioned (i.e. segregated) framework. A detailed derivation of the scheme and proofs of its stability properties can be found in [3].

Methods

To derive our stabilized scheme, we move from energetic considerations on the coupling, at the microscale, between active and passive mechanics models. We show that instabilities are linked to the mismatch between macroscopic and microscopic strains, inconsistently expressed in Lagrangian and Eulerian coordinates, respectively. Hence, we formulate a novel scheme, in which all the variables are framed in a coherent fully Lagrangian reference system. By considering a model problem of active mechanics we prove that the proposed scheme is unconditionally absolutely stable (i.e. it is stable for any time step size), yet within a fully staggered framework.

Results

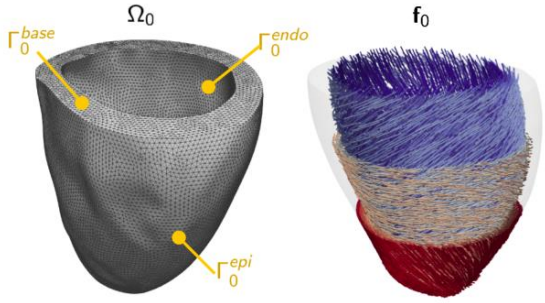

Figure 1: Left ventricle computational domain (left) and distribution of muscle fibers (right).

We apply the proposed method to several force generation models available in the literature, namely the Niederer-Hunter-Smith model [4], the model of Land and coworkers [5] and the mean-field model that we proposed in [5]. We show, by means of several numerical tests, that the proposed stabilization term successfully removes the nonphysical numerical oscillations characterizing the non-stabilized segregated scheme solution. This is verified in two different test cases, namely an isotonic twitch and a test case where a contracted fiber shortens as a consequence of a gradual decrease of the external load, similarly to what happens in the ejection phase of the heart cycle. We show that the new scheme preserves the first order convergence with respect to Δt of the non-stabilized staggered scheme. The numerical error is only slightly larger than the error obtained with the monolithic scheme and it tends to zero with the same rate. Finally, we successfully apply the proposed scheme in the context of a three-dimensional multiscale electromechanical simulation of the left ventricle.

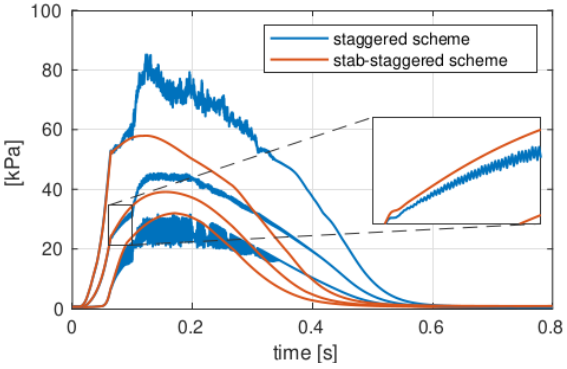

Figure 2: Results of multiscale cardiac electromechanis simulations obtained with the classical staggered scheme (blue lines) and our proposed stabilized-staggered scheme (red lines). The three lines refer to the minimum, average and maximum value over the computational domain.

References

1. S. A. Niederer, N. P. Smith, Progress in biophysics and molecular biology 96 (1-3) (2008) 90–111.
2. P. Pathmanathan, S. Chapman, D. Gavaghan, J. Whiteley, The Quarterly Journal of Mechanics & Applied Mathematics 63 (3) (2010) 375–399.
3. F. Regazzoni and A. Quarteroni, Computer Methods in Applied Mechanics and Engineering 373 (2021), p. 113506.
4. S. Land, S. Park-Holohan, N. Smith, C. dos Remedios, J. Kentish, and S. Niederer, Journal of Molecular and Cellular Cardiology 106 (2017), pp. 68–83.
5. S. A. Niederer, P. J. Hunter, and N. P. Smith, Biophysical Journal 90.5 (2006), pp. 1697–1722.
6. F. Regazzoni, L. Dedè, and A. Quarteroni, PLOS Computational Biology 16.10 (2020), e1008294.

AN IMAGE-BASED COMPUTATIONAL FLUID DYNAMICS ANALYSIS OF HYPERTROPHIC CARDIOMYOPATHY

Ivan Fumagalli(1), Marco Fedele(1), Piermario Vitullo(1), Giorgia Pase(2), Christian Vergara(3), Luca Dede'(1), Sonia Ippolito(4), Roberto Scrofani(5), Alfio Quarteroni(1,6)

1. MOX – Dipartimento di Matematica, Politecnico di Milano, Italy; 2. Bernoulli Instituut, Rijksuniversiteit Groningen, Netherlands; 3. LaBS – Dipartimento di Chimica, Materiali e Ingegneria Chimica "Giulio Natta", Politecnico di Milano, Italy; 4. Radiology Unit, L. Sacco Hospital, Milan, Italy; 5. Cardiac Surgery Unit, L. Sacco Hospital, Milan, Italy; 6. Institute of Mathematics, École Polytechnique Fédérale de Lausanne, Switzerland (Professor Emeritus)

Introduction

Hypertrophic Cardiomyopathy (HCM) is a pathological condition characterized by an abnormal thickening of the myocardium (>15mm), with a prevalence of the 0.2÷0.6% and a mortality rate of 1% in the western world [1]. When it affects the medio-basal portion of the septum, it takes the name of Hypertrophic Obstructive Cardiomyopathy (HOCM) because it induces a flow obstruction in the Left Ventricle Outflow Tract (LVOT), which represents a latent risk that may compromise the cardiac function and possibly lead to cardiac death. In particularly severe cases, this condition may be worsened by the concurrence of a Systolic Anterior Motion (SAM) of the mitral valve. In the present talk, we are going to present computational results comparing the hemodynamics of different HCM patients, with the aim of quantifying the effects of this pathology on the flow and provide clinical indication that may help diagnosis and the design of surgical treatment.

Methods

A novel reconstruction procedure [2, 3] was devised to reconstruct the patient-specific geometry and displacements of the domain boundary and of the mitral leaflets from standard cine-MRI acquisitions. Based on such geometric and functional data, a CFD analysis of the systolic blood flow in the left ventricle and ascending aorta was carried out on HCM/HOCM patients, comparing the hemodynamic effects of their different geometry and contraction. The blood flow was modeled by incompressible Navier-Stokes equations, discretized by the Finite Element Method; the displacement of the endocardium and the aorta was accounted for via an Arbitrary Lagrangian-Eulerian approach, while a resistive method [2, 4] was adopted to immerse the moving valve in the fluid domain. All simulations were performed using the life^x library [5].

Results

The computational pipeline, encompassing image-based reconstruction and CFD simulations, was applied to 3 HCM patients enrolled at L. Sacco Hospital in Milan, one of which also presented SAM. For each patient, blood velocity and pressure distributions were computed, as well as the wall shear stress in significant regions of the ventricular and aortic wall. In order to assess the vortex structures in the ascending aorta, vorticity was also analyzed. Based on the pressure distribution on the septum, we could identify the region of most severe obstruction, thus helping in the design of the possible surgical treatment by septal myectomy.

Discussion

We present a patient-specific computational hemodynamics analysis of the effects of HCM/HOCM and possibly associated SAM of the mitral valve. The results show the diversity of the condition for different patients and allow to quantitatively assess the LVOT obstruction. An effective clinical indication is proposed, helping diagnosis and identifying the most suitable region for surgical treatment.

References

1. Elliot et al, Eur Heart J 35(39):2733-2779, 2014.
2. Fumagalli et al, Comp Biol Med, 123:103922, 2020.
3. Fedele et al, Biomech Model Mechan, 16(5):1779–1803, 2017.
4. Fedele et al, Int J Numer Meth Biomed Engng, e3435, 2021.
5. life^x library. https://lifex.gitlab.io/lifex

Acknowledgements

This project has been funded by the European Research Council (ERC) under the European Union's Horizon 2020 research and innovation programme (grant agreement No 740132, IHEART 2017-2022, P.I. A. Quarteroni). C. Vergara thanks also the H2020-MSCA-ITN-2017, EU project 765374 "ROMSOC - Reduced Order Modelling, Simulation and Optimization of Coupled systems". L. Dede', A. Quarteroni and C. Vergara thank also the Italian MIUR for the research project PRIN17 2017AXL54F. "Modeling the heart across the scales: from cardiac cells to the whole organ".

FLUID-STRUCTURE INTERACTION OF A THIN ELASTIC LEAFLET – A COMPARISON OF COMPUTATIONAL METHODS

Maryrose McLoone (1), Yiling Fan (2), Robert Whiting (1), Claire Conway (3), Ellen Roche (2), Ted Vaughan (1), Nathan Quinlan (1),

1. School of Engineering, National University of Ireland Galway, Ireland, 2. Massachusetts Institute of Technology, USA, 3. Royal College of Surgeons in Ireland, Ireland

Introduction

Numerical modelling of heart valves requires two-way fluid-structure interaction (FSI) to capture the complex coupling between the leaflets and the blood. Three FSI methods are presented in this work; (1) Smooth Particle Hydrodynamics (SPH), a particle based meshless Lagrangian method; (2) Coupled Eulerian Lagrangian (CEL), an immersed boundary (IB) FSI method where the Lagrangian structure moves on top of the Eulerian fluid mesh; and (3) Combined finite volume particle method (FVPM) with the finite element method (FEM), a partitioned FSI scheme with a meshless computational fluid dynamics (CFD) solver and a mesh based finite element (FE) solver. The methods are evaluated for their suitability in FSI modelling of heart valves and are compared against an experimental thin elastomer leaflet deforming under fluid flow.

Methods

A 500 mm long flow channel was built with a cross section of 20 mm x 40 mm and filled with water. A thin leaflet (20mm x 30mm x 1.45mm), made of a silicone elastomer (Dragon Skin 10, Smooth-On), was attached 300 mm downstream from the inlet to ensure fully developed flow. The inlet flow rate was set to 4 L/min and the real-time deformation of the leaflet was captured. The material property of the elastomer was characterized under a uniaxial tensile test, following the ASTM D412 standard.

Three individual FSI simulations were modelled with the dimensions of the experimental flow chamber and thin elastomer leaflet. The leaflet was modelled as Neo-Hookean and a flow rate of 4L/min was prescribed at the inlet.

In the SPH-FE model, the structural domain uses traditional FEM while the fluid domain is discretised into meshfree particles. Each particle properties are interpolated from its surrounding particles. The SPH model was built using Abaqus/Explicit 2017 (Dassault Systèmes, Vélizy-Villacoublay, France). To represent the inlet flow rate of 4 L/min, a block (20mm x 40mm x 100mm) of fluid particles was created and pushed by a rigid plate moving at 70 mm/s.

The CEL model in Abaqus/Explicit 2017 (Dassault Systèmes, Vélizy-Villacoublay, France) was used, whereby the structure was modelled as Lagrangian while the fluid domain is discretised as a fixed Eulerian mesh. The Lagrangian structure is free to deform above the fluid, while the presence of the structure in the fluid mesh is included by an external force in the Navier Stokes equations. The volume of fluid function for the fluid mesh is defined as the fraction of solid structure present in the fluid cells and is updated throughout the simulation.

The FVPM-FE method combines FVPM with FEBio [1], a FE based solid solver. The fluid domain is discretised by a set of overlapping FVPM particles and the solid domain is discretised by finite elements. The fluid and solid domains are solved separately by their respective solvers. Coupling is achieved by passing data between the solvers at the fluid-solid interface. The fluid domain boundaries align exactly with the FEBio element surfaces so data can be passed exactly between the solvers.

Results

The experimental setup is shown in Figure 1a. The deformation of the experimental leaflet in its steady-state condition is compared with the results of the SPH, CEL, and FVPM-FEBio FSI model in Figure 1b.

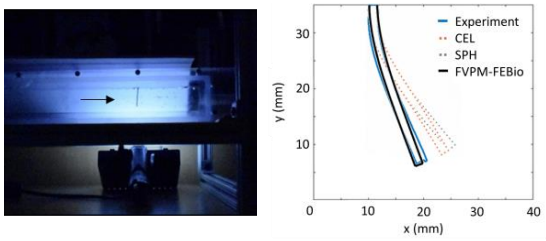

(a) (b)

Figure 1: (a) Experimental rig with arrow indicating the direction of flow. (b) Steady-state condition of the experimental leaflet compared with the results of the SPH, CEL, and FVPM-FEBio FSI models.

Discussion

The three FSI methods were capable of modelling the non-linear elastic deformation of the experimental leaflet in fluid. FVPM-FEBio closely matched the experimental results, while both the CEL and SPH models slightly overpredicted. This demonstrates the methods' ability in the FSI modelling of large deformations of elastic solids in channel flow. This lays the foundation for more complex FSI modelling exhibited in large scale 3D heart valve simulations.

References

1. Maas S. A., Ellis B. J., Ateshian G. A., Weiss J. A. Febio: finite elements for biomechanics. Journal of biomechanical engineering. 134, 2012.

PREDICTING DISSECTION RISK IN ASCENDING AORTIC ANEURYSM USING PATIENT-SPECIFIC IMAGE-BASED CFD

Selene Pirola(1), M Yousuf Salmasi(1), Sumesh Sasidharan(1), Serena Fisichella(1,2), Omar Jarral(1), Alberto Redaelli(2), Declan O'Regan(1), Thanos Athanasiou(1), James Moore Jr(1), Xiao Y Xu(1)

Imperial College London, UK; Politecnico di Milano, Italy

Introduction

Aortic dissection (AD) is one of the main complications of thoracic aortic aneurysm (TAA) and carries a mortality rate of 50% within the first 48 hours if untreated. There is an unmet clinical need in the management of TAA due to a lack of understanding of the mechanisms leading to dissection. The current method of risk stratification relies on size criteria. This is clearly inadequate as the incidence of AD in TAA below the size threshold is being increasingly reported [1]. Our study aims to understand the underlying pathogenic factors associated with aortic medial degeneration in order to develop better risk prediction criteria. In this work, we integrated imaging, computational and experimental biomechanics to study aneurysm dissection in a patient-specific fashion.

Methods

Pre-operative magnetic resonance imaging (MRI) and 4D flow data of 10 patients with TAA were collected. Exclusion criteria were: connective tissue disease (i.e. Marfans), bicuspid aortic valve and redo-aortic surgery. Central aortic pressure was measured prior to the scan. MRI data were used to reconstruct the patients' aortic geometry, while 4D flow images and pressure measurements were used to extract patient-specific boundary conditions for computational fluid dynamic (CFD) analysis, as previously described [2]. All patients underwent surgery for replacement of the aortic root and ascending aorta. Aortic specimens (Fig. 1a) were collected immediately after surgical excision. These specimens were cut into several subsections, which were taken across the whole surface of the aorta in both longitudinal and circumferential directions. For each subsection, tissue thickness was measured using bench top micrometer (~0.1µm accuracy). Samples were then tested with uniaxial tensile testing (after preconditioning) and controlled peel testing, in both longitudinal and circumferential directions. Region specific tensile strength (TS), peeling force and dissection energy function (DEF) were evaluated. Computational results were processed in Ansys EnSight: the aneurysmal region was unwrapped from the outer wall and each patient aorta was segmented to match the regions used for thickness measurement and mechanical testing (Fig. 1b).

Results

In all patients, jet impingement on the outer aortic wall was observed. Local wall shear stress (WSS) distribution was asymmetric, with high values observed in the impingement region: maximum TAWSS was 4.85 ± 2.07 Pa at the outer curvature, 2.67 ± 0.81 Pa at the inner curvature. To assess the influence of WSS on tissue thickness and mechanical properties, linear regression analysis was performed, revealing a statistically significant negative relationship between the maximum TAWSS and tissue thickness (p=0.022, N=107) and DEF (p=0.048). Higher levels of TAWSS were also associated with an increase in TS (p=0.048, N=62).

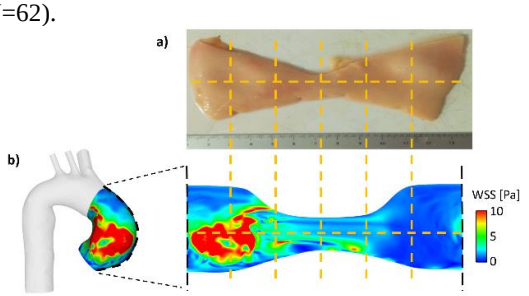

Figure 1: a) Patient tissue sample collected after excision; b) Peak systolic WSS distribution in the ascending aorta. The ascending aorta has been unfolded from the outer wall (dashed line) and subdivided into subsections (yellow lines) in accordance to the experimental procedure.

Discussion

Our results point to a potential link between high WSS and aortic wall degeneration and dissection. Regions of high WSS were thinner and required a lower energy to dissect, suggesting a disrupted aortic medial integrity and increased risk of dissection. Conversely, these regions also showed tissue stiffening, suggesting a reduced risk of rupture. Aortic samples have also been histologically tested to evaluate microstructural density of elastin, collagen and smooth muscle cell content. Further statistical analyses assessing the link between WSS and medial degeneration are currently ongoing. Larger sample sizes and the incorporation of patient-specific finite element modelling will form the basis of future work.

References

1. Kim et al, J Am Coll Cardiol, 68:1209-1219, 2016.
2. Pirola et al. IEEE TBME, 66:3411-3419, 2019.

Acknowledgements

This work was supported by NIHR Imperial College BRC (grant number P74143) and BHF Centre of Research Excellence (RE/18/4/34215).

IN SILICO TESTING: THE PATH FROM MODEL DEVELOPMENT TO VALIDATION FOR A COMPLEX INNOVATIVE SYSTEM

Alissa Zaccaria (1,2), David Contassot (3), Frederic Heim (4,5), Nabil Chakfe (5,6), Giancarlo Pennati (1), Francesco Migliavacca (1), Lorenza Petrini (7)

1. LaBS, Dept. of Chemistry, Materials and Chemical Engineering, Politecnico di Milano, Italy; 2. Intellimech, Italy; 3. ID NEST MEDICAL SAS, France; 4. LPMT, Université de Haute-Alsace, France; 5. GEPROVAS, France; 6. University Hospital of Strasbourg, France; 7. Dept. of Civil and Environmental Engineering, Politecnico di Milano, Italy

Introduction

Before an innovative device can be placed on the market, preliminary trials are required to assess its safety and efficacy, including numerical simulations. To this purpose, in silico models are intended to corroborate experimental data, both providing additional local information not differently acquirable or extending the investigation towards complex scenarios not replicable in vitro. Note that accurate validation is fundamental to establish the model's reliability in supporting decisions. However, only qualitative indications about the procedure to be followed have been provided, and, starting from these guidelines, for each device, it is necessary to implement an ad hoc protocol in light of the intended use and the possible impact of the model.

The present work focuses on the ID Venous System, an innovative device proposed by ID NEST MEDICAL to treat venous compression disorders that involve bifurcations, such as the May-Thurner syndrome (Figure 1.a). The system consists of two components, a laser-cut stent, ID Cav, and a braided stent, ID Branch, which can be combined through a compliant connection [1]. This newly proposed solution allows preventing migration, acting locally on the pathological region, thereby preserving the surrounding healthy tissues.

This project outlines the process followed to implement and validate the ID Venous System virtual twin. The mechanical behavior of the device was investigated both numerically and experimentally. Thus, the model accuracy was assessed following the standard ASME V&V40 [2]. Finally, the reliable prediction of the implant in a realistic geometry was achieved (Figure 1.b).

Methods

The geometries were reconstructed in Solidworks (Dassault Systèmes, Vélizy-Villacoublay, France) and meshed, after a sensitivity analysis, with beam elements. Tensile tests on wire samples were carried out to calibrate the Nitinol materials parameters. Thus, the model, implemented in Abaqus 2018 (Dassault Systèmes, Vélizy-Villacoublay, France), was validated based on the comparison with eight experimental tests. Namely, the validation process runs through increasing complexity scenarios involving both the individual components or the assembled system configuration and reflecting the real use of the device in order to assess the impact of each numerical uncertainty individually. Finally, the deployment in a realistic geometry was performed and numerically replicated to ensure the implant procedure feasibility.

Results

The computational and experimental results were compared in terms of force-displacement curves and deformed configurations. The differences between in vitro and in silico tests lay below 10%, as required to ensure the proper accuracy in the intended context of use.

Therefore, the deployment in an idealized geometry mimicking the anatomical relevant area allowed assessing the implant procedure feasibility without the risk of rupture or plasticity of the components.

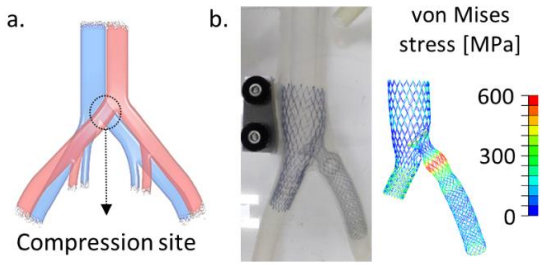

Figure 1: a- representation of May-Thurner syndrome; b- experimental and numerical deployment of the ID Venous System in a realistic geometry. The numerical result is reported with the von Mises stress colored map.

Discussion

The similarity between numerical and experimental data ensures the model reliability, which, in association with the experimentally acquired information, enables the identification of the strengths and weaknesses of the proposed device. Further improvements to the system are currently under investigation, concerning both the design and the delivery procedure.

References

1. Chakfe, N., et al, Eur. J. Vasc. Endovasc. Surg., 2020.
2. ASME. V&V 40, 2018.

VENOUS ANEURYSM MODELISATION USING OPEN-SOURCE TOOLS

Juan C. Cuevas (1), Gerard Fortuny (1), Joan Herrero (1), Josep M. López (1), Dolors Puigjaner (1)

1. Universitat Rovira i Virgili, Av. Països Catalans 26, Tarragona, Catalunya, Spain

Introduction

An aneurysm is a localized dilatation of a blood vessel (Figure 1). It is of interest to study the aneurysm formation in the cardiac veins as it may lead to a variation on the blood flow pattern and on the structural characteristics of the vein tissue. The formation of aneurysms is a fluid-structure interaction phenomenon. A non-linear static analysis, in which the final equilibrium state is resolved by fluid and structural numerical simulations, will be performed.

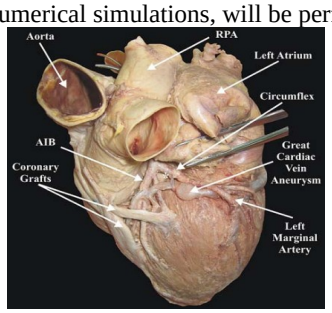

Figure 1: Great cardiac vein aneurysm [1].

Methods

Open-source tools are used to model the fluid-structure interaction problem due to their accessibility, flexibility and high performance. The blood flow and the forces exerted on the vein internal wall are calculated through OpenFOAM using the finite volume method. The deformation of the vein as a consequence of the blood flow increase is computed in CodeAster solver, which employs the finite element method. Mfront is a code generator based on C++ that is used to define the vein material constitutive model.

The Ogden isotropic hyperelastic material model is used in this case to describe the incompressible behavior of the vein tissue. The isochoric strain energy density function is expressed in the form of a series given in terms of the principal stretches $(\lambda_1, \lambda_2, \lambda_3)$ and $2N$ material constants (μ, α) [2]:

$$W^i = \sum_{p=1}^{N} \frac{\mu_p}{\alpha_p} \left(\lambda_1^{\alpha_p} + \lambda_2^{\alpha_p} + \lambda_3^{\alpha_p} - 3 \right) \qquad (1)$$

The vein tissue compressible behavior is described by a simplified volumetric strain energy density function expressed in terms of the bulk modulus (K) and the determinant of the deformation gradient (J), [3]:

$$W^v = \frac{1}{2} K \left(J - 1 \right)^2 \qquad (2)$$

The fluid-structure interaction phenomenon is linearized and modeled as an iterative process. A variation in the blood flow rate will deviate the vein from its equilibrium state. The pressure and wall shear stresses increase on the internal part of the vein tissue will deform the vein geometry. A deformed mesh is obtained from the structure simulation. The new geometry of the vein in turn modifies the blood flow and the forces exerted on the vein walls.

The iterative process is stopped when the forces on the wall and the geometry deformation reach a given convergence criteria.

Python programming language is used to code the scripts that successfully integrate OpenFOAM, CodeAster and Mfront.

Results

The fluid-structure interaction framework coded in Python automates part of the pre-processing, the simulations and part of the post-processing of the computational fluid dynamics and computational mechanics simulations.

As shown in Figure 2, the fluid-structure interaction is an iterative process that may eventually reach a new equilibrium state.

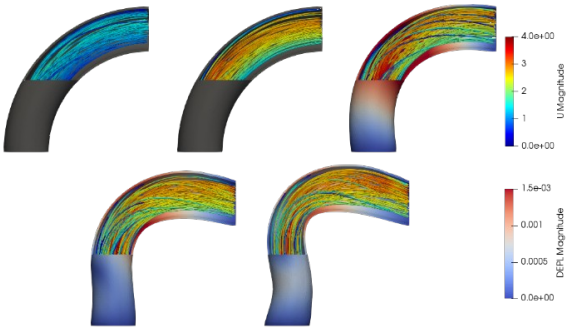

Figure 2: top-left vein: equilibrium state; top-center: flow increase; top-right and bottom: vein deformation and flow pattern for different iterations.

Discussion

More complex material and fluid models can be integrated in order to consider the microscopic properties of the veins and blood, such as the vein anisotropy due to the presence of collagen fibers [4] and the non-Newtonian behavior of the blood.

The fluid-structure interaction framework proposed can be used to study other fluid-structure interaction phenomena in biomechanics.

References

1. Loukas M et al, Surg Radiol Anat, 29:169-172, 2007.
2. Ogden RW et al, Proc R Soc Lond, 326:565-584, 1972.
3. Simo JC et al, Computer Methods in Applied Mechanics and Engineering, 98:41-104, 1992.
4. Holzapfel G et al, Journal of Elasticity, 61: 1-48, 2000.

NUMERICAL MODELLING OF SELECTIVE INTERNAL RADIATION THERAPY FOR THE TREATMENT OF HEPATOCELLULAR CARCINOMA

Elena Cutrì (1), Massimiliano Mercuri (2), Sahadatou Touré (1), Valéry Morgenthaler (3), Pierre-Antoine Eliat (4), Florent Lalys (2), Antoine Petit (2), Anne Landreau (2), Hervé Saint-Jalmes (5), Michel Rochette (3), Yan Rolland (5), Johanne Bezy Wendling (1)

1. Université de Rennes, CHU Rennes, INSERM, LTSI - UMR 1099, F-35000 Rennes, France; 2. Therenva, France; 3. ANSYS France, France; 4. Biosit, CNRS, UMS 3480, Rennes, France; 5. Université de Rennes, CLCC Eugène Marquis, INSERM, LTSI - UMR 1099, F-35000 Rennes, France

Introduction

Hepatocellular carcinoma is a primary malignancy of the liver predominantly occurring in patients with underlying chronic liver disease and cirrhosis. Selective internal radiation therapy (SIRT) has emerged as an effective and safe treatment for patients with unresectable and chemorefractory liver tumors [1-3]. Specifically, such treatment consists in inter-arterial administering of radioactive microspheres, typically Yttirium-90, via catheter directly into the hepatic artery [1]. In order to assess if a patient is suitable for SIRT and to predict the microsphere distribution, a pre-treatment assessment is routinely carried out by infusing Technentium 99mTc-labelled macroaggregated albumin (99mTc-MAA). Based on the pre-treatment assessment, potential extra-hepatic uptake can be evaluated and the dose to be delivered can be estimated. Nevertheless, the reliability of the 99mTc-MAA in mimicking the behavior of microspheres is still controversial. Indeed, a mismatch between the 99mTc-MAA distribution in the pre-treatment and the real microspheres distribution can occur, causing a suboptimal result. A number of factors can play a role in determining different outcomes between the pre-treatment and the treatment itself such as a different catheter positioning, the presence of a bifurcation near the catheter tip, the different size of the injected particles and the injection velocity [4-7]. Starting from these considerations, we aim at developing a patient-specific CFD model of the hepatic arterial tree to evaluate the impact of the aforementioned factors on the outcomes of the therapy. A better understanding of the role of such factors could help the clinicians in improving the treatment outcomes, i.e. an optimal targeting of the tumour(s) while preserving healthy tissues.

Methods

For each patient, medical images of the hepatic arterial tree were acquired via CT or CBCT and hemodynamic data such as pressure and velocity were collected during the pre-treatment assessment at the Centre Eugène Marquis, Rennes, France.

The acquired images were reconstructed by means of standard segmentation method to obtain the patient specific hepatic arterial tree.

To investigate the role of the injection setting, a parametrical CFD model was developed using ANSYS (ANSYS Inc., Canonsburg, PA, USA). Firstly, the geometry of the hepatic tree was complemented with a cylindrical catheter inserted into the hepatic artery. The catheter geometry was parametrized in terms of spatial position and inclination. Secondly, polyhedral meshes were obtained with appropriate boundary layer. Thirdly, a two-phase mixture multiphase method was used to model the blood and the microspheres fluid dynamics pattern with parametric microspheres volume fraction and the injection velocity. Patient specific boundary conditions were set according to the acquired hemodynamic data. Lastly, a reduced order model approach was used. A reliable range of variation was defined for each parameter to build up a series of design points with different combinations of the parameters. A number of simulations are then automatically performed to assess the effect of all the parameters of interests on the treatment's performance.

Results and Discussion

For a given patient specific case, the catheter position (within the HA and its inclination) plays a major role in determining the microspheres distribution, particularly when approaching a bifurcation. The injection velocity has a minor role as long as it is comparable with the blood velocity. The patient specific framework here presented allows to evaluate the impact of a number of parameters on the treatment outcomes in terms of targeting of the tumor.

References

1. Sangro B et al, Int J Radiat Oncol Biol Phys, 66:792–800, 2006.
2. Saxena A et al, J Cancer Res Clin Oncol, 140:537–547, 2014.
3. Kennedy A et al, Int J Radiat Oncol Biol, Phys 68:13–23, 2007.
4. Basciano CA et al, Ann Biomed Eng, 38:1862–1879, 2010.
5. Childress EM et al, Ann Biomed Eng, 42:461–474, 2014.
6. Ulrich G et al, J Nucl Med, 54:516–522, 2013.
7. Aramburu J et al, J Biomech, 49: 3714-3721, 2016.

Acknowledgements

The work was supported by the grant 'AAP Innovation Collaborative Au Croisement Des Filières – Région Bretagne' from the Region of Brittany

FROM CTA TO WALL SHEAR STRESS PREDICTION ON AORTA: A FULLY AUTOMATIC DEEP LEARNING PIPELINE

M.A. Scarpolini (1,2,3), K. Capellini (1,4), S. Longo (4), M. Odino (2), D. Morbidelli (5), M. Cioffi (5), E. Costa (5), V. Positano (1), S. Celi (1)

1. BioCardioLab, Fondazione Toscana Gabriele Monasterio, Italy; 2. TechneValue GmbH, Switzerland; 3. Università di Roma "Tor Vergata"; 4. Dept. of Information Engineering, University of Pisa, Italy; 5. RINA S.p.A., Italy.

Introduction

Computational Fluid Dynamics (CFD) serve as a powerful tool to characterize the hemodynamics of blood vessels. Complex geometries and boundary conditions are just an example of the factors that need to be considered to provide accurate and patient's specific results. However, the time required to segment geometries and the cost associated with CFD make it difficult to integrate numerical simulation in a real clinical environment. In this scenario the emerging Deep Learning (DL) methods offer a new perspective to tackle these problematics. This study aims to propose a DL framework able to segment aortas and to estimate hemodynamic predictors of potential pathological state, such as the wall shear stress (WSS).

Methods

The proposed workflow is schematically reported in Fig. 1, where the two neural networks (NN) of the pipeline are shown. The first is dedicated to the segmentation phase (*NNseg*) and the second one to the WSS computation (*NNwss*).

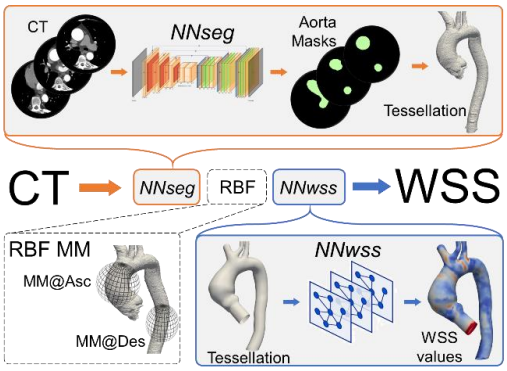

Figure 1: Workflow of the DL pipeline.

The dataset for *NNseg* consisted of 40 CT scans with contrast medium of aortas segmented with 3DSlicer. 25, 5 and 10 scans were used for training, validation and testing, respectively and the dataset was concurrently enriched through data augmentation techniques. *NNseg* architecture is based on 2D U-net [1], and its performance was assessed by means of the Dice and Jaccard coefficients. In order to train *NNwss*, a large-scale CFD dataset was created. The initial 40 aortas of the *NNseg* dataset were meshed and a specific mesh morphing (MM) technique approach, based on the use of radial basis functions (RBFs) [2], was used to obtain a total of 200 different models. The morphing process was applied to the ascending and/or descending portion of the aorta. Stationary CFD simulations were performed and postprocessed by means of ANSYS® Fluent® to obtain the WSS values necessary to train *NNwss*. This network relies on graph convolutional layers to predict the WSS components on each node of the surface mesh. NNwss was implemented with the PyTorch geometric library [3] and absolute percentage error with respect to the CFD results was computed.

Results

The performance of *NNseg* reached a Dice coefficient of 0.96 and a Jaccard coefficient of 0.93 on the test dataset. Our preliminary results for *NNwws* show that the network has predicted the WSS distribution on the given test meshes with an absolute error of 5% per component. In Figure 2 the pointwise absolute percentage error is shown for a random geometry in the test set.

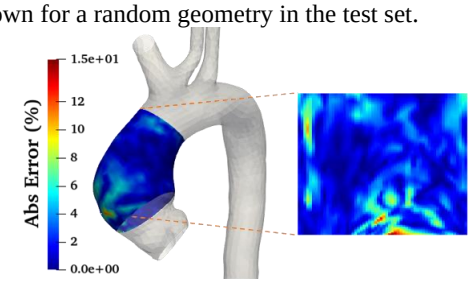

Figure 2: Absolute percentage error on WSS.

Discussion

An automated DL pipeline to enhance the clinical workflow was successfully implemented. The evaluation metrics of *NNseg* are satisfactory and compatible with the ones found in literature. Instead, the preliminary results of *NNwss* show that it is a promising surrogate model for CFD simulations, despite the limited size of the training dataset.

References

1. Ronneberger, O. et al, MICCAI Conf., Springer, Cham, (2015) 234-241.
2. Biancolini, M. et al, *IJIDeM*2020, 14.4: 1227-1238.
3. Fey, M. et al, arXiv preprint arXiv:1903.02428, 2019.

Acknowledgements

This project has received funding from the Marie Skłodowska-Curie grant agreement MeDiTATe project No 859836.

MODELLING THE HAEMODYNAMIC ENVIRONMENT PRODUCED BY THE CREATION OF AN ARTERIOVENOUS FISTULA

George Hyde-Linaker (1), Pauline Hall Barientos (2), Asimina Kazakidi (1)

1. University of Strathclyde, United Kingdom; 2. Image Centre of Excellence, United Kingdom;

Introduction

End-stage renal disease (ESRD) patients require renal replacement therapy (RRT) to filter wastes and excess fluids from blood. The arteriovenous fistula (AVF) is considered the most preferential vascular access for hemodialysis, the most common RRT. Creating an AVF involves surgically constructing an anastomosis between a patient's artery and vein, commonly in the arm. Upon fistula creation, high pressure blood from the artery (a low capacitance system) flows directly to the vein (a high capacitance system). This phenomenon causes an increase in the arterial diameter, permitting consistently high flow rates in excess of 600mL/min. However, in many instances the AVF fails to mature, and vascular access dysfunction remains one of the main causes of morbidity in haemodialysis patients. This clinical problem highlights the need for predicting changes in the haemodynamic environment caused by vascular access surgery. Computational fluid dynamics (CFD) permits a thorough investigation into haemodynamic metrics that are not easily measurable in-vivo. We present a methodology for a patient-specific haemodynamic CFD study from the ascending aorta to the radial artery (proximal to the AVF anastomosis). Furthermore, the haemodynamics juxta-anastomosis for a radiocephalic AVF is simulated (Fig. 1).

Methods

Due to historic contrast-enhanced methods for MRI and CT contraindicating in advanced kidney disease patients [1], ferumoxytol, a superparamagnetic iron oxide nanoparticle preparation, is used as a contrast agent. Three ferumoxytol-enhanced magnetic resonance angiography (FEMRA) datasets were generated for assessing the varying regions of the vasculature. All scans were performed on a 3.0 T Prisma MRI scanner (Magnetom, Siemens Medical Solutions, Erlangan, Germany). All patients were imaged in the supine position. The segmentations from the three scans were then unified into a singular surface mesh using Boolean operations. The patient-specific geometry was then simulated in STAR-CCM+ under the assumptions of a Newtonian fluid with physiologically relevant values (for the aorta simulation) and rigid walls. The juxta-anastomosis simulation used a Carreau-Yasuda non-Newtonian fluid model due to the smaller diameter arteries being considered in the simulation. The three-element windkessel model was implemented in Simcenter Amesim and coupled to the STAR-CCM+ pressure outlet conditions. A triphasic waveform was applied at the domain inlet.

Results

The results of the juxta-anastomosis simulation domain demonstrate the diversion of significant flow from the radial artery to the cephalic vein through the anastomosis (Fig. 1). Additionally, the generation of helical flow in the vein of the radiocephalic fistula is evident. The velocity magnitude throughout the domain after the creation of the AVF are also presented (Fig. 2).

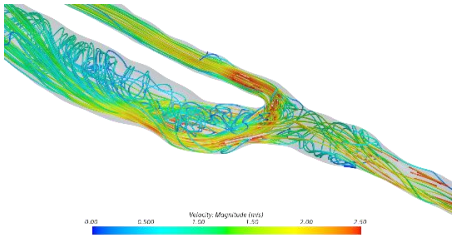

Figure 1: Velocity streamline contour plot juxta-anastomosis at peak systole

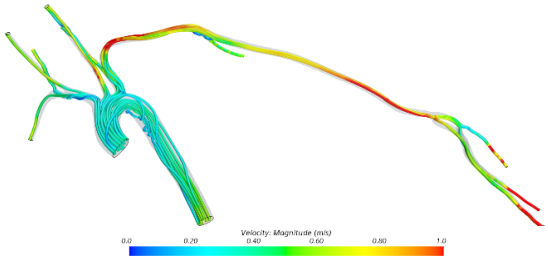

Figure 2: Velocity streamline contour plot from aorta at mid-deceleration

Discussion

FEMRA has been found to produce images comparable to traditional CT. Using FEMRA datasets, a patient-specific CFD study was completed for studying the haemodynamics in a 20-year-old ESRD patient. This methodology and model will be extended to incorporate fluid-structure interaction between the arterial (and venous) walls and blood flow.

References

1. S. Stoumpos, M. Hennessy, A. Vesey, Radjenovic A., R Kasthuri, D. Kingsmore, P. Mark, and G. Roditi. Ferumoxytol-enhanced magnetic resonance angiography for the assessment of potential kidney transplant recipients. Eur Radiol, 28:115–123, 2018.

Acknowledgements

This work is supported partly by the University of Strathclyde International Strategic Partnership, Research Studentships, and the European Union's Horizon 2020 research and innovation programme under the Marie Sklodowska-Curie grant agreement No749185.

A MULTI-PHYSICS MODEL FOR MYOCARDIAL PERFUSION IN THE HUMAN HEART

Simone Di Gregorio (1), Christian Vergara (2), Giovanni Montino Pelagi (1), Paolo Zunino (1), Andrea Baggiano (3), Laura Fusini (3), Gianluca Pontone (3), Alfio Quarteroni (1)

1. MOX, Dipartimento di Matematica, Politecnico di Milano, Milano, Italy; 2. LaBS, Dipartimento di Chimica, Materiali e Ingegneria Chimica "Giulio Natta", Politecnico di Milano, Milano, Italy; 3 Centro Cardiologico Monzino IRCSS, Milano, Italy;

Introduction

Myocardial perfusion is the delivery of blood to the heart muscle, supplied by the coronary circulation. A proper heart function strongly relies on this phenomenon, since reduced coronary flow rate, due for example to atherosclerosis, can lead to ischemic cardiopathy and, possibly, to an infarct of the myocardium.

Methods

We present a mathematical and numerical model for human cardiac perfusion which accounts for the different length scales of the vessels in the coronary tree. Precisely, a clear scale separation can be noticed between the coronaries laying on the epicardium and the smaller vessels penetrating into the tissue [1]. We adopt a multi-physics approach in which the epicardial vessels are represented with a three-dimensional fluid-dynamics description (Navier-Stokes) whereas the intramural vessels are modeled by means of a multi-compartment porous medium (Darcy's law) [2]. These two models are coupled using interface conditions based on the continuity of mass and momentum. Since the heart is composed by regions perfused by distinct epicardial vessels [3], we partition the myocardial domain in perfusion regions. Moreover, in each of these sub-domains a virtual intramural vascular network is generated to estimate the physical parameters of the multi-compartment model. The design of the multiscale model is displayed in *Figure 1*. We also propose suitable numerical strategies for the solution of the coupled problem, which is approximated by means of Finite Element Method. Finally, the multi-physics approach was used to reproduce myocardial blood flow (MBF) maps in nine patients (four healthy and five with detected coronary artery disease) [4].

Results

The application of the multi-physics model to patient-specific scenarios shows an excellent agreement between the computed MBF and MBF measured from clinical data. In all the study population, the relative error was always below 8% over all the myocardium, with an average-in-space value always below 4%.

Discussion

The results of this work proved the accuracy and the reliability of the proposed multi-physics model in reproducing MBF. In this way, we could provide a quantification of the MBF, comparable to invasive MBF clinical measurements, which could be useful for the assessment of the coronary artery disease and for guiding revascularization decisions.

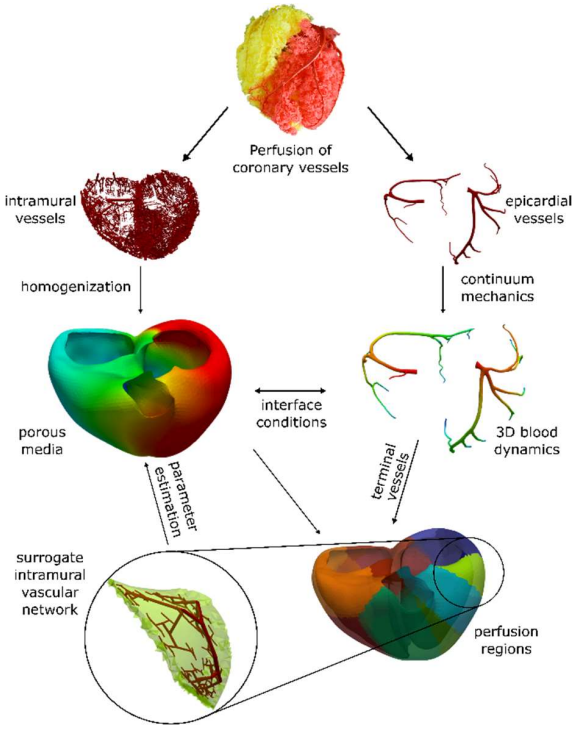

Figure 1: Design of the multiscale model.

References

1. Di Gregorio et al, *J Comp Phys* 424, 2021;
2. Hyde et al, *Ann Biomed Eng*, 42:797-811 2014;
3. Spaan J. et al. *Med Bio Eng Comput, 2005;*
4. Di Gregorio et al. *MOX Report 65/2020.*

Acknowledgements

This project has received funding from the European Research Council (ERC) under the European Union's Horizon 2020 research and innovation programme (grant agreement No 740132).

TURBULENT-LIKE ARTERIOVENOUS FISTULA FLOWS CAUSE WALL VIBRATIONS; A SPECIFIC STIMULUS FOR STENOSIS FORMATION?

Michela Bozzetto (1), Alban Souche (2), Andrea Remuzzi (1), Kristian Valen-Sendstad (2)

1. University of Bergamo, Italy; 2. Simula Research Laboratory, Norway.

Background

Native arteriovenous fistula (AVF) is the preferred vascular access for hemodialysis, but it still has high rate of failure due to stenosis formation [1]. Convincing evidence supports a key role of local hemodynamics in vascular remodeling, suggesting that disturbed flow conditions may have a key role. Recent high-resolution computational fluid dynamics (CFD) simulations have revealed turbulent-like flows in AVF [2] and we hypothesized that the associated high-frequency pressure fluctuations could promote high-frequency AVF wall vibrations. The aim of this study is to investigate the feasibility of assessing wall vibrations in AVF.

Methods

We generated the AVF 3D model from non-contrast enhanced 3D fast spin echo MR images acquired at 3 days after radio-cephalic AVF surgery in one patient.

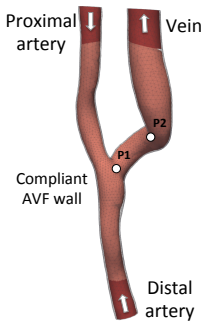

FLUID: 90k elements P2-P1
Navier Stokes equations
Viscosity: 3.5 e^{-2} Poise
Density: 1.025 g/cm^3

SOLID: 27k elements P2
St. Venant-Kirchhof hyperelasticity
Poisson ratio: 0.45
Young's modulus: 1e^7 dynes/cm^2
Density: 1 g/cm^3

Figure 1: AVF model and boundary conditions

We imposed 3 different values of the blood flow entering the computational domain, corresponding to diastolic, average and peak diastolic flow rates acquired with US examination (Table 1).

	Proximal Artery	Distal Artery
Q_{diast} (mL/min)	150	35
Q_{aver} (mL/min)	270	65
Q_{peak} (mL/min)	450	110

Table 1: Blood flow boundary conditions

A validated and formally 2nd order accurate fluid structure interaction solver was used to solve for wall deformation and flow field. The 3D transient problem was modeled taking 10k time steps per second in order to adequately resolve the high-frequency velocity and pressure fluctuations.

Results

Figure 2 shows the temporal evolution of the deformation in 2 selected location on the AVF vein.

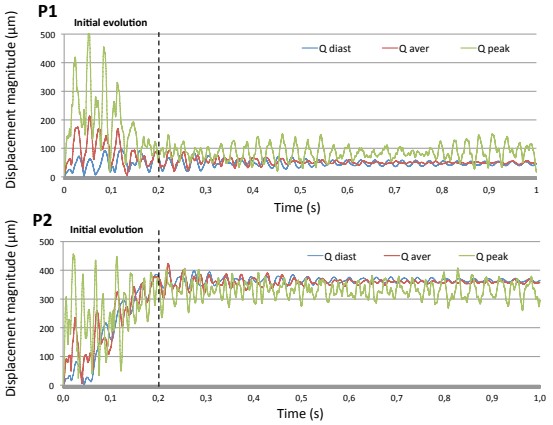

Figure 2: Deformation magnitude for different flow rates at the selected points

Figure 3 shows the time average deformation of the vascular wall over the cardiac cycle for the three different blood flow rates.

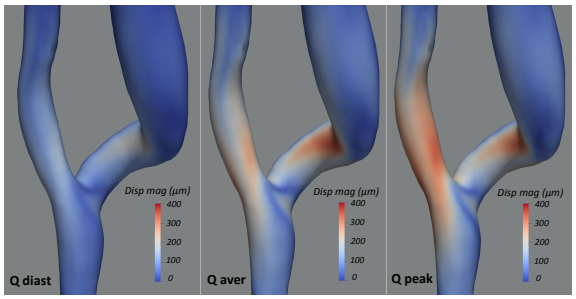

Figure 3: Time average vascular wall deformation.

Discussion

Our preliminary findings demonstrate the feasibility of studying wall vibrations in AVF that could shed light on mechanobiological processes. Our preliminary results under constant flow conditions show that varying the blood flow rate changed both the amplitude and frequency of the deformation. Interestingly, the magnitude and amplitude of wall vibration phenotypically collocate with the formation of stenoses.

References

1. Lee et al. Clin J Am Soc Neprol, 11:1504–12,2016.
2. Bozzetto et al. Ann Biomed Eng. 44(8): 2388-2401, 201

Acknowledgements

We thank Dr. Paolo Brambilla, Dr. Valentina Portalupi and Dr. Stefano Rota for fruitful discussions and data.

ALTERATIONS OF SMOOTH MUSCLE CELL MECHANICS IN THORACIC AORTIC ANEURYSMS

Claudie Petit (1), Ali Akbar Karkhaneh Yousefi (1), Alain Guignandon (2), Stéphane Avril (1)

1. Mines Saint-Etienne, Université de Lyon, INSERM, U 1059 SAINBIOSE, F - 42023 Saint-Etienne France;
2. Université Jean Monnet, Université de Lyon, INSERM, U 1059 SAINBIOSE, F - 42023 Saint-Etienne France

Introduction

Aortic smooth muscle cells (AoSMCs) usually express a contractile phenotype in the aorta and maintain a constant basal tone to contribute actively to the wall biomechanics [1]. However, under pathological conditions as for Ascending Thoracic Aortic Aneurysms (ATAA), the contractile phenotype tends to be turned down in favor of a synthetic phenotype [1], [2]. This may result in alteration of the contractile apparatus, that directly affects the wall biomechanics [3], [4]. We recently developed an *in vitro* technique, based on Traction Force Microscopy (TFM), that permits to quantify the basal tone of AoSMCs [5]. In the present study, AoSMCs of healthy and aneurysmal patients were tested using the TFM technique to assess quantitatively the alteration of AoSMC contractility induced by the aneurysm disease [6].

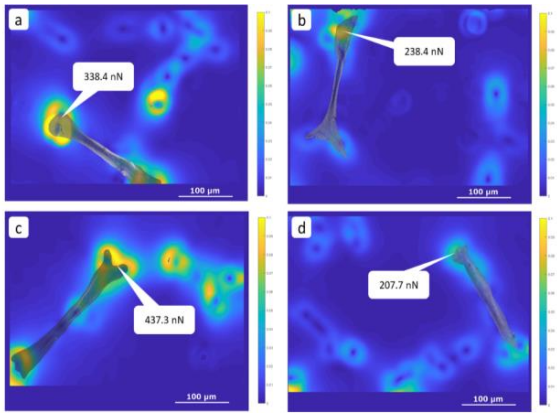

Figure 1: Morphologies of AnevPrim SMC (a,c) and of AoPrim SMC (b,d) obtained from the phase contrast channel of the microscope and superimposed onto the strain maps measured for TFM analyses.

Materials and methods

Cell lines were cultured from ATAA tissue (AnevPrim) collected from 3 patients after informed consent during surgical repair. Then, cell lines from 3 sex and age matched healthy patients (AoPrim) were provided from the biobank of LVTS (INSERM U1148, Paris, France). We used fresh cells at passage 4 for seeding 24-well plates containing ready-to-use hydrogels of varying elastic modulus (4, 8, 12 and 25 kPa), with adhesive collagen I coating and embedded fluorescent microbeads. We deduced the traction forces using a mechanical model based on the Boussinesq solution [5]. After measuring traction forces on about 750 cells, we derived the maximum likelihood traction force for each gel stiffness and compared it between the different cell lines.

Results

Although the range of force generation by AoSMCs suggested some heterogeneity, we observed that: 1. the traction forces were significantly larger on substrates of larger stiffness; 2. traction forces in AnevPrim were significantly higher than in AoPrim cells. We modelled computationally the dynamic force generation process in SMCs using the motor-clutch model and found that it accounts well for the stiffness dependent traction forces. The existence of larger traction forces in the AnevPrim SMCs were related to the larger size of cells in these lineages (Fig. 1).

Discussion

Our results revealed that the basal traction forces applied by representative populations of human primary aortic smooth muscle cells, when cultured onto compliant hydrogels of different stiffness, exhibit large heterogeneity even for cells coming from the same tissue. Despite these heterogeneities, we could conclude that phenotype changes occurring in ATAAs, which were previously known to reduce the expression of elongated and contractile SMCs (rendering SMCs less responsive to vasoactive agents), tend also to induce stronger SMCs [6]. Future work aims at understanding the causes of this alteration process in aortic aneurysms using motor-clutch computational models.

References

1. C. Petit et al, *Advances in Biomechanics and Tissue Regeneration*, 95-114, 2019.
2. P. Lacolley et al, *Cardiovasc Res*, 95(2):194-204, 2012.
3. L.A. Schildmeyer et al, *FASEB J.*, 14(14):2213-2220, 2000.
4. J.D. Humphrey et al, *Circ Res*, 116(8):1448-1461, 2015.
5. C. Petit et al, *Mol Cell Biomech*, 16(2):87-108, 2019.
6. C. Petit et al, *Biomech Model Mechanobio*, in press, 2020.

Acknowledgements

We are grateful to Jean-Baptiste Michel and Véronique Ollivier from LVTS (INSERM U1148) at Hôpital Bichat, Paris, for providing healthy cell lines. This research is supported by the European Research Council (ERC grant biolochanics, grant number 647067).

SYNTHESIS AND CHARACTERIZATION OF A NOVEL BOTTLE-BRUSH MOLECULE INSPIRED BY THE AGGRECAN STRUCTURE

Rossana Romita (1), Javier Rojo (2), Simone Vesentini (1)

1. Dipartimento di Elettronica, Informazione e Bioingegneria-Politecnico di Milano, Italy; 2. Glycosystems Laboratory, Instituto de Investigaciones Químicas (IIQ)-CSIC-Universidad de Sevilla, Spain

Introduction

The mechanical properties of articular cartilage result from the ECM network of collagen and the main proteoglycan, aggrecan, which in combination provide the tensile, shear, and compressive stiffness of the tissue [1]. Aggrecan has a linear-shaped protein core with connected brunches made by sugar chains producing a "bottle-brush" like structure that includes ~100 negatively charged chondroitin sulfate glycosaminoglycan (CS-GAG) chains attached covalently to the core protein. Variations in the structure of aggrecan and its GAG constituents are known to exist as a function of tissue age and pathological conditions such as osteoarthritis. The major challenge is to create constructs having biochemical and structural properties that are functionally equivalent to aggrecan. In this regard, a biomimetic aggrecan was designed mimicking the three-dimensional bottlebrush architecture of the natural molecule.

Materials and Methods

The envisioned molecule is composed by a core protein made by a single collagen molecule, and its lysines exposed on its surface connect bristles made by CS chains (Figure 1).

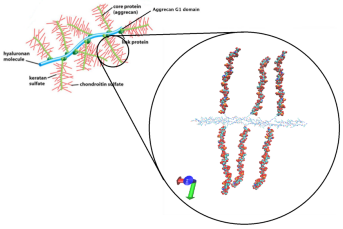

Figure 1 - Representation of the synthesized molecule.

Collagen-free amine content assessment. Ninhydrin is a highly selective indicator for the detection of amino acids with a primary amino group. The free amine residues in collagen molecules react with the 2,2-dihydroxy-1,3-indanedione (ninhydrin assay) to form highly chromogenic derivatives, which can be measured at 570 nm.

Biomimetic aggrecan synthesis. Reductive amination reaction, sketched in Figure 2, is the procedure adopted to obtain the envisioned molecule.

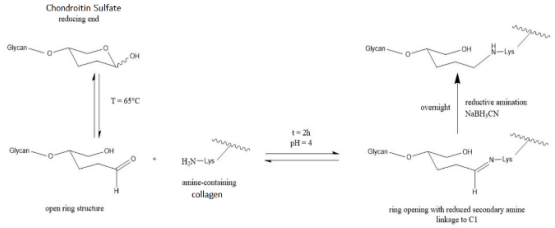

Figure 2 - Scheme of the reductive amination reaction.

Type 1 Collagen (10 mg) and Chondroitin Sulfate type A (600 mg) were mixed in 0.5M Acetic Acid (10 mL), pH = 4. The reaction mixture was stirred at 65°C for 2h, until the imine formation was completed. The imine in AcOH was carefully treated with solid NaBH3CN (3 g) and the reaction was left overnight at 65°C with continuous stirring. In order to purify the product, the precipitated sodium cyanoborohydrate was filtered away using a 100 kDa MWCO Amicon® centrifugal filter and the solvent evaporated at the rotary evaporator and then lyophilized.

Analytical techniques. Lyophilized CS and synthesized molecule samples were reconstituted in deuterium oxide (D2O) and then analyzed with 1H-NMR, HSQC-NMR and DOSY-NMR techniques.

Imaging techniques. Using atomic force microscopy (AFM), it was directly visualized the nanometer scale structure of the synthesized molecule deposited on a mica substrate.

Results and Discussion

Ninhydrin assay on pristine collagen confirms that the 2,7% of the total amino acids present in the collagen are free amine exposed on the surface, available for conjugation [2].

Synthesis. The synthesized molecule has a percentage of functionalization was 48,6%. The success of the reaction was confirmed through a solubility assessment. Pristine collagen is completely insoluble in water, being collagen a largely hydrophobic molecule. After the covalent functionalization of chondroitin sulfate, the obtained product was easily soluble in water.

Analytical techniques. Chemical structures of synthesized molecule samples and unreacted CS were confirmed with 1H NMR. The results suggest that the chemical composition of GAG bristles on the final synthesized molecules was maintained.

Imaging techniques. Atomic force microscopy (AFM) imaging was performed on the molecule (Figure 3).

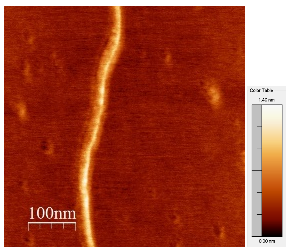

Figure 3 – AFM topography image of the molecule.

References

1. Gautieri et al., Matrix Biol, 34: 89-95. 2014.
2. Chandran and Horkay, Acta Biomat, 8:3-12, 2012.

NANOSECOND-SCALE INTENSE ELECTRIC FIELDS EFFECTS ON KINESIN NANOMOTOR MECHANICS

Jiří Průša, Michal Cifra

Institute of Photonics and Electronics of the Czech Academy of Sciences, Czechia

Introduction

Ultrashort duration intense pulsed electric field (PEF) may represent a unique tool to modulate the function of biological systems with potential applications in bionanotechnology and biomedical therapies. However, a mechanistic understanding of PEF effect on biomolecular mechanics is still lacking for the rational development of any potential biomedical/ bionanotechnological method based on PEF. Earlier, we showed [1] via molecular dynamics simulations that 20 - 100 MV/m nanosecond PEF act on tubulin electromechanics: tubulin conformation, secondary structure and dipole moment are affected. We used these insights in interpreting our findings on nanosecond PEF ability to modulate tubulin conformation to control the self-assembly of tubulin to microtubules in vitro [2]. Here we address the question of how the PEF acts on the nanosecond scale on the kinesin protein – the nanomotor which "walks" on microtubules.

Method

We employed classical full-atom molecular dynamics simulations of the single kinesin motor domain docked on the heterodimer, see Fig. 1, with electric applied of 100 MV/m in several orientations [3].

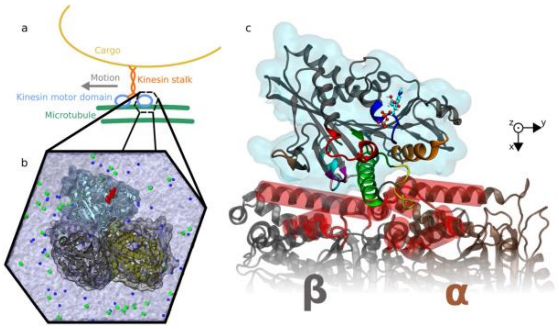

*Figure 1: (**a**,**b**) kinesin motor domain docked on a tubulin heterodimer - subunit of the microtubule track. (**c**) close-up on kinesin motor domain on α, β-tubulin heterodimer.*

Results & Discussion

We found that the magnitude as well as components of the kinesin dipole moment are affected. Furthermore, electric field also seems to affect contact surface area between kinesin and tubulin, as well as the magnitude of fluctuations of functionally important kinesin sites, such as switch in the nucleotide binding pocket and motifs involved in kinesin-tubulin interactions.

These findings indicate that external intense nanosecond-scale electric field can affect kinesin function. Additional new results also indicate that the electric field can detach kinesin from the microtubule track (Fig. 2)

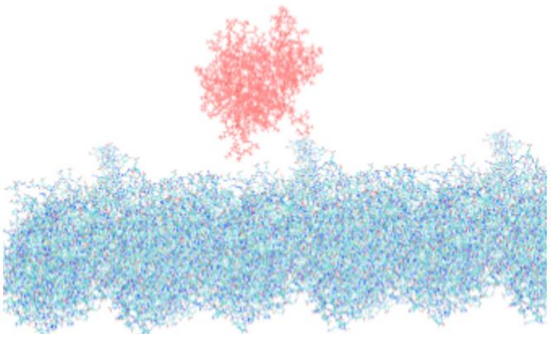

Figure 2: Electric field can cause kinesin motor domain (red) detachment from microtubules (blue)

Our results contribute to developing novel electromagnetic methods for modulating function of biomolecular matter at the nanoscale.

References

1. Marracino et al. Sci Rep, 9: 10477, 2019.
2. Chafai et al. Adv Mat, 31: 1903636, 2019.
3. Průša & Cifra, Sci Rep, 9:19721, 2019.

Acknowledgements

We acknowledge Czech Science Foundation (GAČR), project no. GA20-06873X.

MECHANOSIGNALING IN HUMAN ATRIAL FIBROBLASTS: IMPLICATIONS FOR CARDIAC FIBROSIS

Ramona Emig (1,2,3), Wiebke Knodt (1), Callum M. Zgierski-Johnston (1), Wilfried Weber (2,3), Maximilian Hörner (2,3), Ursula Ravens (1), Peter Kohl (1,2), Rémi Peyronnet (1)

1. Institute for Experimental Cardiovascular Medicine, University Heart Center Freiburg · Bad Krozingen, and Faculty of Medicine, University of Freiburg, Freiburg, Germany; 2. CIBSS – Centre for Integrative Biological Signalling Studies, University of Freiburg, Freiburg, Germany; 3. Faculty of Biology, University of Freiburg, Freiburg, Germany

Fibrosis is associated with most cardiac diseases and a hallmark of atrial fibrillation, a highly prevalent cardiac arrhythmia. It is characterized by excessive accumulation of extracellular matrix produced by activated fibroblasts leading to stiffening of the tissue. This stiffness change is sensed by cardiac cells and contributes to a positive feedback loop, leading to enhanced fibrosis [1].

We use hydrogels with light-tunable stiffness [2] combined with advanced biophysical and imaging techniques to elucidate how human atrial fibroblasts sense and respond to their mechanical environment, to derive strategies to slow, limit or reverse fibrosis.

We show that human atrial fibroblasts adapt to different mechanical environments and that these adaptations are modulated by cell-cell contact and paracrine mediators in mechanically heterogeneous environments. We identified the stretch-activated ion channel Piezo1 to be upregulated in cardiac fibroblasts isolated from atrial fibrillation patients. Up- or downregulation of Piezo1 in cell culture revealed that Piezo1 contributes to the organization of the actin cytoskeleton thereby affecting the mechanical properties of cells. This is mediated by a signaling pathway tightly connected to β1-integrin, as shown by inhibition of focal adhesion kinase and Rho-associated kinase. Using hydrogels with different stiffness, we additionally identified a critical role for Piezo1 in stiffness sensing in human atrial fibroblasts. Therefore, we suggest Piezo1 as new molecular target to slow down or stop the development of fibrosis.

Future experiments will take advantage of the ability to change hydrogel stiffness by light within seconds and target the kinetics of stiffness sensing in cardiac fibroblasts and their relevance for fibrosis development upon cardiac injury.

References

1. Ceccato et al, JAHA, 9/19: e017025, 2020.
2. Hörner et al, Adv Mater, 31/12, 1806727, 2019.

Acknowledgements

We thank the Department for Cardiovascular Surgery of the University Heart Centre Freiburg - Bad Krozingen, and the CardioVascular BioBank Freiburg for providing access to human atrial tissue.

We acknowledge the SCI-MED imaging facility at the Institute for Experimental Cardiovascular Medicine in Freiburg for access to the confocal microscope and support with image acquisition and analysis.

THE EFFECT OF OMECAMTIV MECARBIL ON THE MECHANICAL CONTRACTILE PROPERTIES OF SLOW SKELETAL MUSCLE FIBERS

Valentina Berg, Daniil Shchepkin, Salavat Nabiev, Sergey Bershitsky, Galina Kopylova

Institute of Immunology and Physiology, Russia

Introduction

Omecamtiv mecarbil (OM) is a specific modulator of cardiac myosin function [1]. In slow skeletal muscles, the slow isoform I of myosin heavy chain (MHC) is expressed that is similar to the β-isoform of cardiac MHC. We studied the effect of OM on the mechanical characteristics of slow fiber contraction (*m. soleus*) and its Ca^{2+} regulation.

Methods

The experiments were done according to Directive 2010/63/EU. The effect of 0.5 μM OM OM (Selleck Chemicals LLC) on tension and stiffness of single skinned fibers from rabbit *soleus* muscle was studied using the micromechanical equipment with a temperature jump (T-jump) device [2]. MHC was predominantly isoform I. Effect of OM on the actin-myosin interaction was studied in an *in vitro* motility assay (IVMA) with thin filaments containing skeletal F-actin, troponin, and tropomyosin [3]. The Ca^{2+} dependence of filament sliding velocity over myosin in IVMA was fit to the Hill equation:

$$V = V_{max} \times (1+10^{h(p\mathrm{Ca}-p\mathrm{Ca}50)})^{-1},$$

where V and V_{max} are the sliding velocity of thin filaments and the maximal velocity at the saturating Ca^{2+}concentration, respectively; $p\mathrm{Ca}_{50}$ (Ca^{2+} sensitivity) is pCa at which the velocity is half maximal; h is the Hill coefficient of cooperativity.

Results

In the absence of OM, the T-jump from 5°C to 30°C led both tension and stiffness of fiber to increase by 2.5-2.8 times, i.e., force generation was entirely due to the formation of cross-bridges (Figure 1). At 5°C, 0.5 μM OM increased stiffness by 40% but did not change it at 30°C. The OM adding did not affect tension at 5°C but decreased it significantly at 30°C.

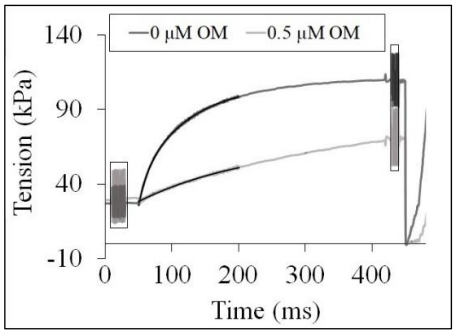

Figure 1: Effect of 0.5 μM OM on tension and stiffness of a single skinned fiber from m. soleus. The change in stiffness is framed.

OM reduced the filament sliding velocity in IVMA in a dose-dependent manner. To decrease the filament velocity by half, 0.036±0.004 μM OM was needed. 0.05 μM OM decreased V_{max} and h of the pCa-velocity relationship but did not affect the $p\mathrm{Ca}_{50}$ (Figure 2 and Table 1).

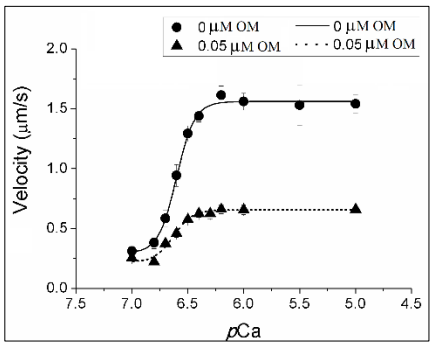

Figure 2: Effect of 0.05 μM OM on the pCa-velocity relationship of myosin from m. soleus in the in vitro motility assay.

OM (μM)	V_{max} (μm/s)	$p\mathrm{Ca}_{50}$	h
0	1.6±0.1	6.60±0.01	2.5±0.1
0.05	0.7±0.01*	6.63±0.01	2.0±0.1*

*Table 1: The effect of OM on the characteristics of pCa-velocity relationship. * denotes significant differences of the characteristics of pCa-velocity relation with OM from that without OM, $p < 0.05$.*

Discussion

We found that therapeutical concentration of OM (<0.6 μM) increases the number of myosin heads in the attached state, decreases the tension of slow muscle fibers at maximal activation, and affects calcium regulation of the actin-myosin interaction. Mechanism of the OM action on cardiac and slow skeletal muscles is similar [4], and so OM might be effective for the correction of contractile function of slow skeletal muscles in pathologies [5].

References

1. Malik et al, Science, 331:1439-1443, 2011.
2. Bershitsky et al, J Physiol., 540:971-988, 2002.
3. Matyushenko et al, Biochemistry, 56(1):250-259, 2017.
4. Nagy et al, Br J Pharmacol., 72(18):4506-4518, 2015.
5. Lindqvist et al, PLoS On, 14(11): e0224467, 2019.

Acknowledgements

This work was supported by State Program № AAAA-A18-118020590135-3.

MICROFABRICATION OF A 3D NICHOID WITH SPECIFIC GEOMETRY FOR THE EXPANSION OF HUMAN MESENCHYMAL STEM CELLS

Bianca Barzaghini (1), Letizia Messa (1), Federica Rey (2), Francesca Fanizza (1), Giulio Cerullo (3), Roberto Osellame (3), Gian Vincenzo Zuccotti (2), Stephana Carelli (2)*, Manuela Teresa Raimondi (1)*

1. Department of Chemistry, Materials and Chemical Engineering "Giulio Natta", Politecnico di Milano, Milano, Italy; 2. Pediatric Clinical Research Center Fondazione Romeo ed Enrica Invernizzi, Department of Biomedical and Clinical Science L. Sacco, Università di Milano, Milan, Italy; 3. Istituto di Fotonica e Nanotecnologie (IFN)-CNR and Department of Physics, Politecnico di Milano, Milano, Italy

** These authors equally contributed to this work*

Introduction

In the body, stem cells (SCs) reside in a specialized niche, characterized by a unique combination of biophysical and biochemical properties. Together, these features allow the maintenance of stemness. Recently, biomaterials have been used to create 3D scaffolds, which mimic the biomechanical characteristics of SCs niches. Raimondi and colleagues applied two-photon polymerization (2PP) technique to fabricate a 3D micro-scaffold, called Nichoid [1], in order to promote cellular proliferation and maintain stemness capabilities without adding any exogenous additive. The Nichoid has the ability to maintain stemness in several stem cells types, to induce the expression of pluripotency genes and potentiate the therapeutic potential of neural SCs [2,3]. Adipose-Derived Stem Cells (ADSCs) represent a promising source for cell therapies because their availability is less invasive compared to the one from other organs or tissue. Indeed, the aim of this study was to investigate the proliferation and stemness properties of human ADSCs expanded in engineered niches with a specific configuration to guarantee isotropic stimuli.

Materials and Methods

Nichoids were fabricated by 2PP using a hybrid organic-inorganic photoresist. The laser source presented in this work is a commercial femtosecond laser with a wave-length of 1042 nm and 1 MHz repetition rate [4]. hADSCs were isolated from lipoaspiarate adipose tissue and elective liposuction procedures were performed in voluntary patients after having received their informed consent.

The validation of the new cubic pore configuration of the scaffold was started by expanding $6x10^3$ hADSCs for 7 days. Then, cells expanded inside the cubic Nichoid have been characterized by viability assay, Real Time PCR and immunofluorescence analysis. Furthermore, neural differentiation was also investigated (Figure 1).

Results

The expansion inside the 3D micro-scaffold permits the potentiation of stemness features by upregulating the expression of pluripotency genes. These observations are in line with the nuclear measurements, confirming the cubic pore Nichoid's ability to induce isotropic cytoskeletal tension which resulted in a roundish nucleus. Furthermore, with this structure of the Nichoid, hADSCs can be efficiently detached and collected in order to be transplanted.

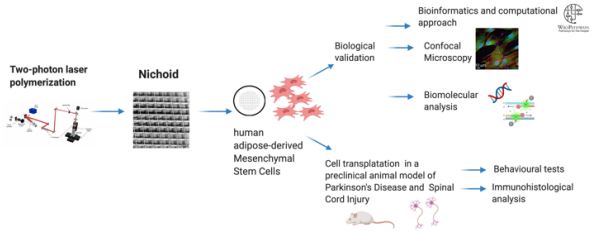

Figure 1: experimental set up of hADSCs expanded inside the cubic pore Nichoid

Discussion

These results represent an incredible improvement needed to reach the biological and clinical demands. Moreover, this approach can be applied also to fabricate any kind of porous Nichoid with different geometries, suitable for different stem cells. In particular, our findings represent a great promise for the Nichoid's application in the field of regenerative medicine, in particular in neurodegenerative diseases as Parkinson's disease and Spinal Cord Injury.

References

1. Raimondi et al., Acta Biomat, 4579-4584, 2013
2. Carelli et al., Nanothno, 5.1: 8, 2021
3. Rey et al., IJMS, 8: 6775, 2020
4. Zandrini et al., Sci Rep, 1:9, 2019

Acknowledgements

European Research Council (ERC projects NICHOID, G.A. 646990, NICHOIDS, G.A. 754467, and MOAB, G.A. 825159); European Commission (FET-OPEN project IN2SIGHT, G.A. 964481); European Space Agency (ESA project NICHOID-ET, G.A. 4000133244/20/NL/GLC); National Centre for the Replacement, Refinement and Reduction of Animals in Research (NC3Rs projects MOAB, G.A. NC/C01903/1 and NC/C019201/1); Italian Ministry of University and Research (MIUR-FARE project BEYOND, G.A. R16ZNN2R9K); Fondazione Social Venture Giordano Dell'Amore, Cariplo Factory, Politecnico di Milano, Fondazione Bassetti and Fondazione Triulza (S2P project EGGS&BEACON) and Fondazione Romeo ed Enrica Invernizzi.

ORBITAL SHAKING FOR ENHANCING CHONDROGENESIS FOR FACIAL CARTILAGE TISSUE ENGINEERING

Thomas H. Jovic (1,2), Feihu Zhao (3), Iain S. Whitaker (1,2)

1. Reconstructive Surgery and Regenerative Medicine Research Group, Swansea University Medical School, Swansea, UK
2. Welsh Centre for Burns & Plastic Surgery, Morriston Hospital, Swansea, UK
3. Zienkiewicz Centre for Computational Engineering, College of Engineering, Swansea University, UK

Introduction

One of the aims of tissue engineering is to regenerate tissue *in vitro*, which will be used for implantation. To enhance cellular activity *in vitro* (e.g. chondrogenesis, proliferation and matrix production) in facial cartilage tissue engineering (CTE), a suitable biological, physical and chemical environment needs to be provided. Previous CTE studies of articular cartilage have found that mechanical stimulation in terms of hydrostatic pressure, fluid-induced shear stress (FSS), and/or mechanical strain can affect cellular behaviours such as proliferation, differentiation and matrix production. However, the effects of different types of mechanical stimulation on human nasoseptal chondroprogenitor (hNC) chondrogenesis cells remain to be investigated with significant implications for facial cartilage regeneration. Therefore, this study aims to investigate the influence of mechanical stimulation on chondrogenesis of hNC cells using a combination of *in vitro* and *in silico* approaches.

Methods

The hNC cell isolation and culturing procedure was undertaken as previously described [1]. The cells were encapsulated within hydrogel constructs, and cultured in the chondrogenic medium. In dynamic culturing, an orbital shaker was used for applying the mechanical stimulation on cells. The cell-laden constructs were cultured for 14 days under both static and dynamic conditions. The relative gene expressions of aggrecan, SOX9 and type 2 collagen were measured for all the samples.

To simulate the mechanical environment within cell-laden struts under orbital shaking, a previously developed multiphase computational fluid dynamics (CFD) model in the study by Melke et al. [2] was used in this study. The cell-laden hydrogel domain was modelled as porous media, and the medium was modelled as incompressible Newtonian fluid (Figure 1a). The volume of fluid (VOF) technique was used for tracking the medium–air interface during shaking.

Results

It was found that the expressions of aggrecan, SOX9 and type 2 collagen were significantly upregulated after 14 days under the dynamic condition, compared to the static condition (Figure 1c). The CFD results showed that the maximum FSS and hydrostatic pressure were 0.02 mPa and 36 Pa respectively, and the maximum interstitial fluid velocity was 3 µm/s (Figure 1b).

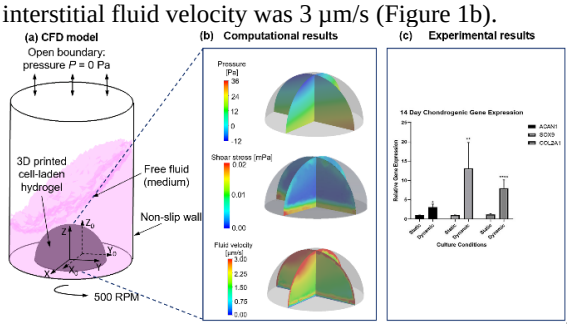

Fig. 1(a) Boundary and loading conditions of the multiphase CFD model for cell-laden constructs in orbital shaker; (b) resultant pressure, shear stress and fluid velocity within the constructs; (c) relative gene expressions of aggrecan (ACAN1), SOX9 and type 2 collagen (COL2A1).

Discussion and Conclusion

Using the orbital shaking system appeared to enhance the chondrogenesis of hNC cells. However, *in silico* modelling revealed that the resultant mechanical stimulation was quite low, comparing to the reported ranges for articular CTE (FSS at 10^{-1} Pa level, hydrostatic pressure at kPa – MPa level) [3]. With the current results, it was hard to conclude that enhanced chondrogenesis of hNC cells was due to the mechanical stimulation rather than convection-enhanced nutrient delivery. Therefore, future work will focus on investigating different levels of mechanical stimulation (e.g. FSS and/or hydrostatic pressure) in cell culturing. Also, cells from different donors will be studied. However, the CFD simulation showed that the mechanical stimulation within cell-laden constructs was still at low level even under maximum loading of orbital shaking system. Therefore, in our future work, we will aim to investigate the role of a suitable bioreactor (e.g. compression and/or perfusion) for applying different levels of mechanical stimulation on hNC cells.

References

1. Jessop et al. Biofabrication 11 045006, 2019.
2. Melke et al, J Orthop Res 38(6): 1228 – 1237, 2020.
3. Fahy et al, J Orthop Res 36(1): 52 – 63, 2018.

Acknowledgements

We thank Ms Kavitha Saw for providing the cartilage samples.

ENGINEERING BREAST CANCER MICROENVIRONMENT: A MECHANICAL STUDY FOR STEM CELL THERAPY

Despoina Nektaria Metsiou[1], Foteini Kozaniti[1] and Despina Deligianni[1]

1. Laboratory of Biomechanics and Biomedical Engineering, Department of Mechanical Engineering and Aeronautics, University of Patras, Rion, Patra, 26504.

Introduction

Breast cancer is the leading cause of cancer-related morbidity and mortality in postmenopausal women, even though its prognosis has improved due to advances in diagnostic and surgical techniques. However, the side effects of anti-cancer chemotherapy remain a major source of concern despite the improved efficacy and enhanced survival offered by modern treatments. Previous studies showed that stem cells can attenuate tumor growth of triple negative cancer and bronchioloalveolar carcinoma [1,2]. Nevertheless, further research is needed to establish the therapeutic effect of stem cells on tumor growth. This study attempted to bring forward and introduce the novel therapeutic opportunities of using culture medium from stem cells in ER+ and HER2+ breast cancer cells but most importantly juxtaposing the static and dynamic culture microenvironment via bioreactor, a condition that simulate satisfactorily human homeostasis and *in vivo* models. Moreover, the metastatic potential of post treatment cells was determined via wound healing assay.

Methods

ER+ and HER2+ breast cancer cells were cultured with the culture medium of stem cells for testing any therapeutic efficiency. Proliferation properties of treated cells were examined in collagen coated surfaces juxtaposing static and dynamic conditions. Specifically, a custom-made bioreactor has been employed to simulate the dynamic cell culture by perfusing the culture medium directly to the seeded cells in steady flow conditions, temperature, and CO_2 level (Fig. 1). MTT test was used for measuring proliferation cell rate in both static and dynamic conditions. Moreover, wound healing assay was performed to examine the post treatment metastatic potential.

Results

In case of dynamic flow conditions, the reduction of cell proliferation rate was 50.4% regarding ER+ treated cells and 17.23% in HER2+ treated cells. In static conditions, MTT assay indicated the decreased post treatment proliferation rate of 16.7% in ER+ cells and 40% in HER2+. Furthermore, the treatment effect of stem cells in ER+ and HER2+ collective cell migration was evaluated using wound healing assay. A significant decrease in ability of cells to migrate was shown in both ER+ and HER2+ cells post treatment 58.3% and 33.5 % respectively.

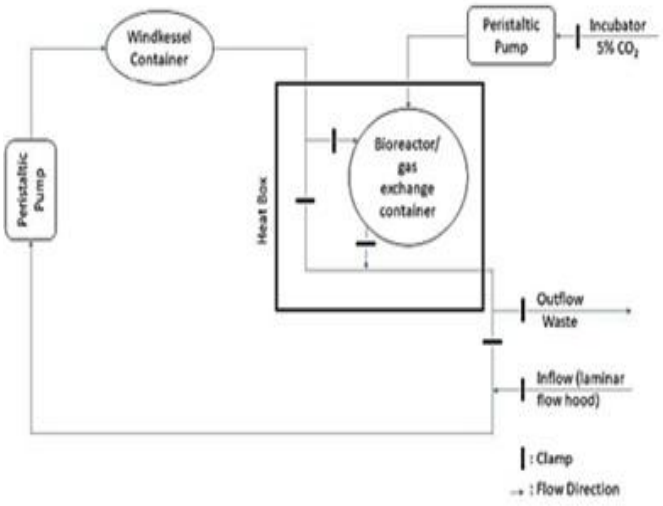

Figure 1: Bioreactor device for dynamic cell culture.

Discussion

Regarding cell proliferation rate of ER+ and HER2+ cancer cells in both static and dynamic culture conditions, the proliferation rate was significantly decreased post treatment. Wound healing assay revealed a significant decrease in migratory potential post treatment in both ER+ and HER2+ cells, implying a limited probability for metastasis. Overall, the reduction in cell viability, proliferation rate and healing capacity in both static and dynamic conditions was greater in ER+ treated cells due to their less aggressive cancer phenotype than HER2+ cells.

References

1. Ayuzawa, R. et al Cancer Lett., 280:31-37, 2009.
2. Matsuzuka et al, Lung Cancer, 70: 28-36, 2010.

Acknowledgements

This research is co-financed by Greece and the European Union (European Social Fund-ESF) through the Operational Programme «Human Resources Development, Education and Lifelong Learning 2014-2020» in the context of the project "Engineering breast cancer and hUMSCs microenvironment in 2D and 3D scaffolds: A mechanical study approach of hUMSCs in anticancer therapy." (MIS 5047131).

MECHANICAL CARACTERIZATION OF LAMIN COILED COIL 1B DOMAIN: FROM MONOMER TO TETRAMER CONFIGURATION

Francesca Donnaloja (1), Federica Rigoldi (2), Emanuela Jacchetti (1), Manuela T. Raimondi* (1), Monica Soncini* (3)

**These authors have contributed equally to this work as senior authors*

1. Department of Chemistry, Materials and Chemical Engineering "Giulio Natta", Politecnico di Milano, Italy; 2. Biology Department, MIT, USA; 3. Department of Electronics, Information and Bioengineering, Politecnico di Milano, Italy;

Introduction

Lamins are the major components of the nuclear lamina, a mesh-like structure, which provides mechanical support to the nucleus. Mutations in lamin A and lamin C cause several heritable diseases, called laminopathies. Even if their pathological mechanism remains so far elusive, mechanical defects in nuclear structure is one of the most plausible hypotheses [1]. In this study we mechanically characterize the already solved coiled coil 1b domain (CC1b) of lamin A. By Steered Molecular Dynamics (SMD) simulations, we investigated lamin hierarchical structure from monomer to tetramer configuration and we estimated viscoelastic features of such configurations.

Materials and methods

We used the X-ray structure of lamina CC1b domain (79-222 residues) [pdbID: 6JLB]. We performed 500ns MD simulations to equilibrate the structure using an NVT *ensemble*. CC1b lamin models were extracted from three different frames randomly selected in the equilibration stable phase. For each frame, a constant force was applied to tetramer, dimer, and monomer configuration simulating a Creep test. SMD simulations were performed in Generalized Born implicit solvent using NAMD software and CHARMM force field, at temperature of 310K and time step of 2fs. Three different force values (48, 70, 138pN) per chain were applied to the C-ter domain of chains A and B and N-ter domain of chains C and D; the opposite terminals have been locked. Kelvin-Voigt model was used to extract the Young's modulus and the viscosity parameter of each configuration.

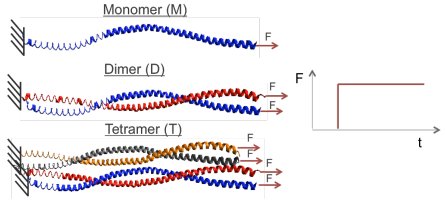

Fig.1: Monomer, dimer, tetramer configurations. The force step (on the right) was applied to each chain (A Blue, B red, C orange and D grey). Each arrow corresponds to the same force value.

Results

The *in silico* mechanical analysis revealed the exponential trend typical of viscoelastic materials, characterized by both stiffness value (Young modulus) and viscosity parameters. For each configuration (i.e. M, D, T) we observed the Young's modulus increasing with the force increment (0.23-0.6 GPa) and the viscosity decreasing. Considering a specific force value (e.g., 48pN), the Young's modulus is almost constant among the hierarchical configurations (about 0.23GPa) suggesting that lamin stiffness is mainly affected by the intra-chain H-bonds, which remain almost constant for all the configurations. Instead, the viscosity increases from the M to the D and T configuration (from 3.6 to 9.4 10^{-4} Pa*s), likely due to the different number of the intra-dimer and inter-dimer H-bonds, respectively. Applying a force of 48 pN/chain, the viscosity term does not change from D to T arrangement (9.4 10^{-4} Pa*s), suggesting that for very low force values the inter-dimer H-bonds do not affect the whole structure behaviour.

Discussion

From our SMD analysis we observed that the monomer filament guarantees lamin stiffness via intra-chain H-bonds. The intra-dimers bonds are instead responsible of the viscous behavior but their effect decreases with the force increment. In case of quite high force values (138pN), only the existence of a tetramer with inter-dimer bonds maintains the sufficient damping effect able to protect the nuclear structure.

The here implemented SMD approach can be replicated on single-point mutated lamin domain [1] to investigate plausible mechanical failure behind the origin of laminopathies.

References

1. Kaufmann A. et al. Nucleus. 2(4):310-9, 2011
2. Donnaloja et al, Frontiers in Physiology, 10:896, 2019.

Acknowledgements

European Research Council (ERC projects NICHOID, G.A. 646990, NICHOIDS, G.A. 754467, and MOAB, G.A. 825159) European Commission (FET-OPEN project IN2SIGHT, G.A. 964481) European Space Agency (ESA project NICHOID-ET, G.A. 4000133244/20/NL/GLC) National Centre for the Replacement, Refinement and Reduction of Animals in Research (NC3Rs projects MOAB, G.A. NC/C01903/1 and NC/C019201/1) Italian Ministry of University and Research (MIUR-FARE project BEYOND, G.A. R16ZNN2R9K) Fondazione Social Venture Giordano Dell'Amore, Cariplo Factory, Politecnico di Milano, Fondazione Bassetti and Fondazione Triulza (S2P project EGGS&BEACON).

DISCOVERY OF SARS-COV-2 MAIN PROTEASE INHIBITORS THROUGH DEEP DOCKING OF 1.36 BILLION COMPOUNDS

Francesco Gentile (1), Anh-Tien Ton (1), Hazem Mslati (1), Fuqiang Ban (1), Artem Cherkasov (1)

1. Vancouver Prostate Centre, Department of Urologic Sciences, The University of British Columbia, Canada

Introduction

Molecular docking plays a major role to investigate interactions between protein targets and ligands as well as to discover new drug candidates for unmet therapeutics needs (virtual screening). We have recently developed Deep Docking (DD), a deep learning program which enables structure-based virtual screening of billions of molecules by predicting docking outputs, resulting in 100-fold acceleration compared to standard docking [1]. As proof of principle, we have used DD to screen 1.36 billion of compounds against the active site of SARS-CoV-2 main protease (Mpro), a key drug target for COVID-19, identifying novel inhibitors with validated antiviral activity. Our results illustrate the advantages of using machine learning approaches to accelerate structure-based drug discovery.

Methods

The structure of Mpro bound to N3 inhibitor (PDB 6LU7) [2] was prepared using Schrödinger's prepwizard tool. 1.36 billion molecules were obtained from ZINC15 database [3]. Virtual screening was performed with DD using the Morgan fingerprints (1024 bits, radius 2) as neural network features, scores as labels, and a recall value of 0.75. Compounds selected for model training at each iteration were prepared using Openeye suite [4] and docked to Mpro using Glide SP [5]. Eleven DD iterations were run. Predicted top hits from the final iteration were prepared and docked to the active site, and top 107 compounds were purchased and evaluated for their inhibitory activity with a Mpro assay using a FRET-based peptide substrate.

Results

The SARS-CoV-2 Mpro proteolytically processes viral polyproteins to initiate the replication of the virus, thus blocking its active site is a promising strategy to develop antivirals for COVID-19. The docking site was defined by structurally evaluating viral Mpros that are closely related to SARS-CoV-2, bound to various substrates and ligands, and included five subpockets responsible for key interactions. Using DD, we were able to reduce the number of ZINC15 compounds from 1.36 billion to 14 million, a 100-fold reduction, by docking less than 1% of the database (Figure 1). Deep learning accelerated screening took only 4 days, while standard docking using the same resources would have taken 295 days. We then docked the top 3 million molecules based on their likelihood to be top scoring, to Mpro. Finally, we selected top ranked compounds whose docking poses recapitulate main Mpro-substrate interactions and consequently were likely to inhibit its proteolytic activity. Out of 107 tested molecules, 16 compounds were confirmed as Mpro inhibitors with IC50 values ranging from 8 to 251 μM. Notably, none of these compounds could be found within to the widely used ZINC15 drug-like in-stock set of about 6.87 million compounds, and therefore could be identified only by screening the entire ZINC15 database.

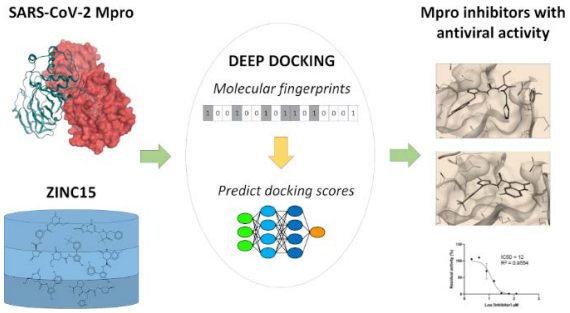

Figure 1. Deep learning accelerated virtual screening of 1.36 billion ZINC15 molecules against the active site of SARS-CoV-2 Mpro.

Discussion

We have developed DD, a machine learning framework that enables routine virtual screening of chemical libraries of billions of compounds. Using DD, we identified SARS-CoV-2 Mpro inhibitors that showed antiviral activity, paving the path towards accelerated discovery of drug candidates for COVID-19 and future pandemics. With the rapid expansion of chemical libraries beyond 10 billion of molecules, we envision that DD will play a pivotal role in the future of drug discovery.

References

1 Gentile, F. et al. ACS Cent. Sci. acscentsci.0c00229, 2020.
2 Jin, Z. et al. Nature 582, 289–293, 2020.
3 Sterling, T. et al. J. Chem. Inf. Model. 55, 2324–2337, 2015.
4 Hawkins, P. C. D. et al. J. Chem. Inf. Model. 50, 572–584, 2010.
5 Friesner, R. A. et al. J. Med. Chem. 47, 1739–49, 2004.

Acknowledgements

We thank Jean lab from the University of British Columbia for experimental evaluation of compounds. This work was funded by the CIHR Canadian 2019 Novel Coronavirus (2019-nCoV) Rapid Research Grant # DC0190GP. FG would like to thank Ermenegildo Zegna Founder's scholarship program, CIHR and Michael Smith Foundation for Health Research for funding support.

INTEGRATIVE MODELLING OF CHONDROCYTE MECHANOTRANSDUCTION AND BIOCHEMICAL STIMULATION

Maria Sequerra-Queralt, (1), Gemma Piella (1), Jérôme Noailly (1)

1. BCN MedTech (Universitat Pompeu Fabra), Spain.

Introduction

Osteoarthritis (OA) is a debilitating joint disease, characterised by articular cartilage (AC) degradation and local inflammation. Through mechanotransduction (MT) processes, mechanical loads induce changes in the gene expressions of AC chondrocytes (CC). Cascades of complex molecular interactions are triggered, converting physical stimuli into cellular responses that favor chondroprotection or cartilage destruction. Systematic representations of those interactions can positively inform early strategies for OA management. To this end, a novel network model of CC activity is proposed. It incorporates important mechanosensors (MS) and the associated downstream signalling cascades.

Methods

Key mechanoregulatory molecular interactions in OA were represented (Figure 1) based on a corpus of 52 journal articles. Then, an interactome was developed, consisting of a set of 108 nodes, i.e., cellular receptors, second messengers, transcription factors and proteins, related to each other through a specific topology of activating and inhibiting links. These were converted into a semi-quantitative mathematical model through a system of differential equations[1]. System solving with different perturbations and initial conditions leads to steady stable states (SSS) that represent patrons of cell expression through systematic descriptions of CC MT molecular mechanisms. To simulate a healthy state of a CC, the network was first stimulated with physio-osmotic according to Phan *et al.*[2] We further assessed whether it could predict expected SSS under inflammation and undue loads such as static compression (ST) or fluid shear stress (FS) when integrin $\alpha_5\beta_1$, PTCH1/2, Wnt or CD40 become activated.

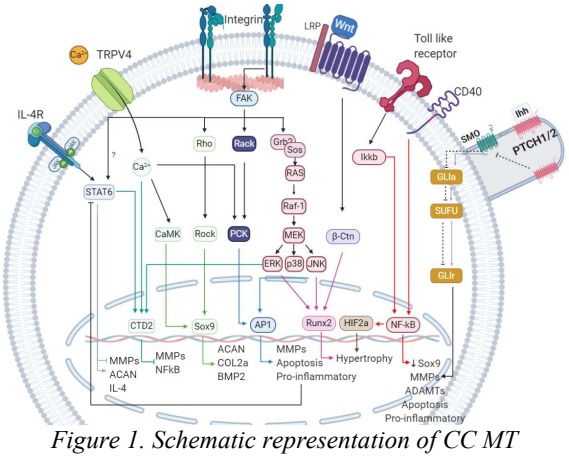

Figure 1. Schematic representation of CC MT

Results and Discussion

Under physio-osmotic conditions, i.e., activation of the TRPV4 and integrin $\alpha_5\beta_2$ MS, the network model evolved towards a basal anabolic SSS (Figure 2, blue). Low levels of MMP expression were achieved, as well as high expression levels of anabolic markers for a healthy CC, such as structural proteins (Collagen and Aggrecan) and growth factors (BMP2 or IGF1). Additional pro-inflammatory perturbations led to a significantly different (t-tests, α=0.05) CC activity, with a catabolic shift of node activations (Figure 2, orange). Pro-inflammatory mediators were fully expressed, as well as degrading enzymes (MMPs and ADAMTs), and markers of hypertrophy (MMP3, BMP2).
Regarding the transcription factors, healthy CC markers, Sox9, FOXO and CITED 2 were activated in the basal SSS, whereas NF-kB, Runx2 or AP1, characteristic of a osteoarthritic CC, were activated by the simulated inflammation. When undue MS were activated in ST or FS the SSS also revealed a catabolic shift (Figure 2, yellow), revealing the potential to reflect load-induced chondroprotection or cartilage destruction.

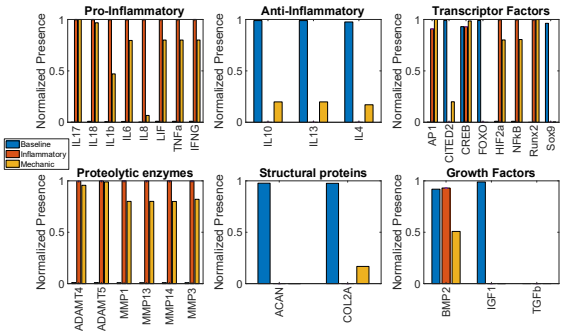

Figure 2. SSS for: the baseline under physio-osmotic conditions (in blue); the pro-inflammatory stimuli (orange); the ST or FS mechanical loads (yellow).

A regulatory network that maps intracellular signaling pathways of a chondrocyte from AC was successfully developed. The model could predict expected MT and inflammation effects on a CC, revealing the potential of exploitation in OA.

References

1. Mendoza et al, Theor Biol Med Model, 3:1-13, 2006.
2. Phan et al, Arthrit & Rheuma, 60:3028-3037, 2009.

Acknowledgements

Spanish (HOLOA-DPI2016-80283-C2-1/2-R, RYC-2015-18888) and Catalan (FI grant) Governments; European Commission (Disc4All-H2020-MSCA-ITN-ETN-2020-955735).

ENTROPY MAXIMISATION DRIVES CELL STRESS FIBRE ALIGNMENT

Ryan J Coleman, Patrick McGarry,
National University of Ireland Galway

Introduction

Extensive experimental evidence characterising cell cytoskeletal morphology suggests that stress fibres (SFs) are highly aligned and elongated. Such alignment appears to be independent of the cell spread shape, with isotropically or irregularly spread cells exhibiting preferential SF alignment (e.g. Fig. 1d [1]). Recent computational models of cell spreading implement a deterministic framework for prediction of SF distributions [2,3]. However, such deterministic frameworks are not capable of predicting the nematic ordering of highly aligned SFs within the cell. Nematic ordering of populations of high aspect ratio cells, spread on narrow adhesive strips, has recently been investigated [4]. However, subcellular nematic ordering of the actin cytoskeleton has not previously been investigated. Here, we propose a thermodynamically based framework for cytoskeletal distributions. We use nested sampling to determine minimum free energy conditions, and demonstrate that nematic ordering of SFs is driven by entropy maximisation.

Methods

The volumetric Gibbs free energy of any cytoskeletal distribution is found as:

$$\hat{G}_{Tot} = \hat{G}_{FA} + \hat{G}_{Col} + \hat{G}_{P} - T\hat{S}_{Nem}, \qquad (1)$$

where $\hat{G}_{FA}$ represents free energy associated with forming focal adhesions on the cell surface, $\hat{G}_{Col}$ represents free energy associated with cell surface collagen recruitment, $\hat{G}_{P}$ acts as a penalising term, and $\hat{S}_{Nem}$ is entropy associated with nematic ordering of sarcomeres within SFs. Free energy associated with the formation of focal adhesions is calculated as,

$$\hat{G}_{\mathrm{FA}} = \frac{C_L}{b}\left(\frac{\mu_L}{k_B T} + \ln\left(\frac{\theta_L}{1-\theta_L}\right)\right)\left(1 + \frac{1}{A_C}\sum A_{\eta i}\right). \qquad (2)$$

Where C_L is concentration of recruited low affinity surface integrins, b is cell thickness, μ_L is enthalpy of low affinity integrins, A_C is cell spread area, $A_{\eta i}$ is contact area of SF "i" with the cell surface, and θ_L is a ratio of recruited low affinity integrins to binding locations, whose computation is influenced by *McEvoy et al.* [2] focal adhesion constitutive models,

$$\left(\frac{1-\theta_L}{\theta_L}\right)^{\mathrm{C_L}/C_H}\left(\frac{\theta_H}{1-\theta_H}\right) = \exp\left(-\frac{\mu_{\mathrm{H}} - \frac{\mathrm{C_L}}{\mathrm{C_H}}\mu_{\mathrm{L}} + \Phi - \mathrm{F}\Delta}{k_B T}\right). \qquad (3)$$

Here C_H is concentration of high affinity integrins, found through a mass balance equation, θ_H is a ratio of recruited high affinity integrins to binding locations, μ_{H} is enthalpy of high affinity integrins, Φ is strain energy, and $\mathrm{F}\Delta$ is work energy, associated with ligand stretch.

Free energy associated with collagen recruitment is computed as; $\hat{G}_{Col} = \frac{1}{A_C b}\frac{1}{k_B T}\frac{\sigma^2}{2\kappa_{Col} C_{Col}}\sum A_{\eta i}$, where σ represents the active contractile stress of a SF, κ_{Col} is elastic collagen stiffness, and C_{Col} is the concentration of collagen fibrils. The nematic entropic contribution of sarcomere distributions are then calculated:

$$\hat{S}_{Nem} = \frac{1}{A_C b}\frac{1}{T}\sum \ln\left(\Gamma(n_i\eta_i + 1)\right). \qquad (4)$$

Where n_i refers to the number of sarcomeres recruited in series, and η_i refers to the number of sarcomeres recruited in parallel, within a SF. We implemented this model within a predefined cellular geometry, within which SFs generate. SF morphology is characterised using probability distributions which enforce preferable SF length, sarcomere concentration in parallel, and orientational alignment. Our random sampling schema predict minimum free energy/ maximum likelihood conditions for a range of cytoskeletal distributions.

Results

Results shown in Fig. 1 display the maximum likelihood SF alignment state, as computed through random sampling. In a circular cell spread, nematic entropy increases as SF length and alignment increases.

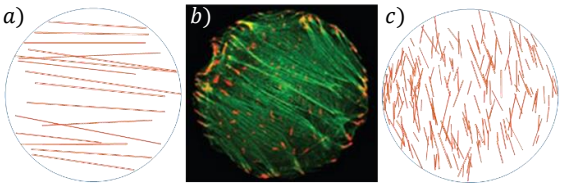

Figure 1: The relationship between SF alignment and energy for a spread cell, (a) maximum likelihood cytoskeletal fibre distribution, (b) Actin cytoskeleton self-organisation into linear arrays (Tee et al [1]), (c) minimum likelihood cytoskeletal fibre distribution.

Conclusions

Our developed framework suggests that high alignment of SFs, as observed experimentally [1], is driven by entropy maximisation, resulting in nematic cytoskeleton ordering. Results suggest that this phenomena is relatively independent of cell spreading, as observed experimentally [4]. Further advances plan for this model to be implemented within a nested sampling schema, to iteratively determine cytoskeletal distributions of increasing likelihoods. The results of this study have significant implications for control of cell spreading and contractility when seeded on tissue engineered substrates/ ECMs.

References & Acknowledgements

1. Y. Tee et al, Nat. Cell Biol, 445-457, 17(4), 2015.
2. E. McEvoy et al, J Mech Behav Biomed Mater, 283-295, 74, 2017.
3. E. McEvoy et al, Biophys. J, 2451-2460, 115(12), 2018.
4. A. Buskermolen et al, Biophys. J, 1994-2008, 116(10), 2019.

The author acknowledge Science Foundation Ireland (grant 18/ERCD/5481) for funding this work.

CARDIAC HYBRID CELLULAR AUTOMATA SIMULATION FOR 2D CARDIAC DYNAMICS

Lilly Maria Treml (1), Alessio Gizzi (2), Ezio Bartocci (1)

1. Vienna University of Technology, Austria; 2. University of Rome Campus Bio-Medico, Italy

Introduction

In a recent contribution [1], we introduced a one-dimensional hybrid cellular automata (HCA) approach considering a free resistance variable to model and simulate cell-cell coupling in 1D cardiac strands. We conducted an extended computational analysis via GPU-accelerated Monte Carlo Simulation highlighting bifurcation phenomena according to conductance statistical features. We extend such an HCA approach to 2D domains to investigate the complex cardiac properties in realistic spatiotemporal scenarios in the present contribution. In particular, parameters heterogeneity is studied according to the recent literature on the subject [2-6].

Methods

We start from the 1D structures presented in [1], introducing a second spatial dimension. Specifically, additional neighbors are introduced to create a virtual 2D uni-directional monolayer of cardiac cells. Figure 1 shows a simplified representative example of the desired structures. Generalizing the 1D coupling shown in Equation 1, we consider Equation 2 in a simplified Von Neumann neighborhood:

$$(u_{i-1} - u_i) * R_v \quad (1)$$

$$(u^i_{j-1} + u^{i-1}_j - 2u^i_j) * R_v \quad (2)$$

Here, j refers to the row index, i to the column index, and R_v is the free resistance variable. The one-directionality of the model allows us to simplify the overall connection such that only the cells in rows >1 comprise an additional neighbor.

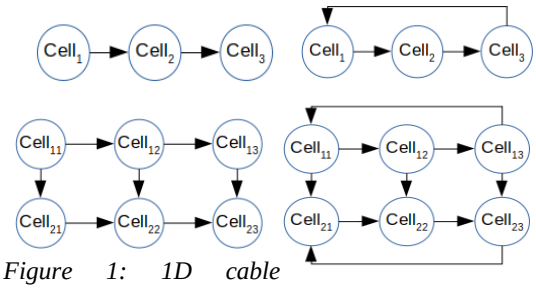

Figure 1: 1D cable structure (top left); 1D ring structure (top right); 2D plane structure (bottom left); 2D circular structure (bottom right).

We test our assumed HCA connectivity by means of standard C codes. Specifically, conduction velocity (CV) validation is provided in terms of planar waves and target patterns over a wide range of numerical and constitutive parameters. We selected resistance values of 0.5, 1.7, and 2.0 in multiple grids of size 5x750, 5x1000, 10x1000, 10x2000 & 20x 2000 cells.

Results

Our analysis shows that the excitation wave propagates successfully in all scenarios for grids < 10x2000 cells. In low resistance cases (Rv = 0.5), no CV could be recovered in bigger grids. The CV computation also failed for the plane structure in the 20x2000 grid with a resistance value of 1.7. The circular design proved self-sustainability as we could compute a CV for the bigger grids with the higher resistance values. Besides, we did not observe any significant deviation between circular and planar structures while observing comparable results with the 1D structure behavior.

Discussion

The estimation of cardiac conductivity in an extended spatiotemporal framework is a well-known open issue in the literature [6,7]. By adopting an HCA approach with a free resistance variable to describe cell-cell coupling, we can get fine control of the underlying spatiotemporal dynamics. In such a scenario, we foresee using advanced strategies of fast simulation and analyses, e.g., machine learning approaches or optimization algorithms that map the free resistance variable to a specific conduction velocity. We plan to improve our numerical model by using GPU-based implementation, thus combining our current approach with hardware accelerators, such as FPGAs that are becoming more and more employed to handle extensive computational problems.

References

1. Treml et al., Mathematics, **9**:164, 2021.
2. Fenton et al., Phys Rev E, **87**:4, 2013.
3. Burger, Inv Probl, **27**:8, 2011.
4. Clerx et al., Biophys J, **117**:2420-2437, 2019.
5. Weinberg, Chaos, **27**:9, 2017.
6. Barone et al., Chaos, **27**:9, 2017.
7. Barone et al., J Comput Phys, 423, 2020.

Acknowledgements

The Authors acknowledge the support of the Italian National Group of Mathematical Physics (GNFM-INdAM).

OSTEOGENESIS IMPERFECTA: BRITTLE BONES FROM STRONGER COLLAGEN FIBRILS

Mathis Nalbach (1), Naoki Motoi (2), Franziska Gantner (1), Orestis G. Andriotis (1), Lauren Battle (3), Anxhela Docaj (3), Aleksandr Ovsianikov (1), Georg Schitter (1), Alessandra Carriero (3), Philipp J. Thurner (1)

1. TU Wien, Austria 2. Kobe University, Japan 3. The City College of New York, USA

Introduction

Osteogenesis imperfecta is a group of genetic disorders that ultimately leads to weak bones and therefore is known as the brittle bone disease. Although familiar as such, it mainly originates by mutations at the molecular level of collagens. Hence, the entire range of a body's collagenous tissues is affected. Here, we mechanically assess single collagen fibrils (CF) of an osteogenesis imperfecta mouse model (*oim/oim*) by performing tensile tests with a novel nano-tensile testing instrument and nanoindentation with an atomic force microscope (AFM). CFs of the studied mouse model are assembled by homotrimeric collagen molecules, caused by substitution of the α2(I) chain by a third α1(I) chain.

Methods

CF were extracted from a tail tendon of each a wild-type B6C3Fe-a/aCol1a2$^{+/+}$ (WT) and a homozygous B6C3Fe-a/aCol1a2$^{oim/oim}$ mouse (severe OI model), both 14 weeks old. After drying, CF were prepared for tensile testing by attaching a magnetic bead with epoxy resin. Each prepared CF was then imaged in contact mode at ambient conditions with the AFM to measure dry diameter and assess the existence of d-banding. Subsequently, CFs were hydrated with phosphate buffered saline solution (PBS) and AFM nanoindentation was performed. By that, indentation modulus, hydrated diameter and swelling are measured. Finally, tensile tests are conducted by lifting one end of the CF by applying a magnetic field. This end is picked up with a two-photon-polymerization printed microgripper that is attached onto a fiber-optic cantilever based force probe (Optics11, Netherlands). CFs are then pulled to fracture using a levered z-piezo stage (Physik Instrumente, Germany) at 5 %/s strain rate.

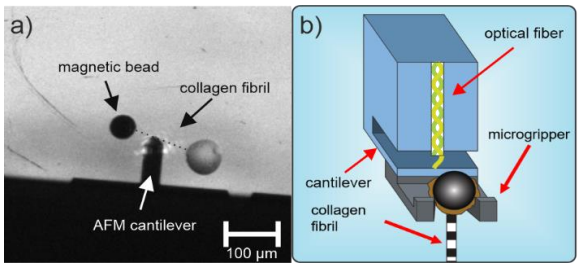

Figure 1: a) AFM measurements on single CF that are prepared for tensile testing. b) Sketch of the force probe equipped with microgripper.

Results

Qualitatively, *oim/oim* CFs exhibit a second phase of stiffening during tensile tests (see figure 2). This leads to about 8-fold higher tensile strength in *oim/oim* CFs. Additionally, the peak tensile modulus within the initial 10% strain regime is higher in the *oim/oim* compared to WT CFs (2.6±0.7 GPa vs. 0.9±0.5 GPa). Concurrently, *oim/oim* CFs swell less when being hydrated in PBS (1.9±0.1 vs 2.1±0.2).

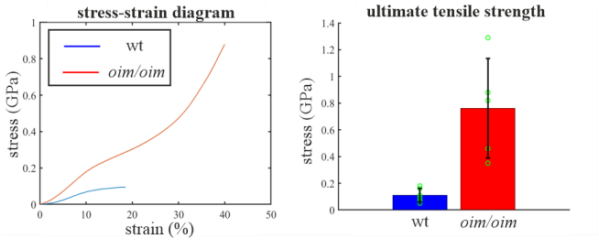

Figure 2: Exemplary stress-strain diagram of a WT and an oim/oim CF and resulting tensile strength at failure of all tested CFs.

Discussion

The overall observation of stronger CFs in *oim/oim* comes as a surprise as fascicles of such mice seem to have lower ultimate strength [1]. Furthermore, molecular dynamics simulations (MD) suggest lower stiffness and less dense packing of *oim/oim* CFs [2]. However, MD does not consider increased levels of advanced glycation end product cross-links in *oim/oim* [3], which can explain the results reported here. Previously reported *in vitro* cross-linking of CFs resulted in similar mechanical properties [4]. Furthermore, lower swelling potentially impacts stiffness in the initial strain regime by higher molecular interaction [5].

Just recently, force controlled tensile loading and therefore direct viscoelasticity testing was implemented in the novel tensile testing instrument. This is achieved by an error-corrected two-degree-of-freedom controller. As of writing, experimental results of this method are being analyzed.

References

1. Misof et al, J Clin Invest., 100(1):40-45, 1997.
2. Chang et al, Biophys J., 102(3):640-8, 2012.
3. Carriero et al, JBMR, 29(6):1392-1401, 2014.
4. Svensson et al, Acta Biomater., 70:270-280, 2018.
5. Andriotis et al, ACS Nano, 12(4):3671-3680, 2018.

GLYCATION INCREASES INDENTATION STIFFNESS AND DECREASES SURFACE CHARGE OF INDIVIDUAL COLLAGEN FIBRILS

Manuel Rufin (1), Mathis Nalbach (1), Orestis G. Andriotis (1), Mathias Poik (2), Georg Schitter (2), Philipp J. Thurner (1)

1. Institute of Lightweight Design and Structural Biomechanics, TU Wien, Vienna, Austria
2. Automation and Control Institute, TU Wien, Vienna, Austria

Introduction

Collagen fibrils (CFs) provide mechanical competence to many biological tissues. The mechanical properties of CFs are in part specified by inter-molecular covalent cross-links; besides biologically steered cross-linking further cross-links result from reaction of collagen with sugars, forming Advanced Glycation Endproducts (AGEs). Such AGEs play a role pathologies e.g. diabetes and ageing [1]. In the presented study, we model AGEs formation through incubation of CFs with methylglyoxal (MGO). We performed *in-situ* atomic force microscopy (AFM) experiments to evaluate nanostiffness and amplitude-modulated kelvin force microscopy (AM-KFM) [2] to assess the presence of MGO mediated cross-links, by measuring surface potentials before and after MGO treatment.

Methods

CFs (source: tail tendons of 6-month old mouse) were placed on microscope slides [3]. Samples were equilibrated for 2 hours in 34°C phosphate buffered saline solution (PBS). After drying in a desiccator (24 hours), AFM and AM-KFM was performed on individual CFs. AM-KFM was performed in ambient conditions at a lift height of 0 nm (Dimension FastScan AFM; Bruker) using the same AFM cantilever for all measurements (OMCL-AC200TN, 9 N/m, 150 kHz). AFM force-indentation tests on a NanoWizard Ultra Speed A (Bruker-JPK) were conducted at the same region of the previously tested CFs, but in aqueous solution (Force Volume Maps @ 1 nN applied force). The indentation modulus was determined via the Oliver-Pharr method [3]. Finally, samples were submerged into a glycation buffer (0.01M PBS, 5mM EDTA and 20 mM MGO adjusted to 7.4pH) for 4 hours at 34°C. After extensive washing, the previously described protocol was repeated in reversed order on the same collagen fibrils.

Results

4h treatment with MGO across all treated CFs led to an increase in indentation modulus +0.44(0.36) MPa at almost constant CF height when tested in PBS, while dry CF diameter increased by 30(9) %. Coincidentally, CF surface potential decreased by 21(9) mV. The control group experienced either insignificant or opposite changes in these properties (See Fig. 1).

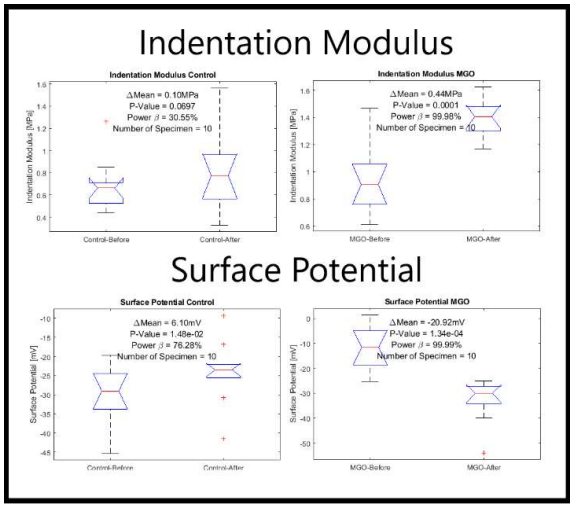

Figure 1: shows the statistical analysis of CF changes in indentation modulus (top) and surface potential (bottom) before and after glycation for both the control (left) and the MGO (right) group (N=10, each).

Discussion

The combination of methods allowed to directly link changes in nanomechanics and cross-linking due to glycation at the individual CF level. Reduction of surface potential of CFs due to crosslinking is in line with literature [2], though we used a different but also physiologic cross-linker in this study. Additionally, the presented results show stiffening of CFs related to cross-linking via a direct before-after indentation test on the same CFs. To further evaluate cross-linking, standard analytical chemistry and tensile tests will be employed and compared to the presented results. Importantly, the application of KFM allows chemo-physical characterization at the same length scale, i.e. at the scale of individual collagen fibrils, which is not possible through standard analytical chemistry tools.

References

1. Snedeker JG, Gautieri A et al, Muscles Ligaments Tendons J. 4(3):303-8. 2014
2. Bansode S et al, Sci Rep. 10: 3397. 2020
3. Andriotis OG et al, JMBBM. 39: 9-26. 2014

THE EFFECT OF TYPE 1 DIABETES ON CONTRACTILE FUNCTION OF CARDIOMYOCYTES IN THE DIFFERENT HEART REGIONS

Galina Kopylova (1), Anastasia Kochurova (1), Valentina Berg (1), Xenia Butova (1), Tatiana Myachina (1,2), Anastasia Khohlova (1,2), Daniil Shchepkin (1)

1. Institute of Immunology and Physiology, Russia; 2. Ural Federal University, Russia

Introduction

Type 1 diabetes mellitus (T1D) is a leading cause of cardiovascular diseases. Cardiomyocyte contractile function and excitation-contraction coupling in different heart regions are poorly understood. We studied the effect of T1D on the contractile function of the left and right ventricular free walls (LV, RV), and interventricular septum (IS) using single cardiomyocytes and isolated sarcomere proteins.

Methods

The experiments were performed according to Directive 2010/63/EU. We used the alloxan-induced T1D in male Wistar rats (12 weeks of age) [1]. Single myocytes from the LV, RV, and IS were isolated by the modified Langendorff method [2]. Cytosolic Ca^{2+} transient and sarcomere shortening during mechanically unloaded contractions were studied at 36-37°C.

The actin-myosin interaction was studied in an *in vitro* motility assay using myosin and native thin filaments (NTF) extracted from the LV, RV, and IS [2]. The Ca^{2+} dependence of the NTF sliding velocity over myosin was fitted by the Hill equation. Protein phosphorylation was analyzed using a 12% SDS-PAGE with Pro-Q Diamond phosphoprotein and SYPRO Ruby staining (Thermo Fisher Scientific, USA).

Results

In the healthy rats, the end-diastolic sarcomere length (EDSL) was similar between the regions. T1D decreased EDSL (Table 1). In control rats, the amplitudes of cytosolic Ca^{2+} transient and sarcomere shortening were not different between the LV, RV, and IS. In T1D, the Ca^{2+} transient amplitude decreased but the shortening amplitude increased significantly in the RV.

The characteristic	LV	IS	RV
EDSL	↓	↓	↓
Ca^{2+} amplitude			↓
shortening amplitude			↑
time to peak of Ca^{2+} transient		↑	↑
time to 50% decay of Ca^{2+} transient		↓	
time to peak of sarcomere shortening			↑
time to 50% relaxation		↓	

Table 1: The T1D effect on the contractile characteristics of single cardiomyocytes.

In the control rats, the time to peak of sarcomere shortening was significantly greater in LV myocytes compared to RV cells. T1D prolonged significantly the time to peak of the Ca^{2+} transient in the IS and RV, and the time to peak of sarcomere shortening in the RV. T1D decreased the time to 50% decay of Ca^{2+} transient and the time to 50% relaxation in the IS only.

T1D decreased the maximal sliding velocity of NTF over myosin by 25-30% and the Ca^{2+} sensitivity of the *p*Ca-velocity relation by 0.2-0.3 *p*Ca (Figure 1). T1D greater affected the actin-myosin interaction in the LV compared with other regions.

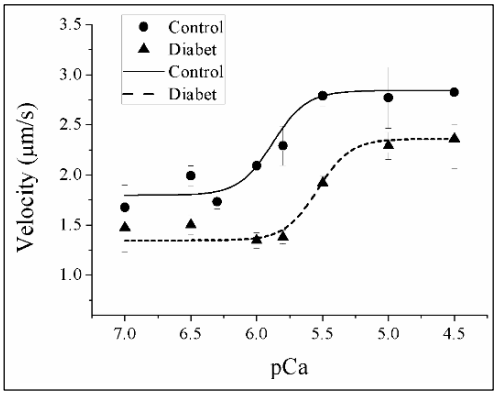

Figure 1: The T1D effect on the pCa-velocity relationship for the LV obtained in the in vitro motility assay.

T1D affected phosphorylation of sarcomere proteins from the heart regions differently. Phosphorylation of the regulatory light chain of myosin decreased in the LV but increased in the RV. Phosphorylation of tropomyosin increased in all heart regions studied. Phosphorylation of troponin T decreased in the RV and IS. Phosphorylation of troponin I decreased, and cardiac myosin binding protein C increased in the LV.

Discussion

T1D affects the amplitude and kinetic characteristics of cardiomyocyte contraction from the heart regions in different ways. Together with a change in the phosphorylation level of sarcomere proteins, this can contribute to the changes in the whole heart function.

References

1. Danilova et al, Anat Rec (Hoboken)., 298(2):396-407, 2015.
2. Khokhlova et al, Biochem Biophys Res Commun., 56(1):250-259, 2017.

Acknowledgements

This work was supported by the RSF grant 18-74-10059.

MOLECULAR DYNAMICS AND BINDING MECHANISMS OF VOLATILE ANESTHETICS TARGETING HUMAN TUBULIN

Eric A. Zizzi (1), Marco Cavaglià (1), Marco A. Deriu (1), Jack A. Tuszynski (1)

1. PolitoBIOMedLab, Department of Mechanical and Aerospace Engineering, Politecnico di Torino, Italy

Introduction

Anesthesia, despite being the cornerstone of modern surgery, is to this date a biological puzzle. While scientific efforts still have not managed to frame its pharmacology in an exhaustive theoretical framework, microtubules inside neurons are thought to be essential for memory formation and consciousness [1]. The potential ability of volatile anesthetics to alter or dampen the vibrational properties of microtubules justifies the spatiotemporal characterization of the interaction between such molecules and the tubulin dimer through the use of computational molecular modelling.

Methods

Human tubulin isotypes βVI, βIIa and βIVa were modeled as αI-β dimers through homology modelling from the PDB 3J6F [2] template, and simulated in GROMACS 2019.1 for 100ns using the AMBER ff99SB-ILDN force field [3], with explicit water and ions at 0.1M, at 300 K and 1 bar, in three replicas. Simulations were performed both without and with Ethylene (ET), Desflurane (DF), Halothane (HT) or Methoxyflurane (MF) in the solvent at 10 mM [4]. Secondary Structure analysis on MD simulations was performed using DSSP, while interaction hotspots were determined as a per-residue contact probability over each frame, which is reported for each sector of the tubulin surface in a spherical coordinate system. Main binding clefts were obtained from the heatmaps and the interaction of the anesthetics therein has been further analyzed using the MM/PBSA method.

Results

The analysis of MD trajectories predicts distinct patterns of interaction of each anesthetic, with a significant fraction of interaction sites located both on the luminal surface ($\varphi<0$), and on the α subunit ($\theta<0$) of the microtubule for all anesthetics except ET, as visible in Fig. 1 for isotype βIVa, the most expressed isotype in the brain [5].

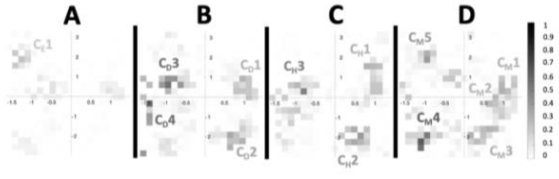

Figure 1: Anesthetic contact heatmaps, i.e. (θ,φ) probability plots, for each anesthetic (A: ET, B:DF.,C:HT,D:MF) on isotype βIVa. Main binding clefts are highlighted. Colorbar is 0 to 1 probability.

No significant interactions occurred with ET, which is the weakest among the four compounds in terms of clinical potency. This analysis highlights the mechanical compatibility of the contact between the three anesthetics DF, HT and MT, and tubulin in specific areas of the surface, hence suggesting the existence of preferential transient binding pockets on the tubulin dimer. These clefts are highlighted in Fig. 1, and a binding energy estimate for each ligand in each of those clefts is provided in Fig. 2.

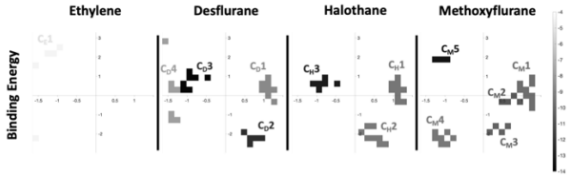

Figure 2: Per-area MM/PBSA binding energy estimate for isotype βIVa. Left to right: ET; DF; HT; MF. Color scale is -4 kcal/mol to -14 kcal/mol.

Binding energy estimates of DF, HT and MT were comparable, between -7 and -14 kcal/mol, while ET confirmed much weaker interactions, below 4 kcal/mol. No significant secondary structure alterations were determined in the presence of anesthetics in the binding clefts, as expected by the transient nature of binding events.

Discussion

The results suggest the lack of a unique and stable binding site for volatile anesthetics on tubulin, but highlight the existence of specific hotspots where anesthetics interact for a relevant fraction of time. These are areas where the contact is mechanically most favorable. The binding events do not follow a *lock-and-key* paradigm, but rather occur frequently inside different, mechanically favorable clefts. This might have consequences on the assembly of protofilaments, on locally induced instantaneous dipoles and on higher-scale vibrational characteristics whose involvement in conscious brain activity and information transmission is currently debated and requires further studies.

References

1. Pan, J. Z. et al., Proteomics, 8:2983–2992, 2008.
2. Alushin, G. M. et al., Cell, 157:1117–1129, 2014.
3. Lindorff-Larsen, K. et al., Proteins Struct. Funct. Bioinforma., 78:1950–1958, 2010.
4. Chau, P. L., Br. J. Pharmacol., 161:288–307, 2010.
5. Huzil, J. T. et al., Nanotechnology, 17:S90-S100, 2006

ULTRASOUND DRIVEN AMYLOID FIBRIL UNFOLDING INVESTIGATED BY MOLECULAR MODELLING

Marcello Miceli (1), Stefano Muscat (2), Morbiducci Umberto(1), Marco Cavaglià (1), Marco A. Deriu (1)

1. PolitoBIOMedLab, Department of Mechanical and Aerospace Engineering, Politecnico di Torino, Italy;
2. Dalle Molle Institute for Artificial Intelligence (IDSIA), Switzerland

Introduction

Alzheimer's disease (AD) is the most common type of dementia. This pathology is characterized by an abnormal aggregation of misfolded proteins into plaques, causing proximal neurons death. Many pharmacological strategies have been proposed to target amyloid aggregation, but regrettably many of them have shown to be ineffective. Ultrasound based technique has shown to be a valid nonpharmacological strategy to reduce plaque size [1]. In this connection, it has been observed that stable cavitation phenomena related to ultrasound can affect protein secondary structures. Modelling techniques and in particular Molecular Dynamics (MD) can provide an adequate tool to observe biological phenomena with fine space (nanometers) and time (nanoseconds) resolution. The aim of this work is to shed light on molecular mechanisms driving the amyloid fibril unfolding during cavitation [2].

Method

Stable cavitation phenomenon was simulated by an ad-hoc computational code, developed in this work starting from information in previous literature [3]. Models of cavitation bubbles consist in dummy beads that varies harmonically their radii, and interact with surrounding waters molecules trough a modified time-dependent Lennard-Jones potential. The stable cavitation was simulated in a molecular systems consisting of a pentameric S-shaped 1-42 Amyloid fibril (PDB:5OQV), in a box filled by explicitly modelled water (TIP3P). 3% of water molecules were replaced by bubble dummy atoms. Different replicas of non-quilibrium MD (NEMD) of bubble stable cavitation were performed in NVT (costant number of particles, temperature and volume) ensemble at 300 K. NEMD simulations were carried out until a complete fibril disaggregation was observed. Moreover, equilibrium MD (EMD) simulations, in NVT ensemble at 300K, with bubbles at fixed radius, has been carried out in order to compare results in absence of cavitation induced phenomena.

Results

Results confirmed that ultrasound stable cavitation affects amyloid fibril stability. Indeed, while root mean squared deviation (RMSD) evaluated on the initial configuration reaches a *plateau* for the EMD simulation, for the NEMD simulation this value constantly increases (Figure 1A). Moreover, time history of contact probability on close chains residues has been studied, (Figure 1B), in order to consider residues involved in non convalent interactions. Fibril compactness is not perturbed during EMD simulation, leading to contact probability values close to 1 for all amyloid residues. On the other hand, in NEMD simulation stable cavitation phenomena results in a chain-chain contact variation, reducing the number of contacts between residues of adjacent chains. Moreover, it is possible to observe that loss of contact starts from residues involved in unstructured regions and propagates to inner residues belonging to ordered secondary structure.

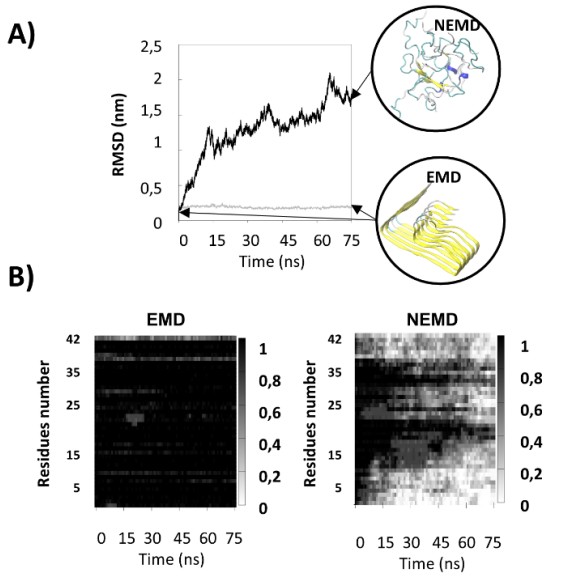

Figure 1: A) Root mean squared deviation for NEMD (black) and EMD (light gray). B) Time history of contact probability

Discussion

Mechanical stimulation in the form of cycles of compression and decompression, obtained by stable cavitation, can drive amyloid fibril to destabilization and disruption. This work clearly depicts how stable cavitation acts at the molecular level. Residues belonging to unstructured regions act as seed of instability, promoting the unfolding process of close structured regions and the entire amyloid disaggregation.

References

1. Nisbet RM et al, eds. *J. Alzheimer's Dis.* 2018; **64**: S517-S527.
2. Miceli M et al,. *J. Mol. Graph. Model.* 2019; **96**: 107518.
3. Hoang Viet M et al,. *J. Chem. Phys.* 2016; **145**: 174113.

THE EFFECT OF TYPE 1 DIABETES ON FORCE-LENGTH RELATIONS IN SINGLE LEFT AND RIGHT VENTRICULAR CARDIOMYOCYTES

Denis Volzhaninov (1), Tatiana Myachina (1,2), Xenia Butova (1), Anastasia Khokhlova (1,2)

1. Institute of Immunology and Physiology, Russian Academy of Sciences, Yekaterinburg, Russia;
2. Ural Federal University, Yekaterinburg, Russia

Introduction

Type 1 diabetes mellitus (DM1) is a risk factor for heart failure. To date, few studies have been devoted to changes in the mechanical function of the heart at the cell level in DM1. Moreover, no analysis of the contractile performance of mechanically loaded single cardiomyocytes has been carried out. The aim of the present work is to explore the effects of DM1 on force-length relations in single cardiomyocytes isolated from the left and right ventricular free walls (LV and RV) and interventricular septum (S).

Methods

Myocyte Preparation. All experiments were conducted in accordance with EU Directive 2010/63 on the protection of animals used for scientific purposes. DM1 was induced in 12-13-week-old Wistar rats using the alloxan diabetic model [1] and then was confirmed after 6 weeks by hyperglycemia and a high glycosylated hemoglobin level. Single cardiomyocytes from the LV, RV, and S were isolated using the Langendorff-perfusion technique in combination with the method of intraventricular injections [2, 3].

Carbon Fiber Technique. In order to apply mechanical preload (diastolic stretch) to a single cardiomyocyte, we used a carbon fiber (CF) technique where four CFs were attached to the cell membrane by electrostatic forces [4]. We used the uMp micromanipulation system (Sensapex, Finland) and self-written control software in the system-design platform LabVIEW 2015 (NI, USA) for CF positioning. The stretch step value was 2 μm, and the time of stretch was 300 ms.

Cell Length and Force Measurements. CF bending during auxotonic contraction was optically recorded using the IonOptix system (IonOptix, USA). Cell force was calculated on the CF bending and CF stiffness. Cell tension was defined as cell force normalized to the cell cross-sectional area.

Force-Length Relation Analysis. The amplitudes of normalized passive (end-diastolic) and active (total minus passive) forces were fitted by linear regression for changes in the cell length. The slopes of the end-diastolic force-length relation (EDFLR) and active force-length relation (F_{active}LR) curves were used as the indexes of cell stiffness and contractility, respectively.

Statistics. All values are presented as mean ± SEM. The two-way ANOVA was used for statistical analyses, and $p < 0.05$ was considered to indicate a significant difference between means.

Results

In healthy rats, no differences in tension amplitudes at slack sarcomere length (SL_0) were found between the regions. LV, RV, and S cells also showed similar slopes of EDFLR and F_{active}LR. DM1 decreased cell tension amplitudes at SL_0 in the LV and RV, but not in the S (Fig. 1).

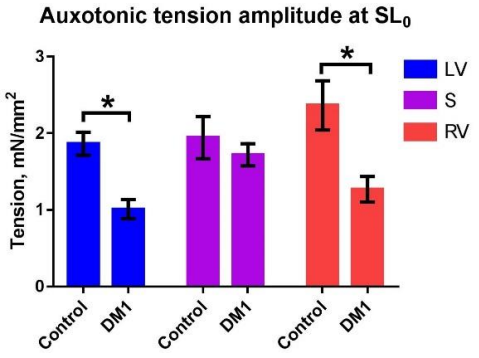

*Figure 1: The effect of DM1 on tension amplitudes of ventricular myocytes at slack sarcomere length (SL_0). * DM1 vs. Control, $p<0.05$.*

In LV and RV cells, DM1 significantly decreased the slope of EDFLR (LV: 0.16 ± 0.05 (DM1, n = 5) vs. 0.45 ± 0.09 (Control, n = 6); RV: 0.22 ± 0.03 (DM1, n = 7) vs. 0.50 ± 0.08 (Control, n = 12) and the slope of F_{active}LR (LV: 0.14 ± 0.07 (DM1) vs. 0.41 ± 0.11 (Control); RV: 0.15 ± 0.04 (DM1) vs. 0.52 ± 0.07 (Control)). However, in S cells, no significant differences were found neither in the slope of EDFLR or F_{active}LR between the DM1 and control groups.

Discussion

Using mechanically loaded cardiomyocytes, we showed that DM1 leads to the changes in force-length relations depending on the myocardial region. We suggest that these intraventricular differences in length dependent force activation may serve as a compensatory mechanism to maintain the cardiac output.

References

1. Danilova et al, Anat. Rec, 298,2:396-407, 2015.
2. Butova et al, MethodsX, 8:101189, 2021.
3. Myachina et al, AIP Conf Proc, 2174:020140, 2019.
4. Iribe et al, J Prog Biophys Mol Bio, 115:103-114, 2014

Acknowledgements

This work was supported by RSF #18-74-10059.

MECHANICALLY CONTROLLED ANTIGEN SENSING BY T-CELL RECEPTORS

Wonmuk Hwang

Departments of Biomedical Engineering, Materials Science & Engineering, Physics & Astronomy, Texas A&M Univeresity, College Station, TX, USA; School of Computational Sciences, Korea Institute for Advanced Study, Seoul, Korea

Introduction

T-cell receptors (TCRs) are essential for recognizing antigenic peptide-loaded major histocompatibility complex (pMHC) molecules and eliciting adaptive immune response. A longstanding question regarding TCR-pMHC recognition was that the binding affinities are very weak and similar, in the range of micro-molar or even lower, whereas the discriminating power between cognate versus non-cognate antigens is on the order of 1 in 10^5. Recent experiments revealed that the TCR-pMHC bond lifetime increases upon application of physiological-level load for the cognate antigen (catch bond), while it exponentially decreases with force for non-cognate antigens (slip bond) [1]. We performed molecular dynamics simulations on TCRs with various truncation schemes and under realistic piconewton levels of load, to find the mechanism by which mechanical force enhances ligand discrimination via catch bond formation.

Methods

For simulation, we used CHARMM [3]. We prepared systems including the pMHC-binding domain only, TCR-only, TCR-pMHC complex, and a TCR mutant that is known to allosterically impair the binding with pMHC. For complexes with pMHC, we applied mechanical load where the average forces are in the piconewton range, which is the same level as in experiments. For each system, all-atom molecular dynamics simulation was performed for more than 500ns.

We developed novel contact analysis methods to monitor dynamics of bond breaking and formation events over time. We also developed a bead-on-chain (BOC) representation to trace the domain motion of TCR and applied principal component analysis (PCA), to find the inter-relation between contact dynamics, domain motion, and applied load

Results

We found that the interface between TCR and pMHC is maintained by formation and breakage of bonds that vary in their average and instantaneous occupancies. When pMHC binds, the domain motion of TCR has a destabilizing effect on the interface, which leads to low binding affinity in the absence of force. Application of 10- to 15-pN range force, which is a typical level present during immune surveillance, leads to suppression of the TCR domain motion and stabilization of the interface with pMHC, which is responsible for the catch bond formation. Alteration of domain motion or the equilibrium conformation of TCR such as by mutation, impact the binding geometry between TCR and pMHC, which results in reduced bond life time even though the mutation is far from the binding interface, which is consistent with experiments on allostery.

Discussion

Our results highlight that mechanical force is a critical component in the operation of the TCR, and they also elucidate the physical mechanism by which catch bonds form. Computational methods developed in this study [2] are applicable to the analysis of other multi-domain immune receptors, including pre-T-cell receptors [4] and antibodies [5].

References

1. Brazin, et al, Front. Immunol. 6:441 (2015).
2. Hwang, et al, Proc. Natl. Acad. Sci. USA, 117:21336-21345 (2020).
3. Brooks, et al, J. Comput. Chem., 30:1545-1614 (2009).
4. Li, et al, Science, 31:181--185 (2020).
5. Burton and Hangartner, Annu. Rev. Immunol. 34:635-659 (2016).

Acknowledgements

This work was funded by the U.S. National Institutes of Health grants P01AI143565 and R01AI136301. Simulations were performed by using computers at the Texas A&M High-Performance Research Computing facility and Texas Advanced Computing Center at UT Austin.

SUCROSE-DRIVEN EFFECTS ON STRUCTURE-FUNCTION RELATIONSHIPS IN HUMAN SWEET TASTE RECEPTOR

Lorenzo Pallante (1), Marta Malavolta (1), Gianvito Grasso (2), Marco Agostino Deriu (1)

1. PolitoBIOMed Lab, Department of Mechanical and Aerospace Engineering, Politecnico di Torino, Italy;
2. Dalle Molle Institute for Artificial Intelligence (IDSIA), Switzerland

Introduction

Human sweet taste receptor is a TAS1R2 and TAS1R3 heterodimer belonging to the C family of GPCR. Each monomer comprises different structural domains, including the transmembrane domain (TMD), a cysteine-rich domain (CRD) and a large extracellular N-terminus (VFTM). This receptor responds to many compounds, e.g. natural sugars, that dock into the orthosteric site in the VFTM. Despite its crucial role in sweet taste prediction, the molecular activation mechanism is still unclear. The most accredited hypothesis for class C GPCR is that after ligand binding into the VFTM the receptor undergoes through a series of conformational changes evolving from the resting state, where the VFTM domains are both in the *open* configuration, to the active conformation, where at least one VFTM is in the *closed* conformation [1]. The transition in the VFTM module propagates up to the transmembrane module, that activates the coupled G protein on the intracellular side [2]. Molecular modelling, thanks to a detailed atomistic resolution, provides tools to characterize the physical and mechanical properties of proteins, and their variations arising after ligand binding. In this work, molecular dynamics (MD) simulations on human sweet receptor underline the sucrose-induced effects on the protein conformational properties. The final aim is to shed light on the molecular mechanism of action of sugars affecting the sweet receptor structure-function relationship, that drives taste perception.

Methods

The 3D atomic structure of the human sweet taste receptor was built by homology modelling starting from a similar class C GPCR, namely the metabotropic glutamate receptor 5 (PDB: 6N51). MD simulations of sucrose-protein complexes and ligand-free receptors were carried out using GROMACS 2020 for at least 300 ns to underline the conformational effects induced by the ligand binding. Structural changes of the sweet receptor were evaluated by computing properties strictly linked to the receptor function, such as the hinge angle in the VFTMs, a measure of the closed/open state, and the distances between the TM domains (Figure 1). Dimensionality reduction techniques, such as principal component analysis (PCA), were also employed to pinpoint major structural rearrangements and global correlations linked to protein function.

Results

The presence of sucrose docked into the orthosteric binding site of the VFTM remarkably affects the conformational behaviour of the receptor. More in detail, the presence of the ligand alters the variation of the VFTM hinge angle (ϑ) and thereby the TM distance (d) (Figure 1). Data reduction techniques highlight the strict mechanical connection between the different domains composing the sweet receptor: the link constituted by the CRD allows the transmission of the conformational changes in the VFTM up to the TM domain, thus linking the compound recognition in the extracellular domain to the structural rearrangements of the TMs.

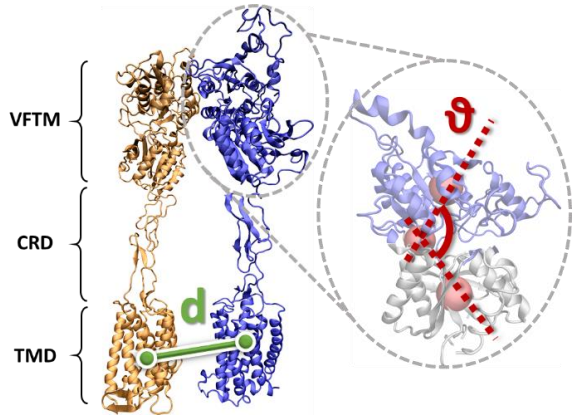

Figure 1: Molecular representation of the human sweet receptor with the reference to the computed VFTM hinge angle (ϑ) and TM distance (d).

Discussion

The detailed atomistic description of the MD simulation sheds light on the molecular mechanism that drives the activation of the human sweet taste receptor. The reported process is in line with the proposed activation mechanisms for other class C GPCRs [3]. These results increase the overall understanding of the complex and multiscale sweet taste perception process and pave the way for further studies aimed at design novel, food-based, enriched compounds to replace natural sugars with non-caloric sweeteners with a great impact on the human health status.

References

[1] K. Masuda et al., *PLoS One*, **7**, e35380, 2012.
[2] S.-K. Kim et al., *Proc. Natl. Acad. Sci.*, **114**, 2568–2573, 2017.
[3] Y. Geng et al., *Elife*, **5**, 1–25, 2016.

Acknowledgements

The research has been developed as part of the VIRTUOUS project, funded by the European Union's Horizon 2020 research and innovation program under the Maria Sklodowska-Curie-RISE Grant Agreement No 872181.

POWER LAW RHEOLOGY TO DESCRIBE CELL MECHANICS

Andreas Weber (1), Barbara Zbiral (1), Jagoba Iturri (1), Rafael Benitez (2), Maria dM Vivanco (3), José Luis Toca-Herrera (1)

1. *Institute for Biophysics, Department of Nanobiotechnology, University of Natural Resources and Life Sciences, Vienna, Austria.*
2. *Departamento de Matemáticas para la Economía y la Empresa, Facultad de Economía, Universidad de Valencia, Spain*
3. *Cancer Heterogeneity Lab, CIC bioGUNE, Bizkaia Science and Technology Park, Derio, Spain*

Introduction

Cells actively control their mechanical properties and respond to the compliance and biochemistry of their surrounding matrices [1]. Due to the complex build-up of cells, different viscoelastic models have been used to describe such properties (2). Interestingly, weak power law rheological models (PLR) can reflect both the frequency- and time-dependent behavior of cells [3-6]. We employed Atomic Force Microscopy (AFM) to study the mechanical properties of HUVECs and breast adenocarcinoma cells and then modelled the F-d and F-t curves using diverse PLR models.

Methods

HUVECs (Human Umbilical Vein Endothelial Cells) and MCF-7 cells were grown on glass substrates and measured using AFM in force spectroscopy mode with cantilevers with pyramidal and spherical tips. To capture the frequency dependent apparent Young's Modulus, cells were indented at different loading rates. In addition, micro-oscillations at various frequencies were performed. Finally, to study time-dependent properties, stress relaxation and creep measurements were done. Indentation curves were fitted using a modified elastic Hertz model, while a PLR models were used to fit the other measurement sets.

Results & Discussion

The apparent Young's Modulus when using both pyramidal tips as well as spherical particles for cell indentation follow weak power laws, as can be seen in Figure 1 and 2.

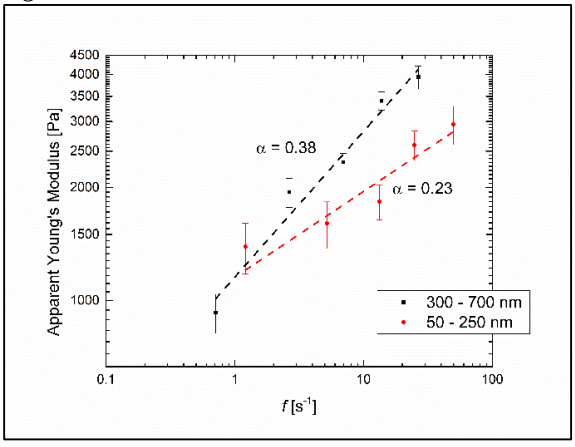

Figure 1: Loading rate dependence of the E-modulus of HUVECs using pyramidal tips and two different indentation depths for calculation.

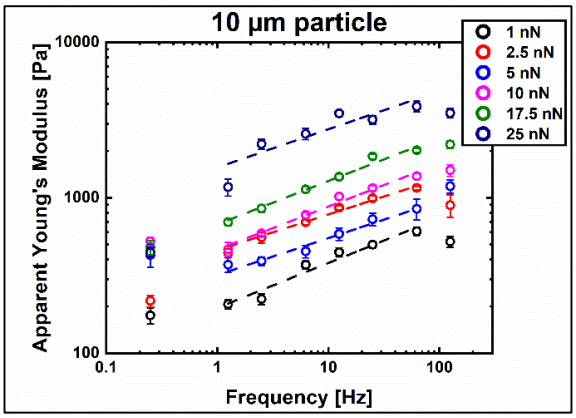

Figure 2: Loading rate dependence of the apparent E (Pa) for a particle at various maximum forces.

Micro-oscillations were used to determine the complex shear modulus which follows a weak power law. Finally, we were able to fit both SR and creep curves using simple PLR models. Figure 3 shows an example of a SR curve fitting.

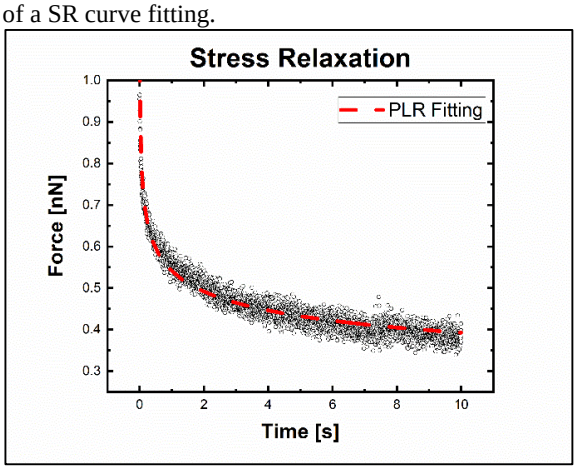

Figure 3: PLR of SR curve.

References

1. Discher D. et al, Science, 310(5751):1139-43, 2005.
2. Lim C. T. et al, J Biomech, 39(2):195-216, 2006.
3. Fabry B. et al, Physical Review E, 68, 041914, 2003.
4. Hecht F. et al, Soft Matter, 11, 4584-4591, 2015.
5. De Sousa et al, Sci Rep 10, 4749, 2020.
6. Weber et al, Micr Res Tec, 1-11, 2020.

Acknowledgements

We want to acknowledge Spela Zemljic-Jokhadar for HUVECs. In addition, we wish to thank Amsatou Andorfer-Sarr for maintenance of the cell culture facilities. This work was funded by the FWF grant P29562-N28.

HALOGENATION AS A STRATEGY TO MODIFY THE PHYSICO-CHEMICAL PROPERTIES OF RESILIN-LIKE OLIGOPEPTIDES

L. Sori (1), A. Pizzi (1), A. Gautieri (2), A. M. Grande (3), F. Baldelli Bombelli (1), M. Soncini (2) and P. Metrangolo (1)

1. SupraBioNanoLab-DCMIC "Giulio Natta"; 2. Biomechanics Group-DEIB; 3. Department of Aerospace Science and Technology of Politecnico di Milano, Piazza L. Da Vinci 32 - 20133 Milan, Italy.

Introduction

Resilin is a natural elastomeric protein found in the exoskeleton of insects. This protein has interesting properties like high resilience and noteworthy energy storage. Indeed, it is commonly studied for potential use in tissue engineering and other fields, e.g., drug delivery.[1,2] Resilin derivatives such as resilin-like oligopeptides, are also used for similar purposes. We focused on the study of a short characteristic repeat sequence of Resilin (7 amino acids, SDSYGAP), with the aim of expressing similar elastomeric properties of the entire protein in a small oligopeptide. The need to use this reductionist approach[3] is that the macromolecule is particularly complex and difficult to produce on a large scale with inevitable negative feedback from the economic and applicability point of view. Among the possible peptide chemical mutations, it is well known that halogenation enhances the intermolecular interactions, promoting self-assembly of peptide systems.[4-7] In fact, halogenation is a minimal structural modification that introduces a great diversity in the supramolecular behaviour of the peptide sequence.[7,8.]

Methods

We explore the halogenation as a strategy with the aim of improving the self-assembly properties of the SDSYGAP sequence. For the experimental activity and the characterization of the compound, several techniques were used including rheology, Differential Scanning Calorimetry (DSC) to understand the thermal behaviour, Scanning Electron Microscopy (SEM) and Polarized Optical Microscope (POM) for the morphological characterization of the peptide samples. In parallel molecular dynamics simulations of clusters of non-modified and halogenated peptide were conducted to verify the stability and molecular behaviour of peptides aggregates.

Results

In this work we have shown that the engineering of the tyrosine residue with bromine atoms promotes the formation of resilient fibril-like aggregates (Figure 1c, 1d). The same behaviour, however, is not visible in its natural counterpart, which is the non-halogenated sequence. Interesting rheological properties were also revealed. In particular, the elastic properties identified are dependent on the temperature and the level of strain applied. The molecular dynamics simulations confirm that the contribution of halogen bonds, due to the presence of bromine atoms, promote the fibrillar aggregation providing greater stability to peptide aggregates (Figure 1a,1b).

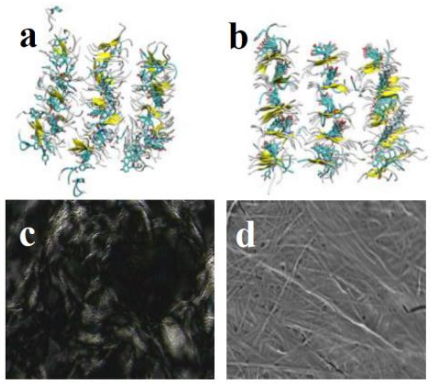

Figure 1: (a) WT peptides forms disordered aggregates; (b) Halogenated peptides forms ordered fibrils; (c) POM image of brominated Resilin; (d) SEM image of the same sample.

Discussion

In this contribution we want to show how halogenation, specifically bromination, has given a mini sequence of Resilin (of only 7 amino acids) exclusive properties. The elastic behaviour we have measured is a unique feature of the halogen sequence as it is totally absent in the natural form of the same mini sequence. Therefore, bromination reintroduces that elastic property which is characteristic of the complete Resilin sequence (> 600 amino acids). Furthermore, we were able to identify a certain self-healing behaviour of the brominated material.

References

1. Sun J et al, Adv. Mater, 32, 1906360, 2020.
2. Balu R et al, Nature Communications, 12:149. 2021.
3. Gazit E, Annu Rev Biochem, 87:533-553, 2018.
4. Pizzi A et al, Nanoscale, 9:9805-9810, 2017.
5. Bertolani A et al, Nature Commun, 6:7574, 2015.
6. Pizzi A et al, Pept Sci, 110:e23088, 2018.
7. Metrangolo P et al, Cryst Eng Comm, 8:946-947, 2006.
8. Cavallo G et al, Chem Rev, 116:2478-2601, 2016.

Acknowledgements

Authors are thankful to the European Research Council (ERC) for funding the projects FoldHalo, no. 307108) and MINIRES, no. 789815. We are also thankful to the PoliMI PhD School for funding a multidisciplinary PhD bursary.

STRUCTURAL AND FUNCTIONAL ANALYSIS OF HUMAN BITTER TASTE RECEPTORS

Marta Malavolta (1), Lorenzo Pallante (1), Marco A Deriu (1)

1. *PolitoBIOMedLab, Department of Mechanical and Aerospace Engineering, Politecnico di Torino, Italy*

Introduction

Taste perception is a prime example of complex signal transduction at the subcellular level. The investigation thereof at the nanoscale is empowered by Computational Molecular Modelling, herein employed to investigate bitter human taste receptors, which protect against the ingestion of toxins. Bitter perception involves TAS2Rs receptors, A-family GPCRs composed of an extracellular N-terminus, an intracellular C-terminus, 7 transmembrane (TM) α-helices, 3 Extracellular (ECLs) and 3 Intracellular Loops (ICLs). TMs and ECLs form the binding site. This work investigates the 25 human bitter taste receptors by using computational methods to underline structural and mechanical differences, as well as functional motions distinguishing *promiscuous* and *selective* receptors.

Methods

The 3D structures of the 25 human bitter receptors were downloaded in PDB format from the BitterDB [1]. Protein-membrane complexes were built with CHARMM-GUI. GROMACS was used to run Molecular Dynamics (MD) simulations. Principal Component Analysis (PCA) was carried out on the MD trajectories to analyze simulation data and distinguish the receptors' main motions. To underline collective atomic motions related to a specific function, Functional Mode Analysis (FMA) was used. The binding pocket volume was analyzed to evaluate promiscuous and selective receptors' opening, with the fpocket tool.

Results

To distinguish the 25 receptors as *promiscuous (PRO)* vs. *selective (SEL)*, different analyses were performed, choosing only 6 of them (TAS2R14, TAS2R10 and TAS2R46 for the promiscuous receptors and TAS2R3, TAS2R5 and TAS2R9 for the selective ones). The analyses were focused on the secondary structure, the identity between receptors, and the residue types: none of those underlined a substantial difference between the two groups. We found the binding pocket volume to be bigger on average for *PRO* receptors, as shown in Figure 1. FMA analysis highlighted a relationship between the ICL3 - C-terminus distance and receptor selectivity: this is in line with previous work highlighting the role of ICL3 in TAS2Rs activation [2]. Ensemble-weighted Maximally Correlated Motions (ewMCMs) were analyzed in every receptor, and the *SEL* receptors were found to have a different behaviour in the ECL2, in the form of greater ewMCM RMSF values with respect to *PRO* ones. The ECL2, located in the extracellular site and near the binding pocket, has a crucial role in the ligand-binding in GPCRs due to its position [3]. RMSF values computed from classical MD simulations confirmed these results.

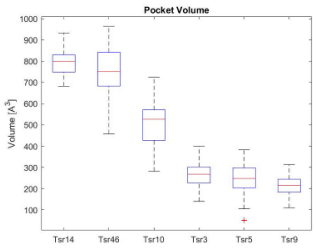

Figure 1: Box-plot of binding pocket volumes of the six receptors. The first three on the left side are the volumes of promiscuous receptors while the others are the volumes of the selective ones.

Discussion

The analyses of the *PRO* vs. *SEL* bitter taste receptors were aimed at functionally linking the intracellular domain, where the G-protein binds to the receptor, to the extracellular domain, where ligand-binding occurs. Binding pocket volume was found to be a differentiating factor between *PRO* and *SEL* receptors. PCA showed the importance of ICL3 and C-terminus fluctuations, the former having previously been found to be fundamental in the activation of the TAS2R receptors [2]. Hence, ICL3 – C-terminus distance was chosen as the function for FMA: ewMCMs were analyzed to investigate the fluctuation related to this function. The main difference between *PRO* and *SEL* receptors appears in the residue fluctuation in ECL2, higher in the selective ones. Such higher fluctuations in ECL2 in SEL receptors may partially explain the receptor selectivity. Also, the analysis of the loop's RMSF confirms this hypothesis. Such structure-function relationship findings represent an important starting point for future analyses, focused on the receptors' capacity to bind ligands in a promiscuous vs. selective fashion.

References

1. Dagan-Wiener, A. et al. Nucleic Acids Res. 47, D1179–D1185, 2019
2. Chen, Z. et al. Mol. Simul. 44, 322–329, 2018
3. Venkatakrishnan, A. J. et al. Proc. Natl. Acad. Sci. 116, 3288–3293, 2019

Acknowledgements

The research has been developed as part of the VIRTUOUS project, funded by the European Union's Horizon 2020 research and innovation program under the Maria Sklodowska-Curie-RISE Grant Agreement No 872181.

THE REGULATION OF PHENOTYPIC CHANGES IN VASCULAR SMOOTH MUSCLE CELLS VIA STRAIN AND NOTCH SIGNALING

Cansu Karakaya (1,2), Valery Visser (1), Tommaso Ristori (1,2,3), Carlijn Bouten (1,2), Cecilia Sahlgren (1,2,4), Sandra Loerakker (1,2)

1. Department of Biomedical Engineering, Eindhoven University of Technology, The Netherlands
2. Institute for Complex Molecular Systems, Eindhoven University of Technology, The Netherlands
3. Department of Biomedical Engineering, Boston University, USA
4. Faculty of Science and Engineering, Biosciences, Åbo Akademi University, Finland

Introduction

There is a clinical need for small-diameter vascular replacements, and *in situ* vascular tissue engineering has the potential to overcome this shortcoming. Despite the advances in strategies over the years, the processes leading to functional remodeling and native-like organization in engineered vascular tissues are not well characterized. Understanding these processes is crucial to steer and control the remodeling and to obtain successful outcomes upon implantation.

Mechanical cues and cell-cell signaling are important mediators of vascular growth and remodeling. Vascular smooth muscle cells (VSMCs) obtain interchangeable synthetic and contractile phenotypes depending on the growth and remodeling state of the vessel, and this plasticity is controlled by mechanical cues and Notch signaling [1,2]. Our computational model has recently predicted that the mechanosensitivity of Notch signaling can regulate the phenotypic switch in VSMCs [3]. Still, these predictions need an *in vitro* confirmation and the combined effects of strain and Notch signaling on VSMC phenotype should be investigated to understand their complex interactions in the context of vascular remodeling.

Methods

Human coronary artery smooth muscle cells were either grown to obtain synthetic VSMCs or differentiated via medium supplements to obtain contractile VSMCs. After growth and differentiation, the cells were either treated with the Notch inhibitor DAPT, or with the vehicle DMSO at a similar concentration as a control. Moreover, cells were equibiaxially stretched with the Flexcell Tension System at 1 Hz for 48 hours. The displacement was tracked with a camera and quantified to calculate the corresponding strain via digital image correlation. Immunofluorescence (IF) imaging and quantitative polymerase chain reaction (qPCR) were performed to characterize the changes in contractility markers (e.g. α-smooth muscle actin (αSMA)) and Notch signaling (e.g. Jagged1) upon stretch and Notch inhibition.

Results

Synthetic and contractile VSMCs showed differences in their gene expression and IF staining. Contractile cells obtained αSMA stress fibers (Figure 1A) and expressed significantly more αSMA compared to synthetic VSMCs (Figure 1B). When Notch signaling was activated, the synthetic cells increased their Jagged1 expression and showed a contractile-like phenotype. The inhibition of Notch signaling resulted in a decrease in αSMA and Jagged1 expression in contractile VSMCs while it hardly affected synthetic VSMCs. Upon stretch, contractile VSMCs lost their αSMA stress fibers (Figure 1A) and significantly decreased their Jagged1 and αSMA expression to the level of synthetic VSMCs (Figure1B).

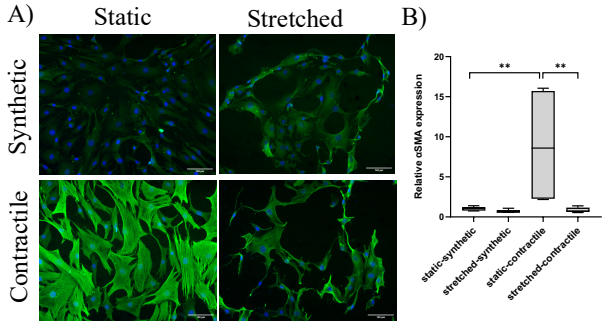

*Figure 1: The representative IF images of αSMA (A) and gene expression (B) in static and stretched synthetic and contractile VSMCs. (green: αSMA, blue: DAPI. Scale bar: 100 um)(**p<0.01, n=5).*

Discussions

The current study suggests that the interaction between Notch signaling and strain has a key role in regulating the VSMC phenotype. Notch signaling is necessary for the maintenance of the contractile phenotype, and the reduced Notch activity in stretched contractile VSMCs might be responsible for the transition of contractile phenotype towards a more synthetic phenotype.

References

1. Rensen et al., Neth Heart J, 15:100-108, 2007.
2. Doi et al., J Biol Chem, 281:28555-28564, 2006.
3. Loerakker et al., PNAS, 115:E3682–E3691, 2018.

Acknowledgements

This project has received funding from the European Research Council (ERC) under the European Union's Horizon 2020 research and innovation programme (Grant agreement No. [802967]).

INVESTIGATING CELLULAR FORCE GENERATION DURING SPROUTING ANGIOGENESIS

Mar Cóndor (1), David Böhringer (2), A. Apolinar (3), J.A. Sanz-Herrera (3), J. Barrasa-Fano (1), Ben Fabry (2) and H. Van Oosterwyck (1)

1. *Department of Mechanical Engineering, KU Leuven, Leuven, Belgium;*
2. *Department of Physics, Friedrich-Alexander University Erlangen-Nürnberg, Erlangen, Germany;*
3. *Escuela Técnica Superior de Ingeniería, Universidad de Sevilla, Seville, Spain;*

Introduction

Most, if not all, organs are dependent on the formation of a functional blood circulatory network for development, growth and regeneration. The mechanisms that control the ingrowth of vessels during angiogenesis have attracted much attention given its importance in the pathogenesis of various disease conditions such as ischemia, cancer and diabetes [1].

Cell invasion through a 3-dimensional (3-D) matrix strongly depends on a cell's ability to generate mechanical forces, which in turn, depend on the matrix properties (such as pore size and fiber stiffness) as well as cell properties (such as cell size and stiffness).

Previous in vitro studies have demonstrated that angiogenesis is strongly affected by ECM stiffness, and depending on the hydrogel used, angiogenesis was found to increase with increasing hydrogel stiffness or to peak at intermediate stiffness [2]. However, the force fields during angiogenesis for different ECM matrix stiffness values has thus far not been quantified.

Methods

We adapted an existing model of endothelial invasion [3] into collagen type I hydrogels for Traction Force Microscopy (TFM) procedures. By performing second harmonic generation (SHG) time-lapse imaging of both invasive endothelial sprouts and collagen fibers, we measured 3D collagen deformation fields (see Fig. 1, left) for three different concentrations of reconstituted collagen gels (2.4, 1.2 and 0.6 mg/ml), which are used to infer cellular tractions during sprouting angiogenesis. To compute these tractions, the mechanical characterization of the collagen gels has been performed by means of shear rheology and extensional rheology experiments.

Results

By examining collagen deformations (see Fig. 1, right) we have observed how endothelial cells mechanically interact with the collagen network mainly at the sprout tip and base region [4]. Protrusions at the sprout tip were mostly applying pulling and not pushing forces, suggesting a prominent role of tip cell pulling for sprout elongation.

When comparing the different collagen stiffness values, we have observed that sprouts formed within the softest collagen gels (0.6 mg/ml) are able to exert the same amount of deformations in the gels than those formed in the stiffest gels (2.4 mg/ml), implying that the cells generated considerably larger tractions in the denser and stiffer gels.

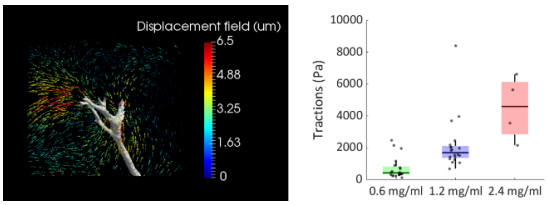

Figure 1: Displacement field (left) generated by a HUVEC-based sprout invading a 1.2 mg/ml collagen gel and differences in tractions (right) for the different collagen concentrations.

Discussion

Previous studies have shown how individual cells -when invading the surrounding ECM- are able to compensate for the steric hindrance, imposed by different matrix stiffness, by using cellular forces in a more efficient way [5]. By observing the process of endothelial sprout formation in differently dense and stiff hydrogels in combination with 3D TFM techniques, we are now able to investigate in detail how multicellular cell systems and their tip cells exert forces to invade the surrounding ECM.

References

1. Potente, M., H. Gerhardt, and P. Carmeliet. Cell, 2011. 146(6): p. 873-887.
2. Mason, E. ; et al.. 2013. Acta Biomat. 9(1):4635-4644.
3. Bayless, K.J., H.I. Kwak, and S.C. Su. Nature Protocols, 2009. 4(12): p. 1888-1898.
4. Vaeyens, M. et al. Angiogenesis, 2020.
5. Cóndor, M.; et al. Biophysical Journal, 2019. 116(7): p. 1305-1312.

Acknowledgements

FWO postdoctoral fellowship 12ZR120N for MC, FWO project G087018N, KU Leuven internal funding C14/17/111, FP7/2007-2013)/ERC Grant Agreement n° 308223 for HVO, DFG FA 336/11-1 for BF and Emerging Fields Initiative grant from Erlangen University for DB.

STEM CELL MORPHOLOGY CONTROLS PROTEIN NUCLEAR IMPORT WITHIN A BIOENGINEERED 3D NICHE

Emanuela Jacchetti(1)[§*], Ramin Nasehi(1)[§], Lucia Boeri(1), Valentina Parodi(1), Alessandro Negro(2), Diego Albani(3), Roberto Osellame(4), Giulio Cerullo(4), Jose Felix Rodriguez Matas(1), Manuela Teresa Raimondi(1).

1.Department of Chemistry, Materials and Chemical Engineering "Giulio Natta", Politecnico di Milano, Milano, Italy. 2.Department of Biomedical Sciences, University of Padua, Padua, Italy. 3.Department of Neuroscience, Istituto di Ricerche Farmacologiche Mario Negri IRCCS, Milan, Italy. 4. Istituto di Fotonica e Nanotecnologie (IFN)-CNR and Department of Physics, Politecnico di Milano, Milano, Italy

[§]These authors contributed equally to this work

Introduction

Smart biomaterials are increasingly being used to control stem cell fate *in vitro* by the recapitulation of the native niche microenvironment. The environment produced by these biomaterials transmits forces through the cell cytoskeleton, activating the mechanotrasduction pathway, guiding the cell fate. We developed an innovative microstructured 3D culture scaffold named "nichoid" that provides a geometric constraint to adhering cells, inducing nuclear deformation and modulating the nuclear import of fluorescent transcription factor Myod-GFP and the inert fluorescent protein GFP in mesenchymal stem cells (MSC).

Methods

3D microstructure scaffolds were produced by two photon polymerization technique [1]. 10^4 rats bone marrow MSC were seeded in the nichoid and on glass coverslip as 2D flat control. Cells were processed for immunofluorescence analysis to characterize focal adhesion localization, actin cytoskeleton organization and the nuclear deformation. To calculate the global influx of transcription factors into the cell nucleus, the MyoD-GFP fluorescent transcription factor and the inert GFP protein were transiently transfected to perform fluorescent recovery after photobleaching (FRAP) assay. A finite element computational model integrating the experimental results was performed to describe the nuclear permeability as function of the nuclear geometry.

Results

By integrating experimental measurements with numerical models, we show that in mesenchymal stem cells grown inside a 3D synthetic niche both facilitated nuclear transport of the myogenic differentiation factor and the passive nuclear diffusion of a smaller inert protein are reduced. We also demonstrate that cell morphology modulates nuclear import through a partition of the nuclear envelope surface exposed to flows, which becomes a thin but extremely permeable annular portion in cells cultured on 2D glass substrates, in which the MSC nucleus has a morphology similar to a thin, stretched disk.

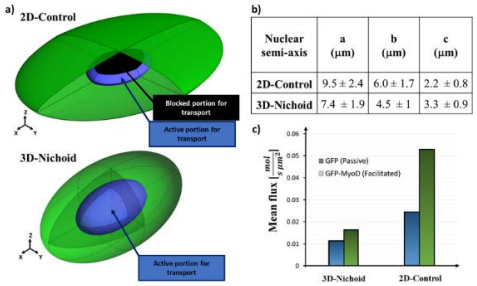

Nuclear semi-axis	a (μm)	b (μm)	c (μm)
2D-Control	9.5 ± 2.4	6.0 ± 1.7	2.2 ± 0.8
3D-Nichoid	7.4 ± 1.9	4.5 ± 1	3.3 ± 0.9

*Figure 1: **a** Representative scheme of the nuclear surface (in blue) exposed for protein transport in MSCs grown into the Control (top) and the Nichoid (bottom). **b** Summary of the nuclear semiaxes length calculated by fitting the nuclear shape with an ellipsoid. **c** Mean fluxes (passive and facilitated), calculated by computational modelling, within the first 22 seconds after photobleaching for cells in Nichoid and on Control.*

Discussion and Conclusion

Our results demonstrate that external forces acting on cell nuclei change the permeability of the nuclear envelope both in the case of facilitated transport and passive diffusion.

Our results support the new emerging hypothesis that in stem cell differentiation, the nuclear import of gene-regulating transcription factors is controlled by a strain-dependent nuclear envelope permeability. The outcomes represent a breakthrough in biomimetic approaches to engineering cell fate.

References

1. Raimondi MT *et al.* Acta Biomaterialia 9: 4579–4584, 2013
2. Ricci D *et al.* Materials 10(1): 66, 2017

Acknowledgements

European Research Council (NICHOID,G.A.-646990, NICHOIDS,G.A.-754467, MOAB,G.A.-825159); European Commission (FET-OPEN: IN2SIGHT,G.A.-964481); European Space Agency(NICHOID-ET,G.A.-4000133244/20/NL/GLC); National Centre for the Replacement, Refinement and Reduction of Animals in Research (MOAB,G.A.-NC/C01903/1 and NC/C019201/1); Italian Ministry of University and Research (MIURFARE: BEYOND, G.A.-R16ZNN2R9K); Fondazione Social Venture Giordano Dell'Amore, Cariplo Factory, Politecnico di Milano, Fondazione Bassetti and Fondazione Triulza (S2P: EGGS&BEACON).

SOFT WALLS PROMOTE VESICLE MIGRATION

Antonio Cerrato (1), Hugo Casquero (2), Joan J. Cerdà (1), Carles Bona-Casas (1)

1. Departament de Física & Institut d'Aplicacions Computacionals de Codi Comunitari (IAC3), Universitat de les Illes Balears, Campus UIB, E-07122 Palma de Mallorca, Spain; 2. Department of Mechanical Engineering, University of Michigan - Dearborn, Dearborn, MI 48128, United States.

Introduction

The study of soft-body motion in shear and Poiseuille flows is of particular interest when studying blood flow in narrow microvessels (diameter below 100 microns). At this scale, the layer of glycocalyx covering the vessel wall plays a crucial role to explain the Fåharæus effect. The glycocalyx is a highly-hydrated fibrous meshwork of carbohydrates located at the surface of endothelial cells and therefore is the outermost part of the endothelium. Its malfunction is related to several diseases such as atherosclerosis, stroke, hypertension, kidney disease, sepsis and cancer.

Methods

Our work studies the mechanical role of this soft and thin layer in cell-scale blood flow by means of the divergence-conforming immersed boundary (DCIB) formulation proposed in [1,2]. The DCIB method follows up on previous works [3-5] where discretizations of the mathematical model proposed by the IB method based on non-uniform rational B-splines (NURBS) and T-splines were developed. In the DCIB method, the Eulerian velocity-pressure pair is discretized using divergence-conforming B-splines, which leads to inf-sup stable, H1-conforming, and pointwise divergence-free Eulerian solutions. The Lagrangian displacement is discretized using NURBS, which enables to robustly handle large mesh distortions. By combining the generalized-α method and a block-iterative solution strategy, the DCIB method results in a fully-implicit discretization, which is key to impose accurately the no-penetration and no-slip conditions at the fluid-solid interface.

Results

Our results focus on the study of the lift velocity of vesicles of different shapes in various shear flows in the presence of both a rigid wall and a flexible wall. It is well known that objects drift away from rigid walls under shear flow either if they are asymmetric or there are strong inertial forces involved. This subject has been studied both experimentally [6] and analytically [7] using the Stokes equations for a rigid wall. We observe the relevance of an elastohydrodynamic lift for deformable objects due to the presence of an elastic substrate. Since we solve the full Navier-Stokes equations, we also observe the presence of an inertial lift even at low Reynolds numbers.

Discussion

The mechanical effect of a soft, deformable coating such as the glycocalyx or even the vessel wall itself is usually neglected in both in vitro and in silico setups. Our results show the presence of forces that are likely to have a significant influence on the behaviour of red blood cells and other bodies in blood circulation and are in line with previously reported experiments [8]. Therefore, the present contribution underlines the important, yet often overlooked, mechanical role that soft walls are likely to play in regulating cell/wall interactions in blood flow.

References

1. Casquero H, et al. J. of Comp. Phys., 2018;374:625-653.
2. Casquero H, et al. Comput. Method. Appl. M., 2015;284:, 943-970.
3. Casquero H, et al. Int. J. Numer. Meth. Eng., 2016; 105: 855-888.
4. Casquero H, et al. Comput. Method. Appl. M., 2017;316: 646-667.
5. Casquero H, et al. J. of Comp. Phys., 2021;425, 109872.
6. Callens, N. et al. Epl 83, (2008).
7. Olla, P. J. Phys. A. Math. Gen. 30, 317–329 (1997).
8. Wang, Y., et al. Phys. Rev. Lett. **115**, 248302 (2015).

Acknowledgements

All the authors thank the financial support of the Spanish Ministry of Economy and Competitiveness (MINECO/AEI/FEDER,UE) through the project Proyecto de I+D (excelencia) DPI2017-86610-P.

IMAGE-BASED ANALYSIS OF FLOW-INDUCED STRAIN ON THE OSTEOCYTE PROCESS VIA TETHERING ELEMENTS

Yuka Yokoyama (1), Yoshitaka Kameo (1,2), Taiji Adachi (1,2)

1. Department of Micro Engineering, Graduate School of Engineering, Kyoto University, Japan;
2. Institute for Frontier Life and Medical Sciences, Kyoto University, Japan

Introduction

Quantification of mechanical stimuli applied to osteocytes is important to understand the osteocyte mechanosensing, which is highly responsible for bone remodeling [1]. The osteocyte is subjected to different levels of mechanical stimuli involving interstitial fluid flow depending on the ultrastructure of osteocyte processes and the surrounding canalicular wall [2,3]. However, it is not clear how their irregular shape affects mechanical stimuli to the osteocyte process. In order to clarify this, we developed a three-dimensional (3D) image-based model of an osteocyte process with a canaliculus, and then evaluated strain distribution by fluid-structure interaction analysis.

Methods

We constructed the 3D model of an osteocyte process in the canaliculus based on ultra-high voltage electron microscopes tomography images [2]. We modelled the osteocyte process as an object covered by thin elastic membrane. We arranged tethering elements (TEs) [3], modelled as linear springs connecting the cell membrane to the canalicular wall. Then we evaluated the cell membrane deformation in response to interstitial fluid flow based on fluid-structure interaction analysis.

Results

Figure 1 shows the results of fluid-structure interaction analysis for bidirectional flow. In forward flow (from left to right), the flow velocity in the canal (Fig. 1a) and strain concentration regions on the osteocyte process (Fig. 2b) were irregularly distributed. The strain concentration was produced by highly tensioned TEs (Fig. 2b).

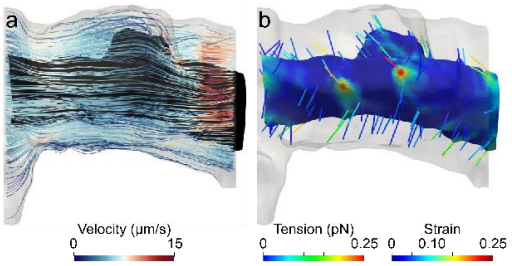

Figure 1: Results of fluid-structure interaction analysis using the image-based model of an osteocyte process and a canaliculus. (a) Distribution of flow velocity of interstitial fluid from left to right direction. (b) Distribution of maximum principal strain on the osteocyte process and tension of the TEs.

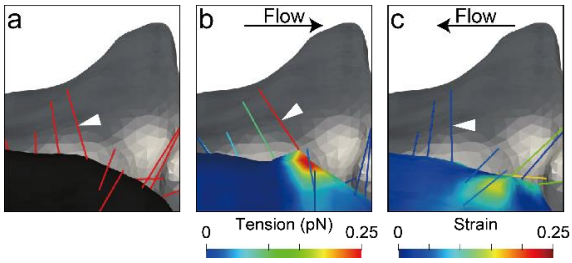

Figure 2: TEs connecting the osteocyte process and the canalicular wall (a) in the initial condition, (b) in the forward flow and (c) in the reverse flow.

The highly tensioned TEs that produced strain concentration on the osteocyte process in the forward flow were initially aligned ones against the forward flow as pointed by arrow head in Fig. 2a. Therefore, the TEs producing large strain in the forward flow (Fig. 2b) did not produce strain concentration in the reverse flow (Fig. 2c). The results altogether imply that inclined TEs produces strain concentration according to the flow direction.

Discussion

Our analysis using the high-resolution image-based model revealed that the initially inclined TEs produce strain concentration on the osteocyte process. In this model, one side of TE was placed randomly on the osteocyte process while the other side was connected to canalicular wall at the nearest point from the process side. Therefore, the inclination of the TEs were caused by irregular shape of canalicular wall as shown in Fig. 2a. It might imply that the same phenomenon also happens *in vivo*. Therefore, the results suggest that the irregular shape of canaliculi is crucial to produce large strain required for osteocyte mechanosensing. To fully understand the detailed mechanism, high-resolution images of TEs placements are required for further study.

References

1. Tatsumi, S. et al, Cell Metab, 5:464-475, 2007.
2. Kamioka, H. et al, Integr Biol, 4:1198-1206, 2012.
3. Han, Y. et al, Proc Natl Acad Sci USA, 101:16689-16694, 2004.

Acknowledgements

We would like to thank Hiroshi Kamioka (Okayama University) for providing us with the UHVEM tomographic data. This work was partially supported by AMED-CREST (JP19gm0810003) from AMED and Grant-in-Aid for Scientific Research (C) (JP19K04074) from JSPS, Japan.

A NOVEL IN SILICO FRAMEWORK CAN PREDICT THE CARTILAGE MECHANICAL DEGRADATION IN EXPLANTS WITH FOCAL DEFECTS

S.A. Elahi (1), P. Tanska (2), N. Famaey (1), R.K. Korhonen (2), R. Lories (1), I. Jonkers (1)

1. KU Leuven, Belgium; 2. University of Eastern Finland, Finland

Introduction

Mechanically induced disruption of cartilage homeostasis, due to *e.g.* presence of defects, contributes to progressive tissue degeneration and loss of joint function [1]. The mechanical degeneration plays an important role in onset and progression of osteoarthritis (OA), a prevalent disease among elderly, but also younger patients due to an injury in cartilage (*e.g.* due to overweight or sport activities) [2]. Despite extensive studies, so far yet, the interaction between mechanical loading and cartilage constitutional changes in mechanically induced OA are not fully understood. This paper aims at studying the onset and progression of degeneration in presence of focal cartilage defects using a novel integrated *in silico* model.

Methods

Finite element (FE) models of four cartilage explants (cylinders of 1.5 mm height and radius) were created within Abaqus: intact explant and explants including a through lesion of 20 µm width and 100, 380 and 750 µm depths mimicking the ICRS defect grades 1, 2 and 3, respectively [3]. A fibril reinforced poroviscoelastic swelling material model was used as the constitutive law to model the cartilage explants with the depth dependent properties given in [4]. The explants were subjected to unconfined compression by applying a 2 MPa compressive pressure in 0.1 sec on the top surface of cylinders simulating the normal gait loading [4, 5].

For the first time, the Cartilage Adaptive REorienetation Degeneration (CARED) model was introduced to predict the interaction between collagen fibril disorganization and degradation and proteoglycan (PG) depletion. The CARED model was used to run the FE simulations within an iterative process. Using the FE model results, fibrils were reoriented towards a preferred direction between the principal strains directions [5]. Fibrils and PG contents were degraded when the strain in fibrils direction exceeded 10% [6] and maximum shear strain exceeded 30% [4], respectively. In the CARED model, fixed charge density (FCD) loss and increase in tissue hydration were for the first time linearly related to the decrease in PG content. The model was run for 50 iterations after which the model reached an equilibrium.

Results

The variations in contents of intact explant under loading representative of normal gait was minimal, in line with our expectations. Fig 1 shows the degenerative changes in constituents of the cartilage explants with the three ICRS defect grades predicted by the CARED model. The grade 2 model presented the maximum fibril reorientation but minimum fibril degradation, indicative of the protective effect of fibril reorientation in cartilage defects. The strain magnitude was pronounced around the cracks, especially at the edges. Especially in the grade 1 model, where the tip of the crack was placed in the superficial zone with minimum fibril density, this contributed to the higher fibril degradation. The larger deformation due to crack opening in the grade 3 model caused higher PG depletion and consequently FCD loss and increase in hydration to occur in the superficial zone and around the crack of this model, which is in agreement with other computational and experimental observations [4]. Altogether, the CARED model provides an insight into the complex interactions that drive cartilage degeneration following cartilage injury.

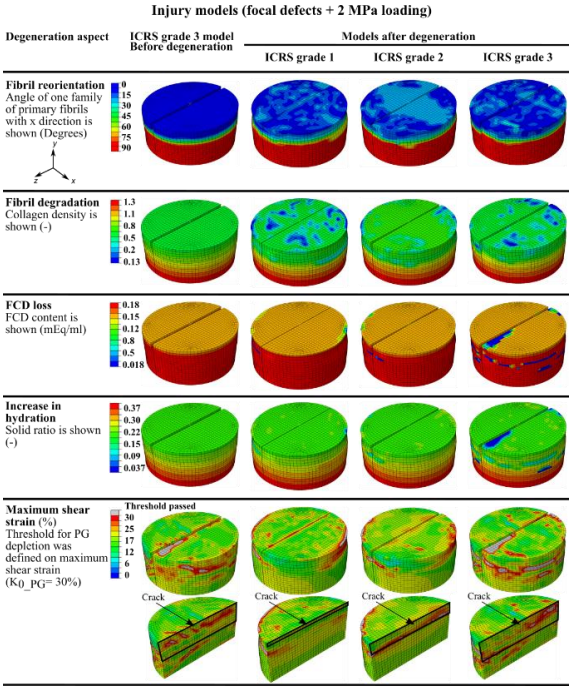

Figure 1: The degenerative variations in constituents of the cartilage explants with the three ICRS defect grades predicted by the CARED model.

References

1. R. Lories et al, Nat Rev Rheumatol. 7, 2010.
2. S. Mukherjee et al, Front Bioeng Biotech 8, 2020.
3. https://musculoskeletalkey.com/articular-cartilage-lesion/
4. A.S. Eskelinen et al, Biomech Model Mechan 18, 2019.
5. P. Tanska et al, Biomech Model Mechanobiol 17,2018.
6. Valentín et al, Int J Numer Method Biomed Eng, 29, 2013.

Acknowledgements

This work was supported by Marie Sklodowska Curie Individual Fellowship (CREATION project: MSCA-IF-2019-893771).

BIOMECHANICAL STIMULATION AND CHARACTERIZATION OF CARTILAGE MICROPELLETS WITH A DEDICATED FLUIDIC DEVICE

N.Petitjean (1,2), P. Cañadas (1), C. Jorgensen (2,3), P. Royer (1), D. Noël (2,3) and S. Le Floc'h (1)

1. LMGC, Univ. Montpellier, CNRS, Montpellier, France; 2. IRMB, Univ. Montpellier, INSERM, CHU Montpellier, Montpellier, France; 3. Hopital Lapeyronie, Clinical Immunology and Osteoarticular Diseases Therapeutic Unit, Montpellier, France

Introduction

Cartilage engineering approaches are being developed for evaluating the repair of articular cartilage lesions following injuries but few of them have reached the clinics. One limitation of current approaches is the lack of mechanical stimulus, which is one main factor regulating tissue homeostasis. With the objective to better understand the impact of mechanical forces on cartilage generation from mesenchymal stromal/stem cells (MSCs) and extracellular matrix production, we relied on the use of cartilage micropellets. The cartilage micropellet is a relevant and widely used in vitro model to study cartilage growth, independently on the presence of an existing matrix [1]. This model is poorly investigated in terms of biomechanical stimulation and characterization because of its small size and imperfect round shape. Thus, the objective of the study was to use a new fluidic custom-made device to stimulate and characterize mechanically MSCs-derived cartilage micropellets.

Methods

Microspheres made of distinct biomaterials with similar size than micropellets were prepared. Alginate microspheres were made with a solution of 3 % sodium alginate extruded into 0,1 M CaCl2. Collagen microspheres were prepared with type I collagen in hydrofluoroether. Human bone marrow-derived MSCs were differentiated into chondrocytes by culture in micropellets with 10 ng/mL TGFβ3-containing inductive medium for 21 days. The fluidic-based device was designed for the concomitant culture of six microspheres placed into the conical wells of a chamber where they were stimulated by a positive pressure (sinusoidal, square or constant). The sinking of each micropellet into the cone was recorded by a camera. The Young's modulus and Poisson ratio were determined after a multi-creep test using a finite element model employing a neo-Hookean hyperelastic law (LMGC90). On day 21, groups of six micropellets were stimulated with different square signals of positive pressure. 24 hours after stimulation, micropellets were harvested for chondrocyte marker quantification by RT-qPCR (SOX9, AGG and COL2B) and histology. Mechanical properties of micropellets were determined.

Results

Alginate- and collagen-based microspheres were first used to validate the reliability of the device for mechanical stimulation. Repeatability and reproducibility of pressure signals were demonstrated. The mechanical properties of microspheres were equivalent to those quantified by a conventional compression test and shown to be reproducible. We then used different parameters (amplitude, frequency, duration) of a square pressure signal to stimulate cartilage micropellets at day 21 and evaluate the expression of chondrocyte markers after 24h. A stimulation with an amplitude of 3.5 kPa superimposed to a minimum pressure of 1.75 kPa, at 1 Hz for 30 min increased the expression of SOX9, AGG and COL2B. The analysis using a finite element model indicated moderate deformation of micropellets with compression, tension and shear that did not alter micropellet structure as shown by histological staining. The mechanical properties of micropellets were measurable and a Young's modulus of 47.6 ± 26.2 kPa and Poisson ratio of 0.46 ± 0.02 were calculated.

Discussion

The interest of this new device lies in the reliability to mechanically stimulate and characterize microspheres with diameters in the range of 600 to 1500 µm and Young's moduli in the range of 1.5 to 90 kPa. Of importance in the case of cartilage micropellets, mechanical stimulation can be performed on six microspheres in parallel allowing both molecular and mechanical characterization on the same group of samples. In the future, the device will be useful to evaluate the growth of cartilage micropellets under mechanical stimuli in a longitudinal study.

References

1. Johnstone et al., Exp. Cell Res. 238, 265–272, 1998.

Acknowledgements

We thank COMPEX team and Yvan Duhamel for their technical support in developing the fluidic setup. We thank Mr Belamie and Ms Berthelot for the preparation of collagen beads. This work was supported by Labex Numev (PIA: ANR-10-LABX-20) and by CNRS (AAP "Osez l'Interdisciplinarité 2018", MoTiV Project).

INVESTIGATING CELL 'VISCO-TRANSDUCTION' IN ENGINEERED VISCOELASTIC HYDROGELS

Ludovica Cacopardo (1), Nicole Guazzelli (1), Simona Piaggi (1), Alessandro Corti (1) Arti Ahluwalia (1)

1. University of Pisa, Italy.

Introduction

Despite tissue intrinsic viscoelasticity, only recently mechanobiology studies started investigating cell response in the light of time dependent substrate properties. However, these studies are usually based on hydrogels where both viscous and elastic properties are altered at the same time [1-2].
For this reason, we engineered hydrogels with a constant equilibrium elastic modulus and different characteristic relaxation times that can be modulated varying the liquid phase viscosity without modifying the crosslinking of the solid network [2].
Here, we optimised agarose gel properties for the culture of adipose-derived mesenchymal stem cells (ADSCs) in order to understand if they are able to sense and respond to substrates with different viscous properties.

Methods

0.5% w/v agarose gel were fabricated using aqueous solutions with increasing dextran concentrations (0, 3, 4 % w/v), and hence viscosities. Mechanical properties were investigated using the epsilon-dot method [3].
aMSCs (50.000 cells/cm^2) were cultured for 21 days on the gels with 0 (high τ) and 4% (low τ) w/v dextran coated with 5% w/v gelatin and in 96-well multiwell plates ($\tau \rightarrow \infty$) as controls. The experimental setup is schematized in Figure 1D. The Alamar blue assay was performed at different time points and cell viability was normalised for the cell number obtained via image analysis. In order to optimise culture times for cell differentiation, at day 7 and 21, controls cells were fixed with 4 % paraformaldehyde and permeabilized with 0.01% w/v Triton-X. Samples were thus incubated overnight with Yes-associated protein (YAP) and CD45 (negative marker for cell stemness) primary antibodies and, then, for 2h with the respective secondary antibody. Finally, nuclei were stained with DAPI and actin with rhodamine-conjugated phalloidin (ThermoFisher, USA). Images were acquired with a confocal microscope (Nikon A1, Japan).
All reagents were purchased from Sigma-Aldrich (Milano, Italy), unless differently specified.

Results

Results showed a significant decrease of the instantaneous elastic moduli (Einst) and of the relaxation time (τ), while the equilibrium elastic modulus (Eeq) did not vary significantly (Figure 1A-B). Moreover, Eeq resulted in the optimal range to mimic the mechanical properties of the stem cell niche (≅ 3 kPa [2]). In all culture conditions, cells showed an increasing viability with increasing culture time (Figure 1C). Finally, in Figure 1E-G, it is possible to observe that, in the controls, cells started to differentiate at 21 days as shown by YAP migration in the nucleus and CD45 expression in the nuclear membrane.

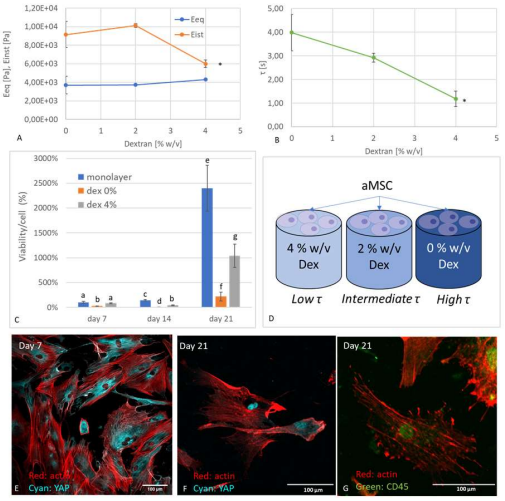

Figure 1: A) Einst, Eeq and B) τ of agarose samples as a function of different dextran concentrations. (= p<0.05, 1-way ANOVA); C) Viability normalised for cell number with respect to day 0 control (different letters indicate significantly different values); D) schematic illustration of the experimental setup; control samples imaging at day 7 (B) and 21 (C).*

Discussion

Hydrogels with tunable viscoelastic properties were adapted for the culture of ADSCs, thus allowing to study cell response to substate with different τ. In particular, culture times were optimised observing cell differentiation in the controls after 21 days.
Further experiments ore ongoing to better analyse cell differentiation in all the substates by means of tissue specific stainings, morphological and gene expression analysis. After the investigation of cell 'visco-transduction', further studies will be performed to understand if cell behaviour is influenced from past viscous stimuli. The final goal is the definition of optimal substrates to preserve their undifferentiated status in culture, in order to develop more physiologically relevant in-vitro models to study cell responses to mechanical alterations of their environment.

References

1. Yang et al., Nature Materials, 13:645-652, 2014
2. Cacopardo et al., J Mech Beh Biom Mat, 89:162-167, 2019
3. Tirella et al, J Biom Mat Res, 102A:3352-3360, 2014

EFFECT OF FLUID FLOW RATE AND DROPLET SIZE ON SPATIAL AEROSOL DISTRIBUTION DURING PRESSURIZED INTRAPERITONEAL AEROSOL CHEMOTHERAPY (PIPAC)

Mohammad Rahimi-Gorji (1,2,3), Ghader Ghorbaniasl (4), Sarah Cosyns (1,3), Wouter Willaert (1,3), Wim Ceelen (1,3), and Charlotte Debbaut (2,3)

1. Laboratory for Experimental Surgery, Department of Human Structure and Repair, Ghent University, Belgium; 2. IBiTech – bioMMeda, Ghent University, Ghent, Belgium; 3. CRIG – Cancer Research Institute Ghent, Belgium; 4. Department of Mechanical Engineering, Vrije Universiteit Brussel, Brussels, Belgium

Introduction

Pressurized IntraPeritoneal Aerosol Chemotherapy (PIPAC) is an innovative drug delivery platform has developed to treat patients with peritoneal metastases using laparoscopy [1]. During PIPAC, a CO_2 pneumoperitoneum is established (12 mmHg) to inflate the abdomen, after which a high-pressure injector delivers the chemotherapy through a nebulizer into the peritoneal cavity. However, some key questions on the ideal technical setup remain unaddressed. Computational fluid dynamics (CFD) allows to study the effects of flow rates and aerosol droplet size on the homogeneity of aerosol distribution.

Methods

The peritoneal cavity was simplified and represented as a box, which was generated by COMSOL Multiphysics (COMSOL, Burlington, VT, USA). The geometry was subdivided in 4 regions to compare different zones (Figure 1a). The geometry of the box was meshed using 98798 tetrahedral-volume elements. First, filling the box with CO_2 gas was simulated until its pressure equaled 12 mmHg (1600 Pa). The inflow boundary condition was set to a pressure of 12 mmHg and no-slip conditions for the walls. Then, nebulization was modeled with a liquid volume of 20 mL , flow rate (Q) of 0.5 mL/s, velocity of 15.92 m/s, density of 1071.9 kg/m3, viscosity of 4.875 mPa·s, and aerosol droplet diameter (d_p) of 30 µm. A freeze condition was assumed at the walls which means droplets adhere to the walls once the distance between the center of the droplet and the wall is less than the droplet diameter. The trajectory calculations were based on the force balance on the droplet, using the Lagrangian approach.

Results and Discussion

Figure 1b shows the typical deposition of aerosol droplets in the model with parameters d_p=1 µm and Q=0.5 mL/s. Figures 2a and 2b show the comparison of the aerosol droplet deposition in 4 regions of the box, obtained from CFD for different sizes and flow rates, respectively. With increasing diameter of the aerosol droplets, most aerosol droplets move to the bottom of the box due to gravitational force. The homogeneity of the distribution of the smaller droplets was better than that of the larger droplets. For a constant droplet size, increasing the flow rate led to an increase in initial velocity, and a concomitant increase in inertial impaction. For low flow rates, more than 90% of the droplets deposited in the lowest region of the box, caused by a phenomenon referred to as sedimentation. When considering high flow rates, due to high inertial impaction, most droplets deposited immediately in Region 1. Homogeneity of the deposition of the droplets was better for flow rate values in the range of 0.314 to 0.7 mL/s. The deposition rate at the top region of the box was zero.

In conclusion, by investigating the trade-off between the droplet size and flow rate, or by considering additional forces, such as the electrostatic force, one can overcome the gravity force and inertial impaction to improve the aerosol droplet distribution in the cavity.

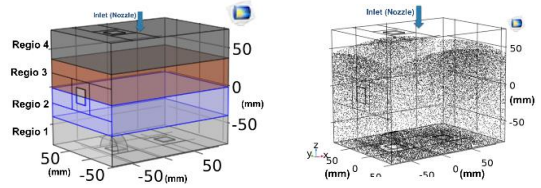

Figure 1: (a) A 3D model of the box model with subdivisions, and (b) Aerosol droplets deposition for the case of d_p=1 µm and Q=0.5 mL/s.

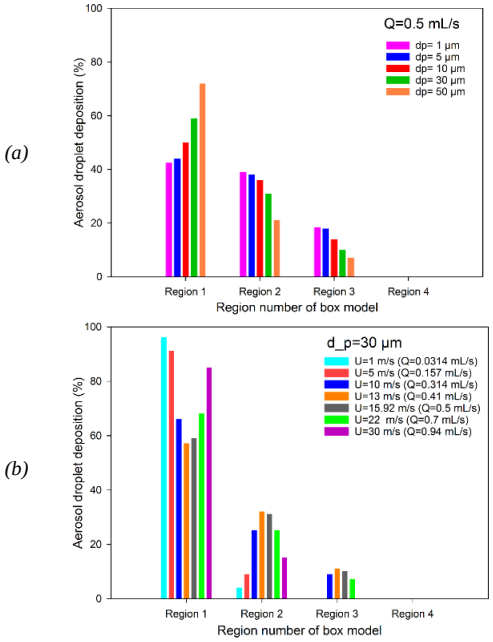

Figure 2: Comparison of aerosol deposition obtained from a CFD model in 4 regions of the box, shown for (a) different diameters (d_p), and (b) different flow rates (Q)

References

1. Rahimi-Gorji et al. Adv Drug Del Rev 160: 105–114, 2020.

QUANTIFICATION OF MECHANOREGULATION FROM TIME-LAPSED IN VIVO MICRO-CT MOUSE DATA

Francisco C. Marques (1), Ariane C. Scheuren (1), Esther Wehrle (1), Ralph Müller (1)

1. Institute for Biomechanics, ETH Zürich, Zürich, Switzerland

Introduction

Impaired bone mechanoregulation is a core mechanobiology indicator of ageing and degenerative conditions such as osteoporosis, which can result in fracture, long-term disability and pain. Investigating the causes leading to an unbalanced bone (re)modelling can advance the development of more effective therapies. Existing tools to study mechanoregulation of time-lapsed micro-computed tomography (micro-CT) images showed that the conditional probability (CP) of formation/resorption events is linked to higher/lower magnitudes of the strain energy density (SED) estimated with micro-finite element analysis (micro-FE) [1]. This analysis focused only on SED, and micro-FE was limited to homogeneous material properties. Assuming load-induced bone adaptation arises from mechanical deformation, the latter can be quantified using SED, SED gradient (SEDG), and effective strain (ES) [2]. Therefore, we expanded on the previous work by investigating the amount of mechanoregulation information recovered when considering homogeneous and heterogeneous material properties as well as the definitions of mechanical signals mentioned above, based on time-lapsed *in vivo* micro-CT data of mice.

Methods

A total of 160 *in vivo* micro-CT scans (vivaCT 40, 10.5µm, 55kV, 145µA, 350ms) were collected from a previously published study [3] investigating the effects of cyclic and static loading frequency on the amount of bone volume change on the sixth caudal vertebra (CV6) of mice after four weeks of extra-physiological cyclic (3x/week, 2, 5 and 10Hz, F=8N), static (F=8N) and sham loading (control group, F=4N, force assigned based on [4]). Simulations were performed with homogeneous (Young's Modulus of 14.8GPa [5]) and heterogeneous (linear relationship between bone mineral density and Young's modulus in trabecular bone [6]) material properties, both with a Poisson's ratio of 0.3. Micro-FE (ParOSol) was used to compute the SED values in the structure, from which all derived quantities were computed after linear scaling to match the *in vivo* force. The mechanoregulation analysis considered SED, SEDG, and ES for the local mechanical signal. SEDG was computed using the central difference scheme, and the norm was used as a proxy for the magnitude of fluid flow in each voxel. The conditional probabilities of a (re)modelling event to occur at each value of mechanical signal were calculated [1]. Mechanoregulation was quantified using Correct Classification Rates (CCR) [7]. Significance was assessed with Kruskal–Wallis test, followed by Dunn's test with Bonferroni correction.

Results

ES combined with homogeneous material properties achieved the highest CCR values for all groups across all time-points (Figure 1). Also, increasing loading frequency yielded higher CCR values, especially for homogeneous material properties.

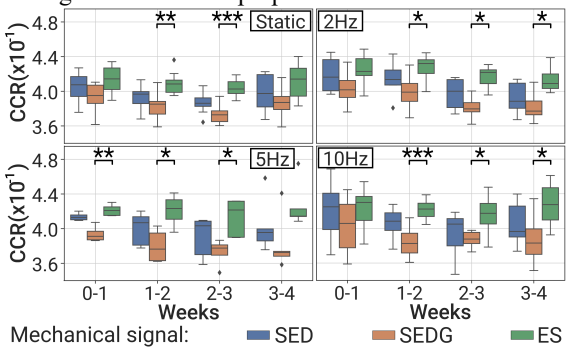

*Figure 1: CCR values from the CP curves computed per group with homogeneous material properties (Control group not shown). *** $p<0.001$, ** $p<0.01$, * $p<0.05$.*

Discussion

Among the three mechanical signals, ES achieved the highest CCR values for both types of material properties, reinforcing previous results that favoured the use of this quantity in events of substantial bone mineralisation, like extra-physiological loading or fracture healing [7]. Heterogeneous (vs. homogeneous) material properties achieved lower CCR scores, suggesting the need for a more accurate conversion of grayscale bone mineral density to Young's Modulus, prior to the micro-FE. The maximum average change in CCR over four weeks was 16%, which could indicate that our ability to quantify the mechanoregulation is not accurate enough, emphasising the need to explore novel methods capable of incorporating additional mechanobiological information from the morphometry.

References

1. Schulte et al., PLoS One, 8(4), 2013
2. Pistoia et al., Bone, 30:6, 2002
3. Scheuren et al., Front Bioeng Biotechnol, 8:1211, 2020
4. Christen et al., Biomech Model Mechanobiol, 11:3-4, 2012
5. Webster et al., Comput Methods Biomech Biomed Engin, 11:5, 2008
6. Mulder et al., Bone, 41:2, 2007
7. Tourolle né Betts et al., Sci Rep, 10:1100, 2020

Acknowledgements

Support from the European Union (MechAGE ERC-2016-ADG-741883), the Swiss National Supercomputing Centre (CSCS) and the Euler compute cluster at ETH Zurich.

THE 3D NICHOID SCAFFOLD AS A MODEL TO DRIVE IN-VITRO STEM CELL FATE

Valentina Parodi (1), Emanuela Jacchetti (1), Arianna Bresci (1, 2), Benedetta Talone (2), Giulio Cerullo (2, 3), Roberto Osellame (3), Dario Polli (2, 3), Manuela T. Raimondi (1)

1. Department of Chemistry, Materials and Chemical Engineering, "G. Natta", Politecnico di Milano 20133, Italy; 2. Department of Physics, Politecnico di Milano, 20133 Milano, Italy; 3. Istituto di Fotonica e Nanotecnologie (IFN)-CNR, 20133 Milano, Italy

Introduction

We developed a 3D in-vitro model for mesenchymal stem cells (MSCs) expansion and differentiation based on the Nichoid scaffold [1]. This engineered scaffold is characterized by precise architectural cues at the microscale thus emulating the tensional states of the native niche. It has been demonstrated that Nichoid culture allows stem cells to proliferate promoting their stemness maintenance. The hypothesis is that the Nichoid controls both the oxygen tension and the cellular shape thus affecting nuclear membrane permeability to transcription factors. In this work, fluorescence microscopy and multimodal label-free microscopy [2] were applied to investigate MSCs phenotypic expression inside and outside 3D Nichoids after exposure to differentiation factors.

Methods

Nichoid scaffolds were obtained via two-photon polymerization of SZ2080 photoresist (Fig. 1) [3]. MSCs at a density of 20,000 cells/cm^2 were seeded on the Nichoids and 5,000 cells/cm^2 on flat control substrates and cultured with complete, adipogenic and chondrogenic culture media for 21 days. To evaluate cell response to the 3D environment, cells were investigated with fluorescence and label-free multi-photon microscopy at different time points. Image processing was performed using MATLAB and Fiji-ImageJ.

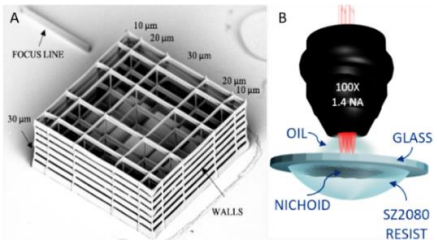

Figure 1: A: Nichoids single unit B: Schematic representation of Nichoid fabrication.

Results

MSCs adipogenesis was studied using label-free microscopy. Results showed lipid vesicle formation and their spatial distribution inside Nichoids (Fig.2).

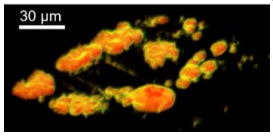

Figure 2: 3D rendering of a label-free image of lipid vesicles produced during MSCs adipogenesis inside the Nichoid.

MSCs induced towards the chondrogenic phenotype behaved in the opposite way. Recent results obtained by fluorescence microscopy in 3D Nichoids and label-free microscopy showed smaller collagen type I production with respect to flat substrates (Fig.3).

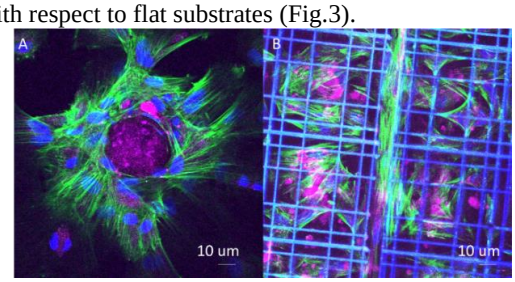

Figure 3: Confocal fluorescence images of MSCs in chondrogenesis at 21 days of differentiation: nuclei in blue, F-actin in green and collagen I in magenta. A: flat substrate; B: 3D Nichoid.

Discussion

Our results suggest that stress states induced by Nichoids promote adipogenesis while limit chondrogenesis in MSCs. This can be related to the stiffness of the material which may regulate stem cell fate [4]. Multimodal label-free microscopy allowed to identify chemical bonds such as lipids in 3D, by filtering out any other signal, without the use of fluorescent probes, representing a promising technique.

References

1. Nava, M. M. et al. Stem Cell Res. Ther. 7, 1–12 (2016).
2. Crisafi F et al. Spectrochim Acta A Mol Biomol Spectrosc 2017;188:135-140
3. Zandrini T. et al. Sci. Rep. 9.1 (2019): 1-9
4. Mao A. S. et al., Biomat. 98 (2016): 184-191.

Acknowledgements

This work received founding from the European Research Council (ERC projects NICHOID, G.A. 646990, NICHOIDS, G.A. 754467, MOAB, G.A. 825159, and VIBRA, G.A. 648615); European Commission (FET-OPEN project IN2SIGHT, G.A. 964481); European Space Agency (ESA project NICHOID-ET, G.A. 4000133244/20/NL/GLC); National Centre for the Replacement, Refinement and Reduction of Animals in Research (NC3Rs projects MOAB, G.A. NC/C01903/1 and NC/C019201/1); Italian Ministry of University and Research (MIUR-FARE project BEYOND, G.A. R16ZNN2R9K); Fondazione Social Venture Giordano Dell'Amore, Cariplo Factory, Politecnico di Milano, Fondazione Bassetti and Fondazione Triulza (S2P project EGGS&BEACON).

THE MISSING LINK IN FROST'S MECHANOSTAT: DIRECT RELATIONSHIP BETWEEN LOCAL STRAIN AND CORTICAL ADAPTATION IN THE MOUSE TIBIA

Edmund Pickering (1), Peter Pivonka (1)

1. Queensland University of Technology, Australia.

Introduction

Frost's mechanostat [1] predicts a direct link between the local loading environment (e.g. local strain) and the adaptive response of cortical bone. However, many studies on bone adaption do not directly test this. Rather, most studies (e.g. [2]) investigate the relationship between total load (instead of local strain) and consider broad adaptive metrics (e.g. bone volume change, cortical area change). Neither of these allow for direct interrogation of Frost's mechanostat.

In this study, we couple local strain predictions with an automated cortical thickness change measurement technique (i.e. a local adaption metric). This novel approach allows us to directly interrogate the link between local strain and the adaptive response in the mouse tibia compression model. We uncover new detail on bone's adaptive response to load. Further, by investigating parathyroid hormone (PTH) dosage, we uncover new insights into PTH's effect on bone adaption.

Materials and Methods

This study used micro computed tomography (μCT) data previously published by Sugiyama *et al.* [2]. In this, female virgin C57BL/6 mice were separated into four groups (n = 3-5 per group). Between 13 – 19 weeks of age, each group was given intermittent PTH injections of vehicle, 20 μg/kg/day, 40 μg/kg/day or 80 μg/kg/day. Between weeks 17 – 19, following PTH injection, the right tibia of each mouse was subjected to 7 min of external loading (left limb acted as a contralateral control). Loading occurred every second day and was strain matched to achieve approximately 1200 $\mu\varepsilon$ on the medial surface of the tibiae 37% along the shaft from the proximal end. On week 19 the mice were euthanised and were μCT scanned with a voxel resolution of 5 μm.

To assess the strain within the mouse tibia, a validated beam theory model was used. Following, a hybrid thickness measurement technique was used to measure the cortical thickness change (cortical thickness difference between left and right tibiae). For each voxel on the periosteum and endosteum, the strain and thickness change was extracted.

Results & Discussion

The periosteal adaptive response as a function of absolute strain and PTH dosage is shown in Figure 1.

For the vehicle, a clear trend relationship is observed between the absolute strain and adaptive response. For strains below 4000 $\mu\varepsilon$, little adaptive response is observed, however for strains above 4000 $\mu\varepsilon$ an approximately linear relationship between absolute strain and adaption. The primary affect of PTH dosage is a reduction in the adaption threshold. For 20 and 40 μg/kg/day PTH, the adaption threshold appears to reduce to approximately 700 $\mu\varepsilon$. For 80 μg/kg/day, large sections of woven bone was observed, leading to errors in the thickness measurement.

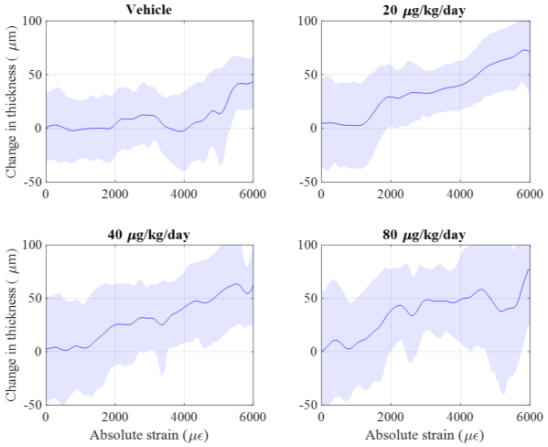

Figure 1: Adaptive response of the periosteum as a function of absolute strain and PTH dosage. The blue shaded area represents one standard deviation.

Conclusion

This study developed a direct link between the local strain within the mouse tibia and the adaptive response. By studying this link, new insights in bone's adaptive response and the effect of PTH can be obtained. It is anticipated that the methods and insights developed in this work, will aid in future treatment of bone degenerative diseases.

References

1. Frost, H. M. (2003). *Anatomical Record - Part A Discoveries in Molecular, Cellular, and Evolutionary Biology*, *275*(2), 1081–1101.
2. Sugiyama, *et al.* (2008). *Bone*, *43*(2), 238–248.

Acknowledgments

The authors thank Sugiyama *et al* [2] for providing the μCT data used in this study and the high performance computing service at the Queensland University of Technology.

NICHOID SUBSTRATE REGULATES MECHANOTRANSDUCTION GENES IN NEURAL STEM CELLS: WHOLE TRANSCRIPTOMIC APPROACH WITH BIOINFORMATIC ANALYSIS

Letizia Messa[1,3], Bianca Barzaghini[1], Federica Rey[2], Cecilia Pandini[3], Gian Vincenzo Zuccotti[2], Cristina Cereda[3], Stephana Carelli[2,*] and Manuela Teresa Raimondi[1,*]

[1] Department of Chemistry, Materials and Chemical Engineering "Giulio Natta", Politecnico di Milano, Milano, Italy

[2] Pediatric Research Center "Romeo ed Enrica Invernizzi", University of Milano, Milano, Italy

[3] Genomic and post-Genomic Center, IRCCS Mondino Foundation, Pavia

** These authors contributed equally to the work*

Introduction

In the field of regenerative medicine, 3D scaffolds are deeply investigated for their ability to mimic the physiological microenvironment and to guide cell fate [1]. 3D substrates create an artificial environment that allows to control in vitro the proliferative and differential potential and to obtain a cellular response more representative of the in vivo behavior with respect to the 2D cell culture conditions. The Nichoid, a 3D scaffold inspired by the natural staminal niche, which its geometry allows stem cells to self-organize inside the pores adhering to the internal grid [2, 3]. Moreover, the Nichoid has shown ability to stimulate the expression of pluripotency genes and potentiate the therapeutic potential of neural precursor cells (NPCs) [2, 3]. In this work, we aim to investigate the effect of the 3D scaffold Nichoid on the NPCs whole gene expression profile through a whole transcriptomic approach, highlighting significant changes in the mechanotransduction.

Methods

Nichoids were fabricated by femtosecond laser two-photon polymerization (2PP) onto circular glass coverslips using a hybrid organic-inorganic SZ2080 photoresist. 10^4 NSCs were expanded inside the engineered niches and in control conditions for 7 days and then analysed through RNA-Seq. Observations were confirmed through Real Time PCR and immunofluorescence analysis.

Results

NPCs grown in standard floating conditions formed spheroids whereas NPCs expanded inside the Nichoid organized themselves in a carpet-like structure, expanding inside the niches. Through RNA-Sequencing we detected 1934 differentially expressed coding and non-coding genes connected to mechanobiology functions, highlighting that the Nichoid impacts the biological and genetic response of stem cells. We fully dissected this mechanism highlighting how the changes start at a membrane level, with subsequent alterations in the cytoskeleton, signaling pathways, and metabolism, all leading to a final alteration in gene expression (Figure 1).

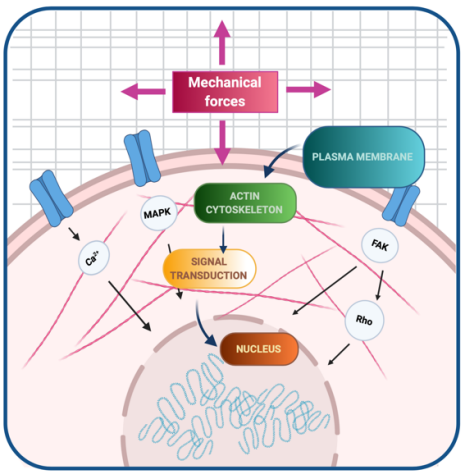

Figure 1: Nichoid's impact on mechanotransduction

Discussion

These results highlight the Nichoid's ability to induce changes in cultured stem cells at any molecular level without the addition any other exogenous chemical agents. The Nichoid recreates the stem cells adhesion, migration, differentiation, proliferation and cell signaling that best mimics physiological conditions, providing new insights in the development of stem cell therapies in regenerative medicine.

References

1. Remuzzi A, et al. Cells. 2020 Aug 11;9(8):1873
2. Carelli S, et al. Nanotheranostics 2021; 5(1):8-26
3. Rey F, et al. Int J Mol Sci. 2020 Sep 15;21(18):6775

Acknowledgements

European Research Council (ERC projects NICHOID, G.A. 646990, NICHOIDS, G.A. 754467, and MOAB, G.A. 825159); European Commission (FET-OPEN project IN2SIGHT, G.A. 964481); European Space Agency (ESA project NICHOID-ET, G.A. 4000133244/20/NL/GLC); National Centre for the Replacement, Refinement and Reduction of Animals in Research (NC3Rs projects MOAB, G.A. NC/C01903/1 and NC/C019201/1); Italian Ministry of University and Research (MIUR-FARE project BEYOND, G.A. R16ZNN2R9K); Fondazione Social Venture Giordano Dell'Amore, Cariplo Factory, Politecnico di Milano, Fondazione Bassetti and Fondazione Triulza (S2P project EGGS&BEACON); Fondazione Romeo e Enrica Invernizzi Milano.

MECHANOBIOLOGY OF EXTRACELLULAR MATRIX ON THE TUMOR GROWTH

Inês G. Gonçalves (1), Daniel Camacho (1), María José Gómez-Benito (1,2), Pedro E. Guerrero (1), José Manuel García-Aznar (1,2)

1. Multiscale in Mechanical and Biological Engineering, Aragón Institute of Engineering Research (I3A), University of Zaragoza, 50018 Zaragoza, Spain

2. Instituto Investigación Sanitaria (IIS-Aragón), Zaragoza, Spain

Introduction

Recently, several works have analyzed the regulatory role of the mechanical properties of the extracellular matrix on tumor growth [1]. In fact, it is well established that matrices of higher density may suppress tumor growth by exerting compressive forces on cells [2]. In addition, experimental studies have also shown that matrices with higher density tend to limit tumor cell movement due to steric hindrance, but matrices composed of lower collagen concentration promote individual cell migration, which can subsequently affect the tumor size [3].

In this work, we aim to investigate the role of matrix mechanics on tumor growth through an agent-based computational framework. In particular, we are going to study how matrix mechanics regulates the growth of two pediatric cancers: neuroblastoma and diffuse intrinsic pontine glioma (DIPG). For this aim, we will develop microfluidic-based cell cultures following the methodology proposed in [3] in order to characterize the general dynamics of individual cellular movement, accounting for the mechanical properties of the ECM.

Methods and Materials

As a first approach, we have simulated the cells as 3D rigid particles, whose spatial location is determined by the balance of forces. Three main forces have been considered: cell locomotive force, cell-cell interactions, and drag forces. In fact, we have introduced the effect of drag forces imposed by the ECM by taking into account the dynamic viscosity of the ECM. Therefore, with this approach, we are able to simulate the 3D migration of the tumor cells.

In addition, proliferation has been simulated considering the effect of the cell cycle, described by a growth phase, in which the cell progressively increases its volume as a result of DNA replication, and by a mitosis phase, in which the cell divides into two daughter cells.

Therefore, tumor growth is the emergent behavior of the multicellular system regulated by the balance between cell proliferation and migration. We clearly show in the results the crucial role of this balance in the tumor growth determined by the mechanical properties of the ECM.

This mechanobiological approach has been applied to simulate both tumor types: neuroblastoma and DIPG. Certainly, different parameters have been used to describe each tumor type.

Results

We have simulated the individual motility of cells in matrices with different properties and consequently stiffness.

Overall, our results show that an increase in the collagen concentration leads to smaller tumor size (neuroblastoma) and how this, in turn, reduces the invasion of single cells, producing larger cell clusters (Fig 1). In contrast, lower density values enable cell migration, resulting in sparser and smaller tumors.

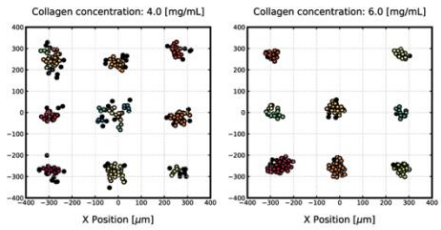

Figure 1: Spatial distribution of tumor cells (neuroblastoma) in matrices with different collagen concentration.

We have found a similar effect in the case of tumor cells from DIPG, where cells migrate much more in the case of lower dynamic viscosity, creating sparser tumors (Fig 2).

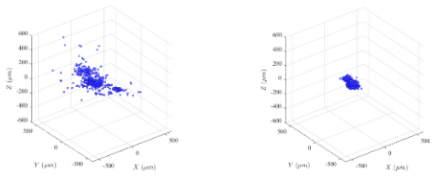

(a) (b)

Figure 2: Spatial distribution of tumor cells (DIPG) in two matrices of different dynamic viscosity.

References

1. Paszek et al, Cancer Cell, 8(3), pp.241-254, 2005.
2. Helmlinger et al, Nat. Biotechnol, 15(8):778-783. 1997.
3. Plou et al, Sci Rep, 8(1):12723, 2018.

Acknowledgements

This work was supported by the European-funded PRIMAGE project (No. 826494), and the Spanish Ministry of Science, Innovation and Universities (RTI2018-094494-B-C21).

NANOMECHANICAL FINGER-PRINTS OF SOLID TUMORS AS A TREATMENT MONITORING BIOMARKER

Andreas Stylianou (1,2), Chrysovalantis Voutouri (2), Fotios Mpekris (2), Triantafyllos Stylianopoulos (2)

1. School of Science, European University Cyprus, Cyprus;
2. Cancer Biophysics Laboratory, University of Cyprus, Cyprus

Introduction

Solid tumors, such as breast tumors and sarcomas, stiffen as they grow in a host healthy tissue. Stiffening is caused by an increase in the structural components of the tumor, mainly collagen fibers, and in cancer and stromal cells content. Tumor stiffening can cause blood vessel inefficiency and hypo-perfusion, and as a result, it poses major physiological barriers to the systemic delivery of drugs. Consequently, there is an urgent need for the development of novel biomarkers, that characterize the mechanical state of a particular tumor so as to support the development of novel therapeutic strategies that target the tumor mechanical microenvironment [1].

In this work, Atomic Force Microscopy (AFM) was employed in order to assess unique NanoMechanical FingerPrints of breast tumor and sarcoma during cancer progression [2]. Also, an approved anti-fibrotic drug, tranilast, was re-purposed so as to target the tumor matrix and alleviate stiffness [3]. The AFM data were correlated with *in vivo* ultrasound studies and polarized microscopy.

Methods

Orthotopic fibrosarcoma and breast tumors were established by implantation of HT1080 and E0771 cells into the left flank and the third mammary fat pad of 6-8-week-old NOD/SCID and C57BL/6 mice, respectively. Mice accepted 4 cycles of treatment with a 3-day interval. Treatment groups included: i)Saline (control), ii)Tranilast, iii)Doxorubicin and iv)Doxorubicin+Tranilast. Biopsies were obtained at 3 different time points. AFM measurements (Molecular Imaging, PicoPlus) on fresh samples were conducted, with silicon nitride cantilevers. Per specimen 15 different force maps (16×16 point grids, 20x20 μm^2) were recorded. The force maps were analyzed by AtomicJ using the Hertz model. Ultrasound elasticity measurements were performed using the shear wave elastography method and microvascular imaging with Doppler (Philips EpiQ Elite Ultrasound), Collagen abundance was evaluated via picrosirius red staining and images were acquired using an Olympus BX53 microscope with linear polarizers.

Results

AFM analysis of tumor biopsies at different times of tumor growth in breast cancer and sarcoma revealed two distinct characteristics as far as the distribution of elastic modulus is concerned: a lower elasticity peak, due to cancer cell softening and a higher elasticity distribution, due the collagen overproduction (Fig.1A). The results also demonstrated that AFM is sensitive enough to monitor nanomechanical alterations during anti-fibrotic treatment with Tranilast (Fig.1B). These results were correlated with collagen content studies (Fig.1C) and ultrasound studies (Fig. 1D). Finally, our results demonstrate that AFM-based NanoMechanical FingerPrints can monitor and predict the effects of the treatments that include the combination of anti-fibrotic drugs (Tranilast) with chemotherapy.

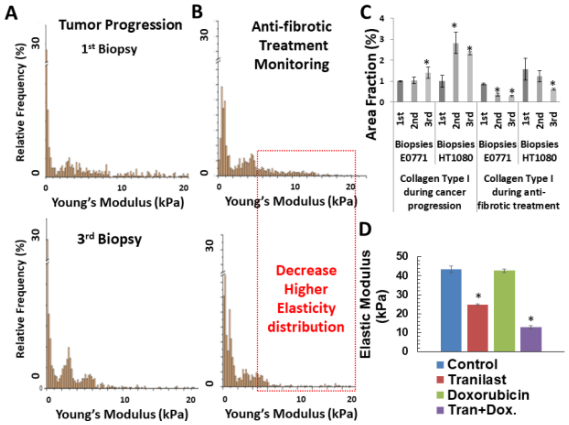

Figure 1: A,B) AFM-based NaoMechanical FignerPrints C) Collagen continent alterations and D) Ultrasound elasticity measurements.

Discussion

We found that AFM techniques are sensitive to access small nanomechanical modifications after solid tumor treatment with drugs, including anti-fibrotic agents and chemotherapy. Further research in this area will reveal the mechanism of different NanoMechanical FingerPrints and will enable the development of mechanical biomarkers.

References

1. Gkrestsi, V., et al., Front Oncol, 5:214, 2015.
2. Stylianou, A, et al., Nanoscale,10:20930, 2018.
3. Papageprgis, P., et al., Sci Rep, 7: 46140, 2017.

Acknowledgements

Part of this work was supported by the European Research Council Proof of Concept (ERC-2018-PoC-838414) and by the Cyprus Research and Innovation foundation (CULTURE/AWARD-YR/0119/0012).

GENERATION OF CONTROLLED HYDRODINAMIC STIMULI ON VASCULAR PLANAR TISSUE SAMPLES IN A NOVEL BIOREACTOR

Elia Pederzani (1), Lorenzo P. Coppadoro (1), Aldo J.S. Roldan (1), Maria Lombardi (2), Chiara Foglieni (2), Monica Soncini (1), Gianfranco B. Fiore (1)

1. *Department of Electronics, Information and Bioengineering, Politecnico di Milano, Italy*
2. *San Raffaele Hospital IRCCS, Milano, Italy*

Introduction

Atherosclerosis is a chronic-degenerative pathological phenomenon that affects the cardiovascular system. One of the main pro-pathological risk factors is the influence of blood flow on the endothelial mechanotransduction mechanisms [1]. Indeed, endothelial cells are extremely sensitive to tangential stress occurring in the vessel wall (wall shear stress, WSS), which is strictly related to local fluid dynamics. It is well known that atherosclerotic plaques are most frequently found in arterial districts with disturbed fluid dynamics. The alteration of WSS is considered the trigger of endothelium permeabilization with consequent lipids' diffusion within the intima. An in-depth literature analysis allowed us to identify three main numerical indexes for WSS description: TAWSS, OSI, CFI. Their combined use enabled an accurate and complete characterization of the disturbed flow and the possibility to discriminate between atherogenic and atheroprotective conditions [2]. Despite this, the relationship between the hydrodynamic stress experienced by endothelial cells and its effect on inflammation and mechanotransduction mechanisms is still far from being elucidated. In this scenario, we have developed a novel device for conditioning human vascular tissue samples of not negligible thickness with multidirectional, complex and over-time variable WSS patterns. Indeed, our device is able to reproduce combinations of specific values of WSS indexes enabling a systematic investigation of effects of specific WSS patterns on vascular cells behaviour.

Culture system

The strategy chosen for bioreactor design is to apply a constant flow rate while the sample rotates with a specific motion function. In this way it is possible to reproduce the complex WSS multidirectional nature experienced by endothelial cells *in vivo*.

The designed bioreactor consists of a vascular sample housing to be inserted in the parallel plates flow chamber (Figure 1(A)). The correct alignment of the endothelium with the bottom layer of the flow chamber is essential to apply a controlled WSS. This is made possible by the joint use of a distance sensor revealing the sample position and a threated piston enabling the manual sample position adjusting. Thanks to the presence of two gears, it is possible to transfer the rotary motion of a stepper motor to the sample housing element and consequently to the hosted biological planar sample (Figure 1(B)).

In order to minimize the risk of tissue damage during sample handling and mounting, we have also devised specific procedures and realized auxiliary accessories.

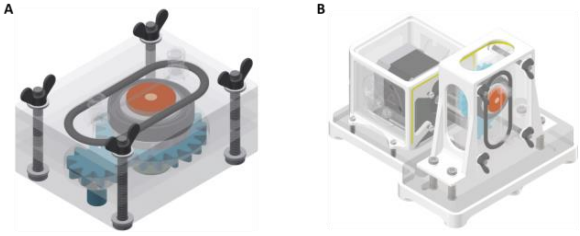

Figure 1 (A) Assembled culture chamber; (B) Entire system hosting the culture chamber and the motor.

The motor movement and the fluidic circuit are controlled by a custom electronic interface aimed at setting and monitoring of the experimental parameters. The WSS acting on the sample can be applied by means of either a parametric protocol or an *in vivo*-like protocol. In the parametric protocol TAWSS, OSI, CFI initial values are set, and the control unit automatically calculates and sets the motion protocol. In the in vivo-like protocol a specific hourly law is applied, as obtained from *in vivo* measurements.

Results and discussion

Up to now, the device has been successfully tested by performing preliminary bench tests: the hydraulic seal is guaranteed up to 780 mmHg and it has been tested for up to 5 days at 100 mmHg; the detection system (distance sensor) average sensitivity has been evaluated approximately 300 *mV/mm*. Biological tests on endothelial cells are ongoing, to verify biological aspects (sterility maintenance, vitality, cell orientation). Thereafter we will perform preliminary experiments with aorta patches to verify the effects of different solicitation patterns on the tunica intima.

The developed system represents a step forward the current state of the art enabling the application of controlled atherogenic/atheroprotective WSS and investigating their effects, no longer only on a cellular layers, but also on whole vascular samples. In this way we will examine the complex mechanobiological interactions that occur in the subendothelial tissue in the early stage of the pathology evolution.

References

[1] Cunningham K.S. et al, *Lab Investig*, 85:9–23, 2005.
[2] Peiffer V. et al, *J Biomech*, 46: 2651–2658, 2013.

EFFECT OF MICROGRAVITY ON CALCIUM AMOUNT USING A BONE REMODELLING MODEL

Andrada Pica (1), Andrea Marinozzi (2), Franco Marinozzi (1), Fabiano Bini (1)

1.Department of Mechanical and Aerospace Engineering, "Sapienza" University of Rome, Italy;
2. Orthopedy and Traumatology Area, "Campus Bio-Medico" University, Italy

Introduction

Spaceflight and prolonged bed rest represent conditions that induce significant increment of bone resorption, especially in the lower limb region. Bone remodelling is based on a feedback loop between mechanical loading and biochemical activity of bone cells that compose the basic multicellular unit (BMU). The bone dynamic behaviour is related also to the local chemical environment, e.g. it is involved in calcium homeostasis. In addition to available studies present in literature, the aim of this work is to investigate the correlation between calcium concentration in bone fluid and the mechanical stimulus.

Methods

The dynamics of bone cells are described by the algorithm proposed in [1]. Mechanotransduction is represented by the response of the osteocytes subjected to a mechanical stress [2]. According to [2], the nitric oxide (NO) and prostaglandin E2 (PGE2) use the RANK-RANKL-OPG pathway to influence bone cells interactions. The rate of change in bone area is function of the areas resorbed and formed by BMUs, activation frequency and normalized cells population [3]. The time variation of calcium concentration in bone fluid is evaluated in function of the normalized osteoblasts and osteoclasts population [4]. The simulation (Figure 1) is performed assuming average values of the BMUs parameters within the human trabecular tissue. Since the value of the activation frequency (f_a) is still debated, we considered two different values, i.e. f_{a1}= 0.006 BMU/mm^2/days from experimental measurements on the iliac crest [3] and f_{a2}= 0.012 BMU/mm^2/days estimated for the femoral head [5]. For 1g gravity conditions, the load is set to obtain a strain ε=1500 με [6] in the trabecular sample, while in microgravity a mechanical stimulus of F=0 N [4] is considered.

Results

We evaluated the influence of the mechanical stimulus and BMU activation frequency on the temporal evolution of mineralized bone area and on the calcium concentration in bone fluid (Figure 2).

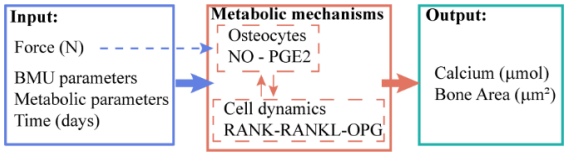

Figure 1: Workflow of the bone remodelling model

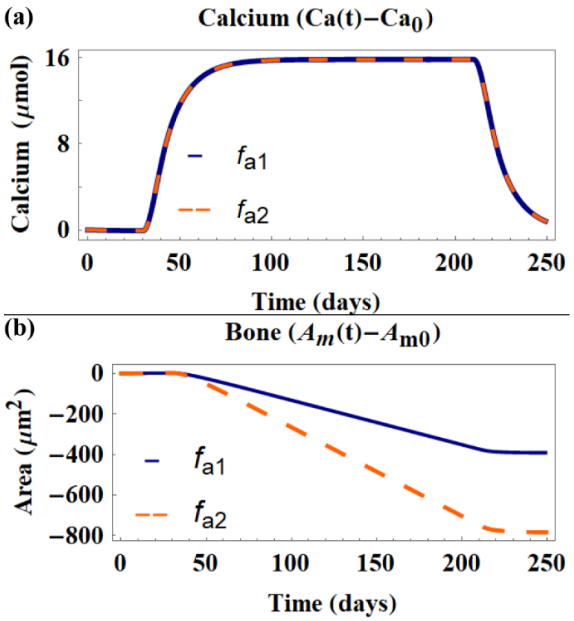

Figure 2: Temporal evolution of bone fluid calcium (a) and bone area (b).

A 250 days simulation is performed: the first 30 days are characterized by 1g gravity conditions, followed by 180 days of microgravity. Finally, the last 40 days are defined by a return to 1g gravity conditions.
For both values of BMU f_a, the decrement of the mechanical force due to microgravity leads to a diminution of bone area and subsequently to an increment of calcium content in bone fluid.

Discussions

BMU f_a represents an important factor in bone remodelling, i.e. increase of f_a contributes to bone loss. Conversely, variations of BMU f_a do not affect the temporal evolution of calcium concentration. In addition, the model highlights that calcium concentration in bone fluid varies in microgravity conditions.

References

1. Lemaire et al, J. Theor. Biol., 229:293-309, 2004.
2. Maldonado et al, Conf. Proc. 28th IEEE EMBS Conference, pp. 3154-3157, 2006.
3. Martin, Yearb. Phys. Anthropol., 28:227-236, 1985.
4. Pennline, NASA/TM—2009-215824, 2009.
5. Hazelwood et al, 49th Annual Meeting of the Orthopaedic Research Society, Poster number: 0454, 2003.
6. Turner, Bone 12:203-217, 1991.

AGING-RELATED BIOPHYSICAL CHANGES LEAD TO T-CELL STIFFENING, LOSS OF MIGRATION AND CELLULAR DIVERGENCE

Blanca González-Bermúdez, [1] Hikaru Kobayashi, [2] Aldo Abarca-Ortega, [1] Miguel Córcoles-Lucas, [1] Mónica González-Sánchez, [2] Mónica de la Fuente, [2] Gustavo V. Guinea, [1] Gustavo R. Plaza [1]

1. Dept. of Materials Science & Center for Biomedical Technology, Universidad Politécnica de Madrid, Spain; 2. Universidad Complutense de Madrid, Spain.

Introduction

To unravel the nature of aging-related changes across immune cells, and its impact on both efficient and dysfunctional immune responses (immunosenescence), we must first gain a better understanding on the mechanical-functional-structural regulatory processes at the cellular level [1]. Although many studies have examined how the T-cell subtype frequency and cell function evolve with age, few have explored the aging-related biophysical changes and their contribution to immunosenescence.

In this work we report a longitudinal biophysical and internal-ordering characterization of mice T cells ($CD4^+$ and $CD8^+$ T cells, in both naïve and memory state).

Methods

Longitudinal strategy for multiple biophysical and biomolecular measurements

To longitudinally characterize the population of T cells, we performed biophysical assays following the specific sequence shown in Figure 1: (i) cell migration, (ii) cell deformability, (iii) internal composition and (iv) morphology.

Mapping correlations with age and heterogeneity

111 biophysical and biomolecular parameters were analyzed to identify: (a) Biophysical signatures of aging (by a Spearman's correlation matrix of the multi-parameter nature datasets and clustering analysis) (b) Inter and intra-individual heterogeneity of cell subpopulations (using a Jaccard similarity approach)

Figures

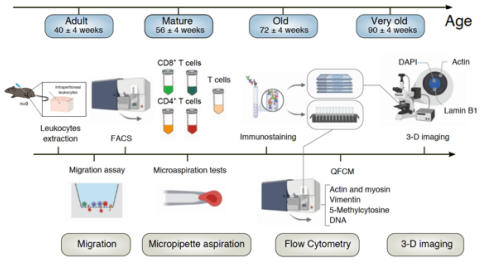

Figure 1: Longitudinal methodology to evaluate T-cell age-related biophysical and biomolecular changes

Results and discussion

Quantifying biophysical and biomolecular changes in T cells across the lifespan.

Many biophysical parameters (e.g. cell's apparent stiffness, relative nuclear size, cell-to-cell heterogeneity) were not stable across lifetime and correlated with a loss of T-cell functionality (i.e. spontaneous migration). We observed a persistent stiffening of T cells across all cell subtypes, which may play a role in immune dysfunction with age.

We further identified correlations between cell's apparent stiffness and relative size of the nucleus (stiffer part of the cell), DNA-methylation (associated with nucleus condensation) and nuclear lamin B1, suggesting a biophysical interpretation of changes at the T-cell level during the process of immunosenescence.

Intra-individual and inter-individual heterogeneity of T cell subpopulations increase by age

Biophysical parameters of all mice and T-cell subtypes clustered distinctly by age group, not by individuals or cell type, demonstrating that the repertoire of changes in cell's biophysical measurements resulted from individual's aging process.

Conclusions

In the study we have found important aging-related changes in various features of the cells and correlations among the parameters, providing support to explain the observed decrease of migration ability with age. The results show also a divergent evolution of T-cell properties for a given individual, revealing the progressive increase of complexity of the immune-cell populations.

References

1. González-Bermúdez et al. Soft Matter, 16:5669-5678, 2020. DOI: 10.1039/D0SM00648C.

Acknowledgments

The authors received support through the projects MAT2016-76847-R and MAT2016-79832-R, and from grants Tec4Bio-CM/P2018/NMT-4443 and NEUROCENTRO-B2017/BMD-376.

CONVERGENCE OF HIPPO/TGF-β PATHWAYS IN MECHANICAL ACTIVATION OF VENOUS AORTO-CORONARY BYPASS FAILURE

Gloria Garoffolo (1), Rosa Vono (2), Giada Andrea Cassanmagnago (3), Anita Thomas (4), Matthijs S Ruiter (1), Matteo Carrara (5), Claudio Saccu (1), Marco Argrifoglio (6), Monica Soncini (7), Gianfranco B Fiore (7), Fabio Martelli (5), Gianluigi Condorelli (3), Paolo Madeddu (4), Gaia Spinetti (2), Maurizio Pesce (1)

1. Centro Cardiologico Monzino, IRCCS, Italy ; 2. IRCCS Multimedica, Italy; 3. Humanitas Research Hospital, Italy; 4. University of Bristol, UK; 5. Policlinico S. Donato, IRCCS, Italy; 6. Università di Milano, Italy; 7. Politecnico di Milano, Italy.

Introduction

Implantation of saphenous vein (SV) grafts in coronary position determines vessel wall remodeling, intimal hyperplasia and graft failure. This causes recurrence of cardiac ischemia in patients with coronary artery disease (CAD). We have recently found that experimentally exposing human saphenous veins (SV) to coronary-like counter-pulsed high flow/pressure regime induces release of matricellular protein Thrombospondin-1 (TSP-1) by resident smooth muscle cells (SMCs) due to cell strain-dependent effects. This release recruits adventitial resident progenitors to a pro-fibrotic phenotype associated to stenosis of the coronary bypass in a large animal model of SV carotid interposition [1]. In the present work, we show the cooperation of TSP-1 (a known component of the TGF-β *pro*-fibrotic pathways) with intracellular pathways activated by strain sensing in fibrotic differentiation of the adventitial SV progenitors (SVPs).

Methods

Human SVs for tissue/cell culture were obtained during coronary artery bypass or SV stripping surgery. SVs were conditioned mechanically with a dedicated coronary pulse duplicator [2] up to two weeks. SVPs were derived as in [3], and subjected to uniaxial strain stimulation (10% deformation; 1Hz) for 1 to 3 days of culture using a commercial platform (FlexCell). RNA of strained cells was extracted and prepared for whole genome RNAseq analysis. Bioinformatic tools were employed to perform pathway analyses of the mostly represented networks in the data set of genes differentially regulated by mechanical stress in SVPs. To validate gene expression data, SVPs were cultured and stimulated with TGF-β, TSP-1, or combinations of the two factors, followed by quantitative real-time PCR (Q-PCR) and immuno-fluorescence/-histochemistry.

Results

SVPs mechanosensitivity was assessed by analysis of nuclear alignment and cell shape index/spread areas after straining. Mechanically stimulated cells showed a significant increase in their basal motility, as verified by migration assays in the presence of medium supplemented with 10% serum. Analysis of transcripts differentially up/downmodulated in strained *vs.* control cells (performed by whole genome RNAseq), showed a significant enrichment of the HIPPO/YAP/TEAD and TGF-β/SMAD transcriptional circuitries in cyclically strained cells. In support of this evidence, immunofluorescence showed an increase in the number of cells with nuclear localized YAP in strained *vs.* control SVPs. This was associated to an increase in direct targets expression (revealed by Q-PCR) and it was mediated by formation of a YAP/TEAD transcriptional complex, as verified by co-immunoprecipitation experiments. Convergence of the Hippo and TGF-β/TSP-1 pathways was confirmed by culturing SVPs in the presence of TGF-β and TSP-1, alone or in combination, followed by analysis of the YAP target genes and fibrosis markers expression. Data showed that in the presence of TGF-β, with or without TSP-1, YAP-dependent targets were upregulated. Conversely, the two factors, only in combination, increased above controls the level of nuclear-localized YAP, that of pSMAD2 (one of the TGF-β pathway nuclear signaling transducers) and collagen secretion. Finally, nuclear localization of YAP was detected in human SVs exposed to coronary flow mechanics *ex vivo* as well as in arterialized SVs in pig carotid interposition model.

Discussion

Our data establish for the first time a cooperation between the matricellular changes occurring in the SV wall exposed to coronary mechanics, and paracrine effects mediated by convergent activation of Hippo/TGF-β pathways in failure of the human aorto-coronary bypass. Since pharmacological inhibition of the YAP/TEAD complex reverted the upregulation of YAP-dependent target genes in SVPs treated with TGF-β (±TSP-1) and reduced their migration *in vitro*, we conclude that targeting YAP *in vivo* may retard the progression of the SV bypass remodeling caused by *pro*-fibrotic activation of adventitial cells, by desensitizing SVPs to the TGF-β biological effects. These results have a strong translational applicability to reduce the burden of venous bypass failure in patients with chronic CAD.

References

1. Garoffolo et al., Theranostics, 2020, 10(6): 2597-2611
2. Piola et al., Ann Biomed Eng, 2017, 45(4):884-897
3. Gubernator et al. Arterioscler Thromb Vasc Biol., 2015 35(3):675-88

CARDIAC CELL IN-SILICO MODEL FOR ENHANCED CELL-EXTRACELLULAR MATRIX INTERACTIONS

Pau Urdeitx (1,2), Mohamed H. Doweidar (1,2)

1. Mechanical Engineering Department, School of Engineering and Architecture (EINA), University of Zaragoza, 50018, Zaragoza, Spain;

2. Aragon Institute of Engineering Research (I3A), University of Zaragoza, 50018 Zaragoza, Spain.

Introduction

Cell processes such as migration, differentiation, proliferation, and apoptosis play a key role in tissue development. These processes are governed by complex mechanical, electrical, and chemical stimuli, as well as cell-cell and cell-extracellular matrix (ECM) interactions. In fact, mechanical and electrical stimulation seems to be particularly relevant to determine the functional properties in cardiac tissues [1]. To determine the adequate conditions to improve tissue properties is not straightforward. In this sense, computational methods can be helpful to reduce the number of *in-vitro* experiments [2].

Here, we develop a computational model to evaluate cardiac cell response into 3D hydrogel matrices, in response to mechanical and electrical stimulation. The purposed model takes into account cell processes such as cell migration, differentiation, proliferation, as well as collective cell response [3,4].

Material & methods

Cell response has been evaluated through the analysis of the cell-cell and cell-ECM interaction. Cells are implemented using the commercial Finite Element software Abaqus, through user element subroutines (UELMAT). Thus, cell internal deformations are obtained as a response to the cell mechanotaxis, and cell migration forces are defined through the balance of the acting forces on the cell. These forces include traction forces, $\mathbf{F}_{trac}$, due to the contraction of the Actin-Myosin machinery, protrusion forces, $\mathbf{F}_{prot}$, due to the random generation of cell protrusions, electric forces, $\mathbf{F}_{elec}$, due to the electrostatic effect, and drag forces, $\mathbf{F}_{drag}$, due to the movement on a viscous ECM. Thus, the force balance is defined as [3,4]:

$$\mathbf{F}_{prot} + \mathbf{F}_{trac} + \mathbf{F}_{drag} + \mathbf{F}_{elec} = 0. \qquad (1)$$

Cell processes such as differentiation, maturation and apoptosis are defined as a function of the mechanical stimulus, $\gamma_c(t)$, of the cell as:

$$\gamma_c(t) = \frac{1}{n}\sum_{i=1}^{n} \mathbf{e}_i : \boldsymbol{\varepsilon}_i : \mathbf{e}_i^T, \qquad (2)$$

where $\boldsymbol{\varepsilon}_i$ is the strain tensor on each membrane node, i, and $\mathbf{e}_i$ is the direction vector from the membrane node towards the cell centroid. Thus, cell state, including cell differentiation and cell apoptosis, is defined as:

$$\text{Cell state} = \begin{cases} m & \gamma_{low} < \gamma_c \leq \gamma_{myo} \\ apop. & \gamma_{apop} < \gamma_c \end{cases}, \qquad (3)$$

Results

Cell behavior has been studied varying the ECM stiffness in the range of 10-40 kPa [3]. Electric stimulation has been applied as continuous, pulsatile, and alternating electric fields, in the longitudinal direction, and for intensities in the range of 50-350 V/m [4].

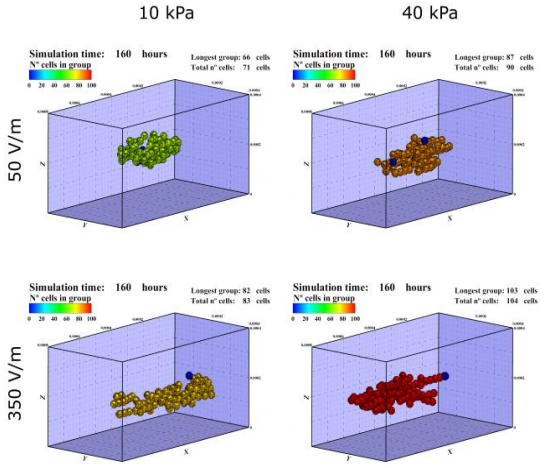

Fig. 2. Cell form elongated groups in response to the electrical field, proportional to its intensity.

Conclusions

A computational model to study cardiac cell mechanical and electrical stimulation has been developed. The model has been applied to study the formation of cellular aggregates in different environments of mechanical and electrical stimulation, which include the variation of the stiffness of the ECM and the application of continuous, pulsed, and alternating electric fields. Cells are polarized in the direction of the electric field, proportionally to its intensity, which induces the formation of elongated cell groups. Increasing stiffness reduces the effect of the electric field. The continuous and pulsating electric fields generate an excessive drag on the cells. Thus, better results have been obtained for alternating electric fields with low stiffness of the ECM.

References

1. W.L. Stoppel, et. al, Adv. Drug Deliv. Rev. 96:135–155, 2016.
2. D. Wendt, et. al, Adv. Mater. 21:3352–3367, 2009.
3. P. Urdeitx et al, Mathematics, 8:1875, 2020.
4. P. Urdeitx et al, Comput. Mech., 66:1003-1023, 2020.

Acknowledgements

The authors acknowledge the financial support from the Spanish Ministry of Science and Innovation (PID2019-106099RB-C44/AEI/10.13039/501100011033), the Government of Aragon (DGA-T24_20R), and the Biomedical Research Networking Center in Bioengineering, Biomaterials and Nanomedicine (CIBER-BBN).

CLUTCH MODEL IMPLEMENTATION FOR RESIDUAL STRESSES IN ECM

Valeria Panzetta (1), Claudia De Clemente (1), Sabato Fusco (2), Paolo A. Netti (1)

1. Centro di Ricerca Interdipartimentale sui Biomateriali, Università degli Studi di Napoli Federico II, 80125 Napoli, Italy; 2. Dipartimento di Medicina e Scienze della Salute "Vincenzo Tiberio", Università del Molise, Campobasso, 86100, Italy

Introduction

The mechanical state of the extracellular matrix (ECM) has a great impact on cell behaviour. The mean by which cells can sense and react to changes in the surroundings are focal adhesions, multi-protein aggregates that connect the actin cytoskeleton to the ECM. Through the actuation of pulling forces exerted on actin fibres by molecular motors, the cell responds differently according to the substrate's mechanical reaction ('motor-clutch' mechanism). Among ECM mechanical cues, it is known that biological tissues develop an internal tension; usually, this tension persists after the removal of any external loading, thus being defined as residual stress. The relevance of this tension has been revealed in many physiological and pathological contexts (1-3). Here, to incorporate the contribution of such residual stress/strain energy on ECM, we propose a modification of the clutch model, a mathematical model that simulates adhesion formation and cell probing of the substrate (4).

Materials and Methods

To incorporate the contribution of strain energy, an additional spring orthogonal to the ones already present in the original clutch model is here introduced; the orthogonal spring takes memory of the ECM strain energy when axially deformed before any interaction with cell molecular clutches can occur (Fig. 1).

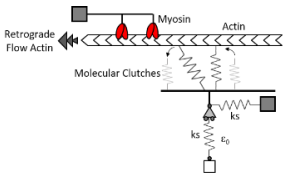

Figure 1: Physical representation of the modified clutch model.

The equation for mechanical equilibrium is:

$$k_s x_s + k_s \Delta l * \cos(\alpha) + k_c n_{ceng} x_s = k_c \sum_i^{n_{ceng}} x_{c,i} \quad (1)$$

where k_s and k_c are the substrate and clutch spring constants, x_s and $x_{c,i}$ are their positions, as consequence of the deformation process, and n_{ceng} is the number of engaged clutches. Δl and α are function of strain ε and length of substrate spring l:

$$\cos(\alpha) = \frac{x_s}{\sqrt{l^2 * (1+\varepsilon)^2 + x_s^2}} \quad (2)$$

$$\Delta l = \sqrt{l^2 * (1+\varepsilon)^2 + x_s^2} - l \quad (3)$$

Results

To evaluate the influence of strain on the optimum number of clutches (indicative of the length of focal adhesions involved in the adhesion process), the model has been implemented with 4 different levels of strain ε (0, 0.25, 0.5 and 1). As shown in Fig. 2, increase of the strain shifts the optimum number of clutches, represented by the minimum of the curve, and, consequently, traction forces towards higher values. Results suggest that cells undergo a reinforcement process, stiffening the cytoskeleton in response to the ECM stress/strain energy. It is hoped that the integration of this environmental feature in a mathematical model could give more insights on the mechanism of cell mechanosensing and explain cell behaviour during physio-pathological processes, such as embryogenesis and tumour onset and progression.

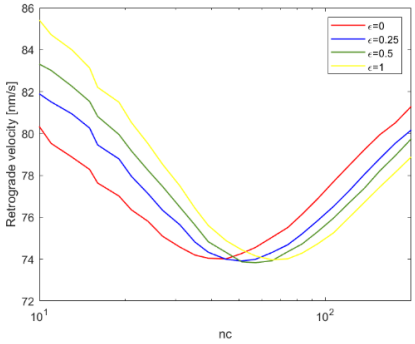

Figure 2: Retrograde actin velocity as a function of n_c predicted by the modified clutch model.

References

1. Han and Fung, Am J Physiol-Heart C, *270*(2), H750-H759, 1996.
2. Nia et al, Science 370.6516, 2020.
3. Panzetta al, PNAS, 116.44: 22004-22013, 2019.
4. Bangasser et al, Biophys J 105.3: 581-592, 2013.

INCREASED NUCLEAR PERMEABILITY BASED ON LAMIN A/C RUPTURES AS A CONSEQUENCE OF APPLIED IN-FLOW FORCES

Maria Isabella Maremonti (1), David Dannhauser (1), Valeria Panzetta (1), Paolo Antonio Netti and Filippo Causa (1)

1. Interdisciplinary Research Centre on Biomaterials (CRIB) and Dipartimento di Ingegneria Chimica, dei Materiali e della Produzione Industriale, Università degli Studi di Napoli "Federico II", Piazzale Tecchio 80, 80125 Naples, Italy

Abstract

The nuclear envelope (NE) comprising the inner and outer nuclear membranes, nuclear pore complexes, and the nuclear lamina, separates the chromatin from the cytoplasm, providing structural support to the nucleus. Particularly, the lamina is a dense protein meshwork, predominantly constituted by Lamin A/C [1]. In general, loss of NE integrity is associated to aging processes or to pathological conditions, such as cancer progression. Tumor cells highly force the nucleus to deform once they move into narrow spaces of the tissues, promoting cancer progression [2]. In recent years, it has been demonstrated that the NE structure integrity is directly associated to trafficking phenomena of different sized molecules and proteins, such as Yes-Associated Protein (YAP). Regardless adhesion or actin cytoskeleton recruitment, it has been verified that the application of a force on the nucleus is enough to induce YAP translocation, from the cytoplasm to the nucleus [3]. This direct effect of nuclear deformation could affect nuclear pores or it could take to rupture-repair mechanisms of the NE, at the Lamin A/C level. These evidences of improved nuclear permeability would place the nucleus and its envelope at the centre stage of mechanosensing phenomena in single cells [3].

To model direct application of forces on the nucleus and subsequently to monitor the YAP trafficking phenomena across the NE, we impose to suspended cells highly precise and controlled fluid-flow compressive forces, based on a viscoelastic solution moving into a microfluidic chip [4]. In particular, our approach permits to analyze cell responses in a wide range of applied forces (1μN-10^2μN), allowing to reach never explored high entities on single cells, in a completely contactless and viable manner. Cells are forced to pass into a sequence of microfluidic cross-sections properly conceived in order to impose variable levels of force, by simply tuning viscoelastic fluid properties, to obtain different degrees of deformation [4]. In fact, multiple force levels allow to recognize healthy or pathological cell types referring to the correlation of biophysical and mechanical parameters [4]. At the highest level of force, cells express a nuclear deformation, resulting in a YAP translocation from the cytoplasm to the nucleus, after the in-flow deformation. Lamin A/C alterations have been addressed to be responsible in such protein redistribution, confirming that possible rupture-repair mechanisms have been induced by the force application. Particularly, we observe that YAP is localized predominantly into the cytoplasm before deformation, whereas it results to be uniformly distributed, up to the nucleus level, after force imposition. To further verify if the Lamin A/C alteration promotes molecular trafficking across the NE, we monitor Hoechst fluorescent dye influx into the nucleus. In particular, we verify that the Hoechst diffusion is more rapid into the nucleus once the cell was deformed, confirming that the molecular trafficking is promoted.

Our results unveil enhanced nuclear permeability mediated by an altered lamina expression and YAP trafficking with potential general applicability in gene transcription.

Figure

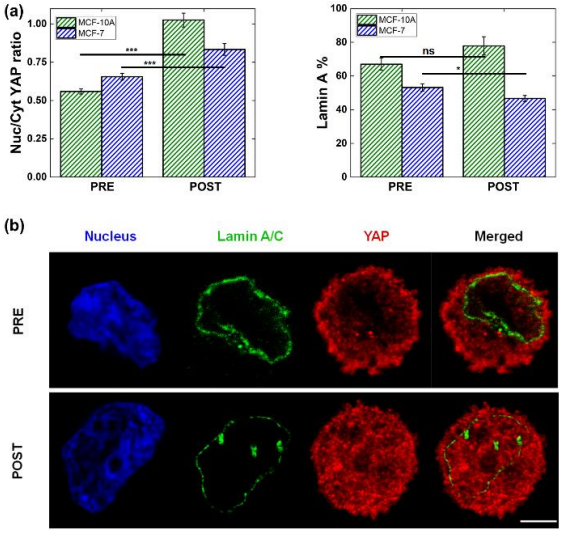

Figure 1: a) On the left we report the change in Nuc/Cyt YAP ratio, in MCF-10A and MCF-7 breast cells, before (PRE) and after deformation (POST). We highlight that both cell lines express a nuclear redistribution of YAP after deformation. On the right, we show the Lamin A/C contour variation. The significative result for MCF-7 presents a reduction in Lamin A/C content after deformation ($^{***}p<0.001$, $^{*}p<0.05$, $^{ns}p>0.05$). b) We present confocal images of nucleus (blue), Lamin A/C (green) and YAP (red), in PRE (top) and POST (bottom) condition for MCF-7. For PRE, the merged image shows how the nucleus is empty from YAP and well delimited by the Lamin A/C contour. For POST, YAP results to be equitably distributed and the Lamin A/C more rarefied.

References

1. P.M. Davidson et al., Trends in Cell Biology, 24:247-256, 2013.
2. C.M. Denais et al., SCIENCE, 353-358, 2016.
3. A. Lomakin et al., Developmental Cell, 43:547-548, 2017.
4. D. Dannhauser et al., Lab On Chip, 20:4611-4622, 2020.

ASSESSING CORTICAL BONE ADAPTATION USING A MULTISCALE, MECHANOBIOLOGICAL APPROACH BASED ON BEAM-THEORY

Corey Miller (1), Edmund Pickering (1), Enrico Dall'ara (2), Peter Pivonka (1)

1. Queensland University of Technology, Australia. 2. University of Sheffield, England.

Introduction

Mechanical loading (i.e., exercise) is well known to influence bone mass [1]. Experimental studies in mice tibia have shown that the adaptation response occurs quasi-linearly with respect to external load magnitude [2]. The response has also been identified to occur at different spatial locations throughout a bone [2, 3].

While μFE modelling is the gold standard to obtain strain distributions in a whole bone, long bones are known to act mechanically like beams [4]; Here, we use beam theory equations as an alternative method to rapidly calculate strain distributions within cortical bone tissue in the mouse tibia.

Using the strain distribution across the tibia, we then formulate a multiscale mechanobiology model of bone adaptation. The aim of this work is to rapidly calculate adaptive strain signals and bone's subsequent adaptation response. Two major objectives are:

1. Determine a numerical link between mechanical loading and localized bone adaptation rates.
2. Guide the development of bone adaptation algorithms to predict bone anabolic and catabolic responses based on applied loads.

Materials and Methods

Data used here was collected by our collaborates from the University of Sheffield [5]. In summary, 6 skeletally mature mice were subjected to a 10 N right tibial axial load three times a week on weeks 2 and 4 of a 5-week schedule. Right tibiae were scanned on weeks 1, 3, 5 and 7 using high resolution μCT (isotropic voxel size = 10.4 μm).

Mouse tibia μCT images were rigidly registered to a common reference frame and, and the bone geometry is extracted through segmentation. The mechanical adaptation algorithm follows the 4 steps outlined in Figure 1, applied to four selected cross-sections: 1) cortical surface points (η_i) are extracted, and cross-sectional properties are calculated, 2) external loads (F) are converted into an adaptive signal (Ψ) through beam theory analysis, 3) the adaptive signal is compared against a mechanostat model, and 4) changes are applied to η_i as required. This process is repeated each day until the end of experiment.

The adaptive response was measured by comparing the position of the surface after the adaptation algorithm to the original state. Changes were calculated as a net distance between the two states. Model parameters were adjusted based on comparison of simulated net distance between experimental and simulated findings.

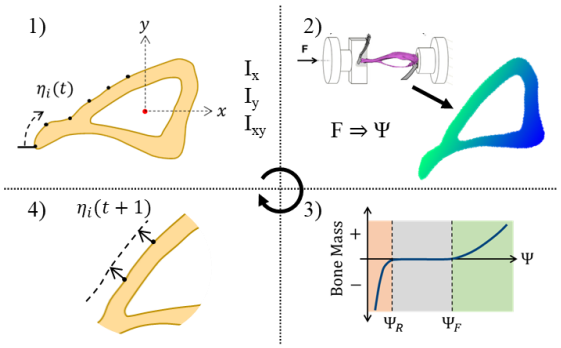

Figure 1: Processing steps of the beam-theory based adaptation model. 1) Geometrical property analysis. 2) Calculate load induced adaptive signal. 3) Compare against mechanostat model. 4) Update geometry

Results

Preliminary results of the simulation for periosteal formation are in good agreement with experimental findings. Considering a 10 N load case, a gradient-based formation response using a longitudinal strain signal provides qualitatively similar trends to those found experimentally as shown in Figure 2.

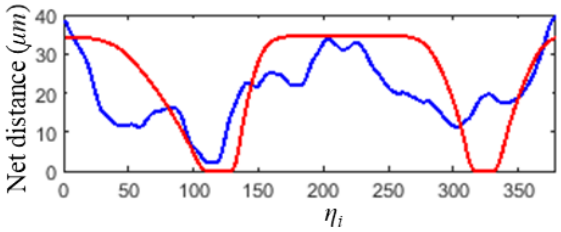

Figure 2: Comparison of adapted (blue) and simulated (red) formation changes across the periosteal surface in the mid-diaphysis of the mouse tibia.

Conclusion and Future Work

The strains calculated through beam theory have been shown as effective drivers of mechanical adaptation on the cortical surface. Additional work will be conducted to transform longitudinal strain into strain energy density, the common metric used in adaptation studies. Furthermore, we intend to expand this model through the inclusion of cell dynamics to present a biologically accurate representation of the adaptation response.

References

1. Wolff J. Das Gesetz der Transformation der Knochen, 1892
2. Sugiyama et al, J Bone Miner Res., 27:1784-1793, 2012.
3. Galea et al, Bone, 133:115255, 2020
4. Ashrafi et al, Biomech Model Mechanobiol. 19:2499-523, 2020
5. Roberts et al, Sci Rep, 10:8889 2020

MEASURING VISCOELASTICITY IN TENSILE LOADED COLLAGEN FIBRILS THROUGH A NONLINEAR RHEOLOGICAL MODEL

Martin Handelshauser (1)(2), Orestis G. Andriotis (1), Martina Marchetti-Deschmann (2), Philipp J. Thurner (1)

1. Institute of Lightweight Design and Structural Biomechanics, TU Wien, Austria;
2. Institute of Chemical Technologies and Analytics, TU Wien, Austria;

Introduction

Soft tissues generally exhibit viscoelastic properties, hence putting forth the research question how this behavior extends to the smallest mechanically relevant structural elements, the individual collagen fibrils. While collagen fibrils have been reported to show viscoelastic behaviour [1], some published methods for the determination of viscoelastic material properties of collagen fibrils are elaborate and complicated by design [2]. From a pragmatic viewpoint it is desirable to find the simplest model that can describe the viscoelastic behaviour of collagen fibrils. In this context, nonlinear rheological models are a promising approach. Here, we propose the use of the nonlinear rheological Maxwell model and its constitutive equation for assessing viscoelastic properties of collagen fibrils experienced during tension testing.

Methods

The nonlinear rheological Maxwell model solved for a constant strain rate was used here. Its constitutive equation for stress (eq. 1) and apparent tensile modulus (eq. 2) are given below:

$$\sigma(t) = \left(\frac{d\varepsilon(t)}{dt}\right)^{\frac{1}{n}} \mu \left(1 - e^{-t/\tau^n}\right)^{\frac{1}{n}} \qquad (1)$$

$$E_{tens}(\varepsilon) = \frac{d\sigma}{d\varepsilon} = \frac{\sigma(t)}{nk\tau^n}\left(e^{\frac{\varepsilon}{k\tau^n}} - 1\right)^{-1} \qquad (2)$$

with the stress $\sigma(t)$[MPa], the apparent tensile modulus $E_{tens}(\varepsilon)$[MPa], the strain $\varepsilon(t)$[m/m], the nonlinearity n[a.u.], the viscosity μ[MPa.s], the constant a[MPa] ($a = \mu/\tau$) and the relaxation time τ[s]. The model was fitted to experimental data, previously published by Andriotis et al. [3], using Matlab. In the analyzed dataset, tensile tests were conducted on collagen fibrils, exposed to varying concentrations of polyethylenglycol (PEG), dehydrating the fibrils with rising concentration.

Results

The nonlinear Maxwell model shows a high quality of fit ($R^2 = 0.99$) and the values for the apparent tensile modulus are in the same range as previously published results (figure 1(a)) [3]. The spring constant a is higher as the tensile modulus due to the viscous nature of the model (figure 1(b)). The viscosity is in a range of 10^{10} MPa.s, which resembles bitumen or molten glass (figure 1(c)). The relaxation time is found in a range between 10^5 to 10^8 s.

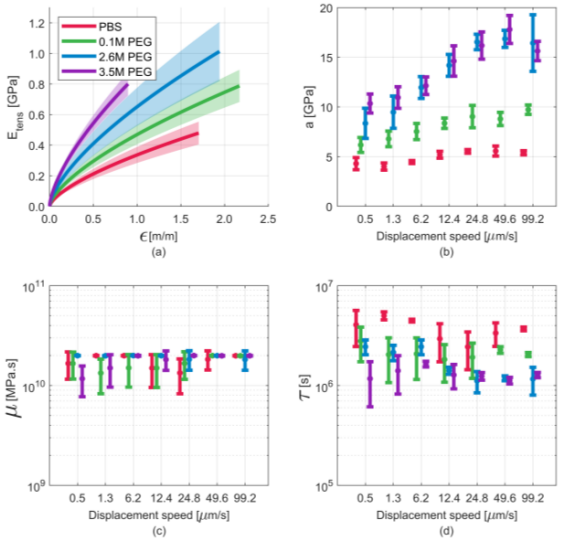

Figure 1: Apparent tensile modulus vs. strain from the nonlinear Maxwell model for different PEG-concentrations (a), spring constant a (b), relaxation time τ (c) and viscosity η (d) as function of displacement speed of the piezo and PEG-concentration; n = 0.6 for all fits (a-d).

Discussion

With the nonlinear Maxwell model, we can describe the viscoelastic behavior of collagen fibrils during tension. The results for the tensile modulus and spring constant seem dependent on displacement speed (figure 1(a,b)), while the viscosity and relaxation time seem not dependent on displacement speed (figure 1(c,d)). The tensile modulus is increasing faster at higher displacement speeds. Per the applicability of the Maxwell model the results also suggest collagen fibrils to be a highly viscous fluid. The nonlinear Maxwell model is a promising first step towards an easy to use rheological model capable of describing the viscoelastic properties of collagen fibrils. In future studies, further validation will be done through creep or stress relaxation experiments.

References

1. Svensson, R.B. et al., JMBBM, 3:112-115, 2010
2. Marino, M. and Vairo, G., JMPS, 73:38-54, 2014
3. Andriotis, O.G. et al., ACS Nano, 12:3671-3680, 2018

MATERIAL STRAIN ENERGY SENSING AS CELL MECHANISM TO RECOGNIZE IN-BORN STRESSES OF ECM

Sabato Fusco (1), Valeria Panzetta (2), Paolo Netti (2)

1. Dipartimento di Medicina e Scienze della Salute "Vincenzo Tiberio", Università degli Studi del Molise, Via F. De Sanctis 1, Campobasso, 86100, Italiy.; 2. Centro di Ricerca Interdipartimentale sui Biomateriali (CRIB), Università degli Studi di Napoli "Federico II", P.le Tecchio, 80, 80125, Napoli, Italy

Introduction

Concepts like in-born and out-born forces generated at cellular and extracellular matrix (ECM) level are pivotal in the field of mechanobiology. In particular, ECMs of musuloskeletal, cardiovascular, and dermal tissues are under tension also when in normal physiological condition and in absence of external solicitations. Such mechanical state is fundamental for morphogenesis contributing to the tissue organization, development and maturation. To date, great uncertainty still remains about the biophysical entity that cells are able to sense through focal adhesion (FAs): force or deformation and along this issue many experimental and modeling studies have been presented [1]. Clutch molecular model, for example, is the most used approach to model the basis of cell mechanosensing mechanism [2]. Its basic constitutive hypothesis is that FAs dynamics depends exclusively upon the stiffness of the ECM, or the force necessary to induce the deformation. This hypothesis does not account for contribution of inborn internal stresses within the ECM on FA dynamics, which, on the contrary, could have relevant effects on cell mechanics and functions. To assess this important issue, the cell-material interactions and mechanical features of the cytoskeleton were measured on substrate with different level of frozen internal stresses realized by imposing increasing percentages of pre-strain.

Methods

During the experimental campaign murine fibroblasts BALB/3T3 and murine preosteoblast MC3T3 were subjected to three different levels of uniaxial deformation (0%, 6%, 9%) via elastic substrates as polydimethylsiloxane (PDMS) and polyurethane (PU). Cell mechanics have been investigated on pre-strained and not pre-strained materials and before and after the stretching application. Intracellular particle tracking microrheology (PTM) was used to investigate the cell stiffness under culture condition [3]. The mechanical response of cells was collected immediately after the deformation and after 2 h.

Results and Discussion

The effect of a pre-strained material on cell mechanics was evaluated seeding cells both on substrates with no pre-strain and on substrate with levels of stretching equal to the percentage of deformations induced in the stretching experiments. Results indicated that cells recognize the existence of pre-strain, exhibiting a stiffer cytoskeleton on pre-strained PDMS compared to cells seeded on unloaded substrate, being equal the stiffness. Also we found that cytoskeleton' mechanics experiencing a pre-strained substrate was comparable to that measured after the stretching of the substrate to the same level of deformation. Along this line, the clutch molecular model has been adopted to simulate the cell response in the particular case of a pre-strained substrate and simulations were in agreement with experimental results only in the case of the addition of a factor accounting the strain energy of the substrate. Taking together simulations and experimental results, become clear that cell mechanosensing is not only driven by the stiffness of the substrate, but rather by the energy of deformation associated with the substrate.

References

1. Yip AK et al, Biophysical Journal, 104:19-29, 2014.
2. Chan CE, Science, 322:1687-91, 2008.
3. Panzetta V, PNAS, 44:22004-13, 2019.

COLLECTIVE MECHANOSENSING IN INFECTED CELL CULTURES

Francisco Serrano-Alcalde (1), María José Gómez-Benito (1), Prathima Radhakrishnan (2), Julie A. Theriot (2), Effie E. Bastounis (2) and José Manuel García-Aznar (1)

1. Aragón Institute of Engineering Research (I3A), University of Zaragoza, Spain; 2. Department of Biology and Howard Hughes Medical Institute, University of Washington, USA

Introduction

Mechanosensing is an important transduction mechanism that cells use to sense the surrounding environment. There are evidences of cell's stiffness adaptation to the extracellular matrix (ECM) [1] and cell migration depending on the ECM's stiffness, both for single cells [2] and collectives [3].

During infection, cells and pathogens communicate through chemical signals, but there are also mechanical variations that cells are able to detect and transduce. Intracellular bacterial pathogen *Listeria monocytogenes* (L.m.) modifies host cell stiffness or cell-cell junction tension [4] in order to facilitate its spread from cell to cell. In response to infection, an increment of the cellular activity of uninfected cells surrounding a locus of infected cells has been shown. These cells push against the infection locus provoking the extrusion of infected cells, leading to the creation of a "mound" of infected cells and limiting the ability of bacteria to spread along the basal cell monolayer.

Thus, it would be important to elucidate the mechanotransduction mechanism that cells internally are using to identify infection domains, as well as what their response is leading to infected cell extrusion.

Methods

We perform a simplified three-dimensional finite element model of a cell monolayer on a soft substrate. This model allows to consider cell-cell and cell-ECM adhesion, the radial geometry effect during cell extrusion and the effect of the vertical direction on mound formation (mound height), which were identified as key mechanisms in promoting cell extrusions [5]. Thus, and based on the experimental results, we propose a mechanotransduction mechanism where cells are able to detect infection loci (Figure 1).

In addition, we assume that a new adhesion is generated (Figure 1) to allow for cell protrusion, also supported by experimental results [5]. We assume protrusion is either constant irrespective of the level of tensional asymmetry or that protrusion is proportional to the tensional asymmetry level experienced by a given cell.

To model the cells, we differentiate two main parts: active (actomyosin contractility) and passive (cytoskeletal stiffness). We superimpose two meshes working in parallel and the infection is modelled by reducing both stiffnesses for infected cell domains.

We study different cases: all cells uninfected (1); infection and uninfected cells do (2) or do not (3) create new cell-ECM adhesions; and infection but none of the cells of the model form cell-cell adhesions (4).

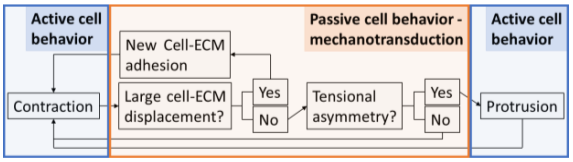

Figure 1: Cell mechanotransduction scheme. We propose a repetitive active contraction and passive behavior, where the cell decides the following active step. Depending on the cell decision, the next step will be a protrusion or a contraction.

Results and discussion

For the uninfected and isolated (no cell-cell adhesions) cases, the stress distribution in the cell is symmetric, so cells do not protrude. Nevertheless, for the other two cases, we observe tensional asymmetry, and those uninfected cells near the infection domain protrude provoking the extrusion of the infected cells. In addition, we propose a lineal protrusion law linking the level of asymmetry with the level of cell protrusion. This law obstructs extrusion when uninfected cells do not create new cell-ECM adhesions, and gives more relevance to the cell-ECM adhesion, as observed experimentally.

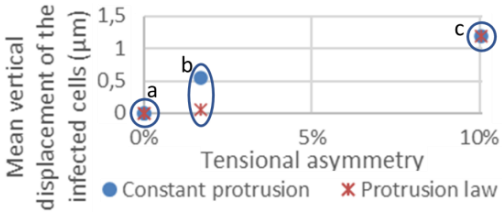

Figure 2: Mean vertical displacement of the infected cells depending on the tensional asymmetry for constant protrusion and applying the protrusion law. a) cases one and four; b) case two where uninfected cells cannot create new cell-ECM adhesions; and c) case three where uninfected cells can create new cell-ECM adhesions.

References

1. Solon et al, Biophysical Journal, 93:4453-4461, 2007.
2. Lo et al, Biophysical Journal, 79:144-152, 2000.
3. Sunyer et al, Science, 353:1157-1161, 2014.
4. Lamason et al, Cell, 167:670-683, 2016.
5. Bastounis et al, Developmental Cell, acepted

Acknowledgements

This research was supported by the Spanish Ministry of Economy and Competitiveness through project RTI2018-094494-B-C21. This project was partially financed by the European Union (through the European Regional Development Fund).

NUMERICAL ANALYSIS OF EFFECTIVE PRESSURE ON MICROFLUIDIC ASPIRATION OF A SINGLE CELL BEFORE CONSTRICTION

Aldo Abarca-Ortega, [1,2] Blanca González-Bermúdez, [1] Miguel Córcoles-Lucas, [1] Gustavo R. Plaza [1]

1. *Center for Biomedical Technology, Universidad Politécnica de Madrid, Madrid, Spain*
2. *Departamento de Ingeniería Mecánica, Universidad de Santiago de Chile, Santiago, Chile*

Introduction

Several techniques exist to evaluate the cell behavior under mechanical stresses, mainly analyzing its stiffness or viscosity, properties related to the internal structure and other biomarkers of cell state [1,2]. Various authors have reported great variability in the results of cellular mechanical properties. A commonly used procedure to test deformability of cells is to study their flow through rectangular constrictions. However, no detailed stress-strain analysis has been performed for the cell during its deformation, but instead simplistic approaches have been used [3,4], which may be an important reason for the variability of the experimental results. We hypothesized that accurate calculations could reduce the variability of results, normalizing the analysis between samples of different sizes and geometric configuration. We performed a study of standardized pressure tests of cells while they are aspirated through a rectangular channel of a microfluidic device over time using numerical simulations.

Methods

A hybrid finite element method with discretization into finite volumes was used. The meshing was performed with linear tetrahedral geometry elements of four nodes, providing good quality of meshing and with an amount according to the size of the geometry. The governing equation of incompressible flow of Navier-Stokes is developed considering a Newtonian fluid with constant viscosity in homogeneous and laminar flow. The study focuses on the development of pressure-velocity of the fluid, so that each proposed time step, or distance traveled by the cell as it enters the channel, is calculated independently from the previous one. The figure 1 shows the boundary conditions of the problem.

Figures

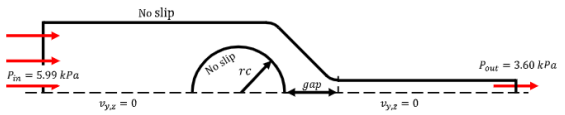

Figure 1: Boundary conditions of the numerical simulation.

Results and discussion

The analysis shows that the effective pressure increases inversely with the ratio of cell radius over width of the constriction, effect that is manifested when this is less than 1, i.e., the cell radius is less than the size of the constriction and there would be no strain by contact with the walls of the device. Less than half of the aspiration pressure is exerted on the cell effectively, the rest of the pressure drop is mainly due to the movement of the fluid in the areas surrounding the cell in the rectangular cross section of the device, which will never be covered entirely by the cell as it happens in other techniques for measuring mechanical properties. In all situations, the smaller the gap, the greater the effective pressure on the cell, growing with the same tendency in all cases, but in different measurements according to the geometric configuration of the associated model. Our model allows understanding the relationship between the observed deformation and the deformability parameters of the cell for a given aspiration pressure, which will be used in future analysis of deformability experiments. The model offers a way to correct equations obtained by dimensional analysis in previous works [4].

Conclusions

An increase in the effective pressure on the cell was found as it approaches the constriction, which responds to the reduction of the cross-sectional area and the corresponding hydrodynamic effects. Our model provides key equations for analyzing experiments involving the aspiration of cells through rectangular constrictions.

References

1. González-Bermúdez et al. Soft Matter, 16:5669-5678, 2020. DOI: 10.1039/D0SM00648C.
2. González-Bermúdez et al., 116:587-594, 2019. DOI: 10.1016/j.bpj.2019.01.004
3. M. Urbanska et al., Nat Methods, 17:587–593, 2020. DOI: 10.1038/s41592-020-0818-8
4. J. R. Lange et al., Biophys J, 109:26-34, 2015. DOI: 10.1016/j.bpj.2015.05.029.

Acknowledgments

This work was supported by grant S2018/NMT-4443 from Comunidad de Madrid, Spain; and by the National Agency for Research and Development (ANID) / Scholarship Program / Doctorado Becas Chile/ 2019 – CEL00011051 and to the Vicerrectoria de investigación, desarrollo e Innovación of University of Santiago.

VERSATILE BIOREACTOR COMBINING PERFUSION AND PEMF STIMULATION FOR BONE MECHANOBIOLOGY RESEARCH

Beatrice Masante (1), Stefano Gabetti (1), Andrea Cochis (2), Giovanni Putame (1), Elisa Fiume (3), Ileana Armando (1), Alessandro Sanginario (4), Francesco Baino (3), Lia Rimondini (2), Enrica Verné (3), Cristina Bignardi (1), Diana Massai (1)

1. Polito^{BIO}Med Lab, Dept. of Mechanical and Aerospace Engineering, Politecnico di Torino, Italy; 2. Dept. of Health Sciences, CAAD, University of Piemonte Orientale, Italy; 3. Dept. of Applied Science and Technology, Politecnico di Torino, Italy; 4. Dept. of Electronics and Telecommunications, Politecnico di Torino, Italy

Introduction

Bone tissue engineering (BTE) aims to develop functional bone tissue substitutes to be used as *in vitro* models for bone research, or ultimately as therapeutic solutions for bone grafting [1]. Bioreactors represent a key technology for *in vitro* generation and investigation of BTE constructs, providing a tightly controlled and monitored environment with user-defined physical stimuli [2]. In particular, flow-induced shear stress obtained by direct perfusion was demonstrated to strongly promote cell proliferation, osteogenic differentiation, as well as bone mineralization [3]. In parallel, non-invasive pulsatile electromagnetic field (PEMF) stimulation is empirically adopted in clinical practice for promoting the endogenous bone healing [4]. In this study, we developed a versatile bioreactor that allows combining tunable perfusion and PEMF stimulation for investigating the mechanotransduction pathways activated by biophysical stimulation applied in clinical practice to promote bone regeneration.

Methods

The bioreactor culture chamber, designed in Solidworks and printed by stereolitography (DentalSG resin, FormLabs), is composed of two hollow cylindrical screwable parts (priming volume = 2 ml), designed to house scaffolds of different sizes press-fit inserted in customized silicone holders (Fig.1A). The culture chamber is part of a closed-loop perfusion circuit, composed of a medium reservoir, a peristaltic pump (G100-1J, Longer), silicone tubing, stopcocks for medium sampling, and injection sites for cell/solution injection. PEMF stimulation is provided by a commercial stimulator (1.5 mT, 75 Hz, 1.3 ms). The bioreactor, suitable for incubator, allows both scaffold cell seeding (bidirectional flow) and perfusion culture (unidirectional flow). Stationary simulations of the magnetic field developing within the culture chamber were performed (COMSOL Multiphysics) and the PEMF stimulator solenoids were modelled as uniform coils with 1400 windings, each one powered by 260 mA. As preliminary biological tests, human mesenchymal stem cells (hMSCs, 4x10^6/scaffold) were seeded into commercial BioOSS porous scaffolds (Geistlich Biomaterials, Italy) and, after 48 h of static culture, transferred into the bioreactor culture chamber and exposed to unidirectional perfusion (0.3 ml/min, w/o PEMF stimulation) for additional 15 days (n=3). Equivalent control constructs were statically cultured for 15 days (n=3). The release of the early osteogenic marker alkaline phosphatase (ALP) was assessed.

Results

Acceptance tests confirmed the bioreactor suitability and ease of use. Simulations showed that the construct is exposed to a homogeneous magnetic field within the culture chamber (1.42 mT, Fig.1B). In biological tests, perfusion significantly increased the release of ALP compared to static culture (Fig.1C, *p<0.05).

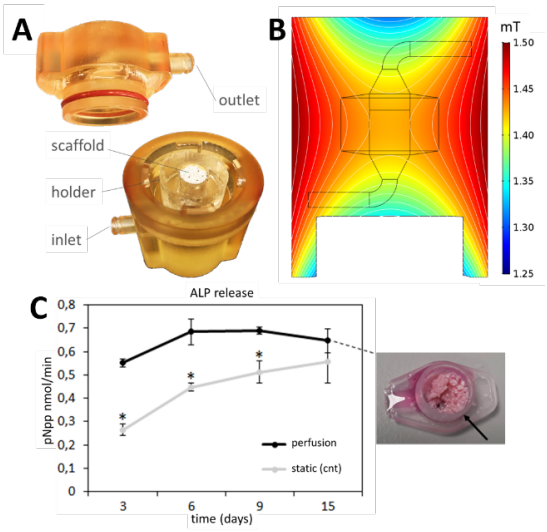

*Figure 1: A) Bioreactor culture chamber; B) Contour plot of the magnetic field modulus across the culture chamber; C) ALP release analysis (*p<0.05).*

Discussion

Preliminary tests confirmed the suitability of the bioreactor and showed that perfusion upregulates expression of ALP osteogenic marker. Systematic tests on BTE constructs cultured under individual or combined physical stimuli (i.e., perfusion and/or PEMF) are ongoing and will enable understanding the links between applied biophysical stimuli and biologic response in view of improved therapeutic treatments.

References

1. Amini et al, Crit Rev Biomed Eng, 40(5):363-408, 2012
2. Carpentier et al, Int J Artif Organs, 34(3):259–270, 2011
3. Wittkowske et al, Front Bioeng Biotechnol, 15;4:87, 2016
4. Massari et al, Int Orthop, 43(3):539-551, 2019

EX VIVO MODEL OF CYCLIC LOADING ON CORTICAL BOVINE BONES INDUCES BONE REMODELING

Jessica Schiavi-Tritz (1), Amala Remo (1), Laoise McNamara (1), Ted Vaughan (1)

1. Biomechanics Research Centre (BioMEC), Biomedical Engineering, School of Engineering, College of Science and Engineering, National University of Ireland, Galway, Ireland

Introduction

Bone remodeling is a continuous process whereby osteocytes elicit biochemical signals (e.g., RANKL/OPG) that regulate osteoblasts and osteoclasts to repair bone damages. Microdamage is formed under daily stresses in bone and can induce an increase of pro-osteoclastogenic markers synthesized by osteocytes around the damaged area [1] and could be at the origin of fatigue fracture in elderly [2]. An *ex vivo* model can be used to understand cell physiology in the presence of the native matrix, whilst also enabling exploration of biomechanical cues [3]. Such approaches might be applicable to study the mechanisms of bone repairing. However, to date an *ex vivo* model of bone remodeling in cortical bone has not been developed. In this study, the objectives were to (1) develop an *ex vivo* model where cortical bone was subjected to cyclic strains and (2) study *ex vivo* the remodeling of bone and its resistance to fracture.

Methods

***Ex vivo* model of bone remodeling induced by cyclic loading:** At the day of culling, bovine beam-shape bone samples were cut and preserved in PBS + 5% Pen/Strep + 2mM L-Glut overnight at 37°C. Cyclic strains were applied with a three-point bend system to induce damage with a regime at 16.66 mm/min for 5,000 cycles in sterile PBS in Evolve® bags (maximum deformation 6%). A control group was cultured under static conditions. **Metabolic activity:** Alamar Blue assays were performed after 1 and 7 days of *ex vivo* culture for each group (**Static**, **Loaded**) and normalized to weight. **Bone remodeling:** ALP activity was assessed in the media at day 1 and 7. After 24 hours cell culture conditioned media (CM) was collected from each group and stored at -80°C. RAW264.7 cells were cultured with CM for 6 days, after which the samples were stained for TRAP, to determine osteoclastogenesis, and imaged.
Histomorphometry: Samples were cultured with calcein for 3 days to label bone formation between day 4 and 7. Fluorescent images were captured at day 7. µCT scanning was performed at 3 µm resolution after labeling samples with $BaSO_4$ precipitate [4].
Fracture tests: Three-point bend flexural tests were performed after 7 days of culture at 1 mm/min.

Results

Bone was sectioned and cultured to maintain live osteoblasts and osteocytes. Calcein (Fig 1A) and HE staining (Fig 1B) indicated the presence of structures similar to bone remodeling cones (white arrow) in both groups after 7 days of culture. CM obtained 24 hours after the fatigue cyclic loading and added to RAW264.7 cells cultures demonstrated significantly increased osteoclastogenic potential compared to that from static samples (Fig.1C). Also, 7 days post-loading, empty space in the stimulated area, detected with the $BaSO_4$ precipitate were substantially increased in loaded samples compared to the static (0.11±0.02% *vs* 0.062±0.01% of bone volume, p=0.1). In addition, the ultimate load to failure was significantly decreased in loaded samples compared to static (478.8±62.05 N *vs* 808.3±119.3 N, p<0.05).

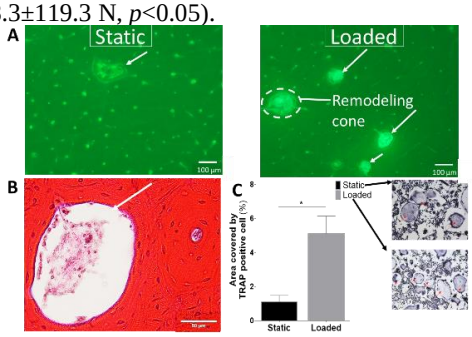

***Figure 1:** (A) Calcein labelling of cone remodeling (white arrow) after 7 days of in vitro culture. B) HE staining of cone remodeling and (C) the area covered by TRAP+ osteoclasts formed after 6 days of culture with CM. Errors bars represents mean ± SEM. * p<0.05.*

Discussion

This study demonstrates that (1) strain induced bone remodeling was successfully induced *ex vivo* in living bovine cortical bones as characterized by the formation of bone resorption cones along with an increase of osteoclast formation, and (2) there was an alteration of mechanical resistance after loading was applied. This supports previous *in vivo* studies with an increase in osteoclastogenesis up to 7 days post loading [1]. This is the first evidence of the development of an *ex vivo* model to study osteon remodeling that could be applied to study bone repair and fracture resistance of the tissue.

References

1. Kennedy et al., Bone 50: 1115-1122, 2016.
2. Acevedo et al., Nature Biomed Eng. 2: 62-71, 2018.
3. Cramer et al., Curr. Osteoporos. Rep.199, 2021.
4. Landrigan et al., Bone 48: 443-450, 2011.

Acknowledgements

This research received financial support of Science Foundation Ireland (SFI), co-funded under the European Regional Development fund (14/IA/2884) and funding from the European Research Council ERC-2018-StG Grant 804108.

DYNAMIC HIP SCREW (DHS): IN SILICO ASSESSMENT OF BONE HEALING USING FINITE ELEMENT ANALYSIS AND FUZZY LOGIC

Pratik Nag, Souptick Chanda
Indian Institute of Technology Guwahati
India

Introduction

Dynamic Hip Screw (DHS) is considered as a gold standard for extramedullary fixation of subtrochanteric or intertrochanteric femoral fractures. Bone healing is a crucial phenomenon for the overall success of the implantation. Secondary bone healing involves production of new soft tissues that gradually converts to callus and further solidifies to become cortical bone. The effect of coupled bio-mechanoregulatory responses to healing is not assessed yet in full-scale 3D models. The primary aim of this study is to preclinically evaluate the bone healing period using Finite element (FE) analysis and fuzzy logics in the DHS fixated construct.

Material and Methods

The 3D FE models of the implanted femur were generated using the manufacturer supplied CAD model of the left femur [1]. A 20mm fracture gap in the subtrochanteric region of the implanted bone was simulated (Fig. 1). The femur models were oriented laterally by 10° in the frontal plane and dorsally by 10° in the sagittal plane as described for fatigue testing [2]. A static load of 2kN was applied vertically downward through the femoral head. A condition of zero displacement was applied at distal femoral surface nodes sufficiently away from the point of application of load. Linear elastic, isotropic and homogenous material properties were applied to cancellous bone, whereas orthotropic material properties were applied to the cortical bone based on the data provided by the manufacturer (Table 1). A total of 96 fuzzy logic rules described the following biological processes: angiogenesis, intramembranous ossification, chondrogenesis, cartilage calcification and endochondral ossification. Dilatational and distortional strain were considered as the mechanical stimulus [3].

Material	Young's Modulus (MPa)	Poisson's Ratio
Cancellous	155[*]	0.3
Cortical	16,700(*compressive*)[**] 10,000(*transverse tensile*)[***]	0.3
Woven bone	4000	0.3
Fibrocartilage	200	0.45
Connective tissue	3	0.3
Plate & screw (Stainless Steel)	193,000[#]	0.3

Table 1: Material Property data based on ASTM D638[***], D695[**], D1621[*] & 308[#].

The callus region in the fracture gap was considered as ROI for the bone healing assessment. The effect of normal walking load case was considered.

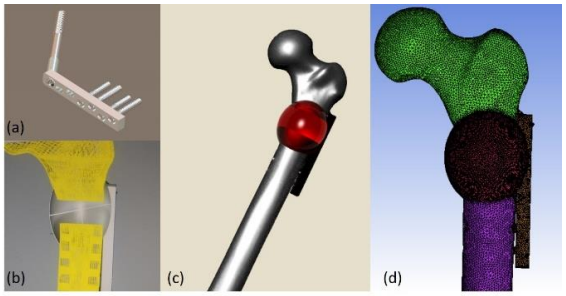

Figure 1 CAD model (a) DHS (b) Callus (c) DHS fixated bone surrounded by callus (d) model after meshing.

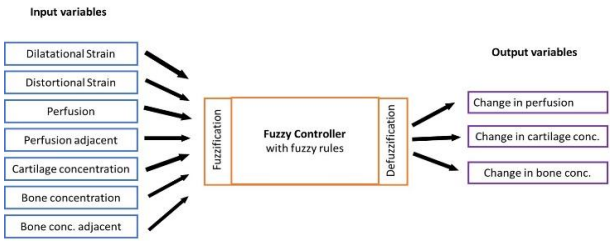

Figure 2 Fuzzy controller with 7 fuzzy input and 3 fuzzy output variables

References

1. Sawbones Europe AB, Malmo, Sweden, model# 3406
2. ISO 720 6-4:2002 Implants of surgery
3. Simon et al, Computer Methods in Biomechanics and Biomedical Engineering, 14: 1, 79-93, 2011.

TAMOXIFEN RESISTANCE LEADS TO SOFTENING OF BREAST CANCER CELLS

Barbara Zbiral (1), Andreas Weber (1), Maria dM Vivanco (2), José Luis Toca-Herrera (1)

1. Institute for Biophysics, Department of Nanobiotechnology, University of Natural Resources and Life Sciences, Vienna, Austria.

2. Cancer Heterogeneity Lab, CIC bioGUNE, Bizkaia Science and Technology Park, Derio, Spain

Introduction

Breast cancer is the leading cause of cancer death in women. Tamoxifen, an estrogen receptor modulator, is widely used in therapy. Resistance to tamoxifen is linked to increased invasiveness and metastatic potential [1, 2]. Cell mechanical properties and tissue integrity are altered during cancer progression [3]. More invasive cells appear softer, both *in vivo* and *in vitro*, due to cytoskeletal rearrangements [4, 5]. This is governed by changes in gene and protein expression. In this work we studied the influence of tamoxifen resistance (TamR) on the mechanical properties of endothelial breast adenocarcinoma cells (MCF-7).

We employed Atomic Force Microscopy (AFM) in force spectroscopy mode to study the viscoelastic properties of said cell lines. Tamoxifen resistant cells appear softer than their counterparts.

Methods

Normal and TamR MCF-7 were grown on glass slides and then measured by AFM using cantilevers with a spherical particle. Cells were first indented up to a given force (1 nN) and then the z-position was kept constant for 10 s, to perform so-called stress relaxation measurements (see Figure 1). A modified Hertz model was fitted to the Force-distance curves to calculate an apparent Young's Modulus. In addition, the stress relaxation Force-time-curves were fitted with either single or double exponential decay function [6]. Viscoelastic parameters were then calculated using either a SLS or a Zener model.

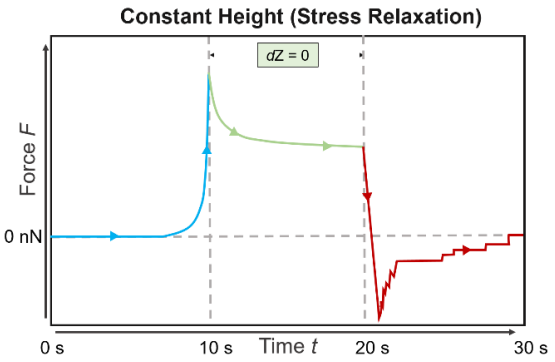

Figure 1: Representative Force-time curve of a stress relaxation measurement on a cell using a spherical particle (blue: approach, green: pause, red: retract).

Results and Discussion

The tamoxifen resistant variant appears softer than normal MCF-7 cells. In addition, they appear to be less viscous, despite showing an increased relaxation time. These results suggest increased invasiveness of TamR cells may be caused by cytoskeletal rearrangements rendering them more pliable. Further studies concerning cytoskeletal rearrangements as well as the expression levels of adhesion proteins such as cadherins are needed.

Parameter	MCF-7	TamR
δ [µm]	1.14	1.4
E [Pa]	199	148
τ_1 [s]	0.15	0.18
τ_2 [s]	3.23	3.60

Table 1: Mechanical properties of the studied cell lines.

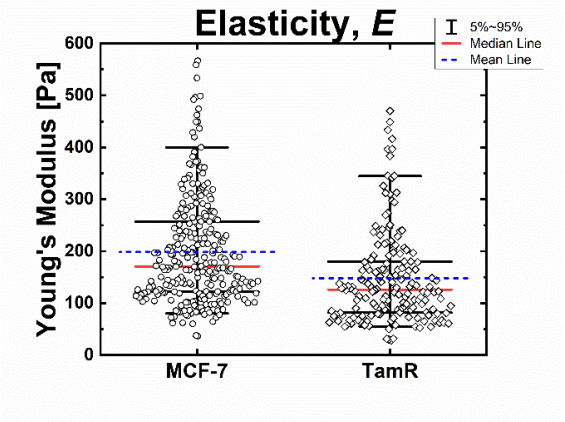

Figure 2: Comparison of Young's Modulus values for MCF-7 and TR cells at an indentation of 500 nm.

References

1. Hiscox S. et al, Int J Cancer, 118(2):290-301, 2006.
2. Ali, S. et al. Nat Rev Cancer, 2:101-112, 2002.
3. Fletcher D., Mullins D. Nature 463, 485-492, 2010.
4. Plodinec et al, Nat Nanotechnology, 7(11):757-65, 2012.
5. Lekka, M. BioNanoScience 6, 65-80, 2016.
6. Moreno-Flores et al. Nanotechnology 21(44):445101, 2010.

Acknowledgements

We would like to acknowledge Amsatou Andorfer-Sarr for maintenance of cell culture facilities. This work was supported by grant 29562-N28 from the Austrian Science Funds (FWF).

AN INTEGRATED EXPERIMENTAL-THEORETICAL APPROACH OF SINGLE CELL MECHANICS AFTER IN-FLOW COMPRESSIVE FORCES

Maria Isabella Maremonti (1), Ida Papallo (2), Massimo Martorelli (3), Antonio Gloria (4), David Dannhauser (1), Valeria Panzetta (1), Paolo Antonio Netti and Filippo Causa (1)

1. Interdisciplinary Research Centre on Biomaterials (CRIB) and Dipartimento di Ingegneria Chimica, dei Materiali e della Produzione Industriale, Università degli Studi di Napoli "Federico II", Piazzale Tecchio 80, 80125 Naples, Italy; 2.Department of Advanced Biomedical Sciences, Università degli Studi di Napoli "Federico II",80131, Naples, Italy; 3. Department of Industrial Engineering, Fraunhofer JL IDEAS, Università degli Studi di Napoli "Federico II", P.le Tecchio 80, 80125 Naples, Italy; 4. Institute of Polymers, Composites and Biomaterials, National Research Council of Italy, V.le J.F. Kennedy 54–Mostrad'Oltremare Pad. 20, 80125 Naples, Italy

Introduction

It is frequently reported how cytoskeletal or nuclear changes are related to cell deformability [1]. Over the past years, great efforts have been devoted to the small-scale measurement of mechanics and biology in single cells. Innovative approaches and hybrid methods have been developed, also involving the use of microscopy and hyperelastic warping to link, for example, intranuclear strain distributions to different cell state conditions [2]. Cell phenotype, development, motility and several biological functions are controlled by mechanical loading. A prolonged or substantial loading can damage cells, eventually leading to their death. Moreover, loading conditions induce specific mechanostructural and mechanobiological responses in different cell types, affecting their internal architecture and morphology as well as the mechanics of the cell components [3]. Accordingly, the aim of the current research was to provide a further insight into the single-cell mechanics through the integration of experimental and theoretical analyses, with a special focus on suspended cells. In particular, an integrated approach based on the combination of reverse engineering (e.g., confocal laser scanning microscopy and image analysis), design and modeling strategies was proposed to understand how the reorganization and redistribution of the inner structural components of the cell (e.g. actin cortex, microtubule network and nucleus) affect the overall mechanical response of the cell under different loading conditions.

Materials and Methods

Confocal laser scanning microscopy (CLSM) was performed on suspended cells before and after deformation. The latter occurred into the microfluidic chip under different viscoelastic fluid flow condition, in order to impose different levels of compressive forces [1]. In particular, cells are seeded into separate wells. For immunostaining, F-actin was stained with Alexa 568 phalloidin, whereas microtubules were stained by using an anti-β tubulin antibody and an Alexa fluor 488 secondary antibody. Nuclei were counterstained with Hoechst 33342. CLSM was employed as an optical imaging technique for the analysis of the cell structural components. Starting from undeformed and deformed confocal *z*-stack images, projection images were then reconstructed. Thus, image capture and analysis techniques were employed to generate 3D virtual models. Specifically, 3D tessellated models of the undeformed and deformed cell were created. The geometric models were imported into a finite element pre-processor to manage the generation of complex models. 3D meshes were suitably generated, appropriate mesh size and mesh refinement techniques were used. Different contact types were properly considered for the several parts of the model. Finite element analysis (FEA) was carried out to analyze the cell mechanical response under different loading conditions. Mechanical properties and constitutive laws were properly defined and implemented according to the different components of the model.

Results

FEA provided important information on the cell mechanical response under different loading conditions. In particular, the contribution of each structural component (actin, microtubules and nucleus) to the overall mechanical behavior of the cell was critically analyzed. Interesting results were obtained in terms of stress and strain distributions as well as of the stress transfer mechanism. A functional correlation between the undeformed and deformed model was also found.

References

1. Dannhauser and Maremonti et al, Lab on a Chip, 20(24): 4611–4622, 2020.
2. Henderson et al., Biophys J, 105(10): 2252–2261, 2013.
3. Saeed et al, Biomech Model Mechanobiol, 19: 1155-1164, 2020.



SIMULATING THE EFFECTS OF BIOMECHANICAL CUES ON NOTCH SIGNALING IN NATIVE CORONARY ARTERIES

Jordy G.M. van Asten (1), Tommaso Ristori (1), David Nolan (2), Caitríona Lally (2), Frank P.T. Baaijens (1), Cecilia M. Sahlgren (1,3), Sandra Loerakker (1)

1. Department of Biomedical Engineering, Eindhoven University of Technology, the Netherlands; 2. School of Engineering and Trinity Centre for Biomedical Engineering, Trinity College Dublin, Ireland; 3. Åbo Akademi University, Faculty of Science and Engineering, Biosciences, Turku, Finland

Introduction

Arteries grow and remodel in response to changing mechanical cues, such as hypertension, to maintain a homeostatic distribution of stress and/or strain across their walls [1]. This response is mediated by vascular smooth muscle cells (VSMCs) populating the tunica media of the arterial wall. The phenotype of these VSMCs is regulated by Notch signaling, a cell-cell signaling pathway that is sensitive to VSMC strain [2,3].

Investigating the role of Notch mechanosensitivity in arterial remodeling requires a computational model able to capture both the native arterial mechanics and Notch signaling dynamics in detail. Therefore, we coupled a calibrated Finite Element (FE) model for arterial mechanics to an Agent-Based (AB) Notch model to investigate the effects of changes in arterial mechanics due to hypertension on Notch signaling and VSMC phenotypic changes in native coronary arteries.

Methods

FE model: A human coronary artery consisting of three distinct layers (tunica intima, media, and adventitia) was modeled as a fiber-reinforced Neo-Hookean material. Heterogeneous residual stresses were accounted for via the theory of kinematic growth [4].

Notch model: A recently developed AB Notch signaling model [2] was used to simulate interactions between Notch receptors and ligands of adjacent VSMCs and predict VSMC phenotype. The circumferential strains in the arterial wall obtained from the FE analysis regulated the production of Notch receptors and ligands informed by experimental data [2].

Calibration: Material parameters for each layer were obtained by fitting experimental stress-strain data from native human coronary arteries [5]. The residual stresses were calibrated to obtain both a homeostatic, contractile VSMC phenotype and an approximately uniform stress distribution in the tunica media at physiological blood pressure (16 kPa).

Results

The material model successfully captured the experimentally observed mechanical response of each of the arterial layers. Increasing the blood pressure by 25% resulted in an increase in circumferential strain in the tunica media (Fig.1A). This affected Notch signaling and, consequently, caused an overwhelming switch in VSMCs from a homeostatic, contractile phenotype to a more proliferative, synthetic phenotype (Fig.1B).

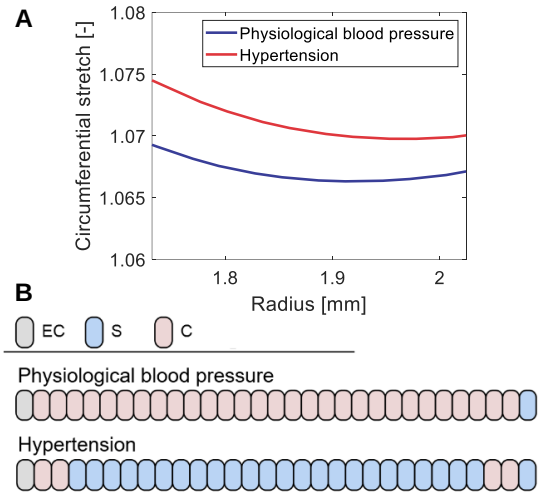

Fig.1: (A) circumferential stretch distribution in the media. (B) predicted phenotype of the cells (EC: Endothelial Cell, S: Synthetic VSMC, C: Contractile VSMC)

Discussion

A FE model simulating the mechanics of a tri-layered human coronary artery was successfully calibrated and coupled to an AB Notch model to study the impact of mechanosensitive Notch signaling on arterial growth and remodeling. The results suggest that Notch signaling may be a key regulator of arterial adaptation by inducing a switch from a contractile to a synthetic VSMC phenotype in response to changes in arterial strain, as synthetic VSMCs cause increased proliferation and matrix synthesis, enabling the artery to grow and remodel to adapt to these changes.

Our model and simulations not only increase our understanding of the growth and remodeling of native arteries in response to changing biomechanical cues but may also be adopted to improve tissue-engineered vascular grafts.

References

1. Humphrey, J.D. *et al.* Hypertension, 52:195-200, 2008
2. Loerakker *et al.* PNAS, 115(16): E3682-E3691, 2018
3. Morrow, D. *et al.* Circ Res, 96:567-575, 2005
4. Oomen, P.J.A. *et al.* Sci Rep, 8:1235, 2018
5. Holzapfel *et al.* Am J Physiol Heart Circ, 289: H2048-H2058, 2005

Acknowledgements

This work has received funding from the European Research Council (ERC) (Grant No. [802967] and [771168]).

INTERPLAY OF MECHANICAL AND INFLAMMATORY CUES IN OSTEOARTHRITIS: A MULTISCALE IN-SILICO APPROACH.

Satanik Mukherjee[1,2], **Raphaëlle Lesage**[1,2], **Liesbet Geris**[1,2,3]

[1]Prometheus, Division of Skeletal tissue Engineering, KU Leuven, Belgium; [2]Biomechanics Section, KU Leuven, Belgium;[3]GIGA In silico medicine, University of Liège, Belgium.

Introduction

Chondrocytes, the primary cells in articular cartilage, require optimum mechanical signals to maintain homeostasis. Abnormal mechanical signals can lead to departure from the stable chondrocyte homeostasis and a switch to hypertrophy, as observed in osteoarthritis (OA). In this context, multiscale models can be used to delineate the translation of mechanical signals from the macro-scale joint level to the micro-scale cell level, as a result of (patho)physiological loading at the joint level, and how these mechanical signals transduce intracellular biochemical processes. The objective of this paper is to develop a multiscale model of articular cartilage of the human knee joint to study the effect of physiological and pathological mechanical signals (post meniscectomy) on the fate of articular chondrocytes, in combination with pro-inflammatory cytokines.

Methods

The multiscale modelling workflow incorporates in-silico models at 3 different length scales i.e. joint-level, cell-level and intracellular level as follows.

Finite Element (FE) modelling of the knee joint: FE model of the right knee of a 70 year old female weighing 77.1 kg was developed in FEBio (geometry obtained from the OpenKnee project [1]). Joint rotations, translations and joint reaction force for stance phase of the gait were used as input boundary conditions for the knee joint (both healthy and meniscectomized).

FE modelling of the chondrocyte: The chondrocyte and its microenvironment (containing the pericellular matrix (PCM) and extracellular matrix (ECM)) for the different zones of the cartilage (superficial zone (SZ), middle and deep zone (DZ)) were developed in Abaqus. The matrix was modelled as fibril reinforced poro-viscoelastic material whereas the cell was considered biphasic [2]. The maximum compressive and shear strains obtained at the different zones of articular cartilage from simulations of the knee joint were used as input boundary conditions for the cell-level model.

Regulatory networks for chondrocyte mechanotransduction: An additive model representing the intracellular gene/protein regulatory network involved in chondrocyte mechanotransduction and inflammation was developed. The 3 stable states or attractors for the network, viz. SOX9, RUNX2 and None (where both SOX9 and RUNX2 are inactive) were identified using a Monte-Carlo analysis. A SOX9 attractor would signify a stable chondrocyte whereas a RUNX2 attractor would signify that the cell undergoes hypertrophy. The forces acting on the integrins obtained from the cell-level model were used as input to trigger the intracellular pathways.

Results

From the joint level simulations, it was observed that meniscectomy lead to increased strains in the different zones of articular cartilage as compared to a healthy joint as seen in figure 1, resulting in higher forces sensed by the chondrocytes in the cell-level model. However, post-meniscectomy, in both the SZ and DZ, the chondrocytes initially remained in their stable state with high expression of stable chondrocyte biomarkers (SOX9, Coll-II, Proteoglycans). With subsequent build-up of pro-inflammatory cytokines with time due to abnormal loading, the SZ chondrocyte underwent a hypertrophic switch as was evident from the high activity of pro-hypertrophic biomarkers (RUNX2, CollX, MMP13,ADAMTS5). Due to this degenerative change in the SZ, the DZ chondrocytes were now subjected to higher strains, which when coupled with inflammatory cytokine build-up over time, led to their subsequent hypertrophic switch.

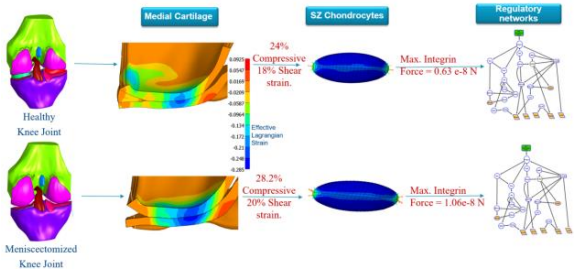

Figure 1: Workflow of multiscale modeling.

Discussion

In this study, we elucidated the ability of the multiscale model to predict that the SZ and DZ chondrocytes undergo hypertrophy at different stages of OA, which was due to the difference in mechanical signals sensed by the chondrocytes in the different zones. The future steps include constructing a feedback loop which will relate expression of molecular factors by the cell to a change in the macro-scale mechanical properties of the cartilage using a computational homogenization approach. This will enable us to predict the onset and gradual progression of OA in an iterative manner.

References

1. Erdemir A. J. Med Device.7(4), 2013.
2. P.Julkunen et al.,Med. Biol. Eng.Cmp.2009,47,1281.

Acknowledgements

This project has received funding from the European Union's Horizon 2020 research and innovation programme under Marie Sklodowska-Curie grant agreement No 721432.

STEM CELL SECRETOME DECREASES ANNULAR MECHANICAL STRENGTH IN A LOADED ANNULUS FIBROSUS ORGAN CULTURE

Graciosa Q. Teixeira (1), Andreas Ekkerlein (1), Raquel M. Goncalves (1,2), Joana R. Ferreira (2), Anita Ignatius (1), Hans-Joachim Wilke (1), Cornelia Neidlinger-Wilke (1)

1. Institute of Orthopaedic Research and Biomechanics, Ulm University, Germany; 2. Instituto de Investigação e Inovação em Saúde (i3S), University of Porto, Portugal

Introduction

Failure of the annulus fibrosus (AF) is often associated with disc herniation and activation of the immune system. Mesenchymal stem cell (MSC)-based therapies have been proposed for disc degeneration/herniation-associated back pain, despite limited knowledge on their mechanism of action after transplantation. Hence, we investigated the impact of a cell-free therapeutic approach with MSC secretome on bovine AF organ cultures (AF-OCs) exposed to mechanical overload and a proinflammatory environment.

Methods

AF rings were isolated from bovine tails of 12-24 months-old animals (n=18). AF-OCs were exposed to upper-physiological cyclic tensile strain (CTS, 9%, 1 Hz, 3 h/day) and 10 ng/mL interleukin (IL)-1β (CTS+IL-1β) in a 6-stations custom-made device [1]. Sub-groups of stimulated AF-OCs were treated with either human MSC in coculture or secretome produced by preconditioned human MSC (n=3, 1 female/2 male, age: 23±1.5 years; preconditioning: 10 ng/mL IL-1β and 6 % O2 for 48 h). Unstimulated AF-OCs were used as controls. AF cells expression for regulators of immune cell function, catabolic enzymes and matrix components was analyzed by real-time PCR using bovine primers. Interleukin (IL)-6 and metalloproteinase (MMP)-3 tissue distribution were analyzed by immunohistochemistry. Glycosaminoglycan, elastin and collagen tissue content were determined by biochemical assays. AF adhesive strength was quantified in the tissue using a peel-force test. Kruskal-Wallis test was used to determine differences between the groups in GraphPad Prism 7 software. P-values < 0.05 were considered significant.

Results

Four days of CTS+IL-1β stimulation upregulated the expression of bovine immune response mediators *IL-6*, *IL-8* and *CD46* ($p<0.05$), and of catabolic enzymes *MMP-1* and *MMP-3* ($p<0.01$). In contrast, treatment of the CTS+IL-1β-stimulated AF-OCs with the MSC secretome downregulated the expression of these markers ($p<0.05$). The changes in IL-6 (Figure 1A) and MMP-3 production were confirmed at protein level. In contrast, the MSC in coculture only downregulated IL-8 expression ($p<0.05$). Interestingly, both the MSC in coculture and the secretome contributed to a downregulation of collagen type I (*COL1A1*) expression by the bovine AF cells ($p<0.001$), but only the secretome induced a significant decrease of total collagen content in the AF matrix ($p<0.05$, Figure 1B) and a decrease of the AF adhesive strength ($p<0.05$, Figure 1C) when compared to the CTS+IL-1β stimulation alone. No differences were observed in glycosaminoglycan or elastin tissue content under the different stimuli.

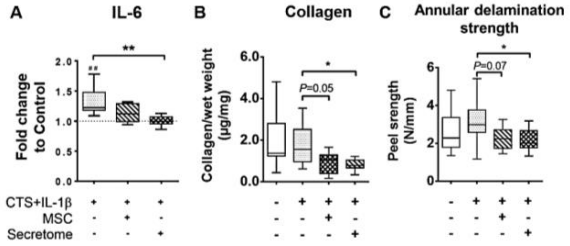

*Figure 1: A) IL-6 staining intensity normalized to the unstimulated control sample for each experiment. B) Collagen content in the AF tissues normalized to wet weight (µg/mg). C) AF peel strength as function of displacement rate (N/mm). n = 6-18, *p<0.05, **p<0.01.*

Discussion

AF cells presented a proinflammatory/degenerative phenotype four days after CTS+IL-1β stimulation. The MSC secretome had a stronger impact than the MSC in coculture on decreasing the immune and catabolic response of AF cells activated by CTS+IL-1β conditions. However, the secretome also contributed to a further decrease of collagen at gene/protein level and of the AF mechanical strength observed in the CTS+IL-1β group. Using the MSC secretome as a therapeutic approach to modulate disc degeneration-associated inflammation seems to be an alternative option to MSC transplantation. Still, it requires further mechanistic investigations and evaluation of its long-term success *in vivo*, before moving to clinical trials.

References

1. Saggese et al, Eur Spine J, 28:922-933, 2019.

Acknowledgements

Supported by Ulm University (LSBN.0157), German Spine Foundation, Humboldt Foundation and DAAD/CRUP.

PRE-OSTEOBLAST CELLS IN THREE-DIMENSIONAL SPHEROIDS EXERT OSTEOCYTE-LIKENESS

Jeonghyun Kim (1), Taiji Adachi (1)

1. Institute for Frontier Life and Medical Sciences, Kyoto University, Japan

Introduction

Three-dimensional (3D) culture system, such as organoid, has been recently attempted to recapitulate various organs for human development and disease studies [1]. While i*n vitro* bone related research was mostly considered from the results achieved on a conventional two-dimensional (2D) culture system where cells were cultured on a stiff plastic or glass dish, effect of 3D culture system on the bone research remained unclear in terms of osteoblast/osteocyte behaviors such as cellular proliferation and differentiation. Osteocytes are embedded inside the mineralized bone matrix and modulate the bone remodeling by controlling osteoclasts and osteoblasts to undergo bone resorption and formation, respectively [2]. During a long period of cultivation for pre-osteoblasts on the 2D *in vitro* model, the cells became proliferated, condensed, and eventually differentiated into osteocyte-like cells [3]. In this study, we hypothesized that the cell condensation of pre-osteoblast cells plays an important role for osteocyte differentiation. In order to prepare for the highly condensed condition for the cells, we utilized the 3D culture system such as spheroid model and further evaluated their differentiation capability.

Method

In this study, mouse pre-osteoblast cell (MC3T3-E1) was utilized. 1,000 cells were subcultured in the super low cell attachment round-bottom dish and incubated for 2 days to fabricate the 3D spheroid. As a comparative model, we used the conventional 2D monolayer reconstructed by MC3T3-E1.

Result and Discussion

After 2 days of incubation, the average projected diameter of spheroid became about 115 μm as described in Fig. 1(A). Using real-time PCR, we measured the mRNA expression of osteocyte markers in Fig. 1(B). In 2 days, all the osteocyte markers were significantly and remarkably up-regulated in the 3D spheroid compared to the 2D monolayer; *Opn* (57-fold change; $p < 0.01$), *Dmp1* (1,266-fold change; $p < 0.05$), and *Sost* (82-fold change; $p < 0.05$). Moreover, the immunostaining results in Fig. 1(C) represented that the spheroid incubated for 2 days had the DMP1 expression, an osteocyte specific marker. In this study, we also conducted a period of 7-day experiment. As a result, the osteocyte gene expressions in 7-day spheroid were increased compared to 2-day spheroid. The results altogether imply that the pre-osteoblast cells in 3D spheroid culture did not only exert the *in vitro* osteocyte differentiation within 2 days, but the osteocyte-likeness was also prolonged after 7 days of incubation. We hereby suggest that the spheroid using pre-osteoblast cells enables to apply for a new *in vitro* osteocyte model. Furthermore, the spheroid is also expected to utilize in the field of tissue engineering by transplantation into the bone defect model for regenerative medicine.

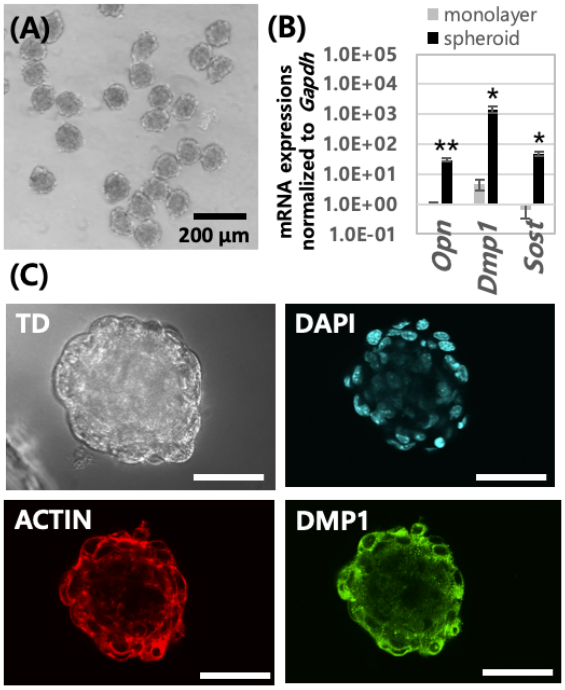

*Figure 1: (A) Spheroid reconstructed by mouse pre-osteoblast cells after 2-day incubation, (B) mRNA expressions of osteocyte markers (Opn, Dmp1, and Sost) for monolayer and spheroid normalized to Gapdh expression (p-value was obtained by Student's t-test; * $p < 0.05$, ** $p < 0.01$), (C) Immunofluorescence staining images of spheroid; DAPI (blue), ACTIN (red), and DMP1 (green). White bars indicate 50 μm.*

References

1. Sasai, Y., Nature, 493: 318-326, 2013.
2. Bonewald, L. F., J. Bone Miner. Res., 26: 229-238, 2011.
3. Bhargava, U. et al, Bone, 9:155-163, 1988.

Acknowledgements

This work was supported by Japan Society for the Promotion of Science (19K23604, 20K20181, and 20H00659), Japan Agency for Medical Research and Development (JP19bm0804006, and JP20gm0810003), and Nakatani Foundation.

CHARACTERIZATION OF DIRECTIONAL FLUID FLOW INDUCED TISSUE GROWTH IN A 3D *IN VITRO* HUMAN BONE DEFECT MODEL.

Bregje W.M. de Wildt (1), Feihu Zhao (2), Iris Lauwers (1), Keita Ito (1), Sandra Hofmann (1)

1. Orthopaedic Biomechanics, Department of Biomedical Engineering, Eindhoven University of Technology, The Netherlands. 2. Biomedical Engineering, Zienkiewicz Centre for Computational Engineering, Swansea University, United Kingdom.

Introduction

Regeneration of bone defects could be guided with smart biomaterials, making use of the bone's innate capacity to regenerate upon implantation [1]. For the development of such materials, animal experiments are routinely used. To enable the investigation of biomaterial-driven human bone regeneration, while addressing the principle of reduction, refinement and replacement (3Rs) of animal experiments, human *in vitro* bone defect models should be developed. Currently, *in vitro* bone defect models are often created from animal specimens which face difficulties in maintaining viability and are mostly only cultured statically [2]. Therefore, we aimed at developing a three-dimensional (3D) *in vitro* human bone defect model using a tissue engineering approach. In addition, we characterized tissue growth and organization induced by directional fluid flow at the defect side.

Methods

Silk fibroin scaffolds were produced with a 3 mm diameter defect in the center. Scaffolds (N = 4) were seeded with human mesenchymal stromal cells (MSCs) and cultured statically or in a flow perfusion bioreactor with a flow of 1.5 ml/min, determined with computational simulation, providing osteogenic medium. Tissue growth over time into the defect was quantified based on histological sections after 2, 4, and 6 weeks of culture. Osteogenic differentiation was visualized using immunohistochemistry for the osteogenic markers RUNX2, alkaline phosphatase, collagen type 1 and osteopontin. To study the effect of fluid flow direction, cell orientation at the defect wall was quantified over time based on a phalloidin staining.

Results and Discussion

In constructs cultured with flow perfusion, bone-like tissue grew away from the scaffold wall reaching into the defect void (Figure 1A+B). In constructs that were cultured statically, this increase could not be seen ($p<0.01$) (Figure 1A+B). All osteogenic markers were present in this newly formed matrix. Interestingly, cells at the scaffold wall aligned in the static and dynamic culture predominantly to the defect's curvature rather than to the fluid flow direction (data not shown), indicating that curvature can overrule directional fluid flow in guiding cell orientation of osteogenically differentiated MSCs in 3D.

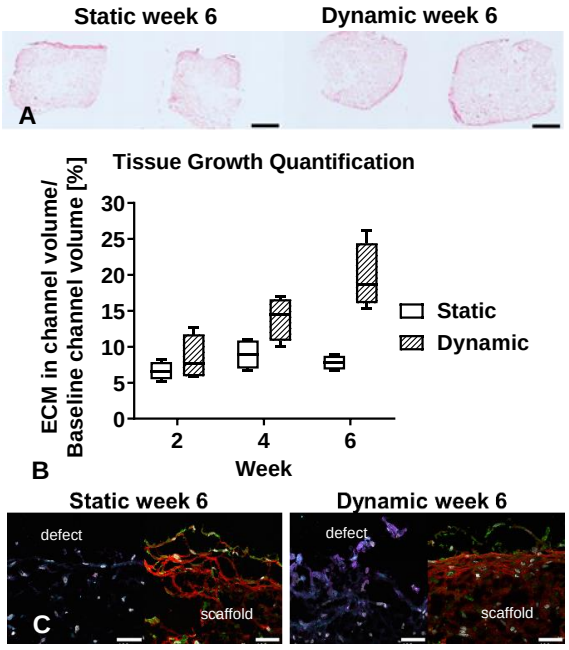

Figure 1. *Tissue sections stained with picrosirius red after 6 weeks static or dynamic culture (A, scale bar: 1 mm) that were used for the tissue growth quantification results over time in the defect void (B). Newly formed tissue was stained positively for the osteogenic markers RUNX2 (cyan), ALP (magenta), osteopontin (green), and collagen type 1 (red) (C, scale bar: 100 μm).*

Conclusion

In this study, we characterized bone-like tissue growth and organization after 2, 4, and 6 weeks with and without fluid flow perfusion in a 3D tissue engineered construct, mimicking an *in vitro* human bone defect. Fluid flow perfusion resulted in more tissue formation at the scaffold's wall. This *in vitro* model could be useful to screen graft materials for biomaterial-driven bone regeneration applications, addressing the principle of 3Rs of animal experiments.

References

1. A.I.P.M. Smits and C.V. Bouten, COBME, 6, 2018.
2. E.E.A. Cramer et al., Curr. Osteoporos. Rep., 2020.

Acknowledgements

This work has been supported partly by the Dutch Organization for Scientific Research (NWO), project # TTW 016.Vidi.188.021.

MAGNETO-RESPONSIVE CORE-SHELL MICROBEADS FOR ENGINEERING PERISTALSIS AND ALVEOLAR BRETHING IN-VITRO

Ludovica Cacopardo (1), Nicole Guazzelli (1), Arti Ahluwalia (1)

1. University of Pisa, Italy

Introduction

Physiologically relevant in-vitro models need to reproduce both structural and mechanical features of the in-vivo environment. 3D scaffolds and cell spheroids are emerging as powerful tools to replicate three-dimensional structures. While, bioreactors are employed to apply uniaxial or biaxial stretching to cell monolayers. However, despite the complexity of these systems, to date, the replication of multidirectional (radial) three-dimensional (out of plane) stretching is a challenge [1, 2].

Here, we present a new bioprinting strategy to obtain core-shell structures, able to replicate the structure and motility of the intestinal and alveolar barrier thanks to magneto-responsive materials (Figure 1). In the case of the alveoli the air-containing beads will be embedded in a magneto-responsive septum-like gel able to mimic the in-vivo deformation mechanism. The core-shell structures were characterised as a function of different extrusion velocities, while deformation was evaluated as on the base of different magnet combinations and magnetite nanoparticle (NP) concentrations.

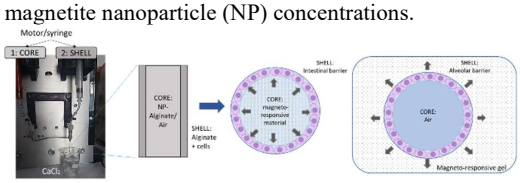

Figure 1: schematic illustration of the core-shell microbead generator and structures.

Methods

A core-shell microbead (COSMIC) generator was designed and fabricated using commercial coaxial needles (16-26 and 9-26 Gauge) connected with two syringes, which are actuated with two stepper motors. The extrusion is controlled via computer thanks to a graphical user interface.

The core-shell structures were characterised using 1 and 2% w/v alginate in the shell and air or 1 - 2 % w/v FITC-alginate (Creative PEGWorks, USA) in the core. A 0.1 M calcium chloride ($CaCl_2$) solution was placed under the needle to allow alginate crosslinking. Spheres dimension was quantified in function of different extrusion velocities (10, 20, 40 µL/s) using brightfields and fluorescence images (Olympus, Japan) and the Image-j software.

The deformation of 1 % w/v alginate beads loaded with 5, 10 or 13% w/v magnetite NP (~ 50 nm diameter) and 0.1% w/v pluronic-127 was measured using image analysis [3]. Different magnet combinations (neodymium permanent magnets with a diameter of 10 mm and 20 mm) were investigated.

Cell viability tests were performed using Caco-2 cells with an encapsulation density of 1M/mL. All reagents were purchased from Sigma-Aldrich (Milano, Italy), unless differently specified.

Results

The obtained diameters range from about 700 to 1700 µm for the core with a shell thickness ranging from 90 to 500 µm. As shown in Figure 2a, the best results in terms of distinction between core and shell was obtained with the following extrusion velocities: core at 20 µL/s and shell at 40 µL/s (c20s40). The best deformation performance was obtained with a combination of the 10 and 20 mm magnets with strain levels from 8 to 12% with increasing NP concentration (Figure 2c).

Cell testing confirmed the cytocompatibility of the beads and of the encapsulation procedure.

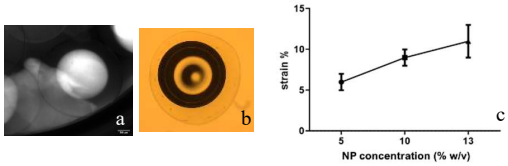

Figure 2: a) c20s40 2% alginate core-shell structures extruded with 19-26G needle; b) c20s40 air core - 1% alginate shell structure; c) strain level as a function of nanoparticle concentration.

Discussion

Results show that our strategy is suitable to obtain cell-laden core-shell structures. The fabrication and characterisation of the septum-like gel and the design of an automated stimulation system based on electromagnets are on-going. Further developments foresee the evaluation of the 3D structure and of the stretching effects on cell morphology, organization and polarization.

In conclusion, the main advantage of our strategy is the combination of structure and 3D stretching, which, to the best of our knowledge, has not been implemented in-vitro. Thus, COSMIC represents a step further towards the definition of physiologically relevant in-vitro models, which improve the translation between research and clinical applications and also have the potential to reduce animal tests as required by EU directives.

References

1. Sakalem et al, J Coloproct, 38:90-93, 2018.
2. Hynes et al. POEU.2020.
3. Zhao et al. PNAS.2011

HYDROGEL VISCOELASTICITY INFLUENCES MECHANOTRANSDUCTION AND CHONDROGENESIS OF MESENCHYMAL STEM CELLS

Matthew Walker (1), Marco Cantini (1)

1. *Centre for the Cellular Microenvironment, University of Glasgow, UK*

Introduction

Hydrogel stiffness has been long recognised to determine human mesenchymal stem cell (hMSC) differentiation, whereas viscous interactions are only recently emerging as powerful regulators of stem cell fate [1, 2]. For example, while viscoelastic hydrogels can promote hMSC spreading and proliferation, elastic hydrogels can inhibit cell proliferation and, in the case of chondrocytes, limit cartilage matrix formation [3]. Moreover, hydrogels can be functionalised with peptide motifs to improve hMSC attachment and influence cell fate: for example, chondrogenesis can be controlled by peptide gradients using integrin receptor RGD and cadherin ligand HAVDI [4]. However, investigations into how the viscoelastic properties of hydrogels influence the chondrogenic differentiation of hMSCs are lacking.

In this work, we investigate whether viscoelastic hydrogels with variable viscous properties and consistent elasticity can provide a cellular micro-environment conducive to the chondrogenic differentiation of hMSCs.

Methods

Polyacrylamide (PAAM) and polyethylene glycol (PEG) hydrogels were prepared using acrylamide and cross-linker N, N'-Methylene bisacrylamide, or PEG macromers and protease degradable VPM peptide cross-linkers, respectively. Elastic and viscous properties of the hydrogels were measured using AFM and rheology. hMSCs were cultured on RGD/HAVDI-functionalised PAAM hydrogels and within RGD-functionalised PEG hydrogels. Cell cultures were analysed by immunoflourescence microscopy and qPCR for adhesion behaviour, as well as markers of mechanotransduction, early chondrogenesis, cartilage matrix, and chondrocyte hypertrophy.

Results

We prepared viscoelastic PAAM and PEG gels with different polymer:crosslinker ratios that maintain similar Young's moduli (~13 kPa), whilst exhibiting differences in viscosity (~two-fold loss modulus change), as measured by AFM nanoindentation and microrheology, and confirmed by bulk rheology.

2D culture on PAAM gels functionalised with RGD showed that more viscous substrates prompted decreased hMSC spreading, modulation of adhesion proteins expression, different mechanotransduction (decreased nuclear YAP and lamin A/C:B1 ratio), increased early chondrogenesis (SOX9 upregulation and RUNX2 downregulation) and late chondrogenesis (COL2A1 and aggrecan upregulation), while preventing an hypertrophic phenotype. hMSC behaviour and fate was also influenced by ratios of RGD/HAVDI. Importantly, 3D culture within viscous PEG gels also promoted enhanced chondrogenesis via similar mechanotransductive mechanisms.

Discussion

These novel findings demonstrate that viscous interactions both in 2D and 3D can be modulated to target key mechanotransductive events, leading to the activation of chondrogenic pathways in hMSCs as a consequence of substrate viscosity.

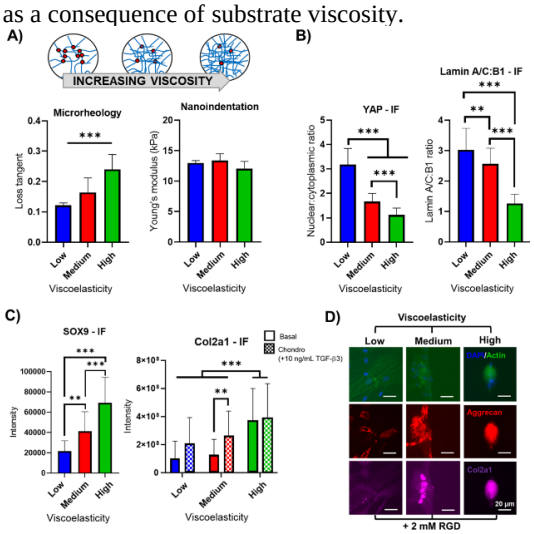

Figure 1. A) Sketch and AFM mechanical characterization by microrheology (left) and nanoindentation (right) of viscoelastic PAAM gels. B) Mechanotransduction (quantification of IF of YAP and nuclear lamins). C) Early chondrogenesis (SOX9) and neocartilage formation (Col II). D) Representative IF images of matrix secretion.

References

1. Chaudhuri O et al. Nat Mater 15:326, 2016.
2. Cantini M et al. Adv Healthc Mater 1901259, 2019.
3. Lee HP et al. Nat Mater 16:1243, 2017.
4. Vega S et al. Nat Comm 9, 2018.

Acknowledgements

The authors acknowledge funding from MRC and UKRMP (MR/S005412/1). Help and guidance by members of the Centre for the Cellular Micro-environment is also acknowledged.

MODELING THE PATHOPHYSIOLOGY OF THE HEART THROUGH A BEATING ORGAN-ON-CHIP PLATFORM

Roberta Visone (1), Andrea Mainardi (1,2), Alberto Redaelli (1), Anna Marsano (2), Paola Occhetta (1), Marco Rasponi (1)

1. Politecnico di Milano, Italy; 2. University Hospital Basel, Switzerland.

INTRODUCTION

The ability to accurately develop advanced *in vitro* models of cardiac pathophysiology represents a breakthrough in the field of cardiac biology and clinical translation. Organs-on-chips have recently emerged as innovative platforms enabling to reproduce key native biophysical conditions with unprecedented precision and to integrate tailored functional readouts.

Here we describe uHeart, the first beating heart-on-chip providing: *i)* a finely controlled mechanical stimulation to 3D microtissue and *ii)* an innovative means to directly extract electrophysiological signals without damaging cultured cells. We exploited the mechanical stimulation of uHeart to: *i)* generate a physiological beating cardiac model for drug screening and *ii)* a scar-like pathological model to elucidate mechanisms of cardiac fibrosis.

METHODS

uHeart was designed i) to provide cyclic controlled uniaxial strain (i.e. 10% stretching at 1Hz) to 3D cell-laden hydrogels [1], and ii) to incorporate an electrical system for non-destructive recording of cardiac field potential (FP). The platform was fabricated through standard photo- and soft-lithography techniques.

Physiological cardiac models were generated from human induced pluripotent stem cell-derived cardiomyocytes (h-iPSC-CMs, FUJIFILM CDI) and human dermal fibroblasts (Lonza). Cells were mixed in a 3:1 ratio ($125 \cdot 10^6$ cells/ml), embedded in fibrin gel (i.e. 10 mg/ml fibrinogen; 1.25 U/ml thrombin) and mechanically stimulated for 7 days. Microtissues' functionality was evaluated on-line by positioning paired electrodes in specific location of uHeart. Ion-channels related gene expression was measured. Drug screening was conducted by evaluating alterations of FP duration (FPD) at incremental concentrations of drugs (i.e. DMSO, Aspirine, Sotalol and Verapamil).

Scar-like cardiac models were generated from primary neonatal rat cardiac fibroblasts isolated from 2-day-old neonatal pups. Fibroblasts were embedded at $14.5 \cdot 10^6$ cells/ml in fibrin gel (i.e. 20 mg/ml fibrinogen; 5 U/ml thrombin). Microtissues in static and dynamic conditions with or without the transforming growth factor β1 (TGFβ1) were cultured for 7 days. The effects on cell proliferation, phenotype and ECM remodeling were assessed through immunofluorescence staining and atomic force microscopy (AFM).

RESULTS

Mechanically trained physiological cardiac models showed striated h-iPSC-CMs which organized in 3D and beat as a syncytium (0.45Hz; FPD 0.5s) (Fig.1a). Mechanical stimulation upregulated potassium channels (i.e. h-ERG, IKs), which influence the repolarization phase. Compounds' effect on FPD was successfully assessed: DMSO and Aspirin did not alter the FPD, while Sotalol (≥15μM) prolonged and Verapamil (≥50nM) shorten cardiac repolarization, respectively.

In the pathological model, the application of mechanical stimulation was sufficient, even in the absence of classical pro-fibrotic biochemical stimuli (i.e. TGFβ1), to induce traits typical of scar formation. Mechanical stimulation significantly increased cell proliferation (3.75 ± 1.33%) as compared to static condition (0.95 ± 0.60%). Mechanical stimulation promoted α-SMA expression (56 ± 21.03%), indicating fibroblasts' switch to myofibroblasts, with respect to static culture (23.92 ± 15.30%) (Fig.1b). Static microtissues showed lower mechanical stiffness (~0.7 kPa) compared to dynamic ones (~2 kPa), which exhibited increased production of scar-like ECM (collagen type-I, aggrecan, fibronectin).

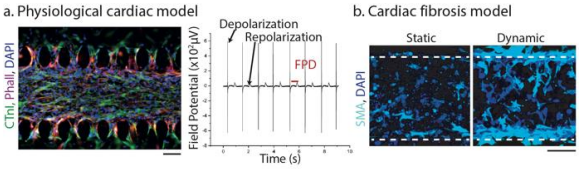

Figure 1: a) Immunofluorescence staining and field potential recording of physiological model; b) Myoblast switching in pathological model (scale bar 100mm).

DISCUSSION

uHeart demonstrated that mechanical cues are great means to reproduce cardiac pathophysiology. uHeart generated functional microtissues reacting to drugs in a physiological way [2], offering a unique on-chip cardiotoxicity screening tool. uHeart also efficiently developed scar-like microtissues covering the principal phases of the wound healing process, fundamental to assess the effects of compounds on reversing cardiac fibrosis [3]. The mechanical stimulation is now being exploited in further studies to investigate the ability of cardiomyocytes to counteract fibroblast proliferation and myocyte switch in fibrotic tissue models.

References

1. A. Marsano *et al.*, *Lab Chip*, 16: 599–610, 2016.
2. H. Ando *et al.*, *J. Pharmacol. Toxicol. Methods*, 2017.
3. P. Occhetta *et al.*, *Integr. Biol.*, 10: 174–183, 2018.

Acknowledgements

This work was supported by Fondazione Cariplo (#2012-0891) and European Commission Horizon2020, MSCA-ITN-ETN (#642458) and MSCA IF (#841975).

MICROBIOME ON CHIP (MOC): A NOVEL MULTI-ORGAN PLATFORM FOR PERSONALIZED THERAPY IN CANCER

Mattia Ballerini (1,2), C. Catozzi (1), Simona Paola Ravenda (3), Nicola Fazio (3), Romario Uberto Fumagalli (3), Marco Rasponi (2), Luigi Nezi (1)

1.Department of Experimental Oncology, IEO, European Institute of Oncology IRCCS, Milan, Italy, 2.MiMic Lab, Department of Electronics, Information and Bioengineering, Politecnico di Milano, Milano, Italy, 3.Division of Gastrointestinal Medical Oncology and Neuroendocrine Tumors, European Institute of Oncology, Milano, Italy

Introduction

It is now evident that the gastrointestinal bacteria contribute in shaping the immune system, etiopathology of cancer and therapy responses [1-2].
In vitro traditional models lack the cellular complexity and physiological architecture present in the human intestine [3-4]. On the other hand, *in vivo* systems often fail to recapitulate results obtained in human and they are limited by poor experimental control.
3D-microfluidic culture systems may overcome these limitations, because they recreate complex multicellular architectures in a finely controlled dynamic environment [4-6].

Methods

A novel microfluidic platform that integrates 3D models of the human intestine, the systemic vasculature and the tumor microenvironment (TME) was developed using soft lithography techniques.
The microbiome-on-chip (MOC) is composed by two modules. The first module consists of a 3D gut-on-chip composed by an epithelial compartment and a vascular one separated by a collagen-based gel. Physiologically relevant luminal flow and peristalsis-like mechanical deformations are applied on the device thanks to an innovative technology recently developed in the lab.
The second module is designed to culture 3D tumor spheroids and test different therapeutic strategies on patient-derived tissue. The whole system allows real-time multiparametric monitoring and could be used as a predictive model to promote patient-specific therapies and improve antitumor responses

Results

The following preliminary results were obtained using single-module devices while the complete platform is currently being developed and tested to study the effect of microbiota on tumor microenvironment and therapeutic responses.

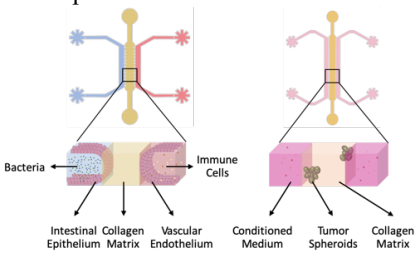

Figure 1: Intestinal and Tumor microfluidic models

The proposed intestinal model allows to obtain a 3D complete and functional intestinal epithelium in 5-7 days of culture (Figure 2A). Epithelium integrity and functionality was assessed using 4.4KDa TRITC-Dextran.
Mucosal samples from patients' intestinal resections were co-cultured on the device to evaluate the influence of tumor-associated microenvironment on intestinal integrity.
Patient-derived tumor spheroids were cultured in the tumor-on-chip module for 4-5 days and different therapeutic strategies were tested. Both tumor and immune cells were successfully cultivated in the device.

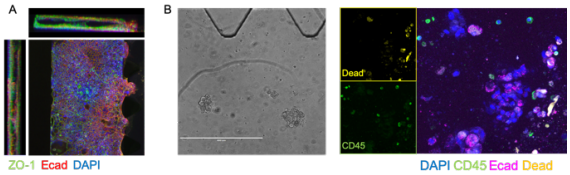

Figure 2: (A) Confocal microscopy image of a complete 3D epithelium stained for tight junctions (ZO-1), E-cadherin (Ecad) and nuclei (DAPI). (B) Tumor spheroids composed by both tumor (Ecad) and immune (CD45) cells.

Discussion

The application of shear stress and the mechanical deformations suggests increasing the ability of cells to create a complete intestinal epithelium. The device is thus suitable to screen combinations of biochemical and mechanical cues to find optimal stimulation parameters.
The use of patient-derived tumor spheroids can promote personalized therapy and help unravel the interaction between microbiota, immune system and cancer.

References

1. Segre et al, Science 349:1058–1059, 2015.
2. Drewes et al, Br. J. Cancer 115:273–280, 2016.
3. Tsilingiri et al, Gut 61:1007–1015, 2012.
4. Kim et al, Lab Chip 12:2165–74, 2012.
5. Kim et al, Proc. Natl. Acad. Sci. 113:7–15, 2016.
6. Jenkins et al, Cancer Discov. 8:196-215, 2018.

TUNABLE MONOPHASIC/BIPHASIC ELECTRICAL STIMULATOR FOR CARDIAC TISSUE ENGINEERING INVESTIGATIONS

Stefano Gabetti (1), Antonio Sileo (2), Federica Montrone (1), Giovanni Putame (1), Alberto Audenino (1), Anna Marsano (2), Diana Massai (1)

1. Polito^{BIO}Med Lab, Department of Mechanical and Aerospace Engineering, Politecnico di Torino, Italy; 2. Department of Surgery and Department of Biomedicine, University Hospital Basel, Switzerland

Introduction

Cardiac tissue engineering (CTE) aims to develop functional cardiac tissue substitutes to be used as *in vitro* models for cardiac research, and ultimately for cardiac repair [1]. Among different physical stimuli applied *in vitro* to promote cardiac tissue maturation [2], pulsatile electrical stimulation was shown to influence rate and duration of action potentials, to increase the percentage of spontaneously beating cells, and to promote cell-cell coupling and calcium handling [3]. Here, we developed the compact electrical stimulator ELETTRA, designed to deliver tunable biomimetic electrical pulses for CTE investigations, and we cultured neonatal rat cardiac cells under monophasic or asymmetric biphasic pulses.

Methods

ELETTRA (18x17x7 cm^3) is based on a microcontroller board (Arduino Due), a lightweight optimized power supply stage, a purpose-built software, and a user-friendly interface (Fig.1A). A sensing resistor allows monitoring the current flowing between the electrodes. To mimic electrical stimuli experienced *in vivo* by human cardiac cells, ELETTRA can deliver tunable monophasic or symmetric/asymmetric biphasic pulses (frequency = 0.5-10.0 Hz, amplitude = 0.5-12.0 V, pulse duration = 1-10 ms). Customized culture chambers were developed molding polydimethylsiloxane (PDMS) housings, embedding two carbon rod electrodes (distance = 1 cm), to be press-fitted into 35 mm wells (Fig.1B). To investigate the electric field distribution within the culture chamber, a stationary computational analysis was performed (COMSOL Multiphysics), imposing a 3 V voltage between the electrodes. For biological tests, neonatal rat cardiac cells were seeded in the customized chambers (70000 cells/cm^2) and cultured for 3 days in static conditions, followed by 4 days under monophasic (3V, 1 Hz, 2 ms) or asymmetric biphasic (+5V/-1V, 1Hz, 2 ms) pulses. Controls were cultured statically for 7 days (n = 8 for all groups). Cardiac cell functionality was assessed applying an external electrical pacing and determining the excitation threshold (ET) and maximum capture rate (MCR).

Results

Preliminary tests confirmed stability and accuracy of electrical stimulation and ease of use of ELETTRA. Simulations showed that the chamber layout guarantees a relatively uniform electric field over a wide region (6 mm) between the electrodes, with an average value of 2.74 V/cm (Fig. 1B). All cardiac monolayer samples stimulated with asymmetric biphasic pulses reproducibly responded to the external pacing, while only 7 and 5 samples for monophasic stimulation and control group, respectively, followed the external stimulation. Asymmetric biphasic experimental group showed lower ET values and higher MCR values (ET = 3.30 ± 0.34 V/cm, MCR = 3.33 ± 0.82 Hz) compared to monophasic group (ET = 4.50 ± 1.04 V/cm, MCR = 3.00 ± 0.53 Hz) and control (ET = 4.94 ± 0.90 V/cm, MCR = 2.63 ± 0.52 Hz).

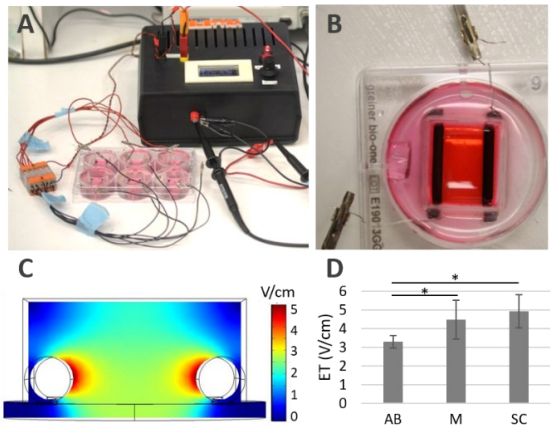

*Figure 1: A) ELETTRA; B) Culture chamber; C) Contour plot of electrical field amplitude within the culture chamber; D) ET values for cardiac monolayer samples cultured under asymmetric biphasic (AB), monophasic (M) pulses, and in static conditions (SC) (*p<0.05).*

Discussion

ELETTRA is easy to use and delivers tunable, stable, and homogeneous cardiac-like electrical stimulation, offering control accuracy, indirect monitoring, versatility, and portability at a competitive cost (~ € 250). Moreover, coupled with existing bioreactors, ELETTRA can be used to provide combined physical stimuli for CTE investigations. Biological results suggest that asymmetric biphasic pulses promote cardiac cell functionality *in vitro*. Further analysis of specific cardiac markers at the mRNA level are ongoing.

References

1. Marsano et al, Biotechnol Prog., 26(5): 1382–1390, 2010.
2. Massai et al, J Healthc Eng., 4(3): 329-370, 2013
3. Stoppel et al, Adv Drug Deliv Rev., 96: 135–155, 2016

OSTEOCHONDRAL BIOREACTOR FOR DRUG SCREENING AND TOXICITY ASSESSMENTS

Francesca Donnaloja(1)*, Giulio De Riccardis(1,2)*, Derek Nichols(3,4)*, Martina Avolio(1,2), Manuela Teresa Raimondi(1), Riccardo Gottardi (2,5,6).

*equally contributing

1 Department of Chemistry, Materials and Chemical Engineering "Giulio Natta", Politecnico di Milano, Milan, Italy; 2 Center for Cellular and Molecular Engineering, Department of Orthopaedic Surgery, University of Pittsburgh, Pittsburgh, PA; 3 Department of Mechanical Engineering and Materials Science, University of Pittsburgh, Pittsburgh, PA; 4 Woodruff School of Mechanical Engineering, Georgia Institute of Technology, Atlanta, GA; 5 Fondazione Ri.MED, Palermo, PA; 6 Division of Pulmonary Medicine, Department of Pediatrics, University of Pennsylvania, Philadelphia, PA

Introduction

Osteoarthritis represents one of the most prevalent and debilitating chronic diseases worldwide. The modest efficacy of available treatments combined with the the significant percentage of failed pre-clinical trials demonstrate an urgent need for realistic tools for *in vitro* drug screening, able to reproduce osteo-chondral interactions in health and disease condition. To generate *in vitro* model of adjacent tissues, we developed and validated an innovative millifluidic bioreactor suitable to accommodate biphasic cell constructs and guarantee real-time optical monitoring.

Materials and methods

Models of the flow path in one-inlet and dual-inlet bioreactors (Fig. 1) were created using SolidWorks and tested using ANSYS Fluid Flow (CFX), with an inlet volume flow rate of 1 ml/day and outlet open to the environment [1].

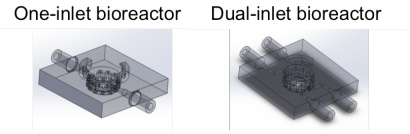

Figure 1: Bioreactors design.

The bioreactors were 3D printed by stereolithography. At day 7 biological tests were performed on the one-inlet bioreactor hosting hMSCs in 8% gelMA construct in the central chamber: Alamar Blue® assay was performed adding the reagent to the inlet medium and analysing the output medium using a plate reader. A Dynamic Live Assay was performed adding Calcein-AM to the inlet medium and collecting bioreactor central chamber z-stacks images. The biphasic bioreactor design fluidic was tested by flowing two different colour media and quantifying the degree of mixing in the outlets using a plate reader. The differentiation of hMSCs towards a chondrogenic and osteogenic phenotype in the two sides of the bioreactor was tested at day 21 via fluorescence test of the Col2 transfected sentinel cells and Col2 PCR analysis.

Results

From the CFD results, one-inlet and dual-inlet bioreactors showed comparable results. Mean velocity of 1.08E-6 μm/s and extremely low shear stress values confirmed simultaneously no cellular damage and suitable nutritional supply in both the devices. Both Alamar Blue® and Live/dead results in one-inlet bioreactor showed no differences in terms of cell metabolic activity if compared to the static culture. Comparing the absorbance intensity of input and output solutions, we validated the absence of fluid mixing inside the chamber. The differentiation of hMSCs towards a chondrogenic and osteogenic phenotype in the two sides of the bioreactor construct was optically validated by fluorescent tests and confirmed by quantitative RT-PCR analysis (Fig 2).

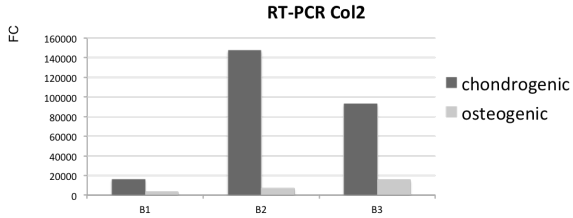

Figure 2: Col2 RT-PCR results for three dual-inlet bioreactors.

Discussion

We validated the millifluidic biphasic bioreactor capability in guaranteeing cell viability, continuous optical monitoring, no mixing of fluids in the culture chamber hosting each tissue phase. Moreover, we validated the designed device in inducing two specific differentiation pathways in the same chamber.

In light of this, the new-designed biphasic bioreactor represents a suitable device for high throughput micro-physiological systems for drug screening and toxicity assessment.

References

1. Nichols, D. A. et al., Biomed. Microdevices 20, 1–8 (2018).

Acknowledgements

We would like to thank Dr. A. Pirosa for help with cell transfection. This work was supported in part by the Ri.MED Foundation, and the National Science Foundation Graduate Research Fellowship (to DAN).

TISSUE REGENERATION IMAGED IN VIVO USING A MINIATURIZED WINDOW FOR INTRAVITAL NONLINEAR MICROSCOPY

Claudio Conci (1), Emanuela Jacchetti (1), Laura Sironi (2), Maddalena Collini (2), Giuseppe Chirico (2), Giulio Cerullo (3), Roberto Osellame (3), Manuela T. Raimondi (1)

[1]Department of Chemistry, Materials and Chemical Engineering Giulio Natta, Politecnico di Milano, Milan, Italy, [2]Univ. di Milano-Bicocca, Dipartimento di Fisica, Milan, Italy, [3]Istituto di Fotonica e Nanotecnologie (IFN)-CNR and Department of Physics, Politecnico di Milano, Milan, Italy

claudio.conci@polimi.it

INTRODUCTION: In many fields such as cancer research and biomaterial testing, intravital microscopy is fundamental to study the evolution and the dynamics of physiological phenomena at the microscale, such as the subcutaneous foreign body response in terms of single cell behaviour and of neovascularization rate. We developed a miniaturized imaging window, the Microatlas, that implanted sub cute, can ectopically guide cell migration and neovascularization into a miniaturized scaffold incorporated in the device. By using two-photon fluorescence microscopy with the Microatlas implanted *in vivo* and repopulated by cells and blood vessels, we can quantify this reaction in the same animal and tissue district, along different time points. Thus, we can *reduce* the number of animals employed in preclinical studies, *refine* and *boost* the analyses and replace old and outdated quantification processes of cellular density, blood vessels sprouting, collagen and fatty infiltrate generation traditionally based on histology. Here, we grafted the Microatlas in living chicken embryos conducting *in vivo* validation assays.

METHODS: The Microatlas micro scaffolds (Fig. 1) were fabricated by two-photon laser polymerization [1] on circular glass coverslips (Ø:5-12 mm), with a biocompatible photoresist, SZ2080. The micro scaffolds consist in several micro grids (500x500x100μm). Reference structures allowed the microscope field-of-view repositioning at different time-points. The Microatlas was implanted in living chicken embryos and it was inspected by nonlinear and linear fluorescence microscopy. At each time point, the embryo was two-photon imaged first, then sacrificed, formalin-fixed, labelled and imaged with a confocal microscope.

RESULTS: Confocal and two-photon inspections at Microatlas implantation sites demonstrated growth of the recipient tissue inside the micro grids and micro vascularization formation with presence of a capillary density six times greater than untreated tissue. Two-photon fluorescence acquisitions specifically showed the presence of a layer of preferentially oriented collagen type I.

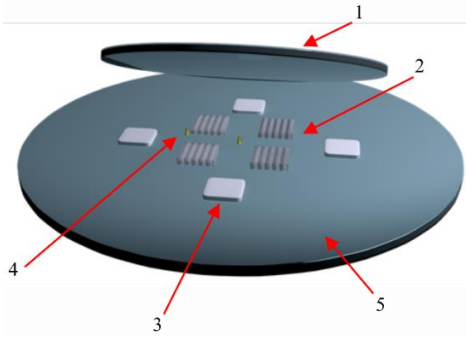

Figure 1: Representation of the Microatlas. A glass coverslip(1) is functionalized with micro scaffolds(2), spacers(3), landmarks for vertical and planar repositioning of the microscope field of view(4). The device can be coupled to a target(5).

Confocal microscope images allowed quantification of cell density with an infiltration rate twofold than untreated tissue and confirmed neo-vascularization inside the Microatlas.

DISCUSSION&CONCLUSION: The Microatlas guided *in vivo* a quantifiable localized reaction inside its micro scaffold, in terms of cell repopulation, collagen generation and capillary formation that we assumed as the primary parameters of the foreign body reaction to an implantation. The device can be used as a reliable and more ethical imaging window for intravital quantifications, which potentially reduces the number of employed animals in preclinical studies.

REFERENCES: [1] Nava MM., T. Eng. Reg. Med. 2016; 4, 524-531.

ACKNOWLEDGEMENTS:

European Research Council (ERC projects NICHOID, G.A. 646990, NICHOIDS, G.A. 754467, and MOAB, G.A. 825159); European Commission (FET-OPEN project IN2SIGHT, G.A. 964481); European Space Agency (ESA project NICHOID-ET, G.A. 4000133244/20/NL/GLC); National Centre for the Replacement, Refinement and Reduction of Animals in Research (NC3Rs projects MOAB, G.A. NC/C01903/1 and NC/C019201/1); Italian Ministry of University and Research (MIUR-FARE project BEYOND, G.A. R16ZNN2R9K); Fondazione Social Venture Giordano Dell'Amore, Cariplo Factory, Politecnico di Milano, Fondazione Bassetti and Fondazione Triulza (S2P project EGGS&BEACON).

COMPLETE TRANSCRIPTOME ANALYSIS OF MESENCHYMAL STEM CELLS CULTURED IN 3D SYNTHETIC NICHES

Carolina Testa (1,2), Stefania Oliveto (3), Francesca Donnaloja (2), Pietro Pinoli (1), Emanuela Jacchetti (2), Roberto Osellame (4), Giulio Cerullo (4), Stefano Biffo (3)‡, Stefano Ceri (1) ‡ and Manuela Teresa Raimondi (2) ‡

1. DEIB, Department of Electronics, Information and Bioengineering, Politecnico di Milano, Milano, Italy; 2. Department of Chemistry, Materials and Chemical Engineering "Giulio Natta", Politecnico di Milano, Milano, Italy; 3. INGM, National Institute of Molecular Genetics "Romeo ed Enrica Invernizzi", Milano, Italy; 4. Istituto di Fotonica e Nanotecnologia (IFN)-CNR and Department of Physics, Politecnico di Milano, Milano, Italy; ‡Co-senior authors.

INTRODUCTION

In the field of cell-based therapies, mesenchymal stem cells (MSCs) attracted increasing attention thanks to their multipotency, ease of isolation and freedom from ethical issues. Moreover, in addition to their potentiality in differentiation and tissue regeneration, MSCs displayed to possess immunomodulatory and anti-inflammatory effects and a marked trophic activity, encoding for a variety of regulatory proteins, including those of the extracellular-matrix (ECM) [1][2]. However, in the body, MSCs reside in specific niches which support MSCs properties through biochemical and biophysical cues. Therefore, many efforts have been put in the design of three-dimensional (3D) synthetic niches, aiming to emulate the native microenvironment and thus efficiently control SCs fate *in vitro* and produce therapeutic cells in large-scale. In this panorama, an innovative engineered niche, named NICHOID, was developed [3]. Its capacity to maintain the pluripotency of different types of SCs without adding any exogenous factor, has been already assessed [4][5]. This phenomenon is linked to isotropic forces that NICHOID provides to cells, inducing a genetic reprogramming by controlling the cytoskeletal tension.
In our work we aimed to investigate, by means of a complete transcriptomic analysis, which are the effects of NICHOID on the whole gene expression of MSCs.

METHODS

Micro-patterned substrates were fabricated through two-photon polymerization (2PP) of a negative hybrid photoresist (SZ2080). Two different scaffold configurations were fabricated: the traditional 3D one (3D NICHOID) and a flat control, composed only by a single layer of polymerized grids (2D NICHOID). The scaffolds were sterilized and seeded with 3×10^4 rat mesenchymal stem cells, obtained from bone marrow of Lewis rats (rBMSCs). After 4 days their morphology and viability were assessed using fluorescence microscopy techniques and the RNA was extracted to study gene regulation. Sequencing data were later quality-checked, processed and subjected to differential expression and enrichment analyses.

RESULTS

rBMSCs were vital in both conditions but displayed different morphologies. Indeed, cells in 3D NICHOIDs were more roundish, attached to the surrounding structure and cells, while on 2D NICHOIDs were elongated on the bidimensional surface. In term of gene expression, this difference in shape was translated in a total of 603 differentially expressed genes (364 up-regulated and 239 down-regulated) between 3D and 2D NICHOIDs. Moreover, interesting pathways turned out to be deregulated, including those related to actin cytoskeleton, immune response, cell adhesion molecules and ECM components.

DISCUSSION

These results highlighted that NICHOID, thanks exclusively to its tridimensional pattern and to the forces it exerts on cells, is able to maintain not only the pluripotency but also other peculiar features of MSCs. This make the NICHOID an appropriate tool for the expansion of MSCs, which can be used not only for regeneration but also to provide physical and trophic supply.

References

1. D. G. Phinney, *Cell Cycle*, vol. 6, no. 23, pp. 2884–2889, 2007.
2. J. Ren *et al.*, *Cytotherapy*, vol. 13, no. 6, pp. 661–674, 2011.
3. M. T. Raimondi *et al.*, *Acta Biomater.*, vol. 9, no. 1, pp. 4579–4584, 2013.
4. M. M. Nava *et al.*, pp. 1–12, 2016.
5. S. Carelli *et al.*, *Nanotheranostics*, vol. 5, no. 1, pp. 8–26, 2020.

Acknowledgements

This study was supported by the following funding: European Research Council (ERC projects NICHOID, G.A. 646990, NICHOIDS, G.A. 754467, and MOAB, G.A. 825159); European Commission (FET-OPEN project IN2SIGHT, G.A. 964481); European Space Agency (ESA project NICHOID-ET, G.A. 4000133244/20/NL/GLC); National Centre for the Replacement, Refinement and Reduction of Animals in Research (NC3Rs projects MOAB, G.A. NC/C01903/1 and NC/C019201/1); Italian Ministry of University and Research (MIUR-FARE project BEYOND, G.A. R16ZNN2R9K).

EXPERIMENTAL EVALUATION OF PERMEABILITY IN TPMS SCAFFOLDS

J. Santos (1), T. Pires (1), B. P. Gouveia (1), A. P. G. Castro (1), P. R. Fernandes (1)

1. IDMEC, Instituto Superior Técnico, Universidade de Lisboa, Lisbon, Portugal;

Introduction

This study presents an experimental evaluation of permeability in triply periodic minimal surfaces (TPMS) based scaffolds, which permit advantageous structural properties for Bone Tissue Engineering (BTE). Three different TPMS structures were considered: Schwartz Diamond (SD), Gyroid (SG) and Schwartz Primitive (SP), with four different porosities (50, 60, 70 and 80%) [1].
Permeability is widely used to characterise scaffolds for BTE applications, as it gives information about the structure porosity, pore size, tortuosity and pore interconnectivity which have an important impact in cell seeding and proliferation [2].
Within this scope, it is important to study which law or method is more suitable for permeability calculation of porous structures. The most used law in literature is the Darcy's law (Eq. 1) but depending on the flow regime, the Forchheimer's law (Eq. 2) can be used as well [3].

$$-\frac{dP}{dx} = \frac{\mu}{k_1} \times v \quad (1)$$

$$-\frac{dP}{dx} = \frac{\mu}{k_1'} \times v + \rho \times \beta \times v^2 \quad (2)$$

Where $-\frac{dP}{dx}$ represents pressure drop, μ is the fluid viscosity, ρ is the fluid density, β the Forchheimer's coefficient, v is the fluid velocity and, k_1 and k_1' are Darcy's and Forchheimer's permeabilities respectively.

Methods

Ten scaffolds (13x13x13 mm) of each TPMS structure were produced using a MJP 3600 MultiJet® (3D Systems, EUA) 3D printer and its material Crystal [2].
Figure 1 presents some examples of samples produced and studied in this work. Experimental determination of permeability was addressed by forcing water flow through the scaffolds at constant flow rates. Eleven flow rates were considered (1, 2, 3, 4, 5, 10, 20, 40, 60, 80 e 100 mL/min) and values for pressure drop were obtained for each flow rate and, type of scaffold and porosity. Subsequently, the distinction of the flow regimes and permeability calculation were performed.

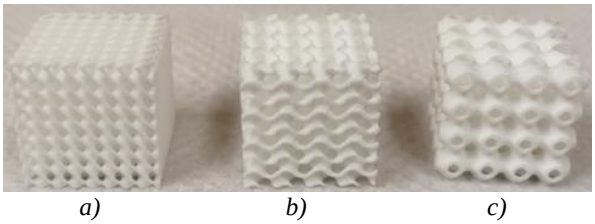

a) *b)* *c)*

Figure 1: Samples of the 80% porosity TPMS scaffolds used in this work: a) SD80, b) SG80 and c) SP80.

Results

It was observed that the behaviour between measured pressure drop and flow rate presented a polynomial tendency (figure 2); this behaviour was aggravated with decrease of porosity, indicating that Forchheimer's law is probably the most suited for permeability calculation.

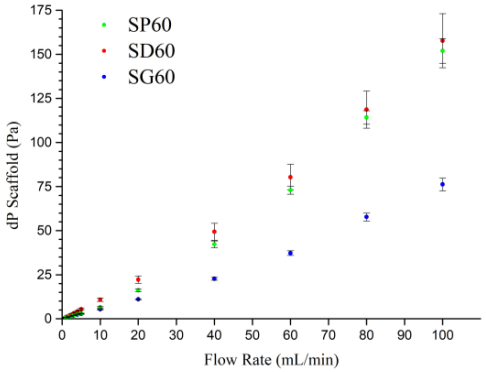

Figure 2: Obtained values of the pressure drops for the 60% porosity scaffolds.

Discussion

Darcy and Forchheimer laws were compared through the obtained permeability values, which were not significantly different. The studied scaffolds presented permeability values in the magnitude of 10^{-10} - 10^{-9} m^2 and 10^{-6} - 10^{-5} m for inertial permeability, well placed within the ones presented in literature for bone TE [3].
For the flow regimes in analysis, it seems both laws can be applied on the evaluation of permeability in TPMS scaffolds and the Forchheimer's equation can effectively be interpreted as an expansion of Darcy's law.
The SG scaffolds were considered the most permeable ones except for the 70 and 80% porosities in which the SP surpassed the SG. Although a higher porosity usually means having a higher permeability, that was not the case when comparing the SG and SD geometries.
Such findings underline the potential of TPMS scaffolds in allowing elevated permeability values with inferior porosities when compared with other conventional scaffolds. Future work will consider new fabrication methods and materials for different applications.

References

1. Montazerian et al, Mater Des, 126:98–114., 2017.
2. Castro et al, Materials, 12(8), 2019.
3. Santos et al, JMBBM, 110:103932, 2020.

Acknowledgements

This work was supported by FCT, through IDMEC, under LAETA project UIDB/50022/2020 and also through project PTDC/BBB-BMC/5655/2014.

DESIGN AND VALIDATION OF A NOVEL PLATFORM FOR LOW COST-BICOMPARTMENTAL CELL AND TISSUE CULTURES

Lorenzo P. Coppadoro (1), Chiara Foglieni (2), Maria Lombardi (2), Elia Pederzani (1), Gianfranco B. Fiore (1), Monica Soncini (1)

(1) Dipartimento di Elettronica, Informazione e Bioingegneria, Politecnico di Milano, Italy; (2) Cardiovascular Research Area, IRCCS San Raffaele Scientific Institute, Milano, Italy.

Introduction

In vitro cell/tissue culture represents a widespread methodology for pathophysiologic studies with good cost/benefit ratio. Despite PDMS-based organ-on-chip technologies are leading the scientific panorama, translation to commercial products is very limited, due to high costs and hurdles for large scale manufacturing [1]. We have developed and validated a novel system based on conventional and low-cost rapid prototyping technologies [2], that allows to host either a microporous membrane on which seeding cells or 3D structures, such as scaffolds or tissue biopsies, to perform compartmentalized cultures/co-cultures and to visualize in real time the sample of interest. Moreover, we have introduced a novel feature to easy recover and reuse the biological material, maintaining the morphological structure and vitality.

Methods

CO_2 Laser cutting (Versa Laser V2.30 ULS) rapid prototyping technology has been applied to realize a novel 12-well plate compatible system suitable to house a porous membrane and perform bi-compartmental cultures. The device is under patenting process. To validate the system, polycarbonate (PC) track-etched 5 µm pore size membranes (Whatmann Nucleopore®) settling on Caco-2 (a cell line, recognized model of colonic epithelium [3]; $4x10^4$ cells/system) and PC track-etched 3 µm pore size membranes (it4ip ipCELLCULTURE™) settling on EAhy-926 (a cell line, recognized model of vascular endothelium; $3x10^4$ cells/system) were inserted. Transwell® inserts served as comparators. Static cultures were run till confluence.

Cell presence/growth was monitored by Acridine Orange stain of living cells (Figure 1A). Confluent cells were then fixed in paraformaldehyde, stained by DAPI (nuclei) and differentiation /lineage-specific antibodies (Caco-2: Human Epithelial Antigen, Junction Adhesion Molecule; EAhy-926: CD-31/PECAM1, von Willebrand factor). Cells were observed at Nikon 55i fluorescence and Leica TSP5 confocal microscopes, and analyzed using FiJi and Adobe Photoshop CS4 software, as opportune. Each experiment (samples in duplicate) was run in at least three times.

Results

The system's production has been scaled up to 70 devices simultaneously, with high reproducibility.

By these systems we obtained confluent monolayers either of living Caco-2 cells or EAhy-926 cells. Cell density was comparable to that on Transwell® inserts, without relevant cell migration across the membrane. Endothelial cells phenotype (Figure 1B) and Caco-2 polarization (Figure 2A, 2B) were observed in all samples.

Conclusions

The optimization of device fabrication processes and assembling protocols led to a highly reproducible and scalable system showing a good compatibility with cultured cells as Caco-2 and EAhy-926 and comparable with Transwell® inserts. The features of our novel system enable controlled and easy to handle cultures. In perspective, we will upgrade the system to subject cells to dynamic stimulation, both in single and co-culture conditions.

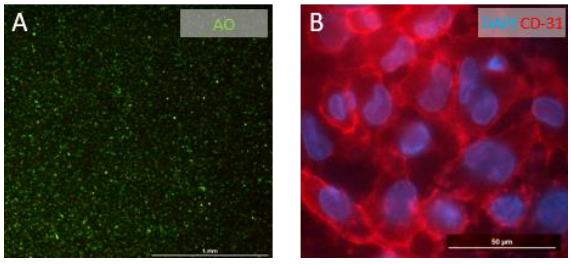

Figure 1: A) Representative live fluorescence images of EAhy-926 cell monolayers labelled with Acridine Orange. B) Representative fluorescence images of EAhy-926 cell monolayers labelled with DAPI and CD-31.

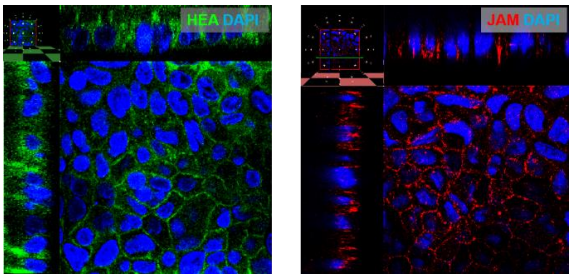

Figure 2: Representative confocal cross-section images of Caco-2 cell monolayers labelled with Human Epithelial Antigen (HEA) and DAPI (left), and Junction Adhesion Molecule (JAM) and DAPI (right), demonstrating cell polarization.

References

1. Walsh D. I. et al, *Trends Biotechnol*, 35:383–392, 2017.
2. Ren Y. et al, *Sci Rep*, 9:1–10, 2019.
3. Cavarelli M. et al., *EMBO Mol Med*, 5: 776–794, 2013.

CFD EVALUATION OF PERMEABILITY IN TPMS SCAFFOLDS

T. Pires (1), J. Santos (1), B. P. Gouveia (1), A. P. G. Castro (1), P. R. Fernandes (1)

1. IDMEC, Instituto Superior Técnico, Universidade de Lisboa, Lisbon, Portugal;

Introduction

In bone Tissue Engineering (BTE), the development of scaffolds has been a major area of research, seeing as they are porous structures that support cell seeding. It is possible to predict what the cells will differentiate into, based on the fluid flow velocity and the shear strain, which are both influenced by a scaffold's permeability [1]. This parameter is crucial in allowing sufficient fluid flow to pass through the scaffold in order to allow the cells to enter it. It also affects the preceding cell proliferation and vascularisation [2]. Permeability of a scaffold is determined by its geometry and its porosity. One of the most discussed design strategies for geometry- and porosity-controlled scaffolds is the triply periodic minimal surfaces (TPMS) method [3]. Accordingly, this study is focused on the analysis on the relationship between the permeability, the porosity and the geometry of TPMS scaffolds, through the combination of a Computational Fluid Dynamics (CFD) analysis using FLUENT® ANSYS® (Ansys Inc., Canonsburg, Pennsylvania, USA) and experimental permeability tests.

Methods

For this study, three different TPMS geometries were studied (Schwartz D (SD), Gyroid (SG) and Schwartz P (SP)), in two levels of porosity (60% and 70%, ahead named from SD60 to SP70). These scaffolds were produced (Figure 1) using a MJP 3600® MultiJet printer (3D Systems, USA). The experimental permeability setup consisted on a syringe pump; a permeability chamber where the scaffold is placed and a pressure transducer that measures the pressure difference. For each scaffold, a total of five different flow rates were tested between 5 and 60 ml/min, with their permeability calculated using Darcy's Law [4].



Figure 1: 3D printed TPMS scaffolds: SD70 (left), SG70 (middle) and SP70 (right).

From a computational cost perspective, it was not feasible to represent the entire 13 mm sided cubic scaffold in the CFD analysis. Therefore, alternative models were built using periodic boundary conditions.

Results

The comparison between the experimental and numerical values shows a good correlation with a R^2 equal to 0.903. However, the obtained experimental pressure drop values are higher than the numerical values (Figure 2, for the 70% porous scaffolds).

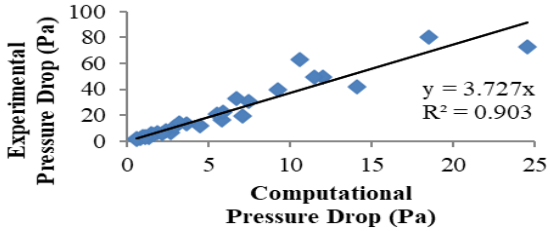

Figure 2: Correlation between the pressure drop calculated from computational and experimental tests for the 70% porous scaffolds.

Discussion

The obtained results are within the range of the permeability values for porous structures used as scaffolds for BTE [2]. In addition, it has been shown that, for the same geometry, a lower porosity results in a lower permeability. However, when comparing different geometries, a lower porosity was not an assurance of a lower permeability, which is in line with previous studies [5].

The insights gained with the CFD outputs, namely the flux streamlines within the scaffolds, support the view that even though porosity is the main factor in determining a scaffold's permeability, its geometry, in particular the surface curvature, also plays an important role. The difference between the numerical and experimental values might be a result of not including of roughness and wettability surface effects in the simulations, which shall be considered in later stages.

To conclude, the SG scaffolds had the overall highest permeability values and permitted more suitable flux streamlines to promote cell-scaffold interactions [1]. Thus, these were recognised as the most advisable scaffolds for most BTE applications.

References

1. Castro and Lacroix, BMMB, 17(2):531–541, 2018.
2. Daish et al, IJNME, 118(13):783-803, 2019.
3. Giannitelli et al, Acta Biomater, 10(2):580-594, 2013.
4. Santos et al, JMBBM, 110:103932, 2020.
5. Pires et al, J Biomech, 110263, 2021.

Acknowledgements

This work was supported by FCT, through IDMEC, under LAETA project UIDB/50022/2020 and also through project PTDC/BBB-BMC/5655/2014.

SCALED UP PROCEDURE TO PRODUCE 'LIVING' PERICARDIUM MATERIAL FOR PERSONALIZED CARDIAC VALVE REPAIR

Stefano Rizzi (1,3), Giacomo Bernava (1), Domenico Ventrella (2), Silvia Ferrari (1), Beatrice Belgio (3), Gianluca Polvani (4), Maria Laura Bacci (2), Federica Boschetti (3), Sara Mantero (3), Maurizio Pesce (1)

1. Centro Cardiologico Monzino IRRCS, Italy; 2. University of Bologna, Italy 3. Politecnico di Milano, Italy; 4. Università di Milano, Italy

Introduction

Diseased and dysfunctional heart valves are routinely replaced by surgical intervention. About 300,000 heart valve procedures are performed annually worldwide; this number is expected to triple by 2050 with the majority of the patients over the age of 65 [1]. Despite their non-modifiable mechanical performance, mechanical prostheses are prone to thromboembolic complications causing patients to require lifelong anti-coagulation therapies. Biological valves, produced with aldehyde-treated animal pericardium, undergo structural deterioration. This is still the principal cause of their failure in the mid/long term. In the present contribution, we propose the scale-up of a procedure to obtain a fully recellularized pericardium material for heart valve engineering. This method has been already tested at laboratory scale [2,3], and is very promising to produce circular patches of 'living' pericardium employable for surgical repair/reconstruction of the aortic valve, also with a 'personalized' approach.

Methods

The decellularization procedure was previously described for porcine pericardium as an improvement of fixation methods and treatment that lead to enhance compatibility of tissue by removing xenoantigens [2,3]. Perfusion tests on decellularized bovine pericardium samples were employed to evaluate and compare the permeability of the tissue from different donors (three samples each). The apparatus used is composed of two coaxial stainless cylinders and a capillary flow meter with the resolution of 1 µl. Fluid pressure was obtained using a column filled with PBS. Permeability was then evaluated using Darcy's law. The bioreactor was designed with the aim to first perfuse a cell suspension through the pores of a scaffold enhancing the uniformity and homogeneity of the distribution of cells and secondly promote cell growth and viability during the culture phase. The system design meets the specifications of a complete standalone bioreactor suitable for industrial scale: sterilisability, ease of use, mass transport enhanced from the media to the construct, reduced overall dimensions and automatic medium exchange. Finally, the design took into account finite element modelling (CFD) with the purpose to assess flow, shear stress distribution and overall fluid dynamic inside the chamber of the bioreactor in relation with characteristics of the decellularized tissue used as a scaffold.

Results

Decellularization consistently increased bovine pericardium permeability: from an overall average value of 3.01E-14 for the native tissue to 1.47E-13 for the decellularized tissue, confirming the possibility to employ a direct perfusion bioreactor to reintroduce cells. Our preliminary recellularization procedure with autologous cells was set in circular patches of 1cm in diameter [2,3], with good results. In order to be clinically employed, diameter of the circular patches will have to be increased until around 5 cm, thus making necessary the engineering of a new cellularization platform.

Provisionally, the new platform will consist of 4 independent bioreactors connected to a flow dynamic loop for seeding phase and one circuit for culture phase composed of a peristaltic pump, a medium reservoir and related tubes.

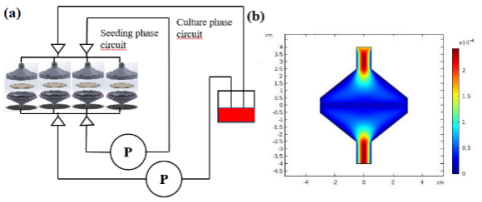

Figure 1:Four independent bioreactor will be connected to the fluid dynamic loops (a), beside the flow velocity field in the chamber (b).

This platform will be realized using chambers and tubing produced with already approved materials for human use (e.g. PSU for the chamber). This will make it easily implementable in the GMP environment.

Discussion

On the basis of our preliminary and published results, the production of living pericardium material with our method appears feasible. In this framework it is very promising the perspective of seeding pericardium with autologous cells (e.g. adipose-derived stem cells), thus prompting, for the first time, the delivery of a personalized therapy for valve disease.

References

1. Head et al, Eur Heart J, 38(28):2183-2191, 2017
2. Amadeo et al, J Tissue Eng Regen Med, 12(6):1481-1493, 2018
3. Amadeo et al, Front Cardiovasc Med, 7:80, 2020

DEVELOPMENT OF A VARIABLE STIMULATION CELL CULTURE SYSTEM USIGN *IN-SITU* FEEDBACK OF THE GENE RESPONSE

Kenjiro Tsuchiya (1), Yusuke Morita, Koji Yamamoto (2)

1. *Graduate School of Life and Medical Sciences, Doshisha University, Japan*
2. *Department of Biomedical Engineering, Doshisha University, Japan*

Introduction

In recent years, regenerative medicine has been applied for the treatment of articular cartilage disease. It is well known that the anabolic function of chondrocyte can be promoted by mechanical stimulation and lots of stimulation conditions have been proposed to improve the function of cultured cartilage tissue. However, the effect of external mechanical stimulation varies depending on the amount and the structure of the extracellular matrix (ECM) around the cell, and those ECM environments dramatically change with culture period. Hence, to maximize the ECM synthesis of cultured cartilage, it is required to alter the stimulation intensity in response to the molecular expression of the cell in the tissue. Here, we developed a variable mechano-stimulation system based on a live imaging of the cellular gene expression under mechanical stimulation using the *Col2a1* gene specific promoter, and verified the validity of the system by quantifying the *Col2a1* gene expression after 6 days culture.

Materials and Methods

Col2al-pZsGreen1-1 vector and CMV-DsRed-Express2 vectors were generated to evaluate gene expression responses *in situ*. The expression level of *Col2a1* were evaluated by the normalized luminance value of pZsGreen1-1 divided by that of DsRed-Express2. Figure 1 shows shape of a silicon sheet where the cells were seeded, and the contour plot shows a strain ε_{xx} profile under an x-axis tensile displacement. Eight displacement patterns were prepared to generate 1-13% strain ε_{xx} within the cell culture area (Fig.1 shows the case of 1-7% strain). The luminance values at each 1-13% strain field were estimated by using an approximate curve with the measured luminance values. By multiplying each luminance value by the area of each strain field and summing them together, we calculated the total luminance value each day. The displacement that showed the largest total luminance values among the eight displacements patterns was selected as the next stimulation condition. As the initial condition of strain ε_{xx}, the displacement was set to 5% of the main strain field in the sheet. ATDC5 induced to differentiate for 7 days was seeded on the silicon sheet at 2.4×10^4 cells/cm^2. After seeding at 18 hours, the vectors were transfected into ATDC5 and the cells were cultured for 6 days, while being loaded to 0.5 Hz tensile stimulation for 5 hours per day. mRNA expression of *Col2a1* was measured by using quantitative real-time PCR (N=4, Student's *t*-test) and the transcriptional normalized luminance value was evaluated using fluorescence observation.

Results and Discussion

Figure 2(a) shows the change in the expression level of *Col2a1*. The expression of *Col2a1* in the stimulated group was significantly increased in comparison to that in the control group (without stimulation). Figure 2(b) shows the change of the tensile displacement for the sheet at each day. It was found that the tensile displacement was altered by using the information of *Col2a1* expression. These results suggest that the feedback to external stimulation based on the stimulus response of chondrocytes can promote the anabolic response even if a heterogeneous mechanical field is generated in the tissue.

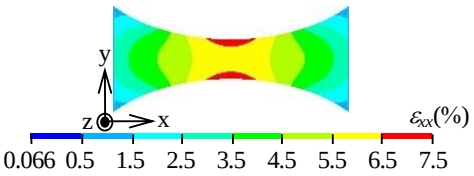

Figure 1. Strain distribution of silicon sheet obtained by finite element analysis (Displacement : 0.96 mm).

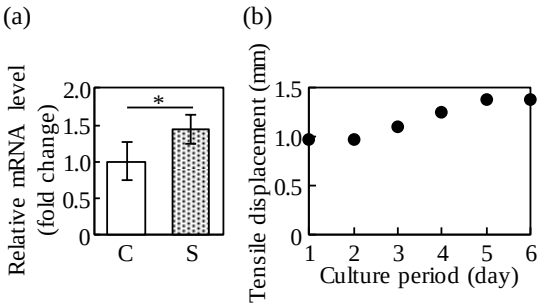

*Figure 2. Results on the effectiveness of variable mechano-stimulation systems, (a) Changes in Col2a1 expression level by qRT-PCR (C: Control, S: Stimulation, N=4, mean±s.d., *:P<0.05). (b) Change of tensile displacement at each day.*

References

1. Zhong, D., et al., *Acta of Bioengineering and Biomechanics*, 20 : 3-10, 2018.

Acknowledgements

This work was supported by JSPS KAKENHI Grant Number JP18H01398.

WRAP ME UP AND LET ME HEAL: *IN SILICO* MODELING OF BONE REGENERATION USING A BIOENGINEERED PERIOSTEAL MEMBRANE

Laura Lafuente-Gracia (1,2), Aurélie Carlier (3), Liesbet Geris (1,2,4)

1. Biomechanics section, Department of Mechanical Engineering, KU Leuven, Belgium; 2. Prometheus, Division of Skeletal Tissue Engineering, KU Leuven, Belgium; 3. Department cBITE, MERLN Institute, Maastricht University, The Netherlands; 4. Biomechanics research unit, GIGA in silico medicine, University of Liège, Belgium

Introduction

Bone healing is a complex, well-coordinated process that starts autonomously when a bone fracture occurs. Due to bone tissue characteristics, successful healing is usually achieved within weeks. However, up to 10% of bone fractures result in delayed healing or non-union, due to fracture severity, anatomical location and host factors such as age, smoking or the presence of other comorbidities. In this work we investigate *in silico* the influence of a bioengineered periosteal membrane, produced using melt electrowriting followed by coating with growth factors and/or cells and combined with oxygen releasing beads, as potential treatment strategy to trigger bone regeneration in cases of non-union occurrence.

Methods

An existing bioregulatory, oxygen-dependent fracture healing model [1] was used to analyze the membrane influence during the healing process in a large skeletal defect. The study was initially classified into three scenarios representing the cases where (S1) only growth factors (GF), (S2) only cells, and (S3) GF and cells were loaded onto the membrane. In S1, different burst-sustained release profiles of osteochondrogenic GF were implemented as boundary conditions (BC). In S2, MSCs, chondrocytes and osteoblasts were implemented as initial conditions (IC) or BC to capture different effects of migration to the fracture callus. In S3, a combination of S1 and S2 best results was investigated. Additionally, additional oxygen experiments were performed. First, since the current model did not simulate the inflammatory phase, simulations with only cells and oxygen were run to represent different IC at the start of the repair phase. Second, the behavior of hypoxia-resistant cells and their influence on the healing process when loaded onto the membrane was explored. Third, the effect of the surroundings, namely the musculature as oxygen source and non-represented cells as oxygen sink, was taken into account.

Results

Key role of GF. S1 predicted bone union when a certain average GF concentration was reached, showing that osteochondrogenic GF loaded alone onto the membrane are capable to provide the necessary conditions for the bone to heal (results not shown).

Key role of chondrocytes. S2 and S3 with hypoxia-resistant chondrocytes loaded onto the membrane predicted bone healing (Figure 1, case B). However, when non-trained cells were loaded alone or in combination with GF, the regenerative outcome depended strongly on other IC (Fig. 1, cases A & C).

Influence of IC. The IC of cells was shown to have less impact in bone healing: the results predicted very little difference in the distribution of bone formation at day 90 when using different values to account for the inflammation time (results not shown). However, different values of oxygen IC predicted different regenerative outcomes, as shown in Fig. 1, case C in comparison with Fig. 1, case A; and thus entailed new oxygen experiments to investigate further hypotheses.

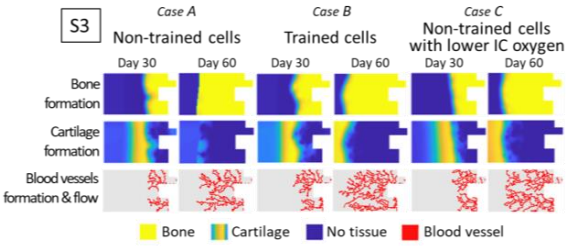

Figure 1: Predicted spatial distribution of bone, cartilage and blood vessels formation at days 30 and 60 for the scenario in which GF and cells were loaded onto the membrane. Due to symmetry, the domain represents one-fourth of the simulated large skeletal defect; and union happens when the bone front, in yellow, reaches the other side. Case A, where bone formation stopped around day 60, predicted non-union. Cases B and C, in which bone was still forming at day 60, predicted bone union by day 90, hence resulting in healing.

Discussion

Bone union was predicted *in silico* with the application of different periosteal membrane types. The different regenerative outcomes indicated that oxygen as IC, chondrocytes and GF play a determinant role in bone healing. Furthermore, the results brought new hypotheses to explore, e.g. the model is very sensitive to oxygen IC, thus implementing the inflammatory phase will provide more accurate IC for oxygen, and also for cells. This study also shows that using models as initial *in silico* screening will allow to identify the most impactful *in vivo* conditions to be tested experimentally.

References

1. Carlier et al., Biofabrication 8:025009 (2016).

Acknowledgements

This work was supported by the European Regional Development Fund - Interreg North West Europe (BONE, NWE 497).

HIGH-THROUGHPUT MECHANICAL SCREENING PLATFORM FOR ENGINEERED TISSUES IN WELL-PLATES

Nelda Antonovaite(1), Joost Nieuwenhuis(1), Ramkumar Raghuraman(1), Kevin Bielawski(1)

1. Optics11 Life, The Netherlands

Introduction

Engineered tissues are fabricated by combining 3D tissue scaffolds, cells, and biomolecules, followed by culturing step for the maturation of the construct, to eventually mimic the composition of native or diseased tissues [1]. One of the major characteristics of engineered tissues is its mechanical properties that influence the morphology and biochemical signaling of the cells [2]. Typically, the mechanical characterization of engineered tissues requires relatively large samples that are transferred out of the well-plate into the larger dish, compatible with conventional mechanical testing systems, which is both destructive and time-consuming. Therefore, a high-throughput mechanical screening device compatible with the well plate format is needed to efficiently characterize mechanical state of engineered tissues.

Methods

In this study, we introduce novel indentation probes with geometry compatible with 96 well-plate combined with X-Y-Z positioning system called Pavone, calibrated for the location of each well, for automatization of indentation procedure (Fig. 1 top). Indentation probes were fabricated by mounting microfabricated cantilever (MEMS) on top of a 1.4 mm diameter and 20 mm length glass ferrule and equipping it with optical fiber to remotely readout the cantilever bending through the interferometric signal [3].

Results

For the proof of principle, we measured mechanical properties of hydrogel coated HTS 96 well-plate ranging in Young's modulus, according to the manufacturer (Matrigen), from 0.2 to 50 kPa in phosphate-buffered saline. The indentation probe of 0.31 N/m cantilever stiffness and spherical tip radius of 24 µm was used to perform static indentations and dynamic mechanical analysis (DMA [4]). The measured Young's modulus varied between 0.2 and 70 kPa (Fig. 1 middle). Furthermore, samples showed non-zero loss modulus E'' and dependency on oscillation frequency which is typical for viscoelastic materials (Fig. 1 bottom).

Discussion

To summarize, our proposed high-throughput indentation system can characterize the viscoelastic properties of various stiffness hydrogels in well-plates in a fast and non-destructive way. Pavone enables mechanical phenotyping of hydrogels and engineered tissue constructs, and has a potential to bring mechanical screening to the clinical and drug testing applications.

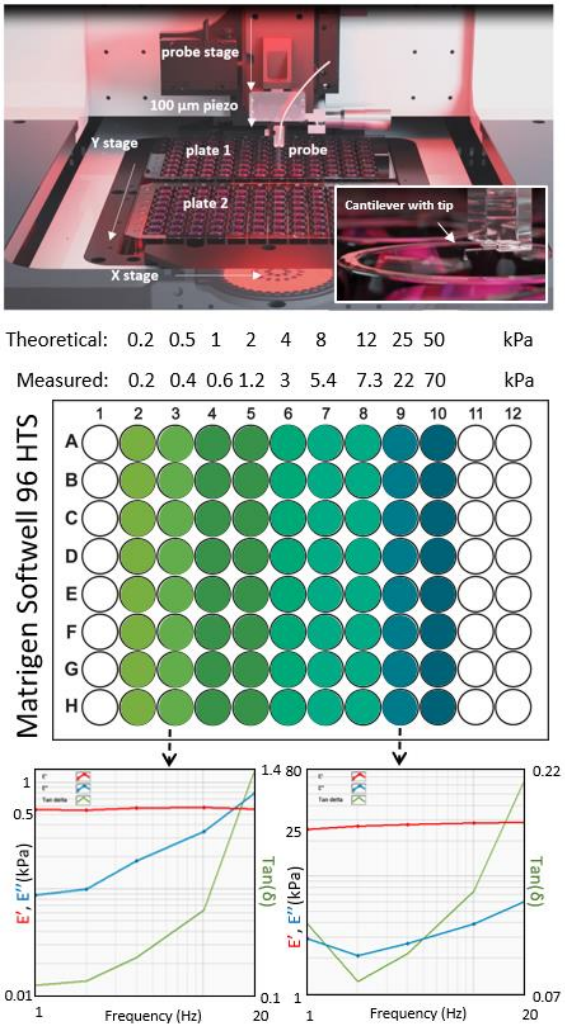

Figure 1: Top: high-throughput mechanical screening platform Pavone. Middle: mean Young's modulus values of hydrogel coated 96-wellplate (Softwell, Matrigen). Bottom: storage and loss moduli E', E'', and damping factor tan(δ) as a function of oscillation frequency.

References

1. Dzobo et al, Stem Cells Intern, 2018.
2. Caddeo et al, Front Bioeng Biotechnol, 5, 2017.
3. Chavan et al, Rev of Sc Instr, 83 (11): 115110, 2012.
4. Antonovaite et al, Sc Rep, 8, 2018.

PREDICTION OF INDIVIDUAL KNEE MOTION: AN IN-VIVO VALIDATION UNDER PHYSIOLOGICAL LOAD

Michele Conconi (1), Nicola Sancisi (1), Filippo De-Carli (2), Giuseppe Monetti (2) and Vincenzo Parenti-Castelli(1)

1. Department of Industrial Engineering, University of Bologna, Bologna, Italy; 2. Primus Medical Center, Forlì, Italy

Introduction

Quantification of individual joint motion may help understanding the articular physiology and designing better treatments and devices. Measurements of such a motion are nowadays invasive or imprecise [1]. We present a numerical model that allows prediction of individual joint motion from the shape of articular surfaces. We hypothesize that the articulations are shaped by an adaptation process to optimally distribute contact loads [2-4]. Individual knee motion under physiological loads can thus be obtained by minimizing a measure of peak contact pressure such as joint congruence [5]: the more congruent the articular surfaces, the smaller the peak contact pressure. This concept was previously applied and validated for cadaveric tibiotalar [6] and knee [7] joints. In this study, the model is validated in vivo on seven knees during weight bearing MRI.

Methods

MRI (3D-HYCE sequences) of the right knee of seven healthy volunteers (males, 32±6-7 years, 177±7.5 cm, 77±7.7 kg) were acquired through a 0.25 T scanner (G-Scan Brio, Esaote SpA). The MRI were segmented (MITK) to reconstruct the articular surfaces of the femur and tibia. Individual knee motion was computed by maximizing joint congruence for a 90° flexion range. The joint motion under load was also measured for validation purposes. For this scope, the scanner was rotated of 90°; the volunteers stood with the right leg in the scanner while the contralateral leg was lowered by a hydraulic, MR compatible rig (Fig. 1.a). The overall motion was similar to stair climbing. For each volunteer, 4 to 5 weight-bearing scans were acquired during flexion. Anatomical reference systems were defined [8] and the femoro-tibial motion was expressed according to [9]. Model predictions were compared to experimental measures by evaluating MAE for rotational and translational motion component.

	Rot. MAE [°]	Trans. MAE [mm]
Knee 1	3.6 ± 2.4	1.4 ± 0.7
Knee 2	1.9 ± 1.3	1.0 ±0 .8
Knee 3	1.2 ± 0.9	2.1 ± 1.1
Knee 4	3.1 ± 1.7	1.1 ± 0.6
Knee 5	4.0 ± 2.5	2.5 ± 1.1
Knee 6	4.3 ± 1.6	1.8 ± 1.1
Knee 7	2.8 ± 1.6	1.3 ± 0.8

Table 1: MAE between model prediction and experimental measure for the seven investigated knees.

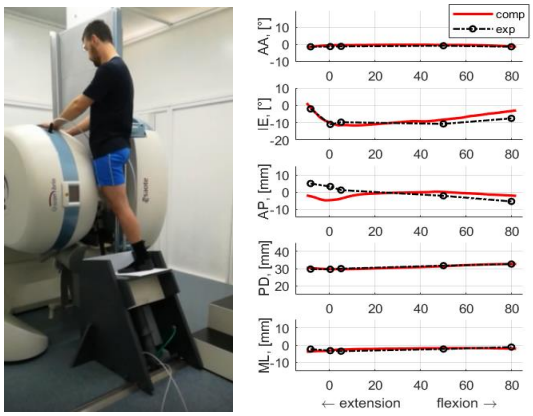

(a) (b)

Figure 1: Setup for the orthostatic MRI scans (a). Comparison between model prediction and experimental measure (b) for one knee.

Results

For all the knees, rotational and translational MAE stay below 4.5° and 2.5mm, respectively (see Table 1). The highest rotational error took place on the internal-external rotation. However, when present errors affect the end of the flexion, while the characteristic screw home motion at the beginning of knee flexion was correctly predicted (Fig 1.b) for all the knees.

Discussion

The presented analysis supports the validity of the predictive model. This approach needs only a 3D representation of the articular surfaces. It may provide a simple and non-invasive way to characterize the individual joint motion. Thus, it may be also useful for the customization of musculoskeletal model, opening the way to their clinical application.

References

1. Masum M. A. et al., *ABEC, 2014*.
2. Radin E. L. et al., *Clin. Orthop. Relat. Res*., 131:288-293, 1979.
3. Frost H. M., *Am. J. Hum. Biol*., 11:437-455, 1999.
4. Heegaard J. H. et al., *J. Orthop. Res*., 17:509-517, 1999.
5. Conconi M. and Parenti-Castelli V., *Proc Inst Mech Eng H.*, 228:935-941, 2014.
6. Conconi M. et al., *J Biomech*, 48:2960-2967, 2015
7. Conconi M. et al., XV ARK: 261-269, 2018.
8. Tashman S. and Anderst, W., *J Biomech*, 46:1–8, 2013.
9. Grood E. S. and Suntay W. J., *J Biomech Eng*, 135:136-144, 1983.

PREDICTION OF INDIVIDUAL CARPAL KINEMATICS DURING HAMMER MOTION: AN IN-VIVO VALIDATION

Michele Conconi (1), Nicola Sancisi (1), Gordon M Best (2), and Michael J Rainbow (2)

1. Department of Industrial Engineering, University of Bologna, Bologna, Italy; 2. Human Mobility Research Centre, Queen's University, Kingston, Ontario, Canada

Introduction

The relationship between form and function of the carpal joint during functionally relevant tasks remains unclear. We hypothesize that the articulations are shaped by an adaptation process aiming at optimally distribute contact loads [1]. The goal of this study was to test this hypothesis by simulating a hammering motion using assumptions of optimal congruence. The hammer motion was chosen because it represents a functionally relevant task, optimized in terms of radiocarpal stability [2]. To test this hypothesis, we developed a congruence-based forward model and validated it with in vivo data. In the model, two degrees of freedom (DOF) were imposed, while the remaining 40 DOF were computed to optimize load distribution by maximizing a measure of the joint congruence [3]: the more congruent the articular surfaces, the smaller the peak contact pressure. This approach was previously validated for the ankle and the knee [4,5] and is here tested on the wrist.

Methods

This analysis was done using the data from a single participant of a larger study. CT scans of the wrist in positions replicating hammering postures were acquired. Cartilage surfaces were acquired using a 3T MRI Scan (VIBE Sequence). Starting from the first hammer motion pose, experimental flexion and ulnar deviation of the capitate were imposed while the remaining 40 DOF were determined by simultaneously maximizing joint congruence of 11 articulations. We then compared the simulated results with the measured CT poses in terms of rotational and translational mean absolute errors (MAE).

Results

Table 1 shows the MAEs between model predictions and experimental measures for each carpal bone.

	Rot. MAE [°]	Trans. MAE [mm]
Capitate	5.2	0.6
Lunate	3.3	0.5
Scaphoid	2.5	0.6
Hamate	2.9	0.7
Triquetrum	5.3	0.7
Trapezoid	3.1	0.8
Trapezium	4.8	1.1

Table 1: MAE between model prediction and experimental measure for each carpal bone.

Rotational errors were generally more apparent than translational errors. The highest errors were in pronation. Model prediction improved toward the end of the motion (Fig. 1, left). This suggests that optimal load distribution is prevalent on the final part of the hammer motion, where impacts take place.

Discussion

The presented analysis supports the predictive capability of the model and confirm the functional relevance of the hammer motion. This model provides a simple and non-invasive way to characterize the individual motion of the wrist, needing only a 3D representation of the articular surfaces. Next activities will extend the analysis on additional subjects.

Acknowledgements

Queen's SARC Award.

References

1. Heegaard J. H. et al., *J. Orthop. Res*., 17:509-517, 1999.
2. Crisco J.J. et al., *JBJS*, 87: 2729-2740, 2005.
3. Conconi M. and Parenti-Castelli V., *Proc Inst Mech Eng H.*, 228:935-941, 2014.
4. Conconi M. et al., *J Biomech*, 48:2960-2967, 2015
5. Conconi M. et al., XV ARK: 261-269, 2018.

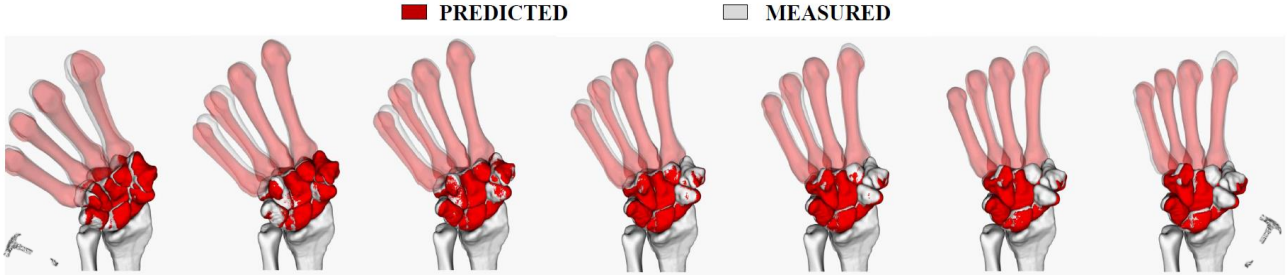

Figure 1: Palmar views of carpal bone motion as predicted (red) and measured (grey) during the hammer motion. The ulnar deviation increases from right to left. The overlapping between predicted and measured bones provide a qualitative assessment of the proposed model. Metacarpal bones and ulna are represented for sake of clarity but were not included in the model.

INTERFERENCE ON PLANTAR AFFERENTS IN BLINDS ALTERS THEIR POSTURAL STRATEGY TO KEEP POSTURAL CONTROL

Rodolfo B Parreira (1), Jamile B P Lopes (1), Lorraine B Cordeiro (2), Deborah C S Cardoso (2), Manuela Galli (3) Claudia S Oliveira (1,2)

1. Master's and Doctoral Program in Health Science, Faculty of Medical Sciences, Santa Casa de São Paulo, Brazil; 2. Master's and Doctoral Program in Human Movement and Rehabilitation, University Center of Anapolis, Brazil; 3. Department of Electronics, Information and Bioengineering, Politecnico di Milano, Italy

Introduction

The central nervous system (CNS) processes and integrates information from sensory inputs (visual, vestibular, and somatosensory) to maintain postural control (CP). However, CP can be affected by lack of vision, leading to abnormalities in sensorimotor information, thus generating typical musculoskeletal deformities and altered gait patterns [1]. Also, a decrease in plantar sensory information, such as the use of soft shoes, interferes with the role of vision on PC [2]. Thus, the objective of this study is to verify the interference (foam block) of the somatosensory system on the CP in blind people through the force platform (PF).

Methods

Seven individuals with total blindness (five women; 48.3±12 yrs, 71.4±14.8 kg, 1.65±0.86 m), and four sighted individuals (three women; 37±4 yrs, 77.4±15.2 kg, 1.66±0.80 m) were included in this study. Ethical approval was received by the number #1.672.635/2016. We analyzed the COP parameter (mediolateral, anteroposterior, and velocity), and the data were interpreted by the SWAY software program (BTS Myolab). The participants stood over an FP (BTS Infinity-T) on both legs, barefooted, and arms parallel to their trunk during 45 seconds, under conditions: open and closed eyes on firm or foam surface.
An independent t-test was performed to determine intergroup differences.

Results

In all COP variables and all conditions analyzed, both groups move more in the A/P plane of movement. However, we found differences in the M/L plane. The main result was in the FoamEO condition, where the blind subjects had a larger M/L displacement (13.8±16.5 mm vs. -5.8±1.5 mm) as well as increased COP speed (25.2±4.7 mm/s^2 vs. 12.7±2.5 mm/s^2) compared to sighted subjects (Figs. 1 a, b).

Discussion

A plantar interference (somatosensorial information), in the case of foam, blind subjects tend to use a hip postural strategy more often (greater M/L displacement) which is used automatically by the CNS to decrease instability [3,4] and improve postural control. On the other hand, the ankle strategy is employed by healthy subjects in the face of minor disorders [5]. The use of the hip strategy allows accelerating the COP without stepping, which explains the use of this strategy in challenging conditions by blind subjects [5]. Thus, these results help in decision-making in the rehabilitation program to improve postural control, as well as to advise the use of certain kinds of shoes in these population.

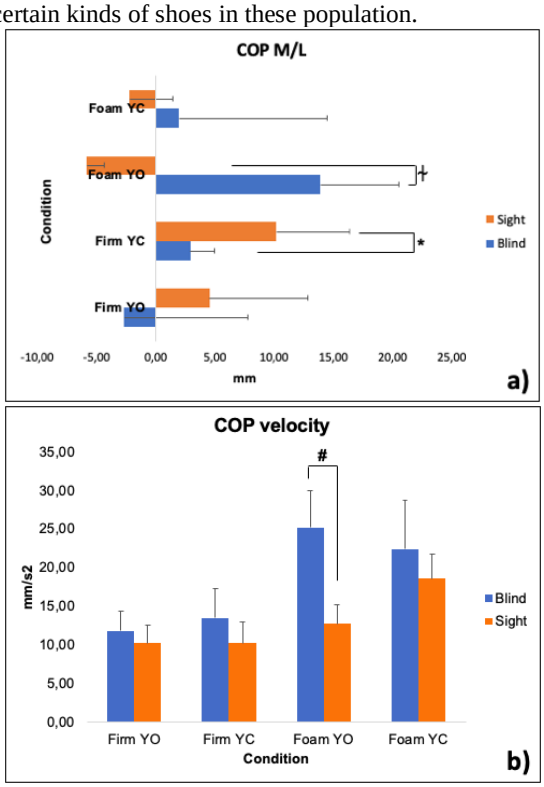

*Figure 1: a) mean ± of mediolateral COP displacement. Negative values are related to left displacement of the COP (+ p < .05; *p < .02); b) mean ± of COP velocity. Positive values are related to anterior displacement of the COP (# p < .001). Note: YO: eyes open; YC: eyes closed; Firm: hard surface; Foam: soft surface*

References

1. Alghadir et al, Brain Behav, 9:e01436, 2019..
2. Foisy and Kapoula, Brain Behav, 7:e00658, 2017.
3. Riemann et al, Arch Phys Med Rehab, 84:90-95, 2003.
4. Afschift et al. J Neurophysiol, 116:1937-1945, 2016.
5. Horak and Nashner, J Neurophysiol, 55:1369-1381, 1986.

Acknowledgements

We thank all volunteers. This work was supported by grant CAPES and CNPq.

MODELING OF MYOFIBRIL MISALIGNMENT IN DYSTROPHIC FIBER

Marco Stefanati (1), Yvan Torrente (2), José Félix Rodríguez Matas (1)

1. Department of Chemistry, Materials and Chemical Engineering "Giulio Natta", Politecnico di Milano, Italy;
2. Stem Cell Laboratory, Department of Pathophysiology and Transplantation, State University of Milan, Italy

Introduction

This work aims to develop a comprehensive chemo-mechanical model of muscle-skeletal tissue accounting for dispersion in myofibril orientations, in addition to the effect of fiber branching, in order to simulate the effect that changes in the muscle microstructure have on dystrophic muscle weakness i.e., reduction in isometric stress and concentric contraction velocity.

Methods

The proposed model of skeletal muscle departs from our recent work [1] where the muscle model is formed by: (i) the myofilament calcium and cross-bridge kinetics, and (ii) the mechanical model of the muscle composed of the fiber and extra-cellular matrix (ECM). The fiber is composed of two elements: (i) the myofibrils and (ii) the elastic passive response of the fiber.

Differently to [1] where the myofibrils are assumed to be perfectly aligned with the myofiber direction, $\mathbf{n}_0$, in the present model this condition is relaxed by allowing the myofibrils to be distributed with a certain dispersion with respect to $\mathbf{n}_0$. To define the fiber dispersion, we assume the existence of a uniaxial myofibril orientation distribution function (ODF) for $\mathbf{r}$ a referential unit vector. Hence, the fiber strain energy is defined as

$$\overline{W}_f = \frac{1}{4\pi}\int_{U^2} \rho(r;b,\mathbf{n}_0)\,\overline{W}_{mf}(\overline{\mathbf{C}},\mathbf{r})\,dA, \qquad (1)$$

where $\overline{W}_{mf}$ is the strain energy of the single myofibril with orientation $\mathbf{r}$. For the ODF, we assume a π-periodic von Mises distribution about the direction $\mathbf{n}_0$ that is a function of the concentration parameter $b \geq 0$. In order to render Eq. 1 operative, the integral is calculated using the unit sphere discretization.

Results

The results indicate that the main difference between the healthy and dystrophic fiber is connected to the myofibril dispersion and myofibril stiffness (see parameters b and η_1 in Table 1).

FIBER		Healthy	Dystrophic
Exp. CAS (-) [2]		0.951 – 0.996	0.844 – 0.951
Model CAS (-)		0.968 – 0.987	0.851 – 0.889
b	(-)	20	3
η_1	(kPa)	0.1192×10^{-1}	0.3254×10^{-1}
MUSCLE		Healthy	Dystrophic
σ_{max}	(kPa)	70.06	41.58
V_{max}	(s^{-1})	-7.19	-5.96

Table 1: Results of CAS, myofibril dispersion, myofibril stiffness, and predicted isometric stress, and concentric velocity of the healthy and dystrophic muscle.

The value of b was found by fitting the ODF to myofibrillar dispersion reported in Schneidereit et al. [2], for healthy and dystrophic fibers characterized in terms of the cosine angle sum (CAS). In this regard, we found the concentration parameter b to be lower for the dystrophic fiber indicating larger dispersion in the myofibril alignment in the fiber, in agreement with the experimental data.

More interestingly, the model predicts that a variation of less than 15% in CAS between the healthy and the dystrophic fiber can account for a 41% reduction in the isometric stress as reported in the literature [2,3,4]. The model is also able to predict the changes in CAS during concentric contraction (see Table 1), showing an excellent agreement with the results reported in [2].

The model also predicts a significant loss of the concentric velocity (V_{max} in Table 1) in the dystrophic muscle, as reported in the literature [5]. This was associated with myofibril misalignment but also with an increase of myofibril stiffness η_1. This difference in η_1 can be associated with the chaotic organization of the sarcomeres present in the dystrophic case [2].

In addition, the model can reproduce the experimental F-V curve (Fig. 1) of the healthy and dystrophic muscle in concentric [5] and eccentric contractions [6].

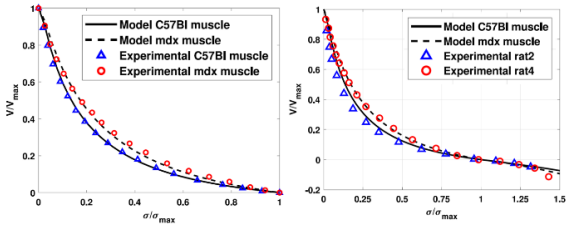

Figure 1: F-V curve for the healthy and dystrophic muscle. Left) Concentric contraction. Right) Eccentric contraction.

Discussion and conclusions

The resulting model includes a specific formulation of the fiber microstructure and represents an original approach to study the defects in the muscle ultrastructure caused by the dystrophy. The results confirm that myofibril disorder in the dystrophic fiber has an important impact on the mechanisms regulating the dystrophic fiber active response.

References

1. Stefanati et al, J Mechanics Physics Solids, 134:1-16, 2020.
2. Schneidereit et al, Light: Science & Appl, 7:79:1-14, 2018.
3. Smith et al, AJP - Cell Physiology, 306:C889-C898, 2014.
4. Bates et al, AJP - Cell Physiology, 304:C873-C880, 2013.
5. Coirault et al, J Applied Physiology, 94:1744-1750, 2003.
6. Till et al, Journal Theoretical Biology, 255:176-187, 2008.

ABOUT GENERALIZATION AND INTERCHANGEABILITY OF HAND KINEMATIC SYNERGIES

Verónica Gracia-Ibáñez, Margarita Vergara, Joaquín L. Sancho-Bru, Alba Roda-Sales, Néstor J. Jarque-Bou, Vicente Bayarri-Porcar

Mechanical Engineering and Construction Department, Universitat Jaume I. Spain

Introduction

The analysis of hand kinematics is complex due to the high number of degrees of freedom involved. However, dimensionality reduction techniques as principal component analysis (PCA) have been successfully used to find the underlying synergies in grasp postures, object manipulation or in performance of real activities of daily living [1]. Furthermore, synergies have been shown to be subject- and task-dependent [2]. This work hypothesizes that synergies obtained from a set of recordings from a high enough number of subjects performing a wide range of tasks could be representative (in terms of variance explained) of other sets of subjects performing other tasks, i.e. synergies could be used interchangeably.

Methods

Two different sets of kinematics recordings from different subjects performing different tasks were considered: set A consisting of 18 subjects performing 24 real ADL from the ICF [3], and set B with 22 subjects performing 26 tasks based on the Sollerman Hand Function test [4]. In both sets, all subjects were right-handed and had no hand pathologies, and 16 joint angles (Table 1) from their right hand were recorded in the same way (100 Hz, with a CyberGlove and a validated calibration protocol [5]). Then, angles were filtered and all tasks were rescaled to 1000 frames. Two PCAs, one per sample, were applied to normalised data (covariance matrix, Varimax rotation) of all subjects and tasks altogether, and Principal Components (PCs) with eigenvalue>1 were extracted. The % of variance explained in each subject by the PCs from the own set and by the PCs from the other set were computed and statistics across subjects were obtained.

			Loadings of PC (set A)					Loadings of PC (set B)				
Joint	Dgit	Mov	1	2	3	4	5	1	2	3	4	5
CMC	1	F/E					0.9			0.8		
MCP	1	F/E			-0.6							-0.7
IP	1	F/E					-0.6					0.8
CMC	1-2	Ab/Ad				0.7					0.9	
MCP	2	F/E			-0.7				0.8			
	3	F/E		0.6	-0.5				0.8			
	4	F/E	0.4	0.7				0.5	0.8			
	5	F/E	0.5	0.8				0.6	0.6			
PIP	2	F/E				0.5		0.7				
	3	F/E	0.9					0.9				
	4	F/E	0.9					1.0				
	5	F/E	0.8					0.9				
MCP	2-3	Ab/Ad			0.8				-0.7			
	3-4	Ab/Ad		-0.7					-0.7			
	4-5	Ab/Ad	-0.5	-0.7				-0.4	-0.5			
Palm Arch						0.7				-0.8		
% variance explained: mean (sd) across subjects												
subjects = set	By PC		24 (2)	19 (2)	12 (1)	11 (2)	8 (1)	27 (1)	24 (2)	6 (1)	9 (1)	9 (1)
	sum		74 (2)					74 (2)				
subjects ≠ set	By PC		24 (2)	18 (2)	12 (1)	11 (2)	8 (1)	25 (1)	22 (2)	6 (1)	9 (1)	8 (1)
	sum		73 (2)					69 (3)				

Table 1: loadings of PCs from each set (absolute values under 0.4 not shown for clarity) & percentage of variance explained: statistics across subjects by PC and the sum, using PCs of the same set (=) and of the other set (≠). Underlined values when significant differences ($p<0.05$) were found in ANOVAs. Joints: CMC (Carpometacarpal), IP (Interphalangeal), MCP (Metacarpo-phalangeal), PIP (Proximal Interphalangeal). Movs: F/E (Flexion/Extension), Ab/Ad (Abduction/Adduction)

Results

Five PCs were obtained in both PCAs. Results (Table 1) show high values of variance explained (~70%) both for subjects of the own and different set.

Discussion

Certain similitudes can be observed in the synergies represented by PCs obtained: PCs 1&2 referring mainly to digit flexion and higher order synergies referring mainly to thumb coordination and palmar arching. However, some differences exist, as for the coordination of thumb and index, appearing in third and fourth synergies in set A, whereas in set B index is coordinated with the rest of digits. Despite the differences, synergies obtained from both sets could be used interchangeably for the other set, since a high crossed variance is explained in relation to that explained within the own set. Results suggest that synergies obtained from a wide set of subjects performing a wide range of tasks are generalizable enough for their use for different subjects performing different tasks. Synergies from the performance of real ADL result slightly more representative (the PCs obtained for set A represent tasks from set B with higher variance than vice versa). This may be because real ADL are more complex in nature than the tasks of the standardized tests (e.g. one ADL from set A consists in putting on pants, and buttoning and zipping them, while a task in set B consists in opening and closing a zipping of a purse attached to a wood vertical board).

References

1. Ingram et al, Exp Brain Res 188: 223–236, 2008.
2. Todorov et al, Conf. Proc. IEEE Eng. Med. Biol. Soc. 6:4637–40, 2004.
3. Gracia-Ibáñez et al, J. Hand Ther. 30: 337–347, 2017.
4. Jarque-Bou et al, Sci Data. 6: 270, 2019.
5. Gracia-Ibáñez et al, Comput. Methods Biomec. 20: 587–597, 2017.

Acknowledgements

Work supported by the Spanish Ministry (project PGC2018-095606-B-C21), by the UJI (project UJI-B2017-51) and by the Regional Government (GV/2020/067).

THE EFFECTS OF TRIPLE ARTHRODESIS ON SOLEUS AND PERONEUS BREVIS MUSCLES, AND ON KNEE FLEXION/EXTENSION DURING GAIT

Shima Hejazi (1), Walter Herzog (2), Gholamreza Rouhi (1)
1. Faculty of Biomedical Engineering, Amirkabir University of Technology, Tehran, Iran;
2. Faculty of Kinesiology, University of Calgary, Calgary, Canada

Summary

We studied the effects of bilateral triple arthrodesis (BTA) on the strength of soleus and peroneus brevis muscles, and on knee flexion/extension during gait using EMG and a kinematic model of the lower limb. We found that the maximum knee flexion and extension was reduced in all patients compared to the average value of normal subjects. Moreover, the peroneus brevis was more active in the early stance phase and soleus EMG patterns were abnormal in early stance, in patients compared to normal subjects.

Introduction

Due to the dependence of movements at one joint on the movements of its neighboring joints, a change in kinematics of a joint can cause alterations in the dynamics of an entire limb [1]. We used gait analysis to determine the effects of a bilateral triple arthrodesis (BTA) on knee kinematics and muscle activation patterns of the soleus and peroneus brevis muscles during gait.

Methods

We performed 3D gait analysis on 10 subjects (five patients with BTA, with a mean follow-up duration of 2.7 years after surgery, and five normal subjects) using a marker system as recommended in [2]. EMG signals of the soleus and peroneus brevis muscles were recorded for each subject, and then normalized to the maximum voluntary, isometric contraction (MVC) values [3]. Knee flexion/extension, was determined using the kinematic data [4], and MATLAB software.

Results and Discussion

The range of knee flexion and extension in the patients with BTA was less than the mean value of the normal subjects (Fig. 1). Moreover, peak soleus activity occurred later in patients than normal subjects (Fig. 2). In addition, the peroneus brevis muscle was more active in the early stance phase in patients compared to controls (Fig. 2). Increased activation of the peroneus brevis at the beginning of the gait cycle, as observed in the patients, has been associated with initial eversion at the ankle joint. Knowing that the calf muscles cause inversion of the ankle, increasing the activation of the calf muscles in patients may help reduce the unwanted eversion. The decrease in knee extension in patients compared to controls, is often caused by pain can cause weakening of the knee extensors, which in turn is a risk factor for the development of knee joint osteoarthritis [5].

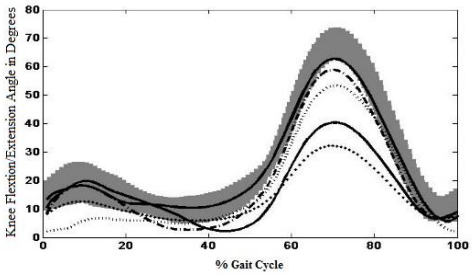

Figure 1: Knee range of motion in the sagittal plane during a gait cycle (approximately 60% of the cycle is spent in stance and 40% in swing). Gray band indicates the variation (± 1 standard deviation from the mean for the normal subjects), while the individual lines correspond to the mean of the five patients with BTA.

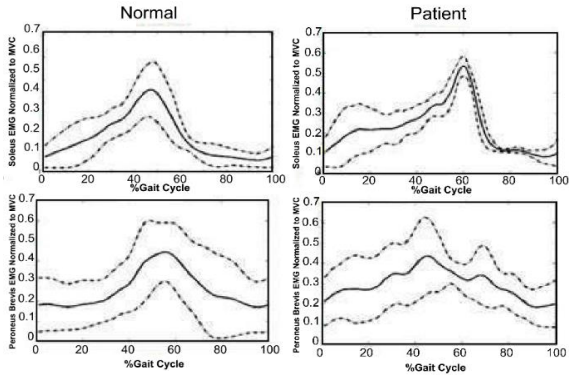

Figure 2: Mean (solid lines), ± 1 SD (dashed lines) of normalized EMG activity in patients (right column) and normal subjects (left column) for soleus and peroneus brevis during a gait cycle.

Conclusions

In BTA patients because of atrophy of a number of ankle muscles and limitation of lower extremity joints, improving surgical techniques, as well as physiotherapy and rehabilitation methods to train activation patterns and strengths in crucial muscles may be helpful for these patients and prevent them from more musculoskeletal disorders.

References

1. Mündermann A et al. (2005). *Arthritis Rheum*, **52**: 2835-2844.
2. Kadaba MP et al. (1990). *J Orthopaed Res*, **8**: 383-392.
3. Perotto AO, (2011), *Anatomical guide for the electromyographer: the limbs and trunk*. Charles C Thomas Publisher.
4. Plug-in gait reference guide. (2016), In: Vicon Nexus 2.5 Documentation, pp. 1–95.
5. Haq I et al. (2003). *Postgrad Med J*, **79**: 377–383.

MUSCLE ACTIVITY IN SLEEP-LIKE STATES OF CONSCIOUSNESS FOR THE VALIDATION OF ACTIVE HUMAN BODY MODELS

Luca Baur (1), Julia Muehlbauer (1), Sylvia Schick (1), Steffen Peldschus (1)

1. Biomechanics and Accident Analysis, Institute of Legal Medicine, University of Munich LMU, Germany

Introduction

Finite-element (FE) human body models (HBM) can be used to assess occupant protection and restraint systems in cars. Their application gains in significance especially in the assessment of future autonomous vehicles' safety technologies. Active FE models enable simulation of different levels of muscle activation (relaxed, braced, sleeping). Currently, it is assumed that sleeping occupants have no muscle activation due to depressed muscle reflexes during non-REM sleep [1]. However, a muscle activation level above 0 % of maximum voluntary contraction (MVC) has already been recorded experimentally for occupants in a relaxed, awake state of consciousness [2]. The present study investigates muscle activity levels of sleeping volunteers to enhance active human models.

Methods

Ethical approval was obtained from the Medical Faculty Ethics Committee of the Ludwig Maximilian University. The study included 20 healthy test subjects, 11 males, 9 females with a mean age of 25,0 ± 6,39 years. Surface electromyography (EMG) was used to measure muscle activity in sleep-like states of consciousness in a potential future seating position in autonomous vehicles [3] (Fig. 1). Bilateral measurement included major neck, trunk and leg muscles. The release of a tennis ball in hand due to increased muscle relaxation was used to determine the point of falling asleep.



Figure 1: Initial testing position in a reclining seat.

During 30 minutes of sleep muscle activity was recorded at 3 intervals of 3 minutes, respectively. For each recording, a period of ten seconds without any artefacts was analyzed. Two measurements in awake state of consciousness in the tested seat position, before and after the sleep period, served as a reference. EMG Data were ECG- and band pass-filtered, rectified and smoothed. MVC tests were used to normalize data.

Results

17 out of 20 test subjects fell asleep (positive ball-sign or personal feedback). In general, normalized muscle activity was very low, ranging from 0,24 to 4,81 % of MVC in all muscles except the neck extensors (ranging from 0,47 to 15,65 % of MVC). Across the time intervals, higher intra- and inter-individual variability was observed in the neck muscles compared to the measured trunk and leg muscles. No global trend was observed across all individuals' muscle activity levels following sleep onset. However, 3 test subjects showed a drop in muscle activity level after falling asleep and an increase after waking up. On an individual level, subjects could be grouped to either a relaxed or a less relaxed activation type based on visual inspection.

Discussion

The setup was reported highly comfortable and proved suitable to derive validation data for active FE models. Although the measured muscle activity was very low, ongoing analyses suggest there is muscle activation over the level of 0 % even in sleep-like states of consciousness as opposed to state-of-the-art definition [4]. It is currently investigated if the differences in intra- and inter-individual variability in the body parts could derive from body positioning, e.g. due to an instable head positioning. It needs to be assessed whether an activity level above 0% of MVC during sleep has an effect upon passenger kinematics in pre-crash phase and thus, should be considered in future active HBM simulations.

References

1. Kryger et al., Principles and Practice of Sleep Medicine, 243-244, 2016
2. Welsch, Master Thesis, TU Munich, 2018
3. Mount et al., NASA TM-2003-104805, 2003
4. Kato et al., IRCOBI Conference 18-32, 2018

Acknowledgements

The authors want to thank all participating volunteers.

ANALYSIS AND COMPARISON OF TRADITIONAL AND OPERATOR-FREE HAND-HELD DYNAMOMETER

Adriana Modrego (2), Roger Marginet i Assens (1), Ricardo Jauregui (2), Simone Balocco (1).

1. University of Barcelona, Spain; 2. DyCare, Spain.

Introduction

Hand-held dynamometers (HHD) are portable devices that assess muscle strength (kg) at compression. The validity and reliability of HHD, mainly depends on the ability of the examiner to provide a stable and consistent base for test [1], especially with large muscle groups and forces over 15 kg [2]. The aim of this study is to determine whether the operator-free dynamometers improve the accuracy of the make tests results which are traditionally done by an operator.

Methods

Nine (9) healthy subjects aged between 22 and 29 years old were selected to perform an isometric knee extension force evaluation. Two configurations were tested in the experiment: The first one was a classical make-test performed with a Manual Dynamometer (Manual Muscle Testing System Model-01165) and an operator. The second configuration is performed without operator and using a portable DyForce V1 (DyCare) dynamometer that is fixed 8 cm from the external malleolus.

The test is performed 10 times each day over a period of 3 days and all measurements were made by the same operator. Before each measurement, the maximum force that the operator could withstand was measured as the force that the operator can apply to a wall in the same position as of the make-test (28,5±2,3 kg).



Figure 1. Test setup using the DyForce V1

Subjects were seated on a table, with a straight back, legs at 90 degrees (Figure 1). Each subject was required to apply the maximum force for a period of 3 seconds. The subject rests for approximately 30 seconds between measurements.

Results

The main results obtained are presented in Table 1 and Figure 2. The results of the experiment are additionally separated for two categories: the subjects stronger and the one weaker than the operator, respectively

	Average differences (kg)	SD (kg)
All subjects	6,65	5,44
Stronger subjects	12,14	6,48
Weaker subjects	3,91	1,89

Table 1. Average difference strength of the results obtained from the tests.

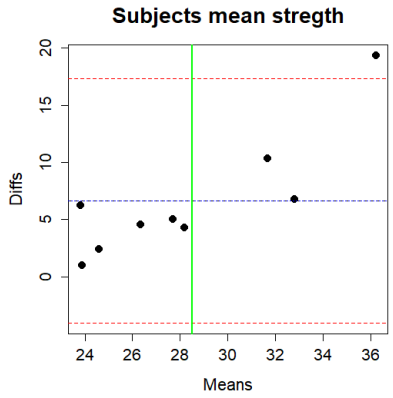

Figure 2. Average difference strength of each subject after performing the tests with both devices

Discussion

Based on the results shown in Figure 2, the mean strength values achieved by the subjects when performing the test using the DyForceV1 are higher with respect to the Manual Dynamometer. This remark is valid for both subjects' categories (stronger and weaker than the operator). Moreover, the average differences of the two groups are substantially differents (Table 1). We believe that the higher measurements obtained are due to different factors:

On one hand, in the case of subjects weaker than the operator the recorded strength is higher due to the test setup. Since the operator is not present, the patient can apply the maximum force without the fear to harm the operator.

On the other hand, in the case of the subjects stronger than the operator, the average difference strengths are larger because apart from the set up, the maximum strength which can be recorded when performing the test with the Manual Dynamometer is limited by the operator's strength, which is counterbalancing the subject force. Instead, when no operator is involved in the test, this limitation is removed and the actual maximum strength of the subject can be registered.

References

[1] B. Alwood and F. Aerts, *Hand-Held Dynamometry: Guidelines for Daily Clinical Practice*. 2018.

[2] D. A. Scott, E. Q. Bond, S. A. Sisto, and S. F. Nadler, "The intra- and interrater reliability of hip muscle strength assessments using a handheld versus a portable dynamometer anchoring station," *Arch. Phys. Med. Rehabil.*, 2004.

Acknowledgements

This work was partially supported by RTI2018-095232-B-C21, 2017 SGR 1742, NEOTEC-SNEO-20171132 and 811755 ReHub2018-2020/H2020-SMEInst.

MODELING HUMAN-SEAT INTERACTION CAN IMPROVE THE ACCURACY OF IN SILICO MAXIMUM VOLUNTARY ISOMETRIC CONTRACTION TESTS

Giorgio Davico (1,2), Francesca Bottin (1,2), Marco Viceconti (1,2)

1. Department of Industrial Engineering, Alma Mater Studiorum – University of Bologna, Italy; 2. Medical Technology Lab, IRCCS Istituto Ortopedico Rizzoli, Italy

Introduction

Over the years, computer simulations of maximal effort tasks, such as maximum voluntary isometric contraction (MVIC) leg extension, emerged as a powerful tool to support clinical diagnosis or rehabilitation programs and to overcome intrinsic limitations of in vivo tests, including poor test-retest repeatability. Experimental data may be used to inform computer simulations, to produce more physiologically plausible estimates of the internal biomechanics, i.e., muscle and joint contact forces; but are not routinely collected in clinical settings. Hence, the overall kinematics is often simplified [1], and human-seat interaction is mostly neglected. Alternatively, more realistic boundary conditions (BCs) may be introduced by adding contact elements, such as Hunt-Crossley forces [2], between the body and the seat. We hereby propose a simulation framework to conduct MVIC tests in silico, with and without the definition of contact elements, and compare the two modelling approaches to provide preliminary evidence on how more realistic boundary conditions affect the outcome measures.

Methods

The OpenSim gait2392 generic model [3] was employed for the simulations. The model was initially positioned with both hip and knee flexion angles set to 90° and the back tilted backwards by 15°, to reflect a typical configuration on a dynamometer chair.

Two sets of BCs were implemented: (i) in line with previous work, pelvis translations were locked, and a static kinematics was imposed, and (ii) Hunt-Crossley forces and spring dampers were added to model human-seat interaction, and a quasi-static kinematics, estimated via forward dynamic simulations, was imposed. Ultimately, a constant flexion torque was applied to the knee joint to elicit muscle activity. The external torque was iteratively increased to identify the MVIC force of the model, i.e. the last torque value that the model was able to sustain (before failure).

Results

Both approaches enabled to produce MVIC force values comparable to those observed experimentally [4]. However, while the model was able to produce a larger maximal knee extension torque (i.e., 161 Nm) when pelvis translations were locked, a lower MVIC value (i.e., 145 Nm) was registered imposing more realistic BCs (i.e., modeling human-seat interaction).

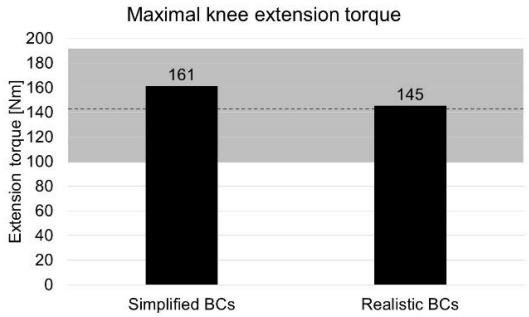

Figure 1: Maximal isometric knee extension torque observed before failure implementing different sets of boundary conditions (BCs): (1) with pelvis translations locked and static kinematics (left) and (2) with Hunt-Crossley forces and quasi-static kinematics (right). Literature data [4] (gray band) are reported for comparisons.

Discussion

Our preliminary results showed that both approaches are feasible and enable to estimate physiologically plausible MVIC force values, in line with literature data [4]. Nonetheless, implementing more realistic BCs led to a MVIC value closer to reported average values for an age-matched population. Further tests on a larger cohort are necessary to confirm our findings. Future work should focus on the validation of the proposed methods, e.g. using available experimental data (e.g., Knee Grand Challenge Data [5]).

References

1. Kainz et al, Gait Posture, 65:213-220, 2018.
2. Sherman et al, Procedia IUTAM, 2:241-261, 2011.
3. Delp et al, IEEE Trans Biomed, 37:757-767, 1990.
4. Driessche et al, PLoS One. 13:e0196838, 2018.
5. Fregly et al, J Orthop Res, 30:503-513, 2012.

Acknowledgements

This work was partly supported by the Mobilise-D project, Grant agreement ID: 820820, funded by the European Commission through the programme H2020-EU.3.1.7.-Innovative Medicines Initiative 2 (IMI2), and by the InSilicoWorld project, Grant agreement ID: 101016503, funded by the European Commission through the Horizon 2020 Research and Innovation Programme.

WRIST LOAD DURING HAND GRIP EXERCISES WITH A NEW INVERSE DYNAMICS HAND MODEL

Lucas Engelhardt (1), Jonas Schwer (1), Maximilian Melzner (2,3), Patrik Christen (4), Sebastian Dendorfer (3,4), Ulrich Simon (1)

1. Scientific Computing Centre Ulm (UZWR), Ulm University, Germany;
2. Laboratory for Biomechanics, Ostbayerische Technische Hochschule (OTH) Regensburg, Germany;
3. Regensburg Center of Biomedical Engineering, OTH and University Regensburg, Germany;
4. Institute for Biomechanics, ETH Zurich, Switzerland

Introduction

The use of musculoskeletal simulations through inverse dynamics has become established as a good approach, when joint, bone and muscle forces are of interest, but rather difficult to quantify.
As shown in [1] and recent presentations [2,3], we developed a new detailed hand model for the AnyBody Modelling System [4]. This model not only includes the possibility of a patient specification but also has been validated by moment arm studies [1,2] and EMG [3].
The aim of this work was to apply the new detailed hand model to a specific hand gripping task, which patients were urged to perform after a conservatively treated distal radius fracture. Especially the transferred wrist load is of great interest, as it is the main mechanical stimulus to the fractured radius healing performance.

Materials and Methods



Figure 1: Hand grip exercise start and compression

The musculoskeletal hand model was adapted to simulate an exercise with a hand gripping tool. This model could be used to determine muscle and joint forces in the wrist that occur as a consequence of this hand grip contraction. The movement has been captured precisely by motion capture analysis in combination with electromyographic (EMG) data of all essential muscles in the forearm and hand. On top, the acting contact forces have been determined with the aid of pressure mapping sensors attached between the fingers and hand grip tool. By determining a characteristic force distribution among the fingers, it was possible to apply the actual forces which act on the individual fingers during the simulation.

Results

Most of the calculated extensor muscle forces showed an increase of not more than 250 N. While the muscle force of the flexor digitorum superficialis (FDS) dominated, with a progressive increase up to over 1200 N. This dominance of the FDS in the compressed position of the hand grip was also reflected in the EMG signals recorded during the exercise.

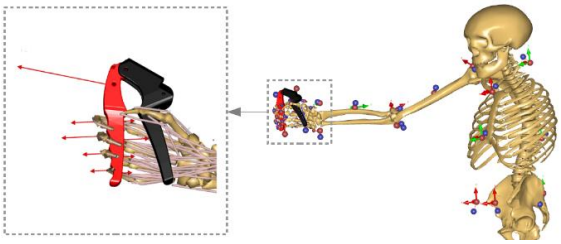

Figure 2: Musculoskeletal model with MoCap protocolled data (right) and applied contact forces(left). The upmost force arrow represents the spring force inside the hand grip tool.

Also, the total wrist load described the same behavior with a progressive increase, creating compressive (mainly axial) forces up to 1136 N, when the hand grip spring force reaches up to 565 N.

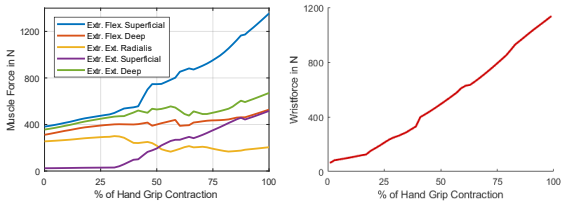

Figure 3: Muscle force during contraction of the hand grip (left). Wrist load course (right).

Discussion

Comparison with in vivo studies by [5] showed a good accordance of the predicted muscle force distribution during a griping task. Nevertheless, the high muscle forces simulated in the beginning movement might be overestimated due to balancing actions, to stabilize the motion. As the investigated movement implies the most severe action in hand motion, intentional co-contraction plays a minor role and their lacking formulations in the inverse dynamic approach can be neglected. The presented study shows the first and successful application of the new developed hand model on a clinical question and might serve for many more.

References

1. Engelh. and Melzner et al. CMBBE 2020
2. Engelh. and Melzner et al. Abstract at ESB 2019, Vienna
3. Melzner and Engelh. et al. Abstract at CMBBE 2019, NYC
4. AnyBody Technology A/S. anybodytech.com
5. An et al. Forces in the n. and a. hand, J Orthop Res 1985

Acknowledgements

Funding from the SNF (320030L_170205), DFG (SI 2196/2-1, IG 18/19-1) and FWF (I 3258-B27) for the DACH$_{FX}$ Project is gratefully acknowledged.

BIOMECHANICAL INVESTIGATION OF BONE SCREW HEAD DESIGN FOR EXTRACTING STRIPPED SCREW HEADS

Mohammad Nikkhoo (1), Arash Azhang (1), Kinda Khalaf (2)

1.Department of Biomedical Engineering, Science and Research Branch, Islamic Azad University, Tehran, Iran; 2.Department of Biomedical Engineering and Health Engineering Innovation Center, Khalifa University, Abu Dhabi, UAE

Introduction

Retained orthopedic implants often cause pain, soft tissue irritation, and/or allergic reactions for patients [1]. Implant removal surgery, on the other hand, is also associated with various complications, including prolonged operations, bleeding, infection, and neurovascular injuries. Improving screw head socket design to prevent stripping and to increase the torque to facilitate unscrewing during removal remains a challenge with only few studies available in literature [2, 3]. The objective of this study was to provide a validated FE model based on experimental tests to investigate the influence of different design parameters for the augmentation of conventional hexagonal socket design in orthopedic biomechanics.

Materials and Methods

A finite element (FE) model was developed to study the biomechanical response of bone screw head design. To evaluate the validity of the model, a hexagonal custom-made socket was manufactured according to the ASTM F543 / ASTM F116. Single load torsional tests using a testing machine (Instron Industrial Products) were conducted to evaluate the mechanical performance of the screws and drivers, and the results were compared with FE simulations. The authorized tolerance of the socket width (SW) and screwdriver width (S) were also determined based on ASTM F543. Four different screwdriver inserted depths (H) (Fig. 1) were chosen to compare 16 different design modes using FE analysis.

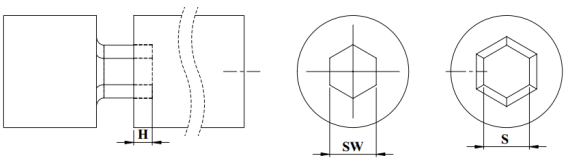

Figure 1: The screw head socket and screwdriver design parameters.

Results

The results from the FE models were well comparable with experimental tests (Table 1) confirming the validity of the FE model.

Table 1: Torque to slippage results for two samples.

Socket Parameters	Test report (N.mm)	FEM (N.mm)
H=1, SW=2.5, S=2.48	4420	4477
H=1.5, SW=2.547, S=2.49	3923	4083

The simulations demonstrated that the maximum torque to failure for the four designs were less than the aforementioned margins based on ISO 6475. The results showed an increasing t maximum torque with increased screwdriver depth (Fig 2).

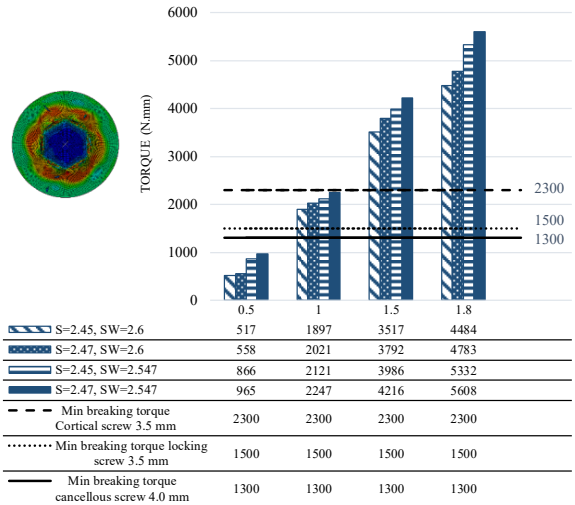

	0.5	1	1.5	1.8
S=2.45, SW=2.6	517	1897	3517	4484
S=2.47, SW=2.6	558	2021	3792	4783
S=2.45, SW=2.547	866	2121	3986	5332
S=2.47, SW=2.547	965	2247	4216	5608
Min breaking torque Cortical screw 3.5 mm	2300	2300	2300	2300
Min breaking torque locking screw 3.5 mm	1500	1500	1500	1500
Min breaking torque cancellous screw 4.0 mm	1300	1300	1300	1300

Figure 2: The screw head socket and screwdriver design parameters.

Discussion

This study provided a validated technique that uses quantitative data towards the investigation of bone screw head designs for extracting stripped screw heads. The results suggest that the effect of width variations for the hexagonal socket or the screwdriver is not as important as the influence of the screwdriver depth to increase the maximum torque for slippage. The results also confirm the possibility of maximum torque prediction which can be used for future design modifications of bone screw heads.

References

1. Musters G.D. et al, Eur J Trauma Emerg S, 39:159-62, 2013.
2. Lin C.H. et al, Injury, 49(3):585-592, 2018.
3. Schwarz N. et al, Eur J Trauma Emerg Surg, 39:339–344, 2013.

THE EFFECT OF ADDITIONAL MASS BY BODY ARMOR ON POLICE SPECIFIC PERFORMANCE

Marvin Zedler (1,3), Maximilian Sanno (1,3), Sandra Grothe (1,3), Anna Droszez (1), Joachim Mester (2,3), Jan-Peter Goldmann (1,3)

1. Institute of Biomechanics and Orthopaedics, German Sport University Cologne, Germany; 2. Institute of Training Science and Sport Informatics, German Sport University Cologne, Germany; 3. The German Research Centre of Elite Sport, German Sport University Cologne, Germany

Introduction

In most police specific tasks, the body must be accelerated or resist external forces. Since acceleration equals force divided by mass, increased body mass needs more force to move the body. An increase in mass by 10 to 40% means a decrease in acceleration at a given force by 9 to 29%. Because police personnel often wear body armor (BA) for protection against punches and shots, the additional mass of BA (Germany 21±1 kg) potentially reduces a) physical performance on the one hand, but 2) enhances officer's resistance against impacts (e.g. by offender's tackling) on the other hand. The objectives of the present study were to analyze individuals on their physical performance with and without body armor and their resistance against external forces.

Methods

Thirty-two physical active (5.3±2.8 hrs/week) women were divided into two groups by body mass (group 1: n=16, 1.57±0.03 m, 55.7±4.5 kg, 25.4±4.7 yrs, BMI 22.6±1.5; group 2: n=16, 1.79±0.02 m, 72.2±7.8 kg, 24.5±5.5 yrs, BMI 22.4±2.5). Two tests (Fig. 1) with and without body armor (m=21 kg) were obtained: 1.) Center of mass (COM) height and mechanical power during countermovement jumps; 2.) Acceleration of the body (Vicon, Oxford, UK) after impact of an oscillating pendulum (E_{kin}=126 J): Simulation of 80 kg heavy offender, who bumps or jolts an officer with a fast walking speed (e.g. body check against officer). Statistics: Kolmogorov-Smirnov test, two-factor ANOVA with Bonferroni's post-hoc test (α = 5%).



Figure 1: Countermovement Jumps on force plate (left); resistance against oscillating pendulum (right).

Results

The mass fraction of the BA in relation to the group's mean body masses amounted to 38% for group 1 and 29% for group 2. BA reduced sig. (P<0.05) jump height and mechanical power (Tab. 1). There were no sig. differences (P>0.05) between the groups in jumping. BA reduced body acceleration after impact sig. (P<0.05) in group 1 (57%) and 2 (66%). There were no sig. differences (P>0.05) between group 1 and 2 without BA. With BA, body acceleration was sig. (P<0.05) lower in group 2 than in group 1.

	Group 1 with/without BA	Group 2 with/without BA
Test 1		
h [cm]	14±4/24±6 [a]	17±4/27±4 [a]
P_{mean} [W/kg]	15±3/22±4 [a]	16±2/23±3 [a]
P_{max} [W/kg]	26±4/38±6 [a]	28±4/40±5 [a]
Test 2		
a [m/s²]	38±9/88±19 [a]	27±8[b] /78±22[a]

Table 1: Jump height (h), COM mean power (P_{mean}), COM maximum power (P_{max}), and body acceleration after impact (a). [a]P<0.05 sig. different to BA; [b]P<0.05 sig. different to group 1.

Discussion

Exercise performance of fit, light- and normal-weighted individuals decreased with increasing additional mass [1]. BA has clearly exceeded the critical weight limits for external loads of less than 15% [2], but the additional mass helped to resist external forces. As additional mass had positive as well as negative effects on exercise performance, fitness tests for the evaluation of job applicants and future employees have to consider police specific tasks. Therefore, precise requirement profiles are needed for the evaluation of police specific work and the choice of fitness tests.

References

1. Cureton et al., Med & Sci Sports, 10:194-199, 1978.
2. Robertson et al., Eur J Appl Physiol, 49:69-78, 1982.

Acknowledgements

We would especially like to thank the Police of North Rhine Westphalia, Germany for providing equipment and body armor.

COMPARISONS OF NATIVE STRAIN DISTRIBUTION ON MEDIAL COLLATERAL LIGAMENT IN TOTAL KNEE ARTHROPLASTY; MECHANICAL ALIGNMENT AND KINEMATIC ALIGNMENT

Min Ji Kim (1), In Jun Koh (2), Dai Soon Kwak (2), Ho Jung Cho (2), Jae Hyuk Choi (1), Seo Yeong Kim (1), Dohyung Lim (1)*

**corresponding author: dli349@sejong.ac.kr*

1. Dept. of Mechanical Eng., Sejong Univ., Korea; 2. The Catholic University of Korea;

Introduction

Advances in implant technology and understanding of knee biomechanics are spurring the ongoing debate about the optimal alignment strategy for total knee arthroplasty(TKA).[1,2] A growing body of evidence supports that kinematically aligned(KA) TKA provides superior clinical outcomes and satisfaction than mechanically aligned(MA) TKA. In theory, KA-TKA would restore knee kinematics closer to the native condition than MA-TKA by reproducing more physiologic ligament strain, but the current biomechanical evidence is lacking.[2] The purpose of this study was to compare the ligament strain between KA and MA-TKA in human cadaveric knees. It was hypothesized that KA-TKA afforded more physiologic strain than MA-TKA.

Methods

We used 13 pairs of knees in this study. For each pair, one knee was randomly assigned to KA-TKA and the other to MA-TKA All specimens were mounted on a customized knee test rig that simulated human standing to squatting motion under physiologic loading condition. Medial collateral ligament (MCL) of all specimen were identified and multiple circle dots were marked on it. Both preoperatively and postoperatively, a non-contact video extensometer that consisted of high-resolution digital camera (ISG, MONET 3D, Sobriety s.r.o, Czech Republic) and real-time image processing (ISG, Mercury RT x64 2.7, Sobriety s.r.o, Czech Republic) monitored real-time MCL strain changes during flexion. Strain patterns between KA and MA-TKA in terms of differences in preoperative and postoperative average and Maximum peak strain according to knee flexion tome were compared

Results

Patterns of average strain in KA-TKA was more similar to the native knee than those in MA-TKA under entire range of motion. The average strain of MCL in MA-TKA(7%±4)($P<0.05$) had occurred 2 times larger than average strain of MCL in Native knee(3%±2). In contrast, the average strain of MCL in KA-TKA(3%±3)($P>0.05$) had occurred very similar to the average strain of MCL in Native knee(3%±2). Therefore, these results might be considered the similarity of KA with the pre-operational knee for MCL strain (Fig.1). Maximum peak strain of MCL for MA-TKA has indicated at the posterior-superior location of 120 degrees flexion (Fig.2).

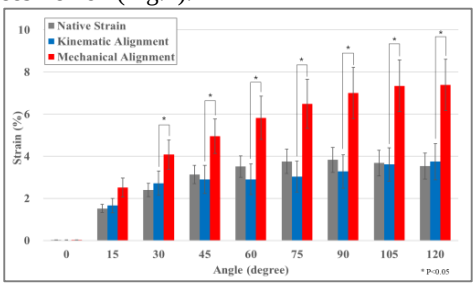

Figure 1: Average of Medial Collateral Ligament Strain can be seen.(Native, MA and KA).

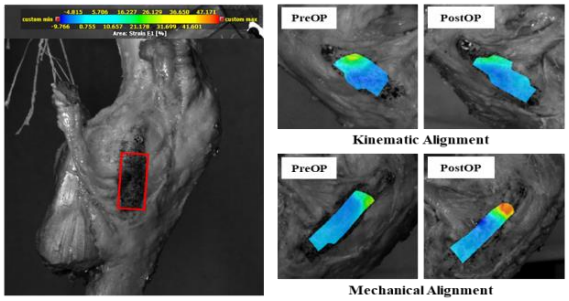

A. Region of strain distribution measure

B. Alterations of strain distributions fc MA and KA

Figure 2: Strain distribution on MCL

Discussion

The results indeed showed that KA-TKA restores MCL strain to the native condition better than MA-TKA. In view of this, the clinical implication of the results obtained in this study suggests that why patients undergoing KA-TKA may experience a more normal knee feeling and better functional performance during activities of daily living

References

1. Koh IJ et al. KSSTA,27:1520-1528,2019.
2. Koh IJ et al. OTSR,105:605-611,2019.

Acknowledgements

This work was supported by the National Research Foundation of Korea(NRF) grant funded by the Korea government (MSIP)(NRF-2017M3A9E9073545) and he Korea Medical Device Development Fund grant funded by the Korea government (the Ministry of Science and ICT, the Ministry of Trade, Industry and Energy, the Ministry of Health & Welfare, the Ministry of Food and Drug Safety) (NTIS Number : 9991007118)

THE EFFECT OF PATHOLOGICAL SCAPULOHUMERAL RHYTHM ON MUSCLE FORCES AFTER REVERSE SHOULDER ARTHROPLASTY

Louis Leuthard (1), Johanna Menze (2), Barbara Wirth (3), Laurent Audige (3), Stephen J. Ferguson (1)

1. Institute for Biomechanics, ETH Zurich, Switzerland; 2 sitem Center, University of Bern, Switzerland; 3. Schulthess Klinik, Zurich, Switzerland;

Introduction

Reverse shoulder arthroplasty (RSA) relieves chronic pain and provides functional improvement [1]. The reversed design of the ball-and-socket anatomy in the glenohumeral joint provides stability [2] and counterbalances the deficient rotator cuff muscles (RCM) [3]. The ratio between the contributions of the glenohumeral (GH) and scapulothoracic (ST) joint to shoulder abduction, also named as the scapulohumeral rhythm (SHR), is often altered after RSA [1]. It is suggested that limited abduction primary results from compromised GH contribution, however corresponding variations in muscle forces have not yet been investigated by musculoskeletal modelling in this context.

The purpose of this study was to investigate the effect of pathological SHR on muscle forces in RSA patients with varying shoulder mobility. It was hypothesized that patients with poor shoulder mobility show decreased forces in the lateral deltoid muscle (LD) which may result in reduced GH abduction.

Methods

Twenty patients (72.1 ± 7.2 years old) with a primary, unilateral Univers Revers^{TM} prothesis (Arthrex Inc, USA) underwent 3D kinematic (Vicon, UK) analysis during bilateral shoulder abduction. Based on their maximum abduction angle, patients were divided into three different mobility groups, poor (<110°), average (110°-140°) or excellent (>140°). The motion capture data was implemented into subject-specific musculoskeletal shoulder models using inverse dynamics analysis (AMMR.v2.2.3, AnyBody Technology 7.2, DK). Each model was scaled to the patient size based on marker positions, body height and weight. In addition, RCM strengths were adapted according to the individually diagnosed RCM deficiencies. Finally, the inverse dynamics analysis was driven with kinematic data for shoulder abduction to 90° in the scapular plane. In the following evaluation, mean muscle forces of the poor (3 patients) and excellent (5 patients) shoulder mobility group were analyzed using MATLAB (MathWorks Inc, USA).

Results

Although no statistically significant differences could be found, LD in the poor shoulder mobility group showed on average 12.6% (min = -4.6%, max = 70.1%) less mean muscle forces during shoulder abduction once muscles were active. Furthermore, LD in the poor mobility group started at higher angles contributing to shoulder abduction compared to the excellent mobility group.

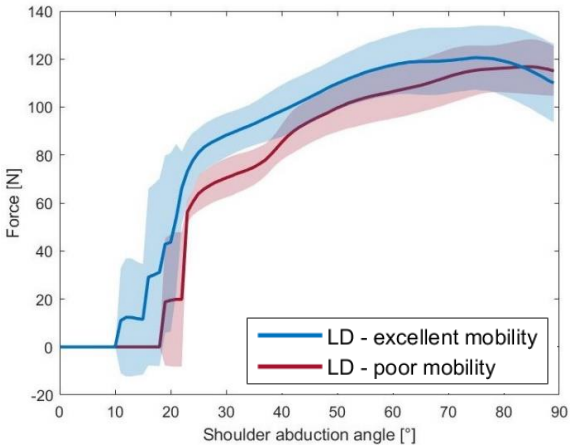

Figure 1: Lateral deltoid (LD) muscle forces (mean and standard deviation) during shoulder abduction in RSA patients with poor and excellent shoulder mobility.

Discussion

Not only started the LD muscle at higher abduction angles to be active, but also decreased forces in patients with poor shoulder mobility were identified. This could indicate that limited abduction primary results from reduced abductor muscle forces. This finding also corresponds to previous research, highlighting the correlation of GH contribution with abduction strength and maximum shoulder abduction [3]. As the SHR is usually consistent in RSA patients at higher abduction angles [1], it remains unclear why the mean muscle force of the excellent mobility group decreases below the poor mobility group above 80° of shoulder abduction.

Future research should focus on more adaptations of the subject-specific models, especially by considering the medialized position of the center of rotation (COR). An altered COR changes the lever arm of the deltoid muscle and subsequently may have an influence on its muscle force during abduction. General limitations of the study are the small sample size, limiting the ability to detect true differences between groups, as well as the applied simple muscle model, neglecting non-linear force-length and force-velocity relationships.

References

1. Walker et al, J Shoulder Elbow Surg, 24:1129–34, 2015.
2. Boileau et al, J Shoulder Elbow Surg, 14:147S-161S, 2005.
3. Friesenbichler et al, Arch Orthop Trauma Surg, 2020.

MEDIAL PROGRESSING AND NON-PROGRESSING KNEE OA SUBJECTS EXHIBIT DIFFERENCES IN LOADING DURING GAIT.

Bryce A Killen[1], Miel Willems[1], Hoa Hoang[2], Sabine Verschueren[3] Ilse Jonkers[1]

1. Department of Movement Science, KU Leuven, Belgium. 2. School of Mechanical Medical & Process Engineering, QUT, Australia, 3. Department of Rehabilitation Science, KU Leuven, Belgium.

Introduction

Osteoarthritis (OA) is a leading cause of disability and a source of high societal burden. The mechanisms underlying patient-specific disease onset and progression are largely unknown. Previous studies have hypothesized that magnitude and location of tibiofemoral joint (TFJ) loading play an important role in development [1,2]. Their role in structural OA progression (represented as Kellgren Lawrence, KL-score) needs further evidence. Model-based, internal joint loading parameters are now available that are suited to investigate these hypotheses. Therefore, this study compared TFJ loading between medial compartment (MC) knee OA subjects that progressed over a 2-year period, subjects that did not progress, and healthy control subjects. It was hypothesized that both progressing and non-progressing OA groups would exhibit altered TFJ loading (magnitude and/or location) compared to the control group where the progressing OA group would present more pronounced differences.

Methods

Data were used from subjects with MC knee OA whereby subjects were tested at baseline and 2-year follow-up. KL scores between time points were used to assign subjects to progressor (P, n=11) or non-progressor (NP, n=15) groups. A KL score increase of ≥1 between time points was defined as progression [3]. Progressors were subdivided into MC and lateral compartment (LC) progressors. Motion capture data was collected during 3 walking trials at self-selected speed and processed through a musculoskeletal modelling framework [4,5] to estimate joint kinematics, moments, and loading parameters (i.e., mean pressure, and centre of pressure (COP)). TFJ loading values at first and second peak were extracted and compared between OA groups and a healthy control group (n=5) using Kruskal-Wallis or Mann-Whitney tests for between group comparisons.

Results and Discussion

TFJ loading (Figure 1): MC-P showed significantly higher medial mean pressures at both first and second peak of TFJ loading compared to all other groups. Further LC TFJ mean pressures were significantly higher compared to the NP group at second peak of TFJ loading. **LC-P** showed significantly lower medial, and lateral mean pressures at second peak TFJ loading compared to the control group. Finally, **NP** showed significantly lower LC TFJ mean pressure at second peak of TFJ loading compared to the control group.

TFJ contact COP (Figure 2): **MC-P** displayed a more lateral COP in both MC and LC TFJ loading compared to all other groups at both time points. Furthermore, a significantly more posterior MC COP, and anterior LC COP was observed compared to all other groups at both time points. **NP** also showed a significantly more lateral COP in both MC and LC TFJ loading compared to LC-P and control subjects at second peak TFJ loading.

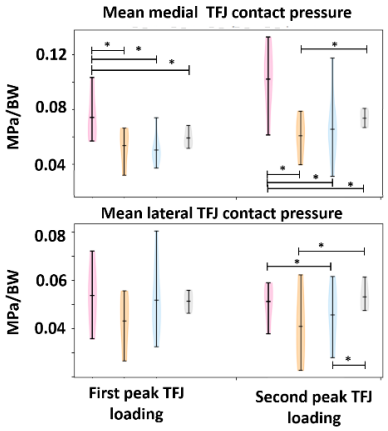

*Figure 1: Medial (middle), and lateral (bottom) TFJ contact pressure at first (left), and second (right) TFJ loading peak. For MC-P (red), LC-P (yellow), NP (blue), and control (grey) subjects. Where * denotes statistically significant differences.*

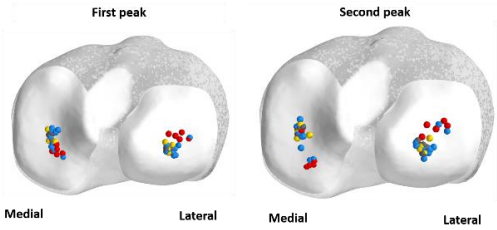

Figure 2: TFJ contact COP at first (left), and second peak (right). For MC-P (red), LC-P (yellow), NP (blue), and control (grey) subjects.

Conclusions

Unique biomechanical markers of **MC-P** were identified. Specifically, **MC-P** were characterised by higher MC mean pressures, posterior-lateral MC COP, and anterior-lateral LC COP compared to **LC-P, NP**, and control groups at first and second TFJ peak.

References

1. Andriacchi et al, J. Bone Joint Surg, 91: 95-101, 2009.
2. DeFrate et al, Osteoarthr. Cartil. 27:392–400, 2019.
3. Wang et al, Arthritis Res Ther, 20:250-261, 2018.
4. Lenhart et al, Ann. Biomed. Eng. 43:2675-85, 2015.
5. Smith et al, J Knee Surg. 29:99-106, 2016.

Acknowledgements

This work was partially supported by H2020 Project OACTIVE SC1-PM17-2017 –and FWO project G-2020-2586.

DEVELOPMENT OF A SUBJECT-SPECIFIC MUSCULOSKELETAL MODEL OF THE THUMB

Dario Sciacca(1), Maarten Vanneste(1), Bryce Killen(2), Evie Vereecke(1)

1. Dept. Development & Regeneration, KU Leuven, Belgium; 2. Human Movement Biomechanics Research Group, KU Leuven, Belgium

Introduction

The trapeziometacarpal (TMC) joint is a biconcave saddle-shaped joint with a high mobility and complexity [1]. To date, we lack a fundamental understanding of the relation between TMC joint morphology and biomechanics which hinders the development of appropriate prevention and treatment strategies for highly disabling diseases such as TMC osteoarthritis (OA). In this study, we use a modelling approach to obtain a fundamental understanding of the biomechanics of the human TMC joint.

Methods

A modular script (Python v3.7.0) has been developed to create a subject-specific model of the thumb. It consists of six main steps:
1) For a specific thumb movement, 3D bone geometries (from CT-scan images) are imported in three different postures: neutral and the two extreme positions.
2) Definition of local coordinate systems for the target bones of the thumb (radius, scaphoid, trapezium and first metacarpal) in the neutral position.

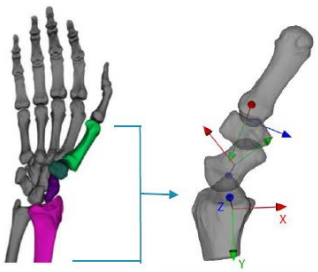

Figure 1: Thumb and wrist joints of the radial column, obtained from CT scan (left); Local coordinate systems for the thumb skeletal chain (right)

3) Calculation of the transformation matrix using markerless registration methods from the neutral to the two extreme positions and computation of the helical axis is computed. In this way, the range of motions (ROMs) are quantified.
4) Intrinsic and extrinsic thumb muscles are added to the model based on image data [2]. The algorithm allows the user to choose the bone meshes with muscle attachment points. These points are obtained by calculating the intersections between the meshes of the muscle and the bones. Muscle paths can also be built by selecting landmark points on the muscle's mesh.
5) The geometry of the model is validated by computing the muscle moment arm during the desired movement and optimizing it to values from literature [3] or experiments.
6) The model is created and imported in OpenSim for further validation and analysis (Fig. 1).

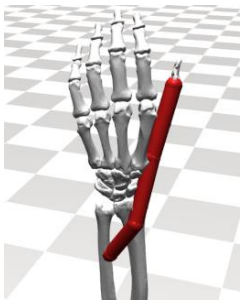

Figure 1: OpenSim musculoskeletal model of the hand with only the extensor pollicis longus

Results

The results for the kinematics of the TMC joint are presented in the Table 1, for both thumb extension-flexion (TFE) and adduction-abduction (TAA). The unit vector representing the helical axis (HA) and the rotation angle are used to define the relative movement of the first metacarpal with respect to the trapezium.

Mov	HA (unit vector)	Rot. angle (deg)
TAA	(-0.71 0.62 0.33)	~ 78
TFE	(-0.98 0.17 -0.15)	~ 85

Table 1: Quantification of the TMC joint kinematics

Discussion

Using a modelling approach we can obtain a profound understanding of the relation between form and function in the TMC joint which is essential to improve treatment options and develop effective prevention strategies.

References

1. Edmunds, J. O. (2011). Current concepts of the anatomy of the thumb trapeziometacarpal joint. Journal of Hand Surgery, 36(1), 170–182
2. Kerkhof, F. D., van Leeuwen, T. & Vereecke, E. E. (2018) The digital human forearm and hand. J. Anat. 233, 557–566
3. Smutz, W. P. et al. (1998) Mechanical advantage of the thumb muscles. J. Biomech. 31, 565–70

BIOMECHANICAL PROPERTIES OF PARASPINAL MUSCLES INFLUENCE SPINAL LOADING - A MUSCULOSKELETAL SIMULATION STUDY

Masoud Malakoutian (1), C. Antonio Sanchez (2), Stephen H.M. Brown (3), John Street (4), Sidney Fels (2), Thomas R Oxland(1,4)

1. Dep. of Mech. Eng., Univ. of British Columbia, Canada; 2. Dep. of Elect. Eng., Univ. of British Columbia, Canada; 3. Dep. of Health., Univ. of Guelph, Canada; 4. Dep. of Ortho., Univ. of British Columbia, Canada

Introduction

Paraspinal muscles are vital to the functioning of the spine. Changes in muscle physiological cross-sectional area significantly affect spinal loading, but the importance of other muscle biomechanical properties remains unclear. This study explored the changes in spinal loading due to variation in four muscle biomechanical properties: passive stiffness, slack sarcomere length (SSL, beyond which passive forces start to develop), in situ sarcomere length, and specific tension (Figure 1).

Methods

An enhanced version of a musculoskeletal simulation model of the thoracolumbar spine with 210 muscle fascicles was used for this study and its predictions were validated for several tasks and multiple postures. Ranges of physiologically realistic values were selected for all four muscle parameters and their influence on L4-L5 intradiscal pressure (IDP) was investigated in standing and 36°flexion.

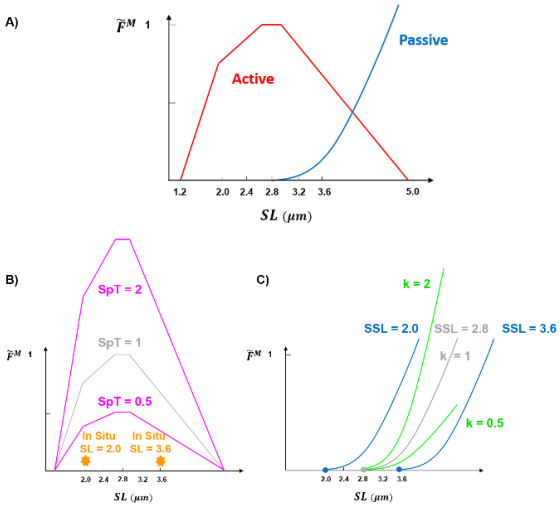

Figure 1: Fundamental muscle force-length curve; force in a muscle varies with certain parameters including (B) posture specific in situ sarcomere length (SL) and the scaling factor for the specific tension (SpT) or (C) slack sarcomere length (SSL) and stiffness scaling factor (k).

Results

We observed large changes in IDP due to changes in passive stiffness, SSL, in situ sarcomere length, and specific tension, often with interesting interplays between the parameters. For example, for upright standing a change in stiffness value from one tenth to 10 times the baseline value increased the IDP only by 91% for the baseline model (Figure 2) but by 945% when SSL was 0.4 µm shorter (Figure 3). Shorter SSL values and higher stiffnesses led to largest increases in IDP. More changes were evident in flexion, as sarcomere lengths were longer in that posture and thus the passive curve is more influential.

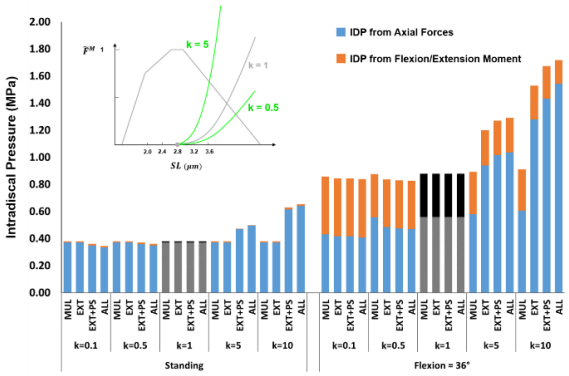

Figure 2: The effect of different stiffness scaling factors (k) on L4-L5 IDP in upright standing and 36° flexion for four scenarios: changes applied to multifidus (MUL), extensor muscles (EXT), extensor muscles and psoas (EXT+PS), and all 210 muscles in the model (ALL). Grey/black bars represent the baseline values.

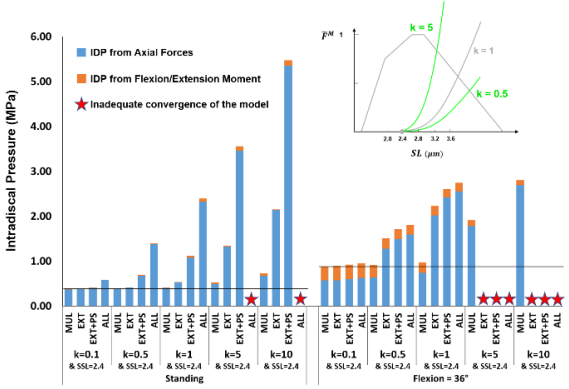

Figure 3. The effect of different stiffness scaling factors (k) combined with a slack sarcomere length (SSL) of 2.4 µm on L4-L5 IDP in upright standing and 36° flexion. The black horizontal lines represent the baseline values.

Discussion

Our results highlight the importance of the muscle force-length curve and the parameters associated with it and motivates further experimental studies on in vivo measurement of those properties.

LARGER MUSCLE FIBERS AND FIBER BUNDLES MANIFEST SMALLER ELASTIC MODULUS IN PARASPINAL MUSCLES OF RATS AND HUMANS

Masoud Malakoutian (1), Marine Theret (2), Shun Yamamoto (3), Iraj Dehghan-Hamani (1), Michael Lee (3), John Street (3), Fabio Rossi (2), Stephen Brown (4), Thomas Oxland (1,3)

1. Dep. of Mech. Eng., Univ. of British Columbia, Canada; 2. Dep. of Med. Gen., Univ. of British Columbia, Canada; 3. Dep. of Ortho., Univ. of British Columbia, Canada; 4. Dep. of Health., Univ. of Guelph, Canada

Introduction

Passive elastic modulus of muscles is important for biomechanical functioning of the musculoskeletal system. While most studies assume that the size of a muscle fiber bundle (i.e. a number of muscle fibers ensheathed in their connective tissue) does not influence elastic modulus after normalizing for cross sectional area, elastic modulus of muscle fibers has been shown to be size-dependent [1]. The objectives of this study were to determine the degree to which this size effect was evident in muscle fiber bundles and to examine the validity of the frequent assumption of a circular cross section of muscle fiber bundles.

Methods

Muscle fibers and fiber bundles were extracted from lumbar spine multifidus and longissimus of three cohorts: group one (G1) and two (G2) included 13 (330±14g) and 6 (452±28g) Sprague Dawley rats, while Group 3 (G3) comprised 9 human degenerative spine patients. A minimum of six muscle fibers and six muscle fiber bundles from each muscle underwent cumulative stretches, each of 10% strain followed by 4 minutes relaxation. Elastic modulus was calculated as tangent at 30% strain from the resulting stress-strain curve. Linear correlations between the fiber/fiber bundle cross sectional area (CSA) and elastic moduli in each group were performed. Major and minor axis diameters of fibers and fiber bundles were measured and their ratios were calculated. The results were contrasted against the theoretical median of 1 (for cylindrical shape assumption) using Wilcoxon signed rank test.

Results

The correlations showed that increasing specimen CSA resulted in lower elastic modulus for both rats and humans, muscle fibers and fiber bundles (all $p<0.05$ except for G2 longissimus bundles with $p=0.21$, Figures 1-2). The median ratio of major to minor axis exceeded 1.0 for all groups, ranging between 1.15 and 1.29 for fibers and 1.27 and 1.44 for fiber bundles.

Discussion

The lower elastic moduli with increasing size can be explained by relatively less collagenous extracellular matrix in the large fiber bundles (Figure 3). Future studies of passive property measurement should aim for consistent bundle sizes and measuring diameters of two orthogonal axes of the muscle fibers and fiber bundles.

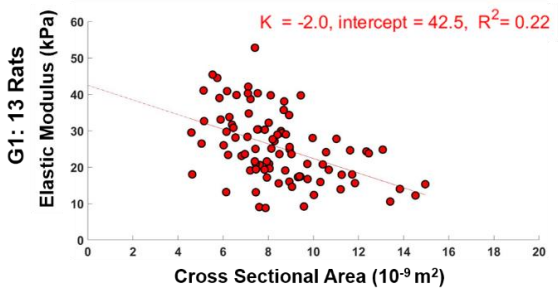

Figure 1: Correlation between elastic modulus and cross sectional area of G1 multifidus single fibers

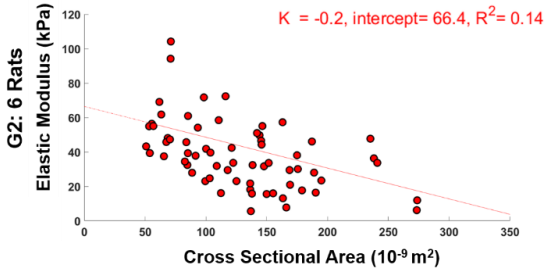

Figure 2: Correlation between elastic modulus and cross sectional area of G2 multifidus fiber bundles.

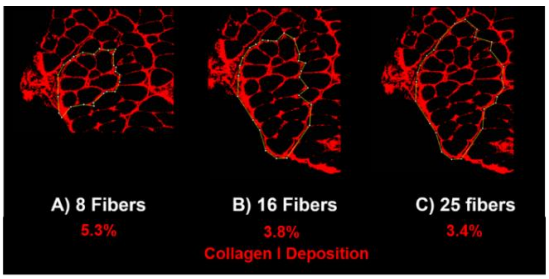

Figure 3: Inverse correlation between collagen I area fraction and size of three bundles of different sizes from multifidus of one rat in G1. Yellow lines represent the borders of selected bundles.

References

1. Noonan et al., J Biomech Eng 142(8), 2020.

Acknowledgements

We thank NSERC and Medtronic Canada for funding.

IN VIVO FORCE ENHANCEMENT IS LARGEST WHEN MUSCLES OPERATE ON THEIR FORCE-LENGTH PLATEAU

Christopher P. Cop (1), Alfred C. Schouten (1, 2), Bart Koopman (1), and Massimo Sartori (1)

1. University of Twente, The Netherlands; 2. Delft University of Technology, The Netherlands

Introduction

The isometric force generated by a muscle after an eccentric contraction is higher than the purely isometric force at the same fiber length and activation level. This phenomenon is known as stretch-induced residual force enhancement (FE). However, several *in vivo* experiments in humans showed that not all subjects display FE, dividing the subject population into responders and non-responders [1].

Previous research has obtained weaker FE *in vitro* in muscle fibers operating on the ascending limb of their force-length (F-L) curve, compared to its plateau and descending limb [2]. Here we investigate whether or not it is possible to observe a similar behavior in intact human muscles *in vivo*.

Methods

One subject (female, weight: 57 kg, height: 1.61 m, age: 27 years) was instructed to keep the tibialis anterior muscle's (TA) activation level between 15% and 20% of maximum voluntary contraction (MVC) while the resulting ankle torque was recorded by a dynamometer. For all trials, the knee angle was set to 150 deg and tracked by a motion capture system.

To determine the region of the F-L curve on which the TA operated, an initial trial was performed in which dorsiflexion (DF) torque was recorded throughout ankle angles ranging from 5 deg DF to 40 deg plantarflexion (PF) (with steps of 5 deg). The plateau region was identified from the torque-angle curve.

The subject then performed six 35-second-trials per ankle angle with a) isometric contractions (n=3) and b) an active stretch followed by an isometric contraction (n=3). Two different initial ankle angles were investigated: one in which TA operated on the ascending limb of the F-L curve (13 deg PF) and another where TA operated on the F-L curve plateau (33 deg PF).

Results

Fig. 1 shows DF torque enhancement after a stretch as the relative increase in torque with respect to the reference isometric contraction. Positive values suggest FE while negative values indicate a torque reduction. When the TA operated on the plateau region of the F-L relationship (blue lines in Fig. 1), we obtained torque enhancements of 17.8% (right after the stretch), 5.6% (10 s after the stretch), and 10.8% (20 s after the stretch). When the TA operated on the ascending limb of the F-L relationship (red lines in Fig. 1), we obtained torque 'enhancements' of -5.5% (right after the stretch), 2.4% (10 s after the stretch), and 2.3% (20 s after the stretch). EMGs remained within the bounds (15-20% of MVC) for the majority of the trials.

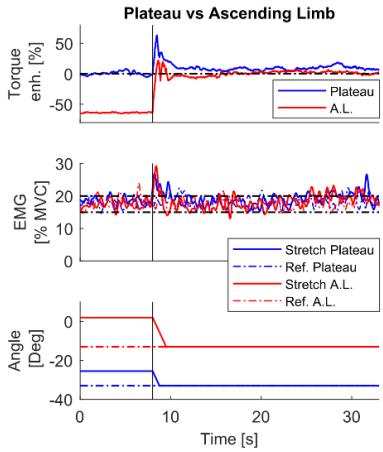

Figure 1: Changes in torque with respect to reference (top), EMG linear envelopes (middle), and ankle angle (bottom) of a representative trial with the reference angle on the plateau of the F-L curve (in blue) and on the ascending limb (A.L.) of the F-L curve (in red). The isometric reference trials are illustrated in dashed lines and the trials with an active stretch are depicted with solid lines. The vertical black solid lines indicate the onset of the stretch applied by the dynamometer.

Discussion

Previous research has not always been successful at eliciting FE in human experiments *in vivo* [1]. We were able to obtain FE in a subject that did initially not show FE with the ankle joint in neutral position, as commonly done in literature. We could obtain FE by first determining the optimal joint angle where TA acted on its F-L plateau. This could suggest that previous failures at eliciting FE might have been due to subjects' muscles operating on the ascending limb of the F-L curve, far from the plateau region. Although experimental data from more subjects is required to corroborate our hypothesis, these results may open new avenues for understanding muscle force generation capacity during complex motor tasks.

References

1. Seiberl et al., J Electromyogr Kines, 25:571-580, 2015.
2. Peterson et al., J Exp Biol, 207:2787-2791, 2004.

Acknowledgements

This work has been funded by ERC Starting Grant INTERACT (803035).

KNEE CARTILAGE LOADING AT DIFFERENT GAIT SPEEDS

Georgios Giarmatzis (1), Konstantinos Moustakas (1)

1. *Visual and Virtual Reality Group, Electrical and Computer Engineering Department, University of Patras, Greece*

Introduction

Knee osteoarthritis (OA) - a degenerative disease of the knee cartilage resulting in pain and movement deficits - has inflicted globally around 86.7 million individuals only during 2020 [1]. Local cartilage dynamics during ambulation has been identified as the main influence on onset and/or progression of the disease which can be explored only through physics-based simulation of human motion. Although knee forces have been previously reported as the main descriptors of cartilage loading, most informative cartilage pressure values have received limited attention, due to the research-intensive calculation methods involved, such as finite element analysis. Since walking is the preferred exercise amongst recreational sports, the main aim of this study is to explore maximum knee contact pressure during different gait speeds and its relation to external joint moments as surrogates of knee loading descriptors. Such knowledge would fill the gap in current literature in terms of intensity-specific cartilage response during walking and inform intervention studies for better OA management.

Methods

Marker-based motion capture system was used to record 11 young individuals walking on a split-belt treadmill with embedded force plates at 3-6 km/h. Knee cartilage contact pressures were calculated during stance phase of the right leg for 265 gait cycles using a 3D musculoskeletal model presented previously [2], scaled to each participant's dimensions and mass. Joint angles were calculated using inverse kinematics. Muscle activations and secondary knee kinematics (11 DoF), required to reproduce the measured primary hip, knee and ankle accelerations were computed using the concurrent optimization of muscle activations and kinematics (COMAK) algorithm [2]. Mean maximum knee contact pressures (max KCP) were calculated and interpolated to 100 points across subjects and gait cycles. Permutation importance maps using Random Forest regression models were estimated to explore correlation between lower limb joint torques and max KCPs across the gait cycle.

Results

Average curves of max KCPs show a double peak profile (Figure 1), also seen in case of knee contact forces [3]. Results show a positive effect of speed on the two peaks of max KCPs, with the latter increasing with increasing speed, ranging from ~7 MPa to 13.3 MPa. Feature importance map (Figure 2) included only knee flexion and adduction moments, as the only non-collinear variables.

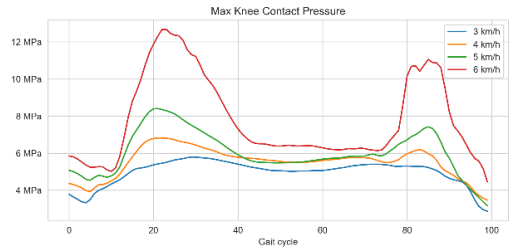

Figure 1 Average curves of maximum knee contact pressures during 100% of gait cycle at different gait speeds.

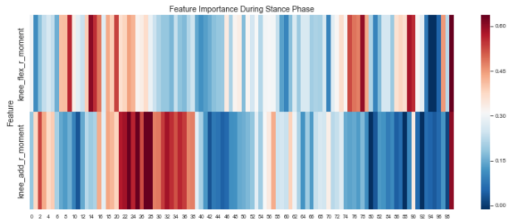

Figure 2 Permutation-based feature importance on max KCPs during the stance phase for knee flexion and adduction moments.

Knee adduction moment's compressive effect is mainly responsible for the first peak whereas knee flexion moment and consequent knee extensors or flexors muscle function correlates with early stance phase and second peak max KCPs.

Discussion

For the first time, KCPs are calculated during stance phase at a wide range of gait speeds. Maximum KCPs exhibit the typical double peak profile during gait stance phase at all walking speeds, reaching peak values well below the cartilage compressive failure limit of 35 MPa [4]. Moreover, novel explainable machine learning algorithms were used to explore the different influence of knee flexion and adduction moments on max PCFs throughout the stance phase and not on just the timings of peak values, as widely done until now.

References

1. A Cui et al, *EClinicalMedicine* **29**–**30** 100587 (2020).
2. C R Smith et al, *Comput. Methods Biomech. Biomed. Eng. Imaging Vis.* **6** 491 (2018).
3. G Giarmatzis et al *Sensors* **20** 6933 (2020).
4. A J Kerin et al *Proc. Inst. Mech. Eng. Part H J. Eng. Med.* **212** 273 (1998).

Acknowledgements

We particularly would like to thank Sabine Verschueren and Ilse Jonkers from KUL for providing the motion capture system and offering their permission to use the motion data. This work was supported by the EC Horizon 2020 project OACTIVE Grant Agreement No.777159.

CURRENT ISSUES ON THE UPPER LIMB MUSCULOSKELETAL MODELS: THE MUSCULAR ACTIVATION ODDITY

Diego A. Rueda (1), Diego F. Villegas (1)

1. Universidad Industrial de Santander, Colombia

Introduction

The intention to depict; how our body works; has encouraged researchers looking for a virtual representation that can emulate the human's body normal behaviour. A musculoskeletal model tries to do this by combining skeletal characteristics with muscle models that use variables like the muscle's length, the contraction length, the contraction velocity, the muscle activation, among other variables.

According to muscle theory, the muscle reacts to stimuli received from the Central Nervous System (CNS). The problem is that there is no idea how the CNS works or how it selects which muscle activated in each movement. To date, many procedures have attempted to decode how muscle stimulation occurs while movements are performed, but none have determined the method of activation that the CNS uses.

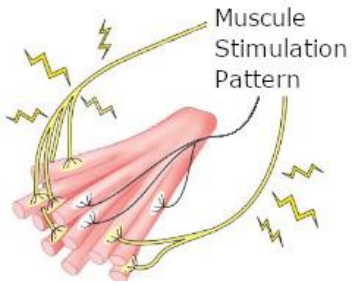

Figure 1: Muscle stimulation schematic: The yellow lines represent a CNS signal and the black lines an inactive state. Each fibre represents a muscle element.

Methods

Through this study, it pretends to expose the current alternatives to predict or approximate muscular activation. Focus on emerging tools imported from other knowledge fields that could have great potential for the proposed task.

Results

The optimization algorithms are widely used in the most popular upper limb musculoskeletal models to determine muscle stimulation patterns; these algorithms implement cost functions related principally to muscle stress and energy expenditure [1]. However, a couple of studies have implemented optimization methods with cost functions based on other approaches, like Pseudo-Inverse and Null-Space approximation concept from control theory [2] and the Entropy concept from applied physics [3], obtaining attractive results and better performance related to base models. On another side, appear methods that use the electromyographic (EMG) signals; this approximation is one of the closest to the real function, but for practical measurements, the data only correspond to the superficial muscles [4].

Current studies are approaching the muscle modelling case using behaviour based analysis, in which based on data can establish a model that fits with the information provided. These are artificial intelligence methods [5], in which the major disadvantage is the lack of real muscle activation data; usually, EMG signals have used as base data.

Ref.	Activations Prediction Method	Validation Method
[1]	Muscle Stress and Energy Expenditure Optimization	In Vivo Measurements
[2]	Pseudo-Inverse and Null-Space Optimization	In Vivo Measurements
[3]	Muscle Stress and Entropy Term Optimization	Inverse Dynamics Measurements
[4]	EMG Patterns Based on Window Sample Entropy and Window Kurtosis	Raw EMG data and Root Mean Square approach
[5]	Neural Networks Prediction	EMG Patterns

Table 1: Current used muscular activation methods and their corresponding results validation approach.

Discussion

The optimization methods are the most regular for approaching muscular activation; cost functions vary depending on the concept to evaluate. These methods regularly propose a unique variable to optimize. So, to approximate the CNS muscular activation pattern, the approach must be more robust and reliable. The artificial intelligence methods accomplish the above requirements but need a solid background of data to train a model that truly represents the system, and that is the hard part.

Interestingly, no info or vague info refers to the muscle function depending on the movement.

References

1. A.A. Nikooyan et al, J Biomech, 43:3007-3014, 2011.
2. A. Terrier et al, Med Eng Phys, 32:1050-1056, 2010.
3. X. Xu et al, J Electromyogr Kines, 33:103-1010, 2017.
4. X. Zhuojun et al, J Bionic Eng, 12:316-323,2015.
5. W.H.K. de Vries et al, J Biomech, 49:73-79, 2016.

HOW DOES THE GLENOID SIZE AFFECT ROTATOR CUFF LOADING ? A MUSCULOSKELETAL ANALYSIS

Johanna Menze (1), Hanspeter Hess (1), Stephen J. Ferguson (2), Matthias Zumstein (1), Nicolas Gerber (1), Jürgen Burger (1), Kate Gerber (1)

1. sitem Center, University of Bern, Switzerland; 2. ETH Zürich, Switzerland; 3. University Hospital Bern, Inselspital, Switzerland

Introduction

The stability of the shoulder joint, being a ball and socket joint with a wide range of motion, is predominantly given by the surrounding rotator cuff (RC) muscles. The smaller the glenoid compared to the humeral head, the stronger the RC needs to act to provide the required stability against subluxation. The resulting excessive loading of the tissue might be a possible explanation why clinical studies have shown a correlation between glenoid size (GS) and RC tear incidence [1,2]. Biomechanical studies, however, have not yet investigated the effect of GS on the RC forces.
Therefore, we aim to understand the influence of the GS on RC forces during shoulder abduction, flexion, internal and external rotation using musculoskeletal modeling.

Methods

The musculoskeletal modelling was performed in Anybody 7.3 using the generic model (male,75kg, 1.80m) of the repository AMMR v.2.3.1. Muscle forces were calculated based on inverse dynamics for shoulder abduction and flexion from 0° to 120° and internal and external rotation from -50° to 50° with the elbow flexed at 90°. All motions were performed against a resistance of 25N. The resulting maximum forces were subsequently extracted from each motion and compared. The glenohumeral joint was kinematically constrained to prevent translations of the humeral head on the glenoid. The GS was determined based on the glenoid width (GW). This was defined as the A-P distance in the inferior portion of the glenoid which was altered from 24 mm to 36 mm according to population variations [3,4]. The glenoid height changed proportionally. The humeral head remained at a constant diameter of 53 mm to solely investigate the influence of the GS to humeral head ratio.

Results

GS variations have an influence on maximum RC forces during abduction and flexion. Throughout internal and external rotation, maximum RC forces remain unchanged despite the varying GS, represented by the respective GW (Figure 1).
When comparing the smallest GW with the mean, the infraspinatus (IS) and subscapularis (SB) both experience the strongest load increase of 46% during abduction and 18% and 99% during flexion, respectively. The supraspinatus (SS) shows only little sensitivity to GS variations.
An increase of the GS does not significantly alter the RC forces, except for the SB force which additionally decreases by 60% during flexion.

Discussion

Various morphological parameters as the acromion shape or glenoid inclination have been investigated in the past and their relation to RC loading have been established [5]. It appears that the GS plays a similarly important role in the evaluation of RC forces. The strong effect on the SB and IS particularly give reason to assume that a reconstruction of their biomechanics is crucial to regain functionality after a RC tear which has also been clinically observed [6]. An impairment could lead to shoulder instabilities or pseudoparalysis which should be further investigated with a model allowing for glenohumeral translations.

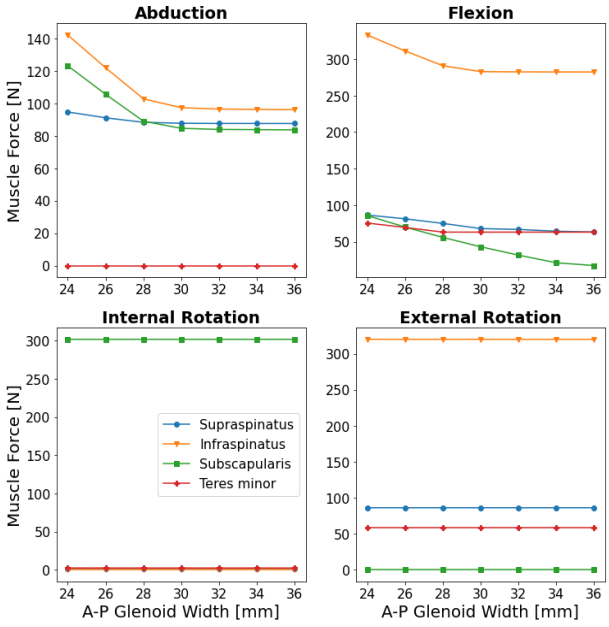

Figure 1: Maximum RC muscle forces during abduction and flexion from 0° to 120° and internal and external rotation from -50° to 50 for various glenoid sizes represented by the A-P glenoid width.

References

1. Saygi et al, J Orthop Surg, 26:2309499018768100, 2018
2. Maalouly et al, Int J Surg Case Rep, 68:74-82, 2020
3. Iannotti et al, J Bone Joint Surg Am, 74:491-500, 1992
4. Churchill et al, J Shoulder Elbow Surg, 10:327-332, 2001
5. Moor et al, Clin Biomech, 32:268-273, 2016
6. Collin et al, J Shoulder Elbow Surg, 23:1195-1202

CHANGES IN MUSCLE ACTIVATION PATTERN DURING GAIT AMONG HEALTHY CHILDREN

Jurgita Ziziene (1), Kristina Daunoraviciene (1), Julius Griskevicius (1), Giedre Juskeniene (2), Kristina Rinkeviciute (2), Juozas Raistenskis (2)

1 Vilnius Gediminas technical University, Lithuania; 2. Vilnius University Hospital Santaros Klinikos, Lithuania;

Introduction

Surface electromyography (EMG) is an essential part of gait analysis. It provides the objective assessment of muscular function during walking and allows to identify the timing of muscle activation during movement. Muscle activation patterns in both adults and children are normed for later use to identify movement changes, dysfunctions, or disorders [1-2]. However, it is observed that the muscle activation in children is very volatile and this is determined by the totality of external and internal factors, which is very difficult to assess. This study aims to define changes in muscle activity of children during gait and determine trends [3-5].

Methods

The study involved 13 healthy kids aged 4-11 years (6 males and 7 females). Parental consent and child assent were obtained prior to the participation in the study. Five muscles (biceps femoris – BF, semitendinosus – SE, tensor fasciae latae – TF, lateral gastrocnemius – LG and medial gastrocnemius - MG) were studied for both lower extremities. Gait was assessed under habitual pace using 8 Vicon motion capture (100 Hz), one force plate Bertec (1000 Hz) and surface EMG Delsys Trigno (2000 Hz) systems. The measurement was repeated 10 times for each subject. Gait cycle was identified using Vicon and force plate data. Collected EMG data were pre-processed: (1) filtered with a high-frequency 4th order zero-phase Butterworth filter with a 50 Hz cut-off frequency, (2) performed full-wave rectification, (3) filtered with a low-frequency 2nd order Butterworth filter with a 3 Hz cut-off frequency. Subsequently, the EMG curves were normalized to full gait cycle (from heel contact to heel contact - strides) in a random 3 strides sequence for each test and the time was normalized. Duration of muscle activation (t, %) was identified and activation change (Δ, %) were determined as the difference between the activation start and end within adjacent strides throughout the gait for each subject. Normally distributed data represented as mean ± SD and not normally distributed data – median (MAD).

Results

The time of muscle activation varies (60– 90 % of cycle) between subjects (fig.1). It may start at the beginning of one stride and end in another, and secondary muscle activation may also occur. Such activation changes presented in the table 1.

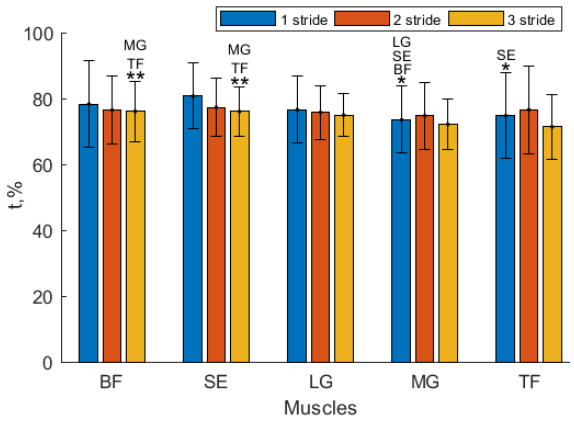

*Figure 1: t (mean± SD) of muscles in % of stride (n=13), * - in 1 stride (p<0.05); ** - in 3 stride (p<0.05);*

		1 vs 2 stride		2 vs 3 stride	
		Right	Left	Right	Left
BF	Δ_{start}	4 (5.3)	3 (3.4)	4 (4.2)	10 (6.3)
	Δ_{end}	6 (6.1)	9 (8.5)	4 (6.4)	(4.3)
SE	Δ_{start}	3 (4.9)	3 (3.4)	4 (3.8)	2 (3.3)
	Δ_{end}	5.5 (4.8)	5 (5.2)	6 (5.2)	7 (4.9)
LG	Δ_{start}	5 (4.7)	4 (2.9)	5 (3.5)	4 (3.3)
	Δ_{end}	3 (4.6)	3 (3.2)	3 (3.4)	3 (4.2)
MG	Δ_{start}	4 (4.2)	5 (4.3)	5 (4.2)	3 (3.4)
	Δ_{end}	3 (3.2)	3 (2.9)	3 (3.4)	3 (3.2)
TF	Δ_{start}	6 (4.2)	5 (4.3)	5 (3.6)	3 (4.2)
	Δ_{end}	5 (5.7)	4 (4.3)	5 (5.0)	5 (4.4)

Table 1: Activation change between adjacent strides, represented in % of stride (median (MAD)), n=13.

Conclusions and Discussion

Changes in the muscle activity pattern during gait not only define the functions of the muscle itself but also define the gait stability of the individual. On the other hand, the large variation indicates the possibilities of musculoskeletal functionality [3,5]. Our study results revealed that there is no permanent pattern of muscle activation even in normal gait of the children. However, to refine the results, the latency period of the muscle should also be taken into account and a larger number of steps should be investigated.

References

1. Rozanski et al., Clinical Neuro, 131(8):1848-1858, 2020.
2. Navacchia et al., Ann Biomed Eng, 47:2416-2430, 2019.
3. Agostini et al., Gait Posture, 32(3):285-289, 2010.
4. Bovi et al., Gait Posture, 33(1):6-13, 2011.
5. Nardo et al., Gait Posture, 46:161-6, 2016.

DYNAMIC ANALYSIS OF TOTAL SHOULDER REPLACEMENTS USING A ROBOT-ASSISTED COMPUTATIONAL TEST METHOD

Maeruan Kebbach (1), Sven Herrmann (2), Robert Grawe (3), Eric Kleist (3), Peter Augat (2), Christoph Woernle (3), Rainer Bader (1)

1. Department of Orthopaedics, University Medicine Rostock, Germany 2. Institute for Biomechanics; BG Unfallklinik Murnau, Germany; 3. Chair of Technical Dynamics, University of Rostock, Germany

Introduction

Despite progressive improvements in surgical technique and clinical research, systematical identification of implant failure mechanisms after total shoulder replacements (TSR) remains difficult. Current experimental approaches are limited in reproducing the complicated dynamic interplay of the implant and the musculoskeletal system. Our present study, therefore, aims to establish a universal robot-assisted hardware-in-the-loop (HiL) test system that combines the advantages of musculoskeletal multibody simulation and experimental testing to enable evaluation of TSR dynamics under reproducible and physiological conditions.

Material and Methods

We deployed a robot-assisted HiL simulation (Fig. 1), in which an industrial robot moved and loaded an anatomical (aTSR) and inverse (rTSR) (Mathys AG, Bettlach, CH) in continuous interaction with a musculoskeletal multibody model (m = 58 kg) of the shoulder complex.

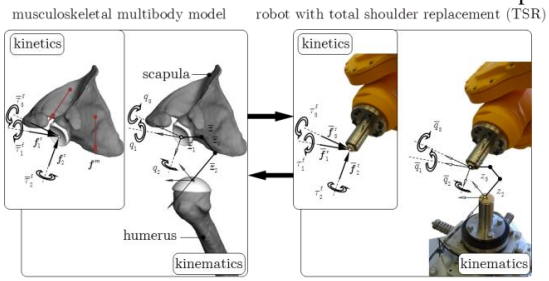

Figure 1: Functionality of the robot-assisted HiL simulation to evaluate TSRs during dynamic activities.

The robot generates the motion of the glenoid component according to the three rotations provided by the model under position control, whereas the forces are applied under force control in the translational directions constrained by the physical contact of the articulating implant components. Occurring resistance torques and displacements of the TSR are measured and transferred back into the computational model (Fig. 1). Based on a previously published inverse kinematic model [1], an inverse dynamic musculo-skeletal multibody model was generated in SIMPACK v9.7 to emulate the dynamics of the upper extremity after TSR during an abduction and flexion movement (Fig. 2A). The model considered muscle structures including muscle wrapping based on a published in-vitro load case [2,3]. Each HiL simulation was repeated ten times to calculate mean values as well as mean and maximum standard deviations (SDs) which allow characterizing of the reproducibility of the test system.

Results

Concerning the reproducibility, the calculated glenohumeral joint force for aTSR/rTSR was repeated by the robot with a mean SD of 5.1 N/1.4 N and a maximum SD of 11 N/5.5 N.

The predicted glenohumeral joint force of the HiL simulation showed good agreement with experimental data provided by Ackland et al. [2,3]. Similar trends were observed in the predicted joint forces qualitatively and quantitatively (Fig. 2).

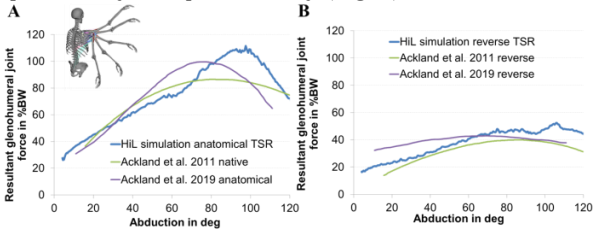

Figure 2: Validation of the HiL test system using the glenohumeral joint force (in %BW) for anatomical (A) and reverse TSR (B) during abduction movement of the right arm in comparison with cadaveric studies performed by Ackland et al. [2,3].

Discussion

Functionality and validity of the robot-assisted HiL test system was successfully demonstrated for anatomical and reverse TSR designs by comparison with both in vitro and in silico data [2, 3]. Furthermore, we validated joint forces and muscle forces during flexion movement. The combination of a musculoskeletal multibody model with an industrial robot enabled the integration of realistic contact conditions, thus mitigating the limitations of solely experimental or numerical methods. Hence, different surgical and implant specific parameters after arthroplasty with anatomical or inverse TSRs can be systematically analyzed by the HiL simulation under reproducible and physiological conditions in the future.

References

1. Herrmann et al. Multibody Dynamics 2019, Springer, Cham, 34-42, 2020
2. Ackland et al. J Orthop Res, 29(12):1850–8, 2011
3. Ackland et al. J Orthop Res, 37(9):1988–2003, 2019

Acknowledgements

The German Research Foundation (DFG, WO 452/11-1, BA 3347/14-1 and HE 7885/1-1) supported the work presented.

KNEE LOADING IN A PRECLINICAL RODENT MODEL BASED ON MUSCULOSKELETAL MODELING AND INTEGRATED XROMM DATA

Judith Piet (1), Falk Mielke (2), Rik Lories (3), Peter Aerts (2), Sam Van Wassenbergh (2), Ilse Jonkers (1,3)

1. Human Movement Biomechanics Research Group, Department of Movement Sciences, KU Leuven, Leuven, Belgium; 2. Laboratory of Functional Morphology, Department of Biology, Faculty of Sciences, University of Antwerp, Wilrijk, Belgium; 3. Department of Development and Regeneration, Skeletal Biology and Engineering Research Center, KU Leuven, Leuven, Belgium

Introduction

Preclinical models are widely used to study cartilage degeneration. The knee can be surgically destabilized to alter joint loading, and induce osteoarthritis. For such interventions, gait is often assessed with hindlimb ground reaction forces (GRF) or paw print intensity (CatWalk system), but internal knee loading is not assessed [1,2,3]. This study presents a workflow to estimate contact forces in the rat knee using musculoskeletal modeling, based on GRF and torques, and accurate motion of hindlimb bones acquired with X-Ray Reconstruction of Moving Morphology (XROMM).

Methods

Two 12-week-old male Sprague-Dawley rats were implanted with radio-opaque tin markers onto the right tibia and femur. After 4 weeks, their gaits were recorded using the 3D²YMOX setup (University of Antwerp) [4]. Rat motion was captured with a biplanar X-Ray video setup, while they ambulated through an instrumented walkway. Synchronous force plate data were acquired using a piezo force plate (Kistler, 20kHz acquisition rate). Forces, torques and center of pressure were computed. Biplanar X-Ray images were processed in XMALab [5]. Bone markers and bony landmarks on the right foot, tibia, femur, pelvis and spine were tracked manually (Fig 1A). A generic musculoskeletal model of the rat hindlimb [6] was scaled in OpenSim [7]. This model includes 38 muscles, has 3 degrees of freedom at the ankle and hip, and 1 degree of freedom at the knee (flexion) (Fig 1B). After inverse kinematics, inverse dynamics, and static optimization of muscle forces, contact forces were estimated in the knee.

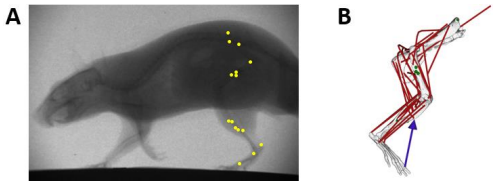

Figure 1: (A) In yellow: markers and bony landmarks on one of the XRay views. (B) Scaled OpenSim model of the rat hindlimb, and ground reaction force.

Results

Both rats had similar resultant GRF (Fig 2A). Rat 2 had deeper knee flexion (Fig 2B, in blue). Forces for the biceps femoris anterior are given as a reference (BFa, Fig 2C). Estimated muscle forces were higher for the vastus lateralis and semi-membranous in rat 2 (VL, SM, Fig 2C, in blue), which are bi-articular muscles connecting the pelvis and tibia. Resultant joint contact forces were higher in rat 2 (Fig 2D, in blue), mostly due to the contribution of anterior-posterior contact forces (not shown here).

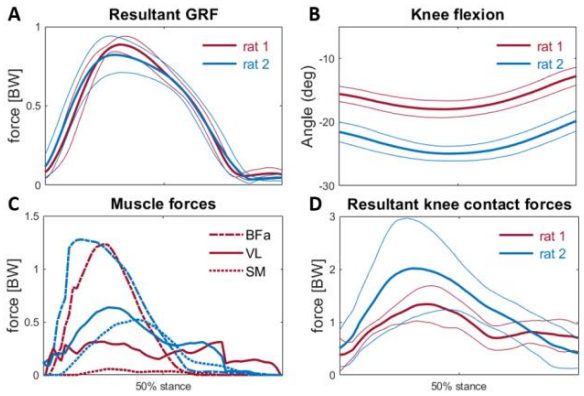

Figure 2: Mean and standard deviation for GRF, knee flexion, knee contact forces. Standard deviation for muscle forces is not shown to avoid crowding. BW = body weight.

Discussion

Even though both rats had similar GRF, estimated knee contact forces were higher in rat 2, likely due to increased knee flexion and higher contribution of muscles spanning across the knee. These estimations emphasize that musculoskeletal modeling is needed to understand internal joint loading in preclinical models of knee injury.

References

1. Fang et al, Sci Rep, 8(1):2855,2018
2. Muramatsu et al, Osteoarthritis Cartil.; 22(6):831-5,2014
3. Ferland et al, Pharmacol Bioch Behav, 97(3):603-10, 2011
4. Sanctorum et al, Meas. Sci. Technol., 30.10: 105701, 2019
5. Knörlein et al.,J Exp Biol.;219(Pt 23):3701-3711.,2016
6. Johnson et al., J Biomech. 2008;41(3):610-9, 2008
7. Delp et al., IEEE Trans Biomed Eng. 54(11):1940-50, 2007

Acknowledgements

This work was supported by the Fonds voor Wetenschappelijk Onderzoek (FWO post-doctoral fellowship #1244221N).

MUSCLE OPTIMIZATION SCALING APPROACH FOR MODEL-BASED MUSCLE FORCES ESTIMATION IN PARKINSONIAN GAIT

Marco Romanato (1), Francesca Volpin (1), Daniele Volpe (2), Zimi Sawacha(1)

1Department of Information Engineering, University of Padova, Padova, Italy; 2Fresco Parkinson Center, Villa Margherita, S. Stefano, Vicenza, Italy

Introduction

Parkinson's disease (PD) is a progressive pathological condition characterized by a dopamine deficiency. Gait alterations are a well-known hallmark of PD patients [1]. Recently, the authors detected further signs of motor impairments in PD's neural strategies, as the timing of the muscle activation peak during the gait cycle and a difference in its amplitude [2] when compared with healthy subjects. Electromyography (EMG) is not representative of the subject's strength and currently, no studies investigated the possibility to assess strength in terms of muscle forces as a biomarker of disease progression in PD subjects. A possible way forward is the use of musculoskeletal modelling which allows the non-invasive estimation of muscle forces. To reach an accurate level of subject-specificity in muscle forces estimation in PD we thus seek in this work the more appropriate musculoskeletal scaling approach.

Methods

Five control subjects ((CS), age=57.8±5.6 years, BMI=27.3±3.9 kg/m^2) and five PD subjects (age=62.8±11.4 years, BMI=27.1±2.9 kg/m^2) were acquired with a 6-cameras motion capture system (60Hz, BTS), synchronized with 2 force plates (960Hz, Bertec) and an 8-channels EMG system (1000Hz, BTS) that recorded bilaterally the activities of 4 muscles: Rectus Femoris, Biceps Femoris, Gastrocnemius Lateralis (GL) and Tibialis Anterior (TA). Data were processed in OpenSim and two different scaling approaches were considered: the standard linear scaling (LS) and the muscle optimizer (MO) scaling [3]. For the latter, two different sets of muscles were included during the process, one including all the muscles of the model (MO_FULL), and one including muscles only spanning knee and ankle joints (MO_MIN). Three different scaled models were obtained for each subject, then inverse kinematics, and static optimization were performed. Coefficient of determination (R^2) between CS predicted and experimental EMGs was computed to assess the physiological validity of the models. Muscle forces were compared via Wilcoxon Signed Rank test, as no evidence of normality assumption was verified.

Results

R^2 (Figure 1) reported a comparable physiological behaviour in the investigated models, suggesting no significant loss of information between the approaches.

Muscle forces obtained for LS and MO_MIN models denoted statistically significant differences in simulated muscles, e.g., Vastus medialis (Figure 2).

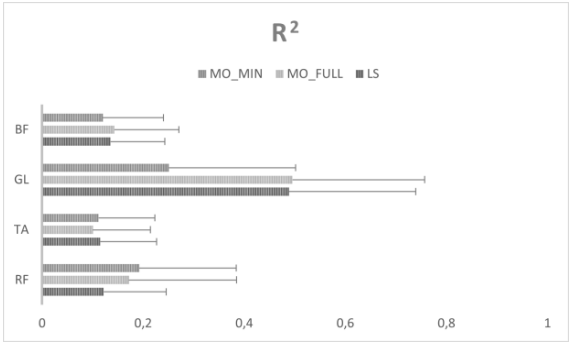

Figure 1: Mean R^2 plus standard deviation of experimental activations for the three different models.

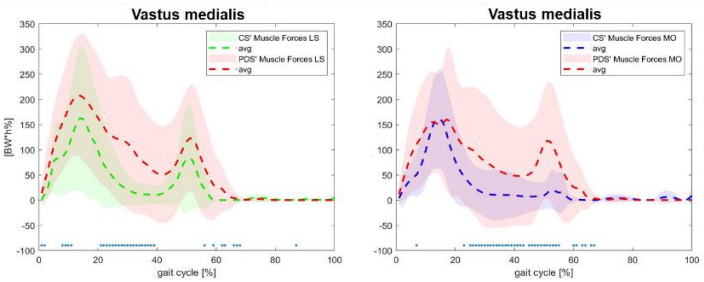

Figure 2: Vastus medialis generated force for CS and PD both with LS and MO_MIN scaling approaches.

Discussion

The MO scaling approach resulted in an enhanced method to detect subject-specific modifications in the lower limb strength production in PD when compared to CS, thus no loss of physiological information was noticed. Further studies are needed to generalize these outcomes.

References

1. D. Volpe et al, Gait & Posture, 52:87-94, 2017.
2. F. Spolaor et al, Gait & Posture, 57:53-54, 2017.
3. L. Modenese et al, Journal of Biomech, 49:141-8,2016.

Acknowledgements

Marco Romanato's PhD course grant is supported by Fondazione Fresco Parkinson Institute Italia Onlus.

ALTERATIONS IN MUSCLE ACTIVITY AND KINEMATICS DURING GAIT IN CHILDREN WITH FRAGILE X SYNDROME

Z. Sawacha (1, 3), F. Spolaor(1), W. Piatkowska(1), A. Ciniglio (1), F. Cibin(1), A. Guiotto(1), R. Polli(2), A. Murgia(2)

1 Department of Information Engineering, University of Padova, Italy
2 Department of Women and Children Health, University of Padova, Italy
3 Department of Medicine, DIMED, University of Padova, Italy

Introduction

Fragile X Syndrome (FXS) is the leading form of inherited intellectual disability and autism spectrum disorder, caused by a tri-nucleotide CGG repeat expansion in the promoter region of the FMR1 gene [1]. In FXS children characteristic musculoskeletal manifestations, which include hypotonia, joint laxity and flexible flat feet [6], may lead to non-physiological gait patterns [2], that justifies a referral for gait analysis. The aim of the present study was to identify the relationship between observed musculoskeletal manifestation and altered motor control in FXS children. Furthermore FXS subjects with classical full mutation of the FMR1 gene (FX-FM) and the ones who carried a full mutation with mosaicism (FX-M) were also compared. For this purpose kinematics and surface electromyography (sEMG) were acquired within standard clinical ambulatory conditions, and sagittal plane kinematics, both duration of muscle activity, its onset and offset during gait cycle were estimated.

Methods

After appropriate informed consent by the parents, 12 FXS children, of whom 7 (FX-FM) (mean (±SD) age and BMI respectively of 9,57 (±2,51) years and 18,97 (±5,54) Kg/m2) and 5 FX-M (mean (±SD) age of 9,00 (±3,74) years and 18,70 (±2,61) BMI of Kg/m2) and 19 controls ((CS) mean (±SD) age of 9,68 (±2,90) years and 21,52 (±4,61) BMI of Kg/m2), were evaluated at the BiomovLab of the Department of Information Engineering and at the Woman and Children Health Department (University of Padua). Kinematics and sEMG data were simultaneously acquired through 4 synchronized cameras (GoPro Hero3, 30fps) and an sEMG system (8 channels FreeEmg, BTS, 1000Hz) that collected the activity of Tibialis Anterior (TA), Gastrocnemius Lateralis (GL), Rectus Femoris (RF) and Biceps Femoris (BF). Each subject performed several gait trials and at least three trials per subject were processed. Sagittal plane kinematics was obtained as in [3] and hip, knee and ankle flexion/extension joints rotations were computed together with spatio-temporal parameters; in terms of sEMG analysis duration of contraction, onset and offset activation timing was obtained [4].

Results

Results consistently showed the presence of an altered muscle activity (Fig. 1). Joint kinematics highlighted a reduced range of motion of all the lower limb joints in both FX-FM and FX-M, while onset and offset activation timing revealed that FX-FM subjects continuously activated and deactivated GL throughout the gait cycle, FX-M subjects displayed a muscle activity closer to controls.

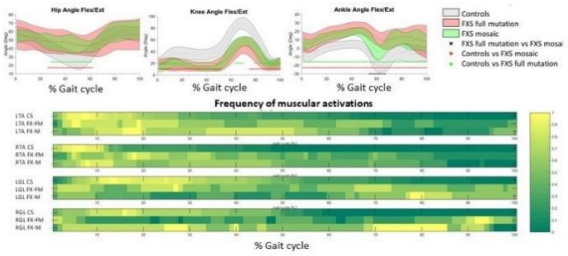

Figure 1: Top: Ankle, knee, hip sagittal plane angles in CS, FX-FM and FX-M groups. Bottom: Frequency of TA and GL activation in CS, FX-FM and FX-M subjects; horizontal bars are color coded as in [5], according to the number of subjects in which muscle activity at each % of gait cycle is observed; yellow: muscle activity is detected in all subjects, dark green: muscle is not active in any subject.

Discussion

Results suggest that FX-FM subjects adopt a muscle compensatory mechanism to cope with the reduced range of motion in the lower limbs. The muscle alterations found in FX-M are milder than in FX-FM. Application of gait analysis in FXS subjects can be a useful tool to plan rehabilitation therapies for affected children.

References

1. Hagerman RJ, et al, Nat Rev Dis Primers, 3, 17065, 2017
2. Davids JR, et al, J Bone Joint Surg Am; 72(6):889-96, 1990
3. Volpe D, et al, Gait & Posture; 52:87-94, 2017
4. Bonato P, et al, IEEE Trans Biomed Eng; 45(3):287-99, 1998
5. Agostini V, et al, Gait & Posture; 32, 285-89, 2010

ESTIMATING MUSCLE FORCES AND ADAPTATIONS DURING PLYOMETRIC HOPPING IN EMULATED HYPOGRAVITY

James Cowburn (1, 2), Gil Serrancolí (4), Steffi Colyer (1,2), Gaspare Pavei (3), Alberto Minetti (3), Aki Salo (1, 2, 5) and Dario Cazzola (1,2)

1. Department for Health, University of Bath, UK

2. Centre for the Analysis of Motion, Entertainment Research and Applications, University of Bath, UK

3. Department of Pathophysiology and Transplantation, University of Milan, Italy

4. Department of Mechanical Engineering, Universitat Politècnica de Catalunya, Barcelona, Spain

5. KIHU Research Institute for Olympic Sports, Jyväskylä, Finland

Introduction

Spaceflight is associated with detrimental adaptations of musculoskeletal tissue [1], which require rehabilitation upon return-to-earth. Plyometric exercises, such as hopping, present an effective way to load the musculoskeletal system when resources are limited during spaceflight [2]. Since peak muscle force is a key stimulus to regulate hypertrophy [3], knowledge of muscle forces during hopping will better inform countermeasure and rehabilitation programs during and after spaceflight. The aim of this study was to quantify muscle i) forces during a hopping task and ii) loading needed to stimulate adaptations in emulated hypogravity.

Methods

A full-body musculoskeletal model [4] was integrated into a direct collocation tracking simulation framework, formulated in Matlab R2017b using IPOPT and CasADi. The foot-ground contact was modelled using six Hunt-Crossley spheres, and muscle activation and contraction dynamics via a Hill-type muscle model [5]. A body-weight support system (BWSS) was modelled by an external force applied vertically to the pelvis' centre of mass equal in magnitude to a load cell placed in series with a harness. The optimiser worked to minimize the sum of squared muscle activations, coordinate accelerations and pelvis residuals, and to minimize the error between simulated and experimental ground reaction forces, coordinate positions and velocities, and net joint moments. Marker trajectories (200 Hz), ground and harness forces (2000 Hz), and seven lower-limb EMG (2000 Hz) were collected on a single healthy male (28 years, 1.82 m, 79.9 kg). Single-leg vertical hopping was performed at a self-selected frequency whilst attached to a BWSS under five gravity conditions (0.17, 0.25, 0.37, 0.50, 1 g). One hop was extracted per condition for analysis. Rectus femoris and Vastus Lateralis, Intermedius and Medialis forces were extracted and input into a muscle adaptation model [6] to estimate the repetitions required to elicit a minimal worthwhile muscle volume increase (3.37%) at each gravity.

Results

Kinematics were tracked with a max error ≤ 1.1°, ground reaction forces ≤ 0.02 BW, and net joint moments < 30 N·m error across all conditions. The shapes of muscle activations were qualitatively similar to EMG data. The range of sagittal plane motion increased at all joints with increased gravity. Total quadriceps force increased but shifted from rectus femoris to vastus lateralis dominant as gravity increased (Figure 1). Repetitions required to stimulate adaption changed proportionally to total force between gravities.

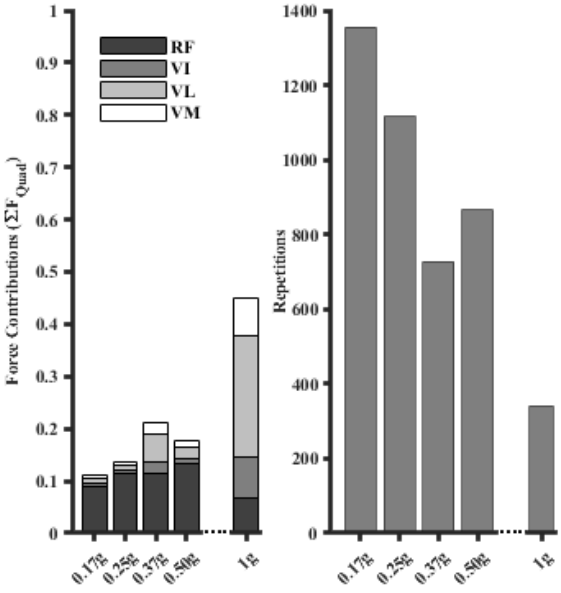

Figure 1: Quadricep muscle contributions to total muscle group force (left) used to estimated repetitions to stimulate muscle volume change (right) at each gravity.

Discussion

The simulation framework highlighted a gravity-dependent organisation of knee extensor muscle forces. All quadricep musculature increased force output to meet the increasing external work demand as gravity increased up to 0.5 g. Increased hip and knee flexion at 1 g may lead to unfavourable muscle geometry for the biarticular rectus femoris, leading to preferential use of the Vasti muscles by the optimiser at this gravity. The results demonstrate it is important to quantify muscle forces in hypogravity as individual muscle forces did not change proportionally to total quadricep force between all gravity levels. Applying this simulation framework to more plyometric exercises in hypogravity will aid rehabilitation programme design by ensuring chosen exercises load the targeted muscles.

References

1. Winnard et al, Front Physiol, 10: 1046, 2019
2. Weber et al, PLoS ONE, 14: e0211263, 2019
3. Martineau & Gardiner, J Appl Physiol, 91: 693-702, 2001
4. Lai et al, Ann Biomed Eng, 45: 2762-2774, 2017
5. De Groote et al, Ann Biomed Eng, 44: 2922-2936, 2016
6. Wisdom et al, Biomech Model Mechanobiol, 14: 195-215, 2015

ALTERATIONS IN SPECTRAL ATTRIBUTES OF SURFACE ELECTROMYOGRAPHY IN CHILDREN WITH FRAGILE X SYNDROME

W. Piatkowska (1), M. Romanato (1), F. Spolaor (1), A. Destro (1), R. Polli (2), A. Murgia (2), Z. Sawacha (1, 3)

1 Department of Information Engineering, University of Padova, Italy
2 Department of Women and Children Health, University of Padova, Italy
3 Department of Medicine, DIMED, University of Padova, Italy

Introduction

Fragile X Syndrome (FXS) is the leading form of inherited intellectual disability and autism spectrum disorder, caused by a tri-nucleotide CGG repeat expansion in the promoter region of the FMR1 gene [1]. In these subjects, the most frequent musculoskeletal manifestations include severe flexible flat feet, excessive laxity of the joints, and possible scoliosis [1], that justifies a referral for gait analysis. The aim of the present study was to identify the relationship between observed musculoskeletal manifestation and altered motor control in FXS children in terms of surface electromyography (sEMG) frequency content. For this purpose sEMG was acquired within standard clinical ambulatory assessment conditions and its spectral attributes extracted.

Methods

After appropriate informed consent by the parents, 23 FXS children ((FXSC) mean (±SD) age and BMI respectively of 9,00 (±3,92) years and 18,77 (3,07±) Kg/m^2) and 20 controls ((CS) mean (±SD) age of 9,68 (±2,90) years and 21,52 (±4,61) BMI of Kg/m^2), were evaluated at the BiomovLab of the Department of Information Engineering and at the Women and Children Health Department of the University of Padua. Kinematics and sEMG data were simultaneously acquired through four synchronized cameras (GoPro Hero3, 30fps) and an 8 channel sEMG system (FreeEmg, BTS, 1000Hz) that collected the activity of Tibialis Anterior (TA), Gastrocnemius Lateralis (GL), Rectus Femoris (RF) and Biceps Femoris (BF). Each subject performed several gait trials and at least three trials per subject were processed. The following sEMG parameters were extracted: instantaneous mean frequency (IMNF) and percentage distribution of signal energy in frequency bands.[2]

Results

Results consistently showed the presence of an altered muscle activity (Fig. 1): FXS displayed increased IMNF in RF and BF; decreased percentage of energy in the band between 10-60 Hz and increased percentage in the bands between 50-400 Hz.

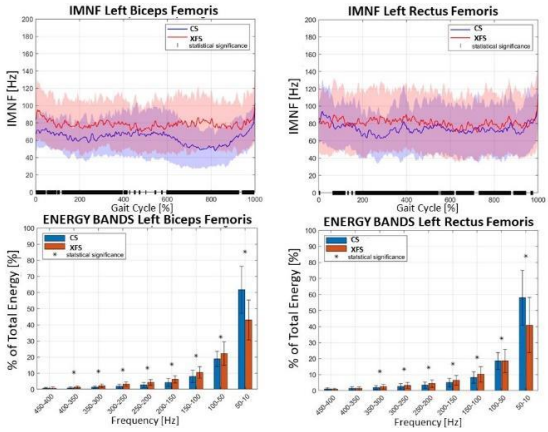

Figure 1: IMNF of left BF and RF (blue CS and orange FXSC; mean±SD) during gait cycle and percentage distribution of energy in the frequency bands of left BF and RF(blue CS and orange FXSC; mean±SD) (| - significant difference)

Discussion

Results suggest that FXSC increases their muscle activity during the gait cycle and also the number of motor units in low frequencies. This information can help to determine the degree of improvement in FXSC walking ability.

References

1. Hagerman RJ, et al, Nat Rev Dis Primers, 3, 17065, 2017
2. Pilkar, R. et al., Front Neurol 8, 449, 2017

SETTING A STANDARD FOR ADHESIVE COUPLANT FOR ACOUSTIC EMISSION TESTING ON SKIN

Polly Blaikie (1), Philip Anderson (2), Davide Crivelli(3), Cathy Holt (4)
1. Cardiff University, UK; 2. Cardiff University, UK; 3. Unaffiliated, UK; 4. Cardiff University, UK

Introduction

Acoustic Emission (AE), a material testing technique, has the potential to be used to monitor human synovial joint health (1,2) and joint implant loosening (3,4). In the future it could replace more expensive and invasive techniques such as MRI and X-Ray for monitoring the progression of degenerative joint diseases such as Osteoarthritis (OA). Additionally, this technique could be used to guide clinicians in treatment decisions which may in turn slow the progression of OA while providing a quantitative measure of joint health. Other studies have investigated this technique but there is a lack of knowledge on best practice for coupling the sensor to skin, and incorrect or unsuitable couplant has a major impact on data quality and transmission.

Good coupling is necessary for transmission of AE signals and this is well established in material testing standards within the engineering community (5,6). It follows that this is also the case for coupling between the participant's skin and the sensor. This study aims to determine the most suitable couplant for use between the AE sensor and skin.

Methods

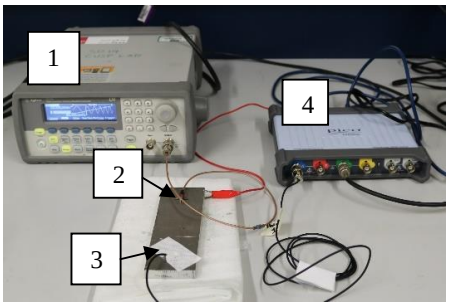

Figure 1 - experimental set up.

Signal was generated from a Waveform Generator (*1.1*) and produced a sweep signal which was pulsed into a sample piece of steel via a NANO 30 sensor [Physical Acoustics] (*1.2*). Five PZT sensors (*1.3*) were coupled in turn to the steel. Five sensors were used in order to check consistency between the sensors. The sensors were held in place with Sterofix (*sf*) Dressing Retention Tape [Steroplast]. The following couplants were tested; Silicone Grease (*SG*) used as the Gold Standard, Petroleum Jelly (*V+sf*) [Vaseline®], GEL103 Tensive Adhesive Gel (*G103+sf*) [BIOPAC Systems Inc.], Aquasonic Clear® ultrasound gel (*USAG+sf*) [Parker Lab, Inc.], Emulsifying Ointment BP (*Em+sf*).

All data was recorded using a PicoScope 5000 (*1.4*) and processed through MATLAB R2019a [MathWorks®]. This initial testing investigated the effects of different adhesive type in comparison to Silicone Grease and if there was an effect from sensor lifting and repositioning.

Results

Maximum recorded amplitude of the signals varies between the adhesives. Treating Silicone Grease (SG) as the gold standard it has a mean maximum amplitude of 30.1mV±2.9mV. Vaseline and Emulsifying Ointment shared similar characteristics to SG with an amplitude of 39.9mV±4.7mV and 32.7mV±3.0mV respectively. Ultrasound Gel showed the least variations between applications with an amplitude of 26.5mV±1.3mV. GEL103 attenuated the AE the most with a mean maximum amplitude of 12.7mV±4.0mV.

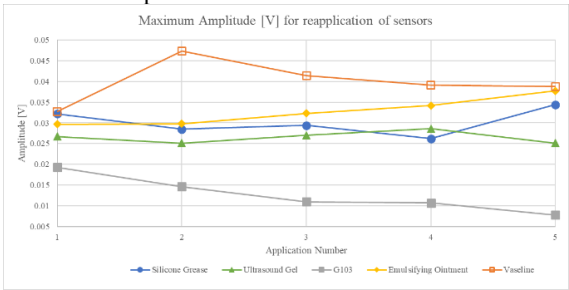

Figure 2 - variation in maximum amplitude with reapplication of the sensor.

Discussion

There is variation between the repeat applications for all adhesives, which shows the importance of consistent application and using a correct amount of adhesive. Silicone Grease and Ultrasound Gel are the most consistent, Vaseline is the best in that its attenuation is lowest. Emulsifying Ointment and the GEL103 show trends in their data, Emulsifying Ointment showing an increase in maximum amplitude for each application and conversely GEL103 showing a decrease in maximum amplitude with each application. For Emulsifying Ointment, this is possibly due to the thickness of the adhesive decreasing with reapplication, and for the GEL103, due to air bubbles becoming trapped following reapplication which then attenuate the sound leading to a decrease in maximum amplitude. Further analysis and testing of other couplant options is required to draw a firm conclusion over the most suitable couplant for skin application.

References

1. Choi D, et al. Sensors Mater. 2018;30(8):1629–41.
2. Shark L-K, et al. Open Med Inform J. 2010;4:116–25.
3. Rodgers GW, et al. IFAC Vol. 47, 2014. 4796–4800 p.
4. FitzPatrick AJ, et al. Biomed Signal Process Control. 2017;33:281–8.
5. Theobald P, et al. J Acoust Emiss. 2008;26.
6. ASTM E650/E650M.

Acknowledgements

This research was supported by the Engineering and Physical Sciences Research Council (EPSRC) doctoral training grant (EP/R513003/1) and by the IMechE Whitworth Senior Scholarship Award.

LIGAMENTS GEOMETRY DEFINITION FOR MUSCULOSKELETAL SIMULATIONS OF HIGH KNEE FLEXION TASKS

D. Pavan (1), S. Van Rossom (2), H. Hoang (2) I. Jonkers (2), Z. Sawacha (1,3)

1. University of Padua, Dept. of Information Engineering, Italy;
2. KU Leuven, Dept. of Movement Sciences, Belgium; 3. University of Padua, Dept. of Medicine, Italy

Introduction

The majority of knee and ACL injuries are often identified as non-contact injuries [1]: immediately disabling, they require long rehabilitation periods, in order to return to the previous level of competition.
ACL ruptures and damages occur when forces applied to the ligament are greater than the loads it can withstand [2]; in order to be effective, screening methods should be linked to ACL mechanical etiology [2].
Biomechanical analysis has been traditionally carried out using both experimental techniques (i.e., motion analysis) and computational methods. Musculoskeletal modelling (MSM) has already been successfully applied in clinic to assess pathological musculoskeletal disorders [3] A musculoskeletal model with enhanced degrees of freedom (DOF) at the knee and knee ligaments has been identified in literature [4], although not specifically developed for deep flexion tasks.
Some works [5,6] have been identified reporting rotations on the frontal and transverse plane [5], and ligaments elongation and spatial orientation [6] in relation to passive knee flexion up to 130 degrees.
The aim of the present contribution is to define the 3D ligaments geometry in a musculoskeletal model having enhanced DOF at the knee, focusing on high knee flexion tasks simulation.

Methods

Once digitalized the data published in [5,6], the insertions of 11 ligament bundles have been redefined through an iterative algorithm: 1. once simulated the knee flexion as in [5], the models' ligaments 3D geometry and elongation are compared with [6] by means of RMSD and Pearson's correlation; 2. comparison are performed only when ligament elongation is higher than its resting length; 3. a tentative insertions cloud is then computed and a simulation run, again, for each combination of tentative insertions; 4. breaking condition are set as the best insertions combination result, equal to the insertions combination given as input; 5. the optimization procedure is performed several times for each bundle, restarting the process with slightly different initial conditions, to avoid for suboptimal solutions, and the best overall solution is stored with the corresponding parameter values.

Results

Ligaments geometry optimization results, reported in figure 1, showed good compliance with [6] geometries and elongation rates, both in terms of correlation and RMSD, when the ligament elongation was higher than its resting length.

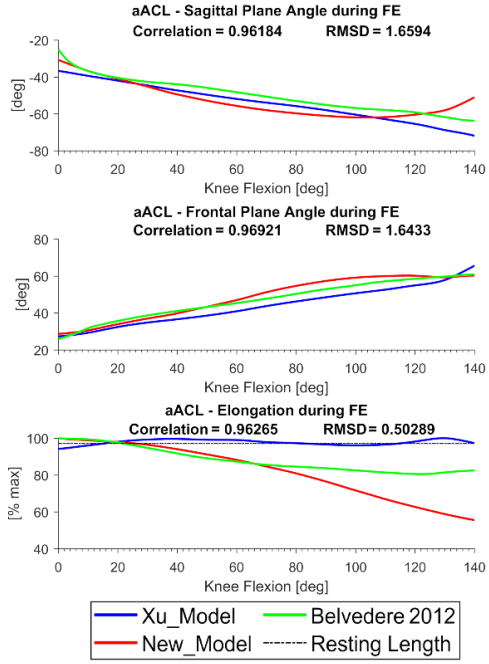

Figure 1: ACL anteromedial bundle - frontal and transverse plane projection of the angle formed against the vertical tibial axis, and ligament elongation trough knee flexion.

Discussion

The repositioned ligaments geometry and the elongation pattern showed good compliance with [6] throughout the knee flexion. Both ligaments lever arms end force exertion are affected by these parameters during MSM simulations, hence by adopting the proposed methodology outcomes would be in line with knee physiology in simulating high knee flexion tasks.
The proposed knee model could be adopted for knee injury prevention screening in high knee flexion tasks. and support the clinical decision making in readmitting an injured athlete to trainings and competitions.

References

1. Boden BP et al, J Am Ac Orthop Sur 18(9): 520–27, 2010.
2. Shin CS et al, J Biomech; 42:280-85, 2009.
3. Scarton, A et al, Gait & Posture, 58:194-200, 2017.
4. Xu H et al, Comp Method Biomec, 18(11):1217-24, 2015.
5. Belvedere C et al, J Orthop Res, 27(11): 1426–31, 2009.
6. Belvedere C et al, J Biomech, 45(11):1886-92, 2012.

A MUSCULOSKELETAL MODEL FOR ACL INJURY PREVENTION IN HIGH KNEE FLEXION CONDITIONS

D. Pavan (1), S. Van Rossom (2), H. Hoang (2) I. Jonkers (2), Z. Sawacha (1,3)

1. University of Padua, Dept. of Information Engineering, Italy;
2. KU Leuven, Dept. of Movement Sciences, Belgium; 3. University of Padua, Dept. of Medicine, Italy

Introduction

Anterior Cruciate Ligament (ACL) injuries have high incidence on athletes [1]: they are instantly disabling and in the majority of cases will require surgery and long rehabilitations; moreover, re-injury has a higher occurrence rate than first ACL injury [1].
Although gait analysis has already identified biomechanical variables strongly related with ACL ruptures, a demanding task is likely to be needed to investigate knee biomechanics in trained athletes.
Musculoskeletal modelling implements experimental measurements with estimates of important variables, as muscle and joint forces, and could be applied focusing on ACL injury prevention [2]. Among the available musculoskeletal models, one with enhanced knee degrees of freedom (DOFs) and ligaments [3], and one specifically developed for the squatting task [4] have been identified, along with the one developed by Delp [5].The aim of the present work is to develop a knee model which overcomes the limitations of the currently available ones, in simulating the knee biomechanics during deep flexion tasks for ACL injury prevention purposes.

Methods

Ten healthy athletes were recruited (mean±SD; age=25,6±1,5 years; BMI=21,7±2,4 Kg/m²). Each participant performed three repeated monopodalic squats: reflective markers were placed as in [6] and data were acquired by means of 3D stereophotogrammetry (BTS Smart-E, 6 cameras, 60 Hz) and 1 force plate (Bertec FP6040, 960 Hz); an electromyography system (BTS Free1000, 8 channels, 1000 Hz) recorded the activation of: Rectus Femoris, Biceps Femoris Caput Longus, Tibialis Anterior, Gastrocnemius Lateralis. MOtoNMS [7] and OpenSim [8] were adopted, and scaling, inverse kinematics, inverse dynamics, and static optimization (SO) computed. Experimental EMG envelope peak occurrence within the task were compared with the related SO outcome (Wilcoxon signed-rank, α=0.05) for validation purposes as in [6]. A new knee model was developed, with enhanced knee DOFs and ligaments repositioned based on published cadaveric geometries [9]. Data were further processed according to [3-5] and results of each simulation compared with the model proposed herein (rm-ANOVA, Tukey post-hoc, α=0.05).

Results

Outcomes underlined differences (Fig.1) mainly associated to the number of knee DOFs (i.e. [4,5] vs the one proposed and [3]). The proposed model was the only one that showed activation in agreement with the experimental EMG.

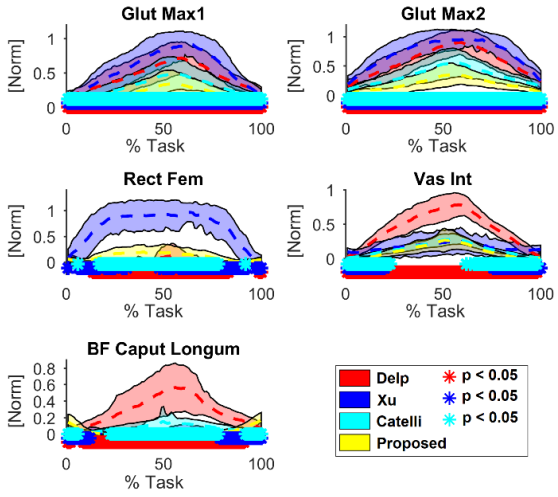

Figure 1: Gluteus maximus 1, Gluteus maximus 2, Rectus femoris, Vastus intermedius, and Biceps femoris caput longum normalized activations. Models: Delp, Xu, Catelli, proposed. Significant differences are flagged referring to the proposed model comparison with the model relative to the flag color in the legend.

Discussion

Xu model showed task-related issues, while Delp, Catelli and the current model showed good compliance with the squat task, even though the models reported in [4,5] have limited DOFs at the knee and no ligaments.
The current study allowed comparing the performances of different knee models in critical conditions, providing further insights on the knee biomechanics during the squat task. The former could be adopted for ACL injury risk evaluation, to better inform the clinical decisions making and to aid in planning prevention and post-rehabilitation return on field programs.

References

1. Paterno MV et al, Am J Sport Med, 42(7):1567-73, 2014.
2. Reinbolt JA et al, Procedia IUTAM, 2:186-98, 2011.
3. Xu H et al, Comp Method Biomec, 18(11):1217-24, 2015.
4. Catelli DS et al, Comp Method Biomec, 22(1):21-4, 2019.
5. Delp SL et al, IEEE T Biomed Eng, 37(8):757-67, 1990.
6. Scarton, A et al, Gait & Posture, 58:194-200, 2017.
7. Mantoan A et al, Source Code BiolMed, 10(1):1-14, 2015.
8. Delp et al, IEEE T Biomed Eng, 54(11):1940-50, 2007.
9. Belvedere C et al, J Biomech, 45(11):1886-92, 2012.

DOES VARUS KNEE DEFORMITY ONLY EFFECT FRONTAL PLANE BIOMECHANICS?

Jake Bowd (1,2), David Williams (1,2), Marina De Vecchis (1,2), Christopher Wilson (2,3), David Elson (2,4), Gemma Whatling (1,2), Catherine Holt (1,2)

1. Cardiff School of Engineering, College of Physical Sciences, Cardiff University, Cardiff, UK; 2. Biomechanics and Bioengineering Centre Versus Arthritis, Cardiff University, Cardiff, UK; 3. Cardiff and Vale University Health Board, Cardiff, UK; 4. Queen Elizabeth Hospital, Gateshead, UK

Introduction

Varus knee deformity increases medial knee joint loading [1] and accelerates osteoarthritis (OA) progression. There is limited research to understand the effect that it has on hip and ankle biomechanics. The purpose of this study was to evaluate hip and ankle kinematics and external moments in patients with knee varus deformity, prior to knee realignment surgery (high tibial osteotomy, HTO).

Methods

Three-dimensional gait analysis was performed on 30 patients before HTO surgery and 28 non-pathological (NP) participants using a modified Cleveland marker-set. Independent samples t-test or a Mann-Whitney U test was performed within MATLAB to compare key biomechanics parameters between the NP group and the pre-HTO cohort. Significance was set at $p \leq 0.05$.

Results

Pre-surgery, individuals had significantly higher external knee adduction moment (EKAM) peaks and knee adduction angular impulse (KAAI) whilst having a significantly lower gait speed (table 2).

Group	NP Group – Mean (SD)	Pre-HTO – Mean (SD)	P-value
n	28	30	
Age (yrs.)	38.14 (11.09)	50.70 (8.71)	**< .000**††
Height (m)	1.70 (.08)	1.75 (.11)	**0.018***
Mass (kg)	71.84 (15.74)	90.57 (20.17)	**< .000**††
mTFA (°)		7.75 (3.72) varus	
KL grade		6 KL2; 19 KL3;5 KL4	

*Table 1: Demographic data for NP and pre-HTO. P ≤ 0.05 = *(†); P ≤ 0.01 = **(††); P ≤ 0.001 = ***(†††) parametric tests(non-parametric) comparisons, respectively. mTFA = mechanical tibiofemoral angle.*

At the ankle, the pre-surgery group had significantly lower peak inversion and significantly higher peak eversion angles. There were no significant differences between the two groups in the sagittal and transverse planes with respect to joint angles peaks.

Group	NP Group – Mean (SD)	Pre-HTO – Mean (SD)	P-value
Gait speed (m/s)	1.21 (0.16)	1.06 (0.23)	**0.008**††
Stance time (sec)	0.65 (.06)	0.73 (.12)	**< .000**††
EKAM, %BW.h			
EKAM1	2.27 (0.65)	3.1 (1.12)	**0.001****
EKAM2	1.5 (0.67)	2.48 (1.1)	**< .000*****
KAAI			
1st half stance	0.43 (0.14)	0.73 (0.25)	**< .000*****
2nd half stance	0.31 (0.16)	0.6 (0.27)	**< .000*****

Table 2: EKAM and KAAI during first and second half of stance. EKAM was calculated using inverse dynamics. EKAM1 and EKAM2 were defined as peaks within 17%-34% and 62%-86% of stance, respectively.

At the hip, there were significant differences in both the sagittal plane (peak hip extension) and the frontal plane (peak hip adduction angle) kinematics (table 3) and in the peak external ankle and hip moments (table 4).

Group	NP Group Mean (SD)	Pre-HTO Mean (SD)	P-value
Ankle kinematics			
Peak ankle dorsiflexion angle (°)	14.97 (3.59)	16.95 (4)	0.054 ns
Peak ankle plantarflexion angle (°)	10.31 (4.24)	9.34 (7.64)	0.549 ns
Peak ankle inversion angle (°)	10.97 (4.55)	7.62 (5.23)	**0.012***
Peak ankle eversion angle (°)	2.99 (4.27)	5.01 (2.79)	**0.012**†
Peak ankle internal rotation angle (°)	0.79 (6.3)	0.83 (7.34)	0.982 ns
Peak ankle external rotation angle (°)	15.42 (6.28)	12.84 (7.01)	0.146 ns
Hip kinematics			
Peak hip flexion angle (°)	32.47 (6.47)	34.01 (7.32)	0.401
Peak hip extension angle (°)	12.89 (5.64)	5.91 (8.32)	**0.000*****
Max hip adduction angle (°)	7.03 (3.41)	2.66 (3.66)	**0.000*****
Max hip abduction angle (°)	8.65 (3.63)	10.01 (3.72)	0.167
Max hip internal angle (°)	4.71 (8.79)	3.72 (7.28)	0.640
Max hip external angle (°)	8.92 (8.76)	9.36 (7.74)	0.840

Table 3: Peak ankle and hip kinematics.

Group	NP Group Mean (SD)	Pre-HTO Mean (SD)	P-value
Ankle			
0-50% (HS to midstance)			
Peak plantar-flexion moment	1.03 (0.28)	0.74 (0.38)	**0.002****
50-100% (Midstance to toe-off)			
Peak dorsi-flexion moment	8.94 (0.74)	8.25 (1.22)	**0.004**††
Peak inversion moment	1.11 (0.34)	0.84 (0.48)	**0.019***
Peak internal rotation moment	1.67 (0.53)	1.37 (0.63)	**0.006**††
Hip			
0-50% (HS to midstance)			
Peak external hip flexion moment	6.61 (2.39)	4.95 (1.73)	**0.003****
50-100% (Midstance to toe-off)			
Peak external hip flexion moment	0.9 (0.7)	0.43 (0.94)	**0.024**†
Peak external hip extension moment	5.09 (1.41)	4.31 (1.56)	**0.050***

Table 4: Ankle and hip external moments. Analysis was undertaken on peak external moments in the first and second half of stance for sagittal, frontal, and transverse planes. Only significant changes shown.

Discussion

Varus knee deformity results in a slower gait speed and an increased joint load, as well as associated significant changes in frontal plane peak ankle kinematics and in peak hip extension and adduction angles and differences in external moments at the ankle and hip. Indicating that the adjacent joints may be involved in compensatory mechanisms associated with knee deformity. Future work should consider whether non-surgical interventions, i.e., gait retraining, can influence these biomechanical differences and establish whether HTO restores healthy knee biomechanics whilst also restoring the biomechanics of the adjacent joints.

References

1. Whatling et al, KSSTA, 2019.

Acknowledgements

Funding: Versus Arthritis [20781], EPSRC [EP/J010111/1].

EVALUATION OF MUSCLE RECRUITMENT AND MUSCLE MODELS IN MUSCULOSKELETAL SIMULATION OF DYNAMIC MOTION

Simon Auer (1,2), Lukas Reinker (1,2), Sebastian Dendorfer (1,2)

1. Laboratory for Biomechanics, Ostbayerische Technische Hochschule (OTH) Regensburg, Germany; 2. Regensburg Center of Biomedical Engineering, OTH and University Regensburg, Germany

Introduction

Musculoskeletal simulation plays an increasingly important role in sports biomechanics. In the last years, the field of application widened from orthopaedics and ergonomics to sports [1]. A muscle recruitment algorithm with a quadratic objective function is usually used to calculate muscle activity in dynamic movements. The agreement of calculated and measured thigh muscle activity has already been investigated [2]. They found a strong agreement for sprinting and running, while the correlation decreased for side-cutting manoeuvres. Nevertheless, the influence of different muscle recruitment criteria on muscle activity in dynamic musculoskeletal simulations is currently unknown. Hence, this study aimed to analyse the effect of different muscle recruitment criteria and muscle models on the correlation of numerical and measured muscle activity in highly dynamic movements.

Materials & Methods

For this study, 50 datasets per muscle from five amateur football players were captured. They performed five knee flexion (prone, 0°-90°) and extension (sitting, 90°-0°) movements for the left and right leg at an audio signal as fast as possible. The muscle activity of vastus lateralis (VL), vastus medialis (VM), rectus femoris (RF), biceps femoris (BF), semitendinosus (ST) was analysed. Muscle activity was measured via surface Electromyography (EMG) sensors (Delsys Trigno EMG, Delsys Inc., UK). Inertial motion capture (MVN Link, Xsens Technologies, NL) was used to record kinematic data. The numerical muscle activity was calculated with the AnyBody Modeling System (AMS, v. 7.3, AnyBody Technology, DK) with four different scenarios: simple muscle model with a quadratic target function for the muscle recruitment (S2), simple muscle model with composite target function (SC), Hill-type muscle model with quadratic muscle target function (H2) and Hill-type muscle model with composite target function (HC). The composite target function consists of a polynomial with infinite exponent and an additional quadratic term [3].

The measured and calculated muscle activity results were processed with Python (v. 3.7.6). Each muscle's activity was normalised to the maximum activity of the five left/right flexion/extension movements. The Pearson correlation coefficient r for numerical and measured activity was determined for each muscle. It was categorised as small ($r \leq 0.3$), medium ($r \leq 0.5$) or strong ($0.5 < r \leq 1$) [4].

Results

The overall correlation of measured and numerical muscle activity is strong for all muscles, although there are differences for flexor and extensor muscles. There is only a small influence of target function on the agreement of numerical and measured muscle activity. On the other hand, the Hill-type muscle model increases r up to 0.72 for the extensor muscles. Table 1 shows the mean r values of the four scenarios for the five muscles.

Table 1: Mean r of the muscles for the scenarios.

	S2	SC	H2	HC
VL	0.59	0.59	0.72	0.72
VM	0.58	0.58	0.72	0.71
RF	0.52	0.52	0.63	0.63
BF	0.67	0.63	0.60	0.57
ST	0.67	0.64	0.66	0.66

Discussion

This study aimed to analyse the effect of different muscle recruitment/model scenarios on the agreement of numerical and measured muscle activity in highly dynamic motion. The overall correlation of numerical and measured activity is strong, with r ranging from 0.52 to 0.72 regardless of the recruitment scenario. This corresponds with the findings of [2]. The target function barely influences the correlation regardless of the muscle model. The changes for the target functions are within the standard deviation. Hence, only the Hill-type muscle model improves the agreement of numerical and measured activity. This effect is limited to the extensor muscles, where the correlation rises from r=0.59 to r=0.72. In the flexor muscles, the Hill-type model does not increase the correlation or even lowers it slightly.

Nonetheless, the investigated movements are relatively simple flexion/extension movements, which might explain the low influence of the target function. However, the flexion/extension motions represent fast and reflex-like movements, which often occur in various sportive activities.

Overall, the Hill-type muscle model should be considered in highly dynamic movements. Furthermore, the data confirms the use of quadratic target function of the muscle recruitment algorithm.

References

1. Auer et al., Sci Med Football, 2020
2. Dupré et al., J Biomech, 84:73-80, 2019
3. https://anyscript.org/tutorials/MuscleRecruitment/
4. Cohen, Statistical Power Analysis for the Behavioral Sciences. 1988

THE ROLE OF LIMB ALIGNMENT ON TIBIO-FEMORAL KINEMATICS: A DYNAMIC VIDEOFLUOROSCOPY STUDY

Barbara Postolka (1), William R. Taylor (1), Renate List (1, 2), Pascal Schütz (1)

1. Laboratory for Movement Biomechanics, Institute for Biomechanics, ETH Zürich, Switzerland
2. Human Performance Lab, Schulthess Clinic, Switzerland

Introduction

Accurate knowledge of tibio-femoral kinematics is not only essential for a clear understanding of knee joint functionality and injury mechanisms to the knee, but can also help to restore physiological knee joint function after orthopaedic interventions. While limb alignment, which exhibits normal anatomical variation among the healthy adult population [1], has been shown to critically affect tibio-femoral joint loading [2], less is known about its role on *in vivo* tibio-femoral kinematics, especially during activities of daily living. Therefore, the aim of this study was to investigate the role of limb alignment on tibio-femoral kinematics during different gait activities using dynamic videofluoroscopy

Methods

12 neutral subjects (hip-knee-ankle angle (HKA): 0.5±1.6° varus), 10 varus subjects (HKA: 5.7±1.8° varus), and 5 valgus subjects (HKA: 5.6±1.5° valgus) were assessed during 5-6 complete cycles of level walking, downhill walking and stair descent using a dynamic fluoroscope [3]. After 2D/3D registration of the subject-specific bone models to the video-fluoroscopic images [4], tibio-femoral rotations, A-P translations of a medial and lateral point on the functional flexion axis of the femur, and the location of the centre of rotation (CoR) [5] were determined.

Results

For all three activities, the rotational ranges of motion and ranges of condylar A-P translation were comparable between the neutral, varus and valgus subjects. However, significant differences occurred between the varus and valgus subjects for A-P translation of the lateral condyle point during mid-stance and early swing (44-55% & 70-75% gait cycle) of stair descent.

A-P translation [mm]		medial	lateral
level walking	neutral	8.8±1.8	10.9±2.2 *
	varus	8.6±1.0	9.9±2.1 *
	valgus	9.8±0.8	10.3±3.0
downhill walking	neutral	8.6±1.9	10.4±1.2 *
	varus	7.3±0.9	9.9±1.7 *
	valgus	9.4±0.8	10.5±1.3
stair descent	neutral	8.7±1.9	11.8±2.5 *
	varus	7.4±1.5	10.5±1.4 *
	valgus	8.7±1.0	12.9±2.2 *

Table 1: Range of condylar A-P translation over complete gait cycles of level walking, downhill walking and stair descent. Mean ± SD for each limb alignment group are presented and significant differences between the medial and lateral condyle are indicated (*).

While the neutral and varus subjects exhibited significantly more A-P translation of the lateral compared to the medial condyle point, resulting in an overall medial CoR, the valgus subjects demonstrated equal condylar translation for level and downhill walking, but significant differences for stair descent (Table 1, Figure 1). Nevertheless, all three groups exhibited high inter-subject variability, with equal or more medial A-P translation observed in certain subjects.

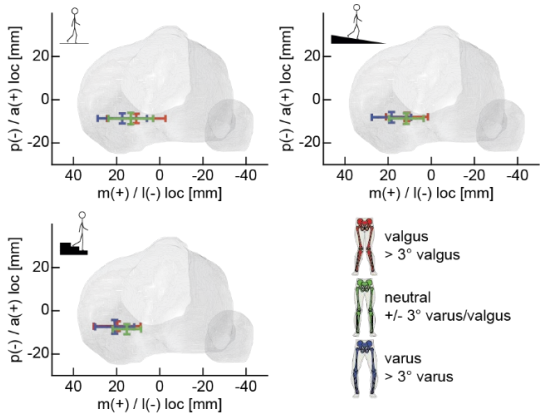

Figure 1: Location of the CoR over the complete gait cycle of level walking, downhill walking and stair descent. Mean ± STD over all subjects are presented for each limb alignment group.

Discussion

Although subject-specific limb alignment only revealed a minor influence on tibio-femoral kinematics, differences between individual subjects were evident and resulted in large standard deviations. Despite axial rotation occurring around a predominantly medial CoR, it is conceivable that changes to the loading of the joint exist among the three limb alignment groups [6]. This data can, in combination with musculoskeletal modelling, provide a first basis for surgical interventions regarding limb alignment and help to further improve restoring physiological knee joint function.

References

1. Bellemans et al., Clin Orthop Relat Res, 470:45-53, 2012.
2. Heller et al., Langenbecks Arch Surg, 388:291-297, 2003.
3. List et al., PloS One, 12:e0185952, 2017.
4. Postolka et al., Med Eng Phys, 77:107-113, 2020.
5. Ehrig et al. J Biomech, 39:2798-2809, 2006.
6. Trepczynski et al. Sci Rep, 9:182, 2019.

Acknowledgements

This study was partially funded by Medacta International and the Commission for Technology and Innovation Switzerland.

MUSCLE STIMULATION LEADS TO BONE TISSUE CHANGES: IN VIVO RESEARCH

Oskar Sachenkov (1), Oleg Gerasimov (1), Maxim Baltin (1), Artur Fedianin(1), Pavel Bolshakov (1), Nikita Kharin (1), Tatyana Baltina (1)

1. Kazan Federal University, Russia;

Introduction

Mechanical properties of bones depend not only on their chemical composition, but also on the nature of their loading. In study some experiments were carried out to determine changes in bone tissue in case of microgravity and some types of stimulation. The aim of work is to determine biomechanical parameters of bone tissue which changes significantly under external loads. This knowledge can help for better understanding the mechanism of bone tissue remodeling.

Methods

To study the effects of microgravity in terrestrial experiments, a model with rats hanging by tail was developed (n=30) [1,2]. Additionally microgravity models with putting on animal's feet (n=10) and spinal cord electromagnetic stimulation (n=25) were carried. Nonlinear laboratory rats (180-200 g) were used in study. All experiments were performed according to bioethical standards and were approved by local ethical committee of the Kazan Federal University. Hindlimbs and forelimbs bones were dissected from all tested rats. Bones was scanned on μCT in diaphysis, metaphysis and epiphysis regions. Fabric tensor was used for analysis of distribution porosity [3]. Numerical experiments to calculate mechanical properties [4] were carried out. Histological parameters such as B.PM, BV/TV, Tb.Th, W.Th etc were measured. Additionally stress tests were performed.

Results

In histological study bone tissue growth was marked. Bone thickness rises up and gets maximum value at 21 days of microgravity. Similar results was get for W.Th. After 21 days W.Th. decreases, but B.PM still increases. Additionally vessel network growth activity was noticed.

The analysis of the results shows difference in the structure of the bone tissue. A clear difference was observed in the epiphysis of the femur, wherein an increase in porosity and a decrease in the degree of anisotropy were noted. Orthotropic directions rotate significantly in diaphysis (see figure 1).

In microgravitational models Young's module decreased slightly (25%), but limits of tension decreased significantly (60%). In case of putting on animal's feet Jung's module restores its value (deviation about 5%) and limits of tension increases up to 33% (in comparison with microgravitational models). In case of cord stimulation Young's module restores its value (deviation about 12%) and limits of tension increases up to 31% (in comparison with microgravitational models).

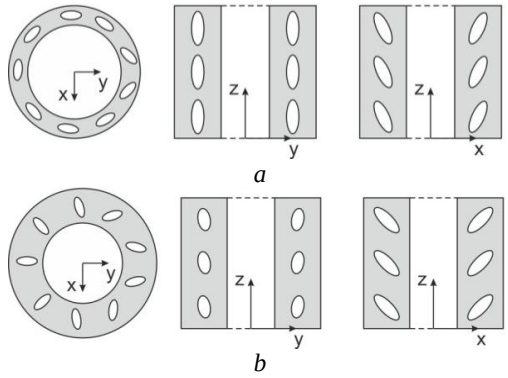

Figure 1: Schematic illustration of distribution of the orthotropic properties in diaphysis area: a – control group; b – 20 days microgravity.

Discussion

Results shows that bone tissue depend on external forces. Having analyzed the obtained data, we can observe a sharp drop in tensile strength under a long-term exposure of an organism to microgravity. Adaptation of bone tissue structure was noticed after 30 days of microgravity. But strength limit still decreases. Putting on animal's feet and spinal cord electromagnetic stimulation influence the process of bone remodeling. The results can be used to verify the mathematical models of evolution of bone tissue. More over the results emphasize that the bone structure can be controlled by influence of external forces. In practice rehabilitation strategy can be planted with taking into account muscle activity.

References

1. Morey-Holton E.R. et al, J. Appl. Physiol., 92: 1367-1377, 2002.
2. Baltina T. et al, BioNanoScience, 8: 864-867, 2018.
3. Kichenko A.A. et al, Russian J. of Biomechanics, 15: 66-81, 2011.
4. Kharin N.V. et al, PNRPU Mechanics Bulletin, 3: 95-102, 2018.

Acknowledgements

The work was supported by the Russian Science Foundation within the scientific project No. 18-75-10027.

COMPARING DIFFERENT COMPLEX TEST DEVICES FOR FRICTIONAL MOMENT MEASUREMENT OF TOTAL HIP IMPLANTS

Paul Henke (1), Rainer Bader (1)

1. Rostock University Medical Center, Germany

Purpose

Aseptic implant loosening is considered to be the main cause for revision surgery after total hip arthroplasty [1]. While there are unified standards for measuring wear by means of simulator tests (e.g. ISO 14242), no standardization for measuring frictional moments within the bearing couple exists. However, higher frictional moments are associated with higher wear [2]. Therefore, two different test devices of different complexity for frictional moment measurement of total hip implants were designed and compared. Both designs are capable of applying loads up to 3 kN according to ISO 14242-1. In present study, frictional moments of ceramic-on-ceramic (CoC) and ceramic-on-polyethylene (CoP) couples each with a head diameter of 36 mm are investigated.

Methods

The test device of lower complexity, the "1-dimensional test rig", is capable of applying a constant load of 3 kN superimposed by an internal-external rotation of ±6° about the taper axis. It consists of an embedding tray supporting the acetabular implant and mounted on a x-y-table which compensates for transverse forces by enabling small translations in the plane orthogonal to the load line. A tension-torsion testing machine (Instron 8874, Norwood, MA USA) combined with an external torque sensor (DRBK-10, ETH messtechnik, Gschwend Germany) was used to apply the load profile.

Furthermore, a complex setup, the "3-dimensional test rig" is built up which simulates the ISO 14242-1 load case and can measure the frictional moment about all three spatial axes of the articulating center of the bearing couple. Ball head and cup implant are assembled with the 6 DOF Vivo™ joint simulator (Advanced Mechanical Technology, Watertown, MA USA) which is used to apply the specific joint forces and motions.



Figure 1: View of the 1-dimensional test rig (left) and the 3-dimenional test rig (right)

The tested implants are made of Alumina Toughened Zirconia (Ceramys®) and vitamin E-stabilized cross-linked polyethylene (Vitamys®) respectively. Bovine serum with a protein ratio of 30g/l according to ISO 14242-1 is used to lubricate the tribological pairings in each case.

In order to investigate the frictional moments in both setups a total amount of 100 cycles are executed, but only the last ten (91st-100th) cycles are taken into account. The last three of n=4 trials for each material pairing (CoC and CoP) are analyzed as the first sample serves as precondition of the setup.

In the 1-dimensional test rig the frictional moment alternates between nearly constant positive and negative values (internal or external rotation) during each load cycle. In this case, absolute values of the measured frictional moments are averaged.

In the 3-dimensional test rig only the highest resultant moment, which occurs at nearly 50% of the gait cycle is taken into account.

Results

Table 1: Measured frictional moments of CoC and CoP bearing couple at both test rigs

Frictional moment	CoC	CoP
1-D test rig [Nm]	0,90±0,03	0,51±0,02
3-D test rig [Nm]	4,92±0,54	6,96±0,29

Frictional moments measured are clearly higher within the 3-D test rig compared to the 1-D test rig only with one load and measurement axis. The reason for the smaller moments detected is based on the fact that highest moments occur at the axes orthogonal to the axial load line which could not be measured within in the 1-D test rig. In the 3-D test setup frictional moments of CoC coupling are smaller than these of CoP couple which is in agreement with literature [3]. In conclusion, only the 3D test rig is appropriate for frictional moment measurement and simulating physiological load profiles.

References

1. Dumbleton et al, Journal of Arthoplasty, 17 (5), 649-661, 2002
2. Haider et al, Journal of engineering in biomedicine 230 (5), 373-388, 2016.
3. Bishop et al, Journal of orthopaedic research: official publication of the Orthopaedic Research Society 31 (5), 807–813.

Acknowledgements

We kindly thank the Robert-Mathys Foundation and Mathys Orthopädie GmbH for supporting the experiments.

DEPENDENCY OF FEMORAL IMPACT FORCES AND STRAINS ON MUSCLE ACTIVATION DURING FALLS IN THE ELDERLY

Giorgio Biesso (1,2), Alexander Baker (1), Pasquale Vena (2), Stephen J. Ferguson (1), Benedikt Helgason (1), Ingmar Fleps (1)

1. Institute for Biomechanics, ETH Zürich, Switzerland; 2. Department of Chemistry, Materials and Chemical Engineering Giulio Natta, Laboratory of Biological Structure Mechanics (LaBS), Politecnico di Milano, Italy.

Introduction

Osteoporosis is a major public health issue worldwide because of its association with bone fracture risk. Falls from a standing or lower height are the most common cause of hip fractures in the elderly. Understanding the conditions that differentiate injurious and non-injurious falls can lead to the development of more effective intervention strategies for hip fracture prevention. In particular, the role played by Muscle Activation (MA) during falls in the elderly is unknown and it is difficult to quantify in volunteer experiments. The aim of this study is to investigate the effect of muscle contraction on femoral impact loads resulting from falls using biofidelic finite element models (FEMs).

Methods

21 muscles, modeled as elastic springs, were added to an existing biofidelic FEM [1]. Insertion points were based on anatomic literature [2]. Prestress in the springs generated muscle contractions (Figure 1). As the relative contractions between muscles is unknown and the hip joint is statically indeterminate, we calculated individual muscle forces (F_i) by minimizing the following objective function [3]:

$$\sum_{i=1}^{m}\left(\frac{F_i}{PCSA_i}\right)^2$$

where $PCSA_i$ is the physiological cross-sectional area of the individual muscles. Four levels of MA were prescribed based on a target joint reaction force magnitude at the hip joint. The MA levels were set to 1, 3, 6, and 9 times bodyweight (BW) of the modeled subject (40.3 kg). Heterogeneous, linear-elastic material properties were assigned to the elements representing bone tissue [4]. A 15ms settling phase with numerical damping was used to achieve quasi-static equilibrium after muscle contraction had been applied. This was followed by a fall simulation with the application of a rotational impact velocity of 3.1 m/s at the greater trochanter.

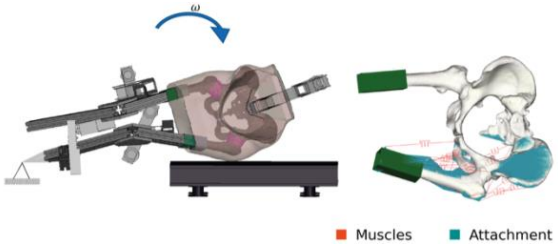

Figure 1: (Left) Biofidelic FEM. (Right) 21 muscles shown attached to the FEM.

The impact force at the hip (femur force) was evaluated along with the 1st principal strains (ε_1) and 3rd principal strains (ε_3) for all elements in the impacted femur at the time of peak force. For comparison, a reference model without any muscle activation was also solved.

Results

For muscle activation levels of 1 BW, 3 BW, 6 BW and 9 BW, the femoral force increased compared to the force in the reference model by 2%, 9%, 21%, and 36%, respectively (Figure 2). At time of peak force in the reference simulation, the average ε_1 was $1.82 \cdot 10^{-3}$ (0.002 SD) and the average $\varepsilon_3$was $-4.07 \cdot 10^{-3}$ (0.006 SD). On average, both ε_1 and ε_3 decreased as more muscle contraction was applied. Strain differences for ε_1 and ε_3 varied greatly from element to element.

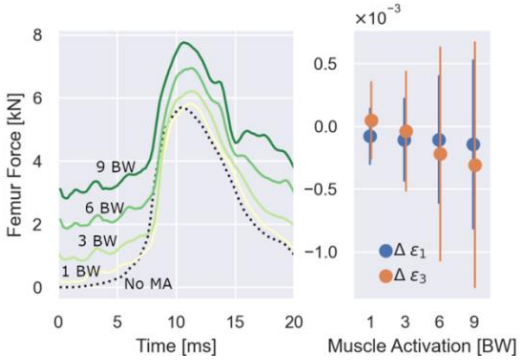

Figure 2: (Left) Femur force throughout the fall simulation for all MA levels. (Right) Average differences (+/- 1 SD) of the 1st (ε_1) and 3rd principal strains (ε_3) over all elements in the femur compared to the reference FEM without MA.

Discussion

With increased muscle activation levels, the peak femur forces increased noticeably which may increase fracture risk; this is supported by increased magnitudes of ε_3. However, the magnitudes of ε_1 decreased which may indicate a protective effect of muscle activation. These results demonstrate that the loads and the strains on the femur are influenced by muscle activation and likely have an appreciable effect on fracture risk and fracture behavior.

References

1. Fleps, I. et al., J. Bone Miner. Res., 2019.
2. Drake, RL. et al., Gray's Anatomy for Students., 2019.
3. Erdemir, A. et al., Clin. Biomech., 2007.
4. Fleps, I. et al., PLoS One., 2018

HOW THE INTRODUCTION OF SUBJECT-SPECIFIC MUSCULOSKELETAL MODELS AFFECTS THE ESTIMATION OF JOINT REACTION FORCES WITHIN THE HUMAN KNEE: A PRELIMINARY ANALYSIS

G. Cassiolas (1), G. Valente (2), G. Marchiori (2), N.F. Lopomo (1) and F. Taddei (2)

1. University of Brescia, Department of Information Engineering, Brescia, Italy

2. Rizzoli Orthopaedic Institute, Bologna, Italy

Introduction

Musculoskeletal modeling has emerged in the clinical practice as useful tool to predict the effect of interventions and, more generally, to enrich available information on human biomechanics that cannot be determined in a non-invasive manner. Developing a subject-specific musculoskeletal model from clinical data is indeed a process that requires a large amount of time and efforts, thus various generic models were made available in years to speed up the modeling process and address the most clinical necessities. On the other hand, subject-specific models are assumed to have greater physiological reliability [1], so the decision on which kind of modeling strategy to adopt depends on cost-benefits evaluation. The aim of this study was to investigate the difference existing between a generic multibody model [2] and a personalized model, focusing on joint reaction forces developed during gait, which are a biomarker for cartilage state of stress.

Methods

One healthy woman (32 years old, BMI=20.8) performed 5 gait trials walking barefoot at self-selected speed. A Plug-in-Gait marker set was utilized, and kinematic and kinetic data were collected by means of 8 Vicon cameras and 2 force plates. Focusing on subject-specific modelling, pelvis and lower limbs anatomy were acquired by means of a 3T MRI scanner. Bones and soft tissues were segmented through Mimics (Materialise, Leuven, Belgium) and a subject-specific was realized in nmsBuilder software [3]. Segments reference systems and joints description were accurately matched with those defined in the generic model to obtain coherent outputs. Muscles architecture was adapted from generic model to subject-specific one by means of a scaling tool within nmsBuilder software. Inertial parameters were calculated by differentiating densities between soft and hard tissues. Muscles pathway was defined by means of intermediate via-points to wrap over underling structures and each muscle maximum isometric force parameter was estimated by assuming muscle fiber length proportional to musculotendon length [4], as in (1)

$$F_{max\,i} = (PCSA)_i \cdot \sigma = \left(\frac{Vol}{l_0^{(gen)} \cdot \frac{l_{MT}}{l_{MT}^{(gen)}}} \right)_i \cdot \sigma \qquad (1)$$

OpenSim software [5] was exploited to estimate gait outputs on both the models; inverse kinematic, inverse dynamic, static optimization and joint reaction analysis were performed on all the trials. Results were averaged on the gait stance cycle.

Results

Whereas the general trend is maintained, differences in the force peaks were observed in the knee joint; in particular generic model overestimated the first peak during stance phase and underestimated the second peak, with respect to subject-specific model outputs (Figure 1).

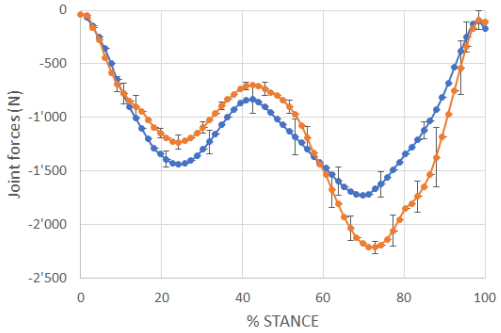

Figure 1: Vertical component of the joint reaction for generic (blue dot) and subject-specific (red dot) models.

Discussion

Subject-specific modelling provided outputs that were different from those obtained with the generic model, depending on the degree of personalization. Since developing a subject-specific model is a data-greedy and time-consuming task, the decision on what kind of model to exploit depends on the application the simulation is intended to. For example, when musculoskeletal modeling is intended to determinate forces to be used in finite element analysis, trustier loading conditions – provided by subject-specific models – is indeed preferred.

References

1. D. Saxby et al, Biomech Model Mechanobiol, 19:1169-1185,2020.
2. Z. Lerner et al, J Biomec, 48:644-650, 2015.
3. G. Valente et al, Comput Methods Programs Biomed, 152:85-92, 2017.
4. T. A. Correa et al, J Biomec, 44:2782-2789, 2011.
5. S. L. Delp et al, IEEE Trans Biomed Eng, 54:1940-1950, 2007.

Acknowledgements

The authors acknowledge Prof. Ilse Jonkers of KU Leuven for providing data here used to build model and simulations.

CALCULATION OF TIBIOFEMORAL FORCE DURING KNEE EXTENSION BASED ON MRI SCANS AND ISOKINETIC TEST

Martyna Białecka (1,2), Jacek Buśkiewicz (1), Tomasz Walczak (1), Jakub Krzysztof Grabski (1), Tomasz Piontek (3,2), Monika Grygorowicz (4,2)

1. Poznan University of Technology, Institute of Applied Mechanics, Poland; 2. Rehasport Clinic LTD, Poland; 3. Poznan University of Medical Sciences, Department of Spine Disorders and Pediatric Orthopedics, Poland; 4. Poznan University of Medical Sciences, Department of Physiotherapy, Poland;

Introduction

Meniscus is a semi-lunar fibrocartilage structure that is integral to the proper knee joint functioning, due to load distribution and amortization. Although knee joint forces (KJF) during isokinetic knee extensions have been already described, none of these studies have analyzed a change in KJF after surgical intervention, especially in meniscus treatment. This is an important problem because proper healing of a meniscus can be a key factor in osteoarthritis prevention.

The aim of this study was to create a simple mechanical model of the knee extension, that will use data usually collected in the treatment process in order to calculate tibiofemoral force (TF) and to investigate a change in its course after the meniscus treatment.

Materials and methods

Data were selected from the patients included and analyzed in study [3] and treated according to the arthroscopic surgical technique presented in [1]. The study group was restricted to 28 patients (8 women and 20 men) according to the following inclusion criteria: medial meniscus tear, without lateral meniscus lesions and with at least one isokinetic test of the operated knee joint in the follow-up period up to five years after the surgery. Exclusion criteria were tears of the ligaments, their reconstruction, as well as partial meniscectomy.

In order to calculate TF, we formulated a two-dimensional mechanical model of the shank and tibial articular surface during isokinetic examination. The model was based on the model presented in [4] and it can be applied only to knee extension. We assumed that the temporary center of rotation during shank extension is localized at the point of contact between tibia and femur, and torque measured in isokinetic test in concentric-concentric mode is balanced by torque exerted by patellar tendon.

The coordinate system in this study was placed on tibial plateau, according to the methodology described in [6]. The distance between tuberosity of the tibia and the center of rotation (tibiofemoral contact point) as well as angle between patellar tendon and tibial long axis were measured separately for every patient, based on MRI scan of extended knee. Then, in order to calculate location of contact point in a function of knee flexion, we applied results of the study [2], where authors provided tibiofemoral cartilage contact points on the medial tibial plateau at different flexion angles during in vivo weight-bearing lunge. Similarly, we applied results from the paper [5] to calculate angle between patellar tendon and tibial long axis in every knee flexion, so it could be used with data measured in isokinetic test.

Results

The mechanical model formulated in this study estimates tibiofemoral force as a function of the knee flexion, dependent on torque measured in isokinetic test. This characteristic was calculated for every patient, separately for every isokinetic test performed postoperatively, usually 6, 12 and 24 months after meniscus regeneration. Results presented as the example in Fig.1 shows that the course of tibiofemoral force changes with time after the surgery what may be a result of meniscus healing and restoration of its biomechanical function in the knee joint.

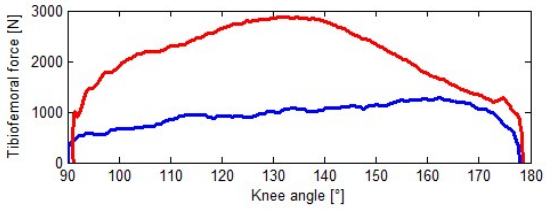

Figure 1: TF calculated with the use of developed model: 6 (blue) and 24 months (red) after the surgery.

Discussion

The point seems to be not the difference in the magnitude of the TF, but the nature of its change together with the change of knee flexion.

Mechanical model presented in this study allows to merge clinical data usually collected during patient treatment process, like MRI scans in knee extension and isokinetic tests of the knee joint, in order to estimate TF course, which is believed to be an important parameter in meniscus treatment and osteoarthritis prevention.

References

1. Piontek et al, Polish Orthop. Traumatol., 77:39-45, 2012.
2. Qi et al, J Biomech, 46:1576-1582, 2013.
3. Piontek et al, Cartilage, 7:123-139, 2016.
4. Masouros et al, Orthopaedics and Trauma, 24:84-91, 2010.
5. Varadarajan et al, J Orthop Res, 28:322-328, 2010.
6. Beynnon et al, J Orthop Res, 32:61-8, 2014.

Acknowledgements

The presented research was funded with grant 02/21/SBAD/3558 allocated by the Ministry of Science and Higher Education in Poland.

A BIOMECHANICAL APPROACH TO EVALUATE PERFORMANCE OF SCOLIOSIS BRACES

Alireza Yahyaiee Bavil (1), Ayda Karimi Dastgerdi (1), Gholamreza Rouhi (1)

1. Amirkabir University of Technology, Iran

Introduction

Bracing is a common method of treatment for scoliosis, which rectifies the unwanted curves in the patient's spine through applying corrective forces [1]. The method of treatment is based on the overcorrection of curves by pushing the spine in the opposite direction of the unwanted curves, which is expected to result in the reduction of Cobb angle. The functionality of bracing has been mostly investigated from a statistical standpoint, and the role of biomechanical factors in this regard has not been extensively tackled yet [2]. In this study, we aimed to provide a biomechanical analysis to investigate the performance of a specific type of part-time brace, i.e. the Providence brace, using experimental and in-silico tools.

Methods

A patient with mild scoliosis (Cobb angle: 17), who was using a night-time Providence brace, was chosen for this study. Applied forces from the brace on the patient's rib cage and pelvis were measured using a Novel Pliance-xf-16(-32) force pad in her supine position (Fig. 1). Moreover, a finite element model of the patient's lumbar spine was developed. The measured forces, in the experimental part, were imported into the model, and the normal stress distribution on the scoliotic lumbar vertebral growth plates was obtained, and alterations in the Cobb angle were observed when wearing the brace, and without using the brace. Finally, a comparison was made between the normal stress distributions and Cobb angle of the model with- and without the Providence brace, and in supine and sitting positions, respectively.

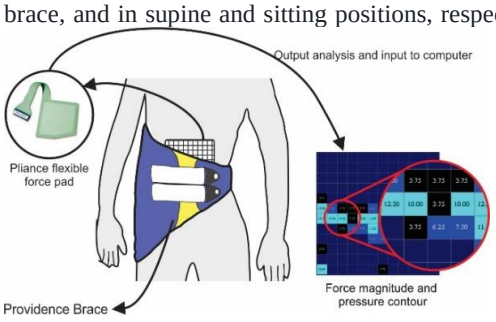

Figure 1: Method used to obtain brace forces on the patient's body.

Results

The measured mean forces applied by the brace were 29.40 N, 24.75 N, 22.429 N, and 37.61 N in the posterior pelvis, anterior pelvis, superior thorax, and inferior thorax, respectively. Furthermore, results of the FE model showed that there is curvature overcorrection, and the Cobb angle was reduced from 17 degrees, in the initial configuration, to 3.4 degrees right after using the brace. The stress distribution in the patient's growth plates, with the brace in the supine position, deviates from that of the scoliotic individual's stress distribution while was not wearing the brace (Fig. 2. a). It was observed that by wearing the brace, unbalanced stress distribution on the growth plates caused by the scoliotic spine's curvatures, can be compensated, i.e. regions in growth plates that experience high compressive stresses in sitting position undergo tensile stress while using the brace (Fig. 2. b).

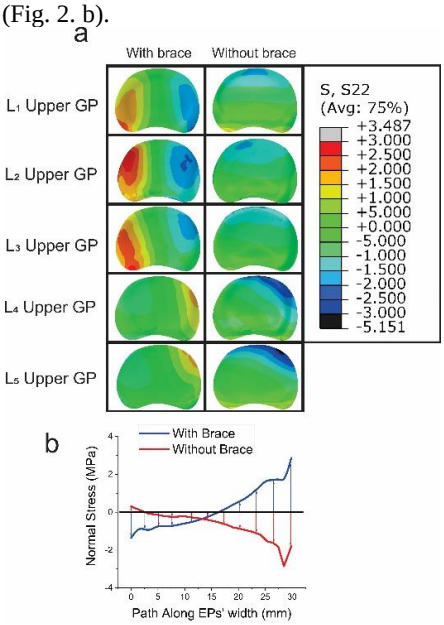

Figure 2: (a) Normal stress distribution on the upper growth plates of lumbar vertebrae, resulted from FEA, (b) Normal stress distribution changes along upper L4 growth plates width.

Discussion

Results of this work indicate that a night-time brace, here Providence brace, can cause alteration in normal stress distribution within the lumbar vertebrae growth plates, which can consequently amend the asymmetric distribution of stress, and ultimately reduce the Cobb angle, in agreement with x-ray photography of the patient. The long-term goal of this research is to design more efficient braces, through discovering new aspects of the biomechanics and mechanobiology of scoliosis.

Acknowledgements

The authors would like to thank Amirkabir University of Technology.

References

1. d'Amato C.R. et al., *Spine*, 26(18):2006-2012, 2001.
2. Clin J, et al., *Spine*, 19 (35): 940-947, 2010.

THE EFFECT OF CURVE LOCATION ON THE SEVERITY INDEX FOR ADOLESCENT IDIOPATHIC SCOLIOSIS

Claudio Vergari PhD (1), Wafa Skalli (1), Kariman Abelin-Genevois (2), Jean-Claude Bernard (2), Zongshan Hu (3), Jack Chun Yiu Cheng (3), Winnie Chiu Wing Chu (4), Ayman Assi (5), Mohammad Karam (5), Ismat Ghanem (5), Tito Bassani (6), Fabio Galbusera (6), Luca Maria Sconfienza (6,7), Marco Bruno-Brayda (6), Isabelle Courtois (8), Eric Ebermeyer (8), Tristan Langlais (9), Raphael Vialle (9), Jean Dubousset (1)

1. Institut de Biomécanique Humaine Georges Charpak, Arts et Métiers ParisTech, France; 2 Department of Orthopaedic Surgery, Centre médico-chirurgical et de réadaptation des Massues, France; 3 Scoliosis Research Laboratory, The Prince of Wales Hospital, The Chinese University of Hong Kong; 4 Department of Imaging and Interventional Radiology, The Prince of Wales Hospital, The Chinese University of Hong Kong; 5 Laboratory of Biomechanics and Medical Imaging, University of Saint-Joseph, Lebanon; 6 IRCCS Istituto Ortopedico Galeazzi, Italy; 7 Dipartimento di Scienze Biomediche per la Salute, Università degli Studi di Milano, Italy; 8 CHU - Hopital Bellevue, France; 9 Department of Paediatric Orthopaedics, Armand Trousseau Hospital, France

Introduction

Adolescent idiopathic scoliosis (AIS) shows a specific geometrical pattern of spinal deformity: a lateral deviation of the apical vertebra, an axial rotation of the scoliotic curve and a flattening of the back. These features were recently combined in a severity index which was developed to detect early those curves at risk of progression [1]. The severity index was preliminary validated in a cohort of 65 patients with Risser sign < 3, i.e. patients who still have growth potential and therefore high progression risk. However, the accuracy of the severity index according to major curve location was not studied; this is an important aspect because a scoliotic curve in the thoracic or lumbar region might not present the same pattern of deformity. In the present work, the effect of the location of the scoliotic curve on the severity index was analyzed.

Methods

AIS patients were included in six clinical centers from four countries (France, Hong Kong, Lebanon, Italy). Inclusion criteria were: Cobb angle < 25°, age > 10 years and Risser sign < 3. They were followed radiologically until decision of treatment ("progressive patients") or until they reached skeletal maturity with no scoliosis progression ("stable patients" Risser ≥ 3 and Cobb angle < 25°). All patients underwent biplanar radiography (EOS system, EOS Imaging, Paris, France) and 3D reconstruction of the spine [2-4]. Three-dimensional geometrical parameters of the scoliotic curve were automatically computed: spinal torsion, apical vertebral axial rotation, inter-vertebral axial rotation at the end vertebrae, the hypokyphosis index [1] and Cobb angle. These parameters were combined in a linear discriminant analysis based on an existing database of 53 asymptomatic subjects, 17 moderate scoliosis and 30 severe ones. The model outputs an index between 0 and 1, i.e., the severity index. In this work, the index was further weighted with a multiplicative factor of 1, 0.8 or 0.7 for patients with Risser 0, 1 or 2, respectively Values lower than 0.4 suggest a stable patient while higher than 0.6 a progressive one. An index in-between is considered undetermined. Patient were grouped by major curve location: thoracic (T, apex above T12), thoracolumbar (TL, apex in T12 or L1) or lumbar (L, apex below L2).

Results

205 patients were included (171 girls and 34 boys, age 12 ± 1 years). 96 patients (47%) were progressive while 109 were stable (53%). 82% were correctly classified as stable or progressive. Positive predictive value was 78%; index's performance is reported in Table 1.

	All	T	TL	L
N	205	88	52	65
Correctly classified (%)	82	83	81	82
Sensitivity (%)	87	93	74	89
Specificity (%)	78	73	88	77

Table 1: Sensitivity and specificity of the severity index by curve topology.

Discussion

The index's specificity was only marginally affected by curve location, while its sensitivity was higher in T and L curves than in TL ones. Further analysis should be conducted on TL curves to determine if they present a different pattern when they tend to progress; for instance, TL curves are between the stiffer spinal region of the ribcage, and the more compliant lumbar spine. Nevertheless, the index showed robust results which are promising for its dissemination in clinical routine.

References

1. Skalli et al, Spine 42:823-830, 2017.
2. Gajny et al, Eur Spine J 28 :658-664, 2019.
3. Humbert et al., Med Eng Phys 31:681-687, 2009.
4. Vergari et al, Eur Spine J 28 :1970-1976, 2019.

ANALYSIS OF MECHANICAL PROPERTIES OF SPAYED CANINE LUMBAR VERTEBRAE

Ernest Kostenko (1), Rimantas Stonkus (2), Algirdas Maknickas (3)

1,3. Department of Biomechanical Engineering, Vilnius Gediminas Technical University, Lithuania; 2. Department of Mechatronics and Robotics and Mechanical Engineering, Vilnius Gediminas Technical University, Lithuania

Introduction

One of the main functions of the spine is to protect the spinal cord; another is to distribute weight while the body is walking, running, or even standing [1]. When the function or mechanical properties of the spine are impaired, disease occurs [2]. One disease of the spine is osteoporosis. Seeking to combat spinal diseases, including osteoporosis, biomechanical engineers and surgeons work together to explore properties of the spine and improve or discover new treatments. [3]

The aim of the current research was to investigate experimentally the mechanical properties of each vertebra in a spayed female eight-year-old dog (bitch).

Methods

For our analysis, we used a spayed female mongrel dog that was approximately eight years old and weighed 28 kg. The dog had been euthanized in accordance with good veterinary practice following diagnosis of a mammary gland tumor. After euthanasia, an autopsy was performed. During the autopsy, the lumbar segment was removed and subsequently stored in the freezer at -20 °C until testing. The day before the test, the segment was removed from the freezer and thawed gradually in saline. When the lumbar section was completely thawed, the muscles and tissues were removed, and the vertebrae were separated. During this process, the vertebrae were kept moist.



a) b)

Figure 1: a) Spayed dog vertebras (Th11-L5) b) Mecmesin MultiTest 2,5-i microcompression machine.

The compression tests were performed using a Mecmesin MultiTest 2,5-i microcompression machine (Mecmesin Limited, Slinfold, UK). The Mecmesin AFG25 load cell had a controlled load of measured accuracy at ±0.01 mm, and it exerted a compression force in the range of 2–2500 with accuracy at ±0.1% where crosshead speed accuracy was ±0.1%. Each vertebra (Figure 1a) was compressed with a force of 950 N. The velocity was chosen equal to 1 mm/min. The vertebrae were adjusted for cyclic loads and selected to work for 10 cycles. After the experiment, the axis of each vertebra was measured. After installing a sample, cyclic loading was applied (Figure 1b).

Results

Comparison of experimental and theoretical data obtained in the first load/unload cycle are presented in Figure 2. The coefficient of determination R^2 of fitted load/unload in the first cycle was [0.9996, 0.9999]. Meanwhile, R^2 of fitted displacement in the first cycle was [0.9999, 0.9998]. These results show good agreement of the fitted curve with experimental data.

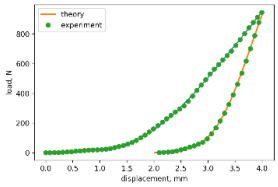

Figure 2: Load displacement relations.

Discussion

Collected experimental data of vertebra load and unload are approximated by using the expressions below:

$$L_k(t) = \sum_{i=0}^{6} a_{ik} t^i \quad (1)$$

$$d_k(t) = d_{0k} + d_{1k} t \quad (2)$$

where L_k is external load, d_k is displacement, t is the independent parameter (time), and a_{ik} and d_{ik} are material constants for each load/unload cycle k. The numerical optimization was applied using the *scipy.optimize.curve_fit* function [4].

References

1. C. H. Turner et al., "Experimental Techniques for Bone Mechanics," in *Bone Mechanics Handbook*, 2nd ed., vol. 7, no. 2, S. C. Cowin, Ed. Boca Raton: CRC Press, 2001.
2. J. B. Volpon et al., "Methods in Bone Biology in Animals: Biomechanics," in *Osteoporosis Research: Animal Models*, G. Duque and K. Watanabe, Eds. London: Springer Verlag, 2011, ch. 29, pp. 34-35.
3. R. Izzo et al., "Biomechanics of the Spine. Part I: Spinal Stability," *European Journal of Radiology*, vol. 82 no. 1, pp. 118-126, 2012.
4. P. Virtanen et al., "SciPy 1.0: Fundamental Algorithms for Scientific Computing in Python," *Nature Methods*, vol. 17 no. 3, pp. 261-272, 2020.

Acknowledgements

We thank veterinarians Dr. J. Šengaut and Dr. L. Labanauskaite for their help in the experiment.

ESTIMATION AND ASSESSMENT OF SAGITTAL SPINAL CURVATURE AND THORACIC MUSCLE MORPHOMETRY IN DIFFERENT POSTURES

Anoosha Pai S (1), Honglin Zhang (2), Nima Ashjaee (1), Thomas R. Oxland (2), David R. Wilson (2), Stephen H.M. Brown (3), John Street (2), Sidney Fels (4)

1. School of Biomedical Engineering, University of British Columbia, Vancouver, Canada; 2. Department of Orthopaedics, University of British Columbia, Vancouver, Canada; 3. Department of Human Health and Nutritional Sciences, University of Guelph, Canada; 4. Department of Electrical and Computer Engineering, University of British Columbia, Vancouver, Canada

Introduction

Clinical imaging for spinal deformity typically consists of a standing x-ray of the whole spine and a supine MRI of only the pathological spinal levels. This does offer coherent data for the development of subject-specific, biomechanical spine models that reflect actual clinical symptoms. Additionally, muscle parameters such as cross-sectional area (CSA) and moment-arms measured from imaging modalities are not perpendicular to the scan slices and must be corrected in order to be appropriately used in models.

Objectives: 1) To develop and validate a method for estimating of subject-specific sagittal spinal geometry in different postures from vertebral body center (VBC) data in a reference posture (standing). 2) To correct for the cosine between the MRI axial scan plane and dominant fiber line-of-action for muscle parameters (CSA and moment-arms) in these postures.

Materials and Methods

Imaging

Thoracic Spines of six healthy participants (age 26±6 y, BMI 24±3 kg/m^2) were imaged (0.5T Open Upright MR scanner) in four postures (supine, standing, flexion, and sitting).

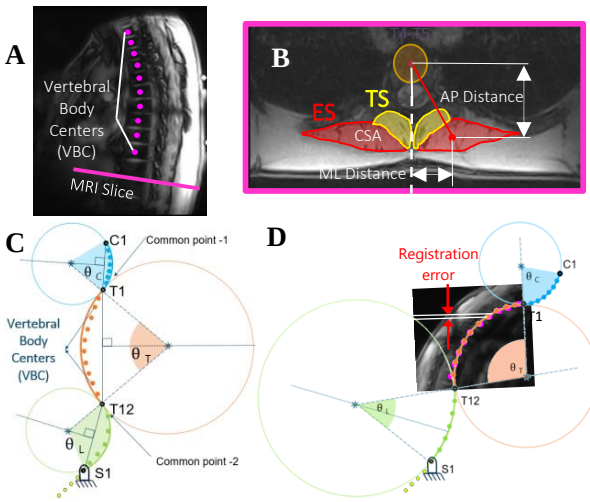

Figure 1: A) Sagittal MR image. B) CSA, A-P and M-L distances of erector spinae (ES) and transversospinalis (TS) on Axial MR image. C) Geometric construct of sagittal spinal curvature (standing). D) Estimated spine geometry (flexion) rigidly registered to ground truth data (MRI in flexion) showing registration error.

VBCs from T1 to T10 were marked on sagittal MR images (Fig 1A). CSA, anterior-posterior (A-P) and medial-lateral (M-L) were computed for two muscles—erector spinae and transversospinalis on axial MR images (Fig. 1B).

Sagittal Spine and Muscle Geometry Estimations

Sagittal spinal curvature was approximated using a circular spline parameterized with the segment angles (kyphosis or lordosis Cobb angle) and segment lengths (assumed constant) (Fig 1C). The subject-spine geometry in any other posture was estimated by modification of these parameters and normalization with the reference posture. The estimated spine geometry was validated against the corresponding MRI data by rigid registration using coherent point drift method [1] (Fig. 1D). From the model, the dominant muscle fiber line-of-action of erector spinae and transversospinalis was computed for each posture. A correction factor based on published literature was then computed and applied to the muscle parameters [2].

Results

The maximum registration error between the estimated spine geometry and MRI data was small (average RMSE~1.2%). The correction factor reduced muscle parameters (~5% for erector spinae and ~25% for transversospinalis) when compared to raw, uncorrected MRI data.

Discussion

Compared to all existing methods for quantitative evaluation of sagittal spinal geometry [3], our method is simple, reliable, computationally inexpensive and easily digitizable for clinical images. Another novelty of this work is reporting trunk muscle properties for postures other than supine. Overall, our data contributes to the growing literature of trunk geometry evaluation and is preliminary step in clinically relevant subject-specific modelling.

References

1. A. Myronenko *et al.*, *IEEE Trans. Pattern Anal. Mach. Intell.*, 32(12): 2262–2275, 2010
2. L. Santaguida, *et al.*, *Clin. Biomech.*, 8:171–178,1993.
3. T. Vrtovec, *et al.*, *Eur. Spine J.*, 18(5): 593–607, 2009.

Acknowledgements

We thank NSERC, CIHR and Medtronic Canada for funding.

EMG-ASSISTED MODELLING PROVIDES PHYSIOLOGICAL NECK MUSCLE ACTIVATION PATTERNS DURING CONTACT SPORT EVENTS

Pavlos Silvestros[1], Claudio Pizzolato[2], David G. Lloyd[2], Ezio Preatoni[1], Harindejit S. Gill[3], Dario Cazzola[1]

1. Department for Health, University of Bath, Bath, United Kingdom
2. School of Allied Health Sciences, Griffith University, Gold Coast, Australia
3. Department of Mechanical Engineering, University of Bath, United Kingdom

Introduction

Replication and estimation of neck muscle activations during impact events is still a great challenge in biomechanics. Experimental in-vitro studies have underlined the importance of neck muscle forces as these can alter the ultimate load [1], but little is still known about how neck muscles are activated in-vivo prior to impacts. In neuromusculoskeletal modelling, EMG-assisted methods combine experimental EMG signals with optimisation procedures to generate muscle activation patterns that satisfy both experimental muscle excitation patterns and the calculated joint moments. The aim of this study is to evaluate the use of EMG-assisted neuromusculoskeletal modelling to investigate neck muscle function in preparation for collisions.

Methods

One academy level front-row rugby player performed lab-based scrummaging and tackling using an instrumented scrum machine and tackle simulator as well as functional neck movements. Full body kinematics, neck flexors and extensors EMG, and full body MRI scans were collected.
A neuromusculoskeletal modelling pipeline that tracks experimental joint moments was used to simulate muscle activation patterns. Two neuromuscular solution modalities were assessed: static optimisation (SO) and EMG-assisted methods. An MRI-derived OpenSim model (Figure 1) was used and its muscle parameters calibrated in CEINMS [2] in two different ways: one where all the model's MTU strengths were calibrated (EMGa) and a second were 44 MTUs were prescribed with estimations obtained from segmented MRI scans (EMGaMRI).

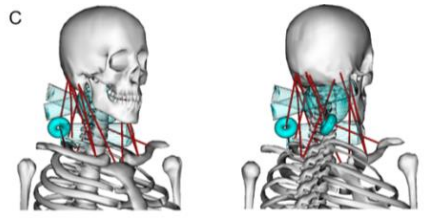

Figure 1:The population specific 'Rugby Model'(https://simtk.org/projects/csibath) was adapted by using MRI scans of the neck region to create wrapping surfaces and update muscle parameters.

The calibrated models were used in CEINMS to estimate muscle activations and MTU forces by tracking experimental joint moments and EMG linear envelopes in an EMG-assisted optimisation approach in remaining trials. Correlative measures across each trial were used to access model performance by comparing the results to experimental joint moments and recorded EMG values and against pure Static Optimisation.

Results

The EMGaMRI neuromuscular solutions tracked experimental net joint moments (NJM) with the same accuracy than SO. The EMGa and EMGaMRI models successfully tracked experimental excitations for the ten MTUs corresponding to the four measured muscles (Figure 2).

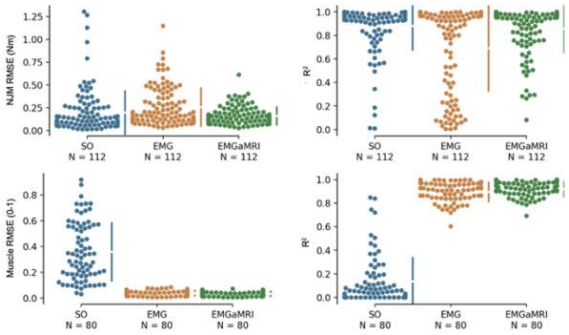

Figure 2: Root mean square error (RMSE) and R^2 for NJM and muscle activation across all neck movements.

Conclusion

EMG-assisted models can reproduce net joint moments with MTU activations that i) track experimental EMG measurements, ii) do not saturate nor display "on-off" behaviour, iii) closely follow experimental co-contraction ratios and v) are estimated without *a priori* objective function. This is a key step forward to investigate cervical spine injury mechanisms during impact events

References

1. Nightingale et al. (2016) *JoB*, **29(3)**:307-318
2. Pizzolato et al. (2-15). *JoB*, **48(14)**: 3929-393

Acknowledgements

The authors would like to thank the Rugby Football Union Injured Player Foundation for funding the PhD scholarship References.

COMPUTATIONAL FRACTURE ANALYSIS OF SCREW-BONE INTERACTION IN A PATIENT-SPECIFIC VERTEBRA MODEL

Cristina Falcinelli (1), Leonardo Molinari (1), Alberto Di Martino (2,3), Alessio Gizzi (1)

1. Campus Bio-Medico University of Rome, Italy
2. University of Bologna, Italy 3. IRCCS-Rizzoli Orthopaedics Institute, Bologna, Italy

Introduction

Screw fixation is a surgical technique in which screws and rods are inserted to connect vertebrae to relieve symptoms of spine diseases. The screws insertion trajectory plays a significant role in arising stress concentrations leading to localized bone failure events, screw loosening and breakage [1]. As such, investigating the effect of screws insertion trajectory on the vertebral mechanical response is crucial to find the trajectory that can minimize the onset of stress concentrations and loosening phenomena. Nowadays, finite element (FE) modeling is widely adopted to investigate the vertebral mechanical response [2] and thus can be adopted to explore the impact of different screw insertion trajectories on vertebral fracture risk. The aim of this study is to evaluate through an extended patient-specific FE analysis the mechanical response of L4 vertebra after screw fixation by varying the screws insertion trajectory to understand its impact on vertebral fracture load, patterns and stress distributions [3].

Methods

A patient-specific 3D FE model of non-osteoporotic L4 vertebra bilaterally instrumented with pedicle screws was generated. The vertebral geometry was derived by segmenting the computed tomography (CT) images. The CAD models of two non-cannulated pedicle screws were designed, virtually inserted in the vertebra model with a depth of 30 mm, and then simultaneously rotated around their insertion points in mediolateral and craniocaudal directions (Figure 1) to maintain fixed the entry point and guarantee different insertion trajectories. Nine trajectories were investigated (combination of three craniocaudal and three mediolateral screws insertion angles). The screws-vertebra system was then discretized with 10-node tetrahedral elements. Isotropic heterogeneous CT-based material properties were computed for the vertebra integrating a custom algorithm ensuring an accurate material properties identification of the thin vertebral cortical layer. For screws, a Young Modulus of 110 GPa and a Poisson's ratio of 0.4 were chosen (Ti-6Al-4V). Physiological motions were simulated (i.e., flexion, extension, axial rotation and lateral bending). The mechanical response of screws-vertebra system was analyzed through a progressive damage procedure, considering a stress-based criterion. Results were analyzed in terms of fracture load and patterns, as well as stress distributions.

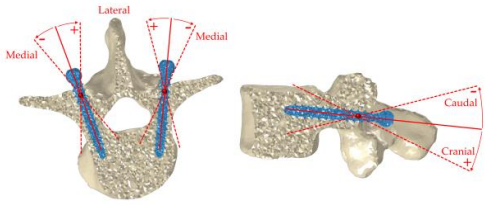

Figure 1: Craniocaudal, mediolateral trajectories [3].

Results

The screws trajectory significantly affected the vertebral mechanics (high variability in fracture loads, ranging from 3139 N to 7680 N, and fracture patterns). In 83% of the cases, the fracture was brittle. Conversely, the caudiomedial trajectory showed a ductile-like fracture in all loading cases that is more appropriate to describe the vertebral failure due to the large amount of trabecular bone that can undergo large plastic deformations prior to the fracture. Moreover, the stress analysis revealed that, among all trajectories, the caudiomedial one exhibited significant differences (p-values<0.05) in terms of Von Mises and maximum principal stress distributions compared to all other configurations, avoiding excessive stresses in trabecular bone and screws. Reducing the stresses in trebecular bone and screws is crucial to avoid trabecular bone failure and subsequent screws loosening and breakage

Discussions

Based on the results, a caudiomedial trajectory may be more suitable in preventing postoperative vertebral fractures, in according with [4]. The results highlighted that the screws' insertion trajectory significantly impacts the vertebral fracture mechanism. As such, the implant positioning should be considered carefully and can significantly affect the postoperative period since an inappropriate choice may lead to a bone structural integrity reduction increasing the fracture risk. Additional work will be necessary to extend the present results to osteoporotic patients, for which the optimal trajectory may be different from that for a healthy subject.

References

1. Ohba et al, SSRR, 3: 79-85, 2019.
2. Jones et al, Med Eng Phys, 30:1287-1304, 2008.
3. Molinari et al, JMBBM, accepted, January 2021.
4. Newcomb et al, Comput Meth Biomech Biomed Eng, 20:1-11, 2017

CERVICAL TOTAL DISC REPLACEMENT CAN RESTORE INTACT RANGE OF MOTION AND 3-D KINEMATICS

Morten Vogt (1), Laura Zengerle (1), René Jonas (1), Hans-Joachim Wilke (1)

1. Institute of Orthopaedic Research and Biomechanics, Trauma Research Centre Ulm, University of Ulm, Germany

Introduction

In contrast to cervical discectomy and fusion, total disc replacement (TDR) aims at preserving the motion at the treated vertebral level. Spinal motion is commonly evaluated with the range of motion (ROM). However, more qualitative information about cervical kinematics before and after TDR is still lacking. Therefore, the aim of this in vitro study was to investigate the influence of cervical TDR on ROM, centers of rotation (COR) and three-dimensional helical axes.

Methods

Six fresh frozen human cervical functional spinal units (FSUs) (C4-5, mean age 32 years, range 19-47 years) were biomechanically characterized in the intact state and after implantation of a cervical disc prosthesis (MOVE-C, NGMedical, Germany). Additionally, to be able to test the prosthesis under in vivo conditions regarding temperature and abundant ambient water, hot water steam was used to create a warm and humid test environment with 37 °C.

In vitro experiments using pure moment loading without preload have been shown to produce reliable cervical kinematics [1]. Thus, following internationally accepted recommendations [2], each FSU was quasistatically loaded with pure moments up to ±2.5 Nm in flexion/extension (FE), lateral bending (LB) and axial rotation (AR) in a universal spine tester [3] for 3.5 cycles at 1 °/s. Motion tracking was performed for each vertebral body individually using Vicon motion capture. For each third cycle of motion the ROM was evaluated and an established method used to determine the helical axis and COR and to project them into three planar X-rays [1]. Statistical analysis was performed in IBM SPSS Statistics 27 using a Friedman-test and post hoc correction with Dunn-Bonferroni-tests ($p < 0.5$).

Results

In FE and AR, the ROM after TDR deviated less than 5 % from the respective intact condition, while in LB the ROM after TDR was decreased less than 20 % (Table 1). No statistical differences between the ROM in the intact condition and ROM after TDR were detected.

The position and orientation of the helical axes after cervical TDR was in good agreement with the results of the intact specimens in all three motion directions (Fig. 1). The COR in FE and AR before and after TDR closely matched, while in LB the COR after TDR were more caudal.

	int+steam	TDR+steam
FE	1.00	1.03
LB	1.00	0.84
AR	1.00	1.03

Table 1: Median total ROM before and after TDR in FE, LB and AR. Values were normalized to the condition int+steam for each specimen individually, then median was calculated.

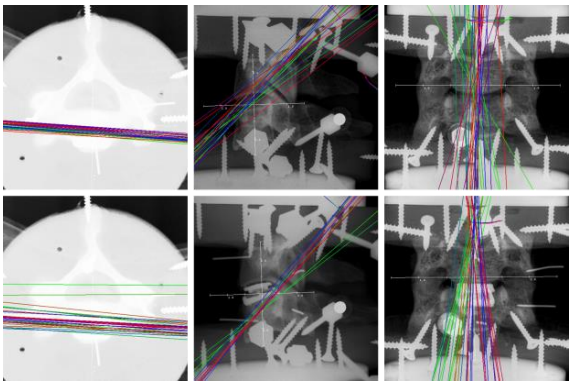

Figure 1: Helical axes in FE (left), LB (middle) and AR (right) of one intact specimen (top) and after TDR (bottom).

Discussion

The results of this in vitro study indicate that ROM of the intact cervical spine can be restored with a cervical artificial disc prosthesis. Additional to the widely used parameter ROM, also the three-dimensional motion pattern was investigated. The kinematics after cervical TDR are in good agreement with the kinematics of the intact specimens under in vitro conditions. This intact kinematics also closely match in vivo data [4].

From these results it can be concluded that this tested unconstrained artificial cervical disc may replicate the quantity as well as the quality of motion of the intact cervical spine under in vitro conditions. Future studies with other types of prostheses are needed.

References

1. Jonas et al, Spine J, 18(3):515-524, 2018.
2. Wilke et al, Eur Spine J, 7(2):148-154, 1998.
3. Wilke et al, Eur Spine J, 3(2):91-97, 1994.
4. Anderst et al, J Biomech, 48(7):1286-1293, 2015.

Acknowledgements

This work was funded by NGMedical GmbH, Nonnweiler, Germany. There are no conflicts of interest.

THE COMBINATION OF TRIANGULAR IMPLANTS WITH ILIAC SCREWS TO ENHANCE SACROPELVIC FIXATION: A FINITE ELEMENT STUDY

Matteo Panico (1,2), Ruchi D. Chande (3), Derek P. Lindsey (3), Tomaso Maria Tobia Villa (1), Ali Mesiwala (4), Scott A. Yerby (3), Marco Brayda-Bruno (2), Fabio Galbusera (2)

1. Politecnico di Milano, Milan, Italy; 2. IRCCS Istituto Ortopedico Galeazzi, Milan, Italy; 3. SI-BONE, Inc., Santa Clara, CA, USA; 4. Southern California Center for Neuroscience and Spine, Pomona, CA, USA

Introduction

Long thoracolumbar fixation is frequently used in combination with sacropelvic fixation for severe spinal deformity correction in order to decrease the instrumentation failure and pseudarthrosis at the lumbosacral joint. The consolidated techniques for sacropelvic fixation include iliac and S2 alar-iliac screws [1,2]. The purpose of this finite element study is to characterize the effects of triangular titanium implants (iFuse Implant System, SI-BONE, Inc., Santa Clara, CA, USA) in combination with iliac screws on L5-S1 and SIJ motion and rod, S1 pedicle screw and iliac screw stresses so as to evaluate the effectiveness of these innovative configurations.

Methods

After the validation of the intact model against in vitro data [1], four T10-pelvis instrumented models were created: pedicle screws and rods in T10-S1 (PED); pedicle screws and rods in T10-S1, and bilateral iliac screws (IL); pedicle screws and rods in T10-S1, bilateral iliac screws and triangular implants inserted bilaterally in a sacral alar-iliac trajectory (SAI, Fig 1); pedicle screws and rods in T10-S1, bilateral iliac screws and two bilateral triangular titanium implants inserted in a lateral trajectory (LAT). The triangular implants were not connected to rods. The models were tested under pure moments of 7.5 Nm in flexion-extension, lateral bending, and axial rotation. The moments were applied to the upper endplate of the T10 vertebra. Measured metrics included flexibility and instrumentation stresses.

Results

This study demonstrates that sacropelvic fixation effectively enhanced L5S1 stabilization and reduced the sacroiliac flexibility. L5S1 and SIJ motion was reduced, respectively, by 85-95% and 55-80% after iliac fixation; the addition of triangular titanium implants reduced the SIJ motion by 80-90% but did not change the L5S1 motion. PED resulted in the highest S1 pedicle screw stresses. IL demonstrated significantly lower S1 pedicle stresses; triangular titanium implants further reduced it. Triangular implants had a protective effect on the iliac screw stresses, especially when placed in the SAI trajectory, except for the lateral bending (Fig. 2). IL resulted in higher posterior rod stresses; Rod stresses were mostly unaffected by the addition of triangular titanium implants.

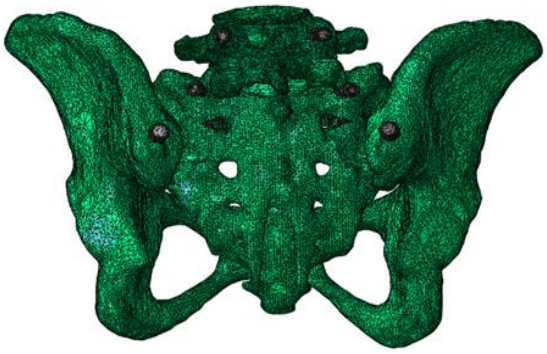

Figure 1: Configuration with pedicle screws, bilateral iliac screws and triangular implants inserted bilaterally in a sacral alar-iliac trajectory, rods not shown.

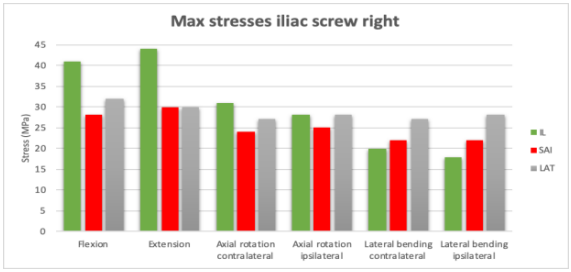

Figure 2: Comparison of the maximal stresses in the right iliac screw in flexion, extension, lateral bending in ipsilateral direction (the same of the side of the implant), lateral bending in contralateral direction, axial rotation in ipsilateral direction (the same of the side of the implant) and axial rotation in contralateral direction.

Discussion

The combination of triangular titanium implants with iliac screws for sacropelvic fixation resulted in a protective effect on the iliac screws themselves, as well as the S1 pedicle screws. This combination can, also, reduce the residual flexibility of the SIJ, suggesting a possible role in patients needing reinforced fixation. With regard to posterior rods, triangular implants did not have a protective effect on the L5-S1 and S1-S2 rods.

References

1. Galbusera et al., Eur Spine J, doi:10.1007/s00586-019-06226-5, 2019
2. Casaroli et al., Eur Spine J, 28(7):1724-1732, 2019

Acknowledgements

This study was funded by SI-BONE, Inc., Santa Clara, CA, USA

AN IN VITRO METHODOLOGY TO ASSESS INTERVERTEBRAL DISC INTERVENTION MECHANICS

Andrew Dixon (1), James Warren (1), Marlène Mengoni (1), Ruth Wilcox (1)

(1) Institute of Medical and Biological Engineering, University of Leeds, Leeds, UK;

Introduction

There are a number of new tissue-sparing interventions for disc degeneration in development, such as injectable hydrogels for nucleus augmentation. Current pre-clinical testing standards were developed primarily for semi-rigid implants and do not take account of the complex interactions between the hydrogel and the tissue. *In vitro* testing presents several challenges as the mechanical properties of the disc change with hydration and time [1]. The objective of this work was to assess the long-term mechanical behavior of intervertebral discs by utilizing novel sequential state testing.

Materials and Methods

Bovine bone-disc-bone units (total n=42) were subjected to sequential mechanical testing where discs were tested in (1) native, (2) degenerated, and (3) treated states. At stage (2), artificial degeneration was enzymatically induced in the discs by injecting papain, followed by a 24-hr static hold at 42C and subsequent injection of an inhibitor. A sham degenerate procedure control group was also completed in which saline was injected in place of the enzyme and inhibitor. At stage (3), the degenerate discs were injected with 0.3 ml or 1 ml of a peptide:glysosaminoglycan mixture [2]. A 1 ml injection control group which substituted the peptide with saline was also completed. Each mechanical testing stage consisted of a hold period under static load followed by cyclic compressive loading between ~350 and 750N at 1Hz. The mechanical behavior of the discs over different numbers of cycles in each of the different states was investigated. A minimum of 1000 cycles was applied at each stage, and the final test on each specimen was extended up to 20000 cycles. Specimens were tested to different final states: native (n=8), degenerate (n=8), saline degeneration (n=6), 0.3 ml treated (n=8), 1 ml treated (n=6), and 1 ml saline:glysosaminoglycan mixture (n=6). Cycle hysteresis and stiffness of the discs was calculated. Linear regression was used to compare low cycle stiffness to the stiffness at 20000 cycles to enable prediction of mechanical behavior.

Results

All specimens in all states showed that, as the number of cycles increased, the hysteresis decreased (Figure 1) and the stiffness increased. The artificial degeneration consistently increased the stiffness of the disc, and the sham degenerate procedure did not result in a significant change of stiffness. Varying degrees of stiffness restoration were observed where the best restoration was found in the 1 ml treatment group. Disruption to the smooth stiffness profile was observed in the treated groups, appearing to be specimen and treatment specific. The stiffness at 20000 cycles was compared to the stiffness at earlier time points through each final test (Figure 2). The root mean squared error (RMSE) reduced up to 8% with diminishing returns as cycle number was increased.

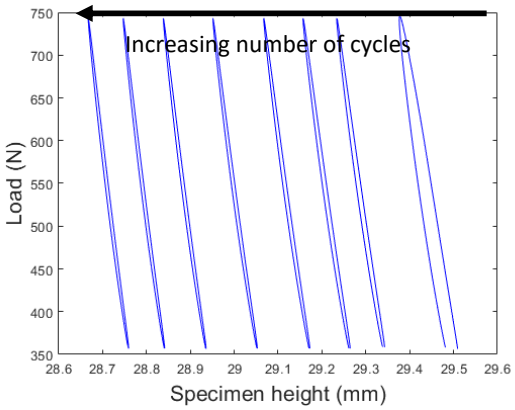

Figure 1: Example hysteresis loops for one specimen

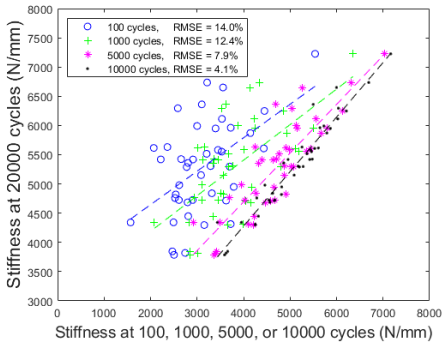

Figure 2: Comparison of stiffness for individual specimens at different numbers of cycles

Discussion

A method was developed to consistently determine intervertebral disc mechanics across multiple states through a longitudinal testing protocol. A window of shortened cyclic testing period was found sufficient to indicate the high cycle behavior, potentially reducing the test time from six hours to 45 minutes at each stage.

References

[1] Showalter BE et al. J Biomech, 47, 2633-2640, 2014
[2] Miles DE et al. J. Mat Chem B, 4, .3225–3231, 2016

Acknowledgements

Funded by EPSRC (EP/R513258/1/2112827, EP/K020757/1).

BIOMECHANICAL INVESTIGATION OF INTERSPINOUS PROCESS DEVICES AFTER LUMBAR DECOMPRESSION – POROELASTIC FINITE ELEMENT ANALYSES

Kinda Khalaf (1), Mohammad Nikkhoo (2), Chi-Chien Niu (3), Chih-Hsiu Cheng (4)

1.Department of Biomedical Engineering and Health Engineering Innovation Center, Khalifa University, Abu Dhabi, UAE; 2.Department of Biomedical Engineering, Science and Research Branch, Islamic Azad University, Tehran, Iran; 3.Department of Orthopaedic Surgery, Chang Gung Memorial Hospital, Linkou, Taiwan; 4.School of Physical Therapy and Graduate Institute of Rehabilitation Science, College of Medicine, Chang Gung University, Taoyuan, Taiwan.

Introduction

Lumbar spinal stenosis (LSS), or the narrowing of the spinal canal at the lumbar level, is one of the most commonly diagnosed and treated pathologic conditions affecting the spine. Despite its increasing prevalence in the aging population, the optimal surgical treatment remains elusive [1]. Recently, different types of interspinous process (ISP) devices have been developed as alternative to spinal fusion [2]. An ISP device serves not only as a distractor, but also as a stress absorber providing rigid, dynamic stabilization in the treatment of LSS. This study aimed to comparatively analyze spinal biomechanics with rigid and flexible ISP devices, as compared to fusion, during daily activities using validated parametric poroelastic finite element models.

Materials and Methods

Using a validated parametric poroelastic FE model of the human spine [3], five subject-specific pre-operative models were developed based on the images of 5 LSS patients. The validity of the FE models was evaluated based on in-vitro [4] and FE studies [5]. Parametric FE models of those lumbar spines were then regenerated based on post-operative images for 4 different clinical cases: (A) posterior fusion (PSF) (B) rigid ISP device (i.e., X-Stop), and (C) flexible ISP device (i.e. DIAM) at the L4-L5 level. The models were compared after 8h rest (200N), following 16h cyclic compressive loading of 500-1000N (40 and 20min, respectively). In addition, different movements (i.e., flexion, extension, lateral bending and axial rotation) were simulated using 10 N.m moment before and after cyclic loading (Fig.1B). Biomechanical responses, including range of motion (ROM), intradiscal pressure (IDP), stress in the annulus fibrosus (AF), and collagen fiber strain were analyzed under the same loading and boundary conditions. The results were compared using one-way ANOVA tests (significant at $p<0.05$).

Results

The intact FE model results were well comparable with in-vitro [4], as well as, FE studies [5]. The flexible DIAM demonstrated slightly increased ROM at the instrumented level (Fig. 1A), but decreased ROM at adjacent levels, as compared to the PSF (Fig. 1B). During cyclic loading, disc height loss, fluid loss, axial stress, and collagen fiber strain in the adjacent IVDs were higher for the PSF construct when compared to intact discs and flexible DIAM (Fig. 1C).

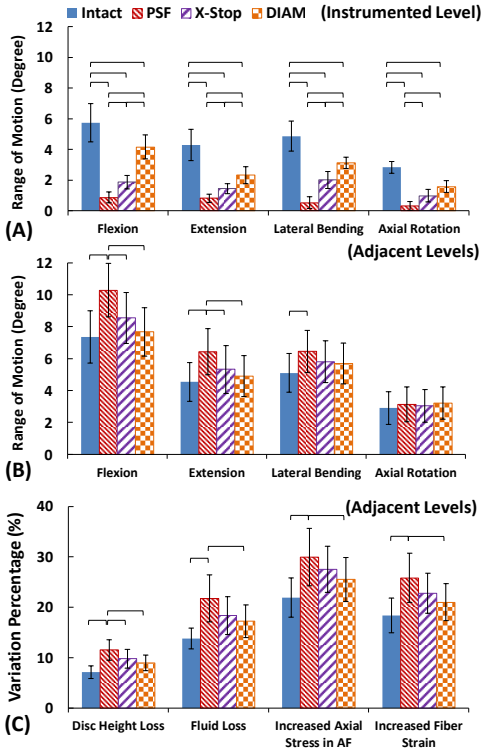

Figure 1: ROM for (A) instrumented and (B) Adjacent levels, (C) variations of results for adjacent IVD.

Discussion

This study provided validated patient-specific FE models towards biomechanically-informed clinical treatment of LSS. Increased ROM, AF stress, and fiber strain at adjacent spinal levels were observed for the PSF group, as compared to the intact and ISP device groups. This suggests an increased risk of disc degeneration at the adjacent levels due to rigid fixation. Similarly, disc height loss and fluid loss were significantly higher at adjacent levels in the PSF group after 16h cyclic loading, suggesting altered fluid-solid interaction of the adjacent IVDs.

References

1. Bresnahan L. et al, Spine, 34:17–23, 2009.
2. Lo H. J. et al, BMC Musc Dis, 20:213, 2019.
3. Khoz et al., Iran J. of Ortho Sur, 15:195-202, 2018.
4. Panjabi et al., J. Bone Joint Sur, 76:413-424, 1994.
5. Schmidt et al., J. Biomech, 43:1849-1856, 2010.

IS IT POSSIBLE TO PREDICT SCREW LOOSENING BY MEASURING THE INSERTION TORQUE? AN IN VITRO STUDY

Jan Ulrich Jansen (1), Laura Zengerle (1), Carsten Hackenbroch (2), Youping Tao (1), Hans-Joachim Wilke (1)

1. Institute of Orthopaedic Research and Biomechanics, University Ulm, Germany;
2. Department of Radiology, German Armed Forces Hospital Ulm, Germany

Introduction

Screw loosening has occurred with rates up to 60 % for osteoporotic and less than 15 % for non-osteoporotic patients [1,2]. In the literature, most cases perform pullout tests, but screw loosening is usually the result of a "windshield-wiper effect", starting with failure of the screw-bone interface as a result of bending [3]. Hence, it would be advantageous to estimate the risk of screw-bone interface failure in order to decide where screw augmentation should be performed or if reducing distraction forces applied during surgery is required. Could the risk be directly estimated without radiation during screw insertion intra-operatively? The purpose of this in vitro experiment was to correlate the screw insertion torque with a bending force necessary to create screw loosening in non-osteoporotic vertebrae.

Methods

In total, 100 pedicle screws were implanted into both left and right pedicles of 50 single vertebrae (14 donors, T9-L4, mean age 41±8) with a median bone mineral density (BMD) of 145 (120-299) mgCaHA/cm^3 which was measured with QCT. After pre-drilling (2.5x20), the appropriate screw (5.5x40, 5.5x45, 6.5x40, 6.5x45, or 6.5x50) was implanted into the pedicle while measuring the insertion torque (Fig. 1A). Both endplates were embedded in PMMA and fixed in a material testing machine. As seen in Fig. 1B, a bending force was applied on the screw head until reaching a displacement of 1 mm (5 N pre-load, 10 mm/min). Afterwards, first a univariate and then a multiple mixed linear model were calculated (SPSS; significant level 0.05).



Figure 1: A) Custom made screw driver with strain gauges for torque measurement. B) Setup for axial loading of ball screw head in material testing machine.

Results

The bending force increased linear with the insertion torque (multiple; p=0.0002) (Fig. 2). The length and the diameter of the screw as well as the vertebral level had a significant impact on the bending force in the univariate model (p<0.0001) but not in the multiple one. BMD did not affect the bending force (univariate; p=0.2483). The screw diameter showed a slight trend for the multiple model (p=0.0584).

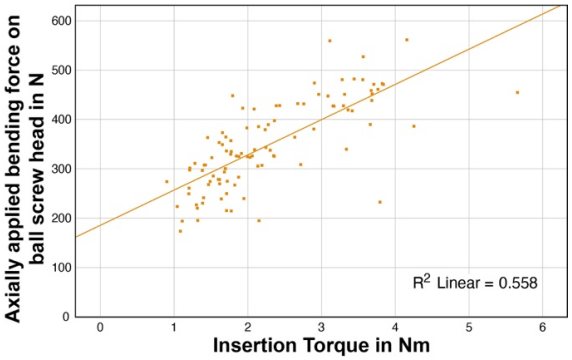

Figure 2: Linear regression between insertion torque and bending force for all 100 tested pedicle screws.

Discussion

The correlation of insertion torque and the bending force suggests an alternative prediction method for screw loosening which could improve the outcome of surgeries and patients' safety. This is potentially a simple, intra-operative, and radiation free method. Differences between the left and right pedicle, which could be due to the operator or the pedicle morphology, were statically tested and considered. Further experiments could further investigate the influence of screw thickness or add to the new findings for non-osteoporotic specimens in this study. Here, the use of a dynamic testing method would provide a deeper mechanical understanding. Non-osteoporotic specimens could, perhaps, indicate a minimum BMD level at which an impact in the clinic is likely to occur.

References

1. Galbusera et al, Eur Spine J, 24(5):1005-1016, 2015.
2. El Saman et al, Eur J Trauma Emerg Surg, 39(5):455–460, 2013.
3. Bostelmann et al, Eur Spine J, 26:181–188, 2017.

Acknowledgements

We thank Apifix Ltd. for providing the pedicle screws and funding the experiment.

ACCOUNTING FOR BIOMECHANICAL MEASURES DOES NOT ENHANCE THE PREDICTION OF CURVE PROGRESSION IN ADOLESCENT SCOLIOSIS

Tito Bassani (1), Dominika Ignasiak (2), Andrea Cina (1), Fabio Galbusera (1)

1. IRCCS Istituto Ortopedico Galeazzi, Milan, Italy; 2. Institute for Biomechanics, ETH Zurich, Zurich, Switzerland

Introduction

Adolescent idiopathic scoliosis (AIS) is a 3D deformity of the spine, the severity of which is quantified by the Cobb angle (Fig.1a). Predictive model for the detection of the progression of scoliosis has been developed by accounting for geometrical parameters of the scoliotic curves [1]. In this regard, biomechanical parameters such as trunk muscle activation and intervertebral loading could provide additional advantageous information. Although not measurable *in vivo* due to the invasiveness of the procedures, such parameters can be obtained by the subject-specific characterization based on musculoskeletal modelling approach. The present study exploits a validated thoracolumbar spine model with articulated ribcage [2], recently adapted for the characterization of the scoliotic spine [3], and evaluates the effect of accounting for the biomechanical parameters on the prediction of scoliosis progression.

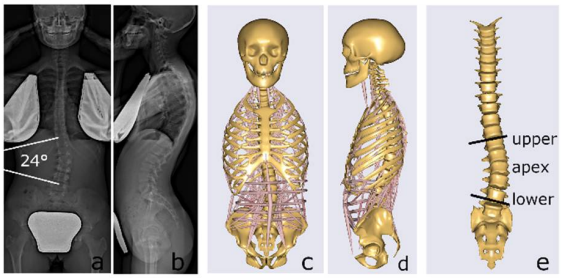

Figure 1: Frontal and lateral radiographic images of one subject (a,b) and musculoskeletal model (c,d,e).

Methods

A dataset of 100 AIS subjects in the early adolescence (age>10 years, Risser sign 0-2) with mild scoliosis (10-25°) at first examination, and identified after at least 6-months follow-up period as 'stable' (Risser>2, increase in Cobb angle <10°) or 'progressive' (Risser 0-2, increase >10°) was exploited (60 and 40 subjects, respectively). The radiographic images acquired at first examination by EOS system (EOS Imaging, France) (Fig.1a,b) were processed for obtaining the 3D orientations of the thoracolumbar vertebrae and the pelvis. Such parameters were used to characterize the subject-specific musculoskeletal model (Fig.1c,d) in AnyBody software (AnyBody Technology, Denmark) [3]. Asymmetry of multifidus and erector spinae muscle activity, as well as intervertebral lateral shear, were calculated inside the curve (the most severe in case of more than one curve) and at apex and upper and lower end levels (Fig.1e). Two sets of predictors for the classification of stable and progressive cases were compared. The 'reduced' model accounted for 12 predictors: age, sex, Risser sign, Lenke type, Cobb angle, number of curves, spino-pelvic and sagittal alignment, and the geometrical parameters of the scoliotic curve. The 'full' model also accounted for the computed biomechanical parameters (11 additional predictors). Six different classification algorithms were compared by repeated cross-validation approach: support vector machine (SVM), predictive discriminant analysis (PDA), naïve Bayes (BAY), decision tree (DET), k-nearest neighbors (KNN) and ensemble approach (ENS). The best fitting ones (providing the largest accuracy) were exploited to compare the classification performance (sensitivity and specificity) for the reduced and full model.

Results

PDA, BAY and ENS were identified as the best fitting algorithms (Table1). In these cases, no significant differences were found in the median value of sensitivity and specificity between the reduced and full model (Fig.2).

	SVM	PDA	BAY	DET	KNN	ENS
reduced	67%	77%	78%	71%	60%	77%
full	64%	73%	80%	68%	64%	77%

Table 1: median accuracy from cross-validation.

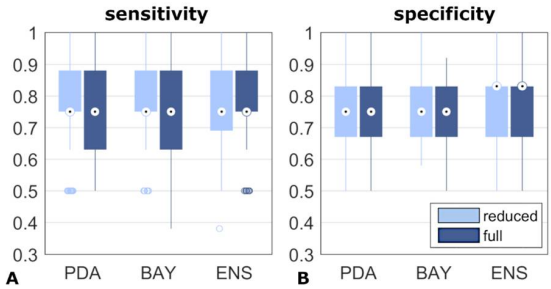

Figure 2: box and whiskers plots for classification performance.

Discussion

Accounting for biomechanical parameters did not enhance the prediction of scoliosis progression. Potential clinical application is not supported at this stage. However, the exploited dataset accounted a moderate number of subjects, and larger sets should be evaluated to refine the classification models and consolidate the results.

References

1. Skalli et al, Spine (Phila Pa 1976) 42:823-830, 2017.
2. Ignasiak et al, J Biomech 49(6):959-966, 2016.
3. Barba et al, J Biomech 114, 110154, 2021.

PROXIMAL JUNCTIONAL FAILURE RISKS WITH DIFFERENT VERTEBRA-ROD ANCHOR TYPES IN ADULT SPINAL DEFORMITIES

Maeva Lopez Poncelas (1,2), Luigi La Barbera (1,2,3), Jeremy Rawlinson (4), Dennis Crandall (5,6,7), Carl-Eric Aubin (1,2)

1. Dept. of Mechanical Engineering, Polytechnique Montreal, Canada; 2. Research Center, CHU Sainte-Justine, Canada; 3. LaBS, Dept. of Chemistry, Materials and Chemical Engineering, Politecnico di Milano, Italy; 4. Medtronic Spinal and Biologics, Memphis, USA; 5. Sonoran Spine Center, Tempe, USA; 6. Mayo Clinic, Phoenix, USA; 7. University of Arizona School of Medicine, Phoenix, USA.

Introduction

Proximal junctional failure (PJF) is a surgical complication following spinal instrumentation surgery which can involve soft tissue disruption, junctional severe collapse, or instrumentation breakage [1]. PJF is a multifactorial complication with several risk factors including the implant type used at the upper instrumented vertebra (UIV). The use of softer fixations such as hooks at the UIV or tethers (bands) at the adjacent level decreased the mobility gradient compared to more rigid pedicle screws and may prevent PJF [2]. Yet, biomechanical studies analyzing the impact of sublaminar bands with additional tensioning on loads distribution have not yet been performed.

The aim was to compare different vertebra-rod anchor types and determine the configuration that minimizes PJF risks in terms of loads at the proximal segment.

Methods

A patient-specific multi-body spinal model was built and validated [3,4] using MD Adams 2014 Multibody Dynamics Simulation Solution (MSC Software, Santa Ana, CA). The model was personalized to simulate the actual surgery followed by standing and upper-body flexion of six adult spine deformity patients who underwent posterior spinal fixation and had developed PJF with junctional subluxation. Using a full-factorial design approach, 12 different anchor configurations were simulated, by combining:

i) upper instrumentation implant type: pedicle screws (PS), supralaminar hooks (SH), PS with sublaminar band at the adjacent level with low (SB-50N) and high (SB-350N) tension;

ii) rod stiffness: high (CoCr, 6mm diameter), medium (CoCr, 5.5mm), and low (Ti, 5.5mm).

The loads held by the anterior spine functional spinal units (FSU) and the instrumentation of the 72 simulations then were analyzed using Kruskal-Wallis statistical tests.

Results

The actual instrumentation procedures were simulated, and the main clinical sagittal and coronal angles were within 5° of the actual postoperative surgical outcome.

SH didn't impact the anterior load distribution at the PJSS and increased the sagittal moment held by the vertebra-implant connection compared to PS (Table 1). Using 50N tension SB smoothed the anterior sagittal moment transition. With 350N tension SB, the sagittal moment held by the adjacent level (UIV+1) decreased significantly but it increased the moment held one level above (UIV+2). It also increased the loads held by the rods around the UIV.

Decreasing rod stiffness decreased the sagittal moment at the vertebra-implant connection (0.7Nm with 5.5 mm Ti vs 1.0Nm with 6 mm CoCr, $p<0.05$).

	PS	SH	SB-50N	SB-350N
UIV+2 FSU	13.4±4.0	13.2±4.2	15.4±4.0	16.2±4.0*****
UIV+1 FSU	13.5±4.5	13.3±4.8	8.3±4.1	2.6±1.4*****
UIV FSU	8.1±5.7	5.8±5.3	7.8±5.6	7.4±5.5
Implant	0.7±0.3	2.8±1.5*****	1.9±2.0	0.8±0.5
Rods	0.9±0.6	2.3±1.1	1.9±0.8	5.9±1.9*****

Table 1: Sagittal moments (Mean±SD, in Nm) on the anterior spine and the instrumentation for different implant configurations and statistical analysis compared to PS (: $p<0.05$)*

Discussion

This numerical study revealed significant variations in representative bending moments for clinical cases with confirmed PJF [4].

The vertebra-to-rod type of connection significantly impacted the bending moments across the instrumented spine. SB with low tension at the top of the construct smoothed the anterior load distribution and reduce PJF risks. However, higher tension SB increased the risks of junctional subluxation at the UIV+2 level and rod breakage. Decreasing the rod stiffness may decrease the risk of vertebra-implant failure, but it increased the risk of rod breakage due to its lower ultimate strength value; the optimal configuration remains to be determined.

References

1. Hart et al, Neurosurgery Clinics, 24:213-218.
2. Bess et al, J Neurosurg Spine, 26 :125-133, 2017.
3. Fradet et al, Clinical Biomechanics, 39:122-128, 2016.
4. Cammarata et al, Spine, 39 :500-507, 2014.

Acknowledgements

This work was supported by the Natural Sciences and Engineering Research Council of Canada (Industrial Research Chair with Medtronic of Canada).

BIOMECHANICAL IMPACT OF INTERVERTEBRAL DISC SIMULATED DAMAGE

Sara Montanari (1), Chloé Techens (1,2), Luca Cristofolini (1)

1. *Department of Industrial Engineering, Alma Mater Studiorum – Università di Bologna, Italy*
2. *National Center for Spinal Disorders - Budapest, Hungary*

Introduction

The intervertebral disc (IVD) has an important role in the load distribution on the adjacent vertebral bodies and in the entire spine motion [1]. Pathological lesions and injuries of the disc occurring during surgical treatment could have a mechanical impact on the spine motion, stability, and in the surrounding tissues (e.g. compression of nerve roots posteriorly). The aim of this work was to evaluate the consequences of different types of intervertebral disc lesions on the human spine biomechanics, in terms of posterior disc height, range of motion (ROM), stiffness and strain distribution.

Materials and method

Eight fresh cadaver thoraco-lumbar FSU's were prepared. The soft tissue around the disc and vertebral bodies, and the posterior element were removed, leaving the anterior ligament intact.The FSU's were horizontally aligned. The extremities were potted into acrylic cement. A white-on-black speckle pattern was sprayed on the specimens to measure displacements and strains with Digital Image Correlation (DIC). The specimens were tested in flexion and extension. Surface images were recorded by a 3D-DIC system (Q400, Dantec). Image correlation was performed using optimized parameters [2]. The displacements were analyzed to compute the change in posterior disc height, ROM, transition displacement, transition load and elastic stiffness [3]. Each specimen was tested sequentially through five conditions (Fig. 1):

- INT: with the intact disc;
- 2CUTS: two vertical incisions on the lateral side;
- 4CUTS: four incisions, forming a square, without removing any part of the annulus fibrosus (AF);
- SQR: after removing the squared plug of the AF;
- NUCL: after removing the nucleus pulposus.

All the defects were executed manually in the opposite side to that observed by DIC.

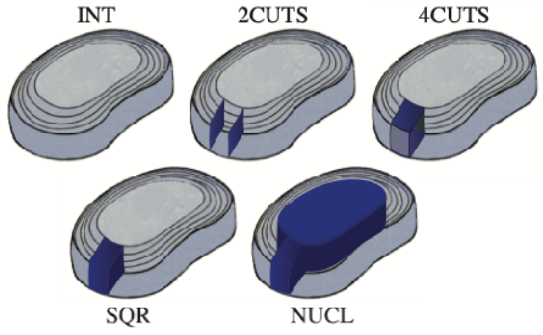

Figure 1: The IVD in the different conditions: the blue portions represent the incisions and removed material.

Results and discussion

The posterior disc height showed a significant 20% decrease in flexion, and 23% decrease in extension from INT to NUCL. These results confirmed the clinical observation [4] according to presence of nucleus inside. A general decreasing trend of the ROM was observed in both loading configurations, but there were no statistically significant differences between the five discs conditions. The level of disc damage did not significantly impact the transition displacement, transition load and elastic stiffness. Different strain distributions were observed for maximum (Ɛ1) and minimum (Ɛ2) principal strains in flexion and in extension (Fig. 2).

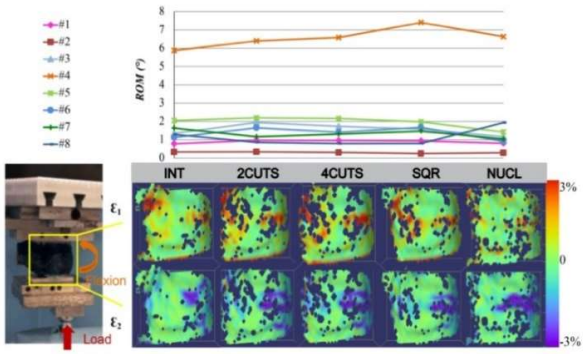

Figure 2: Results for flexion for the 5 disc conditions. Left: specimen with the speckle pattern on the testing machine. Top right: ROM (8 specimens); Bottom: distribution of $\mathcal{E}_1$ and $\mathcal{E}_2$ on the lateral side of the FSU.

Conclusions

The results have shown that sequential damage of the annulus fibrosus does not significantly alter the spine biomechanics in terms of range of motion, stiffness and strain distribution. The main effect observed was the posterior disc height reduction after the nucleus removal due to the lack of support caused by the nucleus loss.

References

1. Newell et al, JMBBM, 62: 420-434, 2017
2. Palanca et al, MEP, 52: 76-83, 2018
3. Tanaka et al, J BiomechEng, 133: 074502-2, 2011
4. Varga et al, Der Ortho, 44: 1-8, 2015

Acknowledgements

European Union's Horizon 2020 Marie Skłodowska-Curie ITN grant SPINNER No. 766012.

Ethics

The study was approved by the bioethical committee of University of Bologna, prot. 76497, 1 June 2018.

SPINE LENGTH EXCURSION DURING WALKING

Veronica Farinelli (1), Chiara Palmisano (2) (3), Federica Camuncoli (2), Alessandra Favata (2), Carlo Albino Frigo (2)

1. Human Physiology Section of the De.P.T., Università degli Studi di Milano, Milan, Italy;
2. Department of Electronics, Information and Bioengineering, MBMC Lab, Politecnico di Milano, Milan, Italy;
3. Department of Neurology, University Hospital and JMU Würzburg, Würzburg, Germany.

Introduction

Human locomotion has been thoroughly analyzed in many aspects, but most studies refer to lower limbs [1], and do not pay much attention to movements of the spine [2, 3]. It is however well known that chronic- or disease-related reduction of trunk mobility may significantly affect the locomotor pattern.
In the present study we aim at describing the typical behavior of the spine during walking in healthy controls, by analyzing few synthetic parameters that can easily be obtained from gait analysis.

Method

Ten healthy young subjects, 5 males, 5 females (aged 25 ± 2 years; body mass 68.2 ± 14.2 kg; body height 171.2 ± 12.2 cm; data shown as average ± standard deviation) were analyzed while walking barefoot at their natural cadence along a straight pathway. The experiment was performed in a gait analysis laboratory equipped with six TV-cameras and a Smart-E motion analyzer (BTS, Milan, Italy). Kinematic data were collected at 60 frames/sec. Retroreflective markers were positioned on the lower limbs, pelvis, and column according to the LAMB protocol [4]. In particular, the cervical process C7, the point of maximum kyphosis, and the Sacrum were considered. In order to include the lower extremity of the spine in our model, an additional virtual point was created in the local reference system of the Pelvis. This point approximately corresponded to the Coccyx, and together with the markers located on the Sacrum and maximum kyphosis, allowed to derive a schematic representation of the lumbar curve. The kyphosis curve was schematically represented by the segments defined by the Sacrum, the point of maximum kyphosis and C7. To synthetically represent spine mobility, we analyzed the time course of the distance between C7 and Coccyx (spinal length) over the gait cycle. Data were averaged across strides and over at least three walking trials for each subject.

Results

Figure 1 represents the time course of the spinal length of one representative subject (25 years old, 1.72 m height, 72 kg of mass). The range of motion of the average curve is about one centimeter, and two peaks of appear at approximately the ipsilateral (0%) and contralateral (50% of stride cycle) heel strike.

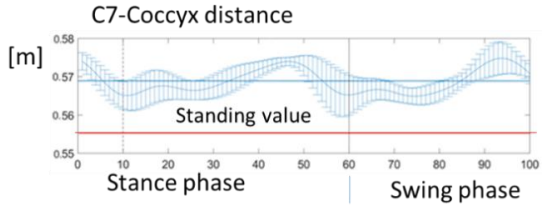

Figure 1: Time course along the gait cycle of the spine length of a normal young subject during walking at natural velocity. Average curve (blue line) and +/-SD (blue band) over three trials are represented. The red line displays the average value of column length obtained during upright standing.

Interestingly, the average spinal length along the walking cycle was considerably greater than during standing upright. From a group level, spine length was on average 1.6% longer during walking than standing (Student's t-test, $p<0.05$). Accordingly, the angle of lordosis decreased from standing to walking on average by 3.5 deg (Student's t-test, $p<0.05$), while the angle of kyphosis did not show significant variations across conditions.

Discussion

During walking, spine length was increased in correspondence of the beginning of the double support phase. Spine length was longer during walking than during upright standing. Lengthening of the column was associated to decreased lumbar lordosis and not to spinal kyphosis. The retroversion of pelvis can be responsible for this phenomenon. The relationship between these biomechanical variables describing spine mobility during walking may be relevant in investigating gait alterations related to spinal musculoskeletal diseases and low back pain.

References

1. Ferrari et al., Gait Posture, 28(2):207–216, 2008
2. Crosbie et al., Gait Posture, 5:6–12, 1997
3. Frigo C, Clin. Biomech., 18:419–425, 2003
4. Farinelli et al., Applied Sciences, 10(5):1606, 2020

APPLICATION OF REDUCED ORDER MODELLING TECHNIQUES FOR STRESS ANALYSIS IN SPINE FIXATION

Marco Sensale (1,2), Leonardo Geronzi (1,3), Marco Evangelos Biancolini (3,4), Tanguy Vendeuvre (5), Michel Rochette (1), Enrico Dall'Ara (2)

1. ANSYS, France; 2. University of Sheffield, UK; 3. University of Rome "Tor Vergata", Italy; 4. RBF Morph srl, Italy; 5. Poitiers University Hospital, France

Introduction

The posterior pedicle screw fixation is a widespread surgical treatment of vertebral fractures [1]. Loosening and failure of screws are complications that could result in loss of correction and kyphosis [2]. Experimental and numerical studies showed that the diameter of screws is predominant in influencing the stability of the instrumented spine after the surgery [3]. The effect of the diameter can be studied numerically by means of computed tomography (CT)-based finite element (FE) models. Nevertheless, parametric modelling is based on time-consuming workflows and can be used to test only some configurations of the diameter within the range of variation. The goal of this study was to use a reduced order model (ROM) based technology to estimate local mechanical quantities continuously in the range of variation of the parameters. A mesh morphing pipeline to build a parametric model with consistent meshes suitable to the application of the method was needed.

Methods

The pre-operative CT-scans of the thoracolumbar spine of three anonymized patients were processed to obtain the geometry of three lumbar vertebrae (L2, L3, L4). Two simplified pedicle screws (no thread, diameter D=6.5mm, length L=45mm) were inserted by a Boolean subtraction in the vertebrae. Two methods were used to change the diameter of the screws from 5.5mm to 7.5mm: a traditional computer aided design (CAD)-based workflow and a mesh morphing based one with RBF Morph™ [4]. Subject-specific FE models were used to simulate a quasi-static compressive load virtually transmitted through the rods to the head of screws (100N vertical load on each screw). The inferior endplate was fixed in the three directions. Both bonded (linear) and contact conditions (nonlinear, friction μ=0.3) at the screw-vertebra interface were tested. The Ti-6Al-4V screw was simulated as homogenous linear elastic material (E=102GPa, ν=0.36) and the bone as heterogeneous linear elastic material (E as function of the bone mineral density, ν=0.3). 10-nodes, 1.0mm size tetrahedrons were used for the bone and 20-nodes, 0.6mm size hexahedrons were used for the screws [5]. The max deflection (d_{max}) of the head of the screws and the max von Mises stress (σ_{VMmax}) of the screws were compared for models obtained with the traditional workflow or the morphing pipeline. A ROM of the deflection (d) and a ROM of the von Mises stress (σ_{VM}) on the screws were built with Ansys Static ROM Builder, for both linear and nonlinear models. The results from models with D=5.5, 6.5 and 7.5mm were used as training, while the results from models with D=6.0 and 7.0mm were used as validation. The maximum relative ROM error was reported.

Results

The average difference in d_{max} between standard and morphed models was lower than 1% and 4% for the linear and nonlinear cases, respectively (Table 1). The average difference in σ_{VMmax} was lower than 1% and 5% for the linear and nonlinear cases, respectively. The average maximum relative ROM error in d was lower than 1% (linear) and 2% (nonlinear) (Table 2). The average maximum relative ROM error in σ_{VM} was lower than 2% (linear) and 3% (nonlinear).

D	% diff - d_{max}		% diff - σ_{VMmax}	
(mm)	Linear	Nonlinear	Linear	Nonlinear
5.5	0.7±0.3	3.5±2.4	0.9±0.7	4.3±0.5
6.5	0.0±0.0	0.4±0.4	0.8±0.4	1.3±0.5
7.5	0.6±0.2	1.3±0.3	0.4±0.3	4.8±0.3

Table 1: Differences (mean ± st dev) between morphing and remeshing.

D	Max % err - d		Max % err - σ_{VM}	
(mm)	Linear	Nonlinear	Linear	Nonlinear
6.0	0.6±0.2	1.5±0.2	1.7±0.5	3.0±0.6
7.0	0.4±0.1	1.3±0.4	1.1±0.2	2.6±0.8

Table 2: ROM error (mean ± st dev) compared to morphing approach.

Discussion

The results of the present study show that the deflection and the von Mises stress on the pedicle screws can be predicted for any given diameter between 5.5 and 7.5mm with good accuracy (average max error of about 5%). This approach will be used to optimize the size of the screws in a large cohort of patients in future studies.

References

1. Wood et al, The Spine J, 14(1):145-164, 2014.
2. Butt et al, Int Orthopaedics, 31(2):259-264, 2007.
3. Bianco et al, Clin Biomech, 68: 190-196, 2019.
4. Biancolini,https://www.designnews.com/design-hardware-software/mesh-morphing-explained.
5. Sensale et al., Frontiers Bioeng Biotech, sub.

Acknowledgements

This project was funded by the EU H2020 programme Marie Skłodowska-Curie grant agreement Spinner No. 766012.

POTENTIALS TO STUDY LOAD SHARING MECHANISMS ADJACENT TO INTERBODY FUSIONS WITH ACTIVE HYBRID LUMBOSACRAL MODELS

Alina Hoffmann (1), Robin Remus (1), Beate Bender (1)

1. Chair for Product Development, Department of Mechanical Engineering, Ruhr-University Bochum, Germany

Introduction

Altered load sharing in spine segments has been identified as one biomechanical factor potentially inducing degenerative changes at levels adjacent to an interbody fusion, named adjacent segment degeneration (ASD) [1]. With a radiological prevalence between 36 % and 84 %, ASD represents one major complication after lumbar spinal fusion [2]. The mechanisms leading to different loading patterns are introduced by changes in height, angle, and material and immobilization of at least one functional spinal unit (FSU). Compensation mechanisms may shift the sagittal balance and the center of rotation (CoR), causing an increased loading of the posterior column and posterior shear force [3]. The aim of the present study was to review active hybrid lumbosacral models compared to finite element (FE), musculoskeletal (MS) and iterative-coupled hybrid models of the lumbosacral spine (LSS), in terms of their capability to represent the mechanisms affecting load sharing in segments adjacent to an interbody fusion.

Methods

Modeling parameters within simulative models affecting the prediction of load sharing mechanisms were reviewed. Principle assumptions of FE and MS models were summarized and compared to the formulation of both iterative-coupled hybrid models and active hybrid models. Potentials for studying load sharing mechanisms adjacent to interbody fusions with active hybrid LSS models were concluded.

Results

In general, two major modeling aspects for the simulative prediction of load sharing mechanisms exist, loading conditions and intervertebral joint formulations. On one hand, muscle lines-of-action, muscle forces and the modeling of the intraabdominal pressure influence the applied loading on FSU components. On the other hand, mechanical responses of the joint depend on material model formulations, stiffness and damping properties, pre-tensioning of ligaments, and the ability of moving CoR. In both, FE and MS models, modeling assumptions disadvantageously influence the prediction of load sharing mechanisms, a simplified formulation of loading conditions by a follower load [4] in FE and reduced intervertebral joint stiffness definitions between rigid bodies in MS. In iterative-coupled hybrid models, loading conditions from MS inverse dynamics are transferred to FE models. Iterative analyses (Figure 1A) enabling model convergence in terms of intervertebral joint properties, leading to quasi-static kinematically converged models [5]. However, the use of iterative-coupled hybrid models neglects passive resistance effects of both trunk musculature and the ligamentous spine [6, 7]. In contrast, active hybrid models (Figure 1B) combine MS and FE methods within a single model and incorporate interactions between passive and active spine structures. Thus, enabling further analyses especially in terms of pre-tensioning interdependencies, muscle force optimizations with ligamentous objectives and stabilizing effects of the musculature on the ligamentous spine.

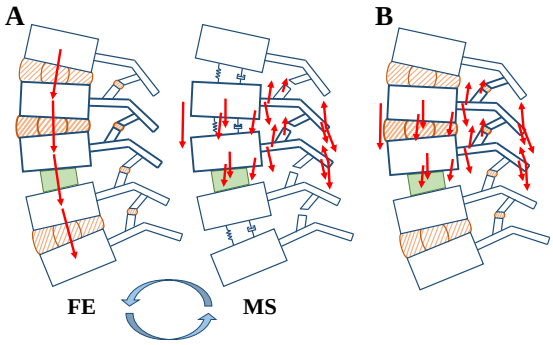

Figure 1: Modeling principles of (A) iterative-coupled hybrid and (B) active hybrid LSS models focusing on the FSU adjacent to an interbody fusion.

Discussion

Considerable insight has been gained within this study concerning potentials for simulating load sharing mechanisms in segments adjacent to lumbar interbody fusions. With active hybrid models, advantages of FE and MS methods for the study of load sharing mechanisms are combined, allowing improved analyses of compensation mechanisms, CoR movement, and mechanical responses. Future work will focus on the simulative verification of these findings by comparing load sharing mechanisms of a passive hybrid LSS model compressed by a follower load [8] with an active hybrid LSS model including a comprehensive muscle set and intraabdominal pressure effects.

References

1. Park et al, Spine 29:1938-1944, 2004.
2. Matsumoto et al, J Neurosurg Spine 26:435-440, 2017.
3. Umehara et al, Spine 25(13):1617-1624, 2000.
4. Patwardhan et al, Spine 24(10):1003-1009, 1999.
5. Khoddam-Khorasani et al, Ann Biomed Eng 46(11):1830-1843, 2018.
6. Hume et al, J Biomech 84:153-160, 2019.
7. Arjmand & Shirazi-Adl, J Biomech 39:510-521, 2006.
8. Remus et al, PLoS ONE, under review.

EVALUATION OF SPINE STABILITY FOLLOWING TREATMENT OF DEGENERATED INTERVERTEBRAL DISCS WITH DISCOPLASTY

Chloé Techens (1), Sara Montanari (1), Ferenc Bereczki (2), Peter Endre Eltes (2), Aron Lazary (2), Luca Cristofolini (1)

1. Department of Industrial Engineering, Alma Mater Studiorum – Università di Bologna, Italy;
2. National Center for Spinal Disorders - Budapest, Hungary

Introduction

Spinal nerve compression is often due to stenosis of the foramen, associated with intervertebral disc degeneration. In ageing population minimal invasive surgical (MIS) solutions can reduce the complication and provide good outcome. Percutaneous cement discoplasty (PCD) is a MIS procedure, that has been recently developed for the polymorbid ageing population with vacuum disc degeneration [1]. The mechanical impact of PCD on the spine stability and on the stress/strain in the surrounding tissues have not been investigated yet. A previous preliminary work on porcine spines demonstrated interesting trends and confirmed the potential benefits of discoplasty on degenerated discs. This study aimed at: (1) testing the stability of human spine segments after discoplasty by monitoring the disc height and the range of motion, (2) assessing the strains on the specimen surface for potentially dangerous peaks.

Methods

27 fresh-frozen human thoraco-lumbar FSUs were obtained from 15 cadaveric spines (35-86 y.o.). The soft tissues around the vertebral bodies were removed, leaving intact the ligaments. The specimens were aligned with the intervertebral disc horizontal; the extremities were potted with acrylic cement. In order to measure surface strains with Digital Image Correlation (DIC), a white water-based speckle pattern was sprayed on the specimens previously stained with methylene blue (Fig. 1). The specimens were tested in flexion and extension under 50% body weight axial load combined to an offset. Images were analysed by a 3D-DIC system (Q400, Dantec) using optimized parameters.

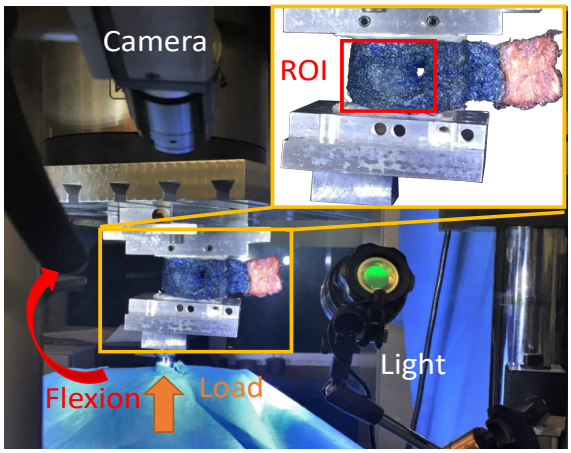

Figure 1: Experimental set-up in flexion. The Region of Interest (ROI) of DIC is located around the IVD.

The Range of Motion (ROM) and the Posterior Disc Height (PDH) were derived. The displacements and principal strains were also computed [2]. Each specimen was sequentially tested under two conditions:

- Simulated degeneration: the intervertebral disc was manually emptied through a hole in the annulus.
- after acrylic cement (Mendec Spine, Tecres) injection (discoplasty).

Results and Discussion

The PDH was significantly restored by discoplasty for both flexion and extension, increasing by 41% and 35% respectively. The ROM was significantly reduced in flexion due to the action of the posterior elements, but not significantly in extension. First and second principal strain concentrations were located on the disc surface for both motions (Fig. 2). Discoplasty decreased strain averages and concentrated first principal strain at the mid-height disc, while the second principal strain was clearly located along the endplates. Additionally, strain peaks were smaller after discoplasty, reducing the risk of local tissue damage.

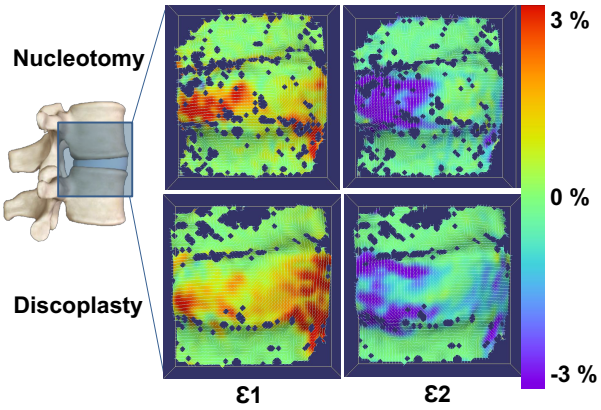

Figure 2: True principal strains (Ɛ1 and Ɛ2) at peak load in extension after nucleotomy, and discoplasty.

References

1. Varga *et al*, Der Ortho, 44:1-8,2015.
2. Palanca *et al*, MEP, 52: 76-83, 2018.

Acknowledgements

European Union's Horizon 2020 Marie Skłodowska-Curie ITN grant SPINNER No. 766012 and the Hungarian Scientific Research Fund (OTKA FK123884).

Ethical approval

The study was approved by the bioethical committee of University of Bologna, prot. 76497, 1 June 2018. The specimens were obtained through an International donation program and the hospital of NCSD.

EVALUATION OF THE NON-LINEAR DYNAMIC RESPONSE OF SILICON NITRIDE BIOCERAMIC

Xiaoyu Du (1), Gurdial Blugan (2), Stephen J. Ferguson (1)

1. Institute for Biomechanics, ETH Zurich, Zurich, Switzerland; 2. Laboratory for High Performance Ceramics, Empa, Swiss Federal Laboratories for Materials Science and Technology, Dubendorf, Switzerland

Introduction

Natural spinal tissues have unique dynamic properties. For instance, vertebral bone and intervertebral disc tissues show a frequency-dependent response, producing non-linear deformations under different loading conditions [1]. These may absorb shock energy and stabilize the spine but may also amplify the load input through resonance. Therefore, it is crucial to investigate the full dynamic response of spinal implants and related biomedical materials to ensure compatibility with the host tissue and fitness for purpose. Silicon nitride is a promising bioceramic for spinal implants [2]. In this study, the dynamic response of silicon nitride has been evaluated using novel and efficient testing methods, at both the material and structural level.

Methods

For the free vibration test, silicon nitride beams (SN) and zirconia beams (TZP) of 40mm*4mm*0.5mm were prepared. Then the fundamental vibration frequency of the beam material was measured experimentally by using a non-contact vibration measurement technique and the damping ratio was calculated from the envelope of the free vibration response using a logarithmic decrement. Porous silicon nitride cylindrical samples were fabricated with porosity range from 66% to 76%. Quasi-static compression tests were applied to test the Young's modulus and compressive strength of the porous samples. As quasi-static compressive tests do not predict well the behavior of structures during impact, a drop tower test [3] was employed to evaluate the impact response of porous silicon nitride scaffolds. Force of impact was measured using a piezoelectric load cell and the impact process was recorded by a high-speed video camera.

Results

The damping ratio was calculated by means of the free vibration decay response of the cantilever beam. Fig.1 (A) shows the comparison of the free vibration response of the different cantilever beams. The free vibration amplitudes decayed faster for the SN beam than for the TZP beam. The exponent of the envelope curve is also higher for the SN beam, reflecting the increased damping ratio, which is in good agreement with the damping ratio calculated using the logarithmic decrement as given in Fig.1(C). For the damped frequency, the SN beam is also significantly higher than the TZP beam.

The results of the quasi-static compression test showed that Young's modulus and compressive strength decreased non-linearly as porosity increased. On the other hand, the results of drop tower testing showed that the average ultimate strength of porous silicon nitride with ~76% porosity was 29.19 ± 4.37 MPa at impact at a speed of 1.7m/s, which is significantly lower than the compressive strength (50.01 ± 1.81 MPa) under quasi-static compression.

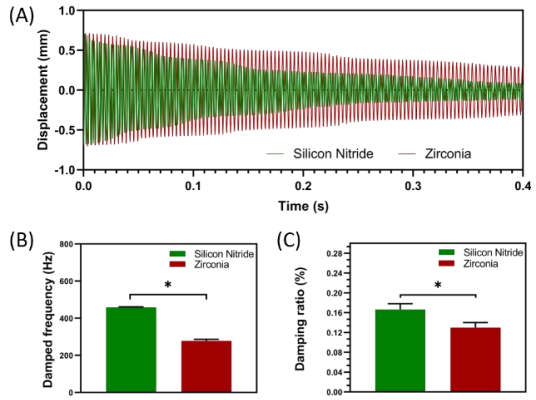

Figure 1: (A) Displacement vs. time curve, (B) Damped frequency, and (C) Damping ratio of the damped silicon nitride beam and zirconia beam.

Discussion

The results of free damped vibration tests of cantilever beams showed that a silicon nitride beam has a higher damping ratio than a zirconia beam. Ceramics with similar Young's moduli therefore can have different energy dissipating capacities. Porous implants have been proposed to promote osseointegration and reduce stress shielding. This study has demonstrated that increasing porosity of silicon nitride scaffolds can decrease the Young's modulus of scaffolds effectively. During the drop tower test, the interface between the dropped ball and scaffold may create a local stress concentration, which initiates failure of the scaffold. This test provides the mechanical behavior of silicon nitride scaffolds under impacts at extremely high strain rates, adding valuable data to allow the pre-clinical assessment of potential catastrophic failure modes of the implant or implant-bone interface.

Overall, silicon nitride possesses high stiffness and strength, but low damping properties. Altering the porosity of silicon nitride is a possible way to tailor its dynamic response.

References

1. Marini et al, J Biomech, 48:479-488, 2015.
2. Bal et al, Acta Biomater, 8:2889-2898, 2012.
3. Enns-Bray et al, J Biomech, 75:46-52, 2018.

THE EFFECT OF DEGENERATION ON INTERNAL STRAINS AND THE MECHANISM OF FAILURE IN HUMAN INTERVERTEBRAL DISC

Saman Tavana (1), Spyros D. Masouros (2), Nicoleta Baxan (3), Brett A. Freedman (4), Ulrich N. Hansen (1), Nicolas Newell (1)

1. Dept. of Mechanical Engineering, Imperial College London, UK; 2. Dept. of Bioengineering, Imperial College London, UK; 3. Biological Imaging Center, Imperial College London, UK, 4. Dept. of Orthopedic surgery, Mayo Clinic, USA

Introduction

Low back pain (LBP) is a common cause of disability, which affect 70-85 % of us in our lifetimes [1]. Previous studies have shown a link between intervertebral disc (IVD) degeneration and LBP [2]. Degeneration changes the mechanical behavior of IVDs and alters the load distribution over the vertebral bodies that can affect the mechanism of spinal fracture [3]. The aim of this study was to 1) compare 3D internal strains in degenerate and non-degenerate human IVD under axial compression and 2) to investigate whether there is a correlation between strain patterns and failure locations.

Methods

9.4T MR images were obtained of ten human lumbar IVDs. Five were classed as degenerate (Pfirrmann = 3.6 ± 0.3) and five were classed as non-degenerate (Pfirrmann = 2.0 ± 0.2). MR Images were acquired a) before applying load, b) after 1 kN of axial compression, and c) after compression to failure using a T2-weighted RARE sequence (resolution = 90 µm). Digital Volume Correlation (DVC) was then used to quantify 3D strains within the IVDs, and failure locations were determined from analysis of the failure MRIs and real-time fluoroscopic images captured during the failure tests.

Results

The average axial strain (ε_{yy}), minimum 3D principal strain, and maximum 3D shear strain in the loaded discs were all significantly larger in the degenerate compared to non-degenerate IVDs, particularly in the posterior and lateral annulus (Figure 1). Specifically, axial strain was -5.37 ± 0.90 % in the degenerate vs -3.39 ± 0.88 % in the non-degenerate discs (p=0.03), minimum 3D principle strain was -9.28 ± 0.76 % in the degenerate vs -6.51 ± 0.56 % in the non-degenerate discs (p=0.002), and maximum 3D shear strains were 8.07 ± 0.65 % in the degenerate vs 5.72 ± 1.02 % in the non-degenerate discs (p=0.01). Generally, peak tensile and shear strains were observed close to the endplates for all IVDs. All samples failed through the endplates with fractures in the nucleus region in all non-degenerate samples, and fractures in the lateral annulus regions in all degenerate samples (Figure 2(a)). Additionally, combining the strain distributions in the transverse plane of the IVD tissue with the location of endplate fracture demonstrated that endplate fractures were always located in the high axial strain regions in the degenerate IVDs (Figure 2(b)) [4].

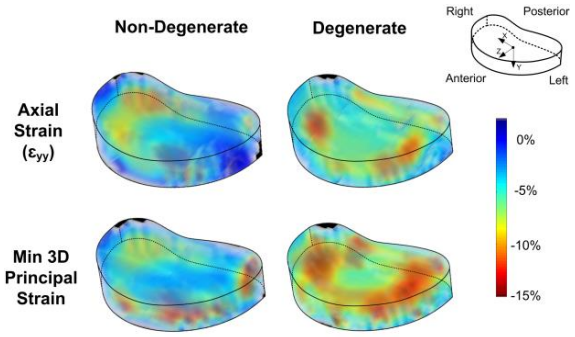

Figure 1: 3D strain maps of axial (ε_{yy}) and min principal strains for non-degenerate and degenerate IVDs [4].

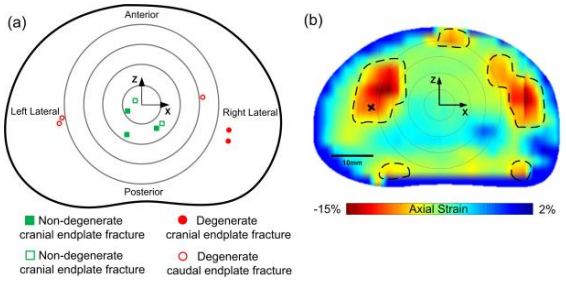

Figure 2: Normalised locations of endplate fracture in each of the samples tested (a). Axial strain distributions in the transverse plane of a degenerate IVD overlaid by the location of endplate fracture (b). Regions inside the dashed lines indicate high axial strain regions, and black crosses denote locations of fracture [4].

Conclusion

Degeneration caused significant changes to strain distributions within IVDs during axial compression, particularly at the lateral and posterior annulus. Degeneration also caused a shift of endplate fracture from the nucleus region to the annulus region. The fact that endplate fractures were seen in regions with high axial strains in the degenerate IVDs makes it reasonable to conclude that IVD degeneration plays an important role in the mechanism of vertebral fracture, and axial strains could be used to identify locations with higher risks of fracture in degenerate IVDs [4].

References

1. Hoy et al, Ann. Rheum. Dis, 73: 968–974, 2014.
2. Luoma et al, Spine, 25:487-492, 2000.
3. Adams et al, Spine, 31, 2151–2161, 2006.
4. Tavana et al, Front. Bioeng. Biotechnol, 8:610907.

TYPE, SIZE AND POSITION OF THE METASTASIS AS INDICATORS FOR BETTER PREDICTING THE BEHAVIOUR OF METASTATIC VERTEBRAE

Marco Palanca[1,3], Giovanni Barbanti-Bròdano[2], Daniele Marras[3], Alessandro Gasbarrini[2], Enrico Dall'Ara[1], Luca Cristofolini[3]

Dept of Oncology and Metabolism, and INSIGNEO Institute for in silico medicine, University of Sheffield, UK
Dept of Oncology and Spine Surgery, Rizzoli Orthopaedic Institute, IT
Dept of Industrial Engineering, Alma Mater Studiorum – University of Bologna, IT

Introduction

In the oncological field, the evaluation of the mechanical weakness of metastatic vertebrae and the rational for their stabilization is still a challenge. The Spine Instability Neoplastic Score (SINS) is the current scoring system that aims to aid the clinicians in deciding whether surgery is needed to stabilize the spine [1]. The SINS relies on radiographical and subjective parameters, but due to the metastasis variability, the actual outcomes are often catastrophic (fracture) or possibly leading to unnecessary treatment [2].
The aim of this work was to identify the metastatic features (among those evaluable in the clinical practice), that explain the variation of the mechanical competence of the metastatic vertebra, in comparison to the clinical spine characterization provided by the SINS.

Materials and Methods

Thirty-five spine segments, consisting of a metastatic vertebra, a control vertebra and two external vertebrae, were obtained from an ethically approved donation program. Each spine segment was scanned with a quantitative computed tomography (qCT) in order to evaluate the type of the metastasis, the position within the vertebral body, and measure the volume of the metastasis with respect to the vertebral body. Biomechanical tests were performed loading each spine segment in four different conditions: flexion, right and left lateral bending, and pure compression. A state-of-the-art Digital image Correlation (GOM Aramis 12M) with four 12MPixels cameras was used to evaluate the strain distribution [3] on the vertebral body surfaces of the metastatic and control vertebrae. The Biomechanical Ratio (BR) was defined as the ratio between the minimum principal strain on the metastatic vertebra and the control vertebra. The BR was used as a surrogate of the competence of the metastatic vertebra in direct comparison with the control one. Finally, the correlations between the different metastatic features and the BR were analyzed.

Results

The vertebrae with lytic metastasis showed more critical BR (>1) with respect to those with mixed or blastic metastasis (Fig, 1). Significant correlation was found between the size of lytic metastasis and BR (r^2=0.42). Poor or non-significant correlations were found for blastic or mixed metastasis (Fig. 2). The correlation between lytic size and BR was further improved (R^2=0.72) when the position of the lesion with respect to the load direction (ipsilateral and contralateral scenario) was taken into account (Fig. 2).

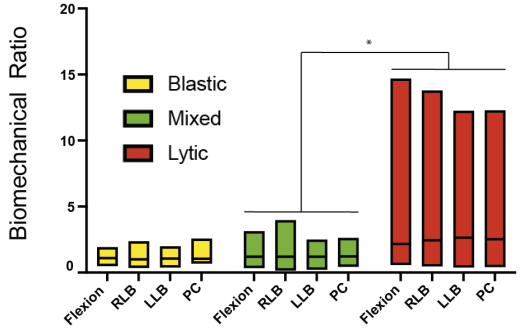

Fig. 1: effect of the metastasis type and loading condition (Flexion, Right and Left Lateral Bending, Pure Compression) on the BR. Different behavior was observed for the different metastasis (Kruskal-Wallis, p = 0.016).

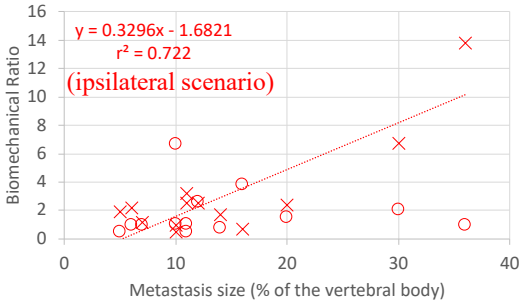

Fig. 2: Correlation between the size of the lytic metastasis in ipsilateral (X) and contralateral (O) scenario and the BR.

Discussion

While there was a weak significant correlation between SINS and BR for the considered specimens (r^2=0.12) [4], the combination of metastasis type, lesion size and position, explained 72% of the variability. In particular, this strong agreement was obtained for the lytic lesions, which affected largely the vertebral mechanical properties. Blastic and mixed metastases, instead, showed a range of minimum principal strains similar to the control vertebrae. This evidence suggested to include the metastatic features as additional parameters to better identify metastatic spines which require a surgical consultation.

References

[1] Fisher et al, Spine 35 (22); [2] Versteeg et al., The Oncologist, 21 (1); [3] Palanca et al., MEP, 52; [4] Palanca et al, Bone, under review

Acknowledgements

The study was partially funded by the AOSpine Discovery and Innovation awards (AOSDIA 2019_063_TUM_Palanca), Marie Skłodowska-Curie Individual Fellowship (MetaSpine, MSCA-IF-EF-ST, 832430/2018) and by the Engineering and Physical Sciences Research Council (EPSRC) Frontier Multisim Grant (EP/K03877X/1 and EP/S032940/1).

MOTION CAPTURE-DRIVEN MUSCULOSKELETAL SPINE MODELING: AN OPENSIM-BASED INVERSE KINEMATICS APPROACH

Stefan Schmid (1), Lukas Conolly (2,3), Greta Moschini (3,4), Michael L. Meier (2), Marco Senteler (3,4)

1. Spinal Movement Biomechanics Group, Department of Health Professions, Bern University of Applied Sciences, Switzerland; 2. Integrative Spinal Research, Department of Chiropractic Medicine, Balgrist University Hospital, University of Zürich, Switzerland; 3. Department of Health Science and Technology, ETH Zurich, Switzerland 4. Department of Orthopedics, Balgrist University Hospital, University of Zürich, Switzerland

Introduction

Being able to non-invasively determine spinal loading during functional activities is crucial for better understanding spinal disorders and to improve treatment modalities. In this work, we present a novel approach for creating subject-specific musculoskeletal full-body models with a detailed spine, modelled according to the external back profile obtained from motion capture data.

Methods

As a basis, we created OpenSim-based female and male full-body models by combining a fully articulated thoracolumbar spine and rib cage model [1,2] with a standard lower body model. Virtual markers were added to enable motion capture-driven simulations based on a previously described configuration [3]. Subject-specific models were created by scaling the lengths and masses of the individual segments as well as by adjusting position and orientation of the intervertebral joints (IVJ) based on a 4th order polynomial fit through the sagittal plane coordinates of the markers placed over the spinous processes. For validating spinal curvature adjustments, we conducted a radiographic analysis using radio-opaque skin markers attached to the back of three healthy adults. To ensure the suitability of the models for estimating spinal loading during functional activities, we conducted motion capture-driven simulations based on data from 17 additional healthy adults and compared the model predictions with *in vivo* measured data obtained from the OrthoLoad database.

Results

IVJ positions were predicted with an average mean error of 0.99±0.68 cm on the frontal and 1.21±0.97 cm on the transverse axis (Figure 1).

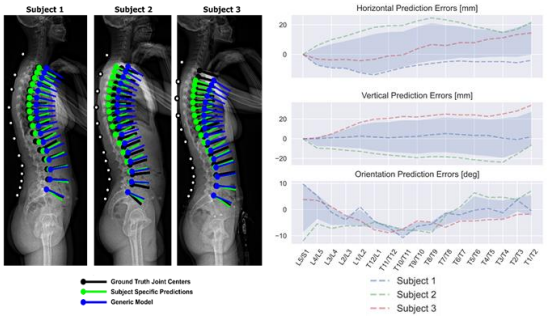

Figure 1: Radiographic evaluation of subject-specific skin marker-derived spinal curvature adjustments with joint center position and orientation prediction errors.

The mean prediction error for vertebral body orientation in the sagittal plane was 4.74°±2.78°.
Estimated segmental compressive forces showed similar characteristics but were considerably larger as compared to the *in vivo* measured data (Figure 2).

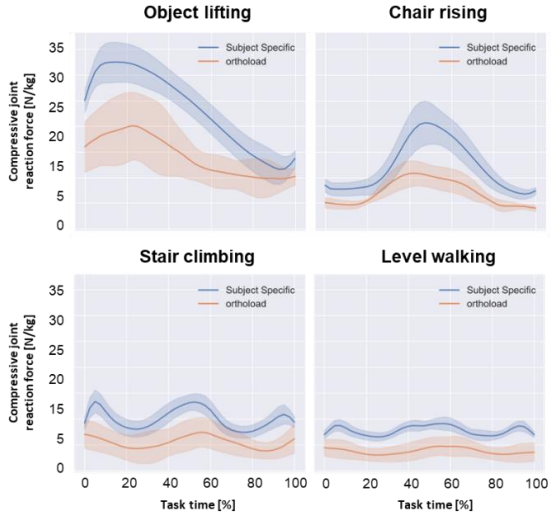

Figure 2: Compressive joint reaction forces at the level L1/L2 predicted by our subject-specific models (blue) and obtained from the OrthoLoad database (orange).

Discussion

This novel method for creating subject-specific musculoskeletal full-body models showed improved accuracy for inverse kinematics-based spinal curvature estimation. In addition, our models were able to perform joint reaction force estimations for a variety of functional activities (including such with large trunk inclinations) with minimal intra-subject variability and clearly distinguishable loading curves between subjects, indicating that the simulation pipeline and the reference models are robust. The proposed workflow represents a powerful tool to address a variety of issues relevant to spinal loading in a scientific and clinical context.

References

1. Bruno et al, J Biomech Eng, 137:081003, 2015.
2. Bruno et al, J Bone Miner Res, 32:1282-90, 2017.
3. Schmid et al, Hum Mov Sci, 54:73-81, 2017.

Acknowledgements

This work was supported by the Swiss National Science Foundation (SNSF, grant-no.: 185123).

ANALYSIS OF EARLY-ONSET SCOLIOSIS INSTRUMENTATION USING GROWING-ROD AND GROWTH GAUIDANCE SYSTEMS

Xiaoyu Wang (1) (2) and Jason Pui Yin Cheung (3)

1. Polytechnique Montreal, Canada; 2. Sainte-Justine University Hospital Center, Canada; 3. Department of Orthopaedics and Traumatology, The University of Hong Kong, Hong Kong SAR, China

Introduction

Growth-friendly instrumentation constructs for early-onset scoliosis (EOS) include distraction-based and growth guidance systems [1]. Biomechanical data are very limited to assist surgeons in their decision-making with regard to the most appropriate surgical solutions for a give patient [2]. Surgeons have to choose between fundamentally different systems and deal with implant pullout, implant migration, rod breakage and bone fracture [3]. The goal was to develop patient-specific biomechanical spine model to assess intraoperative correction and forces in the instrumented spine.

Methods

Geometric models reconstructed from preoperative radiographs of upright, prone, and suspension positions were used to build a simplified spine model (Fig. 1). Stiffness matrices were used to model intervertebral load-displacement relations incorporating the effects of rib cage, intervertebral joints, ligaments and muscles. The stiffness matrices were calibrated such that Cobb angles in simulated upright, prone and suspension positions agreed with those measured on the reconstructed models. Proof-of-concept simulations were done for growth guidance and growing rod (distraction-based) systems.

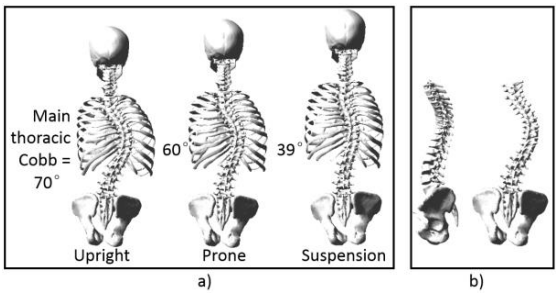

Figure 1: a) Geometric models reconstructed from preoperative radiographs; b) Simplified spine model

Results

Cobb angles in simulated upright, prone, and suspension positions were within 5° to those measured on geometric models reconstructed from preoperative radiographs. Typical primary stiffness coefficients are presented in Table 1. Simulated Cobb angles with the four types of constructs (Fig. 2) were 33°, 31°, 36°, and 30°, respectively. Bone-implant forces were primarily in the transverse plane with growth guidance construct (Fig. 3) and in the caudocranial direction with the growing rod construct.

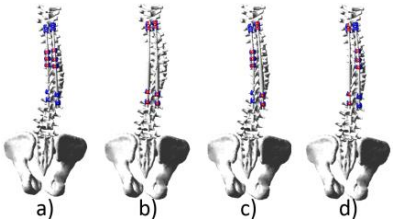

Figure 2: Model views: a) Growth guidance; b) Growing rods; c) Growth guidance and growing rod; d) Growing rod and growth guidance

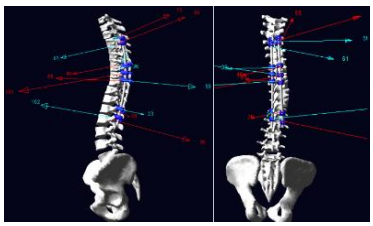

Figure 3: 3D bone-implant force vectors

x-axis (posteroanterior)	y-axis (left-right)	z-axis (caudocranial)
T9-T10 translational stiffness (N/m)		
5.9825E+4	9.739E+4	5.0E+5
T9-T10 rotational stiffness (Nm/Rad)		
98.221335	91.673245	114.59156
L2-L3 translational stiffness (N/m)		
8.8181E+4	1.3864E+5	6.25E+5
L2-L3 rotational stiffness (Nm/Rad)		
27.370595	33.934955	99.42581

Table 1: Typical primary stiffness coefficients

Discussion

The EOS spine model exhibited the spine behavior in terms of Cobb angles in upright, prone, and suspension positions. The model allowed simulations of EOS instrumentation using growth guidance and growing rod systems to assess deformity correction and forces in the instrumented spine. Postoperative spinal growths are expected to be different because of significant difference in force patterns in the instrumented spine.

References

1. Skaggs DL et al. A classification of growth friendly spine implants. J Pediatr Orthop. 2014;34(3):260-74.
2. Vitale MG et al. Variability of expert opinion in treatment of early-onset scoliosis. Clin Orthop Relat Res. 2011; 469(5):1317-22.
3. Akbarnia BA et al. Complications of growth-sparing surgery in early onset scoliosis. Spine (Phila Pa 1976). 2010;35(25):2193-204.

ASSESSMENT OF DEFORMATIONS IN HUMAN METASTATIC VERTEBRAE WITH DIGITAL VOLUME CORRELATION

Giulia Cavazzoni[1-2], Marco Palanca[2], Luca Cristofolini[1], Enrico Dall'Ara[2]
1. *Dept of Industrial Engineering, Alma Mater Studiorum – University of Bologna, Bologna, IT*
2. *Dept of Oncology and Metabolism, and INSIGNEO, The University of Sheffield, Sheffield, UK*

Introduction

Vertebrae affected by metastases have an altered bone tissues distribution that may reduce the load bearing capacity. A comprehensive characterization of the metastatic vertebrae is fundamental to identify, and consequently treat, those at high risk of fracture. Digital Volume Correlation (DVC) is a technique that allows to measure the displacement and the strain field within the bone, through time-lapsed testing within a micro-computed tomography (μCT). Thereby, it could provide a local characterization of the entire metastatic vertebra. However, its effectiveness on tissues with highly variable trabecular pattern, as those affected by the different types of metastases (blastic, lytic, mixed), remains unclear. The aim of the study was to evaluate the potential of a global DVC approach to study the deformation in human metastatic vertebrae.

Materials and Methods

Fresh-frozen human thoracolumbar spines, with mixed or lytic metastases, were obtained through an ethically approved donation program. Ten segments consisting of two central vertebrae (one with metastases and one control) were prepared. Each specimen was mounted in a jig and μCT scanned (Scanco VivaCT80, current 114mA, voltage 70kVp, isotropic voxel size: 39 μm). Each unloaded specimen was scanned twice (the second time only a central portion with metastases was scanned). Then, each specimen was compressed until failure (1200-5000 N) and scanned again. DVC analysis (BoneDVC) was performed with nodal spacing of 50 voxels [1]. The systematic and random errors were computed for each component of strain and for the principal strains, as well as the standard deviation of the error (SDER: standard deviation of the average of the absolute values of the six strain components [2]). The median of the principal compressive strains (eps3) were computed in metastatic and control vertebrae for each specimen. Differences between the median values were tested with Mann-Whitney test for each specimen.

Results

The SDER values ranged over a wide interval from 118 to 840 με over the sample. Larger systematic and random errors were found in the coronal plane in 8 specimens out of 10. The values of eps3 for metastatic and control vertebrae were significantly different (Fig. 1, $p<0.0001$) for five specimens. In most vertebrae with mixed lesions, the eps3 was 20-40% lower than the controls. In vertebrae with lytic lesions the eps3 was 200-600% higher than the controls. The distribution of eps3 in the metastatic vertebrae was highly heterogeneous (Fig 2).

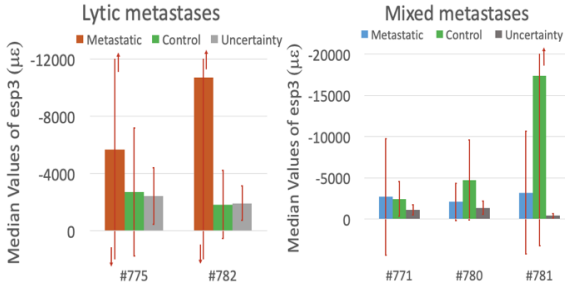

Fig1: Median values of the minimum principal strains (eps3) for metastatic, lytic and mixed, and control vertebrae.

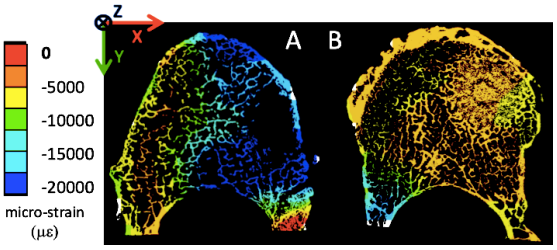

Fig2: Distribution of minimum principal strains in a lytic (A) and mixed (B) metastatic vertebra on μCT cross section.

Discussion

SDER was similar to that found on previous studies on human healthy vertebrae [3].

For each specimen the eps3 for the control and metastatic vertebra were significantly different. However, the lesion increased or decreased the strain in relation to the type of metastasis, highlighting the importance of considering the lesion type in assessing the vertebral mechanical behaviour. In vertebrae with mixed metastases, the blastic regions experienced lower strains when compared with normal tissue or lytic regions within the same vertebra (Fig.2). Thus, the 3D strains field is related to the distribution of the bone tissue within the vertebral body.

In conclusion, this study highlights the potential of a global DVC approach to study the effect of different lesion types on the local deformation of human metastatic vertebrae.

References

1. Dall'Ara E. et al. (2014) *JBiom* **47**: 2956-2963
2. Palanca M. et al (2016) *JBiom* **49** 3882–3890
3. Hussein A.I. et al. (2012) *Procedia IUTAM* ***4***: 116–125

Acknowledgements

The study was partially funded by the AOSpine Discovery and Innovation awards (AOSDIA 2019_063_TUM_Palanca), Marie Skłodowska-Curie Individual Fellowship (MetaSpine, MSCA-IF-EF-ST, 832430/2018) and by the Engineering and Physical Sciences Research Council (EPSRC) Frontier Multisim Grant (EP/K03877X/1 and EP/S032940/1).

RELATIONSHIP BETWEEN POSTURAL ALIGNMENT ALTERATION AND VERTEBRAL STRENGTH

Cecile Heidsieck (1), Laurent Gajny (1), Chistophe Travert (2), Wafa Saklli (1)

1. Arts et Metiers ParisTech, Institut de Biomécanique Humaine Georges Charpak, Paris, France

2. Département de Chirurgie Orthopédique et Traumatologique, Groupe hospitalier Pitié-Salpêtrière, Paris France

Introduction

Osteoporotic fractures are a major health issue because they increase morbidity and mortality [1]. Areal bone mineral density (aBMD) measurement with dual-energy X-ray absorptiometry (DXA) is the reference technique to evaluate fracture risk, but its sensitivity is low [2]. Finite element models (FEMs) based on quantitative computer tomography (qCT) were developed to allow vertebral strength estimation with personalized mechanical properties and geometry. They provide a validated assessment of vertebral intrinsic strength [3]. However, during a CT scan, the subject is evaluated in a supine position, which does not allow personalized loading conditions while sagittal alignment has been proven to evolve with age. Also, an abnormal forward spinal inclination was found in subjects consulting for osteoporosis, even for those without vertebral fractures [4]. The purpose of this study was to analyze the impact of postural alignment changes with age on vertebral strength using finite element analysis and barycentremetry.

Methods

117 subjects were included, 61 male (M) and 63 female (F) from 20 to 83 years old. Three groups were formed, a young group: 20 to 40 years, 61 subjects (32M, 29F); an intermediate group: 40 to 60 years old, 33 subjects (16M, 17F) and an elderly group : 60 years and over, 29 subjects (13M, 16F). EOS biplane radiographs were acquired in standardized free standing position, allowing 3D reconstruction of the spine and body envelope [5,6]. Spinal and pelvic parameters were measured on the 3D reconstructions. A barycentremetry method [7] allowed to compute the mass the of upper body above L1, chosen as the study vertebra, as well as the position of the center of mass (CoM) of this segment against the center of the L1 upper endplate (lever arm).
To isolate the impact of this lever arm on vertebral strength, a previously validated L1 vertebra FEM [3] was used. Vertebral strength of the same model (same geometry and same mechanical properties) was successively computed applying the personalized lever arm of each subject (figure 1a).

Results

A combination of an increase in thoracic kyphosis and cervical lordosis with a loss of lumbar lordosis was observed between the young and the older groups. In addition, pelvic tilt was significantly higher in the older group than in the other two age groups.
The sagittal postural alignment alteration with age resulted in a variation of the lever arm of the center of mass above L1, from 1 mm backwards for the young group, to 7 and 24 mm frontwards, respectively for the intermediate and the elderly group (figure1b).

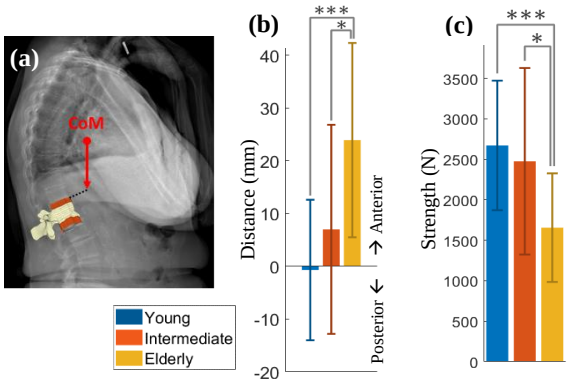

*Figure 1: (a) Example of the personalized loading conditions on the FEM, (b) Antero-posterior distance (mean and 1*SD) between the upper body center of mass above L1 and the center of L1, (c) computed strength (mean and 1*SD) with personalized boundary conditions*

As a result, the vertebral strength decreased from 2547 N for the young group to 1820 N for the older group (figure 1c).

Conclusion

Posture alteration with age was found consistent with the literature [4]. Based on barycentremetry, lever arm of the subjacent center of mass yielded simplified loading conditions. Further refinement of the loading model could be considered. However, given the current results, for a unique vertebral model (same mechanical properties and geometry), posture alteration with age reduced significantly vertebral strength. Postural alignment seems essential to be considered in the evaluation of osteoporotic patients. Also, subject specific FEMs for strength estimation should not only take into account subject specific geometry and material properties, but also subject specific loads.

References

1. Johnell et al., Osteoporos Int, 17(12):1726–33, 2006
2. Cosman et al., Osteoporos Int, 28:1857–1866, 2017
3. Choisne et al., J. Mech Behav Biomed, 87, 190–196, 2018
4. Fechtenbaum et al., Osteoporos Int, 27(2), 559–567, 2016
5. Gajny et al., Eur. Spine J., 28(4), 658–664, 2018
6. Nérot et al., J. Biomech., 48(16), 4322–4326, 2015
7. Amabile et al., J. Biomech, 49(7), 1162–1169, 2016

Acknowledgements

The authors thank the ParisTech BiomecAM chair program on subject-specific musculoskeletal modelling and in particular Société Générale and COVEA.

EXAMINING THE BIOMECHANICAL BEHAVIOR OF THE HUMAN LUMBAR SPINE UNDER COMBINED LOADING USING A NOVEL IN-VITRO TEST PROTOCOL

Nadja Wilmanns (1), Agnes Beckmann (1), Luis Fernando Nicolini (1), Christian Herren (2), Rolf Sobottke (3), Frank Hildebrand (2), Jan Siewe (4,5), Philipp Kobbe (2), Bernd Markert (1), Marcus Stoffel (1)

1. Institute of General Mechanics, RWTH Aachen, Germany; 2. Department for Trauma and Reconstructive Surgery, University Hospital RWTH Aachen, Germany; 3. Department of Orthopaedics and Trauma Surgery, Rhein-Maas Klinik, Germany; 4. Department of Spine Surgery, Klinikum Leverkusen gGmbH, Germany; 5. Faculty of Medicine, University Hospital of Cologne, Germany

Introduction

Most daily life movements require bending of the lumbar spine around all three anatomical axes simultaneously [1]. Nevertheless, the relationship between multiaxial loads on the spine and resulting biomechanical material response have not yet been fully understood. Due to limited experimental data most finite element (FE) models of the lumbar spine, a widely used tool for analyzing biomechanical behavior, could only be validated for simplified uniaxial motions, which limits the possibilities for effective interpretation of physiological motions [2]. In this study, *in-vitro* tests applying a new test protocol with multiaxial bending moments on the human lumbar spine were performed and used to validate a corresponding FE model.

Methods

Range of motion (RoM) of 10 human lumbar spine specimens (L2-L5) were tested with uniaxial moments in all three directions as well as combined loadings - axial rotation (AxRot) with previously applied moments in lateral bending (LatBend) and flexion (Flex)/extension (Ex). A humidified chamber at body temperature was included in the test set up [3]. An FE model was calibrated using the uniaxial and validated using the combined loading RoM data of the performed experiments.

Results

RoM in AxRot was reduced for all combined loading conditions and segmental levels compared to uniaxial loading (all $P<0.001$). RoM in AxRot declined stronger in combination with Ex than in Flex (all $P<0.0001$). A direction-dependent behavior in combination with LatBend was not noted ($P>0.05$). For all segmental levels and directions, the simulated results stand in good agreement with the experimental data (all $R^2>0.79$, Fig.1).

Discussion

A reduction of RoM in AxRot with combined Ex is concordant with previous studies [4,5]. Comparing the results for combined loading in Flex with these studies, a dependency of the RoM on the applied follower load is assumed. Underlying results of the *in-vitro* study and the FE simulation suggest, that the restriction of RoM in AxRot in combination with Flex, Ex and LatBend, is caused by additional loading of both, the facet joints as well as the intervertebral disc (IVD). This study presents a validated FE model of the lumbar spine for multiaxial loading conditions. The applied method and the experimental data of the *in-vitro* study can be used for further investigations of the kinematics of the spinal complex.

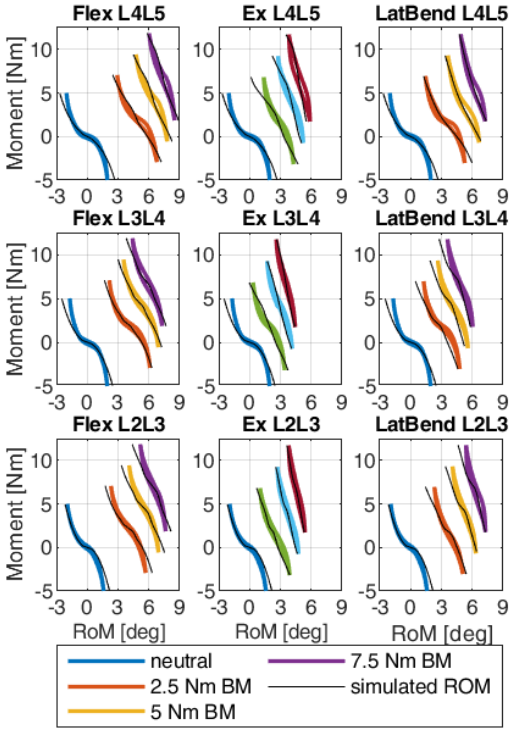

Figure 1: Experimental and simulated RoM curves in AxRot for previously applied bending moments (BM) in Flex, Ex and LatBend. Offsets in x- and y-directions are equal to average RoM and applied moment in Flex/Ex/LatBend direction, respectively.

References

1. Bible et al, J. Spinal Disord Tech, 23(2):106-112, 2010.
2. Dreischarf et al, J Biomech, 47(8):1757-1766, 2014.
3. Beckmann et al, Biomed Tech, 63(4):341-347, 2018.
4. Haberl et al, Eur Spine J, 13(6):560-566, 2004.
5. Burnett et al, Man Ther, 13(4):300-306, 2008.

MECHANISMS OF LUMBAR DISC HERNIATION FAILURE AFTER 6DOF FATIGUE: EFFECT OF MULTIAXIAL LOADING

Michael P Russo (1), Daniel Ciric (1), Dhara B Amin (1), John J Costi(1)

1. Medical Device Res. Institute, College of Science & Engineering, Flinders University, Adelaide, Australia

Introduction

Repetitive lifting (fatigue) and rapid application of high compressive loads (sudden overload) cause disc injuries and herniation [1-3], potentially impinging nerve roots. Fatigue under different combinations of postures (flexion, lateral bending, and axial rotation) may result in altered six degree of freedom (6DOF) mechanics. No study has characterised 6DOF mechanics in these postures, nor compared failure mechanics after fatigue. This study aimed to compare the effect of fatigue loading on 6DOF mechanics and sudden overload failure properties between three combinations of simulated postures.

Methods

The initial 6DOF properties of twenty-four dissected sheep lumbar segments (L4-L5), with facet joint capsules and associated ligaments intact, were measured in a hexapod robot [4]. Specimens were then randomly assigned into one of three combined postures: 13° flexion and 2° left axial rotation (F+R); 10° left lateral bending and 2° left axial rotation (LB+R); 13° flexion and 10° left lateral bending (F+LB), under which 10,000 cycles of combined fatigue loading at 1 Hz with 1.7 MPa of compression were applied [5]. Post-fatigue 6DOF properties were then immediately measured after fatigue loading. Specimens were rotated to their assigned posture and failed at 400 mm/min in compression [2]. A repeated measures ANOVA was performed to identify significant differences in 6DOF stiffness or phase angle (a measure of energy absorption) after fatigue within each posture. A one-way ANOVA compared failure stress and stiffness between postures with post-hoc multiple comparisons using a Bonferroni adjustment. Failure mode was determined by visual inspection.

Results and Discussion

Significant decreases in 6DOF stiffness (Table 1) for all fatigue postures was measured in right lateral shear (p<0.035), left/right axial rotation (p<0.045) and flexion (p<0.012). In addition, posterior shear stiffness significantly decreased after fatigue loading in F+R (p<0.001) and F+LB (p=0.031). Extension stiffness significantly decreased only after F+LB fatigue (p=0.040). No significant change was measured in anterior shear or left/right lateral bending after fatigue for all postures. Facet joint laxity may contribute to stiffness decreases since fatigue loading was applied at extreme ranges of motion. Phase angle significantly increased (Table 1) after fatigue in left lateral shear and anterior shear for LB+R (p<0.030) and F+LB (p<0.015), while right lateral shear only increased in F+LB (p=0.021). Left/right lateral bending phase angle significantly increased for F+R (p<0.045) and LB+R (p<0.010). Left axial rotation phase increased only for F+R (p=0.024), while right axial rotation increased for LB+R (p<0.010) and F+LB (p<0.015). Significant increases in flexion and extension phase angles were seen in F+R (p<0.015) while only extension increased for LB+R (p=0.015) and flexion for F+LB (p=0.003). Overall, significant increases in phase angle indicated that specimens absorbed more energy after fatigue loading in their respective loading directions.

There was no significant difference in sudden overload failure stress between the three postures (p=0.142). While the overall effect of posture was significant for stiffness during the overload failure test (p=0.045), post-hoc comparisons revealed LB+R to be marginally not significantly stiffer than F+LB (p=0.05). All remaining comparisons between each respective posture revealed no significant differences (p>0.242). Visually, posterior or posterolateral herniations were more common in F+R (28%) and F+LB (52%) compared to LB+R (0%).

	Stiffness			Phase Angle		
	F+R	LB+R	F+LB	F+R	LB+R	F+LB
Left Lat Shear		0.007	0.017		0.002	0.013
Right Lat Shear	0.032	0.007	0.010			0.021
Anterior Shear					0.020	0.005
Posterior Shear	0.000		0.031			
Right Lat Bending				0.043	0.006	
Left Lat Bending				0.013	0.023	
Left Axial Rotation	0.034	0.045	0.040	0.024		
Right Axial Rotation	0.000	0.002	0.001		0.010	0.011
Extension			0.040	0.014	0.015	
Flexion	0.001	0.009	0.004	0.004		0.003

Table 1: Stiffness and phase angle p-values for all significantly affected directions after fatigue loading.

Conclusion

Postures that included flexion were the only combinations that led to posterior or posterolateral herniations. Postures with flexion showed reduced posterior shear stiffness, while postures with lateral bending reduced left lateral shear stiffness. A reduced ability to resist shearing deformation may lead to disc annulus tearing from large interlamellar shearing strains. Combined loading in F+LB may explain the higher susceptibility to posterolateral herniation.

References

1. Jordan et al, *BMJ Clin. Evid*. 2011:1118, 2011.
2. Wade et al, *Spine*, 40(12), 891-901, 2015.
3. Adams et al, *Spine,* 1982, 7(3), 184-191.
4. Ding et al. *J. Dyn. Syst-Trans ASME,* 2014
5. Wilke et al, Eur Spine J 25(5): 1363-72, 2016

ON THE SIMULATION OF LUMBAR SPINE LIGAMENTS DEGENERATION

M. I. Godinho (1), V. Carvalho (1), P. R. Fernandes (1), A. P. G. Castro (1)

1. IDMEC, Instituto Superior Técnico, Universidade de Lisboa, Lisbon, Portugal;

Introduction

Low back pain (LBP) is an emerging problem in society, as the lumbar region is a leaning site for spinal diseases to occur. The number of spinal fusion surgeries for treatment of diseases as herniation, stenosis and spondylolisthesis is increasing. As not only the intervertebral disc (IVD) is affected/removed during spinal fusion, the aim of this work was firstly to understand how ligament degeneration links with LBP by determining the role of each ligament per movement and secondly to evaluate the impact of IVD height reduction in degenerative changes. This framework enhances the separation of cause-effect mechanisms in degenerated spines. Thus, treatment decisions can benefit from these finite element (FE) simulations of different scenarios to support clinical practice [1].

Methods

Two different L3-L5 FE models were developed to simulate the abovementioned degeneration/intervention scenarios. The first originated from computed tomography (CT) images of a healthy 40-year-old woman, while the second was based on a 78-year-old woman with marked IVD height reduction on the L4-L5 level (figure 1) [2]. The segmentation software was ITK-Snap [3], followed by Solidworks® for IVD inclusion and Abaqus® for FE simulation (both from Dassault Systèmes SolidWorks Corp., USA).

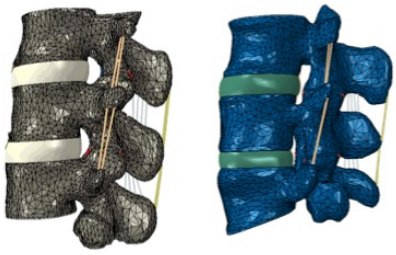

Figure 1: Healthy and degenerated spine models.

The FE models included the seven major ligaments of the lumbar spine: anterior longitudinal ligament (ALL), posterior longitudinal ligament (PLL), facet capsular ligament (FCL), ligamentum flavum, interspinous ligament, intertransverse ligament and supraspinous ligament (superficial ligaments). Four phases for ligament removal around L4-L5 were followed, using the healthy model [4]: (i) removal of superficial ligaments, (ii) FCL removal, (iii) PLL removal, and (iv) ALL removal. Ligament degeneration was then implemented in both models, being modelled as an age-related phenomena in two phases: (i) stiffness decrease (i.e. relaxation) due to reduced mobility, and (ii) increase in ligament stiffness due to growing collagen cross-linking. In all cases, a pre-load of 100 N and a moment of 7.5 Nm were applied on the top of L3, with full restriction of L5 movements [5]. The main outcome was the relative changes in the range of motion (ROM). IVD degeneration was implemented only on the reduced height model, by gradually increasing the stiffness of different components, while reducing the annulus fibres mechanical response.

Results

The outcomes for the healthy IVD model, after ligaments removal, revealed that the superficial ligaments and FCL had no influence for extension movements, being ALL the most influential ligament in that case (ROM increase of 14% when removed). In flexion, FCL removal caused a decrease of ROM up to 19%. After ligament stiffness reduction, there was a 4% ROM increase in flexion when FCL was degenerated, and 1% increase in extension with ALL degeneration. For the model with height reduction, ALL (extension) and FCL (flexion) remained the most active ligaments in extension and flexion. However, their influence was increased, which could be observed on the 11% ROM growth after FCL degeneration.

Discussion

It was interesting to observe that, with IVD and/or ligaments degeneration, ROM variation trends were very similar with both models. This confirms literature indications that ALL and FCL rule the movement, but also that such trends are not altered along the degenerative process [6]. It must also be highlighted that, when comparing the outcomes between models with different levels of IVD degeneration, it was verified that ROM relative changes with mild ligament degeneration were slightly higher in the model with the most advanced stage of IVD degeneration. This is a strong indication that ligament degeneration is primarily linked with IVD degeneration. Further studies will consider more complex material models and a wider patient database.

References

1. El Bojairami et al, Sci Rep, 10(1):1-15, 2020.
2. Korez et al, IEEE T Med Imag, 34(8):1649–1662, 2015.
3. Yushkevich et al, NeuroImage, 31(3), 1116–1128, 2006.
4. Ellingson et al, CMBBE, 19(9):1009–1018, 2016.
5. Park et al, Comput Biol Med, 43(9):1234–1240, 2013.
6. Heuer et al, J Biomech, 40(2):271–280, 2007.

Acknowledgements

This research was funded by Fundação para a Ciência e Tecnologia (Portugal), through IDMEC, under LAETA project UIDB/50022/2020.

The strain distribution in the osteophytes on the vertebral body under different loading conditions.

Daniele Marras (1), Marco Palanca (2), Luca Cristofolini (1)

1. Dept. of Industrial Engineering, Alma Mater Studiorum - Università di Bologna, Bologna, Italy
2. Dept. of Oncology and Metabolism and INSIGNEO, University of Sheffield, Sheffield, UK

Introduction

Vertebral osteophytes are degenerative bony growths. The osteophytes can limit the range of motion, cause pain, and damage the surrounded tissues [1]. Thus, clinicians tend to treat them as degenerative condition, but the actual mechanical role of the osteophytes in the spine is still unclear. Indeed, the biomechanical consequences of osteophytes has never been evaluated in multi-vertebra segments under pseudo-physiological loading condition, and their effect on the surrounding tissues is still unknown. The aim of this study was to evaluate how the osteophytes affect the vertebral body in terms of strain distribution.

Methods

Three segments were isolated from human spines, obtained through an ethically-approved donation program. Each segment included a vertebra with at least an osteophyte, and a control vertebra, without any osteophytes. The spine segments were CT-scanned to detect the position and the type of the osteophytes (Fig.1). Segments with bony bridges between two vertebrae were excluded from this study. Each segment was loaded non-destructively in four conditions: pure compression, flexion, left and right lateral bending. The strain distribution on the entire spine segment was measured using Digital Image Correlation (GOM Aramis 12M) with 4 cameras. The average minimum principal strain was evaluated over the entire vertebra to evaluate the overall effect. Additionally, to evaluate the local effects, a reduced region of interest (ROI) containing the osteophytes and surrounding bone was defined. The principal strain was evaluated on that ROI and on a corresponding ROI, in the corresponding position on the control vertebra. The ratio between the strain in the two ROIs was computed to evaluate if local differences exist osteophytic and normal vertebrae.

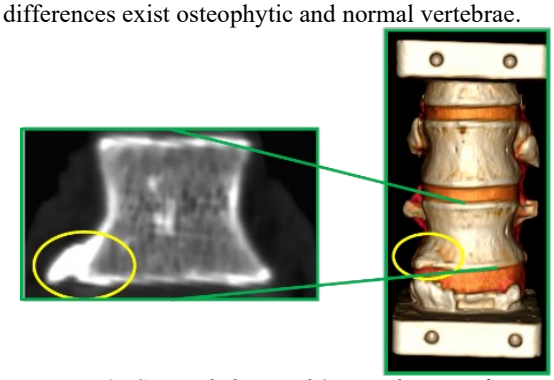

Fig. 1: Coronal slice and 3D rendering of an osteophytic L1 vertebra included in a T11-L2 segment.

Results

Pure compression and right/left bending clearly showed an heterogenous strain distribution in the vertebra with osteophyte. The minimum principal strain was in the order of -9000ue around the osteophytes, while strains smaller than -4000ue were experienced by the rest of the vertebra (Fig. 2). In general, a clear difference in the average deformations between vertebra with osteophytes and control was observed. By contrast, in the local area, the ROI with the osteophyte showed minimum principal strains up to three times larger than the strain over the same ROI of the control vertebra.

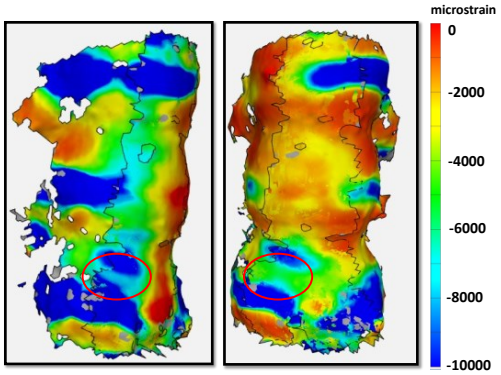

Fig. 2: Minimum principal strains in right bending (lateral view) and pure compression (frontal view). The red circle highlights the osteophyte area.

Discussions

The preliminary results highlighted clear differences between vertebrae with and without osteophytes, especially in local strains distribution. Previous studies, investigating mechanical function of the osteophytes revealed a protective mechanism that they can provide to the vertebra against fractures [2,3]. Here, thanks to a full-field strain analysis, we observed that the amount of mineralized tissues, typical of the osteophytes, lead to strain concentrations around the osteophytes itself. This suggests improving the knowledge around the osteophytes and their behavior during daily motor tasks.

References

[1] Wong et al, Journal of Ortho. & Surg., 24:403-10, 2016.
[2] Wagnac et al., Plos One, 12: e0186779, 2017
[3] Al-Rawahi et al; Spine, 36:770-7, 2016

Acknowledgment This study was funded by the AOSpine Discovery and Innovation Awards (AOSDIA 2019_063_TUM_Palanca) and the charity "Reuse with Love"

PREDICTING PROXIMAL JUNTION FAILURE IN SPINE SURGERY: SAGITTAL ALIGNMENTS AND MECHANICAL INTEGRATED SCORE

Morteza Rasouligandomani (1), Alex del Arco (3), Ferran Pellisé (4), Miguel González Ballester (1,2), Fabio Galbusera (5), Jérôme Noailly (1)

1. BCN MedTech, DTIC, Univ. Pompeu Fabra, Spain; 2. ICREA, Spain; 3. Hospital del Mar, Spain; 4. Univ. Hospital Vall d'Hebron, Spain; 5. Lab. of Biological Struct. Mech., IRCCS Istituto Ortopedico Galeazzi, Italy

Introduction

Proximal Junction mechanical Failure (PJF), is one of the most severe complications in sagittal imbalance spine surgery [1]. The global alignment and proportion (GAP) score has been proposed as an effective predictor for PJF [2]. It uses Pelvic Incidence (PI)-based proportional radiographic parameters in the sagittal plane, but does not explicitly include biomechanical descriptors or global body balance. Hence, the aim of this study is to explore whether full sagittal balance and biomechanical descriptors can improve the discrimination of PJF. As such, a retrospective patient cohort was used to assess the GAP score. We further tested the contribution of the Femoral Obliqueness (FOA) and Pelvic Compensation Angles (PTCA), included in the Full Balance Index (FBI) [3], and the Bending Moment (BM) at the upper fusion level. Cut-off analyses and integrating normalized GAP, FBI and BM lead to introduce new score: Sagittal Alignments and Mechanical Integrated Score (SAMIS).

Methods

We selected 112 patients out of the IRCCS database: 57 as control, including stable proximal junction kyphosis (after 1 year), and 55 as failure, i.e., fracture of Upper Instrumented Vertebra (UIV) or of UIV+1, pullout of instrumentation at UIV and sagittal subluxation [2]. Inclusion criteria were: Age from 50 to 75, Pelvic tilt>20°, SVA>5cm, First immediate standing radiograph after surgery, At least 1-year follow-up, Cobb angle between UIV and UIV+2 >15°. Biplanar low-dose EOS radiographs were collected, 3D full-spine models were reconstructed by using the ster-EOS software and spinopelvic sagittal parameters (Fig. 1) were calculated.

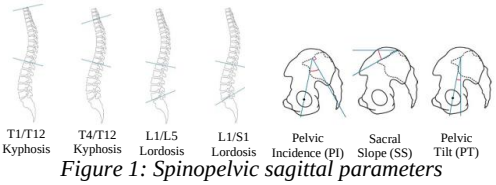

Figure 1: Spinopelvic sagittal parameters

The GAP score was calculated as follow [2]:

$$GAP = RPV + RLL + LDI + RSA + \text{Age factor} \quad (1)$$

RPV: Relative Pelvic Version; RLL: Relative Lumbar Lordosis; LDI: Lordosis Distribution Index ;RSA: Relative Spinopelvic Alignement

Furthermore, FBI was calculated to quantify full body sagittal balance [3]. Also, BM was calculated as the upper body mass times the effective distance to body centre of mass at UIV+1. This effective distance was calculated through the Huygens-Steiner theorem [4]:

$$d_{eff} = \left(\frac{Iz_{eff,UIV+1}}{\sum_{i=1}^{Upper} SBM_i}\right)^{-\frac{1}{2}} \quad (2)$$

The AUC of the GAP, FBI and BM to discriminate PJF cases were analyzed through the Receiver Operating Characteristic (ROC) curve. Parameter Cut-off analyses further provided quantitative thresholds to characterize the control and failure groups.

Results and discussion

Using 3D shape information, we confirmed that the GAP score is able to discriminate possible PJF cases (Table 1), as pointed out by [2]. FBI and BM were also reliable candidates to predict PJF (Table 1).

Table 1: ROC analysis for GAP, FBI and BM

	AUC	Confidence interval	Threshold based on maximizing Youden Index
GAP Score	0.8739	0.70 to 0.92	7
FBI	0.8856	0.71 to 0.93	30
BM at UIV+1 (Nm)	0.9216	0.83 to 0.97	6

Then, in order to optimize the exploitation of the GAP score, FBI and BM at UIV+1, three integrated scenarios were explored in Table 2.

Table 2: AUC & confidence intervals for integrated scenarios

Integrated Scenario	AUC	Confidence interval
FBI+BM	0.9339	0.85 to 0.97
GAP+BM	0.9301	0.84 to 0.96
GAP+FBI+BM	0.9502	0.87 to 0.98

Consequently, a new score was proposed based on normalizing the components respect to the threshold values which calls Sagittal Alignments and Mechanical Integrated Score (SAMIS):

$$SAMIS = (0.142 \times GAP) + (0.033 \times FBI) + (0.166 \times BM) \quad (3)$$

GAP improvement using SAMIS is shown in Fig. 2.

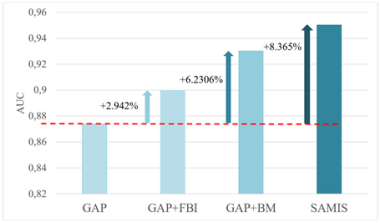

Figure 2: GAP improvement by introducing SAMIS

Importantly, including BM in the SAMIS best improved PJF discrimination (Fig. 2), highlighting the relevance of external mechanical loads in the prognosis of the surgical management of adult spine deformity. This further shows the potential of biomechanical analyses, e.g., finite element analyses, to understand PJF.

References

1. Hyun SJ, et al., Korean J Spine, 14(4), 2017
2. Yilgor C, et al., The Spine J, 17(10), 2017
3. Le Huec, J.C., et al., European Spine J, 2019
4. Toumanidou T, et al., Frontiers in Bioeng. & Biotech., 3, 2015

Acknowledgements

Funds received from DTIC-UPF, IMIM, IRCCS Istituto Ortopedico Galeazzi & Spanish Government (RYC-2015-18888, MDM-2015-0502).

DEVELOPING PATIENT-SPECIFIC FE MODELS OF THE THORACOLUMBAR SPINE USING STATISTICAL SHAPE MODELS AND MESH MORPHING

Morteza Rasouligandomani (1), Alex del Arco (2), Fabio Galbusera (3), Jérôme Noailly (1), Miguel A. González Ballester (1,4)

1. BCN MedTech, DTIC, Univ. Pompeu Fabra, Spain; 2. Hospital del Mar, Spain; 3. Lab. of Biological Structures Mechanics, IRCCS Istituto Ortopedico Galeazzi, Italy; 4. ICREA, Spain

Introduction

Adult spine deformity (ASD) is an abnormal alignment of the vertebral column in the elderly population. Finite Element Models (FEM) have been proposed as effective tools to study the biomechanical etiology of ASD but require structured mesh models, difficult to generate automatically. To address this limitation, we propose a novel tool to generate patient-specific (P-S) FEM models of the thoracolumbar spine. The method is based on a Statistical Shape Model (SSM), built from a retrospective patient cohort. We included the modelling of intervertebral discs (IVD), including all disc tissues, and we validated quantitatively the quality of the approach for individual case modelling.

Methods

We selected 42 non operated patients out of the IRCCS Istituto Ortopedico Galeazzi database. Inclusion criteria were: age 50-75, pelvic tilt>20°, SVA>5cm. 30 cases had pure sagittal deformity and 12 cases had both sagittal and coronal deformity. EOS biplanar images were collected and 3D thoracolumbar spine surface models were reconstructed with the software sterEOS. The overall modelling pipeline is shown in Fig. 1.

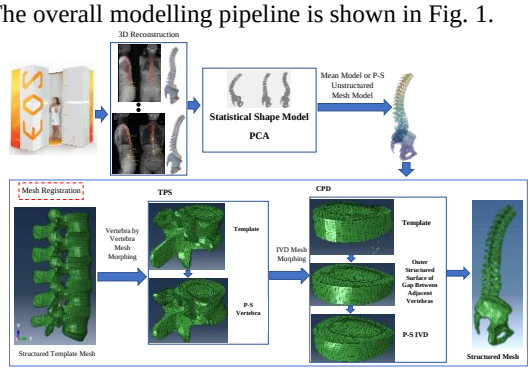

Figure 1: Pipeline of developing P-S spine structured meshes

To train the SSM, all 3D surface models were aligned in a common reference using Procrustes Analysis. Then, a Principal Component Analysis (PCA) allowed to reduce the dimensionality of the data and learn the principal modes of shape variation. The shape model was then [1]:

$$x = x_mean + Pb \quad (1)$$

where x_mean is the mean shape, P is the orthogonal shape variations matrix (principal vectors of the covariance matrix), and b is the weighting shape vector. New spine shapes could be generated by varying b. An adaptation method was developed to find the best b value, to fit the patient data, generating a dense vector field (in our case parametrized via Thin-Plate Splines [2]) representing the deformation from the mean shape to the P-S shape. A reference structured FE mesh of the mean shape was built, and mesh morphing was performed by using the P-S deformation field. Intervertebral disc (IVD) meshes between two adjacent vertebra endplates were interpolated using the Coherent Point Drift (CPD) [3] surface matching algorithm.

Results and discussion

The main SSM shape variation modes are shown in Fig.2, for our population, highlighting coupled spino-pelvic patterns.

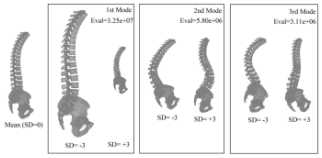

Figure 2: Three main modes of variation from the SSM

Fig. 3 shows one specific case, for which SSM-derived spino-pelvic parameters could be verified (Fig.3).

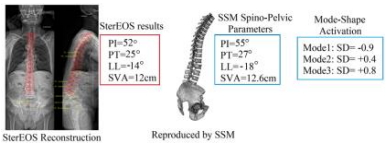

Figure 3: Specific case generated by SSM

The quality of the structured P-S mesh achieved through TPS & CPD is reflected through Table 1 parameters. While the geometrical approximation was excellent (see Euclidian distance), the automatically adapted structural mesh had enough quality for FE simulations. The internal structure of the IVD was also nicely adapted, as reflected by nucleus pulposus (NP) volumetric proportions that compared well with the literature [4].

Table 1: Result of mesh quality for structured meshes

	Euclidean Distance	Mesh Error	Mesh Warnings	Aspect Ratio > 10	Max Angle on Quad Faces > 160	NP Proportio(%)
Vertebras						
Min.	1.423	0%	1.265%	0.145%	0.256%	-
Max.	1.846	0%	8.156%	0.935%	0.478%	-
IVDs						
Min.	0.00018	0%	0.158%	0.587%	0.592%	41.378 [4]
Max.	0.00069	0%	8.634%	4.789%	1.035%	47.357 [4]

We reported a novel framework for the generation of P-S FE structured models of the spine for ASD patients, combining SSM and mesh morphing techniques. This tool shall greatly benefit systematic biomechanical analyses for ASD treatment planning.

References

1. Cootes, T. F., et al., Comp. Vision & Image J, 61(1), 1995
2. Bookstein, F L, et al., IEEE Trans. on Patt. Analyses, 11(6), 1989
3. Myronenko, A, et al., IEEE Trans. on Patt. Analyses, 32(10), 2010
4. Newell, N, et al., Mech. Behavior of Biomed. Mat. J, 69,2017

Acknowledgements

Funds received from DTIC-UPF, IMIM, IRCCS Istituto Ortopedico Galeazzi & Spanish Government (RYC-2015-18888, MDM-2015-0502).

ENZYMATIC DIGESTION WITH CHONDROITINASE OR PAPAIN: METHODS TO INDUCE DISC DEGENERATION FOR IN VITRO TESTING?

Jan Ulrich Jansen (1), Graciosa Quelhas Teixeira (1), Andrea Vernengo (2), Sibylle Grad (2), Cornelia Neidlinger-Wilke (1), Hans-Joachim Wilke (1)

1. *Institute of Orthopaedic Research and Biomechanics, University Ulm, Germany;*
2. AO Research Institute Davos, Switzerland

Introduction

Freshly isolated intervertebral discs (IVDs) from bovine tails are commonly used in vitro for biomechanical and biological investigations because of a limited availability of native human disc specimens. However, their characteristics correspond to very young human discs rather than to degenerated ones. Chondroitinase ABC (ChABC) and papain have been used to induce matrix degradation in bovine IVDs, thereby simulating disc degeneration in vitro. However, biomechanical changes, such as range of motion (ROM), resulting from enzyme degradation have not been evaluated yet. Hence, the aim of this study was to treat bovine IVD organ cultures with ChABC or papain to create "degeneration" for in vitro experiments and to evaluate ROM, disc height, macroscopic morphology and glycosaminoglycan (GAG) content.

Methods

In total, 18 single motion segments (CY3/4) from 18 fresh bovine tails were embedded in PMMA. ChABC (0.25 U/ml), papain (65 U/ml), or DPBS as control (n=6 per group) was injected into the nucleus pulposus. Subsequently, specimens were cultured for 7 days under free-swelling condition, hypoxia (6% O_2) and 37°C, with medium exchange at day 3. Complex loading, as a combination of lateral bending, flexion-extension (both ± 10°) and axial compression (150 N) was applied for 1 hour to mitigate disc swelling during incubation (day 7). The ROM and the change in IVD height were determined before and after enzyme treatment and after complex loading. IVDs were processed for histology with Safranin-O/Fast-Green-Staining and for GAG quantification using DMMB assay. Statistics: Shapiro-Wilk, Mann-Whitney-U, and Friedman test ($p \leq 0.05$).

Results

At day 7, all specimens digested with papain developed a cavity in the IVD space, whereby ChABC specimens macroscopically stayed intact (Fig. 1A). During incubation with papain, the disc height decreased whereas it increased for ChABC and control ($p \leq 0.009$). Complex loading led to a decrease of the disc height in all groups ($p \leq 0.004$). After the 7-day incubation period, the ROM decreased for ChABC and control but not for papain (representatively shown in flexion/extension) (Fig. 1B; $p=0.002$). Complex loading increased the ROM significantly in all groups ($p \leq 0.028$). According to the histological staining and GAG quantification, both enzymes induced GAG loss, but papain showed a more pronounced effect in the nucleus pulposus (Fig. 2).

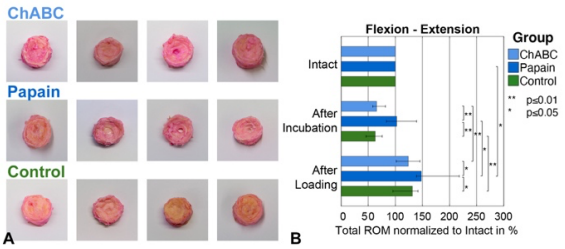

Figure 1: A) Exemplary macroscopic results of 4 IVDs per group. B) ROM after incubation and subsequent complex loading normalized to the intact condition.

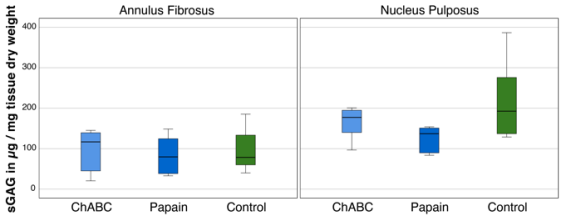

Figure 2: Sulphated GAG content after testing at day 7.

Discussion

Cavities and resulting significant biomechanical changes highlight a stronger digestion of the tissue for papain treatment than for ChABC, supported by the GAG content. The increase in ROM and loss in height for the papain specimens indicate a similar behavior as described for human discs with cavities resulting, for instance, from disc herniation or nucleotomy [1]. The specific digestion of GAG by ChABC led to milder structural defects and biomechanical changes; thus, it mimics more closely real disc degeneration occurring without cavities. ChABC induced milder than expected degeneration, so in future work, higher concentrations will be studied. Overall, these findings enhanced our understanding of the biomechanical impact (especially ROM) of enzyme digestion of IVDs using ChABC and papain, and might enable in future studies the targeted simulation of different disc pathologies in fresh young bovine tail discs for testing purposes.

References

1. Wilke et al, Spine, 38:E587–E593, 2013.

Acknowledgements

This work was supported by Horizon 2020 (iPSpine 825925).

DESIGN AND OPTIMIZATIONS OF AN INTERVERTEBRAL IMPLANT MATERIALS

Michel Mesnard (1), Antonio Ramos (2), Yann Ledoux (3)
1. Institut de Mécanique et d'Ingénierie, Université de Bordeaux, France, 2. Department of Mechanical Engineering, University of Aveiro, Portugal; 3. Institut de Mécanique et d'Ingénierie, Université de Bordeaux, France.

Introduction

Dynamic stabilization devices are under development to treat spine disorders. Unlike arthrodesis, the goal is now to maintain intervertebral mobilities. To transmit loads and control movement, a spinal unit involves interdependent components: two vertebrae, an intervertebral disc, facet joints, and the muscular-ligamentous system. When one of these elements fails (disc degeneration, osteoarthritis, etc.), stability and load transfer are disturbed and generate pain. In that case, arthrodesis was the traditional surgical treatment. However, the hyper rigidity of this technique can create complications in the long-term (screw loosening, disease of the adjacent segment, etc.). "Soft" systems, also called "dynamic" devices, are developed to restore load sharing and allow movements similar to those of the natural unit. This innovative concept associated with the high variability between human beings makes it difficult to design such devices; the rigidity criterion becomes the key to the specifications [1] to reduce intradiscal pressure. The present study focused on a spine dynamic device, the BDyn implant, the objectives were to improve the geometry, the choice of the polymer material, and some components.

Methods

Dynamic spinal implants have been classified into two groups: anterior and posterior devices. The BDyn implant (Figiure 1) is a flexible pedicle screw-based posterior dynamic stabilization device composed of two metal rods and two polymeric elements.

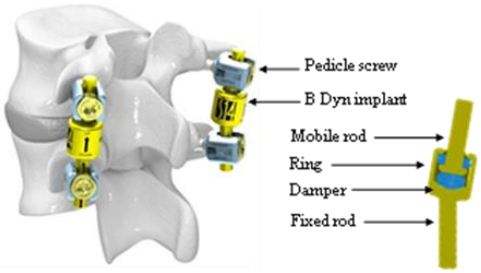

Figure 1: Dynamic stabilization device BDyn (S14 Implants).

Static axial tension tests were carried out for five different elastomeric materials (no#1 up to no#5 in order of increasing rigidity). The device was then tested under dynamic loading (fatigue) using a "spinal" assembly according to the protocol imposed by the international standard ISO 12189, for the multi-criteria analysis, a geometric and mechanical model of the BDyn was produced (Figure 2). The construction was based on data from the experimental biomechanical analysis. To optimize the BDyn implant, the study could combine design variables (materials, stiffness of components, etc.) with observed variables ΔEi and β [2].

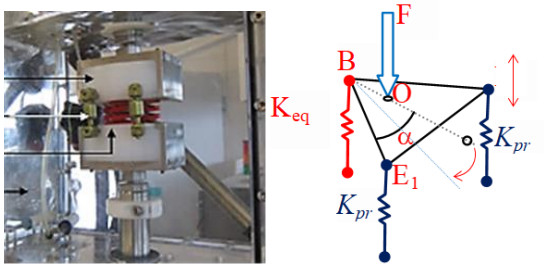

Figure 2: Dynamic mechanical experiment - Geometric and mechanical model.

Results

Static test results were expressed as relative values compared to material #1. For a 2 mm-displacement, the load ratio of materials #2 and #3 were respectively 2.4 and 2.5mm. For material #4 this ratio reached 5.8 and 6.7mm for material #5. Material #1, silicon initially used, deteriorated for a displacement remaining under 2 mm; it cannot ensure the BDyn functions. The measured loads for materials #4 and #5 are twice higher as those of material #1. Previous tests showed that such loads may cause sliding between the implant and the screw's head.

Discussion

According to the features provided by the material manufacturers, material #2 shows better resistance to hydrolysis and oxidation (aging) than material #3. The results of these static trials, therefore, led to select material #2 for the following fatigue tests. Each of the six fatigue tests achieved five million cycles. No broken screw was found and no degradation of metal components of the implants was observed. The results show the BDyn influence on the final position of the vertebra. The closer β is to zero, the better the solution since the implant makes it possible to balance the disc degeneration. The angle β is relatively large for #2 (1.2°) and decreases regularly from #1 to 0.6° for grades #3 and #4 respectively.

References

1. Barrey CY., et al. Int. Jo. for Spine Surgery, 2(4), 159-70.
2. Kaner T, et al. Turkish Neurosurgery; 20(2), 205-15.

ROLE OF TYPE I COLLAGEN-HYALURONAN INTERFACIAL INTERACTIONS ON THE MECHANICS OF ANNULUS FIBROSUS

Shambo Bhattacharya (1), Devendra K. Dubey (1)

1. Department of Mechanical Engineering, Indian Institute of Technology, Delhi, India

Introduction

Tensile, compressive and torsional deformation of the Intervertebral Disc (IVD) is primarily contributed by the AF by undergoing combined tension, compression and shear. Such multi-faceted deformation exhibited is due to the fiber reinforced composite structure, with collagen fibers embedded in a proteoglycan and water matrix. At nanoscale, deformation of an AF lamella is a result of mechanical contributions from collagen, proteoglycan and collagen-proteoglycan shear interactions, with collagen undergoing a combination of backbone stretch and intermolecular sliding [1], hyaluronan component of proteoglycans undergoing backbone straightening followed by intermolecular sliding [2] and aggrecan contributing to maintaining water concentration levels. However, interactions between collagen and hyaluronan at the nanoscale has not investigated, and its role in AF mechanics have not been established.

Present study, employing MD simulations, provides insights into the nanoscale mechanistic role of collagen-collagen (C-C), hyaluronan-hyaluronan(H-H) and collagen-hyaluronan (C-H) interfaces on the mechanics of outer AF.

Methodology and Framework

The atomistic model of hyaluronan is constructed using the monomers N-acetyl Glucosamine and Glucuronic acid. The methodology adopted to construct the atomistic model hyaluronan is outlined in authors' previous work [2]. The atomistic model of collagen microfibril developed using a residue sequence used in earlier works [3]. The atomistic model of C-H interface is developed by concatenating the structures, shown in Fig 1.

All MD simulations are performed using the LAMMPS code using a combination of CHARMM27 and CHARMM36 forcefield, in a water concentration of ~65% (mean of the outer AF). Due to the directional nature of collagen fibres in the AF, tensile deformation of collagen, hyaluronan and the interface is studied in two directions – axial and transverse. The quasistatic deformation and stress computation framework is outlined in author's previous work [2].

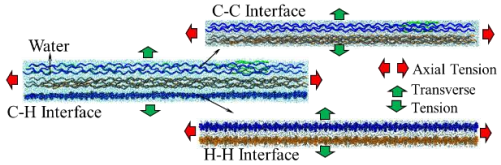

Figure 1: Atomistic Models of C-C, H-H and C-H Interfaces.

Results and Discussion

Results show H-H interface exhibits a stiffer behaviour than C-H and C-C Interfaces under axial tension (Figure 2(a)), but lower strength in both axial (Figure 2(a)) and transverse directions (Figure 2(b)). This is due to the presence of strong water bridges owing to the more hydrophilic nature of hyaluronan molecules. But the ability of hyaluronan to form intramolecular H-bonds results in the rupture of water bridges during axial tension, resulting in a lower peak strain for the H-H interface. Results indicate that the stiffness of H-H interface provides initial stiffness of the AF lamella as postulated in earlier works [4]. Due to lower strength of H-H Interfaces, deformation of AF lamella in the direction of fibers is guided by interfibrillar sliding, resulting from intermolecular sliding of hyaluronan molecules, which is an essential mechanobiological artefact of AF [5].

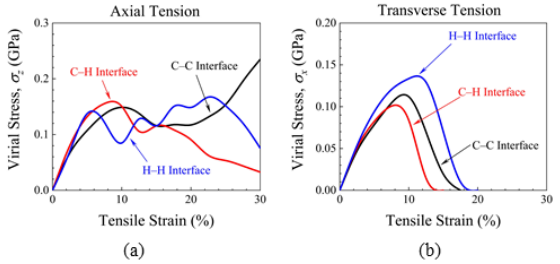

Figure 2: Virial stress-strain - (a) Axial and (b) Transverse Tension

Conclusion

Water bridges provides stiffness to the interfaces but the formation of intramolecular H-bonds in hyaluronan results in rupture of water bridges under axial tension. This results in intermolecular shear between hyaluronan molecules, thus contributing to inter-fibril sliding, which is an important artefact governing cellular mechanobiology in AF.

References

1. Depalle et al, J Mech Bio Mat, 52:1-13, 2015
2. Bhattacharya et al, J Mech Bio Mat, 103752, 2020
3. Dubey et al, Acta Biomater, 5**:**2704–2716, 2009
4. Holzapfel, Biomech. Model. Mechano, 3:125–140, 2005
5. Bruehlmann et al, Spine, 29(23):2612-2620, 2004

Acknowledgements

The authors thank IIT Delhi HPC facility for computational resources.

EFFECT OF CHEMICAL ENVIRONMENT ON THE NANOMECHANICS OF HYALURONAN IN ANNULUS FIBROSUS: A MOLECULAR DYNAMICS INVESTIGATION

Shambo Bhattacharya (1), Devendra K. Dubey (1)

1. Department of Mechanical Engineering, Indian Institute of Technology, Delhi, India

Introduction

Annulus Fibrosus (AF), the fibrous outer jacket of the intervertebral disc (IVD), aid in transferring motion along the spine by undergoing a combination of tensile, compressive and shear deformation, owing to its fiber-reinforced composite structure[1]. However, disc degenerative conditions change the chemo-mechanical interactions between the constituent biomolecules in AF, thus impairing IVD functionality. Understanding the nanoscale mechanical behaviour of constituent biomolecules in AF and its interactions with each other can bring forth important evidence regarding the mechanics of AF at multiple length scales. Present study investigates the effect of chemical environment on the nanoscale mechanics of hyaluronan in the extrafibrillar matrix (EFM) of AF using explicit molecular dynamics (MD) simulations.

Methodology and Framework

The atomistic model of hyaluronan is constructed using the monomers N-acetyl Glucosamine and Glucuronic acid. The methodology adopted to construct the atomistic model hyaluronan is outlined in authors' previous work [2,3] (Figure 1). The tensile and compressive (z-direction) tests are conducted in – (i) plain hydration (~75% water), and (ii) 150 mM NaCl, based on the physiological environment and water content in a healthy AF tissue. All MD simulations are performed using the LAMMPS code using a combination of CHARMM27 forcefield. The quasistatic deformation and stress computation framework is outlined in author's previous work [2].

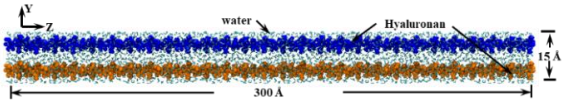

Figure 1: Representative atomistic model of the hyaluronan component in the EFM of the AF

Results and Discussions

The virial stress-strain plots obtained are shown in Figure 2. The elastic modulus in axial tension for hydrated model, in plain hydration and ionic environments, is lower compared to unhydrated model. This is because hyaluronan forms stable intramolecular H-bonds [4] which shield the formation of hyaluronan-water intermolecular H-bonds leading to a reduction in the water-bridges formed. This reduces the load-transfer across the hyaluronan-water-hyaluronan interface. At higher strains, owing to the stiffening of hyaluronan backbone due to bridging of charges [5], the stress carried in ionic environment is higher. During Axial Compression, elastic moduli of hydrated model are higher than unhydrated model. Because the hydrostatic pressure and coiling of hyaluronan due to compression leads to an entrapment of water molecules through intermolecular H-bonds by rupturing the intramolecular H-bonds. This favors the formation of water bridges which aid in bearing the compressive loads.

Overall, analyses show that intramolecular and intermolecular H-bonds play a significant role in governing the nanoscale mechanics of hyaluronan by governing the formation and rupture of water bridges. Furthermore, this study contributes towards understanding the structure-function relationship of constituent biomolecules in the AF and has implications in gaining significant insights into the mechanics of AF at multiple length scales

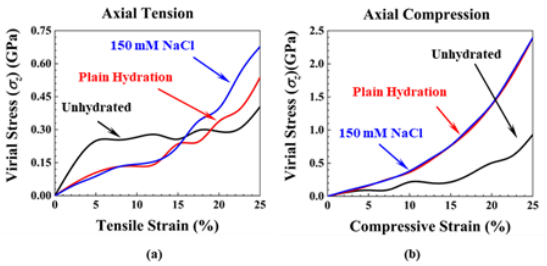

Figure 2. Virial Stress versus strain plot in (a) Axial Tension and (b) Axial Compression

.

References

1. P. P. Raj, 8(1):18–44, 2008
2. Bhattacharya et al, J Mech Bio Mat, 103752, 2020
3. J. R. E. Fraser et al, J. Intern. Med, 242(1):27–33, 1997.
4. G. Giubertoni, J. Phys. Chem. A, 2019.
5. E. Buhler et al, Macromolecules, 37(4):1600–1610, 2004.

Acknowledgements

The authors thank IIT Delhi HPC facility for computational resources.

INSTANTANEOUS AXIS OF ROTATION AS INDICATOR FOR LUMBAR INTERVERTEBRAL DISC DEGENERATION – A SIMULATION STUDY

Robin Remus (1), Alina Hoffmann (1), Beate Bender (1)

1.Chair of Product Development, Department of Mechanical Engineering, Ruhr-University Bochum, Germany

Introduction

Although low back pain is one of the major health issues of the present day, causes are often poorly understood. Many symptoms, however, are associated with changes in intervertebral discs (IVD) that are subject to early degeneration [1]. Degeneration (deg.) is a complex process in which the structure and mechanical properties of IVD alter, characterized by reductions in water content, height, compliance, and swelling pressure [1,2,3]. Understanding spinal kinematics is essential to diagnose degenerative conditions at an early stage. A correlation between deg. and altered kinematics is well known. More differentiated classifications of these kinematic alterations to individual spinal changes, however, are still a matter of debate [2]. Changes in the IVD material properties have been extensively studied [3,4]. We assume that these changes have relevant influences on the lumbar vertebral instantaneous axes of rotation (IAR). Therefore, in this study, we investigate how the IAR motion patterns alter in lateral bending as a result of different degrees of L4/5 IVD degeneration, modeled by changes in material properties.

Methods

We use a calibrated and validated passive hybrid model [5] of the ligamentous LSS built in ArtiSynth [6]. The lumbosacral spine (LSS) model consists of L1-S1 rigid vertebrae interconnected with hyperelastic fiber-reinforced finite element IVD, ligaments, and facet joints. To simulate an increasing grade of L4/5 IVD deg., material properties (bulk modulus K and shear modulus G) of the anulus ground substance (Mooney-Rivlin) and nucleus pulposus (Yeoh) are altered. The materials are fully described by two elastic moduli, assuming homogeneous isotropic linear elasticity, which allows a conversion between Young's modulus E and Poisson's ratio ν with K and G. Based on previous studies [3,4,7] for anulus and nucleus, respectively, ν have been reduced from 0.41 and 0.499 till 0.35 and 0.4, and E have been increased up to factors of 4 and 1.5. For deflections, vertebra L1 or L4 is alternately loaded with a ±7.5 Nm bending moment in frontal plane. The LSS is preloaded via a path optimized [5] follower load (FL).

Results

For the intact L4/5 IVD, IAR progressions of L4 vertebra are smoothest and IAR patterns are least sensitive to variations in preload (500-700 N FL). L4 IAR patterns differ considerably when the LSS or solely subsections (L4-S1 and L4-L5) are deflected (Figure 1). Alterations are more pronounced in moderately deg. IVD but differ for varying preloads. Motion coupling is strongest at 700 N preload and moderately deg. IVD. Facet joint contacts determine the IAR of the vertebrae to a large extent in case of strong coupling. Anteriorly IAR tend to tilt further upward in degenerating IVD. IAR patterns of adjacent vertebrae are little changed.

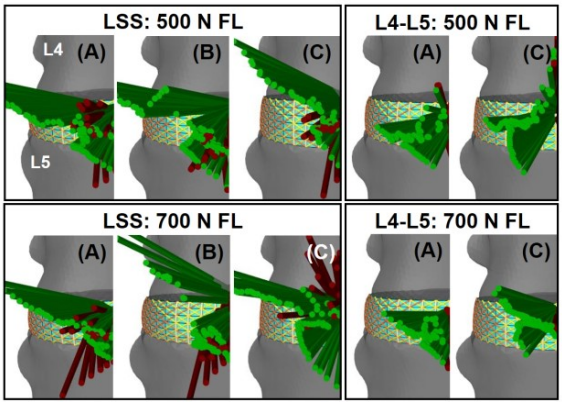

Figure 1: IAR of L4 vertebra for intact (A), moderately degenerated (B), and severely degenerated (C) IVD. The sections shown are cut to the sagittal and frontal plane. IAR in green and red for left and right lateral flexion.

Discussion

Altered IAR motion patterns become apparent in simulated deg. L4/5 IVD due to changes in the material properties. The results suggest essential coupling mechanisms with the adjacent levels, an increased sensitivity to compression, and support findings to an elastic stiffening in severely degenerated IVD due to densifications of the structure [3]. However, predicted IAR pattern changes are less definite than found experimentally [1,2]. This highlights the multifactorial influence of degenerations on the kinematic response. Sole variations of hyperelastic material properties are only one relevant factor, which is why in future studies further structural changes as well as time dependencies and transport processes should be considered. The simplifying loading modes may also limit comparability to in vivo findings. To simulatively account for in vivo similar conditions, the current passive hybrid model may be extended to include skeletal muscles and solved inversely in the context of redundancy problems.

References

1. Krämer et al, 978-3-13-176166-8, 2014.
2. Ellingson and Nuckley, J Biomech, 48(2):361-369, 2015.
3. Iatridis et al, J Biomech, 31(6):535-544, 1998.
4. Natarajan et al, Spine, 29(23):2733-2741, 2004.
5. Remus et al, PloS One, under review.
6. Lloyd et al., 978-3-642-29014-5, 355-394, 2012.
7. Ellingson et al, CMBBE, 19(9):1009-1018, 2016.

EFFECT OF ENDPLATE-TO-ENDPLATE FILLING IN VERTEBROPLASTY

Inês Santos (1), Nicklas Hagenmeyer (1), Yan Chevalier (1), Christoph Birkenmaier (1)

1. *Department of Orthopedic Surgery, Physical Medicine and Rehabilitation, University Hospital, LMU Munich, Germany*

Introduction

Vertebroplasty has been used both in the treatment of painful vertebral compression fractures (VCF) as well as a prophylactic procedure to reinforce the intact but weak vertebral bodies, showing significant and rapid pain relief in these patients [1,2]. Previous studies have shown, however, that this procedure greatly increases the failure strength of augmented vertebrae, thereby inducing new fractures in the adjacent levels [3-5], while others did not find such high incidence. Whether augmenting the fractured vertebrae increases the risk of adjacent-level fractures remains unclear. The purpose of this study was to evaluate the influence of endplate-to-endplate cement injection in failure load and stiffness after prophylactic vertebroplasty.

Methods

Ten specimens consisting each of a central vertebral body with its attached intervertebral discs and upper and lower adjacent vertebrae were harvested from eight human cadavers and screened for bone mineral density. Each specimen was placed in a custom-made fixation apparatus (E10000, Instron, Canton, MA) and subjected to cyclic sinusoidal dynamic compression (500-1000 N, 1 Hz, 1800 cycles) before and after vertebroplasty. The material used for augmentation was commercial bone cement (Biomet, Warsaw, IN) which injection was controlled by fluoroscopy in order to achieve endplate-to-endplate filling. The augmented specimens were further cyclically loaded at steps of increasing load for a total of 4800 cycles and afterwards compressed along their central axis at a constant displacement rate of 0.5 mm/s until failure occurred. All specimens were CT scanned after augmentation and after the fracture test. Pressure was measured in the upper and lower endplates of the adjacent vertebrae using a pressure mapping sensor (4000, Tekscan, Boston, MA). Segmentation and calculation of the cement and vertebral volumes (Figure 1) was performed in 3D Slicer - version 4.11.0. The first peak of the force-displacement curves defined failure load and elastic stiffness was the slope of the linear portion. Cement volume fraction (CVF) was defined as the ratio of cement and vertebral volumes. Linear regression analysis was used to determine the correlation of the mechanical results with augmentation features. The degree of association was measured by Pearson's correlation coefficient (r).

Results

The average volume of cement injected to the central vertebral bodies was 10.8 ± 2.2 cm^3 and mean CVF was 27.4 ± 5.2 %. Mean failure load was 5472.2 ± 1546.7 N and the mean stiffness of the specimens was 3083.3 ± 885.4 N/mm. The results show that CVF correlates positively with both failure load ($r = 0.177$) and stiffness ($r = 0.421$). Failure load is positively correlated with stiffness ($r = 0.339$). No relation was found between the augmented regions and the fracture location in both central and adjacent vertebrae.

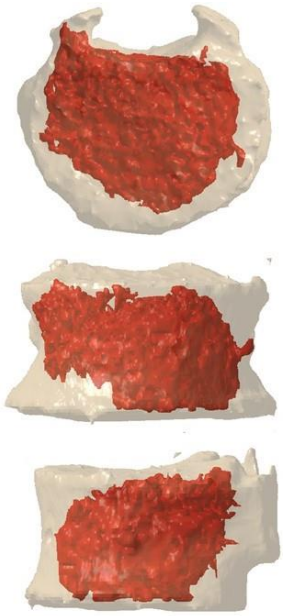

Figure 1: Endplate-to-endplate cement distribution (in red, CVF = 29.5 %) achieved in one of the specimens. Top to bottom: axial view, coronal view, sagittal view.

Discussion

The results of this study are in accordance with previous studies that demonstrated that an endplate-to-endplate filling pattern can have a strong effect on the strength and stiffness of augmented vertebrae. The results obtained by Berlemann et al. [3] for example show, however, that there was a trend towards lower failure loads with increased filling with cement, pointing to a possible risk of fractures in the adjacent, non-augmented vertebrae. These results were contrary to our findings. Further investigation is needed to understand the reported differences.

References

1. Hulme et al, Spine, 226:336-72, 2006.
2. Eck et al, Spine J, 8:488-97, 2008.
3. Berlemann et al, J BJS Br, 84-B:748-52, 2002.
4. Oakland et al, J Neurosurg Spine, 8:442-9, 2008.
5. Aquarius et al, Spine, 38:2092-2097, 2013.

COMPARISON OF LUMBAR SPINE SAGITTAL MOTION BETWEEN EXTERNAL MEASURES AND QUANTITATIVE FLUOROSCOPY

Mona Frey (1), Alan Breen (2), Alex Breen (3), Martha Funabashi (4), Greg Kawchuk (5), Isabelle Pagé (6), Jonathan Williams (2), Arnold Wong (7), Diana De Carvalho (1)

1. Memorial University of Newfoundland, Canada; 2. Bournemouth University, UK; 3. AECC University College, UK; 4. Canadian Memorial Chiropractic College, Canada; 5. University of Alberta, Canada; 6. Université du Québec à Trois-Rivières, Canada; 7. The Hong Kong Polytechnic University

Introduction

Spine biomechanics are commonly measured by external sensors such as motion capture and accelerometers. However, these surface measurements cannot directly measure intersegmental biomechanics of the lumbar spine and have been shown to underestimate spine angles. A great deal of research has been focused on the estimation and modelling of vertebral kinematics of the lumbar spine using static trials only. Thus, the purpose of our study was to investigate errors associated with soft tissue deformation throughout the flexion range of skin-based spine kinematics (accelerometers and motion capture) by comparing these surface measures to quantitative fluoroscopy (QF) in a healthy population.

Methods

Twenty female participants (age 46.3±9.20 years) completed guided standing flexion and extension trials while measuring synchronized QF [1], motion capture and accelerometer data. The sensors were fixed over the spinous processes of vertebras L2, L4, and S1. Changes in intersegmental angles (L2-L4, L4-S1, and L2-S1) from upright standing were compared between the three measures at mid and maximal range positions during the movement trial with a general linear MANOVA and Tukey post-hoc tests. The full movement trials will be compared with a Bland-Altman analysis.

Results

Preliminary data is presented in this abstract. Changes in angle were significantly different between the measurement methods for L2-L4 segment during guided flexion and for the L2-L4 and L4-S1 segment during guided extension ($p<0.05$). The Tukey post-hoc test showed that the motion capture and accelerometers were comparable ($p=0.625$-1.000) but that the skin-based sensors underestimated the change in angle in comparison to QF ($p<0.05$). The maximum change in lumbar angle (L2-S1) during flexion was 29.89±1.73° for QF, 17.31±14.91 for motion capture, and 20.40±11.79° for accelerometers. The maximum change in lumbar angle (L2-S1) during extension was -10.98±4.05° for QF, -11.35±6.05 for motion capture, and -9.43±6.05° for accelerometers. The lumbar angles (L2-S1) at mid and maximal range positions were not significantly different between the three measurement methods for both guided flexion and extension ($p=0.548$-0.984).

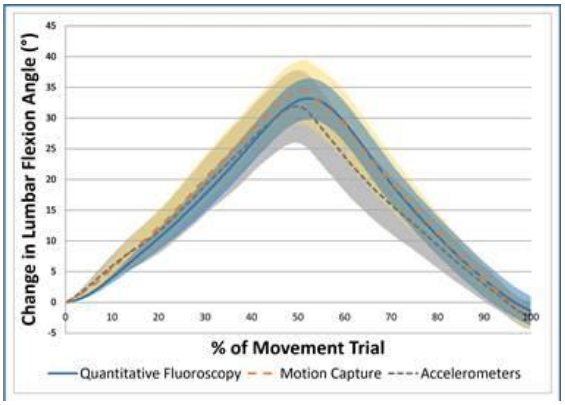

Figure 1: Average Change in lumbar flexion angle and the 95% confidence interval (shaded areas) of 20 participants during the guided flexion trial.

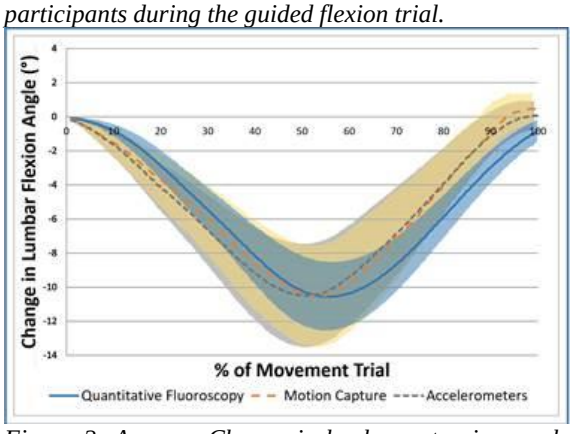

Figure 2: Average Change in lumbar extension angle and the 95% confidence interval (shaded areas) of 20 participants during the guided extension trial.

Discussion

Our results suggests that total lumbar and intersegmental angles vary during dynamic movement when measured directly (QF) or indirectly (skin markers). Skin-based markers underestimate the actual change in vertebral angle. Angles measured by accelerometer and motion capture are comparable throughout spine range of motion.

References

1. Breen et al. (2012). Adv Orthop, vol. 2012, Article ID 802350, 10 pages, 2012.

Acknowledgements

Funding from a NSERC Discovery Grant (#20161771) (DDC) and the Canadian Society for Biomechanics graduate student travel grant (MF).

IN-VITRO MODELLING OF THE HUMAN INTERVERTEBRAL DISC DEGENERATION

Edgar D. Rivera (1), Jude Meakin (1), Tim Holsgrove (1)

1. College of Engineering, Mathematics and Physical Sciences, University of Exeter, United Kingdom

Introduction

The intervertebral disc (IVD) is the connective tissue between adjacent vertebrae which provides stability, movement, and transmits loading through the spine [1]. IVD degeneration is a multifactorial disorder, and this may lead to degenerative disc disease, which can result in substantial pain and disability [2]. Understanding the mechanisms behind IVD degeneration is critical in developing and evaluating treatments and therapies for degenerative disc disease [3]. Existing models of IVD degeneration disrupt the structure of the disc through injury (e.g. needle puncture) [4], hyperphysiological loading [5], or biochemical degradation of extracellular matrix components [6]. These investigations provide valuable details behind IVD degeneration mechanisms; however, there is still a need for clinically relevant disc degeneration models. This study employed mechano-optical analyses to provide novel data with which to understand how micro-structural changes are linked to IVD load-recovery behaviour.

Methods

Sinusoidal cyclic loading was applied to isolated disc specimens (IVD including the adjacent two vertebrae) from bovine tails. Two experimental groups were tested: control (CTL) and overload (OVL). All specimens were submerged in a 37°C saline bath. Both groups were subjected to 2 hours static preconditioning (0.5 MPa) followed by eight periods of 2-hour sinusoidal loading (0.5 ± 0.3 MPa at 1 Hz) and 1-hour static loading (0.2 MPa). The first 8 hours of the protocol was used to equilibrate specimens. The OVL group differed from the CTL group in the 4th period, where a hyperphysiological cyclic load (2.6 ± 1.0 MPa at 5Hz) was applied (Figure 1). The results were evaluated in terms of the cumulative disc height (CDH), which was the change in the disc height after the recovery period with respect to a baseline (the height after the 8-hour equilibration stage), stiffness and microstructure was assessed using polarised light and multi-photon microscopy.

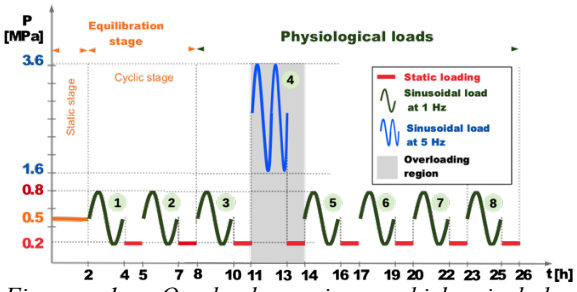

Figure 1: Overload regime which includes loading/recovery periods and testing stages.

Results and Discussion

The CDH did not differ significantly between the CTL and OVL groups during the equilibration period. Similarly, no significant difference was observed in the CDH at any time point with respect to the baseline for the CTL group. This suggests that static preconditioning, and first two loading period were satisfactory in stabilising the specimens load-recovery behaviour. The CDH between the CTL and OVL groups was statistically significant in periods 4 to 8 ($p<0.046$). Similarly, within-subject significance in CDH with respect to the baseline was only detected in the overload group ($p<0.027$) (Figure 2). This suggests that overloading may cause disc height loss which is not recovered in subsequent physiological loading and recovery periods. In contrast, no statistical differences were identified in the stiffness. Imaging revealed minor disruptions in the tissue components of the OVL group when compared with the CTL group (Figure 3), with disruption to the nucleus pulposus and cartilaginous endplates. The damage initiated resembles mild to moderate disc degeneration, as disc height was lost, but the stiffness was unaltered. Therefore, this hyperphysiological loading may be valuable to further investigate the onset of IVD degeneration.

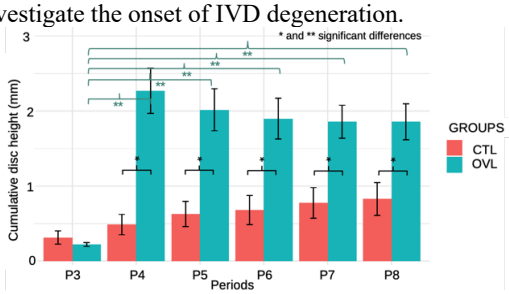

Figure 2: Cumulative disc height comparison.

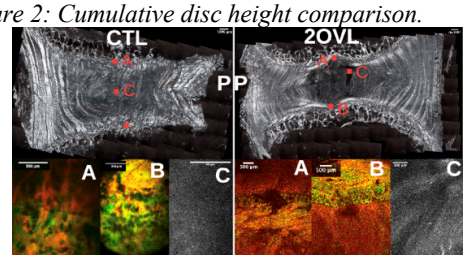

Figure 3: Microstructural analysis of the samples.

References

1. Urban JP, Roberts S, Arthritis Res Ther, 5:120–30, 2003.
2. Vergroesen P et al. Osteoarthr Cartil, 23:1057–70, 2015.
3. Salzmann SN et al, Curr Rev Musculoskelet Med, 10:153–9, 2017.
4. Michalek AJ et al, Spine J, 10:1098–105, 2010.
5. Wade KR et al, Spine (Phila Pa 1976), 40:891–901, 2015.
6. Roberts S et al, BMC Musculoskelet Disord, 9:24, 2008.

A COMBINED IN VITRO – IN SILICO APPROACH FOR LUMBAR SPINE KINETIC AND KINEMATIC CHARACTERIZATION

Simone Borrelli (1), Mara Terzini (1), Giovanni Putame (1), Andrea Ferro (2), Stefano Marone (2), Cristina Bignardi (1), Alberto L. Audenino (1)

1. Polito^{BIO}Med Lab, Department of Mechanical and Aerospace Engineering, Politecnico di Torino, Italy.
2.Oncologic Orthopaedic Surgery Division, CTO Hospital - Città della Salute e della Scienza di Torino, Italy.

Introduction

At present, the modelling of human lumbar spinal segment is giving significant contributions in the understanding of spinal functional mechanisms, and consequently, it is helping to shed light on clinical issues. Nevertheless, the existing multi-segmental multibody models are mainly validated by recurring to data obtained from single functional units' studies which do not fully reflect the real behaviour of the vertebrae once they are combined [1]. Therefore, this study is intended to provide both an extensive and local characterization of a validated rachis phantom, in terms of its global stiffness and single vertebrae's kinematic patterns. This would lead to an exhaustive validation of an entire lumbar spine 3D multibody model.

Methods

A joint approach, embracing experimental tests and multibody modelling, was adopted. The experimental protocol consisted in 4 different motion-controlled loads (flexion, extension, compression, and torsion), designed for a linear-torsion test machine (Instron E3000) and applied to a validated Sawbones lumbar spinal phantom (T12 to S1, SKU3430) in its elastic field. The range of motions were limited in order to perform conservative tests and not to overcome the Neutral Zone of the single FSUs [2].

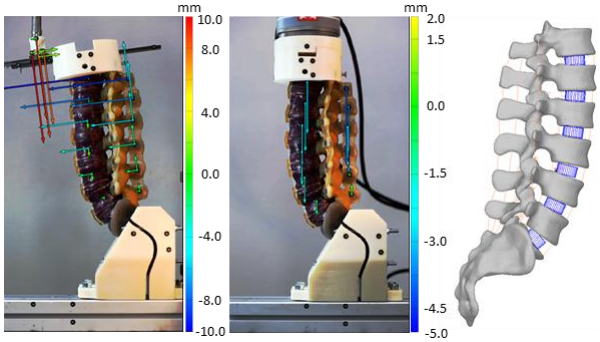

Figure 1: Left and center: experimental setup and kinematic study for the flexion and compression loadings. Right: the lumbar spine multibody model.

Relative displacements between vertebrae, postprocessed in GOM*correlate* environment, were also included by the means of planar motion tracking: markers were positioned on the vertebral bodies surfaces and on their transverse and spinous processes. Furthermore, a multibody model was implemented from the Sawbones CAD geometry in MSC Adams. In accordance with the phantom, the passive elements of the spine were included in the model: ligaments were modelled as pre-strained non-linear tension-only springs, while IVDs were represented as bushing elements oriented coherently with the adjacent vertebrae's endplates [3,4]. To properly compare the results, the experimental loading protocol was replicated in the numerical environment.

Results

Starting from data obtained by experimental testing, the global whole lumbar segment stiffnesses were computed (Table 1). In the investigated ROM, an almost linear behaviour of the dummy was enregistered. Accordingly, the stiffnesses were obtained as the slopes of the angle (T12-L5) - force linear approximation curves (R^2>0.93). The results also revealed a strong correspondence between the experimental and numerical models' kinematic behaviours, with the largest deviation at the maximum amplitude of the motions equal to ± 8%.

Motion	Experimental	Numerical
Flexion	1.49 ± 0.06 Nm/deg	1.75 Nm/deg
Extension	3.45 ± 0.07 Nm/deg	3.03 Nm/deg
Compression	94.4 ± 0.64 N/mm	87.8 N/mm
Torque	2.7 ± 0.01 Nm/deg	2.8 Nm/deg

Table 1: Results and comparison between experimental and numerical lumbar spines' stiffness concerning the global stiffnesses for different motion-loadings. Experimental data reports the mean and standard deviation of 6 replications.

Discussion

The novel multibody model appears to be a promising tool for reliable insights into the dynamic behaviour of lumbar column. Hence, in a short-term perspective, this model could be further exploited to simulate pathological conditions and their corresponding post-operative outcomes, as well as to compare the effects of different surgical strategies. Finally, if coupled with spinal musculature, the model could elucidate load sharing patterns for many kinds of motions.

References

1. C. Zhang et al, J. Biomech, 100:109579, 2020.
2. Panjabi et al, J Bone Jt. Surg. Am 76(3), 413-424, 1994.
3. G. Putame et al, Front Bioeng Biotech, 7:180, 2019.
4. T.K. Rupp et al, Biomech Model Mechanobiol 14(5):1081-105, 2015.

KINEMATIC ANALYSIS OF DYNAMIC LUMBAR SPINAL RHYTHMS DURING FLEXION AND RETURN TO NEUTRAL

Alexander Breen[1], Diana De Carvalho[2], Martha Funabashi[3], Greg Kawchuk[4], Isabelle Pagé[4], Arnold Wong[5], Alan Breen[1]

1 AECC University College, Bournemouth, United Kingdom. 2 University of Newfoundland, St. John's, NL, Canada. 3 Canadian Memorial Chiropractic College, Toronto, Canada. 4 University of Alberta, Edmonton, Canada. 5. Université du Québec à Trois-Rivières, Canada. 6 The Hong Kong Polytechnic University

.

Introduction

The use of fluoroscopy allows for continuous in-vivo intervertebral lumbar spinal motion quantification, the outputs of which are critical to informing musculoskeletal models**.** Furthermore, recent studies using standardised image acquisition protocols have indicated that the sharing of motion between lumbar levels during bending may be a mechanical marker in low back pain [1].

Objective

The aim of this study was to determine the level-by-level distribution of continuous intervertebral rotation for L2-S1 during lumbar flexion and return using a standardised weight bearing protocol in a healthy population.

Methods

Low dose continuous fluoroscopy image sequences (recorded at 15 frames per second) were acquired from a sample of 131 asymptomatic participants during an active, weight-bearing lumbar flexion and return motion using a bending protocol that minimized accessory movements. Intervertebral rotations in the sagittal plane were extracted for each level (L2-S1) in each frame and transformed into the proportional contribution to the total L2-S1 angle. Mean and ± 95% confidence interval (±CI95) values across all participants were computed at each 1% increment of the L2–S1 ROM. Data were separated, to distinguish the flexion and return-to-neutral portions of the bending task. Statistically significant differences between each level's contribution motion was detected by the absence of ±CI95 bands overlap [2].

Results

Full data sets were extracted from 127 participants, 48.8% female, mean age of 38.6 years [range: 21-70]. The proportion of motion performed by each level at moderate and full flexion was similar to previous studies [3]. However, our results also show that there are differences in the contributions to bending throughout the motion both between levels and within levels as participants progress throughout the task [Figures 1 and 2]. Across the study population, each intervertebral level had its own characteristic motion signature, with significant differences ($p<0.05$) between each levels contribution throughout the motion, despite their variability. These findings are likely related to a combination of loading, motor control and inter-joint material properties.

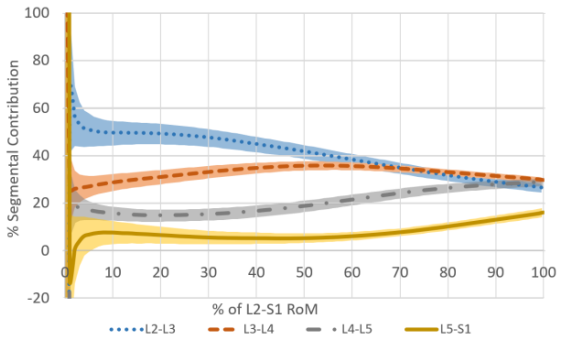

Figure 1: Average segmental contribution to lumbar flexion and the 95% confidence interval (shaded areas).

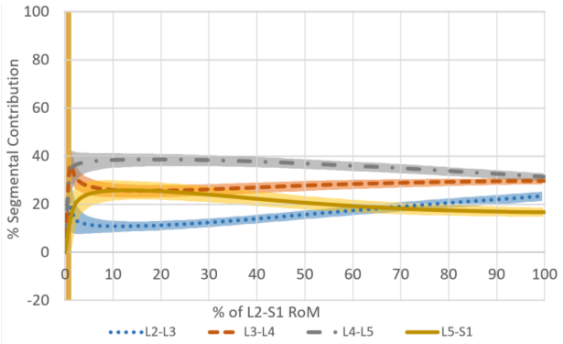

Figure 2: Average segmental contribution to lumbar Return-to-neutral and the 95% confidence interval (shaded areas).

Discussion

This is the largest data-set available to date to present normative values for continuous segmental contributions to motion in the lumbar spine. Unlike previous studies of similar size [4], segmental contribution to motion was found vary throughout the task. The percent contribution patterns in flexion and return are distinctly different as one would expect with the different muscle contractions.

References

1. Breen A, et al. Eur Spine J. 27:145-153, 2017
2. Aiyangar A, et al. J Biomech. 48:3709-3715, 2015.
3. Widmer, J., et al. A of Biomed. Eng., 47:1491-1522, 2019.
4. Wong, K.W et al. Spine, 29(15), pp.1636-1641. 2004.

INFLUENCE OF DOUBLE RODS AND INTERBODY CAGES ON ROM AND ROD STRESS AFTER LUMBOPELVIC INSTRUMENTATION

Aleksander Leszczynski (1), Frank Meyer (1), Yann-Philippe Charles (2), Caroline Deck (1), Rémy Willinger (1)

1. University of Strasbourg, France; 2. Service de Chirurgie du Rachis des Hôpitaux Universitaires de Strasbourg, France

Introduction

Corrections of degenerative lumbar scoliosis and sagittal malalignment are associated with significant complications. Major complications are rod fractures and pseudarthrosis, especially in the lumbosacral junction [1]. The hypothesis of this study is that the use of interbody cages and/or multiple rods could decrease movement and reduce stress on the primary rods and thus prevent complications. The objective of the current work is to evaluate and compare the L5-S1 range of motion (ROM), and the maximal stresses on the primary rods for various instrumentation configurations using a finite element model (FEM).

Materials and Methods

The study was performed using a FEM of the lumbosacral spine (L1–pelvis). Various combinations of interbody cages and device configurations (bilateral single vs. double rod) were investigated. The instrumentation consisted of 5.5 mm diameter of CoCr rods, which reached from L2 to the pelvis for the principal rod and from L3 to the pelvis for the secondary rod. Three configurations, 1 bilateral rod (Config1), 1 bilateral rod + interbody cage at L5-S1 (Config2), and double rod + interbody cage (Config3, shown in Figure1) were simulated. Intact and instrumented model configurations were validated in terms of ROM and strains in the principal rods against experiments from the literature. Loading was applied by pure moments of 7.5 Nm in flexion (FL), extension (EX), lateral bending (LB) and axial rotation (AR) to the superior vertebrae (L1). The pelvis was fully constrained. Results are evaluated in terms of L5-S1 ROM and maximum of von Mises on the primary rods.

Results

The comparison of L5-S1 ROM for the intact and all three instrumented configurations in FL, EX, LB and AR are presented in Table1. All tested instrumentation configurations reduced systematically the mobility of the spine.

	Intact	Config1	Config2	Config3
FL	8.42°	0.39°	0.00905°	0.0069°
EX	2.76°	0.313°	0.024°	0.015°
LB	2.5°	0.033°	0.0075°	0.0068°
AR	1.0°	0.1°	0.032°	0.037°

Table 1: Comparison of ROM at L5-S1.

The maximal von Mises Stress in the principal rods in all three configurations are shown in Table 2.

	Config1	Config2	Config3
FL	195 MPa	178 MPa	170 MPa
EX	157 MPa	142 MPa	142 MPa
LB	86 MPa	69 MPa	69 MPa
AR	139 MPa	146 MPa	109 MPa

Table 2: Comparison of maximal von Mises Stress in the principal rods in all three configurations.

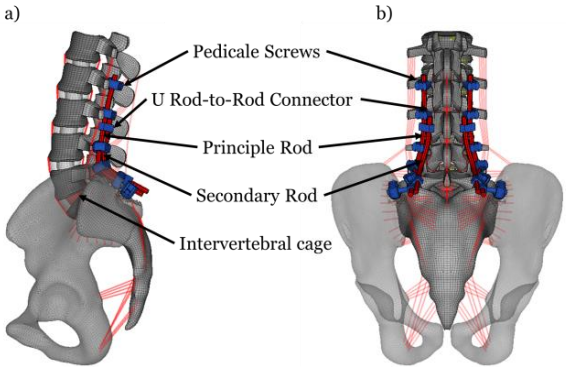

Figure 1: Sagittal (a) and posterior (b) illustration of the configuration config3.

Conclusion

The study evaluated the mechanical performance of various instrumentation configurations after the correction of sagittal imbalance. The results showed that multi-rod constructs and interbody cages increase the stability of the construct, which results in reduced ROM and stress on primary rods. Out of the tested configuration, the bilateral double-rod configuration with interbody cages reduces the stress on the spinal fixators at best, resulting in a minimal risk of rod breakage.

References

1. Godzik et al., Spine J, 19:1121-1131, 2019.

Acknowledgements

The authors would like to thank Clariance for their support.

« TACTILE » – USABILITY OF AN AUTOMATED, TWO-POINT DISCRIMINATION TEST FOR LOW BACK PAIN

Daniel Baumgartner (1), Claudia Höchner (1), Roman Kuster (1), Dominik Textor (1)

1. Zurich University of Applied Sciences ZHAW, IMES Institute of Mechanical Systems, Switzerland

Introduction

A decreased tactile acuity in patients with non-specific chronic low back pain (NSCLBP) results in an increased two-point discrimination (TPD) threshold compared to healthy controls (1). The training of the TPD resulted in a reduction of the TPD threshold of 11.79mm in patients with NSCLBP (2).

Currently, TPD is performed with a calliper by an accompanying physiotherapist. The use of a home based TPD device would be beneficial for an independent training.

Aim of the project

Usability and acceptability of a novel, automated tactile acuity training device (TacTile) in patients with non-specific chronic low back pain (NSCLBP)

.

Material & Methods

In total six participants with NSCLBP participated in the study. A home based training has been performed with the TacTile during three weeks, in total 20 Min a day. Qualitative and quantitative assessments have been performed such as pain intensity and Oswestry disability index.
Additionally, feedback of the users has been collected in a questionnaire in particular to acquire “Median System Usability Scale score” and “adherence rate”.



Fig. 1: Novel device placed at the lower back to apply a stimulus by small motors (solenoids). Recognition of one or two automated punctures had to be confirmed through an app.

Results

The “Median System Usability Scale score” for the application of the TacTile device over 3 weeks showed 71.25 out of 100 points. Median adherence rate has been 85.7%.
No significant reduction in the pain intensity or in the Oswestry disability Index has been detected (Fig. 2).

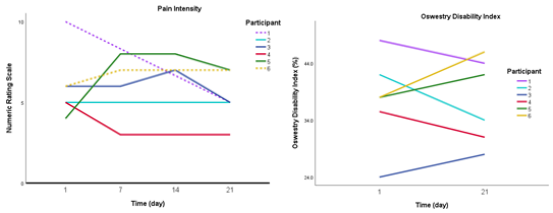

Fig. 2: Pain intensity development and Oswestry disability index over three weeks.

Statements of participants

“For me it was easy to handle, but this has to be the aim, because different people should be able to use it.”

“If you don’t put it on properly or not perfectly, there is a small gap between the bandage and the back and then the pressure is not correct.”

“I can’t tell if it had an effect on the back pain.”

Conclusion

- The TacTile training and the device were well accepted by the participants
- Tactile was considered as helpful device to train the sensory perception of the lower back independentlyat home
- The therapy should be integrated in a multimodal treatment approach in combination with other treatments

The device needs to integrate more patients in an extended study to proove a reduction in pain or in the two-point discrimination distance.

Acknowledgements

[1] Adamczyk et al., 2018, doi: 10.1097/ajp.0000000000000499
[2] Wälti et al., 2015, doi: 10.1186/s12891-015-0533-2

HOW DO INSTRUMENTATION PARAMETERS IMPACT THE 3D CORRECTION OF THORACIC ADOLESCENT IDIOPATHIC SCOLIOSIS?

Luigi La Barbera (1,2,3), A. Noelle Larson (4), Carl-Eric Aubin (1,2)

1. Dept. of Mechanical Engineering, Polytechnique Montréal, Canada; 2. Research Center, CHU Sainte-Justine, Canada; 3. Dept. of Chemistry, Materials and Chemical Engineering, Politecnico di Milano, Italy; 4. Dept. of Orthopedic Surgery, Mayo Clinic, Rochester, MN, USA

Introduction

One major goal of posterior fixation surgery for complex spinal deformities is to achieve optimal 3D correction, while achieving a balanced spinal alignment and preventing curve progression. However, multiple strategies combining widely variable instrumentation parameters, such as the number of fused levels, screw patterns, rods curvatures/stiffnesses, and correction maneuvers are possible [1]. *In silico* patient-specific models can be used to virtually test the biomechanical impact of different instrumentation strategies, while providing detailed information to support the surgical decision-making process [2,3].

The aim of the present modelling study was to assess the correlations between instrumentation parameters and the resulting 3D correction of a representative thoracic scoliosis case.

Methods

A patient-specific biomechanical model of a thoracic scoliotic curve was built using MD Adams 2018 (MSC Software, Santa Ana, CA) [2,3]. An established algorithm analyzed a variety of different widely-used instrumentation parameters [3]:

i) *upper instrumented vertebra* (UIV: from T3 to T6);
ii) *lower instrumented vertebra* (LIV: from L1 to L3);
iii) *screw patterns* [1];
iv) differential *concave-convex rods curvature*: 30°-15°, 45°-15°, 60°-15°, 45°-30°, 60°-30°, 60°-45°;
v) *rod stiffness* (material/diameter): low (Ti/5.5mm), medium (CoCr/5.5), high (CoCr/6).

The simulated primary correction maneuvers were concave rod rotation and *en bloc* derotation.

Factorial ANOVA and correlation analyses quantified how the number of fused vertebrae and implant density (i.e. screws per instrumented level), as clinical (independent) variables of interest, impacted the 3D correction (dependent variables) in terms of Cobb angle, thoracic kyphosis (TK) and apical vertebral rotation (AVR) across the 1080 simulated instrumentation strategies.

Results

The Cobb angle was mainly affected by the LIV and UIV (explaining 84% and 11% of its overall variance), TK by rod curvature and UIV (56% and 36%), while AVR by LIV, UIV, and rod curvature (35%, 32% and 19%). Linear interactions contributed <5%.

3D correction was more correlated with the number of fused vertebrae rather than with implant density. The Cobb angle significantly improved with distal LIV for a given number of fused vertebrae ($p<0.05$, Figure 1.a), and using high-stiffness rods. TK significantly improved using higher curvatures and differentially contoured rods (Figure 1.b), especially with increasing the number of fused vertebrae (from 9 to 13, $p<0.05$), and using a more cranial UIV. AVR was marginally impacted (<5°), compared to Cobb and TK, by the simulated instrumentation parameters.

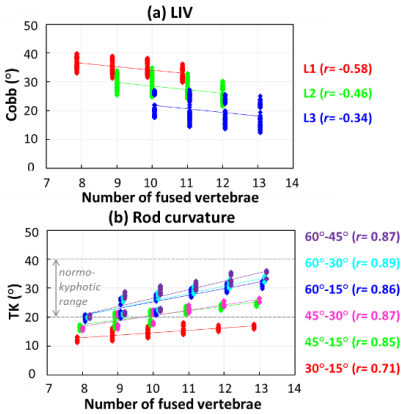

Figure 1: Correlation between Cobb (a) or TK (b) vs. the number of fused vertebrae, respectively, grouped by the lowest instrumented vertebra and concave-convex rod curvature. r=Pearson correlation coefficients ($p<0.05$).

Discussion

The presented *in silico* patient-specific approach provided unprecedented details over a much wider range of instrumentation parameters compared to the published literature [2]. A trade-off between mobility (number of unfused vertebrae) and correction across multiple anatomical planes was required for the thoracic curve herein considered. Such information could support the surgeon in the decision-making process, while enabling to optimize the 3D correction [3].

References

[1] Le Navéaux et al., Scoliosis Spinal Disord, 13:21, 2018. [2] La Barbera et al., Spine Deform, 2021, doi: 10.1007/s43390-020-00275-2. [3] La Barbera et al., Clin Biomech, 2021. doi: 10.1016/j.clinbiomech.2020.105200.

Acknowledgements

Natural Sciences and Engineering Research Council of Canada-Medtronic Industrial Research Chair in Spine Biomechanics, Canada Research Chair in Orthopedic Engineering. Canada First Research Excellence Fund through TransMedTech Institute Postdoctoral Fellowship.

INVESTIGATION OF KNEE FLEXION UNDER ORTHOSTATIC PHISIOLOGICAL LOADS THROUGH DYNAMIC MRI

Michele Conconi (1), Matteo Berni (2), Nicola Sancisi (1), Filippo De-Carli (3), Giuseppe Monetti (3) and Vincenzo Parenti-Castelli(1)

1. Dept. of Industrial Engineering, University of Bologna; 2. Medical Technology Laboratory, Istituto Ortopedico Rizzoli - IOR, Bologna, Italy; 3 Primus Medical Center, Forlì, Italy

Introduction

Measuring the joint motion under physiological loads is fundamental for the comprehension of the normal and impaired musculoskeletal function [1]. Present measurement techniques in vivo are however invasive [2,3] or imprecise [4]. Dynamic magnetic resonance imaging (DMRI) represents an emerging technology that may overcome these limitations [5]. This work presents a procedure to quantify the knee kinematics under physiological loads and about 90° of knee flexion. The accuracy of a new registration algorithm is also discussed.

Methods

Clinostatic MRI of the right knee of three healthy volunteers were acquired (G-Scan Brio, Esaote SpA, 0.25 T, 3D-HYCE) and segmented (MITK Workbench 2018) to reconstruct the reference geometry of the femur, tibia, and fibula bones. The scanner was then rotated 90° to allow weight bearing. The volunteer stood with the right leg in the scanner, while the contralateral leg was supported by a MR compatible hydraulic rig (Fig. 1.a), which guided the knee flexion by lowering the movable step at controlled velocity. The knee flexion was recorded through a planar DMRI (2D-HYCE S Gradient Echo), producing a slice of 5 mm in thickness every 2.9 seconds (roughly 75 frames per motion). The exam was performed on 2 planes (Fig. 1.b). The tibio-femoral kinematics was reconstructed by a new proprietary algorithm, which automatically register the patient bones on the two planes. The algorithm sensitivity to the first guess was investigated by perturbing the initial bone position and orientation up to ±10° and ±10 mm on each component, for a total of 1458 combinations. To establish a reference motion for validation, five static weight-bearing MRI (3D-HYCE) were also acquired, roughly every 20° along the patient flexion. To evaluate the algorithm accuracy and sensitivity to the plane choice, simulated DMRI were generated from the static scans.

	Rot. MAE [°]	*Trans. MAE [mm]*
Knee 1	*1.63 ± 1.15*	*1.67 ± 1.06*
Knee 2	*2.39 ± 2.19*	*1.51 ± 0.56*
Knee 3	*3.05 ± 1.47*	*1.16 ± 0.73*

Table 1: MAE between DMRI reconstructed and static MRI approximated knee motion for the 3 volunteers.

Results

On simulated DMRI, orientation and position MAE were 0.71° and 0.36 mm when tracking a single bone (femur) with 3 orthogonal planes (axial, coronal and sagittal), and 1.38° and 1.66 mm when reconstructing tibio-femoral motion with two optimized planes (Fig. 1.b). Table 1 report orientation and position MAE between real DMRI reconstructed and static MRI approximated knee motion. For the investigated combinations, the initial guess did not affect the algorithm output.

Discussion

Numerical results on simulated data show that the registration procedure may be accurate enough for clinical purpose. The difference between simulated and real data accuracy may be ascribed to several factors, mainly a not perfect synchronization of the two DMRI motions, and differences between static and dynamic evaluation of the tibio-femoral kinematics. The results described well the typical pattern of the tibiofemoral motion (Fig 1.c). The approach can be used for the in-vivo, loaded characterization of joint pathology and for model validation.

References

1. Storheim K. et al., *Ann Rheum Dis*, 73:949-950, 2014.
2. Ramsey D.K. et al., *Knee Surg Sports Traumatol Arthrosc*, 11:344-349, 2003.
3. Miranda, D.L. et al., *J Biomech Eng*, 133:121002, 2011.
4. Dumas R. et al., *J Biomech*, 47:476-481, 2014.
5. Borotikar B., et al., *PloS one*, 12:e0189587, 2017.

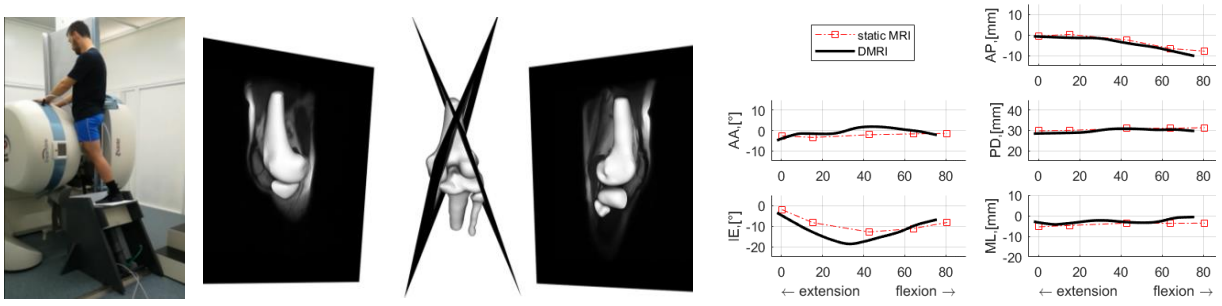

(a) (b) (c)

Figure 1: Setup for the DMRI scans (a). Registration of femur and tibia on DMRI acquired on two optimized planes (b). Comparison between tibio-femoral motion reconstructed from DMRI and approximated from static MRI for one knee (c).

FEASIBILITY OF RIB KINEMATICS AND INTERCOSTAL SPACE MECHANICAL CHARACTERIZATION BY ULTRASOUND

Alisa Hisaund (1), Raphaël Pietton (2) , Raphaël Vialle (2), Wafa Skalli (1), Claudio Vergari (1)

1 Institut de Biomécanique Humaine Georges Charpak, Arts et Métiers ParisTech, France. 2 Department of Pediatric Orthopaedics, Armand Trousseau Hospital, Sorbonne University, France.

Introduction

In severe adolescent idiopathic scoliosis (AIS), pulmonary function impairment has usually been evaluated though respiratory function tests, which partially explain the patient's underlying functional limitations leading to respiratory deficiency. One of the key elements of active respiration is the intercostal space, where thin muscles with alternating pennation angles facilitate the thoracic component of inspiration and expiration [1]. However, no previous report has evaluated the pulmonary impairment of adolescent with idiopathic scoliosis considering the rib kinematics and the mechanical properties of intercostal muscles (ICM), because of the measurement difficulty. In this work, the distance between ribs was measured with ultrasonography and ICM mechanical properties were estimated with shearwave elastography during breathing.

Method

Twenty-eight female subjects between 10 and 17 years old (22 asymptomatic subjects and 6 AIS patients) underwent ultrasound measurement of the intercostal space (figure 1).

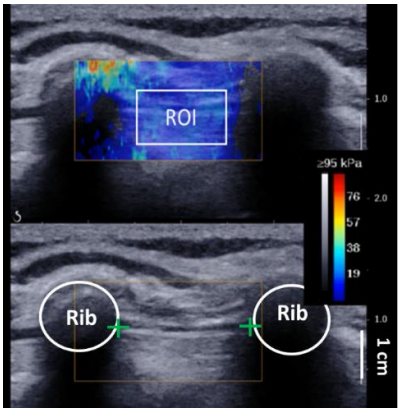

Figure 1 Ultrasound image of the intercostal space. The plus signs indicate the muscle insertions which were tracked to estimate ribs distance. Ribs cross-sections are also visible. The color chart represents local Young's modulus.

30-second movies of ultrasonography and shearwave elastography were acquired at the T8-T9 right and left intercostal spaces during normal breathing. ICM insertions in the ribs (Figure 1) were tracked in each frame with a sampling frequency of 2.5Hz. The distance between the ribs was measured, and the breathing cycles were identified. Shear wave speed (SWS) in the ICM was measured synchronously with ultrasonography (at 1 Hz) and interpolated in terms of percentage of breathing cycle. Measurements were repeated on 4 subjects by two operators to assess reproducibility.

Results

Asymptomatic subjects showed symmetric inter-rib movement and ICM SWS, with no significant differences either during inspiration or exhalation ($p > 0.5$). Reproducibility was 3 mm (17% coefficient of variation). Scoliotic patients showed symmetric ICM properties during exhalation ($p=0.17$), but significantly stiffer ICM in the convex side than in the concave during inspiration ($p=0.02$). AIS patients also showed smaller movements of the ribs (1.5 mm) when compared to asymptomatic subjects (2.4 mm, $p=0.025$ and $p=0.016$ for the distance between ribs at exhalation and inspiration, respectively).

Discussion

Asymptomatic subjects seem to have symmetric motion of ribcage sides and mechanical properties of the IC muscles, which was expected. AIS subjects appeared symmetrical during full exhalation, but their convex side appeared stiffer than the concave during full inspiration. This could be linked to the almost-horizontal orientation of the convex-side ribs in severe scoliosis.

The study confirms that the approach was feasible to measure local rib kinematics and mechanical properties. These findings complement the previous studies on quasi-static ribcage kinematics [2-3] by bringing information on a full cycle of breathing and, for the first time, on AIS patients. This approach was also feasible for the assessment of the IC muscle mechanical properties in AIS subjects during an entirely breathing cycle, completing previous work using this approach but which was only limited to an average value during the cycle [4]. Results must now be confirmed on a larger cohort of AIS patients,

References

1. Beyer et al, Clin Biomech, 29:434-438, 2014.
2. Beyer et al, Resp Phys Neurobiol, 232 :57-66, 2016.
3. Bastir et al, Anat Rrecord, 300 : 255-264, 2017.
4. Pietton et al. (Submitted 2019)

Acknowledgements

The authors are grateful to the ParisTech BiomecAM chair program on subject-specific musculoskeletal modeling (with the support of ParisTech and Yves Cotrel Foundations, Société Générale, Proteor and Covea).

MAGNETIC RESONANCE ELASTOGRAPHY: A TORSIONAL ACTUATION FOR AN ANISOTROPIC MUSCLE-MIMICKING PHANTOM

Chiara Gambacorta, Martina Guidetti, Thomas J. Royston

Richard and Loan Hill Department of Bioengineering, University of Illinois at Chicago, US;

Introduction

The evaluation of the stiffness of a body part has been extensively used by physicians to detect numerous pathologies that affect tissue mechanical properties. Neuromuscular conditions like dystrophy and spasticity may alter muscle tissue elasticity and viscosity. Evaluating tissue stiffness has been traditionally carried out through qualitative manual palpation when the tissue is within reach or via invasive biopsy. Elastography is a noninvasive stiffness imaging method aimed at improving upon the accuracy, resolution and measurement depth. It typically uses ultrasound or magnetic resonance modalities to image mechanical waves in the tissue under examination. The interpretation of the behavior of such waves leads to the mapping of the relevant mechanical parameters, such as elasticity and viscosity values. Magnetic Resonance Elastography (MRE) [1] has become the gold standard for staging liver fibrosis. Unlike liver, skeletal (striated) muscle is highly anisotropic with different elastic properties along versus across the muscle fibers. This makes interpretation of MRE measurements more difficult, but also offers the prospect of more information that may have clinical value if one can actuate wave motion in multiple directions in order to capture the direction-dependent properties of the tissue. The novelty of our current research is the introduction of a new kind of actuation system, which induces torsional shear wave motion into the region of interest. Its initial application to anisotropic phantoms, similar to muscle, is summarized here [2].

Methods

The muscle tissue mimicking phantom is made of PDMS (184 Silicon from DOW) fibers with a diameter of 100 um, inserted in a soft plastic matrix. Such a phantom is inserted into a cylindrical pyrex tube that is connected to a stepper motor in a way to provide torsional oscillatory motion to the cylindrical tube along its axis (See Fig. 1). The phantom within the test tube, in turn, is subjected to radially converging torsional transverse wave motion [2]. The stepper motor is connected to a gradient amplifier system, that contains both the MRI gradients and the Motion Encoding Gradient MEG (needed to encode the signal into its phase component); its activation is triggered by a Matlab sequence that possesses the correct tuning for each of the parameters of the process (MEG cycles, MEG amplitude, vibration frequencies, displacement amplitude for the motor, etc.). Once the complex wave images have been obtained, they can be extracted in the form of matrices and undergo reconstruction (the process of estimating a mechanical property map based on the measured wave motion). A novel strategy is employed in the present study, called Transformation Elastography, in which a directional filtering process is first used to estimate the anisotropic ratio ϕ. The wave image is then spatially distorted by this ratio in order to make the anisotropic problem seem isotropic [2-3], after which a conventional reconstruction algorithm for isotropic materials (e.g. direct inversion) is employed.

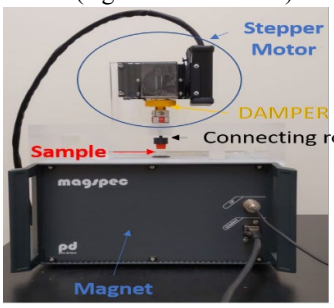

Figure 1: Torsional actuation for MRE in a cylindrical sample inserted in a table-top MRI system.

Results and Discussion

Prior to the experiment, a numerical simulation study using finite element analysis (FEA) was conducted to understand the torsional shear wave field in a transversely isotropic material with its axis of isotropy orthogonal to the axis of the cylindrical container. The TE approach to inversion and reconstruction was found to provide a more accurate estimate of anisotropic shear storage and loss moduli, as compared to an isotropic assumption, and with minimal additional effort (simply distorting geometry based on a k-space-based estimate of the anisotropic ratio ϕ). Results of the experimental study demonstrate the capability of the novel torsional actuation system and show measurement patterns similar to the numerical simulation. Though, as expected, specimen inhomogeneity and inherent measurement noise limit the accuracy of the reconstruction method. Studies are under way to address these issues and improve our ability to quantitatively map anisotropic tissue properties like those found in striated muscle.

References

1. Hirsch S, Braun, Sack I. *Magnetic Resonance Elastography*, Wiley-VCH, Weinheim, Germany, 2017.
2. Guidetti M, Caratelli D, Royston TJ. J. Acous. Soc. Am. 146: EL451-457, 2019.
3. Guidetti M, Royston TJ. J. Acous. Soc. Am. 144: 2312–23, 2018.

Acknowledgement

Financial support from the following is acknowledged: NSF #1852691 (PI: Royston); NIH #AR071162 (PI: Perreault).

WEIGHT-BEARING CT IN BIOMECHANICAL ANALYSES OF THE LOWER LIMBS: BIOMECHANICAL AND CLINICAL MEASURES

Claudio Belvedere (1), Paolo Caravaggi (1), Stefano Durante (2), Alberto Leardini (1)

1. Movement Analysis Laboratory 2. Nursing, Technical and Rehabilitation Assistance Service
IRCCS Istituto Ortopedico Rizzoli, Bologna, Italy

Introduction

Biomechanical modeling of the musculo-skeletal system shall be based on medical imaging, possibly in realistic loading conditions. Standard CT and MRI can provide accurate 3D reconstructions, but the position normally used, i.e. supine, is far from daily living activities, i.e. under load. On the other hand, weight-bearing can be obtained, but only with traditional X-ray pictures in 2D [1]. Recently, medical imaging devices based on Cone-Beam CT (CBCT) technology can provide 3D images in weight-bearing. This fundamental feature [2] adds up to relatively low radiation, high spatial resolution, and convenient ergonomy [3-6]. Therefore CBCT is promising to support clinical and biomechanical analyses. The scope of the present paper is to report on techniques to deduce 3D orientation angles of the foot bones and on preliminary activities of data collection and analyses in a number of different treatments and conditions.

Methods

CBCT scans have been collected ('OnSight 3D Extremity System', Carestream, Rochester, NY), mostly at the foot and ankle, in single-leg upright posture (Figure 1). From these 3D data-sets, Dicom files are generated by virtual slicing at 0.26 mm distance, along most appropriate axes. 3D bone models in STL format are obtained with semi-automatic segmentation (AMIRA, FEI Visualization Sciences Group). The ground is used as 3D reference for global bone orientation. A proprietary software in Matlab (MathWorks Inc., Natick, USA) defines an anatomical reference frame for the foot. Anatomical axes and angles are also defined, according to traditional or novel techniques [1, 4]. The Principal Component Analysis [7], is also used to provide automatically the orthogonal axes of maximum, intermediate and minimum variance of the bone surface points. Axes based on relevant anatomical landmarks or on mean diaphyseal points are also defined as longitudinal directions, still in 3D. Absolute and relative angles characterize foot bone architecture. These measures are combined with kinematics and baropodometric analysis, the latter even simultaneous to CBCT scan. These techniques are exploited in a number of clinical studies, such as flat foot correction, ankle arthroplasty, diabetic foot, patello-femoral instability etc.

Results

CBCT and the present techniques for 3D analyses of skeletal structures finally in weight-bearing enable established angular measurements with more accuracy and open the door to novel 3D measures such as multi-planar inclination of the metatarsal bones, volumetric representations of the longitudinal arches, spatial angles between longitudinal axes, etc. The present initial experience shows that the undesirable projection effect of malpositioning or of major deformity of the foot is considerably reduced by anatomical frame definitions in 3D and the automatic PCA-based calculations. Multi-instrumental analyses are showing correlation between CBCT based 3D measurements and BMI, Year-Of-Disease, and metatarsal loading.

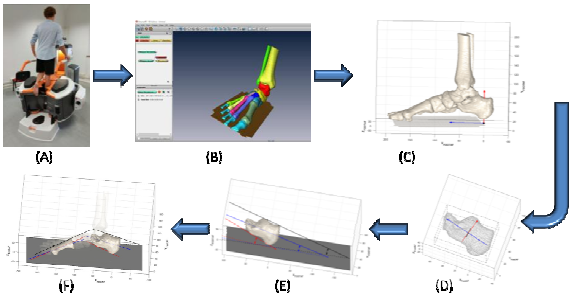

Figure 1: The full process from CBCT scans to 3D geometrical analyses of foot bones: examples on anatomical axes of the calcaneus and first metatarsus.

Discussion

Access to bone structures in 3D and in weight-bearing is finally available in medical imaging, overcoming current 2D X-ray pictures and 3D CT in unloaded conditions, i.e. supine. Clinical studies and biomechanical modelling on physiology, performance, pathology, and treatment of the lower limb can take much advantage of these modern CBCT devices. New 3D measurements are under development, to enlarge traditional planar angular and linear measurements.

References

1. Carrara et al, Foot Ankle Surg, S1268-7731(19)30113-4, 2019.
2. Hirschmann et al, Europ Radiol, 24(3):553-8, 2014.
3. Barg et al, Foot & Ankle Int, 39(3): 376-386, 2018.
4. Lintz et al, EFORT open reviews, 3(5): 278-86, 2018.
5. Ludlow et al, Medical Physics, 45, 4955-63, 2018.
6. Richter et al, Foot Ankle Surg, S1268-7731(19)30096-7, 2019.
7. Parr et al, J Biomech, 45(6):1103-1107, 2012.

Acknowledgements

The authors want to acknowledge the many participants to these studies, not all mentionable in the present author list.

BONE SAMPLE SELECTION FOR SCREW MECHANICAL TESTING BASED ON PERI-IMPLANT CT MORPHOMETRY

Juan D. Silva-Henao (1, 2), Dieter H. Pahr (1, 2), Andreas G. Reisinger (1)

1. Division Biomechanics, Karl Landsteiner Private University, Krems, Austria
2. Institute of Lightweight Design and Structural Biomechanics, TU-Wien, Austria

Introduction

Animal bone surrogate models are frequently used to test the mechanical competence of bone screws since they are generally easier to obtain and test compared to their human counterparts. Despite this, selecting an appropriate sample source which correctly represents the bone architecture in which the implant is placed is oftentimes overlooked. The present study proposed a methodology for surrogate sample selection based on computed tomography (CT) scans which uses a selection criterion based on the peri-implant bone architecture from the real implantation site.

Materials and methods

For this study, 36 HR-pQCT human radius scans, taken from a closely related study [1] each with 10 implanted distal radius screws, were used. A virtual cylinder probe with 4 mm diameter was created for every implanted screw to evaluate the peri-implant CT-derived bone morphometric values (MV). For each peri-implant volume of interest the MVs: cortical thickness, cortical thickness deviation, cortical volume, trabecular thickness, trabecular spacing and bone volume fraction where recorded averaged with the rest of the VOIs on that same location (i.e., average screw 1, 2, 3, etc.). Additionally, 2 animal models were selected, pork and sheep, to be used as potential sample sources. From each animal 6 bones (distal radius, proximal humerus distal and proximal tibia and distal and proximal femur) were scanned with a resolution of 70.6 µm to match, as close as possible, that of the human scans. Surface meshes with sizes ranging between 3000 and 4000 triangles were used to extract cylindrical probes. Each probe was positioned in the centre of each triangle and parallel to its normal vector (done for all bones). From each probe the same MV (BT/TV, Cr.Th. etc.) were recorded.

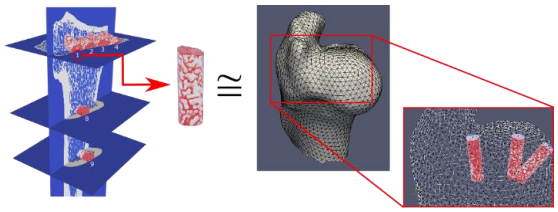

Figure 1: Peri-implant VOI and Mesh-based sample locations.

A bone similarity score (BoSS) based on that presented in [2] was used to compare the morphometry of each probe to that of the target average screw morphometry. For each MV (i) the "distance" between the target (t) and probed point (p) value was defined and then used to calculate the BoSS value for every point:

$$d_i = \frac{MV_t - MV_p}{MV_t}; BoSS_p = \sum d_i \qquad (1)$$

Results

The calculate BoSS values were mapped to the bone surface allowing to locate regions where potential samples could be harvested which morphometric values close (or as close as possible to) the target average screw (Figure 2).

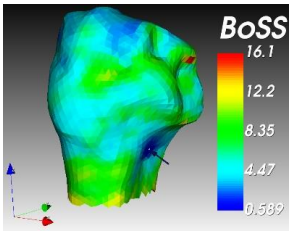

Figure 2: BoSS values mapped to the surface of a pork distal radius. The arrow indicated the minimum BoSS value.

Based on these results, the absolute minimum BoSS for each average screw (Table 1) were found, with all values found in the pork model, more specifically on the distal and proximal femur (PDF, PPF), proximal humerus (PPH) and the distal tibia (PDT).

	S1	S2	S3	S4	S5	S6	S7	S8	S9	S10
BoSS	0.80	0.29	0.34	0.35	0.65	0.33	0.79	0.81	0.93	0.88
Bone	PDF	PPH	PPH	PDF	PPF	PPH	PDF	PDF	PDF	PDT

Table 1: Absolut minimum BoSS for every screw (s1 to s10).

For interpretation, the BoSS value for each of the 360 studies screws when compared to the target screw was also calculated, with the resulting values ranging between 1.15 and 3.67 BoSS units.

Discussion

This study presents a methodology for accurate sample selection based on local CT morphometry from real implantation sites. Not only it was possible to quantify the minimum difference between two bone samples from different species and its location within the bone itself, but also create "maps" indicating potential locations where bone samples could be harvested from. The proposed methodology could be used in studies with any screw type with known peri-implant morphometry and any potential animal model in order to find a sample harvesting location which best represents the real implantation site which of vital importance for applications like mechanical testing.

References

1. Synek et al, J Biomechanics, 48:4116-4123, 2015.
2. Labate et al, J Appl Biomater Func Mater, 14(3): e227-e289, 2016.

Acknowledgements

This project was funded by the NFB Life Science Call 2017 Grand No. LS17-004 and Science call 2019 Dissertationen Grand No. SC19-014

CONTRAST-ENHANCED MICRO-CT FOR 3D VISUALISATION OF GAG CONTENT IN DIFFERENT CARTILAGE TISSUES

Manuela A. Boos (1), Kathryn S. Stok (1)

Department of Biomedical Engineering, The University of Melbourne, Parkville, Australia

Introduction

Auricular cartilage present in the outer parts of the ears is crucial for providing form and function. Understanding its composition and intrinsic mechanisms is thus fundamental for advances in tissue engineering and other regenerative approaches. As part of this composition, glycosaminoglycans (GAGs) have been shown to play a distinctly different viscoelastic response in auricular cartilage compared to articular cartilage [1].

Development of functional tissue-engineered constructs benefits from non-destructive longitudinal imaging methods to assess ECM production. Contrast-enhanced micro-computed tomography (CECT) has emerged as a novel non-destructive technique for 3D visualisation and longitudinal assessment of glycosaminoglycan (GAG) content in articular cartilage tissue-engineered constructs [1]. However, it has not been used for structures which have a different ECM composition to articular cartilage; e.g. auricular cartilage. Therefore, this study aims to test the feasibility of CECT for auricular cartilage compared to articular cartilage and investigate the influence of ECM composition.

Methods

Bovine auricular cartilage plugs (ø5 mm, n = 16 from 6 animals) were harvested from ears and knees of 5 - 8-month-old calves, cut in half and stored at -80°C until further use. One half was incubated in 1 ml of 12 mgI/ml CA4+ (provided by the Grinstaff group, Boston, USA) for 8 h. Plugs were imaged using microCT (µCT50, Scanco Medical, Brüttisellen, Switzerland) at 70 kVP, 57 µA, 4 µm, and 0.5 mm Al filter to obtain their mean attenuation coefficient. Resulting image data were processed using the manufacturer's software. Slices were contoured to only include cartilage samples. A Gaussian filter was applied (σ = 0.8, s = 1), attenuation histograms were generated, and the mean and standard deviation of the attenuation coefficient (cm^{-1}) calculated for each sample. Greyscale images were converted to coloured images to obtain three dimensional images of spatial GAG distribution. Total GAG content was assessed using a DMMB assay. GAG distribution was visualised using microCT images, Safranin-O histology, and immunohistochemistry. All results of GAG content and attenuation profiles were compared to the respective results of articular cartilage using one-way ANOVA and Dunnett's multiple comparison tests. All differences between groups were considered significant at p <0.05.

Results

After immersion of samples in 12 mgI/ml CA4+ for 8 h, colour maps of all cartilage types correspond with measured mean attenuation coefficients and Safranin O staining. GAG content normalised to volume shows a significant difference between articular cartilage (14.17 ± 3.27 µg/mm^3) and auricular cartilage (27.83 ± 5.21 µg/mm^3). Furthermore, mean attenuation is significantly higher in auricular cartilage (2.15 ± 0.12 cm^{-1}) compared to articular cartilage (1.31 ± 0.14 cm^{-1}).

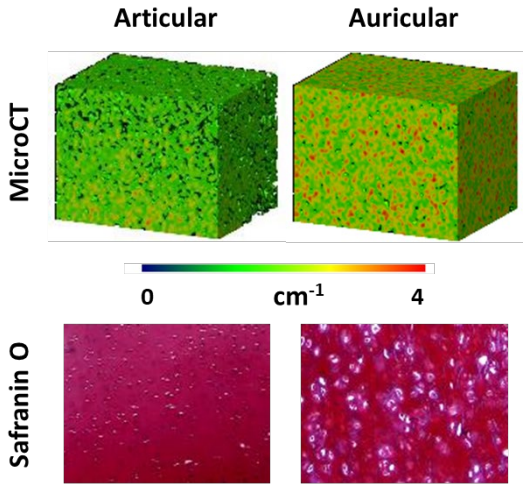

Figure 1: Spatial distribution of GAGs and CA4+ in different cartilage types. MicroCT and Safranin O images of articular and auricular cartilage.

Discussion

In this study, CECT was successfully used to assess spatial distribution and visualisation of GAGs in auricular cartilage. CECT has potential for non-destructive longitudinal assessment and 3D visualisation of ECM production. However, while CECT can clearly be used to visualise GAG distribution in 3D, if detailed structures of fibres and the morphology of cells need to be assessed, additional histological analysis should be performed.

References

1. Nimeskern et al, J Biomech, 49(3):344-352, 2016.

Acknowledgements

Thanks to Professor Mark Grinstaff from Boston University for providing the CA4+. This study was supported by internal funding from the University of Melbourne.

A NANOPARTICLE-BASED CONTRAST AGENT FOR MICRO-COMPUTED TOMOGRAPHY IMAGING OF THE OSTEOCHONDRAL INTERFACE

Mateus O. Silva (1), Kathryn S. Stok (1)

1. Department of Biomedical Engineering, The University of Melbourne, Parkville, Australia

Introduction

Imaging porous channels in the osteochondral interface with micro-computed tomography (microCT) will provide a means to track joint nutrition and study joint health. However, it is necessary to use a contrast agent to better delineate the porous channels of the osteochondral interface from regions with similar X-ray attenuation [1-2].

It has been demonstrated that hybrid metal nanoparticles provide excellent clinical CT contrast at different energies (80-140 kVp) [3]. These nanoparticles are composed of Barium (Ba), Ytterbium (Yb) and Fluoride (F) forming $BaYbF_5$ nanoparticles and are then coated in a silica shell (SiO_2) to ensure biocompatibility. In small animals, porous channels are 50-500 µm requiring microCT for visualization. Since microCT uses a lower energy (45–70 kVp), the aim of this work is to evaluate the $BaYbF_5$- SiO_2 nanoparticles contrast attenuation for subsequent segmentation of mouse subchondral bone in microCT.

Methods

$BaYbF_5$- SiO_2 nanoparticles were synthesized through a series of thermal treatments and coated with silica [3]. A femur (n=1) was extracted from an excess C57BL/10 mouse and fixed in a tube with a two-component resin (Technovit®3040, Hanau, Germany). The femur (n=1) were firstly scanned without any contrast agent. It was then completely immersed in a solution of $BaYbF_5$-SiO_2 (27 nm) in PBS at 250 mg mL^{-1} and was further scanned using microCT (vivaCT80, Scanco Medical AG, Brüttisellen, CH), 3.9 µm voxel size, at 70 kVp, 114 µA, 706 ms integration time. Six (n=6) volume of interest (VOIs) (0.0036 mm^3) were contoured and evaluated for the cortical subchondral bone region. Average microCT attenuation of the VOIs were calculated in grey scale value (1/cm) using the histogram function in Scanco Medical's image processing software (IPL v5.42).

Results

3D color map images of the mouse bone before (Figure 1a) and after (Figure 1b) immersion in the contrast agent $BaYbF_5$-SiO_2 (250 mg mL^{-1}) were obtained via microCT (µCT50, Scanco Medical, CH). Higher mean attenuation was significantly higher ($p < 0.000$) in the subchondral cortical region after immersion in contrast agent (Figure 1b). This was observed in the corresponding histograms (Figure 1c), showing an attenuation shift indicating a higher mean attenuation after the immersion in the contrast agent.

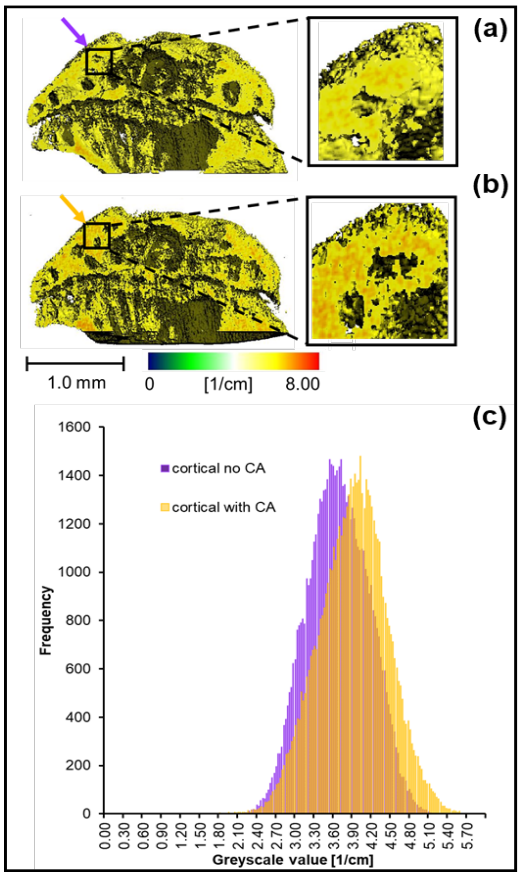

Figure 1: (a) 3D color map images of the mouse bone before (a) and after (b) immersion in the contrast agent $BaYbF_5$-SiO_2 (250 mg mL^{-1}) and (c) their respective histograms (arrow colour in (a) and (b) matched (c)).

Discussion and Conclusion

The subchondral cortical region exhibited higher mean attenuation after immersion in contrast agent. A contrast agent that is able to increase the attenuation of subchondral cortical bone has potential for exploring changes in the osteochondral interface with OA in more detail. In conclusion, $BaYbF_5$-SiO_2 contrast agent is a good candidate for high-resolution imaging of the osteochondral interface with microCT.

References

1. B.A. Lakin, et al., J Orthop Res, 2016. 34(7): pp. 1130-8.
2. N. Willett, et al., Osteoarthr Cart, 2016. 24(9): p. 1604-12.
3. Y. Liu, et al., Adv Healthc Mater, 2012. 1(4): pp. 461-6.

Acknowledgements

ARC Discovery Project (DP180101838) and Selby Research Award. Thanks to Professors Amanda Ellis and Paul Mulvaney for fruitful advice.

ROBUST ALIGNMENT OF RABBIT AND RAT JOINT SCANS FOR PRECLINICAL OSTEOARTHRITIS STUDIES

Pholpat Durongbhan (1), Catherine E. Davey (1), Kathryn S. Stok (1)

1. Department of Biomedical Engineering, The University of Melbourne, Parkville, Australia

Introduction

Visualising and quantifying structural changes due to osteoarthritis (OA) over time provides a means to track disease progression and markers of change. Three-dimensional (3D) imaging methods such as micro-computed tomography (microCT) allow for rapid evaluation of joint tissues in small animal models. Recent preclinical studies developed a quantitative morphometric analysis (QMA) suite for describing the joint as a single unit. Reproducibility and sensitivity were demonstrated in rabbit and rat OA models [1] and shown to be highly dependent on consistent alignment of the long axis of the tibia to a common position. These tasks are manual and time-consuming, requiring specific anatomical knowledge, and prone to human error. Thus, we propose an image processing solution that can automatically align the joint images correctly while remaining robust across different small animal models.

Methods

Raw microCT scans of six tibiofemoral joints from 6 New Zealand white rabbits and 21 joints from 11 Wistar rats from our previous studies were used. Briefly, joints were scanned using microCT (SCANCO Medical, CH) with a nominal voxel size of 18 µm and 10 µm for rabbit and rat joints, respectively. To test reproducibility, contrast-enhanced samples were scanned three times, with repositioning. The femur and tibia, along with their cartilage volumes, were segmented, and a volume of interest between the epiphyseal plates was defined (≈35-40 mm in rabbits, ≈12-15mm in rats).

Fully automated joint alignment was achieved by representing the tibia's basic shape and relative position using a spherical harmonic description method (SPHARM) [2]. SPHARM describes objects of spherical topology as a weighted sum of spherical harmonic basis functions. We used lower-order SPHARM coefficients to extract the coarse tibia shape. Principle component analysis was performed on the resulting shape. The smallest and second-smallest components were used as proxies for the tibia's long axis and the anterior face of the joint, respectively. These were translated into a set of matrices to transform the joint into a common alignment.

Resulting alignment was evaluated using the previously described QMA measure of joint centre of mass, which is a vector with length (λ, mm) and orientation (α, degree; β, degree; and γ, degree) measured along the three principle Cartesian axes, connecting the bone centres of mass. Since λ is independent of orientation, only α, β, and γ were analysed. Reproducibility was expressed using intraclass correlation coefficient (ICC), and precision errors were described in terms of absolute value, PE(SD), and coefficients of variation, PE(%CV).

Results

Visualisation of pre-and post-alignment for a rat joint is shown in Figure 1. The resulting data from both rabbits and rats showed improvements in all reproducibility metrics. In rabbit, ICC improved from unprocessed (α: 0.901, β: 0.739, γ: 0.385) to automatically (α: 0.936, β: 0.920, γ: 0.934) and manually aligned samples (α: 0.978, β: 0.913, γ: 0.981). Similar improvements were observed in rats where unprocessed ICC (α: 0.577, β: 0.890, γ: 0.731) improved when aligned automatically (α: 0.955, β: 0.958, γ: 0.951) and manually (α: 0.990, β: 0.981, γ: 0.998). This was achieved while maintaining very low precision errors for both rat (PE(SD) α: 1.90, β: 1.45, γ: 1.67; PE(%CV) α: 1.80%, β: 1.62%, γ: 1.06%) and rabbit (PE(SD) α: 1.87, β: 1.63, γ: 1.29; PE(%CV) α: 1.96%, β: 1.82%, γ: 0.76%) samples.

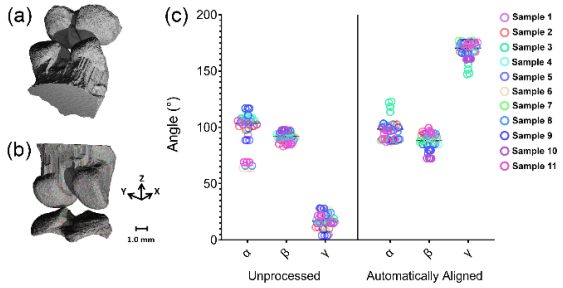

Figure 1: Typical images of a segmented rat knee joint (a) before alignment and (b) after processing through the automated alignment software, with (c) plots of rat joint centre of mass before and after processing.

Discussion and Conclusion

This work demonstrates an automated and efficient solution to the problem of joint alignment for 3D joint QMA that is robust across rabbit and rat models. The software is simple to deploy in new environments and results show reproducible joint alignment with high quality compared to manual alignment. This allows 3D joint QMA to be performed more rapidly in OA studies involving larger cohorts with minimal adjustment between species while maintaining sensitivity and precision. Future work will focus on expanding capability for a complete pre-processing pipeline, as well as expanding capability to allow pre-processing of other preclinical OA models, such as mouse and goat.

References

1. K.S. Stok, et al., PLOS One, 2016. 11(1): e0147564.
2. C.M. Brechbühler, et al., Comput. Vis. Image Underst, 1995. 61(2): 154–170

Acknowledgements

Funded through the ARC Discovery Project (DP180101838).

ENABLING REAL-TIME VISUALISATION OF *IN VIVO* CARTILAGE UNDER PRECISION MECHANICAL LOADING

R. Y. Nigel Kour (1), Joshua Parker (1), Kelvin Wang (1), Hee Seong Yoon (1), Eric Schoof (2), Kathryn S. Stok (3)

1. *Department of Mechanical Engineering, The University of Melbourne, Parkville, Australia*
2. *Department of Electrical and Electronic Engineering, The University of Melbourne, Parkville, Australia*
3. *Department of Biomedical Engineering, The University of Melbourne, Parkville, Australia*

Introduction

The role of mechanical loading in the onset and progression of osteoarthritis (OA) remains an open research problem due to the complex interplay of factors including joint integrity, genetic predisposition, local inflammation, mechanical forces, and cellular and biochemical processes [1]. Using small animal models of OA, the relationship between mechanical forces and other factors can be studied longitudinally to provide new insight into the onset and progression of disease.

This could be achieved using high-resolution micro-computed tomography (microCT), as well as a novel joint loading instrument. In this work, we aim to design and build an innovative instrument that is able to measure and apply precise physiological mechanical loads to the knee joints of live mice, whilst simultaneously visualised using microCT.

The outcomes of this device could provide complimentary data of mechanical load and joint morphology in real-time, during both onset and progression of OA. This would enable future research into the structural and biomechanical changes in the knee joint linked to mechanobiological processes.

Methods

A physical device and application software was designed to complement an experimental procedure by achieving the following functional objectives:

i. Accurate and measurable loading of mouse knees
ii. Compatibility with *in vivo* CT imaging protocols
iii. Safety and comfort of the mouse during application.

This instrument was designed and tested for *in vivo* imaging within the *vivaCT80* (Scanco Medical, CH). Two design-build-test cycles, denoted Alpha and Beta, were completed to produce a fully functional prototype mainly constructed from basic components and materials, Figure 1.



Figure 1: Assembly of the instrument (Beta prototype) with a mouse in the anaesthetic-sealed cylinder.

Results

The custom-built instrument (Figure 2) is comprised of (i) an ergonomic platform which supports and secures the head, body and thigh of the mouse, whilst (ii) an inflatable leg cuff safely grips the foot, ankle and shank. Through the leg cuff, (iii) an actuation system measures and/or applies load to the knee joints with force and displacement precisions of ±10 mN and ±10 µm, respectively. The actuation system can be configured to apply a constant force or constant displacement to the knee. This is powered by (iv) an electronics system and controlled using (v) a MATLAB-based application software (with real-time monitoring of loading data and access to emergency functions). The mouse is located in a detachable gas-sealed cylinder allowing for constant supply of anaesthetic gas.

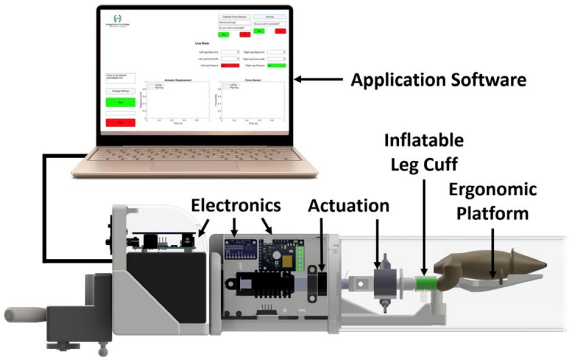

Figure 2: Beta prototype comprised of a platform, inflatable leg cuffs, actuation system, electronics and MATLAB-based application software.

Discussion

Future developments include further validation and enhancements of the inflatable leg cuff and actuation system. This instrument will be used in future studies to reveal insights into mechanobiological changes induced by OA, leading to new strategies for treating the disease.

References

Lespasio et al, Perm J, 21:16-183, 2017.

Acknowledgments

This study was supported by ARC Discovery Project (DP180101838) and internal funding from the University of Melbourne.

KINEMATIC ERRORS IN SCALED-GENERIC MUSCULOSKELETAL MODELS OF THE SHOULDER

Maxence Lavaill (1,2), Saulo Martelli (1,2), Ashish Gupta (1,2,3), Graham Kerr (1,2), Peter Pivonka (1,2)

1. Queensland University of Technology, Brisbane, Australia; 2. Queensland Unit for Advanced Shoulder Research, Brisbane, Australia; 3. Greenslopes Private Hospital, Brisbane, Australia

Introduction

The shoulder joint is one of the most complex joints in the human body, due to its wide range of motion. A better description of shoulder biomechanical function may allow improvements in shoulder surgical techniques and rehabilitation. Musculoskeletal (MSK) modelling is the only viable tool to understand how joint dynamics are produced and what forces are involved during a specific motion. In this context, determining the joint kinematics is the first fundamental step to compute muscle and joint contact forces. However, MSK models of the shoulder are usually scaled to the participant using marker-based measurement of inter-segmental lengths, thereby introducing anatomical errors in the model. Models based on medical images, by nature, may improve these anatomical errors. The aim of the present study was to quantify kinematic differences between scaled-generic and image-based musculoskeletal models of the shoulder.

Methods

Twelve healthy volunteers (7 females, 5 males, age: 28.6 ± 4.2 yrs, weight: 62.6 ± 13.9 kg, height: 166.8 ± 7.8 cm) with no history of shoulder pain or pathology were recruited for the study.

Thorax and upper extremity were imaged using a 3T MR scanner (Ingenia, Koninklijke Philips N.V., The Netherlands) at voxel sizes of 0.4 × 0.4 × 0.8 mm (using T1 dixon sequence). The sternum, clavicle, scapula and thorax in the images were segmented in order to create a 3D anatomical model of the shoulder.

The motion capture protocol included the attachments of 17 retro-reflective markers to the hip, thorax, right shoulder, arm and forearm. A marker cluster was used to track the scapula. [1] Several standardized tasks were then performed by the participants, including shoulder abduction/adduction, flexion/extension, horizontal flexion/extension and internal/external rotations, while markers were recorded at 200 Hz using a 12-cameras *Vicon* motion capture system (Vicon Motion Systems, Oxford, UK).

Two types of shoulder models were used, both with 4 segments and 8 degrees-of-freedom. First, a generic shoulder model was chosen [2] and scaled to each participant's anthropometry using *OpenSim*. Thorax and scapula were scaled in depth, width and height. The humerus was scaled in width and length and the clavicle was scaled in length only. The second model was created using segmented bones from MR images and the use of the freely available software *NMSBuilder*; following the recommendations of the ISB [3] regarding joint coordinate systems and bony landmarks.

Finally, motion data was used to solve for inverse kinematics for the abduction task and both models using *OpenSim*. Joint angles were then compared.

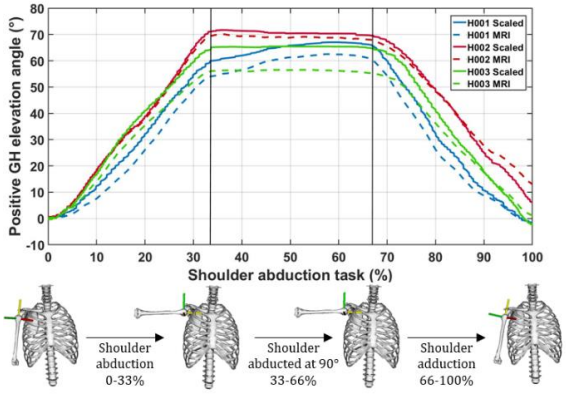

Figure 1: Computed glenohumeral elevation angle against normalized shoulder abduction task for three participants, using generic-scaled models (solid lines) and MRI-based models (dotted lines).

Results

Differences in kinematics were observed between the generic-scaled and MRI-based models of each participant using the same marker trajectories as inputs. A maximum range of motion error of 8.9°, as well as a root mean square error of 6.1° occurred in one of the individuals (see green curve, Fig. 1). From the numerical results, we find that the scaled-generic models always overestimate shoulder elevation angle. Note that the distance between the acromioclavicular and the glenohumeral joints were also varying by 0.2 ± 1.0 cm between both models.

Discussion

Difference in computed kinematics is due to both the differences in joint-to-joint distances and in the definition of joint coordinate systems. This would likely have a big impact on joint dynamics in future modelling steps. Further analysis involving more participants and more types of motions are currently being processed.

References

1. Warner et al., J Visualized Experiments, 96:1-14, 2015
2. Wu et al., J Biomech, 49:3626–3634, 2016.
3. Wu et al., J Biomech, 38:981–992, 2005.

Acknowledgements

The authors would like to acknowledge the support received through the following funding schemes of Australian Government: ARC Industrial Transformation Training Centre (ITTC) for Joint Biomechanics (IC190100020).

ULTRASOUND-BASED EVALUATION OF CARTILAGE DAMAGE AFTER *IN VIVO* ARTICULATION WITH METAL IMPLANTS

Maria Pastrama (1), Janne Spierings (1), Pieter van Hugten (2), Keita Ito (1), Richard Lopata (3), Corrinus C. van Donkelaar (1)

1. Orthopaedic Biomechanics, Department of Biomedical Engineering, Eindhoven University of Technology - TU/e, 2. Department of Orthopaedics, Maastricht UMC+, Maastricht, 3. Cardiovascular Biomechanics - PULS/e, Department of Biomedical Engineering, TU/e; The Netherlands

Introduction

When focal cartilage defects are left untreated, they can progress with further cartilage damage into osteoarthritis [1]. Focal knee resurfacing implants (FKRIs) are an emerging group of implants typically intended for middle-aged patients, to bridge the treatment gap between regenerative therapies and total joint replacement in this age group. Most FKRIs have an articulating surface made of metal, which may damage the opposing cartilage [2]. Furthermore, using metal implants prohibits the use of Magnetic Resonance Imaging (MRI) for follow-up or diagnosis of new emerging problems. In the present study, we propose the alternative use of ultrasound (US) to monitor cartilage quality by assessing an Ultrasound Roughness Index (URI) of tibial cartilage opposing an FKRI in goat knees 6 months post-implantation.

Methods

The medial femoral condyle of Dutch mature milk goats was operated unilaterally. Either a titanium FKRI with a cobalt chromium top layer was implanted (diameter = 9.9 mm; $n = 8$) or sham surgery was performed ($n = 8$). After 6 months the goats were sacrificed, and the tibial plateaus were removed and stained with Indian Ink (Royal Talens, the Netherlands). Macroscopic scoring of the ink staining from 1 (least damaged) to 5 (most damaged) was performed by seven independent observers. This scoring was correlated with the URI in the FKRI articulating plateaus, as it was not sensitive enough to accurately evaluate the relatively low amount of cartilage articulation-induced damage in sham samples. The plateaus were transferred to Phosphate Buffered Saline (PBS) and high-frequency US images were acquired at 9 sections (Figure 1A) using a Verasonics Vantage System (Verasonics, Kirkland, WA, USA) connected to a 31.25 MHz linear transducer MS400 (FUJIFILM Visualsonics Inc., Bothell, WA, USA). B-mode images were reconstructed from the radio frequent data using MATLAB (MathWorks Inc., Natick, MA, USA). The URI was calculated as:

$$URI = \sqrt{\frac{1}{m}\sum_{i=1}^{m}(d_i - \langle d \rangle)^2} \qquad (1)$$

where m is number of scan lines, d_i the distance from the US transducer to the PBS-cartilage interface in scan line i, and $\langle d \rangle$ the average distance from the transducer to the cartilage surface [3].

Results

Significantly higher URI was found in the FKRI knees than in the sham knees in sections articulating against the metal FKRI, i.e., M1 ($p = 0.0093$) and M6 ($p = 0.007$). In the metal group, these locations corresponded to the most damaged and therefore most ink-stained areas and had the highest Pearson correlation coefficient between macroscopic scoring and URI, i.e., $\rho_{M1} = 0.80$ ($p = 0.017$) and $\rho_{M6} = 0.81$ ($p = 0.014$).

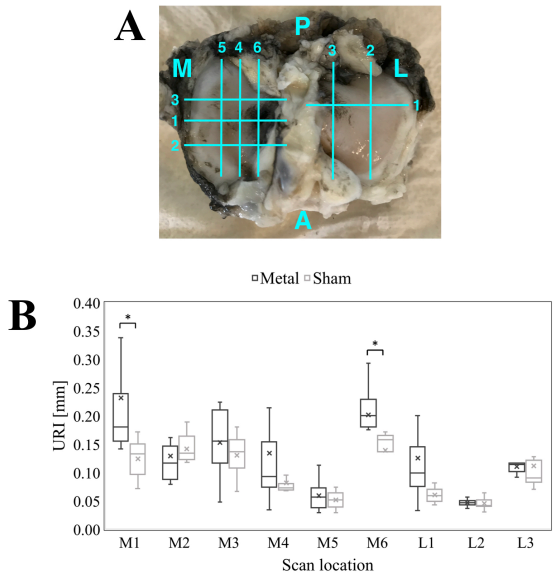

Figure 1: A. Overview of the US scan locations on the tibial plateaus (M = medial; L = lateral; A = anterior; P = posterior); B. Location-specific URI.

Discussion

Locations on tibial cartilage that articulated against a metal FKRI for 6 months *in vivo* had a higher URI than other areas, suggesting a higher degree of cartilage damage. The strong correlation between macroscopic scoring and URI at damaged locations demonstrates the potential of this US-based method to evaluate cartilage roughness and altered surface morphology. This non-destructive approach is faster and less laborious than histology, and it is easier and cheaper than MRI.

References

1. Davies-Tuck et al, Osteoarthr Cartil, 16: 337–342, 2008.
2. Custers et al, Osteoarthr Cartil, 18: 377–388, 2010.
3. Saarakkala et al, Ultrasound Med Biol, 30: 783–792, 2004.

TRABECULAR MICROSTRUCTURE CAN BE QUANTIFIED WITH XTREMECT MORE ACCURATELY USING ADAPTIVE THRESHOLDING

Karen Mys (1,2), Filip Stockmans (3), Boyko Gueorguiev (1), Verena Neumann (1), Caroline E. Wyers (4,5), Joop P.W. van den Bergh (4,5,6), G. Harry van Lenthe (2), Peter Varga (1)

1. AO Research Institute Davos, Switzerland; 2. KU Leuven, Belgium; 3. KU Leuven campus Kortrijk, Belgium; 4. VieCuri Medical Center, the Netherlands; 5. Maastricht University, the Netherlands; 6. Maastricht University Medical Centre, the Netherlands

Parameter	XTremeCT vs microCT		XTremeCT-II vs microCT		XTremeCT vs XTremeCT-II	
	FT	AT	FT	AT	FT	AT
BV/TV	0.86	0.94	0.94	0.97	0.93	0.99
Tb.Th	0.58	0.81	0.85	0.89	0.74	0.93
Tb.Sp	0.88	0.86	0.88	0.89	0.99	1.00
Tb.N	0.86	0.86	0.88	0.88	0.99	0.99

Table 1: Coefficients of determination versus microCT (i.e. accuracy) and agreement between both HR-pQCT scanners increase when using adaptive local thresholding (AT) instead of the manufacturer's standard segmentation filtering technique (FT).

Introduction

High-resolution peripheral quantitative computed tomography (HR-pQCT) can image distal extremities at bone microstructure level *in vivo*, which is highly relevant for investigation of bone diseases. Currently, two HR-pQCT scanners of Scanco Medical AG (Switzerland) are available on the market and frequently used in research: XTremeCT (first generation) and XTremeCT-II (second generation). XTremeCT is inferior to XTremeCT-II in quantifying bone parameters, especially for trabecular thickness (Tb.Th), with moderate agreement between the two scanners [2]. Recently, we presented an adaptive local thresholding (AT) technique for high-resolution cone beam CT (CBCT) which enabled, despite the lower spatial resolution, quantification of bone microstructural parameters at a comparable accuracy as currently obtained with HR-pQCT [3, 4]. This raises the question if AT can also improve the quantification accuracy of HR-pQCT as well as the agreement between both HR-pQCT scanners, which is the aim of this study.

Methods

Nineteen human cadaveric distal radii (donor age: 25 – 93 years, female/male: 14/5) were scanned with three Scanco scanners: (1) XTremeCT at $82\,\mu m$, (2) XTremeCT-II at $60.7\,\mu m$ and (3) the small animal microCT scanner VivaCT40 at $19\,\mu m$ voxel size, which was taken as the gold standard. The HR-pQCT images were segmented and processed twice. Once with the standard approach of the manufacturer (filtering technique – FT) and once with AT (in-house developed C++ software) followed by a direct morphological analysis technique with the manufacturer's script. For all scans, the following microstructural parameters were calculated: bone volume fraction (BV/TV), Tb.Th, trabecular separation (Tb.Sp) and trabecular number (Tb.N). Linear regression analysis was performed and correlation coefficients were calculated to evaluate the accuracy as well as the agreement between the HR-pQCT scanners.

Results

The average accuracy of XTremeCT improved from R^2 = 0.80 (FT) to 0.87 (AT) and reached the same level of accuracy as XTremeCT-II ($R^2 = 0.89$). In more detail, the accuracy of XTremeCT increased for BV/TV and Tb.Th, but not for Tb.Sp and Tb.N with correlations being already high with FT (Table 1). For XTremeCT-II, AT improved the accuracy for most parameters slightly, despite the accuracy of FT being already very high. The agreement between the scanners increased with AT, especially for Tb.Th.

Conclusion

AT demonstrated to enhance the accuracy of XTremeCT in quantifying bone microstructural parameters, reaching the level of XTremeCT-II and increasing the agreement between the two HR-pQCT scanners. The technique could not be only used to improve accuracy, but also to reduce the radiation dosage, to enable faster scanning with XtrememeCT-II. We expect that the use of AT has potential to quantify more challenging regions with lower Tb.Th and hence more partial volume effects e.g. at the knee. Implementation of the AT technique is expected to improve the quality of preclinical and clinical research which use XTremeCT and enhance the comparability of results obtained with the two generations HR-pQCT scanners.

References

1. MacNeil et al, Med Eng & Phys, 29:1096-1105,2007
2. Manske et al, J Bone Miner Res, 32:1514-1524
3. Mys et al, Bone, 114:206-214,2018
4. Mys et al, J Bone Miner Res, 34:867-874, 2019

Acknowledgements

This research was supported by an FWO travel grant and by KU Leuven Internal Funding (Grant C24/16/027).

DEEP LEARNING-BASED PATCHWISE RESOLUTION ENHANCEMENT WITH QUILTING ALGORITHM

Sang Min Sin (1), Bong Ju Chun (2), In Gwun Jang (2)

1. Mobility System Team, SOCAR, Seoul, Republic of Korea

2. The Cho Chun Shik Graduate School of Green Transportation, KAIST, Daejeon, Republic of Korea;

Introduction

Topology optimization has been recently proven to reconstruct the trabecular structure from medical CT scan data [1]. The reconstructed images can provide a more reliable diagnosis for osteoporosis. However, the excessive computational cost of topology optimization with iterative finite element analysis is a critical hurdle for clinical practice.

In principle, deep learning-based imaging technique can resolve the above problem by putting extreme computational cost to the training stage; once trained successfully, this method can reconstruct a trabecular structure in a very short timeframe. However, it is difficult to train an artificial neural network (ANN) with large-size skeletal images over 2000px. In addition, the lack of μCT images for training is another obstacle to overcome.

In this study, a novel resolution enhancement method for skeletal images is proposed based on deep learning. The low resolution (LR) image is first divided into a number of small patches. Each LR patch is reconstructed into a high resolution (HR) patch through the ANN. Then, the HR patches are seamlessly connected into a whole skeletal image by suppressing the image discontinuity along the boundary.

Method

To generate training and testing data, eleven 2D synthetic femur images (1883 x 2080 pixels with a 50μm resolution) were obtained by conducting topology optimization with eleven different loading conditions. These images were downscaled 10 times to obtain the corresponding LR images; then, they were divided into a set of image patches of 8 x 8 pixels. The pairs of HR and LR patches from seven femur images were used to train a network. In this study, the generative adversarial network (GAN) [2] and residual network (ResNet) [3] were used. Adversarial loss, perceptual loss, and bone volume fraction (BV/TV) loss were considered to train the super resolution (SR) GAN. L1 and L2 losses were also used to train the ResNet.

After training, the LR image patches from the remaining four femur images were reconstructed through the trained network. Then, the reconstructed HR images were quilted into the whole image by determining the patch boundary which minimizes the discontinuity in the overlapped region.

The quilted femur images were evaluated in terms of the peak signal to noise ratio (PSNR), structural similarity index measure (SSIM), total bone volume fraction (BV/TV) error, and patch boundary variation (PBV) error. In this study, the PBV was defined as,

$$\mathrm{PBV} = \frac{1}{N_\Omega}\sum_{i}^{N_\Omega}\sum_{p}^{N_{\Omega' i}} |\, \rho_i - \rho_{i,p}\,| \qquad (1)$$

where $\Omega'_i = \{\rho_{x+1,y}, \rho_{x,y+1}\} \cap \Omega^c$; Ω is the set of pixels at the boundary; N_Ω the number of elements in Ω; ρ_i the bone mass density in the *i*th element in Ω, and $\rho_{i,p}$ the bone mass density in the *p*th element in Ω_i'. Finally, the *quilted* femur images were evaluated in terms of apparent stiffness and strain energy density distribution.

Results

The proposed quilting method enables 3.9% and 2.6% improvement in the PSNR and SSIM, respectively, of the reconstructed proximal femur images, compared with that without the quilting algorithm. The whole reconstruction process took maximum 5.9 minutes. Note that a topology optimization-based method typically takes about 12.8 hr. The average apparent stiffness error for the proposed method was 39.7%, whereas that in the conventional deep learning method was 53.0%. By virtue of imposing a seamless boundary, the SED for the proposed method showed a more uniform distribution.

Discussion

A novel method of reconstructing the LR skeletal images into the HR images was proposed based on the deep learning and quilting algorithm. In the proposed method, the patchwise deep learning scheme can be easily trained by using a large number of image patches. The quilting algorithm can suppress a structural discontinuity among the patches. Numerical results show that the proposed method can reconstruct a 2D proximal femur with a relatively low amount of training data within a short computing timeframe.

References

1. Kim, Jung Jin, et al. “Computational Study of Estimating 3D Trabecular Bone Microstructure for the Volume of Interest from CT Scan Data.” *International Journal for Numerical Methods in Biomedical Engineering*, no. November, 2018, pp. 1–13, doi:10.1002/cnm.2950.
2. Ledig, Christian, et al. "Photo-realistic single image super-resolution using a generative adversarial network." *Proceedings of the IEEE conference on computer vision and pattern recognition*. 2017.
3. K. He, X. Zhang, S. Ren, and J. Sun, “Deep residual learning for image recognition,” *Proc*Somebody et al, J Biomech, 45:1-10, 2014.

INTRACELLULAR LABEL-FREE DETECTION OF MESENCHYMAL STEM CELL METABOLISM WITHIN A PERIVASCULAR NICHE-ON-A-CHIP

Simone Perottoni (1), Nuno G. B. Neto (2,3), Cesare Di Nitto (1), Ruslan I. Dmitriev (4), Manuela Teresa Raimondi (1) and Michael G. Monaghan (2,3,5,6)

1: Department of Chemistry, Materials and Chemical Engineering "Giulio Natta", Politecnico di Milano, piazza Leonardo da Vinci, 32 – 20133 Milan, Italy; 2: Department of Mechanical, Manufacturing and Biomedical Engineering, Trinity College Dublin, Dublin 2, Ireland; 3: Trinity Centre for Biomedical Engineering, Trinity Biomedical Sciences Institute, Trinity College Dublin, 152-160 Pearse Street, Dublin 2, Ireland; 4: Tissue Engineering and Biomaterials Group, Department of Human Structure and Repair, Faculty of Medicine and Health Sciences, Ghent University, Ghent 9000, Belgium.; 5: Advanced Materials and Bioengineering Research Centre (AMBER), Royal College of Surgeons in Ireland and Trinity College Dublin, Dublin, Ireland; 6: CÚRAM, Centre for Research in Medical Devices, National University of Ireland, Galway, Newcastle Road, H91 W2TY Galway, Ireland

Introduction

Mesenchymal stromal cells (MSCs) experience many intercellular and extracellular forces and specific oxygen tension (pO2) inside their native in vivo stem cell perivascular niche. Many questions still remain regarding the complexity of this micro-environment and how oxygen concentration gradients and elasticity at the niche-tissue interface can affect MSC metabolism; which could be a physiologically significant feature to enhance differentiation. Here by the use of a miniaturized optically accessible bioreactor (MOAB)[1] coupled with fluorescence lifetime imaging microscopy (FLIM)[2] we profile cellular metabolism of human-MSCs (h-MSCs) in a simulated stem cell niche environment by controlling substrate stiffness and pO2 gradients via interstitial flow velocity levels. The combination of these advanced modalities can profile metabolic activity of cells in very specific micro-anatomic environments to analyse physiology and diseases.

Materials and Methods

h-MSCs were cultured within MOAB with continuous flow at 0.5 - 5 - 10 - 30 µL/min up to 7 days, with and without stiffness tuned polyacrylamide gels. Computational Fluid Dynamic (CFD) analysis was used to predict shear-stress levels and the pO2 gradients within the culture chamber. Real-time FLIM was performed to quantify free and protein bound nicotinamide adenine dinucleotide (NADH) at successive time points. The effect of oxygen depletion on MSC metabolism was assessed by analysis of NADH proportions, glucose consumption, mitochondrial membrane potential, assessment of mitochondrial morphology (fission and fusion) and direct optical measurement of intracellular oxygen.

Results and Discussion

Predictive modelling was employed to engineer a declining gradient in oxygen tension and validated using a previously calibrated non-invasive imaging technology applicable to this miniaturised optically accessible bioreactor (MOAB). Using FLIM (Figure 1) we were able to monitor the adaptive modes of metabolic machinery employed in addition to visualising the correlating oxygen concentrations, glucose uptake and mitrochondrial membrane potential and morphology occuring at these points which were in validation with our in silico model. These results present a new method and technology to preferentially pattern an in silico modelled metabolic gradient which will be of enormous benefit in modelling perivascular niches, the relevant diseases, and also the bioavailability and metabolism-related uptake of pharmaceuticals. Additionally, the imaging toolbox presented in this perivaschular niche example offer the potential to achieve multiparametric single-cell metabolic evaluation in dynamic cultures.

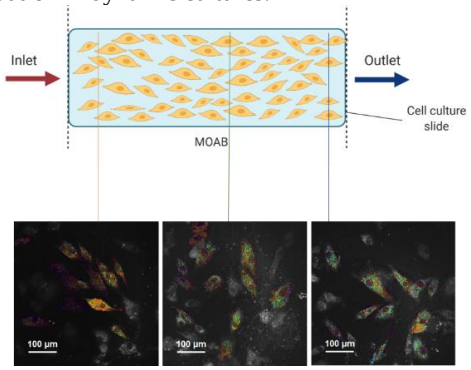

Figure 1: 2P-FLIM NAD(P)H imaging of h-MSC cultured on the MOAB. Representative images after 96 hours cell culture under 0.5 µL min-1 flow rate.

References

1. Izzo L. et Al. Biomed Microdevices, 2019; 21(1)
2. Okkelman I.A. et Al. Redox Biology, 2019 doi.org/10.1016/j.redox.2019.101420

Acknowledgements

NN is supported by a Trinity College Dublin, Provost's PhD Award and the TCD FLIM core unit directed by MM is supported by a SFI Infrastructure Programme: Category D Opportunistic Funds Call (16/RI/3403). This research has received funding from: the European Research Council (ERC) under the European Union's Horizon 2020 research and innovation program (G.A. No. 825159 – MOAB).

FUNDAMENTAL SHAPE ANALYSIS OF HUMAN TRABECULAR BONE USING SURFACE CURVATURE AND MINKOWSKI FUNCTIONALS

Sebastien Callens (1), Duncan Tourolle (2), Ralph Müller (2), Amir A. Zadpoor (1)

1.Delft University of Technology, Delft, The Netherlands. 2.ETH Zurich, Zurich, Switzerland

Introduction

An ongoing effort to advance bone tissue engineering has been to design biomaterial scaffolds that are "bone-mimicking". However, current scaffold designs typically lack the intricate morphology that is observed in trabecular bone, partly due to the absence of a mathematical framework to quantify this morphology. Here, we establish such a framework by applying fundamental tools from differential and integral geometry to compute the surface curvature distributions and Minkowski functionals on micro-CT scans of human bone biopsies. Our analyses show that these local and global metrics are sensitive to subtle morphological differences in bone from different anatomical sites, and unify several traditional bone morphometric indices within the same framework.

Methods

High-resolution micro-CT data from the EU BIOMED 1 project was used [1]. The data set comprised scans of bone biopsies from 70 donors at five different sites, with a 4 mm^3 region of interest (ROI) and 14 µm voxel size. Triangle meshes of the trabecular bone surface were reconstructed using marching cubes, and smoothed using volume-preserving implicit fairing. The principal curvatures were estimated using a multiscale fitting algorithm to create curvature probability density maps for all specimens from the five different sites. Scalar (MS) and tensorial (MT) Minkowski functionals were computed on the same triangle meshes (using Karambola [2]). MS were compared to traditional morphometric indices, such as bone surface (BS), surface area derivative (dS/dr) or Euler characteristic (χ). Different degrees of anisotropy (DA) and ellipticity were computed from the MT eigenvalues, such as the DA/ellipticity w.r.t. surface orientation or w.r.t. curvature, and compared to DA as predicted by the MIL tensor. Moreover, the spatial variations within the bone specimens were quantified by computing MT on smaller sub-volumes within individual specimens.

Results

The curvature probability density maps were found to capture the morphological differences in bone from different anatomical sites, such as the predominant plate-like bone in the femoral head, the mostly rod-like bone in the vertebrae, and the mixed morphology in the calcaneus (Figure 1). MS W_1 and W_2 were found to correlate well with BS and dS/dr. Importantly, MS W_3 was capable of detecting connectivity differences in the different bone types that remained undetected by the Euler characteristic. MT analysis revealed that the different bone types exhibit substantially different DA and ellipticity w.r.t. the different tensors being considered. Moreover, DA predicted by MT $W_1^{0,2}$ was found to be very similar to that predicted by the latest MIL implementation in BoneJ [3].

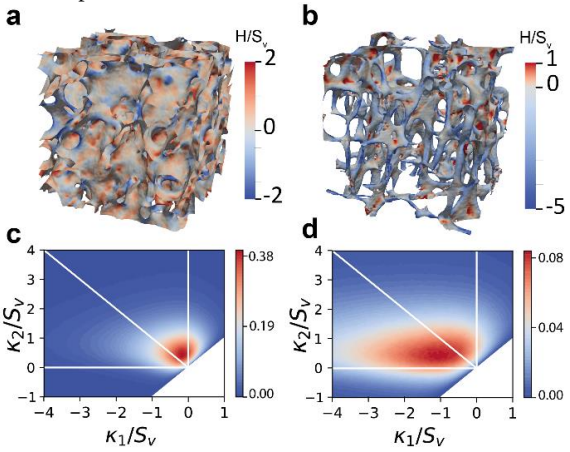

Figure 1: a-b) Local mean curvature on a specimen from the femoral head and second lumbar vertebra, respectively. c-d) Principal curvature probability density maps for all the specimens from the femoral head and second lumbar vertebra, respectively.

Discussion

Our local and global analyses provide a fundamental geometric foundation to the quantification of trabecular bone morphology. In addition to enhancing structure-function relationships of bone, our framework could instruct the design of bone-mimicking scaffolds. For example, our curvature maps reveal that the curvature spectrum of bone is much more complex than that of common scaffold architectures, such as strut-based lattices or triply periodic minimal surfaces (TPMS) [4]. Additionally, our framework could serve as a quantitative basis in the emerging field of geometry-guided tissue growth [5].

References

1. Hildebrand et al, J. Bone Miner. Res. 14:1167-1174, 1999
2. Schröder-Turk et al, New J. Phys. 15: 083028, 2013
3. Doube et al, Bone 47, 1076-1079, 2010
4. Kapfer et al, Biomaterials 32, 6875-6882, 2011
5. Callens et al, Biomaterials 232, 119739, 2020

Acknowledgements

This work was supported by ERC grant agreements no. [677575] and [741883]. The first author is grateful to the IDEA League for facilitating an exchange at ETH Zurich.

PRESERVATION OF CARTILAGE MICROMECHANICS VIA OPTIMISED CONTRAST-ENHANCED X-RAY COMPUTED TOMOGRAPHY

Sarah Davis (1,2), Gianluca Tozzi (2), Greet Kerckhofs (3), Grzegorz Pyka (3), Marta Roldo (1), Gordon Blunn (1).

1. School of Pharmacy and Biomedical Science, University of Portsmouth, UK; 2. Zeiss Global Centre, School of Mechanical and Design Engineering, University of Portsmouth, UK; 3. UCLouvain, Louvain-la-Neuve, Belgium.

Introduction

It is speculated that the pathogenesis of osteoarthritis is associated with changes in the architecture of calcified cartilage and subchondral bone, resulting in abnormal strain distribution in the overlying articular cartilage. This highlights the importance of measuring strain changes at the bone-cartilage interface with techniques such as high-resolution X-ray computed tomography (XCT) and digital volume correlation (DVC). However, DVC requires grayscale contrast which is hard to achieve in soft tissues such as native cartilage due to its lower X-ray absorption. Thus, tissue staining using contrast agents such as phosphotungstic acid (PTA) and polyoxometalate structures (POM) can be used to visualize articular cartilage for XCT imaging [1][2], but most stains bind to matrix components and alter tissue mechanics. Therefore, the aim of this preliminary study is to establish appropriate staining techniques to ensure the generation of significant contrast for XCT imaging of the articular cartilage, whilst maintaining mechanical properties of the tissue for subsequent DVC analysis of the bone-cartilage interface.

Methods

Cylindrical osteochondral plugs (Ø = 4 mm, H = 8 mm were cored from the medial condyle of bovine tibiae. Whole hindlimbs were obtained from ex-breeder Dunkin-Hartley guinea pigs. Tissue samples were stained using either (1) 1% (w/v) PTA in 70% EtOH for 21 h [3] or (2) 3.5% (a Hafnium-based Wells-Dawson) POM [1] in PBS for 72 h. Micromechanical testing was performed on the plugs by indenting the central cartilage surface [4]. All samples were hydrated in PBS and imaged either wrapped in parafilm (whole joints, 60kV/5W, 3µm voxel size, 2401 proj) or in sealed polyamide tubes (plugs, 40kV/3W, 2µm voxel size, 2401 proj) using a high-resolution 3D X-ray microscope (Versa 520, Zeiss, Germany).

Results

Staining osteochondral plugs with PTA showed an increase in stiffness (from 0.61 to 1.14mN/µm) of the articular cartilage from micro-indentation tests (Fig 1A). The use of POM stain showed tissue stiffness (0.61mN/µm) similar to that of fresh (pre-stain) levels (0.68mN/µm) (Fig 1B). POM staining also showed enhanced greyscale contrast in the articular cartilage, calcified cartilage and subchondral bone during XCT imaging (Fig 2A) and was also successful in resolving other soft tissue features such as tendons, ligaments and menisci in guinea pig joints (Fig 2B).

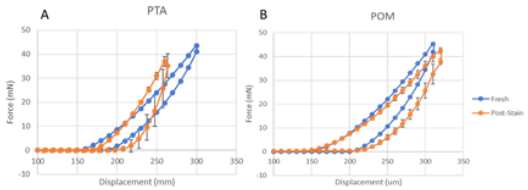

Figure 1: Average (±SD) force-displacement curves before and after (A) PTA and (B) POM staining.

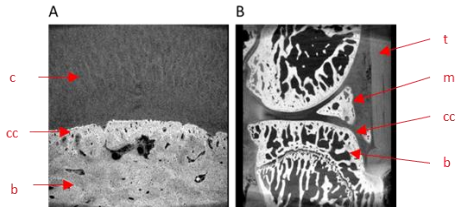

Figure 2: XCT images after POM staining of (A) osteochondral plug and (B) guinea pig joint. Showing bone (b), cartilage (c), calcified cartilage (cc), meniscus (m) and tendon (t).

Discussion

Previous research has included the use of POM staining for the 3D visualization of both mineralized and soft tissues in mouse joints [1]. However, the effect of this stain on tissue micromechanics has not been explored. This study shows that compared to PTA staining which causes increases in tissue stiffness, POM does not alter cartilage micromechanics compared to unstained fresh tissue. This, and the enhanced visualization of cartilage and other soft tissues will allow the strain measurement at the bone-cartilage interface using XCT imaging combined with *in situ* loading and DVC to be further investigated.

References

1. Kerckhofs et al, Biomaterials, 159: 1–12, 2018.
2. Ylitalo et al, J Orthop Res. 37 :855-866, 2019.
3. Clarke et al, Osteoarthritis Cartilage, 28:102-111, 2020.
4. Tozzi et al, Materials, 13: 2579, 2020.

Acknowledgements

The Zeiss Global Centre provided XCT imaging and experimental capability to conduct this study.

CEL-UNET: A NEW CNN ARCHITECTURE FOR AUTOMATIC SEGMENTATION OF KNEE BONES IN CT SCANS

Alberto Faglia (1), Davide Marzorati (1), Luca Mainardi (1), Pietro Cerveri (1)

1. Department of Electronics, Information and Bioengineering, Politecnico di Milano, Italy

Introduction

Three-dimensional (3D) reconstruction of knee bones from images is crucial for different biomechanical applications like anatomical variability analysis, mechanical evaluation of both patello- and tibio-femoral joints [1], [2]. Especially, segmentation of CT scans is made challenging by the presence of strong irregularities at femur condylar level and osteophytes, requiring intensive radiological effort and being prone to inter-operator variability. We propose an automatic segmentation method that leverages an innovative convolutional neural network taking its root from the Unet.

Materials and Methods

The proposed method was based on a 3D neural network trained on segmented CT axial scans of the knee joint anatomy, including tibia, femur, patella and fibula. The dataset was provided in anonymized form by MEDACTA International SA (Castel San Pietro, Switzerland) and included 260 case patients. The training, validation, and test set contained a percentage of the original data equal to 0.75, 0.15, 0.10, respectively.

A previous research of our group [3] was conducted on the topic and the relevant results were used as starting point for this work. The present study was divided into two main parts: the first was a comparison of 2 models sharing the state-of-the-art Unet model [2] as common architecture and trained with two different cost functions, namely boundary and focal loss. The second was the development of a new and innovative encoding-decoding architecture (Cel-Unet) with a targeted loss function (CEL loss) to enhance segmentation accuracy. Cel-Unet (Fig. 1) took its root from the Unet splitting the decoding path in two parallel branches: one to segment the whole bone structure, the other to predict the boundaries of the interested anatomies. The segmentation performances were evaluated on the test set using IoU, Precision and Recall metrics.

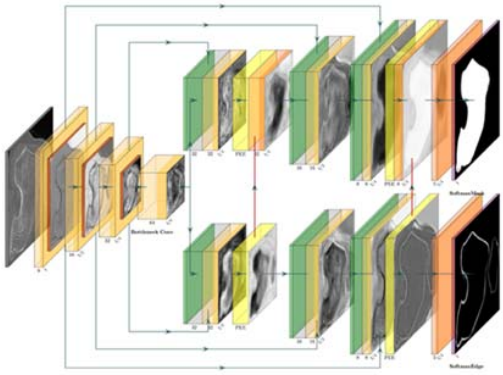

Figure 1: Architecture of the developed CEL-Unet. Top decoding branch segments full bone structures, while bottom decoding path only segments bone boundaries.

3D reconstruction accuracy was measured in terms of root mean squared error (RMSE), as the difference between reconstructed and original shapes.

Results

Table 1 reports the segmentation comparison for femur and tibia between traditional Unet and Cel-Unet. Results, in favor of the proposed network, were greater than 0.95 in all the three metrics. Obtained RMSE are less than 0.5mm on average on the test set. A qualitative analysis also evidenced the improved ability of the CEL-Unet to better delineate irregularities, adjacent surfaces and osteophytes (Fig. 2).

Bone	Architecture	IoU	Prec	Recall
FEMUR	Unet	0.96	0.98	0.98
	CEL-Unet	0.97	0.99	0.98
TIBIA	Unet	0.95	0.97	0.98
	CEL-Unet	0.96	0.98	0.98

Table 1: Comparison between results of Unet and CEL-Unet.

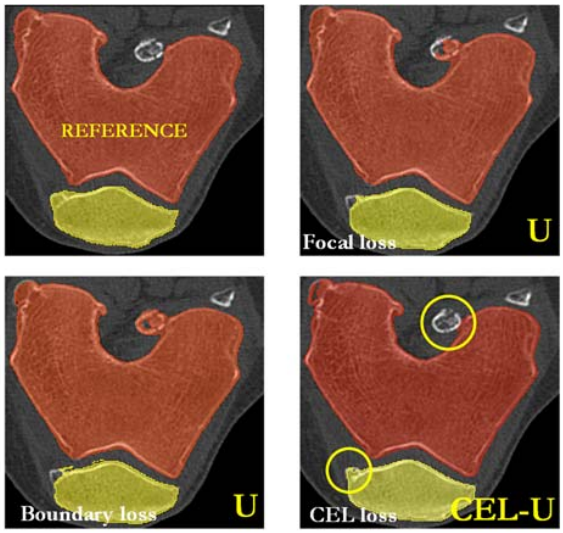

Figure 2: Segmentation details. The Cel-Unet was able to reduce undue both under- and over-segmentation.

Conclusions

The developed deep convolutional network was proved effective and superior to literature methods to concurrently segment distal femur and proximal tibia, exhibiting severe pathological deformations, in knee CT volumes. Prospectively, this can be used as a support tool for biomedical and medical analysis.

References

1. Zhang et al., J of Biomech, 49, 2016
2. Smoger et al., J of Orth Res 33, 2015
3. Marzorati et al., IEEE Access, 8, 2020

EXPERIMENTAL STUDY OF AN ENERGY HARVESTING SYSTEM FOR ENERGY-AUTONOMOUS INSTRUMENTED TOTAL HIP REPLACEMENTS

Hans-E. Lange (1), Nils Arbeiter (2), Rainer Bader (1), Daniel Kluess (1)

1. Department of Orthopaedics, Rostock University Medical Center, Germany

2. Institute of General Electrical Engineering, University of Rostock, Germany

Introduction

For improvement of the clinical outcome of endoprostheses, research is conducted towards so called *smart implants*. Additional sensory or active functions promise enhanced possibilities of therapeutic measures. To power the internal electronics of such devices, the question of optimal energy supply arises. Batteries and external power sources bring drawbacks like their limited lifespan or the dependency on external equipment, respectively. Therefore, energy harvesting approaches are investigated.

In the present study, we continued our work on an energy harvesting system (EHS) for energy-autonomous instrumented total hip replacements [1]. The EHS consists of a piezoelectric multilayer element in an ultra-high molecular-weight polyethylene housing which is placed in a cavity that was excised from the original hip stem geometry (Figure 1). When the implant is loaded, force is transmitted through the implant and through the housing on the piezoelectric element. Thereby, voltage is generated. The aim of this study was to experimentally investigate the energy-conversion performance. Hence, a functional model was manufactured and tested in a simplified set-up.

Methods

The fully assembled hip stem with EHS was embedded in a specimen holder based on ISO 7206-4:2010 [2]. However, the alignment was chosen on basis of preceding iterative finite element analyses (FEA) in ANSYS V18.2. The sample was loaded by a uniaxial testing machine with average patient walking loads from Bergmann et al. [3] for 10 cycles. The piezoelectric element was connected to load resistors and the generated voltage was measured by an oscilloscope, using a voltage divider. We processed the measured data in MATLAB 8.4 and calculated the total voltage and the generated power. According to our previous work [1], we used the approach from Safaei et al. [4] to simulate the voltage and power on basis of the FEA results, using the force acting on the piezoelectric element when loaded with the maximum force during the gait cycle.

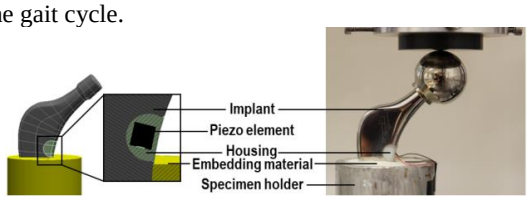

Figure 1: FE model of set-up with cross sectional view (left) and embedded implant with EHS (right)

Results

The simulated force acting on the piezoelectric element amounted to 86.5 N. The voltage curves from testing and simulation were in very good accordance. This is shown for the configuration with the maximum power output (R=0.5 MΩ, P=12.3 µW). Highest deviations occurred for the first cycle. The experimentally determined power was in the lower range of the simulated values (accounting for 20% tolerance for the piezoelectric element's capacity of C=220±44 nF).

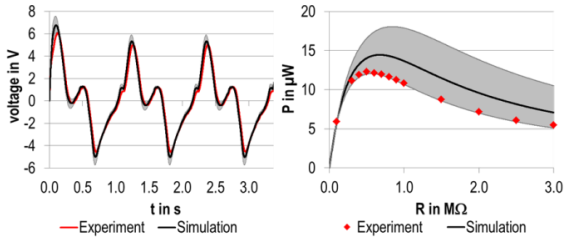

Figure 2: First three voltage cycles at R=0.5 MΩ (left) and generated power against load resistance (right)

Discussion & Conclusion

With this proof-of-concept study, we showed the feasibility of energy harvesting with our proposed EHS. Our numerical simulation was validated by experimental results. The deviations from experiment and simulation in the first cycle are assumed to result from initial controlling by the testing machine leading to slightly different force inputs. Further factors for deviations are differences between real and assumed material parameters and manufacturing tolerances impairing the force transfer on the piezoelectric element. Compared to our previous work [1], the forces on the piezoelectric element were lower due to a different loading situation in this set-up resulting in a lower power output. In future studies, we will implant the functional model of the instrumented implant in an artificial bone and investigate the EHS performance in a more physiological-like loading situation.

References

1. Lange et al., Smart Mater. Struct., 29(11):115051, 2020.
2. ISO 7206-4:2010, 2015.
3. Bergmann et al., PLoS ONE, 11(5), 2016.
4. Safaei et al., SMASIS2017, V001T07A011, 2017.

Acknowledgements

The authors would like to thank Mario Jackszis for technical support. This research is funded by the Deutsche Forschungsgemeinschaft (DFG, German Research Foundation) - SFB 1270/1 - 299150580.

USING A CORONAL FRACTURE MODEL TO COMPARE DOUBLE PLATING METHODS FOR BI-CONDYLAR TIBIAL PLATEAU FRACTURES

Shabnam Samsami (1,2), Robert Pätzold (3,4), Tim Neuy (5) Markus Greinwald (3), Peter E. Müller (2), Yan Chevalier (2), Klaus Püschel (6), Peter Augat (3,7)

1. Department of Mechanical Engineering, Imperial College London, South Kensington Campus, London, UK*; 2. Department of Orthopaedics, Physical Medicine and Rehabilitation, University Hospital, LMU Munich, Munich, Germany; 3. Institute for Biomechanics, Berufsgenossenschaftliche Unfallklinik, Murnau, Germany; 4. Department of Trauma Surgery, Berufsgenossenschaftliche Unfallklinik, Murnau, Germany; 5. Paracelsus Medical University, Salzburg, Austria, 6. Department of Forensic Medicine, University Medical Center Hamburg-Eppendorf, Hamburg, Germany; 7. Institute for Biomechanics, Paracelsus Medical University, Salzburg, Austria*

Introduction

Bi-condylar tibial plateau fractures are one of the most complicated injuries to treat even for expert orthopedic surgeons due to multi-planar fracture splits [1]. Despite diverse internal and external fixation methods, double plating osteosynthesis has been mainly recommended for this trauma [2]. However, the type and position of the plate to achieve adequate fixation stability has been still questionable. This controversy is mainly associated with disregarding the posteromedial fragment in the previous fracture classifications. The Horwitz fracture model, used mainly in previous biomechanical assessments, also did not take this crucial fracture segment into account [3]. Therefore, we aimed to compare two kinds of double locked plating method applying a coronal fracture model developed previously in our institution. Fixation techniques consisted of the lateral and medial locking plates in which the medial plate was implanted medial-anteriorly (MA) or medial-posteriorly (MP).

Methods

Fourteen fresh-frozen tibias were allocated into two groups with similar BMD values. After actualization of the coronal fracture model and fixation of fractures with either the MA method or the MP technique, the specimens were tested under incremental fatigue loading conditions using a customized load applicator. The Aramis camera as an optical motion tracking system was utilized for the evaluation of the interfragmentary movements and relative rotations of the fracture segments (Figure 1).

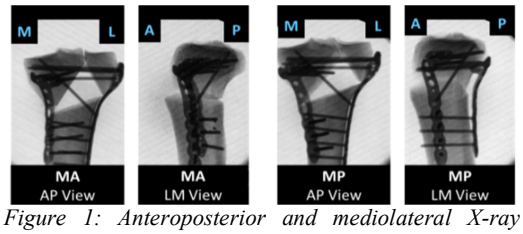

Figure 1: Anteroposterior and mediolateral X-ray images of the MA and MP groups

Results

The obtained biomechanical results showed that there were no statistically significant differences between the two fixation methods in terms of stiffness, failure load, or failure cycles (p= 0.67-0.98, depending on the measured parameter). The kinematic evaluations, however, demonstrated that by changing the position of the medial locking plate, the directions of the frontal and sagittal rotations were changed for the medial-anterior and medial-posterior fracture segments (Figure 2).

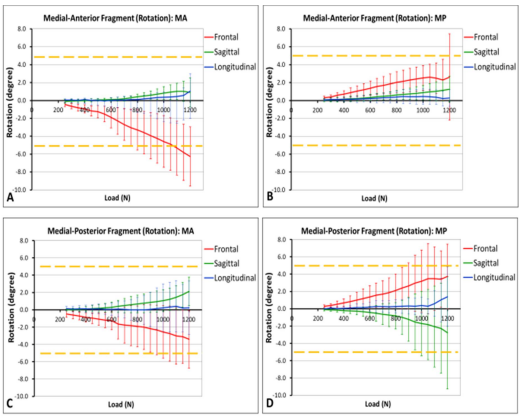

Figure 2: Components of the relative rotations for the medial-anterior and medial-posterior fragments with respect to the tibial shaft for the MA and MP groups

Discussion

Comparing two methods of double locked plating for a coronal fracture model of bi-condylar tibial plateau fractures indicated that the location of the medial locking plate does not affect the biomechanical stability of the tibia-implant construct. However, anterior or posterior insertion of the medial plate changed the movement directions of the medial fracture fragments. Therefore, the slightly larger step-offs were observed for the medial-posterior implantation. In conclusion, according to the surgeon's decisions for clinical conditions of the patients, bi-condylar tibial plateau fractures can be stabilized with the lateral locking plate combined with a medial one located anteriorly or posteriorly.

References

1. Kfuri et al, Injury, 49:2252-2263, 2018.
2. Eggli et al, J.Orthop Trauma, 22:673-679, 2008.
3. Samsami et al, Trauma Surgery, 140:17919-1730.

A FINITE ELEMENT COMPARISON BETWEEN EXTRA- AND INTRA-MEDULLARY IMPLANTS FOR TROCHANTERIC FRACTURE TREATMENT

Atsuki Tanaka (1,2), Luigi La Barbera (1,3), Paolo Sfamurri (1), Claudia Ottardi (1), Tomaso Villa (1)

1. LaBS, Department of Chemistry, Materials and Chemical Engineering "Giulio Natta", Politecnico di Milano, Italy; 2. Department of Orthopaedic Surgery, Kobe University Graduate School of Medicine, Japan; 3. Dept. of Mechanics, Polytechnique Montréal and Research Center CHU Sainte-Justine, Canada

Introduction

For the treatment of trochanteric hip fracture the percutaneous compression extramedullary plate (PCCP, Orthofix) and the intramedullary nail Veronail (Orthofix) have shown clinical effects similar to other intramedullary nails in both stable and unstable fractures [1,2]. Moreover, the PCCP decreases the post-operative hospital stay and overall economical cost compared to the intramedullary [1]. However, from a biomechanical point of view, intramedullary nails have been mentioned to have the advantage of reducing the deforming forces more than the extramedullary plate, because the lever arm from the hip joint to the nail is shorter [2].

The aim of this study is to compare the mechanical behavior, by using finite element (FE) analysis, of four different commercial implants used to treat those fractures: the intramedullary Gamma3 Nail (GN, Stryker), the Proximal femoral nail (PFN, Synthes), Veronail and the extramedullary PCCP in two different fracture models of the femur.

Methods

AO 31-A1 and AO 31-A2 [3] fracture models were replicated in a 3D model of a femur: its distal extremity, corresponding to 40% of the length, was resected with respect to horizontal plane and fully constrained. The four models of the devices were reconstructed using reverse engineering techniques and inserted in the FE model of the femur. A tetrahedral finite element mesh was adopted and convergence analysis was performed to set the proper discretization. In both fracture cases the load was applied to the femoral head: 1866 N for AO 31-A1 and 1088 N for AO 31-A2 [3,4]. Von Mises stresses in the devices were calculated and compared to the static yield stress of the material. The stiffness of the constructs and maximum and minimum principal strains on the bony fracture rims were calculated and compared to the values calculated for the intact femur, without implants. All the simulations were run in Abaqus (Dassault Systèmes, SIMULIA Corp., RI).

Results

The maximum von Mises stresses were at the interface between the nail/plate and the cephalic screw, or between the screw and the support guide (Figure 1). The most stressed device was the GN, but all models had stress levels far from yield. In the AO 31-A2 fracture, only the PCCP and PFN allowed to recover the overall stiffness of the intact femur (Table 1). The minimum value of compressive principal strain was in the posteromedial region of the fracture rim (Table 1).

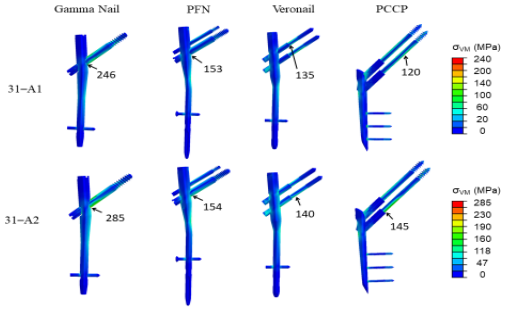

Figure 1: The von Mises stress distribution for each device. The arrows show the maximum.

Fracture type	Model	Stiffness (N/mm)	Strain postero-medial area (%)
–	Intact (reference)	2475	-0.234
31-A1	Gamma Nail	2801	-0.201
	PFN	2854	-0.188
	Veronail	2984	-0.194
	PCCP	3090	-0.203
31-A2	Gamma Nail	2247	-0.997
	PFN	2441	-0.992
	Veronail	2351	-0.936
	PCCP	2491	-0.842

Table 1: Overall stiffness and minimum principal strain of the bone in the posteromedial region of the fracture surface for each model and fracture type.

Discussion

The locations of maximum von Mises stresses in the implants are in agreement with literature [5,6]. The stress distribution of the PCCP was similar to the intramedullary nails having the two screws. In the AO 31-A2 fracture, the principal strain of the PCCP increased about 15% compared to that of the GN. Moreover, the stiffness of the PCCP was higher than other implants due to the stiffer material (stainless steel) and two screws.

These results show that from a biomechanical point of view, the extramedullary implant PCCP could be used safely as the other intramedullary implants, even for the unstable trochanteric fracture. Finally, the PCCP can be a good alternative for the trochanteric fracture treatment, although other drawbacks (i.e. cut-off) have not been completely solved.

References

1. Crespo et al. Eur J Trauma Emerg Surg, 38:443–449, 2012.
2. Kouzelis et al. Open Orthop J, 8:60–68, 2014.
3. Goffin et al. J Orthop Res, 32:39–45, 2014.
4. Damm et al. Clin Biomech, 28:530–535, 2013.
5. Knobe et al. Injury, 46:1475–1482, 2015.
6. Helwig et al. Injury, 40:288–295, 2009.

FINITE ELEMENT ANALYSIS FOR MECHANICAL RESISTANCE OF A 3D PRINTED RADIAL HEAD PROSTHESIS IN CASE OF BONE-RESORPTION

Silvia Pianigiani, Riccardo Verga, Aldo Toni
Adler Ortho, Milano, Italy

Introduction

A common location for radius fracture is the proximal radial head. With the arm in neutral position, the fracture usually happens in the anterolateral quadrant [1].
If traditional surgeries are not enough to induce bone stabilization and vascularization, or the fracture can be defined grade III or grade IV (Mason classification), a radial head prosthesis can be the optimal compromise between bone saving and recovering the "terrible triad".
A commercially available design of radial head prosthesis such as Antea (Adler Ortho, Milan, Italy) is characterized by flexibility in selecting the best matching size for patients and induced osteointegration thanks to the Ti-Por® radial stem realized by 3D printing with laser technique (Figure 1). As demonstrated, Ti-Por® push-out resistance increased 45% between 8 -12 weeks after implantation, hence confirming the ideal bone-osteointegration. Additional features of Antea are: bipolarity, modularity, TiN coating, radiolucency, hypoallergenic, 10° self-aligning.
The osteointegration is of paramount importance for radius, in fact the literature is unfortunately reporting several clinical cases for which the fracture of the prosthesis happened after bone-resorption. Even if related to an uncommon activity, the combination of mechanical resistance provided by the prosthesis and the stabilization due to the osteointegration should cover also accidental movements.



Figure 1: Antea design (Adler Ortho, Milano, Italy)

Based upon [1], after axial compression-load until radii failure, all native specimens survived a compression-load of 500N, while the failure happened for a mean compression force of 2560N.
The aim of this research study was to test the mechanical resistance of a radial head prosthesis obtained by 3D printing.

Methods

In detail, a finite element analysis (FEA) was used to understand the mechanical resistance of the core of the prosthesis and the potential bone fracture induced in the radius with simulated bone- resorption (Figure 2a). The critical level was estimated at the height for which the thickness of the core is the minimum (Figure 2b).
Considered boundary conditions:

- Full-length prosthesis plus radius out of the cement block equal to 60mm;
- Bone inside the cement equal to 60mm;
- Load inclined 10° epiphysiary component;
- Radius with physiological or osteoporotic bone conditions;
- Load (concentrated in the sphere simulating full transmission from the articulation) of 500N or 1300N or 2560N;
- Porous metal as equivalent linear elastic material with E_1=0,75GPa or E_2=1.515GPa or E_3=3GPa.

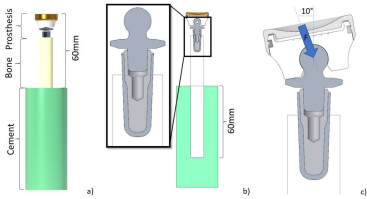

Figure 2: a) configuration of the model used for the FEM; b) level of the simulated bone-resorption up to the level for which the core has the minimum thickness; c) direction of applied load

Results

The maximum stress on the core of the prosthesis and the risk of fracture [2] were observed.
According to the obtained results, the radial head prosthesis shows promising mechanical resistance despite of the different equivalent materials for the porous structure and the simulated bone-resorption for all applied loads except for 2560N. The estimated mechanical limit for the material in use is 200MPa. The risk of fracture is in agreement with the experimental findings [1] and independent by the porous material, in fact bone starts to fail for the minimum reported failure load (Figure 3).

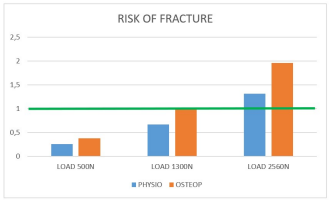

Figure 3: changes of risk of fractures for the different configurations (limit for fracture =1)

Discussion

The presented FEA aimed at investigating the behavior of a femoral head prostheses made by 3D printing with simulated bone-resorption. The prosthesis shows to be a skilled solution even during accidental loads.

References

1. Lacheta et al., BMC Musculoskeletal Disorders, 20:147, 2019
2. Schileo et al, J Biomech, 41:2483–2491, 2008

STABILITY OF REVISION ACETABULAR RECONSTRUCTIONS: CAN A SYNTHETIC MATERIAL REPLACE BONE GRAFT FOR DEFECT FILLING?

Federico Morosato (1), Francesco Traina (2), Ronja A. Schierjott (3), Georg Hettich (3), Thomas M. Grupp (3), Luca Cristofolini (1)

1. Department of Industrial Engineering, Alma Mater Studiorum - Università di Bologna, Bologna, Italy

2. Chirurgia Protesica, IRCCS Rizzoli Orthopaedic Institute, Bologna, Italy

3. Aesculap AG, Research & Development, Am Aesculap-Platz, Tuttlingen, Germany

Introduction

About 10-15% of acetabular implants fails every year, requiring revision surgery. Implantation of the revision prosthesis is generally addressed after restoration of bone defects arising in and around the acetabulum as consequence of implant failure. Morcellised bone graft represents the golden standard solution for defect filling. However, due to the lack of availability of human tissue, synthetic bone graft is becoming more popular in revision surgery.

The aim of the present study was to assess if a calcium-phosphate based substitute (CaP-putty) could provide a primary stability similar to the one provided by morcellised bone graft, when applied to treat central, severe, contained defects. Primary stability was assessed via Digital Image Correlation (DIC).

Materials and methods

Five pairs of fresh-frozen hemipelvises were adopted. The specimens were aligned in a reliable reference frame and potted [1]. To reproduce consistent defects, the procedure illustrated in Figure 1 was applied.

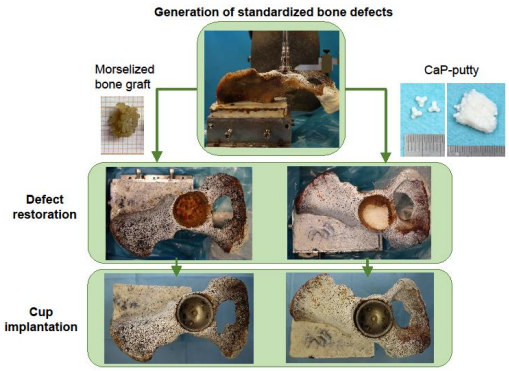

Figure 1: A standardized acetabular defect was implemented [2]. Each hemipelvis and its contralateral side were alternatively reconstructed with morselized bone graft or CaP-based material. Commercial cups were press-fit in the acetabular cavity and two anchoring screws were used.

A black-on-white speckle pattern was applied on each specimen before the test. The loading protocol consisted of cyclic increasing load packages up to 3 BW. The loading direction was chosen so as to replicate the direction of the peak force measured in vivo during level walking. A validated protocol was used to measure the permanent migrations and the inducible micromotions at each load cycle through the DIC system [3].

Results

The permanent migration steadily increased with load, showing a visible settling trend in each load package at low forces. At 3.0 BW the permanent migration measured in specimens reconstructed with CaP-putty was larger than in specimens reconstructed with bone graft (1.39mm vs 0.84 mm, median values), but such difference was statistically not-significant at all load levels (Wilcoxon signed rank sum test, p=0.06-1.0).

A similar trend was found for the inducible micromotions: the largest ones were measured in specimens reconstructed with CaP-putty (0.240 mm vs 0.15 mm, median values), but the difference between groups was statistically not-significant at all load levels (Wilcoxon signed rank sum test, p=0.06-1.0) (Figure 3).

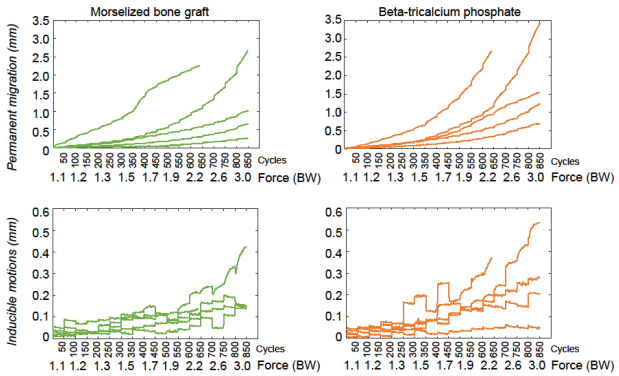

Figure 2: The resultant permanent migration and the resultant inducible micromotions measured during each test are shown for the morcellised bone graft (left) and CaP putty (right).

Discussion

CaP putty granted a mechanical stability comparable with morcellised bone graft when applied in the acetabulum with severe, contained defects. In fact, in both cases the clinical thresholds related to implant failure (i.e. 1 mm for the permanent migration and 150 micrometers for the elastic motions) were not exceeded. In conclusion, this study has shown very promising biomechanical properties of the newly developed CaP putty, when applied to severe contained defects, with remarkable advantages in terms of cost, availability, conservation and body-rejection.

References

1. Morosato et al., J Orthop Res, 36:1645–52, 2018.
2. Schierjott et al., PLoS One,14: e0222511, 2019
3. Morosato et al., Strain, 55: e12318, 2019

What have we learned about the influence of total knee arthroplasty design-based parameters on the in-vivo knee joint kinematic from single plane fluoroscopic analyses?

Moewis P[1], Hommel H[2], Trepczynski A[1], Krahl L[1], Duda GN[1]

[1] Julius Wolff Institute, [2] Krankenhaus Märkisch Oderland

Introduction: Although total knee arthroplasty (TKA) is an established procedure with 95% survivorship, around 14-39% of patients report dissatisfaction with the outcome [1]. Despite a wide number of available TKA designs, there is no clear consensus about the effectivity of specific design geometrical features to achieve a physiological knee joint kinematic pattern of medial pivot and lateral rollback during flexion. The aim of this study was to analyze different TKA designs during in-vivo conditions to achieve an understanding of specific design influence.

Material & Methods: Different cohorts of patients operated with specific TKA designs consisting of; multiradius, gradually changing radius, lateral pivot, bi-cruciate stabilized and high contact area were analyzed in-vivo during weight and non-weightbearing high flexion activities. Single plane fluoroscopy was used to collect the movement from extension until maximal achieved flexion [2]. Specific medial and lateral distal points relative to the tibia component plateau were determined to conduct an anterior-posterior kinematic analysis.

Results: While a tendency towards a design-based kinematic was observed during non-weight bearing conditions, reduced anterior-posterior translation magnitudes or inversed kinematic, like exchanged axial rotation pivots were observed during weight-bearing conditions. An example of this contradicting kinematic can be observed in Figure 1, which shows the kinematic in patients with a lateral pivot implant with unexpected pivot changing.

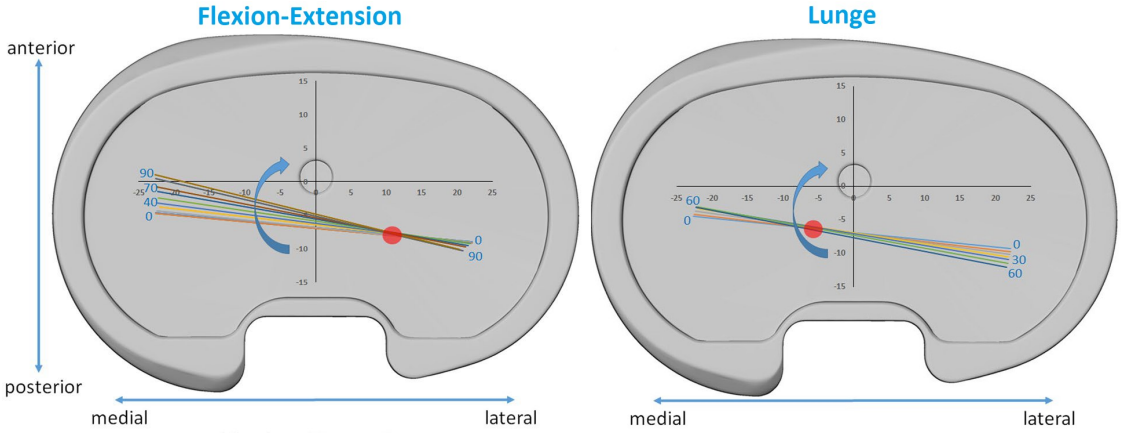

Figure 1. Axial pivot changing between non-weight bearing (left) and weight bearing (right) activities.

Conclusions: Although there is undoubtedly an effect of specific design features, this effect is influenced by the interactions between femoral radius and conformity, loading conditions or cruciate ligament strategy applied. Future designing need to consider the differentiation between loaded and unloaded kinematics, ligament balancing procedure to be applied and also which patient cohort would really benefit from an specific implant.

References:

[1]. Bourne et al. 2010.

[2]. Pitzner et al. 2017

BIOMECHANICAL EVALUATION OF THE IN-SITU STABILITY OF A NOVEL ARTIFICIAL MEDIAL MENISCUS IMPLANT

Matthias Sukopp[1], Maoz Shemesh[2], Elena Pruech[2], Eran Linder-Ganz[2], Scott Hacker[3], Vincenzo Condello[4], Jonas Schwer[1], Anita Ignatius[1], Lutz Dürselen[1], Andreas Martin Seitz[1]

[1]Institute of Orthopaedic Research and Biomechanics, Ulm University Medical Centre, Germany; [2]Active Implants LLC, Memphis, USA; [3]Grossmont Orthopedic Medical Group, La Mesa, USA; [4]Humanitas Castelli Clinic, Bergamo, Italy

Introduction

Severe traumatic meniscal injuries or premature meniscus degeneration requires, in some cases a total meniscectomy. In order to overcome the poor long-term prognosis of total meniscectomy, especially for middle-aged patients, a total meniscus replacement implant (NUsurface®, Active Implants LLC) was developed. Due to individual knee joint anatomy, it can be necessary to perform a notchplasty during the implantation to avoid an impingement of the implant´s lateral wall with the femoral intercondylar notch. However, the effects of such an invasive notchplasty on the device kinematics and its stability in the knee joint have not been investigated. Therefore, the aim of this in-vitro study was to examine the implant kinematics before and after two subsequent notchplasties with increasing tissue removal under realistic loading situations and different limb alignments.

Methods

The Ulm dynamic knee simulator[1] was used to perform realistic loading and motion exercises on six left human cadaveric knee joints (IRB: 34/19). Passive reflective markers were attached to the antero-medial aspect of the implant and to the bony structures of tibia and femur to register the kinematics of the meniscus implant, relative to the tibial plateau (Prime13, OptiTrack, Fig. 1).

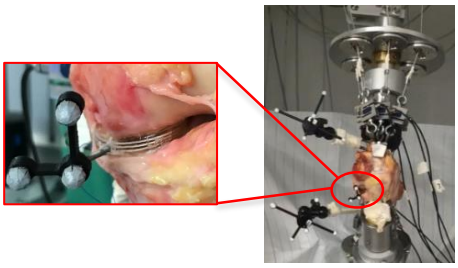

Fig. 1. Specimen in the knee simulator with attached reflective markers to the femur, tibia and the implant.

The specimens were equally divided into two groups to study the effect of knee alignment on implant stability under physiological and 10° valgus alignment of the mechanical axis of the lower limb. The last scenario was chosen to represent a worst-case scenario in terms of implant stability by simulating a reduced contact at the medial joint compartment. Two qualified surgeons (SH & VC) performed the implantation and the notchplasties. For each joint condition, a set of three exercises were randomly simulated: jump landing, squatting and axial ground impacts at 10°, 30° and 60° knee flexion. The data acquisition was performed using an established marker-based motion analysis protocol. Results were calculated using descriptive evaluation.

Results

During all tests, the NUsurface® implant stayed in a safe position without subluxation or dislocation tendencies. The maximum implant translation was less than 12 mm and the maximum implant rotation was below 20° for all exercises. Both, neutral and valgus alignment of the mechanical axis of the lower limb had no influence on implant kinematics. After notchplasty, a trend towards increased translation was observed at axial impacts under 10° knee flexion (Fig.2), while a trend towards a reduction of translation occurred under 60° knee flexion.

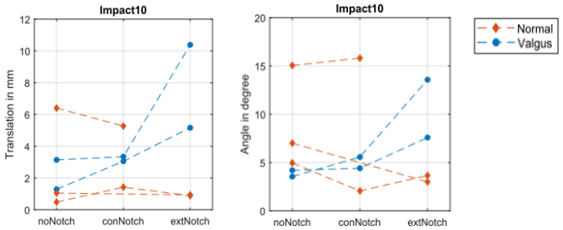

Fig. 2. Axial impact at 10° knee flexion: implant translation and rotation, divided in normal and valgus alignment and under the subsequent notchplasty states.

Discussion

The results of the present study indicate that the NUsurface® implant stayed in a safe position under all of the here investigated conditions. Thus, we can conclude, that the extent of the notchplasty and the malalignment of the leg axis had no influence on the stability and kinematics of the implant. Therefore, patients with valgus up to 10° may benefit from the device. Further, the kinematic behaviour of the implant lies well within the range of implant translations, clinically measured using Magnetic Resonance Imaging in patients without notchplasty[2].

References

1. Schall, F. et al., Frontiers in Bioengineering and Biotechnology, 2019, 7:244.
2. De Coninck, T. et al., Clinical Biomechanics, 2014:898-905

Acknowledgements

This study was funded by Active Implant LLC, USA

ASYMMETRIC VS SYMMETRIC INSERTS IN MOBILE BEARING TOTAL KNEE ARTHROPLASTY, A CLINICAL AND BIOMECHANICAL STUDY

Edoardo Bori (1), Silvia Pianigiani (1), Gianluca Castellarin (2), Bernardo Innocenti (1)

1. BEAMS Department, Université Libre de Bruxelles, Belgium;
2. II Unit Orthopaedic Department, Ospedale di Suzzara, Mantua, Italy

Introduction

This study aims at comparing the clinical and biomechanics effects of symmetric and asymmetric designs for the polyethylene insert currently available for mobile bearing total knee arthroplasty (TKA). The investigation was performed in-vivo, ex-vivo and in-silico.

Methods

The clinical study involved the retrospective analysis of 303 patients with a mobile bearing TKA. All patients received the same femoral and tibial components; concerning the insert, 151 patients received a symmetric design (SD) and 152 an asymmetric design (AD).
The biomechanical study consisted in a 3D finite element model and an experimental cadaveric study.
For the in-silico finite element study (performed in agreement with a previously validated one [1]), a lower leg model was developed, implanted with the same TKAs and analyzed during gait and squat activities; the implant kinematics and bone-stresses were investigated for the two polyethylene insert solutions.
For the ex-vivo study, 5 fresh-frozen cadaveric knee specimens, with no history of musculoskeletal problems, were then investigated following a protocol similar to a previously applied one [2]. The femoral bone of each specimen was clamped to a specific designed frame and optical marker sets were fixed on the tibial and femoral bones and also on the polyethylene mobile bearing insert and tracked during the motion. Each leg was analyzed during 10 passive flexion-extension cycles from 0° to 120° of flexion and the tibio-femoral and insert kinematics were calculated during the motion. The tests were performed in native and replaced configurations, using both symmetric and asymmetric designs of the insert.

Results

The clinical follow-up returned that, after surgery, patients' average flexion improved from 105° (with 5° of preoperative extension deficit) to 120° (AD-group) and 115° (SD-group) at the latest follow-up.
All the clinical scores significantly improved after surgery and there was no postoperative extension deficit. No pain affected the AD-group, while an antero-lateral pain was reported in some patients of the SD-group. Patients of the AD-group presented a better ability to perform certain physical routines.
The finite element analysis results showed that the SD induces higher tibial-bone stresses than the AD; both designs led to similar kinematics, comparable to literature, but however SD insert rotates less on the tray, increasing the relative motion between femoral and insert components, while AD insert permits greater insert rotation.
Experimental ex-vivo tests results, in agreement with the previous findings, showed that the AD allows a better compliance in internal-external rotation: the rotation angle between tibia and insert indeed matches the one found in the tibio-femoral while the SD insert returned instead lower results [see Figure 1], implying a greater relative motion between femoral and insert components.

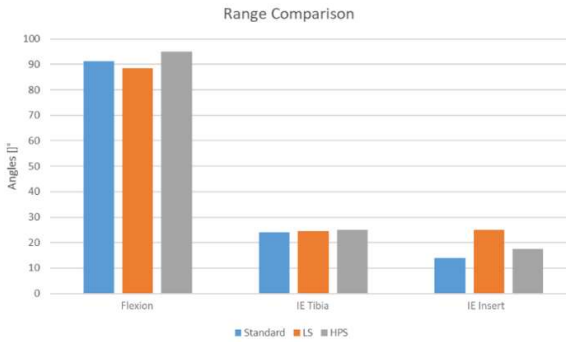

Figure 1: Range of Rotations from the ex-vivo tests, in terms of flexion and internal-external (both of tibia and insert) ranges, for the three different configurations tested.

Discussion

The ex-vivo and in-silico biomechanical analysis justifies the clinical findings: overall joint TKA kinematics is similar for the two designs, although the asymmetric solution shows higher insert rotation and less bone stress, thus resulting as more suitable to be cemented, avoiding lift-off issues, inducing less pain. Clinically and biomechanically, an asymmetric mobile bearing insert could be a valid alternative to symmetric mobile bearing insert.

References

1. Innocenti, Bernardo et al., Load Sharing and Ligament Strains in Balanced, Overstuffed and Understuffed UKA. A Validated Finite Element Analysis. The Journal of Arthroplasty, Volume 29, Issue 7, 1491 – 1498, 2014
2. Victor, Jan et al., The influence of muscle load on tibiofemoral knee kinematics. J. Orthop. Res., 28: 419-428, 2010

ASSESSMENT OF LINER MOVEMENT ON DUAL MOBILITY CUP: PRELIMINARY EX VIVO STUDY

L. Riglet[1], A. Naaim[1], A. Viste[1,2], H. Liebgott[3], R. Dumas[1], MH. Fessy[1,2], and LL. Gras[1]

[1]Univ Lyon, Université Claude Bernard Lyon 1, Univ Gustave Eiffel, IFSTTAR, UMRT_9406, Laboratoire de Biomécanique et Mécanique des Chocs, 69622 Lyon, France

[2]Hospices Civils de Lyon, Hôpital Lyon Sud, Service de Chirurgie Orthopédique, 165 Chemin du Grand Revoyet,69495 Pierre Benite Cedex, France

[3]CREATIS, Univ Lyon, INSA Lyon, UCBL, UJM Saint-Étienne, CNRS UMR 5220, Inserm U1294, Lyon, France

Introduction

The concept of the Dual Mobility Cup (DMC) was developed, in 1974, by G. Bousquet [1]. This hip prosthesis is composed of two joints : a large one, between the metallic cup and the polyethylene liner, and a small one between the femoral head and the polyethylene liner. Compared to standard prosthesis, this design helps to restore the hip joint range of motion, decrease wear, and increase implant stability [3].

The way this prosthesis moves in vivo has not been established yet. Therefore, this study aims at visualizing and quantifying the liner movement in ex vivo experiments, for different leg movements. Ultrasound imaging is used as it is non-invasive, and has already been used to visualize the liner movement in vitro (on immerged DMC) [2].

Methods

A DMC (Serf Novae®) was implanted on a cadaveric subject (male, 78 years old). Six intracortical pins with reflective markers tripods were fixed in the pelvis, left femur and tibia. One rigid tripod was fixed on a 3D ultrasound probe (SuperLinear™ Volumetric SLV16-5). Hip joint range of motion (RoM) was applied manually and recorded using Optitrack (NaturalPoint, Inc.). Ultrasound acquisitions were performed, in a series of static poses, using the 3D probe and an ultrasound system (Aixplorer® Supersonic Imagine®).

Hip kinematics and ultrasound imaging position were obtained using motion analysis data (Figure 1). Liner spherical surface and plane were segmented on the ultrasound imaging data using 3D Slicer. Thanks to these data, change of abduction and anteversion angle of the liner plane, relative to the pelvis, were calculated for different movements using MATLAB (MathWorks®).

Results

Hip movement	RoM (°)	Abduction (°)	Anteversion (°)
Flexion	20.6	8.5	-5.6
Abduction	14.8	-5.7	-7.1
Adduction	5.0	6.9	0.7
Internal rotation	12.9	5.1	-2.8
External rotation	30.2	-7.9	9.0

Table 1: Change of abduction and anteversion angle of the liner plane after hip movement (RoM and angles in degrees)

No clear tendency was found between hip joint and liner plane angles. However, at the end of a series of static poses starting and going back to neutral posture, the liner did not return to its initial orientation (Table 1).

Biomechanical data show a greater liner movement for flexion, external rotation and hip abduction (abduction and anteversion angle greater than 5°), while 5° of hip adduction produce a small anteversion movement (anteversion angle less than 1°) .

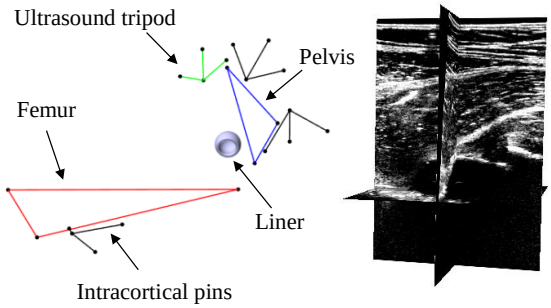

Figure 1: Liner position using fused data (left) – 3D ultrasound imaging (right)

Discussion

This preliminary ex vivo study showed that the liner movement could be quantified and visualised using ultrasound imaging. This result is promising for future in vivo studies, where we expect muscular activity to also affect liner movement. Moreover, even though the study was conducted on only one subject and only for small RoM because of the probe size positioned on the groin area, liner movement could still be observed. The amount of liner movement is not negligible, but remains under 10° of amplitude. Therefore, further experiments should be carried out to better understand the liner movement, and identify movement patterns.

References

1. Noyer, D., Caton, J.H., International Orthopaedics (SICOT), 41(3):611–618, 2017.
2. Desmarchelier, R., et al., Rev. de Chir. Orthop. et Traumatol, 102(7): S179, 2016.
3. Neri, T., et al., SICOT-J, 6:17, 2020.

Acknowledgements

The authors thank Serf company for lending prostheses and materials helping to the implantation. This work was supported by the LABEX PRIMES (ANR-11-LABX-0063).

IMPROVED STABILITY OF DISTAL TIBIA FRACTURES AFTER ANGULAR STABLE INTRAMEDULLARY NAILING – A BIOMECHANICAL STUDY

Ivan Zderic (1), Jan Caspar (1), Michael Blauth (2), André Weber (2), Roger Koch (2), Karl Stoffell (3), Christopher Finkemeier (4), Martin Hessmann (5), Boyko Gueorguiev (1)

1. AO Research Institute Davos, Switzerland; 2. DePuy Synthes, Switzerland; 3. University Hospital Basel, Switzerland; 4. Orthopaedic Trauma Surgeons of Northern California, United States; 5. Academic Teaching Hospital Fulda, Germany

Introduction

Intramedullary nails are frequently used for treatment of unstable distal tibia fractures. However, insufficient fixation of the distal fragment could result in delayed healing, malunion or nonunion. The quality of fixation may be adversely affected by the design of both the nail and locking screws, as well as by the fracture pattern and bone density. Recently, a novel concept for angular stable nailing has been developed that maintains the principle of relative stability and introduces improvements expected to reduce nail toggling, screw migration and secondary loss of reduction. It incorporates polyether ether ketone (PEEK) inlays integrated in the distal and proximal canal portions of the nail for angular stable screw locking (Fig. 1). The nail can be used with new standard locking screws and low-profile retaining locking screws, both designed to enhance cortical fixation. The low-profile screws are with threaded head, anchoring in the bone and increasing the surface contact area due to the head's increased diameter.

The aim of this study was to investigate the biomechanical competence of the novel angular stable intramedullary nail concept for treatment of unstable distal tibia fractures, compared with four other nail designs in an artificial bone model.



Figure 1: Photographs of the proximal (left) and distal (right) portions of the novel nail concept with integrated polyether ether ketone (PEEK) inlays for angular stable screw locking.

Methods

The distal 70 mm of thirty artificial tibiae (Synbone) were assigned to 5 groups for distal locking using either four different commercially available nails – group 1: Expert Tibia Nail (DePuy Synthes); group 2: TRIGEN META-NAIL with Internal Hex Captured Screws (Smith & Nephew); group 3: T2 Alpha with Locking Screws (Stryker); group 4: Natural Nail System featuring StabiliZe Technology (Zimmer) – or the novel angular stable TN-Advanced nail with low-profile screws (group 5, DePuy Synthes). The distal locking in all groups was performed using 2 mediolateral screws. All specimens were biomechanically tested under quasi-static and progressively increasing combined cyclic axial and torsional loading in internal rotation until failure, with monitoring by means of motion tracking.

Results

Initial nail toggling of the distal tibia fragment in group 5 was significantly lower as compared with group 3 in varus ($p=0.04$) or with groups 2 and 4 in flexion ($p\leq0.02$, Table 1). In addition, the toggling in flexion was significantly lower in group 1 versus group 4 ($p<0.01$). Moreover, during dynamic loading, within the course of the first 10,000 cycles the movements of the distal fragment in terms of varus, flexion, internal rotation, as well as axial and shear displacements at the fracture site, were all significantly lower in group 5 compared with group 4 ($p<0.01$). Additionally, group 5 demonstrated significantly lower values for flexion versus groups 2 and 3 ($p\leq0.04$), for internal rotation versus group 1 ($p=0.03$), and for axial displacement versus group 3 ($p=0.03$). A trend to significantly lower values was detected in group 5 versus group 1 for varus, flexion, and shear displacement – with p-values ranging between 0.05 and 0.07 – and versus group 3 for shear displacement ($p=0.07$). Cycles to failure were highest in group 5 with a significant difference to group 4 ($p<0.01$).

Group	Varus (°)	Flexion (°)
1	0.22±0.12	0.23±0.17
2	0.24±0.12	0.43±0.27
3	0.57±0.41	0.38±0.16
4	0.31±0.12	0.68±0.18
5	0.19±0.11	0.08±0.04

Table 1: Initial nail toggling in varus and flexion in the five groups presented in terms of mean and standard deviation.

Discussion

From a biomechanical perspective, the novel angular stable intramedullary nail concept with integrated PEEK inlays and low-profile screws provides ameliorated resistance against nail toggling and loss of reduction under static and dynamic loading compared with other commercially available intramedullary nails used for fixation of unstable distal tibia fractures.

CAN PERIOTEST® QUANTIFY SPINAL PEDICLE SCREW STABILITY IN AGREEMENT WITH PULL-OUT TEST AND ACOUSTIC MODAL ANALYSIS?

Mohammadjavad Einafshar (1,2), Ata Hashemi (1), G. Harry van Lenthe (2)
1. Amirkabir University of Technology, Biomedical Engineering Faculty, Biomechanics Group, Tehran, Iran;
2. KU Leuven, Department of Mechanical Engineering, Biomechanics Section, Leuven, Belgium

Introduction

Pilot hole preparation, in particular pilot hole diameter is one of the most remarkable pretreatments which affects bone screw stability [1]. Pull-out tests are considered the gold standard to assess screw stability but tests are limited due to their destructiveness. Non-destructive acoustic modal analysis is being used to evaluate the primary and secondary stability of bone screws, and has recently been proposed for orthopedic and spine applications [2]. In acoustic modal analysis, deformation modes of a vibrational system can be stimulated, and natural frequencies can be recorded. These natural frequencies are related to mechanical stability [3]. The Periotest® is widely used to assess stability of dental implants [3]; the electromechanical device contains a sensitive tipper that hits the implant 16 times in 4 seconds [3]; the contact time is measured and expressed on a scale from -8 (well-integrated) to +50 (no osseointegration). Considering its widespread use, the aim of this study was to compare the Periotest® values with conventional pull-out test and acoustic modal analysis in quantifying the effect of pilot hole diameter on primary implant stability.

Methods

Twenty specimens (40x40x60 mm^3) were cut from polyethylene (PE) blocks with a density of 947 kg/m^3 and elastic modulus of 1000 MPa. Pilot hole diameters of 5.0, 5.25, 5.5 and 5.75 mm, respectively, were drilled to depths of 20 mm (N=5/group). A self-tapping conical pedicle screw with an outer diameter of 6.5 mm was inserted into the pilot holes.

The screw-block structure was clamped (Figure 1) while two boundary faces were fixed during acoustic modal analysis and Periotest® (Medizintechnik Gulden, Modautal, Germany) methods. Acoustic modal analysis test was performed using a sound recording technique. A microphone (Audio–Control CM-145, Apple Inc. USA) was used to record the sound after small hammer lightly bellows to the head of the screw. The natural frequency of the first vibration mode was extracted by applying fast Fourier transformation (FFT) to the sound data. The Periotest® was carried out with the Periotest® device fixed in another clamp in order to remove undesired deviations (Figure 1). Pull-out test was carried out according to the earlier study [4].

Results

The maximum natural frequency derived from acoustic modal analysis and pull-out force were 1824 ± 3 Hz and 4800 ± 172 N, respectively for the 5.5 mm pilot hole. Moreover, the minimum (most stable) value for the Periotest® was 3.2 ± 0.4 and was found for the same 5.5 mm pilot hole (Table 1).

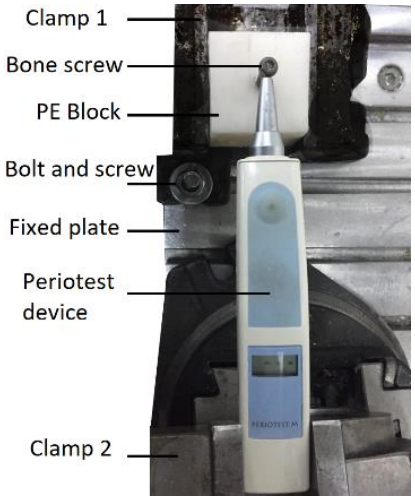

Figure 1: Experimental setup for acoustic modal analysis and Periotest® device tests.

Model	Method		
Pilot Hole Diameter (mm)	Pull-out force (N)	Acoustic Modal Analysis (Hz)	Periotest Scale
5.0	4682 ± 160	1540 ± 6	+6.1 ± 0.3
5.25	4302 ± 37	1505 ± 2	+6.3 ± 0.3
5.5	4800 ± 172	1824 ± 3	+3.2 ± 0.4
5.75	3266 ± 225	1492 ± 6	+6.5 ± 0.2

Table 1: Experimental data on the pull-out force, first natural frequency and Periotest® scale determined for four different pilot hole diameters in polyurethane block.

Discussion

The Periotest® values agreed well with the ones obtained from pull-out tests and acoustic modal analysis. The 5.5 mm diameter was identified as the optimum pilot hole diameter by all three techniques. The The Periotest® values as measured in this study would indicate that "immediate loading is not possible in most cases" [3]. Note that the Periotest scale was developed and validated for dental implants placed in the jaw. How this scale performs for other configurations, such as the pedicle screws placed in PE as in this study, requires further evaluation.

References

1. Silva, P. et al. J EUR SPINE, 22, 1829-36, 2013.
2. Einafshar, M. et al. ESB, 622, 2019.
3. Banihashemi, SA. et al. J DENT MATER TECH, 9(2): 63-68, 2020.
4. Einafshar, M. et al. J Comput Methods Programs Biomed, 2021.

OXIDATION RESISTANCE AND WEAR PERFORMACE OF VITAMIN E BLENDED POLYETHYLENE FOR TOTAL KNEE ARTHROPLASTY

Ana Laura Puente Reyna (1), Arthur Bollinger (1), Marie Anne Mulliez (1), Thomas M. Grupp (1, 2)

1. Aesculap AG, Research and Development, Germany; 2. Ludwig Maximilians University Munich, Department of Orthopaedic Surgery, Physical Medicine and Rehabilitation, Germany

Introduction

Total knee arthroplasty is a well established treatment for degenerative joint disease, which is also performed as a treatment in young and middle-aged adults who have a significant physical activity and high life expectancy. However, complications may occur due to a biological response to polyethylene wear particles as well as delamination of the material [1].

The purpose of the following study was to compare the material properties and wear resistance of a vitamin E blended polyethylene for total knee arthroplasty (MXE) in comparison with a clinically stablished UHMWPE.

Methods

Two polyethylene materials were tested as gliding surfaces: UHMWPE (30 kGy e-beam sterilized) and MXE (0.1 % vitamin E blended polyethylene, 30 kGy gamma sterilized). The gliding surfaces were artificially aged for two weeks according to ASTM F2003-02(2015).

The oxidation index was measured based on ASTM F2102-17 on both materials before and after artificial aging for two weeks up to a depth of 10 mm (whole thickness).

Small punch testing was performed according to ASTM F2977-13 on virgin and aged materials.

Wear simulation was performed on a load controlled 4 station knee wear simulator (EndoLab GmbH, Thansau, Germany) capable of reproducing loads and movement of highly demanding activities measured in vivo on 8 patients [2] and normalized to a patient weight of 100 kg [3]. The load profiles were applied for 5 million cycles in a combination of 40% stairs up, 40% stairs down, 10% level walking, 8% chair raising and 2% deep squatting. Medium size AS emotion PS Pro (Aesculap AG, Tuttlingen, Germany) femoral and tibial components with a ZrN-multilayer surface were tested.

Results

After two weeks artificial aging, the UHMWPE showed oxidation, whereas the MXE material showed a similar oxidation index as the virgin material (Fig. 1).

The small punch test show a reduction in the mechanical properties of the aged UHMWPE material, whereas the aged MXE material showed similar properties as the virgin material.

During the HDA knee wear simulation, the aged UHMWPE showed severe delamination on its surface after 2.5 million cycles (Fig. 3a), whereas the aged MXE showed no signs of delamination after 5 million cycles (Fig. 3b).

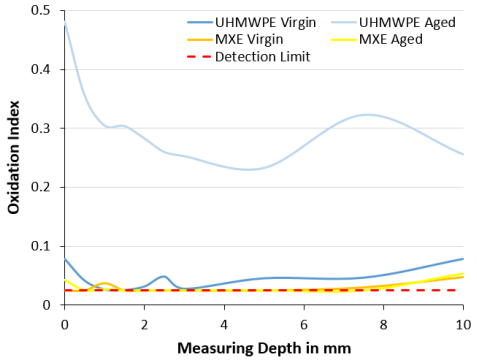

Figure 1: Oxidation index of the tested material.

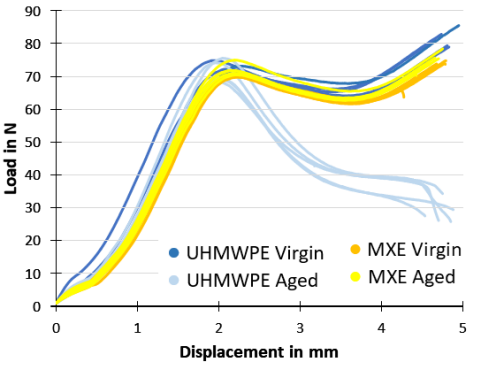

Figure 1: Small punch test results of the material.



Figure 3: (a) delamination of aged UHMWPE after 2.5 million HDA cycles; (b) aged MXE gliding surface after 5 million HDA cycles, no delamination was seen.

Discussion

Even after artificial aging, the addition of vitamin E in the polyethylene prevented its oxidation, kept its mechanical characteristics, and low wear, even under a demanding HDA knee wear simulation.

References

1. Sadoghi et al, J Arthroplasty 2013; 28(8):1329–32.
2. Bergmann et al, PLoS ONE, 9(1): Article ID e86035, 2014.
3. Schwiesau et al, BioMed Research International, 2014: Article ID 567374, 2014.

PILOT HOLE OVERDRILLING INCREASES SCREW PERFORATION RISK IN LOCKED PLATING OF COMPLEX PROXIMAL HUMERUS FRACTURES

Benjamin Burkhard (1,2), Clemens Schopper (1,3), Daniel Ciric (1,4), Dominic Mischler (1), Boyko Gueorguiev (1), Peter Varga (1)

1. AO Research Institute Davos, Switzerland; 2. ETH Zurich, Switzerland; 3. University Hospital Ulm, Germany; 4. Flinders University, Australia

Introduction

The rate of mechanical complications in proximal humerus fracture (PHF) fixations has remained high, up to 35%, despite the wide use of state-of-the-art locking plates [1]. The most frequent mechanical failure mode is post-operative screw perforation through the humeral head's articular surface, with an up to 23% incidence [2]. Non-anatomical fracture reduction and lack of cortical support in the calcar region have been reported as major risk factors [3]. Nevertheless, other surgical mistakes may also contribute to fixation failure, such as in-adverse intraoperative perforation of the articular surfaces during pilot hole drilling, i.e. overdrilling. While commonly neglected in clinics, overdrilling often occurs during PHF treatment due to minimal tactile feedback, especially in osteoporotic bone. Still, its consequences on the fixation stability have not been investigated. This biomechanical study aimed to evaluate whether overdrilling increases the risk of cyclic screw perforation failure in unstable PHFs.

Methods

Nine pairs of fresh-frozen human cadaveric proximal humeri from elderly donors (73.7 ± 13.0 ys, f/m: 3/6) were osteotomized in a standardized manner using subject-specific 3D-printed cutting guides. A highly unstable malreduced 3-part fracture without medial and lateral support of the head fragment was simulated [4]. Fixation was performed with PHILOS plates (DePuy Synthes, Switzerland) according to the surgical technique guide and using six proximal locking screws. The pairs were randomized in two treatment groups, one with all pilot holes accurately predrilled (APD) and the other with the boreholes of the two calcar screws overdrilled (COD). Previously developed experimental setup and protocol was utilized for cyclic testing, with peak load starting at 50 N and progressively increasing by 0.05 N/cycle [4]. The first abrupt increase of displacement at valley load defined screw loosening. The first screw to penetrate through the joint surface closed an electrical circuit when it contacted the artificial glenoid component, stopping the test and confirming perforation failure.

Results

The two groups were highly similar in terms of bone mineral density ($p = 0.91$). The COD specimens demonstrated significantly lower cycles to initial screw loosening (10,310 ± 3,575) compared to the APD ones (12,409 ± 4,569), $p = 0.006$ (Figure 1). Similarly, number of cycles to screw perforation was significantly lower for COD (20,173 ± 5,851) versus APD (24,311 ± 6,318), $p = 0.019$. Failure mode was combined varus collapse and lateral-inferior translation of the humeral head. In all but one specimen, one of the calcar screws was the first to perforate the articular surface.

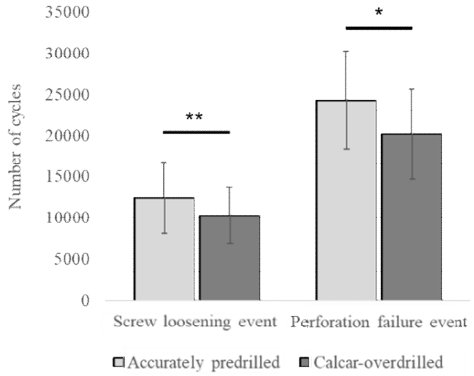

*Figure 1: Plated humeri with accurately predrilled pilot holes sustained significantly more cycles to initial screw loosening (**: $p<0.01$) and perforation (*: $p<0.05$) compared to specimens with overdrilled boreholes of the two calcar screws.*

Discussion

Besides general risk factors such as fracture complexity and osteoporosis, the inadequate surgical technique is crucial source of the high failure rates in locked plating of complex PHFs [5]. This study demonstrates for the first time that correct drilling depth significantly increases the fixation longevity until screw perforation occurs. Study limitations include the fracture model and loading mode. While further investigation about the prevalence and consequences in the clinical setting is needed, raising the surgical community's awareness towards this largely neglected risk source, together the development of devices to avoid overdrilling, are expected to help improve the treatment outcomes.

References

1. Kralinger et al, J Bone Joint Surg Am, 96:1026-32, 2014.
2. Panagiotopoulou et al., Injury, 50:2176-96, 2019.
3. Krappinger et al., Injury, 42:1283-8, 2011.
4. Ciric et al., J Orthop Res, 37:2625-33, 2019.
5. Beeres et al, Arch Orthop Trauma Surg,137:1685-92, 2017.

Acknowledgements

This study was supported by the AO Foundation via the AOTRAUMA Network (Grant No.: AR2018/01).

BIOMECHANICAL ANALYSIS OF DIFFERENT STEM FEATURES IN TOTAL KNEE ARTHROPLASTY

Edoardo Bori (1), Silvia Pianigiani (1), Bernardo Innocenti (1)
1. BEAMS Department,Université Libre de Bruxelles, Belgium

Introduction

Achieving adequate implant fixation and avoiding bone fractures are fundamental requisites in total knee arthroplasty; to cover this aspect, industry currently provides a variety of stems characterized by several designs features. Therefore, surgeons need to determine the correct set-up for each patient, choosing from a wide array of stem solutions for both femoral and tibial components varying in lengths, shapes, bone interfaces and additional features. Even if these many options are available, yet no evidence-based biomechanical guidelines are currently available to quantitatively lead the selection among these possibilities. For this reason, to help the surgeon in the decision-making process, an *in-silico* analysis of different combinations of stem design features was performed to provide a more in-depth insight of their influence on the patient outcomes.

Methods

The development of the model (i.e. soft tissue and bone geometries definition, material models and properties, load and boundary conditions together with the mesh) was performed in agreement with a previously validated finite element model [1]. Different femoral and tibial stems were designed based on currently available products, and a squat activity up to 120° flexion was analyzed combining the following design parameters:
-length/diameter: 120mm/22mm, 160mm/20mm, 220mm/15mm and 280mm/15mm;
-shape: straight and anatomical (bowed stems);
-cross-section: absence or presence of flutes;
-stem-end: full stem or presence of slots;
-bone-prosthesis interface: press-fit or cemented stems.
Examples of these configurations can be seen in Figure 1 and 2.

Von Mises bone stress, Risk of Fracture (RF) and implant micromotions were analyzed in different regions of interest and compared among the models.
The software Abaqus was used to perform the study.

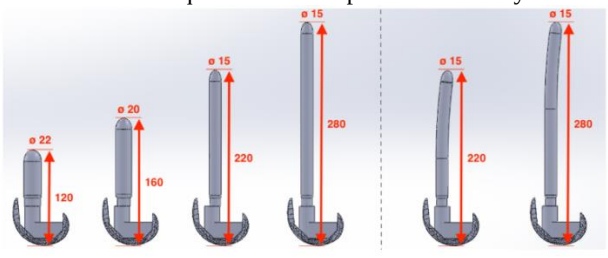

Figure 1: Different stem lengths in straight (A) and bowed (B) configurations

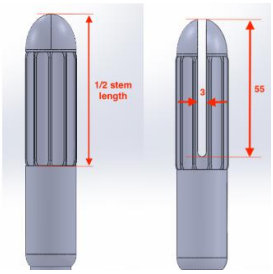

Figure 2: Examples of flutes and slots at the stem end

Results

For femoral stem, the results of this study demonstrated that its presence always induces an increase in bone stress. Proportionally to a length increase, the magnitude of the stress peak and the RF rose, the latter going up to 91% for the 280mm stems; the position of this peak is usually situated close to the stem tip, representing a possible location of failure. Furthermore, long stems implied a stress-shielding effect in the distal femur. Bowed stems led to a reduction of the stress peak at the tip as well as in the overall bone, while straight stems induce a stress concentration at the middle of its length. Regarding the tibial stem, similar outcomes can be found together with the fact that cemented stem showed lower micromotions both at the bone-tibial tray interface and at the stem tip compared to press-fit stems, reducing the risk of implant loosening. The simulations performed showed that the flutes, even if useful in terms of stability, act as stress risers increasing the RF in the bone; opposite behavior is instead referred to the presence of slots.

Discussion

The results of this study demonstrated that among the different stem design features, anatomical shapes and slots reduce the bone stress and the risk of fracture, while flutes have an opposite effect acting as stress risers; no relevant differences were found in this regard when alternating between cemented and press-fit stem configurations. Cemented tibial stems reduce implant micromotions, playing an important role in preventing loosening. The results found are in agreement with previous studies focused on the single features [2,3].

References

1.Innocenti B. et al., J Arthroplasty 29:1491-1498, 2014
2.El-Zayat B.F. et al., Arch Orthop Trauma Surg 136:1741-1752, 2015
3 Andreani L. Er al., J Arthroplasty 35:278-284, 2020

EXPERIMENTAL ANALYSIS OF LIGAMENT TENSION IN NATIVE KNEE TO REACH FUNCTIONAL STABILITY

Edoardo Bori (1), Thomas Paszicsnyek (2), Bernardo Innocenti (1)

1. ULB, BEAMS Department, Bruxelles, Belgium;

2. Privatklinik Ragnitz, Graz, Austria

Introduction

Applying the correct amount of collateral ligaments tension in the knees during knee arthroplasty surgery is a prerequisite to restore normal kinematics. It is well recognized that a low value of ligament tension could lead to an instable joint while a higher tension could induce tissues over-tensioning and problems at later follow-up. In this study, an experimental cadaveric activity was performed to measure the minimum tension required to achieve functional stability in the knee joint.

Methods

Ten cadaveric knee specimens were investigated; each femur and tibia were fixed with polyurethane foam in specific designed 3D-printed fixtures and clamped to a uniaxial loading frame equipped with a load cell.

A constant vertical displacement rate of 0.05 mm/s was applied to the femoral clamp in order to achieve joint stability, and the relative force was measured by the load cell: the lowest force guaranteeing joint stability was then determined to be the one corresponding to the change of slope in the force/displacement curve, representing the activation of the elastic region of both collateral ligaments. The force span between the slack region and the previously found point was considered to be equivalent to the tension required for the functional stability of the joint.

This methodology was applied on native intact knee, after ACL-resection and after further PCL-resection in order to simulate the knee behavior in case of Cruciate Retaining and Posterior Stabilized implants.

The test was performed at 0°, 30°, 60° and 90° of flexion using a specifically designed device. Each configuration was analyzed three times for the sake of repeatability.

Results

Results demonstrated that an average tension of 41.2N (range 30.0-48.0 N) is sufficient to reach stability in a native knee with intact cruciate ligaments. Similar values appear to be sufficient also in an ACL resected knee (average 45.6, range 41.2-50.0 N), while higher tension is required (average 58.6N, range 40.0-77.0 N) in the case of PCL retention. Moreover, in this configuration, the tension required for stabilization was slighter higher at 30° and 60° of flexion compared to the one required at 0° and 90° of flexion.

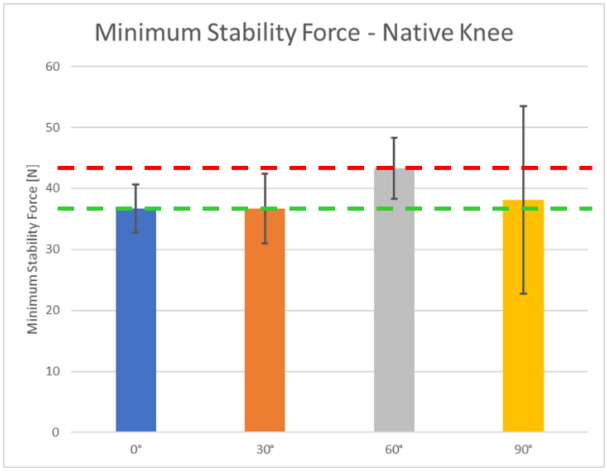

Figure 1: Minimum stability force found in native knee at different flexion angles

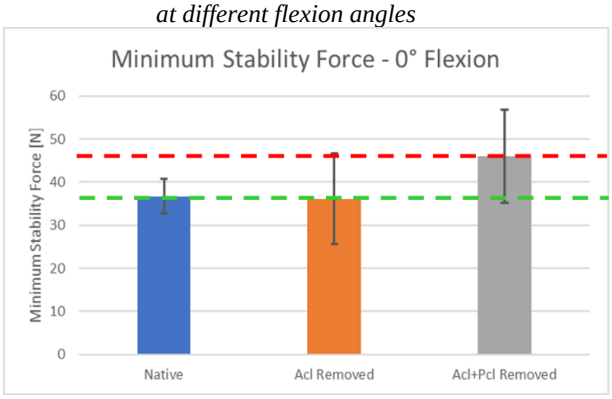

Figure 2: Minimum stability force found in full extended knee with different ligament configurations

Discussion

The current results are in agreement to other experimental studies [1,2] and show that the tensions necessary to stabilize a knee joint in different ligament conditions are way lower than the ones usually applied via tensioners nowadays (up to 200N).
To reach functional stability, surgeons should consider such results intraoperatively to avoid laxity, mid-flexion instability or ligament over-tension.

References

1. Manning WA et al. A load-measuring device can achieve fine-tuning of mediolateral load at knee arthroplasty but may lead to a more lax knee state, Knee Surgery, Sports Traumatology, Arthroscopy, 2019
2. Nowakowski AM et al., Measurement of knee joint gaps without bone resection: “physiologic” extension and flexion gaps in total knee arthroplasty are asymmetric and unequal and anterior and posterior cruciate ligament resections produce different gap changes, J. Orthop. Res., 2012

BIOMECHANICAL ANALYSIS OF CEPHALOMEDULLARY NAILS FOR TROCHANTERIC FEMORAL FRACTURE FIXATION

Torsten Pastor (1,2), Ivan Zderic (1),Dominic Gehweiler (1), Matthias Knobe (2), Boyko Gueorguiev (1)

1. AO Research Institute Davos, Switzerland; 2. Cantonal Hospital Lucerne, Switzerland

Introduction

Trochanteric femoral fractures are associated with increasing incidence due to the aging population and represent a serious adverse effect of osteoporosis. Their cephalomedullary nailing in poor bone stock can be a challenging endeavor associated with insufficient implant fixation in the femoral head. Despite the ongoing implant improvements, the rate of mechanical complications in the treatment of unstable trochanteric femoral fractures is still high. Recently, two novel concepts for nailing with the use of a helical blade – with or without bone cement augmentation – or an interlocking screw have demonstrated advantages as compared with single screw systems with regard to rotational stability and cut-out resistance. However, these two concepts have not been subjected to a direct biomechanical comparison so far.

The objectives of this study were to investigate in a human cadaveric model with low bone density (1) the biomechanical competence of cephalomedullary nailing with the use of a helical blade versus an interlocking screw, and (2) the effect of bone cement augmentation on the fixation strength of the helical blade.

Methods

Twelve osteoporotic and osteopenic human cadaveric femoral pairs were assigned for pairwise implantation using either a short TFN-ADVANCED Proximal Femoral Nailing System (TFNA) with a helical blade head element, offering the option for cement augmentation, or a short TRIGEN INTERTAN Intertrochanteric Antegrade Nail (InterTAN) with an interlocking screw. Following, six osteoporotic femora, classified within the lower DEXA T-score range among the pairs and implanted with TFNA, were augmented with 3 ml TRAUMACEM V+ bone cement. As a result, four study groups were created and combined in two clusters comprising specimens of the same donors each – group 1 (TFNA) paired with group 2 (InterTAN), and group 3 (TFNA augmented) paired with group 4 (InterTAN). An unstable pertrochanteric AO/OTA 31-A2.2 fracture was simulated by means of osteotomies. All specimens were biomechanically tested until failure under progressively increasing cyclic loading featuring a physiologic load trajectory (Fig. 1). Interfragmentary movements were monitored by means of optical motion tracking.

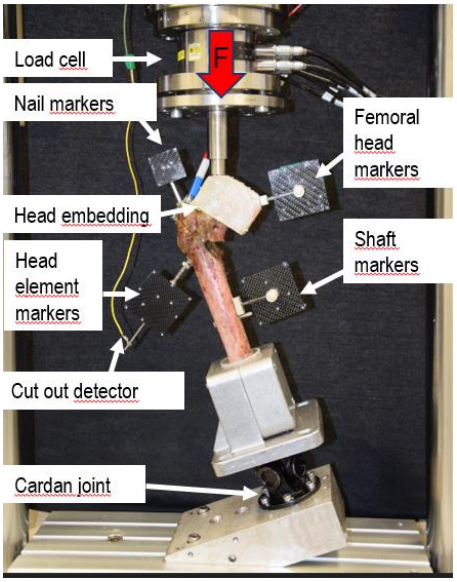

Figure 1: Setup with a specimen mounted for biomechanical testing.

Results

T-score of the osteoporotic femoral pairs in groups 3 and 4 (median -2.8, range -4.6 to -2.5) was significantly lower compared with the specimens in groups 1 and 2 (median -1.9, range -2.6 to -1.0), p=0.03. Initial stiffness (N/mm) in groups 1 to 4 was 335.7±65.3, 326.9±62.2, 371.5±63.8 and 301.6±85.9, respectively, being significantly different between groups 3 and 4, p=0.03. Varus deformation (°) and rotation of the femoral head fragment around the neck axis (°) after 10,000 test cycles were 1.9±0.9 and 0.3±0.2 in group 1, 2.2±0.7 and 0.7±0.4 in group 2, 1.5±1.3 and 0.3±0.2 in group 3, and 3.5±2.8 and 0.9±0.6 in group 4, respectively, both with significant difference between groups 3 and 4, p≤0.04. Cycles to failure and failure load (N) at 5° varus deformation were 21428±6020 and 1571.4±301.0 in group 1, 20611±7453 and 1530.6±372.7 in group 2, 21739±4248 and 1587.0±212.4 in group 3, and 18622±6733 and 1431.1±336.7 in group 4, respectively, being significantly different between groups 3 and 4, p=0.04.

Discussion

From a biomechanical perspective, cephalomedullary nailing of trochanteric femoral fractures with the use of helical blades is comparable to interlocking screw fixation in femoral head fragments with low bone density. Moreover, bone cement augmentation of helical blades considerably improves their fixation strength in poor bone quality.

COMPUTATIONALLY OPTIMIZED IMPLANTS IMPROVE BIOMECHANICAL FIXATION STABILITIY OF COMPLEX PROXIMAL HUMERUS FRACTURES

Dominic Mischler (1), Jana Schader (1, 2), Jan Dauwe (1, 3), Boyko Gueorguiev (1), Peter Varga (1)

1. AO Research Institute Davos, Switzerland; 2. Cantonal Hospital Graubuenden, Switzerland; 3. University Hospital Leuven, Belgium

Introduction

Despite previous advances in the development of treatment strategies, proximal humerus fracture fixations still have a high failure rate, especially in unstable fractures of osteoporotic patients [1,2]. Locked plating is a frequently used joint-preserving treatment with numerous implants available on the market, e.g. the PHILOS plate (DePuy Synthes, Switzerland). However, the standard designs may not always achieve optimal stability. We have previously developed and validated a finite element (FE) simulation tool kit for investigation of proximal humerus fracture fixations [3]. Utilizing this tool kit, it was demonstrated that the screw trajectories of the PHILOS plate can be optimized to achieve significant reduction in the predicted cut-out failure risk compared with the existing design [4]. However, the findings of the computer models have not been corroborated yet with experimental testing. Therefore, the aim of this study was to evaluate the biomechanical benefit of a locking plate featuring optimized screw trajectories versus the PHILOS design in a paired human cadaveric study.

Methods

Eight humerus pairs of elderly female donors (85.3 ± 5.5 years) were selected from a larger sample pool to ensure high pair symmetry of humeral head size and bone mineral density (BMD). The specimens were pairwise randomized into two treatment groups, instrumented with 3D printed metal locking plates featuring either the PHILOS design (PD), or an adjusted optimized design (OD) with screw orientations optimized via a previously established FE analysis approach to minimize predicted failure risk [4]. All humeri were osteotomized to mimic an unstable three-part fracture with no calcar support and the proximal fragments were instrumented with the plates using six proximal locking screws. Specimen-specific 3D printed plastic guides were used throughout the specimen preparation process to ensure inter-pair symmetry and intra-pair consistency in terms of osteotomy setting, implantation, and alignment for biomechanical testing. The constructs were tested to cut-out failure under cyclic loading with the peak force gradually increasing from 50 N by 0.025 N/cycle (Acumen, MTS, USA) (Figure 1). Displacement of the head fragment relative to the plate was monitored using a contactless motion tracking system (Aramis SRX, GOM GmbH, Germany). The numbers of cycles until 1 mm residual head displacement at valley load was defined as cycles to cut-out failure.

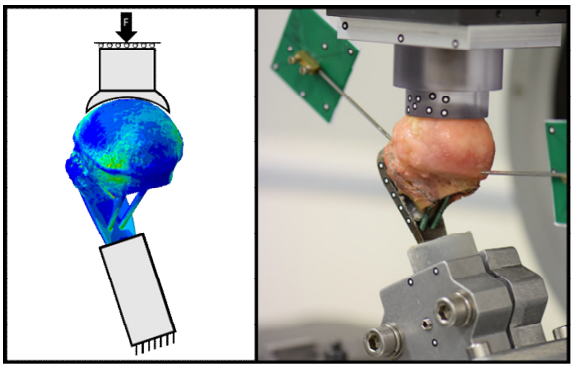

Figure 1: FE model (left) used to optimize screw orientation by minimizing the predicted cut-out risk, which was validated experimentally (right).

Results

BMD (112.0 ± 15.5 HAmg/cm^3, range: 87.5 – 130.0 HAmg/cm^3) was not significantly different between the two groups, p=0.94. Number of cycles to failure in the OD group (18857.8 ± 1970.1, range: 16386 - 21876) was significantly higher compared with the PD group (16252.1 ± 1895.8, range: 13385 - 18511), p = 0.015, leading to a relative benefit of 18% (17.5% ± 19.3%, range: -3.6% - 51.3%).

Discussion

In-silico optimization of implants is a promising approach to tackle the challenging problem of fracture fixation failures. The present biomechanical study demonstrated that implants with FE-optimized screw orientations significantly increase primary stability of a locking plate in complex proximal humerus fractures. Although reaching significance, the relative gain of the adjusted implant design remained moderate. Further research could utilize the validated FE workflow for more generic optimization broadened to other features of the implant design.

References

1. Kralinger et al., J Bone Joint Surg Am, 96; 1026-32, 2014.
2. Krappinger et al., Injury, 50:2176-96, 2019.
3. Varga et al., Med Eng Phys, 57:29-39. 2018.
4. Mischler et al., J Orthop Transl, 25:96-104, 2020.

Acknowledgements

This study was supported by the AO Foundation via the AOTRAUMA Network (Grant No.: AR2019/07).

TARGETING END-OF-STEM PAIN: A BIOMECHANICAL ANALYSIS BASED ON 3-DIMENSIONAL MODELS OF HUMAN FEMORA.

Elisabeth M. Sporer[1,2], Christoph Schilling[1], Adrian Sauer[1,3], Robert J. Tait[4], Alexander Giurea[5], Thomas M. Grupp[1,3]

[1]Aesculap AG Research & Development, Tuttlingen, Germany; [2]Ludwig Maximilians University Munich, Medical Department, Munich, Germany; [3]Ludwig Maximilians University Munich, Dept. of Orthopaedic Surgery, Physical Medicine & Rehabilitation, Munich, Germany; [4] Orthopaedic Institute of Henderson, Henderson, Nevada, USA; [5]Medical University of Vienna, Dept. of Orthopaedic Surgery, Vienna, Austria

Introduction

End-of-Stem Pain is localized pain at the tip of the stem of a prosthesis and a common problem in revision total knee arthroplasty (rTKA) [1, 2].
The elastic modulus mismatch between stem and bone is seen as the main cause for End-of-Stem Pain. However, there is no experimental study analyzing End-of-Stem Pain in rTKA using human specimens. Our goal was to describe the morphological changes of human femora due to the implantation of a long diaphyseal stem.

Methods

We implanted 16 rotating hinge knee implants with cobalt-chrome stems of 177 mm length into 16 fresh-frozen human femora using the hybrid fixation technique.
CT scans before and after implantation were performed and 3-dimensional models of the bones were created using Mimics Medical 21.0 (Materialise NV, Leuven, Belgium). The pre- and postoperative models were brought to spatial overlap (3-matic 13.0, Materialise NV, Leuven, Belgium). An algorithm was developed in Matlab 2020a (MathWorks, Natick, USA), which allowed us to analyze the position of the stem in the medullary cavity as well as to calculate the following changes due to implantation: Reduction in cortical thickness, change in diameter of the medullary cavity and displacement of the femoral axis.

Results

The main contact between stem and bone was located at the tip of the stem, especially anteriorly.
We discovered two different patterns of how the straight stem was positioned in the bended femur (Figure 1). In some bones, the stem lay straight in the medullary canal and the tip of the stem was circumferentially enclosed by the cortex. In other specimens, the stem had a tilted position, so that the tip of the stem only had contact with the anterior cortex but had no contact posteriorly.
The maximum reduction of cortical thickness was found at the tip of the stem with an average reduction in cortical thickness of 933 ± 482 µm anteriorly over the last 15 mm of the stem. This is a relative reduction in cortical thickness of 30%.

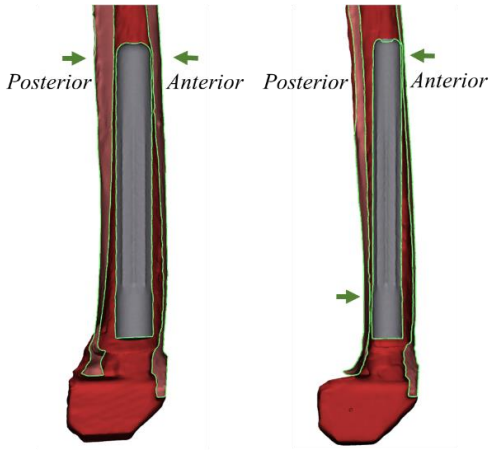

Figure 1: Sagittal sections of two different femoral specimens. Left: Circumferential contact between the tip of the stem (grey) and the cortex (light red). Right: Anterior contact between the tip of the stem and the cortex.

Discussion

We were able to show that the tip of the stem is an important biomechanical region, which has to be payed special attention in the development of revision stems.
Not only was the maximum contact between stem and cortex located in this region, but the maximum reduction in cortical thickness due to the reaming process also lay at the tip of the stem. This may further increase the biomechanical stress at the tip of the stem.
The role of the position of the stem in the medullary cavity has yet to be evaluated for its relevance for the development of End-of-Stem Pain.
Furthermore, the bone models that were created in this study will serve for a FEM-study, which can be used for the development of new stems with a better biomechanical and clinical performance.

References

1. Barrack RL, Stanley T, Burt M, Hopkins S. The Effect of Stem Design on End-of-Stem Pain in Revision Total Knee Arthroplasty. J Arthroplasty 2004; 19(7 Suppl 2):119–24.
2. Albino RB, Santos LS, Gobbi RG, Lamaguchi M, Demange MK, Tirico LE et al. Pain at the Tip of the Stem after Revision Total Knee Arthroplasty. Rev Bras Ortop 2012; 47(1):73–6.

TARGETING END-OF-STEM PAIN: SURFACE STRAINS ON HUMAN FEMORA UNDER DYNAMIC LOAD.

Christoph Schilling[1], Elisabeth M. Sporer[1,2], Robert J. Tait[3], Alexander Giurea[4], Thomas M. Grupp[1,5]

[1]Aesculap AG Research & Development, Tuttlingen, Germany; [2]Ludwig Maximilians University Munich, Medical Department, Munich, Germany; [3] Orthopaedic Institute of Henderson, Henderson, Nevada, USA [4]Medical University of Vienna, Dept. of Orthopaedic Surgery, Vienna, Austria [5]Ludwig Maximilians University Munich, Dept. of Orthopaedic Surgery, Physical Medicine & Rehabilitation, Munich, Germany

Introduction

End-of-Stem Pain is localized pain at the tip of the stem of a prosthesis and a common problem in revision total knee arthroplasty (rTKA) [1, 2]

The elastic modulus mismatch between stem and bone is seen as the main cause for End-of-Stem Pain. Supporting this idea, there is a study which showed increased surface strains at the tip of the stem in synthetic tibiae. However, this could only be shown under an extreme varus load [3].

The goal of our study was to analyze the surface strains on human femora in a realistic scenario applying dynamic load.

Methods

We implanted 16 rotating hinge knee implants with cobalt-chrome stems of 177 mm length into 16 fresh-frozen human femora using the hybrid fixation technique. After implantation, the bones were embedded in a pot and placed in a testing machine (DYNA-MESS, Stolberg, Germany) (Figure 1).

We simulated the maximum force in the knee joint when rising from a chair (**ChairRise90°**) and when climbing stairs (**Stairs20°**). Therefore, a sinusoidal force was applied via the tibial component using a 90° and a 20° flexion angle, respectively. The force was applied with a ratio of 50% medial, 50% lateral. Surface strains were measured using an optical measurement system (PONTOS 5M, GOM, Braunschweig, Germany) and digital image correlation (DIC). In **Stairs20°**, the force was increased until fracture of the bone.

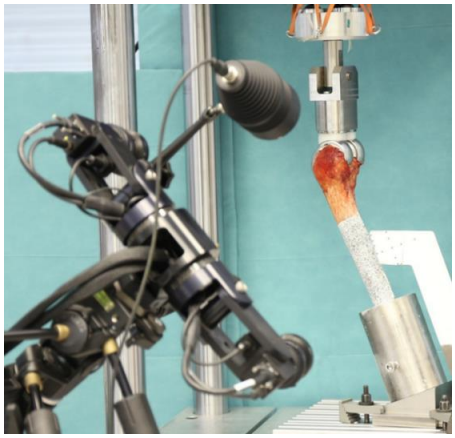

*Figure 1: **Stairs20°**-test. Left: Optical measurement system to measure surface deformations, Right: Femur embedded in a pot, the force is applied from above.*

Results

In both test scenarios, high deformations were measured at the tip of the stem. In Figure 2 for example, the peak strains along a lateral section of the bone were at the tip of the stem. The femora fractured within a range of 1800 N to 4800 N. The analysis of the fractures revealed several fracturing patterns. Some specimen fractured directly where they were embedded in the pot, but most of the fracturing patterns had signs of influence by the tip of the stem. An example for this is a horizontal fracturing line at the anterior tip of the stem.

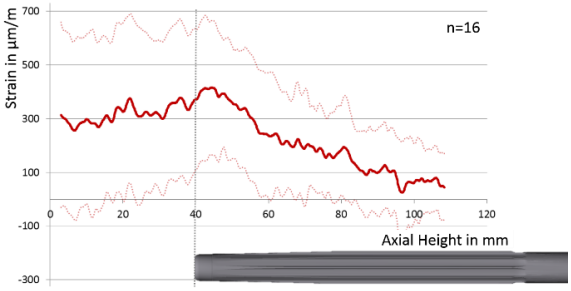

*Figure 2: **ChairRise90°**: Strains in longitudinal direction (direction of the length axis of the femur) along a lateral section of the bone. Axial height 0 mm: Bone embedded in pot, 40 mm: Tip of the stem.*

Discussion

In our study, we were able to measure surface deformations on human femora under dynamic load using digital image correlation (DIC). We detected high deformations at the tip of the stem, which may be relevant for End-of-Stem Pain. The fracturing patterns of the bones also suggested high biomechanical stresses at the tip of the stem. In a subsequent study, we will create a finite element model which will be verified using the data of the deformation testing.

References

1. Barrack RL, Stanley T, Burt M, Hopkins S. The Effect of Stem Design on End-of-Stem Pain in Revision Total Knee Arthroplasty. J Arthroplasty 2004; 19(7 Suppl 2):119–24.
2. Albino RB, Santos LS, Gobbi RG, Lamaguchi M, Demange MK, Tirico LE et al. Pain at the Tip of the Stem after Revision Total Knee Arthroplasty. Rev Bras Ortop 2012; 47(1):73–6.
3. Completo A, Fonseca F, Simões JA, Ramos A, Relvas C. A new press-fit stem concept to reduce the risk of end-of-stem pain at revision TKA: A pre-clinical study. Knee 2012; 19(5):537–42.

IN SILICO DETAILED ASSESSMENT OF THE INTERCONNECTION MECHANISM IN A COMMERCIAL SPINAL FIXATION SYSTEM

Luca Ciriello (1), Francesca Berti (1), Erika Galbusera (1), Giancarlo Pennati (1), Tomaso Villa (1), Luigi La Barbera (1)

1. Department of Chemistry, Materials and Chemical Engineering, Politecnico of Milano, Italy

Introduction

Posterior spinal fixation is a common surgery for the stabilization of spinal segments. Typical assemblies are based on pedicle screws and spinal rods connected through an interconnection mechanism based on various components. *In vitro* pre-market assessment of any new spinal fixator is based on experiments to characterize its static/fatigue behavior according to ASTM F1717 [1] standard (Fig. 1a): the simplified set-up, representative of an average instrumented lumbar spine segment undergoing vertebrectomy (worst-case) [2], allows reproducible loading conditions, improving comparability. Validated *in silico* models have been recently introduced to limit long and expensive in vitro tests [2-4], however, they are over-simplified, especially for what concerns the interconnection mechanism.
The study aims to develop a validated *in silico* model of F1717 standard set-up capable of describing: i) the interactions among components and ii) the residual stresses arising due to the assembly of the interconnection mechanism.

Methods

The finite element model of a commercial device (2B1, Milan, Italy) was built using Abaqus 2018 (Dassault Systèmes, SIMULIA Corp., RI).
A realistic "detailed" model (A), accounting for contacts among components and the initial preload due to nut tightening inside the interconnection mechanism, was developed (Fig. 1b). Preliminary static tests according to ASTM F1798 [5] standard, served to assess the friction coefficient (0.3) and the axial displacement (1.1 mm. Elasto-plastic material properties were assumed for all components.
A simplified model (B), neglecting the assembly step and assuming a tie-constraint among components and elastic material properties were assigned to all components according to the literature [2-4], served as a reference.
In silico fatigue analyses were performed according to ASTM F1717 models applying loading/unloading cycles between 137 and 13.7 N. The life-constant diagram (10^6 cycles) was built for each model components according to Sines criterion:

$$\sigma_{SINES} = \sigma_{VM,a} + K * I_m \qquad (1)$$

where $\sigma_{VM,a}$ is the alternate von Mises stress, I_m is the average first invariant and K (0.6) a material parameter.

Results

The detailed model of nut tightening demonstrated good agreement with preliminary static tests: the overall stiffness and maximum force were predicted within 4%. Following fatigue analyses, the most critical component was detected as the screw neck in both models (Table 1), but the simplified model (B) overestimated the stress components compared to the detailed (A). The nut tightening introduced many elements experiencing negative $I_{1,m}$ in the model (A) compared to model (B) (Fig. 1c).

		Model A	Model B	A vs. B
screw neck	σ_{SINES} (MPa)	616	812	-24%
	$I_{1,m}$ (MPa)	414	694	-40%
	$\sigma_{VM,a}$ (MPa)	368	395	-7%
spinal rod	σ_{SINES} (MPa)	277	597	-54%
	$I_{1,m}$ (MPa)	213	526	-60%
	$\sigma_{VM,a}$ (MPa)	149	282	-47%

Table 1: Maximum Sines stress calculated with Eq (1).

Discussion

The proposed detailed *in silico* model introduced nut tightening, allowing a more realistic description of the components' interactions and the reduction of the overall predicted stresses. Moreover, neglecting the pre-load due to nut tightening and the ideal tie constraint, as assumed in the literature [2-4], represents an over-conservative assumption (Table 1). The higher rates of screw neck failure reported by previous experimental fatigue tests are consistent with our predictions [3], making the presented approach suitable to describe other commercial interconnection mechanisms with similar features [3,4].

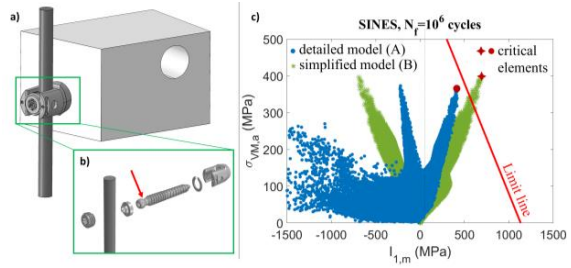

Figure 1: a) one-quarter of the FE set-up; b) interconnection mechanism details; c) life constant diagram of screw elements in model (A) and (B) with highlighted the most critical elements.

References

1. ASTM, F1717, 2019.
2. La Barbera et al, Proc Inst M E H, 228(10):1014-26, 2014.
3. La Barbera et al, Proc Inst M E H, 231(2):176-185, 2017.
4. Chu et al, PLoS One, 14(11): e0224699, 2019.
5. ASTM, F1798, 2019.

COMPARISON OF CEMENTED VS UNCEMENTED TOTAL HIP ARTHROPLASTY AND PERIPROSTHETIC FRACTURE FIXATION

Katherine Wang[1], Eustathios Kenanidis[1,2], Zakareya Gamie[3], Khurram Suleman[1], Mark Miodownik[1], Mahsa Avadi[4], David Horne[4], Jonathan Thompson[4], Eleftherios Tsiridis[1,2], Mehran Moazen[1]

1. University College London, UK; 2. Aristotle University Medical School, Greece; 3. Newcastle University, UK; 4. DePuy Synthes, UK

Introduction

Total hip arthroplasty (THA) is a clinically successful procedure that can be broadly divided into two main categories: cemented and uncemented. Both show good long-term survival [1]. There is debate on the use of cemented vs uncemented stems as the optimal management of THA with no clear evidence demonstrating the increased risk of fracture in one stem type over the other [2]. Periprosthetic femoral fractures (PFF) is a severe complication following THA that is highly studied and can be seen in both patient populations. Our understanding of the impact of stem fixation method in THA on the subsequent management of PFF is still limited. This study aims to investigate and quantify the effect of stem fixation method on the management of Vancouver Type B1 PFF.

Methods

Eight laboratory models of synthetic femora were divided into two groups and implanted with either a: cemented DePuy C-Stem or uncemented DePuy Corail stem to simulate THAs. Constructs were loaded under partial weight bearing anatomical conditions [3]. Stiffness, uniaxial strain, and pattern of strain distribution were measured.

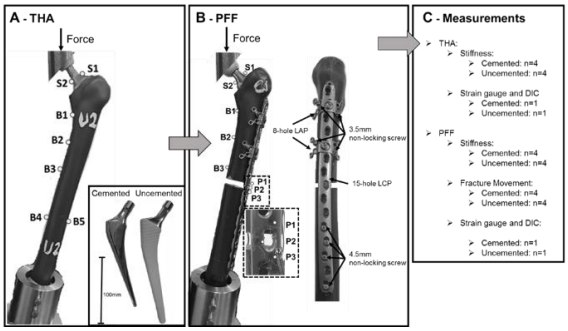

Figure 1: Study overview. Experimental setup of THA, and two different stems used (A), PFF (B), and measurements taken (C). S1-S2 highlight the strain gauge attachment site (SG) on the stem, B1-B5-SG on the bone, and P1-P3- SG on fracture plate.

All specimens then underwent a 10mm osteotomy to simulate B1 PFF's and fracture fixation was achieved using a Ti-64 locking compression plate (LCP, DePuy Synthes, Switzerland). Proximal fixation was achieved using two Ti-64 locking attachment plates with two bicortical screws each (LAP, DePuy Synthes, Switzerland). Distal fixation was achieved using four bicortical screws. Overall stiffness, strain, and fracture movement were taken under the same loading conditions as the THA group (Fig.1).

Results

Stiffness: In the THA models, cemented constructs had higher overall stiffness compared to the uncemented group. In the PFF group, the cemented constructs had a higher overall stiffness. *Strain*: In the THA models strain gauge results showed that the cemented construct had higher strain at B2- B4. In PFF models the mechanical strain on the fracture plate and fracture movement was overall higher for the uncemented constructs compared to the cemented constructs (Fig.2).

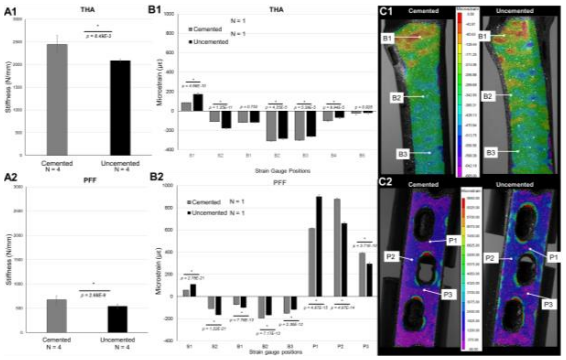

Figure 2: **(A) Stiffness** between cemented and uncemented specimens in (1) THA (2) PFF. **(B) Strain measurement** comparing cemented vs uncemented specimens in (1) THA and (2) PFF. **(C) DIC measurement between the uncemented and cemented** (1) THA-min principal strain across the medial side of the bone (2) PFF-max principal strain across the fracture plate at site of fracture. *: $P < 0.05$

Discussion

The present study raises the question that perhaps the existing treatment algorithms for B1 PFF management need to consider cemented vs. uncemented stem implantation method.

References

1. NJR; 1821:1-202. 2017
2. Karam et al; J Orthop Surg Res, 15:100. 2020.
3. Bergmann et al, J Biomech, 34:859-71, 2001

Acknowledgements

This work was supported by DePuy Synthes (Leeds, UK) and EPSRC Doctoral Training Partnership (DTP) Case Studentship (539270/173067). The authors declare that no competing interests exist.

IN-SILICO AND EXPERIMENTAL DEFORMATION ANALYSIS OF TWO HYBRID PLATE DESIGNS FOR CANINE PANCARPAL ARTHRODESIS

Ivan Zderic (1), Peter Varga (1), Ursula Styger (1), Boyko Gueorguiev (1), Ludmil Drenchev (2), Erik Asimus (3), Brian Saunders (4), Michael Kowaleski (5), Randy J. Boudrieau (5), Loic Déjardin (6)

1. *AO Research Institute Davos, Switzerland; 2. Bulgarian Academy of Sciences, Institute of Metal Science 'Acad. A. Balevski', Bulgaria; 3. École Nationale Vétérinaire de Toulouse, France; 4. Texas A&M University, USA; 5. Tufts University, USA; 6. Michigan State University, USA*

Introduction

Hybrid locking canine pancarpal arthrodesis (PCA) plates are designed with either a round (RH) or an oval (OH) screw hole at the radiocarpal (RC) level. The former is expected to be stronger, whereas the latter enhances varied screw positioning. However, they are have not been subjected to a direct mechanical comparison so far. Therefore, the aim of this study was to compare mechanically the structural properties of these two PCA plates.

Methods

PCA plates with either RH or OH design were assigned to three groups (n=6), pre-bent at 20° and fixed to a canine forelimb model with simulated radius, RC bone, and 3rd metacarpal bone. The OH-plates were instrumented with an RC screw inserted either most proximal (OH-P) or most distal (OH-D). All specimens were loaded axially up to 300 N over 10 ramped cycles at 0.5 Hz (Fig. 1). The test setup was replicated in finite element analyses (FEA) to predict the areas of highest deformations. Plate strains were measured by means of strain gauges at these locations.

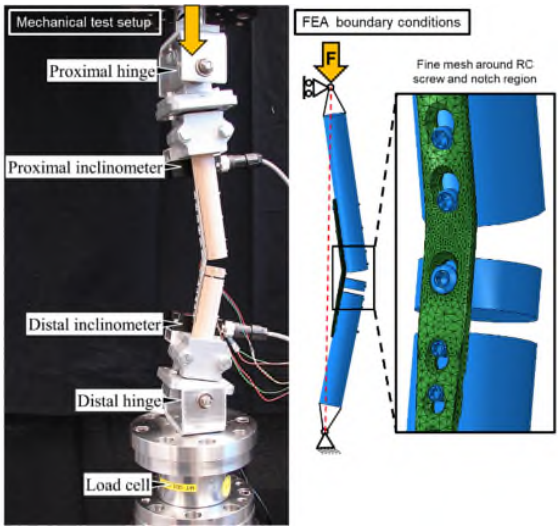

Figure 1: Experimental setup (left) and FEA model with boundary conditions (right).

Results

FEA predicted highest strains located adjacent to the RC screw and plate bending point for all three groups (Fig. 2).

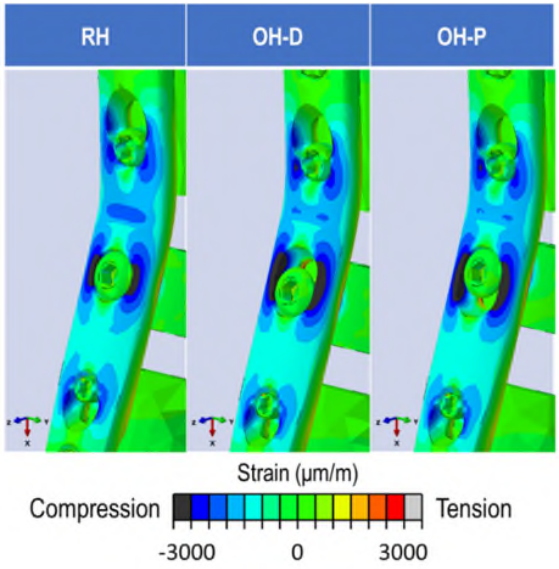

Figure 2: FEA-based plate strain distribution under 300 N axial load visualized for each separate construct.

Experimentally measured peak strains (µm/m) at oval RC screw hole were not significantly influenced by the screw position in this hole (3329±443 [OH-P], 3222±467 [OH-D]; p=0.55). In addition, these strains were significantly higher compared to the group with a round RC screw hole (2123±154; p<0.01). Moreover, peak strains at the bending point of the plates were significantly lower for OH-P (1792±174) and OH-D (1806±194) plates versus RH plates (2158±114, p<0.01). Construct compliance and maximum angular bending plate deformation were not different between three groups (p≥0.12). All FEA findings were in a good agreement with the experimental results.

Discussion

The higher peak strains at the oval RC screw hole in the PCA plates compared to the plates with a round RC screw hole indicate a potential towards a higher mechanical failure risk in the former.

FATIGUE LIFE ASSESSMENT OF TWO HYBRID PLATE DESIGNS FOR CANINE PANCARPAL ARTHRODESIS

Ivan Zderic (1), Peter Varga (1), Ursula Styger (1), Boyko Gueorguiev (1), Ludmil Drenchev (2), Erik Asimus (3), Brian Saunders (4), Michael Kowaleski (5), Randy J. Boudrieau (5), Loic Déjardin (6)

1. AO Research Institute Davos, Switzerland; 2. Bulgarian Academy of Sciences, Institute of Metal Science 'Acad. A. Balevski', Bulgaria; 3. École Nationale Vétérinaire de Toulouse, France; 4. Texas A&M University, USA; 5. Tufts University, USA; 6. Michigan State University, USA

Introduction

Hybrid locking canine pancarpal arthrodesis (PCA) plates with an oval (OH) instead of a round (RH) hole for the radiocarpal (RC) screw (Fig. 1) would improve versatility in surgical application, however, may be more prone to failure due to the enlarged hole dimension. The aim of this study was to mechanically compare the fatigue life of these two PCA plates.



Figure 1: 12-hole hybrid pancarpal arthrodesis plate with a round (top) or an oval (bottom) radiocarpal hole, length 151 mm.

Methods

Ten PCA plates with RH design and twenty PCA plates with OH design were assigned to 3 groups (n=10), pre-bent at 20° and fixed to a canine forelimb model with simulated radius, RC bone and 3rd metacarpal bone. The OH-plates were instrumented with an RC screw inserted either most proximal (OH-P) or most distal (OH-D). All specimens were cyclically tested at 8 Hz under 320 N until failure (Fig. 2). Fatigue life outcome measures were cycles to failure and failure mode.

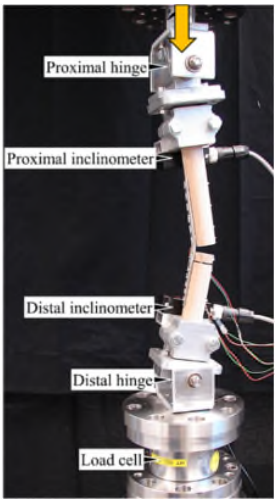

Figure 2: Setup with a specimen mounted for mechanical testing.

Results

Cycles to failure were higher in the group with RH plate fixation (695,264±344,023) versus both OH-P (447,900±176,208) and OH-D plate configurations (391,822±165,116), reaching significance versus OH-D, p=0.03. No significant difference was detected between the OH-P and OH-D groups, p=0.09 (Fig. 2).

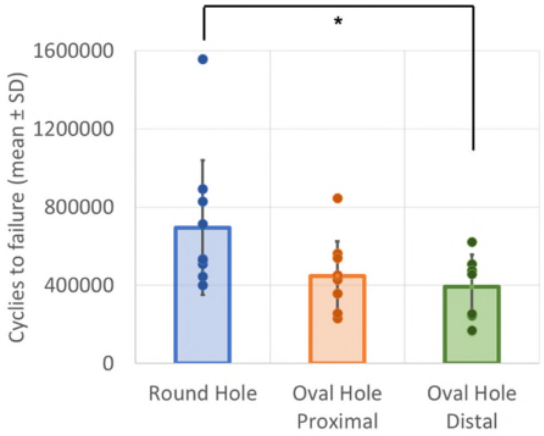

Figure 2: Cycles to failure in the three study groups with a star indicating significant difference.

The constructs failed predominantly by plate fracturing at the most distal radial screw hole with concomitant screw breakage at the shaft-head interface.

Discussion

Despite the surgical advantages of the PCA plate with an oval radiocarpal screw hole, its fatigue life is significantly shorter versus the plate design with a round radiocarpal screw hole and therefore mitigates the potential benefits. Moreover, the failure probability of the plate with an oval hole is increased regardless from the screw position in this hole. Based on these findings, the PCA plate with an oval radiocarpal screw hole cannot be recommended for clinical use.

Acknowledgements

This investigation was performed with the assistance of AO Foundation via AO Technical Commission.

BONE-IMPLANT FIXATION QUALITY MEASUREMENTS IMPROVED BY ATTACHABLE FEMORAL IMPLANT EXTENSIONS

George Athanassoulis Makris (1), Leonard Pastrav (1), Quentin Goossens (1), Michiel Mulier (2), Wim Desmet (3), Kathleen Denis (1)

1. KU Leuven, Department of Mechanical Engineering, Smart Instrumentation, Belgium; 2. UZ Leuven, Orthopaedic Surgery Department, Belgium; 3. KU Leuven, Department of Mechanical Engineering, MSD Section, Belgium

Introduction

Traditionally, when performing a cementless total hip arthroplasty, surgeons sequentially hammer the femoral implant into the femur until they "feel" that adequate fixation is achieved. Since this manner of judging implant fixation is highly subjective, there is a significant risk of fracturing the femur or of leaving the implant sub-optimally fixed [1]. Consequently, a system that objectively assesses the bone-implant fixation has been proposed. The system records and compares the vibrational characteristics of the bone-implant structure after each insertion hit. When the vibrational characteristics have converged, the condition for ideal fixation has been met [2]. Most of the fixation-sensitive modes reside above 2 kHz but are highly damped by the surrounding soft tissue. To deal with this problem, attachable extensions have been designed to shift the sensitive modes within the observable frequency range below 2 kHz. This work investigates experimentally the benefits produced by the extensions and predicted by previous in silico studies [3].

Methods

An artificial femur (Sawbones 3403, Sawbones) and implant (Profemur Gladiator, Microport Orthopaedics) were used together with two attached extensions that are called "Delta" and "Cylindrical" due to their shape. After each insertion hit the structure was excited with an instrumented hammer (PCB 086C03, PCB Piezotronics) and the response was measured in two perpendicular directions using two accelerometers (PCB 352A24, PCB Piezotronics). The signals were processed by a data acquisition device (Simcenter SCADAS, Siemens PLM) and the frequency response functions (FRF) were plotted. The following three configurations were considered: bone-implant (BI), bone-implant-"Delta" (BID) and bone-implant-"Cylindrical" (BIC) (Figure 1).

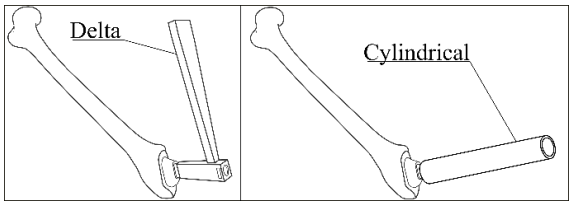

Figure 1 "Delta" extension (left) and "Cylindrical" extension (right) connected to the bone-implant structure .

For each configuration every two subsequent FRFs were compared and the Pearson's correlation coefficients (PCC) were calculated. The insertion was stopped when the implant subsidence was less than 0.1 mm for two subsequent hits.

Results

Figure 2 shows the PCC convergence during the insertion process, while Figure 3 shows the FRFs obtained for the three configurations at the same two subsequent insertion hits, illustrating the modal density difference and the frequency shift.

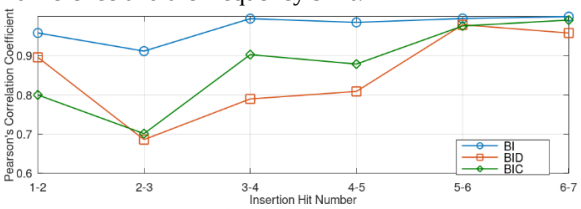

Figure 2 PCC change for three configurations (BI, BID, BIC).

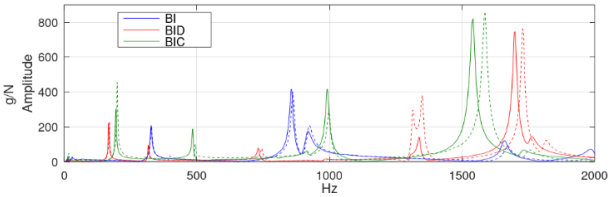

Figure 3 FRFs before (solid line) and after an intermediary insertion hit (dashed line) for the three configurations.

Discussion

The modal density increased below 2 kHz when the designed extensions were added to the BI structure. Additionally, the modes introduced by the extensions are overall more sensitive to fixation changes and some have peaks with significantly higher amplitudes in the range of 1.5-2 kHz. The PCC corresponding to the BI structure shows an early convergence at insertion hit #3, which suggests an optimal fixation, but when an extension was used the PCC converged later, indicating that the implant had a better fixation at insertion hit #5. This observation is explained by the extra sensitive modes introduced by these extensions that make subsequent FRFs more dissimilar.

References

[1] H. Lindahl, Injury, 38(6): 651–654, 2007.
[2] L. C. Pastrav et al, J Orthop Surg, 4: 10, 2009.
[3] Q. Goossens et al, Proc. 25th Congress of the ESBiomech, 2019

Acknowledgements

This work was supported by Internal Funds KU Leuven.

LATTICE STRUCTURES UNDER COMBINED STRESS STATES FOR SCAFFOLDS IN ORTHOPAEDIC IMPLANT APPLICATIONS

Markel Alaña (1), Iñigo Puerta (1), Naiara Rodriguez-Florez (1,2), Aitziber López de Arancibia (1), Asier López (1), Sergio Ruiz de Galarreta (1)

1. Universidad de Navarra, Spain, 2. IKERBASQUE, Spain

Introduction

Additive manufacturing enables the design and production of patient specific porous scaffolds based on lattice structures, which offer mechanical properties comparable to those of bones, while allowing mass transportation and bone ingrowth within the implant [1]. Highly complex stress states arise in the implant as well as in the Bone-Implant Interface (BII), and shear stresses caused by friction phenomena are important to provide primary stability to the implant [2]. Thus, the study of lattice structures under such conditions is crucial for their implementation in orthopaedic implants. Nonetheless, mechanical properties of lattice structures under shear conditions are rarely studied. The present work analyzes a set of lattice structures under different combinations of compression and shear stresses, including pure shear stress.

Methods

Three different types of lattice structures were designed, namely Diamond, FCCm and Gyroid (Figure 1), with porosities of 90%, 80%, 70% and 60%. Finite element models were used to test the mechanical response of the structures for different relative densities. Pure compression and shear loads were studied to obtain the apparent Young's and shear modulus of the lattice structures, as well as the normal and shear yield strength. The interaction between compression and shear loads was studied by applying combined loads to each model. Structures with porosities of 70% were manufactured by stereolitography (SLA) for experimental validation of the numerical models. A modified Arcan shear test was performed to apply combined shear and compression loads, and results were compared to numerical models.

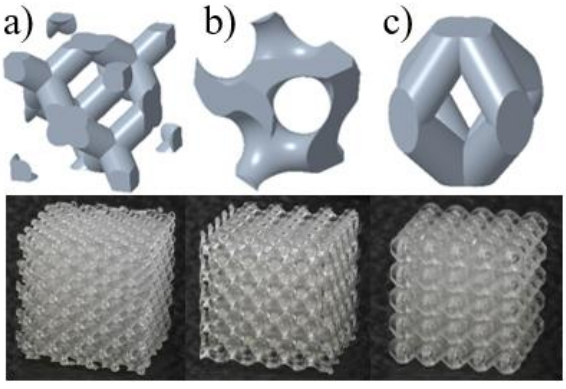

Figure 1: Specimens of a) diamond, b) gyroid and c) FCCm lattice structures with a porosity of 70%.

Results

The elastic and shear moduli and strength of the lattice structures increased exponentially with relative density. Finite element simulations indicated that the interaction of loads has important implications, considerably changing the load carrying capacity of the structures (Figure 2). FCCm lattice had the highest strength in all cases due to the favorable orientation of its struts. A failure criterion was developed for different combinations of normal and shear stresses by fitting a curve to the obtained points. These results were in good agreement with experimental tests.

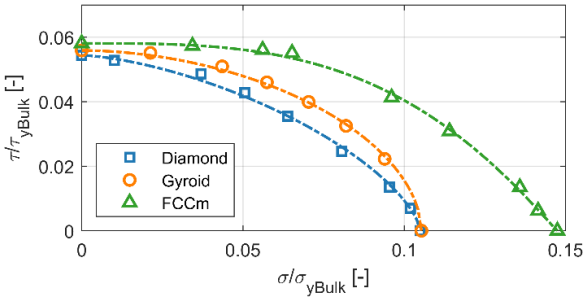

Figure 2: Finite element results of normalized strength of the studied lattice structures with a porosity of 70% under different normal and shear load combinations.

Discussion

The shear, compression, and compression-shear combination behavior of three different lattice structures was studied, being the pure shear strength especially relevant in the BII. Even if the FCCm lattice has the highest strength, the difference diminishes as the proportion of shear stress increases. These results are highly sensitive to the number of unit cells in each direction. The relative density affects not only the normal and shear strength, but also the shape of the failure criterion for combined load cases. These might occur because of larger regions under triaxial stress states for higher relative densities. Thus, the derived failure criterion offers a method to safely implement lattice structures as biomaterials in orthopaedic implants.

References

1. A. Zadpoor, J. Mater. Chem. B, 7:4088-4117, 2019.
2. Gao, X., J. R. Soc. Interface, 16(156):20190259, 2019.

3D STRAIN DISTRIBUTION IN BONE DURING TIGHTENING AND FRACTURE FIXATION WITH NOVEL MG-BASED SCREWS

Marta Peña Fernández (1,2), Alexander P. Kao (2), Frank Witte (3) Gianluca Tozzi (2)

1. Heriot-Watt University, UK; 2. University of Portsmouth, UK; 3. Biotrics Bioimplants GmbH, Germany

Introduction

Bone screws are routinely used for internal fracture fixation to stabilize the fractured bone enabling fast healing, early mobility and full function. Common implant materials (i.e. titanium, Ti) offer high stability but are associated to stress shielding and may require a second intervention for removal [1]. Biodegradable magnesium (Mg)-based screws are increasingly gaining interest as they show good biocompatibility, gradual degradation and similar mechanical properties to those of natural bone [2]. Novel Mg-based screw design aims at providing safe anchorage, while mitigating stress shielding effects to facilitate new bone formation during healing [2]. This study compares the bone deformation induced by Mg-based screws and Ti controls during *in vitro* tightening and fracture fixation combining X-ray computed tomography (XCT), *in situ* biomechanical testing and digital volume correlation (DVC).

Materials and methods

Cylindrical bone cores including both cortical and trabecular bone were extracted from bovine femoral condyles. Self-tapping Mg-based (2.9 mm) and Ti (2.7 mm) cortical screws were used. Time-lapsed tightening (n=3 per screw type) was performed with XCT (Versa 520, Zeiss) and datasets (17µm voxel size) acquired prior to insertion (pre-drilled) and at increased levels of tightening (50, 100, 200 and 300 Nmm). The stability of screws was evaluated in a bone fracture model. Fracture was induced in bone cores at ~30° with respect to the cylindrical axis where Mg-based and Ti screws (n=3 per screw type) were inserted perpendicularly to the cut. A cyclic loading scheme with increasing displacement amplitudes [3] was performed *in situ* (Deben CT5kN) and XCT datasets (Versa 510, Zeiss; 20µm voxel size) acquired under load at each amplitude (0.04, 0.08, 0.16, 0.32, 0.64 and 1.28 mm). DVC (DaVis 10, LaVision) was used to obtain the full-field strain distribution in bone during screw insertion and cyclic loading.

Results

DVC-computed strains increased with tightening. Higher deformations occurred at the bone-screw interface, decreasing radially (Fig. 1A). Ti controls insertion resulted in higher strain accumulation and consequent damage compared to novel Mg-based screws. Comparable bone strain levels were observed with both screw types under compression in the fracture fixation model (Fig. 1B), approaching ~10,000µε around the screw tip.

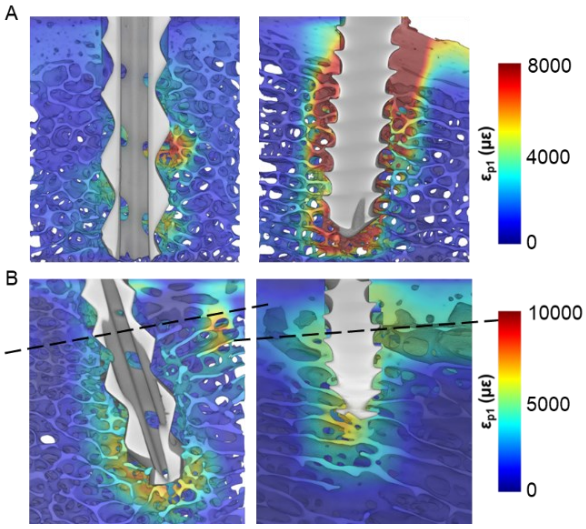

Figure 1: 3D full-field strain distribution of bone around Mg-based screws (left) and Ti controls (right). Maximum principal strains (ε_{p1}) at (A) the maximum tightening level (300 Nmm) and (B) maximum displacement amplitude (1.28 mm) are shown. Dashed black line in (B) indicates location of induced fracture.

Discussion

The novel Mg-based screw design was found to induce less damage in both cortical and trabecular bone during tightening, with a lower bone volume fraction experiencing yielding [4] when compared to the Ti control screws. Additionally, Mg-based screws showed less strain transfer to the surrounding bone radially and mitigated the strain concentration along the bone-screw contact. This bone fracture fixation model suggests that novel Mg-based screws can provide safe anchorage to fracture bone segments, offering high stability as in currently used Ti screws. Future work will investigate the *in vivo* biomechanical degradation of novel Mg-based screws to fully characterize their application as biodegradable implants and how the material degradation and bone regeneration influence the stability of implanted screws.

References

1. Castellani et al., Acta Biomaterialia, 7, 432-440, 2011.
2. Sezer et al, J Magnesium & alloys 6, 23-43, 2018.
3. Voumard et al., JMBBM, 92, 23-32, 2019.
4. Bayraktar et al., J Biomech, 37, 1671-1678, 2004.

Acknowledgements

Funding to support of this project was provided by Biotrics biomaterials (Germany).

POROUS HIP IMPLANT TO PROMOT OSSEOINTEGRATION AND REDUCE STRESS SHIELDING

Seyed Ataollah Naghavi (1). Jia Hua (1,2). Mehran Moazen (3). Steve Taylor (1). Chaozong Liu (1)*

1. Institute of Orthopaedics & Musculoskeletal Science, University College London, Royal National Orthopaedic Hospital Stanmore, London, HA7 4LP, UK

2. School of Science and Technology, Middlesex University, London, NW4 4BT, UK

3. Department of Mechanical Engineering, University College London, London, WC1E 6BT, UK

Introduction

Total Hip replacement is an effective and successful treatment for osteoarthritis. Currently there are over a million patients which undergo this treatment and the number is expected to double in the next two decades [1]. Patients often undergo revision surgery to replace their hip implant due to either peri-prosthetic fracture, aseptic loosening or the severe pain experienced by the patient. Stress shielding is a mechanical phenomenon that refers to the reduction of bone density as a result of altered stresses acting on the host bone. Current orthopaedic prostheses undergo too much bone resorption secondary to stress shielding due to their solid metallic nature, which are much stiffer than the surrounding bone. With the use of 3D printing technology such as selective laser melting (SLM), it is now possible to produce porous graded microstructure hip stems to mimics the surrounding bone tissue properties [2].

Methods

To understand and determine the mechanical and fatigue properties of the hip implant, such as multiaxial yield surface and homogenized stiffness tensor, asymptotic homogenization has been used in many studies. With this method it is now possible to accurately measure the stress distribution within the microstructure [1, 2, 3]. The 3D printed implant needs to have an optimized topology which are defined and affected by the pore size, porosity gradient and the thickness of the manufactured cell elements [1]. In a study by Arabnejad [1], a porous hip stem was designed, produced and experimental studies were performed to measure and compare the bone resorption by analyzing the difference in strain energy between the intact bone and the implanted bone. A novel method [Inverse Homogenization] was introduced by Zadpoor [3] which is reassuring to have a mechanical compatibility among topology optimized microstructures. As a result, the physical properties of the individual cells as well as those of neighboring pairs would be optimized which can then ensure material connectivity and smoothly varying physical properties.

Results

Study done by Gilbert [2] showed that the 3D printed (Ti6Al4V) hip stem implant could survive more than 10^7 cycles and had more than 50% reduction in stress shielding when compared with the current conventional generic hip implants available in the market. Arabnejad [1] showed that fully porous implant with an optimized material micro-structure can reduce the amount of bone loss secondary to stress shielding by 75% compared to a fully solid implant. Zadpoor [3] topology optimization theory (*figure 1*) and results, suggest performance of the individual cells agrees well with the theoretical Hashin–Shrickman (HS) upper bounds, meaning that the optimization of connectivity does not compromise the optimality of individual cells.

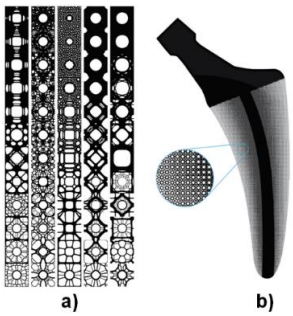

Figure 1: Topology optimization approaches to (a) design and (b) 3D print.

Conclusion

In summary, the graded density implants have a reduced stress shielding compared to conventional hip implants. This is shown by having more areas with higher stresses in the fully solid implants than the graded density implants which have a lower stress value. The architected hip implants presented in recent studies shows clinical promise in reducing bone loss while preventing implant micromotion [2].

Acknowledgements

This project is financially supported by the EU via the H2020-MSCA-RISE-2016 program (grant no: 734156).

References

1. Y. Wang, S. Arabnejad, M. Tanzer, D. Pasini (2018). Hip implant design with three-dimensional porous architecture of optimized graded density, Journal of Mechanical Design 140 (11).

2. He Y, Burkhalter D, Durocher D, Gilbert JM (2018). Solid-Lattice Hip Prosthesis Design: Applying Topology and Lattice Optimization to Reduce Stress Shielding From Hip Implants. ASME. Frontiers in Biomedical Devices.

3. Eric Garner, Helena M.A. Kolken, Charlie C.L. Wang, Amir A. Zadpoor, Jun Wu (2019). Compatibility in microstructural optimization for additive manufacturing, Additive Manufacturing 26 65–75.

IN VIVO BIOMECHANICS ASSESSMENT OF A CR TOTAL KNEE PROSTHESIS DURING SIT TO STAND: COUPLING DYNAMIC RSA AND FE ANALYSIS

Agostino Igor Mirulla (1), Laura Bragonzoni (2), Raffaele Zinno (2), Stefano Zaffagnini (1, 3), Bernardo Innocenti (4)

1. Department of Biomedical and Neuromotor Sciences, University of Bologna, Italy; 2. Department for Life Quality Studies, University of Bologna, Italy; 3. 2nd Orthopaedic and Traumatologic Clinic, IRCCS Istituto Ortopedico Rizzoli, Italy; 4. BEAMS Department (Bio Electro and Mechanical Systems), Université Libre de Bruxelles, Belgium

Introduction

Total knee arthroplasty (TKA) is the gold standard treatment for patients with primary osteoporosis, as it can relief pain and restore joint function. Generally, the prosthesis implant has a survival rate of 82% at 25 years [1] and it provides a patient satisfaction 81% [2]. However, there is stillroom for improvement as far as prosthesis behavior are concerned.

Roentgen Stereophotogrammetric Analysis (RSA) is the most accurate technique assessing the in-vivo joint kinematics.

In this study, an innovative technique, combining RSA dynamic and patient-specific finite element models, was applied to analyze a group of 15 patients who underwent total knee arthroplasty with a cemented PCL highly congruent MB TKA during the execution of a sit to stand from chair.

The aim of our study was to evaluate the position and translation of the femoral polyethylene insert contact points.

Methods

A cohort of 15 patients, underwent cemented CR highly congruent MB TKA (Gemini, Waldemar LINK GmbH & Co. KG, Barkhausenweg 10, 22339 Hamburg, Germany) with patella resurfacing for primary OA, was evaluated after a minimum nine-month follow-up using Model-based dynamic RSA in weight-bearing conditions and during the execution of a sit to stand from chair. The in vivo kinematic data obtained from RSA Dynamic was used as an input for a patient specific finite element models of the implants to calculate condylar contact points between the femoral component and polyethylene insert. The contact points were determined by the FE software as the centroid of the pressure distribution between the femoral condyles and the polyethylene insert.

Results

As shown in figure 1, greater displacements were founded in lateral contact area for AP movement compared with medial area, with peak values of -7.14 mm (LC) and of -3.52 mm (MC). For ML movements, a perfect symmetry was founded comparing LC and MC trends.

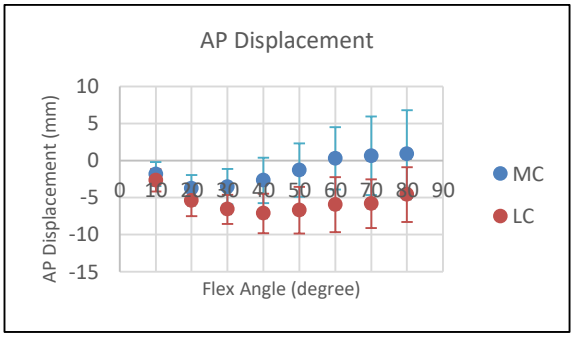

Figure 1: Graph show AP movement of the medial (MC) and lateral (LC) contact points using the FE technique during sit to stand from chair.

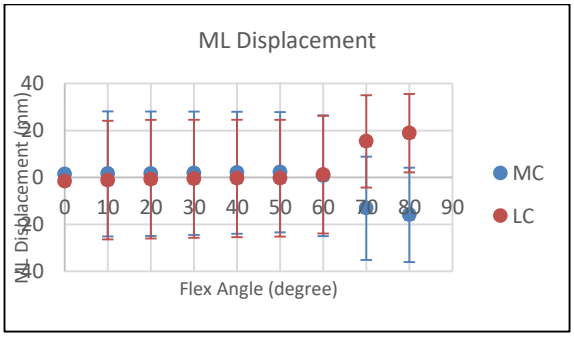

Figure 2: Graph show ML movement of the medial (MC) and lateral (LC) contact points using the FE technique during sit to stand from chair.

Discussion

This study evaluated the knee kinematics in terms of articular surface contacts.

The wider AP displacement of the LC could be interpretated with a slight medial pivot pattern. Concerning the ML movements, results showed a parallel displacement of both condyles with the same wide magnitude, which is in line with the role of the symmetric deep dishes insert.

References

1. Evans JT et al., *Lancet*., 393(10172):655-663, 2019
2. Bourne RB et al., *Clin Orthop Relat Res*., 468(1):57-63, 2010

IS THERE AN INFLUENCE OF DILUTE POVIDONE-IODINE (BETADINE) LAVAGE ON THE INTERFACE FIXATION OF TIBIAL BASEPLATES UNDER CLINICALLY RELEVANT CONDITIONS?

Thomas M Grupp (1,2), Ana Laura Puente Reyna (1), Christoph Schilling (1), Byron Masi (3), Bernhard Fritz (1), William M Mihalko (4), Charles Taunt (5)

1 Aesculap AG Research & Development, Tuttlingen, Germany
2 Ludwig Maximilians University Munich, Department of Orthopaedic Surgery, Physical Medicine & Rehabilitation, Campus Grosshadern, Munich, Germany
3 Aesculap Inc. Research & Development, Center Valley, Pennsylvania, USA
4 Campbell Clinic Department of Orthopaedic Surgery & Biomedical Engineering, University of Tennessee Health Science Center, TN, USA
5 Michigan Orthopedic Center 2815 S Pennsylvania Ave, Suite 204, Lansing, Michigan USA

Introduction

In total knee arthroplasty (TKA), aseptic tibial component loosening remains a major cause of TKA failure, beneath infection, instability and malalignment [1]. This emphasizes the need for a stable primary and long-term fixation of tibial baseplates [2-5].
To reduce the risk of acute post-operative peri-prosthetic joint infection (PJI), dilute betadine lavage has been established in primary and aseptic revision TKA [6]. Thereby, TKA patients receive a 3-minute dilute betadine lavage (0.35 %) before surgical wound closure instead of only normal saline lavage [6].
The objective of our study was to setup a suitable test method to evaluate the influence of dilute betadine lavage on the implant-cement-bone fixation strength for tibial baseplates under clinically relevant time points of dilute betadine application.

Materials & Methods

Using Palacos® R HV bone cement, AS VEGA System® tibial baseplates (size T0) with a ZrN-multilayer coating were implanted in Sawbones® PU blocks (20 pfc) continuously 2 minutes after begin of the cement mixing. After implantation, the tibial baseplates were soaked in either saline solution (0.9 % NaCl) or betadine solution (0.35 %) under constant loading of of 100 N. A total of five testing groups, with six components each, were defined: Control (no use of saline nor betadine solution), early use of saline solution or betadine solution during bone cement application time (start at 4 min 30 sec, 4 minutes duration), late use of saline solution or of betadine solution after bone cement hardening (start at 10 min 45 sec, 4 minutes duration). The timelines for the cementation and use of each solution were based on the working times for vacuum mixing of the Palacos® R HV bone cement. After the cementation procedure, the tibial baseplates were stored upside-down in saline solution at 37 °C for 48 hours.
Finally, each tibial baseplate was mounted into a testing frame and the maximum push-out strength was determined based on an established method [3].

Results

From the final push-out testing no statistical differences between the groups could be seen.

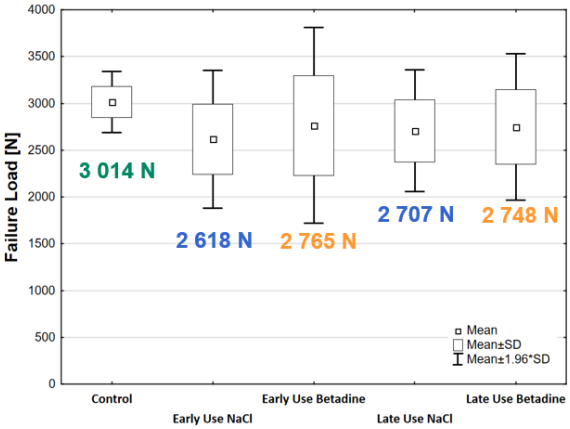

Figure 1: Push-out forces for control, dilute betadine and saline lavage test groups

Discussion

The newly setup method allows to mimic clinically relevant conditions to evaluate the influence of dilute betadine lavage. No significant differences were seen in the implant-cement-bone tibia fixation strength between dilute betadine lavage and normal saline lavage applied during the application phase or after curing of the bone cement. For dilute betadine lavage with a concentration of 0.35 % our results are in accordance with basic compression testing of Bingham et al. [7] on PMMA test cylinders. Further tests for late cement application have to be performed to see if dilute betadine lavage is not influencing tibia fixation.

References

1. Dyrhovden et al., Clin Orth Rel Res, 475:1874-87,2017
2. Cawley et al., Clin Biomech, 27:390-7, 2012
3. Grupp et al., J Arthroplasty, 35(2):579-87,2020
4. Gebert deUhlenbrock et al., Clin Biomech 27:929-35,2012
5. Grupp et al., J Biomech, 59:9-22,2017
6. Calkins et al., J Arthroplasty, 35:538-43,2020
7. Bingham et al., Poster No. 913, ORS 2014

NEW GENERATION OF SHOULDER HEMIPROSTHESIS – A PRELIMINARY IN-VITRO STUDY

Daniel Baumgartner (1), Roger von Mentlen, Stephanie Ruch (1), Daniel Delfosse (2) Viola Mai (2)

1. Zurich University of Applied Sciences ZHAW, IMES Institute of Mechanical Systems, Switzerland
2. Mathys AG Bettlach, Switzerland

Introduction

The use of hemiprostheses are well established as surgical procedure in orthopedics. The humeral part is replaced by an artificial material like ceramics or CoCr. There is evidence that the mechano-compatibility lacks due to a very stiff articulation partner against soft native cartilage on the glenoid. This may be reason of early glenoid failure The idea was therefore to test a ball-on-socket joint with a dense surface layer made of Polycarbonate-Urethane (PCU) articulating against acetabular cups in an in-vitro test.

Aim of the project

The aim of the study was to determine the progression of acting torque moments during flexion/extension over 0.1 Mio loading cycles.

Material & Methods

A) Prosthesis design: The humeral head prosthesis (Ø 32 mm) was coated with thermoplastic Polycarbonate Urethane PCU Bionate I (DSM, USA) with shore hardness 75D. Counterpart of the ball–on-socket joints were congruent ceramic cups (Selexys, Mathys, CH) and congruent sheep acetabulae.

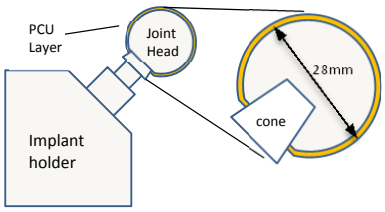

Fig. 1: Mounted humeral head prosthesis with a PCU-layered surface around the base material.

B) Experimental Test setup: The setup was mounted under a universal 2-DoF testing machine (Thelkin, CH). An adapted hip test according ISO-14242 has been carried out, introducing an axial load of 500N, followed by 1000 N after 2500 cycles. The flexural jig applied bending on each side (±30°) in form of a sinusoidal load and a frequency of 1 Hz.
Angular movement and applied load where set to reach their amplitude with a phase shift of 45° to each other (Fig. 2). Phase "A" had a max. load applied at min. bending angle and phase "B" at max. bending angle.
The ball-on-socket joints were fixed on a specific holder providing an angulation of 45° of the joint ball to simulate the CCD-hip angle. The holder was placed in a system that includes a saline water bath at 37°C.

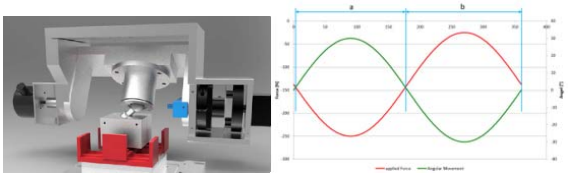

Fig. 2: Test setup including a rotational bending actuator in direction A and B, and an axial loading of 500 N (1st step for 2500 cycles) and 1000 N (2nd step for 95000 cycles).

C) Data Analysis

Mean of resulting bending moments for both bending directions A and B and for the two max. load levels (500 N and 1000 N) were analysed by Matlab.

Results

A slight increase of the moments is generally detected over time although no scratches or abrasion are visible on the PCU-layer. The moments are about 2-6 Nm, which demonstrates the widespread range.

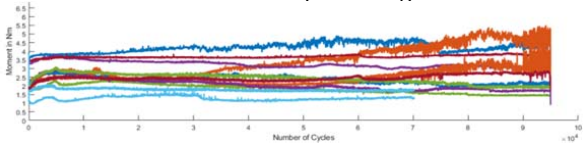

Fig. 3: Moment progression during the application of 95'000 loading cycles for totally 12 humeral PCU-heads on acetabular cups.

The ceramic cup as articulation partner to the PCU heads show slightly increased bending moments in comparison to in-vitro acetabular cups.

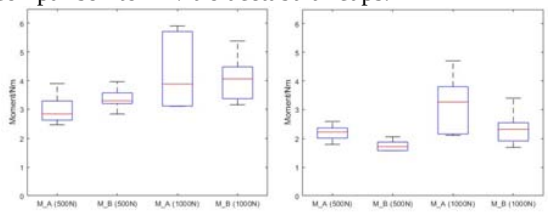

Figure 4: Average moments for PCU head vs. ceramic cup (left) and PCU head vs. acetabular cups (right), each for 500 N and 1000 N loading level.

Discussion & Outlook

The small increase in moment over time may be explained by a swelling effect of the PCU. Ceramic cups show slightly increased bending moments in comparison to sheep in-vitro acetabular cups which demonstrates the applicability of ceramics as a "worse-case" testing scenario.

DEVELOPMENT OF A SIMPLIFIED AND BIOFIDELIC HUMAN SHOULDER SURROGATE FOR TESTING OF PADDED CLOTHING IN RUGBY UNION

Angus Hughes (1), Dr. Heather Driscoll (2), Prof. Matt Carré (1)

1. Department of Mechanical Engineering, The University of Sheffield, Sheffield, United Kingdom 2. Advanced Manufacturing Research Centre, The University of Sheffield, Sheffield, United Kingdom

Introduction

Synthetic human surrogates are used regularly in the sports industry to assess the performance of personal protective and padded equipment following relevant safety standards or regulations. However, these surrogates are often not representative of the human body structure they are modelling due to differences in their material properties (e.g. density, stiffness) and geometries compared with real anatomy [1]. Although these simplifications are made for improved repeatability, the effective assessment of protective and padded equipment's ability to mitigate impact injury can be lost. Padded clothing (shoulder padding) in rugby union is currently governed by test regulations that use a steel cylindrical anvil as a shoulder surrogate which is not representative of a human shoulder [2]. Coupled with this, the impact protective ability of shoulder padding has not been investigated thoroughly. The aim of the study was to construct a human shoulder surrogate for use in the impact testing of shoulder pads that is geometrically and mechanically accurate while also taking into account ease of fabrication to facilitate repeatability. After this a shoulder surrogate biofidelic to the human shoulder would be fabricated.

Anatomical and Mechanical Assessments of the Human Shoulder

Both the external and internal anatomies of the human shoulder were assessed using a data set of semi-professional rugby players. 3D imaging was used to develop a data set of external geometric measurements and computer aided design (CAD) of the shoulder; Ultrasound scanning was used to develop a data set of internal geometric measurements (i.e. muscle thicknesses). Mechanical assessments were made through previously published research [3].

Shoulder Surrogate

After assessments were made, anatomies were simplified so the surrogate was repeatable and easy to fabricate. The shoulder represented a half cylinder with ultrasound showing 2 key layers above the clavicle and scapula, the trapezius muscle and a skin and adipose layer, this area of the shoulder is where shoulder padding sits. Figure 1 shows the simplified shoulder surrogate for impact testing of shoulder padding. After this, work focused on the design of a biofidelic shoulder surrogate with a more representative anatomy to the human shoulder (figure 2).

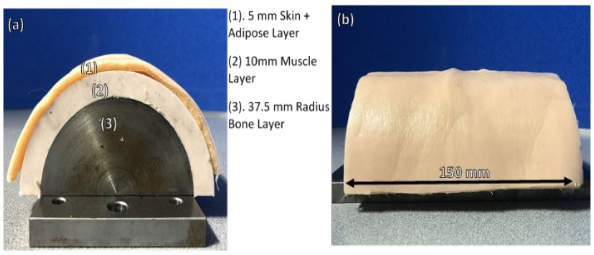

Figure 1: (a) Simplified Shoulder Surrogate (cross-sectional view) (b) - Testbed (side view)

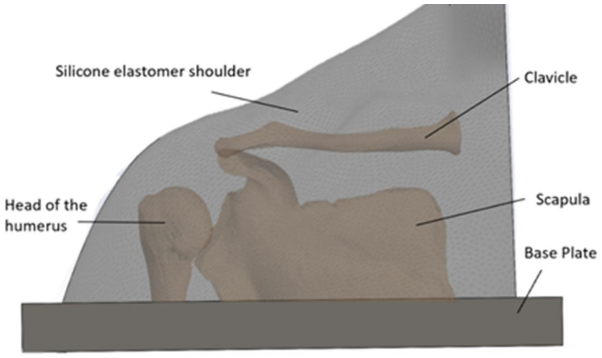

Figure 2: CAD design of Biofidelic Shoulder Surrogate

Discussion

This study presents the development of a simplified shoulder surrogate that can be used in both a testing and an injury preventative research setting. The surrogate demonstrates an effective trade-off between biofidelity and repeatability for use in an impact testing environment. Future work will look to further develop a biofidelic shoulder surrogate with more representative geometries to the human shoulder. This can then be used to further validate the simplified surrogate for improved testing of shoulder padding.

References

1. Payne et al., Crit. Rev. Biomed. Eng, 41(1), 2013.
2. Body Padding Performance Specification, https://playerwelfare.worldrugby.org/body-padding, 2019.
3. Hughes et al., MDPI Proceedings, 49(1):77, 2020.

Acknowledgements

This work is funded by World Rugby and EPSRC. The investigators would like to thank the Sports Engineering Research Group at Sheffield Hallam University for use of their 3D imaging system.

THE KNEE JOINT MENISCUS IS A SHOCK ABSORBER

A. M. Seitz, K. Kreienbaum, J. Schwer, D. Warnecke, A. Ignatius, L. Dürselen
Institute of Orthopaedic Research and Biomechanics, Ulm University Medical Centre, Ulm, Germany

Introduction

"The shock absorbing truth about meniscus" by Andrews et al. [1] initiated a controversial discussion about the until then generally accepted assumption, that the meniscus acts as a knee joint shock absorber. Although there is evidence in literature indicating the shock absorbing potential of meniscus tissue [2,3], there is only one contribution investigating the shock absorbing potential of the meniscus inside the knee [4]. Hence, the aim of this biomechanical study was to investigate the shock absorbing function of the meniscus under cyclic loading in order to finally find a clear answer to the question whether the meniscus acts as a shock absorber in the knee joint or not.

Methods

After soft tissue dissection, eight porcine knee joints were mounted in 45° neutral joint position in a previously introduced and modified drop tower setup [4]. Then the setup was installed in a fatigue testing machine (Instron8871, ITW), allowing for the application of sinusoidal loading. After successful validation (r=.97) of the setup a dynamic mechanical analysis (DMA) was performed applying 10 frequencies (0.1; 0.2; 0.4; 0.6; 0.8; 1; 2; 3; 4; 5 Hz), applying a static load of 1210N and a superimposed sinusoidal load of 910N to the joints. To account for the viscoelastic behaviour of the knee soft tissues the joints were pre-loaded with 300N for about 12 minutes. Four different meniscus states (intact, medial posterior root avulsion, medial meniscectomy, complete lateral and medial meniscectomy) were used to investigate the shock absorbing ability of the meniscus. Force (F) and deformation (l) were synchronously recorded throughout the tests. The time lag $\delta/2\pi f$ between the amplitudes of F_A and l_A (Fig. 1A) was detected by a customized Matlab (R2016b, Mathworks) script. Then, tan δ was calculated representing the ratio between loss modulus M′′ and storage modulus M′, which is considered as damping factor (Fig. 1B).

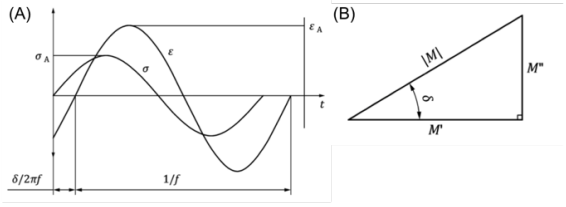

Fig. 1: (A) The phase shift δ /2π f between the stress σ and strain ε in a viscoelastic material subjected to sinusoidal oscillation. (B) The relationship between the storage modulus M′, the loss modulus M", the phase angle δ and the magnitude [*M*] of the complex modulus M*. DIN EN ISO 6721-1:2018-03

After sample size calculation the damping factor tan δ was elaborated by comparing the four meniscus states using a one-way ANOVA followed by Duncan post-hoc testing where differences were observed (SPSS, IBM). p=.05 was considered significant.

Results

Knees with an intact meniscus had the highest damping factors, ranging from .10 to .15 (Fig. 2A). Any treatment lowered the damping factor. After posterior medial root avulsion the mean value of the damping factor was reduced by 15%, while medial meniscectomy resulted in a reduction of 24%. The resection of both, the lateral and medial menisci resulted in a reduction of 18% compared to the intact state. When comparing the meniscal states at specific frequencies in detail (Fig. 2B) Duncan post-hoc testing indicated differences for the comparisons of the intact state and the medial meniscectomy at 0.1Hz; 0.2Hz; 2Hz, 3Hz, 4Hz (p<.04) and for the comparisons of the intact meniscus state and the total meniscectomy at 0.2 Hz (p=.02).

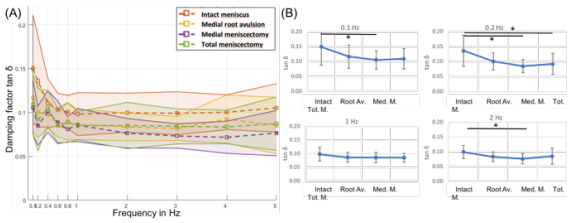

Fig. 2: (A) Mean values (dashed lines) of the damping factor tan δ ±SD (represented by the envelope in the same color) plotted over the 10 different frequencies. (B) Four representative, detailed comparisons of the different meniscus states and their impact on the damping factor tan δ at 0.1Hz, 0.2Hz, 1Hz and 2Hz. The diagrams indicate the mean values ± SD. (n=8; *p < .05 one-way ANOVA and Duncan post-hoc testing)

Discussion

The results of this biomechanical study show, that the damping factor, and thus the shock absorbing ability of a knee joint is lower the more meniscal tissue is resected. Coluccino et al. [6] investigated the viscoelastic response of bovine menisci and found both similar ranges of the damping factor tan δ of e.g. 0.17 at 0.1Hz and a similar frequency dependency of the damping response of the meniscus within the range from 0.1 Hz to 5Hz.

This biomechanical study extends our previous findings, where we identified that the meniscus acts as a shock absorber in the knee joint under impact loads [4]. Therefore, we can conclude that the meniscus significantly contributes to the shock absorption of the knee joint. As a consequence, the results of the present study highlight that care should be taken to save as much meniscal tissue as possible.

References

1. Andrews et al.; J Biomech. 2011; 44(16):2737-40
2. Pereira et al.; Osteoarthritis Cartilage. 2014; 22(9):1271-81
3. Gaugler et al.; KSSTA. 2015; 23(4):1141-6
4. Seitz et al.; Proc ORS2019
5. Taylor et al.; J Biomech. 2006; 39(5): 791-8
6. Coluccino et al. J Appl Biom Func Mat. 2017; 15(1): 77-83

AN EXPLORATIVE IN VITRO STUDY ANALYZING THE DETERMINANTS OF HUMAN RIB FRAGILITY

Christian Liebsch (1), Shamila Hübner (1), Marco Palanca (2), Luca Cristofolini (2), Hans-Joachim Wilke (1)

1. Institute of Orthopaedic Research and Biomechanics, University of Ulm, Germany;
2. Department of Industrial Engineering, University of Bologna, Italy

Introduction

Rib fractures represent a common injury type, occurring in about 10% of all trauma cases [1] and 70% of all blunt chest trauma cases [2]. Fracture mechanisms as well as factors affecting human rib fragility, however, are little investigated so far [3]. The aim of this in vitro study was to explore potential determinants of human rib fragility.

Methods

89 ribs from 13 human donors were prepared for this study. Donor age ranged from 55 to 99 years, including 7 male and 6 female donors and a total of 45 left and 44 right ribs from levels 4 to 8. The ribs were loaded in antero-posterior compression with 1 mm/s until fracture using a material testing machine (Zwick-Roell Z010, Fig. 1). Surface strains were measured using a digital image correlation system (Dantec Dynamics Q400) [4]. The effects of age, sex, bone mineral density, rib level and side, four global morphological factors (e.g. rib length), and seven rib cross-sectional factors (e.g. cortical thickness), determined by µCT (Skyscan 1172), on fracture load were examined using multivariate analysis, group comparisons, and correlation analysis in SPSS.

Results

Significant dependencies on fracture load ($p<0.05$) were found for age, bone mineral density, rib length, cortical thickness, bone volume/tissue volume ratio, trabecular number, trabecular separation, and both cross-sectional area moments of inertia. Age and bone mineral density showed medium correlation coefficients (r=-0.449/ 0.490), while sex did not affect fracture load (p=0.445). Fracture load was significantly higher at rib levels 7 and 8 compared to level 4 (p=0.001/0.013), whereas side had no significant effect (p=0.989). Global morphology did not affect fracture load, while rib length showed highest, but overall low correlation (r=0.287). In total, cortical thickness exhibited highest correlation (r=0.722, Fig. 2), followed by the area moment of inertia around the longitudinal rib cross-sectional axis (r=0.687). Medium correlation with fracture load was found for bone volume/tissue volume ratio (r=0.448), trabecular number (r=0.479), and trabecular separation (r=-0.367) of the rib cross-sectional area. High correlation coefficients were also detected for both bone volume/tissue volume ratio and trabecular number with absorbed energy (r=0.542/0.539), max. external rib surface strain (r=0.631/0.648) and min. internal rib surface strain (r=-0.644/-0.559).

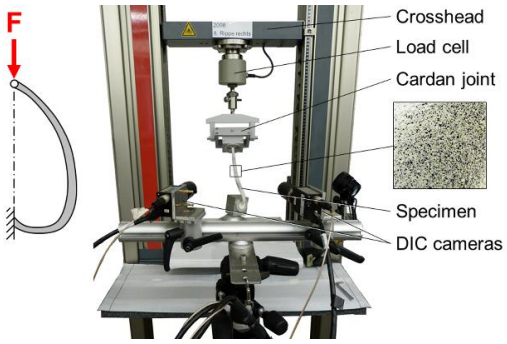

Figure 1: Test principle/setup incl. speckled rib surface.

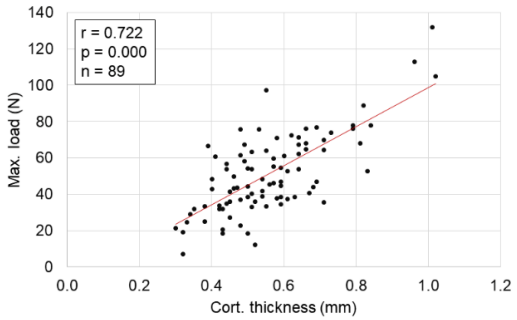

Figure 2: Effect of cortical thickness on fracture load.

Discussion

Together with rib level, the factors cortical thickness, area moment of inertia around the longitudinal rib cross-sectional axis, as well as bone mineral density exhibit the largest effects on human rib fragility with regard to the fracture load. Sex, rib cage side, and global morphology, in contrast, do not affect rib fragility. These findings might be used in future in vitro and in silico studies investigating human rib fracture mechanisms, for the development of novel rib fixation implant designs, as well as for the optimization of novel safety devices in regards to blunt chest trauma.

References

1. Ziegler et al., J Trauma, 37:975–979, 1994.
2. Shorr et al., Ann Surg, 206:200–205, 1987.
3. Liebsch et al., PLoS One, 14(12):e0224105, 2019.
4. Palanca et al., Med Eng Phys, 52:76-83, 2018.

Acknowledgements

This study was funded by the German Research Foundation (DFG, Project WI 1352/20-2).

EVALUATION OF LOCAL FORCES IN EQUESTRIAN HELMETS WHEN EXPOSED TO LATERAL DEFORMATION

Jasmin Stoff (1), Rhosslyn Adams (1), Helen Riley (2), Benjamin Hanna (2), Tony Palkowski (2), Peter Theobald (1)

1. Cardiff University, UK; 2. Champion Manufacturing, UK

Introduction

Twelve percent of all eventing falls resulted in the horse somersaulting, with seventeen percent of those resulting in seriously injured riders [1]. The possibility of the horse falling or stepping on a fallen rider requires a unique resistance to lateral crush not encountered in other sports.

To assess lateral stiffness, equestrian helmets are quasi-statically deformed as prescribed by the international standards PAS 015:2011, VG1 01.040 2014-12 and SNELL E2016. The maximal loads are 800N, 630N and 1000N respectively. The maximum allowable crush is 30mm and the residual crush at 30N must not exceed 10mm [2]. Whilst the literature fails to report the biomechanical consequence of such deformations, Connor et al. reported helmet-headform contact forces when impacted with an equine cadaver. A mean 10kN compressive force was measured inside the helmeted head [3], relative to a 2kN skull fracture threshold [4].

This study seeks to further investigate the lateral deformation test, attempting to quantify helmet-headform contact forces for the above test standards. These forces will then provide insight into potential skull fracture risk, whilst also providing data to inform equestrian safety.

Methods

The external surface of a Hybrid III 50th %ile male headform was instrumented with pressure sensors that had a low-profile construct, to avoid inducing stress concentrations. Multiple helmet models (Champion, UK), certified to PAS015 were fitted to the headform, selecting the appropriate size to accurately resemble a well-fitting product. This test setup was then positioned between two rigid platens, secured to a compression testing machine (Figure 1). The controller, driven by load-control, proceeded to follow the PAS015 lateral deformation test standard. This was considered the most appropriate test standard, given its importance to the UK market. Video cameras were used to capture failure mechanisms.

This protocol was then repeated using just the helmet, without the pressure mat and headform.

Results

Initial data demonstrates that the headform is exposed to significant contact forces from the helmet liner during the lateral crush testing, with different helmet design features appearing to influence these data. Further testing is being completed to understand the potential correlation between these high contact forces and skull fracture, and the potential for future innovative helmet solutions.

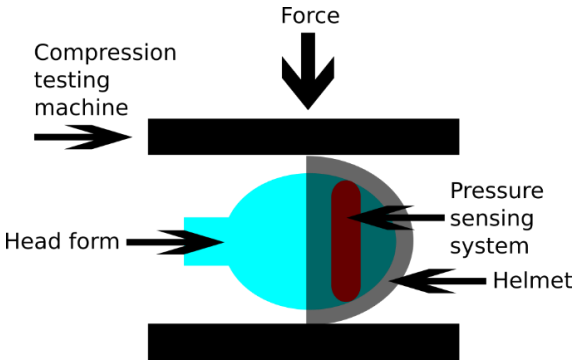

Figure 1: The pressure mat is fitted between the helmet and the head form and force applied, while deformation and pressure are measured.

Discussion

The PAS015 lateral deformation test exposes the equestrian helmet to a substantial load, as it simulates risk posed by the falling horse. Whilst the investigated helmets comply with one of the highest regarded standards (i.e. PAS015) – typically by designing a relatively stiff outer shell, further investigation is needed to establish the relevance of this test when comparing skull compression data to established fracture thresholds. Understanding the force distribution on the head provides greater insight to those engineers tasked with identifying innovative solutions to achieve improved head protection.

References

1. FEI Eventing: Risk Management Program Statistics 2009-2020
2. (2011) PAS015:2011: Helmets for equestrian use, in British Standards Institution BSI, London, BSI
3. Connor, T. A. et al. (2020). An evidence basis for future equestrian helmet lateral crush certification tests. Applied Sciences (Switzerland), 10(7).
4. Schmitt, K. U. et al. (2014). Trauma biomechanics an introduction to injury biomechanics.

Acknowledgements

This research was funded by Champion Manufacturing and Cardiff University. Some of the co-authors are employees of Champion Manufacturing.

A HIGH-FIDELITY FINITE ELEMENT MODEL OF THE CEREBROVASCULATURE FOR BRAIN INJURY SIMULATION

Harry Duckworth (1,2), Adriana Azor (1,2), David J Sharp (2,3), Mazdak Ghajari (1)

1. Dyson School of Design Engineering, Imperial College London, UK; 2. The Computational, Cognitive and Clinical Neuroimaging Laboratory, Imperial College London, UK; 3: Care Research and Technology Centre, Dementia Research Institute, UK

Introduction

Finite element modelling of the brain has been used with increasing frequency to investigate brain biomechanics and pathology of injury [1]. Some models have considered the mechanical effects of vasculature on the response of the brain matter however there are only a small number of studies which investigate vasculature injury, and of these, the focus is bridging vein rupture, meaning diseases such as microbleeding and are unable to be investigated. Here we present a method for inclusion of the complete venous system in the brain from a T1 image and high resolution QSM image for finite element analysis.

Method

A high resolution QSM modality image of the vasculature was segmented using a combination of manual and semi-automatic tools in Mimics (Materialise Mimics Research 20.0). Thresholding was used to identify macroscale veins, a dynamic growth algorithm was used to manually segment remaining veins, and finally, a smart expansion algorithm was applied to add missing edges and discontinuities. The vasculature image was registered to the head segmentation and the centerlines/radii data was transformed to the head coordinate system.

Three steps were taken to build the Finite element (FE) model of the brain from the subjects T1 image. The subcortical structures were segmented using freesurfer, the cerebrospinal fluid (CSF) was segmented using fsl and the skull was created by thresholding the T1 image then removing the brain and CSF segmentation mask. Smoothing was applied at material interfaces.

Four head impact reconstructions were simulated in LS-DYNA for verification purposes [2]. CORA scores, a method for comparison of biomechanical reconstructions, were calculated for each receiver to verify the fidelity of the brain model. Simulations of injury events in sport, road traffic collision, and fall were ran on the model to investigate vasculature strains.

Results

A detailed FE model of the brain was created which included 46 parts, made up of the skull, meninges, CSF, cortical, and subcortical structures (figure 1 left). The biomechanics of the model was verified using head impact data with average CORA scores giving a good/fair biofidelity rating as specified in ISO/TR-9770 (figure 1 right).

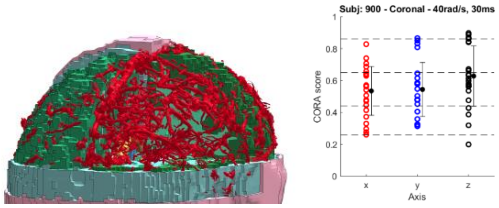

Figure 1: (L) FE brain model with complete venous system, (R) CORA scores for each receiver per axis for reconstruction of UVAB900COR4 [2]

The venous system was successfully segmented and imported onto the brain model. Good alignment of anatomical features was seen and veins < 0.4mm diameter were successfully identified. Strains were seen to peak in patterns in the brain which could indicate pathology.

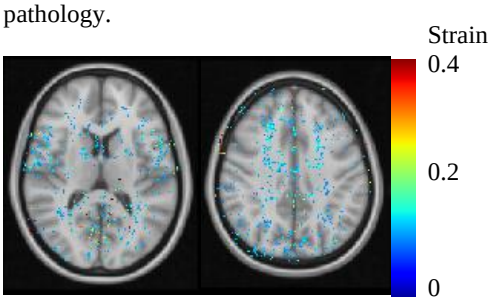

Figure 2: Axial slices of fall reconstruction showing distribution of strains > 0.15

Discussion

Here we present the first FE brain model to use high resolution imaging for identification and inclusion of vasculature in the brain. The brain biomechanics were verified from head impact tests showing fair/good fidelity. Injury recreations show patterns of strain in perivasculature region where vasculature injury is seen.

References

1. Dixit, P. et al. (2017). "A Review on Recent Development of Finite Element Models for Head Injury Simulations." Archives of Computational Methods in Engineering 24(4): 979-1031.
2. Alshareef, et al., (2020). "Biomechanics of the Human Brain during Dynamic Rotation of the Head." J. Neurotrauma 37(13): 1546-1555.

Acknowledgements

We thank Dr. H Mattern for providing the imaging data. This work was supported by EPSRC, grant number EP/N509486/1 and reference 2024686.

INVESTIGATING THE EFFECTS OF INFILL QUANTITY ON THE FRICTIONAL RESPONSE OF *IN VIVO* SKIN

M. MACFARLANE, C. DYSON, M. DOUGLAS, P. THEOBALD

Introduction

Third generation artificial turf surfaces provide a consistent playing experience and enable wider and greater sports participation; however, they are frequently associated with skin friction injuries [1,2]. Whilst not typically preventing elite players training or competing in games, these injuries can be painful and hinder wider acceptance of artificial turfs [3]. The literature poorly describes the epidemiology of skin injuries caused by friction-generating interactions, motivating an investigation into skin-turf friction. A novel test rig was developed to investigate different contact parameters, with the effect of turf pile height the focus of this study.

Methods

Participants (n = 16, 19 – 31 years old) kneeled on a 3G turf surface that slid (2 m/s) against the skin when exposed to an impulse loading, via a pendulum. The cable linking the surface and pendulum was instrumented with a strain gauge to capture resistive force (F_f), whilst the normal force (F_n) was measured via a force plate under the turf. Equation 1 defines the frictional coefficient (μ):

$$\mu = \frac{F_f}{F_n} \qquad [1]$$

Participants performed three baseline tests, for each knee, on control samples (20 mm free pile height) which represented a turf in good condition. The left and right knee were then exposed to a short (5mm) and long (35mm) turf fibres respectively, achieved by an increased/decreased infill quantity. This represented poorly maintained turfs. Data were excluded where participants applied inconsistent pressure across the baseline and intervention tests. This study was approved by the School of Engineering Ethical Approval Committee.

Results

Participants (13 male) performed a full set of control and intervention tests; however, datasets were excluded if they did not meet the pressure requirements. This inclusion criteria accepted 9 and 11 participants for the short (left) and long (right) pile hight test, respectively. Baseline measurements for the free pile height tests achieved a 0.338 (0.075) and 0.341 (0.103) frictional coefficient for the left and right knee, respectively (p = 0.908). Decreasing pile height resulted in non-significant variation between baseline and intervention measurements. Exposing greater pile caused COF to statistically increase by 11.7 (13.6) % (p = 0.03). It was observed that Participant R3 (Figure 1) generated COF approximately 2-fold greater than average. The respective pressures applied to the turf (Figure 2) was calculated as 1.22 (0.369) N/cm^2 for all participants. It was noted that a reduced pressure of 0.50 N/cm^2 corresponded to the peak COF in Figure 1.

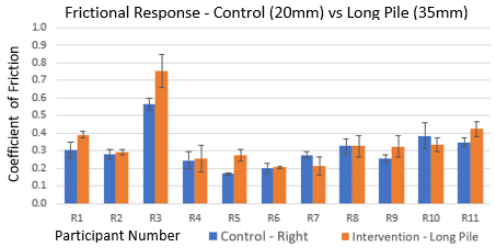

Figure 1: *Comparison of COF - Control vs Long Pile.*

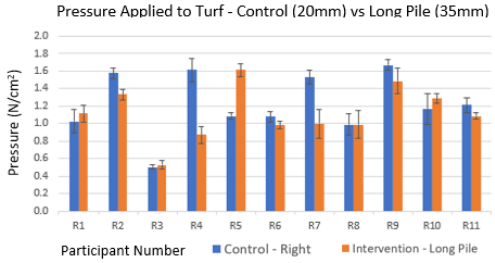

Figure 2: *Pressure applied to the turf - Control vs Long Pile.*

Discussion

As frictional injuries occur unpredictably, the analysis and explanation of anomalous COF values can provide a better insight into the causative factors of these injuries. Exposing a greater pile height caused a statistical increase (p = 0.03) in mean COF. The COF for participant R3 was 2-fold greater than the cohort (Figure 1), which would appear the most injurious result from this study, especially if performed at a greater sliding speed. This participant had the lowest contact pressure, potentially reducing/negating the beneficial ball bearing effects of rubber crumb, whilst presumably achieving minimal infill penetration. This appears a potential cause of higher COF and, presumably, greater risk of frictional injury. Work is on-going to further understand this interaction and those of other surface and skin parameters.

References

1. Fuller et al., Br J Sports Med, **41** (1) 2007
2. van den Eijnde, W., et al., J Sci Med Sport, **17**(1) 2014
3. Tay et al., J Sports Sci, **35**(15) 2017

Acknowledgements

Participants and the team of undergraduates who helped collected the data. This work was supported by SportsLabs and funded by World Rugby.

PLAYER'S PERCEPTION OF INTERACTIONS CAUSING SKIN INJURIES FROM ARTIFICIAL TURF

M. MACFARLANE, C. DYSON, M. DOUGLAS, P. THEOBALD

Introduction

Third generation artificial turf surfaces provide a consistent playing experience and enable wider and greater sports participation, however, they are frequently associated with skin friction injuries [1-4]. The current standard for assessing skin friction has been critiqued for not representing realistic player-turf interactions [5]. This project aims to develop a novel test method that more accurately replicates player-turf interactions, which should ultimately enable improved regulation and reduced skin injuries. The literature fails to identify injurious interactions, whilst a lack of systematically 'flagging' such incidences has hindered a search of historic video footage; hence, appraising player perception is now an important component in understanding turf interactions. This study describes the development and analysis of a survey presented to amateur and elite rugby players, capturing perceptions of artificial turfs and skin injury.

Methods

A survey was designed to capture the opinions of amateur and elite rugby players towards artificial surfaces. The first eight questions captured data describing player status and history. The next six questions, Table 1, explored skin injury history, perceived traits of injurious player-turf interactions and properties. The survey concluded with a free text question, encouraging participants to describe interactions they think are most injurious. This study was approved by the Cardiff University's School of Engineering Ethical Approval Committee and circulated as a Google survey, via the Scottish Rugby Union's social media channels.

Results

Data from 345 participants (306 male) were analysed, including 57 elite male players. Eighty eight percent trained/played at least twice a week. Almost all participants (97.4%) perceived artificial grass as more likely to produce a skin injury, than natural grass. Abrasions (70.4%) or burns (73.6%) were the most common injuries participants thought they experienced. No consensus existed to identify the turf property that was most likely to cause skin injuries, however, participants agreed that prominent bony joints were the most vulnerable anatomical location (elbows – 71.3% & knees – 90.8%). The majority (69%) identified that a situation involving a tackle would most likely produce a skin injury, whilst others thought sliding to score (13.8%) or when going to ground to collect a loose ball (14.1%). The remaining participants suggested a ruck (1.4%) or any interaction with the turf (1.7%) would result in a skin injury.

1. What surface do you think is more likely to produce a skin injury?
i) Artificial Grass ii) Natural Grass
2. Which artificial turf property do you think produces skin injuries?
i) Polymer Grass Fibre ii) Rubber Infill iii) Surface Temperature iv) Not Sure
3. Which body part do you think is most susceptible to receiving skin injuries? Choose one or more:
i) Elbow ii) Knee iii) Face iv) Forearm v) Thigh vi) Shin vii) Other
4. Choose an interaction that you think is most likely to produce a skin injury?
i) Ruck ii) Maul iii) Tackling iv) Tackled v) Sliding for a try vi) Going to ground to collect a loose ball vi) Other
5. Which of the following environmental conditions do you think are more likely to produce a skin injury? Choose one or more:
i) Dry ii) Wet iii) Cold iv) Hot v) Other
6. Which of the following term(s) do you think best describes any injuries you have experienced? Choose one or more:
i) Abrasion ii) Blister iii) Burn iv) Contusion v) Laceration vi) No injury vii) Other

Table 1: *Questions Exploring Player's Perception of Turf*

Discussion

The survey highlighted that the knee was the location most vulnerable to receiving skin injuries. The most likely causative player-turf interactions were "sliding", "tackling" and "tackled". Most players felt they had experienced both abrasions and burns, which suggests the new test method should analyse the abrasive nature of turf and temperature rises under realistic loadings. The high training/playing participation provides confidence in these data, which now inform the design specification of a new assessment apparatus.

References

1. Zanetti, E.M., Appl Ergon, **40**(3) 2009
2. Fuller, C.W., et al., Br J Sports Med, **41** (1) 2007
3. van den Eijnde et al. J Sci Med Sport, **17**(1) 2014.
4. Twomey, D.M., et al., J Sci Med Sport, **22**(5) 2019.
5. Tay, S.P., et al., J Sports Sci, **35**(15) 2017

Acknowledgements

We thank Graham Finnie and Jennifer Griffin from Sports Scotland and SRU, respectively, for their help circulating the survey. This work was supported by SportsLabs and funded by World Rugby.

THE INFLUENCE OF FALL DIRECTION AND HIP PROTECTOR PADDING ON HIP FRACTURE RISK

Ellie S. Galliker (1), Andrew C. Laing (2), Stephen J. Ferguson (1), Benedikt Helgason (1), Ingmar Fleps (1)

1. ETH Zürich, Switzerland; 2, University of Waterloo, Canada

Introduction

Hip fractures in older adults can lead to lasting impairment, a decrease of mobility, and an increased mortality rate. Hip fractures mostly occur as a consequence of a fall from standing height, however only a small percentage of falls lead to hip fractures [1]. Hip fracture risk is multi-factorial in nature, including the risk of falling, the load acting on the femur and the load that the femur can withstand. Hip protectors covering the greater trochanter are a preventive intervention aimed at reducing the impact load applied to the femur. While recent findings indicate that posterior-lateral falls are just as dangerous as lateral falls from a fracture risk perspective [2], most current models focus mainly on assessing lateral impacts. The aim of the present study was to investigate the influence of fall direction and hip protector padding on impact loading and fracture risk using finite element (FE) models.

Methods

We modelled falls for 4 subjects, in 7 different impact directions (15° and 30° anterior, lateral, and 15°, 30°, 60°, and 90° posterior, see Figure 1), at two different impact velocities (2.1 and 3.1 m/s) using pre-existing biofidelic FE models [3]. Two material models were implemented for bone: one with a linear stress-strain response, and another with a non-linear response which enabled prediction of bone failure. We investigated peak forces during impact at the level of the impact surface the greater trochanter, and in the femoral neck, as well as fracture status. The fragility ratio (FR), which is the ratio between the peak femur force predicted with the linear bone model divided by the femur force predicted by the non-linear bone model, was used to quantify the reduction in injury risk.

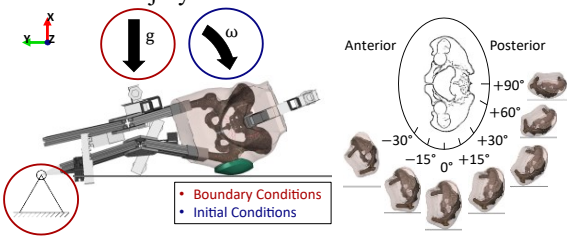

Figure 1: Left - initial and boundary conditions for the fall simulations demonstrated on a sample biofidelic FE model with our hip protector. Right - conceptual illustration of the simulated impact alignments.

Furthermore, we modelled a hip protector and calibrated its mechanical response to match the experimentally measured force-deflection response of commercially available hip protectors [4]. The hip protector model was implemented into the biofidelic FE model and its effectiveness tested under all impact conditions.

Results

Out of 56 impact conditions, we observed 15 femoral fractures in the unprotected falls compared to 9 with the hip protector. Lateral, 15° posterior, and 30° posterior impacts resulted in the highest number of fractures and fragility ratios (see Figure 2). No femur fractures were observed in the 60° and 90° posterior impacts. The mean force attenuation at the femoral neck due to the hip protector was 34.5% for low BMI subjects, but 5.1% for our high BMI subject and showed a small dependence on impact direction with posterior-lateral impacts showing the highest force attenuation.

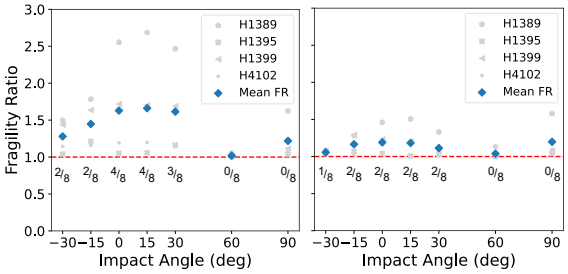

Figure 2: Fragility ratio (FR) vs. impact angles for all subjects. Mean FR depicted with blue diamonds. The fractions represent the number of fractures for each impact direction. Left - unprotected simulations. Right - simulations with hip protector.

Discussion

We found an equal number of fractures in lateral and 15° posterior impacts, suggesting that posterior-lateral falls are at least as dangerous as lateral falls. The hip protector attenuated femur forces for the impact directions that resulted in fractures (-30°, -15°, 0°, +15°, and +30°) but, with the exception of one simulation, only prevented fractures for impacts with low impact speed (2.1 m/s). Our results provide new insight into the risk of hip fracture under different impact conditions and into the efficacy of hip protectors in different types of falls.

References

1. Choi et al, Osteoporos Int, 26: 291-301, 2015.
2. Yang et al, J Bone Miner Res, 35: 1914-22, 2020.
3. Fleps et al, J Bone Miner Res, 34: 1837–50, 2019.
4. Laing et al, J Biomech, 44: 2627–35, 2011.

EXPERIMENTAL HEAD INJURY INVESTIGATION – HEAD IMPACT WITH LOOSE OBJECTS IN VEHICLE DURING VEHICULAR FRONTAL CRASH

Jaroslav Hruby (1), Brad Parker Wham (2), Zdenek Krobot (3), Marek Semela (4), Ales Vemola (5), Filip Wyrwol (6)

1. Brno University of Technology, Czech Republic; 2. Colorado University Boulder, United States of America; 3. University of Defense, Czech Republic; 4. University of Technology, Czech Republic, 5. University of Technology, Czech Republic, 6. Czech Technical University in Prague, Czech Republic

Introduction

Traffic accidents are widespread thanks to the increasing amount of traffic and related human factors such as cell phone calls during driving, stress situations caused by traffic jams, poor driver experience, others. If people are driving on a trip (business, vacation), they usually take several things like bags, drinks, food, and other objects. These objects are placed into the vehicle, and they are mostly unsecured. A typical human assumption "that nothing can happen" causes the unsecured state of several objects placed in the vehicle. Another factor is that people are in a "rush," and they do not have time to think about what these unsecured objects can do when a traffic accident happens. These objects act like projectiles and can hit vehicle occupants and cause serious injury to their bodies. The critical part which is taken into account for the experimental injury potential investigation described in this abstract is a human head. A series of experiments were performed to compute human head injury taking into account Head Injury Criterion (HIC). HIC can determine (from head acceleration response data) the probability of injury that can be caused by the interaction of loose partial elastic objects with the human head (rear part) during a frontal vehicular crash (traffic accident).

Methods

An experimental approach was chosen to determine the situations when the impactor (in our case, partially elastic object – impactor with soft rubber interaction part) interacts with the human head and causes injury. A potential head injury can be determined by the Head Injury Criterion - Eq (1), Eq (2), [2].

$$HIC=\max_{t_1,t_2}\left\{\left(\frac{1}{t_2-t_1}\int_{t_2}^{t_1} a\,dt\right)^{2.5}(t_2-t_1)\right\} \quad (1)$$

$$a=\sqrt{a_x^2+a_y^2+a_z^2} \quad (2)$$

Where a is resultant acceleration, t_2-t_1 is the time interval (15 [ms], [2]), and a_x, a_y, a_z are resultant acceleration components. If the HIC value reaches 1000 [1], it can be considered that the impact can be dangerous and it can harm the vehicle occupant (18% probability of severe head injury; 55% probability of serious head injury; 90% probability of moderate head injury [1]).

For the experimental investigation, purposes were used experimental equipment as follows (see Fig. 1): Self-developed airgun, including pressurizing system and safety valves; Self-developed partially soft rubber projectiles with different masses 0.5, 1, and 1.5 [kg]; Hybrid III 50th percentile male dummy for frontal impacts and DAQ system; Vehicle seats (without head restraint); Vehicle safety belts; DEWE A4 DAQ system. For signal analysis and HIC computations was used software NI DIADEM with Crash Analysis Toolkit.



Figure 1: Experimental Setup in Laboratory

Results

Experimental results generally show (see Figure 2 and Table 1) that the critical speeds of loose partially elastic objects (1 [kg] to 1.5 [kg]) in the vehicle during frontal vehicle impact are in an interval around 50 [km/h] (HIC = 1000 [-]). The results also show that: The increasing mass of the loose object has a significant effect on the critical object speed (mass increases = critical speed decreases; see Table 1); The length of the impulse is short (around 1.5 [ms]), and other tools must be used to verify the injury potential calculated through HIC (Blunt Criterion).

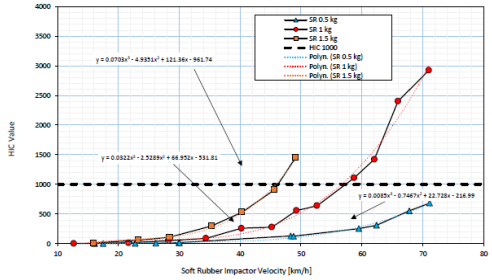

Figure 2: Experimental Results Using Partially Elastic Impactor

Impactor Velocity [km/h]	Resultant HIC [-] *Impactor 0.5 [kg]*	Impactor Velocity [km/h]	Resultant HIC [-] *Impactor 1 [kg]*	Impactor Velocity [km/h]	Resultant HIC [-] *Impactor 1.5 [kg]*
-	-	52.6	638	45.6	908
-	-	58.7	1108	49.1	1453

Table 1: Critical Speed of Partially Elastic *Impactor with Different Masses – Comparison with HIC Equal to 1000*

Discussion

The experimental approach described above does not consider head movement during the vehicular crash and head interaction with airbags and other vehicle parts. It is because the experimental setup will be difficult to build. HIC analysis will also be complicated – problematic to analyze the proper impulse response.

References

1. M. Mackay, Sadhana, 397-408, 2007.
2. B. G. Mc Henry, ATB Users Group, 2-8, 2004.

DEPENDENCY OF FEMORAL IMPACT FORCES ON POSTURE AND FALL DIRECTION ASSESSED WITH BIOFIDELIC FINITE ELEMENT MODELS

Giacomo Catani (1)(2), Alexander Baker (1), Pasquale Vena (2), Stephen J. Ferguson (1), Benedikt Helgason (1), Ingmar Fleps (1)

1. Institute for Biomechanics, ETH-Zürich, Zürich, Switzerland; 2. LaBS-Laboratory of Biological Structure Mechanics, Politecnico di Milano, Milano, Italy

Introduction

Hip fractures are a serious health concern for the elderly population, associated with high mortality, morbidity, and medical expenses. More than 90% of hip fractures result from a fall. Studies investigating the loading of the hip due to falls are mostly limited to sideways falls despite recent data indicating that posterior-lateral falls may be more dangerous than lateral falls [1]. Moreover, the body posture at impact can also affect fracture risk because femoral strength has been shown to be dependent on loading direction [2]. However, the influence of body postures on femoral loading is mostly unknown. Subject-specific explicit finite element models (FEMs) based on an inverted pendulum design can be used to investigate femoral loading and fracture risk for impacts that would be unethical for volunteer testing [3].

The aim of this study was to investigate the interaction between body posture, fall direction and femoral impact forces with biofidelic fall simulations.

Methods

Body alignment was investigated through four postural changes: leg rotation (LR), hip flexion (HF), knee flexion (KF) and pelvis rotation in coronal plane (PC). For each postural change, an existing biofidelic FEM mesh [3] (Fig 1) was morphed to four levels of rotation. Each level was simulated using three different fall directions (lateral fall, 30° posterior fall and -15° anterior fall). In total, 51 impact conditions were simulated.

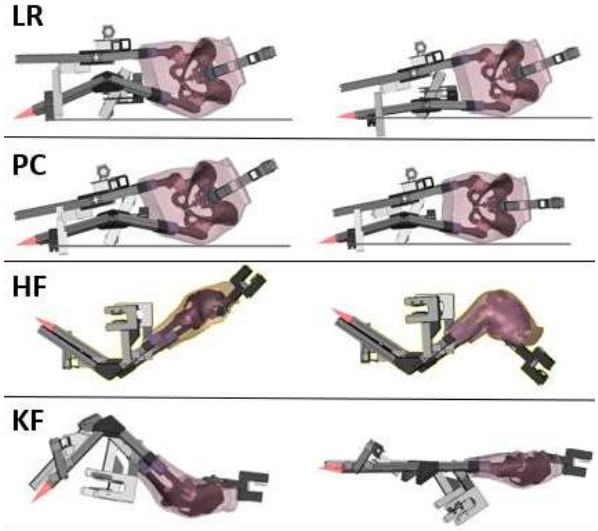

Figure 1: Biofidelic sideways fall FEM with postural changes indicated.

Heterogeneous linear material properties were applied to the bones. Gravity and an initial rotational velocity were applied to reach a target impact velocity of 3.07 m/s at the greater trochanter. Peak femur force (F_{femur}) was quantified between the articular cartilage of the pelvis and the femoral head.

Results

Peak femoral loading varied between 1.49 kN and 5.97 kN depending on impact condition. The average peak femoral forces in anterior, lateral, and posterior fall direction were 4.79kN, 5.51 kN, 3.14 kN, respectively. Impact posture affected peak femur forces more in posterior falls compared to anterior and lateral falls.

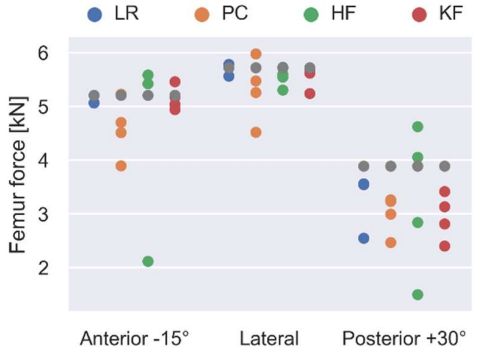

Figure 2: F_{femur} for the four postural changes and three fall directions. Gray markers show the unmorphed reference posture.

Discussion

Our results indicate that femoral loading can vary significantly depending on the impact posture and impact direction. Impact direction had a clear influence on femoral loading, indicating that the femur is less severely loaded in posterior-lateral falls. The influence of postural changes varied with different impact directions, which suggests an interaction between posture and fall direction. To our knowledge, this is the first study that investigates the combination of body posture and fall directions and their association with impact loads generated due to falls from standing height.

References

1. S. N. Robinovitch *et al.*, *Lancet*, 2013
2. T. P. Pinilla et al., *Calcif. Tissue Int.*, 1996
3. I. Fleps et al., *J. Bone Miner. Res.*, 2019

The brain injury mitigation effects of new helmet technologies in oblique impacts

Fady Abayazid[1], Ke Ding[1], Karl Zimmerman[1], Helena Stigson[2], Mazdak Ghajari[1]
[1] Dyson School of Design Engineering, Imperial College London, London, UK
[2] Folksam Insurance Group, Stockholm, Sweden

Introduction

New helmet technologies have been developed to improve the mitigation of traumatic brain injury (TBI) in bicycle accidents. However, their effectiveness under oblique impacts, which produce more strains in the brain in comparison with vertical impacts adopted by helmet standards, is still unclear. Here we used a new method to assess the brain injury prevention effects of 27 bicycle helmets in oblique impacts, including helmets fitted with new technologies dedicated for impact management. We tested whether helmets fitted with the new technologies can provide better brain protection than conventional helmets by assessing mechanical strain in several key anatomical brain regions in three different oblique impact conditions.

Methods

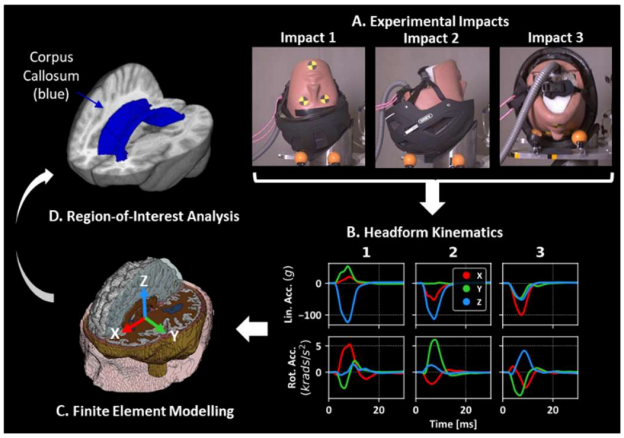

Figure 1: Experimental and Computational Methods

27 commercially available bicycle helmets were selected from the European market. Four new technologies were investigated here and compared with 8 conventional helmets which served as controls. The tested technologies were low friction slip-layer named 'multi-directional impact protection system' (MIPS) [1], a 'wavy' cellular liner called WaveCel [2], add-on shear pads called SPIN, and finally, we included a radical technology, the airbag helmet Hövding 3.0 [3].

Each helmeted headform was dropped onto a 45º inclined anvil at 6.3 m/s at three locations, with each impact location producing a dominant head rotation about one anatomical axes of the head. A detailed computational model of TBI [4] was used to determine strain distribution across the brain and in a key anatomical region – the corpus callosum (Fig. 1).

Results and Discussion

Our results show that most helmets with new technologies tested here have the potential to reduce maximal strain in oblique impacts in comparison to conventional helmets. Nonetheless, a large variation in the strain can be seen across the helmets, from 0.01 with the airbag helmet to 0.19 with a conventional helmet. Strain was within normal ranges in all MIPS helmets for impact 1. In impacts 2 and 3, strain was significantly lower in 60% of MIPS helmets (2: 35 – 66%, 3: 23 – 51%). Likewise, strain was lower in the WaveCel helmet in impact 2 (59%), but not in impact 1 or 3. Strain was also significantly reduced in impact 3 in the SPIN 1 helmet, however no significant reductions were observed for the other impacts nor in the SPIN 2 helmet. The airbag helmet significantly reduced the strain in all three impacts irrespective of analysis duration (Fig. 2).

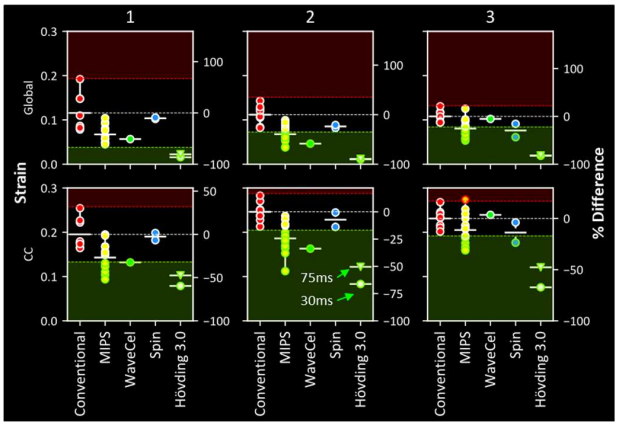

Figure 2: 90th percentile strain in whole brain and corpus collosum resulting from each helmet impact grouped by technology. Green and red margins represent significant improvement or deterioration in performance respectively in comparison to conventional helmets.

In conclusion, incorporating different impact locations in future oblique impact test methods and designing helmet technologies for the mitigation of head rotation in different planes are key to reducing brain injuries in bicycle accidents

Acknowledgments

We would like to acknowledge the financial support ICL's PhD Scholarship and Folksam Insurance Group.

References

1. Halldin, P., Aare, M., Kleiven, S. & von Holst, H. Improved helmet design and test methods to reduce rotational induced brain injuries. 1–8 (2003).
2. Bliven, E. *et al.* Evaluation of a novel bicycle helmet concept in oblique impact testing. *Accid. Anal. Prev.* **124**, 58–65 (2019).
3. Kurt, M., Laksari, K., Kuo, C., Grant, G. A. & Camarillo, D. B. Modeling and Optimization of Airbag Helmets for Preventing Head Injuries in Bicycling. *Ann. Biomed. Eng.* **45**, 1148–1160 (2017).
4. Ghajari, M., Hellyer, P. J. & Sharp, D. J. Computational modelling of traumatic brain injury predicts the location of chronic traumatic encephalopathy pathology. *Brain* **140**, 333–343 (2017).

A GENERIC MATHEMATICAL FORMULATION FOR SOFT TISSUE INJURY SEVERITY IN IMPACT SCENARIOS

Christophe Bastien (1); Clive Sturgess (2); Huw Davies (1); Joseph Hardwicke (3)

1. *Coventry University, Institute for Future Transports and Cities, Coventry, UK;*
2. *University of Birmingham, Department of Mechanical Engineering, Birmingham, UK*
3. *University Hospital of Coventry and Warwickshire, Coventry, UK*

Introduction

Road traffic accidents are catastrophic events leading to serious injury and in some cases fatality. The dichotomy is that traumatic injuries, as a result of road traffic collisions are assessed using the Abbreviated Injury Scale (AIS), which is a measurement of the probability of death, whilst the engineering tools available to support the understanding of injury causation rely on engineering measurements of stress and strain. Further to this, the problem of ageing is not adequately dealt with using existing engineering tools. The research proposes the development of a generic mathematical injury severity model, based on Peak Virtual Power (PVP) [1], to establish relationships between AIS, ageing and collision speed.

Method

A mathematical model is derived, tested and compared against collision cases where the Postmortem (PM) is known. Injuries are non-reversible phenomenon and can be captured by the Second Law of thermodynamics, relating to degeneration and decay. By using the Clausius-Duhem inequality, from the rate dependent form of the 2nd Law (Equation 1), it was demonstrated that AIS was proportional to the maximum rate of entropy inside any soft tissue. This mathematical response is called Peak Virtual Power (PVP) [1] and is illustrated in Figure 1.

$$\sigma : \dot{\varepsilon} - \rho\left(\dot{f} + s\dot{T}\right) - \frac{1}{T} q.\nabla T \geq 0$$

Equation 1: Clausius-Duhem equality [1]

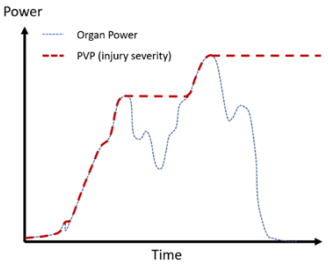

Figure 1: Evolution of injury severity against time [2]

An algebraic formulation of PVP is then derived, expressing AIS as a function of impact speed, ageing, contact stiffness, as well as contact area. It was assumed that human mechanical properties degrade as people age, hence these properties were scaled accordingly. A typical injury severity brain trauma response, based on the mathematical derivation, is illustrated in Figure 2, representing the power needed to cause AIS 4 as function of age and impact speed. Figure 2 confirms that less power is required to injure an older person than a younger one, i.e. as observed in real life [2].

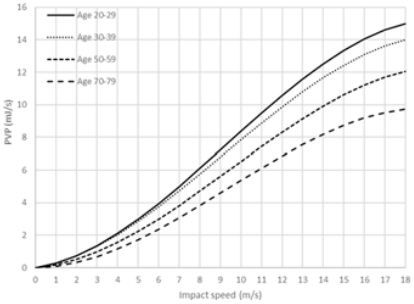

Figure 2: Brain White Matter (DAI) Injury response as a function of age [2]

The four accidents are then reconstructed using Finite Element (3 pedestrian collisions and 1 fall); their numerical AIS predictions, based on the mathematical model, are compared to the AIS recorded from the Post-Mortem.

Results

In 8 organ blunt trauma computer predictions using the mathematical theory derived, 7 were exact AIS predictions and location, while one was slightly under predicting the PM outcome. It this study the standard maximum principle strain (MPS) method, used to detect injuries was inconclusive (1 correct prediction from 7).

Discussion

From this study, it can be concluded that the PVP method, based on theoretical physics, is a good candidate to capture injury severity and location in soft tissues. More data is nevertheless required to confirm whether this method is universal.

References

[1] Sturgess C., et al. (2001) “The relationship of AIS to peak virtual power”. Annual proceedings / Association for the Advancement of Automotive Medicine. 45. 141-57

[2] Bastien, C., et al. (2020) “Computing Brain White and Grey Matter Injury Severity in a Traumatic Fall”, Journal of Mathematical and Computational Applications. Math. Comput. Appl. 2020, 25(3), 61

Acknowledgments

Road Safety Trust (project RST 65 _3_2017), UK Police Force and the UK Coroners.

NUMERICAL OPTIMIZATION OF SCREW POSITIONING OF LOCKING PLATE IMPLANTS ON PROXIMAL HUMERUS FRACTURES

Emin Sünbüloğlu[1], Cemre Yavuz[1], Volkan İgde[1]

1 Department of Mechanical Engineering, Istanbul Technical University

Introduction

Proximal Humerus fractures are one of the most common fractures that affect the mobility of the upper arm and the shoulder joint [1]. Although some of the Proximal Humerus fractures do not require surgical intervention for healing, locking plates are the most common implants for the fixation of them to maintain stability during the recovery period [2]. However, though there have been many improvements in the design and technology, complications due to the plate still occur [3]. Two screws are initially placed at 22,5 degrees' in the sagittal plane with respect to the vertical axis. To overcome this issue, an optimization process to help to prevent complications due to the screw insertion direction must be performed.

Methods

The geometric model of the Proximal Humerus, the locking plate, and the screw is created and then meshed for the analysis. The meshes are generated with different aspect ratios to maintain their quality after morphing. Two screws are initially placed at 22,5 degrees apart. A morphing method without re-meshing is developed to vary the angle of the right and the left screws between 0 to 45 degrees independently. These shapes are created to be used in the optimization process as the design variables to the Global Response Surface algorithm, where the aim is to minimize the response which is the maximum Von Mises stress values at critical regions. The load cases are created according to the muscle attachments as in Figure 1 and combined to form seven different load cases as shown in Table 1. Linear static analysis is performed to see the stress concentration areas on the Proximal Humerus.

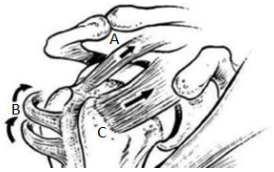

Figure 1: Demonstration of the muscle forces applying to the Proximal Humerus.

Load Case	Force Combinations (as to Fig.1.)
1	Force A
2	Force B
3	Force C
4	Force A+B
5	Force A+C
6	Force B+C
7	Force A+B+C

Table 1: Load Cases and Force Combinations.

Load Case	Optimized Stress	Left Screw Orientation	Right Screw Orientation
1	38,1	36,9	45,0
2	21,0	45,0	33,3
3	90,5	28,1	28,8
4	52,9	45,0	29,7
5	69,8	24,7	45,0
6	98,1	25,4	36,9
7	82,0	36,9	45,0

Table 2: Optimization Results for Proximal Humerus.

Results

The results indicate the angles of the screws which result in minimum stress concentration on the Proximal Humerus as shown in Table 2. It can be inferred that that one can select and perform dynamic or semi-rigid unilateral fixation based on surgical advantages rather than biomechanical considerations. For both left and right screws, the angle placement between 22,5 to 45 degrees in the sagittal plane with respect to the vertical axis results in minimized stress concentrations.

Discussions

Considering the optimized output using all proposed load cases, it can be concluded that the angular position of the screw helps to decrease the maximum stresses on the bone, which is an outcome that is expected to aid the patients during the post-op healing process and will help to decrease the complication rates caused by the instruments with correct screw positioning.

In further studies, some open points, such as combining the search of the screw angles combined with the axial positioning of the screws can be sought. The elastic modulus changes and bone resorption estimates can be input as a parameter to the optimization algorithm. Considering material parameters depending on the patient's age to achieve patient-specific screw positioning of Proximal Humerus Locking Plates is a possibility.

References

1. Iyengar et al, Phys Sportsmed, 39:52–61, 2011.
2. Schumaier et al, Geriatr Orthop Surg, 9, 2018.
3. Harshwardhan et al, Int J Res Orthop, 5: 936, 2019

Acknowledgements

The authors thank Prof. Dr. Ata Can Atalar (Department of Surgical Sciences, Orthopedics, and Traumatology, Acıbadem University, İstanbul, Turkey) for his suggestions and medical support.

THE INFLUENCE OF CORONAL SPLITS OF COMPLEX TIBIAL PLATEAU FRACTURES ON IMPLANT STRESS DISTRIBUTIONS

Shabnam Samsami (1,2), Sven Herrmann (3,4), Robert Pätzold (3,5), Martin Winkler (3), Peter Augat (3,4)

1. Department of Mechanical Engineering, Imperial College London, South Kensington Campus, London, UK*; 2. Department of Orthopaedics, Physical Medicine and Rehabilitation, University Hospital, LMU Munich, Munich, Germany; 3.* Institute for Biomechanics, Berufsgenossenschaftliche Unfallklinik*, Murnau, Germany; 4. Institute of Biomechanics, Paracelsus Medical University, Austria; 5. Department of Trauma Surgery, Trauma Center Murnau, Murnau, Germany*

Introduction

Bi-condylar tibial plateau fractures with the highest frequency in 40-60 years old accounts for 35% of all tibial plateau fractures [1]. Despite the crucial role of posteromedial fragments in the selection of fixation methods [2], there is still a lack of understanding about the effects of coronal fracture lines on load sharings within bone-implant structures. This study aimed to develop validated finite element (FE) models to analyze the impact of coronal fracture lines on stress distributions within fixation constructs.

Methods

FE models with (Fracture C) and without (Fracture H) a coronal fracture were developed in ANSYS based on CT scans of 4th-generation tibial Sawbones and CAD data of Stryker AxSOS Titanium locking plates (Figure 1.A). Corresponding fracture samples were also prepared. To simulate experimental loading, the top surface of the load applicator that included femur condyles of unilateral knee replacements to distribute forces with a 60/40% ratio on the medial and lateral tibia plateaus was coupled to a remote point with vertical translational and sagittal rotational degrees of freedoms. Axial 250-N forces were applied at remote points (Figure 1.B). Screw threads were omitted for bone-screw interfaces. All materials were assumed to be homogenous, isotropic, and linear elastic. Following convergence tests, about 845,000 quadratic tetrahedral elements were considered for meshing. For validation purposes, mechanical tests consisted of three static ramps up to 250N were executed to measure experimental data regarding the global axial stiffness and marker displacements. Von-Mises stresses in the plate and screws were compared between fractures.

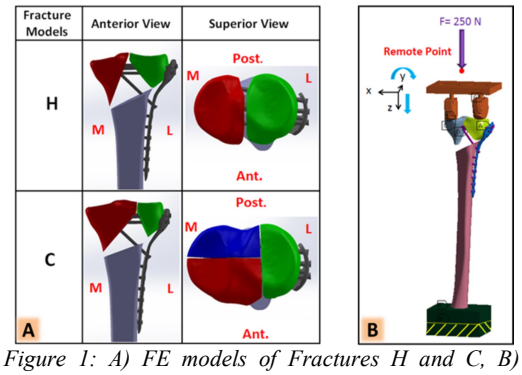

Figure 1: A) FE models of Fractures H and C, B) Loading and boundary conditions

Results

Considering Root-Mean-Square and relative errors of marker displacements and axial stiffness, FEA of Fracture C showed 3-8% deviations from the mechanical tests, while Fracture H's was 3-18% less accurate. Regression curves of marker displacements demonstrated slopes of 0.94-1.08 and R^2 of 0.99 for both fracture models. Von-Mises stress distributions of the inner and outer surfaces of the plate indicated that for Fracture C peak stresses, which occurred around the proximal-inferior and proximal-threadless holes, were 55-65% higher than Fracture H's, observed around the kick-stand hole (Figure. 2). The Kick-stand screw of Fracture C revealed a 65% higher stress than Fracture H's.

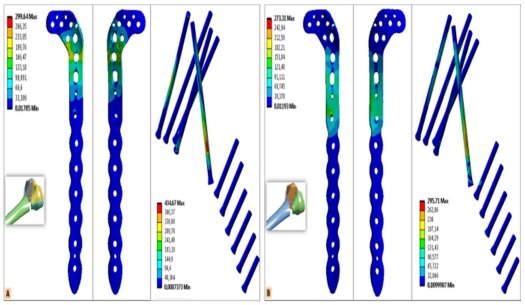

Figure 2: Von-Misses stress contours within locking plates and screws: A) Fracture C, B) Fracture H

Discussion

FEA of both fractures revealed acceptable accuracies, while Fracture C's demonstrated superior agreement with experimental outcomes than Fracture H's. Von-Mises stress distributions demonstrated that the coronal fracture line resulted in a shift in stress concentration areas from the middle section of the plate to the proximal part. Also, the von-Mises stress of the kick-stand screw as the most load-bearing screw was doubled. This suggests that the potential fatigue failure points of lateral locking plates and screws depend on the fracture morphology. Therefore, a clinically-relevant fracture model such as Fracture C should be considered to accurately assess fixation methods and treatment options.

References

1. Elsoe et al, Orthopedics, 38: e780-786, 2015.
2. Barei et al, J.Orthopaedic Trauma, 22:176–182, 2008.

DEVELOPMENT OF A NEW CONCEPT FOR 3D-PRINTED ACETABULAR CUPS SUPPORTED BY FINITE ELEMENT ANALYSIS

Silvia Pianigiani, Fabio Alemani, Aldo Toni
Adler Ortho, Milano, Italy

Introduction

A new concept of less stiff acetabular cup was developed based upon the necessity of obtaining a dome shape made of beams and hole rings connected to a full solid equatorial region. The surface and the region between the beams and hole rings are made of porous titanium. The cobweb cup is intended for index and revision surgery; it presents a spiral hole layout which optimizes the hole/bone contact in case of severe bone loss during revision acetabular reconstruction just by rotating and templating the cup trial before the final cup insertion.
However, a such structure could induce the suspect of a weak mechanical resistance.
For this reason, the aim of this research study is to optimize the number of holes and beams thickness in order of obtaining a mechanical resistant acetabular cup.
In detail, FEA analysis supported the phase of prototyping up to the final design that was finally experimentally tested.

Methods

The worst configuration, was determined by means of finite element analysis (FEA) on size 52 group B. Since the cup can be coupled with a metallic or plastic insert, the effect of the insert was first checked. Then, the most affecting load direction was detected after different simulated positions (Figure 1). The applied load is 3300N. The cup is made by rigid titanium (E=110 GPa, ν=0,32) and porous titanium (E=1,515 MPa, ν=0,39). Friction coefficient between the cup and the insert is μ=0,24 for the metal insert and μ=0,35 for the plastic insert.

Results

For the metal insert, that showed the worst results in terms of mechanical stress, also the most affecting load direction was identified. Once detected that the most stressing boundary conditions, the preliminary design approached 300 MPa of stress, over the estimated limit for the material in use. Thus, the acetabular cup was changed introducing round edges and corners for every link between holes and beams and a higher full thick equatorial region with the aim of decreasing the monitored stress under 200 MPa, the mechanical stress resistance of the materials in use.
Figure 2 shows a comparison between the first and the final design, while Figure 3 shows the final stress for the cobweb structure and porous regions.
Thanks to all the iterative modifications, the last version of the design proofed by FEA was produced and experimentally tested with success under the same boundary conditions: no damage was ever detected in 3 samples tested at 5 million cycle fatigue tests.

Discussion

This study shows a recent example of the use of FEA for helping in prototyping a new concept of acetabular cup. Despite of the dome-web structure, mechanical resistant was proved and confirmed by experimental tests.

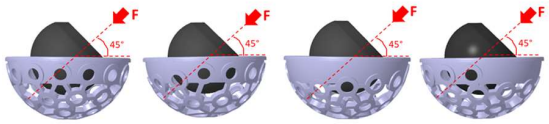

Figure 1: different analyzed positions and load direction (the cup model is presented only for the rigid support)

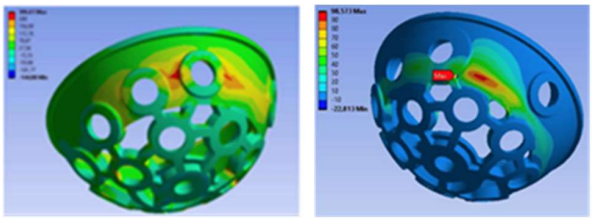

Figure 2: comparison between first design and the final development obtained after the optimizations based upon FEA results

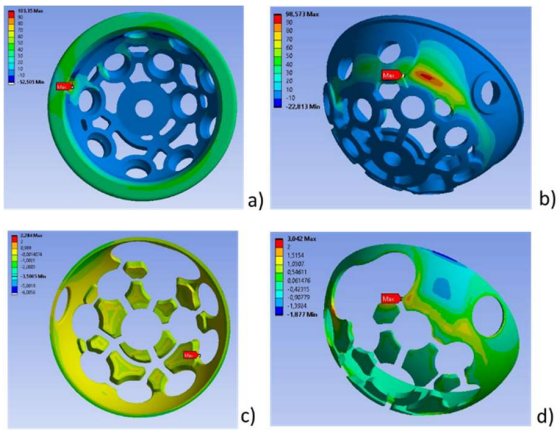

Figure 3: Results for coupling with metal (a,c) or plastic (b,d) insert. Figure a and b show results for the rigid part of the cup while figure c and d the results for the porous areas

SECONDARY STABILITY AND DEBONDING OF OSSEOINTEGRATED ACETABULAR CUP IMPLANTS

Katharina Immel (1,2), Vu-Hieu Nguyen (3,4), Roger A. Sauer (1,5), and Guillaume Haiat (2)

1. Aachen Institute for Advanced Study in Computational Engineering Science, RWTH Aachen University, Templergraben 55, 52056 Aachen, Germany

2. CNRS, Laboratoire Modélisation et Simulation Multi Echelle, MSME UMR 8208 CNRS, 61 Avenue du Général de Gaulle, 94010 Créteil Cedex, France

3. Université Paris-Est, Laboratoire Modélisation et Simulation Multi Echelle, MSME UMR 8208 CNRS, 61 Avenue du Général de Gaulle, 94010 Créteil Cedex, France

4. Université Gustave Eiffel, MSME, 77454 Marne-la-Vallée, France

5. Faculty of Civil and Environmental Engineering, Gdańsk University of Technology, ul. Narutowicza 11/12, 80-233 Gdańsk, Poland

Introduction

Cementless implants have become more and more common for joint replacement surgery. These implants achieve initial stability during surgery, while secondary stability is obtained by bone growing around and into the porous surface of the implant, a process called osseointegration. As debonding of the bone-implant interface due to aseptic loosening and insufficient osseointegration still occur and may have dramatic consequences, predicting implant stability and failure is one of the major goals in implant research.

In most computational models of the bone-implant interface, frictionless contact, Coulomb's friction or perfectly bonded contact conditions are used. However, frictionless and pure Coulomb's friction contact are strong assumptions for the contact behavior between the rough and porous bone and implant surfaces and is not able to model bonding or properly represent the nonlinear contact behavior. Perfectly bonded contact cannot model debonding of the interface and does not account for imperfect osseointegration phenomena [1]. The aim of this work is to develop a contact model that can account for the effect of partial or total bonding due to osseointegration phenomena.

Methods

In this work we model the long-term stability of an osseointegrated acetabular cup implant. The influence of different factors on the long-term stability, such as the degree of osseointegration, distribution patterns of bone tissue on the implant, primary stability, interference fit, and bone stiffness, are studied by considering various osseointegration scenarios.

Each simulation consists of three phases: 1. The insertion phase where the implant is pushed into the hip cavity until a vertical reaction force of 2500 N is reached. 2. The osseointegration phase, where the bone-implant contact ratio is varied between 0 and 100%. 3. The removal phase, where the osseointegrated implant is removed in either a) normal direction, b) tangential direction or c) through torque, in order to assess the implant stability.

The contact model consists of a modified Coulomb's friction law, which can model the tangential debonding of (partially) osseointegrated implants [2]. The friction coefficient $\mu := \mu(\phi)$ is modeled as a function of a state variable ϕ. For every point on the bone-implant interface, this state variable can depend, for example, on the accumulated deformation of the interface, the initial bonding state (i.e. osseointegration or no bonding), and the deformation threshold. The model is extended with a cohesive zone model to account for debonding in normal direction. Furthermore, this model is embedded into an existing enriched finite element contact framework for efficient contact treatment [3].

Results

The stability of the implant, defined by the maximum pull-out force or torque, is determined for different parameter configurations and loading conditions. It is shown that initial stability and the degree of osseointegration, have a significant influence on implant secondary stability and thus the surgical success. Furthermore, implant stability differs depending on the loading condition.

Discussion

Numerical modeling allows controlled analyses of different parameters to determine an optimal configuration of implant and surgery technique for a specific patient and allow for prediction of long-term implant stability. In the future, this model can be coupled with bone remodeling and osseointegration algorithms to accurately account for the osseointegration of implants and increase the accuracy of the prediction of long-term stability.

References

1. Caouette et al, Proc Inst Mech Eng H, 227:209-220, 2013.
2. Immel et al, Biomech Model Mechanobiol, 19:1091–1108, 2020.
3. Corbett & Sauer, Comp Meth Appl Mech Engng, 275:55-75, 2014.

BIOMECHANICAL ANALYSES OF MANDIBULAR FRACTURES TO SUPPORT THE DESIGN OF NOVEL FIXATION SYSTEMS

Vincenzo Orassi (1)(2)(3), Carsten Rendenbach (2), Sara Checa (1)

1. Julius Wolff Institut, Charité – Universitätsmedizin, corporate member of Freie Universität Berlin, Humboldt-Universität zu Berlin and Berlin Institute of Health, Berlin, Germany; 2. Department of Oral and Maxillofacial Surgery, Charité – Universitätsmedizin, corporate member of Freie Universität Berlin, Humboldt-Universität zu Berlin and Berlin Institute of Health, Berlin, Germany; 3. Berlin-Brandenburg School for Regenerative Therapies, Berlin, Germany

Introduction

Mandibular fractures and mandibular resections due to tumors or osteonecrosis are commonly fixated using titanium plates and screws. However, the limitations of current fixation techniques make it necessary to develop new methods to improve the healing outcomes [1].

Animal models are commonly used for testing new designs and biomaterials for bone fixation. However, the choice of a reliable preclinical model is not straight-forward and several drawbacks and complications may occur due to unfitting biomechanical conditions compared to humans.

This study aimed to develop a computational framework to investigate the biomechanics of mandibular bone fixation. More specifically, we investigated 1) the reliability of the sheep mandible as a pre-clinical model for testing fixation devices and 2) the effect of the fixation design on the stability at the fracture site.

Methods

3D finite element models of the human and sheep mandibles were developed. In both models, physiological loading conditions were applied to simulate several clenching tasks. Maximum muscle forces in sheep were estimated by quantifications of the masticatory muscle physiological cross-sectional areas from MRI scans [2]. Fractures in the human and sheep mandibular bodies and the sheep diastema were simulated (Fig. 1a-1c).

Moreover, to investigate the effect of plate design (geometry and biomaterial) on the biomechanics of the fractured human mandible, post-operative muscle forces were applied and fractures in the symphysis, body, angle, and ramus regions were simulated (Fig. 1d-1g). Fracture fixation was performed by using devices in titanium, magnesium, and PLA, in two different plate thicknesses (traditional 1 mm and alternative 1.5 mm).

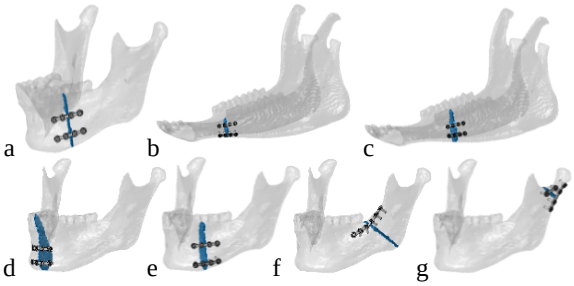

Fig. 1: (a) Human and (b) sheep body fracture, and (c) sheep diastema fracture; (d) symphysis, (e) body, (f) angle, and (g) ramus fractures in the human mandible.

Results

Maximum bite forces of 500 N and 420 N were predicted in humans and sheep, respectively. Mechanical strains within the fracture gap differed considerably between humans and sheep (Fig. 2). Similar stresses within the implants were found in the sheep diastema and the human body fracture scenarios.

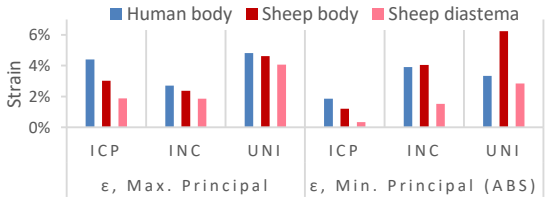

Fig. 2: Tensile and compressive strains (ε) within the fracture gaps during intercuspal (ICP), incisal (INC), and unilateral (UNI) clenching in humans and sheep.

A 100 N post-surgery bite force was predicted in humans. Strains within the fracture gap ranged between 0.3-2.3%, 0.6-3.0%, and 1.7-10.4% by using titanium, magnesium, and PLA plates, respectively (Fig. 3). Plate thickness did not remarkably influence the strains within the fracture.

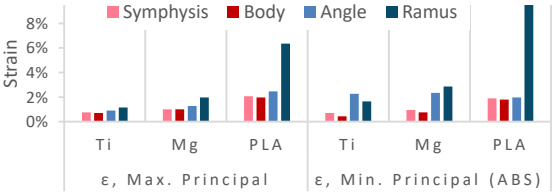

Fig. 3: Tensile and compressive strains within the fracture gap for fixation plates made of titanium (Ti), magnesium (Mg), and PLA during UNI clenching.

Discussion

Our results suggest that: (1) despite lower mechanical properties, magnesium seems to be a good alternative to titanium for mandibular fracture fixation; (2) increasing magnesium plate thickness seems not necessary; (3) the sheep diastema can be considered a valid biomechanical pre-clinical model to test fixation devices; however, studying the influence of fracture fixation on the bone healing in sheep must be done carefully.

Future studies will use this computational framework to investigate the influence of fracture fixation on the biomechanics of reconstructed mandibles.

References

1. Robey et al., Plastic and reconstructive surgery, 122.6: 1733-1738, 2008.
2. Nelson, PhD Thesis. University of British Columbia, 1986.

BIOMECHANICS OF STRUCTURAL ALLOGRAFT IMPACTION IN HIGH TIBIAL OSTEOTOMY: A FINITE ELEMENT STUDY

Alexander Meynen (1,2), Florian Vanquickenborne (1), Stijn Bartholomeeusen (3), G. Harry van Lenthe (4), Lennart Scheys (1,2)

1. Institute for Orthopaedic Research and Training, KU Leuven, Belgium; 2. Division of Orthopaedics, University Hospitals Leuven, Belgium; 3. Department of Orthopaedic Surgery, AZ Herentals, Belgium;4. Biomechanics Section, KU Leuven, Belgium

Introduction

High tibial osteotomy (HTO) is an effective and well-established surgical procedure for treating medial compartment osteoarthritis (OA) of the knee joint. The primary concern associated with HTO procedures is related to delayed recovery after surgery as bone healing after HTO requires a mechanically stable environment and needs time. In a recent clinical study, the use of an impacted patient-specific femoral allograft resulted in high early mobility and good short-term clinical outcome[1]. These results were suggested to be related to an improvement in construct stability and the successful redistribution of axial forces through the allograft. However, biomechanical data supporting this hypothesis are lacking. Therefore, this study focused on quantifying the effect of an impacted bone graft on the stability of the osteotomy site and the loading of the fixation plate.

Methods

Five patient-specific finite element models of the proximal tibia were created from computed tomography (CT) images at three-month follow-up. Each CT scan was imported in Mimics (v23.0, Materialise, Leuven, Belgium). The tibia, structural allograft, plate and screws were manually segmented and converted to 3D models. In order to investigate the influence of the graft, two models were constructed for each patient; one with the structural allograft in-situ and one where the allograft was omitted from the model. The resulting 3D models were converted to finite element meshes with linear tetrahedral elements. Subject-specific material properties based on the Hounsfield units were assigned to the tibial bone and femoral allograft. The titanium fixation plate and screws were assigned homogeneous linear elastic properties.

A gender-specific knee contact load of three times bodyweight was applied as a distributed force on the tibia plateau. Furthermore, a downward intervention-induced load of 200 N was applied at the edge of the superior tibial fragment, simulating the effect of the elongation of the knee ligaments and the extension of the hinge region as a result of the impaction. A frictional contact was defined at the contact interfaces between tibia, graft, screws and plates. Motion of the distal part of the tibia was fully constrained. The von Mises and principal stresses were used to compare the loading of the plate between the models with and without allograft.

The osteotomy stability was quantified as the displacement in response to the knee contact load of the superior to the inferior part at the cortical surface of the osteomy cut.

Results

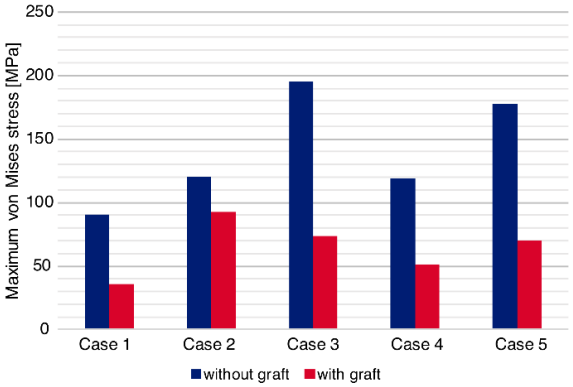

Figure 1: Maximum von Mises stress in the plate in each of the five cases. It decreased from 140.6 MPa to 64.7 MPa, an average reduction of 54 %.

On average, the maximum tensile and compressive stresses in the fixation plate decreased with 55% and 54%, respectively with grafting. The average maximum relative movement in the osteotomy cut decreased from 147.1 µm to 44.8 µm, a reduction of 70 %.

Discussion

This study investigated the biomechanical influence of applying impacted structural allografts in HTO using subject-specific finite element models. Analysis of the von Mises stresses indicates that grafting results in a substantial fraction of the load being shared with the graft and tibia. This decreases stress-shielding of the allograft region and, therefore, promotes callus formation and bone healing. Furthermore, the use of an impacted structural allograft significantly improves the mechanical stability of the osteotomy site evident from the reduced movement.

References

1. Van Genechten et al, Knee Surg. Sports Traumatol. Arthrosc., 28(12):3747-3757, 2020

Acknowledgements

A.M. is a strategic basic research PhD fellow at FWO (Research Foundation – Flanders) grant no. 1SB3819N.

CAN FEMOROPLASTY REDUCE FRACTURE RISK IN CANCER PATIENTS WITH FEMORAL BONE METASTASES?

Amelie Sas (1), Hazem Wafa (2, 3), Esther Tanck (4), An Sermon (2, 5), G. Harry van Lenthe (1)

1. Biomechanics Section, 2. Department of Development and Regeneration, KU Leuven, Belgium;
3. Division of Orthopaedics, 5. Department of Traumatology, UZ Leuven, Belgium;
4. Orthopaedic Research Laboratory, Radboudumc, Nijmegen, The Netherlands

Introduction

Prophylactic treatment is advised for metastatic bone disease patients with a high risk for fracture. Mechanical stabilization can be provided through femoroplasty, a minimally invasive procedure where bone cement is injected into the lesion. However, uncertainty remains whether femoroplasty provides sufficient mechanical strength to the weight-bearing femur [1]. The goal of this study was to evaluate the mechanical effectiveness of femoroplasty through finite element (FE) analysis on a dataset of cancer patients with femoral metastases.

Methods

Dutch patients who were referred for radiotherapy of bone metastases in the femur, were asked to participate. A total of 89 patients (55 male and 46 female, age 39-98), with 101 femurs that were affected with bone metastases were included. During a 6 months follow-up period, pathological fractures occurred in 13 femurs.
Quantitative CT-based FE models were generated for all patients according to a previously validated protocol [2]. Failure load was defined as the maximal reaction force in the loading direction and was normalized for body weight (BW). A critical threshold was defined for the FE failure load in order to classify femurs as having a high or low fracture risk. If the failure force was lower than the threshold, a high fracture risk was assigned. The threshold was chosen that maximized the sum of the sensitivity and specificity when comparing against the actual occurrence of fracture.
For the FE simulation of femoroplasty, the dataset was restricted to 34 femurs with lytic lesions in the proximal femur that were considered eligible for femoroplasty. The lesions were manually segmented from the CT scans. The assumption was made that bone cement would fill the complete lesion as well as the trabecular bone present within 4 mm of the lesion [3]. The FE failure load before and after treatment were compared and evaluated against the critical threshold.

Results

The critical threshold for classification between low and high fracture risk was 8.9 x BW, resulting in a sensitivity of 92% and a specificity of 66%.
Femoroplasty increased the failure load for lesions located in the head/neck of the femur (N = 16) (Fig. 1A). The high risk femurs that actually fractured during follow-up (orange dots), all moved towards a low fracture risk after treatment. In contrast, for the lesions located in the trochanteric region (N = 18), femoroplasty showed almost no effect on the failure load (Fig. 1B). In all 34 femurs from both groups, the FE models predicted femoral neck or subcapital fractures.

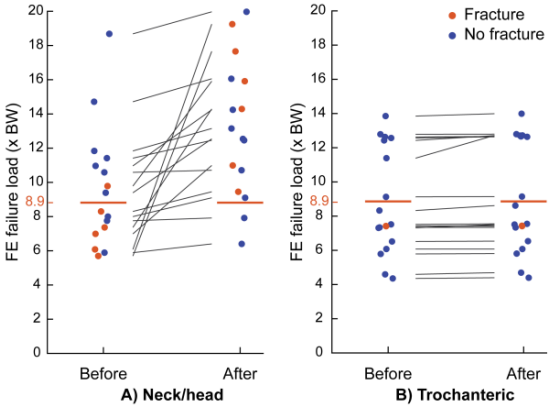

Figure 1: Failure load predicted by FE before and after simulated femoroplasty for lesions located in the head/neck (A) and the trochanteric region (B). The central lines connect points of the same femur.

Discussion

Our data demonstrate that femoroplasty of head/neck lesions can substantially increase failure load and decrease fracture risk. In contrast, femoroplasty of trochanteric lesions showed almost no effect on the failure load. This can be explained by the observation that in these cases fracture occurred through the femur neck, instead of through the lesion, indicating that the lesion was not the critical weak spot. Consequently, cement augmentation of these lesions will not increase the failure load [3]. An important limitation of this study was the exclusion of patients who had been treated with prophylactic surgery, thereby excluding cases with an expected high fracture risk.
To conclude, the results indicate that femoroplasty may be effective to reduce fracture risk in several metastatic bone disease patients with critical lesions in the proximal femur. Yet, future studies on datasets including more high risk lesions are required.

References

1. Dechamps et al., J Vasc Interv Radiol, 23:1311-1316, 2012
2. Sas et al., Bone Reports, 12 :100263, 2020
3. Sas et al., J Mech Behav Biomed Mat, 104:103648, 2020

Acknowledgements

This project was funded by the Research Foundation Flanders FWO (application number 1S34218N; Amelie Sas).

TOWARDS OPTIMIZATION OF PLATE FRACTURE FIXATIONS AT THE DISTAL RADIUS: USING FEA TO REDUCE THE NUMBER OF SCREWS

Alexander Synek (1), Sebastian F. Baumbach (2) Dieter H. Pahr (1,3)

1. Institute of Lightweight Design and Structural Biomechanics, TU-Wien, Austria;
2. Department of General, Trauma and Reconstructive Surgery, LMU Munich, Munich, Germany
3. Division Biomechanics, Karl Landsteiner University of Health Sciences, Krems, Austria

Introduction

Finite element analysis (FEA) has proven useful to predict the biomechanical behavior of intact bone and bone-implant constructs [1]. A potential benefit of FEA is that bone-implant constructs could be optimized by testing a very large number of different implant configurations. A major drawback is that generating models with sufficient level of detail often requires manual intervention, which limits the number of implant configurations that can be tested. Here, we use a previously developed FEA workflow to automatically vary the number of screws used in plated distal radius fractures (DRF) and investigate if fewer screws could be used, as this would save treatment costs and reduce complications. In particular, the effect of the number of screws in volarly plated DRF on (1) axial stiffness and (2) peri-implant principal strains shall be evaluated.

Methods

16 subject specific FEA models of plated DRFs were created following a previous study [1]: High resolution computed tomography scans of the intact bones were used to obtain bone geometry and local bone density, and AO23-A3 fractures treated with volar locking plates with 6 distal screws were created virtually (Fig. 1). These models were previously compared to experimental data [1] (Stiffness FEA vs. experiment: R^2= 0.8) and served as the baseline for this study.

41 different implant configurations were created for each of the 16 subject specific models and loaded with an axial force of 100 N. The configurations comprised all possibilities for removing 1 to 3 distal screws from the implant system (Fig. 1). Two biomechanical parameters were assessed for each of the resulting 41*16=656 FEA models: (1) Axial stiffness to quantify resistance against quasi-static external loading and (2) compressive principal strains, averaged in the peri-implant region around the distal screws, as a surrogate for the number of load cycles to failure [2].

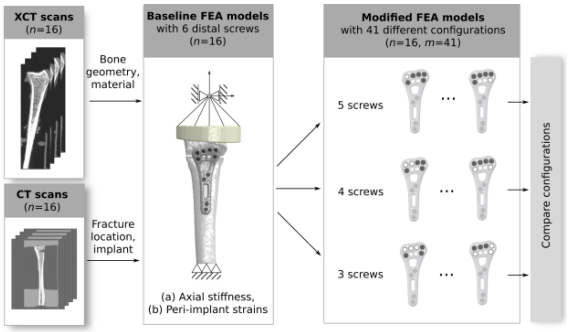

Figure 1: Study outline.

Results

Axial Stiffness (Fig. 2, left): Removing even three screws resulted in only ~11% reduction of stiffness in the subject-specific best configuration, but up to ~46% reduction of stiffness in the worst configuration.

Peri-implant strains (Fig. 2, right): In the best configurations, removing screws even reduced the peri-implant strains (up to ~35% reduction). In the worst configurations and with three removed screws, peri-implant strains were increased by more than 100%.

Interestingly, the configurations leading to the largest axial stiffness were not consistent with the configurations leading to the lowest peri-implant strains.

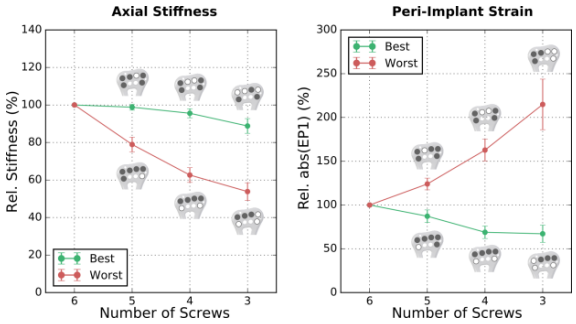

Figure 2: Relative axial stiffness (1) and relative peri-implant strains (2) after removing 1 to 3 screws. Error bars indicate the inter-subject standard deviation (n=16). Insets show the most frequent best/worst configurations across subjects.

Discussion

The results showed that not only how many, but also *which* screws are used in volarly plated DRFs is critical for its biomechanical behavior. The fact that different biomechanical parameters suggest different "optimal" screw configurations might in part explain conflicting results of previous biomechanical studies [3,4] and highlights the need for a more complex optimization procedure taking multiple output parameters into account. While this study highlights the potential of FEA to optimize fracture treatments, several challenges remain to be addressed prior to clinical application, including implementation of non-linear behavior of materials and interfaces as well as more realistic boundary conditions.

References

1. Synek et al., J Biomech, 48:4116-4123, 2015
2. Varga et al., J Mech Behav Biomed Mater, 75:68-74, 2017
3. Drobetz et al., Injury, 44:535-9, 2013
4. Crosby et al., J. Hand Surg., 38:1097-105, 2013

DO PINHOLE LOCATIONS IN MEDIAL UKA IMPACT THE RISK OF TIBIAL PERIPROSTHETIC FRACTURES?

Christine Müri (1), Adam Sanford (2), Philippe Favre (1), Auriane Marret (1), John Kyle Mueller (2)
1. Zimmer Biomet, Switzerland; 2. Zimmer Biomet, USA

Introduction

Periprosthetic tibia plateau fracture after unicompartmental knee arthroplasty (UKA) has been associated with over-resection of the posterior sagittal cut, increased resection depth or malalignment of the tibial implant [1,2]. The impact of multiple cut guide pinholes, which can act as stress risers in the bone, on plateau fracture has not been investigated.
The aim of this study was to create and validate a finite element (FE) model of the tibia bone implanted with a UKA tibia baseplate and to study the influence of the pinhole locations on the risk for periprosthetic fractures following UKA.

Methods

Cadaveric experiments:
Seven cadaveric tibiae were prepared and implanted with a medial, cemented UKA component by experienced UKA surgeons (performing a bi-uni knee surgery), using cutting instrumentation that introduced several pinholes inferior to the transverse cut. The implanted specimens were dissected, potted in cement and axially loaded through the femoral-tibial contact point in extension until fracture of the medial plateau occurred (Figure 1).

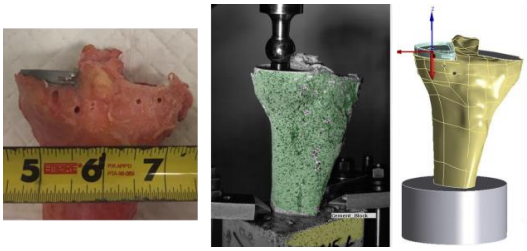

Figure 1: Dissected tibia specimen with implanted medial UKA, experimental test setup with DIC and corresponding FE model.

FE analysis: Specimen specific FE models were created based on pre- and post-operative CT scans, consisting of the tibial baseplate, nominal cement mantle, tibial bone and the cement block. All materials were considered homogenous, isotropic, and linear elastic. The tibia was modelled in two layers (cortical bone: 15 GPa [3], cancellous bone: 0.5 GPa [4]).
The FE models were then validated in terms of overall specimen stiffness (n=7) and local displacement extracted with digital image correlation (DIC) (n=2). The risk of fracture (ROF) in each model was quantified as the volume of cortical bone exceeding 50% of bone strain capacity [5]. The validated FE models were then used to study the influence of pinhole locations on the ROF by varying the number of pinholes and pinhole locations, while subjected to an axial load of 2kN.

Results

Model validation: A close agreement and strong correlation in the overall specimen stiffness (R^2=0.92) and in the local deformations (average differences <11% compared to DIC measurements) was found between experiment and FE models (Figure 2). The ROF at 2kN axial load was inversely correlated (R^2= 0.80) with the measured fracture load of the tibia specimen, supporting the use of ROF as a metric for assessing bone strength.

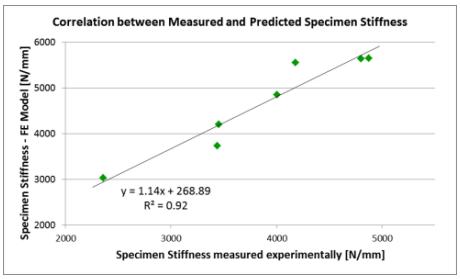

Figure 2: Correlation in specimen stiffness between experiment and FEA.

Influence of pinholes: The relative position of pinholes had a greater effect on the ROF than the number of pinholes: 3 pinholes evenly spread inferior to the transverse resection showed similar ROF volume as the 2 pinholes scenario (student's paired t-test, $p \geq 0.415$). Pinholes spaced underneath the transverse cut significantly reduced the ROF ($p \leq 0.03$) compared to adjacent pinholes in close proximity to the sagittal cut corner.

Discussion and Conclusion

Specimen specific FE models of the tibia with a cemented UKA were validated against an experimental, axial test. The FE model was then used to study the effect of surgical pinhole placement on the risk for periprosthetic fractures.
Surgical pinholes may represent a stress riser in the anterior cortex. To minimize the risk for periprosthetic fracture, ideally, surgical pinholes are distributed inferior to the transverse resection and not in close proximity to the sagittal cut corner.

References

1. Felix et al., Clin Orthop, 345:223, 1997.
2. Brumby et al., J. Arthroplasty, 18: 809-812, 2003.
3. Snyder & Schneider, J Orthop Res, 9: 22-431, 1991
4. Ashman et al., J Biomech, 22: 895-900, 1989
5. Schileo et al., J Biomech, 41: 356-367, 2008

COMPUTATIONALLY EFFICIENT MODEL OF THE IMPLANTED KNEE FOR TIME-SENSITIVE APPLICATIONS

Edoardo Bori(1), Alessandro Navacchia(2), Liang Wang(2), Liz Duxbury(2), Shawn P. McGuan(2), Bernardo Innocenti(1)

1. BEAMS Department, Université Libre de Bruxelles, Belgium; 2. Smith & Nephew, Inc., San Clemente, California

Introduction

To design and analyze orthopaedic devices, finite element (FE) models represent a cost-effective alternative to in vitro experiments. The main problem of such simulations is their extremely long computing time required to perform the simulation; this limitation makes this approach not compatible with time-sensitive applications, such as real-time surgery-planning or intra-operative setting. On the contrary, Multibody (MB) simulations are usually faster than FE simulations, as they consider each component rigid and not deformable. Therefore, the goal of this study was to demonstrate the equivalence in terms of kinematic, contact force, and ligament strain results between a FE and a MB model of an implanted knee under the same boundary conditions.

Methods

The FE model of the knee was composed by the femur, tibia, patella and the patellar cartilage (segmented from the CT scan of a cadaveric specimen); the material properties for those components were taken from literature and modeled as linear elastic. The femur and tibia were implanted with a cruciate retaining total knee replacement. The femoral component, tray, and insert materials were modeled with linear elastic properties. Each component was meshed with second-order tetrahedral elements. The posterior cruciate ligament, medial and lateral collateral ligaments, and patellar tendon (divided in three bundles) were modeled as mono-dimensional linear elastic materials, and their cross-sectional areas were taken from literature. A specular rigid body MB model was then implemented, and the four ligaments were modeled with mono-dimensional geometric nonlinear FE-based elements (available in the multibody solver).

In order to perform the calibration, a dedicated simulation was performed on both models with a ramping compressive force applied on the femur: the femur-insert contact stiffness and damping parameters for the rigid body model were then tuned accordingly to match the FE simulation results.

A squat activity up to 120° of tibiofemoral (TF) flexion was then simulated. The squat loading conditions were derived from a previous model of a cadaveric knee simulator [4]. Six-degrees-of-freedom TF and patellofemoral (PF) kinematics, contact forces on the medial and lateral plateaus, and ligament strain (ligament length - free length) were compared between the two models.

Results

The calibration test was matched with an error of 0.02 mm, and contact area and location also matched the finite element results (See Figure 1).

In the squat simulation, the root mean square differences (RMSD) between the FE and MB models were always below 1.8° and 1.3 mm for both TF and PF kinematics. RMSD for the medial and lateral contact forces were 59.8 and 64.7 N, respectively. Ligament strains were matched with RMSD below 0.016 (See Figure 2). Pearson correlations between FE and rigid body results were always above 0.93. The computational times required by the FE and MB simulations were 155 minutes and 2 minutes, respectively.

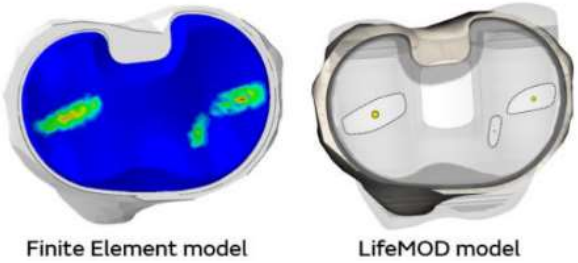

Figure 1: Calibration of the stiffness and damping to match the deformable properties of the FE insert

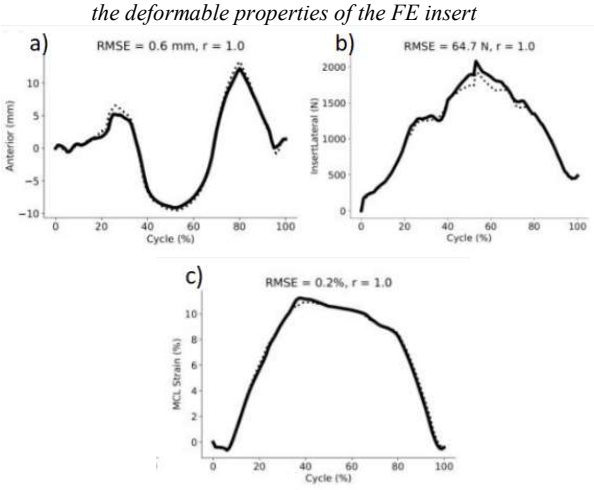

Figure 2: Examples of kinematic(a), contact force(b) and ligament strain(c) results comparison

Discussion

The small RMSD and high correlation coefficients between the results demonstrate the equivalence of the two methods for the knee squat simulation. The comparison between computational times indicate that seventy-seven MB simulations can be completed in the time of one FE simulation. Therefore, rigid body simulations represent a time-effective alternative to FE simulations.

References

1. Erdemir et al., J Biomech, 2012.
2. Halloran et al., J Biomech Eng, 2005.
3. Pianigiani et al., Muscles Ligaments Tendons J, 2017.
4. Pianigiani et al., J Biomech, 2012.

THE IMPORTANCE OF CEREBROSPINAL FLUID AND EPIDURAL FAT IN NUMERICAL MODELS OF BURST FRACTURE SPINAL CORD TRAUMA

Konstantin Arhiptsov (1), Gil Marom (1)

1. School of Mechanical Engineering, Tel Aviv University, Israel

Introduction

Traumatic spinal cord injury (SCI) is a mechanical damage to spinal cord that alters its neurological function. It is estimated that there are 15-40 annual incidences per million people [1]. Cerebrospinal fluid (CSF) has several important functions, including acting as a shock absorber to protect the central nervous system [2]. While numerical models can help predicting the SCI mechanics without putting the subjects in danger, previous studies did not focus on alternations in the CSF conditions, such as its pressure, and did not account for the presence of epidural fat. The current study aims to numerically compare the behaviour of human spine when subjected to several SCI scenarios and under two medical conditions. Specifically, the cord behaviour was compared in SCI scenarios that represent burst fracture [3] with and without epidural fat and the CSF pressure was either normal or in a diseased state of intracranial hypertension [4].

Methods

This research employs numerical methods with focus on the cord and its surrounding tissues and less on the vertebrae and discs. Explicit scheme was used for both the structural analysis and for the fluid parts because of highly dynamic nature of this case. The meshless smoothed-particle hydrodynamics (SPH) method was employed for the CSF and the epidural fat. The fluid structure interaction is intrinsically incorporated into the solver since the SPH and structural solvers can directly transfer contact forces. This approach allowed to account for the CSF pressure alteration and its effect on the cord itself. The anatomical geometries of the vertebral column were obtained from an open database [5]. The internal structure of the cord's gray and white matters was defined based on published anatomic images. The finite element model consisted of T4-T7 vertebrae and burst fracture was modeled at T5 vertebra. The model solver was Radioss (Altair Engineering Inc.).

Results

The model was first validated against published numerical and experimental studies and good correlations were found [6, 7]. The results were able to capture the fluid dynamics of the CSF while demonstrating a considerable change in the stresses of the spinal cord during burst fracture injury (Figure 1). High CSF pressure affected the general shape of the dural sac and increased the stresses by up to 30% in both the white and gray matters of the spinal cord (Figure 2). Due to the additional pressure, the shape of the dural sac tended to be more eliptic while the spinal cord dimensions remained with no significant changes. Exclusion of the epidural fat from the model significantly increased the calculated stresses in the cord by up to 26.7%, indicating on the necessity of the fat presence in future models.

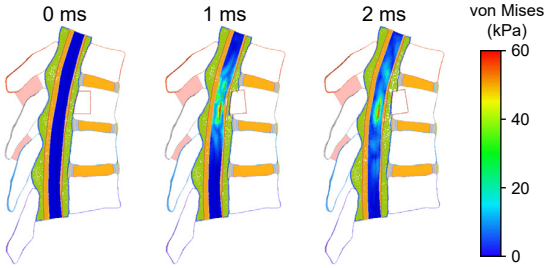

Figure 1: Stress distribution in the spinal cord under impact of fragment with normal CSF pressure

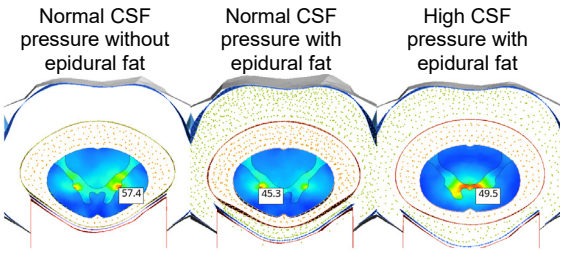

Figure 2: Stress distribution in the T5 section under impact of fragment with normal and high CSF pressure

Discussion

The modeling of the CSF's fluid dynamics allowed to capture the flow field and introduce a consideration that has not been accounted in previous studies, the effect of the CSF pressure. The comparison of two CSF pressures demonstrated that burst fracture impact in patients with intracranial hypertension might lead to worsen spinal cord damage then found in healthy patients. The inclusion of the epidural fat, that was not included in previous SCI models, was also found to have significant effect on the resulted stresses. Therefore, the results show some important aspects that need to be accounted for in future numerical models of SCI while also demonstrating how the injury might aggravate by preexisting conditions.

References

1. Rowland et al. Neurosurg Focus. 25:E2, 2008.
2. Sakka et al. Eur Ann Otorhinolaryngol Head Neck Dis. 128:309-16, 2011.
3. Diotalevi et al. Clin Biomech. 72:186-94, 2020.
4. Rangel-Castilla et al. Neurol Clin. 26:521-41, 2018.
5. Mitsuhashi et al. Nucleic Acids Res. 37:D782-5, 2009.
6. Persson et al. J Neurotrauma. 28:113-25, 2011.
7. Jones et al.J Biomech Eng. 135:101005, 2013.

Finite element modeling of plantar tissue stresses induced by the clinical practice of off-loading of the diabetic heel

Hadar Shaulian (1), Amit Gefen (2), Alon Wolf (1)

1. Technion-Israel Institute of Technology, Israel; 2. Tel Aviv University, Israel.

Introduction

Heel ulceration is a serious and destructive complications of diabetes and the ultimately leading cause of lower extremity amputation [1]. Focal and repetitive stress are causative factors in the development of heel ulceration [2]. A common therapeutic device to treat heel ulceration is a custom-made offloading insole designed with a hole under the active wound site, to reduce constant and shear stresses from the ulcer, also known as "step-shaped" support [3]. The size, location and shape of the hole is based on visual indication and the experience of the therapist, and no scientific guidelines for objective design of the offloading hole have been established. Moreover, with hole-support design, the tissues surrounding the ulcer are prone to higher loads escalating the risk of developing secondary damage. Here, we aim to develop a patient-specific method, based on finite-element (FE) analysis and available patient information, to optimize the offloading design, and thus optimally prevent and treat heel ulcers.

Methods

Since heel ulcers often start internally and progress, we developed a generic FE 3D realistic model of a human heel, to examine heel internal loads during walking on 150 different offloading support configurations. We evaluated the biomechanical efficacy of the offloading support configurations as the reduction in the "total stress concentration exposure" (TSCE) value, defined as the area bounded between the soft-tissue effective stress volumetric exposure curve and the horizontal (stress) axis [4]. We calculated the TSCE from two volumes of interest (VOIs), high risk VOI and peripheral VOI. The high risk VOI represents the tissue at high risk of ulceration, located at the soft tissue layer of the heel under the sharpest point of the calcaneus bone. The peripheral VOI was defined as the lower part of the heel soft tissue surrounding the high-risk area. We then multiplied the two TSCE values of each configuration to find the minimum TSCE for one weighted value.

Results

Distributions of effective stresses and contact pressure in the heel soft-tissue with four representative configurations are shown in cross-section and bottom view respectively (fig 1). Values of the multiplied TSCE for the 150 heel support configurations are shown in fig. 2 in log scale. The two minimum values are represented by blue dots obtained at: (1) geometry that close to the shape of the heel and (2) large offloading hole and depth and relative sharp hole adages.

Discussion

In the current work, we present a method to compare biomechanical efficacy of offloading supports on re-distributing heel stresses. This method enables a quantitative comparison of many heel support configurations considering the volumetric exposure of the tissue at multiple desired areas, such as tissues at high risk for ulceration.

Our generic FE model can be customized to the patient's specific parameters using non-invasive measurements such as MRI, ultrasound and ground reaction forces. Therefore, our method enables patient-specific examination of biomechanical efficiency of offloading solutions to prevent and treat ulcers diabetic heel ulcers.

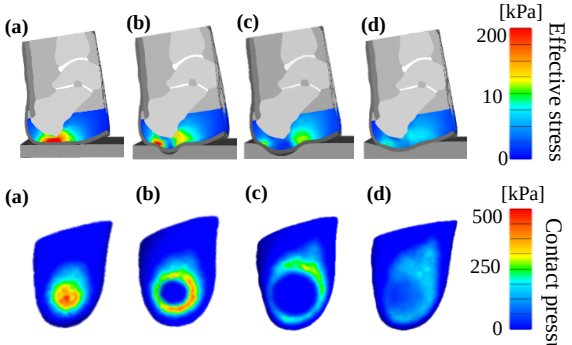

Figure 1: Effective stresses and contact pressure with four heel support configurations: (a) flat; (b) step-shaped; (c) recommended treatment; and (d) total contact for prevention.

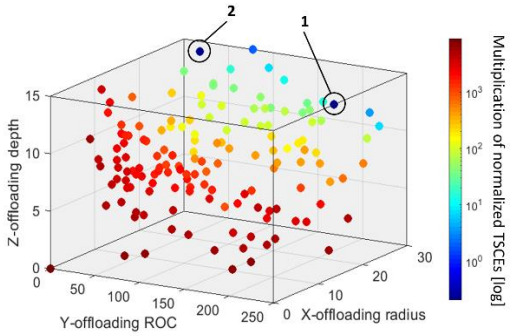

Figure 2: Multiplication of the two TSCE values of each configuration.

References

1. Boulton et al. Lancet, 366:1719–24, 2005.
2. Veves et al. Diabetologia, 35:7 660–663, 1992.
3. D.Armstrong et al. Clin Podiatr Med Surg, 15:105-8, 1998.
4. R. Katzengold et al. Int. Wound J., 1–10, 2019.

The role of interface stresses on implant stability. An experimental-computational approach

Mohammadjavad Einafshar (1,2), Ata Hashemi (1), G. Harry van Lenthe (2)

1. Amirkabir University of Technology, Biomedical Engineering Faculty, Biomechanics Group, Tehran, Iran;
2. KU Leuven, Department of Mechanical Engineering, Biomechanics Section, Leuven, Belgium

Introduction

Bone screw fixation can be quantified with several test methods such as insertion torque, pull-out, push-in and bending tests [1-2]; yet, these are all destructive methods. Non-destructive modal analysis is being used to evaluate the mechanical primary and secondary stability of dental implants, and it has recently been proposed for orthopedic and spine applications [1,3]. In modal analysis, deformation modes of a vibrational system can be excited, and natural frequencies can be recorded. These natural frequencies are related to mechanical stability [3], although a basic understanding of the relationship is still lacking. Computational models could help obtaining a better understanding. Therefore, the aim of this study was to simulate experimental modal analysis through finite element (FE) modeling. We hypothesize that pre-stresses resulting from the insertion process affect the stability behavior of the screws.

Methods

Twenty-four specimens (40x40x60 mm^3) were cut from two polyurethane (PU) foams with densities of 0.16 and 0.32 g/cc, respectively. Pilot holes of 5.5 mm diameter were drilled to depths of 10, 20 and 30 mm, respectively. A self-tapping conical pedicle screw with an outer diameter of 6.5 mm was inserted into the pilot hole. Modal analysis test was performed using a sound recording technique. A microphone (Audio–Control CM-145, Apple Inc. USA) was used to record the sound after slight hammer blows to the head of the screw. Fast Fourier Transformation (FFT) was applied to the recorded sound to extract the natural frequency of the first vibration mode. Three-dimensional models of the PU block and pedicle screw were created using Catia V5R21 and imported in Abaqus CAE 2017 (both software packages by Dassault Systèmes, Vélizy-Villacoublay, France). An elastoplastic material model (yield strain = 5%) with Young's moduli of 23 MPa and 137 MPa was implemented for the low and high density PU foam. For each combination of PU density and insertion depth, two FE analyses were performed: one in which a free-stress tie contact was assumed between screw and foam, and one in which pre-stresses resulting from a 0.5 mm radial displacement to the tapped hole were included. In all models, the lateral faces of the foams were fixed. A modal analysis was performed using linear perturbation moduli in Abaqus and the first natural frequency was extracted.

Results

The experimentally measured first natural frequency ranged from 303 to 2177 Hz (Table 1). Including pre-stresses in the FE models changed the behavior of interface and the simulated response predicted frequency in a range of 1.8% to 18% closer to the experimental one than the simulations without pre-stresses (Table 1).

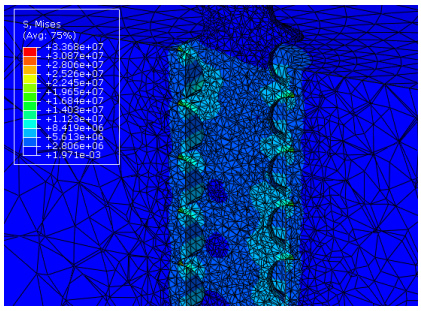

Figure 1: Von Mises stresses due to screw insertion (PU: 0.32 g/cc; insertion depth: 20 mm). A radial seeding gradient was performed to obtain better mesh quality.

Model		First Natural Frequency (Hz)		
PU density (g/cc)	Insertion depth (mm)	FE, stress-free	FE, pre-stressed	experimental
0.16	10	185	209	303 (±19)
	20	516	533	748 (±3)
	30	1023	1042	1182 (±3)
0.32	10	415	459	652 (±3)
	20	982	1006	1108 (±3)
	30	1937	1970	2177 (±6)

Table 1: Experimental and Finite Element data on the first natural frequency determined for two polyurethane foam densities and three insertion depths. FE analyses simulated stress-free screws as well as a screws subjected to pre-stresses resulting from the insertion process.

Discussion

During screw insertion, pre-stresses develop at the foam-implant interface [2]. Inclusion of the pre-stresses into the FE modal analysis increased the natural frequency of the first bending mode. Applying pre-stresses induced internal forces between screw and block elements and these internal forces made the initial positioning of the screw more stable.

The frequency extraction in Abaqus limited the simulation for more details to be included e.g. nonlinear contacts between block and screws.

References

1. Einafshar, M. et al. ESB, 622, 2019.
2. Einafshar, M. et al. *J Comput* Methods Programs Biomed, 2021.
3. Leuridan, S. et al. *J MECH BEHAV* BIOMED *MATERIALS*, 66(1), 12-18, 2017.

FINITE ELEMENT ANALYSIS OF EFFECT OF IMPLANT MALPOSITION IN BI-UNICOMPARTMENTAL KNEE PROSTHESIS

Nicola Armillotta (1), Edoardo Bori (1), Pierluigi Antinolfi (2), Bernardo Innocenti (1)

1. *BEAMS Department, Université Libre de Bruxelles, Brussels, Belgium*
2. *Università degli Studi di Perugia, Perugia, Italy*

Introduction

Unicompartmental Knee Arthroplasty (UKA) is a well-accepted treatment for isolated osteoarthritis (OA) and when both compartments are affected by the disease, bi-UKA could be a possible solution to handle the pathologic knee. Its advantages are retaining of both the cruciate and the minimal invasiveness compared to total knee arthroplasty (TKA), and consequently faster recovery time, superior functional results with the closest restoration of native knee kinematics and range of motion [1]. Patient performance is strongly dependent on implant position, however, due to the high demanding procedure required for the implantation, implant malpositioning could happen during surgery. Among the different errors, wrong slope of the lateral component is one of the most common: therefore, the aim of the study is to investigate the effects of these slight variations in bi-UKA.

Methods

A validated model was used for this study [2]. The medial and lateral components were implanted following the manufacturer guidelines. The medial prosthesis was placed according to the native slope of the tibial plateau, while the lateral was inserted in six different configurations (-5°, -3°, -2°, 0°, 3°, 5°) measured with respect to the slope of the medial tray. All analysis were performed in stance position, loading the femoral head with 2000N along the mechanical axis (equal to 2.55 times the weight of the patient, that is the maximal axial force during gait) and fixing distally the tibia. A mesh size of 2mm was applied for the bearing surface interface and the proximal tibia, and up to 10mm for proximal femur and distal tibial. Similar to previous studies, the outputs were the Von Mises stress in the proximal tibia and polyethylene (PE) insert, shear stress percentage, load repartition on medial and lateral compartments, contact area and pressure on polyethylene insert.

Results

From the literature, the average Von Mises stress in physiological proximal tibia is 1.6-1.7 MPa [2]. From the model, -3°, -2° and 0° slopes achieved 1.5-1.6 MPa, while the -5° and +5° reached the exceeded 1.9 MPa. The load distribution and pressure repartition on the lateral and medial compartment for a healthy knee are respectively 60-40% and 50-50% [2]. Better results were achieved by -3° slope with 63-37% and 53-47%, by -2° with 60-40% and 50-50%, by 0° slope with 48-52% and 38-62%. The -5°, +3° and +5° slopes got detrimental results, exceeding 70% of load on one compartment and achieving a ratio of about 60-40% for the pressure distribution.

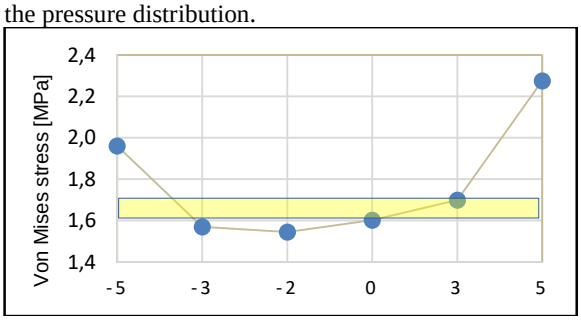

Figure 1: Average Von Mises stress in proximal tibia. In yellow, the physiological range of values.

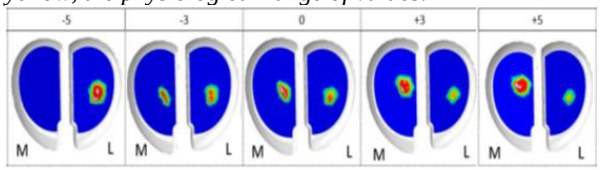

Figure 2: Contact pressure in polyethylene insert.

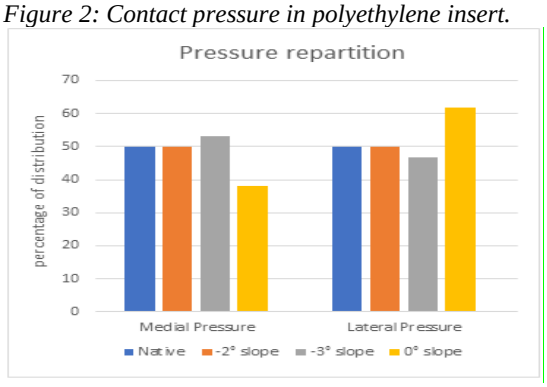

Figure 3: pressure repartition for native and slight negative slopes.

Discussion

Clinically, for this kind of implants, the gold standard is -3° of slope of the lateral component, which means that it's common to insert the lateral component with a different inclination from the medial tray. However, small errors of +-1° can occur during the surgery, and this investigation demonstrates how this occurrence would massively change the outcome of the implant, increasing the chance of revision and failure. The present study indicates that the cut should be always performed to achieve a slight posterior slope, avoiding any positive slope.

References

1. *Romagnoli, et al, Minimally Invasive Surgery in Orthopedics, 2016*
2. *Innocenti et al,J Arthroplasty, 2014*

CEMENTED SHORT-STEM TOTAL HIP ARTHROPLASTY APPEARS PROMISING IN PATIENTS WITH POOR BONE QUALITY

Fahimeh Azari (1), Amelie Sas (1), Karl Philipp Kutzner (2), Andreas Klockow (3), Thierry Scheerlinck (4), G. Harry van Lenthe (1)

1. Biomechanics Section, KU Leuven, Leuven, Belgium; 2. St. Josefs Hospital, Wiesbaden, Germany; 3. Mathys Medical, Bettlach, Switzerland; 4. University Hospital Brussels, Brussels, Belgium

Introduction

Short-stem total hip arthroplasty (THA) is becoming increasingly popular mainly due to the preservation of proximal bone stock and the simplified implantation [1]. Indications of this specific design could be expanded with a cemented version, which potentially offers a solution for patients with poor bone quality or uncommon anatomy [2]. The main objective of this study was to evaluate the mechanical performance of a *cemented* short stem THA and to determine which cementing strategy, i.e., the "line-to-line" or "undersized" technique [3], is preferable.

Materials and Methods

Eight pairs of fresh frozen human cadaveric femora (i.e., 16 femora in total) were implanted with a calcar-guided short stem (optimys, Mathys Ltd, Bettlach, Switzerland); for each pair, the line-to-line cementing technique was used in one femur, and the undersized technique in the contralateral one. Bone geometry, density and cement distribution were assessed with CT-scans. Four of these implanted pairs (i.e. eight femora) were mechanically tested under loading conditions resembling single-legged stance, and stiffness and strength were quantified. Digital image correlation (DIC) was performed during the experiment to measure bone surface displacements. Subject-specific nonlinear finite element (FE) models of the implanted femora were created and subjected to identical loading conditions, as in the experimental tests. Surface displacements were calculated and compared to DIC measurements. Stiffness and strength were determined, and compared to the experimentally measured values. An overview of the procedure is shown in Fig. 1.

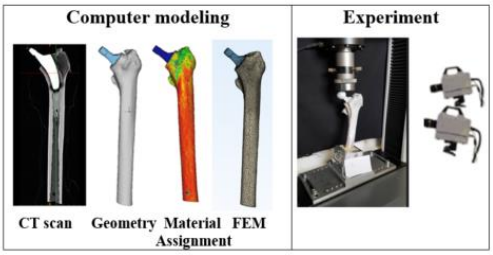

Figure 1: Overview of the validation workflow including computer modelling and mechanical testing.

After confirming that the 8 FE models closely replicated the behavior of the femur as measured in the experimental tests, subject-specific FE models of the other 8 femora were created. The entire set (16 femora) was used to evaluate the behavior under physiological loading conditions resembling level walking [4].

Results and Discussion

The cement distribution of the line-to-line implantation technique was very similar to the cement distribution of the undersized implantation (Fig. 2). The small differences in cement volume (5.8% more cement in the undersized cases) resulted in small and non-significant differences on stiffness (average difference 3.5% ± 3.0%) and strength (average difference 2.3% ± 1.9%). Displacements as calculated from FE corresponded strongly ($R^2 \geq 0.97$) with those measured by DIC. Strength as calculated from FE deviated 8.7% ± 16% from the experimental values, the discrepancy between FE and experimental stiffness was 9.9% ± 15.0%. The validated FE models showed that stresses in the bone, cement and implant during level walking are substantially lower than yield stress.

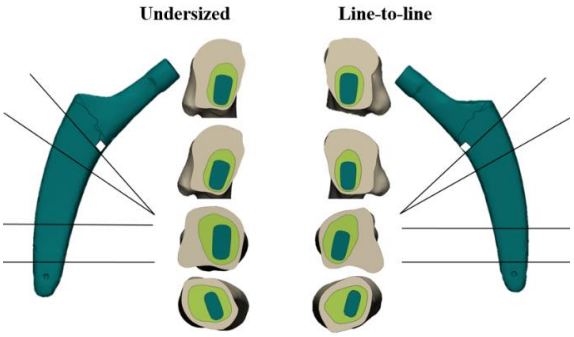

Figure 2: Cement distribution as measured from CT demonstrating that the thickness of the bone cement layer (light green) varies along the length of the stem (dark green).

We conclude that the line-to-line technique withstands similar loads as the undersized technique, and that both are very unlikely to fail under normal physiological loading. Hence, regardless the specific cementation technique, cemented short stems appear promising in patients with low bone quality.

References

1. Burchard et al., BMC Musculoskelet Disord, 18: 343, 2017.
2. Kutzner et al., CLIN BIOMECH, 52: 86-94, 2018.
3. Scheerlinck et al., JBJS (Br), 88: 19-25, 2006.
4. Heller et al., J Biomech, 38: 1155-63, 2005.

EFFECT OF BONY GEOMETRY ON IMPINGEMENT IN TOTAL HIP REPLACEMENTS DURING DISLOCATION-PRONE ACTIVITIES

Simon P. Williams (1), Alison Jones (1), Graham Isaac (1), Ruth Wilcox (1), Alison Traynor (2), Tim Board (3), Sophie Williams (1)

1. Institute of Medical & Biological Engineering, School of Mechanical Engineering, University of Leeds, Leeds, UK. 2. DePuy Synthes Joint Reconstruction, Leeds, UK. 3. Wrightington Wigan and Leigh NHS Trust, UK.

Introduction

Impingement in total hip replacements (THRs), including bone-on-bone impingement, can lead to complications such as dislocation and loosening [1, 2]. The aim of this study was to investigate how the change in bony geometry of a patient would affect the severity of bone impingement in total hip replacements during dislocation-prone activities of daily living.

Method

Nine hips were selected from a cohort of 25 CT scans (50 hips) which had a range of anterior inferior iliac spine (AIIS) locations relative to the hip joint centre. The selected CT scans were converted to solid models (ScanIP) and THR components were virtually implanted (Solidworks) and verified by an orthopaedic surgeon. Dislocation-prone activities of daily living [3] were used with the nine computational models to investigate the effect of different bony geometries on the severity of bone impingement. The severity of bone impingement was measured as a volumetric overlap of bones in the geometric models (Figure 1).

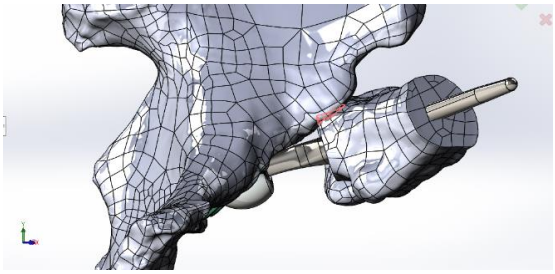

Figure 1 Volumetric overlap of bones during a bone impingement event highlighted in red.

Results

The severity of impingement changed with differing bony geometries. When bone impingement occurred during the anterior impingement activities, the most significant factor was the lateral AIIS measure ($p<0.05$) which affected the severity of bone impingement during the picking an object off the floor (STOOP) activity (Figure 2), increasing the severity of bone impingement by 123mm³ for every 1mm increase of the lateral measure of the AIIS. There were only a few instances of impingement found for the other anterior impingement activities. When bone impingement occurred during the posterior impingement activities, the most significant factor which effected the severity of bone impingement was the anteversion of the natural acetabulum ($p<0.05$). Every increase in 1° of natural anteversion resulted in an increase in severity of 114mm³ during the pivoting one foot through external rotation (PIVOT) activity and 192mm³ during the rolling over in bed (ROLL) activity (Figure 3).

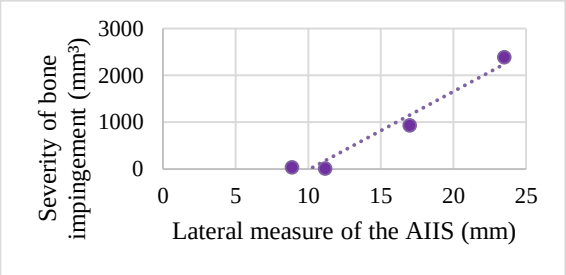

Figure 2 The effect that the lateral measure of the AIIS had on the severity of bone impingement during the STOOP activity.

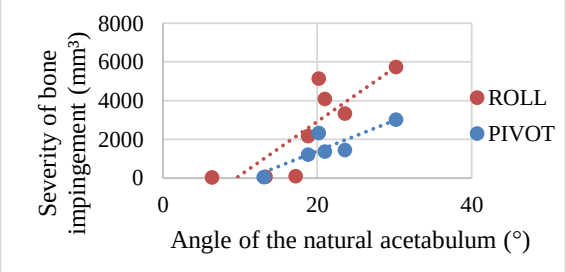

Figure 3 The effect that the anteversion angle of the natural acetabulum had on the severity of bone impingement during the PIVOT and ROLL activities.

Discussion

The bony geometry of the pelvis and femur had an effect on the severity of bone impingement. When bone impingement did occur during the STOOP activity, the AIIS could be used as a predictor for bone impingement severity. When impingement occurred with the posterior impingement activities (PIVOT and ROLL), the anteversion of the natural acetabulum could be used as a predictor for the severity of bone impingement. These severities could be used to assess for potential dislocation.

References

1. Malik et al, J of Bone and Joint Surgery, 89:1832-42, 2007.
2. Brown et al, The Iowa Orthopaedic Journal, 34:1-15, 2014.
3. Nadzadi et al, J of Biomechanics , 36:577-591, 2003.

DEVELOPING A VALIDATED OSTEOCHRONDRAL GRAFT REPAIR FINITE ELEMENT MODEL IN A TIBIO-FEMORAL JOINT

Gavin A Day, Alison C Jones, Marlène Mengoni, Ruth K Wilcox

Institute of Medical and Biological Engineering, University of Leeds, UK

Introduction

Osteoarthritis (OA) is the most prevalent chronic rheumatic disease worldwide with knee OA having an estimated lifetime risk of approximately 14 % [1]. Autologous osteochondral (cartilage-bone) grafting has demonstrated positive outcomes in terms of pain and function in some patients [2], however, understanding of the biomechanical function and how the treatment can be optimised remains limited. Subsidence and graft disintegration are observed in some cases clinically, but factors affecting short term stability of the graft have not been fully investigated. The aim of this study was to develop a robust method for generating specimen specific finite element (FE) models of osteochondral grafts within a full tibia-femoral joint, prior to bone integration. Allowing for future investigation and optimisation of different grafting scenarios. Specifically, this study addressed the challenges of modelling the graft-host interface, using joint pressure data from in vitro tests for validation.

Methods

In vitro tests were conducted on a cadaveric human tibiofemoral joint, which was dissected by removing all soft tissues retaining only the cartilage. The femur and tibia were cemented in pots. Grafts were harvested from the trochlear grove using 6.5 mm chisel (Smith & Nephew, UK), these were trimmed to 10 mm in length. Two 10 mm deep holes per condyle were created using a 6.35 mm drill-bit. Grafts were inserted into two of the holes such that the cartilage layers were flush. The joint was axially loaded at 500 N in a materials testing machine (Instron 3365, UK), before drilling the hole, after hole (defect) creation and finally after osteochondral repair. Contact pressure measurements were obtained using flexible sensors (Tekscan Inc, USA). FE models were created from two registered µCT scans captured pre- and post- test. The joint was segmented and meshed using Simpleware ScanIP (Synopsis, USA). Models of the osteochondral grafts were specimen-specific with material properties based on the initial scan and position given from the post-harvest scan. Settings for the high quality mesh on the graft and hole contact surfaces were based on previously experimentally validated FE models of graft push in tests. Material properties of the bone were based on a (previously calibrated) linear coefficient between the µCT grayscale value and Young's modulus. Interaction properties were also obtained from validated FE models of graft push in tests. FE models were solved in Abaqus (SIMULA, USA). Grafts were first displaced into the simulated defect, creating a pre-strain in the graft and surrounding area that mimicked the experimental press fit caused by the oversized graft. A 500 N load was applied to the femur, with boundary conditions applied that matched the experiment. Pressure maps for the tibial cartilage layers, mean pressure values and contact area, were measured and compared to the experimental data.

Results

Experimentally, repairs ranged from successfully creating a flush, continuous cartilage layer, to inserting the graft too deep. The resultant pressure map changes were well represented in the FE models. Cartilage defects were measurable in the experimental pressure data with good agreement in the FE model pressure maps (Fig 1).

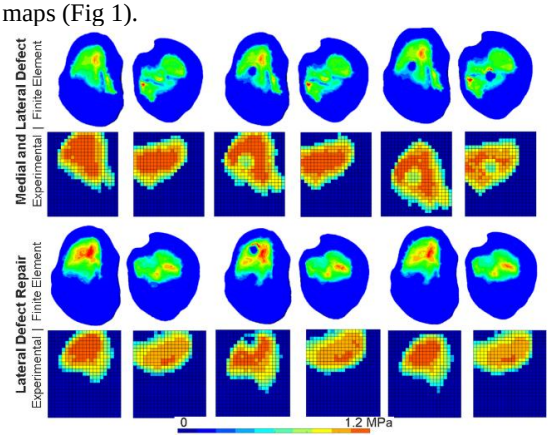

Figure 1: Contact pressure distributions seen using pressure sensors were well replicated in specimen-specific FE models, for both defect and repair cases.

Discussion

The rigorously tested FE models are based upon a range of previously validated testing, including validated models of tibio-femoral contact pressure during static loads, material property calibration and data from graft push-in tests. Experimentally, the graft depth varied, this positioning and alignment was well replicated in FE and evidenced by good agreement between the in vitro and model contact pressure maps. The previously validated testing provided added confidence in the clinically relevant graft behaviours, such as graft subsidence due to defect depth and graft force vectors dependant on the position of the repair relative to the contact area. We have shown that the previously developed, robust method of creating osteochondral graft models within femoral condyles can be used when modelling full tibio-femoral joints. These models can be used to investigate parameters such as cartilage-to-bone ratios and quality of the drilled hole on the efficacy of osteochondral repair.

References

1. Bortoluzzi, A., et al., 2018. *Autoimmunity Reviews.*
2. Pareek, A. et al. 2016. *Arthroscopy*

This work was supported by the EPSRC EP/P001076

PREDICTION OF SCREW PERFORATION IN THE PROXIMAL HUMERUS USING MICRO FINITE ELEMENT ANALYSES

Vasiliki C. Panagiotopoulou (1, 2), Marzieh Ovesy (3), Boyko Gueorguiev (1), R. Geoff Richards (1), Philippe Zysset (3), Peter Varga (1)

1. AO Research Institute Davos, Switzerland; 2. University of Patras, Greece; 3. University of Bern, Switzerland

Introduction

Fractures of the proximal humerus are the third most common fragility fractures with challenging treatment and serious complications. Among those, mechanical fixation failure rates in locking plates reach up to 35% [1-2], 80% of which are related to the screws perforating the glenohumeral joint [3]. Late postoperative, i.e. secondary, screw perforation is a complex process which is not yet fully understood. Biomechanical studies and computational approaches, such as finite element (FE) analysis, are expected to help understand the failure mechanisms and identify the risk factors. Validated FE simulations could be used to predict perforation risk. This study aimed to (1) develop a biomechanical model for single screw perforation in cadaveric humeral heads and (2) evaluate and compare the ability of bone density measures and FE simulations to predict the experimental findings.

Methods

Twenty cuboidal bone specimens, with a cross section of 12 mm x 12 mm, were harvested from four fresh-frozen human cadaveric proximal humeri of elderly donors (aged 85±5 years, f/m: 2/2). Following cylindrical embedding, a 3.5 mm locking screw (DePuy Synthes, Switzerland) was implanted centrally. Quasi-static compression testing was used to induce screw perforation. Specimen-specific linear micro FE (L-µFE) [4] (ParOSol, ETH Zurich, Switzerland) and nonlinear explicit µFE (NL-µFE) [5] (Abaqus, SIMULIA, USA) models were generated from pre- and post-implantation µCT images (vivaCT40, Scanco Medical, Switzerland) (Figure 1) at 38 µm and 76 µm voxel sizes, respectively. µCT images were used to evaluate the bone volume (BV) around the screw and in front of the screw tip, and the tip-to-joint distance (TJD). Both µFE models and the BV measurements were used to predict the experimental force at the initial screw loosening and the maximum force until perforation.

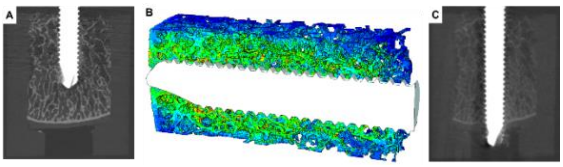

Figure 1: A: µCT image of a cuboidal bone specimen with implanted screw. B: Snapshot of LN-µFE simulation at the time point of screw perforation; colors indicate von Mises stress. C: HR-pQCT image of the perforated specimen.

Results

The first peak of the load-displacement curve defined screw loosening, which occurred at 64.7±69.8 N (range: 10.2–298.8 N) and was best predicted by L-µFE (R^2=0.90), followed by BV around the screw (R^2=0.87). The maximum load, associated with perforation, was at 208±108 N (range: 90–508 N), with NL-µFE providing the best prediction (R^2=0.93), followed by BV in front of the screw tip (R^2=0.89). NL-µFE could better predict screw displacement at maximum force (R^2=0.77) than TJD (R^2=0.70), with quantitative accuracy (Figure 2).

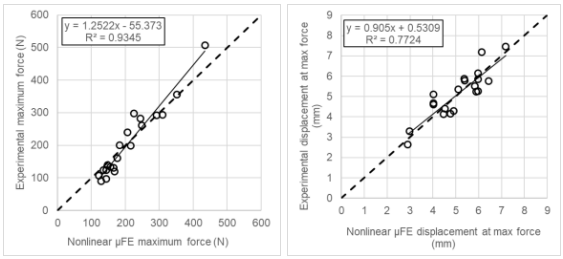

Figure 2: NL-µFE provided the strongest, quantitatively correct predictions of the experimental maximum load (left) and the respective displacement (right).

Discussion

Our results showed that despite density-based measures being strongly correlated with screw perforation force, the predictions by the NL-µFE models were even better and, most importantly, quantitatively correct. Explicit FE models have high potential to be utilized for simulating realistic scenarios involving multiple screws under various loading cases. Towards clinical applications, future studies should investigate if explicit FE models based on clinically available CT images could provide similar prediction accuracies.

References

1. Kralinger et al, J Bone Joint Surg Am, 96:1026-32, 2014.
2. Hengg et al, Arch Orthop Trauma Surg, 139:927-42, 2019.
3. Panagiotopoulou et al, Injury, 50:2176-95, 2019.
4. Pistoia et al, Bone, 30:842-8, 2002.
5. Werner et al, Int J Numer Meth Biomed Eng, 35:e3188, 2019.

Acknowledgements

This investigation was performed with the assistance of the AO Foundation.

THE INFLUENCE OF IMPLANT ALIGNMENT ON BONE STRAIN IN TOTAL ANKLE REPLACEMENT: AN FE STUDY

Bryony Halcrow (1), Ruth K Wilcox (1), Claire L Brockett (1)

1. Institute of Medical and Biological Engineering, University of Leeds, UK

Introduction

Ankle replacement is an end-stage intervention for ankle arthritis, which affects between 1-4% of the population. Revision rates of ankle arthroplasty surgeries are higher than those in the hip or knee, with alignment of the implant thought to play a crucial role in their success rates.

Alignment of the implant during surgery is dependent upon instrumentation and foot positioning, so implant placement can be difficult to implement correctly. Correct positioning is important for good clinical results. Varus and valgus deviation in patients is common.

Finite element (FE) modelling offers a non-invasive approach to estimate malpositioning, as FE methods can be used to identify increased bone strain and therefore the potential risk of bone or implant failure. The aim of this study was to develop image-based FE models of the ankle to investigate the influence of alignment on bone strain in the tibia.

Methods

Five cadaveric ankles were scanned at 82 µm using a µCT scanner and the resulting images segmented into individual bones (Simpleware ScanIP P-2019.09). Neutral alignment of the implant was determined using bony landmarks on the tibia and talus. Bones were virtually implanted with a stemmed ankle replacement device in neutral position. The tibial implant was then rotated by 10 degrees varus, valgus, plantarflexed and dorsiflexed deviation for malpositioned implantation, with virtual implantation representing the post-healed ankle.

Patient specific finite element models of each ankle were created in Abaqus (Abaqus/CAE 2017). Load and flexion values, corresponding to the peak axial load identified from literature, [1] were applied to the superior tibia, with the talus fixed inferiorly. Sliding contact between implant components was applied, with the implant-bone interface fixed. All parts were meshed using linear tetrahedral elements (~115,000 total).

All materials were assigned linear elastic material properties (Titanium E=113.8 GPa ν = 0.34, UHMWPE 850 MPa ν = 0.4). Bone was assigned ν=0.30, with element stiffness being derived from CT greyscale in five material bands. Experimental studies were used to calibrate CT greyscale to material stiffness using tibial specimens. Bone strain was measured at volumes of interest around the tibial implant.

Results

Twenty-five specimen-specific finite element models were created in total, investigating five different alignment scenarios.

In all cases, the highest strain within the tibial bone was found around the tip of the tibial stem. The inter-specimen variation of strain distribution was larger than the variation due to alignment. Changes in alignment by ten degrees showed small changes in strain across individual specimens.

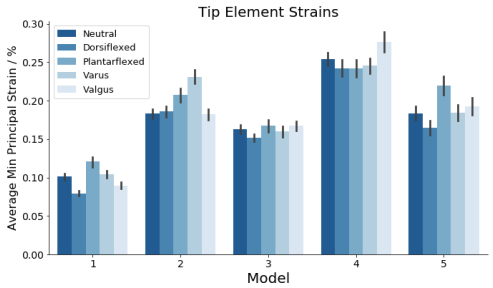

Figure 1: Average minimum principal strain at the tip region of interest showed higher inter-specimen strain variability than alignment variability.

Discussion

Under moderate levels of malpositioning (10 degrees), there was no significant change in strain around the implant with no clear trends evident across five models. Strain levels were consistent with previous studies [2] and below yield strain levels (0.65-0.75%) of the tibia [3]. Within each model, some malpositioning conditions did appear to increase strain, suggesting a subject specific response which may be related to the bone properties.

Modelling assumed a fully bonded bone-implant surface, however strain may increase if the implant is less well fixed. Although varus or valgus deformity is often pre-operative [4], correction to within ten degrees appears to have little influence on bone strain.

References

1. Smyth et al, Journal of Biomechanics, 53:105-110, 2017
2. Sopher et al, Medical Engineering and Physics, 42:80-90, 2017
3. Morgan et al, Journal of Biomechanics, 34:569-577, 2001
4. Kim et al, The Journal of Bone and Joint Surgery, 91:1183-1190, 2009

INTER-OPERATOR VARIABILITY IN A FINITE ELEMENT MODEL OF FEMURS WITH AND WITHOUT SIMULATED METASTATIC DEFECTS

A. Levillain (1), M. Gardegaront (2), S. Ali Agha (1), F. Bermond (2), D. Mitton (2), H. Follet (1)

1. Univ Lyon, Université Claude Bernard Lyon 1, INSERM, LYOS UMR 1033, 69008 Lyon, France;
2. Univ Lyon, Université Claude Bernard Lyon 1, Univ Eiffel, LBMC UMR_T9406, 69622 Lyon, France

Introduction

Femur metastases are associated with severe skeletal complications, including bone fracture [1]. Clinical scores, such as Mirel's, poorly estimate the risk of fracture. A recent study showed that subject-specific finite element (FE) models, based on QCT imaging, outweigh the performance of clinical experts when applied to patients [2]. However, several parameters of the FE models are operator-dependent and may affect the calculated failure load. The uncertainty on these parameters and their effects on the failure load have not been quantified. Therefore, the aim of the current study is to assess the inter-operator variability in a finite element model of femurs with and without created defects representing osteolytic metastases.

Material and methods

Six intact femurs and six femurs with defects were imaged with a clinical CT scan (voxel size: 0.390 x 0.390 x 0.670 mm^3) along with a calibration phantom (Mindways). Three operators performed the FE analysis (FEA) according to three different protocols. The general procedure was as follows. Reconstructed femurs were segmented (3D slicer, 4.10.2) and meshed with 300k tetrahedral elements (Ansys, 2019 R1) in accordance with a preliminary mesh convergence analysis. Each element was assigned a Young's modulus based on the density–elasticity relationship described by Keller [3] (Bonemat, 3.2). The models were orientated such that the angle between the loading axis and the diaphyseal axis was 20 degrees. A load of 5500N was applied on the femoral head, while nodal displacement of the distal diaphysis was fully restrained. Failure was defined when 0.33% of total elements reached a Von Mises stress value beyond their ultimate stress [4].
For "protocol 1" (operator 1), no specific instruction was given. For "protocol 2" (operators 2 and 3), both operators had identical femur orientation for a given specimen. For "protocol 3" (operators 2 and 3), the orientation and the segmentation threshold value were identical. Inter-operator variability was assessed for protocols 2 and 3. For "protocol 1", the failure load was compared to the mean failure load obtained in "protocol 2", where segmentation threshold was set freely.

Results and discussion

When segmentation threshold and femur orientation were set independently between operators, the mean relative inter-operator variability on the failure load was 17.4% and was significantly (p=0.02) higher for the femurs with defects (28.4%) compared to the intact femurs (6.8%) (Figure 1, none fixed parameters). Fixing the femur orientation alone or with the segmentation threshold resulted in a decrease in the relative inter-operator variability, with mean values of 7.5% and 4.9%, respectively, and no significant difference between the groups.

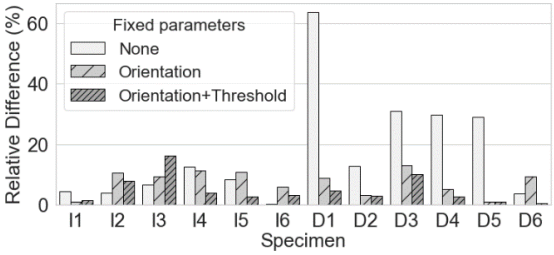

Figure 1: Inter-operator relative difference on the failure load according to the fixed parameters. I: Intact, D: Defect.

Results show that specific guidelines are mandatory for the FEA. Inter-operator variability on femur orientation, and, to a lesser extent, on segmentation, resulted in a large variability on the failure load, especially for the femurs with defects. This study highlights the need to (1) control and estimate the uncertainty on these operator-dependent parameters in the FEA, (2) include the uncertainty on the FE results, and (3) standardize the whole process for a clinical application, as recommended in [5, 6], especially for the femurs with metastatic defects. Other parameters, such as the meshing approach, material properties and failure criteria, vary between the FE models available in the literature [6, 7]. Future work will assess the influence of these parameters on the failure load calculated by the model.

References

1. Decroisette et al, J Thorac Oncol 2011
2. Eggermont et al, Bone, 130:115101, 2020
3. Keller, J Biomech. 27(9):1159–1168, 1994
4. Duchemin et al, CMBBE, 11(2):105-11, 2008.
5. Viceconti et al, Methods, 2020
6. Falcinelli et al, CMBBE, 23(14) :1138-1161, 2020
7. Sas et al, Bone reports 12: 100286, 2020

Acknowledgements

This project has received funding from the European Union's Horizon 2020 research and innovation programme under the Marie Skłodowska-Curie grant agreement No. 895139, LabEx PRIMES (ANR-11-LABX-0063) and MSDAvenir.

INDIVIDUALIZED SIMULATION OF THE MECHANICAL FRACTURE ENVIRONMENT AFTER TIBIAL EXCHANGE NAILING

Michael Roland (1), Marcel Orth (2), Joshua Gawlitza (3), Annchristin Uhl (1), Kerstin Wickert (1), Tim Pohlemann (2), Stefan Diebels (1), Benedikt Braun (4)

1. Saarland University – Chair of Applied Mechanics, Germany
2. Saarland University Hospital – Clinic for Trauma, Hand and Reconstructive Surgery, Germany
3. Technical University of Munich, Institute of Diagnostic and Interventional Radiology, Germany
4. University Hospital Tuebingen, On behalf of the Eberhard-Karls-University Tuebingen, Faculty of Medicine, Department of Trauma and Reconstructive Surgery, BG Hospital Tuebingen, Germany

Introduction

Non-union rate after tibial shaft fractures is among the highest for long bone fractures. Apart from largely uncontrollable biologic, injury and patient-specific factors, the mechanical environment of the fracture gap is the key quantity the healing. The goal of this study was to establish a patient-specific simulation workflow to determine the mechanical fracture environment immediately after tibial nail osteosynthesis and allow for an estimation of its mechanical healing potential.

Methods

A fracture patient with early mechanical failure after nail osteosynthesis of a tibial shaft fracture was referred for a further treatment. After hardware removal and exclusion of infection, two-step exchange nailing was performed. A postoperative computed tomography (CT) scan with a six-rod calibration phantom was used to generate an individualized 3D model of the bone-implant system. Resulting biomechanical forces, computed in a simulation-driven workflow based on patient monitoring and motion capturing data were used as an input for the simulation of the mechanical fracture environment before and after exchange nailing. The motion capturing was realized in a clinical gait course with the Xsens^{TM} tracking system. The patient's motion data was then processed in the musculoskeletal simulation environment AnyBody^{TM} to get individual and patient-specific joint forces and moments which are used as input for the biomechanical finite element (FE) simulations. Implant stresses for the initial and revision osteosynthetic constructs, as well as interfragmentary movement, resulting hydrostatic and octahedral shear strain were calculated and compared to the clinical treatment course [1,2].

Results

The simulation-based workflow was able to adequately predict the implant stresses in the initial treatment situation where mechanical implant failure occurred as well as in the current treatment. In addition, the hydrostatic and the octahedral shear strain of both treatments were computed and compared to the published healing window [1,2]. For the current treatment, the values are within the positive range, accordingly the fracture healed uneventfully during the clinical course.

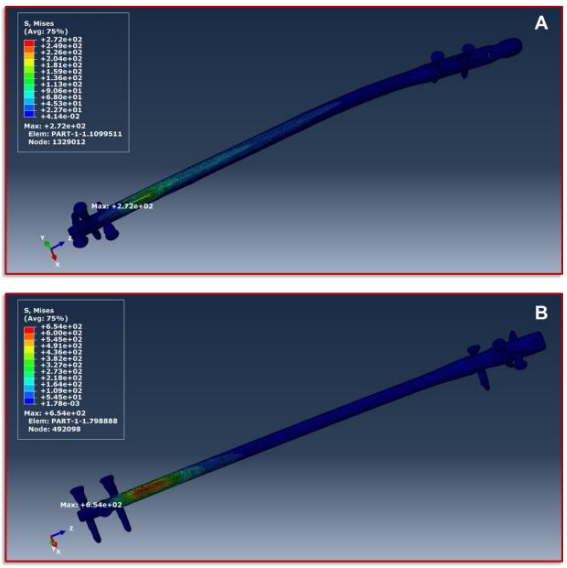

Figure 1: Typical result of the biomechanical FE simulation. Here, an illustration of the von Mises stress distribution of the intramedullary nail and screws is shown. A) current treatment and B) first treatment.

Conclusions

The simulation workflow presented is able to determine the mechanical environment of a fracture and fixation situation, predicting implant mechanical stresses as well as interfragmentary movement and the, resulting hydrostatic and octahedral shear strain. With using this workflow, the critical mechanical boundary conditions for fracture healing can be determined in relation to individual loading parameters during the early stages of fracture healing. Thus, individualized treatment recommendations during the early postoperative phase of patients suffering from fractures of the lower leg may be possible in order to prevent implant failure and development of non-unions.

References

1. Shefelbine S.J., Augat P., Claes L., Simon U. J Biomech 38:2440-2450 (2005)
2. Claes L., Heigele, C.A. J Biomech 32:255-266 (1999)

Acknowledgements

The Werner Siemens-Stiftung supported this work under the grant "Smart Implants 2.0".

ASSESSMENT OF STEM DESIGN ON EARLY POSTOPERATIVE PERIPROSTHETIC FEMUR FRACTURES

Özgür Cebeci (1)(2), Duane Cronin (3), Sara Checa (2)

1. Ingenieurgesellschaft für Automobiltechnik (IAT) mbH, Germany; 2. Julius Wolff Institute, Berlin Institute of Health, Charité – Universitätsmedizin Berlin, Germany; 3. Department of Mechanical and Mechatronics Engineering, University of Waterloo, Canada

Introduction

Periprosthetic femur fractures (PFFs) associated with total hip arthroplasty (THA) are the third most common reason for revision surgeries. Following a PFF, the calculated combined risk of either death or re-operation in the first year is 24% [1], demonstrating a need to better understand and mitigate PFFs.

Epidemiological data shows an increased early postoperative PFF rate with cementless double wedge compared to tapered stem designs [2]. Case reports suggest that early postoperative fractures occur due to low energy impact (LEI) falls and, physiological load cases such as walking, twisting motion, or stumbling [3].

Although the epidemiological data indicates the predisposing factors for early postoperative PFFs, the fracture mechanisms and the role played by the implant design are so far not fully understood.

The main objective of this study was to investigate early postoperative PFFs of artificial hip joints induced during LEI falls and stumbling for the double wedge and tapered stem designs.

Methods

In this study, PFFs were investigated applying LEI and stumbling load cases on implanted finite element femur models using load case specific boundary conditions.

LEI loads were defined based on previously published lateral fall induced proximal femur reaction forces using a contemporary Human Body Model (THUMS V502) [4]. Stumbling load cases were created according to the in-vivo reaction forces measured with telemetric hip implants [5] and applying muscle co-contraction forces for flexion-extension and adduction-abduction groups.

Trabecular and cortical bone were modeled with crushable foam and metal plasticity-based material models, including principal strain-based failure criteria. An average 75-year-old female femur model was generated for fracture assessments using statistical femur models. Finally, generic double wedge and tapered stem designs were inserted into the femur model with a fitting simulation similar to the surgical procedure [6] to consider the intraoperative stress state in early postoperative PPF assessments (Figure 1-a).

Results

Stem insertion simulations demonstrated increased intraoperative stresses in the proximal femur region for double wedge stem design due to the wedging effect and reduced distal support as a result of the rounded and polished distal design. Additionally, fracture assessment results showed an increased postoperative proximal load transfer for double wedge designs. Finally, the combination of the increased proximal loading and intraoperative stresses resulted in increased fracture risk for double wedge stem designs. Both stem designs yield type Al (Vancouver Classification) fractures under stumbling along with type B and A2 fractures under lateral fall load cases (Figure 1-c).

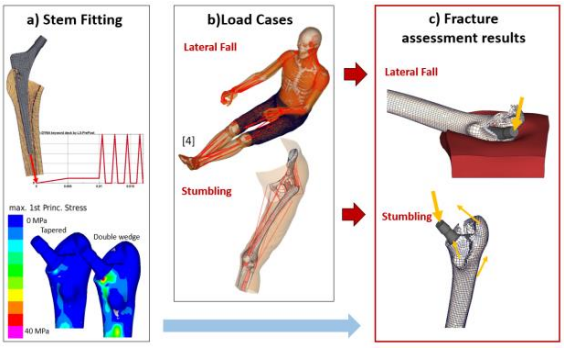

Figure 1: Stem design assessment: stem fitting simulations (a), lateral fall and stumbling load cases (b), detailed femur-implant fracture simulations (c)

Discussion

Combined human body models with statistical femur models can provide detailed insights into the risk of PPFs and quantify epidemiological observations.

Fracture assessment results indicated that double wedge stem designs pose a higher early operative PPF risk due to the increased intraoperative stresses and the postoperative proximal load transfer. In terms of the increased fracture rate of the double wedge design, results provided a similar conclusion as the epidemiological observations.

In the future, commercially available stem designs will be studied based on specific patient cohorts to enable patient group-specific design improvements to mitigate the PFF rates.

References

1. Drew et al, J. of Arthroplasty 10:01611, 2016.
2. Carli et al, Bone Joint J., 99-B:50-59, 2017.
3. Gromov et al, Bone Joint J.,99-B(4):451-457, 2017.
4. Cebeci, IRCOBI, 2020.
5. Bergmann et al, Langenbeck's A., 389: 53-59, 2004.
6. Tijou et al, J. Mec. Beh. of Bio. Mat.,88:102-108, 2018.

CONTRALATERAL IS NOT A CONTROL: AN *IN VIVO* HR-PQCT MICRO-FE STUDY OF HAND DOMINANCE IN THE HEALING DISTAL RADIUS

Caitlyn J. Collins (1), Penny R. Atkins (1), Nicholas Ohs (1), Lukas Horling (2), Kerstin Stock (2), Patrik Christen (1,3), Michael Blauth (2), Ralph Müller (1)

1. Institute for Biomechanics, ETH Zurich, Switzerland; 2. Department for Trauma Surgery, Innsbruck University Hospital, Austria; 3. Institute for Information Systems, FHNW, Switzerland

Introduction

Clinical, radiographic assessment of bone fracture healing lacks detailed information on callus development and consolidation of the fracture at the microstructural level. Moreover, despite evidence indicating poorer recovery in cases involving fracture of the non-dominant arm [1], hand dominance in fracture healing remains under investigated [2]. With the advent of high-resolution peripheral quantitative computed tomography (HR-pQCT), it is now possible to assess changes in microstructural and biomechanical properties *in vivo*. The objective of the current study was to assess the effect of hand dominance on fracture healing using time-lapsed HR-pQCT and micro-finite element (micro-FE) analysis.

Methods

Eleven patients (3 males, Ages 26-70; 8 females, Ages 27-81) with a conservatively treated, unilateral radius fracture provided informed consent prior to participation (Ethics Committee, Medical University of Innsbruck). Standard clinical HR-pQCT scans (XtremeCT II, Scanco Medical AG, isotropic voxel size: 61 µm) were taken of the fractured (F) and contralateral (C) radii (168 slices, starting 9 mm proximal to the radius endplate) at 1, 3, 5, 13, 26, and 52 weeks post-fracture. Additional data, both proximal and distal to the standard scan, were captured for the fractured radii (504 slices). Micro-FE models were generated from previously registered HR-pQCT data [3] via direct conversion of the image voxels to hexahedral elements (Python v3.7). Scaled, linear elastic material properties computed directly from Gaussian filtered (σ=0.8, support=1) image data using [4] and a Poisson's ratio of 0.3 were assigned to all elements. "High friction" axial compression tests with a prescribed 1% displacement were performed on all three models using a CRAY XE6 (Swiss National Supercomputing Centre). Anterior and posterior regions were isolated using a cutting plane, center of mass origin with a surface normal towards the dorsal tubercle of the radius (Figure 1, right). Results were used to evaluate time-lapsed changes in the Effective (Eff) Strain distribution between C- and F-radii and to assess effects of hand dominance (D-dominant, N-non-dominant).

Results

Median Eff Strain was consistently higher (20 to 55%) in the posterior compared to the anterior regions in the C-radii (p=0.027). This discrepancy showed more uniform behavior across the D,C-radii, irrespective of patient age (Figure 1, left). As a result of the fracture, Eff Strain ratios (AP: anterior/posterior) were inverted until weeks 13 and 26 in the D,F and N,F radii, respectively (Table 1). Visual confirmation of cortical bridging in sagittal image slices was strongly correlated (R^2=0.83, p<0.001) with the inversion of the strain ratio.

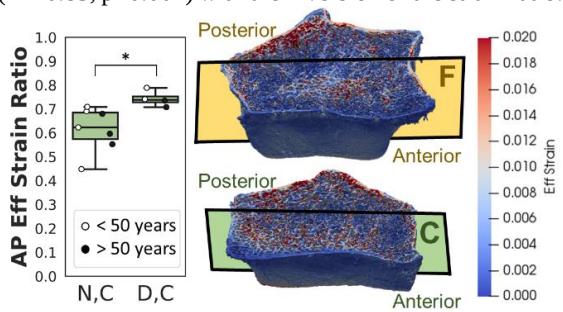

*Figure 1: (Left) Boxplot of the median AP Eff Strain ratio for the N,C and D,C radii. (Right) Contour plots of Eff Strain for F and C radii. *p<0.05.*

	1wk	5wk	13wk	26 wk	56 wk
D,F	1.18 ±0.43	1.22 ±0.65	**0.84 ±0.14**	0.82 ±0.12	0.75 ±0.12
N,F	1.27 ±0.30	1.20 ±0.36	0.98 ±0.18	**0.86 ±0.14**	0.82 ±0.10
N,C	0.62 ±0.09	-	-	-	-
D,C	0.74 ±0.03	-	-	-	-

Table 1: Summary of median AP Eff Strain ratios (±std). Bold indicates point of inversion.

Discussion

The disparity in AP Eff Strain ratio between N,C and D,C-radii suggests that C-radii cannot be used as a patient-specific, "control" reference. The AP Eff Strain ratio shows promise for tracking patient recovery post-fracture, particularly regarding bridging of the cortex. Full recovery may exceed one year, as subjects in the current study have yet to achieve either the target D,C or N,C ratios. Despite the limited size of the current subset, the results indicate that HR-pQCT-based micro-FE is sensitive enough to detect and track dominance-related contributions to bone fracture healing.

References

1. Ashe et al, J Clin Densitom, 10(1):93-101, 2007.
2. de Jong et al, JBMR, 31(5):1114-1122, 2015.
3. Thévenaz et al, IEEE Trans Image Process, 7:27-41, 1998.
4. Mulder et al, Bone, 41:256-265, 2007.

COMPUTATIONAL STATIC COMPARISON OF FEMORAL RECONSTRUCTION MODELS

Iván López (1), Julián Echeverry(1), Víctor Domínguez (2,3), Víctor Araújo (3)

1.Universidad de La Sabana, Colombia; 2. Tecnológico de Monterrey, México. 3. Instituto Nacional de Rehabilitación Luis Guillermo Ibarra Ibarra, México

Introduction

Bone modeling by computational tomography (CT) is a common practice in biomedical engineering for the planning and optimization of surgeries, increasing the biomechanical performance of the prosthesis and implants. The femur is the bone that supports the loads of the upper part of the body, it is connected to the hip by the femoral head and acetabulum. The accurate modeling of this bone is vital for the design of prostheses used in hip arthroplasty [1]. Three different femoral reconstruction models are compared, model 1 a solid bone with one material, model 2 a bone with femoral canal and one material, and model 3 a bone with a different material in each element.

Keywords: Femur, Bone modeling, FEM, CT Scan, Prosthesis design.

Methods

3D solids: Initially, on a heathy patient a CT scan was performed generating a DICOM file. Then, in the software Mimics, bone segmentation was performed for the model 1 and 2. Followed by importing it to the software 3-Matic where the surface of the segmented images for model 1 and 2 was generated. Finally, the 2 surfaces were imported in IGES format in Autodesk Inventor, repairing the surfaces and generating the 3D models which were exported in IGES format.

Meshing: Initially, the IGES file from model 1 and 2 was imported into ANSYS, followed by the meshing of model 1 and 2. For the model 3, the properties to each element were assigned with the software Bonemat. It was necessary to import the ANSYS mesh for case 1 with its respective DICOM images, resulting in the mesh for model 3, and each element with different mechanical properties assigned according to the Hounsfield (HU) scale of the tomography. A convergence analysis was also performed to find out the best element size for the bone modeling.

FEM simulation: With the 3 meshes in the ANSYS software, the boundary conditions and loads shown in the ISO 7206-4 [2]and ASTM F2996[3] standards were placed. Von Mises's Maximum stress and Computation Time were calculated.

Results

Comparisons were made with respect to model 3 of Bonemat see Table 1. The maximum von Mises(vM) stress changes 49% with respect to model 1 and 8% with model 2. The total displacement has a difference with respect to the model 1 of 64% and 46% with model 2. The time used was 71% less for model 1 and 48% with model 2. As shown in Figure 1, the maximum stress is in the neck area.

Model	1: Solid	2: Canal	3:Bonemat
Max vM (MPa)	17.7	31.9	34.7
Max Disp (mm)	0.23	0.35	0.64
Time (s)	64	116	224

Table 1: Results for maximum Von Mises (vM) stress, displacement (Disp) and simulation time.

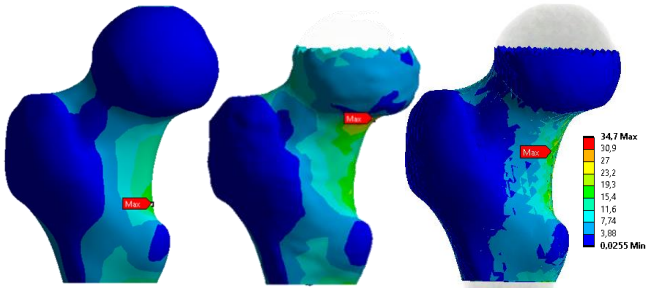

Model 1: Solid | *Model* 2: Canal | Model 3: *Bonemat*

Figure 1: Maximum Von Mises stress for the 3 models.

Discussion

Refining the models with more materials from a CT scan increases the stresses and the displacement, because the mechanical properties across the bone are not constant and the total stiffness of the bone is less than solid and canal counterparts. The 3 models present the maximum stress at the femoral neck as expected, the neck is the most common place of failure.

References

1. F. A, D. H, D. P, D. K. Femoral anatomy, computed tomography and computer-aided design of prosthetic implants. Arch Orthop Trauma Surg. 2002;122:262–8. doi:10.1007/s00402-001-0361-8.

2. ISO. 7206-4:2010 Implants for surgery — Partial and total hip joint prostheses Part 4: Determination of endurance properties and performance of stemmed femoral components. Int Organ Stand Geneva, Switzerland, www.iso.org. 2016;:1–24.

3. ASTM. F 2996-13 Standard Practice for Finite Element Analysis (FEA) of Non-Modular Metallic Orthopaedic Hip Femoral Stems. ASTM Int Conshohocken, PA, www.astm.org. 2013;:1–11.

THE INFLUENCE OF TRABECULAR BONE DENSITY IN THE CEMENTED ARTHROPLASTY – AN EXPERIMENTAL STUDY

Ana Cabrinha (1), António Ramos (2)

1, 2. TEMA-DEM, Biomechanics Group, University of Aveiro, Portugal;

Introduction

Cemented or non-cemented fixation is a controversy decision between surgeons. Some refer that cementless implants are more appropriate for younger patients, rather than cemented ones. In contrast, supporters of cemented implants maintain that it is not reasonable to use an expensive cementless implant that gives the same overall clinical outcomes as a cheaper one, even in younger patients [1-3]. Younger patients are associated with denser bones, whereas older patients are associated with weaker and less dense bones. The degree of osteopenia can affect the integrity of the cement fixation, compromising the implant longevity.

With the purpose of understanding it, this work aims to develop a model that reproduces the bone-cement and the implant-cement interfaces, in order to assess its long-term behavior. For this purpose, experimental samples of a section of a cemented arthroplasty located at the epiphysis of a long bone were fabricated, using different bone densities.

Methods and Materials

A polyurethane foam was used to reproduce the trabecular bone structure with three densities: 7.5,10 and 12 PCF, presented in Figure 1. The highest one regarding younger patients and the lowest one regarding older patients. Manual cementation was used at the same time with the same cement. The samples were subjected to a tensile test and digital image correlation was used to measure the strains in cement. The sample was loaded at the upper end of the stem with a 50N in a quasi-static force (0.5 mm/s increment).



Figure 1: Experimental samples.

Results and Discussion

The mean response force increases 20% for the 10 PCF foam and 60% for the 12 PCF, in relation to the 7.5 PCF, presented in Figure 2. This suggests an increase in the sample mechanical resistance with the increase of foam density. In contrast, the cement strain decreases about 96% for the 10 PCF foam and 92% for the 12 PCF, in relation to the lower density.

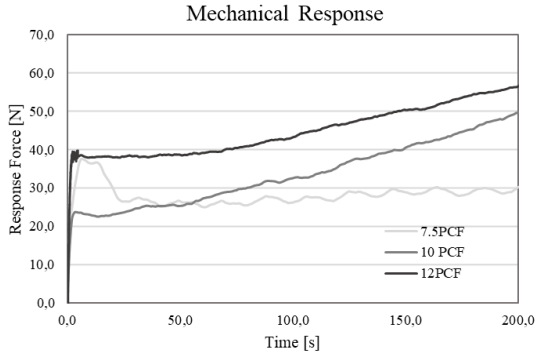

Figure 2: Response in force vs time.

Similarly, the micromovements of bone cement decline 30% and 92%, for the 10 and 12 PCF, respectively, in relation to the 7.5 PCF. These findings indicate that the increase in bone density increases the implant stability. On the other hand, bone cement apposition in the foam decreased with the increase of density. Lower levels of interdigitating are associated with low fracture toughness of cement-bone interface, increasing failure risk [4,5]. Thus, the experimental results indicate that the increase in bone density might compromise the cement-bone interface.

Conclusions

The experimental results suggest that greater bone densities provide stability and a stiffer structure, but the cement-bone interface might be compromised.

References

1. Aprato et al., Ann Transl Med, 4(7):129, 2016
2. Chen et al., J Orthop Surg Res, 14:262-272, 2019
3. Franceschetti et al., Knee Surg Sports Traumatol Arthrosc, 25:1749-1756, 2017
4. Srinivasan et al, J Mech Behav Biomed Mater, 66:181-186, 2017.
5. Waanders et al, J Biomech Eng, 43:1167-1175, 2010.

Acknowledgements

This work was supported by POCI-01-0145-FEDER-032486, UID/EMS/00481/2019, – FCT, by the FEDER, with COMPETE2020 - (POCI), FCT/MCTES.

Finite element model to predict the electric stimuli delivered by planar capacitive systems to stimulate bone-implant interfaces

Dora Videira (1), Marco P. Soares dos Santos (1), António Ramos (1)

1. Centre for Mechanical Technology & Automation (TEMA), Department of Mechanical Engineering, University of Aveiro, Portugal

Introduction

Joint replacement surgery is among the most widely performed surgical procedure worldwide [1]. To avoid revisions, the concept of instrumented implant emerged, which is undergoing increasing scientific evolution, showing in previous studies promising results regarding the stimulation of peri-implant bone regeneration and the monitoring of bone-implant fixation [1]. The main goal of this work is to develop a finite element model to predict the excitation-dependent electrical stimuli delivered by capacitive planar stimulation systems in trabecular structures.

Methods

Electric fields were analysed using finite element model developed with trabecular bone structure as illustrated in Figure 1. Models were developed using a capacitive system comprising four electrodes and a bone structure, reconstructed from micro-CT images of a sheep bone trabecular structure (10x10x10mm). The bone structure was biphasically modelled as a liquid phase (65%) and a mineral phase (35%). The liquid part was modelled to contain water and collagen, while the mineral part only includes hydroxyapatite.

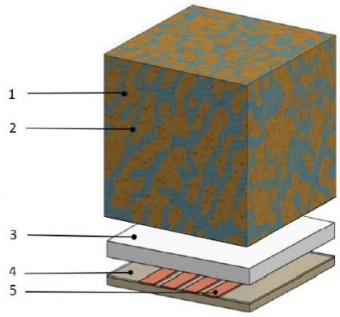

Figure 1: Finite element model (Domains: 1 - Liquid bone part, 2 - Mineral bone part, 3 - Polymeric substrate, 4 - Substrate, 5 - Electrodes).

The capacitive sensor consists of two pairs of striped planar electrodes arranged under the bone structure. Two electrical excitations were used to power the electrodes: 5 V and 10 V peak, both with 60 kHz square waveform. Since there is no contact between the bone structure and the stimulator, this apparatus is based on a non-invasive methodology. The finite element model was developed and simulated in COMSOL Multiphysics (v. 5.3, COMSOL).

Results

The results showed variations in the region-dependent electric field stimuli, with a significant decrease in its magnitude for regions of the bone structure at $x \geq 1.1$ mm away from the stimulator (Figure 2). For $x < 1.1$, this stimulative technology is able to deliver osteogenic stimuli [1]: electric stimuli up to 0.82 V/mm were found (Figure 2.b). The electric stimuli doubled when the excitation is doubled.

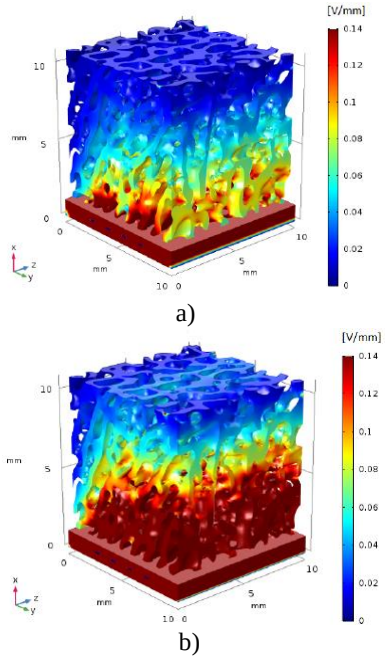

Figure 2: Distribution of the electric field in the model (liquid bone phase is hidden). a) 60 kHz and 5 V; b) 60 kHz and 10 V.

Discussion

Previous studies found the suitable osteogenic electric stimuli provided by planar capacitive systems [1]. Nevertheless, these stimuli were found using in vitro cellular tests. This study provides, for the first time, the distribution analysis of the electric stimuli in a bone structure. We found that the same electric excitations used in cellular tests provided similar osteogenic stimuli using trabecular samples. These results support the design of high-sophisticated stimulative technology to be integrated in future instrumented active implants, such that revision surgeries can be avoided.

References

1. Marco P. Soares dos Santos et al., Sci Rep, 9: 5001, 2019.

Stress changes in growth plates of an adolescent idiopathic scoliotic spine following unilateral muscle weakening

[1]Zeinab Kamal, [2]Gholamreza Rouhi
[1]Department of Biomedical Engineering, University of Twente, Enschede, Netherlands
[2]Department of Biomedical Engineering, Amirkabir University of Technology, Tehran, Iran
Email: z.kamal@utwente.nl

Introduction

In order to investigate the effect of unilateral muscle weakening on the stress distribution in the growth-plates (GPs) of an adolescent idiopathic scoliosis (AIS) spine, the equivalent loads (as an alternative to *in vivo* loading conditions), estimated by our previously-validated trunk musculoskeletal (MS) model of AIS spine [1], were applied on the finite element model of GPs of L1 through L4. Results showed that weakening of the concave-side multifidus lumborum (MFL) and longissimus thoracis pars thoracic (LGPT) muscles rendered a reduction of about 25% in the compressive von Mises stress on the concave side of GPs, which can decelerate the deformity progression during growth.

Methods

A finite element (FE) model of L1 to the L4 vertebrae of one scoliotic 11.5-year-old adolescent was developed based on the subject-specific upright position images (Fig. 1).

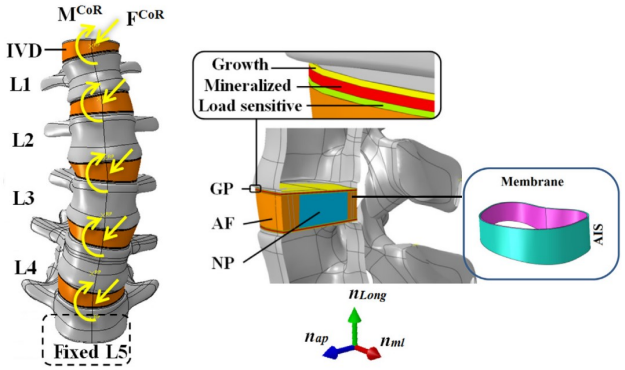

Figure1: Detailed model of scoliotic L1-L2 thorough L4-L5 segments with the schematic depiction of the reaction force (F^{CoR}) and moments (M^{CoR}) about the intervertebral disc (IVD) centroids at each level. The model compromises the annulus fibrosis (AF), nucleus pulposus (NP), GPs in L1 through L4 vertebrae and rebar embedded by membrane elements in each IVD that are illustrated in one level at the right side. The unit vectors of n_{Long} , n_{ml}, and n_{ap} are in the local longitudinal, mediolateral, and anteroposterior directions on the GP surface at each level, respectively. GPs were modelled with three distinct parts: mineralized-, growth-, and load sensitive region.

The equivalent loads, approximated as vector summation of the muscle and gravitational forces at each level as well as the reaction moments about the IVD centroids using our previously-validated MS model in the upright-standing posture [1], were applied on the GPs at each level of the subject-specific FE models, and the stress distribution within GPs were estimated (Fig. 2). Muscle weakening was simulated based on the experimental data related to the 95% loss of strength in rabbits' BTX-A injected muscles [2], by reducing the physiological cross-sectional area of the LGPT and MFL muscles on the concave side.

Results and Discussion

The equivalent loads (Fig. 2a), as an alternative to the *in vivo* loading condition of muscles and gravity loads at each level, were found to be in the physiological ranges of ultimate shear [3], and compressive strength [4].

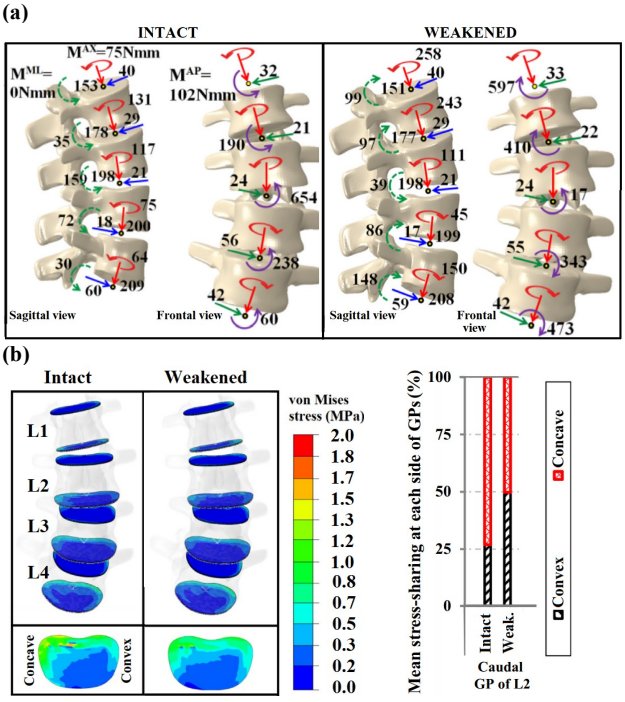

Figure 2. Reaction forces (N) and reaction moments (N.mm) about the IVD centroids of T12-L1 through L4-L5 levels in (a) NFE and (b) SFE models in the sagittal (Left b), and coronal (Right b) views. (c) von Mises stress distribution (MPa) within the GPs under the equivalent loads.

The greatest von Mises stress occurred in the apical GP, i.e., the caudal GP at the L2-L3 level, of the intact model (Fig. 2b). However, results indicate that weakening of the concave-side muscles led to a reduction of 25% in the ratio of the von Mises stresses in the concave- over the convex side of the GPs and a more uniform stress distribution on the apical GP (Fig. 2b).

Conclusions

Unilaterally weakening of muscles caused a reduction in the reaction moments and thus a more uniform stress distribution on the GPs of the weakened model, which in turn can decelerate the deformity progression during growth, in accordance with the Hueter-Volkmann's theory [5]. The intradiscal pressures found in this study were in a satisfactory agreement with the *in-vivo* data[6].

REFERENCES

[1] Kamal Z et al. (2020) J. Biomech. 111: 109997. [2] Fortuna R et al. (2011) J Biomech. 44:39–44. [3] Gallagher S et al. Clin Biomech (Bristol, Avon. (2012) 27(10): 973-978. [4] Ayoub MM et al. Manual Materials Handling, London: Taylor & Francis; 1989. [5] Mehlman C et al. (1997) Am J Orthop (Belle Mead NJ) 26(11): 798–800. [6] Dreischarf M et al. (2016) J Biomech. 49: 833–845.

A COMBINED MOTION ANALYSIS AND FEM APPROACH FOR PLANTAR FOOT ORTHOSIS OPTIMIZATION FOR DIABETIC FOOT PREVENTION

Alfredo Ciniglio (1), Mattia Palladino (1), Annamaria Guiotto (1), Fabiola Spolaor (1), Alessandra Ianniello (2), Eleonora Meggiato (3), Zimi Sawacha (1,4)

1. *Dept. of Information Engineering, University of Padova, Italy; 2. Orthomedica S.r.l., Italy; 3. Podartis S.r.l., Italy; 4. Dept. of Medicine, Italy.*

Introduction

Diabetes mellitus is an epidemic disease: more than 422 million people worldwide presently suffer from T2DM and 10 years after disease onset, between 20 and 50% T2DM patients develop diabetes neuropathy, a major risk factor for diabetic foot problems. This represents the most common cause of non-traumatic amputation (Armstrong et al 2017). Although the use of optimized footwear combined with foot orthotics is inherently implemented in the clinical care path [1], foot orthosis prescription is currently based on clinical experience and static measures. With a re-ulceration risk of 65% in 5 years [1], there is an important potential to optimize foot orthosis prescription by accounting for dynamic foot biomechanical function [2]. As multi-scale modelling has proven to accurately predict both high plantar pressure and even more important internal tissue stresses [3] the aim of this contribution is to devise a simplified pipeline to apply this methodology in ambulatory conditions without the constraints of a gait laboratory.

Methods

The foot geometry of a cohort of 9 neuropathic diabetic subjects ((mean (SD) age 60.89(17.37) years and BMI 29.36(5.41) Kg/m^2) was captured with a 3D scanner. Foot bones geometry was segmented from a database of neuropathic subjects foot MRI [4]. The foot bones were scaled based on every subject foot morphology (Abaqus). Each subject insoles geometries were scanned and meshed with tetrahedral elements (Fig. 1) and material properties were assigned according to the literature [3-4] and to the material characteristics declared by the insole manufacturer. The vertical loads acquired during gait on a treadmill (2 km/h) through a PP insole system (PedarX, Novel gmbh) were applied in the FEM as boundary conditions together with the ankle flexion/extension angle. Loading response and midstance phases of the gait cycle were simulated [3] with and without the insole (see example in Figure 2). The comparison between the experimental PP and the simulated ones (peak and distribution) was used for validation purposes. Both simulated PP and internal Von Mises stresses in plantar soft tissues were compared across the different conditions (Root Mean Square Distance).

Results

A good agreement was reached between the experimental and the simulated PP. Simulated insoles did not completely succeed in assuring a better PP distribution but they reduced Von Mises stresses.

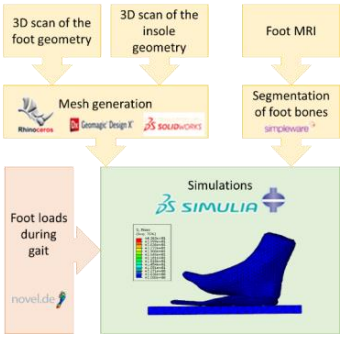

Figure 1: Pipeline for the FEM creation.

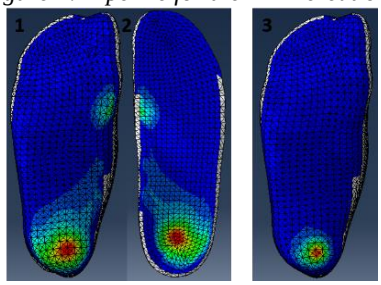

Figure 2: Left, the pipeline for the FEM development; Right, the FEM simulation with (1,2) and without (3) the insole.

Discussion

The behaviour of the insole was successfully simulated through the proposed pipeline by adopting a simple experimental protocol applicable in ambulatory conditions. This approach can be used to predict the effects of the produced insole on the foot function thus resulting in an efficient tool for optimizing its design.

References

1. Armstrong et al, SAGE, 47(2): 145-171, 2017.
2. Telfer et al, J Biomech, 60:157-161, 2017.
3. Scarton et al, Gait & Posture, 60: 279-285, 2018.
4. Guiotto et al, J Biomech, 47(12): 3064-3071, 2014.

Acknowledgements

The study was conducted within the grant "S.F.I.D.A. Scarpa Funzionale Innovativa per Diabetici Attivi" – ID 10230017, financed by "POR FESR 2014 – 2020 Regione del Veneto, Azione 1.1.4 Bando Aggregazioni, DGR 711/2019".

REDUCED TRABECULAR BONE GROWTH IN AN ADOLESCENT FEMALE CYSTIC FIBROSIS RAT MODEL

Maged Awadalla (1), Egon Perilli (1), Saulo Martelli (1), Kaye S. Morgan (2), Marcus Kitchen (2), Patricia Cmielewski (3,4), Alexandra S. A. McCarron (3,4), David W. Parsons (3,4), and Martin Donnelley (3,4)

1. Medical Device Research Institute, College of Science and Engineering, Flinders University, Australia; 2. School of Physics and Astronomy, Monash University, Australia 3. Robinson Research Institute, and 4. Adelaide Medical School, The University Adelaide, Australia.

INTRODUCTION

Patients with cystic fibrosis (CF) have an increased frequency of bone fracture compared to healthy subjects [1] and this is more pronounced in adolescent CF females, compared their male counterparts and healthy females [1]. A CF rat model has recently been developed, which exhibits delayed or no CF-related pancreatic, gut and lung disease [2]; this enables to study bone growth during development without indirect secondary affects (e.g. lung, gut or pancreatic disease) [2]. This model showed a marked reduction in bone content in juvenile CF rats (3-6 weeks) [3], however, it is unknown if this transfers into adolescences, a developmental stage where fractures are observed in CF humans. The aim of this study was to investigate if the reduced bone growth seen in juvenile rats continues during adolescence.

METHODS

Heterozygote (Het) and cystic fibrosis transmembrane regulator (CFTR) knockout Sprague-Dawley rats [2] (n=11 and 7, respectively) were used to investigate the effect of CFTR on trabecular volume fraction. At the start of the study, the two groups did not differ in age (Het: 13.8±2.2 weeks, CF: 12.9±1.6 weeks, p-value=0.3 Mann-Whitney) and weight (Het: 268.8±62.6 grams, CF: 232.6±21.8 grams, p-value=0.1 Mann-Whitney). All experiments were conducted at the AS Imaging and Medical beamline (Clayton, VIC) as part of an ongoing study. Tissues were scavenged under approval from the University of Adelaide animal ethics committee.

Animals were sacrificed using Sodium Pentobarbital overdose. Micro-computed tomography scans of the tibiae were performed (energy of 30 keV) at an isotropic pixel size of 19 µm and cross-section images were reconstructed (X-tract software). The trabecular bone volume of interest (VOI) was selected starting 1 mm below the lower end of the growth plate, extending distally for 3 mm [4] and the following bone morphometric parameters quantified: trabecular bone volume fraction (BV/TV), trabecular number, trabecular thickness and separation (CT Analyser, Skyscan-Bruker, Belgium) [4].

RESULTS AND DISCUSSION

The sample size in this study was not large enough to conduct statistical analysis at different time points. Therefore, the age distribution of our cohort was used to observe only the trend of trabecular growth (Figure 1).

It was observed that CF rats do not show signs of trabecular growth from week 11 to 15. However, Het rats show sign of trabecular growth from week 12 to 16.

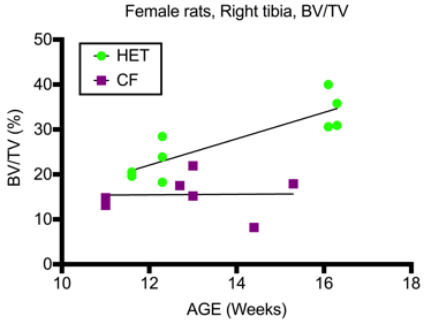

Figure 1: A) Slowed trabecular bone growth (BV/TV) over time in the right tibia of female CF rats compared to female HET (each dot represents an individual rat).

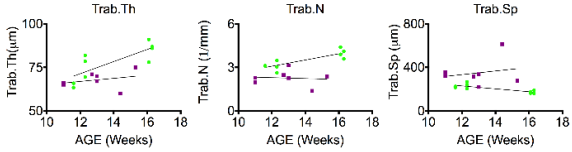

Figure2.: the effect of CF genetic disorder on trabecular thickness (Tb.Th), number (Tb.N) and separation (Tb.Sp). (each dot represents an individual rat).

These preliminary results indicate a trend of reduced trabecular bone growth (lower BV/TV, Tb.Th, Tb.N and increased Tb.Sp) in a female CF rat model (Figure. 2).

CONCLUSIONS

Although preliminary, our results indicate that adolescent CF rats have a trend towards reduced bone growth compared to their healthy HET littermate. This appears consistent with adolescent female CF patients having an increased fracture frequency compared to their male counterpart and healthy females [1]. This rat model provides the opportunity to evaluate bone growth and its strength in CF animals. Further studies are in progress using this technique.

REFERENCES

1. Hendersom R C et al., J Pedictr,125:208-212, 1994.
2. McCarron A et al., Am J Pathology, 2020.
3. Stalvey M S et al., PLoS One, 12:e0188497, 2017.
4. Perilli E. et al., Osteoporos Int, 21:1371-82. 2010.

DEPENDENCY OF LOWER LIMB JOINT REACTION FORCES ON FEMORAL ANTEVERSION

Luca Modenese (1), Christopher P. Carty (2)

1. Dept of Civil Engineering, Imperial College London, UK;
2. Griffith Centre of Biomedical and Rehabilitation Engineering (GCORE), Griffith University, Australia

Introduction

Generic musculoskeletal (MSK) models are employed to investigate the internal forces occurring in the human body under the assumption that "mean" skeletal anatomy can be linearly scaled to adequately match the anthropometry of specific individuals. This assumption may not be broadly acceptable, and personalization of key morphological features may be indicated when calculating joint reactions forces (JRFs) for individuals who deviate from the mean [1]. For example, femoral anteversion (defined as the angle between the plane of the femoral neck axis and that of the femoral axis [2]) has been previously shown to affect muscle moment arms [2] and hip JRFs [3], but its effect on the knee and ankle joints remains unknown. In this work we investigated how variations of femoral anteversion can influence the JRFs in a scaled generic MSK model of the lower limb.

Methods

A generic, full-body MSK model [4] was scaled to the anthropometrics of an elderly participant (86 yo, 75 kg) with an instrumented total knee prosthesis implanted on his left leg [5]. The model was modified by decreasing the maximum isometric force of the muscles crossing the knee joint by 35% [4], obtaining the *baseline model*. Its JRF predictions were preliminarily assessed against in vivo measurements of knee joint contact forces, resulting in overestimation of the largest force peak by 0.59±0.14 BW across five gait trials. Subsequently, the left femur of the baseline model (anteversion angle: 12°) was deformed using a custom MATLAB tool that applies a user-defined torsion profile to the bone long axis, generating a new bone geometry and adjusting its muscle attachments as in [2]. Five *modified models* with anteversion angles ranging from 5° to 40° (Figure 1A) in 7° steps were generated using this approach. The angles range was chosen based on population data [7]. Apart from the left femur alterations, the nominal and modified models were identical. Using a standard workflow (inverse kinematics, static optimization, joint reaction analysis) in OpenSim 3.3 [8], five walking trials from [5] were simulated and JRF peak magnitudes calculated for the left leg joints. These values were then compared against those of the nominal model and correspondent in vivo knee measurements.

Results

The computed JRF magnitudes showed a marked dependency on the femoral anteversion angle (Figure 1B), with second peaks increasing up to 17.6±4.5% of the nominal model values at the hip and 44.6±12.9% at the knee joint for 40° anteversion. JRFs decreased for lower than nominal anteversion angle (hip: -3.1±1.1%, knee: -5.2±0.6% for 5° anteversion). The ankle joint was practically unaffected by the changes in femoral bone morphology (<2% differences for all models).

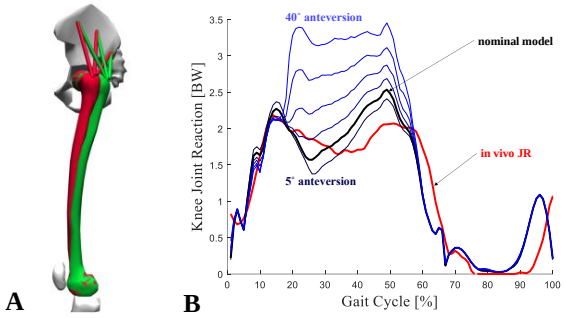

Figure 1: A) Femoral geometries with 5° (red) and 40° (green) anteversion angles. B) Knee JRFs from nominal and modified models for a representative gait trial.

Discussion

The observed variations of hip JRFs are consistent with those reported by [3] using a different MSK model. At the knee joint, the most accurate JRFs were estimated by the nominal model, which had the closest femoral anteversion angle to the actual participant's femur (≈10° estimated from the available CT scans). Our findings suggest caution against using a generic MSK model for estimating JRFs in specific individuals, as variations in a single morphological feature like femoral anteversion can strongly influence the model outputs at the hip and knee joints. This is valid *a fortiori* for populations with bone deformities beyond those reported in [7]. The presented methodology can be used to investigate the dependency of JRFs on bone morphology in other human joints.

References

1. Moissenet et al, J Biomech, 63: 8-20, 2017.
2. Arnold et al, J Biomech, 34: 437-447, 2001
3. Heller et al, Clin Biomech, 16: 664-649, 2001.
4. Rajagopal et al, IEEE Trans BME, 63: 2068-2079, 2016.
5. Fregly et al, J Orthop Res, 30: 503-513, 2012
6. Marra et al, J Biomech Eng, 137: 020904, 2015.
7. Strecker et al, J Bone Joint Surg Br, 79: 1019-1023, 1997.
8. Delp et al, IEEE Trans BME, 54: 1940-1950, 2007.

Acknowledgements

Imperial College Research Fellowship to LM.

STRESS ANALYSIS OF A VERTEBRA USING ARTIFICIAL NEURAL NETWORKS AND MESH MORPHING

Cameron James (1, 2), Mohamed Masmoudi (1, 3), Kateryna Bastova (1), Lingzhong Guo (2)

1. Adagos, France;
2. Department of Automatic Control and Systems Engineering, The University of Sheffield, UK;
3. Toulouse Mathematics Institute, France;

Introduction

Low back pain is recognized by WHO as a priority condition and a leading cause of disability [1]. Despite this, surgical interventions are notoriously challenging [2] and typically are not considered except in chronic cases where conservative treatment options have failed. Biomechanical models have already proved their use in surgical planning. However, slow computational times and manual setups prevent these models from being implemented as tools in intraoperative scenarios.

Recent developments have demonstrated the use of artificial neural networks (ANNs) to substitute finite element analysis (FEA) at a reduced computational cost [3]. To-date, this approach has only been applied to simple geometries, where the mesh of each subject can easily be made topologically consistent by defining its distribution on the geometry's edges. This topological consistency is essential for training the ANN; however, it can pose a challenge in a set of anatomical geometries, where edges are typically not clearly defined.

As a preliminary study, we will discuss here the construction of an ANN substitute for FEA of a single lumbar vertebra, using a mesh morphing approach to solve the issues of mesh topology.

Methods

The morphing approach was based on the algorithm presented in [4] with an adaptation for a hierarchical multigrid approach. The algorithm's inputs are segmentations of a reference vertebra (I0) and a target vertebra (I1), and outputs are the displacement fields that morph I0 to I1. The dataset [5], contained 40 lumbar vertebrae (8 spines) which were used for training the model, while 2 more spines were retained for testing. Initially, every combination of I0 and I1, using the 40 training vertebrae, were tested to investigate how selecting I0 and I1 from different vertebra levels or subjects would influence the results.

After the initial investigation, a 'typical' L3 vertebra was chosen as I0 for building the ANN and a tetrahedral mesh of I0 was generated using MeshLab. The nodal coordinates of the I0 mesh were combined with the displacement fields obtained from the morphing approach to create a set of 40 meshes. Using GetFEM++ to implement FEA, all 40 were simulated under non-physiological loading. NeurEco, a factory for building ANNs with intricate yet minimal structures, was used to train an ANN for predicting the FEA stress results from the mesh coordinates. The testing set was evaluated using the same approach to build the mesh.

Results

On the training set, morphing I0 achieved a mean Sørensen-Dice coefficient of 0.99 compared to I1. The accuracy of morphing between subjects vs. between vertebra levels was not significantly different ($p=0.46$), nor between both simultaneously vs. just one ($p=0.69$, $p=0.59$ respectively). Thus, the entire training set could be used for the ANN, regardless of level or subject.

In evaluating the testing set (10 vertebrae), the stress results obtained from FEA simulation and from the ANN prediction showed excellent fidelity, achieving a mean absolute percentage error (MAPE) of 6.00 % in the Euclidean norm of the output vector.

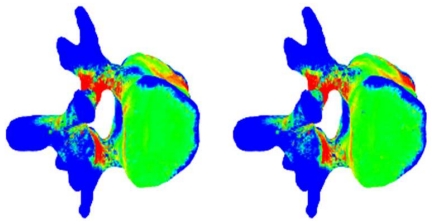

Figure 1: Testing set results for σ_{11} of the Cauchy stress tensor, obtained using FEA (left) and the ANN (right).

Discussion

The morphing approach presented here has allowed the implementation of an ANN substitute for FEA, even in the case of complex anatomical geometries, thus opening the door for biomechanical simulations to be applied in severely time-constrained applications. With the key challenge of obtaining topologically consistent meshes overcome, the approach will be further developed by applying more physiologically relevant loading conditions and by introducing richer subject-specific training data to the ANN, for example: by assigning subject-specific material properties.

References

1. Duthey, WHO Background paper, 6.24, 2013.
2. Kao et al, BMJ open, 8:7, 2018.
3. Liang et al, Journal of The Royal Society Interface, 15(138), 2018.
4. Fehrenbach et al, Comptes Rendus Mathématique, 346(9-10):593-598, 2000.
5. Yao et al, MICCAI, 7512:509-516, 2012.

Acknowledgements

This project has received funding from the European Union's Horizon 2020 research and innovation programme under the Marie Skłodowska-Curie grant agreement No 766012.

INFLUENCE OF FEMORAL TORSION ON HIP LOADING DURING GAIT IN ASYMPTOMATIC ADULTS

Enrico De Pieri (1)(2), Bernd Friesenbichler (3), Renate List (3), Samara Monn (3), Nicola C. Casartelli (3)(4), Michael Leunig (5), Stephen J. Ferguson (2)

1. University of Basel Children's Hospital, Basel, Switzerland; 2. Institute for Biomechanics, ETH Zurich, Zürich, Switzerland; 3. Human Performance Lab, Schulthess Clinic, Zürich, Switzerland; 4. Laboratory of Exercise and Health, ETH Zurich, Schwezenbach, Switzerland; 5. Department of Orthopaedic Surgery, Schulthess Clinic, Zürich, Switzerland

Introduction

The onset of degenerative joint diseases such as osteoarthritis (OA) is often determined by altered joint mechanics due to abnormal joint morphology and/or geometrical limb alignment [1,2]. Hip dysplasia and cam/pincer morphologies, associated with femoroacetabular impingement (FAI) syndrome, have been identified as potential risk factors for developing hip OA. However, other morphological features, such as increased femoral torsion, may also exacerbate or diminish the effects of existing cam/pincer morphologies [3].

The aim of this study was to evaluate hip loading during gait in a group of asymptomatic adult subjects presenting a heterogeneous range of femoral torsion. It was hypothesized that increased femoral torsion may lead to alterations in hip contact forces (HCFs).

Methods

37 healthy volunteers (27.7 ± 4.6 years old, 15 females) underwent a 3D kinematic (Vicon, UK) and kinetic (Kistler, Switzerland) gait analysis session at a self-selected walking speed. Femoral antetorsion (mean angle =15.7° ± 8.8°, min = -7.1°, max = 38°) was evaluated with low-dosage bi-planar radiography (EOS Imaging, France). The collected motion capture data was used as input for a musculoskeletal modelling, inverse dynamics analysis (AnyBody Technology, Denmark) to evaluate HCFs, reported in a pelvis-based reference frame. Subject-specific models were created from a generic lower-limb model [4], which was scaled according to marker data from a static trial and individual segment dimensions from radiographic images. The modelled femurs were morphed (Figure 1a) to match each subject's femoral antetorsion measurements. Correlations between antetorsion angles and 3D HCFs were analyzed using statistical parametric mapping (SPM) canonical correlation analysis (CCA), as well as SPM post-hoc linear regression analyses for the individual force components.

Results

A statistically significant correlation between 3D HCFs and femoral torsion was found in the investigated cohort during terminal-stance and mid-swing (48-52% and 65-79% of the gait cycle) (Figure 1b). In particular, subjects with higher antetorsion have more medially oriented HCFs in mid stance and more anteriorly oriented HCFs during swing phase.

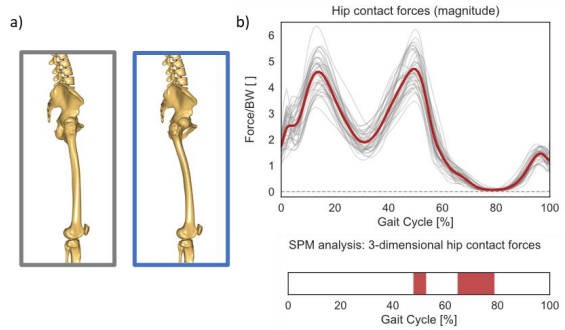

Figure 1a): femoral geometries of the baseline model (grey box) and a morphed model with increased antetorsion (blue box). Figure 1b): predicted HCF magnitude for individual subjects (light grey) and cohort mean (red). Phases of the gait cycle with a statistically significant correlation between 3D HCF and femoral torsion are reported as red bars below.

Discussion

This study investigated potential correlations between femoral antetorsion and hip loads. Subject-specific models were morphed based on individual morphological data and driven with matching individual kinematic data, which would capture potential kinematic compensatory mechanisms, such as in-toeing. A statistically significant correlation was observed between femoral antetorsion and the spatial orientation of the HCF 3D vector during gait. These altered intra-articular loads, in association with other morphological features such as cam/pincer morphology, may become a risk factor for hip degenerative changes. A better understanding of the forces that are produced within the acetabulum is necessary to improve individual diagnoses and to optimally plan targeted realignment of the lower extremities, which could reduce the risk of (over-) loading-induced joint degeneration.

References

1. Tönnis D et al, J Bone Joint Surg Am, 81:1747-70, 1999.
2. Felton DT, Osteoarthr Cartil, 21(1), 10:15, 2013.
3. Zeng WN et al, Sci Rep, 6(1):1–8, 2016.
4. De Pieri et al, PLoS ONE 13(9), 2018.

Acknowledgements

We would like to thank Dr. Morten E. Lund for his help in developing the morphing of the femoral geometries within AnyBody Modelling Software.

DIFFERENCES BETWEEN KYPHOPLASTY AND STENTOPLASTY IN A TRAUMATIC VERTEBRA: IN-SILICO BIOMECHANICAL INVESTIGATION

Rojina Azadkiya (1), Gholamreza Rouhi (1)

1. Amirkabir University of Technology, Iran

Introduction

Vertebral body compression fractures (VBCFs) are one of the most common types of osteoporotic fractures, and one of the most convenient surgical options for osteoporotic VBCFs is minimally invasive Balloon Kyphoplasty (BKP). Clinically, 34% of BKP surgeries do not significantly reduce kyphosis angle, or restore vertebral body's height [1]. Since 2009, vertebral body stent (VBS) was suggested and employed to overcome challenges associated with the BKP. To date, several studies have investigated the effects of various biomechanical factors, which play a crucial role in BKP; however, the biomechanical aspects of VBS approach have not yet been well understood. The aim of this study was to develop finite element (FE) models of both BKP and VBS to explore existing differences between the biomechanical behavior of the two surgical methods under compressive and flexural loading.

Methods

A computed tomography (CT) based- FE model of L_2-L_4 segment was developed. To mimic the geometry of the fractured L_3, it was assumed that the vertebra should experience a 22% reduction in its height, which could be caused under compressive and bending loadings. The L_3 vertebra was then reinforced with bone cement in BKP (Fig. 1 (left)), and with bone cement-stent complex in VBS (Fig. 1(right)) to restore the height of the damaged vertebral body. It was also assumed that the final profile of the cement in the BKP method is similar to that of the stent profile expansion in VBS. Fluid cavity interaction was defined for the inside of the balloon, assuming that it was filled with fluid until the expansion of the balloon can restore the lost height of the fractured vertebra. Embedded region constraint was employed for the bone cement-vertebra, and also for bone-stent interactions. Moreover, the bottom surface of the L_4 was fully constrained in all directions, and a physiological compressive load of 800 N was applied to the upper surface of L_2, and flexion, extension and lateral moment of 7.5 N.m were applied to the center point of the upper surface of L_2 to simulate compression, extension, flexion, and lateral bending movements. Finally, compressive/bending stiffness of L_2-L_4 segment were assessed for BKP and VBS cases and compared with each other.

Results

Compressive and bending structural stiffness of L_2-L_4 segment for the BKP and VBS are reported in table 1. The stiffness analysis of L_2-L_4 segment revealed that the incorporation of a stent in the treatment procedure of the fractured vertebra increases the stiffness of the segment by an average of about 10%.

	Stiffness of L_2-L_4 segment in different compression and bending movements (kN/mm)			
	Compression	**Extension**	**Flexion**	**Lateral Bending**
BKP	**0.587**	**539.56**	**545.55**	**220.55**
VBS	**0.655**	**734.76**	**467.28**	**241.13**
% of relative change between stiffness of VBS and BKP	**+11.6%**	**+36.18%**	**-14.4%**	**+9.33%**

Table 1: The stiffness of the L_2-L_4 segment in BKP and VBS methods for each posture, and percentage of relative change between stiffness of VBS and BKP (with respect to BKP). The "+" and "-" signs indicate an increase or decrease, respectively, in the stiffness of the L_2-L_4 segment in the VBS compared to BKP.

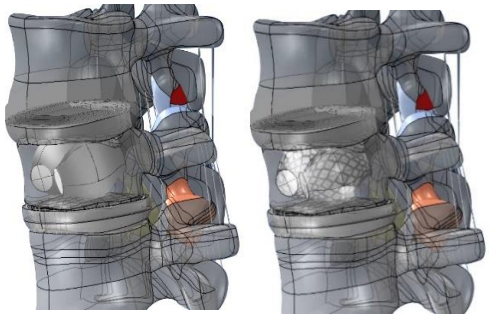

Figure 1: Finite element model of L_2-L_4 segment, including ligaments and intervertebral discs. Height restoration of L_3 with BKP (left) and VBS (right).

Discussion

This study showed that the structural stiffness of L_2-L_4 segment treated by VBS is greater than that of BKP for all postural movements, except for flexion. This may indicate that the VBS can be superior, compared with BKP, if one looks at the stiffness of the fixed segment. Further research is in progress to discover other existing differences between the BKP and VBS methods.

References

1. Rotter, R, et al., European Spine J, 2010. 19(6): 916-23.

Acknowledgements

The authors appreciate Amirkabir University of Technology for supporting this research.

IMPROVING THE COMMUNICATION BETWEEN AN EMG-BASED HMI FOR HAND PROSTHETIC USERS WITH ANN

Marta C. Mora (1), Jeremy Colzy (2), José V. García-Ortiz (1), Joaquín Cerdá-Boluda (3)

1. Dept. of Mechanical Engineering and Construction, Universitat Jaume I, Spain; 2. IUT de Cachan Université Paris Sud; 3. Dept. of Electronic Engineering, Universitat Politècnica de València, Spain

Introduction

The development of anthropomorphic and functional artificial hands remains a challenge for design and control engineering. To date, a variety of artificial hands, robotic and prosthetic, have been designed with different purposes: a) grip stability and human handling skills; b) anthropomorphism and cosmetic appearance. However, an artificial hand should meet both goals, fundamentally if oriented to be a prosthesis. Unluckily, current prostheses are very simple from a biomechanical viewpoint and their manipulation abilities are limited. The main problem lies in the difficulty of establishing a proper communication between the user and the device. In fact, nowadays the communication interface between the user and the prosthesis is a technological bottleneck [1] that explains the simplicity of current prostheses, even when it would be possible to use the most sophisticated solutions developed in the last decades.

This work aims to improve the communication between the user and the prosthesis using an EMG-based Human-Machine Interface (HMI): the MYO armband [2]. The authors found this HMI useful for the control of hand prosthesis in a limited way [3]: it is easy to use but the number of detected hand postures with the manufacturer software is low. In fact, various arm and hand postures can be recognized, but none of them belong to Activities of Daily Living (ADL) [4]. Additionally, deep learning algorithms have become increasingly prominent for their ability to automatically learn discriminant features of experimental data. Still, they have been barely used in the field of grasping posture recognition based on EMG data, even though they have been proven to be valid for gesture classification [5].

In the present work, preliminary work has been done to increase the number and type of detected grasping postures from the EMG signals of the MYO armband with a feed-forward artificial neural network (ANN) implemented in Matlab. A similar ANN provided good results in hand posture prediction in previous works [6].

Methods

The MYO armband is a Bluetooth HMI device with 8 EMG sensors, a 3-axis gyroscope, accelerometer and magnetometer. Once correctly located on the forearm, calibrated and trained, is able to recognize 6 hand gestures with the manufacturer software: tap, fist, open, wave in, wave out, shown in Fig. 1 (up).

In this work, experiments were made with 6 right-handed subjects performing the aforementioned gestures plus two additional ADL grasping postures: pinch and cylindrical grasps [4] (Fig.1, down).



Figure 1: Recognized hand postures from Myo data

The raw signals acquired from the armband were processed to extract the relevant information from the EMG data. In particular, a window of 20 samples was used for feature extraction and the Root Mean Square (RMS) of the samples was computed. These features were used to train an ANN for posture classification with a two-layer feedforward architecture and 100 neurons in the hidden layer. The inputs to the ANN were the RMS values of the 8 EMG sensors and the outputs were 8 values corresponding to the probability of each hand posture. The implementation was carried out with the Matlab "Deep learning toolbox". The performance of the ANN was assessed computing the percentage of success in the classification.

Results and Discussion

The mean percentage of success in hand posture recognition for two subjects whose data were not used for training the ANN was 76.69%, higher that the result reported in [5]. In particular, the ADL grasps had the following success rates: 84% for the cylindrical grasp and 54.1% for the pinch grasp. These results are satisfactory and indicate that this technique could be used for detection of ADL grasping postures and use it for controlling a hand prosthesis. However, the number of subjects used was very low and new features should be computed in order to increase the success rates, especially in the pinch grasp.

References

1. Craelius W, Science 295:1018-1021, 2002.
2. Myo, https://support.getmyo.com, accessed: 2020-01-20.
3. Mora MC et al, 25th Congress ESB, 2019.
4. Vergara M. et al, J Hand Therapy 27: 225-234, 2014.
5. Côté-Allard et al, IEEE T Neur Sys Reh,27(4):760-71,2019.
6. Mora MC et al, Int J Adv Rob Sys, 9(4), 2012.

Acknowledgements

This work was supported by grants GV/2018/125 from the Generalitat Valenciana, UJI-B2018-82 from Universitat Jaume I and DPI2017-89910-R from the Spanish Ministry.

CHANGING THE STRENGTH OF MUSCLES CROSSING SINGLE LOWER LIMB JOINTS ONLY AFFECTS KNEE JOINT REACTION FORCES

Metin Bicer (1), Andrew TM Phillips (1) , Luca Modenese (1)

1. Dept Civil Engineering, Imperial College London, UK

Introduction

Musculoskeletal (MSK) models are used to estimate the muscle and joint reaction forces (JRFs) in clinical patients by personalizing features such as muscle strength [1]. For example, total knee arthroplasty (TKA) can be associated with a 30% reduction of the maximum isometric force (F_{iso}) of the muscles crossing the replaced joint [2]. This study aims to quantify alterations of JRFs in the lower limb when F_{iso} of muscles crossing either the hip, knee, or ankle joints are altered.

Methods

A gait trial of an 86-year old man with a left instrumented TKA [3] was simulated using a generic OpenSim MSK model [4] scaled to the participant's anthropometry. Joint angles and moments were calculated using the inverse kinematics and inverse dynamics tools. Static optimization and joint reaction analysis were used to estimate muscle forces and JRFs at each joint of the lower limb after altering the F_{iso} of the muscles crossing the hip, knee, or ankle joints from their nominal values up to $\pm$40% in increments of 10%. For comparison, analyses where F_{iso} was altered at the same time for all muscles in the model were also carried out. The differences between the peaks of the JRFs estimated by the nominal and modified models were quantified. Also, the second peak of the JRFs at the knee during late stance was compared against the in-vivo measurement.

Results

The JRFs are presented in Figure 1 with respect to varying F_{iso} of different muscle groups. The variation of the peak JRFs from the nominal value ranged from -0.05 to 0.63 BW at the hip, from -1.39 to 1.43 BW at the knee and from -0.15 to 0.6 BW at the ankle. Weakening the strengths of muscles crossing the hip joint increased the knee JRFs by 1.43 BW at maximum, while this had a limited effect (<0.15 BW) on the peaks of the hip and ankle JRFs. Decreasing F_{iso} of the muscles crossing the knee resulted in a maximum knee JRFs reduction of -1.39 BW at its peak load but not significant changes at the hip and ankle (<0.12 BW). F_{iso} of the muscles spanning the ankle joint had influence on the JRFs at the knee (0.76 BW) and the ankle (0.6 BW) but almost none at the hip (0.02 BW). The changes in all muscle strengths resulted in a similar variation of joint loads at each joint (<0.63 BW). In the swing phase of the gait cycle, there were also minor changes in the hip and ankle JRFs (<0.28 BW). The model with the 40% weaker knee-spanning muscles estimated JRFs closer to the in-vivo knee loads (0.28 BW overestimation at the second peak).

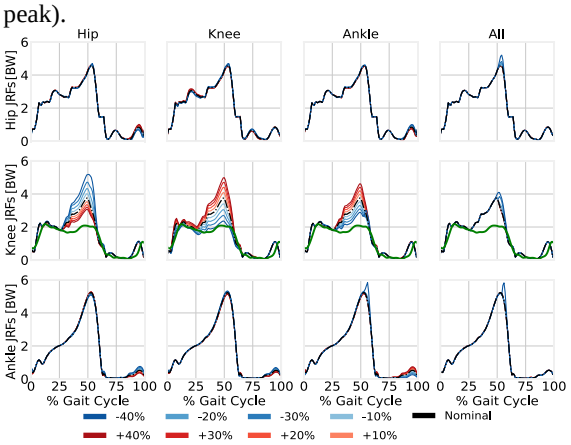

Figure 1: The JRFs at the hip, knee and ankle (rows) for changes in the F_{iso} of the muscle groups of the hip, knee, ankle and all muscles (columns). JRFs from the nominal model are shown in black. Experimental measurement (green) is available for the knee JRFs.

Discussion

As expected, the changes in the strengths of a muscle group altered muscle recruitment and affected other joints via the bi-articular muscles. However, simulation quality was not compromised (muscle forces sustained $\geq$95% of the peak joint moments calculated from inverse dynamics) and joints were differently affected by these alterations. The most and least sensitive JRFs to the changes in strengths of muscles crossing individual joints were the knee and ankle ones respectively, consistently with the findings of [5]. The reduction in the peak JRFs at the knee joint was also comparable to [5] (0.6 BW) although muscle recruitment did not aim to minimize the JRFs and further reduction in F_{iso} of knee-spanning muscles would still be possible. Finally, the best match-up between predicted and recorded JRFs at the knee was found using a 40% decrease in F_{iso} for muscles crossing the knee, consistently with the approach of [1].

Acknowledgements

Turkish Ministry of Education Fellowship to MB, Imperial College Research Fellowship to LM.

References

1. Marra et al, J Biomech Eng, 137: 2015.
2. Silva et al, J Arthroplasty, 18: 605-611, 2003.
3. Fregly et al, J Orthop Res, 30: 503-513, 2012.
4. Rajagopal et al, IEEE T Biomed Eng, 63: 2068-2079, 2016.
5. van Veen et al, J Biomech, 97: 109368, 2019.

BIOMECHANICAL ANALYSIS OF INTRA-ARTICULAR STRESSES CAUSED BY THE RECONSTRUCTION OF THE ACL USING A SECTION OF THE PATELLAR TENDON

Laura Dussán-Delvasto(1), Mónica Gantiva-Díaz(1), Christian Cifuentes-De la Portilla (1)

1. *Ibiomech research group, Biomedical engineering department, Universidad de Los Andes, Colombia.*

Introduction

Anterior cruciate ligament (ACL) injury accounts for 50% of knee ligament injuries and 75% of them occur during sports activities [1]. The main treatment for this tear is ACL reconstruction using autologous or donor tissue. The most common tissues for reconstruction are the patellar and quadriceps tendon. Currently there are different variations of this surgery and, although it is not known with certainty which is the best [2], the option chosen depends on the preference and experience of the surgeon. The objective of this study was to identify changes in intra-articular stresses in the knee to foresee possible future consequences of tendon-to-ligament transfer surgery for ACL reconstruction by means of a computational model of the human knee.

Methods

The finite element model was reconstructed from tomographic images of a healthy patient. This model includes the bones of the joint, cruciate, and lateral ligaments, menisci, femorotibial cartilage, patellar tendon, and quadriceps tendon. The respective Young's modulus and Poisson radius were assigned to them. The model was validated by simulating compression and flexion and comparing the stress results in the menisci with literature [3][4]. The initial model was modified to represent ACL reconstruction surgery with a patellar tendon section. For this, the geometry of the tendon was modified, and the mechanical properties of the ACL were replaced by those of the tendon. Compression and flexion simulations were performed with the modified model. The results obtained were compared with the healthy model.

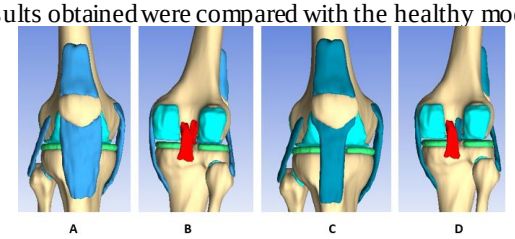

Figure 1: Obtained 3D models: A) Healthy model front view. B) Healthy model rear view. C) Modified model front view. D) Modified model rear view.

Results

Results showed an increase of 40.2% in the maximum tension (fig 1-A-B) of the ACL in the modified model, proved with a compression test, compared to the healthy model.In contrast, there was a 45.5% increase in maximum compression (fig 2-A-B) with respect to the healthy model. In addition, for the ACL flexion movement of the modified model, a 60% increase in maximum tension (fig 1-C-D) and 12% in maximum compression (fig 2-C-D) were obtained compared to the healthy model.

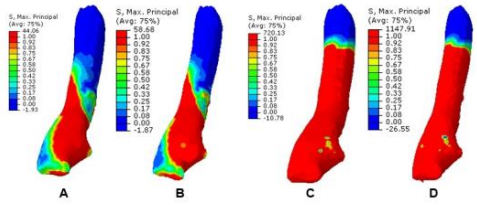

Figure 2: Maximum principal stress calculated in ACL: A) Healthy model subjected to compression force. B) Modified model subjected to compression force. C) Healthy model in flexion motion. D) Modified model in flexion motion.

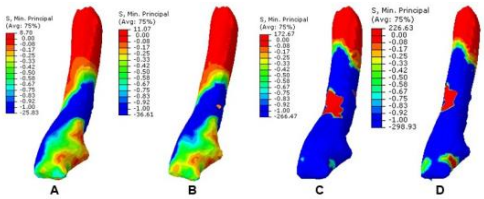

Figure 3: Minimum principal stress calculated in ACL: A) Healthy model subjected to compression force. B) Modified model subjected to compression force. C) Healthy model in flexion motion. D) Modified model in flexion motion.

Discussion

The results show that the intra-articular stress of the knee is modified when performing the ACL reconstruction. The increases in the stress of main maxima and minima are consequence of the change in the Poisson radius when replacing the original material by a section of the tendon, which is incompressible. This parameter changes from 0.3 to 0.49. The greatest increase was presented in the ACL for the main maximums when a flexion was simulated. In conclusion, when an ACL reconstructive surgery use the patellar tendon, the surgeon should consider important stress changes in the new ligament, because it could suffer mechanical stresses considerable different from the original ligament

References

1. Márquez-Arabia J, Márquez-Arabia W. Lesiones del ligamento cruzado anterior de la rodilla. Revista Iatreia. 2009; 22(3): p. 256-271.
2. Shaerf D, Pastides P, Sarraf K, Willis-Owen C. Anterior cruciate ligament reconstruction best practice: A review of graft choice. World Journal of Orthopedics. 2014; 5(1): p. 23–29.
3. Peña E, Calvo B, Martínez M, Doblaré M. A three-dimensional finite element analysis of the combined behavior of ligaments and menisci in the healthy human knee joint. Journal of Biomechanics. 2006; 39(9): p.1686–1701.
4. Yagi M, Wong E, Kanaromi A, Debski R, Fu F, Woo SL.-Y. Biomechanical analysis of an anatomic anterior cruciate ligament reconstruction. American Journal of Sports and Medicine. 2002; 30: p. 660–666.

SUBJECT-SPECIFING MODELING AND SIMULATION OF ANTERIOR CRUCIATE LIGAMENT RECONSTRUCTION SURGERY

Authors
Konstantinos Risvas (1), Dimitar Stanev (2), Konstantinos Moustakas (1)

1. Visualization and Virtual Reality Group, Department of Electrical and Computer Engineering, University of Patras, Greece;
2. École Polytechnique Fédérale de Lausanne - EPFL, Switzerland

Introduction

The Anterior Cruciate Ligament (ACL) rupture is a very common knee injury that can occur in sports. Usually, this leads to the total replacement of the native tissue with a graft. This procedure is known as Anterior Cruciate Ligament Reconstruction (ACLR). In this work, we propose a computational framework that incorporates all the key steps of modeling the ACLR surgery. The aim of the developed workflow is twofold: first, to enable realistic subject-specific modeling of all the parameters and aspects of the ACLR; and secondly, to include these modeled elements in assembling a Finite Element (FE) knee joint model that can be exploited to perform simulations of daily life activities.

Methods

The MRI data used throughout this work are acquired by the OpenKnee database [1] and processed using tailored segmentation tools [2]. The ACLR modeling pipeline is developed in Blender. First, a set of landmarks on the bone surfaces is selected and these are used to drill the tibia and femur tunnels. Then, the graft mesh is created with customized radius, density, and bundle number, which is placed through the tunnels. Modeling of Single (SC) and Double Channel (DC) surgery methods is thus possible. The key steps and results of the modeling workflow are presented in Figure 1.

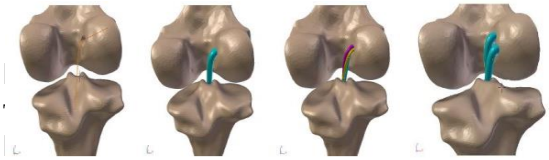

Figure 1: The key steps of the surgery modelling pipeline. A) Surgery planning, B) Single Channel surgery, C) Multiple bundle graft, D) Double Channel surgery.

The created geometries are then used to assembly the FE model utilizing the FEBio software [3], along with meshes that represent the other key anatomical structures such as the menisci and the cartilages. The ligaments are modeled as non-linear springs and proper contact and material models are established. Four versions of the same knee are created that represent the intact ACL knee, the ACL-deficient knee and the SC, and DC ACL reconstructed knees respectively (Figure 2). Subsequently, these models can be used to evaluate the parameters of ACLR when performing an anterior drawer test.

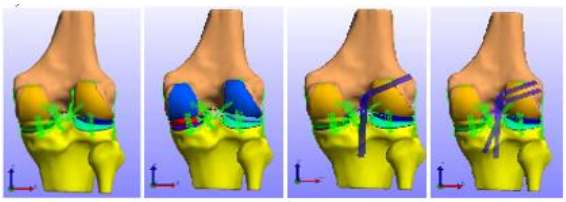

Figure 2: The developed FE models. A) The intact ACL knee, B) The no ACL knee, C) Single Channel ACLR, D) Double Channel ACLR.

The knee is flexed up to 30 degrees and then an anterior force of 134 N is applied on the tibia. The femur is fixed in all degrees of freedom whereas the tibia is free. The measured output is tibial anterior translation. First, the test is performed to compare the intact and deficient ACL models and obtain a reference model. Then, the SC DC models are compared with the reference model. Furthermore, the SC model is used with three different levels of graft pre-tension to assess the impact of graft preparation. Finally, the SC model is used again to compare different angles of graft fixation.

Results

The results demonstrated that the DC ACLR technique is superior to SC in terms of restraining anterior tibial translation. Additionally, increasing the graft pre-tension also improves the graft ability to constrain anterior knee laxity. Finally, graft fixation angles in the 20°-30° are found to be more suitable for graft fixation.

Discussion

In this work, a solid, flexible, and extensible framework for modeling most of the ACL surgery aspects is presented. It can be used to optimize the selection of the ACLR parameters by providing insights into their potential effects on restoration of the knee joint mechanics.

References

1. Erdemir A, *J Knee Surg*. 2016;29(2):107-116
2. Nikolopoulos et al, *IEEE Access*, 8:56766-56781, 2020
3. *Maas SA et al, Journal of Biomechanical Engineering, 134(1) 2012.*

Aknowledgements

This work is supported by the Greek funded SafeACL project (grant agreement T1EDK-04234).

EXPERIMENTAL VALIDATION OF A FINITE ELEMENT MODEL OF PERIPROSTHETIC FEMORAL FRACTURE IN A STUMBLING SCENARIO

Michael Saemann (1), Martin Darowski (1), Rainer Bader (1), Manuela Sander (2), Daniel Kluess (1)

1. Biomechanics and Implant Technology Research Laboratory, Department of Orthopaedics, Rostock University Medical Center, Germany; 2. Institute of Structural Mechanics, University of Rostock, Germany

Introduction

Periprosthetic femoral fracture (PFF) is a severe complication following total hip arthroplasty (THA). The majority of these factures is caused by low-energy traumas, such as stumbling or a fall from standing height [1]. The post-operative cumulative 20-year probability of PFF is 7.7% and the intra-operative probability of PFF is 3% in primary THAs with uncemented hip stems [2]. Regardless of these still high fracture rates, the mechanisms of PFF and its predisposing biomechanical factors are not yet fully understood. Finite Element (FE) studies have proven to be a valuable tool to analyze bone strength and fracture, but they require experimental validation to be reliable. Therefore, the presented study utilizes human cadaveric femurs in a stumbling scenario as experimental validation for FE models of PFFs.

Methods

Experimental testing was conducted on three human cadaveric left femurs implanted with uncemented straight total hip stems by an experienced orthopedic surgeon. Femurs were embedded in pots at a medio-lateral angle of 8° and an anterior-posterior angle of 0°. The native anteversion angles of approx. 15° were reproduced by implanting the hip stems according to clinical routine. The specimens were then axially loaded in an electromechanical testing machine in a quasi-static manner and force and displacement at the contact to the implant ball head were recorded. The stiffness of the femurs at 1 mm axial displacement was calculated. Additionally, surface strain measurements by Digital Image Correlation and five multiaxial strain gauges were carried out. For the creation of the FE models the Image-Based Modeling approach by Kluess et al. [3] was used. First, the CT scans of the femurs were used to semi-automatically segment and reconstruct the femoral geometries based on calibrated HU units. The implant geometries were then virtually positioned according to pre-surgical planning. In a preliminary simple model, the material properties were assumed to be linearly elastic perfectly plastic. Using a custom-developed mapping algorithm, all nodes of the bone mesh were assigned elastic moduli and yield strains depending on the corresponding HU units to reproduce the heterogeneous mechanical properties of femoral bone. A frictional contact between bone and hip stem surfaces was defined. Fracture was assumed when an element reached yield strain.

Results

The results of the experimental tests showed a mean fracture load of 6,686 N or 795% of the patient-specific bodyweight (Fig. 1). The experimental mean stiffness at 1 mm axial displacement amounted to 3,209 N/mm. The load-displacement curve, fracture load and stiffness calculated by the FE models showed only moderate accordance to the experimental data. Initial subsidence of the hip stem was observed in two of the three experimentally tested femurs. This initial subsidence could not be reproduced by the FE models.

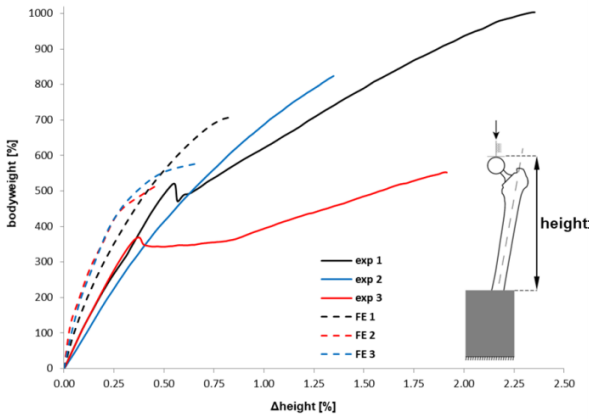

Figure 1: Experimental ("exp") and computational ("FE") load-displacement curves for three left human femurs.

Discussion

Our experimental results showed good agreement with a comparable experimental study by Schwarz et al. [4]. Nevertheless, the preliminary, simple FE models are to be improved to represent the experimental results more accurately. Our study underlines, that especially advanced material modeling is a critical parameter to improve accuracy and reliability of FE modeling of PFFs.

References

1. Sidler-Maier, Waddell. Int Orthop, 39:1673-1682, 2015.
2. Abdel et al., Bone Joint J, 98-B:461-467, 2016.
3. Kluess et al., Comput Methods Programs Biomed, 95:23-30, 2009.
4. Schwarz et al., Clin Biomech, 54:137-142, 2018.

Acknowledgements

This research was funded by the Deutsche Forschungsgemeinschaft (DFG, German Research Foundation) – KL 2327/5-1 and SA 960/8-1.

FEASIBILITY OF A STRAIN BASED EVALUATION OF BONE HEALING IN FRACTURES TREATED WITH AN EXTERNAL FIXATOR

Lorenza Mattei (1), Matteo Gagliani (1), Cristina Curreli (2), Francesca Di Puccio (1)

1. Dip. Ingegneria Civile e Industriale, Università di Pisa, Italia

2. Dip. Ingegneria Industriale, Alma Mater Studiorum – Università di Bologna, Italia

Introduction

In the last decades, the interest towards non-invasive approaches to fracture healing monitoring has rapidly increased. Many different approaches have been proposed from ultrasounds to static angle deflection. Recently, this research group has investigated the application of mechanical vibrations also *in vivo* [1].

In this study, we aim to investigate the feasibility of using strain gauges to monitor fracture healing in cases treated with an external fixator. This approach was considered in the late 90ies but abandoned as not reliable. However, at that time the broken limb was kept unloaded while nowadays the patient can walk after few weeks. Thus, the use of strain gauges placed on the fixator can be re-examined.

The present contribution describes an *in-silico* simulation of a fracture healing process to estimate the trend of 'virtual' strain measurements as possible indicators of bone healing.

Materials and Methods

A Finite Element model of a Sawbone phantom of a tibia with an external fixator was developed. The model of the phantom was provided by Sawbone, while the components of the fixator were added after a reverse engineering operation (Fig.1).

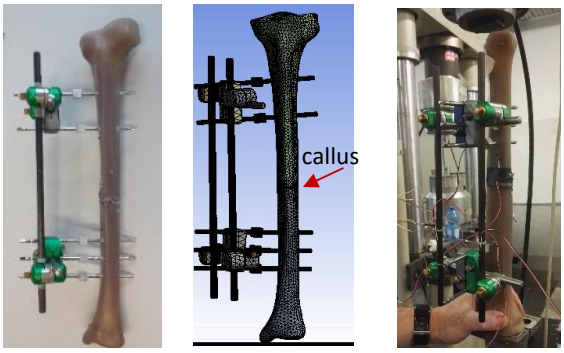

Figure 1: Left: Sawbone tibia with fixator. Centre: FE model with callus in evidence. Right: sample under test.

Bone Healing was simulated by varying the elastic modulus of the callus as 1-12-60-100 % of the modulus of the cortical bone, at weeks 4-8-12-20, respectively. The thickness of the callus was very small (5 mm) to stress the test case.

A static compression (F=500 N) of the phantom without and with fixator was simulated in Ansys® 2019.

Experimental validation of the model was also pursued.

Results

The load distribution in the pins and rods at week 0 is shown in Fig.2. As bone heals, the callus stiffens and the load acting on the phantom increases.

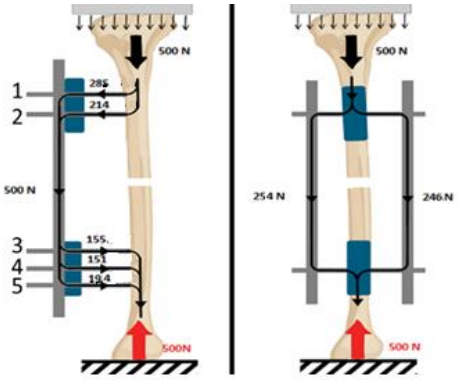

Figure 2: Load distribution in the fixator at week 0.

The strain field highlights that the most suitable points for strain gauges are on the distal pins (1-5), subjected mainly to bending (Fig.3). The trend of strain in the pins during healing is reported in Fig.3, where it is evident that after week 8 there is no significant variation.

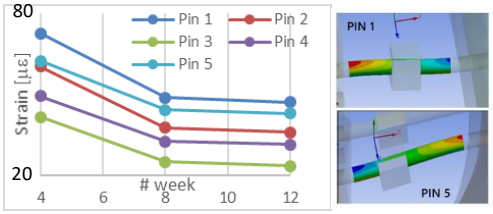

Figure 3: Strain trend in the pins during healing and strain field in pin 1 and 5.

Simulated and measured strains were in good agreement. The strain level appears rather low for achieving reliable measurements *in-vivo*, but this is due to the assumed small thickness of the callus.

The approach could be feasible especially in the first months after fracture. Further analyses with larger callus and other values of elastic modulus will be performed.

References

1. Mattei L, Di Puccio F, Marchetti S. 2018 J. R. Soc. Interface 15: 20180068.

Acknowledgements

The authors gratefully acknowledge the University of Pisa for having funded this research (PRA 2017).

FINITE ELEMENT AND ANALYICAL MODELS FOR WEAR PREDICTION IN HIP PROSTHESES

Lorenza Mattei (1), Cristina Curreli (2), Francesca Di Puccio (1)

1. Department of Civil and Industrial Engineering, University of Pisa, Italy;
2. Department of Industrial Engineering, Alma Mater Studiorum - University of Bologna, Italy

Introduction

Massive wear is recognized as one of the main causes of hip prostheses (HPs) failure. Consequently, the approval for the clinical use a new prosthesis design needs a long and costly campaign of wear tests. Nowadays, *In-silico* clinical trials represent an attractive alternative made accessible thanks to the computational resource available. On the one hand, analytical wear models (AN), though rarely reported in the literature [1], allow parametric formulations and very rapid wear predictions for the running in phase. On the other hand, finite element (FE) modelling can implement the geometry changes due to wear, allowing long-term wear predictions, though this often entails user subroutines and, typically, high computational costs [2,3].
The aim of this study is to compare AN and FE wear modelling of HPs, evaluating strengths and limitations. A new FE wear model of metal-on-plastic HP has been developed which reproduces the case study of the AN model in [1].

Methods

A FE model of a 28 mm MoP HP has been developed using the intuitive ANSYS Workbench® platform, rarely used in literature. The wear is modelled as unilateral, affecting only the cup, neglecting the wear of the metallic head. The Archard wear law is adopted, with a constant wear coefficient. The main boundary conditions, applied to head and cup, are shown in Fig.1: the wear caused by walking is simulated considering a vertical load and all hip joint rotations. Computational strategies, such as rigid body modelling of the head and the submodeling technique [3], were considered to reduce simulation time.

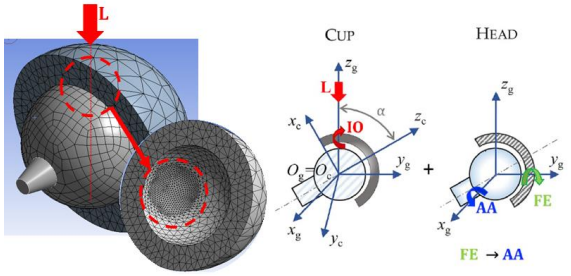

Figure 1: FE wear model of a MoP hip prosthesis (left) and simulated boundary conditions (right).

Results

The main results consist in the evolution of the wear volume *V* and the wear map during walking. As an example, the results obtained for a single gait cycle are shown in Fig. 2. To note that mainly wear occurs during the stance phase, when the load and the contact pressures (green curve, Fig.2) are higher. The wear map is almost circular, with the maximum value located at the nominal contact point, that is fixed on the cup. Results for steady state phase of wear process are not shown for brevity.

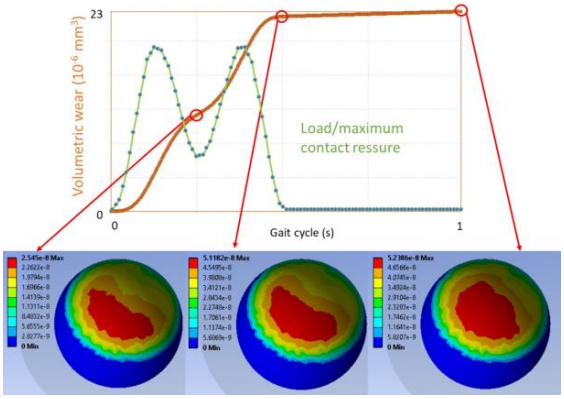

Figure 2: Main results: trend of the volumetric wear and evolution of the wear map during a gait cycle.

Discussion

A first comparison of AN and FE wear models at 1 Mc is considered: the same wear volume (23.3 mm^3) and similar wear maps are obtained, as shown in Fig. 3. This confirms the validity of the AN approach for the running-in phase.
Results suggest the combined-complementary use of the AN and FE wear models for *in-silico* clinical trials of HPs, which would assure the most accurate results at the lowest computational cost.

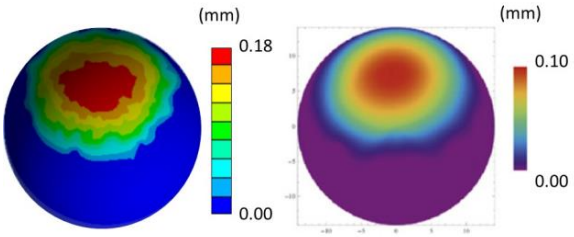

Figure 3: Comparison of the wear maps predicted at 1 Mc by FE and AN [1] models.

References

1. Mattei L. et al, Trib Int, 63:66-77, 2013.
2. Liu et al, Proc IMECHe H: J Eng Med 225: 16-24, 2011.
3. Curreli et al, Int J Num Meth Eng, 116:708-722, 2018.

MECHANICAL AND MORPHOLOGICAL EVALUATION OF CORTICAL BONE THROUGH IN SITU XCT INDENTATION AND DVC

Aikaterina Karali (1), Gordon Blunn (2), Alexander P. Kao (3), Jurgita Zekonyte (1), Gianluca Tozzi (1)

1. Zeiss Global Centre, School of Mechanical and Design Engineering, University of Portsmouth, UK; 2. School of Pharmacy and Biomedical Sciences, University of Portsmouth, UK; 3. Elettra - Sincrotrone Trieste S.C.p.A., Italy

Introduction

Cortical bone mechanical behavior depends on its microstructural properties [1]. High-resolution X-ray computed tomography (XCT) has been widely used to identify the microstructural properties of the cortical tissue (i.e. pore network, Haversian and Volkmann's canals) [2]. However, the connection between its microstructural properties and micromechanical behavior during plastic deformation is unclear. *In situ* XCT indentation, coupled with digital volume correlation (DVC) has been previously employed to study plastic deformation of elephant tusk in relation to its microstructure [3]. Hence, the purpose of this study is to investigate the cortical bone plastic strain and its interconnection with the canal network.

Methods

Bovine cortical bone cylindrical specimens were extracted from the femoral diaphysis (D = 4 mm, H = 6 mm), six in the transverse and six in the axial direction with respect to the long vertical axis of the femur. A novel set up was designed to fit a Vickers' pyramidal indentation tip onto the top plate of an *in situ* loading device (CT5000, Deben, UK). Two consecutive X-ray tomograms (Versa 510, Zeiss, USA) were obtained with the jaws of the loading stage fully open for the calculation of strain uncertainties uncertainty (SDER = 423 ± 213 με). The loading stage was set in depth control with a displacement rate of 0.1 mm/min. The specimens were divided in three different groups of four, two axial and two transverse. In the first group, the specimens were indented once at 0.4 mm displacement. The second group involved two indentation steps; first reaching 0.2 mm and then increasing the depth to 0.4 mm in the same location. The third group included three steps at 0.2 mm, 0.3 mm, and 0.4 mm displacement. DVC analysis (DaVis10, LaVision, UK) was conducted using a multi-step pass processing scheme (128 to 48 voxels) to compute the strain distribution in the volume.

Results

Microcracks were formed in specimens extracted from the axial direction. Additionally, in all the specimens the DVC analysis showed that the region of the imprint is under tension whereas the volume underneath experienced compressive strain. Canal loss was displayed in region of higher compressive strains exceeding -20000 με and crack formation occurred in specimens were Haversian canals were parallel to the indentation tip (Figure 1).

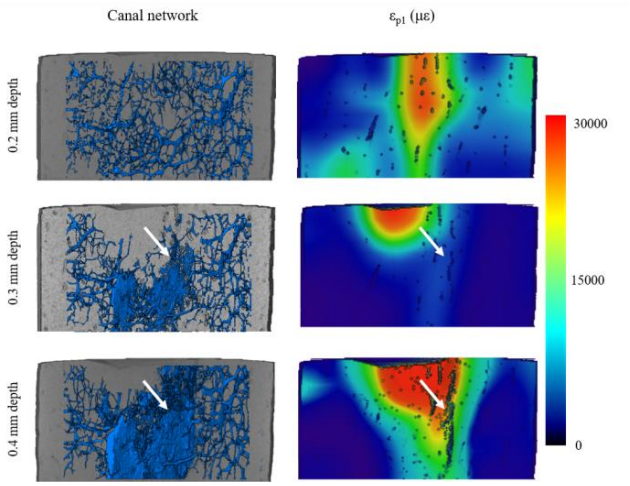

Figure 1: (Left) Visualization of canal network. (Right) strain map of 1st principal strain (ε_{p1}) on axial specimen. Crack forming at the second step of indentation and propagating further at the last (white arrows); white arrows are indicating crack formation.

Discussion

This study evaluated the effect of the orientation of the canal network regarding microcrack formation and prevention. The defect location with respect to the canal network was a major determinant in fracture initiation. Large canals surrounding the indentation defect were allowing uniform deformation in the structure that prevented large crack formation. Additionally it was observed that canal widening induced high tensile strain to the tissue and canal loss showed high compressive strain values. The XCT images revealed that specimens with higher porosity values locally in the defect area, did not crack.

References

[1] J. Rho et al., Med. Eng. Phys. 20 (1998) 92–102.
[2] E. Maire, P.J. Withers, Int. Mater. Rev. 59 (2014) 1–43.
[3] X. Lu et al., Acta Biomater. 96 (2019) 400–411.

Acknowledgements

The XCT imaging and DVC capability was provided by Zeiss Global Centre (University of Portsmouth)

MULTISCALE HOMOGENIZATION AND MICROMECHANICS OF OSTEONAL STRUCTURES

Giuseppe Vairo (1), Pierfrancesco Gaziano (1), Elisabetta Monaldo (2), Cristina Falcinelli (3)

1. University of Rome "Tor Vergata", Dept. of Civil Engineering & Computer Science (DICII), 00133 Rome, Italy; 2. Dept. of Engineering, Roma Tre University, 00146 Rome, Italy; 3. Campus Bio-Medico University of Rome, Dept. of Engineering, 00128 Rome, Italy

Introduction

Bone is a heterogeneous material characterized by a hierarchical structure over multiple length scales. Fracture in bony structures is tricky to predict because the nature of bone constituents at all scales greatly influences the overall mechanical behavior. In addition, any kind of alteration in the quantity and quality of bone tissue with aging and disease results in significant variations in the mechanical response with increased risk of bone fracture. Despite this, some micro-mechanical elements are still not included in the numerical models developed for predicting the bone mechanical response [1]. The aim of the present study is thus to furnish a more detailed modelling of osteons (namely, the structural units of cortical bone) via a multiscale homogenization approach. The brittle behaviour of osteonal bone has been considered by accounting for damage mechanics and for different failure modes. The mechanical response of osteonal structures has been investigated via a nonlinear finite element scheme, revealing a good agreement with experimental findings available in literature [2].

Methods

The structural unit of cortical bone is modelled via a multiscale constitutive rationale, based on micro- and nano-scale parameters having a clear histological meaning. Osteons are constituted of several coaxial, approximately cylindrical lamellae around the haversian canal, herein reproduced as a void. Lacunae, i.e. oblong cavities between the lamellae [3], are modelled as voids having an ellipsoidal shape. Each lamella can be subdivided into a thick lamella and a thin one [1]. Thick lamellae are characterized by considering the features of its nano-constituents, namely hydroxyapatite crystals, collagen fibres and water, which together form the mineralized collagen fibrils (MCF) [4]. Equivalent properties of MCFs are obtained via a first homogenization step, that has been performed following both an analytical and a computational approach. Then, anisotropic elastic properties of thick lamellae are obtained through a subsequent homogenization phase, due to the different arrangements of MCFs in the sublayers constituting the single lamellae [1]. Thin interlamellar areas, made up primarily of non-collagenous proteins [5], are modelled as elastic layers described by 3D spring elements, accounting for normal and tangential stiffness interactions. To simulate the fracture process at the lamellar level, a progressive damage approach is implemented and the possible occurrence of both interlaminar and intralaminar failure is described by adopting two distinct criteria.

Results

The model reliability has been validated by reproducing the mechanical behavior of osteons undergoing experimental tests. In Fig. 1 a comparison between the predicted fracture pattern and the actual one for a single osteon is reported, with reference to a uniaxial tensile test whose data are available in literature [2]. Figure 1 shows that, in this case, fracture originates from the regions with the highest density of lacunae and propagates along a quasi-orthogonal direction with respect to the osteonal axis.

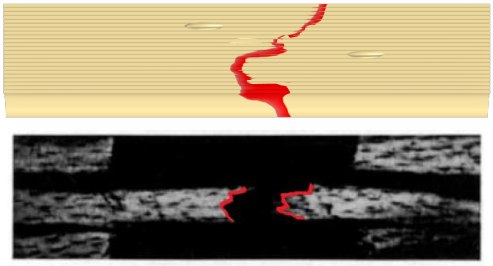

Figure 1: On the top, the fracture pattern predicted by the numerical model. On the bottom, a fractured osteon after a tensile test performed in [2].

Discussion

This work presents a nano-micro multiscale modelling approach to characterize the mechanical behavior of osteonal structures. Comparison of numerical results with the experimental ones allows to confirm the validity of the proposed model. The present study may provide useful indications on microscale failure mechanisms of cortical bone that can be adopted for defining refined bottom-up constitutive descriptions, also accounting for biological aspects. Indeed, biological factors as ageing or disease cause structural changes in bone at all length scales [6].

References

1. Giner et al., J Mech Behav Biomed Mater 37:109-124, 2014
2. Ascenzi and Bonucci, Anat Rec 158(3):375-386
3. Prendergast et al., J Biomech Eng 118:240-246, 1996
4. Jäger and Fratzl, Biophys. J 103:1737-1741, 2006
5. Katsamenis et al., J Mech Behav Biomed Mater 17:152-165, 2013
6. Zimmermann et al., PNAS 108:14416-14421, 2011

INFLUENCE OF STRESS REDISTRIBUTIONS IN µFEA ON THE PREDICTED FAILURE LOAD OF RADIUS SEGMENTS

Monika Stipsitz (1), Philippe K. Zysset (2), Dieter H. Pahr (1,3)

1. Institute of Lightweight Design and Structural Biomechanics, TU-Wien, Austria;
2. ARTORG Center for Biomedical Engineering Research, University of Bern, Switzerland
3. Division Biomechanics, Karl Landsteiner University of Health Sciences, Krems, Austria

Introduction

The Pistoia criterion is often used to predict the strength of radius segments based on linear-elastic µFE simulations. In most cases, tuning of model parameters is necessary to obtain reliable results. One reason might be that in-elasticity or stress redistributions are not taken into account. In this work, we compare the Pistoia criterion with nonlinear µFE simulations up to failure to highlight differences and possible future applications.

Methods

Experimental compression results and µCT scans of 21 radius segments (20 mm height, resolution of 36um) were available [1]. Two simulations were performed per radius segment: (1) A linear-elastic simulation and (2) a materially nonlinear simulation up to failure. For (1), the failure load was predicted with the Pistoia criterion [2]. Since the standard parameters strongly overestimated the experimental failure load, optimal parameters were proposed: The predicted ultimate load was fitted per sample to the experimental value using the overstrained volume as a parameter (Fig 1, left). Elements were overstrained if the effective strain exceeded 0.7%. For (2), a damage-based material with a linear-elastic, a degradation, and a tissue failure region was used. Material parameters were previously validated [3]. Failure load and damaged regions were obtained directly from the simulations. Additionally, the load sharing between cortical and trabecular regions was evaluated as proposed in [4].

Results

The overstrained volume required to reproduce the experimental failure load with the Pistoia criterion was larger than the typically used 2% and highly variable (Tab. 1). The load sharing at the ultimate point obtained from the optimal Pistoia criterion and the materially nonlinear simulations was comparable for all samples (Fig. 1, right). The local distribution of damaged overstrained regions showed only small deviations (Fig. 2).

Table 1: Percentage of overstrained (Pistoia) or damaged elements (NL µFE) at the ultimate load.

	Mean	Standard deviation
Pistoia – Standard	2 %	-
Pistoia – Optimal	33.49 %	19.45 %
Nonlinear µFE	22.91 %	8.24 %

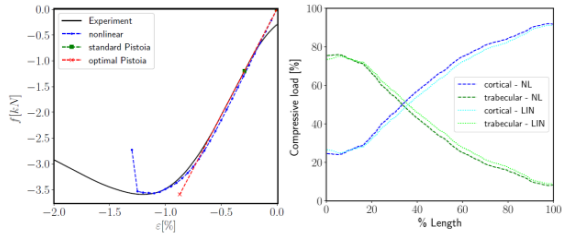

Figure 1: Experimental and model comparisons (left), cortical-trabecular load sharing (right) for a selected radius segment predicted by a linear simulation with the optimal Pistoia criterion (LIN) and a materially nonlinear simulation (NL). The relative length increases from most distal to most proximal.

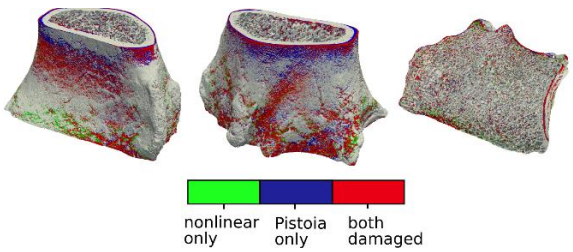

Figure 2: Local difference in the overstrained (LIN optimal Pistoia) or damaged regions (NL µFE) for one selected radius. Three different views are shown.

Discussion

Good agreement between linear (optimal Pistoia criterion) and nonlinear simulations was found on the apparent level, in the load sharing of cortical and trabecular region, and in the local distribution of overstrained / damaged regions. However, the Pistoia criterion required experimental data, i.e. the failure point for the calibration. In contrast, the materially nonlinear simulations needed no calibration based on experiment

References

1. Hosseini et al, Bone, 97:65-75, 2017.
2. Pistoia et al, Bone, 30(6):842-848, 2002.
3. Stipsitz et al, Biomech Model Mechanobiol, 2019.
4. Johnson et al, J Biomech,66:180-185, 2018.

Acknowledgements

The computational results presented have been achieved in part using the Vienna Scientific Cluster (VSC).

THE MICRO- AND NANOSCALE COMPRESSIVE BEHAVIOUR OF REHYDRATED MINERALISED COLLAGEN FIBRES

Alexander Groetsch (1,4), Aurélien Gourrier (2), Daniele Casari (3), Jakob Schwiedrzik (4), Johann Michler (4), Philippe K. Zysset (3), Uwe Wolfram (1)

1. Heriot-Watt University, School of Engineering and Physical Sciences, Edinburgh, United Kingdom; 2. Université Grenoble Alpes, CNRS, LiPhy, 38000 Grenoble, France; 3. University of Bern, ARTORG Centre for Biomedical Engineering Research, Bern, Switzerland; 4. Empa, Swiss Federal Laboratories for Materials Science and Technology, Laboratory for Mechanics of Materials and Nanostructures, Thun, Switzerland

Introduction and Motivation

Musculoskeletal diseases pose a significant socio-economic burden to ageing societies worldwide. Numerical methods could be a cornerstone in digital healthcare by improving diagnosis and treatment strategies. These models critically depend on understanding the complex characteristics of bone as a hierarchical material. Currently, there is limited knowledge on the elasto-plastic behaviour of bone's fundamental mechanical building block, the mineralised collagen fibre, especially under rehydrated conditions. While micro- and nanomechanical data under dry conditions have recently been reported [1], scarce data exist for the quasi-physiologic fibre behaviour. Since the hydration state has a significant effect on the bone mechanics [2, 3], we aimed to develop a testing protocol to identify the rehydrated micro- and nanoscale mineralised collagen fibre behaviour.

Materials and Methods

Micropillars (N = 10) of 6 x 12µm^2 (DxH) were manufactured in individual mineralised collagen fibres of mineralised turkey leg tendon, a model system for bone [4], using a combination of dissection, micro-milling, ultra-short pulsed laser ablation and focused ion beam milling [1]. A portable nanoindenter (Alemnis AG, CH) was integrated into beamline ID13 at the European Synchrotron Radiation Facility to allow simultaneous micropillar compression and SAXS/XRD tests. Samples were rehydrated for 2 hours in Hank's balanced salt solution (HBSS) prior to testing and kept hydrated during testing (Figure 1). Micropillars were uniaxially compressed until 1.5µm displacement at 5nm/s with partial unloading steps of 50nm every 150nm. Micropillars were exposed to X-rays every 5s in a SAXS or XRD regime to extract fibril or mineral strains [1]. Apparent fibre stiffness, yield, ultimate values and strain ratios were extracted from stress-strain data [1]. A statistical constitutive model [5] was used to simulate and evaluate the rehydrated micro- and nanomechanical fibre behaviour including fibril stiffness. Data were compared to dry testing [1] with a statistical significance level of p=0.05.

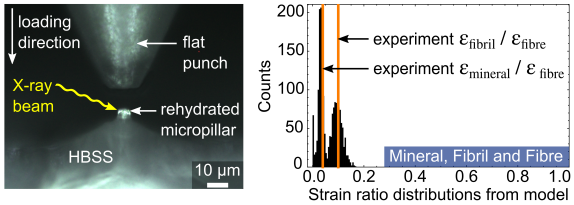

Figure 1: (Left) Experimental set-up for simultaneous micropillar compression and SAXS/XRD for rehydrated fibres. (Right) Experimental and simulated strain ratio distributions between fibre-, fibril- and mineral-levels.

Results

The fibril-to-fibre strain ratio was 0.1±0.03, mineral-to-fibre 0.04±0.01 and mineral-to-fibril 0.40±0.02 corresponding to relative ratios in the elastic region of 53:5:2. Compared to dry conditions [1], fibril-to-fibre and mineral-to-fibre strain ratios were reduced by 62% leaving the mineral-to-fibril ratio unchanged. We found a fibre stiffness of 5.07±1.16 GPa with no reduction also in the plastic region. Hydration led to a 75% reduction of yield stress and compressive strength and a 25% reduction of yield and ultimate strain (Table 1) compared to dry conditions [1]. The model identified a 25% reduced fibril stiffness due to hydration. All changes were significant.

σ_{33}^{yield}/GPa	ε_{33}^{yield}	σ_{33}^{str}/GPa	ε_{33}^{ult}
0.04±0.02	0.03±0.01	0.05±0.02	0.04±0.01

Table 1: Apparent mechanical properties at fibre level.

Discussion

The hydration effect on stress and stiffness values fit well to micropillar compression of ovine bone extracellular matrix [2] but the decrease in stiffness was higher than for microindentation on mineralised turkey leg tendon [4] and trabecular bone [3]. Since our tests were done on individual fibres, this indicates a strong influence of the fibre interfaces on the hydration effect. Hydration had the same effect on fibrils and mineral particles supporting earlier findings on the effect of water in mediating mineral-organic matrix interactions [6]. Smaller fibril strains might result from interfibrillar gliding due to a watery layer. Our fibril stiffness reduction further agrees with molecular dynamics simulations [7]. We identified the rehydrated micro- and nanoscale fibre behaviour by combining experimental and numerical methods. The new insights aim to inform computational models and the design of bio-inspired materials.

References

1. Groetsch et al., *Acta Biomaterialia*, 89:313-329, 2019.
2. Schwiedrzik et al., *Acta Biomaterialia*, 60:302-314, 2017.
3. Wolfram et al., *Bone*, 46:348-354, 2010.
4. Spiesz et al., *J Mech Behav Biomed Mat*, 12:20-28, 2012.
5. Groetsch et al., *Nature Communications*, submitted, 2021.
6. Wilson et al., *Biophysical Journal*, 90:3722-3731, 2006.
7. Fielder et al., *Biomech Model Mechanobio*, 18:57-68, 2019.

Acknowledgements

Financial support: EPSRC (EP/P005756/1), ESRF (ME1472).

EXPERIMENTAL MODAL ANALYSIS FOR THE DETERMINATION OF BONE REPLICATE MATERIAL PROPERTIES.

Maikel Timmermans (1), George Athanassoulis Makris (1), Quentin Goossens(1), Leonard Pastrav(1), Wim Desmet (2), Kathleen Denis (1)

1. KU Leuven, Department of Mechanical Engineering, BMe, Belgium;
2. KU Leuven, Department of Mechanical Engineering, LMSD, Belgium

Introduction

Replicate bone models are frequently used as an alternative testing medium to human cadaver bones. The bone replicates aim to accurately reproduce the biomechanical properties of human bone, while a low inter-specimen variability is maintained [1]. The goal of this study is to investigate the material properties of an ORTHO*bones* femur replicate.

Methods

One replicate of a human femur (ORTHO*bones* left femur ref.1016668, 3B Scientific, Hamburg, Germany) was CT-scanned with a Somatom Force scanner (Siemens AG, Germany) in the University Hospital of Leuven to build a FE model. Using Mimics (Materialise NV, Leuven, Belgium), two separate meshes with linear tetrahedral elements of size 1mm were appointed to respectively the cortical and trabecular region in the FE model. Experimental modal analysis was performed on the bone replicate. It was mounted horizontally with soft rubber bands on either side of the femoral shaft to simulate free-free boundary conditions. Forty equally spread points were marked on the bone and three of them were mounted with a single-axis lightweight accelerometer (PCB A352A24, PCB Piezotronics, Depew, NY, USA, weight 0.8 g) using beeswax. One accelerometer measured in the medial-lateral direction on the femoral shaft and the two others measured in the anterior-posterior direction: one on the femoral shaft and one on the femoral head. Then, the structure was excited by hammer impaction, normal to the surface of the bone model, in all forty points. Data acquisition was performed with LMS SCADAS Mobile (Siemens, Leuven, Belgium). Based on the measured frequency response functions, the resonance frequencies and mode shapes of the specimen were estimated using the Polymax algorithm over a frequency range from 10 to 1000 Hz in Simcenter Testlab (Siemens, Leuven, Belgium).The first seven modes of the numerical model were correlated with the modes of the experimental model. The initial material properties for the numerical model were based on two technical reports provided by the manufacturer of the bone replicate. Two analyses were performed wherein the trabecular region was approximated by an isotropic material and the cortical layer was approximated once by an isotropic material and once by a transversely isotropic material. Then, the elastic material properties of the numerical model were updated through an iterative process as in [2], where the maximum and average error between the resonance frequencies of the experimental and numerical model are minimized .

Results

The numerical model with the isotropic cortical material was improved from an initial average error of 3.71% and a maximum error of 8.69% at mode 3 to a final average error of 2.36% and a maximum error of 3.92% at mode 6. The model with the transversely isotropic cortical material was improved from an initial average error of 1.62% and a maximum error of 3.82% at mode 7 to a final average error of 1.31% and a maximum error of 2.67% at mode 7. The updated material properties are shown in Table 1.

Updated material properties	Before Updating	After Updating	Difference
isotropic			
Young's modulus E_{cort} [MPa]	1530	1455	-4,9%
Poisson's ratio ν_{cort} [-]	0.3	0.38	+26%
transversely isotropic			
Young's modulus $E_{33,cort}$ [MPa]	1530	1492	-2,5%
Shear modulus $G_{13}=G_{23,cort}$ [MPa]	500	503	+0,5%
Poisson's ratio $\nu_{23,cort}$ [-]	0,3	0,28	-7,5%

Table 1: Summary of the updated elastic material properties with their respective values before and after updating and the update percentage.

Discussion

The FE model in which the cortical layer was simulated with a transversely isotropic material approximates the test results most closely. The elastic material properties found in this study are close to the values communicated by the manufacturer. However, these values are significantly smaller than those of human cadaveric bones.[3]

References

1. Gluek et al, J Biomech, 111, 2020.
2. Goossens et al, J. Funct. Biomater., 11: 69, 2020.
3. Mirzaali et al, Bone, 93: 196-211, 2016.

Acknowledgements

This work was supported by Internal Funding KU Leuven.

PATIENT- SPECIFIC MULTISCALE MODELING OF A NORMAL GAIT CYCLE: STRAIN DISTRIBUTION IN FEMORAL NECK

Zainab Altai (1,2), Erica Montefiori (1,2), Bart van Veen (1,2), Margaret Paggiosi (1,3), Eugene V. McCloskey (1,3), Marco Viceconti (4,5), Claudia Mazzà (1,2), Xinshan Li (1,2)

1. INSIGNEO Institute for in silico medicine, The University of Sheffield, UK; 2. Department of Mechanical Engineering, The University of Sheffield, UK; 3. Mellanby Centre for Bone Research, Department of Oncology and Metabolism, The University of Sheffield, UK; 4. Laboratorio di Tecnologia Medica, IRCCS Istituto Ortopedico Rizzoli, Italy; 5. Department of Industrial Engineering, Alma Mater Studiorum, University of Bologna, Italy.

Introduction

There is a need to investigate femoral strains during walking using patient specific data, to enhance our understanding of femur response under physiological loading. Previous studies have used finite element models (FE) of in vivo cadaveric bones coupled with gait data from body-matched volunteers, which could induce inaccuracies in the results [1]. This study aims to report the first fully personalised multiscale model and investigate the strains induced at the femoral neck during a full gait cycle.

Materials and methods

Following ethics committee approval, five postmenopausal women (68.3±5.1 y, 69.8±7.1 kg, 159±3.7 cm) were studied. CT (0.79 x 0.79 x0.63mm) and MRI (1.08 x 1.08 x 3mm) scans of the lower limb were collected. All participants were subjected to a gait analysis protocol during level walking along a 10 m walkway at a self-selected walking speed. The musculoskeletal models (MSKM) were created in NMS Builder (http://www.nmsbuilder.org/) and OpenSim 3.3 (https://simtk.org/), and were used to calculate the muscle and joint reaction forces [2]. FE models of the right femur of all subjects were constructed from CT images using a validated framework [3]. Eighteen muscle forces, estimated by the MSKM, were applied to the FE, at the closest nodes to the centroids of the muscle attachments area. The distance between the application nodes and the estimated centroids varied between 0.1 and 1.6 mm. Boundary conditions were applied to the distal end, where the most distal node of the medial condyle was totally fixed, while the most distal node of the lateral condyle was constrained vertically and in the anterior-posterior direction. An extra node at the mid of the patella groove was also fixed in the anterior-posterior direction (figure 1). Peak principal strains at the neck region were predicted for 100 intervals of the gait cycle, using ANSYS APDL 19.1. The strains were compared with fracture threshold of 0.73% (tension) and 1.04% (compression), respectively [4].

Results

Peak maximum and minimum principal strains ranged from 0.10-0.37% and 0.05-0.67%, respectively. Two peaks were predicted around the 15% (heal strike) and 50% (toe off) of the gait and were observed in 3 of the 5 women, while the other two women were predicted with one peak either at the 15% or the 50% of the gait (Figure 1). Excellent correlation was found between gluteus medius muscle force and predicted strains (R^2 ranged 0.95-0.99). Maximum strains were predicted at the anterior aspect of the neck region (figure 2).

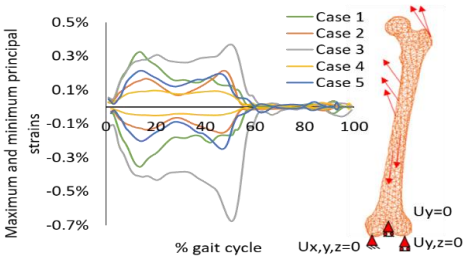

Figure 1: Maximum and minimum principal strain predicted by the FE for 100% of the gait cycle.

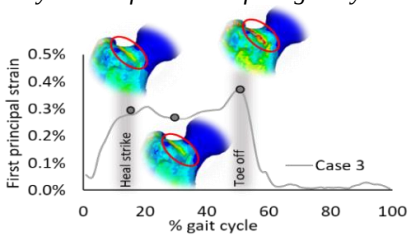

Figure 2: Location of the maximum principal strain predicted at the femoral neck (highlighted in red circle) at 15, 30 and 50 % of the gait cycle for a reprehensive case (Case3).

Discussion

During a normal gait cycle, the highest femoral neck loading occurs when both feet are in contact with the floor (heel strike and/or toe off phases). The current findings suggest that not only joint contact forces but also muscular forces substantially influence the loading at the femoral neck. The activation of major muscles attached to the proximal part of the femur (in particular the greater trochanter) have a considerable contribution to the femoral neck loading during normal gait cycle.

Acknowledgment

The MultiSim and MultiSim2 projects were funded by the EPSRC (EP/K03877X/1 & EP/S032940/1).

References

1. Martelli et al, J Biomech, 44: 1716-1721, 2011.
2. Montefiori et al, Gait & posture, 66S: S1-839, 2018.
3. Schileo et al, J Biomech, 42: 83-91, 2008.
4. Bayraktar et al, J Biomech, 37:27-35, 2004.

MICRO-SCALE CONSTITUTIVE MODEL OF HUMAN TRABECULAR BONE – PART 1: FORMULATION AND PARAMETER IDENTIFICATION

Marek Pawlikowski (1), Krzysztof Jankowski (1)

1. Institute of Mechanics and Printing, Warsaw University of Technology
ul. Narbutta 85, 02-524 Warszawa, Poland

Introduction

In the study an attempt to formulate a micro-scale constitutive model of human bone was made. Also, calibration of the material parameters was presented. The constitutive law can be used to numerically model bone behavior and to predict all or some of the bone-related disorders, as well as to understand the relationship between bone and implants. Formulation of a micro-scale constitutive model for human trabecular bone was based on depth sensing micro-indentation technique [1]. The constitutive model was formulated to implement it in finite element analyses.

Materials and Methods

The bone specimens were resected from a femoral head of a 63-year-old patient to whom a hip joint prosthesis was implanted. The micro-indentation tests were carried out on three trabeculae resected from different areas of the femoral head. A spherical diamond indentator tip of 200 μm in diameter was used. The tests were conducted until the maximal force values 300 mN, 500 mN and 700 mN were reached at the load rates 500 mN/min and 1000 mN/min. A total of 18 tests were conducted.
To model human bone behaviour we proposed a non-linear visco-elastic constitutive model of the general form:

$$\mathbf{S} = \int_0^t g(t-s)\frac{\partial \mathbf{S}^{\mathrm{e}}}{\partial s}\mathrm{d}s, \qquad (1)$$

where: $\mathbf{S}$ – second Piola-Kirchhoff stress tensor, $\mathbf{S}^{\mathrm{e}}$ – elastic second Piola-Kirchhoff stress tensor, $g(t) = g_\infty + \sum_{i=1}^{n} g_i \cdot \exp(-t/\tau_i)$, g_i are characteristic amplitudes and τ_i – relaxation times. In equation (1) s represents the historical time, whereas t is the current time. The form of $\mathbf{S}^{\mathrm{e}}$ was derived from the Mooney-Rivlin strain energy density Ψ:

$$\Psi = c_{10}(I_1 - 3) + c_{01}(I_2 - 3), \qquad (2)$$

where: c_{10}, c_{01} are hyperelastic material constants, I_1 and I_2 – first and second strain invariants, respectively. The relaxation times τ_i and the value of n were determined by fitting the curve described by (1) to the relaxation tests in compression performed on cubic samples of the trabecular bone. The elastic constants c_{10}, c_{01} and the visco-elastic constants g_i were determined on the basis of micro-indentation tests using an indirect method based on finite element analyses [2]. The proposed constitutive model (1) was implemented into Abaqus® finite element method package. The micro-indentation tests were then simulated and the constants calibration was conducted by fitting the simulation curves to those obtained in the micro-indentation experiments [3].

Results

In Fig. 1 the results of curve fitting for one of the micro-indentation case are shown. The solid line represents the curves obtained from the micro-indentation simulations and the squares represent the experiment.

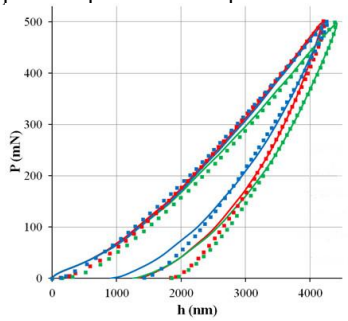

Figure 1: Simulation curves (solid line) fitted to experimental results (squares). Maximal force 500 mN, load rate 1000 mN/min.

The average values of the calibrated constants are presented in Table 1.

Constant	Value	Unit
c_{10}	-2153±76	MPa
c_{01}	2887±81	MPa
g_1	0.11±0.01	-
g_2	0.14±0.02	-
g_3	0.32±0.03	-
g_4	0.02±0.006	-

Table 1: Average values of the visco-elastic constants

Conclusions

The formulated constitutive law for human trabecular bone proved to be capable to model visco-elastic properties of bone at a micro scale. It can be utilized to simulate more accurately bone behavior and to predict its reaction to various load conditions at a macro scale.

References

1. Dall'Ara et al, J Biomech, 48:4073-4080, 2015.
2. Goh et al, Mech Time-Depend Mater, 8:255-268, 2004.
3. Pawlikowski et al, J Mech Behav Biomed Mater, 85:162-169, 2018.

MICRO-SCALE CONSTITUTIVE MODEL OF HUMAN TRABECULAR BONE – PART 2: MODEL *IN SILICO* VALIDATION

Krzysztof Jankowski (1), Marek Pawlikowski (1)

1. Institute of Mechanics and Printing, Warsaw University of Technology
ul. Narbutta 85, 02-524 Warszawa, Poland

Introduction

In the present paper *in silico* validation of the bone constitutive model formulated in the previous study is conducted. The model takes into account visco-elastic properties of human bone trabeculae, i.e. hysteresis loop, load rate dependency and stress relaxation. In the paper the model validation is based on stress relaxation tests.

Methods

The cubic bone samples were resected from a femoral head of a 63 year-old patient such that the two cutting surfaces were perpendicular to the trabecula orientation and the other four surfaces were parallel to the main direction of the trabeculae (Fig. 1).

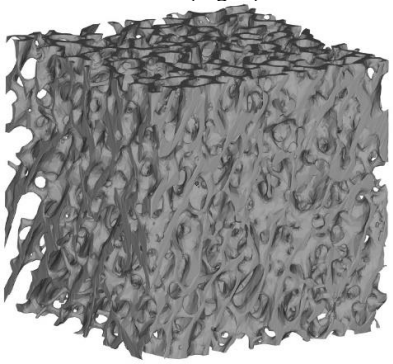

Figure 1: Model of a bone sample

The samples were kept in alcohol. Before the tests they were left in room temperature for an hour to get rid of the excessive amount of the fluid. The relaxation tests were conducted in room temperature, i.e. 20ºC ± 0.5ºC, and air humidity 30% ± 5%. The samples were compressed until stain value 0.01 was reached and then the change of the force was registered for 500 sec.
In order to validate *in silico* the human bone constitutive model formulated in Part 1 of the present study we implemented the model into Abaqus® finite element (FE) package [1]. The general form of the model is described by formula (1):

$$\mathbf{S} = \int_0^t g(t-s)\frac{\partial \mathbf{S}^{\mathrm{e}}}{\partial s}\mathrm{d}s, \qquad (1)$$

where: $\mathbf{S}$ – second Piola-Kirchhoff stress tensor, $\mathbf{S}^{\mathrm{e}}$ – elastic second Piola-Kirchhoff stress tensor, $g(t) = g_\infty + \sum_{i=1}^{n} g_i \cdot \exp(-t/\tau_i)$, g_i are characteristic amplitudes and τ_i – relaxation times. In equation (1) s represents the historical time, whereas t is the current time [2,3]. The values of relaxation times were calibrated by fitting the curve described by (1) to relaxation experimental curves. The average values of relaxation times are shown in Table 1

τ_1 [s]	τ_2 [s]	τ_3 [s]	τ_4 [s]
0.25	22.14	1961.5	8744.2

Table 1: Average values of the relaxation times

The geometrical models of the cubic bone samples were imported into the FE software and the relaxation tests were simulated. The constitutive model validation consisted in comparison of the experimental relaxation curves to those obtained from the FE analyses.

Results

In Fig. 2 one of the results of the curves comparison is graphically presented. The experimental curve is shown by means of squares and the FE analysis curve with a solid line.

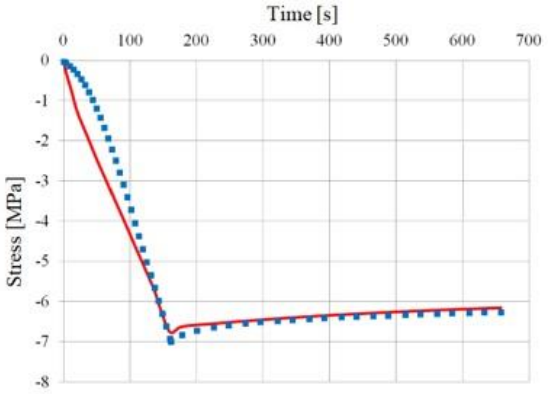

Figure 2: Relaxation curves obtained from: experiment (squares) and FE simulation (solid line)

Conclusions

The formulation of the constitutive model for human trabecular bone and the calibration of the visco-elastic constants proved to be correct. The *in silico* validation presented in the study is based on relaxation tests. Our other studies proved that the model also reliably describes bone behavior under compression loads.

References

1. Pawlikowski et al, Biocybern Biomed Eng, 36:491-498, 2016.
2. Pawlikowski et al, J Mech Behav Biomed Mater, 85:162-169, 2018.
3. Goh et al, Mech Time-Depend Mater, 8:255-268, 2004.

HUMAN TIBIA IMPLANTED WITH TITANIUM PRESS-FIT TRAY: A MICRO-CT ZERO-STRAIN ANALYSIS WITH DIGITAL VOLUME CORRELATION

Lauren Wearne (1), Sophie Rapagna (1), Mark Taylor (1), Egon Perilli (1)

1. Medical Device Res. Institute, College of Science & Engineering, Flinders University, Adelaide, Australia.

Introduction

Achieving primary stability is crucial in tibial press-fit implant fixation [1]. However, experimental data on trabecular and cortical bone deformation during implantation is limited. Advancements in large-gantry micro-CT imaging and the development of digital volume correlation (DVC) allows such data collection. This pilot study assesses the DVC strain errors for a human tibia implanted with a titanium press-fit tray across four scanning configurations using a cabinet micro-CT system. The aim is to optimise such analysis.

Methods

Micro-CT Imaging: One cadaveric proximal tibia was resected, implanted with a titanium press-fit tray and micro-CT scanned (Nikon XT H225 ST) at 42µm/pixel (*Fig.1 A-C*), first in air (150kVp, 227µA, 0.25Sn filter, 2s exposure) with a longer (1h46m, rotation step 0.11°) and shorter (1h6m, rotation step 0.18°) scan time. Both scans were then repeated with the specimen placed in an aluminum cylinder of 2mm wall thickness used for mechanical testing (215 kVp, 195µA, 0.5Sn filter, 2s exposure) [2]. Rescans were taken at each of the four configurations, with specimen repositioning in-between. 3D image co-registration of the rescans was performed (DataViewer, Bruker).

DVC Strain Analysis: Nine cubic volumes of interest (VOIs, 13.4mm side length) were selected via software (CT Analyser, Bruker): five VOIs contained trabecular bone only, and four were centered on the four tibial tray pegs (7mm Ø) with surrounding bone (*Fig.1 D*). DVC analysis (DaVis 8.3.1, LaVision, direct correlation) was performed on the VOIs. Nineteen DVC settings were assessed, including multistep progression (3-6 steps), final subvolume size (0.84-1.68mm) and subvolume overlap. The strain mean absolute error (MAER) and its standard deviation (SDER) were calculated, as indicators of DVC's accuracy and precision, respectively [3].

To perform DVC on the entire proximal tibia, the implant and the volume external to the cortex were masked out (CT Analyser, MATLAB). Optimised DVC parameters (6-step multipass, 0% overlap, final subvolume size of 1.18mm) were hence applied to calculate the zero-strain error values.

Results

Across all VOIs, the accuracy and precision at the four scanning configurations (in air or in the aluminum cylinder, at 0.11° or 0.18° rotation step), were comparable and within the range (MAER) 256-525µε and (SDER) 97-264µε, respectively (*Fig.1 D*). In performing DVC analysis in the entire proximal tibia, the accuracy was 447µε and precision 372µε (*Fig. 1 E*).

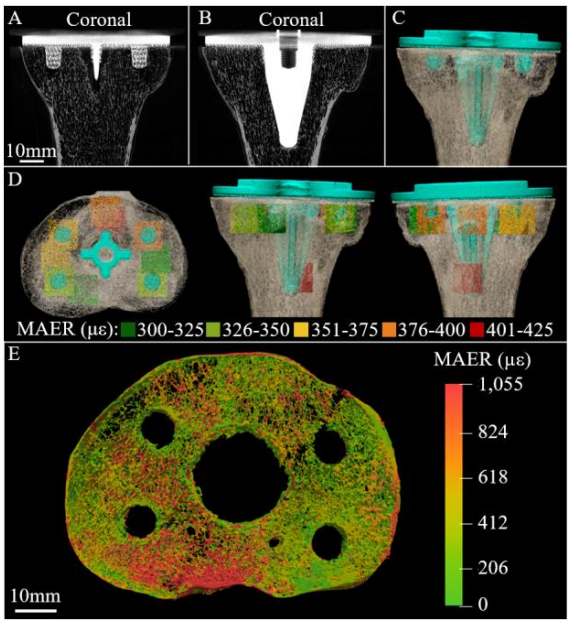

Figure 1: A, B) Coronal micro-CT images (42µm/pixel) and C) 3D micro-CT rendering of the proximal tibia with titanium implant, D) with the 9 VOIs used for DVC (colour represents strain MAER); E) zero-strain MAER across the proximal tibia (peg level).

Discussion

Within the selected VOIs and across the entire proximal tibia, the strain measurements' accuracy was within the range deemed adequate in the literature (less than 10% of the yield strain of bone, 7,000µε)[4]. Moreover, strain errors were comparable across the two rotation steps, in air and the aluminium cylinder. This indicates that the shorter scanning time, preferred for repeated scanning of biological specimens, is suitable for the planned mechanical testing configuration. This study will continue, performing micro-CT imaging of human tibiae implanted with press-fit prothesis under load.

References

1. AOANJRR, Aus Gov Department of Health, 2020.
2. Martelli, Perilli, J Mech Behav Biomed, 84:265-272, 2018.
3. Tozzi, et al., J Mech Behav Biomed, 67:117-126, 2017.
4. Liu, et al., J Biomech, 40:3516-3520, 2007.

Acknowledgements

Australian Research Council Training Center for Medical Implant Technologies

MEASUREMENT OF LINEAR STRAIN FIELDS BY MEANS OF DIGITAL IMAGE CORRELATION

Nedaa Amraish (1,2), Andreas Reisinger (2), Dieter Pahr (1,2)

1. Institute for Lightweight Design and Structural Biomechanics, TU-Wien, Vienna, Austria

2. Division Biomechanics, Karl Landsteiner University of Health Sciences, Krems Donau, Austria

Introduction

Non-homogeneous strain fields can be found on the surface of biological tissues. These strain fields can be captured by means of Digital Image Correlation (DIC). However, DIC strain field measurements are prone to noise [1, 2] which makes it difficult to capture strain gradients. DIC full-field strain measurements can be verified using finite element (FE) methods. At local locations, the normalized strain gradient - which is the difference between the strain at two points divided by their average per unit millimetre - can be used to verify the DIC measurements. The aims of this study are to measure linear strain fields for samples under deformation, and to verify if the DIC measurement can capture the normalized strain gradients at local locations.

Materials and Methods

The sample geometry, w(x), was designed to give a linear strain field along the sample's length when load is applied, see Figure 1. Four strain measurement methods were employed in this study. The analytical strain, strain gauges (SGs) strains, FE strains, and DIC strain measurements. Aluminium, polymer, and bovine bone samples were subjected to a uniaxial tensile load with crosshead movement of 0.5 mm/min till fracture. The strain obtained via the FE model was calibrated for actual experimental values from SG2. The deviation of the DIC strain from the FE strain was evaluated via the root mean square error (RMSE). And finally, the normalized strain gradient was evaluated at the position of SG1 (high-gradient ROI) and SG3 (low-gradient ROI).

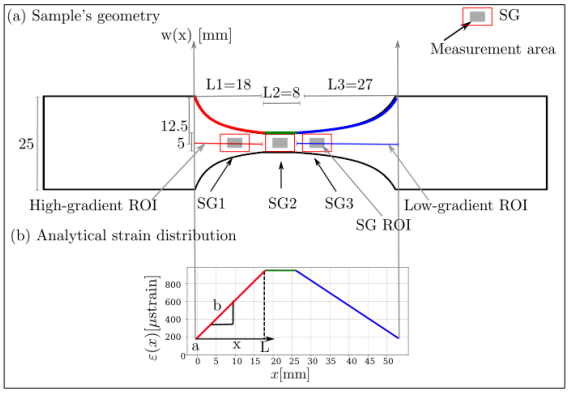

Figure 1: (a) Sample's geometry derived from the analytical solution, (b) The analytical strain distribution along the sample's length.

Results

Figure 2(a) shows the linear strain field along the sample length for bovine bone under 1750µstrain deformation. Figure 2(b) shows the RMSE for the analytical, DIC, and the Gaussian filtered DIC strain in comparison to the FE strain over the full-field. Figure 2(c and d) show how the precision of normalized strain gradient of 6.9% per mm and 3.6% per mm improved with increasing load for SG1 and SG3, respectively. Gaussian low-pass filter (LPF) reduced the noise in the DIC measurement between 25% and 42% on average for all tested materials.

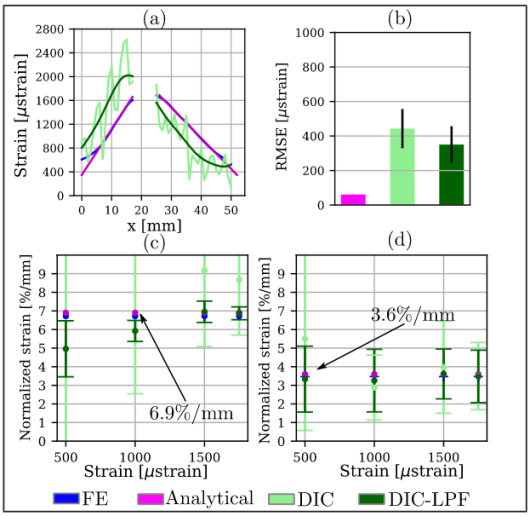

Figure 2: (a) Linear strain gradient, (b) RMSE, (c) and (d) The normalized strain gradient at SG1 and SG3 respectively.

Discussion

Overall, the RMSE of the DIC was less than 500 µstrain for all tested materials which is in line with values reported in the literature [1,2]. No significant difference was found between the SGs' strain and the average strain computed by DIC at the SGs' positions. Finally, DIC can be employed to capture strain gradients.

References

1. Gilchrist et al. (2013). Journal of Biomechanical Engineering, Vol. 135/121001-1.
2. Hensley et al. (2017). Acta of Bioengineering and Biomechanics, Vol. 19, No. 3.

Acknowledgements

This work was supported by the government of Lower Austria, contract No. SC18-006-2019.

MICROSTRUCTURAL ANISOTROPY AND MATERIAL GRADIENTS IN MINERALIZED FIBROCARTILAGE AT THE TENDON-BONE INSERTION

A Tits (1), S Blouin (2), JF Kaux (1), P Drion (1), GH van Lenthe (3), R Weinkamer (4), MA Hartmann (2), D Ruffoni (1)

1. University of Liege, Belgium; 2. Ludwig Boltzmann Institute of Osteology, Vienna, Austria; 3. KU Leuven, Belgium; 4. Max Planck Institute of Colloids and Interfaces, Potsdam, Germany.

Introduction

Tendons attach to bones via a highly specialized interface called enthesis, which ensures load transfer between two strongly dissimilar tissues, for millions of loading cycles [1]. This challenging task is solved thanks to many adaptation strategies, including the presence of fibrocartilage (FC) sandwiched between tendon and bone. Despite the recognized biomechanical importance of FC, which appears either as mineralized (close to bone) or unmineralized (close to tendon), this tissue is much less investigated than tendon or bone. A clear description of the structure-function relationship of FC is still missing, one reason being the small size of this heterogeneous region, spanning less than 200 µm. Yet, this tissue is of high clinical relevance, being involved in enthesis pathologies and degeneration.

Previously, we have characterized the microporosity of FC and the underlying subchondral bone at the tendon-calcaneus bone insertion site of rats (Fig. 1). This location presents attractive aspects: it experiences a relatively simple and localized loading condition (in analogy with a cantilever beam) and it features two types of FC with different mechanical functions: enthesis FC (anchoring tendon to bone) and periosteal FC (facilitating tendon sliding). Using micro-computed tomography, we have highlighted a strong anisotropy of fibrochondrocytes lacunae and vascular canal network at enthesis FC and subchondral bone in comparison with periosteal FC (Fig. 1). Such an arrangement likely reflects adaptation to different biomechanical tasks. To further investigate the structure-function relationship in mineralized FC (mFC) as well as the presence of mechanical gradients at the bone-tendon interface, we characterize the correlation between mineral content and mechanical properties by combining quantitative backscattered electron imaging (qBEI) with nanoindentation (nIND).

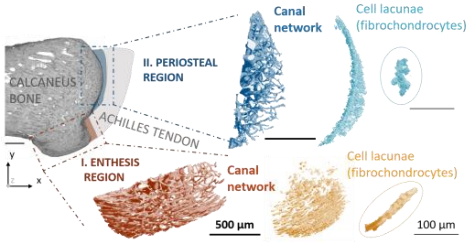

Fig. 1: Rendering of microporosity in bone and mFC.

Methods

After surface grinding and polishing, two-dimensional mineral content maps of bone and mFC (adult Sprague Dawley rat, n = 4) were obtained with qBEI (0.8 µm pixel resolution, Fig. 2). Elastic modulus was measured across the interface and mFC using nIND (Berkovich tip, 500 nm penetration depth, 6 µm spacing between indents). The correlation between mineral content and elastic modulus was obtained superimposing the images obtained from the two measurements and calculating the mineral content around indent positions. Points falling close to voids (lacunae or cracks) were excluded.

Results

The measurement of the elastic modulus across the bone-tendon interface revealed two regions (Fig. 2): a steep increase in tissue stiffness occurring in about 20 µm was followed by a gradual transition in mFC. Interestingly, only the initial increase in elastic modulus could be explained by a corresponding increase in mineral content, while mineralization was practically constant in mFC. Mineral content–elastic modulus correlations were used to generate 2D maps of the elastic modulus, revealing a highly heterogeneous behavior of mFC in comparison to bone (Fig. 2). Additionally, for the same amount of mineral, bone showed the highest stiffness and enthesis mFC the lowest.

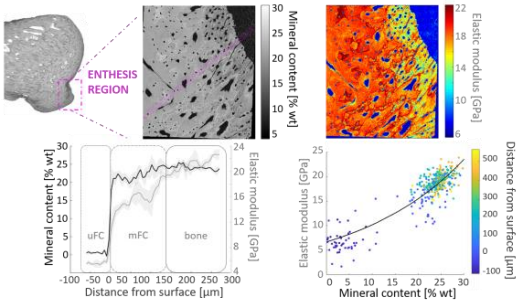

Fig. 2: Maps of mineral content and stiffness (based on modulus-mineral correlation) along with spatial evolution across the bone-tendon interface.

Discussion

Although compositional gradients at the bone-tendon interface have been characterized, information on mechanical gradients is rare. Our work provides a direct assessment of the tissue modulus at the interface, which can be used in finite element simulations of the bone-tendon complex, and reveals the role of mFC to smoothen the transition between tendon and bone. The region-specific mineral-modulus relationship, as observed at the bone-cartilage interface too [2], calls for additional investigations of the arrangement of the mineralized collagen network, especially in relation to the observed anisotropic microstructural porosity.

References

1. Tits et al., Bone Rep, 14, 2021.
2. Gupta et al., J. Struct. Biol, 149(2): 138-148, 2005.

BONE MECHANOREGULATION ALLOWS SUBJECT-SPECIFIC *IN VIVO* ESTIMATION OF MICROSTRUCTURAL TISSUE LOADING HISTORY

Matthias Walle (1), Francisco C. Marques (1), Nicholas Ohs (1), Michael Blauth (2), Ralph Müller (1), Caitlyn J. Collins (1)

1. Institute for Biomechanics, ETH Zurich, Switzerland;
2. Department for Trauma Surgery, Innsbruck University Hospital, Austria.

Purpose

Bone adapts to withstand its habitual mechanical loading environment, leading to bone structure variations and strength across patients. Patient-specific analyses of the mechanically driven bone remodelling process may significantly impact clinical practice; yet, it requires an accurate estimation of day-to-day loads exerted on the skeleton [1]. Where existing estimation approaches assess load history cross-sectionally [2], the growing prevalence of longitudinal studies calls for methods estimating *in vivo* load over time. This study aims to estimate subject-specific loads in longitudinal bone imaging studies by including mechanoregulative principles into a prior reverse engineering estimation approach [2], which is validated using *in silico* and *in vivo* imaging data in humans and in mice. In the future, linking subtle changes in bone strength to changes in day-to-day loading at higher precision may help to identify pathological bone remodelling earlier.

Methods

The proposed mechanoregulated approach (MR) estimates load by superimposing six independent finite element calculations. Using a Nelder-Mead method, strain energy density (SED) was maximised where bone was formed and minimised in regions of resorption. The results were compared to a previously published load history algorithm (LH) [2]. Validation included three unique datasets. First, *in silico* geometries were derived from HR-pQCT images (n=5) and adapted toward nine different target loads using a model of load adaptive remodelling [4]. Receiver operator characteristics (ROC) were used to compare simulated to estimated loads F_{pred} and calculate Sensitivity (Sns), Specificity (Spc) and Accuracy (Acc) (Fig. I). Second, MR and LH algorithms were applied to longitudinal micro-CT scans (vivaCT 40, 10.5µm) of sixth caudal vertebra in mice loaded extra-physiologically (F=8N, 3x/week at 10Hz; n=7) and sham loaded controls (F=0N; n=8) from a previous study [5]. Micro-CT scans were taken weekly at five time points (t=5). Root Mean Squared Error (RSME) between experimentally derived and estimated SED was calculated (Fig. II). Third, HR-pQCT scans (XtremeCT II, 60.7µm) were taken for patients (n=7) six times during one year and handgrip force F_{Grip} was measured using a dynamometer. All patients gave informed consent prior to participation (Ethics Committee, Medical University of Innsbruck, UN 0374344/4.31). Pearson's R between F_{pred} and F_{Grip} was calculated assessing the method's fidelity (Fig. III).

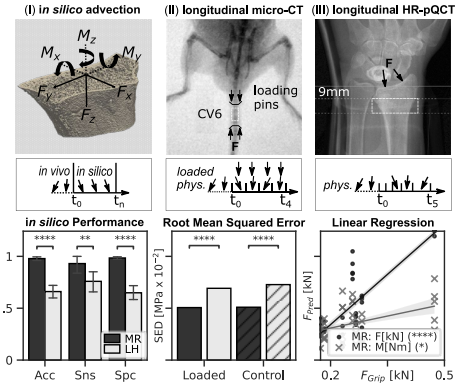

Fig.: Validation of MR and LH. (I) In silico geometries, load cases and patterns over time (t_0-t_5). Bar plots show Acc, Sns, and Spc. (II) Scanninag site and load direction. Load patterns shown for loaded and controls. Barplot shows RMSE of SED. (III) Scanning site and skeletal forces. Lineplot shows F_{pred} and F_{Grip} linear regression.

Results

MR classified *in silico* loads with significantly higher ($p<0.01$) Sns (0.93±0.10), Spc (0.98±0.01) and Acc (0.98±0.02) compared to LH (Sns: 0.76±0.10, Spc: 0.65±0.07, Acc: 0.66±0.06). RMSE was significantly lower ($p<0.01$) for MR compared to LH for loaded (LH: 0.0072 ± 10^{-3} MPa; MR: 0.0051 ± 10^{-3} MPa) and control mice (LH: 0.069 ± 10^{-3} MPa; MR: 0.0051 ± 10^{-3} MPa). Pearson correlation was significant between F_{Grip} and MR's forces ($R^2=0.72$, $p<0.01$) and moments ($R^2=0.18$, $p<0.05$). Similarly, LH predicted forces ($R^2=0.70$, $p<0.01$) and moments ($R^2=0.14$, $p<0.05$) sufficiently.

Discussion

Our findings show that MR is an enhanced *in vivo* load estimation algorithm for longitudinal bone remodelling studies, achieving better *in silico* and *in vivo* performance. Further, we provided extensive validation paving the way for future bone remodelling studies.

References

1. Galibarov et al. (2010) Med Eng Phys 32:1180–1188
2. Christen et al. (2012) BMM 11:483–492
3. Badilatti et al. (2016) BMM 15:83–95
4. Scheuren et al. (2020) Front Bioeng Biotechnol 8:1211

Acknowledgements: We thank Innsbruck University Hospital, Dr. Atkins, and Dr. Scheuren for providing in vivo image and grip strength data. Support from EU-H2020 grant no. 860898 and 841316, SNF 320030L_170205, and CSCS.

MICROSCALE COMPRESSIVE BEHAVIOR OF HYDRATED LAMELLAR BONE AT HIGH STRAIN RATES

Cinzia Peruzzi(1), Rajaprakash Ramachandramoorthy(1), Alexander Groetsch(1), Daniele Casari(1), Philippe Grönquist(2,3), Markus Rüggeberg(2,3), Johann Michler(1), Jakob Schwiedrzik(1)

1. Empa, Swiss Federal Laboratories for Materials Science and Technology, Laboratory for Mechanics of Materials and Nanostructures, Thun, Switzerland; 2. Empa, Swiss Federal Laboratories for Materials Science and Technology, Laboratory for Cellulose and Wood Materials, Duebendorf, Switzerland; 3. Institute for Building Materials, ETH Zurich, Switzerland

Introduction

Bone is a hierarchically structured composite material. Its main components are collagen molecules, calcium phosphate minerals and water. Mineralized collagen fibrils are embedded into an extrafibrillar matrix and form lamellae, 3 to 7 µm thick layers that are wrapped around blood vessels forming osteons in cortical bone. In daily life, bones are subjected to mechanical loading at different strain rates, such as during walking (0.005-0.08 s^{-1}), sprinting (0.05 s^{-1}) and accidental falls (25 s^{-1}) [1]. Microscale tests have been typically conducted at quasi-static strain rates (up to 0.001 s^{-1}). In this study, we investigate the rate-dependent mechanical behavior of ovine bone micropillars at the lamellar length scale across seven orders of magnitude (up to ~830 s^{-1}), under physiologically relevant humidity conditions.

Methods

Micropillars were produced in cortical bone with a focused-ion beam (FIB) [2] using two samples from one ovine tibia oriented parallel (axial) and perpendicular (transverse) to the main osteon direction. 93 micropillars (46 axial and 47 transverse) were fabricated with a diameter of 5.52 +/- 0.14 µm and a height of 10.35 +/- 0.68 µm. Compression experiments were performed under ambient pressure and with a relative humidity greater than 90% using a custom-built nanoindenter. Experiments were performed in displacement control at quasi-static up to impact strain rates (10^{-4} - $8{\cdot}10^{2}$ s^{-1}). High resolution scanning electron microscope (HRSEM) imaging was conducted on all micropillars. To get a better insight into the deformation mechanisms six micropillars were selected for FIB cross sectioning and a further three micropillars that were compressed at high strain rates (10^{2} – $8{\cdot}10^{2}$ s^{-1}) for scanning transmission electron microscopy (STEM) imaging.

Results

The yield stress was found to increase with increasing strain rate (Figure 1). The strain rate sensitivity exponent is defined by the following equation

$$m = \left[\frac{d(ln\sigma)}{d(ln\dot{\varepsilon})}\right]_T \quad (1)$$

and was found to be $m_a = 0.06$ and $m_t = 0.04$ for axial and transverse micropillars, respectively. A clear anisotropy was found in the microscale yield behavior. HRSEM images revealed the main deformation mechanism to be localized shear deformation. At high strain rates, the deformation mechanism and postyield behavior changed, as the energy to fracture and hardening significantly increased. Also, thick shear bands were observed at high strain rates instead of highly localized thin bands in quasi-static experiments.

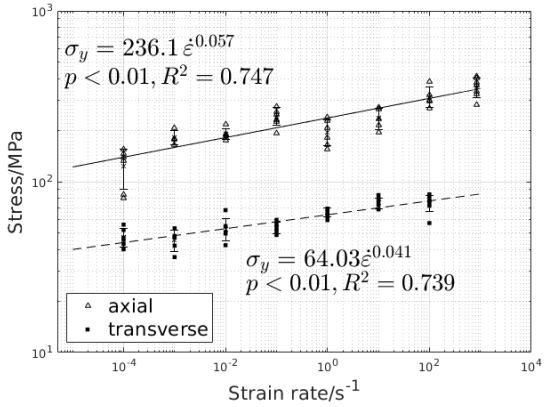

Figure 1: Yield stress extracted from micropillars tested at different strain rates in the axial and transverse direction.

Discussion

This study measured the strain rate dependent yield properties of isolated bone lamellae under hydrated conditions in a large range of strain rates spanning from quasi-static to impact loading (10^{-4} s^{-1} to $8{\cdot}10^{2}$ s^{-1}). The strain rate sensitivity was found to be similar to reported values in literature for different species and higher length scales. This suggests that it is an intrinsic property of the bone extracellular matrix. Furthermore, an increase in energy absorption as well as thickening of shear bands were observed at high strain rates instead of highly localized thin bands in quasi-static experiments suggesting a change in deformation mechanism.

References

1. D.R. Carter et al., Science, 1976.
2. J. Schwiedrzik et. al., Nature Materials, 2014.

Acknowledgements

This work was supported by Ambizione grant 174192 of the Swiss National Science Foundation.

PLATE AND ROD NETWORKS DESCRIBE LOAD TRANSFER IN TRABECULAR BONE

Matthias Walle (1,2), Mohammadreza Abbasian (1,2), Diana Yeritsyan (1,2), Ramin Oftadeh (1,2), Ara Nazarian (1,2,3)

1. *Musculoskeletal Translational Innovation Initiative, Beth Israel Deaconess Medical Center, Boston, USA; 2. Harvard Medical School, Boston, USA; 3. Yerevan State Medical University, Yerevan, Armenia*

Purpose

The trabecular network is perceived as a collection of interconnected plate- (P) and rod-like (R) elements [1]. Previous research has highlighted how these elements and their first-degree connectivity (P-R, R-R, P-P) influence mechanical properties of bone [2]; yet, further work is required to elucidate better the deeply interconnected character of the trabecular network with distinct element formations conducting forces in accordance to their mechanical boundary conditions. Within this network forces act through elements: a rod or plate with a force applied to one end will transmit this force to an element connected to the other end, defining the boundary conditions for loading of each element. To that end, this study has two aims: First, to investigate trabecular bone's morphometric properties of individually segmented elements, with respect to their local boundary conditions as defined by the surrounding trabecular network, and to link them directly to bone's overall mechanical response during loading. Second, to use this model to quantify the side-artefact, a known artefact when testing an excised specimen of trabecular bone, where vertical trabeculae lose their load-bearing capacity due to a loss of connectivity, which ultimately results in a change of the trabecular network topology.

Methods

We used a trabecular specimen model to investigate loss of connectivity within the network, using cylindrical cores taken from 12 bovine femurs. Specimens were, subsequently decreased in diameter (S∅=10 mm, M∅=14 mm, L∅=18 mm) and tested with matching diameter platens (S, M, L). Specimens were scanned using a micro-CT (μCT40, Scanco Medical AG, 40μm). 3D-Images were spatially decomposed using a shape conserving 3D-thinning and topological characterization algorithm to identify plate- and rod-like structures [3], where a sparse connectivity matrix was derived. A weighted graph was constructed using individual element bone volume, being one major predictor of the overall mechanical performance. A Boykov-Kolmogorov maximum flow algorithm was applied to compute the effectively loaded BV/TV following the network layout. The local mechanical environment was derived from voxel-based FE-analysis (E=15 GPa, ν=0.3), and finally ground truth was provided by conducting compressive mechanical testing to failure at 1% strain (Instron 8511, Norwood, MA, USA).

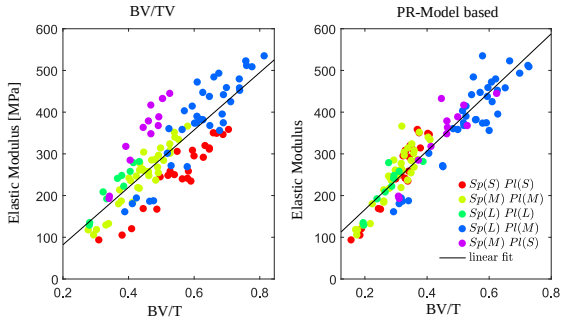

Figure 1: Scatter plots and linear regression lines showing the relationship between BV/TV and apparent modulus based on BV/TV (A) and based on PR-Network (B). Colour code indicating different specimen (Sp) and Plunger (Pl) size (S,M,L).

Results

The max-flow PR-Model successfully identified loaded elements within the trabecular network. Comparison of von Mises stress derived by micro-FE analysis was in good agreement. ROC analysis showed high predictive capabilities (*AUC=0.73*). Max-flow through the network predicted modulus by fitting a linear power law (R^2 = *0.81*) as seen in **Figure 1**. In comparison, prediction using conventional BV/TV results in a lower accuracy (R^2 = *0.72*), demonstrating the PR-Model's ability to estimate compressive elastic modulus independent of specimen size or loading boundary condition. Modulus derived from finite element analysis (E_{FE}) was in good agreement (R^2 = *0.85*) with Young's modulus from the measurements (E_{meas})

Discussion

PR-Network models are a novel approach to describing load and force transfer mechanisms within the trabecular network, incorporating mechanical boundary conditions within the morphological analysis, thus enabling the study of intrinsic material properties of trabecular bone. Ultimately, PR-Network models may be used as an early predictor or may provide further insights in osteo-degenerative diseases.

References

1. Hildebrand, Ruegsegger, CMBBE 1(1), 15-23, 1997.
2. Stauber, et al., JBMR 21(4), 586-595, 2006
3. Stauber, Müller, Bone 38(4), 475-484, 2006.

DXA-BASED 3D MODELS CAPTURE THE EFFECT OF OSTEOPOROSIS PHARMACOLOGICAL TREATMENTS ON BONE STRENTGH

Carlos Ruiz Wills (1), Renaud Winzenrieth (2), Silvana Di Gregorio (3), Luis Del Río (3) , Ludovic Humbert (2), Jérôme Noailly (1)

1. BCN MedTech, Universitat Pompeu Fabra, Spain; 2. 3D-Shaper Medical, Spain; 3. CETIR Grup Mèdic, Spain

Introduction

Millions of people suffer from osteoporosis that affects mostly the elderly. Osteoporotic hip fractures represent a high social and economic burden, and several pharmacological treatments are available in the market. Bone density (BMD) in patients under osteoporosis drug treatment is monitored in clinical practices using DXA. Advanced imaging techniques like DXA-based 3D modelling can improve the quantification of the cortical and trabecular BMD and of the cortical thickness [1]. DXA-based 3D finite element (FE) models add complementary information regarding bone mechanics and have a high potential of discrimination of fracture and non-fracture cases [2]. However, the effectiveness of such methods to capture the effects of pharmacological treatments on bone strength remains unknown. The aim of this study is the evaluation of pharmacological treatment effects on bone strength using DXA-based 3D modelling and FE simulations.

Materials and Methods

Denosumab (DMAB) and teriparatide (PTH) data of 155 patients obtained from CETIR Grup mèdic was used to generate the 3D femur models. 3D models including bone shape and volumetric density were derived from baseline and follow-up DXA scans using the 3D-Shaper® software and statistical average models were computed for each group and each timepoint. Both trabecular and cortical bone were considered as linear elastic material. Young modulus was calculated from bone density using empirical relationships [2].
Lateral fall was simulated through the application of a displacement of 4% of the distance from the femoral head to the greater trochanter [3]. The diaphysis was not constrained, and the trochanter was fixed (Fig.1).

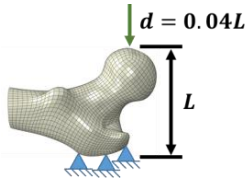

Figure 1: 3D DXA-based FE model with boundary conditions.

Simulations for the inegral bone structure or for only the cortical and only the trabecular bone evaluated the evolution of the strength of both the femur and the individual tissue structures.

Results

The calculated strength for the integral, cortical and trabecular bone increased for both DMAB and PTH treatments (Table 1). The increase in bone strength was higher under DMAB than under PTH, for all bone compartments. Furthermore, under PTH treatment, bone strength in the trabecular bone increased more markedly than in the cortical one.

DMAB	Integral	Cortical	Trabecular
Baseline	3815.08	685.45	1343.97
Follow up	4020.10	700.56	1426.42
Difference (%)	+5.37	+2.2	+6.13
PTH	Integral	Cortical	Trabecular
Baseline	3660.30	626.89	957.94
Follow up	3699.30	628.71	978.65
Difference (%)	+1.04	+0.29	+2.16

Table 1: Femoral strength (in Newtons) for integral, cortical and trabecular models, with DMAB and PTH treatments.

Discussion

The increase in bone strength shown in Table 1 are in agreement with the changes in integral, cortical and trabecular volumetric BMD reported in [1]. Cortical bone strength under DMAD was higher than under PTH. These results are consistent with the respective effect of each drug, since DMAB increases cortical thickness and density. DMAB model captured such effect in the cortical strength value. Interestingly, we found a very slight increase in cortical strength under PTH, whereas the BMD decreased, suggesting that the increment of cortical thickness compensated this BMD reduction. Further simulations using DXA-based models are needed to evaluate the effect of pharma treatments on individual patients to better interpret the current results. To conclude, DXA-based 3D FE models might represent a complementary tool to evaluate pharmacological treatments effect on bone strength in clinical research and practice.

References

1. Winzenrieth R. et al., Osteoporos Int 29(10):2323-2333,2018.
2. Ruiz Wills C. et al., Bone 121:89-99, 2019.
3. Orwoll E. et al., J Bone Miner Res 24(3):475-483,2009.

Acknowledgements

Funds from Spanish Government (ANDAMIO- RTC2019-007413-1, RYC-2015-18888) are acknowledged.

VALIDATION OF MICRO FINITE ELEMENT MODELS OF PORCINE VERTEBRAE WITH INDUCED LESION USING DISPLACEMENT MEASURED BY DIGITAL VOLUME CORRELATION

Marco Palanca, Sara Oliviero, Enrico Dall'Ara

Dept of Oncology and Metabolism, and INSIGNEO Institute for in silico medicine, University of Sheffield, UK

Introduction

Bone lytic metastasis are malignant formation which significantly compromises the competence of the bone. The spine is the site with the most occurrence. The mechanical behavior of vertebrae with mechanically induced lesions has been measured experimentally using Digital Image Correlation [1]. Finite element (FE) models have also been used to predict the mechanical properties of vertebral bodies sections with lesions [2]. Micro-FE models have been found to predict well the local deformation of the vertebra under load when compared to Digital Volume Correlation (DVC) results [3]. However, it is still unclear if these models can predict well the local deformation for vertebrae with lesions. The aim of this work is to validate the displacement predicted by microFE models of porcine vertebras, with artificially induced lesions, through DVC data.

Materials and Methods

Five thoracolumbar three-vertebrae spine segments were obtained from pigs (9 months old) from the alimentary chain. The posterior arcs were removed, the external vertebrae were embedded in PMMA. A tangential hole, in the anterior side in the middle of the vertebral body, was drilled with a diamond core drill (diameter 8mm) to artificially simulate a lytic lesion involving the cortical shell. *In situ* stepwise loading to axially compress the vertebra was performed within a µCT scanner (Scanco VivaCT80, voxel size 39um): two repeated scans were performed with the specimen preloaded at 100N to measure the measurement uncertainty (as standard deviation of the Cartesian components of the displacement for each node) [4]. A third scan with the specimen loaded at 6500N. BoneDVC with a nodal spacing of 50 voxels was used to measure the displacement and strain.

Linear elastic homogenous micro-FE models of the middle vertebrae were generated from the first scan [3]. Elastic modulus of 12GPa and a Poisson's Ratio of 0.3 were assigned to each element. Two different models were prepared for each specimen: one including and one excluding the growth plates (80% and 30% of the vertebral height, respectively). For both cases, the displacement measured by the DVC were interpolated and applied on the top and bottom nodes. The models were solved (ANSYS, APDL) and the displacements within the bone were computed at the location of the DVC nodes. Strains were computed within the bone.

Correlation analyses were performed between the displacements measured with the DVC and predicted by the micro-FE in the middle 75% of the models.

Results

The DVC displacement uncertainty was below the voxel size: 2.2-4.3um for the different directions.

The larger deformations were observed on the growth plates and close to the lesion. The strains close to the lesion were in the elastic range for three specimens (1, 2, 3), or close to failure values for two specimens (4, 5).

When compared to DVC displacement, the linear micro-FE model showed a fair-to-excellent agreement when the growth plates were included ($0.39<R^2<0.98$, $19<RMSE<33$) and excellent agreement for the central region ($0.93<R^2<1.00$, $4<RMSE<70$).

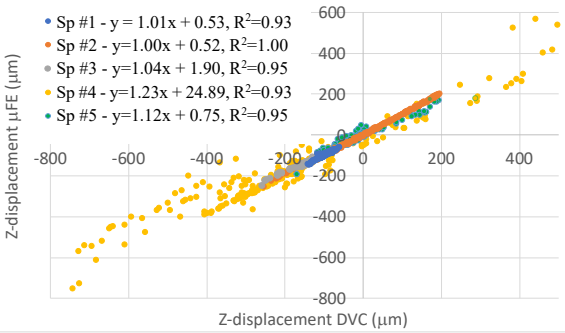

Fig 1: Correlation between micro-FE and DVC axial (z-direction) displacements in the central region.

Discussion

The linear models predicted well the experimental displacements, despite the presence of the lesions. With respect to previous works, the vertebrae were loaded through intervertebral discs, which allowed larger movement of the vertebra. Better correlation was observed when only the central part of the vertebra was modeled highlighting issues in the micro-FE prediction of the displacements in the region of the growth plates. This could be due to the non-linear behavior of these structures that include also soft tissues.

In conclusion, the developed micro-FE pipeline showed excellent ability of predicting local bone displacements in bone with lesions, encouraging future applications on human vertebrae with actual metastases.

References

1. Palanca et al., JBE, 2018, 140 (11): 111005
2. Stadelmann et al., Bone, 2020, 141: 115598
3. Costa et al., PlosOne, 2017, 12 (7): e0180151
4. Palanca et al., JBE, 2015, 137 (7): 071006

Acknowledgements

The study was partially funded by the AOSpine Discovery and Innovation awards (AOSDIA 2019_063_TUM_Palanca), Marie Skłodowska-Curie Individual Fellowship (MetaSpine, MSCA-IF-EF-ST, 832430/2018) and by the Engineering and Physical Sciences Research Council (EPSRC) Frontier Multisim Grant (EP/K03877X/1 and EP/S032940/1).

THE EFFECT OF ADVANCED GLYCATION END-PRODUCTS ON BONE FRACTURE MECHANICS

Marissa Britton, Ted Vaughan

Biomechanics Research Centre, School of Engineering, National University of Ireland Galway, Galway, Ireland

Introductions

Type-2 Diabetic (T2D) patients experience up to a 3-fold increase bone fracture risk [1], [2], despite the fact that their bone mineral density (BMD) is not reduced. This implies that T2D has a deleterious effect on bone quality, whereby the intrinsic material properties of the bone matrix are altered. This creates clinical challenges as current diagnostic techniques are unable to predict fracture probability in T2D as they are based on measures of bone quantity/density. The cause of bone fragility in T2D is thought to be that the hyperglycemic state leads to non-enzymatic glycation in collagen causing the formation of crosslinks, known as advanced glycation end products (AGEs), in collagen, which in turn stiffen the overall collagen network leading to more brittle behavior [3]. While previous studies have examined the relationships between AGE accumulation and some mechanical properties, there is a distinct lack of understanding how AGE accumulation affects the fracture mechanics behavior of bone tissue.

This study will investigate the multiscale fracture mechanics of T2D bone to elucidate the physical mechanisms that of diabetic bone fragility. In the first instance, our objective is to establish an *in-vitro* model of T2D, by artificially inducing AGE accumulation through non-enzymatic glycation of ex-vivo animal tissue and investigating the effect on the mechanical properties.

Materials and Methods

From a single bovine femur, 20 anatomically paired cortical bone samples were obtained through sectioning. *In-vitro* glycation was carried out by immersing the samples (n=20) in a ribose solution at 37°C to induce a diabetic state in the bone by causing non-enzymatic glycation and AGE accumulation [4]. Bone samples in the same solution without the ribose were used as a control (n=20). Bone samples were removed from the solution at day 40 to measure the mechanical properties of the bone. Fracture toughness, three-point bend and nanoindentation testing was carried out along with AGE content analysis. Paired t-tests were used to compare differences between the tested groups.

Results

Using the 95% CI, signifcant evidence was found for increases in AGE content, critical fracture toughness (K_{ic}), yield stress, ulimtate flexural srength in the ribolysated samples after 40 days (See Figure 1). The analysis found that AGE content had an increase of between 698 and 1197 ng of quinine/mg of collagen, where quinine is a fluorescent AGE biomarker. K_{ic} showed an increase of between 0.066 and 0.527 MPa√m. Yield stress had an increase of between 10.71MPa to 30.93MPa and ultimate flexural strength showed an increase of between 4.09MPa to 33.62MPa. There was also a trend observed for increase in secant modulus with a 95% CI of between 1MPa and 2140MPa in the ribosylated samples. Other properties measured that were not found to have a significant difference were flexural modulus, yield strain, modulus of toughness, modulus of resilience, ultimate flexural strain and damage fraction.

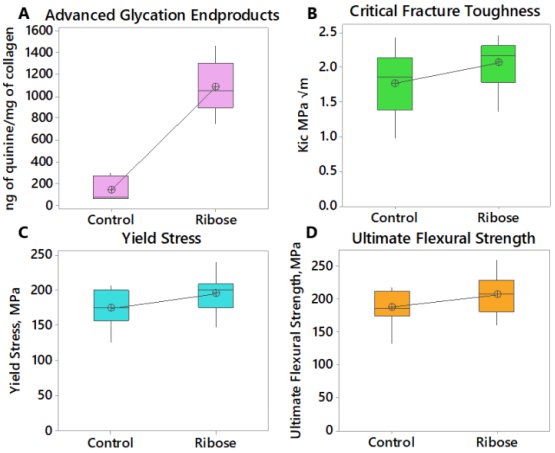

Figure 1: Boxplots for (A) AGEs, (B) K_{ic}, (C) yield stress and (D) ultimate flexural strength, with comparison of control and ribosylated samples.

Discussion

The results above show that *in-vitro* ribolysation has a significant impact on the biomechanical properties of this bone. Following glycation, the fracture toughness, yield stress and ultimate flexural strength increased significantly. The secant modulus also trended towards an increase. A previous study has shown that an accumulation of AGE content increased the yield stress and secant modulus of bone [4], the study referenced also found an increase in yield strain and damage fraction that the current study did not find. To date no other study has looked at the fracture toughness. The observed increase in fracture toughness in this *in-vitro* model contradicts the current theory that AGE accumulation leads to increased brittleness in bone in T2D patients. This study suggests that, despite the *in-vitro* glycation inducing significant AGE accumulation, it may not provide an appropriate representation of bone in T2D patients.

References

1. Cho et al. Diabetes Res Clin Pract 138:271-281, 2018.
2. Janghorbani et al., Am J Epidemiol 166:495-505, 2007.
3. Bank et al., Biochem J, 330:345-351, 1998.
4. Vashishth et al, Bone 28:195-201, 2001.

Acknowledgements

This project has received funding from the European Research Council (ERC) under the EU's Horizon 2020 research and innovation programme (Grant agreement No. 804108)

INDIVIDUALIZED CYCLIC MECHANICAL LOADING ENHANCES THE REGENERATIVE RESPONSE OF BONE IN A MOUSE MODEL OF AGING

Neashan Mathavan (1), Esther Wehrle (1), Graeme R Paul (1), Dilara Yilmaz (1), Gisela A Kuhn (1), Ralph Müller (1)

1. Institute for Biomechanics, ETH Zurich, Zurich, Switzerland

Introduction

The mechanical environment is of fundamental importance to the regenerative capacity of bone [1]. We have recently demonstrated the use of individualized cyclic mechanical loading to augment the regenerative response in a mouse femur defect model [2]. In this approach, *in vivo* micro-CT imaging and micro-finite element (micro-FE) modelling were used to spatially map the mechanical environment at the fracture site. Loading parameters were then adapted to the individual callus properties of each mouse based on the computed strain distribution within the callus at each time point. Individualized cyclic mechanical loading was found to significantly improve bone formation and bone mineralization at the fracture site.

Increasing age is associated with a compromised bone regeneration capacity and an increased risk of delayed or non-unions. Few studies have investigated the efficacy of mechanical intervention therapies in aged bone environments [1]. The findings reported in these studies suggest that the efficacy of mechanical stimulation may be limited by a reduced mechano-sensitivity in aged bone. However, none of these studies made use of an individualized approach to mechanical loading. Our aim is thus to investigate the effect of individualized cyclic mechanical loading on the regenerative response in a mouse model of aging.

Methods

Experiments were performed in PolgA mice, a mouse model of accelerated aging [3]. All animal procedures were approved by the local authorities (license: ZH229/19; Kantonales Veterinäramt Zürich, Switzerland). Female 12-week-old PolgA mice (n = 22) received a femoral osteotomy stabilized with an external fixator [2]. Time-lapsed *in vivo* micro-CT imaging was performed weekly at the fracture site (weeks 0-7; vivaCT 80, Scanco Medical AG, 10.5 µm nominal resolution). Mice which exhibited bridging at 3 weeks post-surgery (n = 13) were subdivided into two groups: Loaded mice (n = 6) and Control mice (n = 7). At weeks 3 – 7, mice received individualized cyclic mechanical loading (6-16N, 10Hz, 3000cycles; 3x/week) or sham-loading (0N). Individualized mechanical loading values were applied 3x per week via the external fixator and were based on weekly real-time computation of the strain distribution within the callus of each mouse [2].

Results

N = 13 mice in the study exhibited bridging at 3 weeks post-surgery. The remaining mice exhibited either delayed union (n = 5) or non-union (n = 4) and were excluded from the study. In comparisons between loaded and control mice, the mean callus volume was 120% larger in loaded mice than control mice at Week 7 (Figure 1). In addition, loaded mice maintained a sustained rate of bone formation between Weeks 3 – 7 (Figure 2). In contrast, the rate of bone formation in control mice peaked at Week 4 and decreased significantly thereafter.

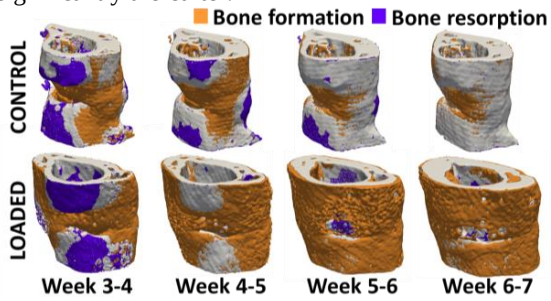

Figure 1: Representative samples from loaded and control mice. Bone formation /resorption sites identified via registration of scans from different time-points [2].

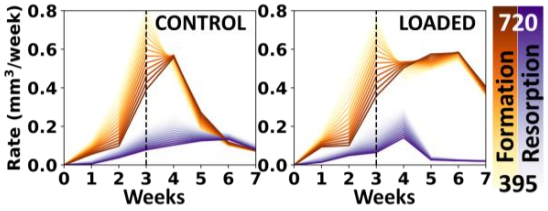

Figure 2: Rates of bone formation / resorption (mm^3/ week) in loaded and control groups at density thresholds between 395 and 720 mg HA/cm^3.

Discussion

In a previous study, we found the same femoral defect in 20-week-old female WT mice resulted in 100% unions [2]. In contrast, 12-week-old female PolgA mice exhibited a compromised regenerative capacity with 41% of fractures resulting in delayed or non-unions. The use of individualized cyclic mechanical loading in this model was found to significantly enhance the regenerative response. This approach therefore has the potential to be a promising intervention in the treatment of recalcitrant fractures in elderly patients.

References

1. Haffner-Luntzer M, et al. Innov. Surg. Sci. (2016).
2. Wehrle E, et al. bioRxiv (2020).
3. Scheuren A, et al. J. Cachexia Sarcopenia Muscle (2020).

Acknowledgements

We thank the EU for funding (ERC-2016-ADG-741883) and S.Freedrich and Y.Fischer for support in animal experiments.

PRELIMINARY RESULTS OF THE EFFECT OF LONG-TERM BISPHOSPHONATE TREATMENT ON PHYSICOCHEMICAL TRABECULAR PROPERTIES

Andrea Bonicelli (1,2), Tabitha Tay (3), Richard Stavri (3), Ulrich Hansen (4), Richard Abel (3), Peter Zioupos (2)

1. School of Health and Life Science, Northumbria University, UK; 2. Cranfield Forensic Institute, Cranfield University, Defence Academy of the UK; 3. MSk LAB, Imperial College, London, UK; 3. Dept Mechanical Engineering, Imperial College, London, UK.

Introduction

Osteoporosis is a metabolic disorder that induces the imbalance between bone resorption and formation that results in trabecular thinning and consequent increase in the risk of fracture. Bisphosphonates (BP) represents one of the most used treatments [1]. Therapy aims to over suppress resorption to prevent excessive bone loss and the consequent increase of fragility. This study aims to achieve a comprehensive, though preliminary, understanding of the changes induced by bisphosphonate on femoral trabecular bone matrix composition and nanoscale mechanical behavior.

Methods

The study involves femoral head trabecular bone samples from 24 donors (77.9 ± 8) divided into three groups: non-fracture control (Control, N = 7), fracture control (FxU, N = 10) and bisphosphonates treated fracture (FxB, N = 8). Experimental procedure involved TGA/DSC3+ (Mettler Toledo®, Indium calibrated, ATR-FTIR (Bruker Optics®, ALPHA T Platinum spectrometer) and XRD (PANalytical X'Pert PRO Multi-Purpose Diffractometer by means of a Cu Kα radiation). The effect of osteoporosis and long-term bisphosphonate therapy on the collagen-mineral matrix and mineral crystal strain was also investigated using synchrotron X-ray scattering and diffraction techniques. Statistical analysis was carried out using the open source software R 3.6.0.

Results

We found several statistical differences across the three groups. Concerning mineral and fibril strain, the FxB group showed significant ($p < 0.05$) lower results compared to the remaining. The same trend, as can be seen in Figure 1b, was also found for tissue strain. These changes in mechanical behaviour are also accompanied by changes in physicochemical matrix composition. Despite not significant, we noted a that fracture groups had a higher mineral content also coupled with the decrease in organic and water content. One most striking result is the differences in collagen maturity between fracture groups and control seen in Figure 1a. Only a minimal difference was found to show increased values of lattice parameter along the 'a'axis for the treated group ($p < 0.05$).

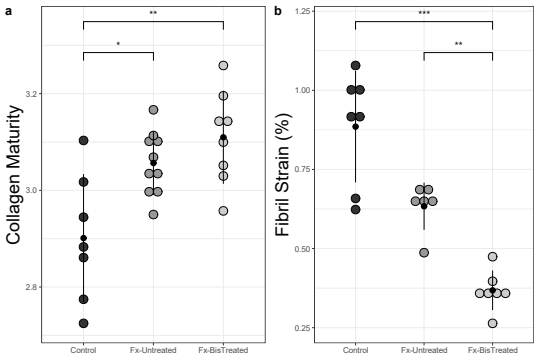

***Figure 1**: group differences show an increase in collagen maturity across control, fracture untreated (FxU) and fracture treated with bisphosphonates (FxB) groups (a). These might reflect on mechanical behavior by decreasing strain capability (b) (* $p < 0.05$; ** $p < 0.01$; *** $p < 0.001$).*

Discussion

Preliminary results in the present study show clear difference between the groups. The expected changes in mineral size were not found here probably due to the high mean age and small sample size. Decrease in mechanical properties have been previously correlated in a similar sample with age related hip-fracture [2]. This is mostly attributed to the decrease in changes in structural properties of trabecular bone [1,2] rather than changes in matrix composition. However, we found, in agreement with other studies [3], that the changes induced by BP might affect organic as much as mineral matrix. For instance, we detected an increasing trend in the accumulation of collagen maturity across the three groups (Fig. 1 a). This is known to result in the stiffening of collagen fibrils that impairs the fibrillar sliding mechanism that reduces bone strain capability.

References

1. Ma, S. et al, *Scientific Reports*, 7: 43399, 2017.
2. Ma, S. et al, *Scientific Reports*, 10:14208, 2020.
3. Zimmermann, E. A. et al, *PNAS*, 108 (35): 14416–14421

Acknowledgements

Wellcome Trust & EPSRC Osteoarthritis Centre of Excellence (088844/Z/09/Z); The Diamond Light Source beam allocations (EE0852, EE9811, SM10458, EE11204, SM13337).

ASSESSING BONE MATURITY: COMPOSITIONAL AND MECHANICAL PROPERTIES OF RIB CORTICAL BONE

Andrea Bonicelli (1,2), Elena F. Kranioti (3), Bledar Xhemali (4), Peter Zioupos (2)

1. School of Health and Life Science, Northumbria University, UK; 2. Cranfield Forensic Institute, Cranfield University, Defence Academy of the UK; 3. Dept of Forensic Sciences, University of Crete, Heraklion, Greece; 4. Institute of Forensic Medicine, Tirana, Albania.

Introduction

Mechanical resistance to fracture relies on the quality of bone and its spatial arrangement. It is well known that the risk of fracture increases dramatically with age and the causes have been largely believed to rely on structural modification especially in relation with certain conditions such as menopause and osteoporosis. This explains only 75% of the increase in risk of fracture [1]. Structural changes cause a considerable decrease in toughness and increase risk of fracture [2]. Regarding the deterioration in matrix composition, they are responsible for a drop of ~80% for bone toughness and ultimate strain that results in a loss of ~30-40% of overall strength [1]. These modifications are independent of bone architecture and mineral density and can be attributed to physicochemical changes affecting the bone matrix at the nanoscale level [1]. Bone matrix is composed by mineral, collagen, non-collagenous proteins and water; its quality and spatial organisation explains a portion of the mechanical behaviour of this tissue.

Methods

Sternal ends (~5 cm) of the fourth right rib from 85 individuals (mean age 45.61), 58 males (mean age 44.78) and 27 females (mean age 47.41). from the Forensic Institute in Tirana were employed in this study. The material was stored at -20°C. Experimental procedure involved TGA/DSC3+ (Mettler Toledo®, Indium calibrated) for collagen thermal stability and gravimetric analysis, FTIR-ATR (Bruker Optics®, ALPHA T Platinum spectrometer) for ion substitution and collagen content and XRD (PANalytical X'Pert PRO Multi-Purpose Diffractometer by means of a Cu Kα radiation) for coherence length (CL), strain and size of mineral crystals. Nano- and micro-indentation was carried out in order to obtain matrix mechanical properties (CSM-NHT (system v.3.75, CSM, 2034 Peseux, Switzerland).

Results

Results show the predominant role in mineral content in the increase in hardness and elastic modulus before the age of 35 years (Fig. 1). This is also combined with the related decrease in organic content. Before maturity, also the increase in crystal length along the 'c'axis is a major contributor in the increase in hardness and elastic modulus. This increment in mechanical capability is also complemented by the decrement in energy dissipation, maintained only by the mitigating effect of collagen stability and bound water. After 35 years, the over-mineralized matrix, is also characterised by the increase in carbonate content and the reduction in crystal growth. Both have a detrimental effect on hardness and elastic properties. As a result, it was possible to identify a decrease in mechanical properties and as well as a drastic increase in brittleness.

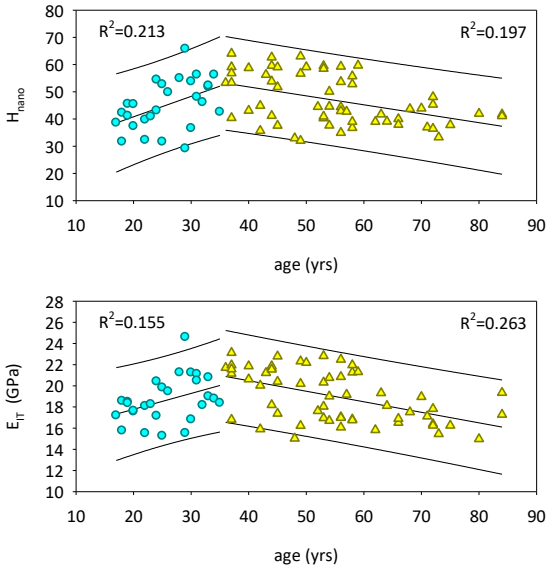

***Figure 1**: the increase in hardness and elastic modulus before maturity is followed by degeneration for the remaining age range (blue circles: <35 years; yellow triangle: >35 years).*

Discussion

By the age of 35 years the bone of the ribs reaches full mechanical maturity and thereafter due to chemical changes of mineral and organic matrix shows a deterioration in functional performance. The variation in physicochemical properties is highly heterogenous and linked to the increase in turnover that reflects in both bone structure and composition.

References

1. Burr, *Bone*, 120:85–93, 2019.
2. Boskey, *Osteoporosis Int*, 14: S16–S21, 2003.

Acknowledgements

Mr. Kostaq Beluri, Head of Control Department Investigation and Prosecution of the General Prosecutor, Ministry of Justice, Tirana, Albania for granting permission for this project (Protocol No. 1797/3 A. Xh. Protocol No. 795)

HEAT IMPACT DURING LASER ABLATION EXTRACTION OF MINERALISED TISSUE MICROPILLARS

Samuel McPhee (1), Alexander Groetsch (1), Jonathan D. Shephard (2), Uwe Wolfram (1)

1. Institute of Mechanical, Process and Energy Engineering, School of Engineering and Physical Sciences, Heriot-Watt University, Edinburgh, UK. 2. Institute of Photonics and Quantum Sciences, School of Engineering and Physical Sciences, Heriot-Watt University, Edinburgh, UK

Introduction

The underlying constraint of ultrashort pulsed laser ablation in both the clinical and micromachining setting is the uncertainty regarding the impact on the composition of material surrounding the ablated region. In orthopaedic hole drilling, for example, thousands of pulses are typically required to mitigate low ablation rates [1]. The cumulative heat deposition here can affect both the cellular viability and the underlying constituents of the extra-cellular matrix. We focused on a used laser protocol for the extraction of micropillars for use in compression testing. The scale at which these pillars are present is below that at which cell seeding occurs. Therefore, we focused primarily on the impact on the underlying collagen, where temperature exposure exceeding 150°C is reported to induce denaturation in dehydrated fibrils [2]. It is essential to know any laser induced compositional changes of the test specimens since it inevitably questions any data interpretation. Therefore, this study aimed to evaluate the micropillar temperature during picosecond laser ablation by implementing a combined ablation and heat model into a finite element suite, and to verify the results by means of Raman spectroscopy and Energy Dispersive X-ray microanalysis (EDX).

Materials and Methods

The used protocol we focused on is that of Groetsch et al. [3], who used mineralised turkey leg tendon (MTLT) as a model system for bone. At the microscale, the MTLT exhibits a similar hierarchical setup as bone. Samples were dissected and ultramilled prior to laser ablation. For the laser ablation, 515 nm light was focused to a beam radius of 10 µm and delivered in pulses of 6 ps (FWHM) every 1 ms. The chosen scanning pattern was an inbound anticlockwise hatch pattern from diameter of 150 µm inward to 50 µm consisting of 4085 pulses, resulting in pillars of 32.85 ± 0.91 µm in diameter and 50.01 ± 4.04 µm in height (Figure 1b). An ablation model was used to produce a directory of meshes representative of the pillar geometry after each pulse (Figure 1a). Using this directory, a heat model representing the laser-material interaction [4] was implemented into Abaqus (2016a, Dassault Systemes). For each pulse, an energy absorption rate function added heat to the system. The temperature field was then mapped to a new mesh with the ablated volume removed and a heat dissipation step of 1 ms was simulated before the next pulse in the pattern. This process was repeated for all 4085 pulses.

Results

The modelling results showed that the micropillar temperature was increased to 70.14°C after 4085 simulated pulses (Figure 2), remaining lower than half of the aforementioned permissible temperature of 150°C. Physiochemically, the Raman and EDX results showed no changes in composition for both the mineral and collagen content. In both analysis techniques, no new phases were identified after the laser-material interaction.

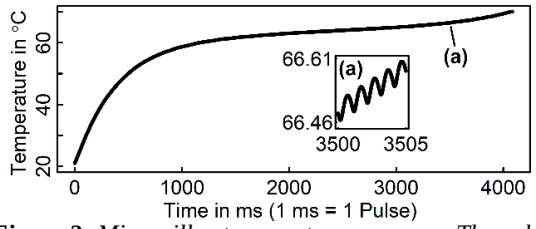

Figure 2: *Micropillar temperature response. The sub plot shows a development of an oscillating response as the dense temperature distribution of each pulse diffuses through the micropillar.*

Discussion

We have established a model allowing us to assess the temperature response of laser ablated tissue samples. The protocol allows for the interchangeability of tissue samples, scanning patterns and laser parameters. We focused on the extraction of mineralised collagen micropillars, which our results indicate are unaffected when fabricated by the protocol reported by Groetsch et al. [3]. The results will allow us to safely and confidently produce micropillars directly by ultrashort pulsed laser ablation. The modelling framework can be extended to soft tissues and may help in the development of minimally invasive surgical strategies.

Acknowledgements

This research was supported by the Engineering and Physical Sciences Research Council (EPSRC), UK (EP/ P005756/1).

References

1. Cangueiro & Vilar, *Appl Surf Sci* 2013, 283: 1012-1017.
2. Bozec & Odlyha, *Biophys J* 2011, 101(1): 228-236.
3. Groetsch et al., *Acta Biomater* 2019, 89: 313-329.
4. Zhang et al., *J Appl Phys* 2015, 117(6): 063104.

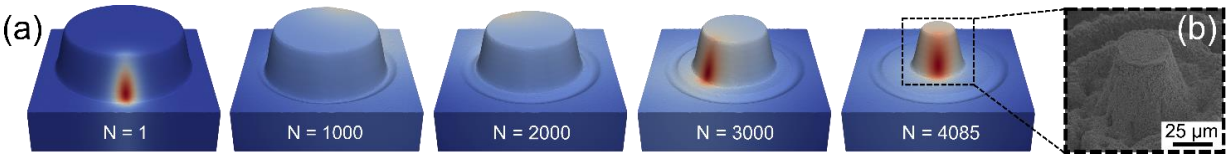

Figure 1: a) *Geometric evolution of pillar, N = pulse number in the 4085 pulse pattern.* ***b)*** *SEM image of the final laser ablated pillar produced by Groetsch et al. [3] Image* ***(b)*** *taken from Groetsch, A., 2019. PhD Thesis.*

THE EFFECT OF MECHANICAL LOADING AND PTH ON BONE ADAPTATION IN AN OVX MOUSE MODEL

Vee San Cheong (1, 2), Bryant Roberts (1,3), Visakan Kadirkamanathan (1, 2), Enrico Dall'Ara (1,3)

1. Insigneo Institute for in silico Medicine, University of Sheffield, United Kingdom, 2. Department of Automatic Control and Systems Engineering, University of Sheffield, United Kingdom 3. Department of Oncology and Metabolism, University of Sheffield, United Kingdom

Introduction

Osteoporosis is characterised by a failure to maintain the balance between bone apposition and resorption, leading to progressive net loss. Simulations of bone adaptation due to mechanical or pharmacological treatment can aid in the optimisation of treatment plans for osteoporosis [1]. However, no study has investigated the adaptive and strain changes due to different treatments in the ovariectomised (OVX) mouse tibia, and their impact on treating impaired bone remodelling. Therefore, this study uses a combined experimental and computational approach to evaluate the effect of separate and combined pharmacological treatment and mechanical loading on bone adaptation in OVX mice.

Methods

Eighteen C57BL/6 female mice were ovariectomised at week 14 of age and the right tibia scanned using *in vivo* micro computed tomography (10.4µm/voxel) at week 14, 16, 18, 20 and 22. Mechanical loading was applied to the right tibia *in vivo* at week 19 and 21 with a 12N peak load, 40 cycles/day and 3 days/week on alternate days (ML, N=6). Mice received either injection of Parathyroid Hormone (PTH, N=6) at 100 µg/kg/day or vehicle. Combined treatments were also studied (PTHML, N=6). Linear isotropic homogeneous microCT-based finite element (microFE) models were created from the tissue mineral density (TMD) calibrated microCT images, and physiological loading based on the weight of the mice were applied [3]. The follow-up images were superimposed to quantify the locations and frequency of apposition and resorption. Regression analyses were performed between bone adaptation and strain energy density (SED) in seven regions above the distal tibio-fibular joint to determine the extent that bone adaptation is linearly strain driven.

Results

Spatio-temporal differences were observed in all three treatment types. ML alone had little effect in inducing bone apposition in the distal tibia between weeks 18-20 and 20-22 (Figure 1). Combined PTHML treatment resulted in higher bone apposition in the proximal tibia than either monotherapy. Compared to the untreated OVX group, all treatments were equally effective in reducing periosteal resorption at weeks 18-20. However, periosteal resorption increased between weeks 20-22, which were also similar between the treatment groups. A moderate correlation between the average SED and surface remodeling was found in the periosteum (R^2 = 0.572 - 0.871). The slopes of the regressions in periosteal apposition were significantly lower for PTH than the ML or PTHML group (Figure 2).

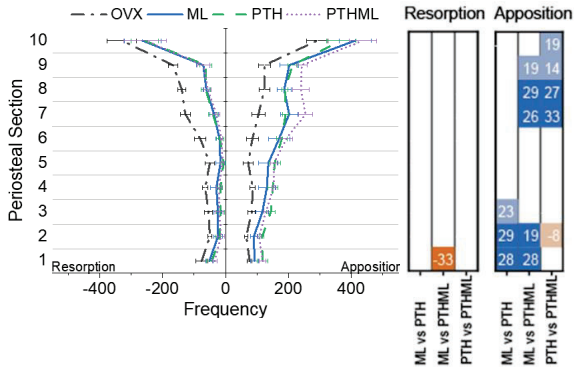

Figure 1: Periosteal bone adaptation at weeks 18-20. Heat maps indicate statistical significant difference. Lighter shade, p<0.05; darker shade, p<0.01. Numbers in heat maps indicate the relative difference.

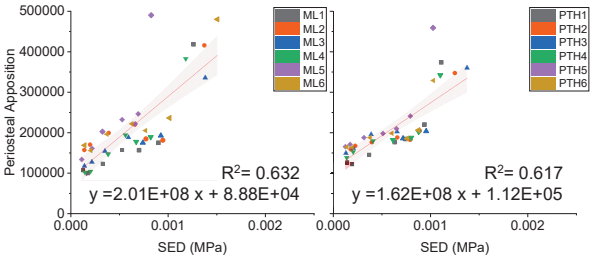

Figure 2: Linear regression of periosteal apposition vs SED at weeks 18-20.

Discussion

The beneficial effects of combining PTH and ML were both additive and synergistic depending on the location. The slopes of the linear regression were different on the endosteum and periosteum across treatment, indicating the importance to have site-specific mechanoregulation models to predict locations of remodelling. Although combined treatment prevented the increase in resorption at weeks 20-22, further optimization of combined treatment is required to improve efficacy, especially in the distal tibia.

References

1. Roberts et al, Sci Rep, 10:8889, 2020
2. Levchuk et al, Clin Biomech, 29:355-362, 2014
3. Charles et al, Front Bioeng Biotechnol 6:61

Acknowledgements

This work was funded by the Engineering and Physical Sciences Research Council (EPSRC) Frontier Multisim Grant (EP/K03877X/1 and EP/S032940/1) and the National Centre for the Replacement, Refinement and Reduction of Animals in Research (NC3Rs; NC/R001073/1).

HOW TOUGH IS THE HUMAN SKULL?

Lilibeth A. Zambrano M.(1,2), Jos Vander Sloten(3), Nele Famaey(3), Joop van Deursen(4), Michael D. Gilchrist(1), Aisling Ni Annaidh(1)

1. School of Mechanical and Materials Engineering, University College Dublin, Ireland; 2. Department of Aerospace, Mechanical and Electronics Engineering, IT Carlow, Ireland; 3. Mechanical Engineering Department, KU Leuven, Belgium; 4. Department of Materials Engineering, KU Leuven, Belgium

Introduction

Fracture toughness has been studied for different human bones and it has been established that it depends on the orientation of the osteons [1]. Nonetheless, little is known about the fracture mechanics properties of human cranial bone [2]. The aim of this work is to determine the fracture toughness of cortical human skull by harvesting samples from the frontal and the left and right parietal bones, with two objectives in mind, firstly to evaluate its resistance and secondly to ascertain whether this property can be also considered as transversally isotropic.

Methods

Five unembalmed human crania (75 – 90yo) provided samples from the external cortical layer of the frontal, left and right parietal bones (ethical approval NH019 2017-09-01 Universitaire Ziekenhuizen Leuven). Single Edge Notched Beam (SENB) specimens were machined (1.5mm x 2mm x 12mm, width x thickness x length) and separated into three groups with mid-span notches (0.9 mm) machined in the radial and the two transversal directions. Samples were kept irrigated with saline solution during machining and refrigerated until tested. The samples were tested on symmetric and asymmetric 3point-bend (Mode I, N = 212) and 4point-bend (Mode II, N = 17) configurations. Load-displacement curves were recorded and stress intensity factors K_I & K_{II}.

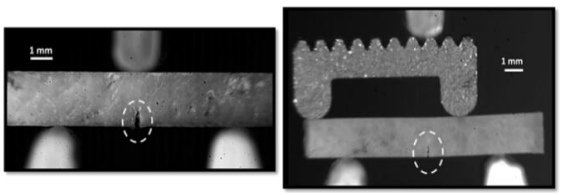

Figure 1: Experimental setup for fracture mechanics tests of cortical cranial bone: Mode I (left: SENB test) and Mode II (right: Asymmetric 4point bending). The dashed line indicates the notch.

Values of K_I were calculated following the procedure presented in the standard ASTM E-1820 [3], whereas the values for K_{II} were obtained by applying the procedure presented by Zimmermann et al. [4]. A Generalized Linear Mixed Effects Model (GLMM) analysis was performed to assess the effect of variables like age, sex, density, location and orientation.

Results

All samples fractured in a brittle manner. In Mode I, the crack propagated in a coplanar way with respect to the original notch, whereas in Mode II the fracture propagated in a kinked path.

Table 1 shows the stress intensity factors found from the Mode I and Mode II tests. For both cases, the GLMM analysis showed no correlation with the type of bone tested (frontal and parietal bones) nor with the orientation, so both factors, K_I and K_{II}, are isotropic and symmetrical with respect to the sagittal plane.

	K_I (MPa*m$^{0.5}$)	K_{II} (MPa*m$^{0.5}$)
Female	2.48 (2.16)	
Male	4.75 (2.58)	
All		0.093 (0.084)

Table 1: Average fracture toughness values found for cortical human cranial bone.

Discussion

Unlike for long bones, osteons do not have a defined orientation within the cranial bone. This random distribution would explain the isotropy found for K_I and K_{II}. For K_I, females' values are 50% that of men which is consistent with what has been found for other bones [1].

The symmetry of these factors is consistent for other properties found for human cranial bone, such as Young's modulus and Poisson ratio. Although for K_{II} no statistical differences were found with respect to sex, more subjects should be tested to discard a correlation between these variables and the human cortical cranial bone fracture toughness.

These values of fracture toughness represent a valid fracture criterion that could be employed in the design and testing of new head protective devices.

References

1. Nalla et al, Nat Mat, 2(3): 164-168, 2003.
2. Botjlar I. et al, Period Polytfjichnica Ser Civ Eng., 38:367-374, 1994.
3. ASTM E-1820, 2015.
4. Zimmerman et al, Biomaterials, 30:5877-5884, 2009.

Acknowledgements

This work was supported by the HEADS ITN (642662) from the European Commission's Marie Sklodowska-Curie Programme.

DETERMINING HUMAN FEMUR BONE MECHANICAL ANISOTROPY: IMAGE-PROCESSING METHOD VS MICRO-FINITE ELEMENT MODELS

Marco Branni (1), Egon Perilli (2), Mark Taylor (2), Saulo Martelli (1)

1. Science and Engineering Faculty, Queensland University of Technology, Brisbane, Australia
2.College of Science and Engineering, Flinders University, Adelaide, Australia

Introduction

Finite Element Models (FEMs) have become common tools for studying the mechanical behavior of the human femur. However, cross-laboratory analyses have shown variable accuracy across the different techniques used at different laboratories [1]. The aim of this study is to compare bone anisotropic mechanical properties determined using an image-processing method against corresponding micro-FEM from micro-CT images of the proximal human femur.

Material and methods

Ten cadaveric femora were scanned with micro-CT (29.81 µm/voxel, Australian Synchrotron Clayton VIC, Australia) [2]. From the stack of grey-level images, contiguous trabecular bone cubes were extracted (5 mm side-length) from the entire femur and analyzed (Fig.1).
Image-processing method: after thresholding, the morphometric parameters Mean Intercept Length (MIL) tensor and bone volume fraction (BV/TV) were calculated (CT Analyser, Bruker, Belgium). Young's moduli, Poisson's ratios and shear moduli were determined using fabric-elasticity relationships based on eigenvectors and eigenvalues of the MIL tensor and BV/TV [3].
micro-FEM: micro-FE models were developed by converting bone voxels into linear hexahedra elements. Sub-sampling by a factor of 2x was performed to reduce computational time. Bone tissue properties were modeled as isotropic linear elastic material (E =17 GPa) with a Poisson's ratio equal to 0.3. For each cube, the anisotropic elastic constants were computed, simulating in displacement control three uniaxial compression and three shear tests (six mechanical loadings) (Ansys, USA) [4].

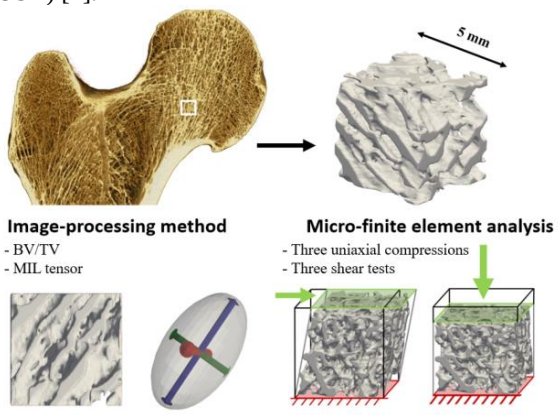

Figure 1: Anisotropic mechanical characterization

The anisotropic elastic constants obtained by the two approaches were compared using linear regression analysis for varying BV/TV ranges. Coefficient of determination (R^2) and the root mean square error (RMSE) were calculated.

Results and discussion

At the time of writing, the analysis was successfully completed for one femur. The BV/TV ranged between 4% and 42%. The linear regression "image-processing-based vs. micro-FEMs" for the Young's modulus along the principal anisotropic direction showed a coefficient of determination of R^2=0.76 (Fig.2). However, a toe region at low Young's modulus values was observed, which primarily includes specimens with very low BV/TV values (below 10%). By considering only cubes within a BV/TV of 10-42% the R^2 increased (R^2=0.80).

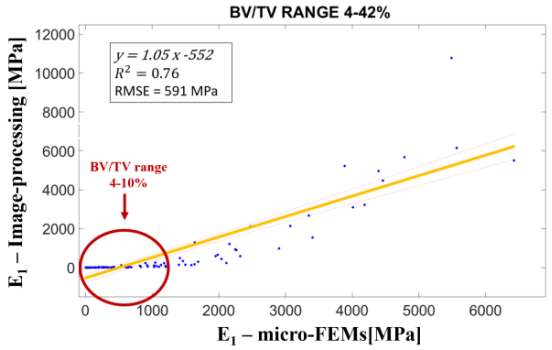

Figure 2: Linear regression analysis of elastic modulus

Conclusion

In our preliminary results, the procedure for determining anisotropic material properties of the human femur reveals a strong coefficient of determination for cubes within a BV/TV range of 10-40%. However, marked discrepancies are shown for bone cubes with lower values of BV/TV. Further investigations are being performed, including other morphometric parameters, such as trabecular thickness, number, and separation, to examine how these variations may influence the global mechanical behavior predicted by FEMs. These studies are needed clarify the large deviation in the numerical data within the biomechanics community.

References

1. Kluess et al, Comput Method Biom, 22.12:1020-1031, 2019.
2. Martelli, Perilli, J Mech Behav Biome, 84:265-272,2018
3. Zysset et al, J Biomech, 36:10:1469-1485, 2006
4. Van Rietbergen et al, J Biomech, 29.12: 1653-1657, 1996

DETERMINATION OF MATERIAL PROPERTIES OF HUMAN TIBIAL CORTICAL AND TRABECULAR BONE

Kerstin Wickert (1), Michael Roland (1), Marcel Orth (2), Tim Pohlemann (2), Stefan Diebels (1)

1. Saarland University – Chair of Applied Mechanics, Germany
2. Saarland University Hospital – Clinic for Trauma, Hand and Reconstructive Surgery, Germany

Introduction

High quality material parameters are a key factor in simulation-driven development of new implants for orthopaedic trauma surgery. Only with the help of experimentally underpinned material models can the mechanical behaviour of bones and bone-implant systems be simulated in a meaningful way and corresponding predictions made possible.
In this study, material parameters of human cadaveric tibia specimens are determined by means of different experiments combined with a simulation-based parameter identification.

Methods and Results

To achieve a broad range of possible material tests, the following experiments were performed: compression tests on cube specimens, tensile tests on shoulder specimens, component experiments using pressure on bone plates and 3-point bending tests on complete human tibias. All experiments are performed with a universal testing machine (Instron™ E10000 linear-torsion floor instrument) combined with a camera-based digital image correlation (DIC) system. In addition, computed tomography (CT) scans were performed of all human cadaveric specimens including a six-rod bone density calibration phantom (see Figure 2b)).
In order to validate the experimental protocols, all experiments are performed in advance with a spare material and the results are compared to the manufacturer's specification. A short fiber filled epoxy is chosen to simulate the cortical bone and the trabecular bone tissue is represented by a solid rigid polyurethane foam (see Figure 1). After validating the protocols, the human cadaveric experiments were performed.

The following steps describe the experimental procedure and the simulation-based evaluation workflow in detail:

1. The different specimen types and samples are prepared in our clinical biomechanics laboratory and the CT scans were performed.
2. After receiving the specimen's shape, all specimens were equipped with a so-called Speckle pattern for the evaluation via the DIC. Figure 1 and 2a) illustrate typical examples.
3. All experiments were performed on a universal testing machine and recorded by a corresponding multi-camera system including real-time triggering.
4. The experiments were evaluated using a combination of the machine sensor data and the DIC evaluation. This process starts with the reference image of the undeformed specimen and calculates the surface displacements and strains with respect to the images of the deformed states.
5. The image stacks from the CT scans of all different specimens are segmented, equipped with the bone mineral density information based on the calibration phantom and passed to a high-quality finite element meshes generator. The image processing was done in Simpleware ScanIP™.
6. A parameter identification was performed for all types of experiments using the Matlab™ optimization toolbox and the finite element suite Abaqus™. The process optimizes the parameters of the material model to match the results of the optical test evaluation as closely as possible with the simulation results.

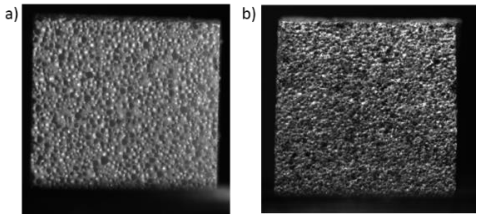

Figure 1: Solid rigid polyurethane foam a) 30PCF without speckle pattern b) 40PCF with speckle pattern

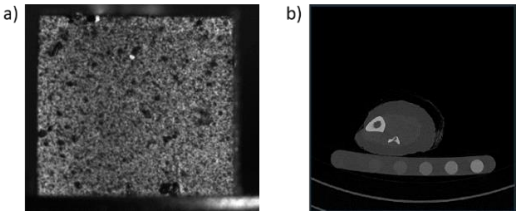

Figure 2: a) Short fiber filled epoxy with speckle pattern b) CT scan of human tibia including six-rod calibration phantom

The presented workflow identifies material parameters with respect to the different experiments and shows their connection to the Hounsfield units (HU) of the underlying calibrated CT images.

Acknowledgements

The Werner Siemens-Stiftung supported this work under the grant "Smart Implants 2.0".

EFFECT OF MGP PROTEIN ON MURINE BONE : A COMBINED MORPHOLOGICAL AND BIOMECHANICAL INVESTIGATION

Cédric Laurent (1), Alexandre Marano (2), Adrien Baldit (1), Maude Ferrari (3), Olivier Perroud (1), Jean-Christophe Perrin (3), Arnaud Bianchi (2) and Hervé Kempf (2)

1. CNRS UMR 7239 LEM3 - Université de Lorraine, Vandœuvre-lès-Nancy, France; 2. CNRS UMR 7365 IMoPA - Université de Lorraine, Vandœuvre-lès-Nancy, France; 3. CNRS UMR 7563 LEMTA - Université de Lorraine, Vandœuvre-lès-Nancy, France

Introduction

Understanding the effect of calcification on skeletal tissue properties is a milestone to propose preventive or therapeutic strategies in response to pathologies involving an alteration of this process. To study the effect of calcification on bone geometry and bone tissue mechanical properties, a mouse model deficient in a calcification inhibitor, the matrix Gla protein (Mgp), compared to non-mutated control, may be very instrumental for this type of investigation [1]. In addition to standard biomechanical studies [2], subject-specific simulations [3] may permit to identify local relations between elastic properties and bone mineral density [4]. At the early stages of growth, such an approach may benefit from multimodal imaging involving both MRI [5] and µCT [6] in order to monitor both calcified and abnormally calcified tissues.

Materials and Methods

Femurs were harvested at postnatal days P21 (n=3) and P28 (n=3) for both mutated ($Mgp^{-/-}$) and normal ($Mgp^{+/+}$) mice. Right femurs were used for three-points bending mechanical testing (Zwicki Z0.50 TN with a 100N load cell), while left femurs were used for histological analysis and 3D imaging using both µCT (EasyTom Nano, RX Solutions) and MRI (Bruker Avance III 600WB spectrometer) modalities. Subject specific non-linear finite element simulations were performed from reconstructed geometries, and used to identify local elasticity-density relations from experimental bending responses.

Results and discussion

Differences were observed between MRI and CT reconstructions at the level of articular cartilage and growth plates, with a clear effect of Mgp mutation (Fig. 1). The skeletal properties were affected by the pathologic calcifications since $Mgp^{+/+}$mice showed an increased stiffness compared to $Mgp^{-/-}$. The mutation also significantly affected the evolution in time of bending properties, since $Mgp^{-/-}$ femurs showed comparable bending stiffness at P21 and P28 while it almost doubled for $Mgp^{+/+}$ femurs. Subject-specific FE models (Fig. 2) enabled to identify suited density-elasticity relationship for each bone group. These results offer wide perspectives concerning the detailed evaluation of the effect of abnormal calcification on the evolution of bone properties during bone maturation and will be extended in the future to stages P14 and P35 to further describe a calcification kinetics.

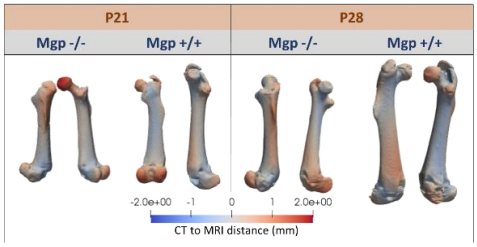

Figure 1: Distances between reconstructions issued from MRI and µCT for mutated ($Mgp^{-/-}$) and non mutated ($Mgp^{+/+}$) femurs at P21 and P28 .

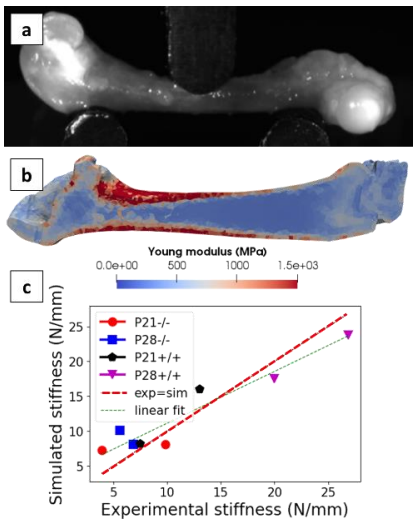

Figure 2: (a) Three-points bending mechanical testing (b) Example of bone material properties distribution in bone cross-section for best fitted density-elasticity relationship (c) Experimental vs *simulated stiffness issued from the selected tissue properties.*

References

1. Leroux-Berger et al, J Bone Miner Res 26, 1543–155, 2011.
2. Mumtaz et al, Bone Reports 12, 100266, 2020.
3. Laurent et al, Proc Inst Mech Eng H 230, 639–649, 2016.
4. Nobakhti and Shefelbine, Curr Osteoporos Rep 16, 404–410, 2018.
5. Singh et al, Clinical Radiology 73, 221–230, 2018.
6. Bouxsein et al, J Bone Miner Res 25, 1468–1486, 2010.

Acknowledgements

This work was supported by the “interdisciplinarity” grant ESCALE from the Université de Lorraine.

CHARACTERISATION OF CRANIAL BONE MORPHOLOGY AND MECHANICS IN INFANTS WITH CRANIOSYNOSTOSIS

Sara Ajami (1,2), Naiara Rodriguez-Florez (3,4), Juling Ong (2), Greg James (2), N U Owase Jeelani (2), David Dunaway (2), Patrizia Ferretti (1), Silvia Schievano (1,2), Alessandro Borghi (1,2)

1. University College London, United Kingdom; 2. Great Ormond Street Hospital, London, United Kingdom; 3. Ikerbasque, Spain; 4. Universidad de Navarra, Spain

Introduction

Craniosynostosis (CS) is the premature closure of one or more cranial sutures, occurring in 1 in every 2,500 births [1]. Limited information is available on the morphological and mechanical properties of CS bone. Determining the material properties of the cranial bone in this paediatric population and elucidating the factors that affect them would not only provide an insight into bone response to surgical procedures [2], but also would improve the accuracy of computational models simulating these surgeries. The aim of this study was to investigate the parietal bone morphology and mechanical properties in infants with sagittal CS.

Methods

Following ethical approval, parietal bone samples were collected from 12 patients (age: 5.2 ± 1.3 months) surgically treated for sagittal CS. Upon retrieval, samples were fixed and kept frozen at until examination. Specimens were imaged using micro-CT (Skyscan 1172) for structural characterisation and mechanically tested using reference point indentation (RPI) (Biodent, Active Life Scientific) and micro-CT based finite element modelling (micro-FE) of three point bending.

Results

Micro-CT scans of the samples demonstrated that bone microstructure was either fully developed into a trilaminar (n=6) or a unilaminar structure comprised of a diploe cavity (n=6) (Figure 1).

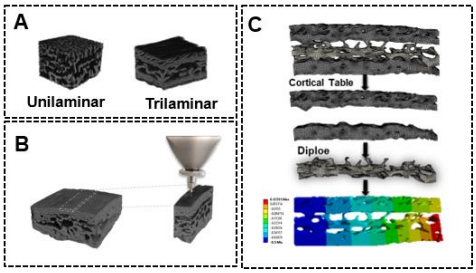

Figure 1: (A) 3D construction of parietal bones with unilaminar and trilaminar structure; Mechanical testing of parietal bone using (B) RPI and (C) micro-FE model of three point bending;

The average values for cross-sectional thickness (Cs.Th), bone volume fraction (BV/TV), specific bone surface (BS/BV), bone mineral density (BMD) of all samples were respectively 1.32 ± 0.29 mm, 59.63 ± 11.23 %, 16.50 ± 4.90 mm^{-1}, and 61.68 ± 8.70 (g/cm^3). A trend towards an increase in BMD (57.15 ± 6.37 $g.cm^{-3}$ vs 66.20 ± 8.77 $g.cm^{-3}$), Cs.Th (1.22 ± 0.29 mm vs 1.43 ± 0.27 mm) and BV/TV (56.76 ± 13.43 % vs 62.51 ± 8.79 %) from unilaminar to trilaminar bone structure was observed. Results from RPI and micro-FE showed a higher elastic modulus for cortical table when compared to diploe (Figure 2). There was a strong correlation between $E_{micro\text{-}FE}$ and E_{RPI} (r=.86, p<0.01). Changes in the microstructure and mechanical properties of bone specimens were found to be irrespective of patients' age.

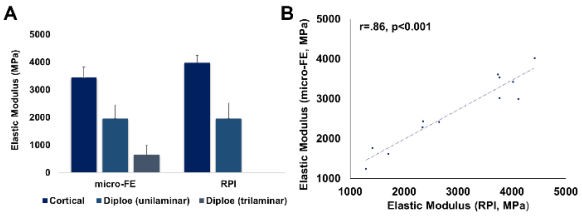

Figure 2: (A) Elastic modulus of cortical and diploe of parietal bone, (B) Correlation between $E_{micro\text{-}FE}$ and E_{RPI}.

Discussion

Certain craniofacial procedures, which rely on the malleability of cranial bone are ideally carried out in the first year of patients' life to achieve desired head shape changes. Our results revealed that age was not a determinant of bone microstructure and elastic modulus. To achieve optimal surgical outcomes, the mechanical and microstructure of the samples should be considered prior to surgery. Since micro-CT cannot be used to assess patients preoperatively, it highlights the need for translatable imaging biomarkers for clinical settings. This study suggests that morphological parameters such as BMD and Cs.Th which could be measured by routine CT clinical examination - should be further investigated as potential imaging biomarkers.

References

1. Morris LM et al, J Facial Plast Surg Clin, 24:517-530, 2016.
2. Rodriguez-Florez N et al, Plast Reconstr Aesthet Surg, 70(11):1589-1597, 2017.

Acknowledgements

This work was funded by the Great Ormond Street Hospital Charity Clinical Research Starter Grant (award number 17DD46).

DENSITY PLAYS A SUPERIOR ROLE OVER SHAPE IN OSTEOPOROTIC HIP FRACTURE RISK ASSESSMENT

Alessandra Aldieri (1), Mara Terzini (1), Pinaki Bhattacharya (2), Margaret Paggiosi (3), Richard Eastell (3), Alberto L. Audenino (1), Cristina Bignardi (1), Umberto Morbiducci (1)

1. Polito^{BIO}Med Lab, Department of Mechanical and Aerospace Engineering, Politecnico di Torino, Torino, Italy; 2. Department of Mechanical Engineering and INSIGNEO Institute for in silico Medicine, University of Sheffield, UK; 3. Department of Oncology and Metabolism and INSIGNEO Institute for in silico Medicine, University of Sheffield, UK

Introduction

Grave predictions have been made about osteoporotic fracture incidence for the next years, with major economic and social impacts in a worldwide greying society [1]. Yet, the predictive performance of the gold standard Bone Mineral Density (BMD)-based T-score in determining the fracture risk in the clinical practice remains limited. In this context, this study explores the potential of a combined statistical shape and intensity modelling approach [2] in predicting hip fracture status in a British postmenopausal cohort. The approach promises to be very effective to get insights into the interrelated role played by geometry and density in osteoporotic risk fracture, with the final aim to empower fracture prediction.

Methods

A retrospective British postmenopausal women cohort of 3D CT-based proximal femur geometries and density distributions was investigated building up Principal Component Analysis (PCA)-based statistical models. The cohort comprised 49 fracture and 49 control subjects, pair-matched for age, body weight and height [3]. In detail, a Statistical Shape Model (SSM) and a Statistical Intensity (i.e. density) Model (SIM) were first built individually. The SSM model construction relied on *Deformetrica* [4], which based on the femur geometries segmented from the CT images allowed to identify the template, i.e. the mean anatomical shape, and the deformation functions, gathering the subject-specific shape patterns, which map the template to the subject-specific shapes. The SIM was built by morphing the meshed template to each patient so that each mesh element was assigned with a Hounsfield Units-based density value [5]. Eventually, a Statistical Shape-Intensity Model (SSIM) [2] was built unifying the independent statistical shape and intensity models, accounting for the shape and density distribution together. For each model, the influence of each PCA mode in explaining the fracture status was quantified.

Results

Considering the first three shape modes, explaining together 50% of the shape variability, a significant difference between fracture and non-fracture groups emerged only for shape mode 3 ($p<0.05$), which alone explained 10% of the total variability. In contrast, distributions of the first PCA intensity and shape-intensity modes, explaining 23% and 15% of the total variability respectively, were both significantly different between fracture and control groups ($p<0.001$). In this regard, the SIM and SSIM turned out to be superior to the SSM in the fracture prediction. For the classification of fracture status in the cohort indeed, shape mode 3 yielded an Area Under the ROC Curve (AUC) of 0.634, the first intensity mode yielded an AUC of 0.822, slightly improved further by the first shape-intensity mode (Figure 1, AUC=0.832).

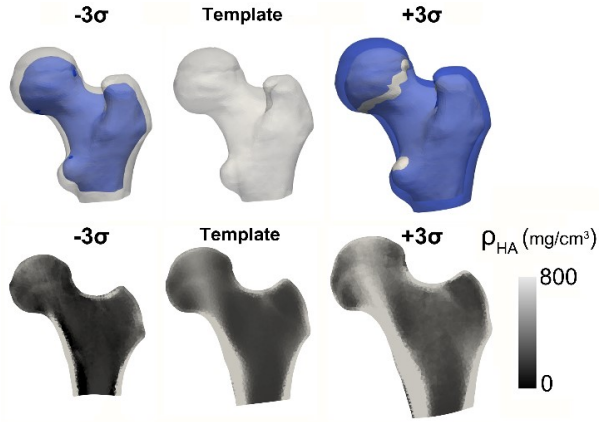

Figure 1: First shape-intensity mode. For ease of visualization, the first row shows only the 3D geometry variations as +/-3σ deviations from the template (white). The second rows shows, beyond the shape variations, also the densitometric variations visualized on a femur slice in the frontal plane.

Discussion

The PCA-based statistical modelling approach for femur fracture prediction presented in this study, based on 3D shapes and density data, suggests a prevailing role for density, compared to shape, in fracture risk assessment. When considered together in a SSIM indeed, the shape contribution to prediction integrated density-based information only moderately, with the SIM discriminatory power only marginally lower than that of SSIM.

References

1. Borgström et al., *Arch Osteoporos* 15:59, 2020.
2. Aldieri et al., *Comput. Biol. Med*, 127, 2020.
3. Yang et al., *Osteoporos Int,* 25:251–263, 2014.
4. Durrleman et al., *NeuroImage*, 101:35-49, 2014.
5. Taddei et al., *Med Eng Phys,* 29(9):973-9, 2007.

CORRELATION BETWEEN NANOSTRUCTURE AND MECHANICAL PROPERTIES OF BIOMATERIAL-MEDIATED REGENERATED BONE

Marta Peña Fernández (1,2), Alexander P. Kao (2), Gordon Blunn (2), Gianluca Tozzi (2)

1. Heriot-Watt University, UK; 2. University of Portsmouth, UK

Introduction

Critical-sized bone defect regeneration is a remaining clinical concern, with several biomaterial-based strategies currently being investigated to enable bone defect healing [1]. However, the mechanisms in which such biomaterials promote bone formation and how the newly formed bone compares to the native tissue remains partially unexplored [2]. Changes in the newly formed bone quality as result of the action of different biomaterials may be involved in the reduction of the global mechanical competence of the regenerated tissue [3], thus increasing the risk of secondary fractures. The aim of this study is to correlate nanostructural changes in the newly formed bone with nanomechanical properties in relation to the osteoregeneration induced *in vivo* by different bone graft materials implanted in critical-sized defects combining X-ray computed tomography (XCT), backscattered electron imaging (BSE), energy-dispersive spectroscopy (EDX), nanoindentation and synchrotron small and wide-angle X-ray scattering (SAXS/WAXS).

Materials and methods

Bone defects were surgically created in ovine femoral condyles and bone grafts (Actifuse, ApaPore, StronBone and StronBone-P) implanted. Samples were extracted from the bone-biomaterial and native bone regions six weeks post implantation, dehydrated, fixed in alcohol, embedded in epoxy resin and polished prior to XCT (Zeiss Versa 510; 7µm voxel) imaging. Nanoindentation was performed in selected regions across the bone-biomaterial interface using a Berkovich tip (Bruker Hysitron). Samples were then sliced (100 µm-thick sections) and SAXS/WAXS patterns collected at I22 (Diamond Light Source, UK). The predominant direction of orientation of the mineral particles, the T and ρ parameters were calculated as in [4] from the integrated SAXS data. Finally, sections were polished and BSE and EDX (Zeiss Evo MA10) images acquired for mineralization and elemental composition analysis.

Results

BSE images allowed visualization of the microstructure of the newly formed bone close to the implanted biomaterials (Fig. 1a). Gradients in the mineral particle thickness and orientation were observed at the bone-biomaterial interface, with the more mature tissue showing thicker mineral particles and higher degree of orientation (Figure 1b, c). Indentation modulus (Er) of the new bone tissue induced by each bone graft ranged from 12.94 GPa to 14.75 GPa, whereas the hardness (H) from 0.46 GPa to 0.57 GPa. One-way ANOVA test revealed a significant effect of StronBone-P on both Er and H ($p < 0.001$) of the newly formed bone compared to the other biomaterials. The regenerated tissue showed significantly lower ($p<0.001$) Er and H than the native trabecular bone (Fig. 1d).

Discussion

This study revealed new insights on the nanomechanical properties of newly formed immature and mature bone following the implantation of commercial biomaterials. Both hardness and indentation modulus of the regenerated bone are significantly lower than those of native bone, due to differences in their nanostructure, with smaller and less organized mineral particles. Full correlations between nanostructural and nanomechanical properties [2] will be performed and compared among the applied treatments to better understand the *in vivo* integration and performance of biomaterials on the regenerated bone quality.

References

1. Roddy et al., Eur. J. Orthop. Surg. Traumatol., 2018
2. Cipitria, A. et al., JBMR, 27, 1275-88, 2012.
3. Peña Fernández et al., ACS Bio Sci Eng, 5, 2543–54, 2019.
4. Pabisch et al, Methods in Enz., 532, 391-413, 2003.

Acknowledgements

We acknowledge Tim Snow, Olga Shebanova and Nick Terril for support at I22 in Diamond Light Source (SM24466-1).

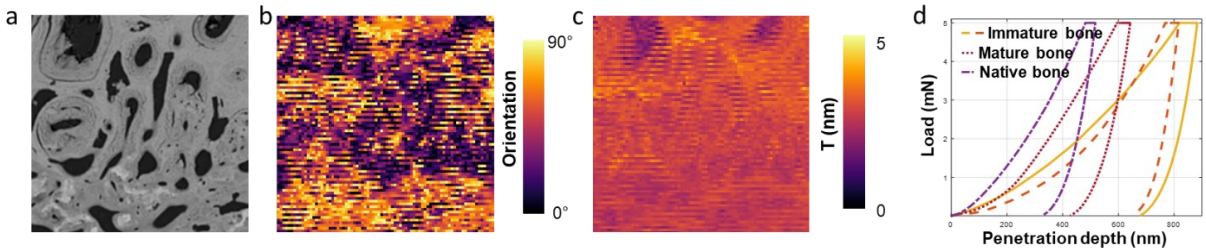

Figure 1. Correlative analysis in a 2 mm x 2 mm region of bone-StronBone system. (a) SEM image of the bone-biomaterial interface. (b) Predominant orientation of the mineral crystals and (c) T-parameter derived from SAXS data. (d) Example of nanoindentation load-depth curve in newly formed immature and mature bone and native trabecular bone from a control bone sample.

INVESTIGATION OF MICROSCALE BONE ANISOTROPY BY POLARIZED RAMAN SPECTROSCOPY AND MICROPILLAR COMPRESSION

Tatiana Kochetkova (1), Cinzia Peruzzi (1), Oliver Braun (1), Jan Overbeck (1,2), Anjani K. Maurya (1), Antonia Neels (1), Michel Calame (1,2), Johann Michler (1), Philippe Zysset (3), Jakob Schwiedrzik (1)

1. Empa, Swiss Federal Laboratories for Materials Science and Technology, Switzerland;
2. Department of Physics & Swiss Nanoscience Institute, University of Basel, Switzerland;
3. ARTORG Center for Biomedical Engineering Research, University of Bern, Switzerland

Introduction

Bone is a natural composite possessing outstanding mechanical properties combined with a lightweight design. The key feature contributing to this unusual combination of material properties is its hierarchical organization, which is present from the nano- to macro-scale. Our study focuses on the microscale, namely on the level of a single lamella – the elementary building block of bone, consisting of aligned mineralized collagen fibrils (MCF) embedded in an extrafibrillar matrix. The goals of this study were to (i) establish a quantitative method for 3D MCF orientation estimation and (ii) investigate the effect of MCF orientation on the yield stress and elastic modulus of isolated bone lamellae.

Methods

Bovine tibia and mineralized turkey leg tendon samples were obtained from a local abattoir, finely cut and polished. Polarized Raman spectroscopy (PRS) was used to estimate the bone collagen fibril orientation from the polarization dependence of amide collagen bands [1] (Fig. 1). We calibrated the PRS data on MTLT samples cut at five angles between 0° and 90°, as verified using SAXS measurements (Bruker AXS, CuKα λ=1.5406 Å). The calibrated method was then applied to the study of structure-property relationships at the lamellar level on bovine cortical bone specimens.

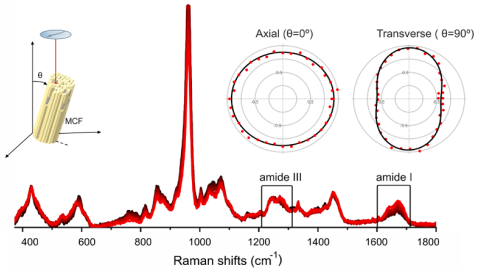

Figure 1: Polarized Raman spectra of cortical bone; Polarization dependence of ∫Amide I / ∫Amide III bands for axial and transverse in-plane fibril alignment.

Microscale compression tests were performed on focused ion beam milled micropillars [1] (N=36, diameter 5 µm, aspect ratio 2) with known collagen fibril orientation measured by PRS. Compression experiments were performed at ambient temperature and pressure, with a controlled relative humidity > 93%, ensuring hydration of the sample. Experiments were run in displacement control up to 10% strain at a rate of $0.001 s^{-1}$.

Results

The new quantitative method for 3D MCF orientation measurement was validated and found to feature an angular uncertainty <10°. This allowed us to measure a unique spectrum of microscale structure-property relationships based on compression data for MCF orientations ranging from 0° to 82° (Fig. 2). We could demonstrate a strong dependence of the microscale compressive mechanical properties of bone on the local MCF orientation. A high degree of anisotropy was found for both the elastic modulus ($E_a/E_t = 3.80$) and the yield stress ($\sigma_a^y / \sigma_t^y = 2.54$). Moreover, the post-yield behavior was found to depend on the MCF orientation with a transition between strain softening to hardening at $\theta = 48°-54°$.

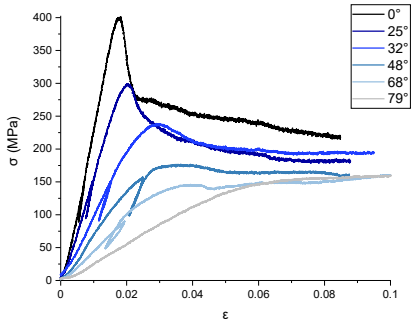

Figure 2: Stress-strain curves of bovine cortical bone lamellae with different MCF orientations [1].

Conclusion

Heterogeneous fibril orientation is a common phenomenon in natural materials like bone, and it significantly affects the measured mechanical parameters. As was shown in this work, measuring the local microstructure and mechanical properties in a site-matched fashion allowed us to reduce the apparent scatter in the collected mechanical data and to reliably determine structure-property relationships of bone at the lamellar level. This is a prerequisite for developing and validating multiscale models predicting bone failure with increased accuracy in the future.

References

1. Kochetkova et al., Acta Biomaterialia 119, 390-404, 2020

Acknowledgements

This work is funded by SFA PHRT iDoc Project 2017-304 (TK) and SNSF Ambizione grant 174192 (JS).

COMPRESSIVE STRENGTH OF OSTEOGENESIS IMPERFECTA BONE MATRIX IS HIGHER THAN CONTROLS AND DEPENDS ON MINERALIZATION

Michael Indermaur (1), Daniele Casari (2), Tatiana Kochetkova (2), Cinzia Peruzzi (2), Elizabeth Zimmermann (3), Frank Rauch (3), Bettina Willie (3), Johann Michler (2), Jakob Schwiedrzik (2), Philippe Zysset (1)

1. ARTORG Center for Biomedical Engineering Research, University of Bern, Switzerland,
2. Swiss Federal Laboratories for Material Science and Technology, Thun, Switzerland,
3. Shriners Hospital for Children, Montreal, Canada

Introduction

Osteogenesis imperfecta (OI) is a group of inherited bone diseases, which affects the collagen quality and increases bone fragility. The three most common disease types are, in order of increasing severity, OI type I, IV and III. Despite previous investigations, the actual mechanisms of OI bone fragility remain unclear. Unlike nanoindentation, micropillar compression allows to determine post-yield properties of bone at the ECM scale [1]. Accordingly, the aim of this study was to investigate compressive mechanical properties of human cortical OI bone extracellular matrix (ECM) and its potential dependency to the degree of mineralization. We hypothesized that strength of OI bone is inferior compared to healthy control bone at the ECM scale.

Materials and Methods

Twelve human, transiliac bone biopsies of healthy controls (n=6), OI type I (n=3), OI type IV (n=2) and OI type III (n=1) were fixed in formalin and infiltrated with PMMA [2]. A total of 65 micro-pillars (healthy n=23, OI I n=16, OI IV n=11, OI III n=15) were milled (ø=5 µm, h=10 µm) in osteonal bone with a focused ion beam and compressed (rate 5 nm/s) with a flat punch in the vacuum of a scanning electron microscope (SEM). Ultimate strength was extracted from the resulting force-displacement curve. In the same osteons, next to each micro-pillar, three nanoindentation measurements were collected and the average indentation modulus per pillar was calculated. Moreover, in the same region, three Raman spectra were recorded to quantify the averaged local mineral-to-matrix ratio (ν_2PO_4/ amideIII). Additionally, global tissue mineral density (TMD) was determined using µCT at the biopsy level.

Results

Global and local degree of mineralization are higher for all OI types compared to healthy control. Interestingly, both elastic modulus and ultimate strength are superior for the OI types compared to healthy bone (see table 1). Finally, indentation modulus and ultimate strength (figure 1) are correlating linearly with the mineral-to matrix ratio ($p= 8.28 \cdot 10^{-7}$ and $p=9.88 \cdot 10^{-15}$ respectively).

	healthy control	OI type I	OI type IV	OI type III
TMD [mgHA/cm³]	1012.7 ±41.6	1097.6 ±17.0	1143.9 ± 42.2	1141.1
ν_2PO_4/ amideIII [-]	0.35 ± 0.12	0.54 ± 0.09	0.69 ± 0.13	0.61 ± 0.13
E [GPa]	19.8 ± 2.2	23.8 ± 3.0	22.9 ± 1.9	22.0 ± 2.0
σ_{ult} [GPa]	0.59 ± 0.13	0.72 ± 0.08	0.79 ± 0.07	0.77 ± 0.12

Table 1: Means and standard deviations of TMD, mineral-to-matrix ratio (ν_2PO_4/ amideIII), elastic modulus (E), and ultimate stress (σ_{ult}) of each group.

Discussion

Surprisingly, the results contradict our initial hypothesis that the compression properties of OI bone ECM are inferior compared to healthy bone. Independently of OI type, the compression properties of bone ECM, especially ultimate stress, increase significantly and substantially with the degree of mineralization. Although our results suggest that OI bone is stronger at the ECM level, we only tested in compression and the collagen defect may have more influence on tension.

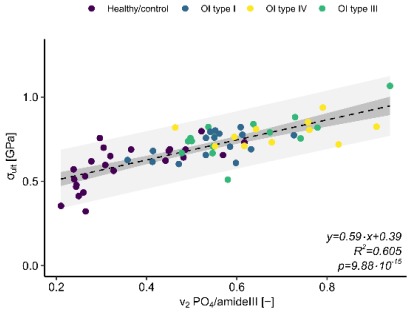

Figure 1: Ultimate stress by micropillar compression versus site-matched mineral-to-matrix ratio by Raman spectroscopy for controls and different types of OI.

References

1. Schwiedrzik et al., Nature Mater, 13:740-747, 2014.
2. Rauch et al., J Clin Endocrinol Metab, 91:511-516, 2006.

Acknowledgements

This study was funded by Mereo BioPharma and SNF grant # 165510.

A MOLECULAR DYNAMICS INVESTIGATION INTO THE STRUCTURAL ROLE OF NON-COLLAGENOUS PROTEINS IN BONE BIOMECHANICS

Mahdi Tavakol (1), Ted J. Vaughan (1)

1. Biomechanics Research Centre, School of Engineering, College of Science and Engineering, National University of Ireland Galway, Ireland

Introduction

Bone is a naturally occurring composite mainly made of Hydroxy Apatite (HAp) mineral phase and an organic matrix composed of collagenous and Non-Collagenous Proteins (NCPs). While NCPs comprise only 10% of the organic phase, it has become apparent that their role in intrinsic toughening, one of the primary contributors towards healthy tissue's excellent fracture resistance, is considerable [1]. Osteocalcin (OC) and Osteopontin (OPN) are the most abundant NCPs [2] and, together, these are known to form protein complexes that mediate bonding at nanoscale mineral interfaces [3] in the extrafibrillar space. It has been established that these NCP complexes facilitate plastic sacrificial sliding, which is a major contributor to the tissue's excellent fracture toughness [3]. Furthermore, knockout animal models have shown that the capacity of sacrificial sliding is impaired when either OC or OPN are removed, leading to reduced fracture toughness [4]. While this highlights their critical role in energy dissipation, the underlying molecular mechanisms that facilitate such behaviour are poorly understood. In this study, we use Steered Molecular Dynamics (SMD) to elucidate the mechanism by which OC and OPN dissipate energy at HAp interfaces.

Methods

MD simulations were utilized to study the nanoscale interfacial energy dissipation potential of OC and OPN proteins. The experimentally resolved 49-residue OC protein structure was used [5], while the 298 residue OPN protein structure was obtained through homology approaches (Figs 1.a and 1.b). Adsorption of proteins on the HAp surface was simulated using the LAMMPS simulation framework. SMD simulations for the adsorption modes with contact residues like the most frequent contact residues were carried out, whereby energy dissipation was calculated via parallel and perpendicular pulling of each protein structure on the HA mineral (Figs 1.a and 1.b).

Results and Discussion

Both the OC and OPN proteins showed strong adsorption on the HA mineral surface. It was found that α-helix structures on the OC protein were responsible for mediating adsorption on the HAp surface. Meanwhile, the OPN protein interacted with the HAp mineral surface thanks to its highly charged phosphoserine residues. It was found that OPN protein could dissipate large amounts of energy, with large deformation of its random coil elements in perpendicular pulling (Fig 1.c). Interestingly, this was not due to protein backbone deformation, but was due to breaking of intra-protein hydrogen bonds and electrostatic interactions of its charged residues and surface ions (which were possible even in the absence of a wider protein network). Although the OC protein was more compact, several key mechanisms directly associated with binding at α-helix structures were observed that enabled excellent energy dissipation behavior parallel to the mineral surface, which included stick-slip behavior and a sacrificial bond mechanism. Also, movement of its 3-calcium motif on the HAp surface provides a unique energy dissipation mode.

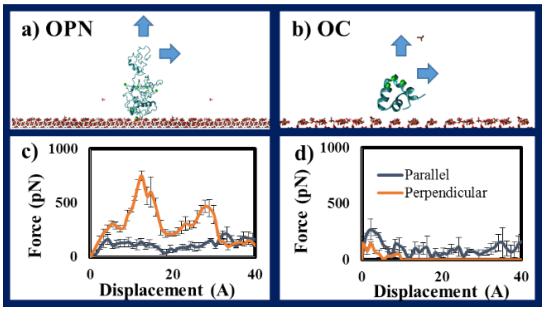

Figure 1: SMD simulation setup for of a) OPN and b) OC with arrows showing pulling orientations. Force-displacement curves for c) OPN and d) OC.

Conclusions

In this study, the role of OC and OPN in bone toughening was investigated. For the first time, it was shown that OC and OPN dissipate energy mainly through stick-slip and the deformation of its random coil elements, respectively. It was also found that OPN does not necessarily need to be in a wider protein network to dissipate energy. These findings provide important insight into large deformation/sliding mechanisms that have been previously observed at mineral interfaces, which are known to contribute the tissue's excellent fracture resistance [3].

References

1. Morgan et al., Calcif. Tissue Int. 97:281,2015.
2. M Tavakol and TJ Vaughan, Sci. Rep. 10:17321,2020.
3. Krauss et al., Bone 44:1105,2009.
4. Nikel et al., J. Biomech. 80:45,2018.
5. Hoang et al., Nature 425, 977 (2003).
6. Fantner et al., Nano Lett. **7** (8), 2491 (2007).

Acknowledgements

This project has received funding from the European Research Council (ERC) under the EU Horizon 2020 research and innovation programme (Grant agreement No. 804108). The authors appreciate the computational resources provided by ICHEC.

EFFECTS OF STRESS GRADIENT BASED ON COLLAGEN ANISOTROPY IN CARTILAGE ON MECHANICAL RESPONSE OF CHONDROCYTE

Shunei Fukuyama, Yusuke Morita, Koji Yamamoto (1)

1. Department of Biomedical Engineering, Doshisha University, Japan

Introduction

Intracellular calcium (Ca^{2+}) signaling is a part of the mechanotransduction pathway which converts mechanical stimulation to molecular signals. The extracellular matrix (ECM) of cartilage is mainly composed by collagen, proteoglycan and chondrocyte. The collagen fiber shows anisotropic arrangements from the surface to the bottom of cartilage and the cell density is uneven, which produces a non-uniform dynamics field and complicates mechanotransduction signals. Hence, to understand the physiological response of chondrocyte in cartilage tissue, it is important to investigate the dynamic Ca^{2+} signal transmitting processes responding to changes of the dynamics field in cartilage. In this study, we analysed them using the calculation model and the cartilage compressing experiment using a round indenter to non-uniform dynamics field.

Materials and Methods

Loading Ca^{2+} dye into chondrocytes in the tissue Porcine articular cartilage (6-month old) tissue punched out from distal femur was molded into a semi-cylindrical shape (diameter: 5mm). All the samples were washed in PBS(-) and stained with Fluo4-AM solution (CS32, Dojindo) to visualize Ca^{2+} signaling.

Analysis of intracellular Ca^{2+} Dynamics under mechanical compression A stained sample was installed on a device which can control strain rate. Forced displacement was applied to specimen at the strain rate of 0.01/s, 0.1/s, and 1/s until achieving 15% strain. The load and displacement of the specimen were measured by the displacement sensor and the load cell. Ca^{2+} images were acquired with a digital CMOS camera (ORCA-Flash 4.0 V3, Hamamatsu photonics).In the analysis of Ca^{2+} luminance value, the Ca^{2+} images were poler-transformed from the center of the round indenter and the area surrounded by dash line in Figure 1(a) was picked up to make luminance profile.

Calculation of stress-strain field The stress and strain field generated in cartilage tissue were simulated by using the visco-anisotropic hyperelastic constitutive equation proposed by Nakamachi et al [1].

Results and Discussion

Figure 1(a), (b), (c) shows the luminance image of 3 s after compression against each strain velocity. When the cartilage is compressed at 0.01/s, the luminance of the surface layer mainly increased and as the strain velocity increases, luminance of the mid-deep zone started to increase in addition with the surface layer. From this result, the Ca^{2+} signaling of the mid-deep zone in cartilage could be affected by compressive strain velocity. Figure 2(a) shows the profile of luminance expression between 1 s to 3 s after compression (The left back corresponds to the initial contact point between the round indenter and the tissue surface). Figure 2(b) shows the mean stress field calculated by using anisotropic collagen structured cartilage model. This result shows that the stress gradient is steep at the mid-deep boundary zone. However, when the mean stress field is calculated by the isotropic collagen structured model, the stress gradient came out gentle at the mid-deep boundary zone. According to the result, we found that the anisotropic transmission of force and displacement due to the arrangement of collagen fiber specifically influenced the stress profile at the boundary between the mid-deep zone. Moreover, the profile of the mean stress field in the anisotropic model closely correspond to the luminance profile. These results indicate that the difference of the stiffness and permeability caused by the anisotropic zonal structure changed the interstitial fluid flow leading to the increase of fluid pressure and the chondrocytes are primarily responsible against those mechanical changes.

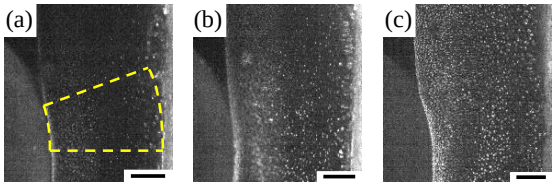

Figure 1. Luminance image of strain velocity (a)0.01 /s, (b) 0.1 /s ,(c)1 /s(×40, Bar:500 µm).

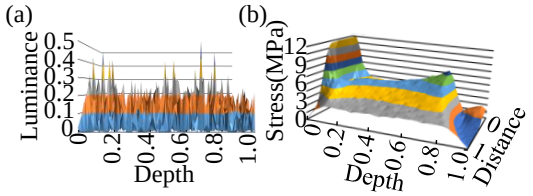

Figure 2. Comparison of the profile between luminance and mean stress. (a) Profile of luminance expression between 1 s to 3 s after compression. (N=3, strain velocity: 1 /s) (b)Calculation result of mean stress field. (Strain velocity:1 /s, Stain amount: 15%.)

References

1. Nakamachi et al, Int J Numer Method Biomed Eng, 33, 2017.

EFFECTS OF H-G SYNDROME ON MACRO AND MICRO MECHANICAL RESPONSE OF MURINE BONE SEGMENTS

Dario Gastaldi (1), Massimiliano Baleani (2), Roberta Fognani (2), Anna Festa (2), Fabio Baruffaldi (2), Stefano Squarzoni (3), Pasquale Vena (1)

1. Politecnico di Milano, Department of Chemistry Materials and Chemical Engineering, Giulio Natta, Italy;
2. IRCCS Istituto Ortopedico Rizzoli, Medical Technology Laboratory, Italy;
3. National Research Council, Institute of Molecular Genetics, Italy

Introduction

Hutchinson-Gilford Progeria Syndrome (HGPS) is a rare genetic condition that appears in the premature aging of the individuals and causes further diseases commonly observed in the elderly, such as cardiovascular disorders, and abnormalities in the development of the skeletal and dental system. Because of its rapid metabolism, the murine progeric model is an excellent tool to investigate the effect of the pathology [1].
The study is aimed a studying the murine models of progeria at two length scales: the macro-scale of the whole femoral bone and the micro-scale of the cortical wall.

Materials and Methods

Healthy (wild) and progeric (heterozygous) murine models have been analysed by means of mechanical test at the scale of the whole bone segment (four-point bending tests), to determine the bending stiffness obtained through the force-displacement relationship, and at the microscale with a nanoindentation test protocol [2], to determine the indentation modulus (Figure 1). The results obtained from the nanoindentation tests were subjected to statistical analysis to evaluate the distribution of mechanical properties in four anatomic regions of the section to evaluate the differences between sample groups.
The four-point bending test was also simulated by means of finite element (FE) models in a subset of six specimens. The real anatomy of the whole murine bone segments was reconstructed from micro-CT scans. The micro-CT FE models were used to determine the tissue modulus value to be set to achieve an estimated stiffness consistent with that determined experimentally.

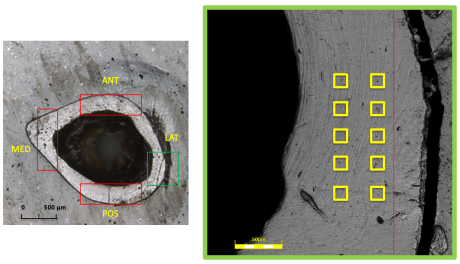

Figure 1: left: transverse section image in the femur central region. right: laser confocal image showing nanoindentations grid in lateral region (10 indentations equally-spaced grid performed in each region).

Results and Conclusions

The bending stiffness resulted from 4-point tests were about 40% higher for healthy samples vs progeric samples. Micro-CT FE models confirmed that this difference is largely explained by the anatomic structural shape (moment of inertia) difference between the two groups. However, the FE analyses must account for a reduction in bone tissue modulus to predict the experimentally determined stiffness. These preliminary results were in agreement with the nanoindentation outcome, which showed an overall reduction of about 6% in bone tissue modulus in the progeric tissue with respect to the healthy case: Er=29.9GPa. and 31.7GPa, respectively. The nanoindentation study revealed that healthy subjects exhibited a non-homogeneous distribution of indentation modulus (with significantly higher values in the Anterior region, based on p-value of 2 tail parametric t-test); while progeric subjects did not feature such regional distribution of the elastic property. The region-by-region comparison between healthy and progeric samples results in statistically significant difference for anterior and posterior regions (Table 1).

Er [GPa]	ANT	POS	MED	LAT
Healthy	34.9±3.6	30.9±4.4	29.9±4.3	31.0±3.2
Progeric	30.2±5.7	29.0±4.6	30.5±5.3	30.0±5.4
p-value	<0.01	0.01	0.14	0.49

Table 1: Regional distribution of the indentation modulus values in the four anatomic regions.

The nanoindentation study revealed peculiar properties of the progeric bone which was not revealed by the bending tests thus emphasizing the relevance of this two scales investigation.
These preliminary results seem to confirm an impact of HGPS on bone tissue structure, as already sustained by Schimdt et al. [3].

References

1. Vo et al., J. Orthop, Res, 28, 1600-1607, 2010
2. Casanova et al. R. Soc. Open Sc., 4, n.160971, 2017
3. Schmidt et al, J Biol Chem, 287:33512-22, 2012.

Acknowledgements

The authors thank Carlos López-Otín (University of Oviedo, Spain) for providing the mouse model.
The contribution of S. Arnardi and L. Calvi to the nanoindentation tests and on the finite element modeling is kindly acknowledged.

SYNCHROTRON IMAGE-GUIDED DAMAGE ASSESSMENT OF HUMAN FEMORAL BONES

Federica Buccino (1), Giacomo Grossi (1), Chiara Colombo (1), Paolo Savadori (2), Luigi Zagra (2), Giuseppe Banfi (2), Laura Maria Vergani (1)

1. Politecnico di Milano, Italy 2.Gruppo San Donato Foundation, Italy

Introduction

One of the most widespread pathologies related to the aging process is osteoporosis, that alters bone microstructure leading to an enhanced bone fragility. Proximal femur fractures are the most common and risky osteoporotic fractures. Nowadays, the reliability of femoral fracture risk needs to be improved and this could be performed by deeply investigating and understanding bone multi-scale damage mechanisms. Within the femur, the trabecular bone structures are arranged along the lines of compressive and tensile stresses resultant from weight bearing activities; these stress trajectories are known to be altered in presence of osteoporosis. In addition to this, the role of femoral micro-scale features (such as lacunae, small cavities where osteocytes reside) in osteoporotic damage progression is still not clear [1]. The aim of this research is to shed some light on the variation of femoral local mechanical properties at the meso and micro-scale in non-osteoporotic and osteoporotic human samples. The exact comprehension of bone damage at the multi-scale can give better insights on the mechanical behavior of bone and on proximal femur fracture development.

Materials and Methods

Three non-osteoporotic and three osteoporotic human femoral heads are collected in agreement with the Ethic Committee, stored in formaldehyde + 70% ethanol and cut in three zones (Z1, Z2 and Z3) with different distances from the frontal plane and 3 sub-zones: medial (M), proximal (P) and distal (D) with respect to the pelvis' position. A total amount of 36 samples is obtained from each femoral head, with a final sample's resistant section of 4x4 mm^2 and an effective length of 6 mm. In order to visualize real-time damage progression in the samples, femoral specimens are tested under wet conditions inside ELETTRA synchrotron in Trieste using a novel-designed portable micro-compression device (MCD). The MCD, compatible with SYRMEP beamline, is characterized by limited height (40 cm) and weight (2 kg), easiness of mounting and disassembling. Samples are tested until failure, at an interval of 0.1 mm/step and at a rate of 0.1 mm/second; each compression step is followed by 5 min relaxation time at constant displacement, providing synchrotron images without any moving artefacts. 4 points are considered in the force-displacement curve with phase contrast at a resolution of 1.6 µm, using white beam at 2.4 GeV.

Results

Local mechanical properties of femoral samples tested with the MCD are expressed in terms of apparent stress and apparent strain, highlighting an exemplificative trend as the one reported in figure 1.

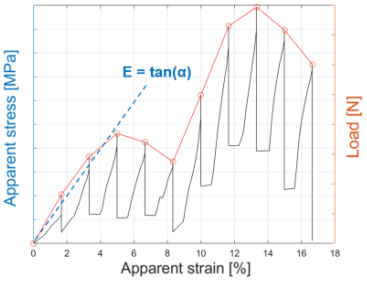

Figure 1: Representative trend of apparent stress- strain curves in non-osteoporotic and osteoporotic samples.

Average values of apparent elastic modulus for non-osteoporotic and osteoporotic samples are reported in table 1.

	Apparent elastic modulus [MPa]
Non-osteoporotic	86.29±38.95
Osteoporotic	53.71±28.16

Table 1: Average apparent elastic moduli in non-osteoporotic and osteoporotic samples

The SR-CT images obtained for non-osteoporotic and osteoporotic specimens at step 0 (prior to the compressive tests), step 1 (pre-yield), step 2 (post-yield), and step 3 (post failure) show that cracks propagate from bigger voids (i.e., canals, vessels) and are influenced by the presence of lacunae.

Discussion and conclusion

Non-osteoporotic and osteoporotic samples show a significative difference in terms of apparent Young Modulus and local mechanical properties of different zones. On the other hand, the sub-zones do not show statistically significative differences between them. The stress-strain curves' trends are coherent with previous literature data [2]. Interesting outputs are shown when correlating local collapses of femoral bone with the SR-CT images, showing crack progression (Fig. 2). Further developments will focus on the comparison among micro-scale morphological features of lacunae in non-osteoporotic and osteoporotic samples and on the definition of local micro-scale fragility indexes, that will help the comprehension of bone damage.

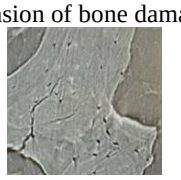

Figure 2: Visualization of cracks deviated by lacunae

References

1. G. C. Reilly, J. Biomech., pp. 1131–1134, 2000
2. I. Aleixo et al., Mater. Sci. Forum, pp. 3–8, 2013.

ISOLATING LACUNAR MORPHOLOGY TO STUDY THE INFLUENCE OF BONE LACUNAR NETWORK IN DAMAGE PROGRESSION

Federica Buccino (1), Sara Bagherifard (1), Marta Ghidini (1), Carlo Alberto Biffi (2), Laura Vergani (1)

1. Politecnico di Milano, Italy 2. CNR, ICMATE, Italy

Introduction

Bone fractures are often caused by pathologies, such as widespread degenerative illnesses (osteopenia (OP), osteoarthritis (OA), etc.) or may happen in presence of rare bone diseases (i.e., osteopetrosis (PET)). While at the macro-scale the identification of those fragility fractures is assured by the clinical practice, micro-scale features are still underexplored: their investigation could lead to a more accurate and early diagnosis of these pathologies. In this research a special interest is devoted to cellular level porosity represented by the lacunar network, a complex system of cavities populated by osteocytes, whose role is still under debate. Lacunae play a dual mechanical role influencing both strength and toughness. In the first instance, lacunae are stress concentrators, contributing to strength reduction. However, considering bone as a damage-tolerant material, lacunae give a beneficial contribution to toughness, by deviating the crack path [1]. The aim of this research is to investigate how a variation in the lacunar distribution or in the lacunar shape in presence of osteopenia, osteoarthritis or osteopetrosis could affect bone resistance to fracture.

Materials and Methods

In order to isolate the effect of lacunar morphology on damage progression, healthy bone lacunae are replicated in Ti6Al4V samples, realized by means of Laser powder bed fusion (LPBF) in CNR (Lecco, Italy). An additional notch is introduced to simulate external surface discontinuities, typical of natural bone samples. The titanium specimens are then analyzed by means of the micro-CT, in order to test the reproducibility of the lacunar disposition and geometry. Mechanical tests are performed including static tensile tests (crosshead speed=1.60 mm/min) and fatigue tests (f=20 Hz, R=0.1). Tensile tests are performed instead of compressive tests, due to the presence of unmolten titanium powder inside lacunae caused by the intrinsic properties of LPBF fabrication method. Both fatigue tests up to failure and interrupted cyclic tests are performed, in order to identify the region where the crack starts and how it propagates. Fracture surfaces are observed by stereomicroscope and by scanning electron microscope. In parallel, both static and fatigue numerical simulations are implemented: fatigue simulations consider the possibility to investigate both the fatigue life of the component and fracture analysis. Once the models based on healthy bone's lacunar network are validated, seven different configurations are explored [2], in order to consider the effects of different lacunar morphological features encountered in OP, OA and PET pathologies (Table 1).

	Characteristics	N° of lacunae	Lacunar aspect ratio
OA	Elliptical lacunae, aligned in the direction of the applied load	20	11:5
OP	Roundish lacunae, aligned in the direction of the applied load	20	11:10
OP_2	The pathological lacunar density is considered	4	11:10
PET	Roundish lacunae, aligned in the direction of the applied load, lower lacunar surface with respect to OP	20	11:10
PET_1	Lacunae are randomly oriented	20	11:10
PET_2	The pathological lacunar density is considered	13	11:10
PET_3	Lacunae are randomly oriented, the pathological lacunar density is considered	13	11:10

Table 1: scheme of different lacunar morphologies. The actual pathological configuration is highlighted in green.

Results

The healthy lacunar network configuration serves as a preliminary validation for the implemented computational models. Three different categories of samples are selected: three specimens without lacunae, three with one lacuna, three with six lacunae and three notched samples with six lacunae. The results for tensile tests show a decrease in elongation at break and a more brittle behavior for samples with a higher number of lacunae. Fatigue tests show a clear effect of the lacunar voids in sample life and in damage propagation. The visualization of the fractured specimens shows that in absence of an external notch, the crack starts from lacunae, while in presence of the notch, crack starts from it and encounters lacunae, as its path is influenced by lacunae arrangement. Samples' toughness and crack patterns are significantly influenced by the presence of different lacunar networks: PET_3 experiences the shortest fatigue life.

Discussion

In the considered titanium samples, damage pattern is influenced by the presence of lacunae, as expected from the past computational studies on bone samples. Stereomicroscope images (Fig. 1) allow a comparison with the crack pattern obtained from computational models on bone lacunae.



Figure 1: Damage pattern around a lacuna.

The main limitations of the experimental study reside in the difficulty to reproduce lacunae as empty cavities. Further developments may focus on considering the effect of bone-like canals and vessels to evaluate damage progression.

References

1. Schneider, P. et al, Biomech. Model. Mechanobiol. 13, 1227–1242, 2014
2. van Hove RP et al, Bone, 321-9, 2009.

IN SITU X-RAY COMPUTED TOMOGRAPHY FOR THE EVALUATION OF BONE REGENERATION INDUCED BY MAGNESIUM-BASED FIBRES

Roxane Bonithon (1), Colin Lupton (1), Gordon W. Blunn (2), Frank Witte (3,4), Gianluca Tozzi (1)

1. ZEISS Global Centre, School of Mechanical and Design Eng., University of Portsmouth, UK; 2. School of Pharmacy and Biomedical Sci., University of Portsmouth, UK; 3. Biotrics bioimplants, Berlin, Germany; 4.Dept. of Prosthodontics, Geriatric Dentistry and CM Disorders, University of Berlin, Germany.

Introduction

Although bone possesses an intrinsic healing capacity following fracture, bone regeneration remains challenging in large defects where the bone is not able to heal spontaneously [1]. In this context, biodegradable magnesium (Mg) alloys are promising candidates due to their density and mechanical properties close to those of trabecular bone [2]. This study aims to employ X-ray computed tomography (XCT) to qualitatively and quantitatively assess the bone regeneration induced by the latest generation of biodegradable Mg-based fibres in large bone defects.

Methods

Cylindrical bone defects (Ø5mm) were created in dog mandibles and filled with either Mg-based fibres (N=24), tetracalcium phosphate (CaP) particles (N=12; Cerabone, Botiss Biomaterials) or left empty (N=12). for 4, 8 or 16 weeks. Each defect site was individually imaged by XCT (2µm voxel size, Xradia 520 Versa, ZEISS) and the bone volume fraction computed. Thereafter, cylindrical specimens (Ø6mm, 10mm length) from the Mg-bone and CaP-bone systems at 16 weeks were cored and mechanically tested *in situ* under compression (CT500, Deben). At different compression stages (2%, 4%, 6% and 8%), XCT tomograms were recorded (20µm voxel size, XT H 225, Nikon). 3D full-field strain was calculated by digital volume correlation (DaVis10, LaVision), using a multipass scheme (110 to 20) and 0% overlap (SDER always <500µε [3]).

Results

At 16 weeks, Mg displayed a significantly higher volume fraction (0.53, 0.54 and 0.79 for empty, CaP and Mg, respectively). The bone was closely integrated with the remaining Mg fibres while a 20-70µm gap separated it from the CaP particles (Fig. 1). Osteocyte lacunae and blood vessels cavities were also found in the newly formed bone in both cases (Fig 1). The overall mechanical properties of Mg-bone and CaP-bone were comparable (e.g. E of 0.15GPa and 0.17GPa for Mg and CaP, respectively). The third principal strain (ε_{p3}) distribution of Mg-bone in the regenerated issue showed local values up to 57 048µε at 2% and 194 545µε at 8% compression (Fig 2).

Discussion

More bone regeneration with closer interaction (Fig 1) was induced by Mg fibres than CaP particles up to the restoration of tissue integrity, probably due to the smaller size of the fibres leading to a faster degradation. The newly formed bone seemed to undergo physiological remodelling (osteocytes cavities) and angiogenesis after 16 weeks, enabling the Mg-bone system to gain sufficient mechanical integrity. This study provides evidence that this novel type of Mg-based fibres has the ability to promote osteointegration, conduction and promotion of newly formed bone allowing the reconstruction of critical-sized defects, while maintaining the mechanical integrity of the injured site.

Figures

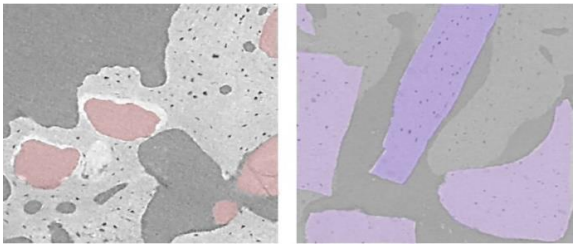

Figure 1: XCT images of the interaction between the Mg fibres (pink) and CaP particles (purple) with the newly formed bone at 16 weeks.

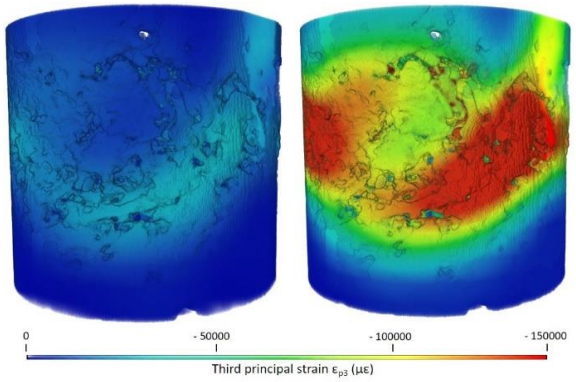

Figure 2: Full-field third principal strain distribution (ε_{p3}) at 2% (left) and 8% (right) compression.

References

1. Oryan et al, Biomed. And Env. Sci., 28:57-71, 2015.
2. Zhao et al, Biomaterials, 112:287-302, 2017.
3. Palanca et al, Journal of Biomechanics, 58:27-36, 2017.

Acknowledgements

The project is co-funded by the University of Portsmouth, Biotrics bioimplants AG and Botiss biomaterials GmbH.

SITE-SPECIFIC CHANGES IN COLLAGEN ORIENTATION IN OSTEOGENESIS IMPERFECTA MOUSE BONE

Anxhela Docaj and Alessandra Carriero

The City College of New York, United States of America

Introduction

In osteogenesis imperfecta (OI) mutations in collagen type I alter the whole bone hierarchical structure and composition, increasing its vulnerability to spontaneous fractures and fragility [1]. Bone fracture toughness of the OI murine (*oim*) model is significantly smaller than its healthy counterpart [1, 2]. We also recently showed that fracture toughness increases with skeletal growth in both healthy and *oim* mice, and that toughening mechanisms to resist crack propagation are different in young and older *oim* mice [3]. Disorganized collagen fibers have often been suggested the reason for the low fracture toughness of OI bone. However, to date it is not known if collagen orientation is site-specific in OI bone. To better understand the brittle behaviour of these bones, we here investigate the structural changes in collagen orientation in *oim* and healthy mouse bone with respect to anatomical directions using second harmonic generation (SHG) microscopy.

Methods

Tibiae from 14 week old *oim/oim* (B6C3fe-a/acolla2$^{oim/oim}$) mice model of OI and their wild type (WT) counterparts (N=5-6/group) were dissected, removed from soft tissue and cross-sections of 3 mm height were generated at 37% of tibial length using a slow speed saw machine with a diamond blade. Bone cross-sections were then glued on microscope slides and maintained hydrated with PBS.

SHG images of the bone cross-sections at their anterior, posterior, medial and lateral sides were collected at a fundamental excitation wavelength of 920 nm using a 40X 0.8 N.A. water immersion objective using a Prairie Tech. Ultima IV Multiphoton Microscope (Bruker; Madison, WI). Objective was focused on each tibia to achieve the maximum birefringence before capturing an image Collagen fibers degree of orientation (weighted-average), and distribution of orientation (second-order susceptibility ratio) were determined (OrientationJ-ImageJ (NIH)) as descriptors of the hierarchical organization of collagen.

Results

The orientation color surveys and histograms for representative sample of WT and *oim/oim* tibiae cross-sections at their anterior, posterior, medial, and lateral sites are shown in Figure 1. Color plots of the collagen fibers orientation show that in WT bone at each site the preferred orientation of collagen fibers are mostly parallel to the bone surface, while in the *oim/oim* bone there are smaller concentrations of fibers following the bone contour, mostly in the medial and lateral sites at the periosteum. Well organized WT collagen fibers along the tibia cross-section are also evidenced by the tall and narrow peaks of the red histograms. The *oim/oim* tibia generally has not well organized collagen fibers, as shown by the small and wide peaks of the green histograms, except in the medial side (showing a tall and narrow peak in the green histogram).

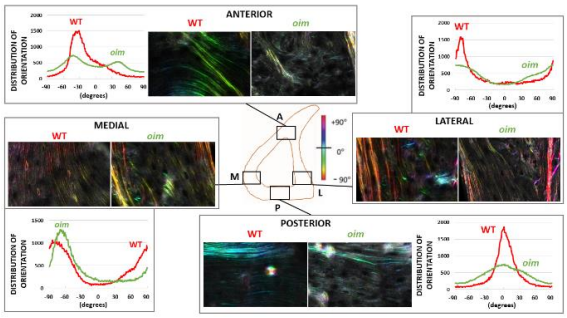

Figure 1: Degree and distribution of collagen fiber orientation for the anterior (A), posterior (P), medial (M) and lateral (L) regions of WT and oim/oim tibiae. Black box indicates region of interest for each site. Peaks of histograms for WT bone are higher and narrower than those of oim bone. FWHM values for oim/oim and WT are in A (79° vs. 34°), M (40° vs. 43°) and P (97° vs. 28°) sites for these representative tibiae.

Discussion

This work reveals the presence of site-specific orientation of the collagen fibers in OI bone. The presence of concentrations of well aligned collagen fibers in the medial and lateral sides of the *oim/oim* bone is important when considering the low bone strength and toughness of these bones. Because of the curved shape of the tibia, when loaded, its medial side is in tension, while its lateral side is in compression [5]. Thus, it seems that the *oim/oim* bone has optimized its collagen structure in an attempt to resist deformations and fractures at these sites of high tensile/compressive strains by having a concentration of well-organized fibers. Our future studies will further explore the relation between site-specific collagen fibers orientation and fracture toughness in *oim/oim* bone during skeletal growth.

References

1. Carriero A., et al., JBMR 29(6) (2014) 1392-401
2. Docaj A., et al., ORS Meeting (2020)
3. Docaj A., et al., ABMRMeeting (2020)
4. Carriero A., et al., JMBBM 39 (2014) 38-47
5. Carriero A., et al., JBMR Plus (2021) in press

Acknowledgements

This work was supported by grant CBET 1829310 from the National Science Foundation

NANOMECHANICAL EVALUATION OF *ARGOPECTEN PURPURATUS* UNDER UPWELLING SCENARIOS

Isabel Benjumeda-Wijnhoven (1), Donna Ebenstein (2), Laura Ramajo (3), Carola Millán (1,) Juan F. Vivanco (4)

1. Facultad de Artes Liberales, Universidad Adolfo Ibáñez, Chile; 2. Biomedical Engineering Department, Bucknell University, Lewisburg, PA, USA. 3. Centro de Estudios Avanzados en Zonas Áridas (CEAZA), Chile; 4. Facultad de Ingeniería y Ciencias, Universidad Adolfo Ibáñez, Chile.

Introduction

Upwelling is a natural phenomenon that depends on winds appearing in the spring-summer and produces an upsurge of deeper waters that are colder and present lower oxygen saturations and higher CO_2 concentrations (acidic) in comparison to surface coastal waters. Upwelling will be increased due to climate change increases in pCO_2, leading to higher acidification rates that will dramatically impact the sustainability of the aquaculture industry of Chilean scallop *Argopecten purpuratus* (*AP*) [1]. Acidification impacts shell growth and mechanical properties, altering crystallographic structure while reducing the ability of shellfish to biomineralize [2]. Changes of the mineral composition have been shown to lead to variations in biomechanical behavior at the tissue level in bone and marine calcifiers. Recent studies have shown that *AP* is highly tolerant and resistant to the stressful phenomenon of upwelling, with an increase in the net calcification rate observed under acidification [3]. However, the effect of acidification due to upwelling on the mechanical properties has not been evaluated. Thus, the purpose of the present study was to evaluate the impact of upwelling on the nanomechanical properties of *AP* valves.

Methods

Materials: *AP* were cultured in natural conditions in Tongoy Bay, Chile and exposed to 4 treatments, namely 2 levels of time (50 or 103 days) to compare the adaptation process; and 2 levels of depth (10 or 25 m) to compare 2 different levels of acidification (the deeper the more acid). One specimen per each combination of treatments was embedded in epoxy resin and subject to polishing using different types of sandpaper (from 600 to 2400 grids) and different concentrations of aluminum oxide (ranging from 1 µm to 0.03 µm) until they presented a flat, smooth surface for their subsequent analysis. Only the external side (calcite) at the newer growth area (Fig. 1) of seashells was analyzed.

Nanoindentation testing and analysis: Nanoindentation experiments were performed with a TI-950 Triboindenter (Hysitron, Minneapolis, MN) equipped with a commonly used sharp Berkovich tip [3]. All indents were performed with the same loading profile: load in displacement control at 35 nm/s to 350 nm, hold for 30 s, and unload at 35 nm/s. A lift off was included at the start of the indent to allow for rezeroing of data. A minimum of 100 indents were collected from each sample. Extreme outliers were removed before analysis.

Results

pH alterations observed at different depths (10m vs 25m) were expected to lead to different levels of shell calcification [3], and differences in nanomechanical properties were observed for shells grown at different depths in this study. A significant increase ($p<0.0001$) in both the elastic modulus (Fig.1) and hardness (data not shown) of the *AP* shells was observed at increased depths for each level of time, suggesting the newest calcite laid down in more acidic conditions is stiffer and harder than the calcite laid down under less acidic condition. These results suggest that *AP* is adapted acclimated to short-term acidic condition due to upwelling, with stronger, stiffer shells.

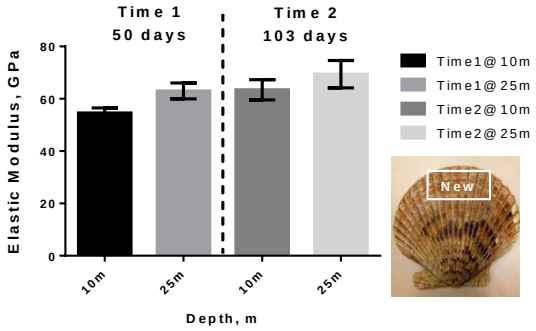

Figure 1: Mean values of elastic moduli of AP extracted from natural environment. Values are reported in GPa. Error bars represent one standard deviation.

Conclusions

This study, despite its limited sample size, complements and improves upon the available results in the field by providing a deeper understanding of the interplay between environmental climate change features of upwelling intensification and material properties of bivalves as *AP*. By combining nanoindentation data with chemical and structural analyses, a greater understanding of the impact of climate change on bivalve mineralization can be achieved.

References

1. Ramajo et al., (2019). ICES J. Marine Sc.76(6), 1836–1849
2. Fitzer et al., (2015). Ecology and Evol. 5(21): 4875–4884.
3. Oliver and Pharr (2011). J. Materials Research. 19: 3–20.

Acknowledgements

PIA-CONICYT ANILLO (ACT 17203).

COMPUTING THE ELASTIC PROPERTIES OF SINGLE HUMAN BONE LAMELLA BY HIERARCHICAL MULTISCALE APPROACH

Hamid Alijani (1), Ted J.Vaughan (1)

1. Biomedical Engineering and Biomechanics Research Centre, School of Engineering, College of Science and Engineering, National University of Ireland Galway, Galway, Ireland.

Introduction

Bone lamella, which forms one of the tissue's primary structural units, is typically composed of many mineralized collagen fibrils (MCF) embedded into Extra fibrillar matrix. The two primary constituents of MCFs are collagen proteins and hydroxyapatite (HA) mineral crystals, distributed throughout the gap zones at the end of collagen molecules [1, 2]. However, the overall volume available in these gaps zones is relatively small and it is now apparent that the majority of the HA mineral phase actually resides *outside* the collagen fibrils. In this extra-fibrillar space, stacks of HA mineral platelets are distributed in an extra-fibrillar matrix comprising of noncollagenous proteins (NCP). However, few finite element-based models have considered the mechanical implications of the mineral residing outside fibrils. The present study aims to provide a detailed hierarchical finite element model of lamellae bone to predict its elastic properties.

Methods

In this study, two levels of structural hierarchy are incorporated to predict the lamellae elastic properties. At the nanoscale, it was assumed the Extra fibrillar matrix comprises aggregated unidirectional HA platelets (C_{11} = 147GPa, C_{33}=185GPa, C_{44}=47.5GPa, C_{12}=47.3GPa, C_{13}=41.3GPa [1]) with ellipsoidal cross-sections embedded into NCP matrix ($V_{f\text{-}HA}$=0.38 and mineral portion in MCF = 0.25[2]). The microstructure of the Extra fibrillar matrix was generated through the representative volume element (RVE) method in ABAQUS, and a single layer of 1.3 nm thick NCP matrix (E = 1.2 GPa, ν = 0.35 [3]) was added to the back of the RVE to justify the tissue periodicity (Fig. 1). Another RVE represents the MCF ($V_{f\text{-}MCF}$=0.53) having a diameter of 50nm [4], and composed of mineral crystals within the collagen matrix was generated following Vercher-Martinez et al. [1] approach (Fig. 1). The distance between adjacent mineral crystals was assumed 27 nm to form the gap and overlap zones. The RVE of Extra fibrillar matrix and MCF was analyzed using the homogenization scheme with periodic boundary conditions to extract their transversely isotropic elastic tensor. At the microscale, the lamella RVE was created based on the properties driven from the smaller scale and depicted in Fig. 1. The anisotropic elastic tensor of lamella was obtained employing by a similar homogenization scheme. Furthermore, two parametric studies were carried out by varying the collagen stiffness among E_C = 1.2 – 7 GPa [5, 6] and varying the fibrils orientation within 0 - 47° [4].

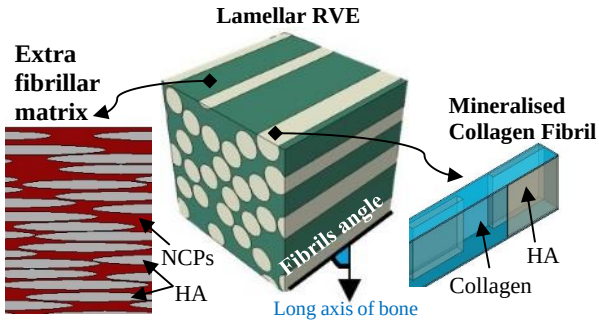

Figure 1: Demonstration of Lamella volume element along with the MCF and Extra fibrillar matrix RVEs.

Results and Discussion

Figure 2 shows the longitudinal and transverse elastic moduli of bone lamella for a range of collagen moduli and fibril orientations. The properties of the tissue were higher with increasing collagen stiffness and lower orientation angles. Interestingly, it was found that in the case of stiffer collagen (E_C = 7GPa), the effect of collagen orientation on longitudinal modulus was less pronounced, compared to the case of more compliant collagen (E_C = 1.2GPa). This suggests a complimentary role of the (anisotropic) extra-fibrillar matrix in determining relative degree of anisotropy at the tissue-level.

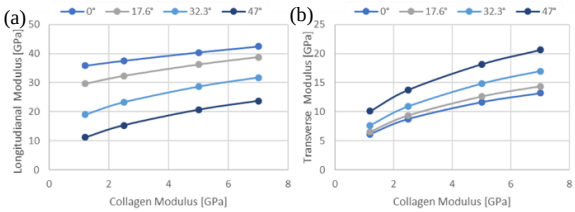

Figure 2: Lamella (a) longitudinal and (b) transverse elastic properties.

References

1. A. Vercher-Martínez et al., J. Mech. Behav. Biomed. Mater., 42:243-256:2015.
2. H. P. Schwarcz et al., Bone, 135:2020.
3. T. J. Lin et al., J. Phys. Chem. C, 120:9: 4975–4992:2016.
4. E. M. Spiesz et al., J. Mech. Behav. Biomed. Mater, 28:195-205, 2013.
5. T. J. Vaughan et al., J. Mech. Behav. Biomed. Mater., 12:50-62:2012.
6. J. A. J. Van Der Rijt et al., Macromol. Biosci., 6:9:697-702:2006.

Acknowledgements

This work was supported by the European Research Council (ERC) under the grant agreement No. 804108.

COMPUTATIONAL INVESTIGATION OF ARTIFICIAL URINARY SPHINCTERS RELIABILITY DEPENDING ON TISSUES DEGENERATION

Chiara Giulia Fontanella (1,2), Ilaria Toniolo (1), Alessandro Arduino (3), Joseph Vannel Fotso Fogang (3), Arturo Natali (2), Emanuele Luigi Carniel (1,2)

1. Department of Industrial Engineering, University of Padova, Italy; 2. Centre for Mechanics of Biological Materials, University of Padova, Italy; 3. Department of Civil, Environmental and Architectural Engineering, University of Padova, Italy.

Introduction

Lower urinary tract dysfunction, with consequent Urinary Incontinence (UI), is a major health concern, with age increasing incidence. UI leads to a miserable quality of life, with huge costs and still sub-optimal solutions by Artificial Urinary Sphincters (AUS). The AUS usually consists of an inflatable cuff and a pressure-regulating system. Commonly, the cuff is placed around the bulbar urethra. AUS cuff pressure is defined based on clinical experience, considering that AUS has to ensure continence up to the case of high bladder pressure conditions. AUS interacts with the urethra, eliciting non-physiological mechanical stimulation of urethral tissues, leading to damage phenomena and potential AUS failure. AUS pressure is often in the order of 50-80 cmH_2O, in spite of the fact that pressures that exceed 40 cmH_2O can lead to risky reduction of tissues blood perfusion and consequent tissues degradation. High surgical revision rates, up to 50%, have been reported, following AUS failure due to urethral tissue atrophy or erosion, perineal pain, or mechanical breakdown. The frequent access of elderly patients to AUS surgery suggests investigating the influence of tissue degeneration because of aging phenomena on AUS functionality and reliability.

Materials and Methods

A specific procedure is developed aiming to analyze the influence of degenerative phenomena on urethral tissues mechanics [1], functionality and interaction with prosthetic devices. Based on data from coupled tensile and inflation tests [2], a specific hyperelastic formulation was defined to characterize the non-linear mechanical behavior of urethral tissues. The investigation of degenerative phenomena occurring because of ageing was performed by considering variations of constitutive parameters. Anatomical sections of urethral duct were collected, leading to the definition of finite element models. AUS cuff represents the fundamental component of the prosthetic device, providing the mechanical action addressed to lumen occlusion. A computational model of the cuff-urethra system was developed (Fig. 1a). Computational analyses made it possible to simulate cuff wrapping (Fig. 1b), inflation and interaction with urethra [3].

Results and Discussion

The computational investigations made it possible to evaluate urethral tissues response in normal and in pathological conditions. Numerical results show how the urethral tissues deform in a non-homogeneous way, determining areas of great strain and stress values that can cause phenomena tissue damage (Fig. 1c). Firstly, the analysis of AUS effects on urethral tissues functionality requires investigating the influence of compressive actions on the urethral vascular system.

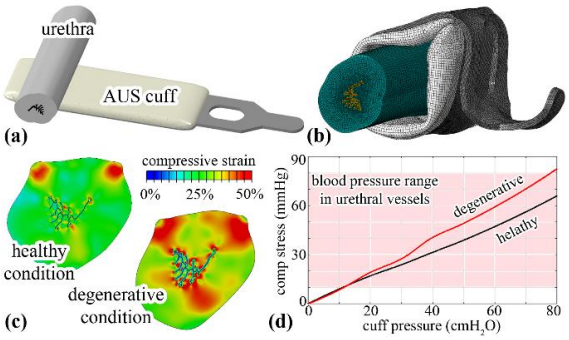

Figure 1: Computational model of cuff and urethra (a); wrapped conformation (b); compressive strains at 50 cmH_2O cuff pressure (c); relationship between cuff pressure and mean compressive stress within urethral tissues (d).

The AUS device acts on the urethral wall leading to significant compressive strain and stress conditions within biological tissues. When compressive stress exceeds blood pressure, vessels occlusion occurs, leading to ischemic phenomena (Fig. 1d). Prolonged ischemic conditions entail urethral tissues infection, atrophy and strictures formation [4]. Such degradation phenomena usually determine a reduction of tissue compressibility that, in turn, may amplify compressive stresses. It follows that after the AUS placement, the urethra may undergo a modification of tissue biomechanical properties with time and a cuff that was initially sized appropriately may become inadequate.

Conclusions

The here reported activities highlight the potentialities of the *in silico* approach for the investigation of surgical procedures. The approach allows overtaking the difficulties of experimental and clinical investigations, which require the identification of patients' conditions, samples acquisition and management.

References

1. Natali et al, J Biomech, 65:75-81, 2017.
2. Natali et al, Exp Physiol, 101:641-656, 2016.
3. Natali et al., Int J Numer Meth Bio, 36:e3308, 2020.
4. Myers et al, Urol Clin North Am, 44:93-103, 2017.

COMPUTATIONAL MODELLING OF GASTRIC TISSUES: EXPERIMENTAL AND COMPUTATIONAL ACTIVITIES ON LSG RESECTED STOMACHS

Ilaria Toniolo (1,2), Carlo Nostran (1), Edoardo Ferrari (1), Edoardo Fongaro (1), Chiara Giulia Fontanella (1,2), Mirto Foletto (2,3), Emanuele Luigi Carniel (1,2)

1. Department of Industrial Engineering of the University of Padova, Italy; 2. Centre for Mechanics of Biological Materials, University of Padova, Italy; 3. Azienda Ospedaliera of Padova, Italy.

Introduction

Obesity is a global health problem and its spread is increasing. Approximately, 4 million deaths worldwide are attributable to obesity [1]. The most effective treatment consists in bariatric surgery. Among the bariatric procedures, Laparoscopic Sleeve Gastrectomy (LSG) is the most performed operation in the world [2]. Currently, the bariatric operation selection depends on surgeon's expertise and patient medical conditions. The actual challenge is to move toward a more rational and customized approach. In this respect, computational biomechanics may provide useful tools. The main difficulty pertains to the development of a reliable computational model of the stomach. Previously, models have been identified by means of data from experimentations that have been performed on animal samples [3]. The aim of this work consists in advancing towards a more reliable computational model of the human stomach.

Materials and Methods

Human resected stomachs from LSG intervention were provided by Azienda Ospedaliera of Padova. The experimentations involved a saline inflation tests to evaluate the pressure-volume relationship (Fig. 1a) [3].

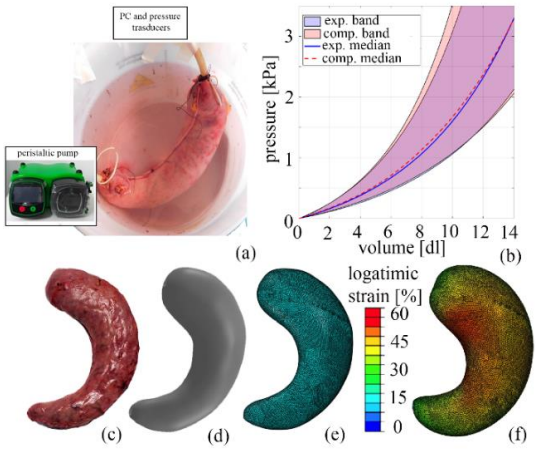

Figure 1: Experimental set-up (a). Comparison between statistical distributions of experimental and computational results (b). Development of the patient-specific FE model of the LSG stomach residual: real photo (c), virtual solid model (d) and finite element discretization (e). Typical results from computational analysis of insufflation tests (f).

Gastric wall thickness was measured for each residual in different locations. Subsequently, a virtual solid model of each stomach was built by photogrammetric reconstruction techniques (Fig 1c/d). The finite element discretisation led to a computational burden ranging from 95,000 to 140,000 nodes. The constitutive characterization consisted in a multi-layered anisotropic visco-hyperelastic formulation, which made it possible to interpret the typical features of gastric wall mechanics, as multi-layered configuration, fibre-reinforced composition, non-linear elasticity and time-dependent behaviour. Despite physiological differences between tissues from different subjects, the same constitutive parameters were adopted for all the stomach residuals. Starting from parameters identified from experimentations on swine model [3], the constitutive parameters were adapted to fit the mechanical behaviour of all the human samples by assuming multiplicative factors. The model of each experimental sample was exploited to simulate the corresponding experimental insufflation process.

Results and Discussion

Results from experimental and computational insufflation tests were statistically processed, leading to distributions of pressure-volume curves. Comparing experimental and computational results, the finite element models revealed to describe reliably the experimentations. In fact, the statistical bands at 75% of confidence interval almost coincided and the numerical median curve respected the trend of the experimental one (Fig. 1b).

The contour of maximum principal strain distribution (Fig. 1f) highlights the capability of computational methods to provide quantitative information about mechanical stimulation of gastric receptor, which play an important role in satiety mediation [4].

Conclusion

Experimentations on resected stomachs from LSG interventions made it possible to update a previously developed computational model of the stomach. Such a computational approach can provide results that allow rationally improving bariatric surgery interventions, comprehending the causes of clinical failures and individualizing the optimal procedure.

References

1. The GBD 2015 Obesity Collaborators, N. Engl. J. Med, 377:13–27, 2017.
2. Angrisani et al., Obes. Surg., 27:1-11, 2017.
3. Fontanella et al., Ann. Biomed. Eng. 47:1237–1249, 2019.
4. Piessevaus et al., Gut, 49:203–8, 2001.

DESIGN AND PRELIMINARY VALIDATION OF A NOVEL, NON-INVASIVE INTRA-ABDOMINAL PRESSURE MEASUREMENT DEVICE

Natasha Jacobson (1), Mark Driscoll (1)

1. McGill University, Canada

Introduction

Intra-abdominal pressure (IAP) is the pressure contained in the abdominal compartment. Unhealthy levels of IAP are often caused by peritoneal inflammation and/or abdominal fluid build-up, typically as a result of acute abdominal injury or surgery [1]. Rates of high IAP have been recorded in 20 to 50% of intensive care unit patients, with rates increasing further in ventilated patients [2]. This increased IAP can reduce blood flow to vital organs, perpetuating further pressure build-up as organs become unable to drain excess fluids [1]. Conversely, low levels of IAP may be representative of poor spinal stability, a phenomenon linked to the onset of low back pain [3]. Thus, measuring and understanding a patient's IAP may improve diagnostics, monitoring, or early treatment of IAP-related complications. That said, existing clinically-accepted IAP measurement techniques are invasive or indirect [4-6]. Therefore, it is the objective of the present research to design and validate a novel, non-invasive IAP measurement tool.

Methods

Research suggests that the abdomen can be represented as a pressurized cylinder of incompressible fluid for mathematical modeling [7]. Some successful IAP measurement tools exploit said model to evaluate the abdominal wall tension and correlate this value with IAP [5-6]. The present research project looks to advance this theory, evaluating the system at a quasi-static equilibrium state to accurately calculate, rather than correlate with, IAP.

Fourteen living participants (7 male, 7 female) were tested with the novel device, 5 cm subxhiphoid, in supine, inclined, sitting, and standing positions. Participants were tested without abdominal activation and at end-exhalation. Measured IAPs were compared to "ideal" IAP values, as suggested in literature. The correlation between the two measurement sets was evaluated with Pearson's correlation (r), where r greater than 0.7 is deemed a "high" correlation [8].

Results

The designed device, Fig. 1, is set against a patient's abdomen at 5 cm subxiphoid. A locally applied suction (2-5 kPa) is created using a hand pump (Qosina 80215). Applied pressure and resulting tissue deformation are measured by sensors 5 PSI-D-HGRADE-MINI and VL6180, respectively. Data is collected via a microcontroller (ESP32), which wirelessly transmits results for further processing.

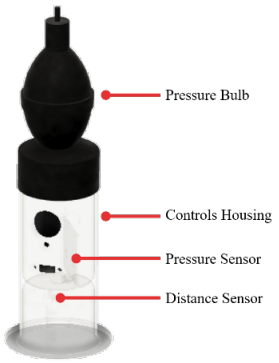

Figure 1: Prototype; major components indicated.

Descriptive statistics of results from living participants are detailed in Table 1. Pearson correlation between ideal IAP values from literature and living participants was 0.982 ($p < 0.0001$), signifying "very high positive" correlation [8].

	Supine	Incline	Sitting	Standing
Avg. IAP	5.2 (1.0)	11.1 (0.9)	17.1 (1.1)	23.9 (1.2)
Ideal IAP	6 (1)	9 (1)	15.5 (N/A)	21.0 (N/A)

Table 1: Mean and standard deviations (SD) [mmHg] of measured and ideal data.

Discussion

A novel device for non-invasive IAP measurement was developed. Initial prototypes posed concerns with air leakage; thus, improved connections were made possible with tee connections, tube reducers, and luer-locks (Qosina). Design iterations were made based on manufacturability, efficiency and function. Positive results, namely high correlation to published values, encourages the need for further research on the novel device, particularly in larger and wide-spread samples.

References

1. D. Roberts et al, Surg Int Care Med, 39(7):621–44, 2016.
2. A. Blaser, et al., Crit Care Med, 47(4):535-42, 2019.
3. I. Stokes et al., Clin Biomech, 26:797-803, 2011.
4. M. Malbrain et al., Anesth Int Ther, 46(5):406–32, 2014.
5. Y. Chen et al., World J Emerg Med, 6(2):137–41, 2015.
6. G. Van Ramshorst et al., J Surg Res, 171(1):240–44, 2011
7. F. Primiano, J Biomech, 15(12):919–31, 1982.
8. M. Mukaka, Malawi Med. J, 24(3):69-71, 2012.

Acknowledgements

We thank Mr Trevor Cotter for his help in the experiments. Funding for this project was provided by NSERC.

LINEAR VARIABLE DISPLACEMENT TRANSDUCERS UNDERESTIMATE GLOBAL LIGAMENT STRAIN

Jonas Schwer (1), Florian Schall (1), Steffen P Hacker (1), Anita Ignatius (1), Lutz Dürselen (1), Andreas M Seitz (1)

1. *Institute of Orthopaedic Research and Biomechanics, Trauma Research Centre, Ulm University Medical Centre, Ulm, Germany*

Introduction

A commonly used method to determine one-dimensional strain in ligaments [1], tendons [2] and menisci [3] is the use of a Linear Variable Displacement Transducer (LVDT). A wide variety of fixation techniques of the LVDT's exist for both *in-vitro* and *in-vivo* applications [1,2,3]. However, it is unknown how these different fixation techniques may affect the strain output. Further, due to the inhomogeneous nature of soft tissues, measurements of local strains may differ from global (grip-to-grip) strains. Thus, we hypothesize that LVDT's underestimate global strain in ligaments.

Methods

Seven porcine lateral collateral ligaments (LCL) were consecutively fixed in a standard material testing machine (Z010, Zwick, Germany) using special clamps. Then, a M-LVDT (LORD Corporation, USA) with a 3mm linear stroke length and an accuracy of ± 0.1% was attached to the center of the ligament using four different fixation techniques (Fig 1): pinned (A), pinned + cross-stitched (B), pinned + entangled ligament (C), pinned + cross-stitched + entangled ligament (D). After reaching a preload of 5N, the initial gauge length of the ligament was automatically detected. All tests were carried out in displacement-controlled mode at a velocity of 10 mm/min until a global ligament strain of 4% was reached. Each fixation technique was tested in random order for three cycles, with the last cycle used for data analysis. For validation of the test setup, the same test was used to measure the strain at seven random positions on a rubber strip (Fig 1, E). Statistical analysis was performed using SPSS (IBM, Inc), while $p \leq 0.05$ was considered statistically significant.

Results

The measured local LCL strains of the four fixation techniques showed no statistical difference ($p > 0.78$) and ranged between 1.44 % (pinned + cross stitch) and 1.92 % (pinned + entangled ligament) (Fig 1, A-D). The validation of the test setup was defined successful, as the LVDT measurements on the rubber strip indicated a median strain of 4.07%, which was similar to the applied global strain of 4% (Fig. 1, E).

Discussion

The main finding of this study is that the local strain measured with the LVDT was up to 60% lower than the grip-to-grip strain for all fixation techniques, confirming our hypothesis. Additionally, the LVDT strain showed no significant difference between the four tested fixation methods. The reason for the comparably low local strains can be attributed to the structural properties of the ligament, mainly composed of parallel aligned collagen fibers exhibiting unique time-dependent mechanical properties and highly inhomogeneous strain patterns [4]. These findings are in accordance with Gijsbertse et al., who also reported lower local strains compared to global LCL strains using two ultrasound systems and digital image correlation techniques [5]. Therefore, we conclude that although the M-LVDT provides a high measurement accuracy by itself, it might lead to an underestimation of total ligament strain. Consequently, users should be aware, when interpreting results from *in-vitro* and *in-vivo* measurements utilizing LVTDs.

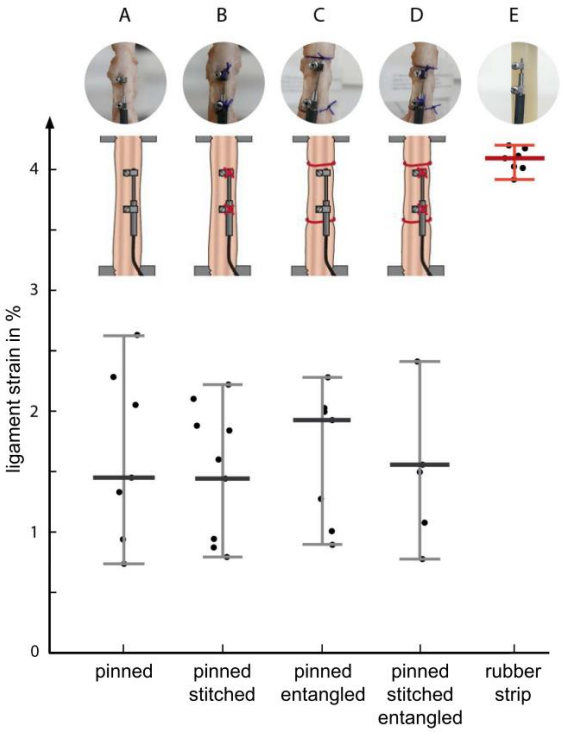

Figure 1: Test results of the four fixation techniques and the validation. A: pinned, B: pinned + stitched, C: pinned + entangled, D: pinned + stitched + entangled, E: rubber strip. The horizontal lines indicate median, minimum and maximum values (n = 7). The four fixation techniques showed no statistical difference ($p > 0.78$).

References

1. Flemming et al, Am J Sports Med, 26(1): 109-18, 1998
2. Lyman et al, Am J Sports Med, 32(2): 457-61, 2004
3. Seitz et al, Knee Surg Sports Traumatol Arthrosc, 20: 1488-95, 2012
4. Phatak et al, Ann Biomed Eng, 35(7): 1175-87, 2007
5. Gijsbertse et al, J Biomech, 73: 233-37, 2018

VISCOELASTIC PROPERTIES OF HUMAN LIVER TISSUE: INFLUENCE OF THIEL PRESERVATION AND COMPARISON WITH ANIMAL TISSUE

Sarah-Jane Estermann (1,2,3), Sophie Förster-Streffleur (1), Lena Hirtler (4), Johannes Streicher (1), Dieter H. Pahr (1,3) Andreas Reisinger (1)

1. Karl Landsteiner University of Health Sciences, Austria; 2. Austrian Center for Medical Innovation and Technology, Austria; 3. University of Technology Vienna, Austria, 4. Medical University of Vienna, Austria

Introduction

In research and medical education, fresh human tissue is often replaced by preserved human or fresh animal tissue due to practical reasons. The *Thiel method* was developed as an improvement to conventional formalin fixation, aiming at maintaining elasticity during embalming [1]. Thus, human Thiel preserved tissue is used when accurate mechanical properties are required. As an alternative, fresh porcine or bovine tissue is also frequently used.

In the current study, we evaluate the effect of Thiel preservation on human liver parenchyma in terms of viscoelasticity. Furthermore, the results of fresh human liver are compared to fresh porcine and fresh bovine liver. Testing is conducted in tension, measuring the stress relaxation of the tissues.

Methods

Strips of liver parenchyma were cut from one fresh human, one Thiel embalmed, one fresh bovine and six fresh porcine organs. The samples were mounted to the mechanical testing machine and tested under uniaxial tension (Fig.1a). Stress was calculated based on the force recording of a 100 N load cell and strain/stretch was calculated based on displacement, measured with digital image correlation. The samples were stretched to a constant strain (~0.06) and held for 5 minutes, causing stress relaxation. 3-element Prony series were fit to the stress over time data, yielding storage and loss modulus (*E'*, *E"*) and loss tangent (tan δ) after transforming to the frequency domain (Fig.1b). The given viscoelastic properties were calculated for a frequency of 1 Hz.

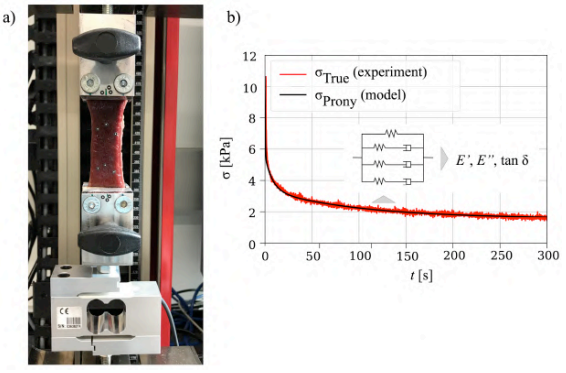

Fig. 1: a) Liver sample in testing machine; b) typical stress relaxation curve with the rheological model used for extracting viscoelastic properties.

Results

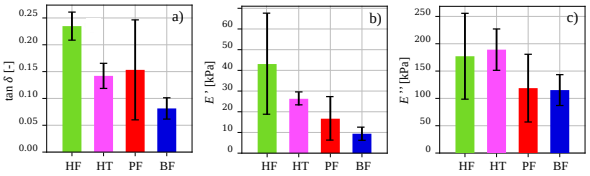

Fig. 2: Viscoelastic properties at 1 Hz for human fresh (HF), human Thiel preserved (HT), porcine fresh (PF) and bovine fresh (BF) liver: a) loss tangent tan δ*, b) storage modulus E', c) loss modulus E"*

Statistical analysis (t-tests with Bonferroni correction, $\alpha = 0.05$) revealed that fresh human liver showed viscoelastic damping (tan δ) to a higher degree than Thiel preserved human and fresh bovine liver. Furthermore, fresh bovine liver exhibited the smallest storage modulus *E'* compared to the other tissues. Concerning loss modulus *E"*, preserved human, fresh porcine and fresh bovine tissues were indiscernible from fresh human tissue.

Discussion

The differing viscoelastic properties might be a result of characteristic microstructural features. The so-called sinusoidal network is responsible for channeling fluid through the liver parenchyma. Differences in viscoelasticity between species could be explained by morphological differences in this sinusoidal network, specifically in the sinusoid endothelial lamina [2, 3]. Altered viscoelastic properties stemming from Thiel preservation can be explained by increased cross-linking and dehydration [4], inhibiting fluid flow.

In conclusion, when substituting fresh human tissue, the relevant properties for the respective application must be considered. The current results indicate that Thiel preserved human liver is the best alternative regarding viscoelastic properties.

References

1. Thiel, Ann. Anat., 174:185-195, 1992.
2. Wood, Z. Zellforsch. Mikrosk. Anat. 58:679-692, 1962
3. Wisse et al., Gene Therapy, 15: 1193-1199, 2006
4. Fishbein et al., Magn. Reson. Med. 57:1000-1011, 2007

Acknowledgements

The project was funded by the NFB Science Call Dissertations 2017 (SC17-016), and the research center ACMIT (funded by COMET, BMVIT, BMDW, the Federal State of Lower Austria, and Standortagentur Tirol).

DEGENERATION DECREASES ELASTIC PROPERTIES OF MENISCAL TISSUE

Daniela Warnecke (1), Mara Kugel (1), Jonas Schwer (1), Martin Faschingbauer (2), Lutz Dürselen (1), Anita Ignatius (1), Andreas Seitz (1)

1. Institute of Orthopaedic Research and Biomechanics, Centre for Trauma Research Ulm, Ulm University Medical Centre, Germany
2. University and Rehabilitation Hospital Ulm, Ulm University Medical Centre, Germany

Introduction

The menisci play a decisive role for the physiological biomechanics of the knee joint. With progressing age, meniscus degeneration occurs, which can finally lead to osteoarthritis [1]. Therefore, research focused on the general biomechanical characterization of meniscal tissue and also on the influence of degeneration on that [2-4]. However, most recent studies performed quasi static tests, although the menisci are mainly loaded dynamically, e.g. during walking. To the best of our knowledge, only PEREIRA ET AL. transferred the Dynamic Mechanical Analysis (DMA) from polymer characterization to biological tissue and examined the material properties of human menisci in more detail [5]. Thus, the aim of this study was to investigate the elastic and damping properties of meniscal tissue with regard to its degree of degeneration using the DMA.

Methods

49 menisci of total knee replacement patients (~69.5 yrs) were harvested and the degree of degeneration (1-4) of each region (PA: pars anterior, PI: pars intermedia, PP: pars posterior) was macroscopically classified according to PAULI ET AL. [6]. From each region, cylindrical samples (Ø 4.6 mm) were punched out resulting in 132 samples (42x PA, 47x PI, 43x PP). For the DMA, a dynamic material testing machine (ElectroForce® 5500, TA Instruments, USA) equipped with a 200 N load cell was configured for an unconfined compression test. After applying a small compressive preload (0.1 N), a dynamic, sinusoidal strain amplitude of 12% was applied over a frequency spectrum of 0.1-10 Hz. Thereby the number of loading cycles ranged between 4, 7 and 20 cycles for low (≤0.25 Hz), mid (≤2.5 Hz) and high frequencies, respectively.

For a detailed characterization of the degenerated menisci, the storage modulus *E'* (1) that relates to the elastic stiffness of the material, as well as the loss factor *tan(δ)* representing the viscous damping properties were calculated with δ being the detected phase shift between the applied strain and resultant stress.

$$E' = \frac{\sigma_0}{\varepsilon_0} cos\delta \qquad (1)$$

To detect any regional or degeneration specific differences, a Kuskal-Wallis with posthoc Dunn's test for multiple comparison were performed.

Results

Both parameters were frequency dependent, with higher values at low (≤0.25 Hz) but also at high (≥2.5 Hz) frequencies. At the typical gait frequency of 1 Hz, *E'* reached values between 0.07-0.72 MPa and *tan(δ)* of 0.06-0.1 (Fig. 1). Additionally, the posterior region (PP) was the stiffest meniscus region by tendency ($p \geq 0.05$). With increasing degeneration, PP showed a decreasing storage modulus from approx. 0.72 MPa (Degen. 1) at 1 Hz to less than 0.1 MPa (Degen. 4) (Fig. 2).

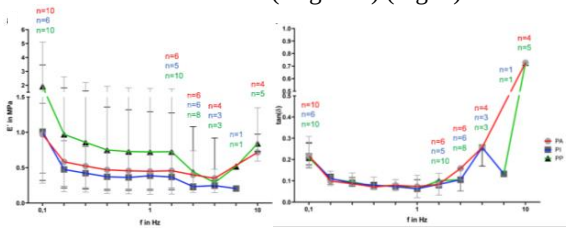

Fig. 1: E' (left) and tan(δ) (right) of the degenerated menisci for each region: PA, PI, PP. (median with range)

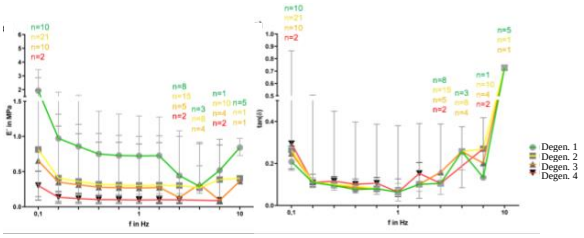

Fig. 2: E' (left) and tan(δ) (right) of PP for each degree of degeneration (Degen. 1-4). (median with range)

Discussion

The current study was the first performing a classical DMA on degenerated human menisci. It could be shown that PP was stiffest at the lowest degree of degeneration in comparison to the other meniscal regions (PI and PA). However, these regional dependencies of *E'* decreased with increasing degeneration. Therefore, it could be assumed that lateral menisci become significantly softer with increasing arthritic changes, whereas the posterior region is mostly affected, while the damping properties remain almost unaffected.

References

1. Lewandrowski et al., Am J Sports Med, 25:486-94, 1997
2. Fischenich et al., J Biomech, 48:1407-11, 2015
3. Sandmann et al., BMC Musculoskelet Disord, 14:324, 2013
4. Warnecke et al., Osteoarthritis Cartilage, 28:1482-91, 2020
5. Pereira et al., Osteoarthritis Cartilage, 22:1271-81, 2014
6. Pauli et al., Osteoarthritis Cartilage, 19:1132-41, 2011

USAGE OF THE ABAQUS – ADAPTIVE QUASI-LINEAR VISCOELASTIC MODEL FOR ARBITRARY LOAD PREDICTION

Martin Frank (1), Othniel J. Aryeetey (1), Dieter H. Pahr (1,2)

1. Karl Landsteiner University of Health Sciences, Austria; 2. Technische Universität (TU) Wien, Austria

Introduction

Soft biological materials can be well modeled in 1D with the adaptive quasi linear viscoelastic model (AQLV), especially for large strains [1]. This model has the advantage of accounting for different strain levels during calibration with ramp and hold experiments. However, the AQLV has only been defined for positive ramp and hold experiments and usage of different loading protocols require complicated mathematical operations. Recently, the AQLV was implemented in Abaqus as finite element (FE) model with 1D rheological connector elements by Smith et al. [2] (see Figure 1- Right). Here, properties of rheological elements and individual load steps had to be adjusted manually. Goal of the current work was to adapt this model for automatized load and stress prediction for arbitrary experimental protocols, such as saw-tooth and sine load with python scripts.

Methods

Porcine liver tissue was tested in ramp-hold experiments to determine the AQLV parameters (see Figure 2 – Top). Experimental vertical strain was measured optically (see Figure 1 – Left) und used as input parameter for the 1D FE AQLV model. In short, python scripts were used to automatize generation of input files that incorporate the non-linear behavior of all spring and dashpot elements, sample geometry and the optically measured strain. Using the exact strain from the experiment is important, since large strains of biological tissue show a hyper-elastic behavior (linear strain ramps as input would cause an artificial deviation). Exemplarily, a cyclic loading protocol was used on a different liver tissue, both experimentally and with the FE model. For the FE model the AQLV parameters were used from the previous sample with the ramp-hold experiment.

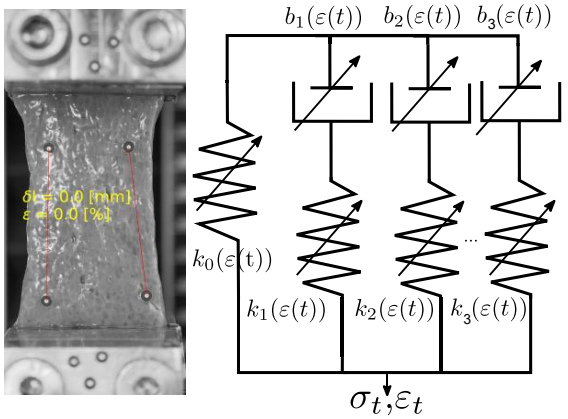

Figure 1: Left: Liver sample with optical strain tracking. Right: AQLV in rheological element representation. Nonlinear springs and dampers are defined with respect to global strain ε.

Results

The ramp-hold experiment used for AQLV parameter identification showed a very good fit for the FE model (see Figure 2 -Top). Further, the calibrated FE AQLV model was still able to predict the overall stress response of a different sample in a cyclic loading protocol (see Figure 2 – Bottom), after correction for differences in sample length and cross-sectional area.

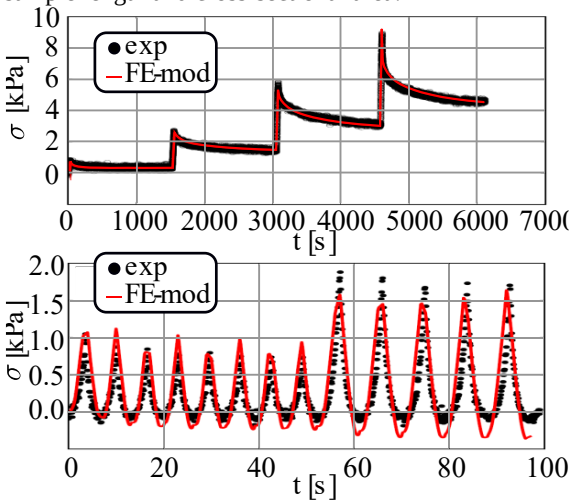

Figure 2: Experimental determined stress response (black) with respect to FE model stress response (red). Top: Ramp and hold experiment used for AQLV parameter identification. Bottom: Cyclic loading of a different sample with used AQLV parameters of sample on top.

Discussion

The AQLV model has been mostly used for ramp-hold experiments so far, limiting its application possibilities. The presented adaptation of the FE Abaqus model also allowed a sufficient prediction of a cyclic loading protocol. Deviations to the experiment are likely caused by biological variation and the inability of the physical liver sample to experience compressive stresses in the experiment because of its softness. In future, further samples will be tested, also in different loading modes (e.g. sine, ramp at different strain-rates) to determine if the FE AQLV can be used in general for soft tissue load prediction. Moreover, determination of stress-strain phase shift and viscous energy dissipation will ease the comparison to other visco-elastic material models.

References

1. Nekouzadeh2007, J Biomech 40: 3070-8, 2007.
2. Smith et al, 2010 SIMULIA Customer Conference.

REDUCED PARAMETER ADAPTIVE QUASI-LINEAR VISCOELASTIC (AQLV) MODEL OF SOFT BIOLOGICAL TISSUE

Othniel J. Aryeetey (1,2), Martin Frank (2), Dieter H. Pahr (1,2)
1. Karl Landsteiner University of Health Sciences, Austria
2. Technische Universität (TU) Wien, Austria

Introduction

3D printed phantoms are demonstrating their benefits in pre-operative planning by improving visualization of key features. However, current models lack kinesthetics feedback suitable for surgical rehearsal. Hence, there is a need to accurately characterize soft biological tissue to develop tissue mimicking materials for surgical rehearsal [1]. Different constitutive models are applied to model the non-linear viscoelastic behaviour of soft biological tissue, whereby Fungs' quasi-linear viscoelastic (QLV) model is the most applied one due to its elegance and ease of use [2]. The standard QLV model requires only 8 parameters for calibration of stress relaxation curves but is limited due to its assumption of a single reduced relaxation function at all strain levels. The standard Adaptive quasi-linear viscoelastic model (AQLV) model [3] overcomes this issue by calibrating its 19 parameters over 4 incremental strain levels. Here, we apply the AQLV model to porcine liver parenchyma tissue and propose a "reduced-parameter" AQLV model which improves the accessibility of the model whilst reducing the experimental burden of calibration.

Methods

Incremental ramp and hold experiments were performed on fresh porcine liver parenchyma tissue (Fig.1A). Stress responses are fitted to standard (3rd order) AQLV model (Fig. 1B). Parameter reduction studies were performed by investigating the effect of reducing the number of parallel Maxwell elements (the order) and the number of experimental steps (n) used for calibration. 3rd, 2nd and 1st order models were compared, in combination with using 4, 3 and 2 ramps (Fig. 1C) for model parameter calibration.

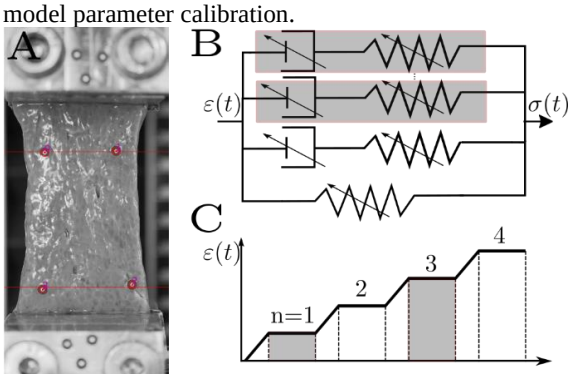

Figure 1: A) Porcine liver tissue sample. B) AQLV model with elective non-linear Maxwell elements (gray). C) strain-time inputs ramp and hold steps (n). Elective steps are colored in gray.

Results

Analysis of the effect of order reduction and sequential step reduction showed that a 2nd order AQLV model calibrated with 2 ramp and hold steps (n=2&4), referred as the 'reduced' model produced the best trade-off when reducing parameters while maintaining experimental data fitting acceptable (see Figure 2). The average coefficient of determination (R^2) and root mean square error (RMSE) is shown in Table 1.

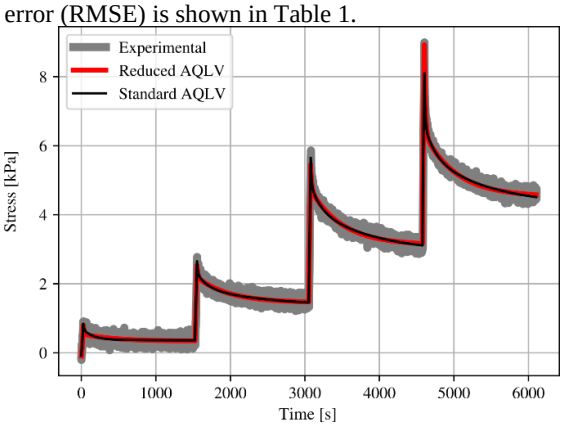

Figure 2: Reduced parameter model (red) and standard AQLV model (black) fits of experimental incremental stress relaxation response (gray) of porcine liver parenchyma.

AQLV Model	R^2 [-]	RMSE [kPa]
Standard (3rd)-4n	0.983 ± 0.030	0.103 ± 0.126
AQLV (2nd)-2n	**0.925 ± 0.029**	**0.203 ±0.148**
AQLV (2nd)-4n	0.964 ± 0.042	0.119 ± 0.141
AQLV (1st) -4n	0.905 ± 0.087	0.191 ±148

Table 1: R^2 and RMSE values between experimental data and standard and reduced parameter AQLV models.

Discussion

The standard AQLV model can accurately model the non-linear viscoelastic behavior of porcine liver tissue over 4 incremental strain levels very well but requires 19 parameters for fitting. In comparison, the 2nd order AQLV model calibrated with 2 ramp and hold steps is sufficiently accurate and produces only 8 parameters. Hence, the model is more accessible and reduces the experimental burden (halved) associated with calibrating the model. This has only been applied to porcine liver tissue so far and other soft tissues, like fat and muscle, will be investigated in future.

References

1. Qiu et al, Advance Material Technologies 3: 1700235,2018
2. Fung et al. J. Biomech, 115(4B): 453-459, 1993.
3. Nekouzadeh2007, J Biomech 40: 3070-8, 2007.

MECHANICAL BEHAVIOR OF INFRAPATELLAR AND SUPRAPATELLAR FAT PADS IN PATIENTS WITH END-STAGE OSTEOARTHRITIS

Chiara Giulia Fontanella (1,2), Elisa Belluzzi (3), Assunta Pozzuoli (3), Marta Favero (4), Pietro Ruggieri (3), Veronica Macchi (5), Emanuele Luigi Carniel (1,2)

1. Department of Industrial Engineering, University of Padova, Italy; 2. Centre for Mechanics of Bioloogical Materials, University of Padova, Italy; 3. Orthopedic Clinic, DiSCOG, University of Padova, Italy; 4. Rheumatology Unit, DIMED, University of Padova, Italy; 5. Department of Neuroscience, Institute of Human Anatomy, University of Padova, Italy

Introduction

The infrapatellar fat pad (IFP) is an adipose tissue situated between the patellar tendon, the femoral condyle and the tibial plateau of the knee, while the suprapatellar fat pad (SFP) is located above the patella and behind the suprapatellar joint (Fig. 1a). The structural functionality of IFP and SFP pertains to a cushioning role in the knee joint, providing to distribute and to damp mechanical actions during articular activity. Recent studies suggest that IFP is involved in knee Osteoarthritis (OA), in consideration of its location and on the metabolic properties of this tissue as a potential source of adipokines and cytokines [1-3]. The purpose of this work is to describe the mechanical characteristics of OA IFP and SFP, with the aim of providing new insights on the implication of IFP and SFP in the development and progression of OA knee.

Methods

Mechanical tests have been performed on IFP and SFP samples collected from patients affected by OA undergoing Total Knee Arthroplasty (TKA) at the Orthopedic Clinic, Padova. Ten patients were enrolled (M: 3, F: 7; age 68±8 years; BMI 27±5 Kg/m^2). Confined compression tests with a spherical indenter (10 mm diameter) were performed via a multi-step procedure (Fig. 1b-c). After preconditioning, each loading step was composed of 15% strain at 3000%/s strain rate, and subsequent 300 s of resting to allow the almost complete development of relaxation phenomena. The mechanical behavior was described using a visco-hyperelastic constitutive model [3]:

$$\psi\left(\mathbf{C},\mathbf{q}^i\right)=W^{\infty}\left(\mathbf{C}\right)+\sum_{i=1}^{n}\int_0^t\frac{1}{2}\mathbf{q}^i\left(s\right):\dot{\mathbf{C}}\,ds \qquad (1)$$

$$W^{\infty}\left(I_1,J\right)=-p\left(J-1\right)+\frac{C_1}{\alpha_1}\left\{\exp\left[\alpha_1\left(I_1-3\right)\right]-1\right\} \qquad (2)$$

$$\mathbf{q}^i\left(t\right)=\frac{\gamma^i}{\gamma^{\infty}\tau^i}\int_0^t\exp\left(-\frac{t-s}{\tau^i}\right)\left(\frac{2\partial W^{\infty}\left(\mathbf{C}\right)}{\partial\mathbf{C}}\right)ds \qquad (3)$$

Constitutive parameters identification required the inverse analysis of confined compression tests, considering both hyperelastic and viscous behavior.

Results

Experimental activities allowed to achieve force-time data depending on strain-time setting. Post-processing gave almost equilibrium force-strain data and force relaxation curves (Fig. 1d-e).

Results from mechanical tests showed the typical features of adipose tissues mechanics, as non-linear stiffening with strain and time-dependent response. OA IFP showed major stiffness compared to OA SFP. During the resting period assumed of 300 s, the micro-structural rearrangement phenomena almost completely developed.

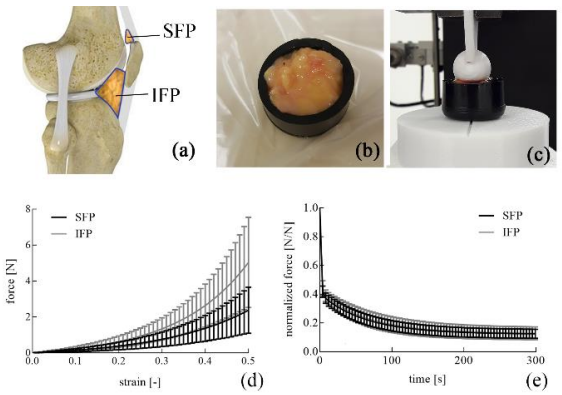

Figure 1: Anatomical localization of IFP and SFP (a). Cylindrical specimen (b) and experimental setup (c) for confined compression tests. Equilibrium force-strain data (d) and normalized force-time (e) (mean and standard error of mean).

Discussion

Experimental results provided the basis for the development of computational tools that will allow investigating the influence of OA on knee mechanics including the presence of IFP and SFP in the knee models. These findings may be of interest during surgical intervention procedures and in the assessment of the possible removal of IFP in case of TKA, in consideration of pain induced by tissue high stiffness. On the contrary, SFP analysis suggested that this fat pad seems not involved in OA, probably due to its localization and physiological function.

References

1. Fontanella, et al.,J Mech Behav Biomed,67:1-9, 2017.
2. Favero, et al., Rheumatology, 56(10):1784-1793, 2017.
3. Fontanella, et al., Annals of Anat, 221:108-114, 2019.

ANTERIOR CRUCIATE LIGAMENT TEAR SIMULATION USING FINITE ELEMENT METHOD

Carla F. Santos (1), Ricardo Bastos (2), Renato Andrade (2), Rogério Pereira (2), Marco Parente (1), João Espregueira-Mendes (2), Renato Natal Jorge (1)

1. INEGI/FEUP- Institute of Science and Innovation in Mechanical and Industrial Engineering, Portugal; 2. Clínica do Dragão, Espregueira-Mendes Sports Centre - FIFA Medical Centre of Excellence, Portugal.

Introduction

The anterior cruciate ligament (ACL) is often injured during sport activities and requires a long time to rehabilitate and not all athletes return to the same level of competition [1]. It is thus important to understand the injury mechanism to implement strategies that aim to decrease the risk of injury and rate of re-tears.
The main objective of the present work is to determine the importance of knee biomechanics in the mechanism of noncontact ACL injury by analysing with finite element method (FEM).

Methods

The knee FEM model used in this work was adapted from the Open Knee project (OKP) [2]. The ACL geometric model was built based in anatomic medical images, including the anteromedial (AM) and posterolateral (PL) bundles inbuilt in the connective tissue. The new ACL developed was assembled with the other structures of the knee in the proper positions of the femoral and tibial insertions (Figure 1). The properties of all structures used in the model are obtained from the literature [3]–[5].

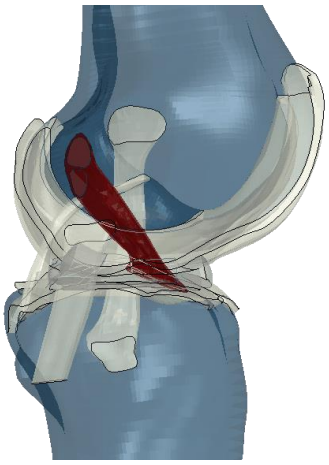

Figure 1: Knee FEM model with the ACL developed highlighted in red.

Once the model was validated, the study was carried out by performing several simulations representing a large set of severe real situations. It included several combinations of tibial rotation, flexion, valgus and axial loads applied to the model in order to evaluate the stress and strain distributions that could lead to ACL injuries.

Results

The peak stress and peak strain of the whole ACL and each bundle (AM and PL) were obtained from all the simulations. The anatomical location where the peak occurs was also identified. The higher stress (11 MPa) and strain (4.8%) values for the different loading conditions tested, were obtained at the AM bundle (Figure 2).

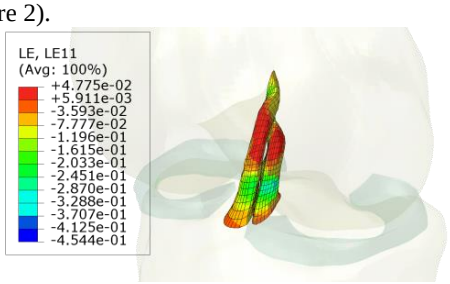

Figure 2: Strain peak in the AM bundle.

Results obtained show that ACL tear is more susceptible to start the damage at the midportion of the AM bundle.

Discussion

The FEM model showed that the ACL tear mechanism is with the knee at valgus, slight flexion, high axial load and tibial external rotation. Interestingly, anterior load displays a low sensitivity in peak ACL stress and strain values during the simulation. Another interesting finding was that there was a significant contribution of axial loads in ACL tear. Most importantly, the external rotation had a superior influence in stress and strain values than internal rotation, which is in line with video analysis studies and against the commonly reported in cadaveric studies.

References

1. C. L. Ardern, N. F. Taylor, J. A. Feller, and K. E. Webster, "Fifty-five per cent return to competitive sport following anterior cruciate ligament reconstruction surgery: An updated systematic review and meta-analysis including aspects of physical functioning and contextual factors," *Br. J. Sports Med.*, vol. 48, no. 21, pp. 1543–1552, Nov. 2014, doi: 10.1136/bjsports-2013-093398.
2. A. Erdemir, "Open Knee: Open Source Modeling and Simulation in Knee Biomechanics," *J. Knee Surg.*, vol. 29, no. 2, pp. 107–116, Oct. 2014, doi: 10.1055/s-0035-1564600.
3. L. Li *et al.*, "Biomechanical analysis of the effect of medial meniscus degenerative and traumatic lesions on the knee joint," *Am. J. Transl. Res.*, vol. 11, no. 2, pp. 542–556, 2019, Accessed: Jul. 15, 2020. [Online]. Available: www.ajtr.org.
4. A. Kiapour, A. M. Kiapour, V. Kaul, C. E. Quatman, S. C. Wordeman, and T. E. Hewett, "Finite element model of the knee for investigation of injury mechanisms: Development and validation," *J. Biomech. Eng.*, vol. 136, no. 1, p. 011002, Jan. 2014, doi: 10.1115/1.4025692.
5. H. Naghibi Beidokhti, D. Janssen, S. van de Groes, J. Hazrati, T. Van den Boogaard, and N. Verdonschot, "The influence of ligament modelling strategies on the predictive capability of finite element models of the human knee joint," *J. Biomech.*, vol. 65, pp. 1–11, Dec. 2017, doi: 10.1016/j.jbiomech.2017.08.030.

Acknowledgements

This work was supported by Arthrex.

A HIGH-RESOLUTION ULTRASONIC APPROACH TO MEASURING INTRA-TISSUE CARTILAGE STRAINS

Maria Pastrama (1), Roy van Hees (2), Isabel Stavenuiter (1), Keita Ito (1), Richard Lopata (2), Corrinus C. van Donkelaar (1)

1. Orthopaedic Biomechanics, 2. Cardiovascular Biomechanics - PULS/e; Department of Biomedical Engineering, Eindhoven University of Technology, The Netherlands

Introduction

Due to its low regenerative potential, local articular cartilage damage may progress into osteoarthritis. Although the exact cause of damage initiation and progression is still unclear, it has been hypothesized that excessive local strain during mechanical overloading is primarily responsible. Correlating locations of excessive strains with damage locations inside the tissue could be an effective approach to test this hypothesis. Nevertheless, determining intra-tissue strains in cartilage is challenging. Existing experimental methods such as Digital Image Correlation (DIC) require a cut surface [1], which may alter tissue structure and deformation behavior. Non-destructive alternatives such as Magnetic Resonance Imaging (MRI) [2] are expensive and restrictive in terms of equipment and resolution. Ultrasound (US) elastography is an affordable, widely available, high-resolution technique, which has been applied and validated for strain determination in tissues such as the heart [3]. This study demonstrates the potential of US elastography to determine the internal strain distribution in articular cartilage during recovery after mechanical loading.

Methods

Osteochondral samples (ca. 1.5 x 1.5 cm^2) were extracted from fresh bovine patellae obtained from an abattoir. Using a hemi-spherical impermeable indenter (R = 2 mm), samples were loaded at 5 mm/min up to 10, 40, or 70 N. After 15 min, the load was removed and samples were translated from the indenter to the US probe using a custom-made sliding panel, such that imaging of strain recovery over time could be performed in the indented area after unloading. Radio frequency (RF) image data were acquired at 37 steering angles with a high-frequency linear probe ('L22-14v', Verasonics, Kirkland, WA, USA; 18 MHz center frequency, 67% bandwidth). Imaging was conducted for 1 h with a frame rate starting at 10 frames/s and decreasing exponentially over time, which resulted in 3600 frames. 1 in 10 frames were selected in MATLAB (MathWorks Inc., Natick, MA, USA) and a region of interest was manually indicated in B-mode images around the indentation zone in the most relaxed cartilage state. The region of interest was meshed using a mesh point distance of 0.2 mm. Starting from the last image, which was considered the unstrained condition, each point was followed over the 360 frames by means of a RF-based speckle tracking algorithm to calculate intra-tissue LaGrangian strains in the axial (indentation) direction [3].

Results

Strain maps show the depth-dependent strain distribution typical for cartilage tissue, with the highest values in the superficial layer below the indenter tip and decreasing values towards the deeper layers (Figure 1). With increasing applied load, the strain magnitude immediately after indentation increased, while the rate and amount of internal strain recovery over time decreased. The average pixel-specific strains in the central region of the samples were -0.39, -0.53 and -0.78 immediately after loading at 10, 40 and 70 N, respectively, and decreased to -0.16, -0.40 and -0.61 after 10 min. The sample compressed at 10 N recovered almost completely after 10 min, while recovery of samples loaded at 40 N and 70 N was not complete after 1 h, which may indicate the presence of tissue damage.

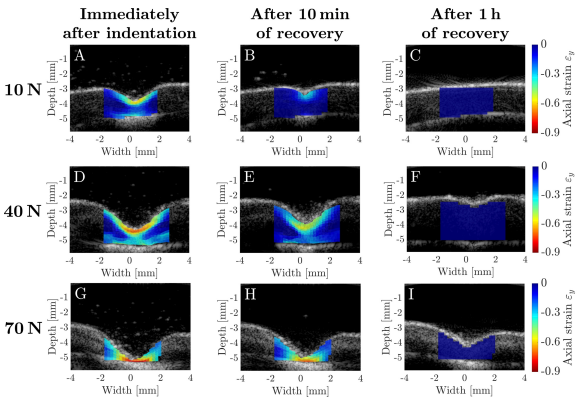

Figure 1: Pixel-specific intra-tissue strain maps.

Discussion

The resulting spatial strain distribution and recovery after various loading regimes demonstrate that high-frequency US imaging and RF-based elastography are very promising for characterization of intra-tissue strains in intact cartilage. With the present approach, the actual tissue strains may be underestimated in case recovery is not complete after the experiment. Furthermore, it is yet unknown whether strain profiles during loading and load-recovery are similar. Therefore, in the future, we aim to develop a technique to determine intra-tissue strains during loading, rather than recovery.

References

1. Lai et al, Osteoarthr Cartil, 18: 1291–1299, 2010.
2. Pastrama et al, J Mech Behav Biomed Mater, 98: 383–394, 2019.
3. Petterson et al, Phys Med Biol, 62: 9112–9126, 2017.

OPTICAL COHERENCE TOMOGRAPHY IMAGING OF SKELETAL MUSCLE FOR MULTISCALE MECHANICAL CHARACTERIZATION

Maxence Maillet (1), Malek Kammoun (1), Jean-François Grosset (1), Stéphane Avril (2), Marie-Christine Ho Ba Tho (1), Olfa Trabelsi (1)

1. Université de technologie de Compiègne, CNRS, Biomechanics and Bioengineering, Centre de recherche Royallieu-CS 60319 -60203 Compiègne Cedex; 2. Center of Health Engineering, Ecole des Mines de Saint-Etienne, CNRS UMR 5307 LGF, Saint-Etienne, France

Introduction

Optical Coherence Tomography (OCT) is a non-invasive optical technique based on the Michelson interferometry principle. OCT measurements can reach 1µm lateral resolution and 2mm in measuring depth and it is the first non-invasive and in-vivo imaging technique that enable to image biological tissue in depth with such lateral solution [1].

To enhance contrast and depth penetration of OCT, optical clearing, which consists of replacing interstitial fluids by an optical clearing agent, can be used on the tissue. Propylene glycol (PG) is an optical clearing agent that has never been used on skeletal muscle, and PG is used for this study.

According to [2], muscle type IID/X fiber is about 63±1.0µm, so that OCT acquisition enhanced with optical clearing might enable to distinguish muscle fibres. This morphological non-destructive imaging technique can be used to perform multiscale mechanical characterization throughout the muscle depth.

Methods

OCT imaging was performed on Extensor Digitorum Longum (EDL) muscle extracted from 6-month-old wistar rats (398±35g). Rats were sacrificed by isoflurane induction followed by exagon injection. Samples were extracted and frozen at -24°C after sacrifice. Before imaging, muscles were thawed overnight at 4°C, and immersed for one hour in a solution of 80% (v/v) PG in Phosphate Buffered Saline. An OCT system (Thorlabs OCT-TEL220C1, central wavelength: 1,300nm, focal length: 18mm, maximum sensitivity range: 111dB at 5.5kHz) was used for imaging. Lateral and vertical resolution were set to 3µm and 2.45µm.

For morphological architecture analysis, EDL muscle, of a wistar rat, was harvested and immediately frozen in an isopentane bath which was cooled by liquid nitrogen to -80°C for histological analyses. 10 µm thick sections were cut parallel and perpendicular to the main axis of the muscle using a cryostat (Cryo-star HM 500, Microm International GmbH, Germany) at -20°C and mounted on glass slides [3]. All sections were stained with azorubine and then visualized under a Leica microscope using a 20× objective, and high-resolution images were acquired with an Olympus cooled digital camera DP-72.

Results

OCT imaging enable to distinguish the different components of muscle and tendon. A similar structure is observed on both OCT imaging and histological observation.

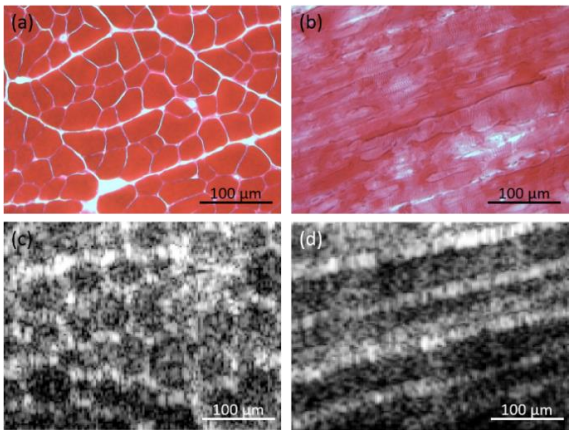

Figure 1: Azorubine staining of rat extensor digitorum longus muscle cross section (a) and longitudinal section (b) compared to OCT acquisition cross section (c) and longitudinal section (d).

To compare structure observed with both imaging technique, fibers diameter has been measured. Mean ± standard variation fiber diameter measured on OCT images is d_{OCT}=45±12µm on that of histological images is d_{hist}=32±7µm. Both are within the same order of magnitude but d_{OCT} is higher than d_{hist}.

Discussion

OCT imaging enable to accurately imaged skeletal muscle structure, which is confirmed by same fibers diameter order values. The difference in diameter is due to different tissue preparation processes for imaging such as tissue clearance for OCT imaging or dehydration for morphological analysis. Image resolution of OCT imaging is also lower than morphological analysis one, which means that measurement is less accurate. To improve this point, our protocol can be use with an OCT which a center wavelength of 900nm to have better lateral resolution and probably thinner details.

However, this technique associated to Digital Volume Correlation can be relevant to study the local mechanical properties of skeletal muscle [4].

References

1. J. G. Fujimoto et al, Neoplasia, 2(1-2):9-25, 2000
2. M. D. Delp et al, J. Appl. Physiol., 80(1):261-270, 1996.
3. M. Kammoun, et al, Eur. J. Histochem., 58(2):163–168, 2014.
4. V. A. Acosta Santamaría, Front. Mech. Eng. 4:1-14, 2018.

NANOINDENTATION OF PDMS SUBSTRATES WITH TUNABLE STIFFNESS FOR CARDIAC MECHANOBIOLOGY INVESTIGATIONS

Gianpaolo Serino (1), Giacomo Bernava (2), Tancredi Lugas (1), Stefano Gabetti (1), Fabrizia Midei (1), Mara Terzini (1), Umberto Morbiducci (1), Alberto Audenino (1), Maurizio Pesce (2), Diana Massai (1)

1. Polito^{BIO}Med Lab, Department of Mechanical and Aerospace Engineering, Politecnico di Torino, Italy; 2. Centro Cardiologico Monzino, Italy

Introduction

Mechanical cues play a continuous, crucial regulatory role in growth, maintenance, and pathophysiology of cardiac tissue [1]. Thus, for studying *in vitro* cardiac cell mechanobiology, it is fundamental to use substrates that mimic the mechanical properties of the native environment. Here, specific polydimethylsiloxane (PDMS) blends with tunable stiffness [2], to be used as model substrates for cardiac mechanobiology investigations, were prepared. By allowing investigations at typical cell-length scales and applying small forces suitable for soft materials, nanoindentation was used to mechanically characterize PDMS blends in physiological conditions (wet conditions, 37°C).

Methods

PDMS substrates with tunable stiffness were prepared using pure Sylgard 184 and Sylgard 527 (Dow Corning, USA). Five different Sylgard mass ratios 184:527 (1:10, 1:20, 1:30, 1:50, 1:100) were blended. PDMS blends were poured into 50 mm diameter petri dishes (cured at 65°C) to create ~3 mm thick films for mechanical testing. The procedure was repeated in three different days producing three lots (seven specimens per lot) for checking the manufacturing reproducibility. Indentation of the specimens, immersed in demineralized water at room temperature (RT) or at 37°C, was performed in displacement-control (indentation depth = 2 µm, cantilever stiffness = 4.4 N/m for Sylgard 184, 0.5 N/m for the other specimens) using the PIUMA nanoindenter (Optics11, NL), which automatically provided the load-indentation curves and their respective elastic modulus (E) values (Hertz model fitting). Each PDMS specimen was indented in three different regions (5x5 points, step size = 50 µm). Three different indentation rates (v_1 = 1 µm/s, v_2 = 10 µm/s, v_3 = 50 µm/s) were set to investigate the viscoelastic response of the specimens. Preliminary indentation tests were performed on bovine myocardium. The specimen (~3x3x0.5 cm^3), immersed in demineralized water at 37°C, was indented in a central region (5x5 points, step size = 100 µm) in displacement-control (indentation depth = 4.5 µm, cantilever stiffness = 0.5 N/m, indentation rate = 2 µm/s). Statistical analysis of variance was performed to assess the impact of manufacturing, temperature and indentation rate on PDMS E values ($p < 0.05$).

Results

No statistical difference emerged among PDMS lots in terms of elastic modulus, proving the reproducibility of the manufacturing. Considering specimens with decreasing mass ratio of Sylgard 184 with respect to Sylgard 527, the average of the measured E values (setting v_1) ranged from 1.80±0.09 MPa to 10.25±2.76 kPa when tested at RT, and from 1.44±0.13 MPa to 10.87±1.47 kPa when tested at 37°C (Fig.1). Interestingly, 1:100 blends matched the E values of healthy cardiac tissue (10-15 kPa), while 1:20 and 1:10 blends matched the E values of fibrotic tissue (20-100 kPa) [3]. Increasing the indentation rate, the measured E values significantly increased, confirming the viscoelastic behavior of PDMS. For preliminary tests on bovine myocardium, the average of the measured E values (11.76±2.81 kPa) was in agreement with literature data for normal heart muscle.

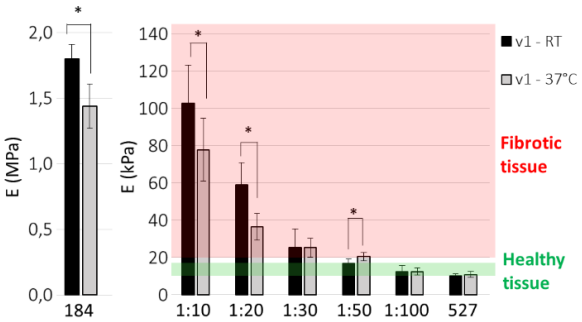

*Figure 1: Average elastic modulus values measured for all PDMS specimens at RT and at 37°C (v_1 = 1 µm/s). The elastic modulus ranges reported in literature for healthy (10-15 kPa, green band) and fibrotic (20-100 kPa, red band) cardiac tissue are shown [3]. * $p < 0.05$.*

Discussion

The findings support the use of specific PDMS blends as model substrates for mimicking *in vitro* the mechanical properties of physiological or pathological cardiac tissue. Interestingly, it emerged that the testing temperature has an effect on PDMS mechanical properties, in particular for blends stiffer than 30 kPa. To our knowledge, this is the first systematic attempt to characterize at typical cell-length scale and in physiological conditions the mechanical properties of specific PDMS blends for mechanobiology applications.

References

1. Zhu et al, Stem Cell Res Ther, 5(5):117, 2014.
2. Palchesko et al, PloS one, 7(12):e51499, 2012.
3. Van Putten et al, J Mol Cell Cardiol, 93:133-142, 2016.

INDENTATION METHOD USING SPHERICAL INDENTERS. DETERMINING THE ERRORS WHILE USING HERTZ EQUATION

Stylianos-Vasileios Kontomaris[1], Anna Malamou[2], Andreas Stylianou[3,4]

1.Athens Metropolitan College, Greece; 2. National Technical University of Athens, Greece; 3. University of Cyprus, Cyprus 4. European University Cyprus, Cyprus

Introduction

Hertzian analysis is probably the most widely used theory regarding data processing in nanoindentation experiments on biological samples [1]. However, there are significant limitations that should be taken into account. For example, Hertz equation assumes a parabolic indenter; however, in practice spherical nano- or micro -indenters are usually employed. Thus, there is a limitation regarding the maximum indentation depth in order to apply the Hertz equation for data fitting. Despite the fact that an analytical solution is available (Sneddon's analysis) [2], the related equation does not directly correlate the applied force on the sample with the indentation depth. As a recent advance, a new equation was developed for the aforementioned purpose [3]. Thus, in this paper the results as provided by the Hertz equation are compared to the results acquired using the accurate solution for spherical indenters to provide a conclusive result regarding the maximum indentation depth that it is valid to employ Hertzian analysis.

Hertzian analysis and spherical indenters

The equation that was initially derived by Hertz correlates the applied force (F) to the indentation depth (h) as follows:

$$F_{par.} = \frac{4}{3}\frac{E}{(1-\nu^2)}R^{1/2}h^{3/2} \qquad (1)$$

In Eq. (1), E, ν are respectively the sample's Young's modulus and Poisson's ratio and R is the indenter's radius. The accurate equation that describes the force-indentation data using a spherical indenter is presented below [3]:

$$F_{sph.} = \frac{4ER^{1/2}}{3(1-\nu^2)}h^{3/2}Z \qquad (2)$$

In Eq. (2), factor Z equals to [3]:

$$Z = c_1 + \sum_{M=2}^{N}\frac{3}{2M}c_M R^{(\frac{3}{2}-M)}h^{M-3/2} \qquad (3)$$

In Eq. (3), the factors $c_1, c_2, \dots, c_N$ and N depend on the indentation depth. For example, the aforementioned values at the domain $0 \le h/R \le 0.6$ (which is a typical domain in indentation experiments on biological samples) are equal to $c_1 = 1.0100$, $c_2 = -0.0750$, $c_3 = -0.1142$, $N = 3$ and $c_1 \ge Z \ge 0.9392$.

Determining errors

If the data is fitted to equation $F = ah^{3/2}$, then $a = \frac{4ER^{1/2}Z}{3(1-\nu^2)}$ and the fitting parameter that is determined is $b = EZ$. Thus, the errors arising from a parabolic approximation will be calculated using the following parameter:

$$\pi(\%) = \frac{E-b}{E}100\% = (1-Z)100\% \qquad (4)$$

The results are presented at the domain $0.05 \le h/R \le 0.6$ (Fig.1).

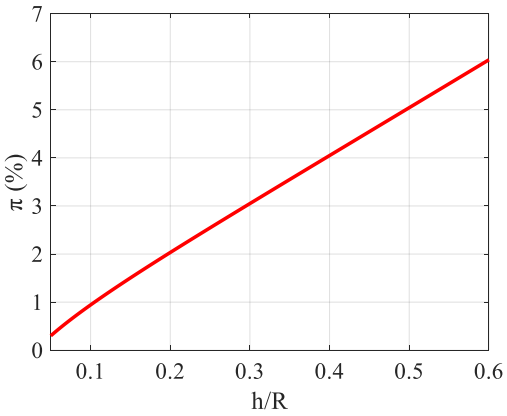

Figure 1: The error of using Hertzian equation for spherical indentation.

As it can be clearly seen in Fig.1 if $h/R \le 0.1$ the error in Young's modulus determination is less than 1%. On the contrary, for $h/R = 0.6$ the resulting error is ~ 6%.

Discussion

Hertz equation can be used for spherical indentations only in the domain $0 \le h/R \le 0.1$. This result is consistent with empirical suggestions in the literature regarding the maximum indentation depth that can be used in spherical indentations on biological samples[4].

References

1. Krieg M et al, Nat. Rev. Phys., 1, 41-47, 2019.
2. Sneddon I N, Int. J. Engng Sci., 3, 47-57, 1965.
3. Kontomaris S V et al, Eur. J. Phys. (in press), doi.org/10.1088/1361-6404/abccfb
4. Radmacher M, Methods Cell Biol., 83; 347-372, 2007.

MECHANICAL CHARACTERISATION OF PANCREATIC TISSUE: PRELIMINARY IN-VITRO RESULTS

Francesco De Gaetano (1), Gennaro Nappo (2), Giovanni Capretti (2,3), Alessandro Zerbi (2,3), Maria Laura Costantino (1)

1. Politecnico di Milano, Milan (ITALY); 2. IRCCS Humanitas – Pancreatic Surgery, Milan (ITALY) 3. Hunimed, Humanitas University

Introduction

Pancreatic cancer is the fourth cause of death from cancer worldwide and surgical resection, when feasible, is the only curative treatment. Pancreatic fistula is a treacherous postoperative complication with a rate of 10-20%. Pancreatic fistula is strongly related to pancreatic parenchyma consistency and structure. There is a lack of knowledge about the mechanical and chemical properties of pancreatic tissue. Therefore, the aim of this project is to investigate the porcine pancreatic parenchyma characteristics towards the definition of a standardized method also suitable for human pancreas in order to obtain the needed parameters to build up a pancreas phantom, a device not yet available and fundamental to improve surgical techniques and training programs in this field of surgery.

Methods

All the samples tested in this work come from porcine pancreas provided by a slaughterhouse. Cylindrical samples (d= 10.91 ± 0.33 mm, h = 4.16 ± 1.08 mm) were cut to perform unconfined compression (stress-relaxation) tests while dog bone specimens (l_0 = 31.54 ± 6.79 mm, w_0 = 4.16 ± 0.32 mm, h_0 = 2.87 ± 0.76 mm) were obtained to perform uniaxial tensile tests. Each specimen was withdrawn from a different lobe of the gland, and all the tests were performed using the MTS Synergie 3200H test machine. Compression experiments were performed using a displacement-controlled protocol (8 steps each one made by 5% deformation) while tensile tests were conducted by imposing strain rate from 3 to 200 mm/min. The stress-strain relationship was obtained, and the elastic modulus was determined. Further tests will be performed using the Anton Paar Bioindenter.

Results

After each stress-relaxation test, ten parameters Prony series were used to well fits results data. Frozen and fresh tissue were analyzed in order to investigate if the conservation method could influence the mechanical properties. According to preliminary results, freezing increases the elastic modulus at both small and large deformations (Fig. 1). Tensile tests were performed at several strains rate and the elastic modulus evaluated at small deformation (ε=0-0.03) is higher than the elastic modulus evaluated at large deformation (ε=0.06-0.08) (Fig. 2 and Fig. 3)

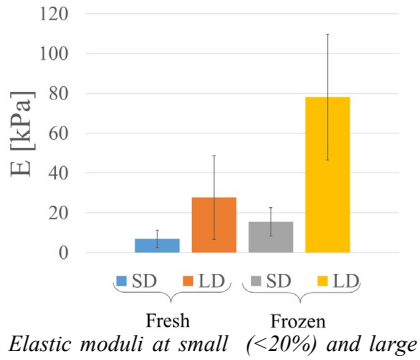

Fig. 1 Elastic moduli at small (<20%) and large (>20%) deformations (SD and LD respectively) for frozen and fresh pancreatic tissues obtained from compression tests.

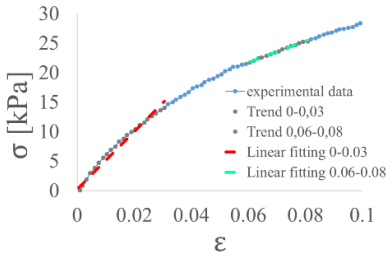

Fig. 2 Stress-strain relationship from tensile test, highlighting the regions where E1 and E2 are evaluated.

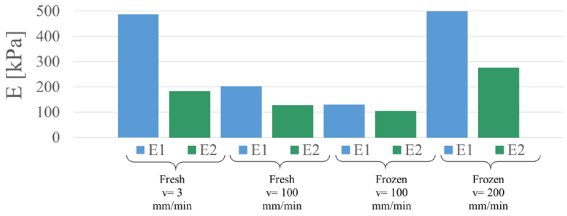

Fig. 3 Elastic moduli E1 (small deformation) and E2 (large deformation) for frozen and fresh pancreas under uniaxial tensile test at different velocities.

Discussion

This work demonstrates that porcine pancreatic tissue has a viscoelastic behaviour like the other abdominal organs (e.g: liver, kidneys, spleen). Further tests should be performed on each pancreatic lobe to assess either a peculiar behaviour of each lobe or heterogeneous properties of the whole gland. This method seems appropriate for the mechanical characterization of the porcine pancreas and could also be applied to the human pancreas, in order to obtain all the needed parameters to build up a pancreas phantom.

ARTICULATING SURFACE PROPERTIES OF THE BOVINE ACETABULAR LABRUM

Matthias X. T. Santschi (1), Stephanie Huber (1), Simon Künzli (1), Casimir Schwank (1), Michael Leunig (2), Stephen J. Ferguson (1)

1. ETH Zurich, Institute for Biomechanics, Zurich, Switzerland
2. Schulthess Clinic, Department of Orthopedic Surgery, Zurich, Switzerland

Introduction

Robust tribological properties of articulating surfaces are essential for the preservation of joint function. In hip joints, the femoral head interacts with an articulating surface that comprises the cartilage of the acetabular socket and the inner surface of the acetabular labrum [1]. While cartilage tissue has been extensively studied, the surface properties of the acetabular labrum remain largely unknown [2]. The purpose of this study was to examine the labrum surface friction, microstructure, and the presence of a lubricating glycoprotein (lubricin).

Methods

Friction. In order to measure and compare the coefficient of friction (COF), cylindrical labrum, cartilage and meniscus samples (n=6 each) with a diameter of 6 mm were loaded using a rotating stainless steel pin with a defined pressure of 0.6 MPa at a rotational speed of 135 RPM. The COF was derived from the recorded normal force and torque using Eq. 1, with μ being the COF, τ the torque and F_N the normal force acting on the tissue surface. Finally, a one-way ANOVA with Tukey post-hoc test was performed.

$$\mu = \frac{3 \times \tau}{2 \times F_N \times r} \quad (1)$$

Microstructure. The microstructure of aldehyde and osmium tetroxide fixed labrum surfaces was characterized using scanning electron microscopy (Hitachi, Japan).

Lubricin. Formalin-fixed paraffin-embedded tissue sections were immunohistochemically stained using a purified mouse monoclonal IgG primary antibody to lubricin and a Novolink Polymer Detection System Kit (Leica, Germany). Cartilage tissue specimens were used as a positive control.

Results & Discussion

The COF between the steel pin and the labral, cartilage and meniscus surfaces were found to be 0.15 ± 0.029, 0.22 ± 0.027 and 0.20 ± 0.026, respectively. To validate our custom-built device, we compared our measured COF between a steel pin and cartilage surface to results reported in the literature [3] and found good agreement. The COF from labral samples were found to be in a similar range to values reported for cartilage and significantly lower compared to meniscus tissue.

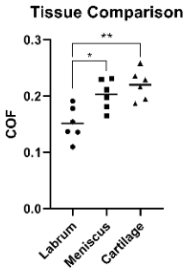

Figure 1: Coefficient of friction of labrum, cartilage and meniscus.

The labral surface microstructure shows a typical mesh-like architecture, as seen in other articulating tissues [2]. In line with recent findings in the human labrum [4], lubricin (Proteoglycan 4) was identified in the bovine labrum as a discrete layer on the tissue surface, within the superficial extracellular matrix, and intracellularly in all regions. This is similar to observations in cartilage and meniscus tissue, indicating that lubricin plays a role in the tribology of these tissues.

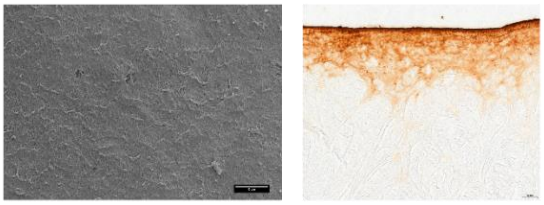

Figure 2: SEM image of the articular surface of the labrum (left) and IHC staining of lubricin in acetabular labrum tissue (right).

The characterisation of the surface properties of labral tissue provides new insight into the normal mechanics of healthy tissue, possible pathomechanisms of degradation, and target properties for regenerative medicine approaches.

Acknowledgment

Funded by Swiss National Science Foundation (205321-176023)

References

1. Tan, V. et al. (2001) American journal of orthopedics (Belle Mead, NJ), 30(11), 809-812.
2. Boettcher, K. et al. (2016) Acta biomaterialia, 29, 180-187.
3. Schmidt, T. A. (2007) Arthritis & Rheumatism, 56(3), 882-891.
4. Zhang, D. et al. (2012). Cartilage, 3(2), 165-172.3(2)

THE BIOMECHANICS OF BEING BORN: CHARACTERISING OVINE PELVIC TISSUES

Harte, K (1), Lennon, A.B.(2), Menary, G (3).
School of Mechanical and Aerospace Engineering, Queen's University Belfast, Northern Ireland

Introduction

The pelvic muscles undergo a degree of stretch in less than 2 hours during childbirth unparalleled elsewhere in the body.[1] This can lead to significant injury in the vagina (VA) and levator ani muscle (LA).[2,3] The LA makes up most of the pelvic floor, creating a sling spanning the pelvic cavity, acting against gravity to provide support to the pelvic organs. Up to 20-30% of women over the age of 20yrs and up to 50% over 50[4] may suffer from pelvic floor disorders. Studying the complicated mechanics of childbirth has moved towards computational models. However, these have been limited by a lack of accurate anisotropic and time-dependent mechanical properties. This research aims to address this gap in understanding by developing a novel test platform for multiaxial static and viscoelastic characterisation of pelvic floor tissues.

Materials and methods

A radial stretcher specifically adapted for soft tissue was designed and built, based on a concept by Schauberger et al.[5] Two cameras were incorporated for imaging failure during tests and enabling digital image correlation, which was used to verify suitability of grip-to-grip displacements for calculating specimen strains (Fig 1A). Three 100 N load cells were placed on three of the eight arms, 45^0 apart, accounting for load in X, R, Y directions (Fig. 1A,B). An environment chamber to hold samples in phosphate buffered solution at 37^0C was also fabricated. Custom velcro-lined grips with a pin and spring-loaded clamp were developed to overcome challenges in gripping specimens. Ovine VA and LA muscles from six sheep (due to similar dimensions and three-level support system to humans) were dissected and removed of all connective tissues. Uniaxial samples (Figs. 1C,E) were cut in fibre (FD) and cross-fibre directions (CF) for the LA (aligned with X and Y directions resp.) and in longitudinal (LD) and circumferential directions (CD) for the VA (X and Y directions resp.) measuring 20mm x 4mm. Radial samples were cut with diameter 20mm. Both tests were carried out at 6 mm/min following 10 preconditioning cycles. A series of ramp and hold tests were carried out to measure stress relaxation in both uniaxial and radial format. Uniaxial tests had 5 steps, with strain increasing by 5% in each step. For radial tests, however, only 2 steps could be achieved in four samples due to frequent failures after the second step.

Results and Discussion

Both tissues were stiffer in the Y direction and softer in the X (Fig. 1D,F). The influence of fibre direction was less evident in the uniaxial tests for LA compared with radial tests (Fig. 1D), which could be due to difficulty obtaining samples with a single dominant FD, small specimen sizes, and dispersion of fibre angles.

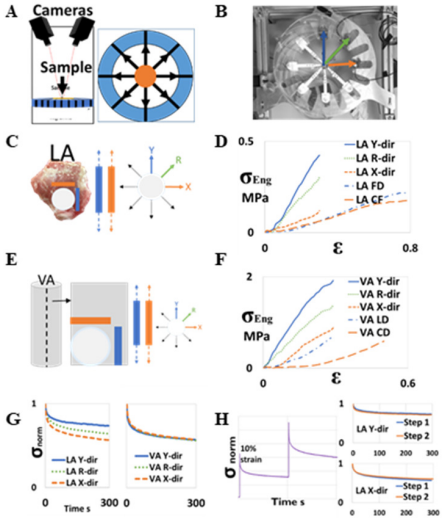

Figure 1: (A) Adapted radial rig. (B) Load cell locations. (C) LA muscle samples for radial and uniaxial in FD and CD direction. (D) Average curves of engineering stress vs strain for both LA failure tests. (E) VA muscle samples for both tests. (F) Average curves of engineering stress vs strain for both VA failure tests. (G) Normalized stress vs time for LA & VA radial relaxation test. (H) Normalized stress vs time for LA radial relaxation test, comparing steps 1 &2 in X & Y directions.

Radial relaxation tests in LA tissues illustrated the influence of directionality in its response: least relaxation in the Y (FD) and most in the X (CF) directions (Fig. 1G). However, VA tissues showed no directional dependence (Fig. 1G). The multiaxial relaxation tests showed little or no change in normalised relaxation rate when the strain was increased for either tissue in all directions, indicating the viscous response can be treated as strain-independent (1H). In conclusion, the accumulated data adds important new information on the anisotropic and viscoelastic properties of pelvic floor tissues, demonstrating both tissues exhibit anisotropic hyperelastic and mostly isotropic quasilinear viscoelastic (QLV) responses (although some directional dependence was observed in LA stress relaxation). Ongoing work will fit a fibre-reinforced hyperelastic model with QLV to the dataset.

References

1. Tracey et al., 2018, J Mech Behav Biomed Mater, 79, 213-218
2. Boyles et al, *AJOG*, *188*(1), 108–115 (2003)
3. Subak et al, Obstet. Gynecol, 98(4), 646–651.
4. Wilson et al,. Obstet. Gynecol. 2001; 98:398–406
5. Schauberger et al., IEEE-Acess (2015)-3, pp. 556-561.

BIOMECHANICS OF FIBROUS LIGAMENTOUS TISSUES: VOLUMETRIC ANALYSIS OF MICROSTRUCTURE UNDER INCREASING STRAIN

G. Marchiori (1), G. Cassiolas (2), N. Sancisi (3), M. Berni (1), M. Conconi (3), S. Zaffagnini (1), M. Fini (1), N.F. Lopomo (2) and A. Parrilli (4)

1. Rizzoli Orthopaedic Institute, Bologna, Italy
2. University of Brescia, Department of Information Engineering, Brescia, Italy
3. University of Bologna, Department of Industrial Engineering, Bologna, Italy
4. Empa, Center for X-ray Analytics, Überlandstrasse 129, Dübendorf (Switzerland)

Introduction

Recently, an advanced experimental procedure has been proposed to highlight the close relationship existing between structure and function in fibrous materials [1], specifically focusing on Anterior Cruciate Ligament (ACL) tissue. A micro-CT system embedding a custom tensioning device was specifically used to acquire the fibrous tissue volume at the micro-scale, considering several levels of strain (i.e. 0÷8%); a biochemical contrasting process optimized fiber visualization and tissue mechanics preservation. After those experimental acquisition sessions [1], this study focused on image data processing and analysis, to identify "fiber" objects, hereinafter called fibers, and estimate mechanical properties, including their mean elastic modulus.

Methods

One healthy ACL sample (H) harvested from a cadaver donor (age 40) was compared to a sample (OA) coming from a patient (age 69), who underwent total knee arthroplasty (ethics committee n.8425). Image processing and analysis included: *1*) defining the region of interest on the central portion of the tensioned sample, thereby excluding clamping distortion; *2*) binarizing the dataset using Niblack local thresholding algorithm (*ImageJ)* and separating the resulting objects combining watershed, distance map and H-Maxima methods (*Avizo)*, as to reveal individual fibers; *3*) calculating for each fiber *i* the mean cross-sectional area A_i, volume V_i and orientation with respect to the loading axis θ_i (*Figure 1*, *CTAn)*; *4*) excluding objects with $V_i < 0.125$ mm^3 to eliminate artefacts; *5*) estimating the experimental stress *F/A* acting on samples, where *F* is the applied load and *A* is the area obtained by summing A_i of all fibres; *6*) modelling the stress σ starting from the analysis reported in [2] applied on a discrete domain:

$$\sigma(\lambda) = 2\pi\lambda^2 E_f \sum_{1}^{N} v_f(\theta) R(\theta) \left(1 - \frac{1}{\lambda_f(\theta)}\right) sin\theta cos^2\theta \Delta\theta \qquad (1)$$

where λ is the tissue finite strain; E_f is the mean fiber elastic modulus and the only unknown parameter; 1:N are the number of orientation (θ) intervals that span from 0 to $\pi/2$ with dimension $\Delta\theta$ and in which θ_i are distributed; $v_f(\theta)$ are the corresponding volume fractions (thus weighting the orientation contribution of fibers by their volume with respect to the total tissue volume); $R(\theta)sin\theta\Delta\theta$ results to be the angular frequency on the N intervals [3] and $\lambda_f(\theta)$ is the fiber strain, calculated as:

$$\lambda_f(\theta) = (\lambda^2 cos^2\theta + \frac{1}{\lambda} sin^2\theta)^{\frac{1}{2}} \qquad (2)$$

7) obtaining E_f by fitting (1) to experimental $F(\lambda)/A(\lambda)$.

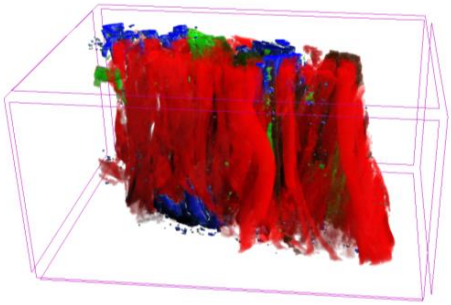

Figure 1: Fiber orientation θ intervals, where red is 0° and blue 90° with respect to the loading axis.

Results

For the sake of brevity, by assuming N=10, E_f resulted 502.6 MPa and 2.9 MPa for H and OA, respectively. A further sensitivity analysis regarding N, as well as the volume of excluded objects, is ongoing.

Discussion

Healthy ACL showed a far higher resistance to deformation with respect to the pathological one. Histology degenerations are expected in OA ACL, which can influence ligament biomechanics [4]. The implemented experimental and modeling procedure can highlight the constitutive and structural components of fibrous tissue behavior and can be useful for testing physiopathological and artificial tissues.

References

1. G. Marchiori et al, *Mater Today-Proc*, 7: 501-507, 2019.
2. C. Hurschler et al, J Biomech Eng, 119:392-399, 1997.
3. T. Mishurova et al, *Int J Eng Sci*, 122:14-29, 2018.
4. M. A. Mont et al, *J Arthroplasty*, 31:284-289, 2016.

Acknowledgements

This study was supported by the "5x1000 2020" funding, provided by Istituto Ortopedico Rizzoli, Bologna (Italy) and by the project GR-2011-02351803 funded by the Italian Ministry of Health.

IN VIVO MECHANICAL CHARACTERIZATION AND TISSUE-SCALE MODELLING OF KELOID AND SURROUNDING HEALTHY SKIN

Aflah Elouneg (1), Audrey Bertin (1), Nicolas Marie (2), Quentin Lucot (1), Danas Sutula (1), Franz Chouly (2), Arnaud Lejeune (1), Thomas Lihoreau (3), Brice Chatelain (4), Gwenaël Rolin (3,5), Stéphane P.A. Bordas (5), Emmanuelle Jacquet (1), Jérôme Chambert (1)

1. Univ. Bourgogne Franche-Comté, FEMTO-ST Institute, Department of Applied Mechanics, CNRS/UFC/ENSMM/UTBM, Besançon, France; 2. Univ. Bourgogne Franche-Comté, Institut de Mathématiques de Bourgogne, Dijon, France; 3. INSERM CIC 1431, CHU Besançon, F-25000 Besançon, France; 4. Service de Chirurgie Maxillo-faciale, Stomatologie et Odontologie Hospitalière, CHU Besançon, F-25000 Besançon, France; 5. Univ. Bourgogne Franche-Comté, INSERM, EFS BFC, UMR1098, RIGHT Interactions Greffon-Hôte-Tumeur/Ingénierie Cellulaire et Génique, F-25000 Besançon, France; 6. University of Luxembourg, Institute of Computational Engineering, Luxembourg

Abstract

Keloids are fibrous benign tumors of the human skin caused by cutaneous trauma. They grow on some specific anatomical sites (arm, abdomen, sternum, *etc.*), subjected to natural mechanical load due to peripheral stress of the tissue and to repeated postures, or to anatomical singularities [1]. Genetic, biological and mechanical factors have an important impact on the occurrence and the propagation to theses tumors. A tight collaboration between researchers from clinical science, biology, mechanics, mathematics and computational mechanics, has been established to analyze and understand the mechanical effects on theses cutaneous alterations. Starting from a multimodal investigation on a patient, a numerical pipeline consisting of several open-source frameworks has been developed leading to stress field analysis in a domain composed of a keloid and surrounding healthy skin. The main objective through this methodology is to conceive specifications of a customized medical device to confine keloid growth or prevent against its growth (Figure 1). In this congress, the experimental and computational contributions of this project achieved at that time are presented as follows : (i) Mechanical characterization with extensometer [2] and ring suction tests [3] combined to medical imagery technique, (ii) Bi-material parameters identification via inverse method of healthy and pathological soft tissues from *in vivo* uniaxial test coupled with digital image correlation and finite elements model (FEniCS-based open-source framework) [4], (iii) Mechanical analysis of multiaxial test of ring suction using digital image correlation to characterize the anisotropy of the skin [5], (iv) Mesh optimization by error estimators [6] applied to a heterogeneous soft tissue, (v) Uncertainties quantification associated with mechanical and topological parameters of 2D and 3D models. The summary of these works in tissue-scale is part of a global project of multi-scale modelling and analysis of mechanical factors influencing the fibroproliferative cellular kinetics.

References

1. Ogawa, Med Hypotheses. 71:493-500, 2008.
2. Chambert et al, J Mech Behav Biomed Mater, 99:206-215, 2019.
3. Elouneg et al, Comput Methods Biomech Biomed Eng, 23:99-100, 2020.
4. Sutula et al, J Mech Behav Biomed Mater, 112:103999, 2020.
5. Rosado et al, Skin Res Technol, 23:429-436, 2017.
6. Duprez et al, Appl Math Model, 77:209-723, 2020

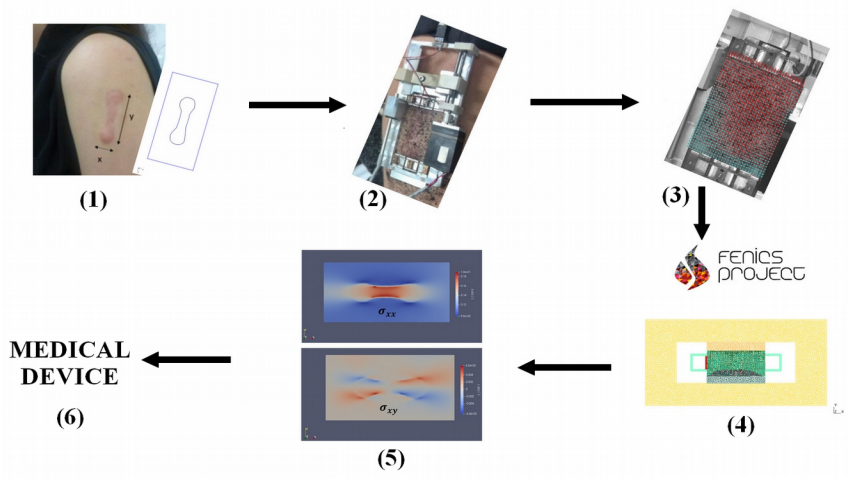

Figure 1: Numerical pipeline: from patient to medical device. (1): Keloid modelling. (2) Uniaxial extensometer test. (3) Digital Image Correlation. (4) Finite Element Model Updating to identify material parameters. (5) Stress field quantification. (6) Medical device to prevent against keloid growth.

Characterization of Viscoelastic Properties of Synthetic Graft Materials and Aortic Tissue using Hysteretic Methods

Rosaire Mongrain (1), Christopher Zikry (1), Stewart McLennan (1), Richard Leask (2), Raymond Cartier (3), Gilles Soulez (4)

1. Mechanical Engineering, McGill, Canada; 2. Chemical Engineering, McGill, Canada; 3. Department of Surgery, University of Montreal; 4. Department of Radiology, University of Montreal

Abstract

In this work, we present the elastic and viscoelastic characterization of aortic tissue and synthetic materials used for the design and fabrication of artificial vessels (Dacron, hydrogels). The materials were characterized using hysteretic methods and a quasi-viscoelastic model. Hysteretic methods are shown to be practical and robust to differentiate the materials. Significant differences in viscoelastic properties are reported between the biological and the synthetic materials

Introduction

Vascular grafts are implanted in the human body in order to replace damaged or blocked vessels [1]. The design of synthetic grafts began in the 1940s [1]. In the 1950s, the concept of porous, fabric vascular grafts were introduced. By the 1960s, most fabrics were abandoned except for Dacron and Teflon. Prosthetic Dacron grafts are widely used as a synthetic substitute following aortic resection. While these polyester grafts are readily available, durable, and biocompatible, they exhibit mechanical properties inconsistent with native aortic tissue. Indeed, aortic tissue which reflects a strong viscoelastic nature [5] was shown to play a key role for the proper functioning of vascular structures (Windkessel effect, pulse traveling wave [3]). For designing the next generation of grafts, the assessment of the needed viscoelastic properties is required.

Methods

Dacron samples were cut from a commercial graft (Hemashield Platinum, MAQUET Cardiovascular LLC). The hydrogel samples (PVA) were prepared using freezing-thawing cycles of a PVA solution 10% (weight) concentration with temperature plateaus at -20°C and 20°C and the tissue samples were obtained from resections. The samples were fastened to an EnduraTEC Electro Force ELF 3200 Biaxial Tensile Tester (TA Instruments). The tests were performed on patches of 15×15 mm^2 affixed with four silk surgical threads with adjusted suture hooks. Equi-biaxial loading-unloading cycles are performed to 60% strain at 0.1 mm/s strain rate.

It can be shown that for a Kelvin-Voigt viscoelastic material, the complex modulus of elasticity is $E^*=E+i\omega\mu$ with E and μ the elasticity and viscosity respectively. Graphically the corresponding hyteresis, on the stress-strain curve, can be approximated with an ellipse with a semi-minor axis b=D/2 (D the width between the loading and unloading curves) from which the viscosity is $\mu=S/(\pi(\omega\varepsilon^2))$. The energy loss is the elliptical hysteretic area $W_d=\pi\mu(\omega\varepsilon^2)$, with ω the heart beat frequency and ε the strain. The elasticity E corresponds to the (global inclination) slope of the ellipse. We recently investigated the loss factor and have shown its capacity to differentiate human aortic tissue [2, 4, 5]. Samples were also studied with the Fung's Quasi-Linear Viscoelastic model.

Results

In Figure 1, we illustrate the results for the stiffness (incremental modulus) at 15% and the viscoelasticity characterization assessed with the energy loss. They are shown for healthy aortic tissue, PVA and Dacron.

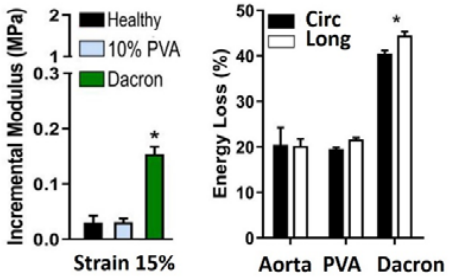

Figure 1: Stiffness and energy loss for aortic tissue, PVA and Dacron

Discussion

One can note the significant differences between the polyester graft material and the soft vascular tissues and the similitude between the aortic tissue and the hydrogel. The correspondence between the methods shows that the hysteretic methods allow to estimate viscoelastic properties from the stress-stretch results and can differentiate the materials. It can serve as a tool to support the design of the next generation of grafts.

References

1. Puskas JE el al, Biomacromolecules. 5(4):1141-54, 2004
2. Shahmansouri N et al, Materials 2016; 9:867
3. Valdez-Jasso D et al, Ann Biomed Eng. 39(5):1438-56, 2011
4. Shahmansouri N et al, J Mech Behav Biomed Mater 2016;64:262-71
5. Alreshidan M et al, J Thorac Cardiovasc Surg 2017;153:781

Acknowledgements

This work was supported by a NSERC grant.

A TORSIONAL WAVE SENSOR FOR MEASURING THE ANISOTROPY OF SOFT TISSUE IS FINALLY REAL

Inas H Faris (1,2), Jorge Torres (1), Antonio Callejas (1,2), Juan Melchor (2,3,4), Guillermo Rus(1,2,3)

1. Ultrasonics Lab, Dept. Structural Mechanics, University of Granada; 2. Instituto de Investigación Biosanitaria, ibs.GRANADA, 18012 Granada, Spain; 3. Excellence Research Unit "Modelling Nature" (MNat) University of Granada, Granada, Spain 4. Department of Statistics and Operations Research, University of Granada, 18071 Granada, Spain;

Introduction

Since most soft tissue is anisotropic[1], it is quite interesting to quantify the tissue's mechanical properties in different directions regarding its fiber orientation. Considering that it has been affirmed that the mechanical biomarkers differ significantly regarding the direction in which the tissue is measured [2,3].

Estimation of the mechanical biomarkers can only be done in one direction at the time. The experimental evidence comes from traditional tensile studies on histological sections that follow the direction of fibers.

To the best of our knowledge, no commercial device can measure tissue anisotropy. Interestingly, our group has developed a torsional wave sensor that emits and receives torsional waves, whose main advantages are the absence of spurious longitudinal waves and a right safety margin since the projected This new TW technique is applied using three independent piezoelectric elements made from PZT ceramic (NCE51), allowing the device to quantify the shear modulus in three different directions. There are three slots arranged to form 0, 90 and 225 degrees, aiming to measure parallel to a selected fiber direction, perpendicular to it and an intermediate orientation, respectively. The sensor is built considering three distinct parts: excitation, reception and casing.

Methods

Scans were done using Torsional Wave Elastography (TWE) technique with the proposed anisotropic probe. Scans were done on cirs phantoms, homemade tissue-mimicking anisotropic phantoms with a fiber arrangement (3D printed) similar to that of the cervix. In addition to *ex vivo* chicken breast and three *ex vivo* human cervix samples obtained from hysterectomies due to prolapses. Figure 1 shows the TWE-anisotropic probe.

Results and discussion

The preliminary results are promising; the transducer can capture the biomechanical properties in different tissue areas. Some of the results are shown in Tables 1 and 2. From tables 1 and 2, one can observe the difference in the stiffness values obtained from the three sectors of the torsional wave probe. In table 1, the probe sector at 0º, that is, parallel to the fiber orientation of the breast fibers returns higher values of stiffness as expected.

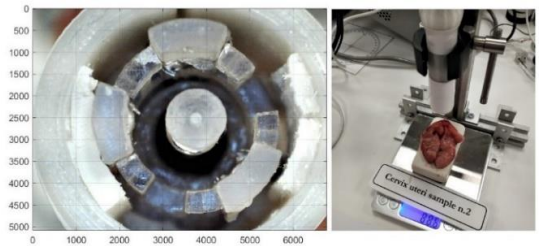

Figure 1: Left: Cross-section of the torsional wave anisotropic probe. Right ex vivo human uterine cervical sample to be scanned.

Freq (Hz)	Channel-I 0º	Channel-II 90º	Channel-III 225º
700	40.75_1.41	16.26_1.63	32.26_0.96
1000	43.57_1.60	17.85_1.07	33.60_2.02
1300	56.25_2.39	19.85_1.64	36.72_1.19

Table 1: Values of stiffness in kPa, of ex vivo chicken breast, measuring using the TWE-anisotropic probe on (0º, 90º, and 225º).

Cervix-sample	Channel-I 0º	Channel-II 90º	Channel-III 225º
1	18.88±1.02	25.35±0.79	12.96±1.63
2	20.53±1.51	26.99±1.58	13.41±1.21
3	32.86±2.74	56.02±3.81	22.23±2.91

Table 2: Values of stiffness in kPa, of ex vivo human cervix, measuring using the TWE-anisotropic probe on (0º, 90º, and 225º).

Results are encouraging; the anisotropic probe has been shown to be able to capture the tissue variability respect to the fiber orientation and frequency with a tendency close enough to the gold standard in elastography. This new technology can be considered as a baseline for future studies on TWE.

References

1. Fung, Y.C. (1993) New York: Springer-Verlag.
2. Gennisson, et al, Ultrasound Med. Biol. 38: 1559–1567 (2012).
3. Brum, J.B et al, Phys. Med. Biol. 59: 505–523 (2014).
4. Callejas et al, Sensors, 17, 2078, 2017.

Acknowledgements

To the Spanish Ministry of Education DPI2017-85359-R, DPI2014-51870-R, EQC2018-004508 and UNGR15-CE-3664 projects. Infraestructuras IE2017-5537, Junta de Andalucía and EQC2018-004508-P, MINECO.

YARN-SCALE STRAIN MEASUREMENTS USING S-DIC IN ABDOMINAL WALL REPAIR MESHES

Baptiste Pierrat (1), Anicet Le Ruyet (2), Damien Simons (2), Stéphane Avril (1)

1. Mines Saint-Etienne, Univ Lyon, Univ Jean Monnet, INSERM, U 1059 Sainbiose, Centre CIS, Saint-Etienne, France; 2. Medtronic – Sofradim Production, Trévoux, France

Introduction

Abdominal wall hernia (AWH) is a protrusion of the abdominal cavity contents through a defect in the abdominal wall. AWH repair is one of the most common surgeries worldwide and the use of mesh has become standard of care. Despite tremendous progress in the treatment, complications remain with AWH repair and reported recurrence rates are still high [1], and represent significant socio-economic burden.

These meshes have been extensively characterized at a global scale, assuming a continuous medium [2]. However such approaches are not suited to apprehend failure modes, as these phenomena are initiated at yarn scale. Local observations pose significant experimental challenges, but are necessary to apprehend the mechanisms leading to failure by relating yarn stretch to global solicitations. In this study, knitted prosthetic mesh implants were loaded using a functional plunger test, and the response at the yarn scale was characterized using an original approach.

Methods

Plunger tests (Figure 1.A) up to rupture were performed with a hemispherical indenter on 4 pre-aged knitted meshes cut in circular samples at a quasi-static rate (0.1 N/s). Two 12MP cameras were placed on top of the specimen with a field of view showing the apex of the hemisphere, and a high enough resolution so that individual yarns were visible. A speckle pattern was sprayed on the yarns using an airbrush. The specimen were backlit and frames were captured at 0.5 frame/s while recording global plunger force and displacement.

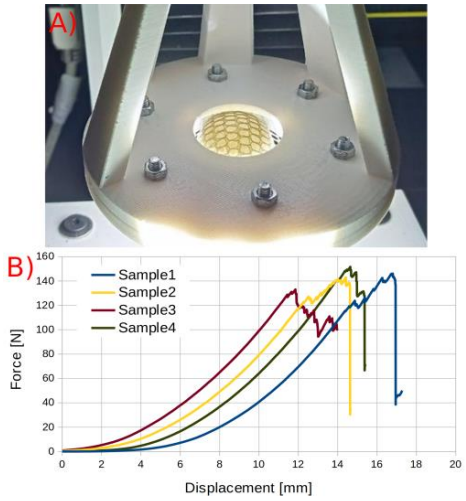

Figure 1: on-going plunger test (A) and force-displacement curves (B).

A custom code was developed in the Julia language to process the image sequences using stereo digital image correlation (S-DIC). In brief, the degrees of freedom of a beam shape function (6 rotations, 6 displacements) were obtained by minimizing the reprojection difference of the deformed beam against the left and right images throughout the full sequence (Figure 2).

Results

The plunger response exhibited a strong non-linear behaviour. Plunger rupture forces ranged from 135 to 150N (Figure 1.B). Rupture consistently happened around the apex of the hemispherical plunger, in an eye-shaped fashion. At the yarn scale, measured strains ranged from 0 to 6%, with the largest values concerning only a few specific yarns.

Discussion

Yarn scale results show that strains did not distribute evenly among the yarns, indicating that some of them may take a majority of the load while others are barely stretched. It highlights the complex behaviour of such structures, suggesting a strong reordering of the network under load, as observed through large loop slidings.

This approach provides promising results to better understand how the load is transferred from the abdominal wall to individual yarns, depending on the knitting pattern. It is the first step towards the design of optimized meshes specifically adapted to their mechanical environment to better accommodate the physiology of the abdominal wall.

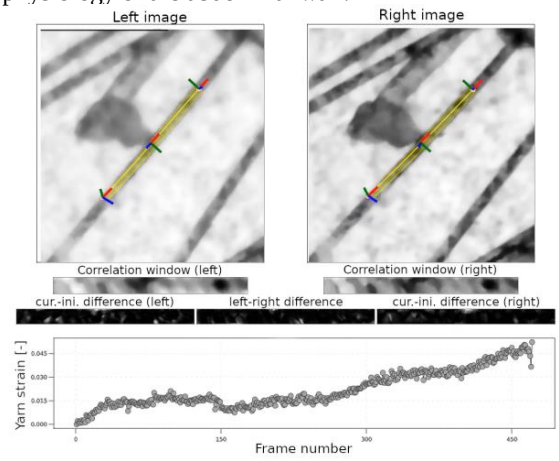

Figure 2: S-DIC progress on a single yarn, showing the images, correlation windows and obtained yarn strain.

References

1. Kadakia et al, Cureus, 12:8, 2020.
2. Röhrnbauer and Mazza, JMBBM, 29:7-19, 2014.

SIMULATION OF RED BLOOD CELL DEFORMATION AND TRANSMEMBRANE MASS DIFFUSION IN A COUETTE SHEAR FLOW

Hristo Valtchanov (1), Renzo Cecere (2), Rosaire Mongrain (1)

1. McGill University Dep. Mechanical Engineering, Canada; 2. McGill University Health Center, Canada

Abstract

Red blood cells (RBCs) are simulated in a Couette shear flow using a fully-Eulerian fluid-structure interaction scheme wherein structural dynamics are solved in the Eulerian reference frame. Simulations are executed for individual spherical vesicles and bi-concave RBCs, as well as for multiple RBCs in a shear flow. The diffusion of hemoglobin through the RBC membrane when pores are opened under stress is also simulated. The effect of cell proximity on peak strain and on the rate of hemoglobin diffusion is evaluated.

Introduction

During hemolysis caused by damage to the RBC membrane, the contents of RBCs (primarily hemoglobin) are released into plasma, which are toxic and thrombogenic. Lower levels of fluid stress on the RBC membrane, called sublethal hemolysis, leads to the formation of pores through which the RBC contents can also diffuse into plasma. High levels of extra-cellular hemoglobin are highly deleterious, but even low levels can cause spontaneous formation of blood clots that may lead to stroke or heart attack [1]. Sublethal hemolysis, being a multi-scale process, is difficult to model at macroscopic scales as pore formation and size, and hence the rate of hemoglobin diffusion depends on distribution of strain on the membrane. Simulation of red blood cell membrane dynamics is not computationally tractable for practical flows, and hence novel approaches to account for the dynamic response of the RBC membrane to varying flow conditions are necessary. Recent work [2] employs a multi-scale approach to estimate sublethal hemolysis. Loading conditions for RBCs are extracted along path lines from CFD simulations, which are then used to solve for the stress distribution on a single RBC that is subject to these stress profiles. RBCs are however densely packed, comprising 40-55% of blood, and have a strong mutual interaction, and it is necessary to examine whether nearby cells effect the strain distribution and the corresponding hemoglobin diffusion rates.

Methods

The RBC membrane stress is computed from the left-Cauchy deformation tensor, which is conserved in the Eulerian reference frame [3] in the CFD simulation, and is applied as a momentum source term to the Navier-Stokes equation using a semi-implicit coupling approach. This provides a computationally efficient method to simulate the fluid-structure interaction of multiple cells within a finite-volume CFD framework. Pore size and hemoglobin diffusion coefficients are computed as a function of local strain at each point on the RBC membrane [4]. The effect of RBC density on the distribution of strain on the RBC membrane, and bulk hemoglobin diffusion rates are evaluated. The size of the computational is increased to accommodate up to 81 red blood cells in the domain. Peak and average area strain are evaluated with multiple cells, and the effect of cell proximity on peak strain on the membrane and average diffusion rate is quantified.

Results

The deformation of a single red blood cell is simulated in a Couette shear flow. Figure 1 illustrates the shape of the red blood cell membrane over time when subjected to a constant shear rate.

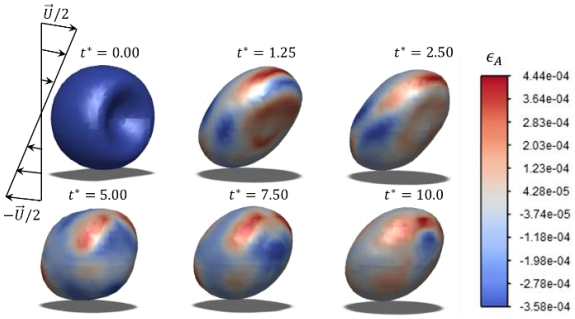

Figure 1: Deformation of RBC. The RBC membrane is coloured by area strain, ϵ_a. $\boldsymbol{t^* = tU/d}$. $\boldsymbol{Ca = \mu\dot{\gamma}d/(2E_s)}$ = 0.2; $\boldsymbol{\dot{\gamma}}$ and $\boldsymbol{E_s}$ are elastic modulus and strain rate.

Discussion

The RBC takes an elliptical shape where the major axis is generally aligned with the principal axis of the velocity gradient tensor. Maximum strain occurs at the elliptical major axis. Local strain varies substantially as the RBC varies between bi-concave and elliptica shape.

References

[1] Helms, C. C. et al. (2013). Mechanisms of hemolysis-associated platelet activation. J. Thromb. Haemost., 11(12), 2148–2154

[2] Nikfar, M. et al. (2020). Prediction of mechanical hemolysis in medical devices via a Lagrangian strain-based multiscale model. Artif. Organs, 44(8), E348–E368

[3] Takagi, S., et al. (2012). A review of full eulerian methods for fluid structure interaction problems. J. Appl. Mech, 79 (1)

[4] Sohrabi, S. & Liu, Y. (2017). A Cellular Model of Shear-Induced Hemolysis. Artif. Organs, 41(9), E80–E91

WIRE-CUTTING TO TEST THE FRACTURE PROPERTIES OF BRAIN TISSUE AND BIOMIMICKING GELS: EXPERIMENTS AND MODELLING

Michele Terzano (1), Andrea Spagnoli (1), Daniele Dini (2), Antonio E Forte (3,4)

1. Dep. of Engineering and Architecture, University of Parma, Italy; 2. Dep. of Mechanical Engineering, Imperial College London, UK; 3. DEIB, Politecnico di Milano, Italy; 4. Sch. of Engineering and Applied Sciences, Harvard University, USA

Introduction

Brain tissue, arguably one of the most complex, delicate, and softest tissues of the human body, is a strongly heterogeneous material, entailing a nonlinear, time- and rate-dependent mechanical behavior [1]. In addition to viscoelastic deformation, the peculiarity of brain tissue is a biphasic nature, in consequence of which it behaves similarly to a soft sponge permeated by cerebrospinal fluid [2], whose interactions are region-dependent and might cause relevant tissue's anisotropy [3]. In light of this picture, experimental characterization of the mechanical properties is a delicate task, and results throughout the literature often display relevant differences [4].

In this work, we have attempted to characterize the fracture properties of brain tissue, which are fundamental to understand and correctly model its behavior for simulations of surgical interventions or delivery of therapeutics.

Methods

Testing the fracture properties of super-soft tissues is a non-trivial task. Therefore, we have employed a wire-cutting setup (Fig.1), previously adopted for testing of foodstuffs and hydrogels [5], and measured the insertion force at various loading rates. In addition to samples of porcine brain, we have parallelly investigated a composite hydrogel, developed at Imperial College to closely mimic brain's mechanical response [6].

We have then developed a poro-hyperelastic model, in which brain and hydrogels are treated as soft deformable matrices completely saturated by an incompressible fluid, and simulated the observed rate-dependent effects through a coupled fluid-stress analysis of the fracture process [7]. Finally, wire-cutting has been treated as a two-dimensional problem and implemented in a finite element software, adopting cohesive elements to describe propagation of the cut during the insertion [8].

Results

Wire-cutting experiments showed a remarkable effect of the rate of insertion in both the materials considered, resulting in an increase of the cutting force at higher velocities. This is also reflected in the fracture toughness of the material, which can be extrapolated from the force. Similarly, coupled fluid-stress finite element analyses showed an effect of the loading rate, although this cannot be directly correlated to the velocity of crack propagation.

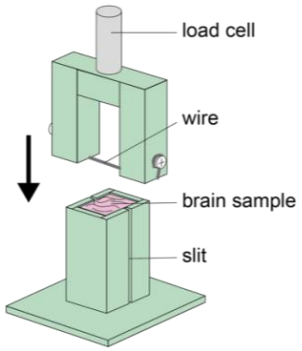

Figure 1: Schematic of the wire-cutting test, employed to test the fracture properties of brain tissue and the mimicking hydrogel.

Discussion

Brain tissue and mimicking hydrogels can be described as soft and wet materials. By a mechanical point of view, rate-dependent effects are among the most peculiar features. Our results confirm the viability of wire-cutting as a method to test the fracture properties of super-soft materials. Furthermore, the approximation of the mechanical behavior of the brain tissue with a poro-hyperelastic model seems to be feasible, although the results appear to be very sensible to the permeability of the material, a parameter which needs to be calibrated accurately. Both experiments and simulations were able to capture an effect of material relaxation, which we argue it might depend on the draining of fluid in the crack-tip region. Viscoelastic relaxation is also known to play an important role in the mechanics of brain tissue. However, classical models cannot adequately describe the viscous effects during fracture, for which micromechanical models and multiscale analyses are needed.

References

1. Budday, S et al, Arch Comput Methods Eng, 27:1187–1230, 2020.
2. Franceschini, G et al, J Mech Phys Solids, 54:2592–2620, 2006.
3. Jamal, A et al, IEEE Trans Biomed Eng, 2020.
4. Forte, AE et al, Biomech. Model. Mechanobiol., 16:907–920, 2017.
5. Forte, AE et al, Food Hydrocoll, 46:180–190, 2015.
6. Forte, AE et al, Mater Des, 112: 227–238, 2016.
7. Terzano, M et al, J Mech Behav Biomed, submitted.
8. Terzano, M et al, Biomech Model Mechanobiol, 19:1809–1825, 2020.

FINITE-ELEMENT MODELING OF VOLUME VARIATIONS IN PLANTAR VEINS

Laure Tsimba (1,2), Miquel Aguirre (1), Cyril Chaigneau (2), Didier Rastel (3), Stéphane Avril (1)

1. Mines Saint-Etienne, Univ Lyon, France 2. Sigvaris GROUP, France 3. Philangio SERURL, France

Introduction

The venous pump of the foot, which is the most distal contributor to venous return from the lower limbs to the heart, is mainly composed of deep plantar veins located between the plantar muscles. The lateral and the medial plantar veins constitute a blood reservoir of about 25 mL emptied at each stage of the gait with weight-bearing and plantar muscles contraction [1-3]. This can happen thanks to the very low venous internal pressure allowing the collapsibility of veins under a bigger external compression. Venous collapse can be represented through a non-linear relation between venous cross-sectional area A and transmural pressure P_{tr} derived from the original Shapiro's tube law [4]:

$$A = Ao\left\{h(p^*).f^+(p^*) + \left(1 - h(p^*)\right).f^-(p^*)\right\}$$

$$p^* = P_{tr}/K_p$$

Where Ao is the cross-sectional area when $P_{tr} = 0$, p^* the dimensionless pressure, K_p the bending stiffness, f^+ and f^- fits of the positive and negative pressure part of the original tube law of Shapiro, and $h(p^*)$ a scaling function. The objective of this work is to develop a 3D finite-element model (FEM) of the foot to predict how the deformations of the plantar soft tissues transmit down to deep plantar veins and how wearing insoles can affect venous return. For that, we study the volume changes of plantar veins and postulate that any volume loss result in blood drained up to the lower leg.

Methods

To reconstruct the foot FEM, bones, soft tissues (skin, fat and muscles) and lateral and medial plantar veins were first segmented from 3D Short TI Inversion Recovery (STIR) MRI images of a non-weightbearing normal foot using Simpleware ScanIP. The initial cross-sectional area Ao of plantar veins and coordinates of their centerlines were extracted. Meshed bones and soft tissues (4-nodes tetrahedral elements) were exported in Abaqus where they were respectively set as rigid body and as isotropic incompressible hyper-elastic material (1st order Ogden; μ=0,0375MPa, α = 5,5 and D = 0) [6].

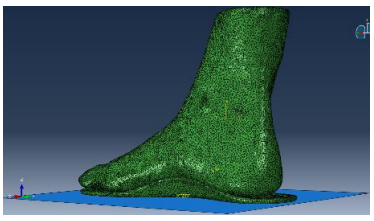

Figure 1: Meshed foot, rigid sole and analytical ground plate

A foot plantar sole was constrained to be tied to a rigid insole placed very close under the foot. An analytical rigid ground plate was also added under the insole and a frictional contact interaction was set between them (coefficient of friction = 0,6).
A ground reaction force in z-direction, corresponding to half bodyweight, were applied under the ground plate which was allowed to move only along this axis.
The obtained hydrostatic pressure HP at each element center was defined in Matlab (R2018a) as the mean of principal stresses components σ11, σ22 and σ33. The local change of cross section was deduced with the (A, p) equation. P_{tr} was derived as the difference between the internal pressure P_{int} and the external pressure P_{ext} which corresponds to the interpolation of HP to the plantar vein centerlines. The cross-sectional area A obtained was then integrated along the entire length of the two vessels to derive the change of volume in lateral and medial plantar veins (V_{LPV} and V_{MPV}).

Results and Discussion

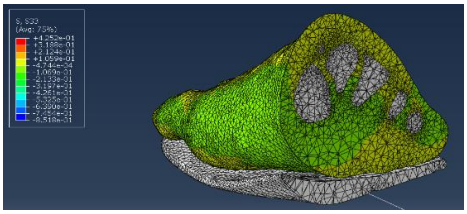

Figure 2: Transmission of stresses (S33) through soft tissues

The effect of the ground reaction forces resulted in localized deformations of the plantar soft tissues (Figure 2). The plantar venous pump PVP was activated since a decrease of plantar veins volume was observed (up to 75%). In the near future, we plan to study whether the insole could have an impact on the PVP efficiency changing its shape and material. Moreover, a more realistic model of PVP would be obtained by using a weight-bearing foot geometry and by considering plantar muscle activity in extravascular pressure. Eventually, the model will also be validated using hemodynamic data collected through an ongoing clinical trial.

References

1. Uhl J-F et al. Phlebology, 27:219–230, 2012
2. Corley et al. The Anatomical Record, 293:370-378, 2010
3. Ricci S et al. Dermatol Surg, 40:225-233, 2014
4. Keijsers J.M. et al. J Biomech., 49(13)2845-2853, 2016
5. Chen et al. Journal of Biomechanics 45:1783–1789, 2012

Acknowledgements

As part of a Cifre thesis project, this work is supported by the company SIGVARIS GROUP and by the Association Nationale Recherche et Technologie ANRT.

ANGIOGENESIS SIGNIFICANCE DURING OSTEOPHYTES EVOLUTION

Ewa Bednarczyk (1), Tomasz Lekszycki (1)

1. *Warsaw University of Technology, Department of Construction Engineering and Biomedical Engineering, Poland*

Introduction

Osteoarthritis is one of the most common diseases. Joint tissues such as bone and cartilage undergo degenerative changes related to the concentration of stress induced by mechanical loading. Mechanically overloaded cartilage cells are compressed which they interpret as having received insufficient nutrition. To address that, they release intensified signals of demand for nutrients. In response to these signals, new blood vessels start to grow from preexisting network located within the bone tissue. Healthy cartilage is avascular and cells receive nutrition through diffusion process from synovial fluid not from blood vessels. Here, expansion of new blood vessels from bone region creates in cartilage favorable conditions for the development of bone tissue and leads to osteophyte onset. Angiogenesis significance during OA is evident [1, 2], however, no mathematical model takes into account blood vessels as integral effect of degenerative changes.

Methods

Presented mathematical model consists of four integro-differential equations. The model describes evolution of selected variables which determine formation of the osteophytes.

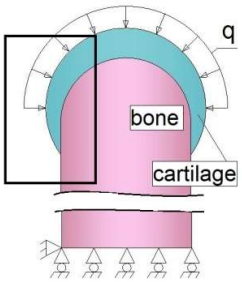

Figure 1: Geometrical model of computational domains corresponding to the joint.

Mathematical model:

Evolution of blood vessels density

$$\dot{\rho}_V(\zeta^A,t) = S(\zeta^A,t)B(\zeta^A,t)N(\zeta^A,t)$$

$$N(\zeta^A,t) = \int H\left(\Delta N(\zeta^i,t)\right) e^{-\frac{R(\zeta^i,\zeta^A)}{\beta}} d\Omega$$

$$B(\zeta^A,t) = \int \rho_V(\zeta^i,t)\, e^{-\frac{R(\zeta^i,\zeta^A)}{\gamma}} d\Omega$$

$$S(\zeta^A,t) = \left(2 - e^{\frac{-U(\zeta^A,t)}{m}}\right) P_m(\zeta^A,t)$$

Evolution of bone cells density

$$\dot{\rho}_B(\zeta^A,t) = \rho_B(\zeta^A,t)\rho_N(\zeta^A,t)$$

Evolution of nutrients density

$$\dot{\rho}_N(\zeta^A,t) = B(\zeta^A,t) - \eta(\zeta^A,t)\rho_B(\zeta^A,t)$$

Evolution of Young modulus

$$\dot{E}(\zeta^A,t) = \rho_B(\zeta^A,t)S_{ME}(\zeta^A,t)$$

$$S_{ME}(\zeta^A,t) = \int U(\zeta^i,t)\, e^{-\frac{R(\zeta^i,\zeta^A)}{U}} d\Omega - U_E$$

Simulations were conducted in COMSOL Multiphysics software.

Results

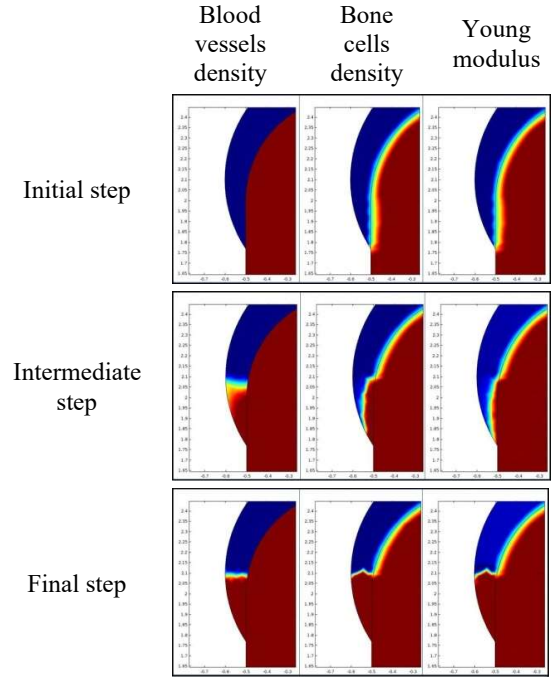

Figure 2: Evolution of variables in selected time steps.

Discussion

The mathematical model describes phenomenon of the growth of osteophytes. It couples mechanical loading with the development of new blood vessels and cell signaling. Results show evolution of selected variables which determine osteophyte invasion into cartilage domain. The results correspond with medical reports.

References

1. Moskowitz R., Bone remodeling in osteoarthritis: subchondral and osteophytic response. Osteoarthritis and Cartilage, 7:323-324, 1999.
2. Mapp P.I. et al., Angiogenesis in two animal models of osteoarthritis, Osteoarthritis and Cartilage, 16:61-69, 2008.

Acknowledgements

This research was supported by the National Science Centre, Poland, under the scientific project 2017/27/N/ST7/01490 ("Novel bio-mechanical model of osteophyte development during osteoarthritis").

SIMULATING THE STOMA EFFECT ON THE ABDOMINAL WALL

Lluís Tuset (1), Dolors Puigjaner (1), Joan Herrero (2), Josep M. López (1), Gerard Fortuny (1)

1. Departament d'Enginyeria Informàtica i Matemàtiques, Universitat Rovira i Virgili, Catalunya;
2. Departament d'Enginyeria Química, Universitat Rovira i Virgili, Catalunya

Introduction

An ostomy is a surgery to create an artificial opening to reroute the exit of urine and faeces from the inside of the body to the outside. One of the most common complications of ostomies is the appearance of parastomal hernias (PSH) around the stoma [1]. One of the risk factors associated with the appearance of PSH is the location of the stoma. The goal is to simulate the behaviour of the abdominal wall in the presence of an stoma with the purpose of finding out the best zone where practice an ostomy.

Methods

A model of the abdominal wall has been designed as a way to simulate its behaviour. *Figure 1* shows that model which was made using the open source software Salome-Meca. Commonly in these kind of simulations, the model includes the main muscles of the anatomical region.



Figure 1: the linea alba (LA) in blue, the two rectus abdominis muscular (RA) in yellow, the two internal oblique muscles (IO) in green, the two external oblique muscles (EO) in brown and the two transverse abdominis muscles (TR) in green.

Several models have been created with different positions of holes which exemplify the stoma all over the abdominal wall (*Figure 2*). The Code_Aster [2] open source finite element software was used to simulate the behaviour of the abdominal wall. This tool is part of Salome-Meca package, which in addition allows to represent the solutions graphically.

Results

A static and linear behaviour has been considered with several values of the intraabdominal pressure up to 20 kPa [3]. The calculated strain and stress fields were very similar for all of the stoma models, with a maximum abdominal expansion of about 52.38 mm at 20 kPa, except in the case with the stoma on the LA, for which the maximum deformation was 61.23 mm instead. The latter simulation would reflect a extreme case in which LA is cut during surgery.

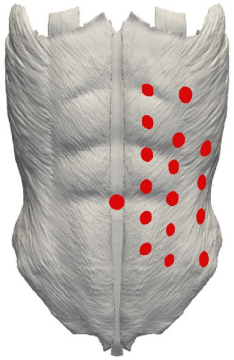

Figure 2: The seventeen holes (in red) that simulates the stoma location all over the abdominal wall. The central one is on the LA and divides it in two different parts. The other ones are above three imaginary lines parallel to LA.

Discussion

The experimental results show that in a surgery of these characteristics if the stoma is practised correctly and the evolution of the patient is adequate, no problems should appear from a biomechanical point of view unless the LA is damaged during the operation. In the near future, we want to consider the abdominal wall as a transversely isotropic hyperelastic material which assume the anisotropy and non-linearity of the soft tissue.

References

1 Cingi A, Cakir T, Sever A, Aktan AO (2006) Enterostomy site hernias: A clinical and computerized tomographic evaluation. Diseases of the Colon and Rectum 49:1559–1563
2 ASTER. Electricité de France, Open source on www.code-aster.org, Finite element code_aster, Analysis of Structures and Thermomechanics for Studies and Research,1989-2020.
3 Cobb WS, Burns JM, Kercher KW, Matthews BD, James Norton H, Todd Heniford B (2005) Normal intraabdominal pressure in healthy adults. Journal of Surgical Research 129(2):231–235

COMPUTATIONAL ANALYSIS OF QUASI-BRITTLE FAILURE OF FEMURS VIA A NON-LOCAL DAMAGE FORMULATION

Pierfrancesco Gaziano (1), Cristina Falcinelli (2), Elisabetta Monaldo (3), Giuseppe Vairo (1)

1. Dept. of Civil Engineering & Computer Science, University of Rome "Tor Vergata", 00133 Rome, Italy.
2. Dept. of Engineering, Campus Bio-Medico University of Rome, 00128 Rome, Italy.
3. Dept. of Engineering, Roma Tre University, 00146 Rome, Italy.

Introduction

Over the last two decades, Computed-Tomography (CT)-based Finite Element (FE) modelling was widely adopted to investigate the femoral mechanical behavior [1]. An effort-intensive work to validate the FE-derived predictions of both strain patterns and fracture load was performed by different groups [2-4]. Although these groups adopted radically different modelling strategies, very similar, yet not optimal, accuracy levels were achieved. Many differences exist among the various FE-based femoral modelling approaches, principally in terms of bone constitutive modelling and way of detecting the fracture location. On the other hand, these features have a pivotal role in the effectiveness of numerical models. Thereby, the adoption of advanced mechanics-based theories describing the fracture process may furnish a more accurate description of bone mechanical behavior, thus enhancing the accuracy level. As such, in this work a refined CT-based FE modelling approach for describing the femur mechanical response is presented. In particular, the quasi-brittle behavior of bone is modelled by employing a Continuum Non-local Damage Mechanics (CNDM) approach, which revealed more appropriate for modelling the fracture onset and evolution, than the more conventional local damage models [5].

Methods

The 3D femoral geometries were reconstructed by segmenting the CT-images (ITK-Snap software). Heterogeneous isotropic material properties were adopted by deriving local values of bone density (ρ) from the CT grayscale data and then converting ρ into local values of Young modulus [6]. To simulate the progressive loading-induced loss of structural integrity in a stance loading configuration, the linear elastic constitutive description of bone was coupled to a quasi-brittle non-local damage formulation. Specifically, a damage regularization approach based on an integral-type averaging of strain local values was adopted [5]. Three different meshes based on tetrahedral quadratic elements, labelled as "rough" (mean element size 4.0 mm), "average" (2.0 mm) and "fine" (1.0 mm), were built to test the objectivity of results upon mesh refinements. The numerical procedure has been implemented by using a displacement-controlled incremental loading path. FE analyses were performed by employing home-made Matlab codes integrated within the FE software Comsol Multiphysics.

Results were analyzed in terms of load-displacement response, damage patterns and fracture loads.

Results

The adopted approach was able to reproduce a quasi-brittle failure mode of femurs as Independent from the mesh size (Fig. 1). Computed fracture loads did not result sensitive to the mesh refinement level (percentage difference of 0.4% compared to the experimental value). In addition, FE load-displacement curves showed a convergent trend of solution upon mesh refinements (Fig. 1a). Damage patterns agreed with those experimentally detected (Fig. 1b).

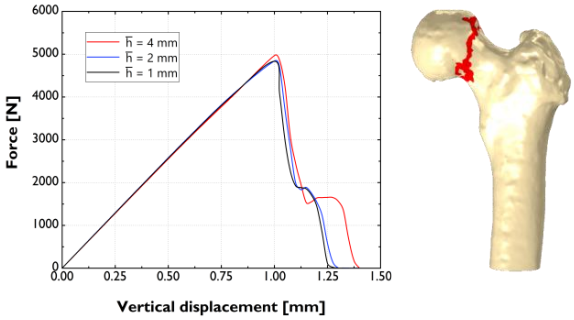

(a) (b)

Figure 1: (a) FE load-displacement curves of a femur tested under a stance loading configuration with three different mesh refinements using a CNDM approach. (b) Detected fracture pattern for the "average" mesh.

Discussion

The proposed approach is able to accurately detect the quasi-brittle behavior experienced by femur at stance position in agreement with experimental findings [7]. As such, the proposed approach may be adopted to improve the accuracy of CT-based FE models and thus obtain a more comprehensive understanding of femoral failure mechanisms.

References

1. Pahr et al., Curr Osteoporos Rep, 14:374-385, 2016
2. Keyak et al., Med Eng Phys, 23:65-173, 2001
3. Bessho et al., J Biomech, 40:17-45-1753, 2007
4. Schileo et al., J Biomech, 47:3531-3538, 2014
5. Jiràsek, Int J Solids Structures, 35: 4133-4145, 1998
6. Juszczyk et al., J Biomech, 44:2259-2266, 2011
7. Falcinelli et al., J Mech Behav Biomed Mater, 93:9-22, 2019

IN-SILICO MODELLING OF THE COMBINED EFFECT OF ANTI-ANGIOGENIC TREATMENT AND METRONOMIC CHEMOTHERAPY

Myrianthi Hadjicharalambous (1), Eleftherios Ioannou (1), Vasileios Vavourakis (1, 2)

1. University of Cyprus, Cyprus; 2. University College London, United Kingdom

Introduction

Tumour-induced angiogenesis is considered a key event in cancer progression, marking the transition to an aggressive, metastatic phase. Importantly, angiogenesis results in a pathological network, associated with hypoperfusion, high permeability and large interstitial fluid pressure (IFP), which hinder the delivery of drugs to the tumour site. Due to the pivotal role of angiogenesis, significant effort has been devoted to the development of anti-angiogenic (AA) drugs. They can have a direct effect, by hindering the formation of new vessels and by reducing the density of the existing vasculature. Importantly, AA drugs can also have indirect benefits, by improving the delivery of chemotherapy. This is due to increased perfusion, as a result of vascular normalisation (changing vessel pore size and diameter) and of a reduction in IFP.

Despite their potential, AA therapies have seen limited use in the clinic, necessitating an improved understanding of their highly intricate course of action. In this work, we present an in-silico tumour growth model, offering the ideal framework for systematically investigating the role of individual mechanisms of action of AA drugs in tumour progression. AA treatment is also considered in combination with metronomic chemotherapy, where the optimal drug dosage and timing of administration are examined.

Methods

Our in-silico model of tumour growth encompasses angiogenesis and blood flow through the vasculature and the interstitium [1]. It also simulates tissue biomechanics, the transport of chemical agents and the interaction between different cells' populations, along with the delivery of cytotoxic agents. Our framework was used to investigate several mechanisms of action of AA drugs. Initially, the effect of reducing the vascular density was examined, by employing four discrete vascular representations, corresponding to different doses of AA drug. The role of vascular normalisation was also investigated, by altering pore size and diameter. Finally, the tests were extended to metronomic chemotherapy, whereby the dosage and timing of drug administration were varied.

Results

Computational simulations revealed that the higher the dose of AA drug (which causes a higher reduction in vascular density), the larger the impact on tumour volume (Figure 1). However, a very high dose of AA drugs caused severe damage on healthy cells too.

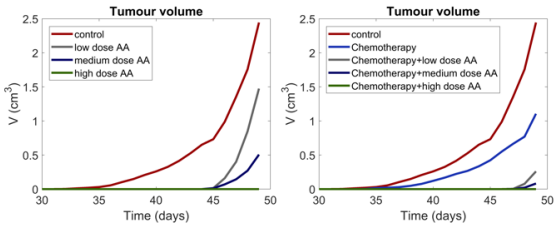

Figure 1: Effect of AA drugs on tumour volume as a monotherapy (left) or combined with drugs (right).

Importantly, when combined why chemotherapeutics, a lower dose of AA drugs was found able to shrink the tumour (Figure 2), without causing such severe effects on healthy cells. Vascular normalisation treatments were also considered in combination with chemotherapy, presenting promising results in enhancing drug delivery to the tumour site.

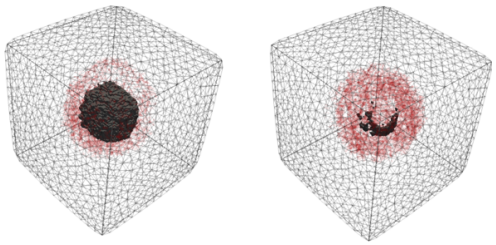

Figure 2: Tumour and new vessels in control (left) and when treated with low dose AA + Chemotherapy (right).

Discussion

Our preliminary results suggest that combinatory treatment protocols might be more beneficial than monotherapies, hindering tumour growth without causing excessive damage on healthy tissue. Equally important is the careful planning of treatment dosage and timing of administration. Finally, our results highlight the potential of our in-silico framework to evaluate treatment strategies in a non-invasive and cost-effective manner, paving the way for an improved understanding of AA therapies and thus for more effective cancer treatments

References

1. Vavourakis et al, PLoS Comput. Biol, 14, 2018.

Acknowledgements

The authors acknowledge funding from the University of Cyprus, and from the European Regional Development Fund and the Republic of Cyprus, as part of the RESTART 2016-2020 Programmes of the Research and Innovation Foundation of Cyprus (OPPORTUNITY/0916/MSCA/0012).

PERFORMANCE ANALYSIS OF HEXAHEDRAL MESH-MORPHING FOR THE MENISCUS OF THE KNEE

Adam G. Kelly, Alison C. Jones, Marlène Mengoni

Institute of Medical and Biological Engineering, School of Mechanical Engineering, University of Leeds, UK

Introduction

Generating high-quality hexahedral meshes of highly irregular tissues for finite element (FE) simulations is a laborious and time-consuming endeavour. The meniscus is an important component of the knee and challenging structure to simulate due to multi-body contact, large deformations and nearly incompressible material properties. Simulations of this nature are more accurate and likely to converge with hexahedral meshes.
Mesh-morphing has been chosen to automatically create accurate, high-quality hexahedral meshes of meniscus geometries from a single template mesh. This work aims to assess the performance of an in-house mesh-morphing strategy against a state-of-the-art hex-mesh procedure – the multi-block method (IA-FEMesh).

Methods

A set of 20 geometries (10 lateral and 10 medial) were selected which represent a variety of challenging meniscus features. Using their surface representation, 2x20 volumetric meshes were produced with either a multi-block method or our morphing strategy, using one high-quality but generic template. FE simulations with FEBio were performed as a single-condyle of the tibio-femoral joint subject to a standing compression of 500 N, incorporating idealised tibial and femoral cartilage meshes. Cartilage and meniscus were modelled as hyperelastic materials. The time taken to derive each mesh, surface error, mesh-quality and differences in simulated contact pressure and area were compared.

Results

The mesh-morphing strategy operates faster for all geometries with generation times between 83-184 s, compared to 279-8040 s for the multi-block. Overall, the multi-block method produces mesh with a lower surface error averaging 0.22 mm compared to 0.43 mm. The multi-block meshes had a lower surface error for 17/20 geometries. Mesh-morphing produces fewer very low-quality elements with an average of 0.85%, compared to 1.19% for the multi-block.

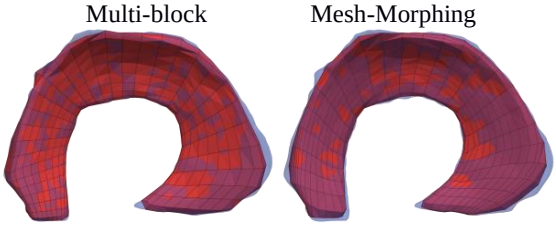

Figure 1: Surface error of the multi-block method and mesh-morphing strategy

However, the multi-block method produces fewer low-quality elements on average with 9.1% compared to 11.7%. The contact pressure distributions between the two simulations generally show strong similarities but can have different max. contact pressure locations.

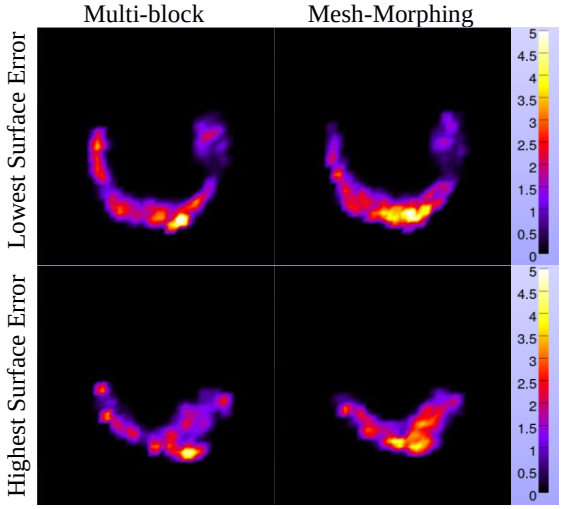

Figure 2: Contact pressure distributions (MPa) for the multi-block method and mesh-morphing strategy, for two geometries with very different surface errors

Discussion

One template was used to generate a total of 20 valid hexahedral meshes of the meniscus with reasonably low surface errors. Some differences in the contact pressure occur, mostly from mesh artefacts from the multi-block method. Other differences occur from subtle local and global surface errors. The morphed meshes distribute contact pressures more evenly due to having a smoother geometry. Although, morphed meshes that have larger surface errors tend to produce higher contact pressures.
Larger surface errors are caused from a shrinking effect from the morphing strategy and can lead to a smaller mesh than the target geometry. This will require optimizing the default mesh-morphing parameters.
The mesh-morphing strategy offers a faster, competitive and automated alternative to the semi-automatic multi-block method, with no significant difference in FE simulation outcomes.

Acknowledgements

We thank Prof. D. M. Pierce, Dr. Rodriguez-Vila and Dr. Day for supplying and curating the target meniscus geometries. This work was supported and funded by EPSRC.

TOWARDS VALIDATION OF AN IN SILICO MODEL OF TRABECULAR BONE REMODELLING IN CAUDAL MURINE VERTEBRA

Daniele Boaretti (1), Francisco C. Marques (1), Esther Wehrle (1), Ralph Müller (1)

1. Institute for Biomechanics, ETH Zurich, Zurich, Switzerland

Introduction

The acquisition and analysis of *in vivo* data has highlighted the effects of aging and loading in bone mechanobiology. On the other hand, *in silico* models of bone remodelling are not yet fully validated, impeding their recognition and application. The validation of these models would require a synergy of *in vivo* and *in silico* data and methods. Recently, our laboratory has examined the effects of ageing and loading *in vivo* on mice with premature ageing (PolgA) and their wild-type littermates (WT) [1]. In addition, we have implemented a 3D *in silico* model of trabecular bone remodelling in mice [2]. The *in vivo* data and the *in silico* model can be used together to validate the mechanobiological assumptions of the signalling pathways and cells included in the *in silico* model.

Methods

The anabolic effect of cyclic mechanical loading of the sixth caudal vertebra in WT and PolgA mice were previously shown [1]. Micro-CT scans were acquired on a weekly basis and these two groups of mice were subjected to either sham or 8N cyclic loading. Trabecular mask with (T_{Full}) and without ($T_{Cropped}$) the middle region were computed using a previously established procedure [3]. T_{Full} is used for computing the static bone morphometry parameters of the corresponding time-lapsed image, whereas dynamic parameters are obtained by superimposing the $T_{Cropped}$ for each time-lapsed image.

The first image is masked with T_{full} and used to start the *in silico* bone remodelling simulations on CSCS (Swiss National Supercomputing Centre) as described before [2]. Bone mechanobiology is simulated through signalling pathways and cells. The subsequent simulated mineral images are thresholded and used to compute the dynamic and static bone morphometry parameters along with the initial $T_{Cropped}$ and T_{Full}.

Results

The *in vivo* experimental findings have been further expanded with the corresponding *in silico* trabecular bone remodelling simulations (*Figure 2*). Their output is used to compute the static and dynamic bone morphometry parameters to establish if the *in silico* model can quantitatively reproduce the same morphological features we observe *in vivo*. On the other hand, visual inspection is carried out to inspect if the same regions are remodelled *in vivo* and *in silico* and to inspect their shape and extent which is not visible only with the numerical output of bone morphometry.

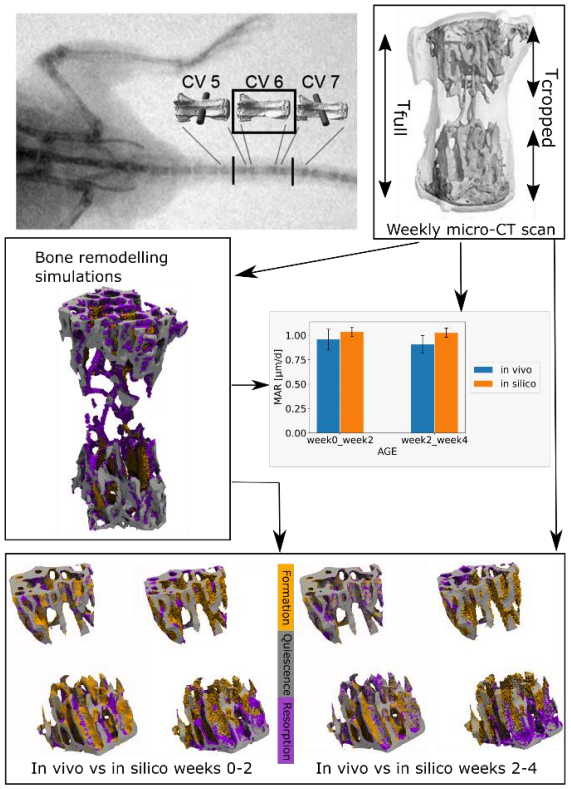

Figure 1: Outline of the validation: from acquisition of in vivo data to the quantitative and qualitative comparison between in vivo and in silico results.

Discussion

The validation of our *in silico* model of trabecular bone remodelling is the ultimate synthesis between *in silico* and *in vivo* data. As a result, the assumptions of bone mechanobiology in the *in silico* model can reproduce bone morphometry parameters. We plan to present the validation of the *in silico* model of trabecular bone remodelling in aging mice in the near future.

References

1. Scheuren et al, J Cachexia, Sarcopenia and Muscle, 11(4), 1121-1140, 2020.
2. Boaretti et al., Abstracts 25th Congress of the European Society of Biomechanics, Vienna, Austria, 7-10 July 2019.
3. Lambers et al, Bone, 49(6), 1340-1350, 2011.

Acknowledgements

Support from EU (MechAGE ERC-2016-ADG-741883), the Swiss National Supercomputing Centre (CSCS)

MATHEMATICAL MODELING OF CORTICAL TO CANCELLUS BONE TRANSFORMATION BY REMODELING

Yoshitaka Kameo (1,2), Nobuaki Sakano (2), Taiji Adachi (1,2)

1. Institute for Frontier Life and Medical Sciences, Kyoto University, Kyoto, Japan
2. Graduate School of Engineering, Kyoto University, Kyoto, Japan

Introduction

The microstructures of cortical and cancellous bones are continually altered by remodeling to adapt to the mechanical environment. The cellular mechanisms of these bone remodeling are extremely similar, despite their remarkably different porosity [1]. The intracortical remodeling that occurs at the cortico-cancellous transitional zone promotes transformation from dense cortical bone to porous cancellous bone, which is known as the main cause of bone loss with age [2]. To effectively prevent and treat age-related bone loss, it is crucial to understand the fundamental behavior of cortical-to-cancellous bone transformation. Therefore, in this study, we developed a mathematical model of cortical and cancellous bone remodeling, in which bone porosity is determined by the local balance between bone formation and resorption, and simulated cortical-to-cancellous bone transformation [3].

Methods

We proposed a mathematical model of bone remodeling based on the assumption that bone formation is induced by a mechanical factor in mineralized bone, and bone resorption is induced by a biochemical factor in bone marrow. As a bone formation factor, we introduced the mechanical stimulus to bone cells, S_{sf}, defined as a weighted average of von Mises equivalent stress. On the other hand, as a bone resorption factor, we considered a hypothetical molecule supplied from blood vessels. The concentration of the molecule, ϕ, was assumed to be governed by the diffusion equation. The remodeling stages on the bone surface, *i.e.*, formation, resorption, and quiescence, were determined by S_{sf} and ϕ (Fig. 1a).

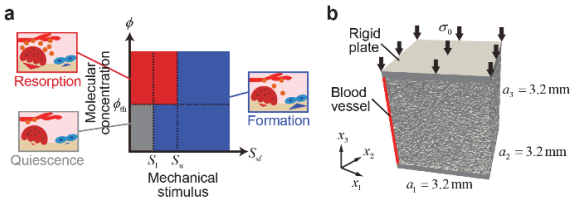

Figure 1: Methods for bone remodeling simulations. (a) Mathematical model of bone formation and resorption. (b) Initial simulation model of a cancellous-like bone.

By combining the proposed mathematical model with a voxel finite element (FE) method, we conducted bone remodeling simulations. A voxel FE model of a cancellous-like bone cube with an isotropic porous structure was constructed (Fig. 1b). A blood vessel, as a source of bone resorption molecules, was placed in the region of analysis. A uniform uniaxial compressive load σ_0 = 1.0 MPa was applied on the upper rigid plate.

Results and Discussion

The ratio of the threshold for the molecular concentration, ϕ_{th}, (Fig. 1a) to the concentration in the blood vessel, ϕ_0, is an important model parameter that regulates bone formation/resorption balance. Here, we investigated the effects of ϕ_{th}/ϕ_0, on the bone morphology after 100-day remodeling (Fig. 2a). To clearly show the porosity difference between cortical-like and cancellous-like bones, we also showed the corresponding distribution of mean bone volume fraction (BV/TV) (Fig. 2b). When the value of ϕ_{th}/ϕ_0 is relatively high, Haversian-like canal was formed around the blood vessel. With the decrease in ϕ_{th}/ϕ_0, the small canal was enlarged, and multiple trabeculae replaced the cortical-like bone. This process is remarkably analogous to the trabecularization process of the cortex via intracortical remodeling [2]. These results suggest that the proposed mathematical model of bone remodeling has the potential to reproduce cortical-to-cancellous bone transformation.

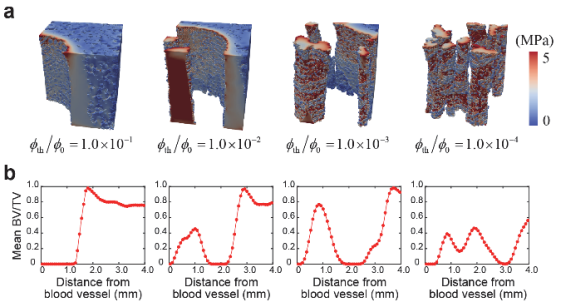

Figure 2: Reproduction of cortical-to-cancellous bone transformation by altering ϕ_{th}/ϕ_0. (a) Bone morphology with the distribution of von Mises equivalent stress. (b) Distribution of mean bone volume fraction (BV/TV).

References

1. Parfitt, J Cell Biochem, 55:273-286, 1994.
2. Bala et al, Curr Opin Rheumatol, 27:406-413, 2015.
3. Kameo et al, Bone Rep, 12:100206, 2020.

Acknowledgements

This work was partially supported by Grant-in-Aid for Scientific Research (C) (JP19K04074) from JSPS and AMED-CREST (JP19gm0810003) from AMED, Japan.

ANALYSIS OF THE INTRASTRIATAL DELIVERY OF COLLAGEN USING A BIPHASIC COMPUTATIONAL MODEL

Ioanna Marina Syntouka, Philip Riches, Asimina Kazakidi

Biomedical Engineering Department, University of Strathclyde, United Kingdom

Introduction

Parkinson's disease is a degenerative disorder that affects dopaminergic neurons in the basal ganglia. Cell therapy has emerged as a promising therapeutic strategy, and biomaterials acting as scaffolds are used to minimize the immune reaction to the graft and to prolong the cell viability. However, the existing delivery approaches have shown limited success in clinical translation [1]. This study aims to develop a device for the delivery of an *in situ* forming collagen hydrogel. A biphasic solute computational model is used to gain insight into different parameters affecting the delivery. Finally, the model of the collagen delivery to the striatum is validated by comparing it to *in vivo* experimental data.

Methods

The delivery of collagen was modelled computationally in the three-dimensional space. The striatum was modelled as a sphere, with a radius of 2.78mm corresponding to the mean volume of putamen in rats [2]. Within the finite element method framework, the biphasic solute method was used, modeling the brain tissue as a permeable hyperelastic solid matrix. MRI images of rats injected with collagen hydrogel were provided by MIRCen, CEA, France.

Results

The interaction between the collagen and the brain tissue was analyzed, and the volume of the collagen delivered in the computational model was compared to the experimental results. It was shown that a similar volume was achieved.

Discussion and Conclusions

The intrastriatal injection of a hydrogel is a complex process and computational analysis of the delivery can help identify the obstacles facing clinical translation. The validation of the biphasic computational model when compared to experimental results was successful, and this model will be used to investigate how different syringe designs may affect the intrastriatal delivery.

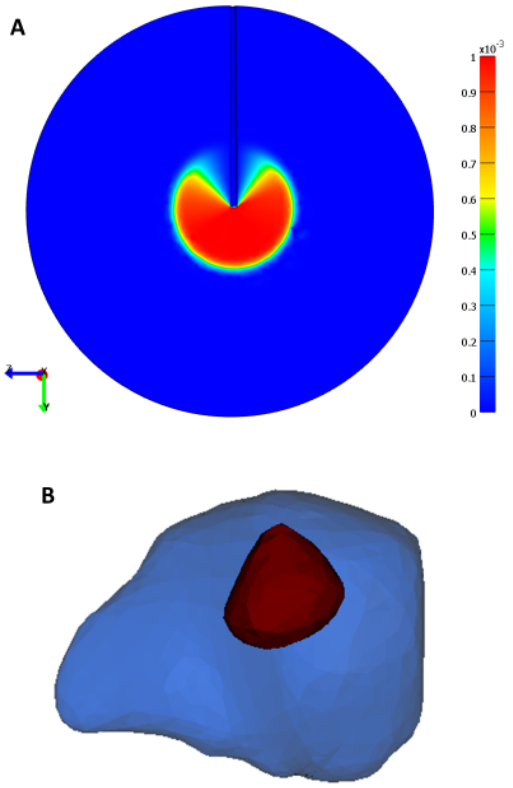

Figure 1: Three-dimensional model of collagen delivery to the striatum. A) Effective concentration of collagen when injected into the striatum, modelled as a biphasic material. B) 3D reconstruction of MRI images of collagen (red) injected to the rat striatum (blue).

References

1. Amer M et al. *npj Regen. Med.* 2(1):23,2017.
2. Mengler et al, NeuroImage, 84:35-44, 2014.

Acknowledgements

This work is supported from the European Union's Horizon 2020 research and innovation program under the Marie Skłodowska-Curie Innovative Training Network grant agreement No 676408. We would also like to thank Dr F. Gubinelli and Dr E. Brouillet for providing the MRI images.

CONSTRUCTION OF A THREE-LAYER SKIN FINITE ELEMENT MODEL BASED ON IN VITRO INDENTATION

Bastien Eydan (1), Baptiste Pierrat (1), Jérôme Molimard (1)

1. Mines Saint-Étienne, Univ Lyon, Univ Jean Monnet, INSERM, U 1059 Sainbiose, Centre CIS, F-42023, Saint-Étienne, France;

Introduction

The skin is subject to daily mechanical stress when in contact with objects. Being able to make predictions about the skin's ability to withstand interactions with every day used products is therefore of great interest.
Skin mechanical behaviour has already been widely studied [1, 2]. However, the current understanding of the through layer behaviour of skin is insufficient to explain discomfort and mechanical irritation phenomenon.
The aim of this work was to build a 2D three-layer finite element model of skin on the base of full field through thickness strains measured during indentation.

Methods

Full field through thickness deformation results were obtained using digital image correlation after the indentation of a porcine skin sample on a home designed device. The geometries of the layers interfaces were built thanks to a Fourier fit of a segmented histological image of human skin.
Each layer of the model was defined homogeneous, linear and elastic. Indeed, the anisotropy of the skin is essentially resulting from the orientation of the collagen fibres, predominantly in a plane orthogonal to the one studied here. The Young moduli of each layer were calibrated through the inverse identification process described in Figure 1. The objective function compared the horizontal and vertical displacements of every node of the model to an interpolation of digital image correlation experimental results, as well as the reaction forces on the probe, at every indentation step.

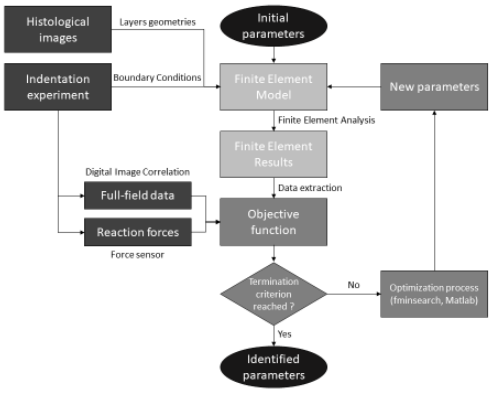

Figure 1: Identification process of the material properties of the skin

Results

For the skin sample considered in this work, the optimization process led to a minimum of the objective function for the values of the Young moduli for the epidermis, dermis and hypodermis layers of respectively 0.81MPa, 5.81MPa, and 10.01MPa. The corresponding numerical strain maps were compared to the experimental ones as shown in Figure 2.

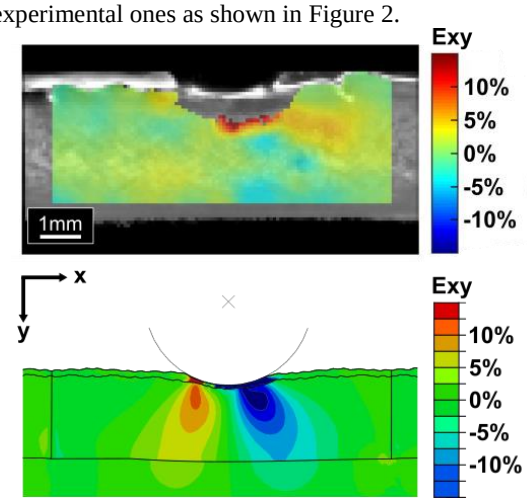

Figure 2: Experimental shear strain map obtained using digital image correlation (top) and numerical shear strain map obtained using the material properties resulting from the identification process (bottom).

Discussion

The found parameters are a little higher than the average of those found in the literature, but remain within the range of skin layer parameters [1, 2, 3]. The relative softness of the epidermis could partly be explained by the limited experimental data obtained in this layer. The unusual rigidity of the hypodermis might result from the hard metal layer underlying the skin sample during the experiment.
The overall deformation behaviour was fairly well approximated by the model defined in this study. Yet, the comparison of the experimental and numerical strain maps highlight that this type of model is not able to capture heterogeneities in the skin. The reproduction of this work on more samples will allow refining these results. The use of hyperelastic material properties could enhance the model. Accessing such detailed information about the through-layer deformation of the skin is a promising result. By perfecting this method, it will be possible to study with accuracy the viscoelastic and non-linear properties of the skin.

References

1. H. Joodaki and M. B. Panzer, Eng Med, 232:323-343, 2018.
2. A. Pissarenko and M. A. Meyers, Prog Mater Sci, 110:100634, 2020.
3. S. Derler and L-C Gerhardt, Tribol Lett, 45:1–27, 2012.

MECHANOSTAT ESTIMATION FROM TIME-LAPSED IN VIVO MICRO-CT MOUSE DATA

Francisco C. Marques (1), Ariane C. Scheuren (1), Esther Wehrle (1), Ralph Müller (1)

1. Institute for Biomechanics, ETH Zürich, Zürich, Switzerland

Introduction

Ageing or degenerative conditions such as osteoporosis precede an impaired regulation of bone (re)modelling, which can result in fracture, long-term disability and chronic pain. Understanding the causes leading to unbalanced bone (re)modelling can help expedite the development of more effective therapies. Available tools to study mechanoregulation of time-lapsed *in vivo* micro-computed tomography (micro-CT) images showed that the conditional probability of formation/ resorption events is linked to higher/lower magnitudes of the mechanical signal estimated with finite element analysis (micro-FE) [1]. Still, such conditional probability curves do not have a direct biological interpretation and cannot serve as input for *in silico* models of bone adaptation, which often rely on implementations of the mechanostat theory [2]. Hence, alternative approaches that estimate such parameters directly from *in vivo* data are desirable. This study aimed to develop a mechanoregulation analysis method to estimate sample-specific mechanostat parameters based on time-lapsed *in vivo* micro-CT data of mice.

Methods

First, formed, quiescent and resorbed volumes and surfaces are identified between scans. A distance transform of the follow-up and inverted follow-up images estimates the thickness of formed and resorbed volumes per surface voxel on the baseline image. Next, a micro-FE step computes the local effective strain (ES). A 2D histogram relates the voxel-wise surface ES with the estimated thickness. The ES values are capped at the 99th percentile to eliminate high (unphysiological) instances and binned at 1% of this value. Thickness values are binned at 1% of the maximum value. A curve is obtained by taking the average of the thicknesses, weighted by the number of bin counts. Multiplication and division by the voxel size and the interval between the time-points, respectively, convert the result to 'rate' units. The mechanostat parameters are estimated by fitting a piece-wise linear function. A total of 160 *in vivo* micro-CT scans (vivaCT 40, 10.5µm, 55kV, 145µA, 350ms) were collected from a previously published study [3] investigating the effects of cyclic and static loading frequency on the amount of bone volume change on the sixth caudal vertebra (CV6) of mice after four weeks of extra-physiological cyclic (3x/week, 2, 5 and 10Hz, F=8N), static (F=8N) and sham loading (control group, F=4N, force assigned based on [4]). Rates are given in "µm/week", and formation (F) and resorption (R) saturation and threshold values in ES values (dimensionless).

Results

The method can produce sample-specific and group average mechanostat parameter estimations (Table 1).

Param.	Control	Static	2Hz	5Hz	10Hz
$R_{saturation}$	-9.89	-7.01	-7.53	-5.76	-8.63
R_{rate}	18615	7232	17530	20424	35845
$R_{threshold}$	0.53	0.97	0.43	0.38	0.24
$F_{threshold}$	2.0	3.6	0.8	0.6	0.4
F_{rate}	972	1241	1723	2070	2180
$F_{saturation}$	0.36	1.78	2.32	2.99	3.39

Table 1: Parameters of the piece-wise linear curve fitted to the average mechanostat curve per group (F: formation, R: resorption; $R_{threshold}$ and $F_{threshold}$ x10^{-3}).

Figure 1 shows that peak surface velocity was achieved in the second week, from which the rates decreased over time. Higher frequencies showed higher surface velocities and lower formation thresholds. The range of ES values also decreased towards a defined interval with smaller amplitudes for higher frequencies.

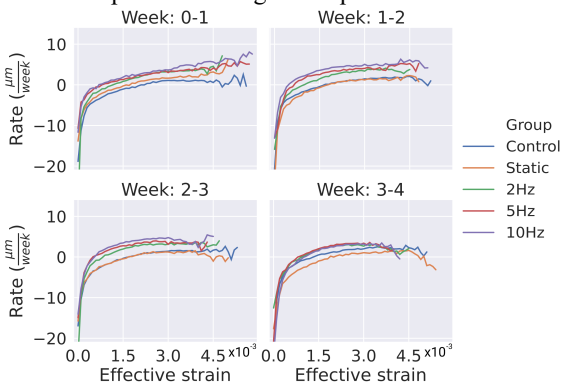

Figure 1: Group average mechanostat estimation for all samples of all groups, across all pair of time-points.

Discussion

ES values converged to a small interval, suggesting a more homogeneous ES distribution at week 4 [4]. Future work will explore if such estimations allow accurate individualised *in silico* modelling of bone adaptation.

References

1. Schulte et al., PLoS One, 8:4, 2013
2. Frost, H. M., Bone Miner. 2, 73–85, 1987
3. Scheuren et al., Front Bioeng Biotechnol, 8:1211, 2020
4. Christen et al., Biomech Model Mechanobiol, 11:3-4, 2012

Acknowledgements

Support from the European Union (MechAGE ERC-2016-ADG-741883), the Swiss National Supercomputing Centre (CSCS) and the Euler compute cluster at ETH Zurich.

“COUNT ON ME”: AN AUTOMATED, NEURAL NETWORK-BASED SYSTEM FOR DETECTION OF APOPTOTIC NUCLEI

Gaetano Iannuzzi (1), Federica Bussa (1), Pietro Cerveri (1), Stefano Casarin (2,3,4), Eleonora Dondossola (5)

1. Dept. of Electronics, Information and Bioengineering, Politecnico di Milano, Italy; 2. Dept. of Surgery, Houston Methodist Hospital, Houston, TX; 3. Center for Computational Surgery, Houston Methodist Research Institute, Houston, TX; 4. Houston Methodist Academic Institute, Houston, TX; 5. GU Medical Oncology, The University of Texas MD Anderson Cancer Center, Houston, TX.

Introduction

Apoptosis is the programmed form of cell death, a highly regulated process responsible for cellular turnover in living tissues. Alterations of this mechanism play a key role in different diseases, including cancer.
The identification of apoptotic cells in preclinical samples provides valuable insights into disease progression and allows to evaluate therapy response.
Various apoptosis detection modalities are available, and they largely rely on empirical assessments from biologists. The process is laborious, time consuming and subjected to human error. To overcome this gap, we propose an automatic computerized system to detect and quantify apoptotic cells in fluorescence microscopy images to optimize the time of analysis, improve the accuracy and abate the incidence of human errors.

Materials and Methods

The proposed method is based on a deep learning algorithm [1] and was applied to confocal microscopy images of human melanoma and prostate cancer cells [2]. Our system performs semantic segmentation over each entire image, distinguishing among intact nuclei, apoptotic fragments, and the remaining background.
The dataset included 94 images (80% employed for the training and 20% for the validation) that were manually labelled under the supervision of an expert biologist. Data augmentation was performed on available annotated images in order to instruct the network more efficiently – see Fig. 1a.
A UNet architecture [3] was chosen and adapted to this specific purpose, together with a customized loss function to target the class imbalance issue.

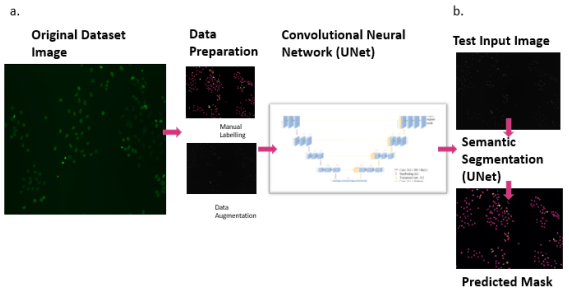

*Figure 1: Workflow: **a.** Training of the network; **b.** Test of the semantic segmentation technique.*

Results and Discussion

We calculated the Intersection over Union (IoU) to estimate the performance of the proposed framework and the results are summarized in Table 1.

	Validation
Max IoU Apotosis	0.6709
Max IoU Intact	0.8483

Table 1: UNet performance parameters

Fig. 2 shows an example of segmentation results. The network was overall accurate in predicting the presence of the intact nuclei in the entire image. The detection and localization of apoptotic events was good with a true positive rate of 73.07% and a false positive rate of 3,15%. The computational time required for a single image was in the order of few seconds.

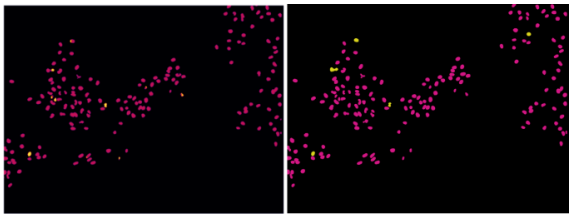

Figure 2: Output mask of the algorithm (left) compared with the true mask (right). In yellow apoptotic nuclei.

Conclusions

We presented an innovative CNN-based solution for individuation of apoptosis in microscopy images. The proposed approach can significantly reduce the time of analysis, improve the accuracy and reduce the incidence of human errors.
As next step, an improvement of the learning process will be targeted, along with an increase in the quantity of input data applied to new class of images to study different cells populations.

References

1. Klang E., J Thorac Dis. 10(3):1325-1328, 2018
2. Veelken,, C et al., Methods 128: 139-149, 2017
3. Ronneberger O. et al, Miccai, 9351:234-241 ,2015

AUTOMATIC NEURAL NETWORK-BASED BONE METASTASIS TUMOR VESSEL ANALYSIS ON MICROSCOPY IMAGES

Giulia Alessandrelli (1), Pietro Cerveri (1), Stefano Casarin (2,3,4), Eleonora Dondossola (5)

1. Dept. of Electronics, Information and Bioengineering, Politecnico di Milano, Italy; 2. Dept. of Surgery, Houston Methodist Hospital, Houston, TX; 3. Center for Computational Surgery, Houston Methodist Research Institute Houston, TX; 4. Houston Methodist Academic Institute, Houston, TX; 5. GU Medical Oncology, The University of Texas MD Anderson Cancer Center, Houston, TX.

Introduction

Bone metastasis is a lethal complication of prostate cancer (PCa) (84% incidence) [1] with a survival rate of ~30% at 5 years from the diagnosis [2].

Blood vessels in bone are key players of metastasis development and progression and a target of anti-angiogenic therapies. Thus, detecting tumor vasculature is necessary to monitor the performance of these agents. However, due to the highly irregular structure of the vessels, their manual quantification is complex, time-consuming, and subjected to human errors.

To fill this gap, we propose an automatic computer system to segment blood vessels in microscopy images.

Materials and Methods

The proposed method is based on a neural network algorithm applied to images of PCa bone metastasis. Briefly, mouse tibiae are injected with human PCa cells, collected after 10 days, processed, cut at the vibratome, stained (endomucin) and acquired at a multiphoton microscope.

The dataset includes 163 images referring to two different cancer cell lines: PC3 and C42B. A C42B image example is shown in Fig.1a. For each image, a ground truth mask was manually developed in ImageJ under the supervision of an expert biologist. Given the high shape irregularity of tumor vessels in bones, we approximated each vessel with an ellipse (Fig.1b).

The proposed method employed a U-Net neural network to perform semantic segmentation [3]. Data augmentation was executed to increase data availability by applying the same geometrical transformations to both images and masks. The augmented dataset was split into a "training subset" (280 images) and a "validation subset" (120 images) to tune the model hyperparameters and to monitor the model performance. First, the convolutional neural network (CNN) was trained with the relative subset; second, the trained model was validated with the relative subset. Then, the model was employed to perform semantic segmentation, generating predicted vessel masks for every image of the entire dataset. From each mask, vessel features were extracted, including centroid coordinates, major and minor axis length, eccentricity, orientation and the total number/image.

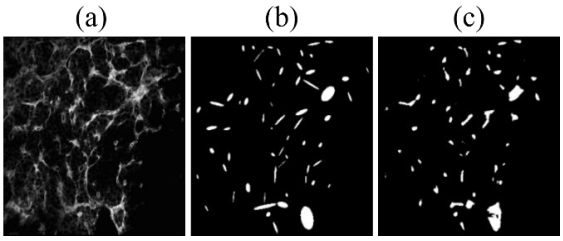

Figure 1: Original image (a), manual ground-truth mask (b), mask automatically predicted by the CNN model (c).

Results and Discussion

A qualitative evaluation and validation of the semantic segmentation results have been performed by an expert biologist in the field with a satisfying outcome. The maximum Intersection over Union (IoU) is 0.468. However, its choice as quantitative indicator of segmentation quality is questionable due to the approximation of vessels into ellipses.

Detection of 53 vessels		
	Vessel # 1	Vessel # 2
Centroid	(287, 328)	(324, 104)
MajorAxisLength	52.9	32.2
MinorAxisLength	23.6	17.9
Eccentricity	0.90	0.83
Orientation	-88.2	49.4

Table 1: Results of the first 2 vessels, related to Fig. 1c, sorted by area dimension.

Conclusions

An innovative neural network-based solution for automating blood vessels analysis in bone metastasis is presented. Our automatic method highly improves the time of analysis and abates the incidence of human errors. In future developments, we will boost the semantic segmentation performance by improving the quality of the ground truth mask. Moreover, an increased quantity of images is beneficial to widen the data variability that the algorithm can manage.

References

1. Shah, R., et al., Cancer Res., 64(24):9209-16, 2004
2. Gandaglia, G., et al., Prostate, 74(2):210-6, 2014
3. Ronneberger, O., et al., https://arxiv.org/abs/1505.04597, 2015

COMPUTATIONAL STUDY OF SURFACE-BASED CELLULAR STRUCTURES FOR BONE TISSUE ENGINEERING

Reduan Asbai-Ghoudan (1), Sergio Ruiz de Galarreta (1), María Ángeles Pérez (3), Patrina S.P. Poh(4), Naiara Rodriguez-Florez (1,2)

1. University of Navarra, Spain; 2. IKERBASQUE, Spain; 3. University of Zaragoza, Spain; 4. Charité - Universitätsmedizin Berlin, Germany

Introduction

Cellular porous structures, such as triply periodic minimal surfaces (TPMS) have become increasingly popular in the design of scaffolds for bone tissue engineering. The need for a deeper understanding of TPMS structures is required to find optimal bone scaffold designs, which could adequate to the needs of each patient and bone site. Fluid flow dynamics also play a critical role in the diffusion of nutrients and scaffold properties such as permeability and wall shear stress (WSS) are directly involved in the proliferation and cell differentiation [1]. The aims of this study are to create computational models that will allow designing scaffolds which match the mechanical and fluid flow properties of the host tissue.

Methods

Prismatic samples according to ASTM D695 (12.7x12.7x25.4 mm) compromising 4x4x8 cells were designed based on four different TPMS structures (Double Diamond *DD*, Fisher-Koch S *FKS*, Diamond *D* and Gyroid *G*) of three porosities (60%, 70%, 80%). Compression tests were modelled with Finite Element Analysis (FEA) [2] using polycaprolactone (PCL) as the biodegradable material (E_0=271 MPa). Apparent moduli (E/E_0) were calculated for each relative density (ρ/ρ_0) to obtain the coefficients of Gibson-Ashby analytical model (C_1, n):

$$\frac{E}{E_0} = C_1 \left(\frac{\rho}{\rho_0}\right)^n \qquad (1)$$

Computational Fluid Dynamics (CFD) was used to obtain values of intrinsic permeability and WSS [3].

Results

Figure 1 shows the Gibson-Ashby fitting for all structures, indicating an increase in the apparent moduli with increasing relative density.

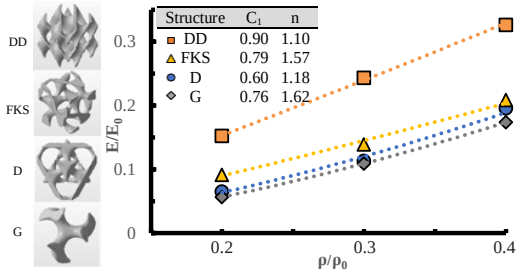

Figure 1: Unit cell architecture and Gibson–Ashby fitting for all structures.

When using PCL as the bulk material, elastic modulus (Figure 2) ranged from 75 MPa (DD-60%) to 13 MPa (G-80%), corresponding to the smallest and biggest pore size respectively. Figure 2 shows that permeability increased with porosity from $1.39x10^{-9}$ m^2 (DD-60%) to $19.45x10^{-9}$ m^2 (G-80%). As for WSS, the values ranged from a maximum of 0.211 Pa (DD-60%) to a minimum value of 0.017 Pa (G-60%).

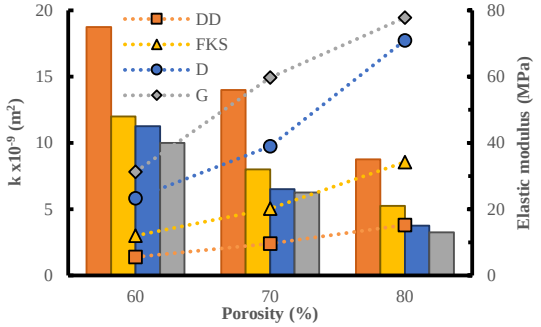

Figure 2: Calculated permeability (k) values from the CFD models (lines) and elastic moduli (E) obtained from the FE simulations (columns).

Discussion

The correlation between the apparent moduli and relative density followed a power-law, as reported by Gibson-Ashby. Young moduli of PCL structures led to lower values than the ones reported for trabecular bone. However, although PCL was used for its biodegradability, its mechanical properties can be improved when combined with hydroxyapatite or bioactive glass nanoparticles. The obtained permeability and WSS are in the range described for osteogenic differentiation [1]. Based on the relations inferred from this study, novel functionally graded structures could be designed to combine the characteristics of various models and/or porosities in order to design scaffolds specific for each patient or bone site.

References

1. Ali et al, European Journal of Mechanics-B/Fluids,79,376-385, 2020.
2. Ruiz de Galarreta et al, Materials & Design, 189, 2020.
3. Pires et al, Journal of Biomechanics, 2021.

PREDICTING TWO CORRECTIVE OUTCOMES FOR SAGITTAL CRANIOSYNOSTOSIS

Connor Cross, M. Eng[1], Roman H Khonsari, MD, PhD[2], Giovanna Patermoster, MD[4], David Johnson, MD, Ph.D[3], Yiannis Ventikos, Ph.D[1], Lars Kölby, MD, Ph.D[5], Mehran Moazen, Ph.D[1]

[1]Department of Mechanical Engineering, University College London, London, UK

[2]Service de Chirurgie Maxillo-Faciale et plastique, Necker – Enfants Malades University Hospital, Université de Paris Paris, France

[3]Oxford Craniofacial Unit, Oxford University Hospital, NHS foundation trust, Oxford, UK

[4]Department of Neurosurgery, Necker – Enfants Malades University Hospital, Université de Paris Paris, France

[5]Department of Plastic Surgery, Sahlgrenska University Hospital, The Sahlgrenska Academy, University of Gothenburg, Gothenburg, Sweden

Introduction

Sagittal synostosis is the premature fusion of the sagittal suture, affecting 1 in 10,000 live births [1]. Various corrective techniques have been developed. Craniofacial surgeons continue to debate which technique provides the most optimum outcome [2]. Finite element method is a powerful tool used for craniosynostosis management. This study aimed to (1) develop a validated patient-specific model of skull growth in sagittal synostosis patients under 2 or 3 spring-assisted cranioplasty (2 SAC & 3 SAC, respectively) correction; (2) compare biomechanics of SAC vs. a classical technique that used to be used for treatment of the same condition based on modified strip cranioplasty (MSC).

Methods

CT data of 2 SAC (n=10) and 3 SAC (n=10) patients were obtained for validation purposes. A 3-month old preoperative CT was used for 3D reconstruction. Calvarial bone, sutures and intracranial volume (ICV) were all segmented. Calvarial growth was undertaken up to 36 months of age (Fig 1). Spring cranioplasty was modelled and springs were removed at 9 months. Bone formation across the sutures and calvaria were simulated based on a previously described validated algorithm [3]. Contact parameters were established between the bone-ICV surfaces. Cephalometric, morphological and distractor distance outcomes were evaluated at 9 & 36 months.

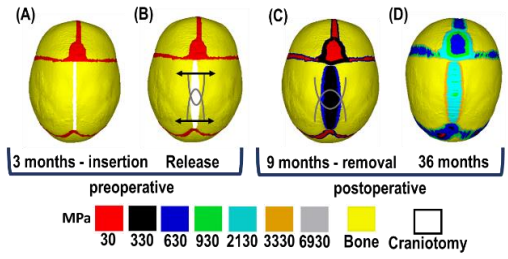

Figure 1: *Simulation workflow: where spring insertion (A), release (B) are replicated. Skull growth & bone formation are simulated up to 9 months (C) and 36 months (D).*

Results

SAC opening and morphology matched well against CT data outcomes by 36 months of age. Relapse in the cephalic index was visible in both predictive and reported outcomes (Fig 2). Predictive craniotomy closure time differed between the considered techniques, leading to altered sutural closure. Increased anterior pressure was observed in 3 SAC predictions compared to 2 SAC outcomes.

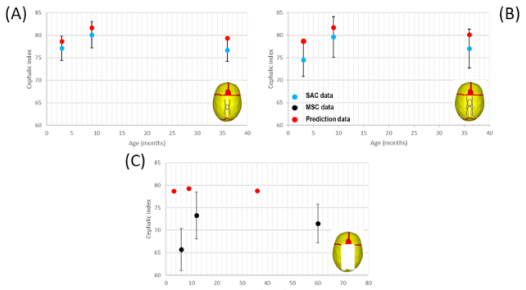

Figure 2: *Mean cephalic index over time with standard deviations. Showing 2 SAC (A), 3 SAC (B) & SMC (C) predictions vs. CT/literature data.*

Discussion

This study attempts to predict and compare various sagittal synostosis techniques using a FE approach. Our predictive outcomes in replicating SAC agree well with CT morphology. Reported morphological characteristic seen postoperatively were also predicted here. Bone formation cannot be validated but plays a large roll in predictive outcomes. Contact pressure across the ICV hope to aid in minimising functional deficits postoperatively.

References

1. Jin et al., J Korean Neurosurg Soc, 59:192-96. 2016
2. Magge et al., J Neurosurg Pediatr, 23:708-14. 2019
3. Marghoub et al., Phys Rew Lett, 122:048103. 2019

Acknowledgement

This work was supported by the Rosetrees Trust (A1899). The authors declare that no competing interests exist.

LINKING LOCAL MECHANICAL STIMULI AND MINERAL FORMATION - A SURFACE STRAIN DILATION APPROACH FOR TISSUE BIOMECHANICS

Julia K. Griesbach (1), Gian N. Schädli (1), Nicholas Ohs(1), Graeme R. Paul (1), Caitlyn J. Collins (1), Ralph Müller (1), Marina Rubert (1)

1. Institute for Biomechanics, ETH Zurich, Switzerland

Introduction

Dynamic mechanical loading increases bone density both *in vitro* and *in vivo* [1,2]. While micro-computed tomography (micro-CT) and micro-finite element (micro-FE) analysis have shown a relationship linking bone formation, resorption and mechanical environment *in vivo* [2], current methods have several limitations. Tissue engineering approaches [1] rely on manual, time-consuming and subjective correlation of formation sites with the mechanical environment. Notably, the association of multiple strain values to single formation voxels on concave surfaces (Fig. 1a) leads to faulty probabilities for remodeling predictions using the method introduced by Schulte et al. [2]. To overcome these limitations, we developed and validated an automated surface strain dilation (SSD) method to accurately link local mechanical stimuli to mineral formation in tissue biomechanics.

Methods

The newly developed SSD method uses a remodeling image, obtained through registered and superimposed time-lapsed micro-CT images, and local micro-FE strains of the baseline image as input. Strain and formation are associated by a dilation of the surface strain onto the newly formed mineral. The surface data is extrapolated iteratively layer by layer: dilating the surface strain values and keeping only the newly dilated values (Fig. 1b). This prevents a distortion of the original data. For validation, we applied the SSD method to three datasets and compared results to the Schulte method (Fig. 1a) [2]. First, we created synthetic images representing bone formation on uneven surfaces (Fig. 1c) or multiple layers (Fig. 1d) to assess if every formation voxel is associated with exactly one strain value. Second, we applied the SSD and Schulte method to five *in silico* remodelled micro-CT images of human distal radii (Fig. 1e) and computed the correct classification rate (CCR) to assess reliability. Third, to evaluate the capabilities for *in vitro* applications, cell-seeded scaffolds (n=6) were cultured in compression bioreactors. Cyclic loading was executed 3x/week using a 3 % strain at 5 Hz for 5 minutes [3]. Time-lapsed micro-CT-images were acquired weekly. To obtain remodeling images and local strains, images were registered, superimposed and converted to Young's moduli for subsequent micro-FE. Both SSD and the Schulte method were applied and the amount of linked strain and formed mineral were compared to the input data. The area under the curve of the Receiver Operating Curve (AUC-ROC) and the probability of formation were then computed.

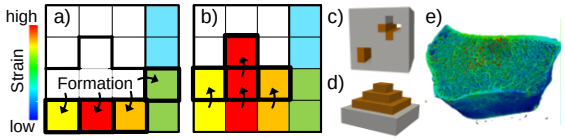

Fig. 1: Association of formation and strain for a) Schulte method [2], b) SSD method; c) concave surface, d) multiple formation layers: synthetic images (quiescent: grey, formation: orange); e) human distal radius after FE for in silico remodeling

Results & Discussion

The SSD method associated exactly one strain value with each formation voxel, while the Schulte method associated 2.25 and 0.64 strain values per voxel for Fig. 1c and Fig. 1d, respectively. Additionally, the *in silico* data showed an improved performance of the SSD method, visible in the resulting probability curves and a significantly higher CCR (Fig. 2). The results of the *in vitro* study confirm this: The SSD method associated exactly one strain value per formation voxel, compared to 2.09 strain values per voxel for the Schulte method. Furthermore, the SSD method (0.653) showed a better AUC-ROC than the Schulte method (0.544).

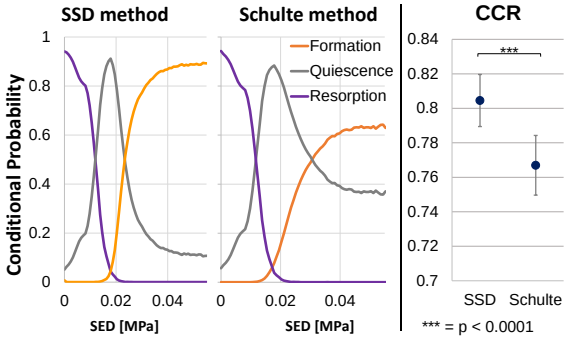

Fig. 2:Validation on in silico radius data. Left: Conditional probability plots, Right: CCR results

Conclusion

We have developed and validated a versatile novel algorithm that allows accurate association of local strain and formation on uneven surfaces, overcoming limitations of existing methods. Hence, it allows the investigation of mechano-regulation for tissue engineering applications such as cell-laden bone-organoids. This can lead to new insights in mechanical and experimental design in tissue biomechanics.

References

1. Baas et al., J.Biomech., 43(4), 2010
2. Schulte et al., PLoS One, 8(4), 2013
3. Schädli et al., Commun. Biol., 4(1), 2021

COMPARISON OF SINGLE VERTEBRA MODELS INCLUDING ENDPLATES FOR FAILURE LOAD ESTIMATION

V. Allard[ab], J-P. Roux[b], C. Confavreux[bc], F. Bermond[a], D. Mitton[a] and H. Follet[b]

[a] *Univ Lyon, Université Claude Bernard Lyon 1, Univ Gustave Eiffel, LBMC UMR_T9406, 69622 Lyon, France;*

[b] *Univ Lyon, Université Claude Bernard Lyon 1, INSERM, LYOS UMR 1033, 69008 Lyon, France;*

[c] *Centre Expert des Métastases et d'Oncologie Osseuses (CEMOS), Service de Rhumatologie Sud, Hospices Civils de Lyon, Lyon, France*

Introduction

Vertebral fractures are frequent especially with rising age due to loss of bone density [1]. Voxel-based models of bone failure have been proposed to estimate failure load of single vertebrae including vertebral endplates [2], but there is no international standard for these Finite Element (FE) models. One methodology, based on non-linear voxel FE model, is known to show good results in predicting incident vertebral fractures [3]. The aim of this study is to compare our tetrahedral models to voxel-based models found in literature [4, 5, 6].

Material and Methods

Ten L3 vertebrae without posterior arch (4 females, 6 males, 74.5±8.2 y.o.) were compressed until failure as described in [7]. Image acquisitions before failure were performed using a HR-pQCT device (High-Resolution peripheral Quantitative Computed Tomography, XtremeCT, Scanco Medical AG, Bassersdorf, Switzerland,) with a voxel size of 82 µm.

For our model, two types of mesh were created: an isotropic voxel mesh of 0.984 mm^3 size and a quadratic tetrahedrons mesh. A hydroxyapatite phantom was used to calibrate grey levels into bone densities. Average grey levels for each element were assigned with a custom script for the voxel meshes and using Bonemat (Bonemat v3.2, Bonemat software, Bologna, Italy) for the quadratic tetrahedral meshes. Then the same law as proposed in [8] was used to attribute Young's modulus and yield strength. The plastic modulus was set to 1 MPa for all elements. Each vertebra was then compressed to reach a total deformation of 1.9% according to failure criteria in [6]. Non-linear finite element analysis was performed with ANSYS (v19R2; Swanson Analysis, Houston, PA).

Results and Discussion

Differences between simulated and experimental failure loads for our tetrahedral and voxel models are not significantly different (Wilcoxon-Mann Whitney test, p-value = 0.65). There are no significant differences between failure loads computed using our quadratic tetrahedral and voxel meshes (Wilcoxon signed rank test, p-value = 0.49). Our models are similar to the literature in terms of mean difference and Standard Deviation (SD) between numerical and experimental failure load (Table 1).

Studies	Mesh	N	F_{num}-F_{exp} (N)
Current study	Tetrahedron	10	-179 ± 938
	Voxel	10	43.7 ± 967
Chevalier et al. [4]	Tetrahedron	12	1829 ± 1141
	Voxel	12	1631 ± 1061
Buckley et al. [5]	Voxel	17	68.3 ± 677
Wang et al. [6]	Voxel	52	-492 ± 880

Table 1: Differences between numerical and experimental failure loads (F_{num}-F_{exp}), mean ± SD

Non-linear voxel-based models [4, 5, 6] also add thin layers of polymethyl-methacrylate over endplates to transmit loads which was not reproduced in the current models. This may have an effect on the results. Various bone densities - mechanical properties relationships were found in the literature (e.g. [4, 5, 6]). The choice of this relationship should be included in a future standard. After conversion of the grey levels, the mechanical properties attribution to elements has not been depicted in literature which could induce uncertainties [9].

Conclusion

As there are no significant differences between our quadratic tetrahedral and voxel model in a non-linear analysis, we could keep either one of them for the simulation of vertebral failure load. The selection between the two meshes could be made according to the automation and the reproducibility of the process which are key factors to transfer these simulations to clinical applications. Even if the simulations performed in the current study and in the literature were performed in different laboratories and are consistent, international standard would improve reproducibility and should be defined for application in clinical settings.

References

1. Silverman, S. L., Bone, **13**, pp. S27–S31,1992
2. Bailey et al., Bone, 138, 115159, 2020
3. Keaveny et al. Osteoporos Int 31 :1025–1048, 2020
4. Chevalier et al. J Biomech Eng., 131(11): 111003, 2009
5. Buckley et al. Spine 32 (9), 1019–1027, 2007
6. Wang et al. J Bone Miner Res 27(4) : 808–816, 2012
7. Wegrzyn et al. J Bone Miner Res ;26 : 739–46, 2011
8. Kopperdahl et al. J Orthop Res.;20(4):801–5, 2002
9. Zannoni et al. Med. Eng&Ph, 20-10, 735-740, 1999

Acknowledgment

This project has received funding from LabEx PRIMES (ANR-11-LABX-0063) and MSDAvenir.

A MATHEMATICAL MODEL FOR RADIATION-INDUCED PULMONARY FIBROSIS

Eleftherios Ioannou (1), Myrianthi Hadjicharalambous (1), Stelios Angeli (2), Stavros Kassinos (1), Vasileios Vavourakis (1,3)

1. Mechanical & Manufacturing Engineering Dept., University of Cyprus, Cyprus
2. Prognosis Advanced Diagnostic Center, Larnaca, Cyprus
3. Medical Physics & Biomedical Engineering Dept., University College London, UK

Introduction

Pulmonary Fibrosis (PF) is a condition where lung tissue becomes damaged and scarred. It is caused by an abnormal wound healing response to an injury in the alveolar region of the lung which leads to the formation of excess fibrous connective tissue. This reduces the ventilation capacity of the lung and the transfer of oxygen to the blood vessels resulting in breathing difficulties and even respiratory failure. Currently, there is no known cure for PF and treatments are limited to slowing the progression of the disease and relieving symptoms. A cause of PF is the exposure to radiation due to radiotherapy (RT). Considering the large number of patients undergoing external beam RT in the chest area, there is a need to characterize the development of radiation-induced PF and to determine appropriate radiation dosages that minimize the risk of fibrosis development while ensuring tumour regression.

Methods

Staging and prognosis of PF remain elusive, mainly because of the highly heterogeneous course of the disease in different patients [1]. Existing prognostic models rely on demographic characteristics and/or clinical indices and have had limited success. In this work, we present a 3D mathematical model of tumour regression and radiation-induced fibrosis in the lung which incorporates patient-specific information and enables the accurate description of PF development. The model is a continuum-based formulation that features a system of three partial differential equations that govern the evolution of cancerous cells, fibroblasts and lung parenchymal tissue. It includes cell transport processes as well as the growth and death of cancerous cells and fibroblasts in response to radiation and lung tissue biomechanics. The equations are solved numerically using the finite element software FEB3 [2].

Results

The model is applied on physiologically accurate lung geometries, reconstructed from Computed Tomography (CT) scans of patients diagnosed with PF. Patient data were obtained with informed consent and anonymised by Prognosis Advanced Diagnostic Center in Cyprus. The initial conditions are set based on the location of the cancerous tumour and the radiation distribution as shown in figure 1. The numerical solution exhibits the development of fibrous tissue in the lungs which is in good agreement with the fibrotic tissue observed in the CT scans of patients and resembles the irregular "honeycombing" appearance seen in widespread pulmonary fibrosis.

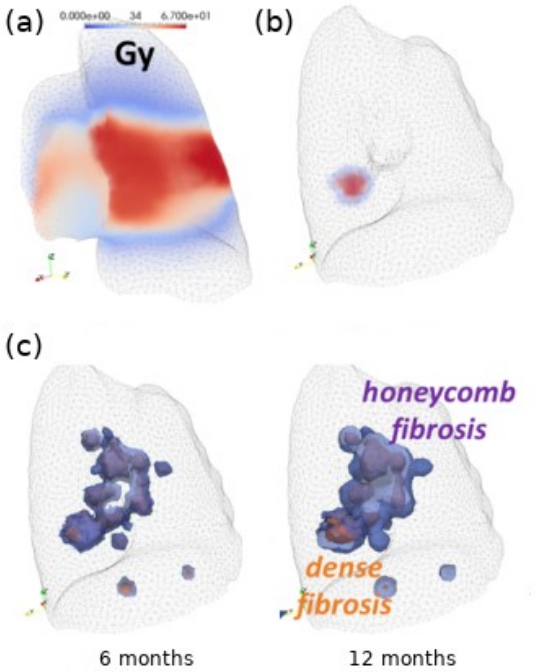

Figure 1: (a) Spatial distribution of radiation applied on the lung. (b) Location of the initial cancerous tissue. (c) Development of fibrous tissue in the months following radiation exposure.

Discussion

Our results demonstrate that the model can realistically reproduce tumour regression and fibrosis progression exhibited in lung cancer patients who received RT as part of their treatment. In future work, we plan to employ the model in biomechanical simulations to study the effect of PF on lung function.

References

1. Kolb, M. and Collard, H. R. *Staging of idiopathic pulmonary fibrosis: past, present and future*. European Respiratory Review (2014) DOI:10.1183/09059180.00002114
2. Vavourakis, V., et al. *Multiscale Mechano-Biological Finite Element Modelling of Oncoplastic Breast Surgery - Numerical Study towards Surgical Planning and Cosmetic Outcome Prediction.* PLOS ONE (2016) DOI:10.1371/journal.pone.0159766

MODELIZATION OF ENDOTHELIAL GLYCOCALYX WITH DIVERGENCE-FREE IMMERSED BOUNDARY METHOD AND INTERACTING PARTICLES

Antonio Cerrato (1), Hugo Casquero (2), Joan J. Cerdà (1), Carles Bona-Casas (1)

1. Departament de Física & Institut d'Aplicacions Computacionals de Codi Comunitari (IAC3), Universitat de les Illes Balears, Campus UIB, E-07122 Palma de Mallorca, Spain; 2. Department of Mechanical Engineering, University of Michigan - Dearborn, Dearborn, MI 48128, United States.

Endothelial glycocalyx

The endothelial glycocalyx (EG) is a soft polymer coating made of proteoglycans and glycoproteins that recovers the luminal surface of all mammalian blood vessels and has a thickness that oscillates between 0.1 and 1 micron. This organ weighs over 1.4kg and, unlike other organs, it reaches every part of our body. This biological gauzy mantle plays many crucial roles in our bodies [1]: as a selective barrier of those molecules that can pass from the blood to the rest of the body, as a shield against the loss of fluids (edema), as a lubrifying layer for the transport of red blood cells, as a controller of the appearance of thrombosis, inflammations and oxidative stress, as well as transductor of information from the blood flow towards the endothelial cells that form the walls of veins and arteries so they can change their shape and other properties allowing the body to have a dynamical control over the blood transport. The malfunction or loss of the EG has been associated with the appearance of several diseases [2] like atherosclerosis, ictus, hypertension, preeclampsia and acute bacterial infection, as well as a dramatic death rate increase in malaria. The EG has been also recently associated with the control of the growth and migration of tumoral cells, and experiments show a strong relation of the EG with side-effects related to diabetes in eyes, kidneys and wet gangrene in toes and feet.

Numerical approach

The objective of our work is to find a suitable model to reproduce in silica the behavior of the EG in blood flow in micro-vessels and its interaction with other elements in real physiological conditions.

The modelization of blood flow in micro-vessels is already a high complex numerical problem that involves the solution of the Navier-Stokes (NS) equations for incompressible fluids interacting with highly deformable solids [3]. Including the EG complicates the subject further as the use of complex constitutive models is needed. In order to tackle this problem, we present a formulation based on the Isogeometric Divergence-Conforming Immersed Boundary method (DCIB) [4,5] which is coupled to a Coarse Grain Particle Model (CGPM).

In the DCIB method for the NS equations, the Eulerian velocity-pressure pair is discretized using divergence-conforming B-splines, which leads to inf-sup stable, H1-conforming, and pointwise divergence-free Eulerian solutions. The numerical method has an MPI implementation written on top of PetIGA and PETSc. The interaction between the particles forming the polymeric structure is managed by ESPResSo [6], taking advantage of its parallel implementation and its wide variety of short and long-range interacting forces between particles.

Results and discussion

The proposed numerical coupling strategy has been tested with different benchmark problems, including comparisons with fully Dissipative Particle Dynamics (DPD) models. The model is able to describe complex inner flow within the soft brush-structure layer, as well as provide a description of the inner shear stresses that affect the wall where the polymers are anchored, as shown in Figure 1.

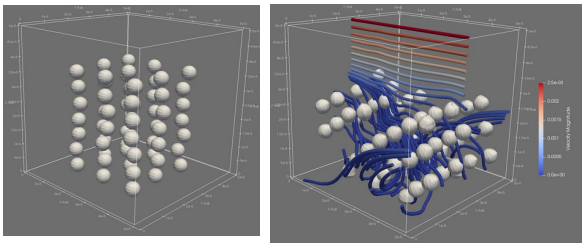

Figure 1: Flow description at the interior of an anchored polymeric brush-structure subjected to a shear flow in a canal. Left: initial configuration. Right: transient fluid flow.

More complex problems approaching the real physiological conditions of blood flow in micro-vessels have been also solved showing promising results.

References

1. S. Dognè et al, Arterioscler Thromb Vasc Biol, 38:1427-1439, 2018.
2. R. Mitra et al, Curr Atheroscler Rep, 19(12):63, 2017.
3. H. Casquero et al, Comput Method Appl M, 316:646-667, 2017.
4. H. Casquero et al, J of Comp Phys, 374:625-653, 2018.
5. H. Casquero et al. J of Comp. Phys., 2021;425, 109872.
6. HJ Limbach et al, Comp Phys Comm, 174:704-727, 2006.

Acknowledgements

All the authors thank the financial support of the Spanish Ministry of Economy and Competitiveness (MINECO/AEI/FEDER,UE) through the project Proyecto de I+D (excelencia) DPI2017-86610-P

Investigation of Stress Distribution in Growth Plates of Adolescents with Normal and Idiopathic Scoliosis Spine

[1]Zeinab Kamal, [2]Gholamreza Rouhi
[1]Department of Biomedical Engineering, University of Twente, Enschede, Netherlands
[2]Department of Biomedical Engineering, Amirkabir University of Technology, Tehran, Iran
Email: z.kamal@utwente.nl

Summary

This study used finite element (FE) analysis to determine the stress distribution within the growth plates (GPs) of the growing spine under the equivalent loads (as an alternative to *in vivo* loading conditions) estimated by our previously-validated trunk musculoskeletal (MS) model of normal and scoliotic spines. Results of the present work showed the compatibility of the presented approach to investigate the effect of muscle forces on the stresses in GPs.

Introduction

Adolescent idiopathic scoliosis (AIS) is the most common type of spine deformity in adolescents [1]. There have been a number of passive, i.e. devoid of muscles, FE models developed to simulate a growing spine with AIS [2]. However, stress distribution within a GP under subject-specific muscle exertions has not yet been investigated. The aim of this study is to evaluate stress distribution on the GPs of the FE models of normal (NFE) and scoliotic (SFE) spines under the equivalent loads. For this purpose, a nonlinear 3D FE model of rigid L1 to L4 vertebrae of one normal and one scoliotic thoracolumbar spine, consisting of GPs attached to the vertebrae, were developed using CT images.

Methods

Two FE models of L1 to the L4 vertebrae of one normal and one scoliotic 11.5-year-old adolescent were developed based on the subject-specific upright position images (Fig. 1).

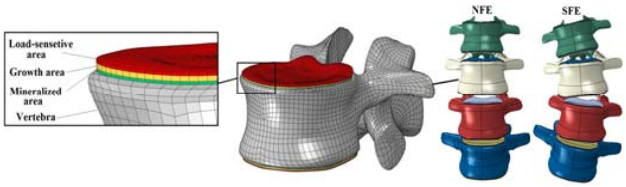

Figure 1: NFE and SFE models of L1-L4 vertebrae, including the detailed model of the GP of a rigid vertebra which consists of mineralized, growth, and load-sensitive areas [4].

The equivalent loads were approximated as vector summation of the muscle and gravitational forces at each level as well as the reaction moments about the intervertebral disc (IVD) centroids, calculated by our previously-validated MS models. In the upright-standing posture, muscle forces and reaction moments were estimated using an optimization algorithm, which was constrained to equilibrium and stability conditions [4]. Afterward, the equivalent loads were applied on the GPs at each level of the subject-specific FE models, and the stress distribution within GPs of the fully-fixed L1 to the L4 vertebrae were estimated (Fig. 2).

Results and Discussion

The equivalent shear and compressive loads (Fig. 2 a, and b), as an alternative to the *in vivo* loading condition of muscle force components and gravity loads at each level, were found to be in the physiological ranges of ultimate shear [5], and compressive strength [6], respectively. The shear force at the mediolateral direction (F^{ML}) in the normal spine was found ~0N, which is consistent with the symmetric stress distribution on the growth plates of the normal model of spine.

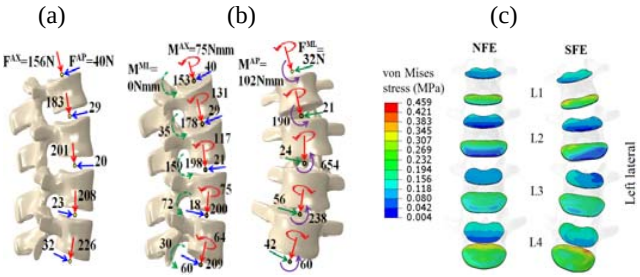

Figure 2. Reaction forces (N) and reaction moments (N.mm) about the IVD centroids of T12-L1 through L4-L5 levels in (a) NFE and (b) SFE models in the sagittal (Left b), and coronal (Right b) views. The ML, AP, and AX directions were alongside the local mediolateral, anteroposterior, and axial directions at each level, respectively. (c) von Mises stress distribution (MPa) within the GPs under the equivalent loads.

The greatest von Mises stress occurred in the apical GP, i.e. the caudal GP at the L2-L3 level, of the SFE model (Fig. 2c). The greater stress level on the posteroconcave side of the GPs (Fig. 2c) can confine the bone growth rate in that region, and in turn can promote increasing spine deformity in accordance with the Hueter-Volkmann theory as well as anterior spinal overgrowth in AIS consistent with the literature [7].

Conclusions

The approach presented in this study might be used to investigate the effects of long-term strengthening of the muscles and alignment correction exercises in order to devise more effective plans for conservative clinical therapies, such as exercise therapy or bracing, for patients with AIS.

References

[1] Wajchenberg M et al. (2016) *Scoliosis Spinal Disord* **11**: 4.
[2] Lin H et al. *Med Biol Eng Comput* (2009) **47**(4): 357-66.
[3] Moga PJ et al. (1993) *Spine* 1**5:** 2305-9.
[4] Kamal Z et al. (2018) *Med Eng Phys*, Doi: 10.1016/j.medengphy.2018.12.015.
[5] Gallagher S et al. *Clin Biomech (Bristol, Avon.* (2012) **27**(10): 973-978.
[6] Ayoub MM et al. Manual Materials Handling, London: Taylor & Francis; 1989.
[7] Guo X et al. *Eur Spine J* (2005) **14**(9):862-73.

POLYESTER SCAFFOLD DEGRADATION MODEL: FROM IN-VITRO TO IN-SILICO PREDICTIONS

Simone Russo , Pilar Alamán-Diéz, Francisco Serrano-Alcalde, José Manuel García-Aznar, Maria Ángeles Pérez

Multiscale in Mechanical and Biological Engineering (M2BE), Aragón Institute of Engineering Research (I3A), Aragon Institute for Health Research (IIS Aragón), University of Zaragoza, Zaragoza, Spain.

Introduction

Tissue Engineering (TE) development is strictly related to changes in materials fabrication technology. Biomaterials design and their properties play a critical role in the success of designed scaffolds for TE. [1] A better understanding and control of biodegradation process may help in the development of successful TE strategies. Computational modelling offers an efficient framework to predict and understand the behaviour of biomaterials. This work's aim is to develop a combined *in-vitro/in-silico* method to quantify scaffold's degradation.

Materials and methods

In-vitro model. 3D printed hybrid poly(e-caprolactone) (PCL) and poly(D,L-lactic-co-glycolic) acid (PLGA) scaffolds (50:50) were fabricated. The scaffolds were degraded in simulated physiological environment under static conditions or perfusion within a customised perfusion bioreactor (Figure 1a). Scaffolds were soaked in Phosphate-Buffered Saline (PBS) and incubated at 37ºC for 14 and 28 days. Degradation was monitored by measuring the weight-average molecular weight, weight loss, polydispersity index and scanning electron microscope (SEM) images.

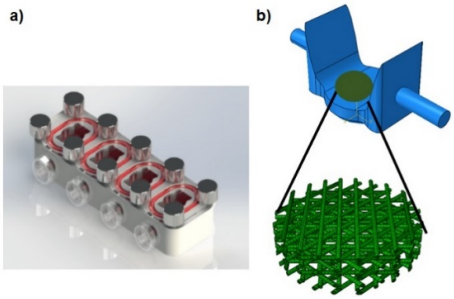

Figure 1: a) Custom bioreactor chamber; Computational model of the PCL-PLGA scaffold within the bioreactor chamber.

In-silico model. The hydrolytic degradation mechanisms of PCL and PLGA has been previously modelled [2]. The degradation process is a random hydrolytic chain scission and the rate of degradation also strongly depends on the monomers used and the ratio of copolymers [2]. In this study, we assumed that the hydrolytic degradation of aliphatic polyesters is an autocatalytic mechanism. The produced oligomers/monomers cannot diffuse but shall instantaneously disappear. The kinetics of this reaction is following the Michaelis–Menten scheme and the hydrolysis rate equation is given by Equation (1):

$$\frac{\partial C_C(x,t)}{\partial t} = k(x,t)C_E(x,t)C_w(x,t)C_c(x,t) \quad (1)$$

Where $C_C(x,t)$, $C_W(x,t)$ and $C_E(x,t)$ are the concentrations of the carboxylic end groups, water and ester groups, respectively. The reaction rate coefficient of hydrolysis $k(x,t)$ depended on the strain energy. The model was implemented in ABAQUS 6.14. We used a thermal analogy to solve the diffusion problem of water and user material definitions to solve the differential equations. A Fluid-structure interaction approach was used to estimate the load and displacements acting on the scaffolds due to perfusion (Figure 1b).

Results

Each polymeric molecule is randomly broken at a given ester group. Thus, the number of carboxylic end groups will increase with degradation time, whilst the number of ester groups decrease. The variation of ester bonds molar concentration was used to estimate the molecular weight variation. Figure 2 represented the comparison between the in-vitro results after 14 and 28d under static and perfusion conditions and predicted in-silico results. Perfused scaffolds degraded faster than static ones. Computational predictions are accurate enough.

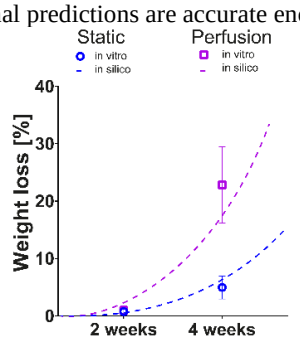

Figure 2: In-vitro and in-silico weight loss (%).

Discussion

In-silico modelling offers an efficient framework to predict and understand the behavior of biomaterials and as it has been here demonstrated it can be successfully applied to biodegradation prediction studies.

References

1. Khan F et al., Int. J. Mol. Sci. 2018, 19, 17
2. Wang Y et al., Biomaterials 2008, 29:3393-01

Acknowledgements

Authors have received funding from the EU Horizon2020 project No. 722535 and SMEC DPI2017-84780-C2-1R.

ESTIMATION OF ULTRASOUND INTENSITY FOR IN-VITRO STIMULATION OF CELLS

Meysam Majnooni (1,2), Philippe Lasaygues (3), Vincent Long (3), Jean-Claude Scimeca (4), David Momier (4), Carine Guivier-Curien (2), Cécile Baron (1)

1. Aix-Marseille Université, CNRS, ISM UMR7287, France; 2. Aix-Marseille Université, CNRS, Centrale Marseille, IRPHE UMR7342, France; 3. Aix-Marseille Université, CNRS, Centrale Marseille, LMA, UMR7031, France; 4. Université Cote d'Azur, CNRS, iBV UMR7277, INSERM iBV U1091, France

Introduction

Ultrasound stimulation of bone regeneration (USBR) was first reported in the early 1950s [1]. Although it has attracted the interest of clinicians, biologists and acousticians over the past 70 years, its therapeutic effectiveness remains controversial. The resolution of this controversy requires a better understanding of the mechanisms that drive the ultrasound mechano-transduction of bone tissue. An unavoidable first step is the implementation of an in-vitro ultrasound stimulation model. In that context, one of the key issues remains the control of the ultrasound intensity. In this study, an innovative experimental set-up coupled with a finite element (FE) numerical model is proposed in order to characterize and control the acoustic intensity delivered inside a Petri dish (PD).

Methods

Experimental set-up: A transducer of 13 mm diameter is positioned underneath a polystyrene PD (diameter 35 mm) and delivers a pulsed signal (Figure 1). In order to avoid chaotic distribution of the intensity in the near field, the distance between the transducer and the PD is set to h = 25 mm. The PD only contains water and is covered by a custom innovative absorbing system (IAS) (Figure 1). The role of the IAS is to avoid any perturbing phenomena such as standing waves [2] and its performance has been investigated and validated. The acoustic pressure is measured in the XY plane at z = 28 mm inside the PD. Then, the temporal average and spatial average temporal average intensities (I_{TA} and I_{SATA}) are calculated from these acoustic pressure measurements [3].

Numerical Model: In order to reach a precise and quantitative understanding of the phenomena, a 2D axi-symmetric numerical model based on the experimental set-up is developed in COMSOL Multiphysics. The pressure signal is $p(t) = p_0 \sin(2\pi ft\text{-}z/c_w)$ where p_0 = 57 kPa, f = 1 MHz, z, and c_w are the pressure amplitude, frequency, wave propagation direction and sound speed in water with a duty cycle of 20% at 1 kHz pulse repetition frequency. A transient acoustic pressure simulation is performed over a 1 ms cycle.

Results

I_{TA} is estimated experimentally and compared to the numerical model (Figure 2). The corresponding I_{SATA} are calculated by averaging the I_{TA} over the effective radiating area where $I_{TA} \geq 0.25 \times \max(I_{TA})$ [3]. Numerical and experimental I_{SATA} are 36.8 and 38.4 mW/cm^2 respectively.

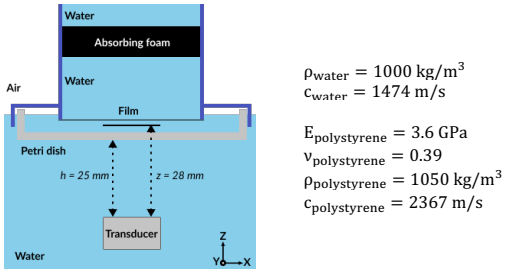

Figure 1: Schematics of the experimental setup

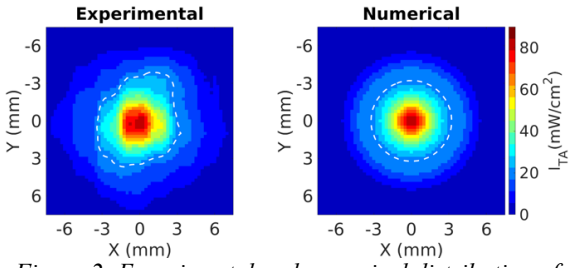

Figure 2: Experimental and numerical distribution of I_{TA}. The dashed contour represents the effective radiating area [3].

Discussion

This work proposes an innovative experimental set-up designed to properly control the ultrasonic intensity delivered inside a PD. A great accordance between experimental and numerical results (~ 4% difference) can be observed which indicates that the numerical model can capture the characteristics of the experimental set-up. In addition, the numerical model would help to perform parametric studies in order to better understand the acoustic field. This will help to study the bone cell mechano-transduction in USBR context.

References

1. Corradi et al, J Arch Ortop, 66:77-98, 1983.
2. Hensel et al, Ultrasound Med Biol, 37:2105-2115, 2011.
3. Preston, Springer Science & Business Media, 1991.

APPLYING LARGE SCALE TOPOLOGY OPTIMIZATION IN COMPUTATIONAL DESIGN OF BIOMECHANICAL STRUCTURES

Thijs Smit (1), Niels Aage (2), Stephen J. Ferguson (1), Benedikt Helgason (1)

1. Institute for Biomechanics, ETH Zurich, Zurich, Switzerland

2. Solid Mechanics, Technical University of Denmark, Denmark

Introduction

Topology optimization is a numerical method to optimize the design of an object such that a given performance metric is maximized. Currently, topology optimization (TO) is not widely used in biomechanics and biomedical engineering. However, there is a large potential for using TO in the design of implants and scaffolds tailored to e.g. patient-specific loading and enhanced bone ingrowth. This study describes an open source Python wrapper for the parallel large-scale topology optimization framework introduced by Aage et al. (2015). The Python interface simplifies the problem definition, is intended to expand the potential user-base and to ease the use of large-scale topology optimization for biomechanical applications. Furthermore, the functionality of the topology optimization framework is extended to include, among other things, local volume constraints, which contributes to its usability for real-world design applications. The framework is available at https://github.com/thsmit/, repository TopOpt_in_PETSc_wrapped_in_Python.

Methods

The wrapper allows the user to setup a TO problem via a Python script. Figure 1 conceptually illustrates the work-flow supported by the wrapper using a classic TO bracket example.

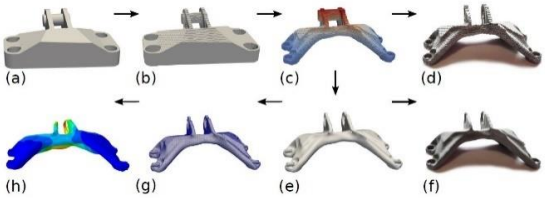

Figure 1: Work flow: from idea to a 3D printed object (a) input (.stl file) that describes the design domain (b) voxelization (c) computational design by TO and volume (.vtu file) generation for visualization (e.g. displacements) (d) 3D printing of non-smooth design (e) surface smoothing (f) 3D printing of smooth design (g) mesh generation of smooth design (h) FEM analysis of final smooth design for verification.

The topology optimization of a proximal femur is used to demonstrate the capabilities of the framework, in a biomechanical context. The example illustrates the use of physiological loading and classical TO vs. TO of porous structures, using a local volume constraint, which restricts the amount of material locally, as defined by Wu et al. (2018). A final example for demonstrating the capabilities of the framework is a scaffold, optimized for maximum porosity and a target stiffness under compression loading.

Results

The result of the TO of the proximal femur is shown in Figure 2. A clear difference between classic TO (c) and the porous infill constraint (d) is visible. A familiar cancellous bone-like internal porous structure emerges. Analysing the results of the TO under different constraints can thus enhance our understanding of nature's own design constraints and targets.

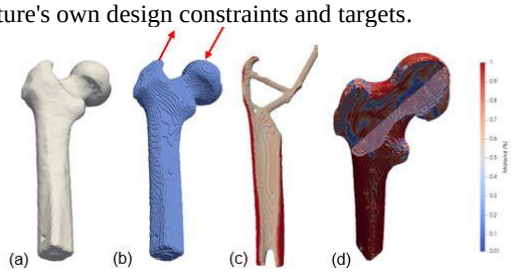

Figure 2: (a) geometry of femur (b) voxelization and application of physiological loads (c) Classical TO (d) Controlling the internal porous structure results in a bone like structure

In Figure 3, a cross-section of the scaffold designed by the framework is shown, demonstrating an interconnected porous structure with targeted pore size and porosity.

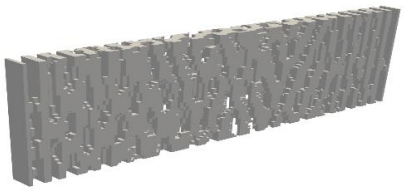

Figure 3: Slice of an interconnected porous scaffold design by the topology optimization framework

Discussion

We are releasing a large scale TO framework, available in Python. The introduction of the framework will allow a larger user group access to a state-of-the-art large-scale (high-resolution) topology optimization code. Extending its functionality increases its applicability to the design of real-world 3D biomechanical structures.

References

1. Aage et al. (2015) Topology optimization using PETSc: An easy-to-use, fully parallel, open source topology optimization framework. DOI 10.1007/s00158-014-1157-0
2. Wu et al. (2018) Infill Optimization for Additive Manufacturing-Approaching Bone-Like Porous Structures. DOI 10.1109/TVCG.2017.2655523, 1608.04366

COMMBINI: COMPUTATIONAL MECHANOBIOLOGICAL MODEL OF BONE INJURY IMMUNORESPONSE

Edoardo Borgiani (1,2), Laura Lafuente Gracia (1), Liesbet Geris (1,2)

1. Biomechanics section, Department of Mechanical Engineering, KU Leuven, Belgium;
2. GIGA in silico medicine, Biomechanics Research Unit, University of Liège, Belgium.

Introduction

Bone fracture regeneration is characterized by the cooperation of numerous biological and mechanical factors regulating the process to successfully repair the injury without leaving scars. Bone fracture regeneration is characterized by three subsequent stages: (i) the inflammatory response, (ii) the repair stage, and (iii) bone remodeling. Among them, the inflammatory response is playing the main role as it is the dance opener of the whole process. After a bone injury, inflammatory cells are the first responders and it is therefore described that their dysfunction or suppression affects the whole regenerative process, leading to delays or non-unions. In vivo studies of the inflammatory response to bone injury remain particularly challenging due to the numerous immune-response factors interacting at different time- and length-scales. To date, only Trejo et al. (2019) entrusted computer models to simulated the interactions between the inflammatory cells and their relative signals during the initial stages of fracture regeneration [1]. With COMMBINI we proposed a novel multiscale approach to better capture the stochastic nature of the events during the early stages of healing. The inclusion of a discrete approach highlighted the hidden processes at the cellular scale, which are challenging to study experimentally but whose understanding could provide interesting insights to therapeutic clinical perspectives and treatments.

Methods

COMMBINI follows a computational approach to simulate and predict the mechano-biological environment within the bone fracture opening. The model is a combination of finite element and agent-based modeling. The finite element model, which simulates the mechanical environment, is based on an existing bone fracture healing study [2]. However, the innovative aspect of COMMBINI regards the introduction of an agent-based model to simulate the cellular and sub-cellular dynamics during the inflammatory stage of bone regeneration. It simulates the behavior of immune and repair cells by reproducing their spatio-temporal distribution within the fracture domain. Besides, at sub-cellular level, it simulates the concentration dynamics of pro- and anti-inflammatory cytokines, and bone regeneration enhancing growth-factors. These signaling molecules up- or down-regulate the activities of the cells in their surroundings. The model has a double-way relationship: on one hand, the mechanical environment predicted by finite element model influences the activities of the cellular populations; on the other hand, the cellular distribution regulates the tissue formation within the region of interest, thereby updating the mechanical properties of the finite element model. The iterative nature of the simulation allows to follow how the mechano-biological environment changes during the inflammatory and repair phases of bone fracture regeneration (Figure 1).

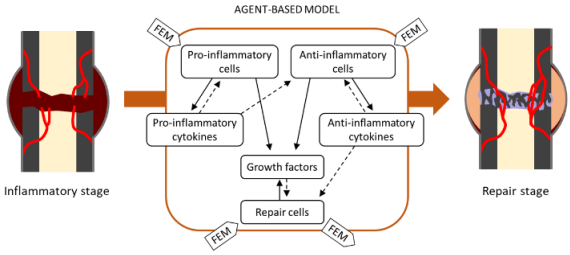

Figure 1: COMMBINI simulates the mechano-biological interactions that happen at different scale levels of bone fracture healing to investigate how inflammation influences the subsequent repair stage.

Results

To date, COMMBINI is delivering its preliminary results. The analysis of the simulation outcomes at different scales nicely highlights the spatial distribution of tissues, cell populations, and sub-cellular signals through the development of healing. Over the numerous factors involved, the model spots the most influential ones to determine their role during the inflammatory response and, consequently, their impact on the overall bone healing process.

Discussion

The principal aim of COMMBINI is to extend the vast collection of bone fracture regeneration computer models with a brand new one that explores the healing process since the initial inflammatory stage. The in silico nature and the inclusion of an agent-based model to reproduce the stochastic mechanisms at cellular and sub-cellular levels are essential to explore the numerous mechano-biological interactions that are challenging to investigate experimentally. The platform has the potentialities to become a clinical tool to explore critical healing case scenarios and provide insights about the effectiveness of treatments and therapeutics since the first instants post-injury.

References

1. Trejo et al, Math Comput Appl, 24:12, 2019.
2. Geris et al, Biomech Model Mechanobiol, 9:713-24, 2010.

A PENALTY CONTACT IMPLEMENTATION ON A HIGHLY PARALLELISABLE CARTESIAN MESH FINITE ELEMENT SOLVER

Frederik Trommer (1,2), Pinaki Bhattacharya (1,2)

1. Insigneo Institute for in silico Medicine, University of Sheffield, United Kingdom; 2. Department of Mechanical Engineering, University of Sheffield, United Kingdom

Introduction

Micro finite element analysis (uFE) is a validated tool for non-invasively quantifying bone mechanics using high resolution computed tomography (CT) images. MicroFE solvers for Cartesian mesh (or voxel) models, such as ParOSol [1], can efficiently solve problems with billions of degrees of freedom. As yet, such solvers do not accurately compute contact induced stresses due to the artificially jagged Cartesian mesh surface. The novel simulated smoothed surface, sliding contact (SS-SC) formulation [2] addressed this by simulating a smooth surface within a penalty contact approach, resulting in a reduction of errors associated with contact from 42% to 2%. The usability of the SS-SC formulation is limited by the fact that it is currently implemented in an in-house FE solver. As an intermediate step towards implementing the SS-SC formulation in the highly parallelized octree-based multigrid ParOSol solver, the present study implements the standard penalty contact formulation in ParOSol.

Methods

The disjoint deformable bodies involved in contact are assumed to occupy initially the same Cartesian grid. New data structures are defined in HDF5 file format to read in to ParOSol the geometry of these bodies, their contact surfaces and weighted master–slave contact pairings. Initial rigid-body transformations orient these bodies such that contact is incipient. An incremental solution strategy is implemented to capture intermediate contact states leading to the final state of deformation and/or load. Within each increment, contact iterations are performed to solve the inherently nonlinear contact boundary conditions. Specifically, in each iteration, the global stiffness matrix and the global load vector are updated by contributions from the tangent contact stiffness and the contact reaction forces. These contributions are computed based on [3].

The implementation was used to analyse the problem of two linear elastic, homogeneous and isotropic bodies (A and B) with hard, frictionless contact interaction (Figure 1a). The nine nodes on the bottom plane of body B (comprising four voxels) are fixed in all dimensions; the 4 nodes on the top of body A, comprising a single voxel, are restricted in x and y directions; body A is displaced downwards ($-z$ direction) onto body B such that the bodies penetrate by 6.25% of the voxel size. Two equally weighted master–slave pairs were defined with the opposing surfaces of A and B as master and slave respectively and vice versa. Model prediction is verified against an identical formulation in the commercial FEA solver Abaqus v6.14.

Results

Figure 1b and 1c compare, respectively, the predictions from ParOSol and Abaqus for contours of the normal strain in the z-direction overlaid on the deformed shape.

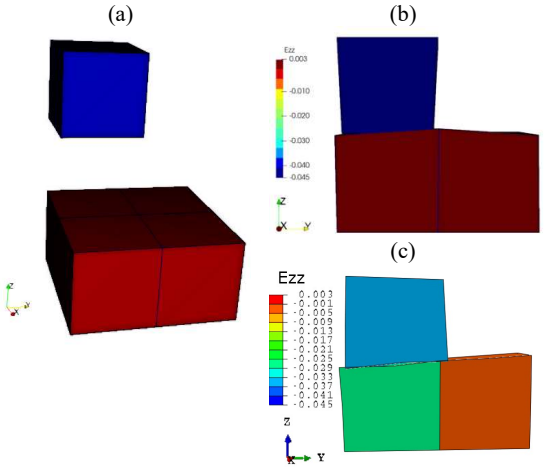

Figure 1: a) Model geometry in reference configuration with body A in red and body B in blue. Contact induced deformations and strains predicted by b) ParOSol enriched with penalty contact and c) Abaqus.

Discussion

The penalty contact formulation implemented in ParOSol reached convergence and predicted contact induced deformations and strains comparable to a commercial solver. Future implementations will engage the multigrid cycles in the solution process and include a simulated smooth surface definition, thus integrate the SS-SC formulation more completely into ParOSol.

References

1. Flaig, PhD Thesis, ETH Zürich, 2012.
2. Bhattacharya et al, Int J Numer Meth Eng, 115(4):411–26, 2018.
3. Parisch, Int J Numer Meth Eng, 28:1803–12, 1989.

Acknowledgements

This work was supported by partially supported by the EPSRC UK grant MultiSim2 (No. EP/S023940/1).

ALTERATIONS OF BILATERAL GAIT SYNERGIES IN DOWN SYNDROME

Diana Catalina Pardo Ramos (1), Alessandro Santuz (2,3,4), Matteo Zago (1), Gabriella Casarico (1), Marta Elisa Manunza (1), Claudia Condoluci (5), Adamantios Arampatzis (2,3), Manuela Galli (1)

1. Dipartimento di Elettronica, Informazione e Bioingegneria, Politecnico di Milano, Italy;
2. Department of Training and Movement Sciences, Humboldt-Universität Zu Berlin, Germany;
3. Berlin School of Movement Science, Humboldt-Universität zu Berlin, Berlin, Germany;
4. Atlantic Mobility Action Project, Brain Repair Centre, Department of Medical Neuroscience, Dalhousie University, Halifax, Canada; 5. IRCCS San Raffaele Pisana, Roma, Italy

Introduction

The hypothesis that the central nervous system activates muscles in blocks instead of individually to simplify the production of movement has been suggested since the 20th century under the name of Muscle Synergies (MS). MS extracted from electromyographic (EMG) data might reflect the modular organization of the neural strategies adopted by the central nervous system to simultaneously control functionally similar muscles [1]. Although MS have been used to study motor control in some neuro-motor pathologies such as stroke, Alzheimer and cerebral palsy, less is known about Down Syndrome (DS). In particular, no study to date described the specific bilateral activation of lower limb muscles in this pathology.

Methods

This cross-sectional study involved two age-matched (25-28 years) cohorts of 11 patients with DS and 10 healthy subjects (control group, CG). Surface EMG of four muscles were recorded bilaterally (eight muscles in total) at 1000 Hz (FreeEmg300, BTS, Italy) while performing level overground walking: rectus (RF) and biceps femoris (BF), tibialis anterior (TA) and gastrocnemius lateralis (GL). EMG data streams were high-pass filtered (*Fc*=50 Hz), full-wave rectified, low-pass filtered (*Fc*=20 Hz) to obtain the linear envelope of the signal and normalized to the maximum amplitude of each trial [2]. MS were calculated using Non-Negative Matrix Factorization as the product of two matrices: the motor modules or muscle weightings and the motor primitives or time-dependent coefficients. Differences in motor primitives between DS and CG were assessed using Statistical Parametric Mapping unpaired t-tests.

Results

The preferred walking speed was significantly lower in DS vs CG (0.6±0.2 vs 1.3±0.2 ms^{-1}, $p<0.001$).
Four synergies described bilateral muscle activations during the following gait cycle phases:

(1) in Synergy 1, (right side-weight acceptance) DS patients showed a reduced contribution of right BF and RF, and a higher contribution of the left BF;
(2) primitives of Synergy 2 (propulsion and late contralateral swing, Figure 1), were active earlier (just after foot strike or contralateral toe-off) in DS ($p<0.001$) and a greater contribution of the right RF and BF was observed, while this was reduced in the left RF and BF;
(3) in Synergy 3 (right late stance), no differences in either primitives or motor modules were found;
(4) in Synergy 4 (right late swing), only a non-relevant difference between 20-40% of the stance phase was found ($p<0.001$).

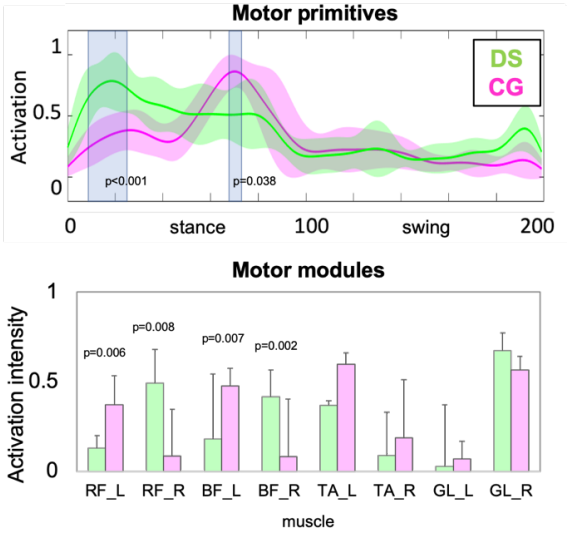

Figure 1: Synergy 2, motor primitives (top, gait cycles are time-normalized to 200 points, 100 for the stance and 100 for the swing phase; shaded areas are significant SPM clusters) and motor modules (bottom, p-values refer to Mann-Whitney rank sum test).

Discussion and Conclusion

In this study, we extracted MS from bilateral EMG activity of the lower limb to evaluate inter-limb muscle coordination during walking. In Synergy 1, a lack of activity of knee flexors and extensors was found in DS, potentially disrupting stability during step negotiation and in the weight acceptance phase [3]. Conversely, an augmented contribution of the same muscles was observed in Synergy 2.

References

1. Bizzi and Cheung, Front in Comp Neurosci, 7:51, 2013.
2. Santuz et al., Int J Neural Systems, 27:5, 2017.
3. Zago et al., IEEE Trans Neural Syst Rehab Eng, 27:8, 2019.

GAIT FATIGABILITY DURING THE 6-MIN WALK TEST IN PATIENTS WITH MUSCULAR DYSTROPHIES: A COMPARISON STUDY

Fabio Alexander Storm (1), Gianluigi Reni (1), Emilia Biffi (1)

1. Scientific Institute, IRCCS "E. Medea", Bioengineering Laboratory, Bosisio Parini, Lecco, Italy.

Introduction

Wearable sensors are becoming increasingly popular for complementing classical clinical assessments of gait deficits [1]. They have been used to inform on additional aspects of gait, especially walking-related fatigue. Literature shows that gait fatigability measured using both traditional and novel outcome parameters can be significantly correlated with physical fatigue, gait disability, and fall history [2].

The 6-minute walk test (6MWT) is a simple, non-invasive, standardized and reproducible test to assess exercise capacity. Monitoring gait during the 6MWT offers a unique opportunity to investigate the dynamic changes that occur over the entire walk.

The aim of this study is to determine which gait parameters become worse during sustained walking and to examine the clinical correlates of gait fatigability in patients with different types of muscular dystrophies.

Methods

Twelve patients with mitochondrial myopathy (MM), myotonic dystrophy type 1 (DM1) and facio-scapulo-humeral muscular dystrophy (FSHD) were enrolled and recruitment is ongoing. Data was collected during a standard 6MWT: patients were instructed to walk as far as possible along a 25-m flat hospital corridor for 6 minutes, turning 180° every 25 m. During the test, a wearable sensor (GSensor, BTS) was worn around the waist and attached to the lower back, at L5 level. The sensor included a 3D accelerometer and a 3D gyroscope, and collected data at 100 Hz. Spatial–temporal parameters of gait were extracted from raw signals using validated algorithms [3], corresponding to early (1st minute), middle (3rd and 4th minute) and late (6th minute) segments of the 6MWT. Non parametric test were performed to compare gait parameters between segments and within type of dystrophy.

Results

Preliminary results show a significant decrease of cadence (p=0.042, Table 1) and gait symmetry (p=0.030, Table 2) in the DM1 group, but no significant deterioration in patients with MM or FSH.

	6MWT segment		
	Early	***Middle***	***Late***
DM1*	*131 ± 20*	*129 ± 15*	*127 ± 18*
MM	*125 ± 35*	*119 ± 27*	*124 ± 29*
FSP	*90 ± 47*	*86 ± 45*	*86 ± 44*

*Table 1: Results for cadence (steps/min) in the patient populations across the three segments of the 6MWT. *p<0.05.*

	6MWT segment		
	Early	***Middle***	***Late***
DM1*	*96.3 ± 6.0*	*94.6 ± 8.3*	*95.0 ± 8.1*
MM	*96.3 ± 11.1*	*96.7 ± 3.7*	*96.9 ± 5.1*
FSHD	*93.8 ± 4.0*	*93.9 ± 7.5*	*94.2 ± 4.1*

*Table 2: Results for gait symmetry (%) in the patient populations across the three segments of the 6MWT. *p<0.05.*

Discussion

Fatigue is a well known complaint in patient with muscular dystrophies, but has not yet been well investigated [4]. Our preliminary results suggest that gait parameters associated to fatigability can be measured during a standard 6MWT using an unobtrusive, wearable device, and that the method allows to highlight differences in gait fatigability between types of dystrophies.

References

1. Ben Mansour et al, Gait & Posture 42 (2015) 409–414
2. Shema-Shiratzky et al, J Neurol. 2019 Dec;266(12):3022-3030.
3. Bugané et al, Comput Meth Prog Bio 2012; 108: 129–137.
4. Angelini & Tasca, Neuromuscul Disord. 2012 Dec 1; 22(3-3): S214–S220.

Acknowledgements

We thank Ms Eleonora Diella for her help in the experiments. This work was supported by the Italian Ministry of Health (Ricerca Corrente 2018/2019/2020 to Eng G. Reni and Dr. E. Biffi).

Gait analysis to establish an individual postoperative treatment after fractures of the tibia

Annchristin Uhl (1), Michael Roland (1), Kerstin Wickert (1), Marcel Orth (2), Tim Pohlemann (2), Stefan Diebels (1)

1. Saarland University – Chair of Applied Mechanics, Germany
2. Saarland University Medical Center – Clinic for Trauma, Hand and Reconstructive Surgery, Germany

Introduction

Limited gait-load during the healing process after fractures of the tibia can be defined by measurement and monitoring of postoperative gait analysis in patients compared to reference data of healthy subjects. For this purpose, kinematic and kinetic types of gait analysis are required. The findings of this analysis demonstrate that it is possible to collect data for individually adapted implants and to create individual loading recommendations.

Methods and Results

The inquiry of the project uses Xsens™ (Xsens Technology B.V., Enschede, Nederland) for motion capturing as kinematic analysis and sensor insoles (Moticon™ ReGo AG, Munich) for the kinetic gait analysis. Besides that, the physiological gait parameters such as gait line and centre of pressure are analysed. The Xsens system uses 17 trackers, which are inertial measurement units placed at strategic locations on the body by straps in order to measure the motion of every segment. The Moticon insoles use the ground reaction force to create a gait analysis by applying 16 pressure sensors and an inertial measurement unit inside the insoles. The measurement process proceeds such as follows: First, the surgeon decides whether a patient may be considered for the study by analysing the pattern of injury using initial X-rays and CT-images (computed tomography images). If patients signed the informed consent form, the gait analysis with the two systems starts shortly after the surgical intervention depending on the mobility level of the patient. The two systems are used simultaneously during the measurement taken along physiotherapy. By this means, the patient learns to walk and take stairs in consideration of the prescribed limited gait load by using crutches. The recorded gait data are compared with the data of a healthy subject. This workflow is repeated after 6 and 12 weeks after the surgery to monitor the complete healing process. After the data collection, values are implemented into the software AnyBody™ (AnyBody Technology A/S Aalborg, Denmark) in order to analyse the ground reaction- as well as muscle forces by creating a digital avatar of the patient.

The results show clearly the impact of the physical condition of the patient on the healing process and the impact of the physiotherapy. In fact, physiotherapy can be supported by this analysis to visualize and monitor gait pattern and the development of a physiological gait pattern during the healing process. Thereby pathological processes, which may lead to the development of non-healing fractures, can be detected at an early time point after surgery and may be prevented by early adaption of the postoperative treatment protocol. Furthermore, it is possible to understand the forces that affect the fracture and its healing process permanently in much more detail.

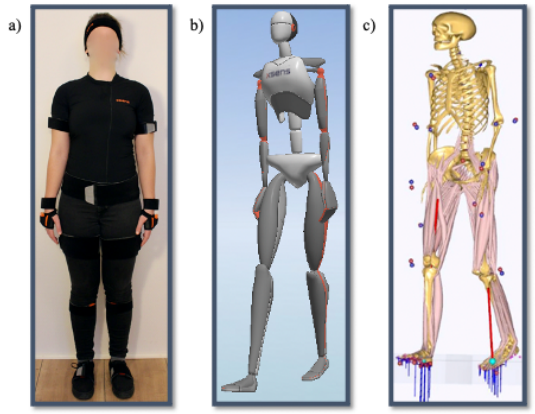

Figure 1: Systems to generate the kinematic gait cycle
a) Subject wears motion capturing system from Xsens
b) Analysis using the Xsens software
c) Analysis using the AnyBody software after creating a digital avatar

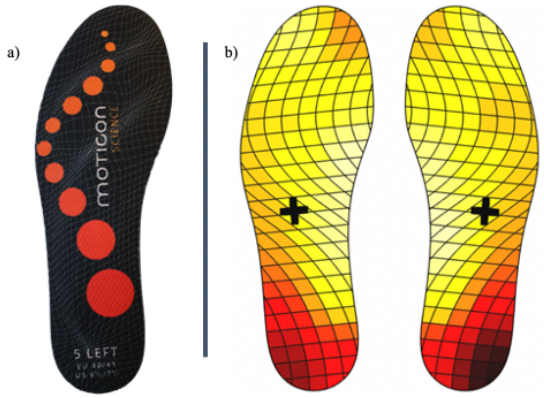

Figure 2: Moticon System to generate the kinetic gait cycle
a) Moticon sensor insole
b) Mean pressure distribution while walking

Acknowledgements

The Werner Siemens-Stiftung supported this work under the grant “Smart Implants 2.0”.

QUANTIFICATION OF MULTI-SEGMENTAL SPINE KINEMATICS: THE RELIABILITY AND OUTCOMES OF A NEW PROTCOL

Jennifer Fayad (1,2), Peter Eltes (2), Aron Lazary (2), György Szőke (3), Tamás Terebessy (3) Luca Cristofolini (1), Rita Stagni (4)

1. Department of Industrial Engineering, Alma Mater Studiorum – Università di Bologna; 2. National Centre for Spinal Disorders, Budapest; 3. Department of Orthopaedics – Semmelweis University, Budapest; 4. Department of Electrical, Electronic and Information Engineering "Guglielmo Marconi", Alma Mater Studiorum – Università di Bologna

Introduction

Motion abnormalities have been found to impact the prevalence and recurrence of spine disorders [1]; a better understanding of spine kinematics is necessary to improve treatment, surgical planning and assess the role of spine pathologies on activities of daily living (ADL) [2]. Several marker-based motion analysis protocols have been proposed however, assessment of the reliability and functional significance of the kinematic variables is lacking for healthy and pathological cohorts. Additionally, the role of coordination between spinal segments, and with respect to other body segments is often disregarded. The lack of protocol standardization and the limited analysis of kinematic alterations restrict the distinction between a pathological alteration and a potential functional compensation during ADL.

The aim of the present study is to fill this gap: to develop and validate a comprehensive protocol for spinal kinematics assessment that provides clinically significant data. This study included experimental assessment of methodological reliability, identification of kinematics reference patterns and timings during simple mobilization and ADLs.

Methods

Protocol: The marker setup included 9 markers attached on the trunk at C7, T3, T7, T12, L3, clavicle, sternum, right and left acromia; to define four spine segments: upper thoracic (UT), lower thoracic (LT), upper lumbar (UL) and lower lumbar (LL) in addition to the pelvis. 3D angles between adjacent segments and in respect to the pelvis were quantified during standing, full flexion (FF), thoracic flexion (TF), lateral bending (LB), sit-to-stand, ball-lifting, and level walking.

Experimental Setup: 19 healthy participants were recruited [10F, 9M; age: 26.6±4; height: 175.6±7.4cm; weight: 71.1±14.9kg]. Marker kinematics was acquired using stereophotogrammetry (VICON, UK).

Protocol Testing: Two marker placement techniques were tested to quantify soft tissue artefact (STA) and marker misplacement.

Data Analysis: 3D angular data was normalised over task duration and synchronised with respect to key events identified in the motion to analyse segment coordination and event timing. Reference bands of motion were generated showing the median angle of motion and the 25th-75th percentile range.

Results

Marker Placement: Differences in intersegmental kinematics were found due to marker placement and STA accounting for a maximum of 25% change in the LT/UL angle during TF (fig.1, A). The maximum difference in key event timings was equal to 5% change in the coronal plane during LB, changes in the sagittal plane were limited to <2% for FF and TF.

Reference Bands: After event synchronization, angular intersegmental kinematics exhibited high inter- and intra- subject repeatability in both flexion/extension and lateral bending (fig.1, B). Segmental coordination analysis showed differences in the timing of segments with UL/LL starting the motion before UT/LT during FF, the opposite was seen during LB. Differences in motion contribution were also seen, LT/UL contributed the most to the sagittal plane motions accounting for double the angle of motion detected at the UT/LT joint.

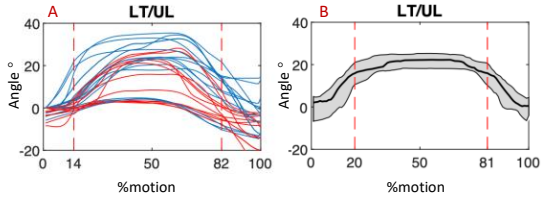

Figure 1: LT/UL angles in the sagittal planes during thoracic flexion(A) and full flexion(B).

Discussion

The preliminary testing of the proposed protocol highlighted a repeatable approach for the characterisation of spine intersegmental kinematics. Marker misplacement and STA were found to influence intersegmental kinematics to a different extent for different segments. Based on the variability assessed in the study, the number of cohorts for the identification of significant reference bands will be increased and compared to pathological patient motion.

References

1. Gombatto et al., Gait Posture, 42:539-544, 2015.
2. Christe et al., J. Orthop. Res., 38:1248-1256, 2020.
3. Grood et al., J. Biomech Eng.,105:136-144,1983.

Acknowledgements

The project leading to the scientific results was supported by the European Commission (766012 -SPINNER – H2020-MSCA-ITN-2017) and the Hungarian Scientific Research Fund (OTKA FK123884).

THE STUDY OF UPPER EXTREMITY MOTIONS UNDER PARTIAL GRAVITY

Tatiana Volkova (1), Claude Nicollier (1), Volker Gass (1)

1. Space Innovation, École Polytechnique Fédérale de Lausanne, Switzerland

Abstract

According to biomedical research, the effect of partial gravity (PG) on the human body is crucial [1, 2, 3]. In the long-term, this can create health problems, reduce well being, and affect the capacity to perform assigned tasks.

This exploratory study provides valuable insights into the effect of PG on the joints of the upper extremity (wrists, elbows, shoulders, etc.). The main focus is on learning the seated posture of a person and performing various tasks in the workplace.

To simulate the different tasks in the workplace in PG, we conduct an experiment in a hydro-laboratory. To provide a comparison, the same tasks were performed in earth gravity conditions. This experiment involved seven healthy males and seven healthy females (all aged 35±5years). Data collection equipment included force plates, dynamometers, load cells built into the experimental workplace, and video cameras, as well as survey on subjective mental workload assessment [4].

Both the static postures [5] as well as dynamic motions were the subject of this study. The static equilibrium were studied using the d'Alambert's principle, while the analysis of dynamic motions was based on the recursive Lagrangian formulation [6].

The results of this exploratory study facilitate better understanding of the relation between different gravity levels, joint profiles' results, and anthropometric parameters of the upper extremity of subjects by means of linear regression techniques.

For simple motions, we find minor deviations between the relations predicted by the mathematical simulations and the actual hydro-laboratory environment experiments. Another parameter that is measured is the level of subjects' fatigue [7]. While the linear relation between joint workload and gravity is well understood, its long-term effect remains understudied. Our work contributes to the understanding of joint profiles and fatigue levels of upper extremity of subjects under PG and earth gravity while performing the similar tasks.

The data obtained from these experiments and the proposed methods for studying movements can be applied to improve the ergonomic conditions of the workplace in PG. The findings of this study can also be applied for improving the human digital modeling approach under PG conditions.

References

1. Richter C., Braunstein B., Winnard A. 5, Nasser M., Weber T., Human Biomechanical and Cardiopulmonary Responses to Partial Gravity – A Systematic Review, original research article, Front. Psysiol, 2017.
2. Sylos-Labini F., Lacquaniti F., Ivanenko P., 2014, Human Locomotion under Reduced Gravity Conditions: Biomechanical and Neurophysiological Considerations, Biomed Res Int., 2014.
3. Chappell, S.P. and Klaus, D.M., Enhanced simulation of partial gravity for Extravehicular Activity. Journal of Human Performance in Extreme Environments, 10(2), p.1, 2013.
4. de Winter, J. C., Controversy in human factors constructs and the explosive use of the NASA-TLX: a measurement perspective. Cognition, technology & work, 16(3), 289-297, 2014.
5. Rohmert, W., Wangenheim, M., Mainzer, J., Zipp, P., & Lesser, W., A study stressing the need for a static postural force model for work analysis. Ergonomics, 29(10), 1235-1249, 1986.
6. Abdel-Malek, K., Yu, W., & Jaber, M., Realistic posture prediction. SAE Digital Human Modeling and Simulation, 2001.
7. Frey Law, L. A., & Avin, K. G., Endurance time is joint-specific: a modeling and meta-analysis investigation. Ergonomics, 53(1), 109-129, 2010.
8. Bigland-Ritchie, B. W. J. J., & Woods, J. J., Changes in muscle contractile properties and neural control during human muscular fatigue. Muscle & Nerve: Official Journal of the American,1984.
9. Chang, S.W. and Wang, M.J.J., Digital human modeling and workplace evaluation: Using an automobile assembly task as an example. Human Factors and Ergonomics in Manufacturing & Service Industries, 17(5), pp.445-455, 2007.
10. Vink P., Bazley C.M., Jacobs K., 2016, Modeling the relationship between the environment and human experiences, Environmental Design, Work, vol. 54, no. 4, pp. 765-77, DOI: 10.3233/WOR-162374, 2016.
11. Vogler. A, Design study for an astronaut's workstation, Journal of aerospace, SAE Transactions, p. 529-540, 2005.

REAL WORLD MOTION ANALYSIS IN CHILDREN: A RELIABILITY AND REPEATABILITY ASSESSMENT

Alfredo Ciniglio (1), Francesca Michieletto (1), Federica Cibin (2), Fabiola Spolaor (1), Annamaria Guiotto (1), Zimi Sawacha (1,3)

1. Dept of Information Engineering, University of Padova, Italy

2. BBSoF S.r.l., Padova, Italy

3. Dept of Medicine, University of Padova, Italy

Introduction

Gait analysis is a process of instrumented measurement and evaluation of walking ability in patients, recognized as a useful assessment tool and a support in medical decision-making [1]. Standard gait analysis is performed within a gait laboratory by means of stereophotogrammetric systems. Recently great attention has been given to the possibility of assessing children's motion for gait and posture evaluation purposes, in real world conditions [2]. The aim of this study was to evaluate the reliability and repeatability of a methodology for gait and posture assessment in real world conditions by means of commercial video-cameras and automatic tracking of features techniques in children. This approach could be exploited in ambulatory conditions, in school or sport facilities, for the prevention of postural alterations in children with foot deformities [3], scoliosis [4] and temporomandibular disorders [5]. Furthermore the reliability and repeatability of the methodology was assessed with respect to stereophotogrammetry. Results are encouraging as good reliability and repeatability were observed.

Methods

Eleven subjects (mean±SD age 9.7 ± 2.6 years, BMI 20.6 ± 3.5 kg/m2) were acquired simultaneously with a stereophotogrammetric system (6 TVC, 60-120 Hz, BTS) and 4 GoPro Hero 7 cameras. Each subject performed several gait cycles and 4 different set-up were adopted: reflective markers on anatomical landmarks ("BTS"), markers made with double colored tape ("Tape") [6], without applying any marker ("NoTape"). Reflective markers were applied as in [7] and trajectories were reconstructed through stereophotogrammetry ("BTS") or video tracking ("Marker"), using Track on Field (BBSoF, S.r.l), based on a self-developed tracking of feature algorithm [6]; in the other 2 conditions (Tape and NoTape), a simplified version of [7] was applied and only video tracking was used to reconstruct anatomical landmarks trajectories. Joints angles were determined as in [6] for "BTS" and "Marker" set up, while only sagittal plane kinematics was retrieved for "Tape" and "NoTape". Comparison among the four set-up was performed through the estimation of the mean root mean square distance (RMSD) and Wilcoxon signed-rank test ($p<0.05$). For the inter-trial variability, the Coefficient of Multiple Correlation ("CMC") [8] was calculated for each biomechanical variable. Normative bands were created, for each condition, including only trials with a CMC>0.7 [9]. To verify the inter-operator variability the Standard Error ("SE") [9] was calculated (2 operators).

Results

Although statistically significant differences were observed, results showed that the 4 set up were comparable in terms of occurrence of the joint angles peak within the gait cycle (Fig. 1, right) and range of motion (Fig.1, left). Good inter-operator repeatability was found.

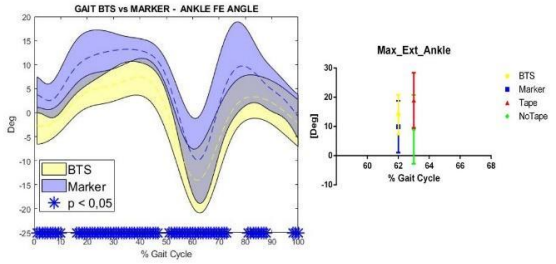

Figure 1: Left side:, Ankle Flexion-Extension Angle, "BTS" & "Marker"; right side:, Ankle Extension Angle Peaks.

Discussion

Results are encouraging toward the adoption of a wider use of motion analysis in real world conditions as in sport or rehabilitation facilities, and schools, for prevention of children musculoskeletal alterations.

References

1. Wang et al, Sensors; 19(8): 1925, 2019.
2. Benedetti et al, Gait & Posture, 58: 252-260, 2017.
3. Root et al, JAPMA, 89: 268-269, 1999.
4. Negrini et al, SOSORT, 7:3, 2012.
5. Mason et al, Otolaryngologists, 4(4): e110, 2014.
6. Magalhães et al, J Sports Sc & Med, 58:194-200, 2013.
7. Leardini et al, Gait & Posture, 26(4): 560-71, 2007.
8. Ferrari et al, Gait & Posture, 31(4): 540-542, 2010.
9. Schwartz et al, Gait & Posture, 20: 196-203, 2004.

A SUPERVISED CLASSIFICATION OF CHILDREN WITH FRAGILE X SYNDROME BASED ON GAIT ANALYSIS

W. Piatkowska (1), M. Romanato (1), F. Spolaor (1), A. Huang (1), F. Cibin (1), A. Ciniglio (1), R. Polli (2), A. Murgia (2), Z. Sawacha (1, 3)

1 Department of Information Engineering, University of Padova, Italy
2 Department of Women and Children Health, University of Padova, Italy
3 Department of Medicine, DIMED, University of Padova, Italy

Introduction

Fragile X Syndrome (FXS) is the leading form of inherited intellectual disability and autism spectrum disorder, caused by a tri-nucleotide CGG repeat expansion in the promoter region of the FMR1 gene [1]. In these subjects, the frequent musculoskeletal manifestations; such as ligamentous laxity and flat foot [1], justifies a referral for gait analysis.
Supervised classification is generally used to find the relation between the input parameters and the target variable [2] that in our contest is represented by the presence of musculoskeletal alterations associated with FXS in the examined subjects. The aim of the present study was to find out which set of kinematics and sEMG parameters were the most useful to discriminate between controls and FXS subjects, for assisting in clinical decision making.

Methods

After appropriate informed consent by the parents, 20 FXS children ((FX) mean (±SD) age and BMI respectively of 10,00 (±3,74) years and 18,57 (±3,46) Kg/m^2) and 16 controls ((CS) mean (±SD) age of 10,22 (±3,19) years and 22,84 (±3,93) BMI of Kg/m^2), were evaluated at the BiomovLab of the Department of Information Engineering and at the Woman and Children Health Department of the University of Padua. Kinematics and sEMG data were simultaneously acquired through 4 synchronized cameras (GoPro Hero3, 30fps) and an 8 channel sEMG system (FreeEmg, BTS, 1000Hz) that collected the activity of Tibialis Anterior (TA), Gastrocnemius Lateralis (GL), Rectus Femoris (RF) and Biceps Femoris (BF). Each subject performed several gait trials and at least three trials per subject were processed. The following sEMG parameters were extracted: duration of muscle contraction, onset and offset activation timing [3], peak of the envelope and its occurrence [4], number of co-contraction and its occurrence. The following kinematic parameters were estimated: minimum and maximum values of lower limb joints angles (hip, knee and ankle) and their range of motion (ROM) [5]. Supervised classification by means of 7 different classifiers was performed: Decision Tree, Random Forest, CN2 Rule Induction, SVM, k-NN, Neural Network and Naïve Bayes was performed on 3 different sets of vectors: S1. sEMG parameters only; S2. kinematic parameters only; S3. combined sEMG and kinematic parameters.

Results

The best classification on a training set (66% of subjects) were obtained by applying k-NN algorithm for S2. and Random Forest for S1 and S3; hence it was further tested on a test set (33% of subjects) (Table 1 and Fig. 1).

Set of vectors	S1	S2	S3
Algorithm	Random Forest	k-NN	Random Forest
Training set acc (%)	98,3	100,0	99,2
Test set acc (%)	98,3	100,0	96,7

Table 1: Performance of the most performant classification algorithms on training and test data.

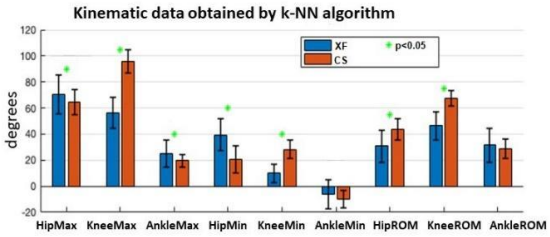

*Figure 1: Kinematic parameters in subjects classified as FX and CS by k-NN classifier, *-statistically significant difference ($p<0.05$)*

Discussion

All the analyzed solutions allowed a good classification of FXS subjects, yet using only kinematic data allowed a better classification. This suggests that the most evident differences in motor control between CS and FX subjects can be detected by analyzing the kinematic parameters.

References

1. Hagerman RJ, et al, Nat Rev Dis Primers, 3, 17065, 2017
2. Alloghani, M. at al., Springer Int. Publishing, Cham, pp. 3–21., 2020
3. Bonato P, et al, IEEE Trans Biomed Eng, 45(3):287-99, 1998
4. Sawacha Z, and Spolaor F, et al, *Gait Posture*, 35(1):101-5, 2012.
5. Sartori M, et al, Neurophysiol 114: 2509–2527, 2015.

COMPARING THE KINEMATICS OF STROKE SURVIVORS AND HEALTHY INDIVIDUALS IN A 360-DEGREE TURNING TASK USING INERTIAL MEASUREMENT UNITS

Masoud Abdollahi [a], Pranav Madhav Kuber [a], Christopher Hoang [b], Michael Shiraishi [b], Rahul Soangra [b,c], Ehsan Rashedi [a*]

[a] *Industrial and Systems Engineering Department, Rochester Institute of Technology, Rochester, NY, USA*

[b] *Department of Physical Therapy, Crean College of Health and Behavioral Sciences, Chapman University, Orange, CA, USA.* [c] *Fowler School of Engineering, Chapman University, Orange CA 92866, USA*

Introduction

The experience of a severe ailment like stroke is known to affect the neuro-musculoskeletal system of the human body, engendering difficulty in performing daily activities as observed even in recovered survivors [1]. Consequently, stroke patients encounter physiological alterations (e.g., muscle weakness, whole-body fatigue, and partial sensory impairment) leading to asymmetric movement that hinder regular movement patterns. Even a simple movement like turning, which requires a combined effort of multiple systems of the body, may not be successfully completed by a stroke survivor thereby resulting in a slip, trip and/or fall [2]. Although rehabilitation is possible, analyzing and comparing the motion of such individuals with healthy individuals (HI) using wearable sensors may help researchers to identify the critically affected aspects of the movement during 360-degree turn. This may expose opportunities for the development of potential assistive remedies (e.g., design of more effective rehabilitation program) to reduce injury among stroke survivors (SS). Through this study, our efforts will be geared towards identifying and comparing the most prominent features that exhibit differences in the kinematics between HI and SS during a complete turning task using wearable sensors.

Methods

A laboratory experiment was conducted by recruiting 10 participants (5HI, 5SS) as they performed in-place 360-degree turning. Prior to conducting the experiment, 4 Inertial Measurement Units (IMUs) were secured over-the-body (one on each shank, another on the sternum and one on the sacrum). The analysis was performed in three major steps: filtration, segmentation and feature extraction. Looking at the foot movement, duration between each of the two consecutive intermediate foot placement was classified as one cycle and used for segmentation. Finally, we identified 11 features (i.e., duration of task, number of cycles, mean angular velocity of shank, sacrum and sternum per cycle; ratio of stance-time to the duration of task, rotational angles for sternum and sacrum about each axis, flexion angle for shank) and compared them between HI and SS.

Results

We observed a significant difference (p-value < 0.05) between SS as compared to HI for number of cycles, duration of turn, range of trunk lateral bending, and range of sacrum lateral bending. HI completed 3.8 cycles in 4.4 secs at an average, whereas SS needed 7.4 cycles per turn at a mean duration of 9.5 secs. Further, SS showed increased wobbly motion while performing the turn, seen from the lateral bending angles of trunk and sacrum. Although not significant, all features (except angular velocities) displayed higher mean values for SS. Table 1 below demonstrates the mean values of the parameters in SS and HI, along with the p-values.

Table 1. Statistical comparison and mean (SD) of spatiotemporal features for Healthy Individuals and Stroke Survivors

Feature Name	Healthy Individuals Mean (SD)	Stroke Survivors Mean (SD)	p-values
Number of Cycles	3.8 (0.8)	7.4 (2.3)	**0.040**
Duration of Turn (sec)	4.4 (1.9)	9.6 (3.5)	**0.041**
Mean Angular Velocity of Trunk Flexion (deg/sec)	1.1 (0.2)	0.3 (0.8)	0.156
Mean Angular Velocity of Sacrum Flexion (deg/sec)	1.1 (0.2)	0.2 (0.9)	0.139
Mean Angular Velocity of Shank Flexion (deg/sec)	2 (0.3)	1.6 (0.5)	0.153
Ratio of Stance Time to Duration of Turn (%)	42.9 (7.6)	57.9 (16.6)	0.066
Range of Trunk Lateral Bending (deg)	5.8 (1.0)	12.7 (4.8)	**0.017**
Range of Sacrum Lateral Bending (deg)	6.7 (0.8)	10.9 (2.3)	**0.006**
Range of Trunk Flexion-Extension (deg)	6.5 (1.9)	9.5 (2.9)	0.110
Range of Sacrum Flexion-Extension (deg)	6.9 (0.9)	7.7 (3.8)	0.613
Range of Shank Flexion-Extension (deg)	11 (1.8)	17.7 (8.1)	0.179

Discussion

According to the results, there was no significant difference between the angular velocity and range of motion for the shank, sacrum and trunk in flexion-extension. This reveals the fact that the required pace of body movement for the HI was not excessively large to be reached by SS. However, the range of lateral bending for trunk and sacrum was significantly larger in SS vs HI. The larger wobbling in upper body could stem from the degraded ability of the SS in balance retaining. The identified features in this study can help in designing/improving rehabilitative programs for SS. For example, including a task targeting the core stability in patients can lead to an improved rehabilitation program.

References

1. Carlsson et al, Cerebrovascular Diseases, 16(4):383-8, 2003.
2. Walsh et al, J Epidemiol Community Health, 70(5):513-9, 2016.

PROOF-OF-CONCEPT EXPLORATORY STUDY: MARKERLESS MOTION CAPTURE METHODOLOGY BASED ON DEEP LEARNING

Silvia Zampato (1), Azza Bouleimen (1), Francesco Piemontese (1), Silvia Fantozzi (2), Giorgio Gatta (3), Matteo Cortesi (3), Michele Rossi (1), Zimi Sawacha (1,4),

1. Dept of Information Engineering, University of Padova, 35131 Padova, Italy;
2. Dept of Electrical, Electronic and Information Engineering, University of Bologna, 40136 Bologna, Italy;
3. Dept for Life Quality Studies, University of Bologna, 47921 Rimini, Italy;
4. Dept of Medicine, University of Padova, 35128 Padova, Italy

Introduction

Markerless motion capture methods are becoming valid alternatives to marker-based optical systems. The main objective of such techniques is to overcome the intrinsic limitations of marker-based ones. Spurred by the advent of deep neural networks and by their successful application in images and videos, we propose a specific machine-learning based processing pipeline for the motion capture field to move towards the realization of a markerless joints' tracker that estimates natural poses on field.

Methods

Forty two gait trials performed by 3 subjects (mean age 27.3 ± 5.5 years, mean BMI 21.3 ± 2.6 kg/m^2) were acquired both in a laboratory environment (out-of-water, OW) and underwater (UW) in a swimming pool. Six synchronized underwater color analog wide-angle cameras (720×576 pixel resolution TS-6021PSC), were used. The system was synchronized automatically employing a custom-made software application as in [1]. The synchronization delay was found to be inferior to a frame duration, which in our study is 20 ms. Calibration of the intrinsic parameters was performed in dry conditions, filming a black and white checkerboard as in [1] and then corrected for UW condition [1]. Extrinsic calibration was performed with a 12-control points calibration grid (2 m×1.1 m×1.1 m) [1]. The processing pipeline can be summarized as follows: 1. the video frames are extracted and undistorted; 2. a person detector [2] identifies the subject's presence in the set of 6 synchronized frames and, if found, the region of interest in the image is processed by a pose estimator [3] that provides the probability maps for each joint in the 6 regions of interest, separately; 3. the information from different point of views are merged by means of triangulation: at this step, the three-dimensional pose is reconstructed; 4. a subject-specific model is utilized to match the lengths of the subject's limbs in the obtained pose model; 5. the lower limb joints sagittal plane rotations are estimated as planar angles between anatomical segments for each gait cycle and low-pass filtered. In order to assess reliability of the proposed approach the same gait trials were processed by automatically tracking anatomical landmarks (Track on Filed, BBSOF S.r.l.) marked on the subjects skin with a waterproof black marker, according to CAST [4]. Mean and Standard deviation, across trials, of each planar angle were computed for each technique and compared (Paired T Test $p<0.05$).

Results

No statistically significant differences were observed between the two techniques both OW and UW (Fig.1).

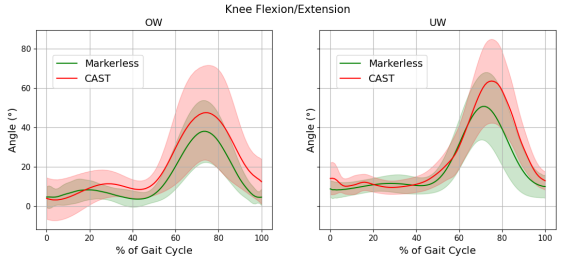

Figure 1: Knee flexion-extension angles during gait for the same subject in OW and UW environments.

Discussion

The proposed approach can be used in a real-time acquisition setup. These results can be used to address further improvements towards a fast and accurate tool for gait analysis, also in challenging environments such as UW.

References

1 Ceseracciu E. et al, Journal of Biomechanics, 44(12):2236-2242
2 Ren S. et al, IEEE Transactions on Pattern Analysis and Machine Intelligence, 39:1137-1149, 2017
3 Sun K. et al, IEEE/CVF CVPR, 5686-5696, 2019
4 Cappozzo A. et al, Clinical biomechanics, 10:171–178, 1995

A FACE TRACKING APPROACH TO EVALUATE HYPOMIMIA IN PARKINSON'S DISEASE SUBJECTS

Elena Pegolo (1), Lucia Ricciardi (2,3), Daniele Volpe (4), Zimi Sawacha (1,5)

1. Department of Information Engineering, University of Padova, Italy; 2. St George's University of London, Molecular and Clinical Sciences Institute, United Kingdom; 3. Medical Research Council Brain Network Dynamics Unit, Nuffield Department of Clinical Neurosciences, Oxford, United Kingdom 4. Fresco Parkinson Center, Villa Margherita, S. Stefano, Vicenza, Italy; 5. Department of Medicine, University of Padova, Italy

Introduction

Parkinson's disease (PD) is a neurodegenerative disorder that mainly causes gait disturbances and postural abnormalities. Among other symptoms, hypomimia is one of the hallmark manifestations of PD. Patients experiencing this condition usually exhibit an impaired facial expressiveness (*masked face*) with respect to healthy subjects (HS) [1]. The aim of our study is to quantify the degree of hypomimia comparing HS and PD subjects exploiting a face tracking approach based on the Facial Action Coding System (FACS) [2]. FACS is a human observer-based system that encodes facial muscles movements identifying action units (AUs); AUs are related to either single or sets of muscles and they can entirely describe the human basic emotions: anger, disgust, fear, happiness, sadness, surprise and neutral [3].

Methods

Data from 17 HS (10 women and 7 men; mean(±SD) age: 66.53(±7.16) years) and 29 PD subjects (13 women and 16 men; mean(±SD) age: 68.48(±7.80) years) were considered. A video recorded session was performed while subjects were seated at 1.36 m from a commercial camera with a white background behind them. They were instructed by a clinician to randomly perform the following expressions: anger, disgust, fear, happiness, sadness, surprise and neutral. Data were analyzed using a self-developed software (*TrackOnField, BBSoF S.r.l.*) [4]. Videos were segmented into 4 frames; per each obtained image, a set of 56 features was tracked in the 2D-image space and 35 distances were calculated. Values outside the interquartile range were excluded from the analysis. A face mobility index (FMI) was defined as follows:

$$FMI_j = \frac{\sum_{i=1}^{n_dist} |1 - ratio_j| \cdot 100\%}{n_dist} \; j = 1 \dots 6$$

Per each emotion ($j=1\dots6$) the ratio between the i-th distance and its corresponding one in the neutral expression was calculated (*ratio*). FMI was defined as the summation of the percentage changes from the neutral expression, normalized to the number of available distances (*n_dist*). In order to compare the FMI in the two cohorts of subjects, the non-parametric Kruskal Wallis test ($p<0.05$) was performed.

Results

Results highlighted statistically significant differences in the FMI in two expressions: anger and happiness (Figure 1).

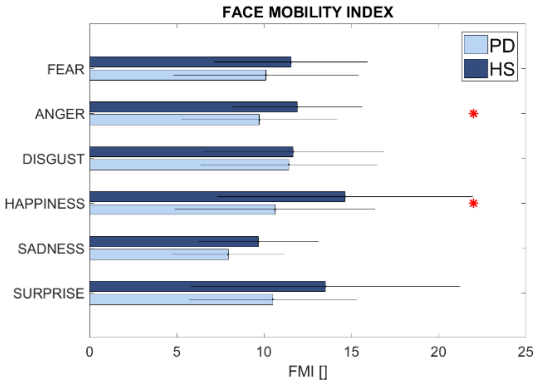

Figure 1: Face mobility index (FMI) for the six expressions in PD and HS subjects ($p<0.05$), the zero value corresponds to the neutral expression.

Discussion

Besides some limitations (subjectivity in the interpretation and expression of the emotion and numerosity of the sample), encouraging results were achieved. Indeed, as expected, HS showed a larger face mobility with respect to PD patients. The index we proposed is clinically easy to interpret. Furthermore, FMI could be used to quantitatively track the disease progression.

References

1. Ricciardi L. et al, PLOS One, 12(1):e0169110, 2017.
2. Ekman, P., Facial Action Coding System: Investigator's Guide; Consulting Psychologists Press, 1978.
3. Wu P. et al, Comput Math Methods Med, 2014.
4. Magalhaes FA et al, J Sport Sci Med; 12:660, 2013

QUANTIFICATION OF THE EFFECTS OF A TREATMENT OF HYPOMIMIA IN PARKINSON'S DISEASE: A PRELIMINARY STUDY

Elena Pegolo (1), Lucia Ricciardi (2,3), Daniele Volpe (4), Zimi Sawacha (1,5)

1. Department of Information Engineering, University of Padova, Italy; 2. St George's University of London, Molecular and Clinical Sciences Institute, United Kingdom; 3. Medical Research Council Brain Network Dynamics Unit, Nuffield Department of Clinical Neurosciences, Oxford, United Kingdom 4. Fresco Parkinson Center, Villa Margherita, S. Stefano, Vicenza, Italy; 5. Department of Medicine, University of Padova, Italy

Introduction

Parkinson's disease (PD) is a neurologic disorder characterized by a progressive motor impairment, that can also affect facial muscles. Indeed, PD patients often exhibit a *masked face*: a reduction of emotion expressivity termed hypomimia. Patients experiencing this symptom have a limited facial expression that can lead to a significant reduction of their quality of life. Despite the high prevalence of this feature in PD, hypomimia still remains under-investigated [1]. In particular, no validated treatments nor quantification of their effects are available. The aim of our study is to quantify the effects of a tailored rehabilitation treatment comparing the pre- and post-treatment conditions. A face-tracking algorithm based on the Facial Action Coding System (FACS) is used [2].

Methods

Data from 10 PD patients (mean(±SD) age: 68.4(±8.46) years) were investigated. They underwent 9 sessions of 60 minutes each of hypomimia rehabilitation treatment in a time window of two months. Data acquisition took place before (T_0) and after the treatment (T_1). MDS-UPDRS values were collected (Table 1). Moreover, frontal face videos of the subjects were recorded while they were instructed by an operator to perform the face expressions described in [3]. Data were recorded with a GoPro Hero 3 camera (1920x1080 pixels, 30 fps) placed at eye level at 1.36 m from the patient, seated with a white background behind. Videos were segmented into 4 frames per each emotion; using an ad-hoc set of 56 features tracked in the 2D-image space (with a self-developed software *TrackOnField*, *BBSoF S.r.l.* [4]), 35 distances were calculated. Each distance was then normalized with respect to the corresponding one in the neutral expression. Wilcoxon signed-rank test was performed to compare the two conditions ($p<0.05$).

Results

Along with the improvements in the MDS-UPDRS scale values (Table 1) results showed an enhancement in facial mobility at T_1. Figure 1 highlights the statistically significant distances between T_0 and T_1 per each emotion.

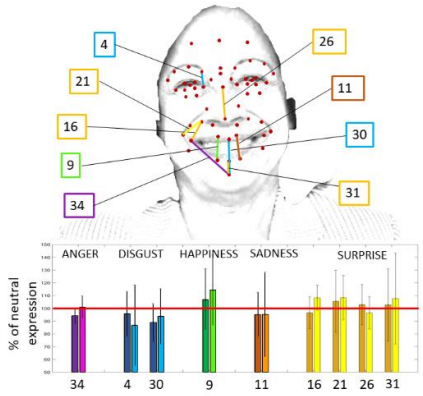

Figure 1: Significant distances ($p<0.05$) per each emotion. Darker colors refer to T_0, lighter colors to T_1. The red line represents the neutral expression (100%).

	total UPDRS score	Facial expression (III.2)
T_0	116.3 ± 27.93	1.90 ± 0.32
T_1	87 ± 33.11	1.40 ± 0.52

Table 1: UPDRS values (total score and facial expression item) at T_0 and T_1. Mean ± SD data are reported.

Discussion

Preliminary results on the quantification of the treatment outcomes are encouraging. This method can be used in future investigations increasing the dataset and studying different rehabilitation treatments.

References

1. Ricciardi L. et al, PLOS One, 12(1):e0169110, 2017.
2. Ekman, P., Facial Action Coding System: Investigator's Guide; Consulting Psychologists Press, 1978.
3. Wu P. et al, Comput Math Methods Med, 2014.
4. Magalhaes FA et al, J Sport Sci Med; 12:660, 2013

COMPARING LAND AND UNDERWATER GAIT CHARACTERISTICS WITH INERTIAL MEASUREMENT UNITS

Cecilia Monoli (1), Isabella Gasparini (2), Luigi Piccinini (3), Jeffrey A. Tuhtan (1), Manuela Galli (2)

1. Centre for Biorobotics, Tallinn University of Technology, Tallinn, Estonia; 2. DEIB, Politecnico di Milano, Milan, Italy 3. IRCCS "La nostra famiglia" Bosisio Parini, Italy

Introduction

Underwater rehabilitation, or hydrotherapy, offers an alternative to traditional land-based therapy, which can be challenging for subjects with important motor impairments [1]. Patients affected by pathologies of the musculoskeletal system, with a limited joint range of motion and balance may especially benefit from hydrotherapy. Despite the advantages of in-water rehabilitation, the quantitative analysis of underwater motion remains limited due to technology gaps. Few studies have investigated the application of wearable devices to water rehabilitation, especially considering underwater gait analysis [2]. The main limitation to the use of Inertial Measurement Units (IMUs) underwater is the difficult data interpretation, especially without the support of motion capture systems and or video tracking observations. To address these gaps, we have carried out gait analysis in air and underwater using data collected in a motion laboratory with optoelectronic gold standard system and with IMU sensors suitable to work underwater. The goal of the investigation is to systematically record, characterize and interpret the kinematic differences in the walking gait caused by the presence of the fluid. This preliminary investigation focuses on step detection and the identification of spatiotemporal gait parameters.

Methods

Over January 2021, gaits were recorded from 10 volunteer healthy subjects (23.4 ±1.3 years old), with no previous history of pathologies of the lower limbs in a motion laboratory (Figure 1a) equipped with a reference optoelectronic system (BTS-SmartDX, Italy, sf:100Hz) following Davis protocol for markers placement [3] and with 6 wearable devices (30 x 12 x 4 mm, 6.9 ± 0.3 g) which had an IMU sensor (BMX160 Bosch Sensortec GmbH, Germany, sf:100Hz). Similarly, the same subjects performed gaits underwater using a rehabilitation pool (Figure 1b) (1.20m depth, 33°C) wearing only the IMU devices. In both trials, subjects were wearing (Figure 1c) For the first trial, on land, a two-pose calibration procedure allowed to synchronize the data from both measurement systems. Matlab R2020a was used to identify primary gait events, including initial foot contact and toe-off, to determine the average stance and swing time over the gait cycle.

Results

Evidence of consistency between IMU and optoelectronic data was given comparing accelerometer data and the acceleration of the foot center of mass extrapolated by the gold standard system achieving on average correlation coefficient *r* of 0.91 ±0.02 and root mean squared error (RMSE) of 1.8 ±0.2.

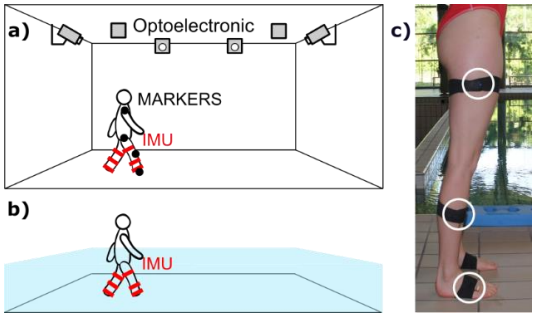

Figure 1: a) Gait analysis with optoelectronic and IMU systems in motion laboratory; b) Gait analysis in rehabilitation pool; c) IMU positioning on lower limbs.

The measured gait parameters revealed that on average, a underwater walking gait cycle has a 41 % longer duration than a gait cycle from the same subject on land. The average step time was 1.2 ± 0.1 s on land, and nearly 3 ± 0.1 s in water. Concerning the stance and swing time partitioning; it was found that the underwater stance time was reduced to 50% from 60%, and consequently the underwater swing time had an average duration some 10% longer underwater than on land.

Discussion

Preliminary results showed the resemblance between IMU data in and out water while highlighted important differences caused by the fluid-body interactions during the walking gait. Further investigation will be conducted to automatize the data processing by developing and testing new sensor fusion algorithms using both the IMU and Optoelectronic data to classify and interpret the IMU data collected during underwater rehabilitation based on walking gaits.

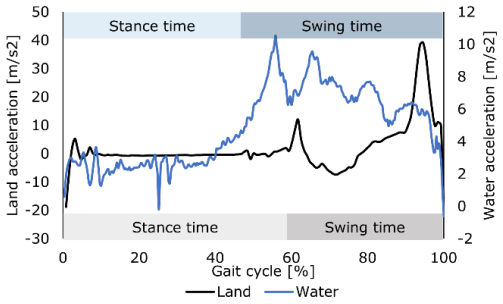

Figure 2: Accelerometer data over the gait cycle [%], for both Land and Water trial. Stance and Swing time are reported.

References

1. Mooventhan A et al, N Am J Med Sci, 6(5):199-209, 2014.
2. Marinho DA et al, Int J Environ Res Public Health, 16(24):5067, 2019
3. Davis RB et al, Hum Mov Sci, 10(5), 1991

ASSESSMENT OF PATIENT POSTURAL STABILITY ACCORDING TO THE FORCE PLATE AND VICON

Elvira Mukhametova (1), Regina Khamatnurova (2), Alena Militskova(1), Irina Dyatlova(3), Elena Semenova(1,3), Viktoriya Yaikova(1,3), Oskar Sachenkov(3)

1. Scientific and Clinical Center of Precision and Regenerative Medicine, Russia;
2. Goethe-Universität Frankfurt am Main, Germany; 3. Kazan Federal University, Russia

Introduction

Quiet standing activates ankle and hip strategies for balance control. Analysis of postural stability using a force plate is one of the popular methods for the diagnosis of diseases of various etiologies. The method is quite informative, and the obtained data is often enough to generally determine the violation of the body's ability to maintain balance. However, the force plate detects the center of pressure movements which substantially related to ankle strategy.

Methods

We used a complex comprised of a force plate and a Vicon system (see figure 1). Markers were installed on a dorsal side of the body. To analyze the Vicon data the geometric centerline of a patient was restored. The geometric axis can be defined as a line equidistant from the Vicon markers. For analyses, the point set of the intersections of the centerline and floor plane was found to assign both ankle and hip strategy. Stabilometric parameters were used. To determine statistically significant parameters, the method of singular decomposition was used.

Results

Force plate data analysis showed balance quality rate decrease in subjects with latent myogenic trigger points comparing to control subjects which is confirmed by Vicon data obtained by axis up to floor plane. However, analysis of movement of the point set of the axis restored across of centerline showed significant increase both in frontal and sagittal planes. Moreover the proportion of movements of pointset across the floor plane and the centerline significantly increases in subjects with myogenic trigger points comparing to healthy subjects that indicates on prevalence of hip strategy in subjects with trigger points of cervical muscles.



Figure 1: Scheme of the experiment complex: a force plate and a Vicon system.

Discussion

Normally, during quiet standing, the most prevalent control strategy is an ankle strategy as a more energy-efficient one. The “hip strategy” is activated in conditions of perturbed standing as an unstable surface or narrow area of supports. Previously it was shown that the free chain system compensates the center of mass shifts increasing vertical posture stability. Multiple cervical myogenic trigger points restrain neck movements which cause a compensatory increase of range of movement of the underlying segment.
Thereby body axis reconstruction and further segmental analysis can be more sensitive in the event of the hip or mixed strategy activation which could help to reveal minimal inferiority in balance control integration.

Acknowledgements

The reported study was carried out on equipment of DNA Research Center Autonomous Nonprofit Organization

DYNAMIC ANALYSIS OF HUMAN GAIT USING FULLY CARTESIAN COORDINATES WITH MIXED COORDINATES

Ivo F. Roupa (1), Sérgio B. Gonçalves (1), and Miguel Tavares da Silva (1)

1. IDMEC, Instituto Superior Técnico, Universidade de Lisboa, Lisbon, Portugal

Introduction

Inverse dynamic analysis (IDA) is a powerful tool to obtain important insights regarding human movement, such as, joint moments or joint reaction forces. In sports it is used to enhance athlete's performance and to reduce injuries [1], while in clinics it is usually used for studying disease etiology, support medical decision, and evaluate treatment effects [2]. When applied to ergonomics it can provide valuable insight into the risk of occurring musculoskeletal injuries while performing manual tasks in industrial settings.

MultiBody System Dynamics is an efficient and validated methodology that has been successfully applied to perform IDA of biomechanical systems with large number of degrees-of-freedom (DOF) in a non–invasive way. Here, Fully Cartesian Coordinates (FCC) [3] are combined with Mixed Coordinates (MC) [4] to assure the solution of the IDA and, simultaneously, the kinematic consistency of the underlying biomechanical model with the experimental data.

Methods

In planar systems the FCC formulation requires the use of 4 generalized coordinates per rigid body (RB), respectively the Cartesian coordinates of a point located at its center of mass (CoM) and the Cartesian coordinates of the components of a direction unit vector [3]. Additionally, if MC are considered, an additional angular coordinate expressing the orientation of each RB needs to be added to the vector of generalized coordinates (**q**). Consequently, the number of constraint equations becomes less than the number of generalized coordinates. To overcome this situation, additional kinematic constraints in the form of trajectory constraints, are added. Each trajectory constraint adds two equations per marker, leading to an overconstrained system that is solved, for each timestep, using a least square approach. The proposed methodology was implemented in an in-house software developed in Python and applied to the analysis of 3 gait cycles, at natural cadence, of a female subject. Kinematic and kinetic data were acquired at 100 Hz using 14 infrared Qualysis™ cameras and 3 AMTI force plates. The biomechanical model has composed by 12 segments [5]. IDA results are compared with similar ones obtained from the literature [6].

Results

The IDA solution procedure showed good convergence for the analyzed gait cycles. Calculated results (Fig. 1) presented similar patterns and values to those from the literature [6], exhibiting a maximum and minimum normalized ankle moments of 1.95 $Nm.Kg^{-1}$and -0.07 $Nm.Kg^{-1}$ and a maximum and minimum ankle power of 5.99 $W.Kg^{-1}$and -0.79 $W.Kg^{-1}$, respectively.

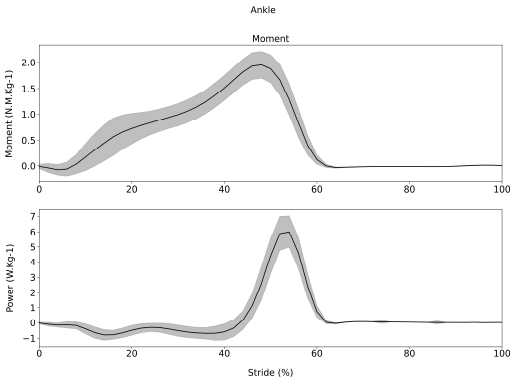

Figure 1: Representation of ankle moment (upper) and ankle Power (lower) during normalized gait cycle. Grey area – literature data. Black line – experimental data.

Discussion

The use of the local coordinates of each experimental marker with respect to the segment where it's located computed during the static trial, in association with the use of MC and the least square approach ensures model kinematic consistency and minimizes the difference between model segments positions and orientation with respect to experimental markers. Future work will address the implementation of the proposed methodology for spatial models.

References

1. Cruz et al, RSMIJ, 21(4), 330-342, 2013
2. Kuo et al, PO, 16(1), 1-14, 2020
3. Roupa et al, Proceedings of IMSD, 2018
4. Roupa et al, Proceedings of VPH, 2020
5. Pàmies-Vilà et al, MMT, 58:153-164, 2012
6. Winter, University of Waterloo Press, 2nd, 1991

Acknowledgements

This research was supported by the Fundação para a Ciência e a Tecnologia through grants IDMEC, LAETA (UIDB/50022/2020), UID/CEC/50021/2020, ARCADE (PTDC/CCI-COM/30274/2017).

GENDER DIFFERENCES OF PASSIVE KNEE KINEMATICS.

Francesca Bucci (1), Rami AlDirini (1), Mark Taylor (1), Saulo Martelli (1,2)

1. Medical Device Res. Institute, College of Science & Engineering, Flinders University, Adelaide, Australia;
2. School of Mechanical Medical & Process Engineering, QUT, Brisbane, Australia

Introduction

Women experience higher rates of knee ligament injuries than men [1], different anatomical features [2] and different knee kinematics during weight bearing activities [3]. However, kinematic differences between genders show mixed results [3,4]. Knee passive motion has been studied in large cohort of male donors [4] and along selected axes of motion. The present study aims at studying gender differences of the knee passive kinematics over the six degrees of freedom in intact adult specimens.

Methods

Twenty-nine healthy knee specimens (19 males and 9 females between 43 and 82 years of age) were obtained from a body donation program (Science Care, Phoenix, USA); exclusion criteria included no reported history of knee surgery and osteoarthritis. Ethics approval was obtained from the institutional Ethics Committee. Specimens were CT scanned (Somaton FORCE, Siemens, Germany; in-plane voxel size: 0.33 mm). Femoral and tibial bone surfaces were segmented with ScanIP (Simpleware, Exeter, UK). Custom 3D printed potting cups were created for the tibia and the femur. Reflective markers (12) were placed on dedicated features on the femur and tibial potting cups and the assembly was CT scanned to determine the relative position of the marker and the knee. Two trials of complete flexion-extension movements were performed respectively by manually applying a medial a lateral force to the femoral cup [6-8N](Fig1). Five repeated cycles were recorded for each trial. The marker trajectories were recorded using a 10-camera stereo-photogrammetric system (VICON, Oxford, UK), sampling at 100 Hz, and filtered (fourth-order Butterworth filter, 10Hz cut-off frequency). Anatomical bony landmarks were identified on the bone surfaces according to the ISB standards using NMS Builder [5]. The anatomical joint coordinate system was created according to Gray at al. (2019) [6]. The knee kinematics for the six motion axes was estimated using the Kinemat toolbox (Matlab, MathWorks Inc., USA). Preliminary results for 13 males and 7 females were processed. The range of passive motion was the difference between the knee motion measured applying medial and lateral pressure. Mean and standard deviation were calculated and compared to earlier findings [7] and across genders using two tails t-test and statistical parametric mapping (SPM, Matlab toolbox, $\alpha = 0.05$); variations were reported as mean and peak differences.

Results

Tibio-femoral kinematics were consistent with earlier reports. The largest difference between was medial and lateral force trials was 20º mean adduction-abduction rotation (peak: 29º). Smaller differences were found for internal-external rotation (mean: 2º) and medio-lateral translation (mean: 2 mm) (Fig1). Females presented significantly greater flexion angles than males by applying a medial force (mean difference: 6º) whereas no gender-specific differences were found for the remaining axes of motion (Fig1).

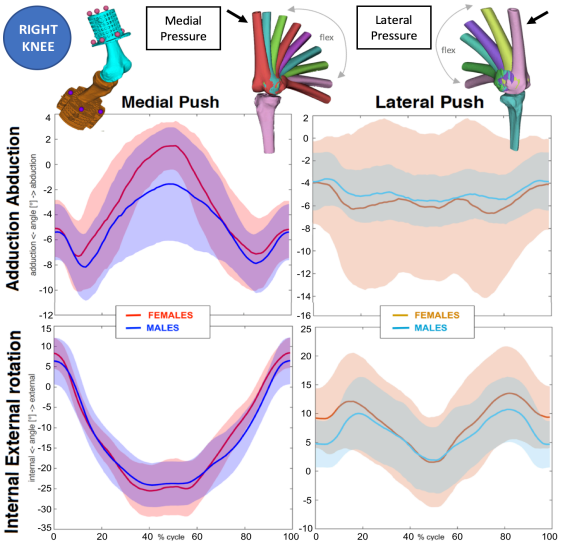

Figure1: Gender differences in knee passive kinematics.

Discussion

Preliminary results demonstrate a gender-specific passive knee motion observed for two extremes of the envelope of passive motion obtained by applying medial and lateral force. Females display higher adduction-abduction and lower internal-external rotation than males, in partial agreement with literature [3]. These founding may complement current understanding of gender differences kinematics.

Acknowledgments

Australian Research Council (DP180103146)

References

1. Arendt et al., J.Athletic.Train,34:86-92,1999.
2. Conley et al, J.Am.Acad.Orthop.Surg.,15:S31-6,2007.
3. Roger James et al, Res.Q.Exerc.Sport,75(1):31-38, 2005.
4. Cyr et al. Proc.Inst.Mech.Eng.H., 228: 494-500, 2014.
5. Wu et al., J.Biomech.,35:543-548, 2002.
6. Gray et al., J.Biomech.Eng.,8:141, 2019.

MOTION SYNERGIES IN TENDON-DRIVEN PROSTHETIC HANDS ACTUATED BY ABLE-BODIED SUBJECTS

Immaculada Llop-Harillo, Antonio Pérez-González, Javier Andrés-Esperanza

Departamento de Ingeniería Mecánica y Construcción, Universitat Jaume I, Spain

Introduction

The advent of 3D-printing technologies has led to the spread of affordable tendon-driven prosthetic hands due to their availability and easy customization. Many of them can be freely downloaded from CAD repositories. The tradeoff between the number of motors and the grasping ability of these hands is a relevant issue to analyze during the design process. Fewer motors allow reducing weight and cost, but at the expense of lesser motion versatility. Nevertheless, linking the movement among the joints of each finger is a preferred option in the do-it-yourself context due to their easier assembly and maintenance. In addition, in the literature [1,2], synergies have successfully applied to create novel design and control concepts for artificial hands. The analysis of motion synergies or *eigenpostures* among fingers is a common method used to reduce the number of DoFs that can be controlled in an independent manner without losing dexterity significantly. The fingers of the affordable hands for which the motions of the tendons are highly correlated can be candidates to be moved by a single controller, or even a single actuator. Therefore, the purpose of this study is the assessment of motion synergies during grasping of different tendon-driven hands using an able-bodied adaptor (ABA). The use of this adaptor to control the hands using the fingers of healthy subjects allows taking advantage of the human brain control mechanism while obtaining the synergies directly from the artificial hand.

Methods

Four tendon-driven artificial hands (Figure 1), three of the currently available online 3D-printed electrical prostheses for transradial amputees: Limbitless (5 tendons and 1 actuator), Dextrus v2.0 (5 tendons and 5 actuators), InMoov (5 tendons and 5 actuators); and the IMMA hand (6 tendons without defined actuation) designed by the authors [3]; were confronted with the Anthropomorphic Hand Assessment Protocol (AHAP) [4]. This benchmark is composed of 26 tasks involving grasping with the eight most relevant human grasp types during activities of daily living and two non-grasping postures, accounting for more than 90% in grasp frequency. Three subjects performed the tests by means of an especially designed ABA [5]. It allows controlling each tendon by a different human finger while the tendon motions are registered. A set of analyses using Pearson Correlation Coefficient (CC) and Principal Component Analysis (PCA) among tendon displacements during grasps performed successfully were used to obtain the motion synergies. The Principal Components (PCs) (Figure 1) were obtained using Varimax with Kaiser Normalization as rotation method.

Results

According to CC, for all the hands and subjects, the highest synergies were obtained for pairs of long fingers, being the lowest the coordination between index and little fingers and the highest middle and ring fingers. The coordination between thumb and long fingers was lower than that observed among long fingers.

The results from the PCA (Figure 1) show that, for all the hands, two similar PCs explained near or more than 80% of the variance. First PC includes mainly the motion of little, ring and middle fingers and second PC that of the thumb, with the index participating partially in both.



Figure 1: Eigenvectors (spline connected) for the PCs of the tendon displacements for the hands analyzed.

Discussion

The scores of the PCs obtained can be useful for the design of transmission systems to underactuate the hands or for control design. This underactuation is essential to simplify the control of the hand, especially for affordable designs. The dimensionality reduction using only two motors to actuate these hands should not affect their dexterity significantly.

References

1. Santello et al, Phys Life Rev, 17:1-23, 2016.
2. Salvietti et al, Front Neurorobot, 12:1-6, 2018.
3. Llop-Harillo et al, Int Biomech, 4(2):50-59, 2017.
4. Llop-Harillo et al, Rob Auton Syst, 121:1-12, 2019.
5. Llop-Harillo et al, Front Neurorobot, 14:57, 2020.

Acknowledgements

This work was supported by grant DPI2017-89910-R from the Spanish Ministry of Economy and Competitiveness, AEI and ERDF; and by grant UJI-B2017-70 from Universitat Jaume I.

DESIGN OF 3D PRINTED HINGED ANKLE-FOOT ORTHOSIS BASED ON IN-VIVO KINEMATICS ANALYSIS WITH CUSTOM RIGID SHELLS

Carlo Ferraresi (1), Carlo De Benedictis (1), Daniela Maffiodo (1), Walter Franco (1), Alberto Leardini (2)

1. *Department of Mechanical and Aerospace Engineering, Politecnico di Torino, Torino, Italy*
2. *Movement Analysis Laboratory, IRCCS Istituto Ortopedico Rizzoli, Bologna, Italy*

Introduction

Hinged ankle-foot orthoses (HAFOs) are used to partially immobilize the ankle joint and to reduce the range of motion according to the medical indication. The placement of the mechanical hinge is one of the most critical aspects in the design of such devices, as well as the number of degrees of freedom (DOF) allowed to the joint. If not correctly positioned, HAFO can lead to unnatural gait [1]. Unphysiological restrictions to dorsi/plantar-flexion can be harmful. In-vivo kinematics analysis of the ankle can provide valuable information for the design of these devices, but marker positioning and soft-tissue artefacts make this critical [2]. An original methodology for the development of a custom-made HAFO is presented, based on in-vivo kinematics identification of the patient by means of rigid shells. A prototype has been designed, fabricated in additive manufacturing and equipped with a novel 6 DOF mechanical hinge joint replicating original joint kinematics as resulted from previous motion analysis on the same healthy subject.



Figure 1: Three phases of kinematic shells design.

Methods

A handheld 3D optical scanner was used to get two separate point clouds on a healthy subject, 23 years old, respectively of: left shank and dorsal aspect of foot, and plantar aspect of the foot in loaded condition. Two corresponding meshes were defined and merged, then used to design the kinematic shells (Fig. 1). These were 3D-printed in ABS, and a technical cluster of four markers was stuck for tracking. These shank and foot shells are used both to collect kinematics trials to assess ankle joint motion, and eventually to manufacture the HAFO after design of the appropriate connection (Fig. 2, left). Kinematics analysis during passive flexion and level walking was performed, using a stereo-photogrammetric system (Vicon Motion Capture, Oxford UK) and IOR-gait protocol [3]. Marker coordinates were processed to calculate the Instantaneous (IHA) and Mean (MHA) Helical Axes, along with relevant linear and angular dispersion parameters [4]. The MHA and these parameters were used to design the complete custom-made HAFO; a relevant prototype was 3D printed and tested back on the subject (Fig. 2, right). Finally, kinematic analysis was replicated with the subject wearing the device, with the same experimental procedure.



Figure 2: The separate rigid shells and relevant marker positions (left), the HAFO prototype (right).

Results and discussion

The overall procedure worked well and provided consistent results. The custom-made rigid shells and relevant elastic belts limit considerably relative motion between markers. This seem to limit also motion with respect to the underlying bones; only a very small sliding with respect to the skin was noticed in a few trials. IHAs axode at the natural ankle, i.e. without shell connector, showed similar location and variability with respect to the literature, though relevant accuracy of the technique is still questioned [5]. The 3D printed HAFO prototype was found stiff enough to support the ankle, resulting as planned in almost-free joint motion in the sagittal plane and very limited motion in the other planes, as demonstrated by the strong reduction of dispersion parameters after shell connection. For the final clinical exploitation, consideration on the most appropriate kinematic reference shall be made, i.e. whether the target motion should be the restricted motion of the affected or of the contralateral joint.

References

1. Leardini A. et al, Gait Posture, 40:274-277, 2014.
2. Leardini A. et al, Gait Posture, 21:212-225, 2005.
3. Leardini A. et al, Gait Posture, 26:560-671, 2007.
4. Ferraresi C. et al, Proc Inst Mech Eng H, 231:831-838, 2017.
5. De Rosario H. et al, J Biomech, 62:60-67, 2017.

THERMAL EFFECTS DURING BONE PREPARATION FOR- AND DURING INSERTION OF OSSEOINTEGRATED TRANSFEMORAL IMPLANTS

Emir Benca (1), Beatrice Ferrante (1,2), Martin Zalaudek (3), Lena Hirtler (4), Alexander Synek (5), Franz Kainberger (3), Reinhard Windhager (1), Rickard Brånemark (6,7), Gerhard Hobusch (1), Ewald Unger (8)

1: Department of Orthopedics and Trauma Surgery, Medical University of Vienna, Austria; 2: Politecnico di Milano, Italy; 3: Department of Biomedical Imaging and Image-guided Therapy, Medical University of Vienna, Austria; 4: Centre for Anatomy and Cell Biology, Medical University of Vienna, Austria; 5: Institute of Lightweight Design and Structural Biomechanics, TU Wien, Austria; 6: Department of Orthopaedics, Gothenburg University, Sweden; 7: Biomechatronics Group, Massachusetts Institute of Technology, USA; 8: Center for Medical Physics and Biomedical Engineering, Medical University of Vienna, Austria

Introduction

Bone anchorage represents an alternative to conventional suspension techniques for transfemoral amputees with increasing popularity. The preparation of bone for- and insertion of the osseointegrated transfemoral implant is performed at very low speeds in order to avoid thermal damages of bone tissue which may potentially jeopardize implant stability. The aim of this study was to quantify the temperature increase in the femur at different sites and insertion depths, relative to the final implant position during the stepwise implantation procedure.

Methods

Graphical abstract of the project is given in Figure 1.

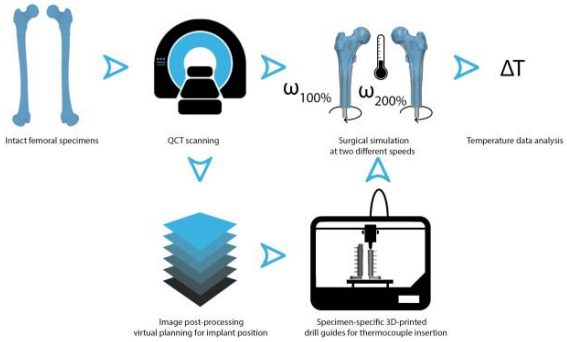

Figure 1: Graphical abstract of the project: Twenty-four paired femoral specimens were scanned using a QCT scanner. Images were post-processed to create specimen-specific drill guides to facilitate placement of thermocouples in each specimen. The surgery was performed at the clinically practiced speed ($\omega_{100\%}$) in one femur of each pair and the doubled speed in the contralateral specimen ($\omega_{200\%}$). Consequently, data analysis was performed to assess if a higher speed generates more heat.

The procedure for installation of the osseointegrated implant was performed on twenty-four femoral specimens. In one specimen of each pair, the surgery was performed at the clinically practiced speed, while the speed was doubled in the contralateral specimen. Six thermocouples were inserted into the specimen in a distance of 0.5 mm, and six at 1.0 mm from the final implant surface, respectively.

Results

Drilling caused a temperature increase of <2.5°C and was not statistically significantly different for most drill sizes ($0.002 < p < 0.845$). The mean increase in temperature during thread tapping and implant insertion was <5.0°C (Figure 2), whereas the speed had an effect on the temperature increase during thread tapping.

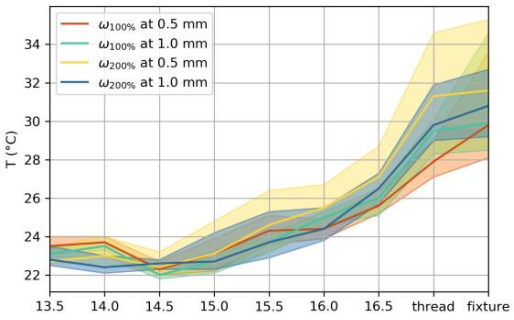

Figure 2: Cumulative heat generation during the simulated surgery for the two different speeds at 0.5 mm and 1.0 mm from the implant surface. The solid lines represent the median and the shaded area the corresponding 25th to 75th percentile.

Discussion

Drilling is the most time-consuming part of the surgery. Doubling the clinically practiced speed did not generate more heat during this step, suggesting the speed and thus the time- and cost-effectiveness of the procedure could be increased. The frequent withdrawal of the instruments and removal of the bone chips is beneficial to prevent temperature peaks, especially during thread tapping.

The duration of the surgical procedure for bone preparation and insertion of osseointegrated implants could be significantly shortened by increasing the speed during drilling without risk of thermal damages to the bone tissue.

Acknowledgements

This study was partially funded by the Austrian Research Promotion Agency (FFG) project "Additive Manufacturing for M3dical RESearch, M3dRES" (Nr. 858060).

DEVELOPMENT OF A NUMERICAL 2D MODEL OF AN AMPUTATED LOWER LIMB FOR OBJECTIVE EVALUATION OF THE LINER

Vasja Plesec (1), Gregor Harih (1)

1. Laboratory for Intelligent CAD systems, Faculty of Mechanical Engineering, University of Maribor, Slovenia

Introduction

The loss of a lower limb has been a significant problem since the beginning of humankind. As in all disciplines, prosthetics has made significant progress with the development of numerical simulations, which is reflected in a considerable number of limb, liner and socket models [1]. Such models help us to understand the behaviour inside the limb under different loads.

Models based on a specific geometry provide us with results for a particular patient, which is useful when making socket or liner for the specific subject. On the other hand, in the case of a relative comparison of liners' mechanical properties, it is useful to use a generic geometry that covers a broader population of leg amputations. By changing the boundary conditions, we can easily simulate different load cases that can be used to make a relative comparison between the liners.

Methods

Limb loss is a highly subjective problem, yet there are only a limited number of liners with specific characteristics that cover all subjects and provide limited suitability. For this reason, our numerical model is based on a generic geometry, which is useful for relative comparison of different liners.

An axisymmetric generic 2D geometry of bone, soft tissue, liner, and socket was modelled. Similar simplified geometries have been used by previous researchers and have shown good correspondence with experimental measurements [3-5]. In the case of the generic geometry, the 2D model allows us to perform simulations faster with similar results to the volumetric model.

Obtaining material data for soft tissue can be quite difficult due to its complex structure. The properties differ from patient to patient as well as from the site of the measurement [6]. We decided to use established material models from previous studies. Soft tissue and liners were defined by a hyper-elastic model [2,6], while bone and socket were defined by a linear-elastic material model [3,6].

Boundary conditions have been determined to simulate most common load cases:

- donning of the liner and the socket,
- loading or displacement of the bone.

Results

From the developed numerical model, the contact pressure at the tissue-liner and liner-socket interface was extracted. It is a useful parameter for evaluating the prosthetic fit and can also be easily measured, which can be used to validate the numerical model. Moreover, it is an indicator of comfort, since by minimizing and providing uniform contact pressure distribution, we increase comfort and prevent tissue damage.

In addition, the developed numerical model allows analysing the internal stresses, strains, and the relative displacements between the components. The results are compared with previously validated simulations and experimental measurements.

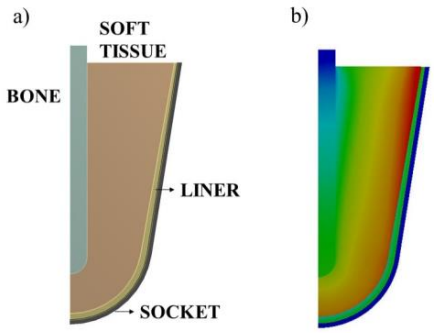

Figure 1: a) geometry of 2D limb-socket model; b) total deformation [mm] after donning the liner and the socket.

Discussion

The numerical model developed and presented serves as a tool for objective evaluation and development of prosthetic liners.

The model consists of a generic geometry and pre-validated material models from previous studies. The main advantages of the generic 2D model are:

- lower computation time,
- control over input parameters,
- allowing relative comparison,
- simple boundary conditions.

References

1. Dickinson et al, Medical Engineering and Physics, 43:1-18, 2017.
2. Cagle, A dissertation, University of Washington, 2016.
3. Ramalho et al, Materials Today, Proceedings, 2020.
4. Silver-Thorn et al, Journal of Rehabilitation Research & Development, 34(2):171, 1997.
5. Filep et al, Applied Mechanics & Materials, 658:429, 2014.
6. Kallin et al, arXiv preprint arXiv:1907.13340, 2019.

Acknowledgements

The authors acknowledge the financial support from the Slovenian Research Agency (research core funding No. P2-0063).

SENSORY FEEDBACK INTERFACE FOR BODY-POWERED AND MOTORIZED 3D PRINTED PROSTHETIC HANDS

Yair Herbst (1), Derick Sivakumaran (2), Shunit Polinsky (1), Yoav Medan (3), Alon Wolf (1)

1. Faculty of Mechanical Engineering, Technion, Israel; 2. Faculty of Mechanical Engineering, Swiss Federal Institute of Technology (ETH Zurich), Switzerland; 3. Faculty of Electrical Engineering, Technion, Israel and Haifa3D organization, Israel.

Introduction

The field of prosthetic hands in general and sensory feedback specifically have been widely studied but sensory feedback in prosthesis is not yet common in commercial devices. Moreover, current commercial designs have a very high price tag making them inaccessible to large portions of the population and mainly to children who are constantly growing out of their devices [1]. The growing availability and improvements of 3D printers offer a solution to this problem. The Raptor Reloaded, similarly to the Cyborg Beast [2] is a basic hand prosthesis that is fabricated by a 3D printer, it is designed mainly for children with a congenital amputation below the wrist. This is shareware design and the manufacturing is low-cost (approx. 40$). While there are many rejection reasons for prosthesis, such as weight, social acceptance etc. [3] that could be resolved with the benefits of 3D printers, one drawback that remains unsolved in low-cost devices and prosthesis in general is the lack of sensory feedback.

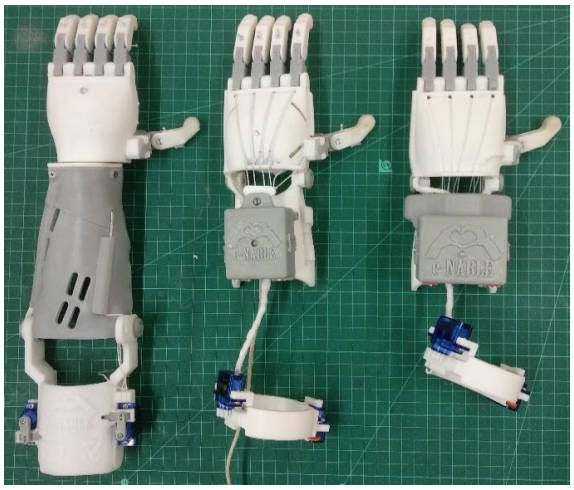

Figure 1: The designed sensory feedback interface connected to (from left to right) a body powered prosthetic (below and above wrist) and motorized hand.

Methods

To add the missing sensory component we offer a solution comprised of four components: (1) Sensing- pressure sensors to evaluate the normal forces applied on the object grasped, location sensor to predict object slippage and a temperature sensor, all are based on variable resistance response. (2) Data acquisition and analysis- based on an Arduino Nano interface. (3) An electronic, multi-sensory biofeedback system- consists of two servo motors, a vibration motor and an RGB LED. (4) A mechanical feedback system- consists of rods that convey texture sensation. The interface was incorporated into three hand designs, a body powered hand (below and above wrist) and a motorized hand as shown in Figure 1. To calibrate the system and validate its performance we designed an emulator that enables able-bodied users to wear the hand.

Results

The final design is based on standard off-the-shelf parts that maintain the high availability and low cost of the original design, as most of the parts can be reused when the recipient grows out of his hand. Additional cost is ~$50 for the first hand and another ~$10 for every new one. The circuit can run a full day without recharging and the weight of the entire hand increased by ~150gr. Preliminary results with healthy subjects and validations done show the improved usability of our modified model. The graph in Figure 2 illustrates the ability of the hand to measure the force applied on a grasped object.

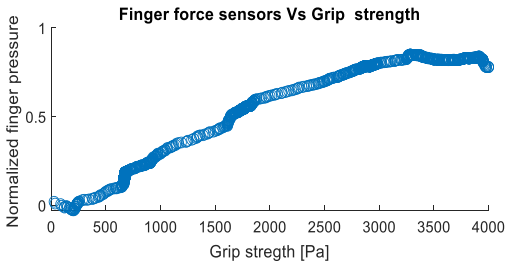

Figure 2: Normalized average measurement by the five finger force sensors vs grip strength applied on the object.

Discussion

In this research, we present the addition of a sensory feedback interface to low-cost 3D printed prosthetic hands. The described improvement can help overcome a major gap in the field of prosthesis in general and advance the field of low cost prosthetic hands. The entire design is open-source and shared online to be used by recipients worldwide.

References

1. Krebs et al. Phys Ther. 71: 920–934, 1991.
2. Zuniga et al, BMC Res. Notes, 8, 2015.
3. Meurs et al, J Biomech Eng, 30:165-173, 2006.

WALKING WITH ANKLE FOOT ORTHOSIS IN CHILDREN WITH HEMIPLEGIA

Federica Camuncoli[(1)], Alessia Barbonetti[(1)], Luigi Piccinini[(2)], Eugenio Di Stanislao[(3)], Manuela Galli[(1)]

1.Department of Electronics, Information and Bioengineering, Politecnico di Milano, Milan, Italy;
2.Scientific Institute IRCCS Eugenio Medea, Bosisio Parini, Lecco, Italy;
3.ITOP SpA Officine Ortopediche, Palestrina, Rome, Italy;

Introduction

Hemiplegic children are characterized by deviation in gait pattern due to plantarflexors spasticity, dorsiflexors weakness, and deformities [1]. To overcome these functional limitations, among all the possible treatments (botulinum toxin, muscle and tendon lengthening, …), the use of ankle foot orthosis (AFO) is often prescribed [2]. The aim of the study was to characterize the most common types of AFO currently available on the market, in order to identify their main limitations and to propose technical improvements.

Method

This retrospective study was conducted using gait data from the database of ITOP SpA (Officine Ortopediche, Palestrina, Rome, Italy) and from the gait laboratory of IRCCS Eugenio Medea (Associazione La Nostra Famiglia, Bosisio Parini, Lecco, Italy). A total of 26 hemiplegic subjects (17 males and 9 females, age: 9.3 ± 1.5 years, height: 134.46 ± 11.8 cm, weight 34.4 ± 11.2 kg (mean ± SD)) was selected following these inclusion criteria: (a) right or left hemiplegia, (b) AFO users, (c) age 6-11 yo, (d) GMFCS level I-II.
An optoelectronic motion analysis system composed of eight cameras was used for kinematic data acquisition (BTS Smart DX 700 Bioengineering, Milano, Italy), whereas kinetic data were collected by four paired force platforms (BTS P-6000, Bioengineering, Milano, Italy). Twenty-two reflective markers were applied on anatomical landmarks according to Davis protocol [3]. Two conditions have been tested: (i) barefoot, (ii) walking with different prescribed AFOs. In both cases the children were asked to walk along the walkway at their self-selected speed. For the kinematic and kinetic data one dimensional Statistical Parametric Mapping (SPM) was applied. Subjects were subdivided in three groups, based on the type of the prescribed AFO: (i) solid or hinged AFO, (ii) carbon posterior leaf spring AFO [2], (iii) supra-malleolar orthoses. An ANOVA 2x2 repeated measure analysis was performed ($\alpha = 0.05$) followed by post-hoc two-tailed paired t-test ($\alpha = 0.01$). Dynamic ankle joint stiffness (1) was also evaluated as in [4].

$$DAJS = dM/d\theta \quad (1)$$

Results

All the subjects showed in the barefoot trial gait deviations that are in accordance with the "equinus" condition, such as initial contact with the forefoot, persisting plantarflexion throughout the gait cycle and great reduction of power generated at push-off (Fig. 1). Known AFOs effects, such as improvement in the first and second rockers, along with detrimental effect on the third rocker, were also observed.

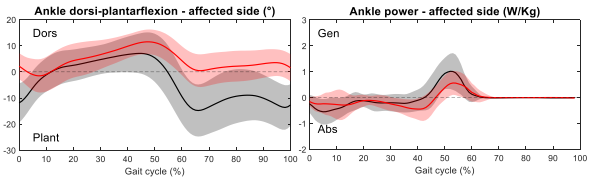

Figure 1: Ankle kinematic and power of the affected side during the gait cycle. Mean and SD of the barefoot (in black) and the orthotics (in red) trials are represented.

Solid, hinged and carbon posterior leaf spring AFOs determined significant (SPM{t}) changes in the kinematics of the affected ankle at initial contact (0–5%, p=0.007 and 0–5%, p=0.004 respectively) and at push-off (50–65%, p=0.001), and seemed to be effective in reducing asymmetries between the two limbs. They also determined a significant increase in the affected ankle stiffness. Power generated at the ankle during push-off was reduced in all the three groups while wearing the AFO (42%, 50%, 23% respectively).

Discussion

The subdivision of the population in groups allowed a more in depth evaluation on the effects of different types of AFO. Patients prescribed with solid, hinged and carbon posterior leaf spring AFOs showed comparable gait patterns during the barefoot trial, while the use of the orthoses lead to a significant reduction in the ankle range of motion at push-off, which is believed to be the cause of the great reduction in power generation (42% and 50% less than the normality value). In particular, carbon posterior leaf spring AFOs seem to determine the greatest decrease, thus being even more limiting than the traditional designs. On the other hand, supra-malleolar orthoses showed a lesser impact on the third rocker, allowing a significantly higher power generation at push-off with respect to the other groups ($p<0.001$).
In accordance with the existing literature [5], the reduction in power generation at push-off is confirmed to be the main limitation of currently prescribed AFOs.
The foundations have been laid for the definition of the design specifications of a new device that allows the performance of sports activities.

References

1. Abe et al., *Tohoku J. Exp. Med.*, 218(3):193–199, 2009.
2. Tavernese et al., *NeuroRehabilitation*, 40(3):447–457, 2017.
3. Davis et al., *Hum. Mov. Sci.*, 10(5):575–597, 1991.
4. Gabriel et al., *Phys. Ther. Sport*, 9(1):16-24, 2008.
5. Desloovere et al., *Gait Posture*, 24(2): 142-151, 2006.

FUNCTIONAL EVALUATION OF A NOVEL CUSTOM ANKLE-FOOT-ORTHOSIS IN PATIENTS WITH SEVERE DROP-FOOT

G. Rogati (1), A. Leardini (1), A. Zomparelli (2), G. Lullini (1), L. Berti (1), C. Fanciullo (1), A. Cinquepalmi(1), F. Cevolini (3), M. Ortolani (1), L. Boriani (1), P. Caravaggi (1)

1. IRCCS Istituto Ortopedico Rizzoli, Bologna, Italy; 2. MHOX Design, Modena, Italy; 3. CRP Technology, Modena, Italy.

Introduction

Ankle Foot Orthoses (AFO) can be prescribed to address functional impairment of the main ankle dorsiflexor muscles in drop-foot patients affected by neuromuscular pathologies. Current 3D scanning devices, in combination with additive manufacturing technology, allow to design and produce custom AFOs with improved fit and comfort [1, 2]. In this pilot study, a procedure was established to design and manufacture a novel custom AFO with improved comfort capable to address the functional deficit of drop-foot patients who are not satisfied with standard solutions. The AFO is designed on the foot/leg morphology, can compensate for foot postural alterations and is produced via Selective Laser Sintering (SLS) of a lightweight composite material.

Methods

Two patients (67 years, 83 kg, 1.80 m; 80 years, 96 kg, 1.95 m) with drop-foot diagnosed after spine stabilization surgery T9-S1 and herniated disc surgery L4-L5, respectively, volunteered in the study. The patients' feet and lower limbs were scanned in bipedal upright posture using a 3D foot scanner based on the Microsoft Kinect depth sensor [3]. According to the procedure, the 3D shape of the foot and leg was used to design a custom AFO in Blender (Blender Foundation, Amsterdam). AFOs were 3D sintered using a glass-fiber reinforced polyamide composite material (Windform GT®, CRP Technology, Modena). Functional evaluation (Figure 1) was performed using the IOR-gait lower limb protocol [4] in three conditions: 1) wearing the custom AFO, 2) wearing a standard off-the-shelf AFO in polyethylene (Molla di Codivilla, Ottobock) and 3) without the AFO. The perceived comfort while wearing the two AFOs was assessed via a 0-10 VAS scale.

Results

Both subjects walked with increased stride length while wearing the custom AFO (1.22 ± 0.03 m; 1.07 ± 0.04 m) with respect to the Codivilla (1.17 ± 0.03 m; 1.06 ± 0.08 m) and the no-AFO (1.09 ± 0.02 m; 1.06 ± 0.07 m) conditions. The ankle maximum dorsiflexion in the swing phase was larger while wearing the custom AFO (16.9 ± 0.3 deg; 12.0 ± 0.6 deg) with respect to the Codivilla (14.7 ± 0.3 deg; 3.8 ± 1.5 deg) and the no-AFO condition (33.4 ± 0.4 deg; 24.7 ± 0.8 deg). Both subjects scored the custom AFO more comfortable than the Codivilla (9.7 vs. 7.3; 9.6 vs. 6.9); in particular in the shank support (9.6 vs. 7.5; 7.9 vs. 4.4), the plantar aspect (9.8 vs. 3.5; 9.8 vs. 9.5) and in the perceived elastic return (9.7 vs. 6.9; 7.5 vs. 6.4).

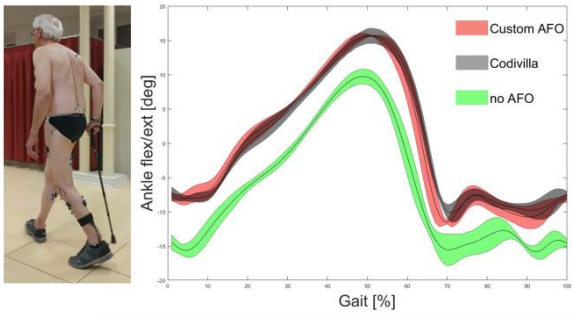

Figure 1: Left, gait analysis of one patient while wearing the custom AFO on the left foot. Right, mean temporal profiles of ankle flexion/extension angle [deg] during normalized gait-cycle in the three conditions: custom AFO, Codivilla and no-AFO.

Discussion

Designing personalized orthoses is becoming increasingly feasible and useful to improve the functional outcome of patients with lower limb pathologies, when standard off-the-shelf solutions are not effective. The novel SL-sintered custom AFO has proved to be more comfortable than a standard off-the-shelf AFO and allows faster gait and a longer stride length. The positive outcome of the present pilot study is encouraging a thorough validation in a larger population of drop-foot patients, and further customization of the mechanical properties with respect to the patient-specific functional impairment.

References

1. Telfer S, et al, BMC Muscolskeletal Disord, 13: 84, 2012.
2. Wojciechowski E, et al, J Foot Ankle Research, 12(1): 11, 2019.
3. Rogati G, et al, J Foot Ankle Research, 12(1): 1-8, 2019.
4. Leardini A, et al, Gait & Posture, 26(4): 560-71, 2007.

Acknowledgements

This study was partially funded by the Italian 5x1000 funding scheme.

VECTOR AND GEOMETRIC EXACT SOLUTION IN SINTHESYS OF TOTORONTO MECHANISM APPLIED IN TRANSRADIAL PROSTHESIS.

Luis A. Bautista (1) and Diego F. Villegas (2).

1. Industrial University of Santander, Colombia; 2. Industrial University of Santander, Colombia.

Introduction.

This document is related to the design of a transradial mechanism prosthesis[1] and the synthesis of a Toronto Mechanism problem (STMP) [2] as a possible choice. Two possible solutions have been proposed in STMP, the first one is related to the development of a vector form and the second one is a geometric and exact solution [3] of the STMP.

Method.

Toronto mechanism is an assemble composed of six linked bars as figure 1.

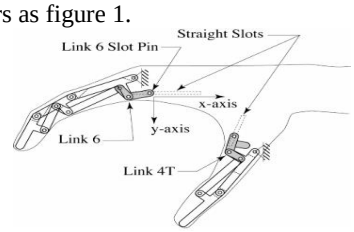

Figure 1: Toronto mechanism and its implementation. Image modified. Source [2].

The two initial equations considered in synthesis of TM are the equations 1 and 2.

$\overline{AB} + \overline{BC}Cos(\beta) + \overline{CD}Cos(\varphi) = \overline{AD}Cos(\alpha)$ **(1).**

$\overline{AD}Sin(\propto) + \overline{CD}Sin(\varphi) = \overline{BC}Sin(\beta)$ **(2).**

To solve the complex relation between trigonometric approach, has been found a dot vector product associated and consequently easy to implement it in STMP summarized in next equation.

$\overrightarrow{BD} \cdot \overrightarrow{BC} + \overrightarrow{AB} \cdot \overrightarrow{AD} = K2$ **(3).**

To prove the success of this equation applied to STMP have been developed a MATLAB program like figure 2. and the results can be found in figure 4.

Finally, here have been developed a geometric and exact solution, how it is shown in figure 3, of STMP which gave an easy way to solve the problem. To prove the success of the geometric exact solution, it was employed the AUTOCAD software with the reference tool and the results were completely exact.

Results.

The input data and numerical results are: p1=p2 where p1 and p2 are constant K2 relative to equation 3 in which this value have to stay constant before and after of TM movement. Next, the numerical values considered.

```
%Values considered in simulations of an index
finger. Values in centimeters.
A=[0 0];B=[1.16518934 -0.00236043];
C=[1.2218565
2.64633777];D=[2.086730391.37853015];
```

```
p1=6.137965589729951; p2=6.137965586464713
```

Consequently, numerical results confirm the validation of preliminary assumptions.

Discussion.

The first vector method related to dot product is a math tool that reduces the difficulty of the problem and the second geometric solution gave the final and successfully solution. It is proposed a geometric and exact solution of the STMP and future works should be implemented in an optimum way.

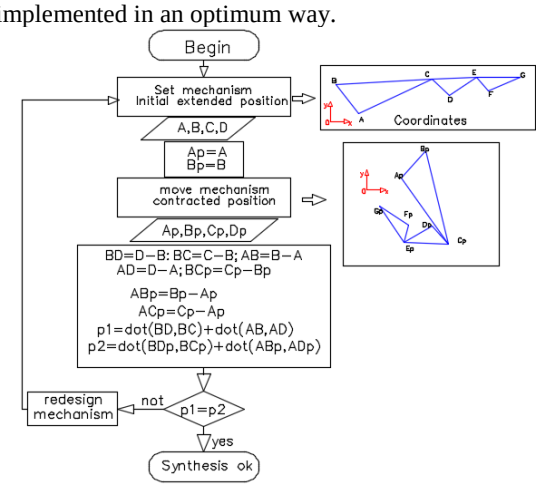

Figure 2: MATLAB algorithm. Source, the authors.

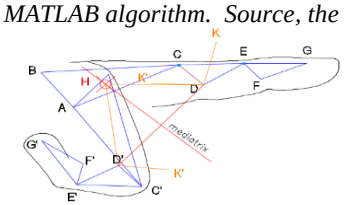

Figure 3: Geometric approach to synthesis of TM. Source, the authors.

References.

[1] C. L. Semasinghe et al "Transradial prostheses: Current status and future directions, October, 2016.

[2] N. Dechev et al, "Multi-Segmented Finger Design of an Experimental Prosthetic Hand, 1–8, 1999.

[3] T. Kulkarni and R. Uddanwadiker, "Overview: Mechanism and control of a prosthetic arm,". 147–195, 2015.

Acknowledgements

This research has the support of the Bicentennial scholarship proposed by MINCIENCIAS.

ANALYSIS OF THE SCOLIOSIS BRACE DESIGN PROCESS USING 3D IMAGING AND POINT CLOUD PROCESSING SOFTWARE

Inigo Sanz-Pena (1), Shanika Arachchi (2), Dilani Dhammika (3), Sanjaya Mallikarachchi (4), Jeewantha Sasika (3), Alison H. McGregor (5), Pujitha Silva (4), Nicolas Newell (1)

1. Department of Mechanical Engineering, Imperial College London, United Kingdom; 2. Department of Applied Computing, University of Kelaniya, Sri Lanka; 3. Rheumatology and Rehabilitation Hospital Ragama, Gampaha, Sri Lanka; 4. Center for Biomedical Innovation, University of Moratuwa, Sri Lanka; 5. Department of Surgery and Cancer, Imperial College London, United Kingdom.

Introduction

Adolescent Idiopathic Scoliosis (AIS) is an abnormal curvature of the spine that occurs in approximately 2.5% of the general population [1]. Brace treatment, the most common non-surgical AIS treatment has been found to be effective to stop curve progression and prevent surgery [2], [3]. Casting is the most adapted fabrication technique of braces, but requires a substantial amount of resources and time, and the generated geometry of the rectified mold is highly dependent on the orthotist expertise. Alternative design approaches make use of CAD/CAM techniques [4]. Despite the implementation of CAD/CAM, mold rectification still requires input from an orthotist to ensure an effective brace design. Therefore a detailed analysis of the manual rectification process is needed. This study aims to determine whether it is achievable to characterise the manual rectification process.

Methods

Five AIS patients (10-15 years, Cobb angle = 20-45°) prescribed with brace treatment were recruited for this study. A 3D scanner Mark II (*Occipital Inc. Colorado, USA*) was used to obtain scans of the patient's body and plaster cast molds. Seven spherical markers were used to locate the main anatomical landmarks. Characterization of the manual rectification was divided in three analyses. The first two focused on strategies that correct postural changes of the torso during the mold design phases, and the third focused on volume rectifications of the plaster mold, related to the pressure pads and brace geometry. First, changes in the Anatomical Landmark Positions (ALP) between the patient and post-rectification mold scans were compared using Blender open-source sculpting software. Second, the surface centroid locations of transverse sections were analysed. Third, the volumetric deviations between the patient and the post-rectification mold scan were analysed using CloudCompare 3D point cloud processing software.

Results

ALP deviations of the post-rectification scan with respect to the patient's body scan were obtained for each patient. ALP lowest mean deviations were located at the pelvis (3-12mm) compared to deviations in the thoracic areas (16-39mm). The centroid coordinates results at different transverse sections showed medial shift in the range of 1 to 54mm in all patients, indicating the same trend found in the ALP analysis. Centroid trajectories in the coronal and sagittal plane indicated convergence of the rectified molds towards the centroid of the pelvis section (Fig. 1.a). Volumetric differences between the post-rectification mold and patient's body scans were represented using 3D surface deviation plots (Fig. 1.b). A rectification factor determined by the reduction at the waist with respect to the patient's pelvis width showed mean values of 0.21±0.01 and 0.13±0.06 for the convex and concave side of the curve respectively. Furthermore, lateral (Fig. 1.c) and sagittal tilt angles were obtained from the external contours of the scans showing mean tilt angles on the rectified mold of 80.5±3º (convex side) and 83.2±2.8º (concave side), and 82.4±2.4º and 85.2±2.3º on the anterior and posterior side respectively.

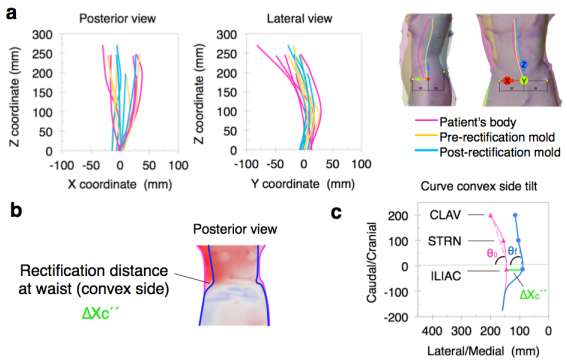

*Figure 1: **a** the centroid trajectories for the different patients. **b** the lateral contours from the patient and mold and **c** the lateral tilt angles and rectification distance at the waist.*

Conclusions

This study characterised the manual rectification using geometry parameters that can be used to define scoliosis brace shape. These results can be fed into a digital design flow towards automated brace design reducing the design time and resources.

References

1. W. J. Kane, Clin. Orthop. Relat. Res., 126:43–46, 1977.
2. J. B. Emans et al, Spine, 11:8, 1986.
3. J. O. Sanders et al., *JBJS*, 96:8:649–653, 2014.
4. Sy N et al, Curr Pediatr Rev., 12(1):36-42, 2016.

SYMMETRY FUNCTION IN PATIENTS AFTER UNILATERAL TFA USING A MECHANICAL OR MICROPROCESSOR PROSTHETIC KNEE

Sławomir Winiarski[1], Mateusz Kowal[2], , Ewa Gieysztor[2], Anna Kołcz[2,3], Karolina Walewicz[4], Wojciech Borowicz[5], Alicja Rutkowska-Kucharska[1], and Małgorzata Paprocka-Borowicz[2]

[1] Department of Biomechanics, University School of Physical Education in Wroclaw, Wroclaw, Poland
[2] Department of Physiotherapy, Wroclaw Medical University, Wroclaw, Poland
[3] Laboratory of Ergonomics and Biomedical Monitoring, Wroclaw Medical University, Wroclaw, Poland
[4] Faculty of Health Sciences, University of Opole, Opole, Poland
[5] Department of Nervous System Diseases, Wroclaw Medical University, Wroclaw, Poland

Introduction

Transfemoral amputations (TFAs) contribute to gait asymmetry [1]. The level of asymmetry is i.a. affected by the type of knee prosthetic module [2,3]. There is limited evidence suggesting that more technically advanced solutions (microprocessor modules; MicPK) are superior to less advanced ones (mechanical modules; MechPK). **The study aimed** to evaluate the variable range of hip and pelvic joint movements during gait and look for differentiating areas with an increased asymmetry of the gait cycle in individuals who underwent a unilateral TFA and are equipped with MicPK or MechPK.

Methods

Twenty-eight individuals participated in the study; 14 were assigned to a study group of individuals who underwent a unilateral TFA, and the other 14 were healthy participants (a control group). The movement task was recorded using the optoelectronic SMART-E system following the standard Davis protocol (the Newington model). A new method of quantifying gait symmetry using the symmetry function (SF) is proposed. SF is an integral measure of absolute differences in time-standardized signals between sides standardized throughout the whole cycle of motion variability.

Results and Discussion

There were significant differences between groups in the asymmetry of the range of movement in the hip joint of the intact limb in the frontal plane (Table 1). In the middle of the support phase, the intact limb was more adducted in individuals with MicPK and less abducted in people with MechPK (differences in mean 180%, $p < 0.000$; max 63%, $p < 0.000$; min 65%, $p < 0.000$). In the sagittal plane, the range of asymmetry of the flexion and thigh extension of the intact limb was similar to and only slightly different from the physiological gait. In the transverse plane, higher asymmetry values were noted for individuals with MicPK. In the final stage of the swing phase, the thigh was more rotated both externally and internally. The size of the asymmetry, when compared to gait of healthy individuals, reached 50% (differences in mean 115%, $p < 0.232$; max 62% $p < 0.26$; min 50, $p < 0.154$).

	Mean		Range	
	MicPK	MechPK	MicPK	MechPK
POBLI	3.1	17.6	63.6	54.9
PTILT	-0.1	0.7	142.4	138.7
PROT	51.3	50.3	78.7	68.7
HPAA	-6.5	103.9	121.4	93.7
HPFE	0.3	-1.7	59.8	48.9
HPIE	-56.1	-30.1	117.8	117.6

Table 1: The mean and range values of the symmetry function characterizing pelvic movements in frontal (POBLI), sagittal (PTILT), and transverse (PROT) planes as well as hip joint movements in frontal (HPAA), sagittal (HPFE), and transverse (HPIE) planes.

Conclusions

MicPK reduces the asymmetry values compared to healthy individuals' movements, especially the movements in the sagittal plane and pelvic rotations. Participants equipped with MechPK and MicPK develop a different type of gait expressed by changing the size of the pelvic and thigh movements' asymmetry in the hip joint. In the study group, the assessed ranges of pelvic and thigh movement in the hip joint differed only in the frontal plane. Individuals who underwent a unilateral above-knee amputation may gain less from using MicPK than anticipated. Less technically advanced prostheses are similar to the more advanced solutions in restoring a pattern of the gait cycle. The prosthetic supply type should be considered, due to differences in gait compensation, especially in the frontal plane.

References

1. Ray, S. F., Wurdeman, S. R., and Takahashi, K. Z., 2018, "Prosthetic Energy Return during Walking Increases after 3 Weeks of Adaptation to a New Device," J. Neuroeng. Rehabil., 15(1).
2. Kaufman, K. R., Frittoli, S., and Frigo, C. A., 2012, "Gait Asymmetry of Transfemoral Amputees Using Mechanical and Microprocessor-Controlled Prosthetic Knees," Clin. Biomech., 27(5), pp. 460–465.
3. Taheri, A. R., and Karimi, M. T., 2012, "Evaluation of the Gait Performance of Above-Knee Amputees While Walking with 3R20 and 3R15 Knee Joints," J. Res. Med. Sci., 17(3), pp. 6–11.

CLINICAL ESTIMATION OF THE USE OF THE HIP AND KNEE EXTENSORS DURING ATHLETIC MOVEMENTS

Rachel K. Straub (1), Alex Horgan (2), Adam J. Barrack (1), Leana Mosesian (1), Christopher M. Powers (1)

1. University of Southern California, USA; 2. Trinity College, Ireland

Introduction

The knee is the most commonly injured body region, accounting for as high as 59% of all injuries.[1] Identified causes of knee injury in sport are many and include movement behaviors that increase knee loading. Athletes who land with greater knee relative to hip extensor moments display greater knee valgus moments,[2] which have been shown to predict ACL injury.[3] Although the hip/knee extensor moment ratio (HKR) can be used to characterize movement behavior that is indicative of greater use of the knee relative to the hip extensors, quantification of hip and knee extensor moments requires sophisticated laboratory equipment. There is a need for a clinic friendly method to characterize movement behavior that may expose individuals to knee injury.

Characteristics of movement behavior associated with higher knee extensor moments include an upright trunk and forward tibia.[4] Therefore, the difference between sagittal plane trunk and tibia orientations may be a practical method to characterize movement behavior that may expose individuals to knee injury. The purpose of the current study was to determine whether the difference between sagittal plane trunk and tibia orientations obtained from 2D video (2D trunk-tibia) could be used to predict the average HKR during a wide range of athletic movements. We hypothesized that the 2D trunk-tibia angle would be predictive of the average HKR during the deceleration phase of a wide range of athletic movements.

Methods

Thirty-nine healthy athletes (15 males, 24 females) participated. Lower-extremity kinematics and kinetics (3D) and sagittal plane video (2D) were collected simultaneously during 6 tasks (Step Down, Drop Jump, Lateral Shuffle, Deceleration, Triple Hop, Side-Step-Cut). Linear regression analysis was performed to determine if the 2D trunk-tibia angle at peak knee flexion predicted the average HKR during the deceleration phase of each task. Each equation was adjusted for body mass. To distinguish between a hip bias (average HKR>1.0) or knee bias (average HKR<1.0), the cut-off for the 2D trunk-tibia for each task was derived by solving the regression equation for the value when the average HKR equaled 1.0.

Results

For each task, an increase in the 2D trunk-tibia angle at peak knee flexion predicted an increase in the average HKR when adjusted for body mass ($p<0.013$, R^2: 0.17 to 0.77) (Figure 1). The 2D trunk-tibia angle cut-offs necessary to achieve a hip extensor biased movement strategy (average HKR>1.0) ranged from -2° for the step down and 31° for the triple hop.

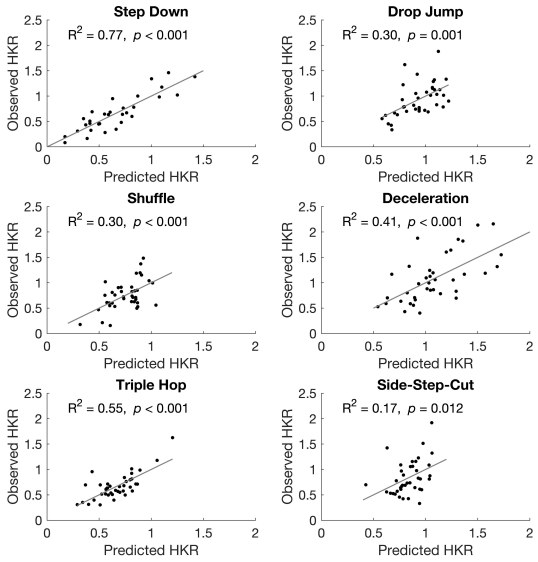

Figure 1. Linear regression models to predict the average hip/knee extensor moment for each task based on the 2D trunk-tibia, co-varied for body mass.

Discussion

Consistent with our hypothesis, the 2D trunk-tibia angle was be able to predict the average HKR for a wide range of athletic movements. Therefore, the 2D trunk-tibia angle may be useful to screen individuals at risk for knee injury. This is relevant clinically, given that greater use of the hip extensors has been proposed to be protective against various knee injuries.[2] A secondary analysis was undertaken to distinguish between hip and knee bias movement strategies. Thresholds ranged from -2° (step down) to 31° (triple hop), with higher cut-offs observed in tasks with higher knee extensor moments. Further study is needed to determine the optimal position of the trunk relative to the tibia to minimize loading (and possible injury) at the knee.

References

1. Kay et al, J Athl Train, 52(2):117-28, 2017.
2. Pollard et al, Clin Biomech, 25(2):142-146, 2010.
3. Hewett et al, Am J Sports Med, 33(4):492-501, 2005.
4. Biscarini et al, J Sports Sci, 29(5):457-469.

KNEE KINEMATICS OF ACL INJURY IN PROFESSIONAL FOOTBALL PLAYERS USING A MODEL-BASED IMAGE-MATCHING ANALYSIS

Susanna Stillavato (1), Manuela Galli (1), Marco Tarabini (2), Simona Lucarno (3), Francesco Della Villa (4), Matteo Zago (1,2)

1. Dip. di Elettronica, Informazione e Bioingegneria, Politecnico di Milano, Italy; 2. Dip. di Ing. Meccanica, Politecnico di Milano, Italy; 3. Athletic Area, AC Milan SpA, Italy; 4. Isokinetic Medical Group, Bologna, Italy

Introduction

Anterior Cruciate Ligament (ACL) injury is among the most debilitating injuries in professional football players. Despite the improvement of prevention programs, the rate of ACL injuries continues to rise, and only 65% of players still play at the top level 3 years after ACL rupture [1]. This is probably due to a still incomplete understanding of the multifactorial nature of the ACL injury mechanism. Video analyses based on television coverage have the potential to provide an ecological description of the injury mechanism [2]. An advancement of estimated injury kinematics obtained from 2D camera images, the model-based image-matching technique is a promising way of capturing subtler and more detailed 3D information during the injury itself. Unfortunately, contrarily to other court sports (basketball, handball [3-4]), few examples are available to date in élite football.

Methods

The situational pattern [2] and injury mechanism of five consecutive non-contact and indirect-contact ACL injuries occurred in the main European Leagues (season 2020-21) were analyzed. Once an injury was identified, (i) multiple-angles television images were inspected to exclude direct-contact injuries and to identify the injury frame (IF); (ii) for each injury, camera views were taken every 0.1 s from 0.5 s before IF to 0.1 after IF; (iii) a size-matched pitch was modelled within Blender and was used to calibrate the cameras by matching reference elements in the images (e.g. pitch lines); (iv) a 3D body model was adjusted to fit the body segments arrangement in each frame and view; (v) model's poses were interpolated, and (vi) Euler's sequences knee joint angles were extracted (Figure 1).

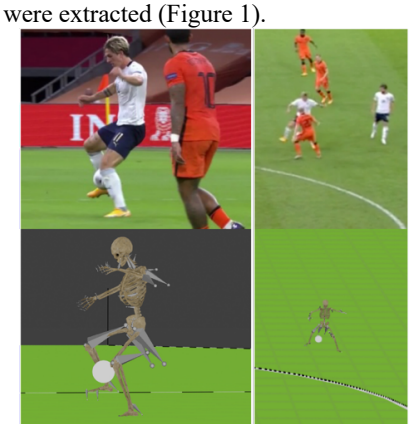

Figure 1: Example of a video matched in Blender, double-camera ACL injury at the Injury Frame.

Results

Four non-contact and one indirect-contact injury were analyzed. Situational patterns were: offensive situation and dribbling (n=1) or defending the ball (n=1), defensive situation and tackling (n=2) or pressing (n=1). Knee kinematics across the injury event is reported in Figure 2: at IF, knee flexion ranged from 18° to 56°, knee rotation from -15° to 12° degrees, while the knee was abducted (1° to 17°).

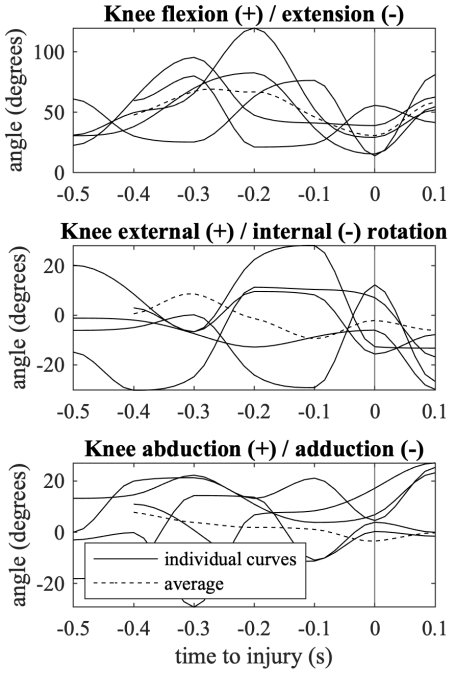

Figure 2: knee kinematics (dashed average curve) from 0.5 s before to 0.1 s after the injury frame (vertical line).

Conclusion

While confirming the risk associated with a fully extended knee landing or sidestepping, preliminary results outlined differences in kinematics, potentially depending on the situation (offensive/defensive) preceding injury. Extending the analysis could unveil still not considered features of the ACL injury mechanics, helping in designing ad-hoc neuromuscular training and ACL injury prevention programs.

References

1. Waldén et al, Br J Sports Med, 50: 744-750.
2. Della Villa et al, Br J Sports Med, 54**:**1423-32, 2020.
3. Koga et al, Am J Sports Med, 38:2218-25, 2010.
4. Krosshaug, Gait Posture, 26:378-85, 2007.

FATIGUE ALTERS TURNS KINEMATICS IN FEMALE SOCCER PLAYERS

Matteo Zago (1,2), Filippo Bertozzi (3), Francesca Salaorni (1,2), Claudia Brunetti (1,2), Alice Gatti (1,2), Chiarella Sforza (3), Manuela Galli (1,2)

1. Dip. di Elettronica, Informazione e Bioingegneria, Politecnico di Milano, Italy; 2. E4Sport Lab, Politecnico di Milano, Italy; 3. Dip. di Scienze Biomediche per la Salute, Università degli Studi di Milano, Italy

Introduction

Anterior Cruciate Ligament (ACL) rupture is among the most severe injuries in women soccer, accounting for 43% of absence from match play [1]. ACL injury mechanism involves multiplanar movement patterns that can occur during landing, turning, cutting or pivoting actions [2]. Despite fatigue may have an effect in enhancing ACL injury risk [3], its impact on movement mechanics is still unclear [4]. A deeper understanding of these mechanisms would expand the base of evidence for the development of prevention programs.

Methods

Nine élite female soccer players (age: 20-31 years, BMI: 18.4-22.7 kgm^{-2}) belonging to the first or second Italian division ("Serie A" and "B") completed a 5-m shuttle-run test until exhaustion, paced at 70% of their own maximal aerobic speed (2.6±0.2 ms^{-1}).

The three-dimensional position of 37 reflective markers was acquired during the test with an optoelectronic motion analysis system (BTS, Italy). Peak blood lactate concentration was measured at the end of the test. Hip, knee and ankle 3D kinematics were obtained from a biomechanical model developed in Visual 3D (C-Motion, USA, Figure 1). Statistical parametrical mapping paired t-tests were used to compare joint kinematics during the stance phase between the turns 6-10 and the last 5 turns performed with the preferred leg.

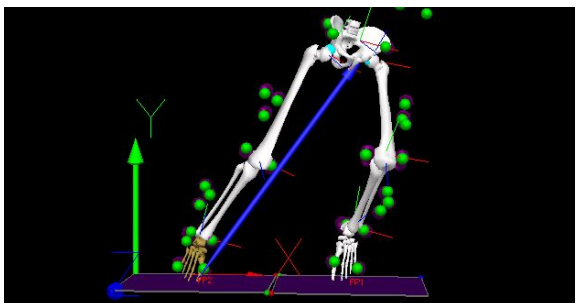

Figure 1: Visual 3D model of participants' lower limbs during the stance phase of a single turn.

Results

Post-exercise blood lactate concentration was 10.7±3.0 mM. The hip was more extended at mid-stance (t=2.398, p=0.038), as well as the knee (t=2.635, p=0.005). The tibia was more internally rotated from 20% to 80% of the stance phase (t=2.677, p<0.001, Figure 2). No significant differences were observed at the ankle level.

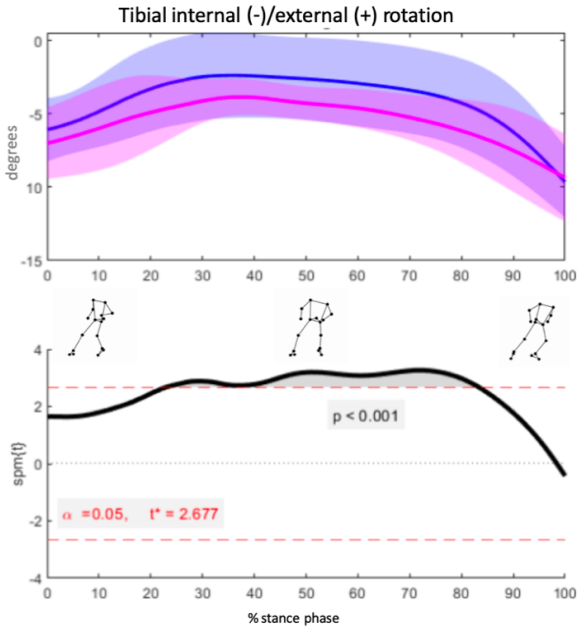

Figure 2: Tibial rotation during the stance phase (see Fig. 1 and stick diagrams). Blue/pink curves refer to turns performed at the beginning/the end of the test.

Discussion and Conclusion

These findings depict a sequence of concatenated alterations to the mechanics of changes of direction that are commonly described as biomechanical risk factors for ACL injury [2]: reduced knee and hip flexion ("stiff" landing), tibial internal rotation and knee dynamic valgus. Surprisingly, we did not observe alterations in knee kinematics on the frontal plane: it could be either that the high training level of the assessed cohort did not let such difference emerge, or that while the drop between the fresh and the fatigued condition was not significant, the baseline value (10-15 degrees of knee abduction) is potentially hazardous *per se*, even before the onset of fatigue.

As outlined in our recent work on men [3], it is confirmed and reinforced (given the higher incidence in women [4]) the need of planning specific neuromuscular training at the end of trainings, as when players are fatigued they can get the highest benefit from tackling modifiable biomechanical risk factors.

References

1. Larruskain et al, Scand J Med Sci Sport, 28:237-245, 2018.
2. Fox et al, Sports Med, 44:815-832, 2014.
3. Zago et al, Eur J Sport Sci, 19:1072-1081, 2019.
4. Bourne et al, Sports Med, 49:1629-1635, 2019.

OPTIMIZATION OF THE CYCLING KINEMATIC ANALYSIS. METHODOLOGY COMPARATIVE.

Ezequiel Martín-Sosa (1), Elena Soler-Vizán (2), Juana Mayo (1), Joaquín Ojeda (1)
1. Department of Mechanical and Manufacturing Engineering, University of Seville, Spain.
2. Health System of Andalusia, Spain

Introduction

Pedalling 3D kinematic analysis using videogrametry technology shows some specific problems which are not fully resolved. The main trouble of the use of this technique compared to other task such as the gait analysis is that movements outside the sagittal plane show a range of movement that can be of the order of errors due to the soft tissue artefact (STA), therefore the location of the markers must be carefully selected. On the other hand, when the cyclist sits on the saddle, hemi-pelvises are rearranged, causing relative movement between markers. These difficulties are responsible for the fact that there is no extensive literature related to the topic and, as a result, a gold standard has not been established. Consequently, the kinematics studies based on videogrametry technology found in the literature tend to reconstruct the body system of the subject using different markers protocols and calibration processes from one another, most of them adapted from gait analysis [1]. The use of processes developed by the gait analysis can cause serious inconveniences in cycling, such as the concealment of markers due to an inappropriate choice of anatomical points. It can also cause alteration of the trajectory of the markers because of the effect of phenomena such as rearrangement of soft masses or muscle contractions, which are more pronounced than in the case of gait.

To our knowledge, the previous problems have not been addressed in form of a specific action protocol for the cycling kinematic analysis. The aim of this project is to analyse the effect of different methodologies for the placement of markers.

Methods

The marker protocol developed by Martín-Sosa et al [2] was used for the cyclist kinematic analysis. Each capture session was divided into two steps. First: capture preparation, consisting of marker placement and static calibration. Second: kinematic capture. Two different methods of capture preparation were carried out on each studied subject. Method A applies imported gait analysis techniques. Placement of markers and static calibration are performed with the subject standing and anatomically positioned. Method B, proposed in this work, uses techniques aimed at the cycling particularities. Markers are located when the subject is sitting on the bike and in pedalling position, due to the relocation of fatty zones and hemi-pelvis. Static calibration is carried out with the subject sit on the bike, in anatomical posture and the feet resting on the floor. Two capture sessions were carried out per subject, one per method.

When static calibration was finished, kinematic captures were carried out at 150 W of pedalling power with automatic pedals cleat. Saddle height was established using the methodology developed by Holmes et al [3]. The duration of each trial was 6 seconds. Seven subjects, males, adults, amateur and without pathologies were analysed.

Results and Discuss

Table 1 shows the value of the range of motion (ROM) and maximal value (θ^{max}) of pedal cycle for method A and B. The values are the average ± standard deviation of the 7 subjects and related to the right leg, due to the behaviour of these variables are similar between right and left leg.

		Method A		Method B	
		ROM	θ^{max}	ROM	θ^{max}
H	F	47.5±2	99.7±4	47.5±2	99.7±6
	A	6.9±4	-5.3±4	8.5±5	-3.7±4
	I	26.8±3	6.6±2	27.2±6	0.8±8
K	F	81.8±4	114.3±2	81.6±3	115.5±3
	A	16.3±2	5.7±4	16.9±3	-1.2±7
	I	11.0±7	3.1±5	11.2±7	3.3±5
A	D	27.0±6	17.2±7	26.3±6	16.8±6
	A	11.9±3	2.1±4	17.7±6	3.7±5
	I	9.4±3	18.9±15	8.6±2	17.1±12

Table 1: Effect of the methods in the ROM and θ^{max}. Results in degrees. H: hip. K: knee. A: ankle. F: flexion. A: adduction. I: internal rotation. D: dorsiflexion.

Table 1 reflects differences on the values of ROM and θ^{max} between methods. The significant differences are located on the ROM value of ankle adduction and the θ^{max} value of knee adduction and hip internal rotation. This last case shows the significant effects of the used methodology and how the reorientation of bones and fatty zones can affect the kinematic analysis. This case is affected by a relocation and reorientation of the pelvis when the subject sit on the bike and a readjustment of the fatty zones near to the great trochanter.

In the absence of a gold standard to follow and in view of the differences obtained, this study concludes that the employ of specific cycling methods seems more appropriate due to it considers the effects that the readjustment of muscles, bones, and fatty zones may have on the location of markers when subject adopts pedalling position.

References

1. Umberger B. R. et al, J. Appl. Biomech, 2001, 17, 55-62
2. Martín-Sosa et al. ESB Vienna, 2019
3. Holmes J. C. et al. Clin. Sprt Med, 1994, 13,187-205

Acknowledgements

The authors thank the Ministry of Economy and Competitiveness for funding the project DPI2016-80796-P.

UNATTENUATED VERTICAL WALLS IN TRAMPOLINE PARKS ARE SAFER THAN ATTENUATED VERTICAL WALLS

David Eager (1), MD Imam Hossain (1), Edward Lind (1), Karlos Ishac (1)

1. University of Technology Sydney, Australia

Introduction

This paper discusses a novel use of vibration equipment to assess the safety of whether to pad or not to pad the vertically orientated walls within trampoline parks used specifically for an activity known as *walk-the-walk*.
The CEN/TC 136 WG 17 is currently drafting EN ISO 23695:202x Trampoline Parks – Safety requirements. The joint CEN/ISO Working Group is divided on whether to allow a padded or rigid vertical surface for the *walk-the-walk* activity. In general, all surfaces within the falling space of a forced movement device such as a trampoline shall be impact attenuated.
This paper presents the finding of research undertaken by the University of Technology Sydney to provide the CEN/ISO Working Group with guidance.
The *walk-the-walk* activity is where a trampolinist walks up a vertical wall using a high-performance trampoline to obtain sufficient vertical height and momentum.

Method

Acceleration data was obtained from a triaxial accelerometer mounted adjacent to the trampolinist's sternum. The acceleration data was then fused with video data and analysed.

Results

As can be seen from Figure 1, initially the trampolinist experienced a 1g acceleration which is due to the reaction force from the ground as he was standing on the platform at the top of the wall. While performing on the trampoline which starts at roughly 6 s the trampolinist experienced a very high peak acceleration with a maximum acceleration of approximately 11.5g due to the trampoline reaction force [1], during trampolinist bottom dead-centre location as shown in Figure 2. Between each trampoline reaction force acceleration spikes which can be seen from Figure 1, there are small variable peaks indicating walk-the-wall activities.

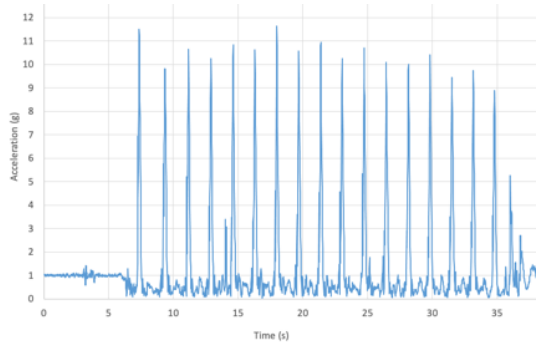

Figure 1: Vector sum of a triaxial accelerometer.



Figure 2: Trampolinist at bottom-dead-centre.

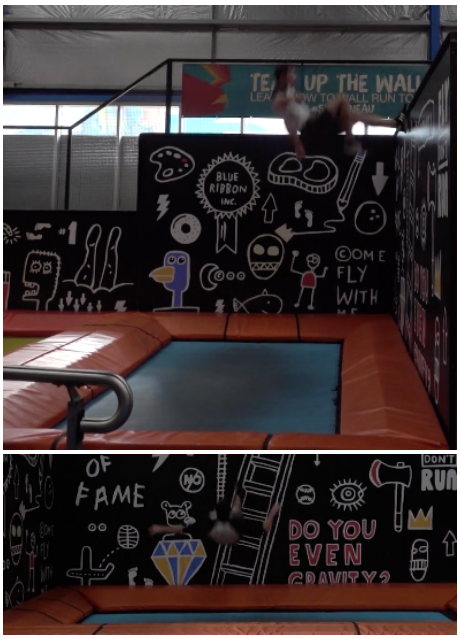

Figure 3: Trampolinist walking-the-wall.

Conclusion

Rigid vertical walls allow the trampolinist to obtain greater control and retain spatial awareness greater than what is achievable a non-rigid surfaces. In the presence of a padded wall, the reaction force from the wall can be considered a variable force, and might not always give the same outcome the trampolinist need to balance with each climb of the wall and fall from the height. It was concluded that unattenuated vertical walls are safer than attenuated vertical walls for *walk-the-walk* activities within trampoline park facilities. Non-rigid walls provide an unstable surface which reduced the trampolinist's control and stability. Control and stability are both critical while performing the complex walk-the-wall manoeuvrer.

References

1. Pendrill, A-M., Eager D. Free fall and harmonic oscillations - analysing trampoline jumps, Physics Education 50(1):64-70, Jan 2015. doi:10.1088/0031-9120/50/1/64.

EFFECTS OF LEG DOMINANCE AND BALL CONDITION ON PEAK LOWER LIMB MUSCLE ACTIVATION DURING MAXIMAL INSTEP KICKS

Rodrigo Rabello (1), Filippo Bertozzi (1), Matteo Zago (2, 3) Chiarella Sforza (1)

1. Università degli Studi di Milano, Milan, Italy; 2. Politecnico di Milano, Milan, Italy; 3. E4Sport Lab, Politecnico di Milano, Italy

Introduction

Soccer is a very popular sport, with 265 million players in 207 countries [1]. To score, players need to kick the ball with a high velocity, giving the goalkeeper less time to react. In a match, players often need to kick a moving ball and, to be more successful, need to be able to kick the ball with both feet proficiently. Although muscle activation during the kicking task has been studied [2,3], it is still unclear how limb dominance and ball condition affect lower limb muscles activation during an instep kick.

Methods

Ten experienced male soccer players (age: 21.9±1.9 years; BMI: 21.9±2.9 kg·m2; experience: 13.5±3.3 years) participated in the study. Eight surface EMG probes (FreeEMG 300, BTS, Italy), with a sampling rate of 1000 Hz, were positioned on the muscle belly of the vastus medialis (VM), biceps femoris (BF), gastrocnemius medialis (GM) and tibialis anterior (TA) of both limbs. To obtain the maximal functional activation, volunteers kicked the ball as fast as possible, without regard for direction, three times with each foot. Subsequently, they were asked to kick the ball inside a 1.5 X 1.5m target 3m away as fast as possible in four conditions: stationary ball and rolling ball with both the dominant and non-dominant feet (the ball rolled from behind the subjects at 2 m·s−1). sEMG signal was rectified and filtered (20 Hz Butterworth, 2nd-order high-pass filter) and normalized peak activation was obtained for each kick. A repeated measures two-way ANOVA was used to identify differences between conditions and partial eta-squared (ηp2) was used to measure effect size, in both the kicking and the supporting limbs.

Results

There were no significant differences between positions or limbs. However, there were large partial eta-squared values for some comparisons: the swinging limb BF activation was higher when kicking with the dominant foot (ηp2 = 0.19) and when kicking a stationary ball (ηp2 = 0.25); the GM and the TA activation from the supporting limb were higher when kicking a moving ball (ηp2 = 0.35 and ηp2 = 0.18, respectively).

Conclusions

Although we found no significant differences in this pilot study, the large effect sizes in some comparisons suggest that there could be a trend toward different muscle activations in these comparisons. The larger swinging BF activation in the stationary and dominant conditions suggest that there is greater co-contraction when performing these kicks; the larger support GM and TA activations when kicking a rolling ball suggest that muscles that act on the ankle joint could be more active to stabilize the joint during this task. Future studies with a greater sample size can clarify how lower limb muscle activation function in different kicking conditions and possibly help to direct training and consequently improve player's performance.

References

1. Kunz et al, FIFA Magazine, 2007
2. Brophy et al, J Bone Jt Surg, 92:2050-58, 2010
3. Scurr et al, J Sports Sci, 29: 247-251

OPTIMIZATION THE MOVEMENT OF A SKIER WITH A DOUBLE POLING TECHNIQUE: MATHEMATICAL MODEL BASED ON THE RACE DATA

Daniil Parshin (1), Anna Kubyak (2)
1. Lavrentyev Institute of Hydrodynamics SB RAS, Russian Federation;
2. Novosibirsk State University, Russian Federation

Introduction

In modern high-performance sports, we notice that even in technical sports such as cross-country skiing, not the most depends on the technical support of the skier (his equipment), but very much depends on his physical readiness and running technique. There are quite a large number of studies in the literature devoted to the development of physical training skills [1], as well as certain aspects of the energy efficiency of skiing techniques [2], however, the latest results are based on, in our opinion, oversimplified models and have no specific application in sports.

The aim of our work is to determine the parameters of the optimal course depending on the individual anthropometric characteristics of the skier. As a basis, we considered a simplified biomechanical model of a skier having an inclined position to the track at a constant angle alpha, as well as with angles: Φ_0-angle between the body and shoulder, Φ_1-between the shoulder and elbow joint and Φ_2 between the elbow joint and the stick.

Methods

Using the virtual displacement method, the dependence of the transmitted force with respect to the virtual skier configuration parameters is analyzed. The time dependence of the angles were determined statistically from the video of the competition (the Olympic Games and the stages of the world cup). The double poling technique of movement of three elite level skiers: A. Bolshunov, A. Chervotkin, R. Juve is analyzed.

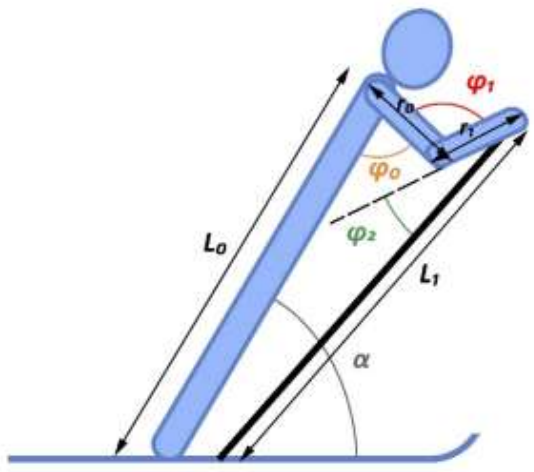

Figure 1: Virtual skier configuration and parameters.

Results

At the moment, we analyzed the dependences of the angles Φ_0, Φ_1, Φ_2 as a function of time for three repulsion cycles for each of the skiers.

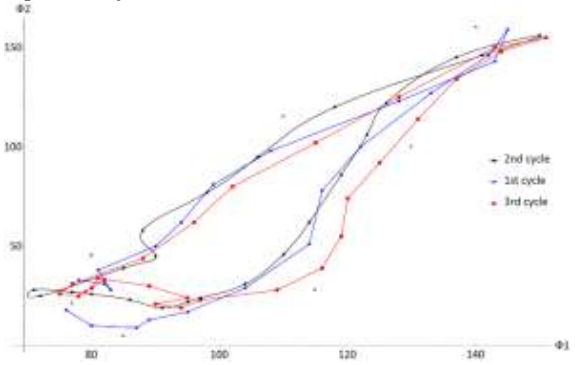

Figure 2: Dependence between Φ_2 and Φ_1 during repulsion cycle. Three cycles considered. The second cycle is interpolated by spline.

The repetition of the repulsion cycle for each of the skiers is determined and determined by the formula:

$$\Delta = \frac{\sqrt{(1/N)\sum_{j=1}^{N}(\varphi_2^{(analysis)} - \varphi_2^{(interp)})^2}}{|(1/N)\sum_{j=1}^{N}\varphi_2^{(interp)}|}$$

and it amounted to 11.29% between the first and second cycles and 18.39% between the second and third cycles, which is the norm of deviations of periodic processes for living systems. We have written the equilibrium equation, which allows us to evaluate the influence of the anthropometric parameters of the model on its energy efficiency.

As the prospects of this work, we note the possibility of further complicating the model using the statistics of video recordings and identifying the model features for male and female skiing techniques.

References

1. Johny E. Nilsson et al., 2004, 10.1007/s00421-004-1042-4;
2. L.J. Holmberg and A.M. Lund, 2008, 10.1243/17543371JSET10;

Acknowledgements

The study was supported by a grant of Russian Science Foundation, No 20-71-10034

RELIABILITY AND ACCURACY OF ACL QUICK CHECK, AN ON FIELD METHODOLOGY FOR ACL RISK OF INJURY SCREENING

Alfredo Ciniglio (1), Mattia Donadello (1), Fabiola Spolaor (1), Annamaria Guiotto (1), Davide Pavan (1), Federica Cibin (2), Zimi Sawacha (1,3)

1. Dept of Information Engineering, University of Padova, Italy; 2. BBSoF S.r.l., Padova, Italy; 3. Dept of Medicine, University of Padova, Italy.

Introduction

Anterior cruciate ligament (ACL) injury is multifactorial and involves biomechanical, anatomical and neuromuscular factors, such as excessive knee valgus moments or large anterior tibial translation [1]. Hence, screening methods should be linked to the mechanical etiology of ACL injuries in order to effectively identify 'at-risk' athletes [2]. This study aims at validating the adoption of a biomechanical assessment that can be performed on the field by means of video cameras and plantar pressure for ACL injury risk assessment [3].

Methods

After signing informed consent, 7 subjects were acquired: 6 controls (age 27.3 ± 4.4 years, BMI 27.8 ± 1.9 kg/m$^{2)}$, 1 ACL-injured subject (ACL-S) 3 months after the surgery (age 27 years, BMI 22 kg/m^2). Data were simultaneously acquired by means of a stereophotogrammetric system (6 TVC, BTS) synchronized with two force platforms (Bertec), a video-based system (8 TVC, GoPro Hero 7) and plantar pressure insoles (PedarX, Novel). Controls performed three mopodalic and bipodalic squats, while the ACL-S performed only bipodalic squats. Reflective markers were applied as in [4] and trajectories reconstructed through stereophotogrammetry and automatic tracking [3] (a self-developed software Track on Field (TOF), BBSoF S.r.l., validated in [6] was used). Joint kinematics [4,5] and kinetics [3,4] provided through the following set-up were compared: Stereophotogrammetry and force plates (set-up_1) [4]; Stereophotogrammetry and plantar pressure (set-up_2) [3]; video cameras and force plates (set-up_3); video cameras and plantar pressure (set-up_4) [3]. Wilcoxon signed rank test (α=0.05) was used to compare the data across the different set up and the asymmetry index (AI) was calculated [6]. The comparison between controls and ACL-S was performed through Wilcoxon rank sum test (α=0.05). To assess the inter-operator variability of the video tracking, the Standard Error ("SE") [7] was calculated (2 operators).

Results

Reliability and repeatability results showed good agreement between angles calculated with both systems, (Fig.1, Up) and a good inter-operator repeatability. In the comparison of the joint moments across the different set-up, larger differences were observed in the monopodalic squats, especially in the central phase, at the hip joint, between set-up_1 and 4. Statistically significant differences were observed on joint angles, moments and the AI (Fig. 1, Down) between controls and ACL-S in every tested condition.

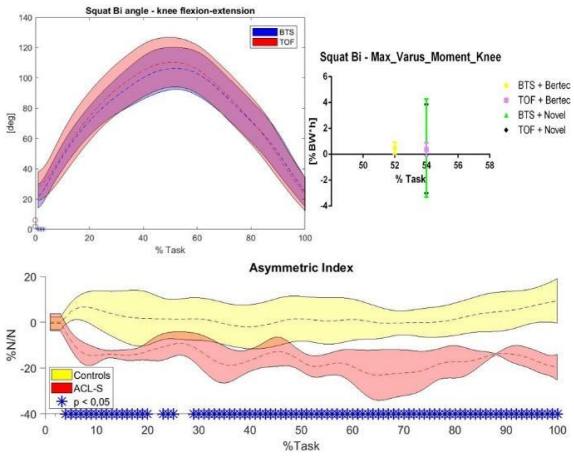

Figure 1: Up Left, the knee flexion-extension angle, BTS, in blue and TOF, in red. Up Right, the knee varus torque peak occurrence and values, for each set-up. Down, the AI, controls in yellow and ACL-S in red.

Conclusions

Reliability and repeatability tests results are encouraging toward the adoption of set-up 4 which can be easily applied on field. Comparison in terms of joint kinetics, showed good agreement among the different approaches. The significant differences observed between set-up_1 and 4 were mainly due to differences between force plate and plantar pressure measures.

References

1. Shin et al, J of Biomech, 42(3): 280-5, 2009.
2. Fox et al, Curr Rev Musculoskelet Med, 10(3): 307-314, 2017.
3. ACL Quick Check® patent: https://www.bb-sof.com/
4. Del Din et al, Med Biol Eng Comput, 49(7): 801-9, 2011.
5. Magalhães et al, J Sports Sc & Med, 58: 194-200, 2013.
6. Jordan et al, JSHS, 7: 416-424, 2018.
7. Schwartz et al, Gait & Posture, 20: 196-20, 2004.

ON FIELD COM ACCELERATION ASSESSMENT IN HOCKEY PLAYERS: COMPARISON OF 3 APPROACHES BASED ON VIDEO ANALYSIS AND PLANTAR PRESSURE DATA

Alex Scaldaferro (1), Alfredo Ciniglio (1), Giacomo Maistrello (1), Fabiola Spolaor (1), Annamaria Guiotto (1), Federica Cibin (2), Zimi Sawacha (1, 3)

[1]BiomovLab, Dept. Engineering Information, University of Padova, Padova, Italy
[2] BBSoF S.r.l., Padova, Italy
[3]Dept. Medicine, University of Padova, Padova, Italy

Introduction

Field Hockey is a popular sport that is played through an implement: the hockey stick. Using the hockey stick while playing has been proved to affect players in terms of body posture [1]. In this study data acquired directly on field, relative to a sprint task performed by female elite-field hockey players while holding the stick, are presented. The purpose of this contribution is to analyze the center of mass (CoM) acceleration of the athletes directly on field, while performing a sport specific task, by means of video analysis or pressure insoles. To this extent three approaches were adopted: 1. track the anatomical landmark L5, 2. apply the anthropometric approach as in De Leva [2], 3. apply the Winter's formula to the plantar pressure data [3].

Methods

Nine athletes of the female field hockey team of CUS Padova (mean (SD) age 21,56 (4,67) and BMI 22,01 (0,99) kg/m^2), signed the informed consent and took part in the study. Outdoor acquisitions were carried out directly on the field by means of four GoPro Hero 3 cameras and a plantar pressure system (Novel Pedar X). The automatic tracking software TrackOnField (BBSoF S.r.l.) was used and Matlab codes were developed to implement the three approaches. The 3-dimensional trajectory of the anatomical landmark L5 was reconstructed from the video sequences and its instantaneous acceleration was calculated. The anthropometric measures of the athletes were used to apply De Leva's equations [2] and estimate the COM trajectory, hence its acceleration was computed. Then Winter's [3] formula (1) was applied to the center of pressure (COP) data extracted from the plantar pressure system.

$$COP\text{-}COM = k * \ddot{C}OM \quad (1)$$

Results

The results showed a good agreement between the COM acceleration estimated with the anthropometric approach and the trajectory of L5 (Fig.1), while COM acceleration retrieved with Winter's formula was higher than the others.

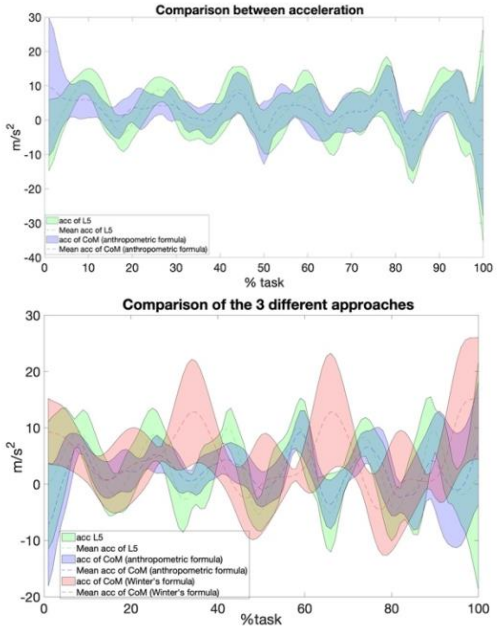

Figure 1: *In the top figure is represented the comparison between the instantaneous acceleration of L5 and the COM acceleration estimated with the anthropometric approach; in the bottom figure the comparison across the acceleration extracted from L5, the anthropometric approach and Winter's formula is reported.*

Discussion

The current study showed that in dynamic conditions, COM acceleration could be estimated through different approaches that only in two cases led to comparable results. For validation purposes this approach should be further applied in static conditions with the aid of a force plate that could represent a gold standard.

References

1. Podgorski T. et al, *Hum Mov*, **12**: 108-123, 2011
2. De Leva P. et al, J Biomech, **29**: 1223-30, 1996
3. Winter D. A. et al, Biomech & Motor Control of Human Movement, **4,** 2009.

SPM DIFFERENCES IN TOPSPIN BACKHAND BETWEEN CHINESE AND POLISH FEMALE TABLE TENNIS PLAYERS

Sławomir Winiarski & Ziemowit Bańkosz

Department of Biomechanics, University School of Physical Education in Wroclaw, Wroclaw, Poland

Introduction

The research aimed to compare the kinematics (the movement pattern in the most important joints, and accelerations of the playing hand) between female table tennis players coached in Poland (POL) and China (CHIN) during the performance of a topspin backhand stroke (so-called quick topspin).

Methods

The study involved 6 female table tennis players at a high sports skill level, playing in Poland's highest league. Three were national team members of Poland (age: 20.3±1.9), whereas three were players from China (age: 20.0±0.0). Kinematics was measured using MR3 myoMuscle Master Edition Inertial Measurement Unit (IMU) system [1]. The participants performed one task of topspin backhand as a response to a topspin ball, repeated 15 times. Statistical Parametric Mapping (SPM) was calculated using SPM1D in a Python package that offered a high-level interface to 1D SPM [2].

Results and Discussion

The SPM method allowed for the determination of differences between the Chinese and Polish female athletes (Fig. 1). The differences found are probably mainly due to differences in the training methodologies caused by different coaching systems. The observed differences include, i.a., greater use of the so-called small steps in order to adapt and be ready during the back to ready position and backswing phases, which gives the CHIN players slightly better conditions for preparation for the next plays. The CHIN players' position is also more universal than the POL players and favours a quicker transition to the forehand play. This difference is probably related to the difference in the dominant playing styles of the groups studied. Despite the differences in movement patterns in both groups, the same value of playing hand was achieved. This may be a manifestation of the phenomenon of equifinality and compensation.

Conclusions

The examinations carried out in this study allowed for a detailed description of the technique of performing a fast topspin backhand stroke. The SPM method allowed for the determination of differences between the Chinese and Polish female athletes.

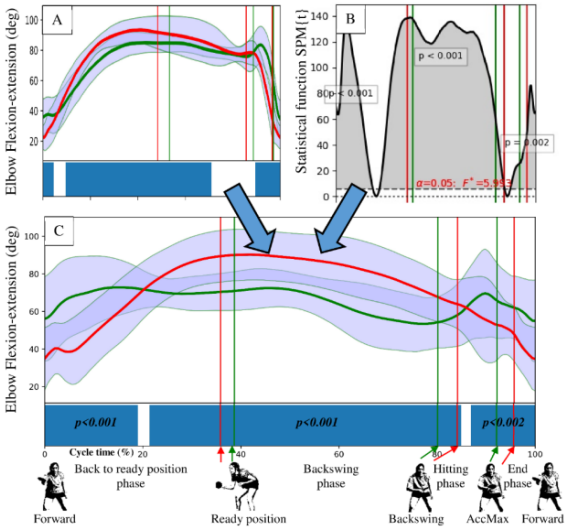

Fig 1: The statistical parametric mapping (SPM) procedure. For each data set (A), an SPM{t} function (B) was calculated. The SPM statistical information was transformed into a horizontal bar representation (C), designating the most significant differences between the compared patterns.

The differences found are probably mainly due to differences in the training methodologies caused by different coaching systems. The observed differences include, among others, greater use of the so-called small steps in order to adapt and be ready during the back to ready position and backswing phases, which gives the CHIN players slightly better conditions for preparation for the next plays. The position of the CHIN players is also more universal than in the POL players and favours a quicker transition to the forehand play. This difference is probably related to the difference in the dominant playing styles of the groups studied [3].

References

1. Bańkosz, Z.; Winiarski, S. Statistical Parametric Mapping Reveals Subtle Gender Differences in Angular Movements in Table Tennis Topspin Backhand. International Journal of Environmental Research and Public Health 2020, 17, 6996.
2. Pataky, T.C. One-dimensional statistical parametric mapping in Python. Comput Methods Biomech Biomed Engin 2012, 15, 295–301.
3. Bańkosz Z, Winiarski S, Malagoli Lanzoni I. (2020). Gender Differences in Kinematic Parameters of Topspin Forehand and Backhand in Table Tennis. International Journal of Environmental Research and Public Health. 2020; 17(16):5742.

MUSCULOSKELETAL LOWER BACK LOAD OF ACCOUCHEURS DURING DELIVERY

Maximilian Melzner (1,2), Khaled M. Ismail (3,4), Zdeněk Rušavý (3,5), Vladimír Kališ (3,5), Franz Süß (1,2), Sebastian Dendorfer (1,2)

1. Laboratory for Biomechanics, Ostbayerische Technische Hochschule (OTH) Regensburg, Germany
2. Regensburg Center of Biomedical Engineering, OTH and University Regensburg, Germany
3. Biomedical Center, Faculty of Medicine in Pilsen, Charles University, Pilsen, Czech Republic
4. Department of Obstetrics and Gynecology, Faculty of Medicine in Pilsen, Charles University, Czech Republic
5. Department of Obstetrics and Gynecology, University Hospital, Pilsen, Czech Republic

Introduction

With the progress in modern medicine, it was possible to significantly reduce the risks of birth for mother and child. One aspect that has received less attention so far is the risk of injury to the accoucheurs (obstetricians and midwives) during the birth process. Indeed, studies indicate that 92% of midwives suffer from musculoskeletal disorders, with the lower back being the main cause of complaints (72%) [1]. The aim of this study was to investigate two commonly used postural techniques used by accoucheurs during childbirth and to analyze the resulting load on the lower back using the AnyBody™ [2] musculoskeletal simulation software.

Material and Methods

To create a kinematic data set for musculoskeletal analysis, we recorded two male obstetricians performing a simulated deliveries using a birthing simulator (Sophie and Sophie's Mum Birth Simulator, MODEL-med, Melbourne, Australia) placed on a table. For each obstetrician, three different birthing trials were conducted. Obstetrician 1 was kneeling on his right knee, whereas obstetrician 2 was in an upright position pivoting his right elbow on his right thigh.

To determine the obstetricians' movement, an Xsens IMC System (Xsens Link, Xsens Technologies BV, Enschede, Netherlands) was applied to the test subjects. Two gloves, on top of each other, were placed on the accoucheur's hand - one glove to obtain the kinematics of all fingers of each hand (Prime I Xsens, Manus VR, Geldrop, Netherlands) and one glove, measuring the forces acting on the right thumb, index, and middle finger [3].

For the analysis of the loads acting on the accoucheur's musculoskeletal system, only the time interval of the final contraction of the delivery was considered. The musculoskeletal simulation software AnyBody™ (AnyBody Technology A/S, Aalborg, Denmark, V.7.3.1) was used as a modelling environment.

Results

Figure 1 shows the force acting on the lumbar spine of one exemplary trial of obstetrician 1 (Figure 1a) and obstetrician 2 (Figure 1b). The tendency of increased force between the lumbar spine segments was seen in all three trials. The average maximum total load between the segments of the lower back decreased by 677 N (mean force 638 N) from obstetrician 1 to 2. Also, the shear forces showed a mean reduction of the maximum force of 295 N (276 N) for the anteroposterior direction and 92 N (66 N) for the mediolateral direction.

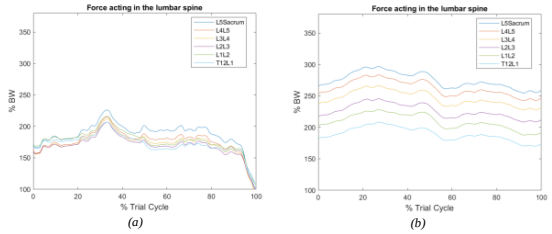

Figure 1: Force (normalized to the body weight - BW) acting between the segments of the lumbar spine for subject 1 (a) and subject 2 (b) during a delivery.

Discussion

The results of musculoskeletal simulations indicate that the kneeling position of the accoucheur does not stress the low back as much as standing posture. One limitation, however, is that the force transmission between the elbow and thigh was not included in the simulations of subject 2 as this force could not be measured. We appreciate that the measurements were only test measurements on a simulator, nonetheless have potential significant practical implications. In the next step of our work, we intend to apply an identical test setup to real deliveries.

References

1. Okuyucu, Kubra, et al. (2019), Midwifery, 79: 102546.
2. AnyBody Technology A/S. anybodytech.com
3. V. Kalis et al. (2020), BMC Pregnancy Childbirth 20 (1), pp. 1–6

Acknowledgements

Funding from the EFRE (INTERREG Project 182) and BayWISS is gratefully acknowledged.

DEVELOPMENT OF A SMART MATERIAL ABLE TO USE AS SOFT ACTUATOR OR SENSOR IN HEALTHCARE

António André (1), Ana Margarida Teixeira (1), Pedro Martins (2)

1. INEGI, Porto, Portugal, (aandre, ateixeira)@inegi.up.pt; 2. INEGI, LAETA, Porto, Portugal, palsm@fe.up.pt

Introduction

Smart materials, defined as materials with the ability to change their properties in function of an external physical stimuli, have been increasingly adopted as soft actuators or sensors. Considering this scenario, electroactive polymers (EAP) have been the primary option, among all possibilities [1].

EAP materials are characterized by the ability to mechanically deform their shape and size in presence of an electrical field, which makes them ideal to be used as soft actuators i.e. in rehabilitation solutions [2]. Moreover, for the same material to be used as a sensor (e.g. in cardiorespiratory [3] or motion monitoring [4]), it must have the opposite behavior - it must generate a measurable voltage or current when externally deformed. This reversible process is designated by piezoelectric effect, while the materials are called by piezoelectric-based materials [5].

Polyvinylidene fluoride (PVDF) is a commonly used piezo-based material, exhibiting excellent properties, such as large dielectric constant, high polarity, biocompatibility, ionic conductivity, high mechanical strength, easy processing and the most important, high piezoelectric coefficients [6]. PVDF could evidence, at least, five polymorphic modifications in its crystalline phase (α, β, γ, δ and ε), being some more desirable for piezo effect than others, in particular, the β phase [7]. This phase, exponentiated in different ways [7], gives PVDF its piezoelectric properties.

Materials

The smart material was developed considering a mixture of three different materials: PVDF powder (Solef 6020) offered by Solvay Lda; a ionic liquid (IL) (1-Methyl-3-propylimidazolium bis(trifluoromethylsulfonyl)imide, >99%) responsible for increasing β phase and purchased from IoLiTec-Ionic GmbH; and finally the solvent, dimethylsulfoxide (DMSO, 99.5%) purchased from Fisher Scientific, Lda.

Methods

The sample was prepared by blending the products previously mentioned and following a similar protocol established by Correia et al [1].

First, the IL was mixed in DMSO, considering a ratio of 40% w/w (IL/PVDF). After that, PVDF was added to the solution in a ratio of 15/85% w/w (PVDF/DMSO). During the dissolution of the PVDF, the beaker should be sealed, and the mixture stirred by a magnetic stirrer and maintained heated, around 65ºC (Figure 1). This temperature eases the dissolution, while avoids agglomerates of the powder.

After a transparent and homogeneous solution achieved, the resultant is casted to a glass substrate, followed by solvent evaporation at the oven with temperatures above 70ºC.

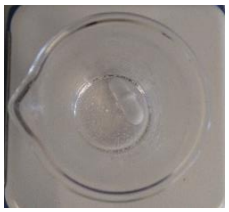

Figure 1: Mixture being stirred.

Results and Discussion

The result obtained is a translucent PVDF film, as shown by the figure 2. Additionally, electrodes must be embedded into the film to establish electrical conductivity with the signal generator - if used as actuator, or the signal analyzer – if used as sensor. Only after this last step, the PVDF film is ready to be used.



Figure 2: Polymer film achieved.

References

1. Correia et al, The J of Physical Chemistry, 123:12744-12752, 2019
2. Billah et al, Materials Today: proceedings 3:572-577, 2016
3. Wang et al, J of Int Material Systems and Structures, 14:185-190, 2003
4. Yang et al, Sensors and Actuators A: Physical, 301:111789, 2020
5. Anton et al, Smart Mater. Struct., 16:R1-R21, 2007
6. Cardoso et al, Polymers, 10:161, 2018
7. Ruan et al, Polymers, 10:228, 2018

Acknowledgements

The authors gratefully acknowledge funding from FCT, Portugal, under grant SFRH/BD/147807/2019, and from project MImBI - PTDC/EME-APL/29875/2017 financed through FEDER and from research unit LAETA. The help of Solvay Lda, was gratefully appreciated.

POLICE SPECIFIC PHYSICAL FITNESS OF MEN AND WOMEN WITH DIFFERENT BODY HEIGHTS

Jan-Peter Goldmann (1,3), Maximilian Sanno (1,3), Sandra Grothe (1,3), Anna Droszez (1), Joachim Mester (2,3)

1. Institute of Biomechanics and Orthopaedics, German Sport University Cologne, Germany; 2. Institute of Training Science and Sport Informatics, German Sport University Cologne, Germany; 3. The German Research Centre of Elite Sport, German Sport University Cologne, Germany

Introduction

In many occupations, standards for body height are used to evaluate job applicants and future employees [1]. Especially in jobs where physical fitness is required, precise cut-off values are widely discussed. More than 50% of the countries of the European Union defined minimum height requirements for police officers, but none of the defined minimum sizes is supported by scientific research [2]. Several studies examined the effects of body height on typical parameters of general fitness and health but without considering police specific work [3]. Therefore, the objectives of the present studies were to analyze tall and short men and women on their physical fitness in police specific situations. For this purpose, the entire work was divided into four sub-studies, which included both laboratory tests and field tests.

Methods

Sixty one physical active (5.3±2.8 hrs/week) participants were divided into four groups. 16 short women (1.57±0.03 m, 55.7±4.5 kg, 25.4±4.7 yrs), 16 tall women (1.79±0.02 m, 72.2±7.8 kg, 24.5±5.5 yrs), nine short men (1.66±0.02 m, 64.1±3.7 kg, 26.8±3.8 yrs) and 20 tall men (1.91±0.05 m, 85.5±8.0 kg, 26.1±4.2 yrs). For analyzing police specific physical fitness, four sub-studies (Fig. 1) were obtained: 1.) Center of mass height (h) and max. mechanical power (P_{max}) during vertical jumps with body armor (BA, m=21 kg); 2.) Resistance against impacts with BA; 3.) Pulling forces in different grip heights pertinent to overcoming disturbers; 4.) Performance while rescuing and recovering a person from a car. Statistics: Kolmogorov-Smirnov test, one-factor ANOVA with Bonferroni's post-hoc test (α = 5%), Friedman's non-parametric test (α = 5%), Wilcoxon test.

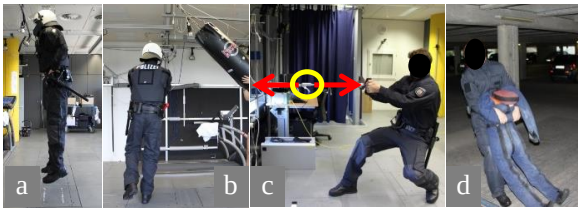

Figure 1: Set up of the sub-studies. a) Countermovement Jumps on force plate; b) resistance against oscillating pendulum (E_{kin} 126 J); c) pulling forces in different grip heights with strain-gauge load cell (circle); d) dummy (m=70 kg) rescue and recovery about 37 m.

Results

The results of the studies (Tab. 1) showed that compared to tall men and women 1.) resistance to impacts was 45% and 39% lower (P<0.05) in short men and women; 2.) short men and women generated 31% to 42% less forces (P<0.01) in both grip heights; 3.) during rescuing and recovering a person from a car, short men and women needed 17% and 43% (P<0.05) more time.

	Men short/tall	Women short/tall
h [cm]	24±3/25±4	14±4/17±4
a [m/s²]	32±8/22±6*	38±9/27±8***
F_1 [N]	186±17/289±38**	125±22/217±38**
F_2 [N]	372±40/538±76**	296±47/433±56**
t [s]	34±3/29±4*	64±19/45±8*
v [m/s]	1.55±0.1/1.9±0.06*	0.9±0.08/1.2±0.1*

*Table 1: Jump height (h), body acceleration after impact (a), absolute forces in head height (1.80 m, F_1) and hip height (1.10 m, F_2), time (t) and mean velocity (v) for rescue and recovery. *P<0.05, **P<0.01, ***P<0.001 significantly different to short.*

Discussion

Considering the sample of this study, short men (<1.68 m) and women (<1.61 m) demonstrated less police specific physical fitness than tall men (>1.86 m) and women (>1.77 m). The results are contrary to the results of the study by Lagestad [3], who found that short police students performed similar or even better in classical fitness tests (e.g. bench press, standing long jump) than tall students. One should consider that these tests were mainly focused on moving own body weight rather than resisting external forces or moving external weights. Based on the results of our studies, a minimum height requirement should therefore be advocated as a prerequisite for the recruitment of applicants to the police service. However, it would be advisable to offer a fitness test with police specific tasks in the limits of the minimum heights.

References

1. Judge et al., J Appl Psychol, 89:428-441, 2004.
2. Kirchengast, J Pol Sci Pract, 1:52-61, 2011.
3. Lagestad, Int J Pol Sci & Managm, 14:322-333, 2012.

Acknowledgements

We would especially like to thank the Police of North Rhine Westphalia, Germany for providing equipment and body armor.

CATEGORIZATION OF REHABILITATION EXERCISES FROM MOVEMENT SIGNALS USING NEURAL NETWORKS

Adriana Modrego (1,2), Alex Llobet Martínez-Pons (2), Andrea Masi (2), Kevin David Rosales Santana (2), Ricardo Jauregui (1)

1. DyCare, Spain; 2. FIB-UPC, Spain;

Introduction

The increase of rehabilitation demand wobbles the sustainability of health care services, requiring new models such as remotely-controlled rehabilitation or tele-rehabilitation.

ReHub, is a tele-rehabilitation platform which registers patients' movements with a single inertial measurement unit (IMU). One big challenge is to identify which exercise is the subject performing because several different exercises are described by very similar signals.

The aim of this study is to classify 5 rehabilitation exercises performed by patients using ReHub. The captured signals during exercises' execution will be treated as time-series problems and different Convolutional Neural Networks (CNN) and Recurrent Neural Networks (RNN) models will be designed to study their capability to generate the needed deep features to correctly classify the selected exercises [1].

Methodology

Firstly, the initial 1650 time-series signals files, regarding five different exercises carried out by some patients, were split by repetitions leading to 16166 files. Then, feature selection and instance reduction methods were applied. After this step, the dataset was composed of 16053 instances with 10 features each.

From this point, the tensors (i.e. multidimensional matrices) required to feed the selected deep learning models were built. These were mainly of two types: one tensor for repetition (independent cycle), and one tensor with all the repetitions of one exercise (entire exercise). Later, some signal adjustment procedures were deployed to obtain tensors of the same size.

Finally, the experimental models were designed. They were based on Convolutional Neural Network (CNN) architectures and on the new hybrid Long Short-Term Memory (LSTM) and CNN architecture that combines advantages from both CNN and LSTM techniques.

Results and discussion

The main results obtained are presented in Table 1.

Input data	NN type	Test accuracy
Entire exercise	CNN	0.905
Independent cycles	**CNN**	**0.979**
Entire exercise	LSTM-CNN	0.921

Table 1: Accuracy achieved by the different implemented approaches.

The accuracy values indicate that among all the proposed methods the best option is to use a CNN model and feed it with independent cycles.

Considering the best approach and the test set, a confusion matrix was obtained, and it was detected that the main errors were misclassification between *standing hip flexion* and *knee flexion* and misclassification between *knee flexion-extension* and *hip extension*.

Taking into account the execution of the exercises, these pairs of exercises are quite similar. Thus, the obtained signals have very similar patterns. Even though, the CNN architecture designed is able to discover deep features even to classify exercises with very similar patterns.

Furthermore, the results achieved proved that the studied CNN models are able to retrieve the underlying features of the data of each exercise and use them to classify new queries. Additionally, the hybrid CNN + LSTM models, which are state-of-the-art in time-series problems, allow the memorization of samples through time, thus improving the performance.

Conclusions

Based on the results presented in the last section and regarding the accuracy achieved by the best model (0.979), it is a high enough score to consider implementing this model to analyze and assess in real-time the repetitions of an exercise performed by a patient.

To further improve this work, an optimization of the parameters of the hybrid architectures should be done (e.g. using GridSearch), which will yield a fair comparison among models as all would be optimized.

Finally, this work led to believe that an appropriate CNN architecture could help to identify if a particular exercise is well executed or not in real-time even if the captured signals are very similar. Consequently, it will make possible an accurate real-time biofeedback which will increase patient empowerment.

References

1. Oonagh Giggins, Kevin Sweeney, and Brian Caulfield. Rehabilitation exercise assessment using inertial sensors: A cross-sectional analytical study. Journal of neuroengineering and rehabilitation, 2014.Somebody et al, J Biomech, 45:1-10, 2014.

Acknowledgements

This work was partially supported by 811755 ReHub2018-2020/H2020-SMEInst.

ACCURACY OF INERTIAL SENSOR IN THE ANALYSIS OF CENTER OF MASS DISPLACEMENT

Federico Temporiti (1,2,4), Alessandro Vagnini (3), Roberta Furone (3), Giulia Zanotti (1), Manuela Galli (4), Roberto Gatti (1,2)

1. Humanitas Clinical Institute, Rozzano, Milan, Italy; 2. Humanitas University, Pieve Emanuele, Milan, Italy; 3. BTS SpA, Garbagnate Milanese, Milan, Italy; 4. Politecnico di Milano, Milan, Italy

Introduction

The displacement of centre of mass is usually used to quantify postural stability [1]. Centre of mass displacement can be measured using different techniques, which are complex and time-consuming [2]. Inertial sensors have been proposed to evaluate the centre of mass displacement, but their accuracy have never been compared to the gold standard. The aim of the study was to evaluate the agreement in terms of centre of mass displacement measured by an inertial sensor (G-sensor, BTS, Italy) with respect to an optoelectronic system (SMART-DX, BTS, Italy) assumed as gold standard.

Methods

Thirty young (age: 22±2.5 years) healthy subjects (15 male and 15 female) were assessed during a single evaluation session at the Motion Analysis Lab of Humanitas Clinical Institute, Milan, Italy. Subjects were asked to perform four balance tasks, one minute each, consisting of: quiet standing with eyes open and close and single limb stance with open eyes on the right and left legs. An inertial sensor with a retro-reflective marker over it was placed at the level of the second sacral vertebrae (S2). All tasks were recorder by an inertial sensor and an optoelectronic system, simultaneously. Medial-lateral (ML), anterior-posterior (AP) and Total Path Length, ML and AP Speed, Confidence Ellipse of centre of mass and Root Mean Square (RMS) acceleration were calculated. The results of the four tasks were gathered and the agreement between the two systems was assessed using the Intraclass Correlation Coefficient (ICC 3,1) and the Bland-Altman plot.

Results

High ICCs scores were found for Speed-ML (r=0.93), Speed-AP (r=0.95) and Total Path Length (r=0.91). Good ICCs scores were found for ML-Path-Length (r=0.88), AP-Path-Length (r=0.89) and RMS-ML (r=0.77). Moreover, moderate ICCs scores were found for RMS-AP (r=0.65) Confidence Ellipse (r=0.75) and Range-ML (r =0.7), whereas ICCs revealed poor scores only for Range-AP (r=0.47) (always p<0.001, Table 1). Bland-Altman revealed a good agreement, especially for AP-speed (Figure 1). On the other hand, the greatest limits of agreements were found for Confidence Ellipse.

	Optoelectronic system	Inertial sensor	ICC
Range-ML (m)	0.02 (0.013)	0.019 (0.232)	0.70
Range-AP (m)	0.032 (0.02)	0.037 (0.028)	0.47
Speed-ML (m/s)	0.004 (0.004)	0.034 (0.003)	0.93
Speed-AP (m/s)	0.004 (0.003)	0.003 (0.002)	0.95
P-Length-ML (m)	0.21 (0.232)	0.2 (0.183)	0.88
P-Length-AP (m)	0.214 (0.186)	0.22 (0.132)	0.89
P-Length-TOT (m)	0.336 (0.186)	0.348 (0.247)	0.91
RMS-ML (m/s^2)	0.004 (0.002)	0.004 (0.003)	0.77
RMS-AP (m/s^2)	0.008 (0.004)	0.007 (0.005)	0.65
Confidence Ellipse (m^2)	0.147 (0.094)	0.134 (0.093)	0.75

Table 1. ICCs (3,1) between optoelectronic system and inertial sensor parameters gathering the four tasks. Data are shown as median and interquartile range.

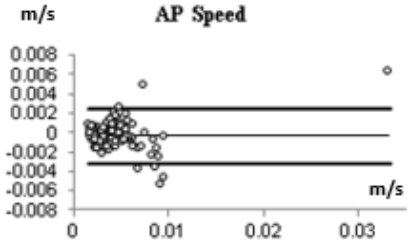

Figure 1. Bland Altman plot for Speed-AP (mean difference: -0.0003, limits of agreements (-0.0032; 0.0025). Data are presented gathering the four tasks.

Discussion

Inertial sensor can offer an accurate method to study centre of mass displacement in all conditions (eyes open, eyes close and single limb stance). These findings may enable the assessment of postural stability also in a clinical setting.

References

1. Mancini et al, Eur J Phys Rehabil Med, 46:239-248, 2010

2. Doheny et al, Conf Proc IEEE Eng Med Biol Soc, 3300-3, 2012.

VALIDITY AND RELIABILITY OF KINEMATIC INDEXES DURING NINE HOLE PEG TEST FOR MANUAL DEXTERITY ASSESSMENT

Federico Temporiti (1,2,3), Serena Mandaresu (1), Alessandra Calcagno (1), Stefania Coelli (1), Erica Monfardini (1), Ilaria Lozza (1), Roberto Gatti (2,3), Anna Maria Bianchi (1), Manuela Galli (1)

1. Politecnico di Milano, Milan, Italy; 2. Humanitas Clinical Institute, Rozzano, Milan, Italy; 3. Humanitas University, Pieve Emanuele, Milan, Italy

Introduction

Nine Hole Peg Test (NHPT) is one of the most used tools for manual dexterity assessment. However, the time to accomplish the test represents the only outcome score, without providing quantitative parameters on the quality of motor performance [1-2]. The study aim was to investigate test-retest and intra-rater reliability, convergent and discriminant (dominant versus non-dominant arm) validity of kinematic indexes during NHPT.

Methods

Twenty-five healthy right-handed volunteers performed NHPT twice for dominant and non-dominant upper limbs. After 6 hours, the session was repeated by the same operator. Retro-reflective markers were placed on upper limbs and trunk to detect kinematics and segment the performance into different phases based on the velocity profile of a marker on the finger index. Specifically, nine consecutive peg-grip, peg-transfer, peg-in-hole, hand-return phases and one removing phase were identified, and the following parameters were extracted: total and phases times, normalized jerk, mean, peak and time-to-peak of velocity, curvature index during peg-grip and hand-return phases, and trunk 3D displacement during the entire performance. Test-retest and intra-rater reliability were assessed using Intraclass Correlation Coefficients (ICCs), convergent validity using Pearson's correlation and discriminant validity using the paired t-tests and Cohen's *d* for effect size estimation.

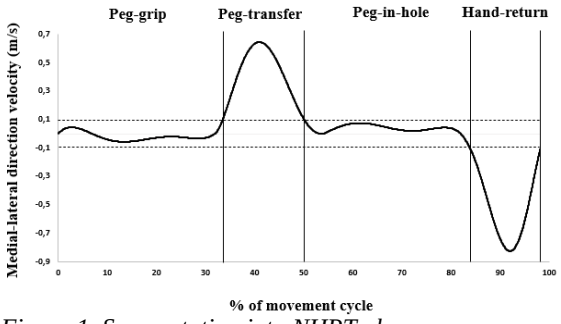

Figure 1. Segmentation into NHPT phases.

Results

Test-retest reliability was excellent for trunk rotation (ICC: 0.91) and good to moderate for kinematic indexes (ICCs: 0.89-0.61). Intra-rater reliability resulted excellent for total and removing times (ICCs: 0.91 and 0.94) and good to moderate for the other indexes (ICCs: 0.84-0.66), except trunk inclination (ICC: 0.37). NHPT phases, normalized jerk, mean velocity, peak of velocity, time-to-peak and curvature index correlated with total time, indicating convergent validity (r-score: 0.8-0.3, $p<0.001$). As shown in Table 1, NHPT phases and most kinematic indexes discriminated the dominant from non-dominant arm, with the greatest effect size for normalized jerk during hand return (d=1.16).

Variables	Dominant limb	Non-dominant limb	p-value	Effect size
Time (s)	18.1±1.7	19.7±1.9	**<0.001**	1.01
Removing (s)	5.5±0.7	5.8±0.8	**<0.001**	0.57
Peg-grip (s)	3.6±0.7	4.0±0.7	**0.001**	0.51
Peg transfer (s)	2.5±0.3	2.7±0.3	**<0.001**	0.61
Peg-in-hole (s)	3.2±0.5	3.7±0.6	**<0.001**	0.56
Hand return (s)	2.0±0.2	2.2±0.2	**<0.001**	1.07
Normalized Jerk PT	1.14±0.23	1.32±0.25	**<0.001**	0.83
Normalized Jerk HR	0.92±0.13	1.07±0.14	**<0.001**	1.16
Mean velocity PT (m/s)	0.32±0.04	0.31±0.04	0.156	-
Mean velocity HR (m/s)	0.36±0.04	0.35±0.04	0.090	-
Peak velocity PT (m/s)	0.64±0.11	0.61±0.11	**0.029**	0.31
Peak velocity HR (m/s)	0.83±0.12	0.78±0.11	**0.002**	0.47
Time-to-peak PT (%)	40.1±5.6	36.6±5.2	**<0.001**	0.55
Time-to-peak HR (%)	55.6±4.8	59.7±4.6	**<0.001**	0.66
Trunk inclination (°)	0.6±0.3	0.6±0.2	0.693	-
Trunk rotation (°)	1.9±0.5	2.2±0.8	**0.004**	0.43
Trunk flexion (°)	1.1±0.5	1.0±0.4	0.275	-
Curvature index PT	112.0±4.9	112.9±5.2	0.167	-
Curvature index HR	112.8±4.7	114.7±5.3	**0.007**	0.40

Table 1. Discriminant validity of kinematic indexes during NHPT with the dominant and non-dominant upper limbs (PT: peg-transfer; HR: hand-return).

Discussion

Kinematic indexes during NHPT resulted in valid and reliable parameters for manual dexterity assessment. These results may play a role in detection of subtle manual dexterity changes in healthy subjects or features of dexterity impairments in patients with disability.

References

1. Grice et al, Am J Occup Ther, 57:570-3, 2003.
2. Johansson et al, J Neuroeng Rehabil, 14:8, 2019.

L5-S1 JOINT MOMENT DOES NOT PREDICT INTERNAL BACK LOADING AND CONSEQUENT RISK ON LOW BACK INJURY

Arthur van der Have (1), Wei Wang (1,2), Sam Van Rossom (1), Ilse Jonkers (1)

1. *Human Movement Biomechanics Research Group, Katholieke universiteit Leuven, Belgium*
2. *Shenzhen Institutes of Advanced Technology, Chinese Academy of Sciences, Shenzhen, China*

Introduction

Back and muscular pain in the upper limbs are work-related musculoskeletal disorders (WMSDs) reported by three out of five workers in the EU, mainly in relation to excessive physical workloads[1]. It is well-know that excessive muscle and joint contact forces are important risk factors for developing WMSDs, however these forces cannot be measured *in-vivo*. Therefore, most ergonomic risk assessments rely on external joint moments and measured muscle activity as an estimation of the internal musculoskeletal loading [2]. The aim of this study is to evaluate if these external moments are an accurate representation of the back loading during various industrial tasks measured in a lab-based setting. The correlation between peak compression force, calculated using a complex full body musculoskeletal model, peak L5-S1 moment and peak m. erector spinae longissimus activation was evaluated.

Methods

One healthy participant pulled laces through holes (50 cm above shoulder height), lifted a 10 kg box from ground to knee height, from elbow to shoulder height, from shoulder to 50 cm above shoulder height, from ground level to elbow height and lifted a 10 kg box from ground to elbow height with 45 degrees rotation. 3D full-body marker trajectories and ground reaction forces were measured and used to calculate joint angles, moments, muscle and joint contact forces using OpenSim[3]. A full body-musculoskeletal model with articulated spine and shoulder [4] was used of which the spine includes nonlinear bushing elements representing the spine joint stiffness[5]. The model was scaled to the anthropometry of the participant. Bushing forces in the spine were calibrated and spine kinematics were optimized in order to minimize the difference between the modeled and measured marker trajectories as well as minimizing the intersegmental forces while satisfying skeletal dynamics[6]. In addition, bilateral muscle activations of the m. erector spinae longissimus (ESL) were recorded, using surface electromyography. Raw EMG signals were band pass filtered (20-400Hz), full-wave rectified, low pass filtered (6Hz) and normalized to maximum voluntary contraction. Next, we investigated the correlation between the peak joint contact forces, peak moment at the L5-S1 joint and with the peak erector spinae activity in all ergonomic tasks studied.

Results

Peak L5-S1 joint moment has a good correlation with peak compression force in L5 (R^2 = 0.8257). However, a high root mean square error (RMSE = 37.37) is observed. Peak muscle activations of the ESL bilaterally did not correlate well with peak compression forces in L5 (R^2 = 0.05836).

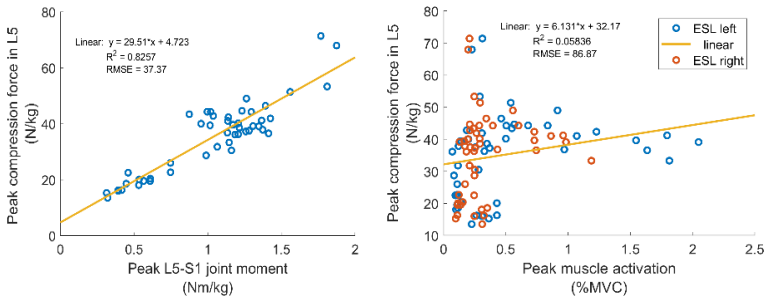

Figure 1: Correlation between peak L5-S1 joint moment and peak compression force in L5 (left). Correlation between peak compression force in L5 and peak ESL muscle activation (right).

Discussion

Our findings indicate that despite the high correlation (R^2 = 0.83), the L5-S1 joint moment might not be the best proxy for lower back loading given the high RMSE value. The correlation between peak compression force in L5 and the peak ESL activations did not correlate well (R^2 = 0.05836) as the highest compression forces were not correlated with the highest muscle activations. Regardless, joint moments and EMG are often used in order to quantify the risk on developing WMSDs on the work floor. Based on the high correlation between L5-S1 joint moment and peak compression force, joint moments it is however valid to use peak external moments to compare two work situations and investigate the relative workload. It is important to indicate that given the substantial normalized RSME (= RMSE/(Ymax-Ymin)) of 64%, joint moments should not be used to investigate the absolute internal musculoskeletal loading. Indeed, given the high residual variance of the linear regression, we advise against the use of the external L5-S1 moment for the absolute quantification of musculoskeletal loading. It is therefore extremely important that accurate musculoskeletal modelling workflows are designed using in the field measurement set-ups to evaluate musculoskeletal loading to assess the risk for WMSDs development.

References

1. Publications office of the European Union et al.1–164, 2017.
2. Gallagher et al.*Ergonomics 60*, 255–269, 2017.
3. Delp et al.*IEEE Trans. Biomed. Eng. 54*, 1940–1950, 2007.
4. van der Have et al.*Appl. Sci.* 1–20, 2019.
5. Wang et al.*J. Biomech.* 109437, 2019.
6. Wang et al.*25th Congr. Eur. Soc. Biomech.* 2019.

ANALYSIS OF LOWER LIMB ACTIVATION MODALITIES OF PARKINSON'S DISEASE PATIENTS DURING GAIT

Marco Romanato (1), W. Piatkowska (1), Fabiola Spolaor (1), Daniele Volpe (2), Zimi Sawacha (1)

1. Department of Information Engineering, University of Padua, Italy; 2. Fresco Parkinson Center, Villa Margherita, S. Stefano, Vicenza, Italy

Introduction

Parkinson's disease (PD) is the second most prevalent neurodegenerative disorder affecting people worldwide. Modified pattern of motor unit activation and rigidity might be the causes of gait alterations associated with PD [1]. State of the art showed that basal ganglia dysfunction affects not only the automatic maintenance of the movement [2] but also each component of the motor plan in terms of timing [3]. The aim of this work was to analyse how PD affects the motor plan. We hypothesized that the electromyography (EMG) sequence can be considered as a motor program. To be able to address and quantify the motor control abnormalities will allow us to identify how the PD disrupts normal control processes.

Methods

The data of eighteen PD subjects (age 65.6±10.5 years, BMI 26.5±3.5 kg/m^2) and ten controls subjects ((CS) age 62±6.5 years, BMI 26.4±3.7 kg/m2), have been acquired at the Human Movement Bioengineering Laboratory (10m walkway) of the Department of Information Engineering at the University of Padova (Italy). Data from an 8 channels EMG system (1000Hz, BTS, Italy) were collected to record the electrical activity of four lower limb muscles bilaterally: Tibialis Anterior, Gastrocnemius Lateralis, Rectus Femoris and Biceps Femoris. The EMG signals were band pass filtered with a double 5th order Butterworth filter and full wave rectified. The cut-off frequencies varied between 15 and 20 Hz for high pass filter, and between 450 and 495 Hz for low pass filter. A double-threshold statistical detector [4] was applied for activation detection. Peak of the envelope (PoE) and its position (PPoE) per each accepted burst were extracted together with burst duration. Subjects were then grouped per activation modality types. PoE and PPoE were extracted also considering the entire gait cycle. A co-contraction index has been extracted as in [Sartori et al].

Results

Results for the TA and GL muscles were presented within Figure 1. In the upper part, results reporting analysis on the entire signal envelope were displayed. In the bottom part maps representing frequency of activation patterns divided for activation modalities were reported. Additional information on the PPoE were given within the figure.

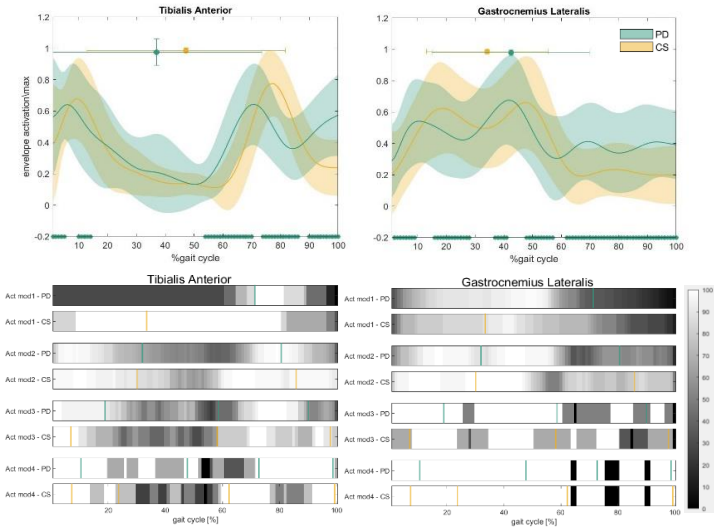

Figure 1: Upper part: Mean activation envelopes ± standard deviation for PD (in green) and CS (in yellow). Statistically significant differences are reported as green asterisks in the bottom axes. PoE is presented as a dot with errorbars associated with its position (horizontal) and value (vertical). Bottom part: map of the activation occurrence per activation modality types. Vertical bars indicate the peak of the envelope within the burst.

Discussion

PD subjects displayed a different motor plan during walking. The results obtained with the adoption of a statistical detector (bottom part of Figure 1) allowed us a deeper understanding and characterization of the information derived from the EMG signals. The objective assessment of a different motor control strategy could be useful for planning interventions aiming at improving the walking pattern of PD's subjects.

References

1. Volpe D et al Gait & Posture. 2020: 80:185–191.
2. Horak FB et al. J Neurol Sci. 1992;111(1):46-58.
3. Crenna P, Frigo C. J Physiol. 1991; 437: 635–653.
4. Bonato P et al. IEEE Trans Biomed Eng. 1998;45(3):287-99.
5. Sartori M et al, J Neurophysiol. 2015; 114: 2509–2527.

Acknowledgements

Marco Romanato's PhD course grant is supported by Fondazione Fresco Parkinson Institute Italia Onlus.

BIOMECHANICAL ANALYSIS OF CYCLISTS DELIVERIES POSTURE'S

Brayan David Solorzano Q (1), Kevin Alejandro Giraldo (1), Nicolas Yanguma Muñoz (1), Christian Cifuentes-De la Portilla Ph.D (1)

1.Biomechanics group (IBIOMECH), Department of biomedical engineering, Universidad de los Andes, Colombia.

Introduction

Cyclist deliveries are carried by people who work riding bikes, transporting essential and non-essential goods in backpacks on their backs. These people tend to suffer several injuries in their backs and shoulders [1, 2, 3], mostly because they carry items that weigh more than 15 percent of their body weight. Thus, this study aimed to analyse cyclist' deliveries kinematics and kinetics varying the backpack's load as a percentage of a cyclist's body weight.

Methods

The kinematic analysis was done using the software Kinovea; this procedure consisted of 2D motion analysis with seven markers on the subject (fig. 1A-B). The tests were carried out with 4 different percentages of body weight (0,10,20,30) in steady state for 64 seconds. The reference of data capture was the craniocaudal axis, using the sagittal plane. On the other hand, the kinetic analysis was done implementing a computational model through the software COMSOL Multiphysics. This study included a backpack and body with standard measurements (fig 1C). The kinetic simulations were carried out with the method of finite elements by a module of structural mechanics, changing the percentage of body weight in the backpack, and the inclination of the subject.

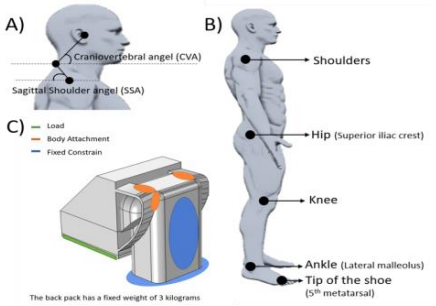

Figure 1. Overall kinematic and kinetic methodological considerations. **A-B)** Markers position kinematic analysis, **C)** Boundary conditions computational kinetic model.

Results

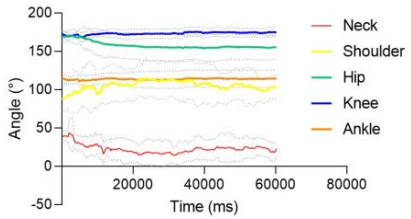

Figure 2. Angular variation as a function of time for a load of thirty percent of the subject's body weight.

Figure 2 shows the subject's angular variation overtime for a load of thirty percent of the subject's body weight. As can be seen, the lumbar overload has a significant impact on the angular variation of the shoulders, hips, ankles, and neck. Furthermore, figure 3 illustrates the subject's kinetic behaviour under steady-state conditions and a loading weight of thirty percent of body weight. On the other hand, figure 4 illustrates tension and compression variations varying subjects' angular inclination under the same steady-state conditions.

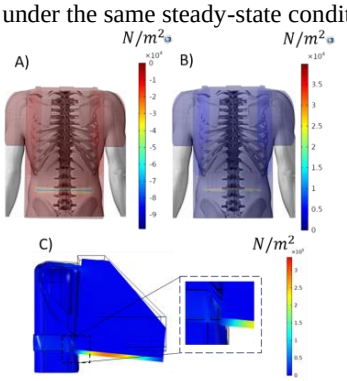

Figure 3. A) Compression and **B)** tension forces involved on deliveries cyclists under loads of thirty percent of their body weight, **C)** Von mises stress with lumbar backpack's crust representation.

Discussion

Most affected areas by lumbar overload are the hips, neck, and shoulders; while neck angle decreases, the shoulders angle increases because it balances out the anatomical disturbance, thus shoulders angle is inversely proportional to the neck angle. Moreover, hips angular variation is affected with the load over time, due to, as greater loads are supported, the subject tends to reduce the angle to release pressure on the shoulders and transfer it to the lumbar area; which is anatomically counterproductive because the compressive force decreases, but shear' force increase on lumbar vertebrates, leading to injuries [3]. Regarding backpack's involve forces, momentum and torque are generated on the rigid bar at the bottom of the backpack; resulting in critical tension and compressions forces over the subject's lumbar area. Overall, although data suggest that lumbar overload has consequences over the health of deliveries cyclists, deliveries backpack design may also play a critical role in developing injuries in cyclists.

References

1. Atreya, S., Joshi, D., Anand, S., Singh, U., & Ribeiro, R. (2010). Effects of Backpack Carriage on Gait and Posture-Design Studies. In *6th World Congress of Biomechanics (WCB 2010). August 1-6, 2010 Singapore* (pp. 155-158). Springer, Berlin, Heidelberg.
2. Ren, L., Jones, R. K., & Howard, D. (2005). Dynamic analysis of load carriage biomechanics during level walking. *Journal of Biomechanics*, *38*(4), 853-863.
3. Goh, J. H., Thambyah, A., & Bose, K. (1998). Effects of varying backpack loads on peak forces in the lumbosacral spine during walking. *Clinical Biomechanics*, *13*(1), S26-S31.

STRESS REACTIVITY OF MUSCULAR IMBALANCES IN HEALTHY AND BACK PAIN PATIENTS: THE INFLUENCE OF PERSONALITY

Simone Kubowitsch (1), Franz Suess (1,2), Sebastian Dendorfer (1,2)

1. Ostbayerische Technische Hochschule (OTH) Regensburg, Labratory for Biomechanics, Germany;
2. Regensburg Center of Biomedical Engineering, OTH and University of Regensburg, Germany

Introduction

The muscular response to stress is thought to play a central role in the development and maintenance of back pain. In addition to the known muscle activation under stress in healthy participants [1], an increase of muscular imbalances as contralateral muscle activation asymmetries may significantly increase spinal loading [2]. Back pain patients often show a symptom-specific higher muscular reactivity to short-term stressors [3] and this reactivity could be influenced by variables of personality [4].
Whether these changes also occur under stress in relation to muscular imbalances has not yet been systematically investigated. The aim of this study is to compare changes of muscular imbalances in the back caused by stress between healthy and back pain patients and to investigate the influence of personality variables on stress reactivity.

Methods

Thirty-six healthy participants (M = 22.39, SD = 2.30) and 34 low back pain patients (M = 41.19, SD = 14.01) took part in the study. After completing two personality questionnaires, the General Self-Efficacy Scale and the Center for Epidemiological Studies Depression Scale, they were exposed to a baseline measurement and an experimental condition with an additional cognitive stressor (PASAT) [5], both in a sitting position. The muscular activity of six muscle pairs in the back was measured by surface electromyography. Muscular imbalances were calculated as ratios of the mean signals (left/right) of the filtered and normalized EMG data [6]. A mean value for the upper and lower back was calculated as average from three ratios each and for the whole back as average from all six ratios. Stress reactivity was computed by simple change scores (stress trial - baseline).

Results

A multivariate analysis of covariance with the variable "age" as a covariate and the independent variables "imbalances in the upper back" and "imbalances in the lower back" revealed a significant effect for the factor "condition", $F(2, 134) = 16.78$, $p < .001$, $Wilks' \Lambda = .800$, $\eta p^2 = .20$, and the factor "health", $F(2, 134) = 11.83$, $p < .001$, $Wilks' \Lambda = .850$, $\eta p^2 = .15$. The significant effect for factor “condition” resulted from higher imbalances in the stress condition compared to the baseline condition, both in the upper back, $F(1, 135) = 30.52$, $p < .001$, $\eta p^2 = .18$, and in the lower back, $F(1, 135) = 10.36$, $p = .002$, $\eta p^2 = .08$. With regard to the factor "health", there were comparable imbalances in the upper back for healthy participants and back pain patients, $F(1, 135) = 1.20$, $p = .28$. In the lower back, however, significant differences were observed, $F(1, 135) = 23.79$, $p < .001$, $\eta_p^2 = .15$.
Among back pain patients, there were significant correlations between the stress reactivity of muscular imbalances for the whole back and general self-efficacy ($r = -.51$, $p = .001$) as well as depression ($r = .59$, $p \leq .001$).
A stepwise regression analysis showed that general self-efficacy and depression explained 37.0% of the variance in muscular stress reactivity, $R^2 = 0.370$, $F(2, 31) = 9.11$, $p = 0.001$, see Table 1.

Predictor	Regression Coefficient	β	t	p
Self-efficacy	-0.17	-.420	-2.81	< .01
Depression	.009	.333	2.23	< .05

Table 1: Result of the stepwise regression for the prediction of static imbalances by the general self-efficacy and depressiveness

Discussion

In both healthy participants and back pain patients, muscular imbalances increased from the baseline to the stress condition, although both subsamples did not differ in terms of their stress reactivity. However, back pain patients had higher muscular imbalances in the lower back than healthy participants in both conditions. Thus, there was no symptom-specific increase in stress reactivity. However, muscular stress reactivity was significantly influenced by personality variables general self-efficacy and depression in back pain patients, but not in healthy participants. To our knowledge, this is the first time that a positive buffer effect of self-efficacy on the neuromuscular stress response has been demonstrated.

References

1. Marras et al., Hum Factors, 54(6): 881-889: 2012.
2. van Dieen et al, J Orthop Sports Phys, 49(6), 370–379, 2019.
3. Glombiewski et al, Psychosom Med, 70(1), 125–131, 2008.
4. Flor et al, J Consult Clin Psychol, 53(3), 354–364, 1985.
5. Gronwall, Percept Mot Skills, 44(2): 367-373, 1977.
6. Oddson et al., J Appl Physiol, 94(4): 1410-1420, 2003.

CONTINENT WOMEN MAY HAVE A BETTER BALANCE BETWEEN ABDOMINALS AND PELVIC FLOOR MUSCLES THAN INCONTINENT

Alice Carvalhais (1), Thuane Da Roza (2), Renato Natal Jorge (3)

1. LAETA, INEGI, CESPU-Instituto Politécnico de Saúde do Norte, Granda, Portugal; 2. Laboratory of Biomechanics, Center For Health and Sports Sciences (CEFID), Universidade do Estado de Santa Catarina (UDESC), Florianópolis, Brazil; 3. LAETA, INEGI, Faculdade de Engenharia, Universidade Do Porto, Porto, Portugal

Introduction

During physical exertion the muscles that surround the abdominopelvic cavity work together to raise the IAP [1]. The increase of IAP leads to a downward displacement of the abdominal contents, stressing the pelvic floor muscle (PFM) [2]. If the PFM does not co-contract with appropriated timing and strength to resist this downward force, urine leakage can occur, which is called stress urinary incontinence (SUI) [3]. In a biomechanical perspective, we hypothesized that a strength balance is needed between the muscles of the abdominal cavity and the PFM to prevent SUI.

Methods

This was a cross-sectional study. A convenience sample was recruited from staff and students from the University of Porto. Demographic and medical history data were collected by questionnaire. The International Consultation on Incontinence Questionnaire–Urinary Incontinence-Short Form [4] was applied to assess continence status and the type of UI. After the eligibility criteria, women were divided into continent and incontinent group according to the ICIQ-UI-SF. Vaginal resting pressure (VRP), PFM strength, and endurance were assessed by the Peritron 9300 manometer. Peak torque of trunk flexor muscles was used as a surrogate measure of superficial abdominal muscles (RA and OE) strength [5], using the Biodex System 4 Pro dynamometer (Biodex Corp., Shirley, NY). Maximal Expiratory Pressure (MEP) and Maximal Inspiratory Pressure (MIP) were used to measure the deep abdominal muscles (TrA and OI) [6] and the respiratory diaphragm strength [7], respectively.

For each participant all tests were performed on the same day, using standardized protocols, and following the same order: MEP, MIP, VRP, PFM strength, PFM endurance, and Isokinetic evaluation. Written informed consent was obtained from all participants.

Results

The sample comprised 58 women aged 19 to 49 years, 38 were continent and 20 had SUI symptoms. No differences were found in age, body mass index (BMI), parity, constipation, and exercise practice.

Table 1 demonstrated the difference between the continent and incontinent group regarding the study variables. Incontinent women had stronger diaphragm and superficial abdominals than the continent women.

	Continent (n=38) mean (sd)	Incontinent (n=20) mean (sd)	p
VRP	48.1 (8.7)	44.1(11.7)	.149[a]
PFM strength	52.4 (19.5)	51.7 (21.9)	.906[a]
PFM endurance	51.1 ±45.9	47.1 ± 50.9	.477[b]
Diaphragm	61.7± 21.8	74.2 (19.2)	.036[a]
Superficial abd	106.9 (28.8)	132.9 (28.4)	.006[a*]
Deep abd	61.8 (20.6)	71.6 (17.6)	.077[a]

Table 1: Vaginal resting pressure (VRP), pelvic floor muscle (PFM) strength (cmH2O) and endurance (s), diaphragm (cmH2O), deep (cmH2O) and superficial (Nm) abdominal muscles (abd) strength, among continent and incontinent women. [a]T test for independent variables; [b]Mann-Whitney U test; [*]adjusted to BMI.

Discussion

Regarding PFM variables, no difference was found between the continent and incontinent women. Contrarily, incontinent women have stronger superficial abdominals and diaphragm strength, leading us to suspect that PFM strength should be view in relation to these muscles of the abdominal cavity. As happened in other studies, we found great overlaps on PFM strength and endurance between the continent and SUI women. A recent study found that incontinent athletes had greater PFM strength, and this variable had a positive association with abdominal muscle strength [8]. However, the effect of physical exercise on the pelvic floor remains controversial. Further research is necessary.

References

1. Shaw et al, J Sports Sci, 32:1176–1185, 2014.
2. Shafik et al, Eur J Surg, 163:883-887, 1997.
3. Haylen et al, Int Urogynecol J, 21:5–26, 2010.
4. Avery et al, Neurourol Urodyn, 23:322-330, 2004.
5. Guillem et al, J Electromyogr Kinesiol, 24:986-993, 2014.
6. Ito et al, J Electromyogr Kinesiol, 28:76-81, 2016.
7. ATS/ERS Statement on respiratory muscle testing. Am J Respir Crit Care Med, 166:518-624, 2002.
8. Dos Santos et al, Int Urogynecol J, 30:693-699, 2019.

STIMULATION OF THE FOOT SOLE BY A NOVEL, 3D-PRINTED SHOE TECHNOLOGY – A PRELIMINARY USER STUDY

Daniel Baumgartner (1), Patrick Bischof (1), Bettina Sommer (2), Christoph Bauer (2)

1. Zurich University of Applied Sciences ZHAW, IMES Institute of Mechanical Systems, Switzerland
2. Zurich University of Applied Sciences ZHAW, IPT Institute of Physiotherapy; Switzerland

Introduction

Today's footwear often focuses on shock-absorbing shoe soles to damp impacts on the ground. Consequently, the foot only gets a reduced stimulation input from the ground, because ground unevenness is absorbed by the sole [1].
Some activities in shoe technology focus therefore on so called "minimal shoes" to increase the stimulating effect by the ground. Nevertheless, a tilting (heel gradient) is only partially realised due to the thin sole between foot and ground.
It would be beneficial to have a system which is able to reproduce a comfortable foot bed by simultaneously transferring a micro-stimulating effect to the foot. To have such a shoe available, a solution had to be found for a first user experience study.

Aim of the project

The aim of the project was the development and testing of an ergonomic shoe sole technology to transfer the ground composition through a sole to the foot.

Material & Methods

A) Shoe development
A new technology of stimuli-transmitting shoe sole has been iteratively developed with soft and hard elements integrated in the shoe.
Injection moulding of elastomeric material and 3D-printing (SLA) have been used to manufacture a first series of prototypes. The idea is to transfer the uneven surfaces on the floor through a flexible sole (Figure 1).

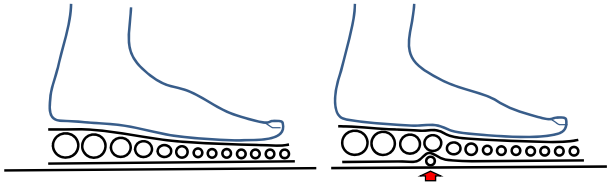

Fig. 1: Technical concept which allows the transfer of uneven surfaces to stimulate the foot mechanically.

B) User Study
User experience was the main focus in the user study, focusing on feedback about walking sensation, comfort, complaints and intensity of sensory transmission by a questionnaire. The study included 20 participants (Ø 64 years) wearing the shoes in daily life (2hrs a day) and 10 participants (Ø 41 years) absolving a parcours (paved, unpaved, nature trails).

Results

A) Shoe sole prototypes
Several iteration steps resulted in a compact design, which may be manufactured in a series production. Spherical balls are printed in form of an interconnected grid, surrounded by a flexible, injection moulded structure.
The foot bed and the sole tilting angle (heel gradient) have been integrated to maintain the ergonomic structure of a shoe.

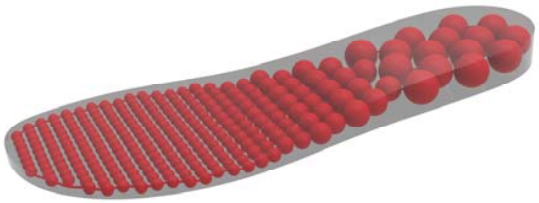

Figure 2: Shoe sole with hard balls (red) integrated into an injection moulded, dense shoe sole (grey).

B) Preliminary user experience study
Comfort & complaints: The new shoe was considered to be "very or rather comfortable" by approx. 85% of the users. Participants perceived the stimuli strongest in the forefoot, where also most of the complaints occurred.
Ground composition: Nature trails seemed more comfortable than hard grounds, even though the opinions about hard grounds diverged. The most uncomfortable walking was on unpaved, downwards grounds.

Discussion & Outlook

A) Shoe development: The shoe technology has been developed to fulfill requirements of an industrialised manufacturing. It seems to be feasible to integrate the currently 3D-printed prototype into a series production.
B) User study: the user study prooved the concept of an increased stimulation on the feet. Nevertheless, aspects with regard to comfort need to be improved.

Acknowledgements

The authors would like to thank Innosuisse for funding this study (LS-28381.1) and for the Industry partner Vadret Schneiter AG for providing the prototypes.

[1] Altman and Davis (2012). Current Sports Medicine, Reports, 11: 244-250

DIABETIC SHOE UPPER PRESSURES: PRELIMINARY APPROACH TO IDENTIFY RELATIVE LEVELS OF COMFORT AND INJURY

Pedro Martins (1), Arcelina Marques (2)

1. CIETI - Centro de Inovação em Engenharia e Tecnologia Industrial, ISEP, 1160308@isep.ipp.pt, Portugal;
2. CIETI - Centro de Inovação em Engenharia e Tecnologia Industrial, ISEP, mmr@isep.ipp.pt, Portugal

Introduction

Diabetic foot is one of the most serious complications affecting the feet of diabetic patients. It is characterized by a progressive loss of protective skin sensitivity and requires an early diagnosis due to the imminent possibility of infection, ulceration, and amputation [1]. Frequently, the anatomical deformation of the foot and the use of misfit shoes compromise the biomechanics of the foot, causing abnormal overload and minor trauma that can precipitate ulceration. The most critical pressure points, located in the plantar and dorsal region of the foot, are already well identified. In this sense, in addition to increased clinical attention, the use of appropriate footwear is also an essential factor in preventing injuries. The shoe must have an internal length between 1 and 2 cm greater than the foot, it must be adapted to the widest part of the foot and the height of the toecap must guarantee sufficient space for the toes. The choice of shoes should be evaluated with the patient standing and preferably at the end of the day when the feet are more likely to be swollen. In more complex cases, the use of custom-made shoes should be advised [2]. This results in evident losses in the patient's ability to move.
The pressures that the shoes impose on the feet are extremely important and, although the plantar pressures are already well studied [3], the pressures involved between the upper of the shoe and the dorsal region of the foot is still a little addressed topic.
In this paper, we propose a preliminary approach to measure dorsal pressures and quantify relative levels of potential injury, to maintain a compromise between the comfort and safety of the diabetic patient's foot.

Methods

Looking for objective evidence that a concrete dorsal pressure threshold will jeopardize the integrity of the foot, our methodology consisted of: recognizing the critical locations of the dorsal region already described in the literature; create a method to locate sensors and measure pressure while walking; define a test procedure; and define groups of trial participants.

Results

In the acquisition of the measured pressure values it is proposed to use circular FSR sensors with an area of approximately 1 to 2 cm^2. In data processing and recording, a microcontroller based on the ATmega328, equipped with a memory card and powered by a battery, will be essential. After identifying the most critical dorsal pressure sites, the location of the FSR sensors and the method of data acquisition and recording were defined (Figure 1). These sensors can be attached to the inner lining of the shoe or sewed on a sock created for this purpose.

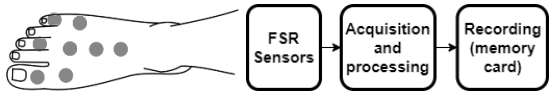

Figure 1: FSR locations and acquisition method.

As shown in Figure 2, for the implementation of a test protocol to identify standards and relative levels of comfort and injury, a group of participants (healthy, without diabetic foot and ages between 20 and 45 years) will be selected who will do a walk with different shoes (more or less tight). At the end they will answer a questionnaire to perception of comfort, whose answers will be analyzed and crossed with the pressure values acquired. It is expected to obtain standards that indicate relative levels of comfort and injury that can later be applied to patients with diabetic foot.



Figure 2: Test protocol and identification of comfort standards and relative injury levels.

Discussion

This method is shown as a practical approach to identify characteristic thresholds of dorsal pressures in the foot associated with different levels of comfort. But it is important to identify whether the pressure that will be considered as the injury threshold is the same for all users. The threshold that puts a given patient at risk may be different from another. However, this approach is essential to obtain more objective and concrete values of dorsal pressures.

References

1. S. Mishra, K. Chhatbar, A. Kashikar, and A. Mehndiratta, "Diabetic foot," *BMJ*, vol. 359, no. SUPP 1, pp. 1–7, 2017.
2. N. Schaper, J. Van Netten, J. Apelqvist, et al., "Practical Guidelines on the prevention and management of diabetic foot disease (IWGDF 2019 update)," *Diabetes Metab Res Rev.*, vol. 36, no. e3266, pp. 1–10, 2020.
3. S. Ahmed, A. Barwick, P. Butterworth, and S. Nancarrow, "Footwear and insole design features that reduce neuropathic plantar forefoot ulcer risk in people with diabetes : a systematic literature review," *J. Foot Ankle Res.*, vol. 13, no. 30, pp. 1–13, 2020.

T-CHAIR - NOVEL THERAPY DEVICE IN NEUROREHABILITATION

Patrick Bischof (1), Michaela Wenger (1), Daniel Baumgartner (1)

1. ZHAW, IMES Institute for Mechanical Systems, Switzerland

Introduction

Per year, 16 million people experience a stroke for the first time, of which 5 million have a limited mobility. Loss of mobility early post stroke is due to an impaired trunk function [1]. Trunk exercises seem to have a beneficial effect on trunk function, standing balance, and mobility [2]. Patients post stroke whose trunk function improves faster start earlier with gait and balance training.
However, safe and resource efficient therapy approaches enabling high intensity training are missing.

Purpose

A robot assisted therapy chair in sitting (T-Chair) that supports trunk stability and control training early post stroke has been developed. The T-Chair is designed to support improving trunk control and stability.
The aim of this study was to assess its usability from a patients' and a physiotherapists' perspective.

Methods

In total fifteen stroke patients with trunk impairments and 11 physiotherapists were recruited. A moving seat to mobilise the pelvis and the lower spine is the core technology of T-chair. The seat describes a physiologic motion pattern to perform stability and balance exercises including Flexion/Extension (+/-10°) and lateral Bending (+/- 11.5°).

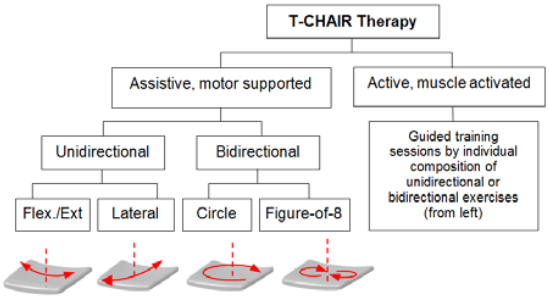

Fig. 1: Variation of therapy sessions with the mobile seat.

The seat may move the patient in an assistive way by motors or by the patients' trunk muscles. The T-chair has been integrated in the patients' therapy program. Each patient performed four individual therapy sessions on the prototype T-Chair under the physiotherapists' supervision. Usability from the patient's perspective was assessed using a diary and a questionnaire; usability from the physiotherapists' perspective with a focus group interview and a questionnaire. The study focused on time expenditure, safety aspects, and unsupervised therapy potential.

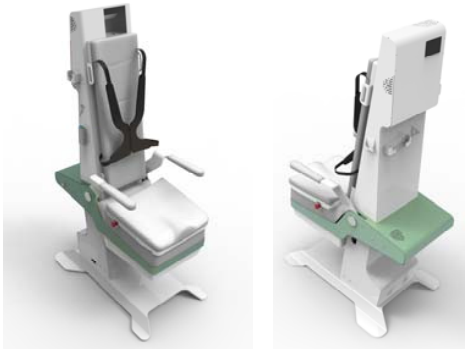

Figure 1: T-CHAIR allowing the seat to swing laterally and in Flex-/Ext direction (isometric views).

Results

64 % of the physiotherapists had a positive view of the novel therapy concept, while 33% considered the current prototype version a useful rehabilitation device. Therapists were recognizing the potential for an unsupervised therapy.

- The T-Chair facilitates proprioception and allows unlimited repetition of movement.
- Physiotherapists recommend integrating computer games into the T-Chair.
- Patients reacted positively to the T-chair and enjoyed training with it, while others found the training intensity too undemanding.

Conclusions

The T-Chair might become an adequate training tool for patients post stroke at an intermediate trunk control level, between exoskeletons and bedside exercises. Improvements in time expenditure, exercise difficulty, safety as well gamification aspects are desired.

Implications

The T-Chair represents a therapeutic device to train trunk control with substantial repetitions early post stroke, and thus helping patients to regain mobility.

References

[1] Verheyden G., Clin Rehabil. 2004 May; Vol. 18(3): 326-34.
[2] Viswaja K., Int J Physiother. Vol 2(6), 925-932, December (2015)

ASSESSING CREDIBILITY OF CT-BASED FINITE ELEMENT MODEL TO PREDICT BONE STRENGTH

Cristina Curreli[1,2], Antonino A. La Mattina[1,2], and Marco Viceconti[1,2]

1. Department of Industrial Engineering, School of Engineering and Architecture, Alma Mater Studiorum - Università di Bologna, Bologna, Italy

Medical Technology Lab, IRCCS Istituto Ortopedico Rizzoli, Bologna, Italy

Introduction

Subject-specific finite element (FE) models derived from computed-tomography (CT) are powerful tools to non-invasively estimate bone strength, and to predict the risk of bone fracture [1]. During the last decades, many different studies demonstrated the possibility to apply this technique in a number of clinical scenarios (e.g. identifying patients who are at high risk of vertebral fracture [2], investigating the likelihood of self-inflicted humeral fracture in infants [3]); however, if such methods are to be used to provide evidences in clinical trials of new bone drugs, a systematic evaluation of model credibility is required, based on accepted verification, validation, and uncertainty quantification (VV&UQ) practices.

The aim of this work is to define a VV&UQ plan that can be submitted as evidence for qualification of the method to a regulatory authority.

Methods

The modelling technology here analyzed and tested through the credibility assessment framework is mainly based on one of the most recent patient specific CT-FE methods used to classify patient under risk of hip fracture [4]. A retrospective validation study demonstrated that, using this technique, the stratification accuracy between fractured and non-fractured patients was higher than 80% [4].

The only technical standard currently available for the assessment of the credibility of predictive models to be used in healthcare is the ASME V&V-40. While this standard specifically aims to models to be used to assess medical devices, it has already been used also to assess models for drugs testing.

According to the V&V-40, the VV&UQ plan requires the following essential elements:

1. Definition of the Context of Use (CoU)
2. Risk analysis and definition of the extent of the VV&UQ assessment
3. Code and Solution verification
4. Technical and clinical validation
5. Applicability assessment

Results

The *CoU* we selected is to use the model to predict the minimum side fall strength (MSS) [4] as a predictive biomarker of the risk of hip fracture, an accepted clinical endpoint to evaluate the efficacy of new bone drugs. Since this primary endpoint requires at least a five years follow-up, some recent clinical trials used changes in bone density as a surrogate endpoint. Our long-term goal is to demonstrate that our model's predictions have a much greater discriminative power than densitometry.

The result of the *Risk analysis* suggests that the risk of obtaining an incorrect prediction from the computational model can be considered medium-high. This drives the selection of all the VV&UQ activities and goals for each credibility factors.

The *Code verification* will be ensured by pursing certification according to the standard EN 62304::2006 +A1:2015 "Medical device software — Software life-cycle processes". Other existing implementations based on the ANSYS solver are already compliant with this standard.

The *Solution verification* will primarily focus on the evaluation of the discretization error, through convergence studies of the mesh refinement and of the fall direction sampling.

The *Technical validation* will be mostly based on a number of studies where we compared the model's predictions with experimental measurements on cadaver femurs, and on the evaluation of the stratification accuracy against two retrospective cohorts.

Sensitivity analysis will be conducted along the lines of [5].

The *Clinical validation* will be conducted by evaluating the discriminatory power of the MSS against that of densitometry, in two group of patients treated with two different bone drugs, over two controls 12 months apart.

Last, the *Applicability Analysis* will be performed by defining the limits of validity of the model with respect to the range of inputs used in the clinical validation.

Discussion and Conclusions

The systematic procedure proposed here provides an overview of all the important steps that are needed to support the credibility assessment of a computational model to be used in drug trials.

This work will provide the basis for a request for Qualification Advice we plan to submit soon to the European Medicine Agency.

References

1. Viceconti M, *et al.* DOI: 10.1007/s11914-018-0438-8.
2. E Dall'Ara, *et al*. DOI: 10.1007/s00198-011-1568-3
3. Altai, Z, *et al.* DOI: 10.1016/j.crad.2019.08.026
4. Altai, Z, *et al.* DOI: 10.1016/j.clinbiomech.2019.06.004
5. Taddei F., *et al.* DOI: 10.1109/TBME.2006.879473

A BIOMECHANICAL APPROACH FOR FRACTURE RISK ASSESSMENT FOLLOWING TUMOR CURETTAGE

Azadeh Ghouchani (1, 2), Gholamreza Rouhi (2), Mohammad. H Ebrahimzadeh (3)

1. Department of Biomedical Engineering, Mashhad Branch, Islamic Azad University, Iran; 2. Faculty of Biomedical Engineering, Amirkabir University of Technology, Iran; 3. Orthopedic Research Center, Mashhad University of Medical Sciences, Iran

Introduction

There is no firm criterion for identifying patients with a bone tumor at high risk of postoperative fracture. Hence, surgeons' recommendation for prophylactic actions is based on pathologic fracture criteria, such as Mirels' or clinical experience, both suffering from poor specificity. Recently, attempts were made on employing more accurate methods, such as Quantitative-CT (QCT)-based finite element models (FEM), to predict bone strength as a key determinant of its fracture risk, but with a focus on the fracture risk of a metastatic bone, and not the post-operative fracture risk [1]. Additionally, such models suffered from low validity and accuracy, due to lack of inclusion of non-linear behavior or non-homogeneous material properties of bone, or mere validation against FEM results [2]. Thus, there exists a great need to present a validated and accurate biomechanical approach to identify patients who are at high fracture risk, following tumor curettage.

Methods

Tumor curettage was mimicked in 7 human distal femoral bones (Fig.1-A), and the contralateral bone of each specimen was kept intact. All the specimens were put in a container of water and QCT scanned along with a calibration phantom, which was used to convert Hounsfield Units to bone ash densities. Then, the specimens were tested under compressive load until they experience failure, to determine the fracture load (F_{Test}). Three-dimensional FEMs of the specimens were created considering non-homogeneous material properties, calibrated by bone ash densities, and based on the non-linear behavior of distal femur [1], which were assigned to each element of the model (Fig.1-B). Loading conditions, mimicking in-vitro tests, were applied and bone strength was calculated (F_{FE}).

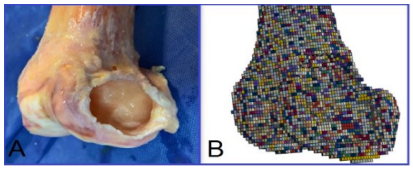

Figure 1: (A) Tumor curettage simulation in human distal femoral bone, and (B) 3D heterogeneous model of the bone with the simulated defect following curettage.

The accuracy and precision of FEMs were evaluated using the method introduced in [2], considering $P<0.05$ to be statistically significant. After validating the FEMs, bone defects, mimicking tumor curettage, with different sizes were created with the scope of determining the critical size of defects, causing considerable reduction of the bone strength as compared to the intact bone.

Results

Results of statistical analyses showed the accuracy and precision of the FEMs, with P-values of 0.474 and 0.396, respectively; which imply that there is no significant difference between F_{Test} and F_{FE}. Regression analyses also showed a good linear relation between F_{Test} and F_{FE} with the slope=1.12 and intercept=0.57kN. It was found that under compressive load, there is a positive correlation in the bone strength reduction with the size of the defect. Nonetheless, this correlation was found to be non-linear, and it was interestingly found that a notable reduction, in the bone strength, was occurred when the defect volume exceeds 65 cm^3, i.e. 38% of the epiphyseal volume (EPV) (Fig. 2). The reduction in bone strength was less than 5% for defects smaller than the critical defect size, i.e. 38% of EPV. On the other hand, for a defect of 44% of EPV, a 30% reduction in bone strength was observed, compared to the intact femur.

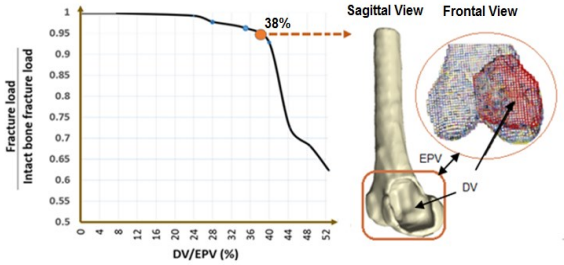

Figure 2: (Left) Fracture load/Intact bone fracture load versus DV/EPV, which shows considerable reduction when DV/EPV exceeds 38%; and (Right) Sagittal and frontal views of the FE model with DV/EPV =38%.

Discussion

QCT-based FEM is a powerful tool in predicting post-operative distal femoral strength. A retrospective study demonstrated a high risk of post-operative fracture for defect sizes larger than 60cm^3 [4], which is in agreement with the results obtained in this study. The approach presented here can be used to derive a biomechanical criterion for post-operative fracture risk in patients with bone tumors.

References

1. Ghouchani, A. et al, Sci Rep, 10, 21319, 2020.
2. Ghouchani, A. et al, J Med Biol Eng, 37: 454-467, 2017.
3. Keyak, J. et al, Clin Orthop Relat Res, 437:219-228, 2005.
4. Hirn, M. et al, Acta Orthop, 80: 4-8, 2009.

CLINICAL VALIDATION FOR REGULATORY QUALIFICATION OF IN SILICO TRIALS METHODOLOGIES

Marco Viceconti (1, 2), Giorgio Davico (1, 2), Cristina Curreli (1, 2), and Antonino La Mattina (1, 2)

(1) Department of Industrial Engineering, Alma Mater Studiorum – University of Bologna
(2) Medical Technology Lab, IRCCS Istituto Ortopedico Rizzoli, Italy

Introduction

Patient-specific, physiology-based predictive models are more and more frequently used as clinical decision-support system. To use such technologies in the clinical practice, they need to receive a marketing authorization from competent regulatory authorities, which will consider it as "software as medical device". Instead, when the models are to be used to evaluate the safety or efficacy of new medical products (in silico trials), the regulatory pathway is less clear. While this is not mandatory, it is convenient, especially for innovative technologies, to pursue the so-called qualification of new methodology: essentially this is a regulatory evaluation of the new methodology; once approved, the methodology can be used to produce evidence in the marketing authorization request of a new medical product, without any further methodological evaluation.
If we now focus on medicinal products, the regulatory philosophy is that no methodology can really be validated only with laboratory tests. Thus, in addition to the so-called technical validation, where you assess the accuracy, precision and robustness of a new methodology through laboratory tests, most regulators expect new methodologies to be used in drug trials, to be extensively validated also in a clinical setting. The logic of clinical validation is quite different from that of a technical validation; thus, it may be worth to present it systematically, using the qualification of the so-called Biomechanical Computed Tomography (BCT), a model-based estimation of the biomechanical strength of a patient's bone.

Construct validity

The clinical validation of a new methodology requires one demonstrates construct validity, predictive capacity, and ability to detect change of the biomarker, in this case an in silico prediction.
If the clinical concept that our model predicts cannot be directly measured, then the first step is to demonstrate that the quantity we predict is a valid *construct* of that clinical concept. For example, if we want to use the femoral BCT to represent the risk of proximal femur fracture (PFF), first we need to demonstrate that BCT correlates with other variables affecting the risk of PFF such as age, or bone density (convergent validity). We also need to demonstrate that the BCT does not correlate with other variables that do not affect the risk of PFF, such as the low-density lipoprotein cholesterol levels (discriminant validity). Another evidence in support of construct validity is that BCT is significantly different between two groups with markedly different risk, such as post-menopausal women and age-matched men (known-group validity).

Predictive capacity

Probably the most important evidence to qualify an in silico trial is the predictive capacity. To demonstrate predictive capacity, we would use the BCT to separate in a cohort a group of patients who just experienced a PFF from those who did not; the area under the ROC curve or relative risk can be used to quantify predictive capacity.

Ability to detect change

In the context of drug assessment, it is essential that a biomarker shows a significant ability to detect the changes the new drug induces. To the purpose, we need to demonstrate that changes in our model's predictions correlate with changes in the clinical quantity of interest (longitudinal validity). For example, we need to show that the change over time of the BCT in a group of osteoporotic patients correlates with the change over time of their risk of PFF. It is also necessary to establish the minimal change in a treatment outcome that would indicate a change in the patient's management, or that an individual patient would identify as important (minimal important difference). But the most important evidence is the *responsiveness*, defined as the ability of the model's prediction to discriminate between the two arms of an interventional randomized clinical trial.

Discussion

The aim of this paper is to provide, using BCT as biomarker of risk of PFF as a guiding example, a gentle introduction to the concept of clinical validation of new methodologies for drug testing. For a more authoritative guide please refer to the official guidelines of the regulatory agencies, e.g. [1, 2].
The philosophical background of this regulatory process is very far from that of the credibility assessment for physics-based predictive models our community is used to. The first submissions for qualification of in silico trials tools will require a considerable effort to realign these two substantially different cultures.

References

1. Qualification Process for Drug Development Tools Guidance for Industry and FDA Staff. FDA-2010-D-0529.
2. Qualification of novel methodologies for medicine development (2014), EMA/CHMP/SAWP/72894/2008.

REPORTING AND STANDARDISATION OF PLATE WORKING LENGTH (BRIDGE SPAN) IN FRACTURE HEALING STUDIES

Mark Heyland (1)*, Gabriele Russow (1,2)*, Luis Becker (1,2), Georg N. Duda (1), Dag Wulsten (1), Katharina Schmidt-Bleek (1), Ricarda Seemann (2), Sven Märdian (2)

*1. Julius Wolff Institut, Charité – Universitätsmedizin, Berlin, Germany; 2. Center for Musculoskeletal Surgery, Charité – Universitätsmedizin, Berlin, Germany. * These authors contributed equally to this work.*

Introduction

Fracture healing is affected by fixation stiffness [1], which can be modulated by choosing an appropriate plate working length (PWL) [2, 3]. To date, the reporting of the mechanical boundary conditions relies on an individual basis [4, 5] and has so far hampered the development of a more harmonised mechanotherapy of fracture fixation. Especially the definition of the essential parameter "PWL" remains heterogeneous. This study aimed first to illustrate the lack of a standardised reporting and definition of PWL, second to highlight the significance of PWL in fracture fixation with relative stability, and third to suggest how to improve the definition and reporting of working length definition in a standardised manner.

Methods

A systematic literature search (www.ncbi.nlm.nih.gov/pubmed, January 2021) was conducted [query: ((("plate" AND ("locking" or "locked")) AND ("tibia" or "tibial" or "femur" or "femoral")) AND ("working" or "bridge" or "bending" or "bridging")] yielding 138 relevant publications (manually identified), which were classified (Tab.1, Fig. 1, A).

Furthermore, a finite element analysis (FEA) examined PWL in plate configurations of long bone fixation with varying screw configurations (Fig.1, B). A cylinder was modelled (ABAQUS 2019, Dassault Systèmes®) to represent a long bone (30mm diameter, 5mm cortical thickness). A 4.5mm locking compression plate (LCP) and matching screws were modelled in titanium. Screw-plate interface was modelled by an isotropic ring structure with elastic properties (Fig. 1, C). Young's modulus of the ring (isotropic, homogeneous) was determined experimentally through comparison of displacement of the screw upon loading (Fig. 1, C). Axial loading was performed (500 N).

Results

The majority (56%) of studies do not report PWL (class A), less than 7% report a mean and variation (class D) or individual case values (class E, Fig.1 A). Our FEA confirms other study results [2,3,5] and supports that PWL is one of the main determinators for interfragmentary movement (IFM) which controls secondary fracture healing (Fig.1 B). When mapping maximum deformation perpendicular to the direction of the load, a point of inflection could be found on the central axis of the screw.

Discussion

Our literature review showed that <50% of the included studies report PWL. Thus, the assessment of the mechanical environment and a profound failure analysis remains impossible. Even if the mean/median of PWL is reported, varying conditions can hardly be evaluated. We suggest defining the PWL as the distance between the central axes of the nearest screws proximal and distal to the fracture/osteotomy. Thereby, comparability of future clinical and biomechanical studies can be achieved. Besides this, reporting of bone-plate distance, fixation implant type and material, and additional fixation (cerclage wires and/or lag/positional screws) should be included in fracture healing studies.

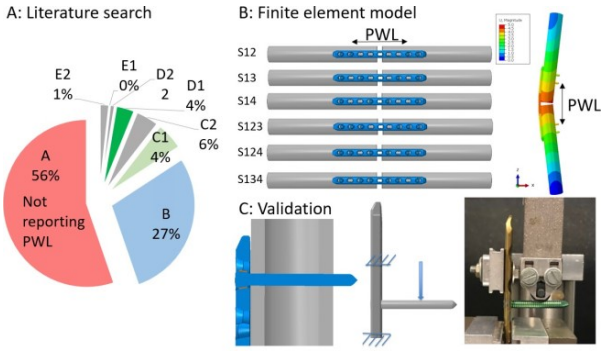

Fig. 1: Reporting of plate working length, PWL (A) does not conform to its biomechanical importance as assessed by finite element analysis, FEA (B). Parameter identification and validation of FEA were performed (C).

CLASS	CATEGORY DESCRIPTION	N= 138
A)	NO value for PWL reported	**77**
B)	any value for PWL reported, e.g. number of empty screw holes	**37**
C)	a quantitative scalar distance, e.g. in mm/cm	
C1)	a clear definition for PWL provided	**6**
C2)	NO clear definition for PWL provided	**8**
D1)	mean + variation reported, a clear definition of PWL	**5**
D2)	mean and variation reported, NO clear definition	**3**
E1)	individual values of PWL for singular cases reported (especially failure cases), clear definition of PWL	**0**
E2)	individual values of PWL for singular cases reported (especially failure cases), NO clear definition of PWL	**2**
STUDY TYPE		
1)	clinical in vivo	**56**
2)	animal in vivo	**10**
3)	experimental in vitro, human cadaver	**23**
4)	experimental in vitro, animal	**8**
5)	experimental in vitro, artificial bone (sawbone)	**31**
6)	numerical study	**10**

Tab. 1: Literature search study classification.

References

1. Epari et al, J Bone Joint Surg Am, 89(7):1575-85, 2007.
2. Heyland et al, Injury, 46 S4:24-32, 2015.
3. Märdian et al, Clin Biomech, 30(4): 391-6, 2015.
4. Grant et al, J Biomech, 48(15): 3989-94, 2015.
5. MacLeod et al, Bone Joint Res, 7(1): 111-20, 2018.

COULD PATIENT-SPECIFIC LOCKING PLATES IMPROVE PRIMARY STABILITY OF PROXIMAL HUMERUS FRACTURE FIXATION?

Jana Felicitas Schader (1, 2), Dominic Mischler (1), Jan Dauwe (1, 3), Boyko Gueorguiev (1), Peter Varga (1)

1. AO Research Institute Davos, Switzerland; 2. Cantonal Hospital Graubuenden, Switzerland; 3. University Hospital Leuven, Belgium

Introduction

Treatment of proximal humerus fractures remains an unresolved clinical problem. State-of-the-art locking plates have high failure rates, ranging up to 36% [1,2]. The potential benefit of surgical over conservative treatment has been critically discussed [3]. A possible reason for this high rate of failures is that generic implants do not accommodate the considerable variability of the clinical cases. In turn, patient-specific fixation designs are becoming increasingly available given recent advances of additive manufacturing and may help to improve stability and reduce failure risk. Validated computer simulations could guide the design of custom implants via in silico optimization of the predicted mechanical performance. This study aimed to investigate via finite element (FE) analysis whether patient-specific locking plates with optimized screw angles could improve fixation stability versus a standard implant.

Methods

Nineteen low-density (73.5–139.5 mg/cm^3) proximal left humeri from elderly donors (83 ± 8.8 years) were scanned with high-resolution CT, virtually osteotomized mimicking an unstable three-part fracture and fixed with the PHILOS plate (DePuy Synthes, Switzerland) using six proximal locking screws. FE models of the constructs were created using a previously developed and validated simulation framework [4] and loaded in three physiological shoulder activities. The orientation of each locking screw was varied in a parametric study based on an established methodology [5] to minimize peri-implant bone strain, being a validated predictor for cyclic cut-out risk [6]. By repeating this process for each specimen individually, subject-specific optimized screw orientation configurations (SSC) were obtained, requiring more than 300 simulations. SSC were compared with the previously published cohort-specific implant design featuring screw orientations optimized for all nineteen humeri (CSC) and the original PHILOS-specific configuration (PSC). The potential benefit of SSC was further evaluated in a two-part fracture model.

Results

The optimal screw orientations in SSC showed a large scatter and were considerably different from both CSC and PSC. Peri-implant bone strain was significantly lower in SSC versus CSC (-6.8 ± 4.0%, p=0.006) and PSC (-25.24% ± 7.93%, p<0.001) (Figure 1). The two-part fracture model showed generally lower strains compared to the three-part fractures, but the relative benefit and statistical significances between the screw orientation configurations remained similar.

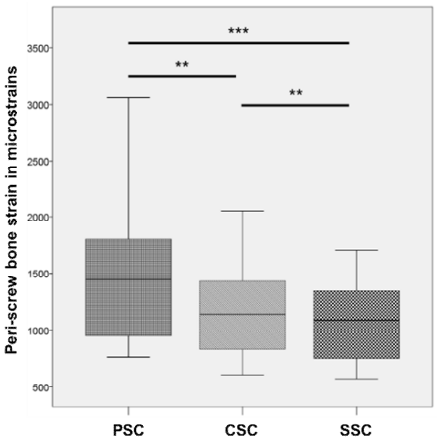

*Figure 1: Subject-specific screw orientations exhibited significantly lower peri-implant bone strain versus the cohort-specific (CSC, **: p<0.01) and PHILOS (PSC, ***: p<0.001) configurations.*

Discussion

This study demonstrates the efficiency and potential of computer simulation approaches in improving implant performance. Although the benefit of SSC versus both CSC and PSC was significant, the magnitude of the benefit was rather modest. Including other design features into the optimization process may provide further improvement, as a clearly superior mechanical fixation performance is required to justify the substantial extra costs and efforts related to the design and manufacturing of custom implants. These computational results require biomechanical and clinical corroboration. The presented simulation methodology and optimization approach may be utilized to optimize screw trajectories for variable-angle plates.

References

1. Kralinger et al., J Bone Joint Surg Am, 96:1026-32, 2014.
2. Panagiotopoulou et al., Injury, 50:2176-96, 2019.
3. Handoll et al., Bone Joint J, 99-B:383-92, 2017.
4. Varga et al., Med Eng Phys, 57:29-39. 2018.
5. Mischler et al., J Orthop Transl, 25:96-104, 2020.
6. Varga et al., J Mech Behav Biomed Mater, 75:68-75, 2017.

Acknowledgements

This study was supported by the AO Foundation via the AOTRAUMA Network (Grant No.: AR2019/07).

RECOVERY OF HYPOXIC REGIONS IN A RAT MODEL OF MICROEMBOLISM

Theodosia Georgakopoulou* (1), Anne-Eva van der Wijk* (1), Erik N.T.P. Bakker (1), Ed van Bavel (1)
On behalf of the INSIST investigators

1. Department of Biomedical Engineering and Physics, Amsterdam University Medical Centres, University of Amsterdam, the Netherlands;

**Theodosia Georgakopoulou and Anne-Eva van der Wijk contributed equally.*

Introduction: The introduction of Endovascular treatment (EVT) has led to a breakthrough for the therapy of acute ischemic stroke. Although in the large majority of cases successful recanalization is attained, only one third of the patients is left with a good clinical outcome [1]. Human MRI studies have shown that during and following EVT, a shower of micro clots releases from the initial thrombus and spreads in the arterial bed distal to the thrombus, possibly causing new ischemic lesions [2]. Several animal models have been developed to map tissue damage caused by micro-embolisms, but quantitative 3D data on their effect on hypoxia and infarction are lacking. Such data are required as part of in silico clinical trials on ischemic stroke treatment.

Methods: In our rat model, micro-embolisms were generated by injection via the left common carotid artery of a mixture of polystyrene fluorescent microspheres (25000 of 15, 5500 of 25, and 625 of 50 micron in diameter). The animals were then sacrificed at three time points: day (D)1 (n=6), 3 (n=6) or 7 (n=7) and the brains were harvested for further immunohistochemical analysis. Hypoxyprobe was used as a marker of hypoxia, lectin as a marker of perfusion, anti-NeuN antibody as a marker of infarct volume. AMIRA and IMARIS software was used for 3D reconstruction of brain tissue and damage, respectively.

Results: Macroscopic observation showed multiple perivascular hemorrhages on the brain surface as well as within the brain parenchyma at all three days. Microscopic analysis revealed multiple areas of hypoxia, but much less infarcts in a 500 µm thick brain volume. On average, 50 hypoxic areas were present at D1 with the majority of the lesions being less than $1.5 \cdot 10^6$ µm^3. Both the amount and total volume (Fig. 1A) of hypoxic areas declined over time. On average, four infarctions were present at D1 and their amount and total volume did not significantly decline over time (Fig. 1B).

Discussion: Micro-embolism induces hypoxia and infarction, yet hypoxic lesions became significantly less pronounced over time, implying the recovery capacity of the brain.

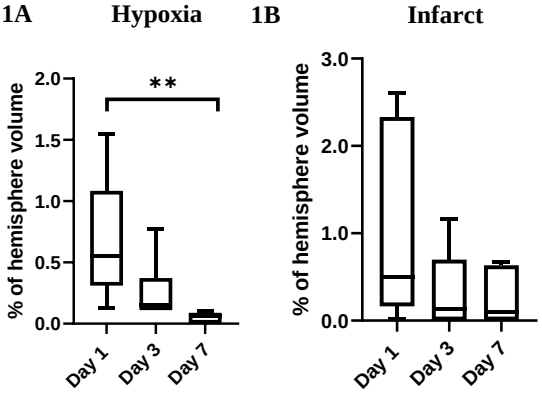

***Figure 1**. Time course of brain damage following micro-embolism in a rat ischemic stroke model. **A:** Total hypoxic volume declines over time. **P<0.05, One-way ANOVA. **B:** Total infarction volume does not change over time.*

References

1. Pereira VM, Yilmaz H, Pellaton A, Slater LA, Krings T, Lovblad KO. Current status of mechanical thrombectomy for acute stroke treatment. Journal of neuroradiology Journal de neuroradiologie. 2015;42(1):12-20.
2. Zhu L, Wintermark M, Saloner D, Fandel M, Pan XM, Rapp JH. The distribution and size of ischemic lesions after carotid artery angioplasty and stenting: evidence for microembolization to terminal arteries. Journal of vascular surgery. 2011;53(4):971-5; discussion 5-6.

Acknowledgements

This work is supported by grant 777072 from the European Union's Horizon 2020 research and innovation program.

FLEX-EXTENSION ANGLE CHANGES DURING GAIT MIGHT INCREASE KNEE WEAR IN PATIENTS WITH OSTEOARTHRITIS

Ruiz Wills C.[1], Tassani S.[1], Tío L.[2], Monfort J.[2,3], Monllau JC. [2,4], Gonzalez Ballester MA.[1,5], Noailly J.[1]

1. BCN MedTech, Universitat Pompeu Fabra, Spain; 2. IMIM, Spain; 3. Rheumatology service, Hospital del Mar, Spain; 4. Orthopaedic Surgery and Traumatology Service, Hospital del Mar, Spain; 5. ICREA, Spain

Introduction

Knee OA represents a tremendous burden for both patients and society [1]. Its prevalence increases with age, affecting seriously the quality of life of the patients, and OA is highly multifactorial, which hinders adequate prevention. In the last years, finite element (FE) models have risen as a tool to explore OA at the tissue level in proper organ contexts. FE studies focus on contact pressure when the knee is in full extension. However, the effect patient gait style, defined by flex-extension angle on cartilage composition remains unclear. Hence, the aim of this study is to explore specific relationships between gait descriptors of OA subjects, and water content variations and contact pressure in knee cartilage.

Material and methods

Gait analyses were performed for 10 OA subjects (KL grade 2-3), using 8 cameras Smart-DX 700, 1.5 Mpixels 250 fps and 2 force plates P-6000, 500 Hz sampling (BTS, Milan, Italy), and the Helen Hayes marker protocol with medial markers [2]. Gait flexion-extension angle and load at the knee and weight acceptance times were used as inputs for simulations with a FE model adapted from the OpenKnee [3]. Composition-based poromechanical tissue models were used for cartilage and menisci, and rebar elements simulated collagen fibre reinforcements (Fig.1) [4]. Ligaments were modelled as fibre-reinforced incompressible materials and femur and tibia as rigid bodies. The tissue initial composition parameters were generic for all subject [4].

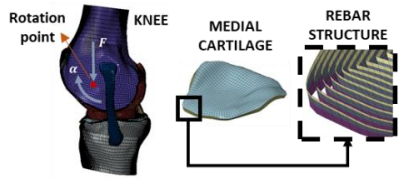

Figure 1: 3D knee FE model with depth-dependent fibre reinforcement of cartilage layers.

The knee forces and rotations determined in each patient were applied on the rotation point of the model according to their corresponding weight acceptance times, leading to 10 simulations with patient-specific (PS) knee joint loads and rotations. The bottom of the tibia was fixed. The influences of PS load and rotations on the water contents and contact pressures of the lateral and medial tibial plateau cartilage were analysed.

Results

No relationship was found between the force, time and rotation and the water content (Fig.2). In contrast, the rotations influenced the contact pressure in both medial and lateral cartilage. The pressure decreased in the medial side and increased in the lateral side with significantly high correlation coefficients (Fig.3).

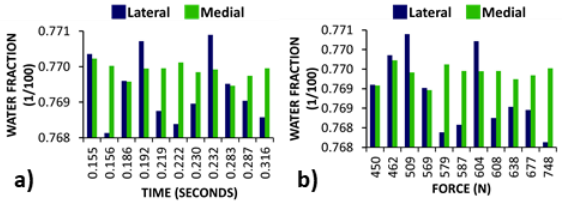

Figure 2: Lateral and medial water content vs a) time, and b) force.

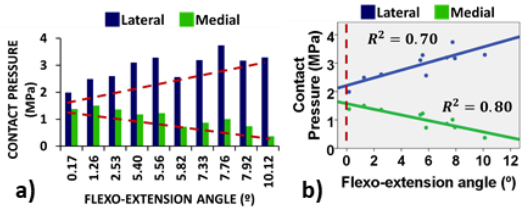

Figure 3.a) Contact pressure vs rotation angle b) Linear regression for contact pressure and rotation angle.

Discussion

The dot line in Fig. 3b represent the 0 flex-extension angle, commonly used in the literature to define PS boundary loads on knee FE models [5]. According to other Authors [6], the contact pressure was higher in the lateral compartment, with pressure values around 2 and 1.5 MPa in the lateral and medial compartments, respectively. However, our results further show that when the PS flex-extension angle increases, pressure levels decrease in the lateral cartilage, whereas they increase in the medial cartilage. This result suggest that lateral side is most affected, in contrast to evidence that point the medial side as most damaged. However, medial load scenario might trigger cell responses that could disintegrate cartilage. Overall, the implemented couplings can be used to explore links between knee joint biomechanics and OA.

References

1. Hiligsmann M et al, Medicographia, 35:197-202,2013.
2. R.B. Davis, Hum. Mov. Sci. 10 575–587, 1991.
3. Erdemir. A, J Knee Surg 29(2):107-116, 2016.
4. Parraga Quiroga J.M. et al, J Biomech, 48(8):1371-6,2015.
5. Shriram D. et al, Sci Rep 7:1-11,2017.
6. Łuczkiewicz P. et al, Plos ONE 11:1-13,2016.

Acknowledgements

Funds from Spanish Government (HOLOA-DPI2016-80283-C2-1/2-R, RYC-2015-18888) are acknowledged.

RAPID MODELING: A SURGICAL PROOF-OF-CONCEPT EXPLAINED BY HEMODYNAMICS MODELING

Nicolas Golse (1,2,3), Florian Joly (3), Quentin Nicolas (3), Eric Vibert (1,2), Pal Dag Line (4,5), Irene Vignon Clementel (3)

1. Paul-Brousse Hospital, AP-HP, France; 2. INSERM, France; 3. Inria, France; 4. Oslo University Hospital, Norway; 5. University of Oslo, Norway.

Background

The RAPID (Resection And Partial Liver Segment 2/3 Transplantation with Delayed total hepatectomy) concept is an innovative surgical procedure that was recently proposed to increase the availability of grafts (transplantable organs) for patients with unresectable metastases (1). The RAPID technique (Fig.1) includes total hepatectomy (Hx, liver resection) in two steps. First, partial Hx is performed and the recipient receives a small partial liver. Then, portal flow, the main input flow to the liver, is diverted to the graft to facilitate its fast regeneration. However, to avoid graft portal hyperperfusion or barotrauma, portal vein (PV) pressure monitoring is required (2). As soon as the graft reaches the target volume, the second stage resection is performed, ending the native diseased liver removal.
For such complex and innovative procedures, numerically simulating hemodynamics in RAPID patients would be useful for surgical planning (3).

Methods

Recently, our team performed hemodynamic 0D modeling to simulate major Hx in pigs (4) and understand disease development in cirrhotic rats (5). To the aim of tailoring the RAPID procedure, we adapted the 0D model in this setting to assess its clinical applicability.
The modified 0D model was retrospectively tested on 3 patients. We compared our estimated PV pressures and portocaval gradients to those intraoperatively measured, as indication to modulate portal flow relies on these measures.

Results

Portal vein pressures measured at the end of the first stage in patients 1, 2 and 3 were respectively of 14, 16 and 12 mmHg while the simulated pressures were of 13.1, 14.8 and 11.5 mmHg. Portocaval gradients measured after right PV clamping in the 3 patients were respectively of 10, 11 and 7 mmHg while the simulated gradients were of 9.9, 11.6 and 8.3 mmHg. Spearman correlation for the 12 paired values was high (r coefficient =0.94, p=0.02).
In order to anticipate the minimal graft weight that should be chosen to avoid the need for portal flow modulation (according to fixed maximal pressure or gradient), we virtually changed the graft weight of each patient. The minimal graft weight required to avoid portal hypertension with different thresholds proposed for PV pressure and portocaval gradients was below the real graft weight in all cases, except for the most restrictive portocaval gradient threshold: patient 1 was borderline, while patient 2 real size was too low. This result highlights the need for a consensus in appropriate thresholds.

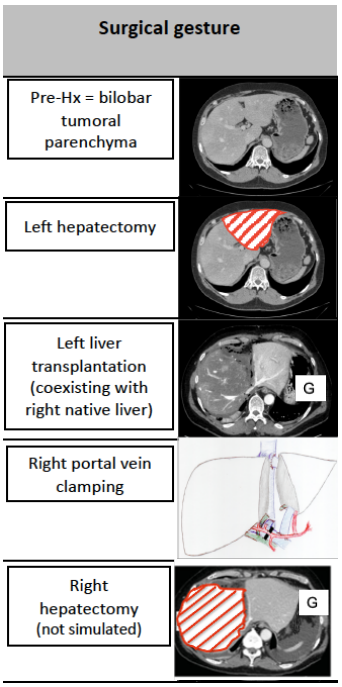

Figure 1: Different steps of the RAPID procedure. The red part corresponds to the liver piece which is removed during partial Hx. G indicates the graft.

Conclusions

Although more work is warranted to validate it on a larger cohort, as recently done focusing on major Hx on 47 patients (6), this promising report demonstrates that 0D simulation could be a useful tool to evaluate this new surgical procedure and how to tailor it in the future.

References

1. Line P-D et al, Ann Surg, 262(1):e5–9, 2015.
2. Yagi S et al, Transplantation, 81(3):373–8, 2006.
3. Golse N et al, Clinical Biomech, 73:95-200, 2020.
4. Audebert C et al, J Biomech, 50:202-208, 2017.
5. Audebert C et al, IEEE Trans Biomed Eng, 65(11), 2450-58, 2018.
6. Golse N et al, J Hepatol, online 2020

Acknowledgements

This work was supported by an Inria-APHP fellowship.

MAINTAINING BONE HEALTH IN THE LUMBAR SPINE: ROUTINE ACTIVITIES ALONE ARE NOT ENOUGH.

Clément D Favier (1), Alison H McGregor (2), Andrew TM Phillips (1)

1. Department of Civil and Environmental Engineering, Imperial College London, United Kingdom;
2. Department of Surgery and Cancer, Imperial College London, United Kingdom

Introduction

To maintain a healthy musculoskeletal (MSK) condition, public health organizations recommend a combination of routine activities such as walking or cycling, and regular demanding physical activities such as heavy gardening or carrying heavy shopping. With the COVID-19 pandemic, self-isolation restrictions make these guidelines difficult to follow [1]. As bone adapts its structure to withstand the mechanical loads it is subjected to [2], the current global situation is particularly problematic for maintaining bone health in areas at risk of bone loss such as the lumbar spine. A multiscale simulation pipeline combining MSK and structural finite element (FE) modelling coupled with an optimisation algorithm was developed to investigate how the lumbar bone structures adapt to their mechanical environment and identify which activities are influential in maintaining lumbar vertebral health.

Methods

For each lumbar vertebra, a physiological loading envelope consisting of muscle and joint reaction forces is obtained from MSK simulations for a range of physical activities representative of a healthy lifestyle using a subject-specific MSK model of the lumbar spine and lower limbs [3]. Activities of interest include spine movements restricted to each anatomical plane, locomotion activities (walking, sit-to-stand and stand-to-sit, stair ascent and descent) and spine-focused more demanding activities involving twisting and lifting tasks. The obtained load cases are used as loading conditions for the structural adaptation of base FE models of the lumbar vertebrae. The initial structural mesh of the base models consists of a randomized network of truss element (radius=0.1mm) representing trabecular bone and shell elements (thickness=0.1mm) representing the cortex. All elements are assigned linear isotropic material properties (E=18GPa, ν=0.3). An iterative strain-driven adaptation algorithm [4] is used to optimize the shell thicknesses and truss radii until they withstand the loading conditions. All models and simulations are based on activities and MRI scans recorded on the same healthy participant to ensure consistency of the modelling framework. The converged structural FE models allow direct visual observation of the predicted cortical and trabecular bone architecture subject to a loading scenario representative of a healthy lifestyle. A sedentary scenario was also investigated, with load cases corresponding to the more demanding activities removed from the loading envelope.

Results

The structural FE models of the lumbar vertebrae adapted to the healthy scenario show a cortical and a trabecular architecture similar to observations made in the literature [5]. For trabecular trusses, a difference can be made between the primary structure (radius>0.1mm) and the secondary structure (radius=0.1mm). Clear trabecular trajectories resisting vertical compression in the vertebral bodies can be seen in the primary structure (Figure 1A). Trusses of the secondary structure appear to give a base stiffness to the bone in the transverse plane. Areas at risk of bone degradation with a sedentary behaviour are located in the anterior part of the vertebral bodies and the spinous processes (Figure 1B).

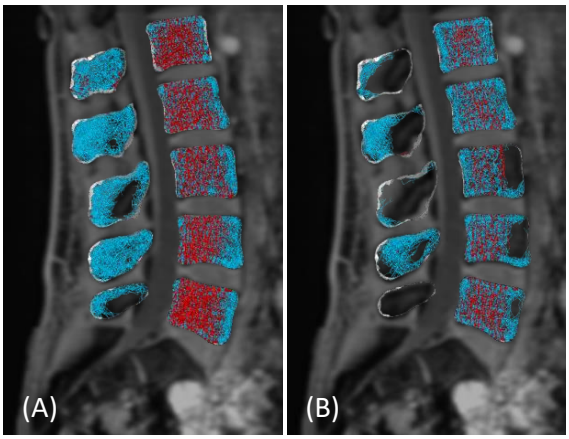

Figure 1: mid-sagittal slices for the converged models adapted to the healthy (A) and sedentary (B) scenarios. Cortical shell elements are in grey. Trabecular truss elements of the primary and secondary structures are in red and blue respectively.

Discussion

The developed simulation pipeline is a computationally efficient tool for predicting areas at risk of bone degeneration under a particular loading envelope. This study suggests that demanding activities involving large spine movements and lifting tasks are necessary to maintain lumbar spine bone health. In the current pandemic situation where self-isolation becomes the norm, such movements should be practiced regularly.

References

1. Narici et al., Eur J Sport Sci, 1-22, 2020.
2. Frost, The Anat Record, 275A:1081-1101, 2003.
3. Favier et al., Comp Meth Biomec, Under Review, 2021.
4. Phillips, Eng Comp Mech, 165(2):147-154, 2012.
5. Gallois et al., Revue Chirurgie, 63:687-708, 1925.

DEVELOPMENT OF A LOW DIMENSIONAL PARAMETRIC MODEL OF HIGH-FIDELITY VIRTUAL INTRA-ARTERIAL THROMBECTOMY

Sara Bridio (1), Giulia Luraghi (1), Mattia Belloni (1), Alberto García-González (2), Sanjay Pant (3), Francesco Migliavacca (1), José Félix Rodriguez Matas (1), on behalf of the INSIST investigators (4)

1. Department of Chemistry, Materials and Chemical Engineering "Giulio Natta", Politecnico di Milano, Italy; 2. E.T.S. de Ingeniería de Caminos, Universitat Politècnica de Catalunya-BarcelonaTech, Barcelona, Spain; 3. College of Engineering, Swansea University, Wales, UK; 4. www.insist-h2020.eu

Introduction

Intra-arterial thrombectomy (IAT) is a minimally invasive mechanical treatment for acute ischemic stroke (AIS) where a stent-retriever is navigated to the occluded artery through a micro-catheter, entraps the blood clot (thrombus) and is retrieved out of the patient. The recanalization fails if the stent loses the clot inside the vessel or if high stress/strain in the clot causes its fragmentation, leading to embolization. In this work, a low dimensional parametric surrogate model, based on the finite-element (FE) simulations of IAT [1], is developed, allowing to substitute FE simulations in predicting the stress and strain state of the thrombus during the IAT procedure.

Methods

The FE model of the IAT procedure (Fig.1a) is made of a tapered vessel, a blood clot and a Trevo ProVue (Stryker, USA) stent-retriever. The model has 5 independent parameters (blue text in Fig.1a) varying in ranges determined on the basis of literature data [2, 3]. A design of experiment was conducted: 50 combinations of the parameters were uniformly sampled and used to run 50 simulations of IAT with the FE solver LS-DYNA (ANSYS, USA) as described in [1] (Fig.1b). The evolution of the maximum first-principal (Max1P) strain inside the thrombus is extracted during the procedure as output of interest, obtaining a total of 73 values per simulation. Thus, an initial training set of 73x50 parametric simulations was used. A Principal Component Analysis was carried out to reduce the dimensionality of the system to the first 15 eigenvectors (accounting for the 92% of the manifold information). Next, 15 independent Gaussian Process surrogate models were built to correlate each of the 15 components with the corresponding 5 input parameters.

Results

The predictive ability of the developed surrogate model was tested with 10 additional FE simulations of the IAT procedure. For 7 cases the model predicted the strain curve with less than 2% error (normalized Euclidean distance) with respect to the FE simulation strain curve (Fig.2). In 2 cases the prediction was suboptimal, with ~6% error, while in 1 case the prediction had ~18% error. The proposed model provides instantaneous predictions for the strain curve, while each FE simulation runs in ~40 hours on 20 CPUs of an Intel Xeon64 with 120 GB of RAM.

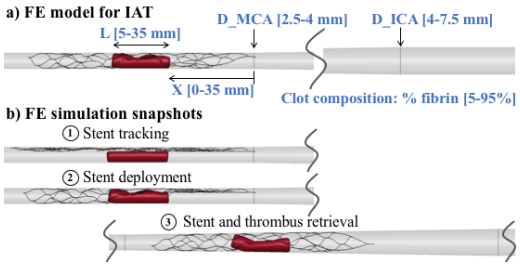

Figure 1: a) FE model of IAT procedure and ranges of the 5 parameters (MCA: middle cerebral artery, ICA: internal carotid artery); b) FE simulation of IAT.

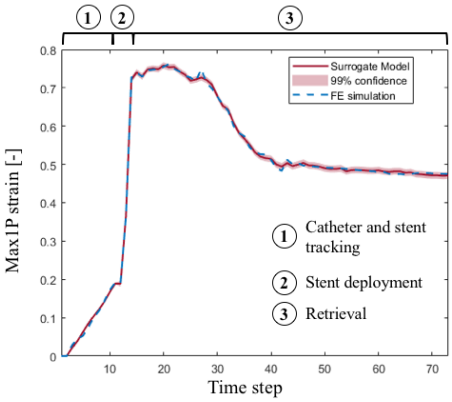

Figure 2: Max1P strain curves FE vs. surrogate model.

Discussion

The developed low dimensional surrogate model based on the FE simulations of IAT was able to predict the evolution of Max1P strain in the thrombus during the procedure. This proved the feasibility of these type of low dimensional models to evaluate the grip of the stent on the clot or to provide data for studies on the mechanisms of clot fragmentation. Reliable surrogate models can also be useful for running *in silico* clinical trials for AIS treatments, where the procedure outcome must be assessed on a big volume of virtual patients.

References

1. G. Luraghi et al, Interface Focus, 11:20190123, 2021.
2. N. Boodt et al, Stroke, 51:1727-1735, 2020.
3. A.T. Rai et al, J NeuroIntervent Surg, 5:371-375, 2013.

Acknowledgements

This project has received funding from the European Union's Horizon 2020 research and innovation programme under grant agreement No 777072 (www.insist-h2020.eu, "In silico clinical trials for treatment of acute ischemic stroke").

A FINITE ELEMENT MODELLING FRAMEWORK TO PREDICT SPRING ASSISTED POSTERIOR VAULT EXPANSION OUTCOMES

L. Deliège[1,2], K. Ramdat Misier[1,2], S. Bozkurt[1,2], W. Breakey[2], G. James[2], J. Ong[2], D. Dunaway[2], N U O. Jeelani[2], S. Schievano[1,2], A. Borghi[1,2].

[1] University College London, UK, [2] Great Ormond Street Hospital, London, UK

Introduction

Spring Assisted Posterior Vault Expansions (SAPVE) is a surgical procedure adopted in Great Ormond Street Hospital (GOSH) for reshaping and enlarging the calvarium of patients affected by syndromic craniosynostosis (SC – premature suture fusion causing abnormal skull growth [1]). In this procedure a surgical bony cut is performed on the skull and elastic distractors (Fig. 1) are inserted to dynamically reshape the skull and increase the intracranial volume (ICV). The outcome is uncertain due to the complexity of the procedure and the lack of knowledge of the interaction between spring and skull. Finite Element (FE) modelling has proved suitable to accurately predict the outcome of spring expansion in other populations [2,3]. We developed, tested and validated a three-dimensional FE simulation platform to predict SAPVE outcomes, using information retrievable from Computed Tomography (CT) scans.

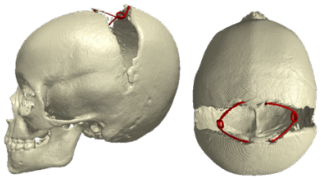

Figure 1: Post-operative CT (Side view and top view) 3D reconstruction of a representative SAPVE patient (spring distractors are shown in red).

Method

Retrospective spring expansion measurements (n=80) relative to a population of 50 patients (age at surgery = 2.1 ± 1.6 years) were used to tune a skull viscoelastic model for SC patients. Data relative to fourteen patients who underwent SAPVE in GOSH (age at surgery= 2.0 ± 1.7 years), having preoperative CT (44 ± 60 days before surgery) and postoperative CT (147 ± 144 days after surgery) were collected and processed to create 3D models. Osteotomy dimensions, spring models and location were recorded from postoperative CT scans and notes (Fig.1). Surgical cuts were replicated and the spring expansion was simulated in ANSYS 2019 (Canonsburg, Pennsylvania, US). For each patient, the predicted postoperative skull shape was retrieved and compared with the respective postoperative 3D model. Predicted and postoperative ICV (ICV_{FE}, ICV_{CT}) were extracted and compared.

Results

Material model optimization showed that the relaxation time of the SC calvarial bone is around 20 times larger than previously reported for non-syndromic craniosynostosis patients [3]. The comparison of the sagittal cross sections of the simulated end-of-expansion calvaria and the postoperative skull shapes extracted from CT images showed a good shape matching for the whole population (Fig.2). The average postoperative ICV recorded was 1454 ml ± 230 ml and the simulated model yielded comparable values with an average of 1400 ml ± 240 ml ($R^2 = 0.92$, $p<0.0001$ - Fig.3).

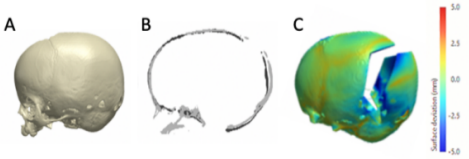

Figure 2: (A) Pre-operative 3D model for a selected patient. (B) Comparison of sagittal plane cut between postoperative CT (light grey) and simulated expansion model (dark grey). (C) Surface deviation between the simulated FE model and the post-operative skull model reconstructed from CT image.

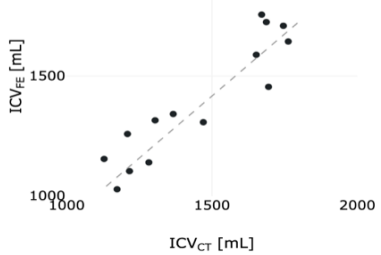

Figure 3: Comparison between post-operative ICV_{CT} and ICV_{FE} ($R^2 = 0.92$, $p <0.0001$).

Discussion

This work shows that our FE model can reliably predict the effect of spring insertion on SC patients. Further developments will investigate the modelling of crack propagation allowing an even more accurate prediction of the calvarial expansion. This modelling framework is currently being tested as a preoperative planning tool.

References

1. Hoey et al, Craniosynostosis. Eplasty, 12, ic2, 2012
2. Borghi et al, Spring assisted cranioplasty: a patient specific computational model. Med Eng Phys 53:58–65, 2018
3. Borghi et al, A population-specific material model for sagittal craniosynostosis to predict surgical shape outcomes. Biomech Model Mechanobiol 19: 1319–1329, 2020

A RADIATION FREE NUMERICAL MODELLING FRAMEWORK TO PREDICT SPRING ASSISTED CRANIOPLASTY OUTCOME

Begona Garate Andikoetxea (1), Sara Ajami (1,2), Eimer O'Sullivan (1,2) Naiara Rodriguez-Florez (3,4), N U Owase Jeelani (2), David Dunaway (2), Silvia Schievano (1,2), Alessandro Borghi (1,2)

1. University College London, United Kingdom; 2. Great Ormond Street Hospital, London, United Kingdom; 3. Universidad de Navarra, Spain; 4. Ikerbasque, Spain

Introduction

Sagittal Craniosynostosis (SC) is a congenital craniofacial malformation, which involves premature closure of the sagittal suture, leading to restricted brain growth and aesthetic problems. Spring-Assisted Cranioplasty (SAC) is an established method for treating SC in young children (figure 1). Our group showed that surgical outcomes can be predicted using a numerical model. However, our method relies on the availability of CT scans, which is not routinely performed. We hereby investigated a method for creating a simplified numerical model for predicting the SAC outcomes, which only relies on the availability of head surface details, retrievable from radiation-free 3D scans.



Figure 1: Sample of cranioplasty spring (left); 3D reconstruction of a patient skull after SAC (right).

Methods

Eight SAC patients with preoperative CT scans were retrospectively recruited. Information on osteotomy locations, spring model and post-operative spring opening were recorded in theatre. Each patient received a preoperative 3D scan (Rodin4D®). For each patient, two models were created: i) full anatomy, FA; and ii) 3D scan, 3DS. In the FA model (figure 2A), calvarium and sutures were extracted from 3D scan using automatic and manual segmentation implemented in ScanIP (Simpleware). The head scalp and skull thickness were extracted for each patient. Averaged values were used to produce the 3DS model (figure 2B), where the preoperative 3D scan head model was offset to produce a simplified calvarium model. Each model was imported into ANSYS and spring cranioplasty was simulated [1]. Spring openings (OP) were retrieved and averaged for each model (OP_{FA}, OP_{3DS}), and compared with post-operative on-table measurements (OP_M). For each model, simulated post-operative occipitofrontal diameter (OFD, maximum anterior-posterior dimension) and biparietal diameter (BPD, maximum lateral dimension) were extracted and cranial index (CI - defined as BPD/OFD) was calculated.

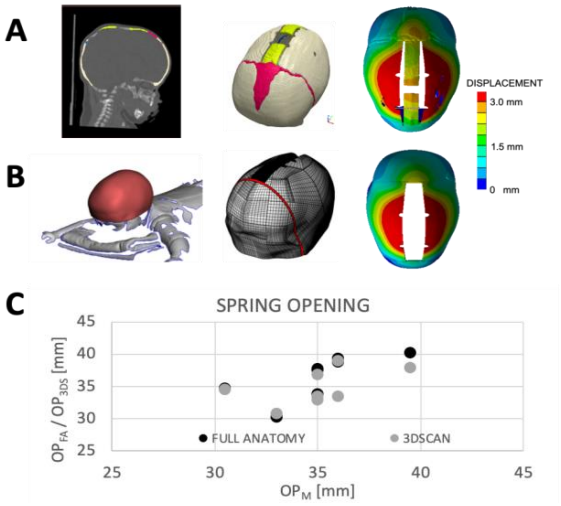

Figure 2: Image processing (left), FE model (centre) and simulation of spring expansion (right) for a patient in the FA (A) and 3DS (B) groups; comparison of spring expansion prediction in the two groups (C).

Results

The patient age was 5.1 ± 0.4 months at the time of procedure. Average spring opening measured in theatre was OP_M = 35.0 ± 2.6 mm. Simulations resulted in spring expansions of OP_{FA} = 36.5 ± 3.4 mm and OP_{3DS} = 34.8 ± 2.8 mm for the FA and 3DS models respectively (figure 2C). Predicted post-operative CI was quantified in both groups: CI_{FA} = 72.2% ± 5.7% while CI_{3DS} = 73.4% ± 3.2%.

Discussion

Finite element modelling is a suitable technique for predicting the outcome of SAC. This work shows that a simplified model created from the head surface shape using averaged skull and scalp thickness yields an average outcome prediction error of 6.9% of the measured values. Further modelling refinements will allow the use of this predictive tool during preoperative planning.

Acknowledgements

This work was funded by the Great Ormond Street Hospital Charity Clinical Research Starter Grant (award number 17DD46).

References

1. Borghi A et al, Med Eng and Phys, 53: 58-65, 2018.

TOWARDS IN SILICO PHASE III CLINICAL TRIALS FOR OSTEOPOROSIS DRUGS: COHORT EXPANSION WITH ANATOMIC STATISTICAL ATLAS

Antonino A. La Mattina (1,2), Mark Taylor (3), Fabio Baruffaldi (2), Marco Viceconti (1,2)

1. *Department of Industrial Engineering, Alma Mater Studiorum – University of Bologna, Italy*
2. *Medical Technology Lab, IRCCS Istituto Ortopedico Rizzoli, Bologna, Italy*
3. *Medical Device Research Institute, Flinders University, Adelaide, Australia*

Introduction

Osteoporosis is and will be an ever-growing burden for western societies, with a great and steadily increasing fraction of elder population [1]. This urgent health need conflicts with the drug slow development cycle, which has to ensure new drug safety and efficacy. In particular, the last phase of clinical trials (phase III) requires thousands of patients to be followed-up for a few years [2].

To reduce time and costs, often a surrogate fracture risk predictor (namely, areal bone mineral density measured with dual-energy X-ray absorptiometry (DEXA)) is used instead of the population measured fracture rate along 5-10 years.

However, patient-specific CT-informed finite-element (CT-FE) models have been demonstrated to have a better stratification accuracy between fractured and non-fractured patients with respect to DEXA, with an area under the ROC curve of 0.85 vs 0.75, respectively [3]. The introduction of FE modelling as a fracture risk predictor, if validated, would allow a reduction of the enrolled patients and/or the follow-up period, with consequent time-to-market and cost reduction.

As a step towards in silico augmented clinical trial [5], the aim of this work is to expand a physical cohort with derived synthetic patients in order to create a population sample suitable for phase III clinical trial simulation.

Methods

A virtual cohort of over 1000 synthetic patient CT-FE proximal femur models was stochastically generated with active shape and appearance modelling based on principal component analysis [4] of 94 pair-matched (47 fractured and 47 non-fractured) women CT-FE models.

A series of non-linear boundary conditions simulating side-fall in different directions was simulated using ANSYS, and a multiscale stochastic approach was used to estimate patient proximal femur fracture risk [3]. Two fracture risk estimators were considered, namely: Minimum Side-fall Failure Load (MSFL), and Absolute Risk of Fracture at time 0 (ARF0).

The synthetic and physical population results were fitted with a 2-component gaussian mixture model to evaluate the population bimodal composition.

Receiver Operating Characteristic (ROC) curves were used to identify the best thresholds to discriminate between fractured and non-fractured populations in the physical cohort, and the same threshold were then applied to the synthetic population.

Results

The synthetic cohort can be described with a bimodal gaussian distribution, as well as the physical cohort. In particular, the non-fractured gaussian components of the two populations are not statistically different (about (2000 ± 500) N and (31 ± 15)% for MSFL and ARF0, respectively), while the fractured component of the synthetic population has a higher fracture risk with respect to the physical population ((1060 ± 400) N vs (1370 ± 310) N, and (70 ± 16)% vs (60 ±13)%).

However, by using the optimal thresholds calculated for the physical population (1560 N for MSFL, and 45% for ARF0), the number of synthetic patients classified as fractured and non-fractured is approximately the same (51.5% population is classified as fractured by using MSFL criterion, 57.1% by using ARF0).

Discussion and Conclusions

The synthetic cohort retained several biomechanical characteristics of the physical cohort, even when employed in non-linear mechanical models. The increased fracture risk of some synthetic patients could be ascribed to osteopenic and osteoporotic patient overrepresentation in the starting physical cohort (T-score -1.37 ± 1.24, range -4.2 to 1.4).

Thus, a physical cohort can be used to train an anatomic statistical atlas to generate synthetic patients with known biomechanical characteristics (BMC, femur biomechanical length, height, weight). If validated, such cohort expansion can be leveraged in the future to reduce the number of participants to enrol in a phase III clinical trial to obtain the desired significance level.

References

1. WHO, Prevention and management of osteoporosis: report of a WHO scientific group, 2003.
2. Van Norman, J Am Coll Cardiol Basic Trans Science, 1: 399–412, 2016.
3. Bhattacharya et al, Biomech Model Mechanobiol, 18:301–318, 2019.
4. Bryan et al, J Biomech, 45:1952–1958, 2012.
5. Pappalardo et al, Brief Bioinform, 20:1699–1708, 2019.

Acknowledgements

This work was supported by grant CompBioMed2 (H2020, number 823712) from the European Commission.

3D MEASUREMENT OF TROCHANTERIC SOFT-TISSUES THICKNESS IMPROVES HIP FRACTURE RISK CLASSIFICATION ACCURACY

Alessandra Aldieri (1), Mara Terzini (1), Alberto L. Audenino (1), Margaret Paggiosi (2), Richard Eastell (2), Pinaki Bhattacharya (3)

1. Polito^{BIO}Med Lab, Department of Mechanical and Aerospace Engineering, Politecnico di Torino, Torino, Italy; 2. Department of Oncology and Metabolism and INSIGNEO Institute for in silico Medicine, University of Sheffield, UK; 3. Department of Mechanical Engineering and INSIGNEO Institute for in silico Medicine, University of Sheffield, UK

Introduction

The majority of osteoporotic hip fractures result from a fall to the side. Hence, fall impact attenuation forces due to passive Soft-Tissues (ST) surrounding the trochanter influence fracture risk. ST-induced impact force attenuation (η_{ST}) can be assessed from ST Thickness (STT) [1], where STT at the greater trochanter can be estimated from the subject's Body-Mass Index (BMI) [2]. A recent multiscale model [3] predicted the current absolute risk of hip fracture (or ARF0) adopting an orientation-independent η_{ST}, estimated using BMI, for all considered impact orientations. This model – henceforth ARF0$_{STT0\text{-}BMI}$– classified hip fracture status in a British postmenopausal cohort with high accuracy (AUC=0.85), considering that ignoring the effect of ST-induced attenuation (i.e. $\eta_{ST} = 0$) in the same model reduced AUC to 0.75. The present study investigates the relative improvement in fracture classification accuracy, with respect to ARF0$_{STT0\text{-}BMI}$, when subject- and orientation-specific STT is included.

Methods

A previously reported cohort comprising 47 fracture and 47 control postmenopausal British women was analysed [3]. Unlike the orientation-independent η_{ST} defined in [3], computed using STT(BMI), models developed in this study adopted a modified definition of η_{ST} dependent on impact orientation (α,β) given by

$$\eta_{ST}(\alpha,\beta) = 0.0986 \cdot \mathrm{STT}(\alpha,\beta),$$

but were otherwise identical to the model in [3]. Two different approaches were used to estimate STT(α,β), leading to as many ARF0 models. In the ARF0$_{STT\text{-}CT}$ model, the pelvic outer surface, i.e. the outer limit of the tissues overlying the greater trochanter, was segmented from proximal femur CT images and the closest distance between the femoral and pelvic surfaces was defined as STT(α,β). In the ARF0$_{STT\text{-}BMI}$ model instead, a k-fold cross-validated linear regression was trained between the CT-based STT(α,β) and BMI of the cohort subjects. STT(α,β) estimates from BMI could then be used in the $\eta_{ST}(\alpha,\beta)$ definition.

Results

Average STT measured using CT at any orientation exceeded average STT as estimated from BMI [3] by 5 mm or more. Nearly 60% of the cohort reported highest STT at the simultaneously anterior- and medial-most orientations. Pairwise differences between ARF0$_{STT0\text{-}BMI}$ and ARF0$_{STT\text{-}CT}$ were statistically significantly greater than zero for the fracture and non-fracture groups separately ($p < 0.001$).

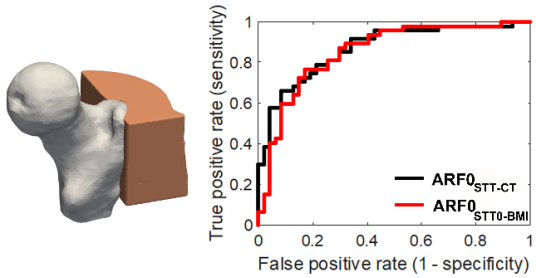

Figure 1: Left: a representative proximal femur with soft tissues overlying the trochanteric region. Right: ROC analysis performance curves using ARF0$_{STT0\text{-}BMI}$ (red) and ARF0$_{STT\text{-}CT}$ (black) as classifiers.

Performance curves from ROC analyses (Figure 1) showed that the classification was the most optimal for ARF0$_{STT\text{-}CT}$ = 21% threshold with 79% sensitivity (95% CI: 64–89%) and 79% specificity (95% CI: 65–89%). Area Under the ROC Curve (AUC) = 0.87 (95% CI: 0.78–0.93) of ARF0$_{STT\text{-}CT}$ only slightly exceeded AUC = 0.85 (95% CI: 0.76–0.92) of ARF0$_{SST0\text{-}BMI}$. AUC = 0.84 of ARF0$_{STT\text{-}BMI}$ fell below that of ARF0$_{SST0\text{-}BMI}$.

Discussion

This study investigated for the first time the STT heterogeneity in the hip region and its influence on hip fracture risk prediction accuracy. Orientation-specific STT was measured using CT and estimated by a BMI-based regression. Accuracy with respect to an orientation-independent STT estimate improved only when STT was measured using CT. Yet, the magnitude of improvement, as estimated by this study, is likely to be outweighed (in a clinical setting) by cost considerations of CT imaging.

References

1. Robinovitch et al., *J. Orthop. Res.* . 13:956–962, 1995.
2. Bouxsein et al., *J. Bone Miner. Res.* 22:825–831, 2007.
3. Bhattacharya et al., *Biomech Model Mechanobiol* 18:301–318, 2019.

Acknowledgements

This study was partially supported by the UK EPSRC grant MultiSim2 (No. EP/S023940/1).

PAIN CATASTROPHISM AND GAIT COORDINATION IN TOTAL KNEE REPLACEMENT DECISION MAKING

Tassani S.(1), Tio L.(2), Castro-Domínguez F.(2,3), Monfort J.(2,3), Monllau JC.(2,4), Gonzalez-Ballester MA.(1,5), Noailly J.(1)

1 BCN MedTech, DTIC, Universitat Pompeu Fabra, Barcelona, Spain; 2 IMIM, Barcelona, Spain; 3 Rheumatology Department, Hospital del Mar, Barcelona, Spain; 4 Orthopedic Surgery and Traumatology Department, Hospital del Mar, Barcelona, Spain; 5 ICREA, Barcelona, Spain;

Introduction

Healthy gait is a coordinated motion, but musculoskeletal pathologies, like Osteoarthritis (OA) of the knee, change the gait patterns of the patients. In particular, it is well known that maximum ranges of motion can decrease during the progression of OA [1], but this simple descriptor does not fully characterize the changes in gait. Moreover, our previous studies are pointing out that emotional factors, like pain catastrophism, might drive the decision to undergo a total knee replacement (TKR) more than pain itself or mechanical factors. This abstract aims to investigate the relationship between pain catastrophism and gait-coordination in TKR decision making.

Material and Methods

Eighty-six OA subjects with KL grades 2-3 were selected based on 4 clinical factors: Gender (male – female), Age (60-67 – 68-75), BMI (25–29.9 – 30+) and Therapy (TKR – conservative treatment). Gait analysis was performed using 8 cameras BTS Smart-DX 700, 1.5 Mpixels 250 fps and 2 force plates BTS P-6000 500 Hz sampling (BTS S.p.A., Milan, Italy). Helen Hayes marker protocol with medial markers was used.

Range of motion: Dynamical range of motion of the lower limbs were computed during the gait cycle. A multifactorial ANOVA was performed to identify the articulation motion related to the factor Therapy.

Pain Catastrophism: pain catastrophizing score (PCS) was computed for each patient. A score higher than 30 was considered clinically relevant.

Results

ANOVA analysis identified hip abduction-adduction and pelvis obliquity as significantly related to the TKR decision ($p<0.005$). Most subjects presented singularities in which the coordination among body segments was lost (Figure 1, red circles) and these singularities increased in intensity in patients requiring TKR (Fig. 1a). Classifying patients against differences in PCS (clinically relevant or not) revealed no influence of PCS on the range of motion, but an increased loss of coordination was visible at increasing PCS (Fig. 1b).

Discussion

In healthy subjects, the singularities shown in the red circles are not present and the movement is smoothly coordinated [2]. The variations in pelvis obliquity compared to the limited variations in hip abduction-adduction angles suggest a limping gait.

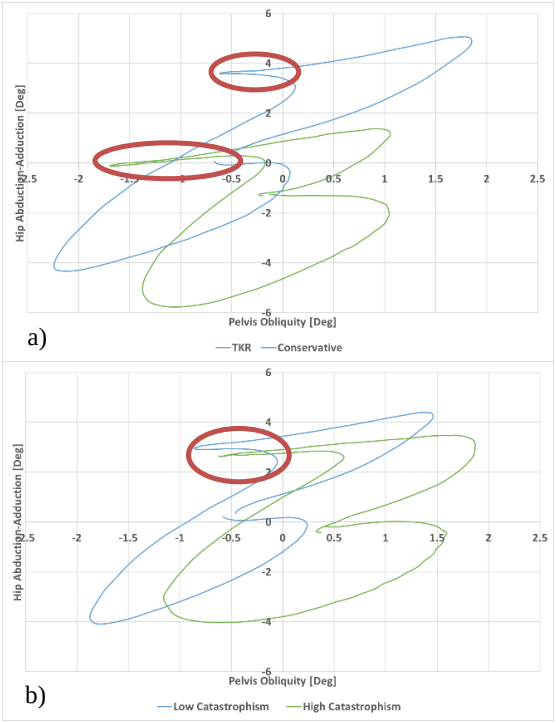

Figure 1 Coordination between Hip Abduction-Adduction angle and Pelvis Obliquity shown in a) patients selected for TKR or conservative treatment b) patients with clinically not relevant or high levels of PCS.

From previous analyses of the current cohort, we know that patients with high PCS are more likely to undergo TKR. This study further shows that similar gait patterns in terms of loss of hip-pelvis coordination are present in patients both requiring TKR and with high PCS, even if PCS does not alter the range of motion, in contrast to Therapy. Patients with high PCS can present a limping gait, and related discomfort, therefore showing a relation between emotional factor and gait that can influence the decision to undergo TKR. Dynamic analyses of different gait perturbations in terms of range of motion and segment coordination may help identifying those patients that might be wrongly referred to TKR because of high levels of catastrophism.

References

[1] K. Mills et al. *Arthritis Care Res.*, 65, 2013.
[2] J. R. Franz et al. *Gait Posture*, 2009.

Acknowledgements

Funds from the Spanish Government (HOLOA-DPI2016-80283-C2-1/2-R, RYC-2015-18888) and from DTIC-UPF.

MULTIFACTORIAL AND MULTIVARIATE ANALYSIS OF FUNCTIONALITY AND DYNAMICS IN OSTEOARTHRITIC GAIT

Tassani S.(1), Tio L.(2), Castro-Domínguez F.(2,3), Monfort J.(2,3), Monllau JC.(2,4), Gonzalez-Ballester MA.(1,5), Noailly J.(1)

1 BCN MedTech, DTIC, Universitat Pompeu Fabra, Barcelona, Spain; 2 IMIM, Barcelona, Spain; 3 Rheumatology Department, Hospital del Mar, Barcelona, Spain; 4 Orthopedic Surgery and Traumatology Department, Hospital del Mar, Barcelona, Spain; 5 ICREA, Barcelona, Spain;

Introduction

Osteoarthrosis (OA) is a multifactorial disease. This means that several factors, like age and gender, interact among each other in different, non-linear, ways. Hence, the impact of each factor on OA might be interpreted differently, depending on these interactions. The issue becomes evident when clinically and radiologically similar patients are referred to radically different management strategies, i.e. total knee replacement (TKR) or conservative therapy. In gait analysis, the variability of outcomes among different publications is known [1] and might be related to the difficulty to perform multifactorial analyses. Accordingly, this study aims to investigate whether any rationality can be identified in the selection of OA management strategies, through a multifactorial and multivariate analysis of gait dynamics and function in a patient cohort.

Material and Methods

A multifactorial and multivariate analysis of gait dynamics was developed. 86 OA subjects with KL grades 2-3 were selected based on 4 clinical factors: Gender (male – female), Age (60-67 – 68-75), BMI (25–29.9 – 30+) and Therapy (TKR – conservative treatment). Gait analysis was performed using 8 cameras BTS Smart-DX 700, 1.5 Mpixels 250 fps and 2 force plates BTS P-6000 500 Hz sampling (BTS S.p.A., Milan, Italy). Helen Hayes marker protocol with medial markers was used [2]. Each volunteer was asked to perform a minimum of 5 valid gait sequences.

Functionality: The velocity of gait and the time needed to perform a gait cycle were computed.

Dynamics: The reaction forces and moments at the ankles, knees and hips were computed through inverse dynamic analyses. Temporal analysis was also performed at three different times point of the gait, where the vertical reaction force derivative was zero. Multivariate analysis of variance was performed for the four factors described among the functionality and dynamics parameters.

Results

The multivariate analysis showed functionality values to be more dependent on the studied factors than the dynamics ones.

Functionality seems to be directly related to the clinical treatment. Patients who selected TKR needed more time to make a step, spent more time in double stand position and walked slower, need more time for each step and spend more time in double stance ($p<0.001$). Older subjects also need more time for each step. However, this dependency seemed to variate with age (interaction between clinical treatment and age – $p<0.01$ – Figure 1).

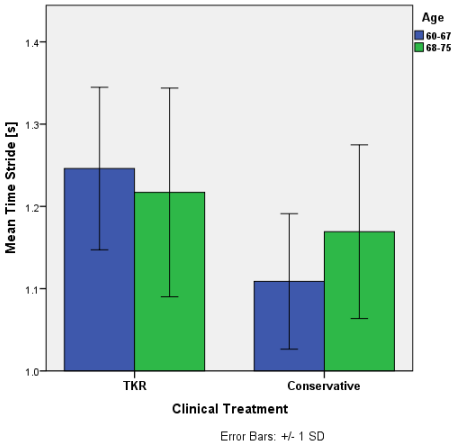

Figure 1: Effect of the interaction between Clinical treatment and age over Mean Stride Time

Dynamics: Forces at the joints seemed affected by the gender ($p< p<0.005$) and moments were affected by age ($p<0.015$) but not by the chosen therapy. Moments showed statistical influence on the selected therapy only in three or four level interaction (Age-BMI-Therapy $p<0.005$; Age-BMI-Therapy-Gender $p<0.01$). Age was also significant as was the interaction between age and BMI (both $p<0.015$).

Discussion

Reduced functionality seems to be the main reason driving the selection of therapy. In contrast to current paradigm, forces at the joints may have no role in the definition of the best therapy for OA subjects. Remarkably, subject requiring TKR do not present higher loads at the joints. Instead of forces or moments, kinematics and posture assessments might support rational treatment decisions and future multifactorial analysis should take them into consideration.

References

[1] K. Mills et al. *Arthritis Care Res.*, vol. 65, no. 10, pp. 1643–1665, 2013.

[2] R. B. Davis et al. *Hum. Mov. Sci.*, vol. 10, no. 5, pp. 575–587, 1991.

Acknowledgements

Funds from the Spanish Government (HOLOA-DPI2016-80283-C2-1/2-R, RYC-2015-18888) and from DTIC-UPF.

A PIPELINE FOR IN SILICO PREDICTION OF CORONARY STENTING SHORT TERM OUTCOMES

Luca Antonini (1), Gianluca Poletti (1), Francesca Berti (1), Panagiota Tsompou (2), Antonis Sakellarios (2), Georgia S. Karanasiou (2), Dimitrios I. Fotiadis (2), Giancarlo Pennati (1), Lorenza Petrini (3)

1. LaBS – Dept. of Chemistry, Materials and Chemical Engineering, Politecnico di Milano, Milan, Italy; 2. Dept. of Biomedical Research, FORTH-IMBB, GR 45110 Ioannina, Greece; 3. Dept. of Civil and Environmental Engineering, Politecnico di Milano, Milan, Italy.

Introduction

With the advent of in silico clinical trials, patient-specific simulations increased their attractiveness in the scientific field. Several literature works deal with the computational reproduction of the stenting procedure in patient-specific arteries. Generally, the realism of the vessel geometry is guaranteed by 3D reconstruction based on clinical images and the mechanical properties are assigned relying on the literature [1, 2]. Although the computational methods proposed in the literature are generally applied to single cases or to comparison scenarios, the present work proposes a comprehensive workflow for the realization of patient-specific stent deployment simulations and presents the results related to the simulation of a cohort of ten clinical cases. The numerical pipeline aims at a detailed description of the quantities of interest from the point of view of the accuracy of the stent model, the reliable representation of the diseased artery and considering the various steps of the deployment procedure.

Methods

Models of delivery systems (stent and balloon) previously validated through comparison with experimental tests were coupled with arteries reconstructed on the basis of Optical Coherence Tomography images (OCT) and angiographic data. The arterial wall was divided into three layers, namely adventitia, media and diseased intima in which, on the basis of the analysis of clinical images, any calcific and/or lipidic plaques were inserted.

Finite element simulations were performed using Abaqus/Explicit solver and were set to faithfully replicate the various steps of the real clinical procedure regardless of its complexity. Given the need to potentially perform a large number of simulations, a semi-automatic process has been developed to limit operator intervention in the setup phase. The results obtained by simulating stenting procedures in virtual patients were suitably compared with clinically observed quantities, namely lumen gain and possible malappositions.

Results

Figure 1 reports, as an example, a simulation related to one of the analyzed clinical cases, showing the configurations at the end of the various phases of stent deployment. The performed post-processing has allowed to extract values of interest to be compared with the clinical end-points measured in real cases. Through this comparison the goodness of the computational method specifically developed was evaluated.

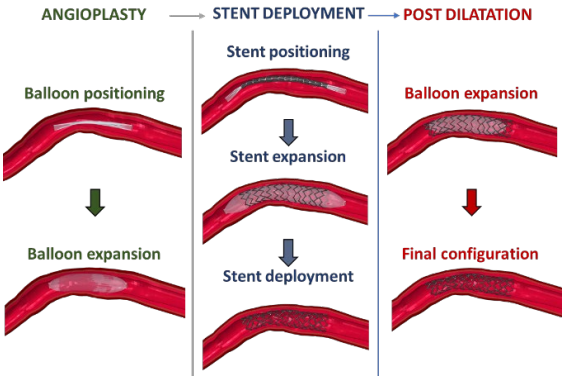

Figure 1 Numerical simulation of stenting patient-specific procedure.

Discussion

Numerical simulations can be effectively exploited for in silico clinical trials only if the used models are validated with respect to the context of use, the computational time are compatible with the time to market strategy and the manual steps in the setting up of the computational tool are limited. In this work, a pipeline able to satisfy those requirements is proposed for the prediction of short term outcomes in coronary stenting. Clearly, the intrinsic uncertainties related to clinical data have to be opportunely considered both during modelling and results evaluation. The pipeline extension to middle- long term outcomes is ongoing in the frame of "Insilc" European project (GA n. 777119).

References

1. Morlacchi et al, Med Eng & Physics, 35:1272-1281, 2013.
2. Mortier et al, Ann of Biomed Eng, 38:88-99, 2009.

Acknowledgements

This project has received funding from the European Union's Horizon 2020 research and innovation programme under grant agreement no 777119. This article reflects only the authors' view and the Commission is not responsible for any use that may be made of the information it contains.

IN SILICO TRIALS ON OSTEOPOROTIC HUMAN BONE FIT DENOSUMAB WITHDRAWAL REBOUND EFFECT SEEN IN CLINICAL PATIENT DATA

Charles Ledoux (1), Daniele Boaretti (1), Duncan C. Tourolle né Betts (1), Ralph Müller (1), Caitlyn J. Collins (1)

1. Institute for Biomechanics, ETH Zurich, Zurich, Switzerland

Introduction

Incidence of osteoporosis (OP) is increasing with our aging population. Denosumab, a common treatment for OP, is a monoclonal antibody that binds to RANKL and thus reduces osteoclastogenesis, osteoclast-mediated bone resorption and remodeling rates. As a result, bone mineral density (BMD) increases and fracture risk decreases. Upon cessation of treatment, however, resorption rises quickly to levels even higher than baseline and thus rapid bone loss occurs [1]. Recent experimental studies have postulated that this rebound effect may be attributed to accumulation of osteoclast precursors as a result of blocked differentiation to osteoclasts - the so-called gate-blocking effect - [2]. In this work, we used *in silico* modelling to explore mechanisms responsible for the rebound effect following cessation of denosumab treatment.

Methods

The micro-multiphysics (micro-MP) agent-based model used in this work was adapted from a model of fracture healing [3]. Briefly, osteoblasts, osteoclasts, osteocytes, MSCs, HSCs, pre-osteoclasts, pre-osteocytes and lining cells are represented as agents on a voxel-based lattice and are motile and capable of producing or resorbing tissue and signaling molecules. Micro-computed tomography (micro-CT) data serves as input for the baseline model structure. Signaling molecules diffuse and react on the same lattice where the cells reside using a multiphysics solver. Concomitantly, the bone mechanical environment is simulated using micro-finite element analysis to determine the internal strains, which serve as stimulus for the osteocytes and osteoblasts. Starting from 7 micro-CT scans of iliac crest biopsies from postmenopausal women (age: 72±5 years)[4], simulations were run for 2 years of denosumab treatment with an additional 2-years of follow-up without treatment. For the current work, changes in concentrations and cell numbers were tracked and linked to changes in BMD, which were assessed at timepoints matching the measurement intervals from an *in vivo* study on denosumab withdrawal [1].

Results

Simulations of 2 years of denosumab with a 2-year withdrawal follow-up closely match *in vivo* BMD trends (Fig.1). In both *in vivo* trials and the simulated iliac crest micro-MP models, BMD dropped rapidly starting 6 months after the last denosumab injection and stabilized below baseline but above placebo levels by month 48.

After 2 years of simulated denosumab treatment, mean effective strain was lower and osteoclast precursor numbers were significantly higher than at baseline ($p=0.033$ using a paired Student's t-test, N=7).

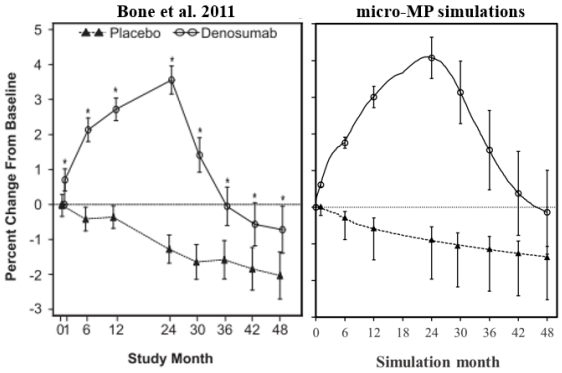

Figure 1: (Left) total hip BMD [1] and (Right) simulated BMD percent changes from iliac crest biopsy micro-MP models during Denosumab treatment and withdrawal.

Discussion

A novel micro-MP agent-based model reproduced trends in BMD observed experimentally after withdrawal of denosumab. The model predicted increases in osteoclast precursor numbers over the course of treatment with denosumab, in accordance with recent experiment data demonstrating significantly higher numbers of cells expressing CD14+/CD11b+ in a group of 10 postmenopausal women treated with denosumab for 3 years relative to a control group of 69 postmenopausal women [2]. The model also predicted a decrease in mean effective strain over the course of treatment with denosumab, leading to higher RANKL and sclerostin production by osteocytes. The micro-MP model may provide a fast and inexpensive tool to test hypotheses relating to bone mechanobiology and OP treatment sequence and assist in formulating *in silico* trials to help reduce and refine human clinical trials.

References

1. Bone et al. (2011) J Clin End & Met 96(4):972-80
2. Fontalis et al. (2020) Bone Reports 13:100457
3. Tourolle (2019) ETH Library
4. Tourolle et al. (2021) JBMR Plus, *under review*

Acknowledgements

Support from the Swiss National Supercomputing Centre and the Euler compute cluster at ETH Zurich.

SENSITIVITY ANALYSIS OF MENISCUS ASSUMPTIONS IN A VALIDATED TIBIOFEMORAL FINITE ELEMENT MODEL

Jiacheng Yao, John Crockett, Mathias D'Souza, Gavin Day, Ruth Wilcox, Alison Jones, Marlène Mengoni

Institute of Medical and Biological Engineering, School of Mechanical Engineering, University of Leeds, UK

Introduction

Validation of finite element models is a key step to enable their practical use with confidence in their ability to replicate some known conditions. However, "valid" models are never valid for everything: the validation process is done for a specific set of conditions and specific outputs of interest. Understanding the sensitivity of results to input parameters can contribute to define the contexts for which a modelling methodology remains valid [1].

The aim of this work was to provide information on the context of use for validated models of the tibiofemoral joint, analysing the sensitivity of FE model outputs to assumptions used to model the meniscus.

Methods

Previous work validated knee contact outputs (total contact area and mean contact pressure) for three image-based human tibio-femoral joint models in axial compression against in-vitro data of the same knees. Cartilage properties of meniscectomy models were calibrated against corresponding in-vitro contact area (achieving errors below 10%). Models with meniscus were validated against in-vitro contact area and mean contact pressure on each condyle (with errors lower than 15% on most outputs). The baseline meniscus had a geometry based on MR and CT images, with meniscus roots each represented by 15 linear springs attached to one point on the tibia (Figure 1). It was modelled with transversely isotropic linear elasticity with axial modulus equivalent to the cartilage normal modulus, and circumferential to axial modulus ratio of 3.5 [2].

A one-at-a-time sensitivity analysis was performed for the value of the cartilage to meniscus axial modulus ratio, the value of the circumferential to axial modulus ratio in the meniscus, the root attachment position (from its baseline location, to a location more anatomically realistic based on bone landmarks or slightly away from the latter), the root attachment shape (from a single point to an area covering the core root attachment or its total attachment), and the methodology used to model the roots (linear spring, rigid bars or 3D model of the root). In addition to the contact outputs already mentioned and measured in the in-vitro work, maximum relative displacement of the meniscus with respect to the cartilage and, where relevant, stretch values of the linear springs were extracted.

Results

Contact pressure and area showed high sensitivity to the meniscus axial modulus, albeit non-systematic, but low sensitivity to the circumferential modulus (with the axial sensitivity 10 to 20 times higher). Similarly, changing the meniscus root attachment location or shape had only a low and non-systematic effect on the contact area or contact pressure. Where the baseline position was furthest from its more realistic one, the differences were lower than 8%. The springs' stretch showed a systematic increase with increasing attachment surface area. The relative displacement showed a systematic decrease with adjusting the spring attachment shape or the root modelling methodology (Figure 1).

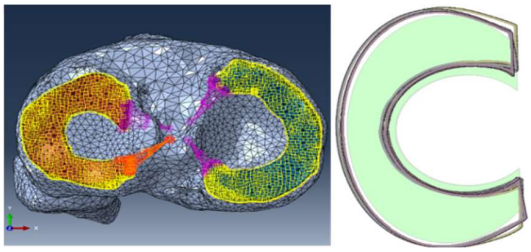

Figure 1: Axial view of the baseline meniscus model (left) and imprint of the meniscus movement on the tibia with different root modelling methodology (right)

Discussion

The meniscus material assumptions in FE modelling do not have a systematic effect on contact pressure and area for a knee loaded in axial compression, with axial stiffness dominating the behaviour. Assumptions used for the roots have an effect on the meniscus displacement (hence the contact location) and root behaviour but not on contact pressure and area. This shows that a model valid for contact in axial compression is not necessarily valid for localized behaviour of the meniscus. It is likely that dynamic gait loading or static flexion have higher sensitivity to the meniscus model. The validation performed for the baseline models can be used for studying effects linked to the cartilage or the inter-patient variability but should not be considered valid for movements involving more displacements of the meniscus. This work provides more evidence on the importance of understanding the sensitivity to modelling assumptions in a "valid" model, which can help defining the context of use of models.

References

1. Viceconti et al, Methods, 2020
2. Cooper et al, JMBBM 2020: 103797

Acknowledgements

This work was funded by the EPSRC (grant EP/P001076/1).

VALIDATION OF ANALOG INSTRUMENTS ON A NOVEL MINIMALLY INVASIVE SPINAL FUSION SIMULATOR

Brittany Stott (1), Mark Driscoll (1)

1. McGill University, Canada

Introduction

The Halstedian approach is a traditional training method for surgical residents founded on apprenticeship in the operating room [1]. With the advancements of medical technology, the progression of complex minimally invasive (MI) procedures is evolving [1]. As a result, MI surgical simulator development is progressing [2], with the aim of allowing clinicians to acquire skills and knowledge through safe and repetitive training. A novel MI spinal fusion surgical simulator was developed, complete with physically and virtually realistic analog instruments.

Validation of medical surgical simulators is crucial to ensure a reliable transfer of skills and knowledge between the training device and the operating room. However, surgical simulators are typically validated as a complete training device, absent of the explicit validation the instruments themselves.

The purpose of this study was to assess face (realism) and content (appropriateness) [3] validity of novel analog surgical instruments.

Methods

Seven male expert orthopedic surgeons (n=4) and neurosurgeons (n=3) participated in the ethically approved study. No participants had prior experience on the surgical simulator. Each participant performed a MI single-level spinal fusion procedure on a cadaver prior to performing an equivalent operation on the surgical simulator. The time taken to complete each task during the procedure and the participants' interaction with the surgical instruments were recorded. Immediately after the completion of the simulator trials, participants responded to a questionnaire assessing face and content validity. Participants ranked their responses on a 5-point Liker-scale where 5 indicated strongly agree and 1 strongly disagree.

Results

Variations in length of time required to complete each task were detected between participants and training devices (cadaver vs simulator). However, participants were observed to interact with the instruments in a similar manner, judged by grasp position and location on the instruments, regardless of the training device and despite their unfamiliarity with the surgical simulator.

The participants ranked the overall average score for the analog instruments 3.7/5 on the Liker-scale. When asked to compare the simulator instruments to those utilized in the cadaver experiments, mean values of 3.9/5, 3.6/5, and 3.3/5 were allotted for overall physical resemblance, virtual impression, and maneuverability, respectively.

Discussion

The observed lack of association for the time spent completing each step in the procedure was expected. Patient anatomy, and as a result collapsed disc space, varied between cadaver specimens, resulting in a unique surgical approach from each participant. Participants were observed to interact with the instruments in a comparable manner during the cadaver and simulator trials. Participants grasped the instruments with similar finger placement and location on both training devices. The ease with which the participants adapted to the analog instruments further supports their physical realism when compared those handled during the cadaver trials.

Face and content validity were demonstrated as a result of the participant questionnaire feedback. The mean physical appearance and maneuverability of the simulator instruments were rated >3.5 and >3, respectively, indicating above average realism.

To conclude, the analog instruments were successfully validated on the novel surgical simulator. Moreover, this study highlights the importance of independently validating the simulator instruments. The results of this study encourage further investigation regarding the effect that implementing realistic instruments on surgical training devices has on novice user experience.

References

1. Shaharan and Neary, World J Gastrointest Endosc, 6:436-447, 2014.
2. Neary et al, Surgical Endoscopy, 22:2301-2309, 2008.
3. McDougall, J of endourology, 21:244-247, 2007.

Acknowledgements

We thank our research partners, CAE Healthcare Inc. (Montreal, Canada) and Depuy Synthes (Raynham, USA). This work was supported by grant CRDPJ 515768-17 funded in part by the Natural Sciences and Engineering Research Center (NSERC), MEDTEQ, Depuy Synthes Spine, CAE Healthcare Inc., and McGill University.

REPRODUCIBILITY OF THE DENSITOMETRIC AND MECHANICAL PROPERTIES OF THE MOUSE TIBIA FROM *IN VIVO* MICRO-CT

Sara Oliviero (1,2), Vee San Cheong (2,3), Bryant C Roberts (1,2), William Griffiths (2,3), Enrico Dall'Ara (1,2)

1. Department of Oncology and Metabolism, University of Sheffield, UK; 2. INSIGNEO Institute for in Silico Medicine, University of Sheffield, UK; 3. Department of Mechanical Engineering, University of Sheffield, UK

Introduction

Osteoporosis is one of the most common chronic diseases of the musculoskeletal system. New treatments require *in vivo* testing before clinical translation, and the mouse tibia is one of the most commonly used animal models [1]. For clinical translation, bone density and strength are relevant endpoints for preclinical studies. Recently, a method for evaluating the densitometric properties of the whole tibia has been proposed [2], based on *in vivo* micro-Computed Tomography (microCT). Micro-CT-based Finite Element (microFE) models can assess non-invasively the tibia structural mechanical properties [3]. However, the microCT image processing pipeline includes operator-dependent tasks that could affect the measured properties.

The aim of this study was to evaluate the intra- and inter-operator reproducibility of the densitometric and mechanical properties of the mouse tibia estimated with *in vivo* microCT.

Methods

Five C57BL/6 mice were microCT scanned *in vivo* (VivaCT80, Scanco Medical; 55kVp, 145µA, 10.4µm voxel size) from the age of 14 to 24 weeks, every two weeks in a previous study [4]. The images acquired at week 18 were used in this study (N=5). An operator rigidly registered each image to a reference in order to align all tibiae in the same spatial orientation. Subsequently, the operator selected a volume of interest (VOI) below the growth plate, including 80% of the total length. Each operator-dependent task (registration and selection of VOI) was repeated three times by the same operator and once by two additional operators, in order to evaluate both intra- and inter-operator reproducibility. The spatial distribution of bone mineral content (BMC) was evaluated by dividing each tibia into 10 longitudinal sections and four quadrants (anterior, posterior, medial and lateral, Fig 1A) [2]. Lastly, microCT images were converted into voxel-based homogeneous linear elastic (E=14.8GPa, ν=0.3) microFE models (Fig 1B) for estimating structural stiffness (S) and failure load (Fu) [3].

Reproducibility was evaluated for each parameter by using precision error (PE, [%]) [2], defined as

$$PE = \sqrt{\sum_{j=1}^{5} \frac{CV_j^2}{5}} \; ; CV = \frac{SD}{\mu} \qquad (1)$$

where µ is the average of the three measurements and SD is the standard deviation.

Results

High reproducibility was obtained for densitometric parameters (PE < 3%, Table 1) for both intra- and inter-operator. Operator-dependent tasks had the largest influence on bone stiffness estimated with FE models (PE < 4%). Reproducibility was higher for intra-operator than inter-operator (Table 1).

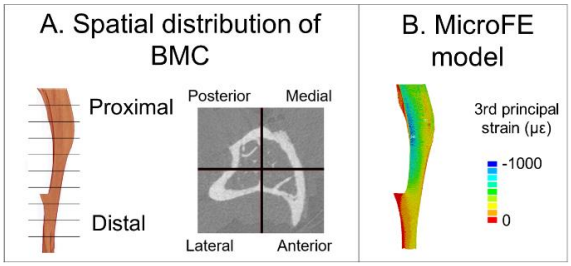

Figure 1: Overview of the methods.

	Intra-operator PE [%]	Inter-operator PE [%]
TotalBMC	0.05	0.21
TotalBMD	0.15	0.29
BMC in 40 sectors	0.15 – 2.01	0.18 – 2.34
S	3.06	3.94
Fu	1.51	1.96

Table 1: Intra- (3 repetitions) and inter-operator (3 operators) precision error (PE) obtained for densitometric and mechanical properties of the mouse tibia (N=5 tibiae) measured from in vivo microCT.

Discussion

Densitometric and mechanical properties measured from *in vivo* microCT were highly reproducible. Further analyses will be carried out to evaluate reproducibility at different time points to study the effect of interventions on bone properties.

References

1. Bouxsein et al, JBMR, 25:1468–1486, 2010.
2. Lu et al, JBiomech, 49:2095-2099, 2016.
3. Oliviero et al, JMBBM, 113:104190, 2021.
4. Roberts et al, SciRep, 10:8889, 2020.

Acknowledgements

This study was partially funded by the NC3Rs (NC/R001073/1) and by the EPSRC (EP/K03877X/1 and EP/S032940/1).

TOWARDS OBJECTIVISATION OF PAIN: RESEARCH AND DEVELOPMENT OF PAIN STIMULUS DEVICE

Kotryna Šileikytė (1), Julius Griškevičius (1)

1. VILNIUSTECH university, Lithuania

Introduction

Pain is described as a sensation that occurs when nerve endings, which are mostly in the skin, are irritated. The feeling of pain is caused by various stimuli, such as: stabbing, pressure, excessive heat in one place, stretching, shock. However, there is a difference in the response to pain. When the pain signal reaches the spinal cord, it is passed on to the brain, where the pain signal turns into pain [1]. All brain activity induced by stimuli can be monitored using devices such as an electroencephalograph (EEG) [2] and nuclear magnetic resonance imaging (MRI) [3] equipment. Hence, causing pain as an irritant in the aforementioned studies helps to study brain activity. The feeling of pain is judged very subjectively, therefore various scales and methodologies [4] have been introduced to quantify pain. However, there is no unanimous decision on how to assess the pain, necessitating a study using a multi-contact tactile pain stimulus device that would allow the physician / investigator to cause pain to the subject in a controlled manner using pneumatically actuated stimulus. Functional MRI – based pain research requires MRI – compatible device, since current devices like digital pressure algometers allowing to measure pressure pain threshold are not compatible [5,6]. The device allows replicating the same amount of load on all subjects when the load is applied at different points to assess the individual human response during functional MRI study.

Methods

The study was conducted in two stages. The first stage comprised of laboratory tests, where the pressure dependence of the load in kilograms per square cm (kg/cm^2) was measured to estimate what air pressure is required to maintain a particular load. The second was studies with subjects to find out how particular load values are related to an individual pain threshold in subjects. Laboratory tests were performed using a BIOPAC MP36 signal acquisition and processing system and variable pressure sensor SS12LA, when the load is increased every 50 grams to reach one kilogram. Six volunteers (mean age ± standard deviation 23 ± 3.933) were recruited in the study. Following inclusion in the study criteria have been defined: persons have no complains of skin irritation and did not experience additional pain in the hand areas. The study was performed by placing the hand in a box in which one of the mechanical stimuli was randomly triggered at different places on hand 20 times to avoid predictability and increase accuracy. Each time, the subject had to assign a pain value in Verbal Rating Scale (VRS), ranging from 1 to 10, where 1 means no pain, 5 moderate pain and 10 extreme pain. A statistical review was performed.

Results

The results of the study are best seen in the diagram presented in Fig. 1, in which shows relation between the load size and pain scales.

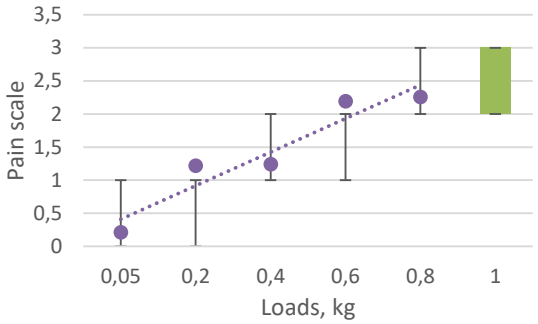

Figure 1: The distribution of pain scale results for the assigned loads.

Correlation coefficient calculations were used to obtain coefficients for the load on the pain scale evaluation averages: r_{xy1}=0.983, r_{xy2}=0.966, r_{xy3}=0.962, r_{xy4}=0.958, r_{xy5}=0.983 and r_{xy6}=0.968. Correlation coefficients approach the value of 1, but are not 1. This may be influenced by the small number of subjects, which does not allow to fully objectify the pain.

Conclusions

The study shows that the pneumatic pain stimulus device we offer ensures constant and equal amounts of load, making it suitable for application fMRI based pain research because it is fMRI compatible. However, there are limitations in this study because the number of subjects was small and, the maximum value of the pain scale was not reached.

References

1. Roberts et al, Medical Life Sciences, 2020.
2. Tu et al, J frontiers in Computational Neuroscience, 2014.
3. Brown et al, J Pain, 19:1-21, 2018.
4. Ramirez et al, Pain scales, 2020.
5. Park et al, J Ann Rehabil Med, 412-417, 2011.
6. Computerized Pressure Algometer, 2020.

IN-SILICO AND IN-VITRO UNCERTANTY QUANTIFICATION OF INLET CONDITIONS OF THE AORTIC COMPLEX

Emanuele Vignali (1), Emanuele Gasparotti (1,2), Alessandro Mariotti (3), Maria Vittoria Salvetti (3) Simona Celi (1)

1. BioCardioLab, Fondazione Toscana Gabriele Monasterio, Italy; 2. Dept. of Information Engineering University of Pisa, Italy; 3. Dept. of Aerospace Engineering, University of Pisa, Italy

Introduction

The importance of hemodynamic analysis of the aortic complex has been established in different works [1]. Both in-vitro and in-silico investigation tools are available for this purpose, but inaccuracies still affect the models [2]. Great interest is given by MRI investigation on mock circulatory loops (MCLs), which usually require long tubes from the pump to the MR scanner to avoid any metallic components in the scanning room. To improve these approaches, the quantification of uncertainties from conditions modeling, including tubing length, is pivotal.

To this purpose, this work proposes a method for the stochastic quantification of effects of aortic inlet conditions for in-vitro and in-silico characterization of aortic complexes. The Generalized Polynomial Chaos approach was used for a study of uncertainty deriving from the stroke volume (SV), cycle period (T) and profile distribution (P) of the aortic flow for a healthy (Hlt), an aTAA and a CoA case. The same approach was adopted in-vitro with a set of experimental tests on a MCL [3].

Methods

Anatomic and functional flow data were extracted from MRI patient data from Hlt, aTAA and CoA cases. The numerical approach consisted in CFD simulations to investigate the SV, T and P effects. Four points of quadrature for the SV and T parameters were set, ranging from 41 to 134 ml and from 0.67 to 1.14 s. Plug and fully-developed flows were imposed as P conditions. For all the simulations, RCR model outlet boundary conditions were imposed at supra-aortic branches (Br1,2,3) and descending aorta (Dsc).

The same approach was imposed for the in-silico cases. The MCL was actuated with a custom piston pump to reproduce the quadrature points. 3D printed phantoms were manufactured for Hlt, aTAA and CoA cases. The outlet conditions were managed with lumped RCR models. Different tubing lengths for the inlet section, ranging from 4 (~plug) to 66 cm (~fully-developed), were used as different P conditions. The parameters influence was quantified through the Sobol Indexes (SI) analysis and Probability Density Function (PDF).

Results

The in-vitro pressure and Br1 flow PDFs are reported in Figure 1 a and b, respectively. The higher variability was reached in the systolic peak. The same trends were confirmed by both in-silico and in-vitro simulations. The SI uncertainty analysis demonstrated that SV and T have the strongest influence on the output parameters all cases, as reported in the flow SI trend example of Figure 1 c. The systolic phase variability is linked with SV, while the early diastole is influenced by T uncertainties. The P of the input profile instead produced negligible variations, regardless of tube length.

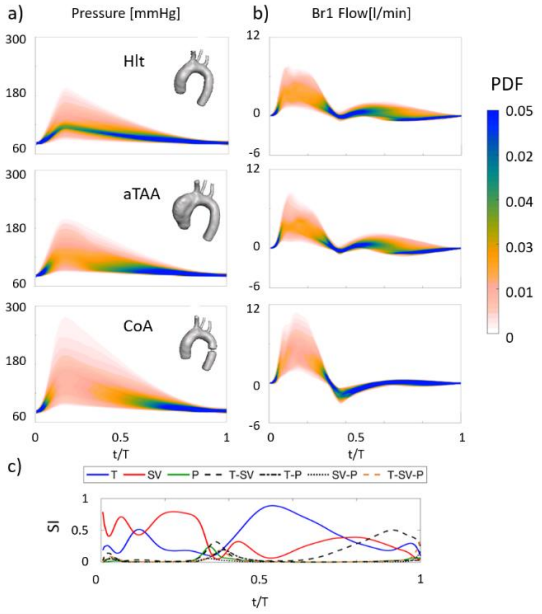

Figure 1: In-vitro PDF for pressure (a) and Br1 flows (b) for Hlt, aTAA and CoA case, with an example of flow SI trend (c)

Discussion

The workflow demonstrated the influence of inlet parameter uncertainty on fluid dynamic models of the aorta. The inlet condition modeling produces inaccuracies propagations directly on the outlet features, regardless of healthy/pathological state. As patient specific conditions modeling is acquiring importance, the current work demonstrated the pivotal role of SV and T estimation, while the tube length did not influence the outcome.

References

1. K. Capellini et al, Med Eng Phys, 2020.
2. A. Boccadifuoco et al, CVET 9.4: 688-706, 2018.
3. E. Vignali et al, AIMETA Conference: 908-919, 2019.

CFD/UQ INTEGRATED APPROACH FOR PATIENT-SPECIFIC STUDIES OF AORTIC COARCTATION

Maria Nicole Antonuccio (1,2), Sandra Perondi (3), Benigno Marco Fanni (1,3), Katia Capellini (1,3), and Simona Celi (1)

1. BioCardioLab, Fondazione Toscana G. Monasterio, Italy; 2. École MINES Saint-Étienne, France; 3. Dept. of Information Engineering, University of Pisa, Italy.

Introduction

Among all the known Congenital Heart Disease (CHD), the Aortic Coarctation constitutes around 5-10% of them, occurring in four new-borns out 10,000 [1]. The hemodynamic features of a CoA, such as altered flows and high-pressure gradients (ΔP) across the coarctation site, make the modelling of this disease challenging and particularly prone to Computational Fluid Dynamics (CFD) analyses. The main issue is prescribing appropriate boundary conditions (BCs) that consider further resistance to the flow offered by the narrowing. The state-of-the-art approach consists in prescribing a lumped parameters Windkessel model as outlet BCs [2]. *A-priori* known values of two resistances and one capacitance (RCR) are then split among the different outlets. In this work, the effect of an uncertain parameter α, introduced in the splitting equations, and calibrated through a stochastic methodology, was compared against another uncertain parameter, i.e. the coarctation diameter (ϕ).

Materials and Methods

Two patient-specific geometries of CoA were reconstructed from Magnetic Resonance Imaging (MRI) data. The inlets of the CFD models were placed at the ascending aorta; the three supra-aortic branches and the descending aorta were the outlets. The BCs were prescribed as in [3]. The proximal (R_P) and distal (R_D) resistances at the outlets were computed as in Eq. (1):

$$R_{p|i}=(1+\alpha)\frac{A_{tot}}{Ai}R_p, \quad R_{d|i}=(1+\alpha)\frac{A_{tot}}{Ai}R_d \ , \quad i=1\ldots4 \quad (1)$$

The uncertain parameter α varied in the range [-0.15, -0.08] for the first model. To further validate this new procedure, α was also used in the second model, varying in the range [-0.2, -0.1]. The effect of the CoA severity was evaluated through four different models, obtained varying the diameter of the second model in the range [6, 11] mm. The combined effect of BCs and CoA diameter was assessed, assuming a uniform Probability Density Function (PDF) for both uncertain parameters. The generalized polynomial chaos [4] was used to statistically characterize the response of the quantities of interest as a function of the uncertain parameters (ϕ, α).

Results

The PDF distribution of the volume flow rate at CoA level along the cardiac cycle for the two geometries are depicted in Figure 1a and 1b, respectively. The results obtained for α=0 (standard procedure) are shown in dotted line, whereas data obtained from MRI are reported in dashed red lines. In the first case, a remarkable variability of the volume flow rate waveform is observed in correspondence of the systolic peak (Figure 1a), whereas slighter variability is observed in the second case (Figure 1b). Figure 1c shows the partial sensitivity to ϕ (blue line), α (red line), and their interaction (green line) of ΔP across the CoA site during the cardiac cycle.

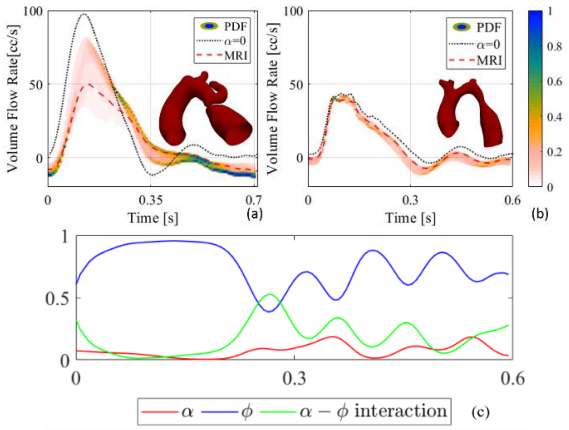

Figure 1: PDF of volume flow rate at CoA sections (a, b); partial sensitivity to ϕ and α of ΔP across the CoA site during the cardiac cycle (c) (second geometry).

Discussion

In both CoA models, a significantly better agreement between clinical data and numerical results was found introducing the parameter α, strengthening the validity of this approach in prescribing outlet BCs when dealing with CoA cases. A satisfying agreement between the simulation results and the patients' flows was found, and the physiological ΔPs were correctly reproduced. The partial sensitivity analysis showed that the impact of ϕ on ΔP is higher than the effect of α. ϕ is indeed the main responsible of the variation of ΔP. Finally, the interaction (green line in Fig. 1c) between the two parameters slightly affects ΔP.

References

1. Canniffe et al, International J Card, 167:2456–2461, 2013.
2. Clementel et al, Comp Meth Biomech., 13:625–640, 2010.
3. Boccadifuoco et al, Comput Fluids, 165, 96-115, 2018.
4. Xiu et al, SIAM J on Scientif Comp, 24:619–644, 2002.

SENSITIVITY ANALYSIS TOWARDS A MODEL OF THE HUMAN HEART

Giulio Del Corso (1), Roberto Verzicco (1,2), Francesco Viola (1)

1. GSSI (Gran Sasso Science Institute), Italy; 2. Università di Roma "Tor Vergata", Italy

Introduction

Cardiac modeling entails the epistemic uncertainty of the input parameters, such as bundles and chambers geometry, electrical conductivities and cell parameters, thus calling for an uncertainty quantification (UQ) analysis. The numerous inputs combined with the high computational cost of solving even single components makes this problem difficult to tackle. However, the presence of a marked individual variability and the uncertainty related to medical data collection procedures provide fertile ground for UQ analysis. To circumvent the computational difficulties inherent in the problem, an electrophysiology model is proposed, divided into distinct components and developed specifically for the study of UQ. Indeed, the crucial components of the model are fully described in a parametric way in order to be able to act automatically taking into account individual variability. Some preliminary studies that exploit this model on the atrial component alone provide promising results allowing a drastic reduction of input parameters for quantities of medical interest.

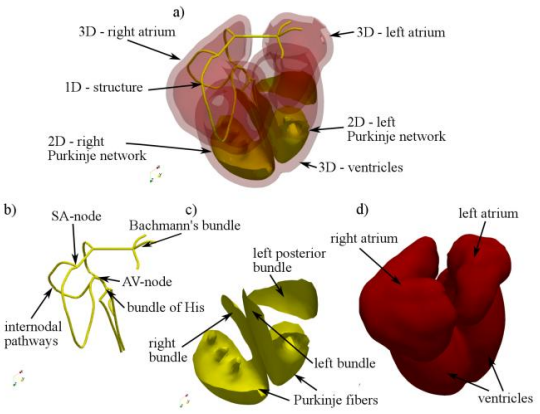

Figure 1: a) Human heart model divided into components: b) fast conduction structure c) Purkinje network d) conductive 3D structure. The arrangement of the conduction fiber, as well as the communication points of the Purkinje Network and the orientation of the muscle fibers are described parametrically.

Methods

The UQ analyzes of cardiac electrophysiology are approached with Polynomial Chaos Expansion (PCE) techniques [1], using an adaptive variant based on quasi-Montecarlo samples and validated in the case of ventricular electrophysiology [2]. The model reductions are based on the first and total order Sobol' indices (whose confidence intervals have been obtained through the use of bootstrap techniques [3]).

Results

The sensitivity analyzes performed on single cardiac components allowed a drastic reduction of the input parameters for physiological propagations. In particular, in the case of the atria, out of 12 parameters considered (including both electrical and geometric parameters, characterization of the stimulus and cellular models, differentiated for males and females) only 3 have been shown to have a relevance on atrioventricular activation times.

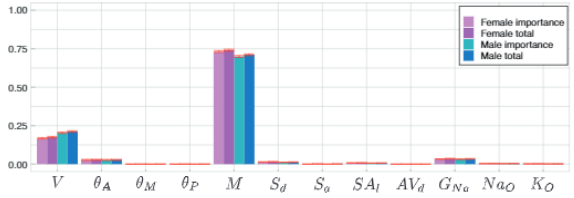

Figure 2: First and total order Sobol' indices for the atrial variables that impact the activation of the atrioventricular node. Of these 12 parameters, only the conductivity values M and the atrial chambers volumes V play a relevant role. The cases are differentiated for male and female hearts, as they are characterized by a high difference in volume.

Discussion

The preliminary results obtained from the atria confirm the high predictive capacity of the model and its applicability to UQ contexts. The same component structure was then implemented for the other components of the heart (Bundle of His, Purkinje fibers, etc. [4]), providing a highly parametric model that is optimal for UQ analyzes. The model so structured, combined with the obtained model reduction, lends itself well to inverse calibration of electrical parameters on the basis of medical observations [5,6].

References

1. Blatman et al, J. Comput. Phys., 230.6, 2011
2. Del Corso et al, J. R. Soc. Interface, 17.171, 2020.
3. Dubreil et al, Reliab. Eng. Syst. Saf., 121:263-275, 2014.
4. Dossel et al, MBEC, 50(8), 773-799, 2012
5. Whittaker et al, WIREs Systems Biology and Medicine, 12.4: e1482, 2020
6. Barone et al, J. Comput. Phys., 423: 109810, 2020

EFFICIENT ESTIMATION OF CARDIAC CONDUCTIVITIES: A PROPER GENERALIZED DECOMPOSITION APPROACH

Alessandro Barone (1,4), Michele Giuliano Carlino (2), Alessio Gizzi (1), Simona Perotto (3), Alessandro Veneziani (4)

1. *Department of Engineering, Campus Bio-Medico University of Rome, Rome, Italy*
2. *INRIA, Bordeaux, France*
3. *MOX, Department of Mathematics, Politecnico di Milano, Milano, Italy*
4. *Department of Mathematics, Emory University, Atlanta (GA), USA*

Introduction

Personalized computational models of cardiac ElectroPhysiology (EP) are gaining remarkable interest in medical research and clinical practice. However, the complete translation of numerical simulations to the bedside is hindered by several factors, generally related to the required physiological accuracy of patient-specific simulations and the corresponding high computational costs, not compatible with clinical timelines. Several reduced-order models (ROMs) have been investigated to replace the high-fidelity Bidomain/Monodomain models with educated and cheaper surrogates. In this work, we apply for the first time the Proper Generalized Decomposition (PGD) method to direct and inverse problems for cardiac conductivity estimation.

Methods

The PGD approach is a technique introduced by F. Chinesta and co-workers [1] for generic parametrization problems. PGD relies on a classical off-line/on-line paradigm based on the idea that the parameters in a model of interest can be treated as independent variables, leading to an augmented variational formulation. The off-line stage concerns the construction of appropriate basis functions set by solving the equations in the parameter space. A special separation-of variable technique is used to perform this step efficiently. Should the solution of this extended variational formulation be available, the computation of the parametrized solution is performed nearly real-time for any value of the parameters (on-line stage), being the solution of an algebraic problem. This accelerates any data assimilation, optimization, uncertainty quantification iterative procedures. The appealing aspect of PGD vs. other model reduction methods is that no snapshot of the solution for specific values of the independent variables and the parameters is needed.

Results

Here we illustrate some preliminary results obtained using the PGD method to reduce the Monodomain model and then solve the Monodomain Inverse Conductivity Problem (MICP) [2]. Fig. 1 shows the color maps of one snapshot of the 2D transmembrane potential computed by the Full Order Method (FOM) based on the Finite Element (FE) compared with the corresponding solutions of the PGD approach varying the quotient of longitudinal and transverse conductivities and the tolerance of the construction of the basis functions in the offline phase. As expected, when the tolerance constraint is more restrictive, the overall accuracy of the PGD approximation improves. The on-line stage enables real-time simulations: in fact, the computation of the reduced solution is two-orders of magnitude cheaper than the FOM one. The extreme rapidity of the on-line phase can dramatically reduce the computational costs of MICP. In fact, the PGD approach for MICP is remarkably convenient since the estimation is obtained in less than one minute as opposed to using the FE solution, requiring several hours, keeping reasonable accuracy of the estimates (more details in [3] including 3D results).

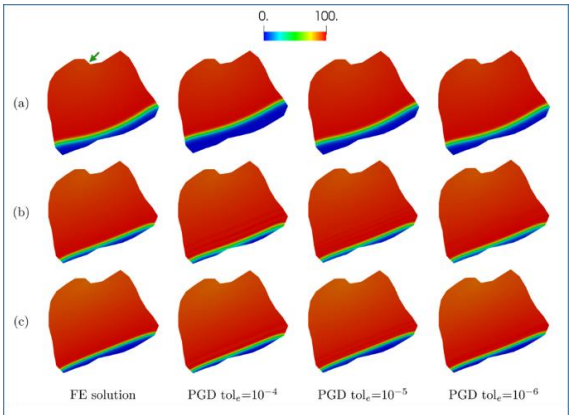

Fig. 1 – Testing the PGD on a 2D canine tissue. Comparison of the solution with the FE method and the PGD varying the tolerance tol$_\varepsilon$. The lines (a), (b) and (c) show the solution for three different values of the quotient r (2,4,6 respectively). As expected, the accuracy improves when the tolerance decreases.

Discussion

In this work, we successfully use a snapshot-free model order reduction such as the PGD to solve EP problems mostly in real-time. This is just the first preliminary step of a more complex series of possible developments, such as (i) the extension to more complex ionic and tissue models, (ii) application to realistic cases in the clinical practice (iii) Uncertainty Quantification.

References

1. F. Chinesta et al, Springer International Publishing, 2014.
2. H. Yang et al, Inv Prob, vol.31, no. 11, p. 115001, 2015.
3. A. Barone et al, J Comp Phys, 423 p. 109810, 2020.

UNCERTAINITY QUANTIFICATION OF HYPERELASTIC SOFT TISSUE

Mahmut Pekedis
Department of Mechanical Engineering, Ege University, Izmir, Turkey

Introduction

The soft biological tissue materials often exhibit intrinsic variability due to inhomogeties once subjected to large deformation For *in-vitro* specimens, the uncertainties and variability in these specimens are high which may be raised by many factors such as the death age of cadaver, preservation time, and some other specific factors regarding to the soft tissue specimens and also measurements [1]. Although hyper elastic material parameters that calibrated for each singular specimen using deterministic approach is useful, stochastic calibration based on Bayesian estimation allows to quantify the uncertainties in useful bonds and also gives the correlation for the calibrated parameters. Here, we quantify the uncertainties and calibrate the hyper elastic parameters for *in-vitro* human head skin specimens.

Methodology

Initially, a total of 8 rectangular cross sectional male human skin samples are dissected from 8 various fresh frozen preserved cadavers. Then, these specimens are tested longitudinally at low stretch rate in order to obtain stress-stretch data. Then, a deterministic calibration approach is implemented for each specimen to obtain prior data for the Bayesian estimation.

This estimation operates by updating the posterior beliefs of parameters as new data become available. The general form Bayes' equation is

$$P(\theta|D,M)=\frac{P(D|\theta,M)P(\theta|M)}{P(D|M)} \tag{1}$$

where θ is the vector of unknown model parameters, M represents the hyperelastic constitute model, and D shows the observed stress-stretch curves. The main goal of Bayesian analysis is to establish an expression to compute by random sampling, the posterior joint probability density function (PDF) of $P(\theta|D,M)$.

The prior PDF of the parameters $P(\theta|M)$ is based on the knowledge of distribution of model parameters. The parameters are generally uninformed, but prior values typically are predicted using non-linear least square fit.

Considering hyperelastic polynomial form with two term, the energy potential is,

$$U=C_{10}(I_1-3)+C_{01}(I_2-3)+C_{20}(I_1-3)^2 + C_{11}(I_1-3)(I_2-3)+C_{02}(I_2-3)^2 \tag{2}$$

where C_{10}, C_{01}, C_{11}, C_{20} are model parameters and I_1, I_2, I_3 are deviatoric stretch invariants.

For uniaxial loading, the stretches in 3 axis are

$$\lambda_1=\lambda_U,\quad \lambda_2=\lambda_3=\lambda_U^{-0.5} \tag{3}$$

and the deviatoric invariants are

$$I_1=\lambda_U^2+2\lambda_U^{-1},\quad I_2=\lambda_U^{-2}+2\lambda_U \tag{4}$$

Once invoking the principle of virtual work, the nominal stress-stretch relationship can be derived as,

$$T_U=\frac{\partial U}{\partial \lambda_U}=\frac{\partial U}{\partial I_1}\frac{\partial I_1}{\partial \lambda_U}+\frac{\partial U}{\partial I_2}\frac{\partial I_2}{\partial \lambda_U} \tag{5}$$

$$=2(1-\lambda_U^{-3})(C_{10}\lambda_U+C_{01}+2C_{20}\lambda_U(I_1-3)+ C_{11}(I_1-3+\lambda_U(I_1-3))+2C_{02}(I_2-3)) \tag{6}$$

The idea here is to determine the uncertainties of each calibrated parameter by evaluating all specimens measurements together. Uniform type (lower = -30, upper = 30) prior distribution are assigned for each parameter. In this work, we implemented the Sampler (NUTS) within the PyMC3 Python package to sample the joint posterior of parameters [2].

Results

Experimental observations and 95 % confidence contour of the model are represented in Figure 1. The range of stochastic calibrated parameters can capture the uncertainty for all specimens. From that point, we hope the implement the similar methodology for other hyperelastic models such as reduced polynomial and Ogden strain energy potential (with 2, 3 and 5 term).

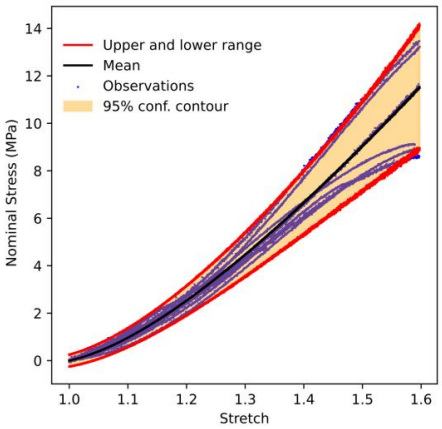

Figure 1: Calibration of hyperelastic polynomial form with N=2

References

1. Mihai LA, Woolley TE, Goriely A. 2018 Stochastic isotropic hyperelastic materials: constitutive calibration and model selection. Proc. R. Soc. A 474: 20170858.
2. Salvatier J., Wiecki T.V., Fonnesbeck C. (2016) Probabilistic programming in Python using PyMC3. Peer J Computer Science 2:e55.

ON THE VALIDATION OF CORONARY STENT DEPLOYMENT SIMULATIONS: IN-VITRO AND IN-VIVO DATA AS COMPARATORS

Luca Antonini (1), Francesca Berti (1), Gianluca Poletti (1), Georgia S. Karanasiou (2), Dimitrios I. Fotiadis (2), Francesco Migliavacca (1), Lorenza Petrini (3), Giancarlo Pennati (1)

1. LaBS – Dept. of Chemistry, Materials and Chemical Engineering, Politecnico di Milano, Milan, Italy;
2. Dept. of Biomedical Research, FORTH-IMBB, GR 45110 Ioannina, Greece;
3. Dept. of Civil and Environmental Engineering, Politecnico di Milano, Milan, Italy.

Introduction

Validation is defined as the process of evaluating the predictive capabilities of a model against a reality of interest. In this context, ASME V&V 40 [1] provides a framework for defining the credibility of a computational model applied to a specific context of use through comparison with purposely collected data, referred as comparators. The aim of this work is to analyze and discuss the possibility of validating in-silico coronary stent deployments, when the context of use is the prediction of acute outcome of human coronary treatment. To this purpose either in-vitro and in-vivo comparators were used, paying particular attention on how their intrinsic uncertainties might limit the validation activity.

Methods

Experimental deployments in 3D printed vessels, data from animal studies and from clinical trials were chosen as in-vitro and in-vivo comparators, respectively. The objective is to explore the compromises between the controllability of the experiment and its realism, intended as closeness to the context of use. If, in principle, the in-vitro deployment using 3D printed vessel could ensure a high level of test control (known vessel geometry and measurable vessel mechanical properties), data from clinical cases should allow the maximum realism at the expense of greater uncertainties (e.g. the mechanical properties of the wall are necessarily based on the literature). In all the cases, the deployment simulations (Abaqus/Explicit) were performed mimicking the real procedures. The differences between numerical results and data from comparators were evaluated considering suitably selected quantities of interest, namely the diameter-pressure curve during in-vitro deployments and the lumen gain across the procedure for in-vivo cases.

Results

Concerning in-vitro tests, the state of the art of printable elastomeric vessels allows only a limited quality control, in terms of shape/dimension and homogeneity of the deposited material. Hence, it could be quite challenging to develop an accurate digital twin of the 3D printed vessel, which means adding uncertainties on the input data of the in-silico deployment. For animal studies, mechanical properties of the wall can be measured at the end of the test, after animal sacrifice, to be used as input of the model. However, the disease created in the animals does not lead to coronary arteries with plaques representative of human plaques. Finally, dealing with an in-vivo comparator (animal or human data) implies having large uncertainties on input data and as well as on the quantities used for the comparison, since both are affected by the limitations associated to clinical imaging techniques.

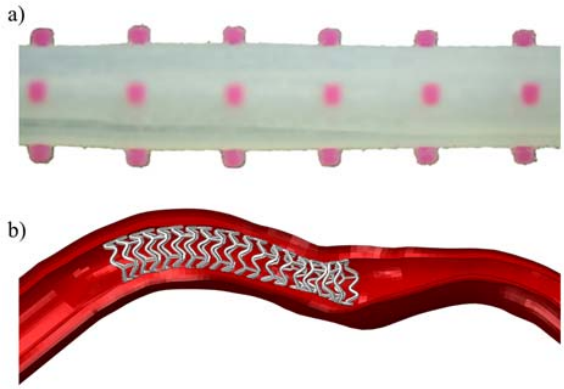

Figure 1: a) example of 3D printed vessels used for stent deployment experiments: the pink markers were used as reference points for a more accurate measurements of external diameter variation; b) stent deployment simulation in a patient specific anatomy used to compare in-silico result with clinical outcomes.

Discussion

This study evidenced a number of possible uncertainties associated with the comparators used to validate coronary stent deployment. The various considered comparators show different levels of uncertainty and realism, suggesting a combined use of them to validate in-silico models of stent deployment.

References

1. ASME Standard, V&V 40, 2018.

Acknowledgements

This project has received funding from the European Union's Horizon 2020 research and innovation programme under grant agreement no 777119.
This article reflects only the authors' view and the Commission is not responsible for any use that may be made of the information it contains.

SIMULATIONS OF COMPETITIVE LIGAND BINDING AT THE CELL – EXTRACELLULAR MATRIX INTERFACE

Zeynep Karagöz (1), Thomas Geuens (1), Vanessa L.S. LaPointe (1), Martijn van Griensven (1), Aurélie Carlier (1)

1. Department of Cell Biology–Inspired Tissue Engineering, MERLN Institute, Maastricht University, Universiteitssingel 40 (UNS40), 6229 ER, Maastricht, the Netherlands

Introduction

Integrin transmembrane proteins mediate mechanotransduction at the cell–extracellular matrix interface. This process is central to cellular homeostasis and therefore particularly important when designing instructive biomaterials and organoid culture systems. Previous studies suggest that fine-tuning the extracellular matrix (ECM) composition and mechanical properties can improve organoid development [1]–[3]. Although experimentally very complex, computational models provide novel avenues to testing the effect of numerous different ECM ligands and mechanical properties on cell decision-making mechanisms.

Methods

We developed an ordinary differential equation–based model that enabled us to simulate three main interactions, namely integrin activation, ligand binding and integrin clustering (**Figure 1**). In contrast to previously published computational models, we account for the binding of more than one ligand to the same type of integrin. Binding rates of integrin α5β3 (**i** and **I**) and its two ligands, fibronectin (**L1**) and von Willebrand Factor A (**L2**), were obtained from the literature [4]. The binding rate constant for **L1** (**k3**) was 10^4 times higher than the binding rate for **L2** (**k5**). The initial conditions for the ECM ligands (**L1** and **L2**) were retrieved from proteomics analysis of kidney organoid ECM, performed in our department [5].

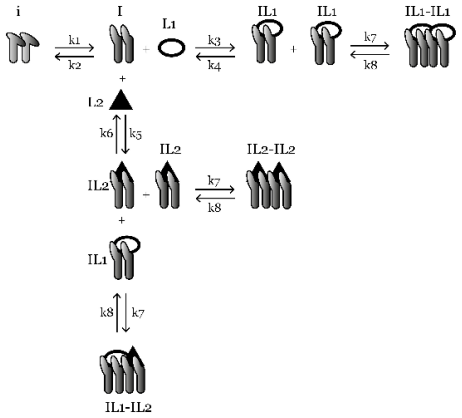

Figure 1: Schematic overview of the ligand competition model.

Results

Our results clearly indicate that this competition between ligands defines the fate of the system. By simulating the model with different initial conditions for competing ligands and testing different sets of binding rates, we demonstrated that the ligand with the higher binding rate (**L1**) occupies more integrins at the steady state than does the competing ligand (**L2**). We have also demonstrated that an increase in the initial concentration of ligands does not ensure an increase in the steady state concentration of ligand-bound integrins**.** Parameter sensitivity analysis was in accordance with these observations. The L2-bound integrin concentration (**IL2**) was most sensitive to changes in binding and unbinding rates of the two competing ligands (k3, k4, k5, k6). Furthermore, the **IL2** concentration was sensitive to the decrease in **L1** initial concentration but not to changes in **L2** initial concentration (**Figure 2**).

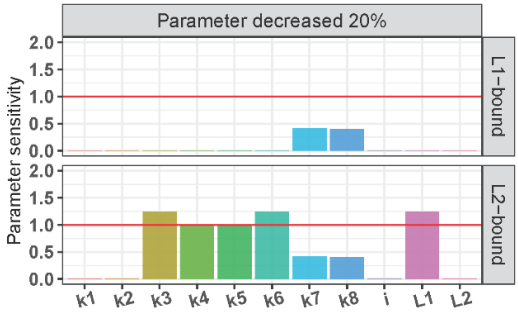

Figure 2: Sensitivity of IL1 and IL2, ligand bound integrin molecular species to the 20% decrease in the model parameters.

Discussion

The model highlights the importance of correctly estimating the ligand–integrin binding rates in the design of advanced cell culture systems. Future work will focus on extending the computational model with intracellular pathways, including developing data-driven approaches to identify and calibrate the pathways of interest. With cell type specific, quantitative input on integrin-ligand binding rates, this model can be used to develop instructive cell culture systems.

References

1. Geuens *et al.*, *npj Regenerative Medicine*, 5.1: 1–6, 2020.
2. Gjorevski *et al.*, *Nature*, 539.7630 : 560–564, 2016.
3. Garreta *et al., Nat. Mater.*,18.4:397–405, 2019.
4. Hudson *et al.*, *Sci. Rep.*, 7.1:1–13, 2017.
5. Geuens *et al.*, bioRxiv preprint, 2020.

Acknowledgements

We gratefully acknowledge the Gravitation Program "Materials Driven Regeneration" funded by the Netherlands Organisation for Scientific Research. (024.003.013)

DETAILED BLOOD CELL FLOW MECHANICS IN CURVED VESSEL GEOMETRY

Christian J. Spieker (1), Gábor Závodszky (1), Max van der Kolk (1), Pierre H. Mangin (2), Christian Gachet (2), Alfons Hoekstra (1)

1. Computational Science Laboratory, Informatics Institute, Faculty of Science, University of Amsterdam, Science Park 904, Amsterdam 1098 XH, the Netherlands; 2. Université de Strasbourg, INSERM, EFS Grand-Est, BPPS UMR-S 1255, FMTS, France

Introduction

The connection between the flow mechanics of the cellular components of blood and the emerging bulk flow parameters, such as the red blood cell free layer (CFL) width, the wall shear rate and the level of hematocrit are well investigated both experimentally and computationally in simple straight channel flows. Currently, there is a substantial lack of extensive analysis in case of non-trivial geometries. Therefore, we investigate the effects of curvature on cellular blood flow by utilizing a thoroughly validated cell-resolved blood flow model[1–2] to simulate the accurate cellular movement in a U-shaped channel for multiple wall shear rate and hematocrit values. Furthermore, the simulation results are compared to indirect measures of experimental platelet adhesion in a collagen coated curved microfluidic device of similar geometry.

Model

The *in silico* experiments in a U-shaped square duct channel with a cross section of 25*25 µm (see Figure 1B) are performed via the lattice Boltzmann method based HemoCell (www.hemocell.eu) for wall shear rates of $\dot{\gamma} = 1600\ s^{-1}$ and $\dot{\gamma} = 300\ s^{-1}$, as well as hematocrit values of $H = 30\%$ and $H = 5\%$. The complementary *in vitro* blood experiments use the same parameter variation in an upscaled microfluidic device (see Figure 1A) and quantify fractional thrombi coverage on surface collagen via microscopic assay.

Results

The simulations show significant differences in shear rate and shear rate gradient distributions between the inner and outer arc of the channel curve (see Figure 1D), leading to the presence of elongational flow fields, while the analysed cell distributions as well as the CFL width and platelet availability remain largely uninfluenced close to the wall. The areas at the inner curve correlate with the location of increased thrombi formation in the experimental results, as shown in Figure 1C.

Conclusion

The amplified platelet adhesion intensity in the experimental results, visible in Figure 1C II. cannot be attributed to a higher platelet concentration or increased volumetric flow in the region, when correlated with the simulation results. However, there is a significant effect

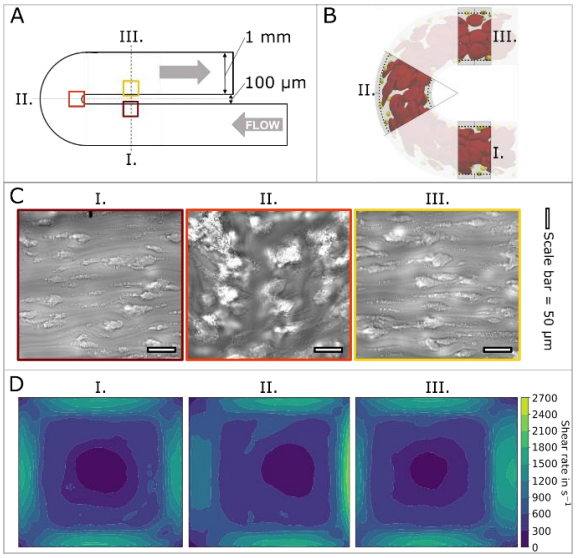

Figure 1: (A) Setup of microfluidic device with highlighted regions of interest. (B) Simulation setup with highlighted regions of interest. (C) Microscopic thrombi surface coverage images referring to regions of (A). (D) Simulated 2D cross-sectional shear rate profiles referring to regions of (B) from outer to inner arc of channel curvature (left to right).

on the shear rate, the shear rate gradient, and on the intensity of elongational flows.

These augmented values, that appear on the inner side of the curve are not in the pathological region, but could cause the uncoiling of von Willebrand factor (vWF)[3].

We propose, that the curvature influenced flow pattern changes are responsible for the changes in the surface platelet thrombi formation, and that this change might be driven by vWF mediated adhesion of platelets to collagen on the microfluidic device surface[4].

References

1 Závodszky, G. *et al. Procedia Computer Science* 108, 159-165 (2017)

2 Závodszky, G. *et al. Front. Physiol.* 8, 563 (2017)

3 Schneider, S.W. *et al. Proceedings of the National Academy of Sciences* 104, 7899–7903 (2007)

4 Sing, C.E. & Alexander-Katz A. *Biophysical Journal* 98, L35-L37 (2010)

Acknowledgements

The authors acknowledge financial support by the European Union Horizon 2020 research and innovation programme under grant agreement no. 675451, the CompBioMed project. The use of supercomputer facilities in this work was sponsored by NWO Exacte Wetenschappen (Physical Sciences).

THROMBOSIS IN PORTAL VEIN RECONSTRUCTIONS: SIMULATION OF POSTSURGICAL BLOOD CLOT FORMATION

Veronika Dušková, Alena Jonášová, Stanislav Plánička, Jan Vimmr

Department of Mechanics and NTIS, Faculty of Applied Sciences, University of West Bohemia, Czechia

Introduction

Pancreaticoduodenectomy as a form of surgical treatment of advanced pancreatic cancer is often accompanied by resection and reconstruction of portal vein segments infiltrated with tumour cells. Currently, not much is known about the usability of allogeneic cadaveric venous grafts, which compared to autologous ones are always available and more often than not have the right proportions (lumen, length etc.). However, similarly to other non-native grafts/patches, the allogeneic ones are prone to failure due to thrombosis (Fig. 1) that cannot always be attributed to technical errors, see, e.g., the results of the multidisciplinary experimental-computational study [1].

Because of the non-negligible role of haemodynamics in the development of thrombosis, the present study aims to provide an insight into the postsurgical development that includes the formation of blood clots in interaction with flowing blood in small- and middle-sized vessels. For this purpose, a computational model of flow-mediated thrombosis is proposed and tested for selected postsurgical geometries of reconstructed portal veins obtained from experimental animals (piglets), see [1].

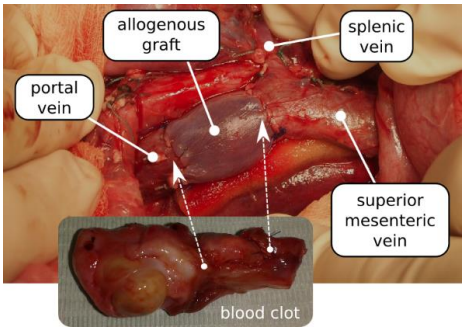

Figure 1: Example of an experimental portal vein reconstruction with an allogeneic porcine graft.

Methods

Compared to other similar studies, the proposed computational model of blood clotting is comprised of three linked submodels describing the processes of platelet plug formation, hemocoagulation and fibrin polymerisation. The governing equations of the first two submodels are inspired by the continuous model of platelet aggregation introduced in [2] and by the chemical interaction of clotting factors expressed through a system of convection-diffusion-reaction equations [3]. The submodel of fibrin clot formation is based on the Smoluchowski coagulation-fragmentation equation and is made up of an infinite system of differential equations for fibrin chains [4] that is modified by the method of moments [5]. The thrombosis model and the two-way interaction model between the portal haemodynamics and the growing blood clot are implemented and numerically solved in the Ansys Fluent software.

Results and Discussion

Assuming hepatopetal blood flow modulated by respiration, the thrombosis in the postsurgical portal vein geometries is triggered by low concentrations of the tissue factor–factor VIIa complex located at one or both anastomosis (injury) sites (Fig. 2). In line with expectations, the obtained numerical results highlighted the key role of vascular geometry and the influence of chemical and haemodynamic stimuli on the thrombosis process. They also provided additional information on the evolution and structure of blood clots, which showed a strong tendency to fill out adjacent low-flow zones of implanted grafts (Fig. 2).

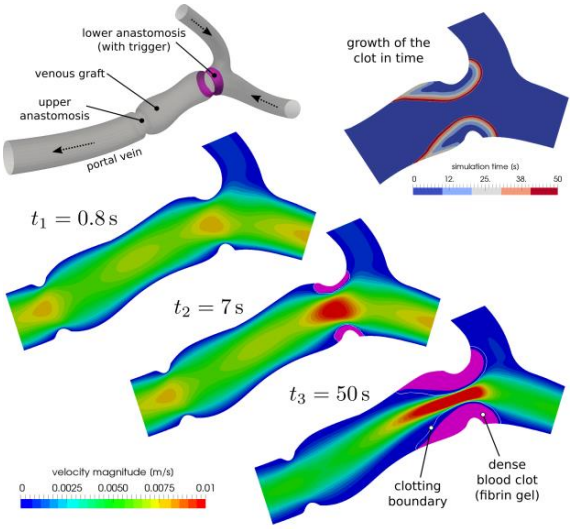

Figure 2: Fibrin clot formation at selected times.

References

1. Pálek R. et al, Anticancer Res, 39:6603-6620, 2019.
2. Link K. et al, Multiscale Model Sim, 18:1489-1524, 2020.
3. Biasetti J. et al, Front Physiol, 3:266, 2012.
4. Rukhlenko O.S. et al, PLOS One, 10:e0134028, 2015.
5. Mastan E. et al, Eur Polym J, 68:139-160, 2015.

Acknowledgements

The study was supported by the European Regional Development Fund-Project "Application of Modern Technologies in Medicine and Industry" (No. CZ.02.1.01/0.0/0.0/17_048/0007280).

COMPUTATIONAL MODELING OF TOXIN TRANSPORTERS IN A BIO-ARTIFICIAL KIDNEY

Jasia King, Sangita Swapnasrita, Stefan Giselbrecht, Roman Truckenmüller, Aurélie Carlier
MERLN Institute for Technology-Inspired Regenerative Medicine, Maastricht University, the Netherlands

Introduction

Millions of people worldwide suffer from varying stages of kidney disease. Regrettably, kidney transplantation is not possible for all. Consequently, dialysis is offered as a bridge-to-transplantation option. Protein-bound uremic toxins (PBUT) accumulate in the patient's system due to their high affinity to large serum protein such as albumin resulting in a large molecular weight complex that cannot be removed by ultrafiltration[1]. Epithelial transport of PBUTs in the proximal tubule is predominantly performed by organic anion transporters (OAT). The complex binds to the OATs, and albumin is released back to the bloodstream. The toxin unbinds from the transporter and is transported across the cell basolateral membrane. Often in toxin-transport modelling, the transport steps are lumped together to model the overall removal of the toxin[2]. We have modelled the individual toxin transport steps to bring more insight into the influence of the transporters' activity and density on toxin transport when these are decoupled from each other.

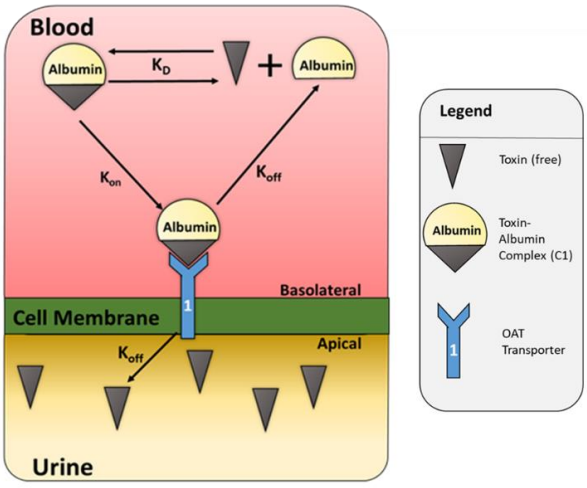

Figure 1: Kinetic model for binding of toxin, albumin and transporters in the proposed computational model.

Quantity	*Value used*
K_{on} *(Binding rate to OAT)*	*0.5* $(\mu M^{-1}s^{-1})$
K_{off} *(Unbinding rate from the complex-OAT across the cell basolateral membrane)*	*10* (s^{-1})
K_{rev} *(for both)*	*0.0*

Table 1: Parameter values for binding and unbinding rates. Toxin is assumed to be initially bound to albumin.

Methods

Equation based modelling of the kinetic binding system was developed using Virtual Cell- an open-source platform for computational modelling of biological systems[3]. The initial toxin concentration was fixed at 1 µM, the binding rates and initial OAT concentration was calibrated using *in vitro* data. The influence of channel length, transporter density, albumin concentration, toxin generation on the rate at which the toxin was transported into the apical compartment was investigated.

Results

We have shown that the final toxin concentration saturates after a specific increase in both the transporter uptake activity and density but increases steeper with the latter. It affirms that transporter activity and density are both essential to toxin transportation.

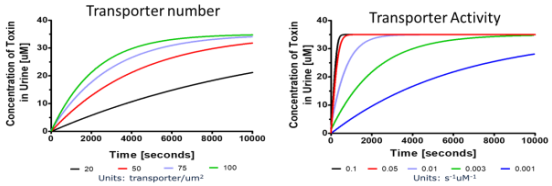

Figure 2: Influence of tranporter density (20, 50, 75, 100 molecules/µm²) and transporter activity (0.001, 0.003, 0.01, 0.05, 0.1 $\mu M^{-1}s^{-1}$*). The toxin removal increases with increase with both parameters.*

Conclusion

Independent kinetic modelling of transporters offers a more accurate portrayal of the toxin removal process by showing the competitive binding between multiple toxins and provides interesting avenues to inform organ-on-chip development.

References

1. Jansen J, Jankowski J, Gajjala PR, Wetzels JFM, Masereeuw R. Disposition and clinical implications of protein-bound uremic toxins. Clin Sci [Internet]. 2017;131(14):1631–47.
2. Eloot S, Schneditz D, Cornelis T, Van Biesen W, Glorieux G, Dhondt A, et al. Protein-bound uremic toxin profiling as a tool to optimize hemodialysis. PLoS One. 2016;11(1):1–18.
3. Blinov ML, Schaff JC, Vasilescu D, Moraru II, Bloom JE, Loew LM. Compartmental and Spatial Rule-Based Modeling with Virtual Cell. Biophys J. 2017;113(7):136 72.

Acknowledgements

This work is supported by the partners of RegMed XB and Powered by Health~Holland, Top Sector Life Sciences & Health.

A COMPUTATIONAL MODEL OF PROSTATE CANCER BONE METASTASIS GROWTH AND RESPONSE TO RADIUM223

Luca Marsilio (1), Michele Grimaldi (1), Pietro Cerveri (1), Eleonora Dondossola (2), Stefano Casarin (3,4,5)

1. Department of Electronics, Information and Bioengineering, Politecnico di Milano, Italy; 2. GU Medical Oncology, The University of Texas MD Anderson Cancer Center, Houston, TX; 3. Dept. of Surgery, Houston Methodist Hospital, Houston, TX; 4. Center for Computational Surgery, Houston Methodist Research Institute, Houston, TX; 5. Houston Methodist Academic Institute, Houston, TX

Introduction

Radium223 (Rad223) is an alpha emitter that localizes in bone upon systemic injection and has emerged as the first bone-targeting agent showing an overall survival improvement in patients with advanced metastatic prostate cancer [1]. Its direct toxicity on cancer cells has been detected after high-dose application *in vitro*; however, the relevance of this effect *in vivo* remains unclear and clinical response is often followed by relapse and disease progression [2]. Since research efforts require a significant investment both in time and resources, computational models, integrated with experimental data, can support scientists in preclinical studies and lead them towards more promising therapeutic approaches. Accordingly, we developed an Agent-Based Model (ABM) of pre-established prostate cancer lesion in bone and applied this platform to test Rad223 outcome throughout a defined follow-up time. We identified maximum Rad223 efficacy towards micro lesions, which was further confirmed by *in vivo* validation.

Materials and Methods

The model, implemented in Matlab®, was integrated with *in vivo* data retrieved from multiphoton microscopy experiments. The ABM lays on a hexagonal grid where each site corresponds to a single cell endowed with individual probabilities of mitosis, apoptosis and interphase status. In Control regimen, a random spatial distribution was assigned to these events. In Rad223 regimen, the spatial- (maximum efficacy within 100 μm of distance from bone) and time- (half-life 11.4 days) dependent effects of this agent were integrated in the model by modulating the probabilities with a logistic and an exponential function, respectively [3]. In both procedures we used a Monte Carlo simulation to define which cell undergoes mitosis and apoptosis at the end of its cell cycle. Finally, the ensemble of the cellular events over a follow-up time of $T = 15\ days$ determines tumor regression, persistence or progression.

Results

We validated our model by comparing the temporal dynamics of tumor growth *in silico* (Fig. 1 – red line) with *in vivo* data retrieved from dedicated experiments (Fig. 1 – black line). We obtained a high level of confidence with a percentile normalized root mean squared error of 1.7% and with the *in silico* trend fully matching the *in vivo* within its standard deviation range.

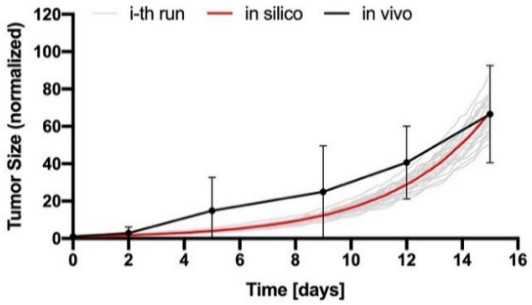

Fig. 1: in silico model validation – tumor growth in vivo (black) compared to in silico simulation output (red).

We then investigated the effect of an increasing initial tumor size on Rad223 efficacy spanning across micro- (elliptical shape with axis of [2x1], [8x7] pixels), middle-sized ([64x53], [128x106]), and macro-lesions ([256x213], [500x416]). As shown in Fig.2, the optimal response was recorded towards micro-lesions where the ΔSize between control and treated regimen was maximum. This evidence was then validated *in vivo* [3].

Conclusions

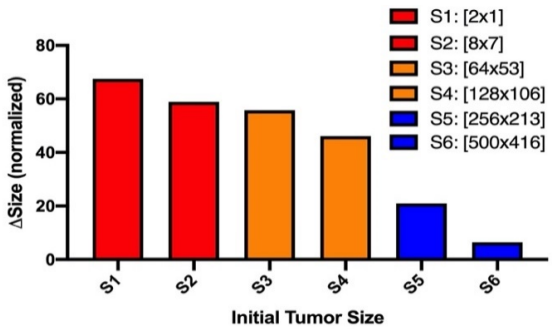

Fig. 2: in silico predictions. Quantification of the difference in tumor's size (normalized on its initial value) under Rad223 treatment for each initial size of interest. In red: micro lesions; in orange: middle-sized lesions; in blue: macro lesions.

The proposed model identified micro-tumors as the best target for Rad223-based therapies in terms of tumor regression. Aspects influencing tumor's dynamics and response to treatments will be addressed in future developments, as well as the potential to test additional bone targeting agents, including other radiopharmaceuticals or bisphosphonates.

References

1. Parker, CS et al., N Engl J Med, 369: 213-23, 2013
2. Suominem, MI et al., JNCI, 105:908-16, 2013
3. Dondossola, E et al., JNCI, 111(10):1042-1050. 2019

BIOMECHANICAL LINK BETWEEN RED BLOOD CELL DYNAMICS AND VASCULAR REMODELLING DURING ANGIOGENESIS

Qi Zhou (1), Lowell T. Edgar (2), Timm Krüger (1), Miguel O. Bernabeu (2)

1. School of Engineering, Institute for Multiscale Thermofluids, The University of Edinburgh, UK; 2. Centre for Medical Informatics, Usher Institute, The University of Edinburgh, UK. Email:g.zhou@ed.ac.uk

Introduction

Sprouting angiogenesis is an essential vascularisation mechanism consisting of two well-differentiated phases: sprouting and remodelling. The remodelling phase was revealed to be driven by rearrangements of endothelial cells (ECs) within the primitive vasculature in response to flow-induced wall shear stress (WSS) [1]. However, the role of red blood cell (RBC) dynamics during this process remains unknown. In this work, we aim to simulate blood flow as a suspension of RBCs within developing vasculature for characterisation of the RBC dynamics in the context of angiogenic remodelling.

Methods

Confocal images of mouse retina stained for ICAM2 (luminal reporter) and Collagen IV (labelling matrix sleeves) were obtained. The Col.IV images were used to reconstruct the flow domain [2] and the ICAM2 images used to assess the state of remodelling (Figure 1B). We simulated cellular blood flow within selected regions of interest (ROIs) as a suspension of deformable RBCs using the Lattice Boltzmann and Immersed Boundary methods implemented in the software package *HemeLB* (access via https://github.com/hemelb-codes/hemelb). Inflow/outflow boundary conditions for each ROI were specified based on a whole-plexus simulation assuming generalised non-Newtonian blood rheology (Figure 1A).

Results

Our image-based 3D simulation of microvascular blood flow predicted volume flow rates, RBC velocities and RBC fluxes showing good agreement with recent in vivo measurements from mouse retina [3]. A striking finding from the simulations was the high-level heterogeneity of RBC perfusion in primitive vascular networks (Figure 1C). Furthermore, we uncovered a strong association between vessel regression/stenosis and RBC depletion (Figure 1D), which was attributed to the plasma skimming effect through evaluation of our simulation data against an established empirical model [4].

Discussion

This study proposes a new mechanism for the enhancement of WSS differences driving vascular remodelling in angiogenesis via the highly heterogenous dynamics of RBCs within the primitive plexus, which are capable of locally modulating the effective viscosity. Additionally, we speculate with these findings that vascular remodelling is driven on the principle of removing RBC-depleted vessels from the primitive vasculature towards an optimised network that avoids portions of the tissue being vascularised but with poorly oxygenated blood.

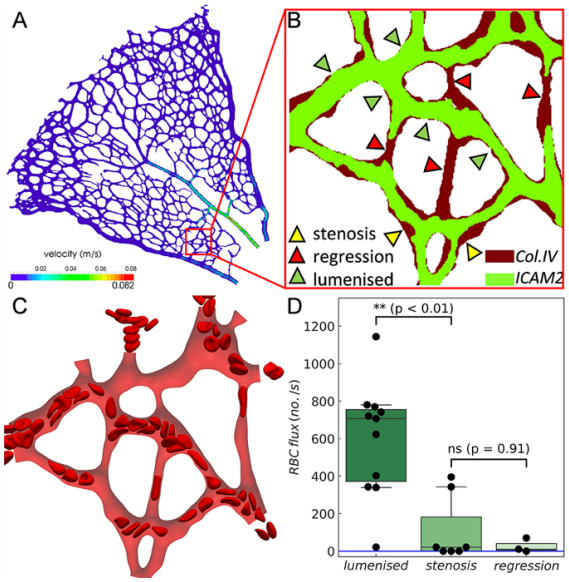

Figure 1: Simulation of RBC flow in developing plexus of mouse retina. (A) Velocity patterns from a whole-plexus simulation using a generalised non-Newtonian blood rheology model. (B) Overlaying ICAM2 over the Col. IV map indicates areas of vessel lumen, stenosis (an intermediate step of regression [1]), and regression. (C) Example of heterogenous RBC flow in a retinal ROI. (D) Association between RBC depletion (low/negligible RBC fluxes) and vessel stenosis/regression.

References

1. Franco et al, *PLoS Biol*, 13(4):e1002125, 2015
2. Bernabeu et al, *Biophys J*, 114(9):2052–2058, 2018
3. Joseph et al, *eLife*, 8:e45077, 2019
4. Pries et al, *Microvasc Res*, 38(1):81–101, 1989

Acknowledgements

We thank the laboratory of Prof. Holger Gerhardt at the Max Delbrück Center for Molecular Medicine in the Helmholtz Association (Berlin, Germany) for the experimental data enabling this study. This work was supported by a Transatlantic Network of Excellence grant (17 CVD 03, https://www.mdc-berlin.de/leducq-attract) from the Leducq Foundation. Supercomputing time on the ARCHER UK National Supercomputing Service was provided by the "UK Consortium on Mesoscale Engineering Sciences (UKCOMES)" under the EPSRC Grant No. EP/R029598/1.

NETWORK MODELLING OF ARTICULAR CHONDROCYTE MOLECULAR REGULATION IN HEALTH AND OA

Maria Segarra-Queralt, (1), Michael Neidlin (2), Gemma Piella (1), Laura Tio (3), Leonidas Alexopoulos (2), Miguel Ángel González-Ballester (4), Jérôme Noailly (1)

1. BCN MedTech (Universitat Pompeu Fabra), Spain; 2. Department of Mechanical Engineering, National Technical University of Athens, Greece; 3. IMIM, Spain 4. ICREA, Spain

Introduction

Pharmacological treatments for osteoarthritis (OA) are based on painkillers, and none can stop OA progression because mechanisms that control the pathophysiology are not well understood. However, overstimulation of catabolic events of cartilage chondrocytes (CC) compared to the biosynthetic activity is common in OA. To enable mechanistic explorations of key molecular players, we propose a network-based model of CC that incorporates the action of key inflammatory mediators at cell level, often reported in OA. The model was further calibrated against experimental data.

Methods

We selected OA-related interactions through careful examination of 63 expert journal articles. An initial CC model based on an OA-specific protein interactome (IOA) was developed. Anabolic interactions not related to OA were further included by enriching the interactome (ENR) with the high throughput tool STRING. The interactomes consisted in a set of nodes, related to each other through a specific topology of activating and inhibiting links. They were translated into a semi-quantitative mathematical model thanks to a system of differential equations that converges to steady stable states (SSS)[1]. These represent patrons of cell expression as systematic descriptions of CC regulation by microenvironmental cytokines. The ENR model was calibrated against experimental data[2] by minimizing the mean absolute difference (MAD) between predicted and measured molecules through a genetic algorithm (GA), giving a new network topology (OPT). The latter was validated against independent experimental data[3] and assessed qualitatively in terms of prediction of expected SSS in diverse anabolic and catabolic environments. As proof of concept, an OA treatment based on anti-inflammatory cytokines[4] was eventually simulated.

Results and Discussion

Independent validation showed that the OPT model reduced MAD to 0.0239, against 0.3412 for the ENR model. Fig. 1 shows the change of topology between the IOA and the OPT models. Qualitative evaluation of the OPT against literature knowledge led to 87% accuracy.

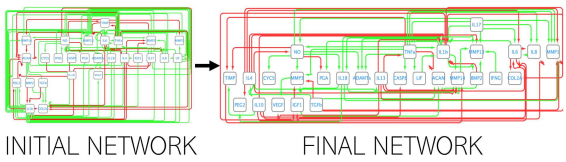

Figure 1: Initial vs final networks topology.

Analysis of the network basal SSS without any imposed perturbation (Fig. 2, blue), revealed that the IOA model was catabolic per-se. In contrast, the OPT and the ENR networks were anabolic by default, with low levels of MMP expression and high levels of anabolic markers. When the networks were perturbated with pro-inflammatory stimuli (Fig. 2, orange), t-tests (α=0.05) revealed no significant differences of the perturbed vs basal responses in the IOA model. In contrast, the OPT network was able to shift from its anabolic basal state to catabolic node activity.

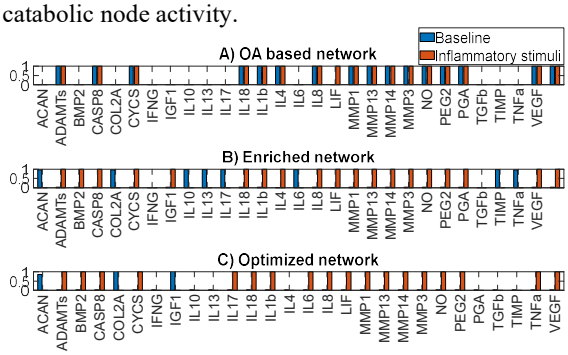

Figure 2: SSS of the base (blue) and the inflammatory stimulation (orange) of the OA based network (A), the enriched network (B) and the optimized network (C).

When the OPT model was initially stimulated to be catabolic and further perturbed with anti-inflammatory cytokine to simulate OA treatment based on biologics[4], predictions were consistent with the experimental results: matrix degradation (ADAMTS, MMP), pain mediators (PEG2, VEGF) and hypertrophy markers (MMP13, BMP2) were reduced, but cartilage matrix was not restored, highlighting the challenge to regenerate the cartilage. A CC regulatory network that maps measurable inflammatory mediators was successfully developed. Guided network enrichment and topology optimization defined a viable strategy to achieve a predictive CC regulation model and explore mechanistically anti-degenerative therapies.

References

1. Mendoza et al, Theor Biol Med Model, 3:1-13, 2006.
2. Melas et al, Sci. Rep; 9:151-176, 2019.
3. Neidlin et al, Osteoarthr. Cartil; 22:509-518, 2014.
4. Richards et al, The Phys Sports Med 44: 101-108, 2016.

Acknowledgements

Spanish (HOLOA-DPI2016-80283-C2-1/2-R, RYC-2015-18888) and Catalan (FI grant) Governments; European Commission (Disc4All-H2020-MSCA-ITN-ETN-2020-955735).

ON PARAMETER FITTING FROM IN VITRO IMAGES OF CELL BEHAVIOR. A DEEP LEARNING APPROACH

Marina Pérez-Aliacar (1), Jacobo Ayensa-Jiménez (1), Mohamed H. Doweidar (1,2), Manuel Doblaré (1,2,3)

1. Aragón Institute of Engineering Research (I3A), University of Zaragoza, Spain
2. Centro de Investigación Biomédica en Red en Bioingeniería, Biomateriales y Nanomedicina (CIBER-BBN)
3. Aragón Institute of Health Research (IIS Aragón)

Introduction

Glioblastoma (GBM) is the most lethal primary brain tumor, and unfortunately also the most common. Its evolution is complex, being lack of oxygen (hypoxia) one of the main driving forces of its aggressiveness.

The response of GBM cells to hypoxia follows the so-called *go or grow* paradigm, which states that cell resources are consumed either in proliferation or in migration [1], depending on whether oxygen concentration is above or below a hypoxia threshold, respectively. This threshold, together with the proliferation and migration rates, characterize the invasion properties of the tumor, being, therefore, determinant for the patient prognosis. However, the intra and interindividual variability inherent to any biological parameter makes it impossible to determine universal values for these parameters.

Computational techniques have a great potential for the study of cancer, being able to test new hypotheses in a cheap way and to answer *what-if* questions, that are sometimes impossible to reproduce experimentally due to technical or ethical reasons. However, thanks to the flexibility and miniaturization of microfluidic devices, a huge amount of data can be generated nowadays, enabling us to study these types of problems from a data science perspective.

In this work, we focus on the prediction of the parameters regulating the *go or grow* tumor behavior from images of microfluidic devices. The long-term aim is the development of a patient-specific tool, able to predict the tumor evolution from a patient sample grown on a chip.

Methods

In our microfluidic experiments, GBM cells were seeded within a central chamber with controlled oxygen provision through two lateral channels. Fluorescence images were obtained and processed to obtain the profiles of live and dead cells, which are the input to our deep learning model.

A convolutional neural network (CNN) was then built to predict, from a chip image, the non-dimensional parameters describing the proliferative and migrative behavior of the tumor, namely proliferation rate (G), migration rate (K), and hypoxia threshold (K).

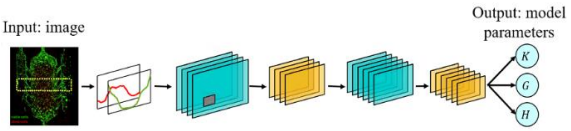

Figure 1: CNN scheme for predicting model parameters from culture image

The training dataset was generated employing a dimensionless version of our previously published mathematical model [2], which is able to describe glioblastoma evolution in microfluidic devices.

Results

The developed model provides very accurate responses for all the parameters. In particular, the Pearson's correlation coefficient ρ, obtained from validation, is greater than 0.99 for all the parameters.

The network also proved to be robust under different starting values for the parameters while good agreement was found with the experimental data available.

Discussion

We have developed a new methodology based on deep learning, more precisely on convolutional neural networks. The model is trained by synthetic data that is obtained using a previously validated mathematical model of GBM invasion under hypoxic conditions. With this approach, the model parameters, that can be used to simulate the evolution and progression of the tumor, and eventually to make clinical decisions, can be obtained.

References

1. Hatzikirou et al, Math. Med. Biol., 29: 49-65, 2021.
2. Ayensa et al, Sci. Rep., 10(1):1-21, 2020.

Acknowledgements

The authors gratefully acknowledge the financial support from the Spanish Ministry of Economy and Competitiveness (MINECO) and FEDER, UE through the project PGC2018-097257-B-C31, the Spanish Ministry of Science and Innovation through the project PID2019-106099RB-C44/AEI/10.13039/501100011033 and the Government of Aragon (DGA).

PATIENT-SPECIFIC VASCULAR MODELS FOR HANDS-ON TRAINING IN TRANSCATHETER OPERATIONS

F. Perico (1), M. Jaworek (1), E. Salurso (1), G. Gelpi (1,2), F.A. Viola (3), M. Caironi (3), G.B. Fiore (1), R. Vismara (1)

1. Department of Electronics, Information and Bioengineering, Politecnico di Milano, Milan, Italy;
2. Cardiovascular Surgery Department, ASST Fatebenefratelli Luigi Sacco University Hospital, Milan, Italy;
3. Center for Nano Science and Technology @PoliMi, Istituto Italiano di Tecnologia, Milan, Italy

Introduction

The diffusion of new transcatheter approach to treat heart pathologies goes hand in hand with the need for surgeons to acquire new skills, other than those involved in conventional open-heart surgery. In this context, the need for an adequate surgical training phase is growing. If carefully designed, in vitro simulators can provide realistic platforms for training operators in these challenging procedures.
We aimed to design and develop training-oriented vascular models with realistic anatomy and haptic feedback.

Methods

A computer tomography image derived from a female patient with aortic arch aneurysm was used as a starting point.
Semi-automatic segmentation of the aorta and common iliac arteries was performed using ITK-SNAP software to obtain a 3D computational model (Figure1-A).
The model was used to design the internal and external mold through CAD modelling (Fusion 360, Autodesk) (Figure1-B).
The molds were 3D printed (Ultimaker 3, Ultimaker B.V.) by PLA (Figure1-C); the surfaces were cured by sanding and covered with epoxy resin, in order to minimize the surface roughness of the vessel and obtain greater transparency of the polymeric model (Figure1–D).
Once this process was completed, the mold was assembled, and Sorta Clear 18 silicone (Smooth-On, Inc.) was injected into the mold. Polymerization at room temperature lasted for 24 hours (Figure1-E).
Two models were obtained. The inner surface of one model was coated with Parylene-C [1] in order to improve the haptic feedback during the insertion of endovascular instruments, by reducing friction (Figure1-F).

Results

Figure 2 shows one of the two silicone models that were used to simulate a transcatheter procedure by an experienced operator. The test involved the insertion in the phantoms of a guide wire (0.35mm), a catheter pigtail (6Fr) and the delivery system of Medtronic (Enveo) Evolut R TAV.

The haptic feedback during the procedure in the Parylene-coated model was considered more realistic than those with the uncoated model.

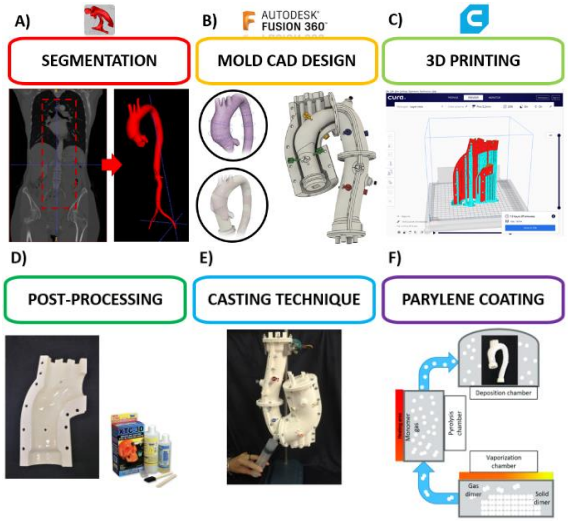

Figure 1: Workflow process for patient-specific vascular model.

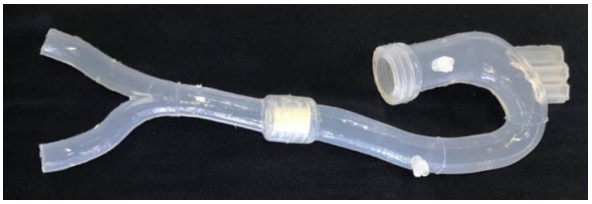

Figure 2: Patient-specific silicone model obtained with the described method.

Discussion

The proposed method is an effective way to produce patient-specific, transparent vascular models with silicone casting technique. The silicone models are a promising tool for realistic surgical trainings in transcatheter procedures.

References

1. Cosseddu, P., et al. “Tactile Sensors With Integrated Piezoelectric Polymer and low voltage Organic Thin-Film Transistors” 13th IEEE Sensors Conference, SENSORS 2014, Valencia 2-5 November 2014.

EXTRUSION BIOPRINTING: SIMULATIONS FOR CELL VIABILITY ASSESSMENT

Gianluca Santesarti (1), Michele Marino (1), Francesco Viola (2), Roberto Verzicco (3), Giuseppe Vairo (1)

1. Department of Civil Engineering and Computer Science, University of Rome "Tor Vergata", Italy;
2. Gran Sasso Science Institute, L'Aquila, Italy;
3. Department of Industrial Engineering, University of Rome "Tor Vergata", Italy;

Introduction

The final outcome of extrusion-based bioprinting procedures is highly affected by a number of process variables, such as bio-ink properties, nozzle diameter and extrusion pressure [1]. Introducing in silico (computational) models as an integral part of the bioprinting design pipeline would allow to increase innovation, productivity, scalability and robustness. To date, simulations are not employed in the field since theoretical and computational models for describing the physicochemical mechanisms occurring during/after bioprinting are not available or refined enough for giving quantitative predictions. The objective of this work is to develop a computational model for the extrusion of non-Newtonian shear-thinning hydrogels with a cellular component. In fact, cell densities affect both the extrusion flow rate and the final cell viability. The aim is to explicitly describe the extrusion of cells through the nozzle, predicting the cellular membrane stresses during the process which are related to the cell damage or apoptosis [2].

Methods

Since the multiscale dimensionality of the problem due to the different magnitude orders between the extruder, the micro-nozzle and the printed cells, an adimensional computational framework based on immersed boundary formulation has been employed [3]. Furthermore, to take into account the significant cell deformations within the hydrogel during the printing process, a moving-least-squares method has been implemented in order to accurately reproduce the fluid-structure-interaction [4].

Results

As a first case study, this work addresses the case of a single cell immersed in the hydrogel, flowing through different nozzle reference geometries. In Fig. 1. are reported the velocity field along the zx plane and the cell shear stress field in a convergent-shaped nozzle at adimensional time $t^* = 2$. In Fig. 2 is reported the cell shear load evolution during the extrusion acting on the whole cell surface. Due to the gradient velocity increase, as the cell approaches to the nozzle throat section, the shear stress rises, as highlighted by the peak in Fig. 2. Then, it sharply decreases in the constant cross section zone and in the outflow region.

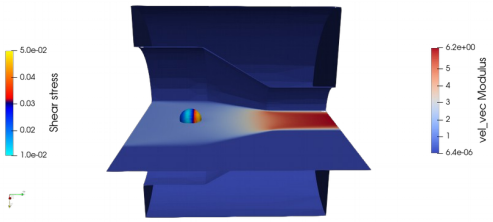

Figure 1: Velocity field along the zx plane and cell shear stress field in the convergent-shaped nozzle at time $t^* = 2$.

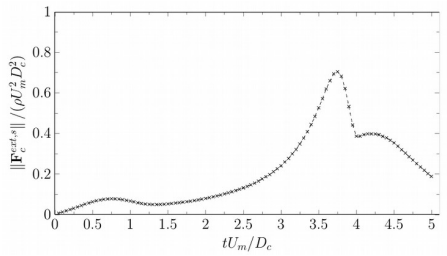

Figure 2: Shear load evolution on the cell during the extrusion through the convergent-shaped nozzle.

Discussion

The proposed model is a first step towards a predictive tool for the optimal setting of process variables in bioprinting. Through this computational framework, it would be possible to investigate for example the optimization of hydrogels material properties and of nozzle geometries, in order to guarantee a delicate balance between the biological requests of high cell density and viability and the engineering constraint of bio-inks printability.

References

1. Ozbolat, I. T., Hospodiuk, M., Biomaterials, 76: 321-343, 2016.
2. Chang, R. et al., Tissue Eng., Part A 14.1: 41-48, 2008
3. Fadlun, E. A., et al,, J. of Comp. Physics 161.1: 35-60, 2000
4. de Tullio, Marco D., Pascazio G. J. of Comp. Physics 325: 201-225, 2016

FABRICATION BY TWO PHOTON POLYMERIZATION OF 3D BIOCHIPS FOR CELL MOTILITY STUDIES

Federico Sala (1,2), Carlotta Ficorella (3), Rebeca Martínez Vázquez (2), Josef A Käs (3), Roberto Osellame (2,1)

1. Department of Physics , Politecnico di Milano, Italy; 2. Istituto di Fotonica e Nanotecnologia (CNR), Italy; 3. Peter Debye Institute for Soft Matter Physics, Leipzig University, Germany

Introduction

Cell migration constitutes one of the main process in pathology on multicellular organisms and it is strongly affected by extracellular environment, like in case of metastasis infiltrations. In particular, mechanical and topological constrains influences cellular migration velocity and strategies [1]. Standard analysis methods consist in studying the chemotaxis on specific cells through porous media, but these techniques neither allows the complete visualization of the cell during the motion, nor permits the design of the extracellular matrix to induce specific types of stimuli. In this framework, micro-additive manufacturing techniques, like two photon polymerization (2PP), allows the fabrication of three-dimensional structures for controlled cell migration onto optical accessible substrates [2-3].

In our work we present the fabrication and validation of a microfluidic platform for controlled cell motility analysis that allows live-imaging during the migration. The specific design of the device can be easily tailored on the cell type, thanks to the versatility of 2PP microfabrication technique. We used our biochip to characterize the migration of murine neuronal cancer cell under high physical confinement.

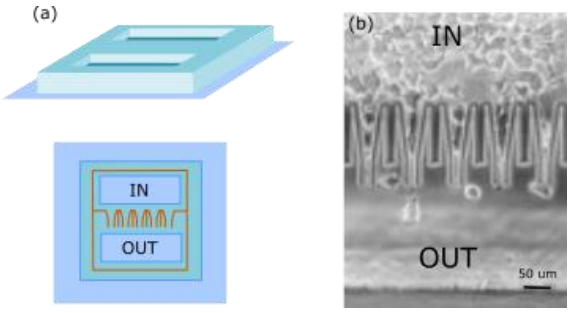

Figure 1: (a) Scheme of two possible biochip design; (b) microscope image of cell migration assay

Methods

The device consists in a deposition chamber and one or more recollection chambers, connected by a migration channels where engineered microconstrictions are placed. The constrictions have minimum dimension of about 3-7 μm, in order to simulate a high confinement environment.

The biochip has been realized with a hybrid technique combining glass microstructuring and 2PP, using femtosecond laser direct writing [3]. It consists in a multilayer structure: a main glass frame with the chambers; a polymeric film where the migration constrictions are realized; a microscope thin cover glass that allows complete optical accessibility. A scheme of the device possible designs is reported in Figure 1.

We used one specific device design to study the migration strategy of murine neuronal cancer cell. The cell line used was NG108-15, stained on filamentous actin and on nuclei in order to track both the cell outline and position during the migration. Regular culture medium was used during the migration assay.

Results

Our fabrication technique allows rapid prototyping and great freedom in the design and realization of the biochips. The number of reservoirs can be arbitrary chose. Here we present two types of device: a two-reservoir chip for live-imaging of cell migration and a five-reservoir chip, where a single inlet leads to 4 collection chambers, in order to parallelize multiple.

The shape of the constrictions can be chosen depending on the required physical stimulus. We successfully realized 4 different types of geometries as a proof of concept. The specific geometry used in our biological experiment consist in a funnel-like geometry with a minimum dimension of 5 μm and an appended tunnel structure, to apply a protracted compressive stress after the first deformation.

Our experiments show for the first time the highly invasive nature of NG108-15 cells, in a highly compressive and rigid environment. In particular, the microtubule-driven axon outgrowth seems to be quite active during the assay.

Discussion

We showed the possibilities offered by 2PP in terms of device design, realization and minimum features. We realized different devices, meant for different types of analysis. We successfully used one of these biochips to characterize neuronal cancer cell motility behavior, highlighting the possible role of axon in the migration strategy.

References

1. O. Ilina *et al*, *Nat. Cell Biol.*, 22:1103–1115, 2020.
2. A. K. Nguyen *et al*, Mater. Today, 20, 314–322, 2017.
3. C. Ficorella *et al*, *New J. Phys.*, 21, 2019.

3D BIOPRINTING OF HYDROGELS FOR RETINAL TISSUE ENGINEERING

Beatrice Belgio (1), Andrea Mantelli (1), Filippo Iervolino (1), Marinella Levi (1), Federica Boschetti (1), Sara Mantero (1)

1. Dept. of Chemistry, Materials, and Chemical Engineering "Giulio Natta", Politecnico di Milano, Italy

Introduction

Retinal diseases are the leading causes of vision-loss globally. Currently no effective treatments exist to restore normal retina function from lost vision.
Retinal tissue engineering may be helpful in providing better solutions. Conventional scaffold fabrication methods lack precision and are incapable to produce scaffold with complex designs [1]. Three-dimensional (3D) bioprinting can mimic the complex multilayered hierarchical architecture of the retina.
In this study, we present a strategy to develop a biomaterial ink suitable for retinal tissue engineering. Sodium alginate and gelatin were selected due to their high biocompatibility [2-3].

Materials and Methods

Three biomaterial inks (B1, B2, B3) were prepared combining sodium alginate (SA, SR00449, MP Biomedicals) and type B gelatin (G, G9391, Sigma) at different concentrations reported in table 1.

Biomaterial ink	SA concentration	G concentration	Mixing ratio SA:G
B1	4%	10%	50:50
B2	6%	10%	50:50
B3	4%	10%	70:30

Table 1: Concentrations (weight/volume) of SA and G in the inks.

A rotational rheometer (Discovery DHR2, TA Instruments) and an electromechanical testing machine (Bose EnduraTEC ELF 3200) were used to investigate rheological and mechanical properties of the inks, respectively.
A 20 mm x 20 mm x 0.2 mm cube was designed with Solidworks® and printed using an extrusion-based 3D bioprinter (INKREDIBLE+, Cellink) with a 22G conical nozzle. The printing speed was set at 15 mm/s for all the inks, whilst the printing pressure was optimized for each ink. Crosslinking was obtained after printing with a solution of calcium chloride.
The printed scaffolds, realized with B1, B2, and B3 inks, were characterized in terms of morphology with an inverted optical microscope (Eclipse Ti2, Nikon), repeatability, and swelling behavior. Regarding the repeatability of the printed grids, the difference between the pre-established and the effective measurements was estimated.

Results

The flow curves showed a shear thinning behavior for all biomaterial inks B1, B2, and B3. The yield stress increased when increasing SA concentration in the hydrogel. In addition, with the increase in SA concentration, an increase in compressive modulus was encountered demonstrating an improvement in the mechanical properties.
The optimized printing pressure for B1, B2, and B3 were 88 kPa, 120 kPa, and 100 kPa, respectively.
Results of repeatability suggested that the networks of B1 ink better maintained shape fidelity (Fig. 1A). These outcomes were confirmed by morphological analysis: filaments obtained with B1 ink were characterized by a more regular profile. Figure 1B displays the printed scaffold realized with B1 ink.

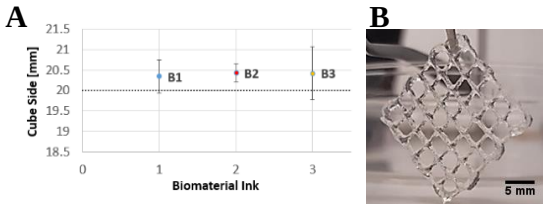

Figure 1: (A) Shape fidelity of scaffolds made of B1, B2, and B3 inks (dotted line is the pre-established side); (B) Scaffold made of B1 ink.

No statistical difference in the swelling behavior was found between the scaffolds made of B1, B2, and B3 inks (Fig. 2).

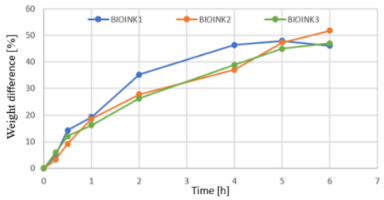

Figure 2: Swelling behavior of B1, B2, and B3 inks.

Discussion and Conclusion

The choice of the optimal SA and G blend, performed in this study, is the first step to obtain a suitable bioink with well-defined characteristics for retinal tissue engineering. Our findings showed that, among the three inks, B1 is the most promising bioink. The next step will be incorporating retinal cells in B1 ink.

References

1. P. Shi et al, Int J Bioprinting, 3:1-9, 2017.
2. J. Sun et al., Mater, 6: 1285-1309. 2013.
3. T. Jiang et al., Biofabrication, 12: 1-13. 2019.

TWO-PHOTON POLYMERIZATION OF SYNTHETIC SCAFFOLDS ON DEFORMABLE SUBSTRATES FOR MICROGRAVITY APPLICATIONS

A. Nardini (1), C. Conci (1), E. Jacchetti (1), G. Cerullo (2), R. Martínez Vázquez (2), R. Osellame (2), G. Ciofani (3), M. T. Raimondi (1)

1. *Department of Chemistry, Materials and Chemical Engineering "Giulio Natta", Politecnico di Milano, Milano, Italy*
2. *Istituto di Fotonica e Nanotecnologie (IFN)-CNR and Department of Physics, Politecnico di Milano, Milano, Italy*
3. *Istituto Italiano di Tecnologia (IIT), Smart Bio-Interfaces, Pontedera (PI), Italy*

I. Introduction

In the last two decades tumor research focused onto microgravity cell cultures, analyzing the epigenetic effects in malignancy cellular behavior [1]. Nowadays, no dynamic culture system in use with microgravity conditions showed the capability to generate truly in vitro 3D tissue models by having a controlled geometry at the cellular scale [2]. Those systems, engineered to reach orbiting laboratories, as the ones into the International Space Station, are limited to non-frangible substrates due to regulations.

II. Materials and Methods

Here, we developed synthetic 3D cell culture scaffolds for microgravity and zero-gravity applications with a resolution beyond the diffraction limit (~100 nm) [3], by two-photon polymerizing (2PP) a biocompatible photoresist [4, 5] on a commercial non-frangible cyclic-olefyn-copolymer as substrate (Figure 1).
The 3D model stability under the stress conditions involved by the flexibility of the substrate, was computationally evaluated first. Then, we developed a brand-new protocol for substrate preparation and polymerization.

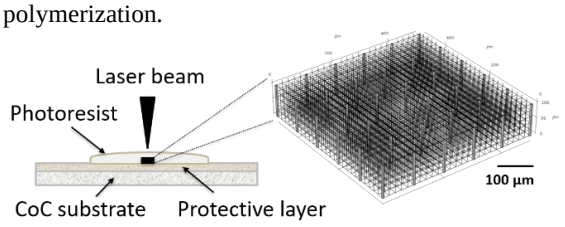

Figure 1: Qualitative representation of the study model.

III. Results

Scanning Electron Microscopy (SEM) inspections demonstrated stable 3D structures (Figure 2).
The computational simulations enhanced the possibility to scale up the process without compromising the microscaffolds stability (Figure 3).

IV. Discussion

As shown by the fabrication outcomes, this study proved the feasibility of the 2PP microfabrication of biocompatible scaffolds on deformable non-frangible substrates, thus representing a great promise in 3D cell culture substrates production for microgravity and zero-gravity applications.

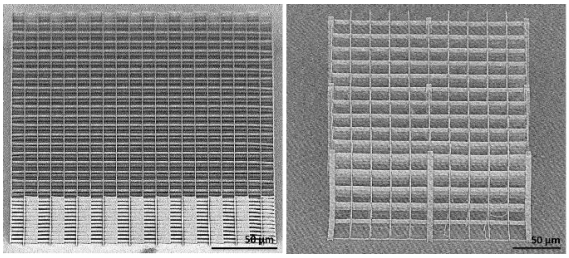

Figure 2: SEM acquisitions of the fabrication outcomes.

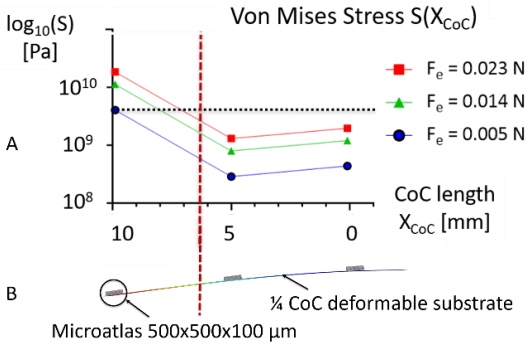

Figure 3: Von Mises Stress distribution involved in the scaffolds due to the CoC bending (A) and qualitative representation of the model (B)

References

1. G. G. Genchi *et al.*, *Nanomedicine*, vol. 13, 22:2821–2833, 2018.
2. S. L. Wuest *et al.*, *Biomed Res. Int.*, vol. 2015, 2015.
3. C. Conci *et al.*, vol. 3, 4:7–8, 2019
4. M. T. Raimondi *et al.*, *J. Appl. Biomater. Biomech.*, vol. 10, 1: 0–0, 2012.
5. C. N. LaFratta *et al.*, *Angew. Chemie - Int. Ed.*, vol. 46, 33: 6238–6258, 2007.

Acknowledgements

European Research Council (ERC projects NICHOID, G.A. 646990, NICHOIDS, G.A. 754467, and MOAB, G.A. 825159);European Commission (FET-OPEN project IN2SIGHT, G.A. 964481);European Space Agency (ESA project NICHOID-ET, G.A. 4000133244/20/NL/GLC); National Centre for the Replacement, Refinement and Reduction of Animals in Research (NC3Rs projects MOAB, G.A. NC/C01903/1 and NC/C019201/1); Italian Ministry of University and Research (MIUR-FARE project BEYOND, G.A. R16ZNN2R9K);Fondazione Social Venture Giordano Dell'Amore, Cariplo Factory, Politecnico di Milano, Fondazione Bassetti and Fondazione Triulza (S2P project EGGS&BEACON).

DESIGN, MANUFACTURING AND ASSESSMENT OF A CUSTOMIZED TI6AL4V TALUS PROSTHESIS THROUGH SELECTIVE LASER MELTING

Francesca Berti (1), Francesca Danielli (1), Adelaide Nespoli (2), Luigi La Barbera (1), Giulia Mancinelli (1), Gaia Motalli (1), Marco Cavicchio (1), Martina Colombo (1), Fabio Galbusera (3), Nicolò Martinelli (3), Tomaso Villa (1,3), Lorenza Petrini (4)

1. Department of Chemistry, Materials and Chemical Engineering "G. Natta", Politecnico of Milano (Italy); 2. CNR ICMATE, Lecco (Italy); 3. IRCCS Istituto Ortopedico Galeazzi, Milano (Italy); 4. Department of Civil and Environmental Engineering, Politecnico di Milano (Italy)

Introduction

Selective laser melting (SLM) is an established additive-manufacturing technology for the realization of custom-made implantable devices [1]. This could be an advantage in ankle replacement prostheses, where traditionally-manufactured implants are affected by a significant failure rate (50% at 5 years), especially for talus reconstruction devices [2]. Due to the talus' complex morphology and reduced dimensions, traditional surgical treatments aiming at substituting the whole bone are very invasive [3].
The current study proposes a new method for designing a custom-made device for talus resurfacing with a trabecular-like core, obtained through SLM of Ti6Al4V ELI powder. The workflow is also demonstrated on a clinical case with advanced talus arthrosis.

Materials and methods

A custom resurfacing prosthesis was designed starting from the reconstructed CT images of an arthrotic patient (Fig. 1,a). A multistructured implant was conceived. The external articular layer of the device was meant to be solid (Fig. 1,b). The inner core had a trabecular lattice structure to promote stability through trabecular bone ingrowth and implant osseointegration.
Two different lattice structures (A and B) were selected and designed with average strut diameter of 0.6 mm (Fig. 1,c). The samples' CADs were discretized to obtain a finite element (FE) model of the samples, which could support the device design and verification phases: 1D beam elements were used, allowing for a reduced computation time, while providing reliable information on detailed implant loadings. Simulations of compressive tests were performed on the samples to evaluate the maximum force before failure (Fmax), to choose the one capable of supporting at least 4 BW=3.2kN (in the average case of body mass of 80 kg) [4]. Moreover, the FE model was used to evaluate the stress distribution in the lattice. For validation purposes, three samples for each lattice design were produced in Ti6Al4V ELI (AM400, Renishaw plc.) and tested to assess the goodness of the simulations.

Results

All printed samples showed high density (>95%). From the dimensional analysis conducted on the samples, a variation of about ±4% compared to the average strut thickness was found and it was accounted in the FE models. Both the designs exhibited good resistance (Fmax: A=4.6kN, B=3.8kN), with a more homogeneous stress distribution in the Sample-B design. A good agreement between the numerical and experimental tests was found (Fig. 1,d).

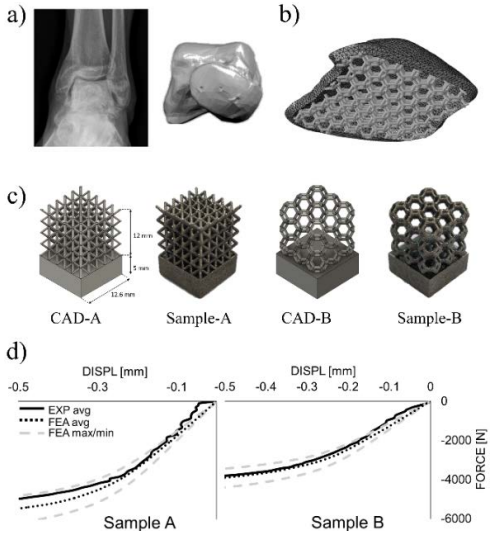

Figure 1: a) CT images and reconstructed geometry of the talus;b) schematics of the multistructured implant; c) different CAD and samples of the trabeculae; d) force-displacement plots after compressive tests

Discussion

The reduced computational approach was successful in supporting the design of the custom-made talus prosthesis. The FE model provided detailed results on the trabecular design which nicely agreed with the compressive tests. The very short computation time (few seconds on a standard PC), make this approach suitable to investigate alternative implant designs, while describing complex functional loadings.

References

[1] Trevisan et al., (2017), J Appl Biomater Funct Mater, 16(2):pp.57–67
[2] Bowes et al., (2019), Front Surg, 6(11):pp. 1–7
[3] Tracey et al., (2019), Foot Ankle Spec, 12(1):pp.39–48
[4] Fan et al., (2020), J. Orthop. Surg. Res, 15(1):pp. 1–8

IMPROVING SURGICAL OUTCOMES IN CRANIOFACIAL SURGERY BY MEANS OF BIOFIDELIC 3D PRINTED DIGITAL MATERIALS

Sara Ajami (1,2), Begona Garate Andikoetxea (1), Naiara Rodriguez-Florez (3,4), Juling Ong (2), Greg James (2), N U Owase Jeelani (2), David Dunaway (2), Silvia Schievano (1,2), Alessandro Borghi (1,2)

1. University College London, United Kingdom; 2. Great Ormond Street Hospital, London, United Kingdom; 3. Ikerbasque, Spain; 4. Universidad de Navarra, Spain

Introduction

Craniosynostosis (CS) is the premature closure of one or more cranial sutures leading to restricted skull growth and often neurological disorders [1]. Spring-Assisted Cranioplasty (SAC) is an established method for treating scaphocephaly in young children at Great Ormond Street Hospital, using stainless steel spring distractors [2]. Although the procedure is safe and effective, final head shape outcomes remain variable due to the lack of an accurate surgical tool to predict and plan head reshaping in infants. The aim of this project was to develop 3D printed patient-specific accurate models of infant skull using a biofidelic 3D printed digital material that replicates the mechanical behaviour of an infant skull to reliably predict surgical outcomes of SAC.

Methods

Specimens in Vero yellow, Rigur, Digital ABS Plus, and Durus were 3D Printed (Stratasys Connex 3 Objet260V, Stratasys Inc, Israel) in dumbbell (n=5) and rectangular shapes (n=5), and mechanically tested. Tests were carried out according to ASTM D638-14 and D790-04 for tensile and 3 point bending, respectively. Tensile and Flexural modulus were retrieved. Upon selection of a material, CT data were collected for 8 patients in order to create anatomical 3D models of the skull (Materialise Mimics®). Surgical cuts, as well as spring locations, were replicated from post-operative notes. Each model was 3D printed using the selected material to create a patient specific phantom. Two cranioplasty springs were inserted in each phantom, one anteriorly and one posteriorly (Figure 1) and the spring opening (OP_P) was retrieved for each 3D model, averaged and compared with measurements gathered during surgery (OP_M).



Figure 1: Phantom models of the skull with springs inserted.

Results

The tensile and flexural modulus of the tested materials are reported in Table 1. The elastic modulus of Vero yellow is close to that of unilaminar parietal bone (1.95 ± 0.56 GPa) measured by reference point indentation, therefore patient specific models were printed using this material. The recorded anterior and posterior average spring openings OP_P were 26.86 ± 3.24 mm and 27.02 ± 3.56 mm, while OP_M was 33.38 ± 2.67 mm for the anterior and 36.33 ± 4.24 mm for the posterior spring. When OP_P and OP_M for each patient were compared an error of 14.01±6.41% was found.

Material	Tensile Modulus (GPa)	Flexural Modulus (GPa)
Vero Yellow	2.28 ± 0.06	1.85 ± 0.002
Rigur	1.54 ± 0.05	1.25 ± 0.05
Digital ABS	2.07 ± 0.03	1.01 ± 0.02
Durus	0.785 ± 0.03	1.31 ± 0.02

Table 1: Tensile and Flexural modulus of 3D printed Stratasys materials.

Discussion

The development of a range of 3D printing techniques has proven useful to produce anatomical phantoms to understand physiology and test new medical devices. Here we developed a phantom model of an infant skull and used it to predict the outcome of SAC, with a prediction error of 14% when compared with surgical measurements. The main limitation of this work lies in the assumption of calvarial bone structure: the parietal bone in CS patients <1 year old is of either a trilaminar structure - composed of cortical bone and diploe - or a unilaminar diploe. Here we considered the bone as a unilaminar structure when printing all the phantom models. Moreover, the effect of sutures was neglected.
Our future work will include further refinements by mimicking patients' bone microstructure in the phantom model, to improve the prediction accuracy and move to clinical application as a predictive tool.

References

1. Morris LM et al, J Facial Plast Surg Clin, 24:517-530, 2016.
2. Rodgers W et al, Plast Reconstr Surg. 140(1):125-134, 2017

Acknowledgements

This work was funded by the Great Ormond Street Hospital Charity Clinical Research Starter Grant (award number 17DD46).

3D PRINTING AGAROSE: PARAMETERS EVALUATION

Ana M Teixeira (1), António André (1), Pedro Martins (2)

1. INEGI/FEUP, Portugal; 2. INEGI, Portugal

Introduction

3D printing is a growing technique that has recently been used in tissue engineering. Customized scaffolds with complex internal morphology and desired properties are produced in a layer-by-layer fashion from a computer aided design (CAD) [1]. The material printability (defined as the ability to form filaments and to incorporate cells at 15-37ºC [2]) and structural integrity after printed are key points influenced by viscosity, surface tension, cross-linking, among others factors [3]. Bertassoni et al. [4] found a direct correlation between printability and the hydrogel mechanical properties, by using methacrylated gelatin (gelMA) hydrogels. Murphy et al. [5] also focused in the printability of different hydrogels, concluding that the ones with higher viscosity, have more accurate results and the hydrogels with the lowest viscosity need a crosslink. Negrini et al. [6] investigated the potential of methylcellulose-based hydrogels as bioinks, optimizing its printing process. Hydrogels are used in soft tissue engineering since they mimic the natural extracellular matrix (ECM), presenting an inherently biocompatibility, low inflammation, and suitable mechanical properties [7]. Studies have successfully been developed by printing hydrogels, such as alginate, collagen, gelatin, chitosan, or agar, for skin, cartilage, cardiac, adipose or neural tissues for example [8].

Methods

Agarose is a hydrogel that is not often used either for 3D bioprinting or tissue engineering, however it seems to have good mechanical and biological properties for tissue engineering applications [9]. The 3D bioprinting process using agarose was optimized in this study by evaluation the influence of different parameters, such as printing pressure (40, 60, 80 and 100kPa), printing speed (1, 2, 4, 6, 8 and 10 mm/s), polymer concentration (1.5, 2 and 2.5%) and needle gauge (25, 27 and 30G). Agarose powder was dissolved in distilled water, then the solution was poured into the printer cartridge and printed at 40ºC, using an Inkredible+ printer (CellInk, Sweden). An alternating line was designed using SolidWorks with 10mm wide, 40mm long and the line diameter equal to the needle diameter. The gcode was obtained using Sli3er and the line height was defined as 0.4mm. The line thickness was measured using ImageJ and the root mean square (RMS) was calculated by equation 1:

$$RMS = \frac{1}{\sqrt{n}} \times \sqrt{\sum (t - t_i)^2} \qquad (1)$$

where n is the total number of points, t is the thickness in the CAD and t_i is the experimental thickness.

Results and Discussion

In the image below (Figure 1), it is shown an example of four alternating lines.

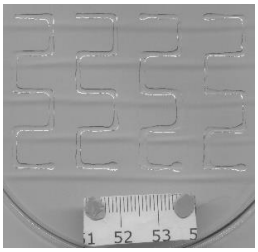

Figure 1: Printed alternating line with 80kPa, 25G and 8mm/s (first two lines) and 10mm/s (last two lines).

In each line, the thickness was measured at different points and the mean calculated. It was confirmed that the thickness decreases with the increase of velocity and needle gauge and with the decrease of pressure and agarose concentration.

Moreover, the error was measured using equation 1 and as expected the error decreases with the decrease of thickness. The error of the prints is inversely proportional to accuracy, i.e. lower errors correspond to higher accuracy and, hence, to the best printing parameters. Through the results, it is observed that the best printing combination for 1.5%, 2% and 2.5% of agarose concentration is, respectively: 100kPa, 10mm/s and 30G (error=0.860); 100kPa, 10mm/s and 27G (error=0.798); and 60kPa, 10mm/s and 25G (error=0.166). This shows that agarose is a printable hydrogel at different concentrations and under these experimental conditions, being a promising material to produce 3D bioprinted scaffolds for tissue engineering.

References

1. Chae et al, *3D Bioprinting for Reconstructive Surgery*. 15:305-353, 2018
2. Mouser et al, *Biofabrication*, *8*(3), 035003, 2016
3. Cleversey et al, *Micromachines*, *10*(8):501, 2019
4. Bertassoni et al, *Biofabrication*, *6*(2), 024105, 2014
5. Murphy et al, *J Biomed Mater Res*, *101A:* 272–284, 2013
6. Contessi Negrini et al, *Bioprinting*, *10*: 1–10, 2018
7. O'Halloran et al, *J Tissue Eng Regen Med.*, *12:* 2234–2247, 2018
8. Mandrycky et al, *Biotech Advances*, *34:* 422–434, 2016
9. Zarrintaj et al, *Carbohydrate Polymers*, *187*, 66–84, 2018

Acknowledgements

The authors gratefully acknowledge funding from FCT, Portugal, under grant 2020.08718.BD, and from project MImBI - PTDC/EME-APL/29875/2017 financed through FEDER and from research unit LAETA.

BIODEGRADABLE IMPLANTS FOR PELVIC ORGAN PROLAPSE REPAIR: 3D PRINTING AND CHARACTERIZATION

Rita Rynkevic (1), Maria Silva (2), Jorge Alves (3), Antonio Fernandes (4)

1. LAETA, INEGI, Faculty of Engineering, University of Porto, Portugal
2 LAETA, INEGI, Faculty of Engineering, University of Porto, Portugal,
3 LAETA, INEGI, Faculty of Engineering, University of Porto, Portugal
4 LAETA, INEGI, Faculty of Engineering, University of Porto, Portugal,

Introduction

Surgery is the mainstay of therapy for pelvic organ prolapse (POP) [1]. However, the use of meshes may cause graft related complications (GRCs). It is believed to be due to insufficient biocompatibility and inappropriate mechanical properties of these meshes, besides patient and surgeon factors [2]. Pore stability also plays an important role in tissue integration [2]. A completely different approach may be the use of non-textile biodegradable implants. Electrospinning, combined with 3D printing enables using biocompatible materials with personalized dimensions [3]. This research presents biodegradable polycaprolactone (PCL) novel implants for POP repair, produced using melt electrospinning technology; and preliminary mechanical behaviour and geometry deformation analysis results.

Materials and Methods

The polypropylene (PP) Restorelle mesh (for POP correction) will be used as a benchmark - it is a simple square-patterned mesh (2mm pore dimension), composed by 3 filaments with a diameter of 80µm knitted around each other. Simple square-shaped PCL meshes were produced, using own assembled melt electrospinning prototype: 3 layers of 80µm filaments; 1 layer of 240µm filament. A total of three specimens (60x8mm) were obtained for each mesh and tested by uniaxial tensile. Outcome measurements describing the mechanical behaviour were stress-strain curves. The comfort zone (physiological range of native tissue deformation) was defined for 10-20% of the total elongation. Digital camera records were used to analyse implant cell deformation.

Results

The printed implants had similar mechanical behaviour, despite differences in fibre diameter; however, mesh with 240µm filament diameter was stiffer ($p<0.05$) (Figure 1). Once the elastic deformation stage is completed, the plastic deformation dominates and a horizontal path is registered. The behaviour of the mesh prototypes is utterly distinct from Restorelle mesh ($p<0.05$). The printed meshes follow the biomechanical properties of native tissues more closely, unlike PP implant, particularly in the comfort zone. Geometry deformation analysis showed that PP mesh (Figure 2), had pore narrowing and hourglass effect, which possibly contributes to the emergence of associated GRC's. PCL printed mesh pores appear to be stable.

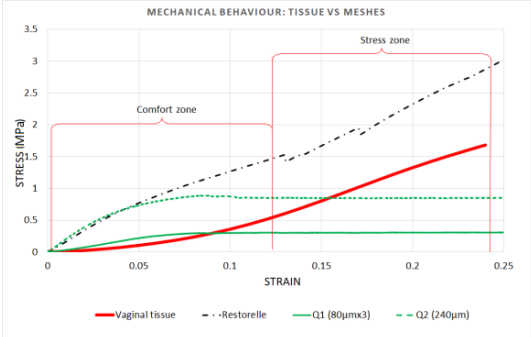

Figure 1: Mechanical behaviour of printed PCL meshes, Restorelle mesh and vaginal tissue

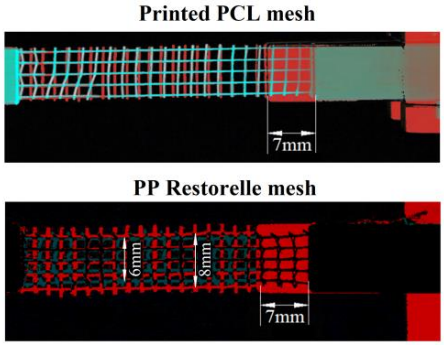

Figure 2: Mesh geometry deformation analysis: red-initial, blue and black- deformed.

Discussion

Printed implants match the natural tissues more closely and appear to be stable with no border curling and the hourglass phenomenon. The fact that the geometrical pattern and the fibre diameter were efficiently reproduced highlight the built prototype's success.

References

1. Geynisman-Tan, et al, Rambam Maim. Med J,8:2-7, 2017.
2. Barone W.R., et al, Am. J. Obstet. Gynecol, 215:1-9. 2016.
3. Wunner F., et al., In Comprehen Biomat II, 217–235, 2017.

Acknowledgements

The authors gratefully acknowledge the FCT, Portugal and POCI, the project SPINMESH - POCI-01-0145-FEDER-029232.

AN MRI-BASED PATIENT-SPECIFIC RCR ESTIMATION OF PULMONARY BIFURCATION USING IN-VITRO AND IN-SILICO APPROACHES

Benigno Marco Fanni (1-2), Emanuele Gasparotti (1-2), Emanuele Vignali (1), Claudio Capelli (3), Vincenzo Positano (1), Simona Celi (1)

1. BioCardioLab, Fondazione Toscana G. Monasterio, Italy; 2. Dept. of Information Engineering, University of Pisa, Italy; 3. Institute of Cardiovascular Science, University College of London, United Kingdom

Introduction

Cardiovascular Heart Diseases (CHDs) represent a huge portion of the cardiac pathologies among children, such as Pulmonary Artery (PA) defects like regurgitation and stenosis. In this context, there is lack of research works related to the investigation of the PA hemodynamics in pathological conditions using experimental and numerical methods. Such tools would enhance the spread of individualized healthcare, setting up patient-specific fluid dynamics simulations, both in-vitro, using ad hoc mock loop circuit (MLC) [1], and in-silico, with the advance of Computational Fluid Dynamics (CFD).
In this work, the PA, including its main branch with right (RPA) and left (LPA) arteries, was investigated. A specific Genetic Algorithm (GA) was developed to estimate the three-elements Windkessel (RCR) model based on patient-specific Phase Contrast Magnetic Resonance Imaging (PCMRI) data. This code took into account not only for the physiological pressure range, but also for the replica of the patient-specific right-left (R/L) flow split, thus providing specific RCR values for RPA and LPA.

Methods

A custom GA tool was developed to estimate two sets of patient-specific RCR values, one for each PA main branch (i.e. RPA and LPA), taking into account for the R/L flow split of the subject based on the individual PCMRI flow curve and pressure range. The outcomes of the code were validated using experimental tools and CFD simulations. In-vitro, an MLC was set up including a 3D printed phantom of a representative pathological PA (Figure 1a). The selection of the printed geometry was based on the statistical shape analysis performed on 3D-MRI images of a population of CHD patients (n = 21) affected by PA regurgitation. The custom piston pump [2] was used and opportunely programmed to provide an averaged pathological PA flow within the circuit. The inputted flow curve was adapted based on the mean flow obtained from the PCMRI data of the population. Pinch valves and compliance chambers were set according to the RCR values obtained from the GA code. In-silico, the experiment was replicated with a CFD simulation (LS-Dyna, LSTC, Livermore, USA). Same boundary conditions were imposed in terms of RCR values and input flow.

Results

The R/L flow split of the selected patient was 79-21%, as measured from PCMRI. Experimental and simulation results showed high agreement with the prediction of the GA (Figures 1b-c), demonstrating that the computed RCR values were suitable to provide the correct R/L flow split, both in-vitro and in-silico. Pressure were successfully replicated in a physiological range (5-25 mmHg).

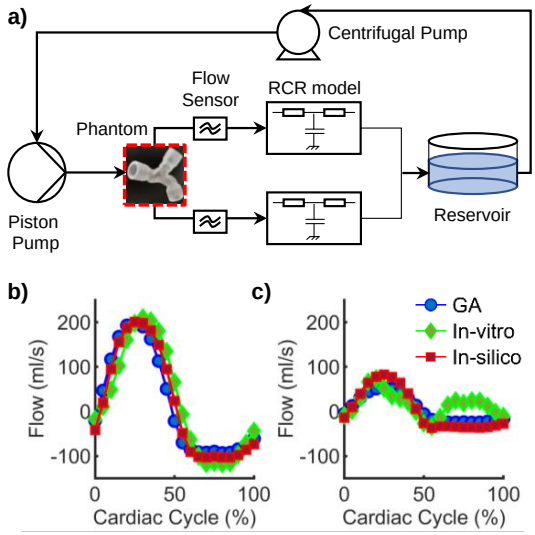

Figure 1: a) MLC representative scheme; b-c) Flow curve from RPA (b) and LPA (c) as resulted from GA code, in-vitro experiment and CFD simulation.

Discussion

In this study a novel method based on a custom GA script for the estimation of patient-specific RCR parameters for the PA bifurcation, considering the flow split of the subject, was presented. The effectiveness of the computed RCR values, from solely imaging data, was demonstrated in-vitro and in-silico. Further investigations involving more case studies may increase the confidence of experimental setups and CFD simulations for the investigation of PA pathologies, thus facilitating the translation of engineering tools in clinics for individualized healthcare.

References

1. Knoops et al, Artif Organs, 41(7):637-646, 2017.
2. Vignali et al, Proceedings of AIMETA 2019.

Acknowledgements

This work was funded by the VIVIR (PE-2013-02357974) and 4RTender (JRC/IPR/2018/F.3/0035/OC) projects.

NI-TI STENTS PRODUCED BY SLM: DESIGN, MANUFACTURING AND FUNCTIONAL PROPERTIES

Valentina Finazzi(1), Francesca Berti(2), Ali Gökhan Demir(1), Lorenza Petrini(3), Barbara Previtali(1)
1. Department of Mechanical Engineering, Politecnico di Milano, Milan, Italy; 2. Department of Chemistry, Materials and Chemical Engineering, Politecnico di Milano, Milan, Italy; 3. Department of Civil and Environmental Engineering, Politecnico di Milano, Milan, Italy

Introduction

Selective Laser Melting (SLM), allowing the production of customized biomedical prosthesis, in now on widely used in orthopedics applications. The cardiovascular field is a still unexplored but promising candidate for exploiting potentialities of SLM patient-specific devices. The challenges that have to be faced are: the design of "printable" optimized geometries, requiring ad hoc strategies and computational tools, and the definition of appropriate production processes [1]. In this paper, focusing on the additive manufacturing. of Ni-Ti stents by SLM, the following aspects are discussed: i) process parameter selection for thin structures; ii) design for additive manufacturing; iii) adjusting temperature-dependent material properties; and iv) surface finishing. This work aims to produce functional Ni-Ti stents through SLM and to set a validated FE model for pre-clinical assessments of these novel devices.

Methods

Powder feedstock with an initial chemical composition of $Ni_{50.8}Ti_{49.2}$ was employed (SAES Getters, Italy) (Fig. 1A.1-3). An industrial SLM system with pulsed wave laser emission was used (Renishaw AM250, Stone, UK). The SLM parameters were investigated to guarantee high density, correct chemical composition, and adequate mechanical properties. Energy density was varied from 49 to 277 J/mm^3, producing thin struts with an average nominal diameter of 300 µm (Fig. 1B.1-2). Sample characterization included internal defect and density analysis (Fig. 1B.3), and surface roughness measurements (Fig. 1B.4). Differential scanning calorimetry (DSC) was performed on ad hoc specimens (Fig. 1C.1), while mechanical properties were measured through uniaxial tensile tests at 37° on struts with dogbone shape (Fig. 1C.4). Stents with a closed-cell geometry [2] was considered for studying the mechanical behaviour of SLM produced Ni-Ti devices (Fig. 1D.1). A FE model was calibrated using the mechanical properties obtained in the testing phase (Fig. 1D.5).

Results

Samples produced with an energy density of 185 J/mm^3 was found to be suitable, having a measured diameter of 469 ± 10 µm, density of 99.6 ± 0.1 % and R_a = 3.09 ± 0.14 µm. Mechanical testing on the specimens showed superelastic behavior in tension up to 6% strain, with less than 1% permanent deformation. The stent FE model was prepared from the reconstructed geometry from µCT scans (Fig. 1D.2-3). The 1D centerline (Fig. 1D.4) was discretized with beam elements, allowing for numerically investigating stent performance under different loading conditions in a reduced computation time.

Discussion

This study presents some solutions to the gaps in the state of the art of designing and manufacturing superelastic thin structures, such as Ni-Ti stents. The use of ad hoc developed FE model allowed to predict stent performance giving useful information for future shape optimization.

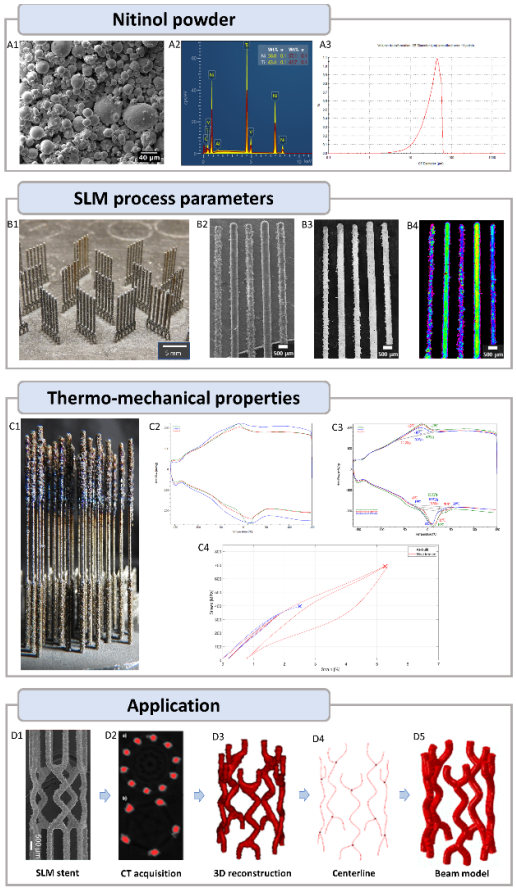

Figure 1: Graphical abstract outlining the phases of the research work, from the powder to the final application.

References

[1] Demir et al., (2017), Mater. Des., 119

[2] Finazzi et al., (2020), J. Manuf. Process., 55

Acknowledgments

The authors acknowledge SAES Getters for the support provided during this work.

3D-PRINTED SAW-GUIDE FOR COLLE'S FRACTURE MODELING AND ADJUSTEMNT OF DIAPHYSEAL FRACTURE GAP DISTANCE

Martin Frank (1), Ewald Unger (2), Francesco Moscato (2), Emir Benca (1)
1. Dept. of Orthopedics and Trauma Surgery, Medical University of Vienna, Austria,
2. Center for Medical Physics and Biomedical Engineering, Medical University of Vienna, Austria

Introduction

Recently, 3D printing has been gaining popularity for pre-operative planning, including the field of trauma surgery. Especially complex fractures of the pelvic ring might benefit from 3D visualization of cracks and selection and pre-shaping of implants prior surgery. However, basic knowledge about the effect of different pre-processing steps, such as selection of computer tomography (CT) settings and segmentation algorithms, on the obtained 3D models are still lacking. Thus, it is essential to establish a simple, reproducible fracture model to investigate these effects. The Colle's fracture (distal radius) is the most common fracture in humans and exact anatomical fracture specifications have been reported previously [1], making this fracture suited for a basic fracture model. The main goal of this work was to design a 3D-printed saw-guide for establishing a Colles's fracture model. Further, the size of the smallest detectable fracture gap is unknown. Thus, the fracture model should be extended with an additional diaphyseal fracture (better contrast of cortical bone to surrounding tissue, in comparison to cancellous bone), whereby gap distance should be adjustable.

Methods

Twenty fresh frozen radii were dissected from forearms (distal half) using the Henry approach. Then, bones were macerated at 60°C for two weeks to remove remaining soft tissue. Distal radii were scanned with a CT (Siemens Somatom Edge+, 120kV, sd/ri 0.6/0.4, kernel Ur77). Obtained DICOMs were segmented in Mimics (V21.0, Materialise) using a 50% threshold between bone and air, based on two intensity profiles across the radial head (for cancellous bone) and the diaphysis (for cortical bone). Saw-guides were designed in 3-matic (V13.0, Materialise) to enable exact fracture simulation of the distal radius, with a dorsal inclination of 26.1° (see Figure 1), and fixed in place with glued carbon wedges. In addition, the diaphysis was fractured, and sample specific fixators were designed for adjustment of the fracture gap distance (see Figure 2). In that way, bones with defined fractures can be scanned again with CT to determine the effect of different CT settings and segmentation algorithms on final 3D-printed models.

Results

3D-printed, bone sample-specific saw-guides were successfully designed for establishing a model for Colles's fracture (same anatomical location, same dorsal inclination). Further, a sample-specific fixator at the diaphysis was developed to allow an exact adjustment of the fracture gap (from closed to several mm) with a lock nut, mounted on thread pins (see Figure 2).

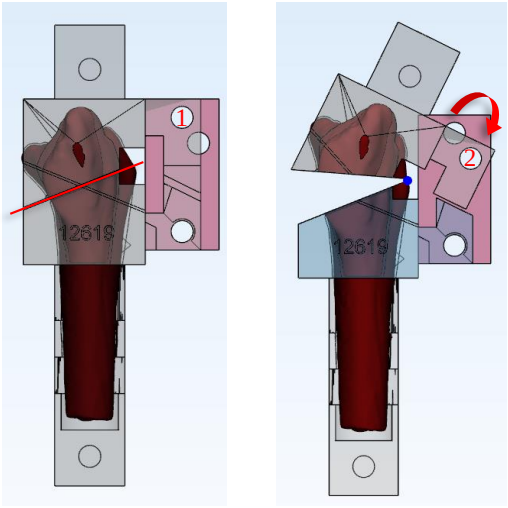

Figure 1: Left: Saw guide with defined anatomical fracture location (red). Right: Dorsal inclination of distal radius around Lister's tubercle (turn point, blue) and fixation from position 1 to 2 of the top saw-guide.

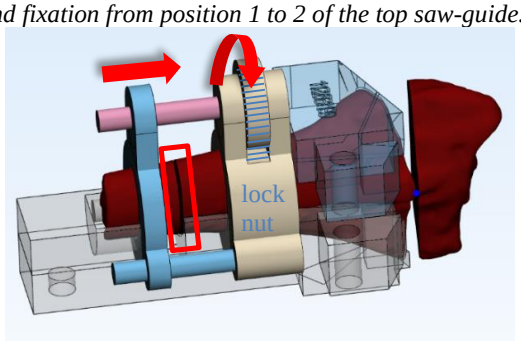

Figure 2: Fracture of diaphysis and adjustment of fracture gap distance with thread pins and a lock nut.

Discussion

The developed saw-guide enables an exact anatomical fracturing and dorsal inclination to establish a model for Colle's fracture. As such, influencing factors on obtained 3D printed bone models, such as different CT settings or segmentation algorithms, can be determined, independent from different fracture patterns or differences in anatomical locations. Moreover, the diaphyseal fixator allows the determination of the minimal detectable fracture gap, also in dependency on different CT settings or segmentation algorithms.

References

1. Baumbach et al., J. Orthop. Res. 2010

Acknowledgements

This study was partially funded by the Austrian Research Promotion Agency (FFG) project "Additive Manufacturing for M3dical RESearch, M3dRES" (Nr. 858060).

ANALYSIS OF DIFFERENT GEOMETRICAL FEATURES TO ACHIEVE CLOSE-TO-BONE STIFFNESS MATERIAL IN MEDICAL DEVICE: A FEASIBILITY NUMERICAL STUDY

Agostino Igor Mirulla (1,2), Giulio Maria Marcheggiani Muccioli (2,3), Stefano Fratini (2), Stefano Zaffagnini (2,3), Tommaso Ingrassia (1), Laura Bragonzoni (4), Bernardo Innocenti (5)

1. Department of Engineering, University of Palermo, Italy; 2. Department of Biomedical and Neuromotor Sciences, University of Bologna, Italy; 3. 2nd Orthopaedic and Traumatologic Clinic, IRCCS Istituto Ortopedico Rizzoli, Italy; 4 Department for Life Quality Studies, University of Bologna, Italy; 5. BEAMS Department (Bio Electro and Mechanical Systems), Université Libre de Bruxelles, Belgium

Introduction

The purpose of this article was to investigate if a material could vary itself based on both patient and surgeon necessities. We thought geometry of the material could be a valuable way to address rigidity changes in the material. Rigidity is an important characteristic which is different from bone in all materials actually used, and it has been considered in several recent studies where the most rigid material has shown an higher stress-shielding. [17, 18]

The aim of this study was to evaluate with computer simulation and trough Finite Element Method (FEM) if a porous material with variable gaps dimension and different in-body vacuum geometrical shapes could modify the material rigidity. The goal of this work is to evaluate how empty spaces geometry could influence the material rigidity. In our thoughts, a "close-to-bone" material could have positive implications for orthopaedic implants, not only in TKA but also in other joint replacements.

Our hypothesis was that a closer-to-bone rigid material could improve prostheses performances, allowing for a better bone integration and a more rigid articular interface.

Methods

Five cubes with a 20 mm thickness were generated with computer simulator and analyzed under compression load by means of finite element (FE) analysis. The displacement calculated in four cubes, containing four internal gaps with different geometry shape (quadratic, hexagonal, octagonal and cylindrical), were compared with a full body used as control. FE analysis was conducted to assess the displacement in the axial direction in five points located inside each cube, dividing the latter into four layers (α, β, γ, δ).

Results

The hexagonal and cylindrical internal gaps provide the greater displacements compared to the full body, so reaching lower stiffness than the other in-body vacuum geometries. Specifically, the displacement reduction values are 5.1 µm (cylindrical) and 5.0 µm (hexagonal) in layer α, 10.6 µm (cylindrical) and 10.2 µm (hexagonal) in layer β, 19.1 µm (cylindrical) and 19.6 µm (hexagonal) in layer γ, 47.2 µm (cylindrical) and 47.7 µm (hexagonal) in layer δ.

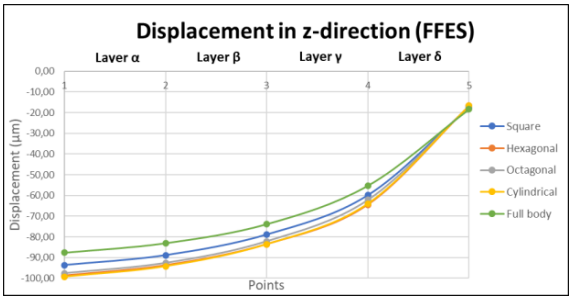

Figure 1: Figure 5. Displacement in z direction (first simulation) for quadratic (blue), hexagonal (orange), octagonal (grey) and cylindrical (yellow) in-body vacuum geometries, compared to full body trend (green).

Discussion

The most important finding of the present study was that cubes with hexagonal and cylindrical geometries show the lowest rigidity at each point, compared to the other geometries analyzed and compared to the full body cube. This study also suggests that to achieve reduced rigidity, the size range of the in-body vacuum was from 1 mm to 4 mm.

References

1. Martin JR, Watts CD, Levy DL, Kim RH (2017) Medial Tibial Stress Shielding: A Limitation of Cobalt Chromium Tibial Baseplates. J Arthroplasty 32:558–562.
2. Srinivasan P, Miller MA, Verdonschot N, Mann KA, Janssen D (2017) Strain shielding in trabecular bone at the tibial cement-bone interface. J Mech Behav Biomed Mater 66:181–186.

NOVEL METHOD OF PREPARATION OF GELMA/XANTHAN GUM-BASED BIOMATERIAL WITH IMPROVED PRINTABILITY

Andrea Mantelli (1), Filippo Iervolino (1), Beatrice Belgio (1), Federica Boschetti (1), Sara Mantero (1), and Marinella Levi (1)

1. *Dept. of Chemistry, Materials and Chemical Engineering "Giulio Natta", Politecnico di Milano, Italy*

Introduction

In the three-dimensional (3D) bioprinting work frame, the development of novel highly biocompatible materials with good printability and tailored mechanical properties is one of the main targets. Even though, either natural or synthetic biomaterial are employed in 3D bioprinting, naturally derived materials are inherently bioactive. [1] Gelatin is one of the natural materials employed in 3D bioprinting. To exploit its use in 3D bioprinting it can be either functionalized, enabling the ultraviolet (UV) light crosslinking or, more recently, crosslinked with enzymes avoiding the presence of harmful chemicals. [2,3] Nevertheless, gelatin methacrylate (gelMA) is widely used in 3D bioprinting. [4-6] The study of a bioink based on gelMA additivated with a natural gum has demonstrated good printability and high cell viability. [7] Besides, the miscibility and the foam stability of xanthan gum (XAN) and gelMA have been reported, opening its use in 3D bioprinting. [8,9]

Methods

Porcine skin gelatin was dissolved in phosphate buffer solution (PBS). After the dissolution, methacrylic anhydride was added to the solution. Then PBS was added to dilute the reaction mixture. The mixture was dialyzed for 72 h at 50 °C. After dialysis, 20 wt.% of xanthan gum with respect to gelMA was added. The solution was kept under vigorous stirring to allow the formation of a foam. Then, the foam was dried at 55°C for 48 hours. The gelMA/XAN foam was diluted in PBS Table 1 shows the compositions of the prepared inks. The inks were printed using an Inkcredile+ by Cellink 3D bioprinter using different speeds and pressures. Several characterizations were performed. Cytotoxicity assays were carried out on the gelMA/Xan inks to assess the biocompatibility using an established cell line. Rheological measurements were performed to evaluate the effect of the addition of XAN to gelMA. The tests were carried out on a Discovery DHR2 rotational rheometer by TA instruments. Finally, compression tests were carried out using a Bose EnduraTEC ELF3200 to evaluate the correct polymerization of the material.

Ink	GelMa (wt%)	XAN (wt.%)	PBS (wt.%)
GelMA/XAN 20%	8	2	90
GelMA/XAN 30%	7	3	90
GelMA/XAN 40%	6	4	90

Table 1: Compositions of the inks used for this study.

Results

Cytotoxicity assays showed that the materials are biocompatible. The rheological behavior of the gelMA/XAN inks was assessed. Each ink showed a pseudoplastic behavior with the presence of a yield stress due to the addition of xanthan gum.
Two different geometries were printed: arrays of lines and scaffolds (Figure 1). The array of lines was printed at different speed and pressures to find the optimal process parameters. While, the grid was printing with a different number of layers. Finally, compression tests verified the correct polymerization of the material.

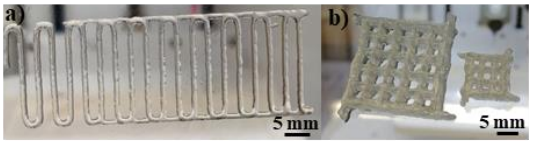

Figure 1: Array of lines printed (a) and scaffolds (b) printed with gelMA/XAN 30% ink.

Discussion

The use of xanthan gum as an additive allowed to use a novel method of preparation, i.e., the drying of a gelMA/XAN-based ink. This method had the advantage of substituting the lyophilization step. Furthermore, the use of XAN improved the printability of gelMA-based inks without affecting cell viability. Therefore, this novel strategy for the preparation of Gelma/XAN-based inks led to the development of a material exhibiting an excellent compromise between printability and biocompatibility.

References

1. P. S. Gungor-Ozkerim *et al.*, *Biomater. Sci.*, 6: 915-946, 2018
2. H. Mao *et al.*, *Prog. Nat. Sci. Mater. Int.*, 30: 618–634, 2020
3. M. Zhou *et al.*, *Biofabrication*, 11: 2, 2019
4. L. Valot *et al.*, *Chem. Soc. Rev.*, 48: 4049–4086, 2019
5. X. Zhao *et al.*, *Adv. Healthc. Mater.*, 5: 108–118, 2016
6. J. Yin *et al.*, *ACS Appl. Mater. Interfaces*, 10: 6849–6857, 2018
7. F. P. W. Melchels *et al.*, *J. Mater. Chem. B*, 2: 2282–2289, 2014
8. K. C. Basavaraju *et al.*, *J. Appl. Polym. Sci.*, 109: 2491–2495, 2008
9. M. Abdollahi *et al.*, *Eur. J. Lipid Sci. Technol.*, 122: 1–9, 2020

4D PRINTED SUTERELESS CLIPS FOR INTESTINAL ANASTOMOSIS

Irene Chiesa[a], Silvia Bittolo Bon[b], Davide Morselli[c], Micaela Degli Esposti[c], Paola Fabbri[c], Carmelo De Maria[a], Giacomo Giorgi[d] , Antonino Morabito[e] and Luca Valentini[b]

[a]Department of Information Engineering and Research Center E. Piaggio, University of Pisa, Italy

[b]Dipartimento di Ingegneria Civile e Ambientale, Università degli Studi di Perugia, Terni, Italy

[c]Department of Civil Chemical, Environmental and Materials Engineering, Università di Bologna, Italy

[d]Dipartimento di Ingegneria Civile e Ambientale, Università degli Studi di Perugia, and CNR-SCITEC, Perugia, Italy

[e]Department of Pediatric Surgery, Meyer Children's Hospital, Firenze, Italy and Dipartimento Neuroscienze, Psicologia, Area del Farmaco e della Salute del Bambino NEUROFARBA, Università degli Studi di Firenze, Italy

Introduction

Manual suturing is the current gold standard for intestinal anastomosis, remaining a difficult and time-consuming procedure [1-2]. In this study, we designed and four-dimensional (4D) printed hollow cylindrical structures made of biobased and biocompatible regenerated silk (RS) and poly(3-hydroxybutyrate-co-3-hydroxyvalerate) (PHBV) to be used as suterless clips in intestinal anastomosis. The rationale of our innovative 4D structures is based on the negative thermal expansion coefficient of RS when heated in high relative humidity (HRH), as in the human body.

Methods

Material preparation: Bombyx mori cocoons were degummed in sodium bicarbonate ($NaHCO_3$) at 100°C for 30 min. Then, two RS solutions were prepared: i) RS/$CaCl_2$: RS fibers were dissolved in calcium chloride ($CaCl_2$)/formic acid (FA) solution; ii) RS/$CaCl_2$/KNO_3: potassium nitrate (KNO_3) was added to the RS/$CaCl_2$ solution. PHBV was dissolved in chloroform with a final concentration of 150 mg/ml.

Structure fabrication: Hollow bilayer cylindrical structures were 4D printed using a piston-driven extrusion-based 3D printer (Fig. 1A), featuring a rotating spindle (spindle diameter = 5 mm, spindle speed = 15 rpm, needle diameter = 0.8 mm). The inner layer was obtained extruding the PHBV solution over the rotating spindle, whereas the external one was obtained depositing the RS compounds (i.e. RS/$CaCl_2$ or RS/$CaCl_2$/KNO_3) over the PHBV (Fig. 1B).

Structure characterization: The structures were characterized by weight variation in HRH, Fourier transform infrared spectroscopy and compression test. Then, finite element (FE) simulations were performed to analyze the capability of the 4D printed structures to contract under thermal stimulus. Finally, the structures were used as sutureless thermoresponsive clips *ex vivo* (Fig. 1C), measuring the bursting resistance once applied on an anastomized porcine intestine.

Results

In this work, we fabricated hollow biobased and bilayer cylindrical structures with a thickness of approx. 50 μm, exploiting extrusion-based 4D printing. Structure characterization showed that adding KNO_3 promotes the formation of the β-sheet intramolecular crystalline structures, stabilizing the tubes and enhancing its resistance to collapse. FE models indicated that at 37°C the tubes contracts radially, compressing the intestine wall, with a bigger compression when RS/$CaCl_2$/KNO_3 compound is used. This result agrees with experimental evaluation of bursting pressure, showing that the use of the RS/$CaCl_2$/KNO_3 + PHBV structure increases the burst pressure to approximately 90 mmHg. This represents an increment of over 140% in comparison to the value recorded for sutured intestine.

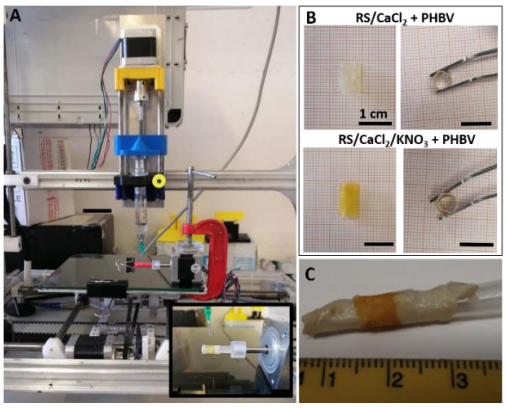

Fig. 1: (A) 3D printing equipment based on an extrusion system featuring a rotating spindle. (B) Top and side view of the 4D printed cylindrical structures. (C) Assembly of the fabricated device for the ex vivo testing.

Discussion

The 4D printed RS/$CaCl_2$/KNO_3 + PHBV structures resulted in a promising biobased device for sutureless anastomosis [3]. In the next future, this device will be used in mices to verify anastomosis capabilities *in vivo*, and complex RS deposition patterns (e.g. helix, honeycomb) will be explored to maximize the contractive mechanism.

References

1. Yauw, S. T. et al.,
2. Yao, L., *et al.*, Med. Sci. Monit., 22:4570, 2016
3. Bittolo Bon, S., *et al.*, Mater. Des., 18:109492, 2021.

Acknowledgements

S.B.B., I.C., D.M., M.D.E., P.F., C.D.M., L.V., are supported by the Italian Ministry of Education, University and Research under the PRIN Project VISION (grant 2017FWC3WC). This work was carried out in collaboration with the CrossLab Additive Manufacturing Laboratory of the Department of Information Engineering (University of Pisa).

3D PRINTING OF MICROFLUIDIC DEVICES FOR CELL CULTURE

Désirée Baruffaldi (1,2), Candido Fabrizio Pirri (1,2,3), Francesca Frascella (1,2).

1. Dipartimento di Scienza Applicata e Tecnologia, Politecnico di Torino, C.so Duca degli Abruzzi 24, 10129 Turin, Italy; 2. PolitoBIOMed Lab, Politecnico di Torino, C.so Duca degli Abruzzi 24, 10129 Turin, Italy 3. Center for Sustainable Futures @Polito, Istituto Italiano di Tecnologia, Via Livorno 60, 10144 Turin, Italy;

Introduction

Digital light processing (DLP) is widely used in 3D printing, because of its scalability, mild working condition and fast printing speed. DLP consists in the photopolymerization of photo-curable precursors starting from a CAD project and commonly used inks are acrylates and their derivatives [1]. Light-based 3D printing techniques may represent a valuable instrument for its precision and the flexibility. Herein, we tested the biocompatibility of three different acrylate-based formulations to assess the feasibility to use them to realize device for cell culture. After adjusting printing parameters, we optimized washing and sterilization protocol to improve cell viability [2].
Since, microfluidic devices enable to control cell culture environment and may be used for drug screening or other cell-based assay to improve reproducibility [3], we design a DLP printed microfluidic device mimicking a 96-well plate, suitable for cell culture and cell-related assays.

Methods

Bisphenol A ethoxylate diacrylate (BEDA), 1,6-hexanediol diacrylate (HDDA) and polyethylene glycol diacrylate (PEGDA) with 0,2% or 1% of a phospine oxide-based compound (BAPO) were printed using a PICO 2 DLP-3D printer (Asiga, Australia) with a LED light source (405 nm). Washing protocol consisted in incubation or sonication in selected solvent (Ethanol or acetone). The sterilization was performed 30 minutes of UV light before cell seeding. Cell viability was assessed using MTT assay [2]. The design of the microfluidic device was done using SolidWorks and the dimension recapitulated the well of a 96-well plate.

Results

The 3D printed samples were deeply washed, to remove un-reacted materials, following four specific protocols which may be divided into two main groups: incubation and sonication. For incubation, the samples were incubated for 2 h in ethanol or acetone; then then UV post-curing for 5 min. Sonication protocol consisted in sonication for 5 minutes in a solvent (ethanol or acetone) and then UV post-curing as described above. Finally, the samples were kept in the same solvent overnight. Among the protocols, incubation seems to be too mild to remove toxic product leading to cell death. On the other hand, sonication gave better result, but acetone strongly affect the optical properties of the samples and in some cases lead to the break of the material. Among the resins, BEDA is associated to lower cell proliferation. Although, HDDA showed the higher cell viability after but the loss of transparency after washing step made it impossible to use for imaging analysis. After testing all the formulations, PEGDA 0,2% BAPO sonicated in ethanol represents the best candidate to be used as main material for a 3D printed device for its printability, transparency and cell compatibility [3].
Next, we designed a PEGDA based microfluidic plate that recapitulates 96-well plate dimensions (Figure 1). Fluidic test shows that the channel succeeds in filling all the wells when connected to a peristaltic pump and the precise design makes its suitable to be used in normal plate reader. Cells can be seeded in these wells and analyzed by optical and fluorescent imaging or by proliferation assays.

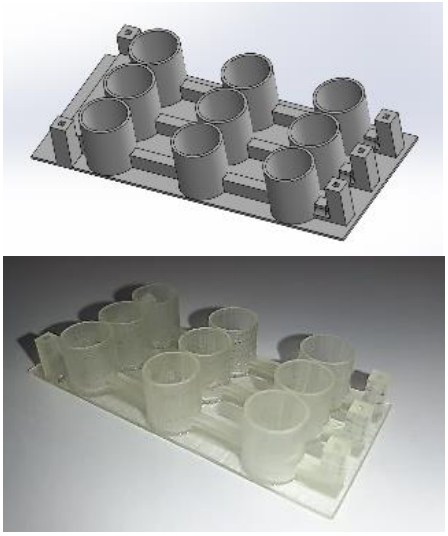

Figure 1: This figure shows the CAD design of the microfluidic plate (left) and the 3D printed one (right).

Discussion

We produce biocompatible 3D printed polymer parts using a commercial DLP-3D printer. Our results underlined the importance of post printing processing, indeed, washing steps are essential in removing non-reacted monomers and photoinitiators to reduce the toxicity of printed parts towards cells.

References

1. Zhang et al., J of Material Chemistry C, 8:13896-13917, 2020.
2. Gonzalez et al, Nanomaterials, 10:1788, 2020.
3. Lee et al., JALA, 12(6): 363–367, 2007

THREEDIMENSIONAL RECONSTRUCTION OF THE FEMALE PELVIC ORGANS FOR BIOMECHANICAL MODELING AND DEVICE TESTING

Paola Ulacia-Flores (1), Stewart McLennan (1), Lucy Gilbert (2), Rosaire Mongrain (1)

1. Department of Mechanical Engineering McGill University, Montreal, Canada; 2. Department of Obstetrics & Gynecology, Gynecologic Oncology, McGill University Health Centre, Montreal, Canada

Abstract

To date, most gynecological models available focus on pregnancy. Using imaging data from pelvic magnetic resonance (MR) images, we extracted the specific anatomy of the non-pregnant, post-menopausal uterine cavity and surrounding tissues for the creation of 3D anatomically correct and biomechanically representative solid models. These models aid in the visualization of the anatomical features *in silico* and can easily be translated into physical models and dedicated experimental setups for the evaluation of new technologies such as liquid biopsies, by means of rapid prototyping.

Introduction

Mechanical alterations of the female reproductive organs can lead to different pathological states [1]. The generation of anatomically accurate and biomechanically representative models is of great importance for the analyses and simulation of therapeutic or surgical interventions, as well as the study of the biomechanics of the onset of disease. Hydrogels (Polyvinyl alcohol (PVA), chitosan, alginate, etc.) and silicone rubbers have been used to mimic the mechanical properties of soft tissues, allowing for different model generation techniques [2]–[4].

Methods

Anatomically correct 3D reconstructed structures of the female pelvic organs were obtained from MR images through user-guided segmentation and used to generate molds for additive manufacturing techniques.

Sagittal and axial T2 weighed FRFSE MR images were loaded on slicer 4.10.1[5], and ITK SNAP 3.8.1[6], where semiautomatic segmentation tools, followed by user auditing and correction were used to identify the bladder, uterus, vagina and uterine cavity, as well as reference anatomic landmarks. Three dimensional solids were generated for each structure and exported as .STL files to Inventor 2019 [7] where 3D-printable molds were designed.

Two main manufacturing processes have been identified: 1) 3D-printed molds for hydrogel casting and 2) 3D-printed scaffold for direct hydrogel deposition through bioprinting.

Thus far, PVA thermal cycling and mechanical characterization has been completed. Different hydrogel compositions and cross-linking techniques are being tested for further biomechanical compatibility and manufacturability of the generated models.

Results

Anatomically accurate solid models of the uterus and uterine cavity were extracted, molds were designed and casted on silicone rubber with a shore hardness of 00-10, with a 100% modulus of elasticity of ~ 55kPa (Figure 1). The characterization of 10% and 15% w/w PVA solutions determined that to obtain similar properties in the linear region, 6 to 10 thermal cycles are required at a freeze rate of 0.333°C/min (to -20°C) and a thawing rate of 0.111°C/min. (to 10°C).

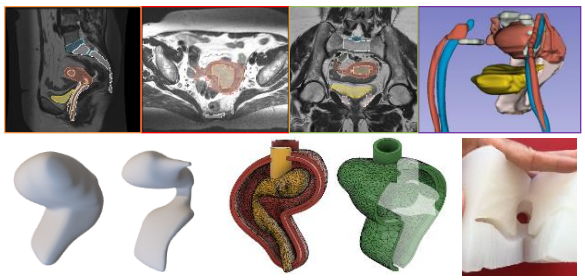

Figure 1: 3D reconstruction of the pelvic organs. Top: Y. Sagittal, R. Axial, G. Coronal planes. P. 3D volume. Bottom, left to right: uterus and uterine cavity solids, casting moulds, and silicone rubber model.

Discussion

Automated segmentation of complex structures is not always achievable and requires user intervention. The use of hydrogels for biomechanically representative models is feasible, however, it represents manufacturing challenges particular to the cross-linking methods of the selected materials. These fine-tuned mock-ups are useful in the assessment of new technologies, training and surgical planning.

Further work is required to streamline the process from medical imaging to bio printed biomechanical models. If successful, these could potentially facilitate the generation of patient-specific, biomechanically compatible engineered tissues.

References

1. A. Baah-Dwomoh, et al, App.Mech.Rev, 68(6):1-12, 2016
2. S. Jiang, et al, JMBBM. 4:1228-33 2011
3. S. Jiang, et al, Mater. Sci. Eng. C, 33(7):3768-74, 2013
4. P. Li, et al, JMBBM,49 :220-234, 2015
5. Fedorov A. et al, Magn. Reson. Imaging, 30(9):1323-41, 2012. https://www.slicer.org/
6. Yushkevich et al, Neuroimage, 31(3):1116-28, 2006
7. Autodesk Inventor, 2019

Acknowledgements

We thank Mrs. Valerie Josset. This work was supported by the Valerie Josset and Gary Aitken Cancer Research Award.

AVOIDING CELL DEATH IN 3D BIOPRINTING – COMPUTATIONAL FLUID DYNAMICS (CFD) MODLLING OF EXTRUSSION SHEAR STRESSES

Patricia Santos-Beato (1), Deepak M. Kalaskar (2), Ryo Torii (3)

University College London, UCL
1. UCL,UK; 2. UCL,UK; 3. UCL,UK

Abstract

In vitro tissue modelling is a growing field which is currently being enhanced with new manufacturing techniques such as 3D bioprinting. This revolutionary technique enables the production of complex hierarchical structures while allowing high cell densities encapsulated in bioinks to be deposited in a controlled manner[1]. However, it has been shown that high shear stresses produced during the extrusion process can compromise cells' ability to survive[2] and grow[3]. Currently, the printing process is optimised by trial & error, which requires large quantities of cells and materials, and time. A more efficient process of printing optimisation, e.g. towards maximum cell survival post printing, is much needed for the further advancement of 3D bioprinting. Computational fluid dynamics (CFD) modelling used to simulate the extrusion process of bioinks under different extrusion pressures, nozzle and needle diameters, is expected to play an important role in the optimisation of the printing process.

The aim of this work is to develop a CFD model to establish a quantitative understanding of the association between the extrusion pressure, choice of bioink material, nozzle or needle size, and shear stress within the nozzle/needle.

The CFD model was developed using ANSYS Fluent software. The geometrical model of nozzle/needle and the air bodies combined, were made in a 2D axisymmetric manner and subsequently meshed using quadrilateral elements. After mesh sensitivity test, the simulations were conducted using different bioinks – mixtures of xanthan gum and gelatine, and gelMA 5% – to assess the optimum printing conditions for each material. The materials were characterised rheologically to find their viscosity and fitted into the Herschel-Bulkley model, when non-Newtonian, as inputs for the CFD model. The shear stresses generated were analysed in three different nozzle sizes and three needle sizes (22G–410 µm, 25G–250 µm and 27G–200 µm). The results showed the correlation between smaller nozzle sizes and higher shear stresses generated for the same material and extrusion pressure, which was expected. Additionally, a comparison of the maximum shear stresses showed that the xanthan gum-gelatine mixtures generated lower shear stresses (140 Pa) than gelMA (845 Pa) when extruded with the same nozzle diameter and extrusion pressure. Additionally, the flow rate was assessed and compared to experimental gravitational measurements to validate the model. By examining the flow rate and the experimental results, a further correlation between the maximum pressure and maximum printing velocity that can be used without losing filament continuity was found. Although the simulations and experimental validation tests were conducted under acellular condition, the results provide a quantitative indication which can narrow down the number of possible printing parameter combinations towards a low potential cell damage and high printing output.

Ongoing work will be aimed at establishing the potential association between the predicted shear stress and the cell-specific tolerance of shear stress that causes cell damage in experimental printing, which will make this model a strong tool to design 3D bioprinting processes.

References

1. C. K. Chua and W. Y. Yeong, *Bioprinting: principles and applications*, World Scientific Publishing Co Inc, 2014.
2. R. Chang, J. Nam, W. Sun, *Effects of dispensing pressure and nozzle diameter on cell survival from solid freeform fabrication-based direct cell writing*, Tissue Engineering – Part A, 2008, 14, 1, 41-48.
3. B.J.H Zoro, S. Owen, R.A.L Drake and M. Hoare, *The Impact of Process Stress on Suspended Anchorage-dependent mammalian cells as an Indicator of Likely Challenges for Regenerative Medicines*, Biotechnology and Bioengineering, 2008, 99, 468-474.

DESCRIPTION OF VISCOELASTIC BEHAVIOUR OF 3D PRINTED PHOTOPOLYMERS THROUGH A GENERALIZED MAXWELL MODEL

Stefania Marconi (1), Gianluca Alaimo (1), Ferdinando Auricchio (1), Andrea Vigliotti (2)

1. Università degli Studi di Pavia, Italy; 2. CIRA Centro Italiano Ricerche Aerospaziali, Italy

Introduction

In recent years, Additive Manufacturing (AM), mainly known as 3D printing has widely spread and developed within the engineering landscape. The diffusion of this technology has also affected the biomedical context, and in particular the production of patient-specific anatomical models, which can be used for a lot of purposes, including surgical training as well as *in vitro* experiments. For such applications, the model should be able to return a sensory feedback to the surgeon as much as possible in line with the operative reality and, moreover, it should be possible to accurately predict its mechanical response.

Highly deformable 3D-printed photopolymers are well suited to simulate the mechanics of biological tissues. In the literature, they are commonly described through a linear elastic model, which is an excessive approximation for soft rubber-like materials known to have a not negligible viscoelastic behaviour.

The aim of this work is the experimental evaluation of the parameters of a constitutive model that can effectively describe the behaviour of 10 specific photopolymers Agilus30™, VeroCyan™ - Stratasys©, and their 8 possible mixtures S30-S95 (where the number refers to the Shore A of the material. Stratasys© *Material Jetting* 3D printers can simultaneously deploy all the 10 materials during the same print: this means that they can be combined in a single multi-material anatomical model.

Methods

A generalized Maxwell model, in which the shear relaxation modulus is expressed by means of a Prony series was selected, being available in the majority of Finite Element (FE) commercial software. It is formulated as follows:

$$G(t) = G_0 + \sum_{i=1}^{N} G_i e^{\frac{-t}{\tau_i}} \qquad (1)$$

where G_0 is the shear relaxation modulus at equilibrium, N is the number of terms, G_i is the shear relaxation modulus of the ith Maxwell element and τ_i its relaxation time.

The aim of the work is to determine through experimental tests $G(t)$ and subsequently theoretically derive the bulk relaxation modulus $K(t)$. For the determination of the parameters involved in (1), the shear frequency response is evaluated through a Discovery HR2 rheometer (TA instruments) in the range 1-100 Hz, applying a sinusoidal strain history. Frequency responses were evaluated at different temperatures.

For each material, the transition temperature T_g was computed [21] and all the frequency responses obtained at different temperatures were shifted to compute the *master curve*, by means of the Williams-Landel-Ferry (WLF) approach. WLF constants were retrieved using the approach of Andreozzi et al. [22], while a manual shift of the curves was implemented following the *Equivalent slope method* [23]. The Krein Nudelman + Honerkamp Weese (KN+HW) method [24] was selected to get the values G_0, G_i and τ_i in (1) without imposing a priori the number of Maxwell elements N.

Results

Table 1 reports the values G_0 and G_i, while Table 2 reports the relaxation times τ_i. The procedure identifies 5 τ_i for all materials except for S85, for which 4 are found. For the sake of brevity, values for materials S30, and S40-S60 are not reported, being close to S35 values.

Mat.	G_0	G_1	G_2	G_3	G_4	G_5
Agilus30	0,126	0,030	0,073	0,170	0,444	3,154
S35	0,136	0,038	0,098	0,222	0,639	2,637
S70	0,156	0,052	0,125	0,293	0,871	4,242
S85	0,229	0,118	0,300	0,632	1.630	
S95	0,244	0,149	0,323	0,612	1,219	1,828
VeroC.	0,770	0,348	0,882	1,816	2,578	2,930

Table 1: Shear moduli G_0 and G_i in MPa.

Mat.	τ_1	τ_2	τ_3	τ_4	τ_5
Agilus30	0,503	0,049	0,007	0,001	0,000
S35	0,406	0,038	0,006	0,001	0,000
S70	0,459	0,040	0,006	0,001	0,000
S85	0,312	0,027	0,004	0,001	
S95	0,711	0,052	0,007	0,001	0,000
VeroC.	1,422	0,163	0,034	0,008	0,001

Table 2: Relaxation times τ_i in sec.

Discussion

This work provides a valuable contribution to the understanding of the mechanics of several 3D-printed photopolymers and a methodology to obtain the required parameters for the use of the selected constitutive model within the most common commercial FE software. Future works will explore the possibility of including hyperelasticity in the model, to account also for nonlinear effects.

References

1. ASTM D7028. ASTM International, 2015.
2. Andreozzi et al, XX Congresso dell'Associazione Italiana di Meccanica Teorica e Applicata, 1–8, 2011.
3. Saboo et al, Indian Highways, 46(2): 19–28, 2018.
4. Jalocha et al, Int J Solids Struct, 67:169–181, 2015.

3D BIOPRINTING OF A PHOTOCURABLE AND THERMOSENSITIVE BIOINK FOR SKIN TISSUE ENGINEERING.

Miranda Torre[1], Sara M. Giannitelli[1], Emanuele Mauri[1], Manuele Gori[2], Marcella Trombetta[1], and Alberto Rainer[1,3]

1. Department of Engineering, Università Campus Bio-Medico di Roma, via Álvaro del Portillo 21, Rome 00128, Italy; 2. Institute of Biochemistry and Cell Biology (IBBC), National Research Council (CNR), via E. Ramarini 32, Monterotondo Scalo (Rome) 00015, Italy; 3. Institute of Nanotechnology (NANOTEC), National Research Council (CNR), via Monteroni, Lecce 73100, Italy.

Introduction

Multicomponent bioinks have emerged as an optimal solution to overcome the drawbacks of single-hydrogel compositions, such as the limited printability of natural polymers or the lack of cell-specific activity of synthetic ones, thus integrating the advantages of each component (e.g., different crosslinking mechanisms) and widening the biofabrication window [1][2][3]. The present study reports an innovative formulation consisting of Pluronic F127 (PF127) and gelatin methacrylate (GelMA), which integrates the advantages of both hydrogels, maximizing the ink printability and biocompatibility to fabricate 3D constructs as skin tissue models.

Methods

A GelMA-PF127 aqueous system was prepared and characterized in term of its temperature-dependent rheological properties.

Squared multi-layered scaffolds laden with human dermal fibroblasts were obtained by micro-extrusion bioprinting. After printing, constructs were exposed to 365 nm UV radiation (using Irgacure 2959 as a photoinitiator) to induce GelMA polymerization. Dissolution of Pluronic component from crosslinked constructs was performed by washing steps (Figure 1).

At selected time points (up to day 14), constructs were analyzed for cell viability (MTT assay) and cell distribution within the hydrogel (by labelling actin filaments).

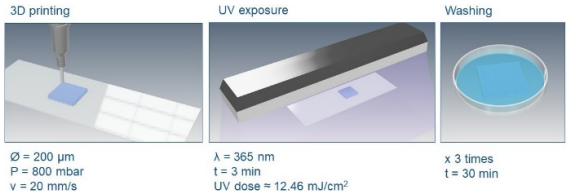

Figure 1: Schematic illustration of the printing process of GelMA-PF127 hydrogel with the relative parameters.

Results

Due to its thermosensitive properties (Figure 2-a) and shear-thinning behaviour (Figure 2-b), the ink was suitable for bioprinting at physiological conditions, showing excellent structural integrity and shape fidelity after fabrication (Figure 2-c).

Encapsulated cells remained viable for 2 weeks after printing (Figure 2-d) and cell proliferation was reported.

A remarkable cell alignment along the fiber deposition direction was observed already after 4 days in culture (Figure 2-e).

Discussion

Due to the intrinsic bioactive properties of GelMA and the mesoporosity provided by the elution of PF127 micelles [4], the bioink was used for the biofabrication of fibroblast-laden constructs with the aim to recapitulate the dermis compartment of the human skin. The bioprinted constructs showed high levels of cell viability and proliferation in long-term cultures, thus representing a technological platform for the future development of a construct recapitulating the physiological complexity of the entire dermo-epidermal layers.

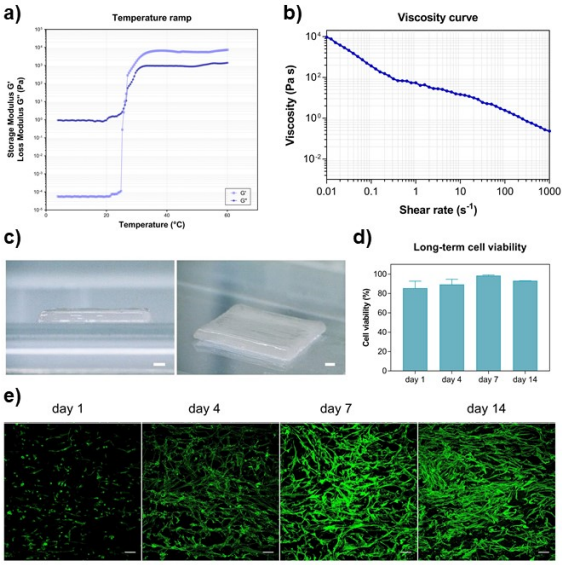

Figure 2: (a) Storage and loss moduli as a function of temperature showing the sol-gel transition; (b) shear thinning behaviour of the ink; (c) 3D printed constructs (scale bar: 1 mm); (d) long-term cell viability of human dermal fibroblasts up to 14 days post printing; (e) cell distribution over the selected time interval.

References

1. Cui et al, Adv Healthc Mater, 9.15:1901648, 2020.
2. Rastin et al, ACS Appl Bio Mater, 3:3, 1815-1826, 2020.
3. Schwab et al, Chem Rev, 120:19, 11028-11055, 2020.
4. Gori et al, Adv Healthc Mater, 9, 2001163, 2020.

A CLINICAL TRIAL TO ASSESS THE EFFECTIVENESS OF 3D MODELS FOR COMPLEX CARDIAC SURGICAL PLANNING

Katia Capellini (1,2), Emanuele Gasparotti (1,2), Emanuele Vignali (1), Lamia Ait Ali (3), Massimiliano Cantinotti (4), Paolo Tripicchio (5), Michele Murzi (6), Simona Celi (1)

1. BioCardioLab, Fondazione Toscana G. Monasterio, Italy; 2. Dept. of Information Engineering, University of Pisa, Italy; 3. Institute of Clinical Physiology, CNR, Italy; 4. Paediatric Cardiology Unit, Fondazione Toscana G. Monasterio, Italy; 5. Perceptual Robotics Lab, TeCIP Institute, Scuola Superiore Sant'Anna, Italy; 6. Adult Cardiology Unit, Fondazione Toscana G. Monasterio, Italy

Introduction

The adoption of 3D models is of great interest in different medical fields [1]. Complex heart diseases (CHD) represent an ideal field to assess the medical effectiveness of 3D models, considering the level of complexity that affects a lot of surgical procedures. Moreover, the anomalous anatomical arrangement of CHDs, requiring a personalized approach, would benefit from 3D models [2-3]. Nevertheless, the effectiveness of these strategies applied in real clinical workflow has not been evaluated yet. The aim of this work is the comparison in terms of accuracy and added diagnostic value provided by 3D printed and virtual models in the planning of cardiac surgery.

Methods

CT and MRI volumetric datasets of about 60 patients affected by CHD scheduled for surgical repair were segmented to obtain 3D models of cardiac structures (Fig 1a). Three different 3D printing techniques were used: the fused deposition modelling (FDM), the stereolithography (SLA) and the selective laser sintering technique (SLS). TPU Elasto85 filament (3ntr), Elastic 50A resin (Formlabs) and Flexa Bright powder (Sinterit) were adopted in the FDM, SLA and SLS approaches respectively. A 3D virtual web platform was developed in JavaScript linked to clinical records. This application allows scene rotation, virtual cutting and spatial measurements. The enrolled clinical cases were evaluated by a multidisciplinary heart team, following two steps: first, the clinical case was discussed by using only the traditional imaging dataset, then the virtual and 3D printed models were introduced to plan suitable procedures and to assess the added value provide.

Results

For the analysed cases, the adoption of the two techniques reported a significant improvement in comparison with standard clinical images alone. The main advantages reside in the possibility to manage the 3D geometry to plan the surgical or interventional procedure and to facilitate communication within the heart team's members. Table 1 reports the 3D printed models scores associated to technical aspect of the post curing time (PC_{time}), printable model size (MS), clinical feedbacks in terms of surface finish (SF) and applicability of models to simulate procedure in a surgical room (cch) or via catheterization (cathlab).

	PC_{time}	MS	SF	SA
FDM	**	***	*	cch
SLA	*	*	***	cathlab
SLS	***	**	***	cch/cathlab

Table 1: Associated scores for the, PC_{time}, MS, SF and the simulation approach (SA).

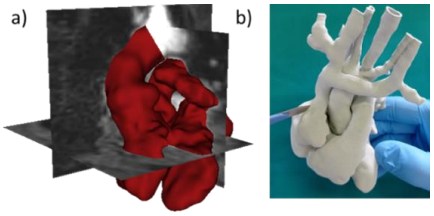

Figure 1: Reconstructed 3D heart model (a); example of surgical planning on 3D model printed with SLS (b).

Table 2 reports a comparison between 3D printing and virtual models in terms of perceived effectiveness by each medical team.

	cch <10	cch >10	cathlab
3D	***	**	***
virtual	**	***	**

Table 2: Resulting scores for the 3D printed models and virtual models assigned by cch members with more or less than 10 years of expertise and cathlab.

Discussion

The 3D model adoption to test the feasibility of the determined surgical technique gave a positive feedback from clinicians. The 3D printing resulted as the most appreciated approach in terms of perceived usefulness. The SLS was the best among the 3D printing techniques. However, it is worth to stress out that the virtual approach is cheaper since it is not associated to printing costs and the 3D model can be edited several times in a reversible manner.

References

1. S. Celi et al, Curr Pharm Des. 2020.
2. Z. Sun et al, Int J Clin Med, 8(4): 522. 2019.
3. C. Ong et al, Congenit Heart Dis, 13(3): 357-361. 2018.

Acknowledgements

This work was supported by 3D Virtual Baby Heart project (GR-2016-02365072).

UNCOVERING STABILITY PRINCIPLES OF AVIAN BIPEDAL UNEVEN LOCOMOTION.

Emanuel Andrada (1), Oliver Mothes (2), Dirk Arnold(1), Joachin Denzler(2), Martin S. Fischer(1), Reinhard Blickhan (3)

1. Institute of Zoology and Evolutionary Research; 2. Science of Motion; 3. Computer Vision Group, all Friedrich-Schiller-University Jena, Germany.

Introduction

To understand control strategies implemented by any system, it is necessary to characterize how the system responds to external perturbations. By measuring global, joint mechanics and motor responses to a range of perturbations, we can learn about the control strategies implemented by small birds to cope with perturbation during bipedal locomotion.

Methods

To better understanding of the neuromechanics of avian bipedal uneven locomotion, 10 quails moved on a walking-track at their preferred speeds. Uneven locomotion was analyzed by combining X-ray fluoroscopy (500 frames/sec) with 3D ground reaction forces (1 kHz), and electromyographic (EMG, 2 kHz) analysis (see fig. 1). Uneven experiments were divided into steps perturbations and sudden drops perturbations (with and without camouflage). Three different perturbation heights (1 cm, 2.5 cm, and 5 cm) were tested. The complete experiment setup was conducted with and without EMG measurement.

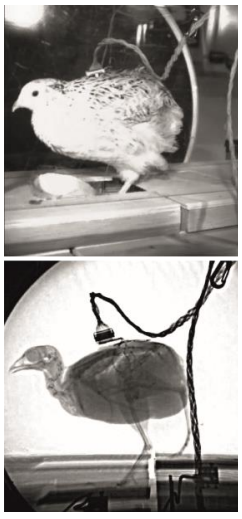

Figure 1: Combining high speed biplanar fluoroscopy, ground reaction force measurement and electromyography. A quail step into a camouflaged hole.

To measure muscle activation, it was necessary to implant electrodes (iridium-platinum alloy) into the muscles. This kind of surgery was never made before in such small birds like quail. We collected ca. 500 videos encompassing steps and drops. The time necessary to manually label landmarks and center of mass (CoM) at 500 Hz is prohibitive. Consequently, we developed semi-automated labeling method for the anatomical landmarks [1] and automated method to estimate 3D-potion of the CoM [2]. Our landmarks localization technique combines deep feature representation of the input image, landmark regression task and 3D reconstruction. Deep features are learned representations of images extracted from a Convolutional Neural Network (CNN). Landmarks regression are trained linear models.

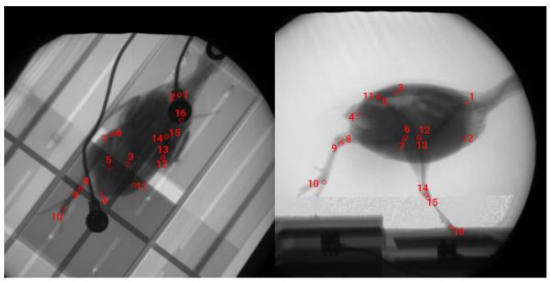

Figure 2: Semi-automated labelling of anatomic landmarks based on biplanar fluoroscopy during uneven locomotion of a quail.

Ongoing work

We now combine 3D-kinematics with 3D-ground reaction forces to analyze global and joint dynamics. Numerical models [3] are used to test stabilization strategies. We expect to start analyzing EMG soon.

By measuring motor responses to a range of perturbations, we expect to define the functional mapping between deviations in limb state (i.e., the position, velocity, acceleration of joints or muscles) and the resulting motor output (i.e., muscle activations). This functional mapping defines the control strategy.

References

1. Mothes, O. and Denzler, J. In International Conference on Pattern Recognition (ICPR) -VAIB, 2018
2. Hasse et al, J Biomech, 46(12), 2082-6, 2013.
3. Andrada et al, Proc Roy Soc B. 281(1797), 2014.

Acknowledgements

Supported by the German Research Foundation DFG-grants (De 735/8-1/3, Bl 236/22-1/3, Fi 410/15-1/3, AN 1286/2-1) to DJ, RB, MSF and EA, respectively.

MICROMECHANICAL CONSEQUENCES OF OCEAN ACIDIFICATION FOR COLD-WATER CORALS

Uwe Wolfram (1), Ali Ozel (1), Marta Peña-Fernández (1), Ewan Smith (1), Sebastian Hennige (2)

1. School of Engineering and Physical Sciences, Institute of Mechanical, Process and Energy Engineering, Heriot-Watt University, United Kingdom; 2. Changing Oceans Research Group, School of GeoSciences, University of Edinburgh, Edinburgh, UK

Introduction

Ocean acidification is a threat to deep-sea coral reefs and could lead to dramatic and rapid loss of the habitats they make. Increases in porosity in structurally critical parts of the coral reef framework will lead to structural weakening and physical habitat collapse on an ecosystem scale, reducing the potential for biodiversity support [1]. *In situ* evidence highlights that cold-water coral (CWC) can survive beneath the aragonite saturation horizon, but in a fundamentally different way to what is currently considered a biogenic cold-water coral reef, due to a loss of the majority of reef habitat [1]. The weakening mechanism has a striking similarity with osteoporosis [2] and similar 'fracture risk' analyses techniques could help to investigate 'tipping points' in CWC reefs. Therefore, this study aims to develop a multiscale constitutive model to investigate the consequences of ocean acidification on CWC stiffness and strength.

Materials and Methods

CWC skeletons are multiscale materials whose building block is the aragonite ($CaCO_3$) crystallite. Crystallites form needles (~5 µm) conglomerated around rapid accretion deposits and in thickening bands making up the skeletal wall [1]. We used molecular dynamics simulations to approximate crystal stiffness and strength [3, 4]. Unit cell dimensions are a = 4.961 Å, b = 7.967 Å and c = 5.740 Å with 4 calcium, 4 carbon and 12 oxygen atoms. Periodic boundary conditions were used on relevant elementary volumes of 24 unit cells in each direction. Time-step was set to 0.001 ps and monotonic loading was applied at a strain rate of 0.01 1/s until after ultimate strength was reached. Three tension and three shear tests were simulated. Computed elasticity was verified against experimentally identified stiffnesses [3].

We developed a three-scale micromechanical model to scale up stiffness and strength and implemented it in Abaqus (v6.16). The skeletal wall was modelled as a polycrystalline material with randomly oriented aragonite needles [5] and dissolution porosity was included via a Mori-Tanaka scheme [6]. We used a Mohr-Coulomb strength criterion [5] for the aragonite crystals to identify a porosity dependent strength criterion [7] at the skeletal length scale to incorporate strength loss due to ocean acidification. Cell wall elasticity was compared to quasi-static nanoindentation tests (1 µm depth) of CWC material unaffected by ocean acidification.

Results

SEM and EBSD images confirmed that crystal arrangement can be assumed as random. Molecular dynamics derived aragonite stiffness compared well with the literature (Table 1) so that strength values (3.93-5.33 GPa) are considered usable for our micromechanical model.

in GPa	C_{11}	C_{22}	C_{33}	C_{44}	C_{55}	C_{66}
Exp	171.1	110.1	85.0	41.3	25.6	42.7
Comp	164.4	112.0	71.3	40.1	26.6	43.8
MD	156.1	96.0	66.5	34.1	24.6	38.7

Table 1: Normal and shear components of the aragonite stiffness tensor. Exp and Comp are literature values [3] and MD denotes our molecular dynamics results.

Polycrystalline stiffness (no dissolution) was comparable to nanoindentation results. Significantly increasing porosity due to ocean acidification (Figure 1a) has a detrimental effect on macroscopic stiffness (Fig 1b) while the underlying material properties of the polycrystal are not significantly affected (p=0.08). Strength of the skeletal wall follows a similar trend (Fig 1c).

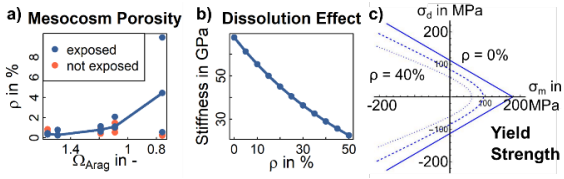

Figure 1: Porosity ρ significantly increased with increasing aragonite concentration (a) for exposed CWC skeletons in 12 months long experiments simulating future oceanic conditions [1]. *Porosities reached up to ~40% so that stiffness (b) and yield strength (c) of the skeletal wall were significantly decreased.*

Discussion

We developed a multiscale model that allows us to investigate the effect of ocean acidification on exposed CWC structures. Aragonite concentration dependence of porosity (Fig 1a) allows us to use an *in situ* biochemical marker as an independent variable. The shift from a habitat of high 3-dimensional complexity provided by both live and dead coral framework, to a habitat restricted primarily to live coral colonies with lower 3-dimensional complexity represents the main threat to future CWC reefs and the biodiversity they support. The presented model may help to determine critical exposure times and may allow 'tipping points' to be quantified for future management of these vulnerable ecosystems.

Acknowledgements

This project was supported by Leverhulm Trust Research Project Grant 2020-215.

References

1. Hennige et al. Sci Adv, In review (MS available)
2. Hernlund et al. Arch Osteopor 2013.
3. Liu et al. Phys Chem Miner 2005, 32(2): 97-102.
4. Plimpton, J Comp Phys 1995, 117(1): 1-19.
5. Sanahuja et al. J Eng Mech 2010, 136(2): 239-253.
6. Speed et al. JMBBM in press
7. Schwiedrzik et al. BMMB 2013, 12(6): 1155-1168.

MODELLING SALBUTAMOL PARTICLE TRANSPORT AND DEPOSITION IN THE CAT UPPER AIRWAYS

Rocío Fernández-Parra (1,2), Pascaline Pey (3), Ghita Benchekroun (1), Carol R. Reinero (4), Mauro Malvè (5)

1. École Nationale Vétérinaire d'Alfort, Maisons-Alfort, France; 2. Universidad Católica de Valencia, Spain; 3. Department of Veterinary Medical Science, University of Bologna, Ozzano dell'Emilia, Italy; 4. University of Missouri, Columbia, USA; 5. Universidad Pública de Navarra, Pamplona, Spain

Introduction

The cat is the only animal species that spontaneously develops allergic asthma with all the major features of the human disease, and serves as an important pre-clinical model. Inhaled medications allow topical treatment of affected large airways while decreasing systemic side effects. While the intent of inhaled medications is to reach the lower airways, substantial amounts of drug are deposited in the upper airways leading to drug waste and undesirable local high dosages. Knowledge of inhaled drug deposition has relevance both for pet cats and humans with asthma. Computational fluid dynamics (CFD) is used in humans for non-invasively studying aerosol deposition. Little is known in animals, and only few studies have been performed in the rabbit [1], rat and monkey [2]. In this study, we analyze particle transport and deposition in the airways of a cat. Results will help improve drug delivery strategies and benefit pet cat health.

Materials and Methods

One adult client-owned healthy cat was enrolled in this study. The cat required sedation for a computed tomography scan for reasons unrelated to this study. The medical images were imported into the geometry reconstruction software Mimics (Materialise Software). A manual reconstruction of the geometry of the upper airway (nose, nasopharynx, larynx) and trachea was performed.

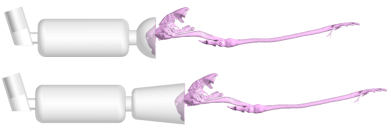

Figure 1: Geometry baseline models illustrating the metered dose inhalant, spacer of 10 cm, and spherical (top) or conical (bottom) masks.

The CFD analysis was performed with the software Ansys CFX (Ansys Inc.) after the imposition of an inspiratory flow of 3.7 L/min [3]. The drug transport and deposition consider particles of aerosol with size of 10 μm and density of 1000 kg/m^3 [4]. Six different combination device models' simulations were done: two masks with a spherical and a conical shape and two spacers of 10 and 20 cm respectively were used for inhalation (see Figure 1). Particles released from the simulated inhaler traveled along the airways until they impacted the walls or exited from the model outlets.

Results

The CFD simulations of the cat inspiration and the obtained drug transport and deposition show that a consistent number of particles deposits in the masks, in the spacers and/or in the upper airways, especially in the nasal regions (Figure 2). This insinuates drug waste and it suggests that prolonged treatment with repeated inspiratory efforts would be needed for adequate drug concentrations to reach the lower airways.

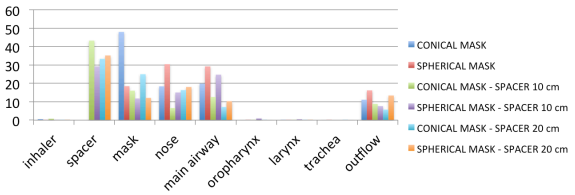

Figure 2: Regional particle deposition (plotted in % on the y-axis) within the cat airways (specified on the x-axis) and the different devices. Outflow represents regions downstream of the trachea, the target of drug deposition.

Discussion

CFD is used to compute the aerosol particle deposition and transport valuable in a number of human respiratory diseases. Drug waste has been reported in humans even in the presence of spacers that should improve the delivery [4]. A non-optimal drug distribution is also revealed in cats in this study. Only small percentages of particles reach the regions downstream of the trachea even in the presence of spacers. Because cats serve as an animal model for human asthma in particular for investigations of novel treatments and pet cats spontaneously develop asthma, thus, application of CFD in the feline species has relevance for bidirectional improvements in cat and human health.

References

1. J. Xi et al, Anat Rec, 299:853-868, 2016.
2. R. A. Corley et al, Toxicol Sci, 128(2):500-516, 2012.
3. P. Pang et al, J Exp Biol, 219:1866-1874, 2016.
4. C. Kleinstreuer et al, J Aer Med, 20(3):294-309, 2007.

Acknowledgements

Dr. M. Malvè and Dr. R. Fernández-Parra are supported by grant DPI2017-83259-R (AEI/FEDER, UE) from the Spanish Ministry of Economy, Industry and Competitiveness.

FEM SIMULATION OF KNEE JOINT IN DOGS: EFFECTS OF JOINT LOADING CORRELATE WITH BONE DENSITY

Heiko Stark (1), Emanuel Andrada (1), Martin S. Fischer (1)

1. Friedrich-Schiller-University Jena, Institute of Zoology and Evolutionary Research, Germany

Introduction

The domestic dog is the only species with more than 300 breeds. These have different body sizes (chihuahua – great dane) and variable body types (sighthound – bulldog). Thus, it is possible to study size-dependent effects without major morphological differences in musculature and innervation. Fischer et al. [1] showed that the hindlimb kinematics differ in relation to body shape and leg posture. The French bulldog, having more abducted hindlimbs, exhibited significant differences in terms of trajectories (abduction/ adduction) and long axis rotation of the femur. This unusual leg kinematics can yield into pathologies, due to the irregular loading of the joints.

To better understanding of if the relationship between joint pathogenesis and joint dynamics is necessary to bring light in how the interplay between breed related joint's passive properties, gait-typical kinematics and forces, and bone density influences bone stress. In the present study, we started the analysis of this interplay on the knee of a Beagle.

Material & Methods

The knee model was built using computed tomography (CT) data of an adult Beagle (13.8 kg [2]). The resulting CT data set consisted of 3370 (spacing 0.33 mm) sections with a resolution of 512×512 pixels (spacing 0.279×0.279 mm). The femur, tibia and soft tissue were reconstructed from this data set with Amira (Thermo Scientific Amira Software; Fig. 1).

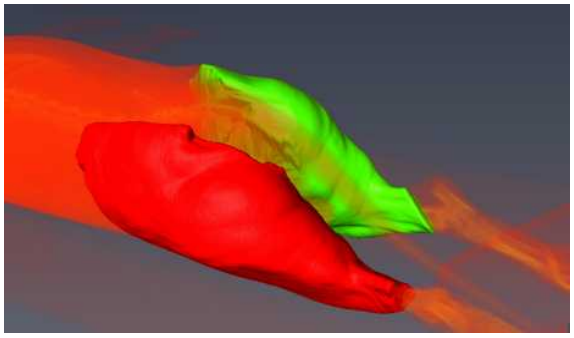

Figure 1: Three-dimensional knee models considering the knee bones and soft tissue (left: red; right: green). The reconstruction was created with Amira.

In the second step, a FE-model with a resolution of 1x1x1 mm hexahedrons was created from the reconstruction. The soft tissue was implemented in two different model variants. The first one included a homogeneous distribution of the material properties. The second considered the musculature, ligaments, skin and connective tissue. For the simulation, the femur was fixed and a load was applied to the tibia. The load was limited to extension, flexion, adduction and abduction in the preliminary tests. The FEBio and the Postview software tools from the MRL and MBL [3] were used for the simulation and evaluation.

Results & Discussion

As expected, the regions on the joint surfaces showed the highest stress, where the bone density was also highest. The simple (homogeneous soft tissue) and the complex model displayed similar stress-distributions. It has to be pointed out that there was no additional control in the joints or further constraints. The force and the geometry constraints of the surrounding tissue stabilized the motion (Fig. 2).

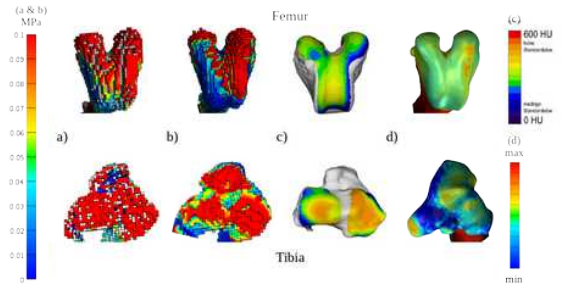

Figure 2: Inter-articular view of the knee simulation (flexion) of the simple (a) and complex model (b) without the connective tissue. As well as the bone density measurement by Riegert [4] (c) and our CT data (d).

Based on our the results, it can be hypothesized that for the different breeds the specific geometry of the bones and the distribution of the soft tissue constraint motion and forces transmission. This body plan might face important problems for highly unusual joint kinematics, increasing the risk of emergence of degenerative diseases. This hypothesis needs more investigation.

References

1. Fischer, Lehmann & Andrada. Sci Rep 8, 16982, 2018. DOI:10.1038/s41598-018-34310-0
2. Andrada, Reinhardt, Lucas & Fischer. Am. J. Vet. Res.78, 804–817, 2017. DOI: 10.2460/ajvr.78.7.804
3. Maas, Ellis, Ateshian, Weiss. J. Biomech. Eng., 134(1):011005, 2012.
4. Riegert. Tierärztlichen Fakultät der Ludwig-Maximilians-Universität München, vet. PhD thesis, 2004 .

Acknowledgments

We thank all the involved members of the Institute of Zoology and Evolutionary Research for their stimulating discussions and support. This research work was supported by the company 'Biologische Heilmittel Heel GmbH'.

HIERARCHICAL CLUSTERING OF MUSCLE ACTIVATION DURING DOG LOCOMOTION: A SIMULATION STUDY

Heiko Stark (1), Martin S. Fischer (1), Emanuel Andrada (1)

1. Friedrich-Schiller-University Jena, Institute of Zoology and Evolutionary Research, Germany

Introduction

Dogs are an interesting object of investigation due to their different body sizes (chihuahua – great dane) and their variable body type (sighthound – bulldog). The domestic dog is the only species with more than 300 breeds. Thus, it is possible to study size-dependent effects without major morphological differences in musculature and innervation.

Material & Methods

For this purpose, we developed a dog model, which has 84 DoFs and 134 (67 per side) muscles (Fig. 1). Our model includes the majority of fore- and hindlimb muscles and the most important epaxial muscles used for locomotion.

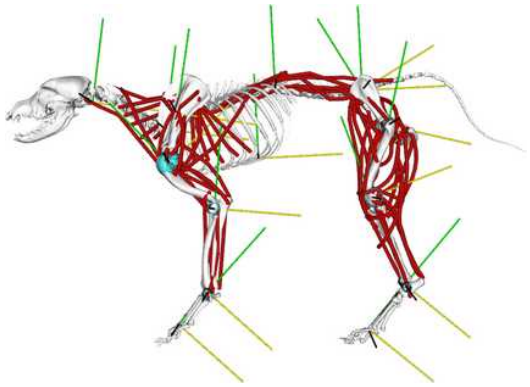

Figure 1: Three-dimensional dog model considering the musculature (red) and the specific joints (cyan) as well as the local segments (bones). The local axes are aligned laterally (red), longitudinally (green) and transversely (yellow) to the bone.

By using static optimization in the software package "OpenSim" we estimated muscle activation patterns and forces in a dog at walk [1, 2]. For this purpose, we used 3D-limb kinematics and ground reaction forces recorded experimentally [3, 4].
The muscle activation's estimated by the model were further analyzed using a hierarchical cluster analysis (R – Ward2 algorithm) to identify similar activation patterns among the muscles. This method permitted us to find muscle groups that showed a similar pattern of innervation. By integrating literature data [5, 6] into the cluster analysis, we ensured a more objective comparison between simulation results and published data.

Results & Discussion

For most muscles, our simulations delivered comparable results to the literature. Additionally, our analysis allowed us to detect inconsistencies in the data and to describe previously unmeasured muscles (Fig. 2 [7]). Apart from numerical errors and optimization goals, inconsistencies can be caused by the fact that EMG studies are largely based only on surface EMG's and can therefore only provide a diffuse and local representation of muscle activation's.

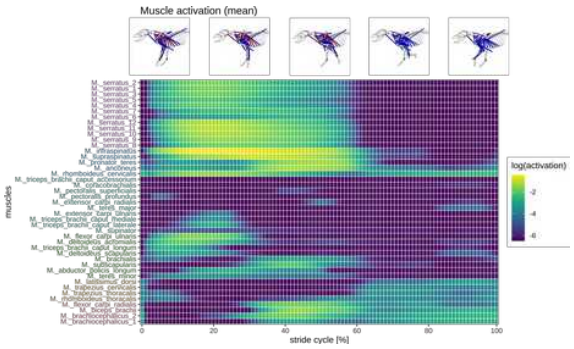

Figure 2: Muscle activation pattern for 43 muscles of the dog forelimb. Blue indicates no activation and yellow ~30% muscle activation. The muscle names are colored according to their hierarchical clustering.

References

1. Seth, Hicks, Uchida, Habib, Dembia, Dunne, Ong, DeMers, Rajagopal, Millard, Hamner, Arnold, Yong, Lakshmikanth, Shermann & Delp, Plos Computational Biology, 14(7), 2018.
2. Delp, Anderson, Arnold, Loan, Habib, John, Guendelman & Thelan, IEEE Transactions on Biomedical Engineering, 55: 1940-1950, 2007.
3. Andrada, Reinhardt, Lucas & Fischer, American Journal of Veterinary Research, 78, 2017.
4. Fischer, Lehmann & Andrada, Scientific Reports, 8, 2018.
5. Tokuriki, The Japanese Journal of Veterinary Science, 35(5): 433-446, 1973.
6. Deban, Schilling, & Carrier, Journal of Experimental Biology, 215(2): 287–300, 2012.
7. Stark, Fischer, Hunt, Young, Quinn & Andrada, 2020. BioRxiv:2020.07.16.205856; DOI:10.1101/2020.07.16.205856

Acknowledgments

We thank all the involved members of the Institute of Zoology and Evolutionary Research for their stimulating discussions and support. We especially thank Jonas Lauströer and Amir Andikfar for providing the muscle data for the model. This research work was supported by the company 'Biologische Heilmittel Heel GmbH'.

INJURIES IN GREYHOUND RACING: NUMBER OF STARTERS

Karlos Ishac (1), David Eager (1)

1. University of Technology Sydney, Australia

Introduction

As with children falling in playgrounds [1-5] and trampolines [6], long-bone and neck [7] fractures can occur in racing greyhounds caused usually by collisions and falls [8,9]. The number of injuries occurring on the first turn of an ovoid track is largely due to the congestion. The hypothesis discussed herein is that reducing the congestion will result in a decrease in the injury rate in greyhound racing. The variable explored in this study is the number of greyhounds in a race. Australia has races with 8 starters, whereas in England and Ireland races have 6 starters.

Methods

Over a two-year period from June 2018 to July 2020, race injury data were recorded from all 13 greyhound tracks in Victoria, Australia. Even though races are usually conducted with 8 greyhounds, there were races with fewer greyhounds due to low numbers of dogs being nominated and/or one or more dog being scratched. The injury rates were recorded and compared for 6 and 8 dog races on the same track and varying race distances. The hypothesis was having more space between greyhounds during a race would reduce the congestion, especially while the greyhounds negotiate their way around the first turn, and this reduced congestion would result in fewer serious injuries. All race injuries were assessed by professional on-track veterinary surgeons. The injuries were categorised by the stand-down (or incapacitation) period given to the greyhound, ranging from 0 - 90 days. Major 1 were greyhounds given a stand-down of between 28 and 42 days, Major 2 were greyhounds given more than 42 days stand-down and Catastrophic injuries were fatal (see Figure 1).

Results and Discussion

In total 3,445 races with 6 starters, examining 20,670 greyhounds and 16,051 races with 8 starters, examining 128,408 greyhounds were observed. All injury data was normalised per 1,000 starters for each venue and racing distance. Figure 1 shows the normalised number of injured greyhounds per 1,000 starters for all 6 and 8 dog races for Victoria, Australia. Figure 1 shows that there were significantly lower number of injured greyhounds in 8 dog races compared to races with 6 greyhounds. The results showed that 8 dog races have a statistically significant lower number of greyhounds with Major injuries compared to 6 dog races. The 6 dog races recorded 394 Major 2 injuries compared to only 246 Major 2 injuries in 8 dog races. However, both 6 and 8 dog races showed similar numbers of Catastrophic injuries on a normalised basis.

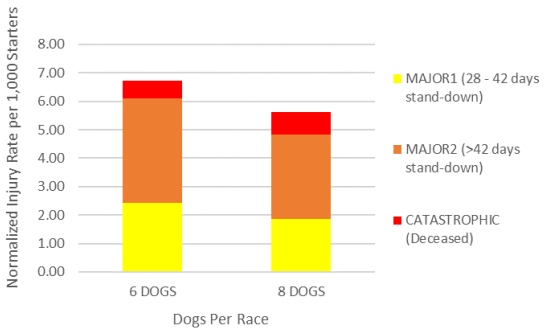

Figure 1: Comparison of normalised injury rates for all 6 and 8 dog races from June 2018 to July 2020 in Victoria, Australia.

Conclusions and Recommendations

The data showed that having 8 dogs per race resulted in a lower number of greyhounds sustaining Major injuries than having 6 dog races. However, having either 6 or 8 dog races did not significantly affect the number of fatalities observed. These results are counter-intuitive, as it was expected that having fewer greyhounds in a race would reduce congestion and result in a lower number of injured greyhounds. It is recommended that more research be undertaken to understand why there are more Major injuries in 6 dog races compared to 8 dog races.

References

[1] Nixon J.W. et al. (2004) *Preventing injuries on horizontal ladders and track rides*. Injury Control and Safety Promotion Journal, 11(4):219-224.

[2] Sandseter E.B.H. et al. (2017) *Risk and safety in outdoor play*, The SAGE handbook of outdoor play and learning, pp113-126, ISBN 978-1-47-3926608.

[3] Davidson P.L., et al. (2013) *Analysis of energy flow during playground surface impacts*, Journal of Applied Biomechanics, 29:629-633.

[4] Eager D. et al. (2016) *Impulse force as an additional safety criterion for improving the injury prevention performance of impact attenuating surfaces in children's playgrounds*. ASME, Safety, Eng and Risks Analysis.

[5] Eager D., Hayati H. (2018) *Additional injury prevention criteria*, ASCE-ASME J. Risk Uncertainty Part B.

[6] Ashby K. et al. (2015), *Influence of voluntary standards and design modifications on trampoline injury in Victoria, Australia*. Inj Prev 9-041598.

[7] Whyte T. et al. (2016) *Mechanisms of head and neck injuries sustained by helmeted motorcyclists in fatal real world crashes - Analysis of 47 in-depth cases*, Journal of Neurotrauma. doi:1089/neu.2015.4208

[8] Hayati H. et al. (2017) *A study of rapid tetrapod running and turning dynamics utilizing inertial measurement units in greyhound sprinting*, ASME-IDETC/CIE29017.

[9] Hayati H. et al. (2017) *A novel approach to analysing rapid tetrapod locomotion using inertia measurement units and stride length as a speed indicator in fast quadrupeds*, ISB, Brisbane, Australia

FLUID MECHANICS AND GENE EXPRESSIONS OF THE CHICK EMBRYONIC MODEL OF HYPOPLASTIC LEFT HEART SYNDROME

Sheldon Ho (1), Wei Xuan Chan (1), Choon Hwai Yap (2)

1. Dept of Biomedical Engineering, National University of Singapore, Singapore;
2. Dept of Bioengineering, Imperial College London, UK

Introduction

Past investigations showed that biomechanical forces can influence cardiovascular development and cause congenital heart malformations, but the mechanism is unclear. We investigate the role of abnormal fluid mechanics in causing Hypoplastic Left Heart Syndrome (HLHS), using the chick embryonic model of HLHS. This model is achieved via left atrial ligated (LAL) on the HH21 chick embryo, which disrupts ventricular inflow, and causes a hypoplastic left heart by HH28 [1].

Methods

In vivo 4D high-frequency ultrasound imaging was performed on chick embryonic hearts (5 normal, 4 LAL). Temporal ensemble averaging was performed to improve blood-tissue contrast. Cardiac motions were tracked with a validated algorithm [2]. Image-based dynamic mesh computational fluid dynamics (CFD) simulations were performed on whole embryonic heart, as per previously published methods [3].

At HH30 (E6.5), the LV free wall were extracted from 4 normal and 4 LAL embryos for single-cell RNA-sequencing. 392 cells were sequenced (130 endothelial, 171 myocytes, 91 others), approximately 50%-50% between Normal and LAL groups. The Louvain method was used to cluster the 2D UMAP profiles of the 392 cells. The subsequent cell annotation was performed by combining Seurat's marker analysis, gene ontology and gene set enrichment analysis.

Results and Discussion

LAL reduced atrial size and stroke volume. At E4.5, the ventricle apex became more pointed, and a medial shift in the atrioventricular junction is observed. By E5.5, the left ventricle (LV) size and stroke volume were smaller than controls, even before full ventricular septation, but right ventricle (RV) size and stroke volume compensated and were above controls.

Reduced atrial function led to weak inflow into the LV, and reduced velocities in the LV. Velocity fields are shown in figure 1A. The LV geometric changes led to regions near the LV free wall and apex to be further away from the streams of flow in the LV, leading to sluggish flow at the LV free wall, where fluid particles bobbed around with contraction motion, but are only washed towards the outlet slowly. This led to weak and oscillatory wall shear stresses (WSS) on the LV, which could be linked to the hypoplastic LV at E6.5. Particle tracking demonstrated high particle retention in the LV free wall regions (Figure 1B).

RNA-seq showed that differential expression of several mechanosensing-related genes, including VEGFR2 and glypicans in the endothelial cells, and focal adhesion genes, Cadherins and NOTCH1 in myocardial cells. Expression levels for calcium signaling genes (PI3K, Caveolin, SERCA) and myosin contractility genes (CALM, MLCK, MLCP) were altered. Many ECM remodeling genes (9 types of collagen, laminin, 3 types of MMP, and TIMP3) were upregulated, suggesting myocardial fibroelastosis, which agreed with previous findings. Endothelial-myocardial signaling gene expressions (TGF-b, BMP, FGF, and PDGF) were also altered.

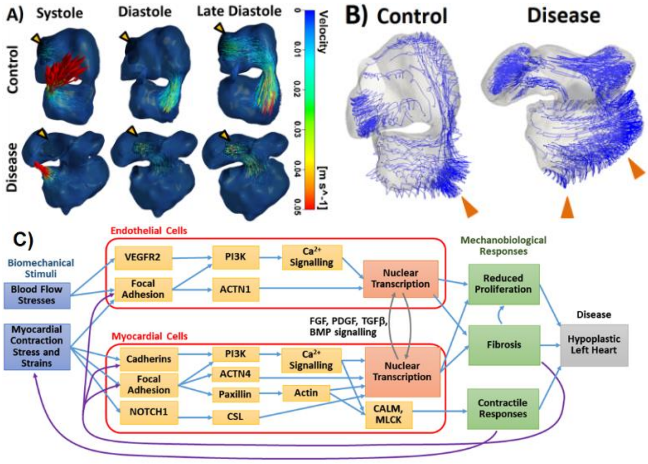

Figure 2: (A-B) CFD results: (A) velocity field, (B) particle tracking analysis, showing high particle retention in LAL LV due to weak and oscillatory flow near the LV. (C) RNAseq provided clues to possible mechanobiological pathways leading to HLHS in the LAL model.

Conclusions

We discovered that hypoplastic LV can occur in the LAL chick embryonic model of HLHS even before septation is complete, and that this is likely related to WSS becoming weak and oscillatory at the LV free wall, due to compromised atrial function, and ligation induced alteration in cardiac geometry. We also discovered potential mechanobiological pathways for HLHS.

Acknowledgements

Funding by Singapore Ministry of Education Grant number MOE-T2-1-003, and Imperial College Startup.

References

1. Tobita, K., et al. *Am J Physiol Heart Circ.*(2002),282, H2386-2396
2. Wiputra, H., et al. *Sci Rep.* 10, 18510 (2020)
3. Ho, S., et al. *Sci. Rep.*, (2019), 9, 18072

INFLUENCE OF PATIENT BREATHING AND COORDINATION ON INHALED DRUG DEPOSITION IN IMAGE-BASED MODELS

Josh Williams (1), Steve Cunningham (2), Ali Ozel* (1), Uwe Wolfram* (1)

*1. School of Engineering and Physical Sciences, Heriot-Watt University, Edinburgh, UK; 2. Centre for Inflammation Research, University of Edinburgh, Edinburgh, UK. * Authors share last authorship*

Introduction

Respiratory patients often suffer from poor inhaler technique, which hinders treatment effectiveness and disease management. Patient breathing speed and coordination with inhaler actuation is particularly problematic for children [1]. Delayed inhaler actuation has been modelled in a simple mouth-throat geometry with constant air inflow [2]. Understanding the deposition change with delayed or early actuation in transient breathing will give a better understanding of which patients may require breath-actuated inhalers. Therefore, we aimed to evaluate drug deposition change due to (i) airway structure and (ii) rapid vs normal patient breathing. We then evaluated deposition change due to device coordination in a child patient, by adjusting when drugs were released during breathing.

Materials and Methods

We compare drug deposition in the airways of a healthy male, a female lung cancer and a child cystic fibrosis patient [3]. Deposition of 10 and 4 µm particles was compared in each patient to evaluate the differences due to patient anatomy. We used airways extracted from clinical computed tomography scans for simulations (Fig. 1a). We used a computational fluid dynamics-based solver (MPPICFoam) coupled with Lagrangian particle tracking in OpenFOAM [4], allowing us to track individual particles and account for effects of fluid-particle momentum transfer. We validated the gas velocity field against *in vitro* data [5]. Due to computational limitations, we modelled a 0.1 µg dose (200,000 particles at 10 µm diameter, 1000× lower than a real dose). The implications of modelling realistic dosages on predicted drug deposition will be investigated in a future study.

Results

We show upper airway deposition ranged 50-95% of the total dose across patients for 10 µm particles with rapid breathing. Both diseased patients had 30% upper airway deposition with 4 µm particles during rapid breathing, and the healthy patient had 20%. During rapid breathing, all patients had deposition hotspots over 100× the mean concentration, mainly in the throat (Fig. 1a). For 10 µm particles during normal breathing, 40% of the total dose reaches the juvenile cystic fibrosis patient's deep lung when released at the start of inhalation (Fig. 1b, ii). With a delay of 0.5 s (Fig. 1b, iii), the deep lung receives 18%. Conversely, when released 0.5 s before inhalation begins, the deep lung receives 35% of the dose (Fig. 1b, i). At a delay of 1.8 s only 25% of the dose deposits. As inhalation is nearly finished, most of the drug is still floating as the patient transitions to exhalation (which was not modelled). In that case, 75% of the drug is exhaled and is wasted.

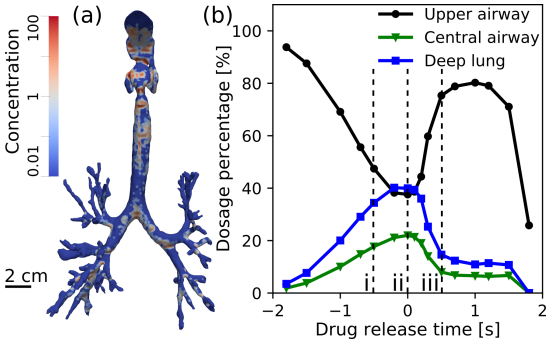

Fig. 1: Deposition in a cystic fibrosis patient for 10 µm particles and normal breathing. Panels: (a) Deposition concentration normalised to a mean of one. (b) Drug delivery change with inhaler coordination, where negative time is early, positive time is delayed, and t = 0 s is perfect coordination.

Discussion

Our results show 10 µm particles were sensitive to patient airway shape and breathing profile (figure not shown). With more ideal conditions (small particles, healthy breathing), upper airway deposition varied less across the three patients (range only 10%, compared to 45% in rapid breathing and 10 um particles). The change in deposition caused by delayed actuation (Fig. 1b) is due to the acceleration and deceleration of the flow creating flow structures that do not appear with constant inlet conditions [6]. Our models show deposition is influenced most by coordination during acceleration and deceleration stages of inhalation.

Our models were limited by not including ventilation variation across different lung lobes. We believe that our results pave the way to integrate such models into patient care to improve and maintain good technique.

References

1. O.S. Usmani, Ther Clin Risk Manag, 15, p.461, 2019
2. Á. Farkas et al, Int J Pharm, 547(1-2), pp.480-488, 2018.
3. J. Williams et al, MedRxiv, doi: 10.1101/2020.06.08.20118513, 2020.
4. D.M. Snider, J. Comput. Phys, *170*(2), pp.523-549, 2001.
5. A. Banko et al, Exp Fluids 56:117, 2015.
6. S. Jalal et al, Phys Rev Fluid, 5(6), p.063101. 2020.

Acknowledgements

JW was supported by a 2019 PhD scholarship from the Carnegie-Trust for the Universities of Scotland.

IMPLEMENTING PHYSIOLOGICAL PROCESSES IN COMPUTATIONAL FLUID DYNAMICS MODELS OF THE CEREBROSPINAL FLUID

Sarah Vandenbulcke (1), Tim De Pauw (2), Frank Dewaele, PhD (2), Patrick Segers, PhD (1)

1. Ghent University, IBiTech-bioMMeda, Department of Electronics and Information Systems, Belgium; 2. Ghent University Hospital, Department of Neurosurgery, Belgium

Introduction

The brain and the spinal cord are surrounded by the cerebrospinal fluid (CSF). This clear, water-like liquid provides protection against impacts and shocks and plays a crucial role in the maintenance of homeostasis in the central nervous system [1]. Disturbances in its normal production, absorption and/or movement modifies the neuro-biomechanical environment through changes in CSF and brain tissue pressures. This can lead to severe neurological complications as observed in patients with Chiari malformation, hydrocephalus and dementia [2]. However, the mechanisms underlying these disorders are not well understood, neither are the CSF dynamics under normal physiological circumstances. The aim of this study is to investigate, through computational fluid dynamics (CFD) modeling, the physiological processes affecting the dynamical behavior of the CSF by incorporating them as boundary conditions. Adequate boundary values were retrieved from clinical literature (Sakka et al. [3]) and numerical and magnetic resonance imaging (MRI) studies performed by Sweetman et al. [4], Khani et al. [5] and Matsumae et al. [6].

Methods

A three-dimensional model of the ventricular CSF space was constructed (figure 1). The geometry was obtained via segmentation of clinical T2 MRI images from Ghent University hospital, taken from a middle-aged female, using Mimics (Materialise, Leuven, Belgium).

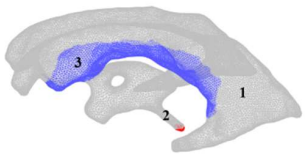

Figure 1: Geometry of (1) the lateral ventricles, (2) the cerebral aqueduct and (3) the choroid plexus.

An unstructured computational mesh was generated in ICEM (Ansys, Canonsburg, USA), with the final number of elements (650971) determined in a mesh sensitivity study. The CFD analysis was performed within the numerical software Fluent 2019 R3 (Ansys, Canonsburg, USA). The CSF was modeled as an incompressible Newtonian fluid with properties similar to water at body temperature (density 998.2 kg/m³ and dynamic viscosity of 0.8 mPa.s). Further, the flow was considered laminar because of low Reynolds numbers. Problem-specific boundary conditions are as follows. First, CSF production by the choroid plexuses, which are specialized cell structures in the cerebral ventricles, was implemented as a continuous bulk flow of 0.4 ml/min. Secondly, the arterial pulse causes the cerebral arteries to expand during systole, leading to periodic brain tissue displacement that induces pulsatility in the CSF flow. This effect was taken into account by inclusion of a pulsatile flow at the ventricular walls based on boundary conditions applied by Sweetman et al. [4]. Finally, the fluid leaves the ventricular space through the cerebral aqueduct, to normally flow via the fourth ventricle into the spinal and cranial subarachnoid space. At this outlet, the effects of pressure build-up and damping within the CSF space were implemented by imposing windkessel model boundary conditions to produce a realistic pressure distribution.

Results and discussion

The maximal velocities and flow rate through the center of the aqueduct were selected as a reference and compared to phase-contrast MRI measurements reported by Sweetman et al. [4] and Matsumae et al. [6]. Adequate finetuning of the boundary conditions allowed to simulate velocities and pressures within the physiological range (20 mm/s and 550 Pa above venous pressure respectively) as depicted in figure 2.

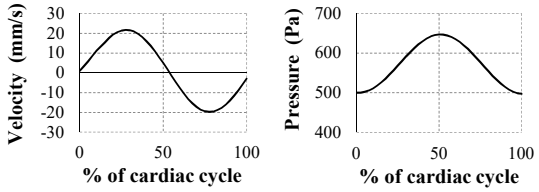

Figure 2: Velocity (left) and pressure (right) magnitude in the cerebral aqueduct simulated for one cardiac cycle.

These boundary conditions can be implemented into future models, hereby requiring appropriate validation, for investigation of the normal CSF circulation as well as for research of CSF-related neurological disorders.

References

1. R. Spector et al., Exp. Neurol., 273, 57–68, 2015.
2. B. A. Martin et al, in R. R. Lonser et al. Eds. Academic Press, 73–89, 2019.
3. L. Sakka et al, Eur. Ann. Otorhinolaryngol. Head Neck Dis., 128, no. 6, 309–316, 2011.
4. B. Sweetman and A. A. Linninger, Ann. Biomed. Eng., 39, no. 1, 484–496, 2011.
5. M. Khani et al, Fluids Barriers CNS, 17, no. 1, 1–17, 2020.
6. M. Matsumae et al, Neurol. Med. Chir, 59, no. 4, 133–146, 2019.

COMPARING TIME-EFFICIENT PARTICLE RELEASE MAPS FOR LIVER TUMOR TARGETING WITH EMBOLIZING MICROPARTICLES

Tim Bomberna (1,2), Geert Maleux (3,4), Charlotte Debbaut (1,2)

1. IBiTech-bioMMeda, UGent, Belgium; 2. Cancer Research Institute Ghent (CRIG), Belgium; 3. University Hospitals Leuven, Belgium; 4. KU Leuven, Belgium;

Introduction

Hepatocellular carcinoma (HCC) is one of the leading causes of cancer mortality worldwide [1]. During transarterial radio- (TARE) and chemoembolization (TACE) for the treatment of unresectable HCC, damaging microparticles are injected in the hepatic arteries to selectively destroy tumor tissue [1]. Since the impact of clinically variable parameters (e.g. injection location, particle size and density, etc.) on the target specificity of the procedure is currently unclear, computational fluid dynamics (CFD) may be used to investigate this impact [2]. While transient simulations are typically run for these purposes, their high computational complexity and cost may limit eventual clinical applicability. In this study, it is investigated whether computationally less complex steady-state (SS) alternatives can offer a time-efficient alternative.

Methods

The hepatic arterial geometry was obtained by combined vascular corrosion casting and micro-CT imaging of an explanted human cirrhotic liver [3]. The arteries were segmented and 3D reconstructed using Mimics and 3-matic (Materialise, Leuven, Belgium). A volume mesh containing $9 \cdot 10^6$ tetrahedral elements and three prism boundary layers was created in ICEM CFD (Ansys Inc., Canonsburg, USA). Blood flow was modelled using a shear-thinning fluid (Quemada viscosity model) and a density of 1060 kg/m³. The dispersion of microparticles (diameter: 40 µm, density: 1600 kg/m³; mimicking SIR-Spheres (Sirtex, Australia)) inside the bloodstream was calculated using the Discrete Phase Model in Ansys Fluent (Ansys, USA). The outflow boundary conditions (BC) were set according to Aramburu's perfusion methodology [4], corresponding with a moderate tumor (565 ml) in the 4th liver segment. A transient simulation of seven cardiac cycles was run, during which particles were released throughout the third cycle. For the inflow BC, a transient inflow waveform of 0.8s was specified (see Fig. 1). At four selected timepoints, separate steady-state simulations were run: t=0.01s (Sim. 1), t=0.09s (Sim.2), t=0.35s (Sim. 3), t=0.65s (Sim. 4). For each simulation, the % of particles exiting through each outlet of the domain (particle exit fraction, or PEF) was obtained.

Results

Inspecting the global particle distribution, Sim. 1 (t=0.01s) provides the closest match with the transient PEF, with an average difference of 0.565% per outlet (max: 1.86%). Sim. 2 (t=0.09s, systolic rise) provides the worst prediction, with an average difference of 0.824% (max: 5.91%). In Fig. 1, Particle Release Maps (PRMs) for Sim.1-4 are given. PRMs are visualizations of the injection plane, showing where particles should be injected cross-sectionally to reach the tumor (green outlets). The PRMs in Fig. 1 were generated by comparing each SS PRM with the transient PRM generated at the corresponding timepoint. Here, green zones indicate the tumor targeting zones as predicted in both simulations, red zones indicate the non-tumor targeting zones, while orange zones indicate a mismatch in prediction of particle fate between the two simulations (the % mismatch is given at each timepoint in Fig. 1, which is minimal for Sim.2 (34.2%)).

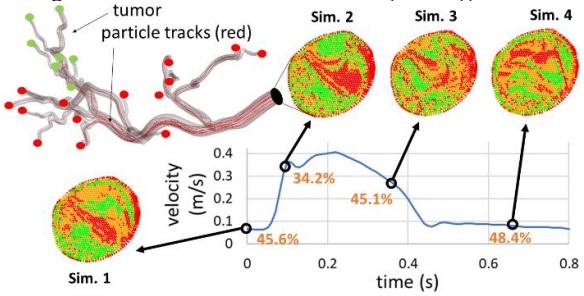

Figure 1: Comparing tumor targeting zones (green) and non-tumor zones (red) between SS and transient results at specific timepoints (t=0.01s, 0.09s, 0.35s, 0.65s). Orange zones indicate a mismatch in prediction.

Discussion

While SS simulations at selected timepoints can provide a relatively accurate prediction of global particle distribution throughout the liver network (e.g. Sim. 1, t=0.01s), the large orange zones in Fig. 1 show that there are considerable discrepancies between the tumor targeting zones in the PRMs of the SS and transient simulations. Next, the accuracy of the global SS prediction should be verified for varying injection conditions and particle characteristics.

References

1. Salem, R et al., *Clin Gastroeneterol Hepatol*, 11:604–611,2013.
2. Aramburu, J et al., *Curr Med Chem*, 25:1–15,2018.
3. Debbaut, C et al., *J Anat*, 224:509–517,2014.
4. Aramburu, J et al., *Int J Numer Method Biomed Eng*, 32:2016.

Acknowledgements

This research was supported by the strategic basic FWO grant 1S10421N.

COUPLING OXYGEN DELIVERY AND RADIATION DAMAGE THROUGH A 3D-1D MULTISCALE MODEL OF MICROVASCULAR FLOW

Riccardo Rosati (1,2), Luca Possenti (2,3), Daniele Cerroni (1), Alessandro Cicchetti (3), Maria Laura Costantino (2), Tiziana Rancati (3), Paolo Zunino (1)

1. MOX, Dept. of Math., Politecnico di Milano; 2. LaBS, Dept. of Chemistry, Materials and Chemical Engineering, Politecnico di Milano; 3. Prostate cancer program, Fondazione IRCCS Istituto Nazionale dei Tumori

Introduction

The microcirculation delivers oxygen and nutrients to the tissue. For this important role, the microvasculature has been studied with different methods. To this aim, we present here a sophisticated mathematical tool, based on a mesoscale model. Such models represent an important tool to investigate microcirculation because a brute force computational approach is not yet viable in this case. Indeed, microcirculation represents a significant challenge because of the intrinsic complexity of this problem. Additionally, several non-linear effects are required to properly model phenomena involved in microcirculation, especially when describing oxygen delivery. We present also an application case in the context of radiotherapy. Even if the complexity of the micro-environment (ME) and the oxygen presence have certainly an effect on the treatment outcome, the mechanism of these phenomena is still not completely understood.

Methods

The advanced mathematical model describing a microvascular network embedded in the surrounding environment has been detailed and improved in subsequent works [1-4], including the following features: (i) interaction between the microvascular network and the surrounding environment due to capillary wall leakiness; (ii) handling of complex network geometry; (iii) heterogeneous vascular radius; (iv) description of vessel curvature; (v) rheological effects of red blood cells; (vi) the heterogeneous distribution of red blood cells when flowing through bifurcations; (vii) possible inclusion of lymphatic absorption.

We present here the modeling of oxygen transport in the ME (i.e. oxygen delivery to tissue) with non-linear oxygen consumption (Michaelis-Menten kinetics). Also, the key role of RBC in oxygen transport has been considered, modeling the transport enhancement due to the presence of hemoglobin. We used the model to obtain the oxygen concentration in tissues considering different artificially generated networks. Then, based on that results, we have applied the well-known linear-quadratic model with oxygen enhancing ratio (OER) to describe radiation damage.

Results

Simulations allow us to describe the fluid flow through the microvasculature, the interstitium, and the microvascular wall. Leveraging on that results, we have described the oxygen transport through the network and its delivery to the tissue (Figure 1). Then by assuming a uniform radiotherapy dose over the domain considered, we have computed the cell survival ratio in different cases, based on the oxygenation of the tissue. Results show how the oxygen delivery by microvasculature determines the heterogeneous oxygen distribution in the tissue leading to heterogeneous cell survival.

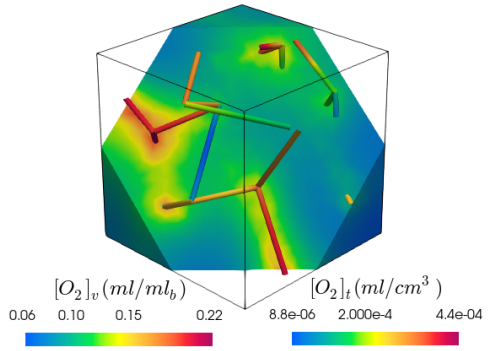

Figure 1: oxygen concentration within the vasculature and the interstitial space.

Discussion

The model enables the spatial description of the microenvironment explicitly accounting for the microvasculature, allowing the analysis of radiotherapy effects accounting for the spatial distribution of solutes, cells, and gasses. Therefore, differences in treatment outcomes related to microvascular network morphology can be directly investigated. This represents a step towards the mechanistic description of radiation damage to tissues (considering both tumor and healthy tissue) which explicitly includes ME features.

The model can be applied to compare different treatment options, considering also combined treatments, enabling the analysis of drug concentrations, metabolization rates, and eventually cell surviving fractions.

References

1. Cattaneo and Zunino, *Networks and Heterogeneous Media* 135– 159, 2014
2. Possenti et al., *IJNMBE,* 35:e3165, 2019
3. Possenti et al., *Microvascular Research* 122:101–110,2019
4. Cattaneo and Zunino, *IJNMBE*, 30:1347– 1371, 2014

Acknowledgments

L.P. is supported by the AIRC fellowship within the grant IG21479 for the AIRC - Fondazione AIRC per la Ricerca sul Cancro.

MODELLING LYMPH PROPULSION IN A 3D RECONSTRUCTED MURINE COLLECTING VESSEL WITH 3 LYMPHANGIONS IN SERIES

Ghazal Adeli Koudehi (1), Carlos Alejandro Silvera Delgado (1), Matthias Van Impe (1), Pieter Cornillie (2), Christophe Casteleyn (2), Christian Vanhove (3), Charlotte Debbaut (1), Patrick Segers (1)

1. Ghent University, IBiTech-bioMMeda, Belgium; 2. Ghent University, Department of Morphology (Veterinary Medicine), Belgium; 3. Ghent University, IBiTech-MEDISIP-INFINITY, Belgium

Introduction

The lymphatic system transports the excess fluid from the interstitium and ultimately returns it to the venous circulation against an adverse pressure gradient and gravitational force. The spontaneous contractions of the lymphangions, which are the building blocks of collecting vessels, and unidirectional valves play key roles in lymphatic propulsion [1]. Currently, higher dimensional models of lymph transport are scarce. On the other hand, the morphology of the lymphatic system has proven to be very difficult to capture. In this study, we model lymph propulsion in a 3D reconstruction of a collecting lymphatic vessel with contracting lymphangions originating from the hind limb of a mouse. A parametric study was also performed to better understand the factors impacting lymph propulsion.

Methods

Ex-vivo animal experiments were performed to collect morphological data from collecting lymphatic vessels as approved by the Ethical Committee of Ghent University Hospital. 18 C57BL/6 mice were sacrificed in total. The mice were imaged by high resolution µ-CT scans after interstitial contrast injection. The images, with a resolution of 40 µm, were then segmented using Mimics (®Materialise, Leuven, Belgium) to be incorporated as the simulation morphology. The 3D computational model was further developed and computed using COMSOL Multiphysics® to study the behavior of flow within the collecting vessel, the deforming vessel wall, and the poroelastic interstitium (Figure 1a). Four unidirectional valves were modelled as porous media with the permeability changing in function of the transvalvular pressures. The vessel wall was assumed linear elastic. The total length of the vessel was 1.83 mm with diameters ranging between 50-130 µm. Lymphangions' contractions were implemented as boundary loads. The pressure boundaries at the inlet and outlet of the collecting vessel were both set to zero. The studied parameters included the elastic modulus of the interstitium, the elastic modulus of the lymphatic collecting vessel wall, the magnitude of the lymphangions' contraction load, the refractory period in between contraction cycles, the adverse pressure at the outlet, the load applied at the interstitial boundaries, and the maximum permeability of the secondary valves.

Results

The deformations of the collecting vessel wall as a result of lymphangion contractions is shown in Figure 1b. Figure 1c shows a representative pressure-volume (P-V) loop of lymphangion 1, as well as the definition of some significant points throughout its contraction cycle.

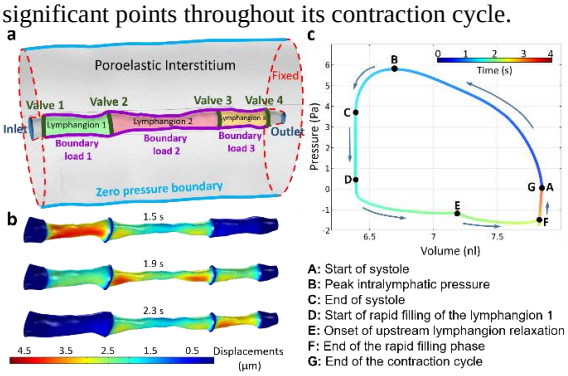

Figure 1: The different domains and boundary conditions of the model, (a), the deformation contours of the vessel wall, (b), and the P-V loop of lymphangion 1, (c).

When increasing two of the studied parameters, namely the maximum valve permeability and the elastic modulus of the interstitium, the P-V loops were shown to shorten, with intralymphatic pressures variations decreasing, and shrink, due to less wall deformations, respectively (Figure 2).

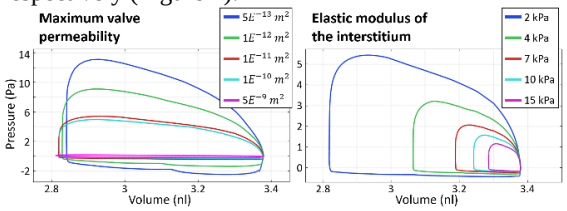

Figure 2: The effect of changing maximum valve permeability (left) and elastic modulus of the interstitium (right) on the P-V loops.

Discussion

Amongst the evaluated parameters, the maximum valve permeability and the elastic modulus of the interstitium proved to have the most impact on the accumulated volume propelled by the collecting vessel. Very high values of valve permeability as well as increased interstitial elastic modulus drastically reduced the conveyed volume. Our results showed how specific parameters could affect lymph propulsion.

References

Reddy NP et al, Microvasc Res, 10(2):214-6, 1975.

THE INTERPLAY BETWEEN FLUID MECHANICS AND ENCRUSTATIONS ON INDWELLING URETERAL STENTS

Shaokai Zheng (1), Dominik Obrist (1), Dario Carugo (2), Sarah Waters (3), Fiona Burkhard (4), Francesco Clavica (1)

1. ARTORG Center, University of Bern, CH; 2. Dept. of Pharmaceutics, University College London, UK; 3. Mathematical Institute, University of Oxford, UK; 4. Dept. of Urology, Bern University Hospital, CH

Introduction

Double-J ureteral stents are commonly used in urological practice to maintain and reinstate drainage of urine in presence of obstructions. One of the paramount drawbacks of long-term indwelling stents is the encrustation, which leads to further complications and significantly impacts patients' quality of life. Previous studies have suggested that the encrustation process is strongly influenced by the local fluid mechanical characteristics [1] but results from in-vitro fluid mechanical models are limited [2]. This study presents the first quantitative investigation of stent encrustations in a physiologically realistic model with commercially available stents.

Methods

An in-vitro model was designed to mimic the physiological geometries of the upper urinary tract. The flow is driven by a peristaltic pump into a silicone ureter model with two conical ends representing the ureteropelvic junction (UPJ) and ureterovesical junction (UVJ), respectively (figure 1a, b). The tested stent features side holes over its entire length, which are 1mm diameter openings on the wall, connecting the lumen of the stent to the extraluminal space. These holes are designed to facilitate urine passage in case of obstruction.

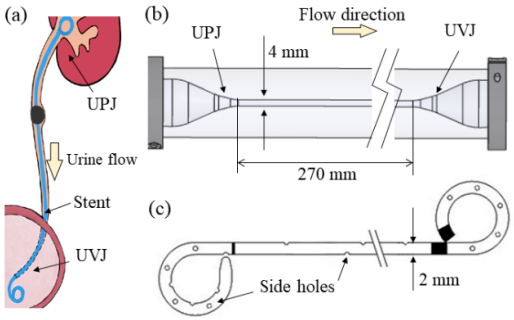

Figure 1 (a) Illustration of a stented ureter, (b) side view of the ureter model, and (c) typical stent geometry with side holes over its entire length.

Quantitative measurements were taken using a microscopic Particle Image Velocimetry (µPIV) setup with neutrally buoyant fluorescent particles of 20µm diameter. A high-speed camera (Photron FASTCAM Mini AX100) equipped with a long-distance microscope (Infinity K2) was used to capture the images. To ensure accurate results, velocity profiles within the ureter model without stent were examined against the theoretical solution of Poiseuille flow. A stent was then inserted without further obstruction, and the flow above the side hole was measured. Various measurement locations along the ureter at different flow rates were tested.

Results

Velocity profiles without inserted stent agree well with the Poiseuille flow. The contour of mean streamwise velocity and streamlines for one stented case are given in figure 2(b).

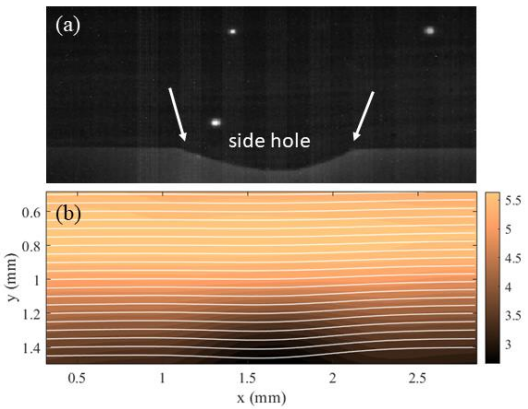

Figure 2 (a) Partial side view of the inserted stent, white arrows mark the edge of the side hole. (b) The streamwise velocity (color) and streamlines (white linnes). Colorbar shows velocity scale in mm/s.

Discussion

The streamlines are deformed towards the side hole (figure 2b), where a local region of low streamwise velocity is observed. Such transverse flow promotes the interaction between suspended microparticles and side holes, suggesting a faster growth rate of encrustations in these regions. Further measurements at different locations along the ureter will allow for critical comparison to clinical evidence of stent encrustations.

References

1. Clavica F, et al., PLoS ONE, 2014.
2. Zheng S, et al., WIREs Mech. Disease, 2021.

Acknowledgements

This work was supported by the SNSF grant number IZCOZ0_182966 and the ENIUS COST action grant number CA16217.

VESSEL COMPRESSION BIASES THE PARTITIONING OF RED BLOOD CELLS AT A DOWNSTREAM BIFURCATION

Romain Enjalbert (1), David Hardman (1), Timm Krüger (2), Miguel O. Bernabeu (1)

1. Centre for Medical Informatics, Usher Institute, The University of Edinburgh, Edinburgh, UK; 2. School of Engineering, Institute for Multiscale Thermofluidics, The University of Edinburgh, Edinburgh, UK

Introduction

The tumour microenvironment is abnormal and is reported to be hypoxic. One of the abnormalities in tumours is vessel compression, resulting from high solid stress in tumours [1]. Studies have shown that compressed blood vessels take an elliptical cross-section [2]. Experimentalists have shown in animal models that vessel decompression reduces tissue hypoxia, oxygen heterogeneity and increases the survival rate of animal models [3]. However, the mechanistic link between vessel decompression and changes in tissue oxygenation is unclear. We hypothesise that vessel compression leads to an altered partitioning of red blood cells (RBC) at vascular bifurcations due to the change in vessel shape, and that this effect compounds in networks and leads to tissue oxygenation heterogeneity.

Methods

We model blood as a suspension of deformable particles in a plasma phase [4]. The RBC membrane is modeled as hyperelastic, isotropic and homogeneous with a membrane energy model. The plasma is modeled as a continuous and Newtonian fluid, the non-Newtonian properties of blood arising from the deformable particles [4].

We solve the models in *HemeLB*, an open-source software (https://github.com/hemelb-codes/hemelb). The RBC model is solved with the finite element method. The fluid model is solved with the lattice Boltzmann method. The fluid structure interaction is solved through the immersed boundary method [4].

We use idealised geometries to investigate the effect of a compression on the downstream bifurcation, see Figure 1.



Figure 1: Snapshots of two geometries used. (a) is the control geometry, without a compression. (b) is the long compression, no recovery geometry.

Results

At 10% haematocrit, our simulations show that vessel compression alters the partitioning of RBCs at a downstream vascular bifurcation. Figure 2 shows the comparison of the control geometry (Figure 1a) with the long compression, no recovery geometry (Figure 1b).

Figure 2 also shows that in the presence of a compression, the higher flowing child branch is quasi-depleted of RBCs, whereas in the control geometry there is only a slight reduction in haematocrit of the child branch.

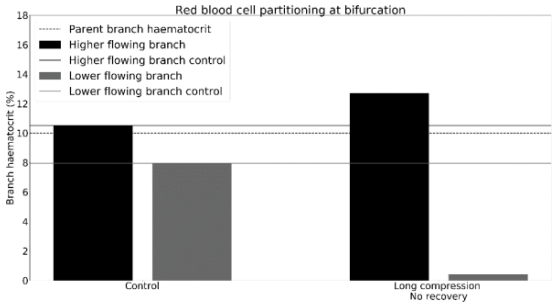

Figure 2: Phase separation in child branches at 10% haematocrit. Black/grey bars show higher/lower flowing child branch respectively. Solid lines are control haematocrits, the dotted line illustrates the parent branch haematocrit.

We find that the abnormal RBC partitioning due to vessel compression is less pronounced at higher haematocrit values, and is in fact negligeable at 30% haematocrit.

We investigate the mechanism leading to the altered partitioning of RBCs due to a compression. We report that it is due to cross-streamline migration of RBCs towards more central streamlines, leading to a narrowing of the cross-sectional distribution of RBCs in vessels. This effect is caused by the increased shear rate and shear rate gradient in the compression. The narrower RBC cross-sectional distribution leads to a more biased partitioning of RBCs towards the higher flowing branch.

Discussion

In summary, our simulations show that vessel compression biases the partitioning of RBCs to the higher flowing child branch. Our findings show a mechanism whereby vessel compression may lead to tumour tissue hypoxia and provide a mechanistic explanation as to why decompressing vessels improves tumour tissue oxygenation.

References

1. Stylianopoulos et al., PNAS 109:15101-15108, 2012
2. Fang et al., Oncotarget, 8:30092-30099, 2017
3. Chauhan et al., Nature Communications, 4, 2013
4. Krüger et al., Computers and Mathematics with Applications 61:3485-3505, 2011

PATIENT BREATHING SIMULATOR FACILITATES THE DEVELOPMENT OF SPONTANEOUS MODE IN NOVEL VENTILATOR DESIGN

J. Frattolin (1), D.J. Watson (1), M. Madekurozwa (1), W. Bonneuil (1), A.C. Moore (1), J.E. Moore Jr. (1), J. Mathiszig-Lee (2,3), J. van Batenburg-Sherwood (1).

1. Department of Bioengineering, Imperial College London, UK; 2. Department of Surgery and Cancer, Imperial College London, UK; 3. Department of Anaesthesiology and Perioperative Medicine, Royal Marsden Hospital, UK.

Introduction

The COVID-19 pandemic resulted in increased demand for critical care ventilators, leading to unprecedented strain on the global ventilator market. In order to meet the growing demand, new approaches to ventilation were required.

Critical care ventilators typically provide a supported breathing mode that can sense when the patient is attempting to breathe and then assist that breath. This allows for a gradual decrease in the level of respiratory support a patient receives, aiding their recovery towards breathing independently. To facilitate the testing and optimisation of a spontaneous breathing mode, a patient breathing simulator was developed. This novel simulator can be used to test how patient effort effects the level of support and the response time of the ventilator, as well as its robustness to patient coughing.

Methods

The patient breathing simulator mimics breathing effort by adding and subtracting up to 300ml of air from a test lung; this is achieved through two mechanically coupled pneumatic cylinders. The first cylinder, the driving cylinder, is connected to a compressed gas supply, while the second cylinder, the driven cylinder, is connected to the test lung. Solenoid valves are used to mediate these connections (Figure 1), allowing the driving cylinder to be advanced either forwards or backwards. This changes the volume of the driven cylinder, which is connected to the test lung with the opening of the output valve.

To simulate a patient inhalation, a set volume of air is removed from the test lung at a controlled rate. The resulting drop in pressure is dependent upon the compliance of the test lung. The ventilator then detects this drop in pressure or the resulting flow and delivers a breath. During exhalation, the cylinder is advanced to its original position, replacing the volume in the test lung, increasing flow out of the lung. A displacement sensor measures the volume added or subtracted. The valve timings can be adjusted to vary the work, or breathing effort, achieved by the simulator. Rapid actuation of the system, with a small set volume of air, can be used to simulate coughs. This system was used to test the spontaneous mode of a proposed ventilator design.

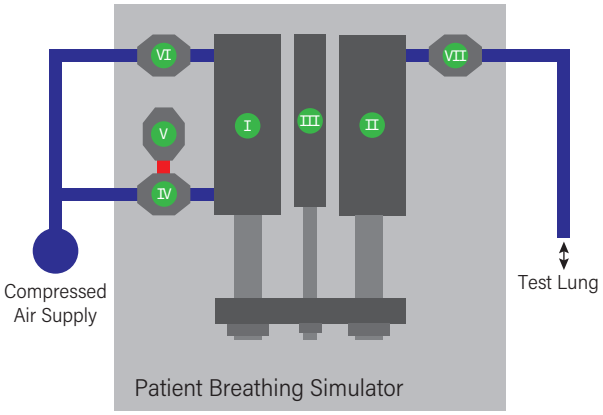

Figure 1: An overview of the patient breathing simulator: I) driving cylinder; II) driven cylinder; III) displacement sensor; IV) return actuator valve; V) hold actuator valve; VI) forward actuator valve; VII) output valve.

Results

The breathing simulator supported the development of a spontaneous mode. The robustness of triggering, the response time and other clinically relevant parameters were assessed to optimise the control algorithms. As the patient simulator breathing effort increased, the work done by the ventilator fell, validating the design approach to spontaneous ventilation.

Discussion

The motivation to meet exceptional ventilator demand creates the opportunity for a re-examination of the fundamental approaches to ventilator design. New tools have been developed to artificially simulate the mechanics of breathing and aid the development of novel methods for supported-breathing ventilation.

Acknowledgements

The authors acknowledge financial support from the Royal Academy of Engineers and Imperial College London. The authors also wish to thank all those who supported and contributed to this project.

IN-VITRO PLATFORM FOR WAVE PROPAGATION INVESTIGATIONS IN THE LOWER URINARY TRACT

Lukas Bereuter (1), Lorenzo Ferrari (1,2), Maria Laura Costantino (2), Yoan Civet (3), Yves Perriard (3), Bernhard Kiss (4), Dominik Obrist (1), Fiona Burkhard (4), Francesco Clavica (1)

1. ARTORG Center, University of Bern, CH; 2. Dept. of Chemistry Materials and Chemical Eng., Politecnico di Milano, IT; 3. Integrated Actuators Lab., EPFL, CH; 4. Dept. of Urology, Bern University Hospital, CH

Introduction

Application of the impedance pump principle to the urethra has been proposed as a novel non-invasive approach to aid bladder emptying in urinary retention patients [1]. External cyclic compression of the urethra results in wave propagation and wave interactions, which can lead to a directed net flow. Hence, urine is actively pumped out of the bladder, while contact with urine is avoided. To systematically study the pumping effect and the wave propagation, an in-vitro platform that mimics the lower urinary tract (LUT) was developed.

Methods

The platform consists of a Polydimethylsiloxane (PDMS) part which models the penis (including corpus cavernosum and urethra) and is connected to a reservoir that mimics the bladder. Since we focus on wave propagation, the mechanical and geometrical properties of the model are crucial. Formulations formed by blending SYLGARD™ type 527 and 184 (Dow Chemical, USA) can cover a wide range of physiological elastic moduli spanning from 5 kPa to 1.7 MPa [2]. Based on literature data [3], a Young's modulus of 20 kPa was targeted for the model. A weight ratio of 20:1 of SYLGARD™ 527:184 was used as suggested in [2]. The PDMS was casted into a mold and cured for 24h at 60 °C. The geometry of the mold was designed based on mean anatomical dimensions. The mechanical properties of the model were measured with the MyotonPRO digital palpation device (Myoton AS, Estonia), which is designed for soft tissue assessment. The model was connected to a reservoir and a 2F pressure catheter (SPR-320, Millar, USA) was introduced from the open urethra outlet. A mechanical stimulator was actuated to achieve cyclic compression of the urethra part of the model.

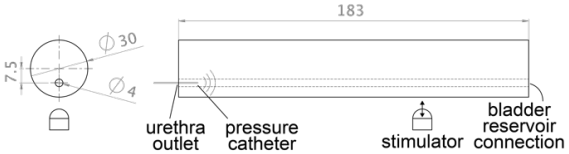

Figure 1: Front view (left) and side view (right) of the model, stimulator and pressure sensor (units are in mm).

Results

The mechanical properties of the model, measured with the MyotonPRO device, are within the physiological range (considering linear fitting for soft tissues [4]). Upon cyclic compression of the urethra, pressure waves are generated, which are eventually reflected at the urethra outlet and the bladder interface. The recorded pressure is a superposition of these waves. The pressure waveform changes depending on the stimulator position, frequency and duty cycle of the compression. Net flow up to 0.9 ml/s was achieved using impedance pumping.

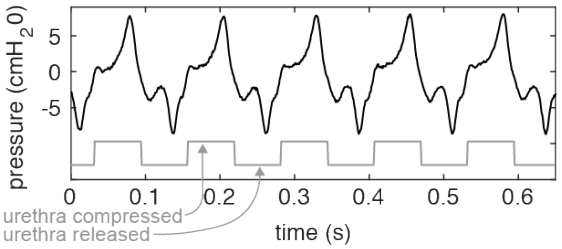

Figure 2: Typical pressure recording (black) during cyclic urethra compression. Position of the stimulator = 38 mm from bladder, frequency = 8 Hz, duty cycle = 50%.

Discussion

So far, wave-propagation theory mainly has been investigated on thin-walled axis-symmetric tubes only. The proposed platform allows for a realistic systematic investigation of the wave propagation and impedance pumping principle on the LUT.

The MyotonPRO device provides an alternative to conventional methods for assessing mechanical tissue properties (e.g. tensile test). This measurement approach appears particularly suitable for our purpose as i) it is very close to our application (stimulator compressing soft tissue) and ii) it allows assessments on living subjects. We anticipate that a clinical study will be conducted (using the MyotonPRO) to collect data on penile mechanical properties

References

1. Clavica et al, ICS, 38:S44-S45, 2019.
2. Palchesko et al, PLOS ONE, 7(12):e51499, 2012.
3. Udelson, J. R. Soc. Interface, 4:1031-1047, 2007.
4. Feng et al, Sci. Rep., 8(1):17064, 2018.

Acknowledgements

We would like to thank Benjamin Voumard and Philippe Zysset from the Muscoloskeletal Biomechanics group of the ARTORG Center of the University of Bern for their advice in mechanical testing.

PROTOCOL TO EVALUATE THE RELATIONSHIP BETWEEN BREATHING, POSTURE AND STABILITY

Alejandro Buritica (1), Clara Matencio (2), Jerome Noailly (2) Juan Ramírez (1), Simone Tassani (2)

1. Universidad Nacional de Colombia, Medellín, Colombia; 2. BCN MedTech, DTIC, Univ. Pompeu Fabra, Barcelona, Spain

Introduction

When referring to corporal stability, the first thing to point out is that its importance lies in the functionality that it provides and represents for the human body at daily performance, since this is defined as the ability to control the position and movement of the body. Therefore, it is essential to focus on the factors that could affect the level corporal stability permanence of a person, as are breathing and posture.

The aim of this study is to propose a protocol for the measurement and establishment of quantitative relationships between different parameters of breathing, posture, and stability, through non-invasive methods such as optoelectronic plethysmography (OEP), Stabilometry and the application of statistical analysis.

Methods

The proposed protocol collect: for breathing the volumes of the thoracic area and their changes over time when performing the cycle of breathing [1]; for posture, angles between notable points of the upper body such as craniovertebral angle, sagittal shoulder – C7, and sagittal head tilt [2][3], and for stability, the COP and related time and frequency estimators [4]. For the measurement of parameters of breathing and posture were used 8 BTS Smart-DX 700 cameras, 1.5 Mpixels 250 fps, and 102 markers located on the body of the volunteers for OEP protocol [1] and posture. In the case of the stability parameters, 1 BTS P-6000 force plates are used, sampling 500 Hz.

For data collection three conditions of respiration were defined, these are: control, the standard position of the subject; tense, the subject exerts a muscular contraction without any type of joint movement; and relaxed, the subject takes a deep diaphragmatic breath. Similarly, 2 states referring to the eyes are defined, these are open and closed. Thus 6 combinations of states are obtained for the conditions to be evaluated with the protocol. The protocol was tested over 10 adult healthy volunteers.

Multifactorial ANOVA analysis for repeated measures was applied to study the effect of the two factors (kind of respiration and state of the eyes) over the dependent variables.

Results

The complete development of the proposed protocol has applied on the respiration and stability data. Figure 1 show comparison between the results obtained for the trace length [mm] of the COP [4] under 4 combinations of factors and two ways of breathing (Abdominal and Pulmonary). N is the control condition, R relaxation condition, O eyes open, and C eyes closed.

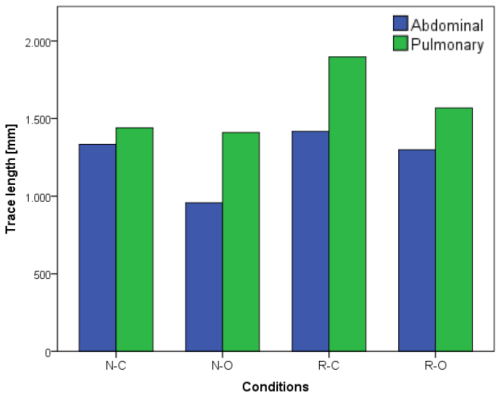

Figure 1: Differences between subjects with abdominal and pulmonary breathing along the four different conditions for trace length. Factors: N (normal/control), R (relaxed), O (eyes open), C (eyes closed).

Discussion

The results suggest that only a minority of the population is able to perform abdominal breathing. This is itself a troubling result since abdominal breathing is a basic vital activity. Subjects capable of deep abdominal breathing seems more stable but the stability is reduced when it is explicitly asked to perform deep abdominal breathing. Results must be confirmed over a larger cohort of volunteers. Equations may be included in the abstract, using either the “Equation” style or by using the Word equation editor. The text fonts in the equation should be Times New Roman and Symbol, 10 point. Equations should be indented one tab stop from the left. Equations may be sequentially numbered.

References

1. Aliverti et al, Eur Respir J, 33:49-60, 2009.
2. Shaghayegh et al, Eur Spine J, 25:3577-3582, 2016.
3. Singla et al, J Chiropr Med, 16:131-138, 2017.
4. Mello et al, International Conference of the IEEE Engineering in Medicine and Biology Society, 31:1351-1354, 2009.

Acknowledgements

Funds from the Spanish Government (RYC-2015-18888) and from UPF (BYMBOS - PLAWB00420)

DETERMINING LUNG OBSTRUCTION USING FORCED OSCILLATION TECHNIQUE AND MACHINE LEARNING

Jensen Xi (1), Mohamed Talaat (2), Xihua April Si (3), Jinxiang Xi (2)

1. *Martin Luther King High School, Riverside, CA 92508, U.S.A.*
2. *Department of Biomedical Engineering, University of Massachusetts, Lowell, MA 01854, U.S.A.*
3. *Department of Aerospace, Industrial, and Mechanical Engineering, California Baptist University, Riverside, CA, 92504, U.S.A.*

Introduction

A key factor in devising the treatment plan for patients with obstructive airways disease is being able to measure their lung functions accurately. Impulse oscillometry (IOS) is a new technique that use impulse acoustics to measure the levels of obstruction in the human respiratory tract (Fig. 1). It does not require patient cooperation, which makes it well suited for children, seniors, or patients with respiratory distress [1]. In this project, we will study the sensitivity of the IOS in detecting airway obstructions in an anatomically realistic lung cast model.

Methods

A lung model with 11 generations of bifurcation and 1240 outlets was developed following Hiroko Kitaoko [2] and was manufactured using 3-D printing techniques (Fig. 2). This hollow lung cast was put in 5-later container that is equivalent to the human total lung capacity (TLC) of an adult. Impulse sound singles of 5-20 Hz generated by the IOS were released into the lung cast, while tidal breathing was simulated using a gas pump. The reflected signals were collected by IOS and translate into airway-obstruction-related parameters such as resistance and resonance frequency. To study the airway obstruction effects, the outlets of the lung cast model was covered using playdoh by 0%, 10% and 20%. For each blockage, 400 tests were performed in order to develop a database. Machine learning was then used to learn the common features of the parameters from different blockages. New test samples were used to test the prediction accuracy of the machine-learned model [3].

Results

Statistically significant differences were found in the measurements with different airway blockages, indicating that the IOS is sensitive enough to detect the airway obstructions with a difference of 5% blockage. The prediction accuracy of the classifier (i.e., the machine-learned model) is around 70%.

Discussion

IOS can detect blockage in the 3-D printed lung model. However, future work is needed to determine how it works in human patients. It is still unclear, but is of high interest to doctors, whether the IOS can detect the locations of the airway obstructions. Our future studies will address this problem by blocking different sections of the lung case model and testing it with IOS.

Figures

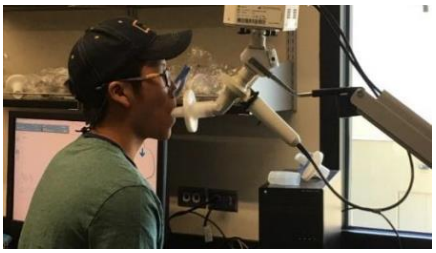

Figure 1: Impulse oscillometry (IOS) in operation to measure obstruction in the human respiratory tract.

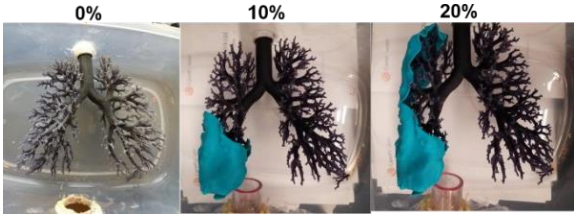

Figure 2: Lung casts with different blockages.

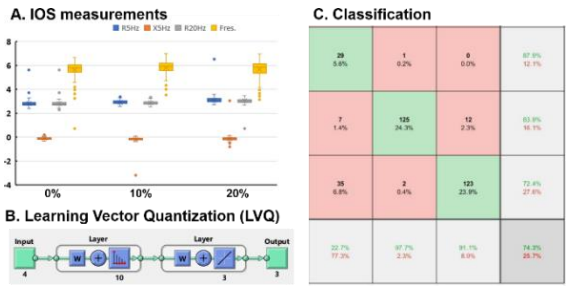

Figure 3: Results: (a) IOS measurements with different blockages, (b) Classification method, (c) classification result.

References

1. Bickel S., et al, Chest, 146: 841-847, 2014.
2. Kitaoko H., J Appl Physiol, 87:2207-2217, 1999.
3. Matlab Deep Learning Toolbox https://www.mathworks.com/products/deep-learning.html.

Acknowledgements

We thank Garcia Christian for his help in the experiments.

INFLUENCE OF *IN VITRO* CORROSION ON THE MECHANICAL BEHAVIOR OF POROUS MAGNESIUM-BASED SCAFFOLDS

Roxane Bonithon (1), Colin Lupton (1), Marta Roldo (2), Gordon W. Blunn (2), Frank Witte (3,4), Gianluca Tozzi (1)

1. ZEISS Global Centre, School of Mechanical and Design Eng., University of Portsmouth, UK; 2. School of Pharmacy and Biomedical Sci., University of Portsmouth, UK; 3. Biotrics bioimplants, Berlin, Germany; 4.Dept. of Prosthodontics, Geriatric Dentistry and CM Disorders, University of Berlin, Germany.

Introduction

The mechanical and biological properties of degradable magnesium(Mg)-based materials make them attractive candidates for orthopaedic applications [1]. However, the influence of their degradation behaviour on the mechanical integrity of Mg scaffolds have not been fully investigated. The aim of the present study is to employ high-resolution X-ray computed tomography (XCT), coupled with in situ mechanics and digital volume correlation (DVC) to evaluate the influence of *in vitro* degradation on the Mg scaffolds mechanical behaviour.

Methods

Cylindrical Mg-based scaffolds (Ø6mm x H10mm; N=6) were dynamically corroded in Hank's balanced solution (0.3 mL/min, 37°C and 5% CO_2) for 2, 8 and 14 days. After each incubation time, the scaffolds were embedded in endcaps and mechanically tested *in situ* under compression (CT500, Deben). At different compression stages (1%, 3%, 6% and 10%), XCT tomograms were recorded (27µm voxel size, XT H 225, Nikon). 3D full-field strain was calculated by digital volume correlation (DaVis10, LaVision), using a multipass scheme (110 to 20) and 0% overlap (SDER always <200µε [2]).

Results

The volume of material loss increased with the corrosion time (8%, 10% and 15% of the total volume at 2, 8 and 14 days, respectively). Accumulation of corrosion products was clearly visible after 8 days and more pronounced after 14 days (Fig 1). The mechanical curves trend was relatively similar while the yield stress slightly increased at 14 days (1.60MPa to 2.13MPa at 0 and 14 days, respectively). The maximum strain accumulated was higher after corrosion (Fig 2), however, a slight decrease was observed at 14 days. In addition, while the third principal strain distribution was homogeneously distributed over the structure before corrosion, it was then localized around specific areas mostly affected by corrosion. The pore diameter was reduced with the corrosion time (387µm to 335µm at 0 and 14 days, respectively).

Discussion

The corrosion rate (0.42 and 0.37mm.year^{-1} at 8 and 14 days) was found to be in the range of those reported *in vivo* [3]. The corrosion induced mass loss that seemed to be correlated with the third principal strain distribution where higher strain was found in higher mass loss areas (Fig 2). However, no global failure was observed, and the mass loss appeared to be partially counterbalanced by the accumulation of corrosion products trapped in the inner pores at 14 days (Fig 1) which strengthened the global structure [4]. Additionally, hard callus tends to form after 14 days which will further contribute to maintain the mechanical integrity of the injured site [5].

Figures

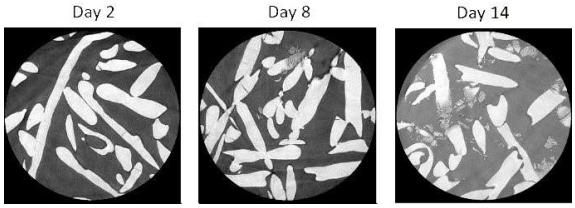

Figure 1: 2D XCT images of the Mg-based scaffolds after corrosion.

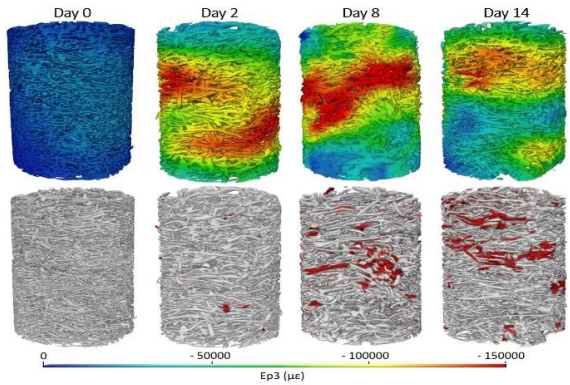

Figure 2: Full-field third principal strain distribution (Ep3) at 10% compression (top) and their corresponding 3D scaffolds where the red parts indicated the corroded volume (bottom).

References

1. Witte, Acta Biomaterialia, 23:28-40, 2015.
2. Palanca et al, Journal of Biomechanics, 58:27-36, 2017.
3. Martinez et al, Acta Biomaterialia, 13:16-31, 2015.
4. Hedayati et al, J. Biomed. Mat. Res., 106:1798-1811, 2018.
5. Wang & Yeung, Bioactive Materials, 2:224-227, 2017.

Acknowledgements

The project is co-funded by the University of Portsmouth, Biotrics bioimplants AG and Botiss biomaterials GmbH.

THERMOPLASTIC GRAIN REFINMENT OF THE COMMERCIALY PURE TITANIUM FOR THE BIOMEDICAL APPLICATIONS

Jakub Bańczerowski (1), Marek Pawlikowski (1), Konstanty Skalski (2) Tomasz Płociński (3)

1. Warsaw University of Technology - Institute of Mechanics and Polygraphy, Poland;
2. Łukasiewicz Research Network - Institute of Precision Mechanics, Poland;
3. Warsaw University of Technology - Faculty of Materials Science and Engineering, Poland

Introduction

One of the most commonly used in biomedical implants alloys, due to its great strength, is Ti6Al4V alloy. However, its prolonged use is dangerous for the human body due to toxic effect of the aluminum and vanadium ions released into it [1]. Commercially pure (CP) titanium does not have this disadvantage but it has lower strength than TiAl64V alloy, therefore it is required to improve its properties by grain refinement [2]. Due to nature of titanium deformation mechanism, plastic deformation in elevated temperature was chosen as a method of grain fragmentation [3].
Additionally, to further improve control over plastic deformation process, constitutive equations were employed.

Methods

CP titanium samples were compressed at elevated temperatures (775 K÷875 K) at different strain rates ($\dot{\varepsilon} = 10^{-2} \div 10^{1}$) to a constant strain $\varepsilon = 0.6$ on a Gleeble thermomechanical simulator. The data from the experiments allowed for plotting stress-strain graphs. The hardness of the samples before and after deformation was measured.
Titanium microstructure was observed with a scanning electron microscope (SEM) and scanning transmission electron microscope (STEM) in order to assess the changes in grain size and to determine the deformation mechanisms. The electron backscatter diffraction (EBSD) tests were performed to reveal grain size distribution.
Arhhenius constitutive equation was chosen to describe the process.

Results

For the compression in the temperature 775 K maximum stresses were 250-350 MPa, while at 875 K this value was 150-250 MPa.

The Arhenius equation was used for representing the elevated temperature flow behaviour of the material.

$$F(\sigma) = \begin{cases} \sigma^{n_1}, & \text{for} \quad \alpha\sigma < 0.8, \\ \exp(\beta\sigma), & \text{for} \quad \alpha\sigma > 1.2, \\ [\sinh(\alpha\sigma)]^{n}, & for\ all\ \sigma, \end{cases}$$

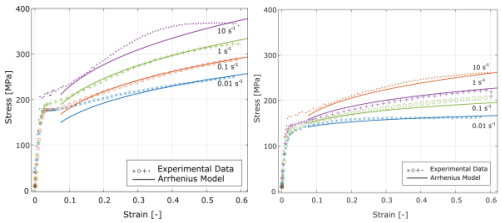

Figure 1: Stress-strain and Arrhenius model graph for the titanium sample a) compressed at temperature T = 775 K, b) T = 875 K

Using experimental data and aforementioned equation, flow stress values have been calculated and compared to the experimental results (Fig. 1). The comparison indicates that the model predicts material behavior correctly only in the plastic domain.
The microstructure analysis indicates that grain was fragmented mostly as a result of twinning mechanism. Initial grain size was 2–8 μm, while after deformation in 875K, those values were below 2 μm (Fig. 2).

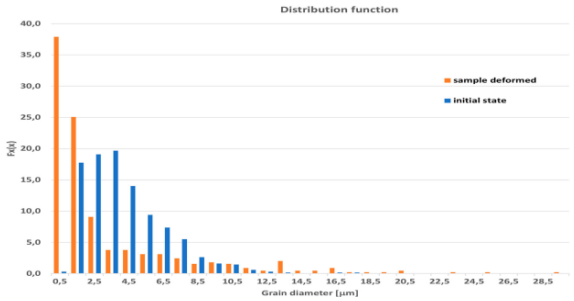

Figure 2: Histogram of the frequency of equivalent grains diameter of initial state size of 2–8 μm (blue) and sample deformed with the maximum frequency size in the range below 2 μm (orange).

Discussion

The applied method of the CP titanium plastic deformation allowed for controlled grain fragmentation. Hardness after the deformation increased averagely by 120 HV0.1, which implies an increase of the material strength. Grain fragmentation was confirmed by microstructure observations and EBSD analysis.

References

1. I Ansarian et al, J Alloy Compd, 776:83-95, 2019.
2. Zhang S et al, Mat Sci Eng A, 641:29–36., 2015;
ng Agency. Zhang S et al, Mat Sci Eng A, 641:29–36., 2015.

THE OSMOTIC SWELLING POTENTIAL IN HYDROSPACERS CAN BE USED TO CREATE LOAD-BEARING CARTILAGE IMPLANTS

G.H. Schuiringa[1], K. Ito[1], C.C. van Donkelaar[1]
[1]Orthopaedic Biomechanics, Dept. Biomedical Engineering, Eindhoven University of Technology, The Netherlands

Introduction

Cartilage defects occur frequently and can lead to osteoarthritis. Hydrogels are a promising regenerative strategy for treating such defects, using their ability of mimicking the native extracellular matrix [1]. However, such hydrogels are too soft to resist loadbearing in the joint [1]. To overcome this, it may be possible to use a hydrogel to mimic the natural load-bearing mechanism of healthy cartilage, whereby swelling from the proteoglycan-rich ground substance is restricted by the collagen network [2]. Such an implant is being developed in which the mechanical loadbearing function originates from the osmotic pressure generated by the swelling potential of a charged hydrogel, which is restricted from swelling by a textile spacer fabric. This This study aims to quantify the relationship between the swelling potential of the hydrogel and the compressive stiffness of the implant.

Methods

Solutions with different molecular weight ratios of poly 2-hydroxyethyl methacrylate (pHEMA) and sodium methacrylate (NaMA) (20:0, 19:1, 18:2, 17:3) were used to create either plain hydrogels (Ø8 x 3 mm) or HydroSpacers, which were obtained by injecting the hydrogel in a poly amide 6 (PA6) warp knitted spacer fabric (Ø8 x 3 mm)(n=6 per group). The hydrogels and HydroSpacers were polymerized in Teflon moulds using UV light (365 nm) for 3 hours. Subsequently, they were either placed in free swelling or in a custom-made Ø8 mm confined compression set-up.

After equilibration in 0.15 M or 0.015 M sodium chloride (NaCl) solution, samples were mechanically tested in stress relaxation with a step deformation of 15% strain at a strain rate of 15% strain/sec and held till equilibrium was reached. Afterwards, samples were lyophilized to assess water and polymer content.

The fixed charge density (fcd) of the samples was calculated by dividing the molar charge of NaMA, based on the polymer content and the molecular weight ratio's, by the sample water content under each experimental condition. Using fcd and bathing solution, the osmotic pressure was determined. Significance was set at $p<0.05$ for two-way ANOVA analysis.

Results

Hydrogels alone swelled up to 9-fold the initial weight, whereas HydroSpacers swelling was restricted to 1.2-fold (Fig 1A). Regression analysis revealed a significant linear relationship between osmotic pressure and peak and equilibrium stresses in HydroSpacers (Fig 1B-C).

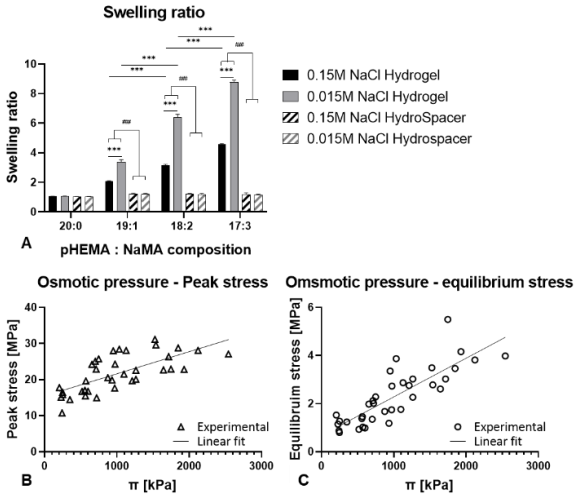

Figure 1. Swelling ratio of free swelling pHEMA hydrogels and confined HydroSpacers (A). Linear regression of osmotic pressure (π) versus peak (B)(R^2=0.48) and equilibrium stress (C)(R^2=0.69) of HydroSpacers.

Discussion

Restricted swelling of pHEMA-NaMA hydrogels in warp knitted PA6 spacer fabrics lead to an internal osmotic pressure. This osmotic pressure correlated positively with the compressive stiffness of the HydroSpacers. This mechanism concurs with the load-bearing mechanism of native cartilage [2].

With the development and optimization of bulk materials and spacer fabric designs, mechanical properties may be steered towards that of healthy cartilage. Moreover, a regenerative cartilage construct might be feasible by using cell-seeded biodegradable hydrogels and spacer fabrics.

In conclusion, this proof of principle demonstrates that by combining spacer fabrics and swelling hydrogels, load-bearing hydrogels can be developed.

References

[1] Neves et al, *Trends Biotechnol.*, 38, 3, 292–315, 2020.

[2] Quiroga et al, *Biomech. Model. Mechanobiol.*, 16, 1, 151–158, 2017.

Acknowledgements

This research was performed under the framework of Chemolot InSciTe, supported by the partners of Regenerative Medicine Crossing Borders (www.regmedxb.com) and powered by Health~Holland, Top Sector Life Sciences & Health.

DESIGN AND *IN VIVO* VALIDATION OF CERAMIC SCAFFOLDS FOR OVINE LONG-BONE DEFECTS

Pablo Blázquez-Carmona (1), José Antonio Sanz-Herrera (1), Carlos Rodríguez-Andrade (1), Francisco Javier Martínez-Vázquez (2), Jaime Domínguez (1), Esther Reina-Romo (1)

1. Escuela Técnica Superior de Ingeniería, Universidad de Sevilla, Spain; 2. Escuela de Ingenierías Industriales, Universidad de Extremadura, Spain

Introduction

Tissue engineering is a biomedical engineering discipline that emerged as an alternative to traditional autografts for bone regeneration using porous structures called scaffolds. Bioceramic scaffolds printed by additive manufacturing stand out for their biocompatibility, osteoconductivity and bioabsorbable properties [1]. In the literature, scaffolds tested *in vivo* in long-bone defects are usually of a generic design and stabilized by internal fixations [2,3]. The present work aims to numerically optimize the structure of externally stabilized patient-specific scaffolds by considering the mechanobiology of the bone defect. The mechanical integrity of the implant and the bone regeneration process are then monitored *in vivo* in an ovine model as a preliminary validation.

Materials and Methods

3D-printed hydroxyapatite scaffolds were structurally optimized to regenerate a sheep metatarsus defect stabilized by an external fixator. Three geometric variables define their orthogonal layer-wise log pile microarchitecture: the diameter of the rods (*D*), the center-to-center distance between adjacent rods of the same layer (*s*), and the vertical spacing between consecutive layers (*h*). Different combinations of these variables were selected to define 300 candidates as *in silico* models to perform the simulations. The optimization problem includes both biological parameters (porosity, pore size and specific surface area) and mechanical constraints [4] (maximum principal stress) to guarantee the cell adhesion and proliferation and the mechanical integrity, respectively. The selected structure was manufactured by robocasting and preliminarily tested *in vivo* in a sheep metatarsus. Surgery was performed to implant an external fixator with an axial stiffness of 593 N/mm. Two osteotomies were subsequently performed and the resulting 15 mm long fragment was replaced by the patient-specific scaffold. After seven days of the latency period, the ground reaction force (GRF) was monitored weekly using a load platform embedded in a wooden gate circuit to evaluate the bone regeneration.

Results

Geometric variables have a different impact on each objective (cost) function (Fig. 1). Assuming the same weight for all biological parameters, the compromise structure was defined by the following geometric values: *D*=264 μm, *s*=625 μm, and *h*=228 μm. Thereby, the biological parameters took the following values: 59.3% of porosity, 5768.9 m^{-1} of specific surface area, and 360.8 μm of pore size. Regarding the *in vivo* experiment, the operated sheep progressively reduced its bearing capacity to a minimum of 0.2 GRF (% BW) at day 36 after surgery. After that day, the sheep progressively recovered healthier GRF values [5].

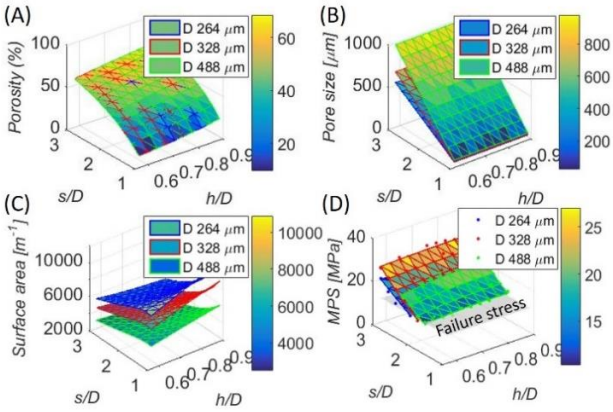

Figure 1: Evolution of the parameters analyzed in the optimization problem as a function of the variables D, s and h: (a) porosity; (b) pore size; (c) specific surface area; (d) maximum principal stress (MPS).

Discussion

The optimal implant shows a porosity and pore size values similar to other successful *in vivo* works in similar models [2,3]. The operated limb of our specimen seems to reduce its bearing capacity until bridging the bony fragments. This reduced mobility period does not appear in other bone regeneration processes, such as distraction osteogenesis, due to the early bone callus formation during the distraction phase [5].

References

1. Karageorgiou et al., Biomaterials, 26:5474-91, 2005.
2. Cipitria et al., Biomaterials, 34:9960-8, 2013.
3. Pobloth et al., J Tissue Eng Regen Med, 12:897-911, 2018.
4. Miranda et al., J Biomed Mater Res A, 83:646-55, 2007.
5. Blázquez-Carmona et al, Ann Biomed Eng, Online ahead of print, 2020.

Acknowledgements

We thank the funding of the Junta de Andalucía and the Ministry of Economy and Competitiveness of the Government of Spain through the projects US-1261691 and DPI2017-82501, and the grant FPU17/05361 awarded to the first author of this abstract.

OPTIMIZING THE STRUCTURE OF NYLON 6,6 ELECTROSPUN BUNDLES TO MIMIC THE MECHANICS OF TENDON FASCICLES

Alberto Sensini (1), Michael H. Santare (2,3), Emily Eichenlaub (3), Ellen Bloom (3), Carlo Gotti (4), Andrea Zucchelli (1,4), Francesco Zoli (4), Maria Vittoria Ricioppo (4), Luca Cristofolini (4,5)

1. CIRI-MAM, University of Bologna, Italy 2. Department of Mechanical Engineering, University of Delaware, USA 3. Department of Biomedical Engineering, University of Delaware, USA 4. Department of Industrial Engineering, University of Bologna, Italy; 5. CIRI-HST, University of Bologna, Italy

Introduction

Tendons have a complex, multiscale nanofibrous structure [1]. Two key features for the mechanical properties of tendons are the transition point (i.e. end of the toe-region) and the inflection point (i.e. stress-strain curve shifts from strain-stiffening to strain-softening, the real starting point of tendon damage) [2]. Electrospinning allows us to replace these tissues [3] and by tuning the process parameters, it is possible to obtain bundles of nanofibers similar to those in tendon fascicles. The electrospun nylon6,6 has demonstrated a suitable structure and mechanics for this purpose [4]. In this study, we produced nylon6,6 bundles with varying nanofibrous anisotropy, characterizing their morphology and mechanical properties. In particular we focused in the strain range corresponding to the toe region up to the inflection point, mechanical features generally not considered in the scaffold's characterization, but fundamental for the physiological range of motion and failure of tendons and the extracellular matrix (ECM) regeneration.

Methods

A solution of 15% (w/v) of nylon6,6 dissolved in TFA:AC = 50:50 (v/v) was used to electrospin mats of nanofibers on a drum collector rotating at different speed: 19.6 m s^{-1} (drum rotation = 2500 rpm); (B) 13.7 m s^{-1} (1750 rpm); (C) 7.9 m s^{-1} (1000 rpm). The mats were wrapped up on the drum to obtain ring-shaped bundles (diameters = 400 - 600 µm) with a consolidated procedure [4]. The nanofibers were studied with SEM images (Fig. 1A-C) obtaining their diameters and orientation. The mechanical properties were investigated (n=12 for each category) with a monotonic tensile test to failure (Fig. 1D) with a strain-rate of 0.33%/s.

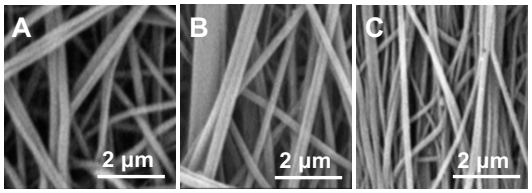

Figure 1: SEM images of nanofibers at: B) 1000 rpm, C)1750 rpm and D) 2500 rpm.

The stress-strain curves were analysed to determine the inflection point (σ_I), (ε_I), the transition point (σ_T), (ε_T) and the slope in the linear region (E_L). A MATLAB routine was developed for curve fitting and quantification of these parameters [2-5].

Results & Discussion

Increasing the drum speed, caused the nanofibers to obtain an increasing biomimetic morphology and orientation (Fig. 1). The nanofibers and bundles showed diameters similar to the ones of tendon fibrils and fascicles [1]. The mechanical behavior of the bundles went from ductile at low rpm (1000 and 1750) to elastic brittle at higher rpm (2500) (Fig. 2B). The mechanical properties of the bundles (Table 1) were in the same range as tendon fascicles [6]. The inflection properties, σ_I, ε_I and E_L were lower than the yield properties σ_Y, ε_Y and E (considered the gold standard for the scaffold characterization). This study provides a method that highlights the fundamental role of the transition and inflection points in the mechanical performances of electrospun scaffolds for tendon tissue replacement and regeneration, focusing the attention to the actual physiological range of work of these tissues.

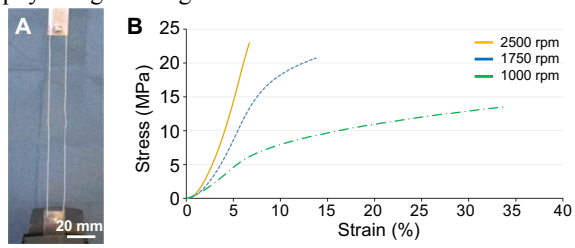

Figure 2: A) Bundle mounted in the mechanical test setup; B) mechanical behavior of the bundles.

	1000 rpm	1750 rpm	2500 rpm
σ_T (MPa)	1.9±0.5	4.6±1.2	6.5±1.6
σ_I (MPa)	3.8±0.8	10.3±2.2	17.4±3.9
σ_Y (MPa)	5.6±1.1	16.3±4.0	-
σ_F (MPa)	13.7±2.3	21.5±2.4	23.9±6.0
ε_T (%)	2.8±0.3	3.4±0.4	3.1±0.4
ε_I (%)	4.5±0.2	5.4±0.4	5.4±0.5
ε_Y (%)	6.1±0.2	7.7±0.8	-
ε_F (%)	6.1±0.2	13.8±3.7	6.7±0.7
E_L (MPa)	110±23	275±49	445±78
E (MPa)	113±25	288±47	486±94

Table 1: Mechanical properties of bundles.

References

1. Kannus, Scand J Med Sci Sports, 10(6):312-320, 2000.
2. Lee et al, Acta Biomat, 57: 363-372, 2017.
3. Sensini & Cristofolini, Materials, 11(10): 1963, 2018.
4. Sensini et al, Med Eng & Phys, 71: 79-90, 2019.
5. Tanaka et al, J Biomech Eng. 133(7):074502, 2011.
6. Hanson et al, Ann Anat, 194(5):457-60, 2012.

COMPUTATIONAL MODELLING AND CRACK ANALYSIS OF BIOINSPIRED VOXEL-BASED MULTI-MATERIAL COMPOSITES

Mauricio C. Saldivar (1), Mohammad J. Mirzaali (1), Eugeni L. Doubrovski (2), Amir A. Zadpoor (1)

1.Department of Biomechanical Engineering, Faculty of Mechanical, Maritime, and Materials Engineering, Delft University of Technology (TU Delft), The Netherlands; 2. Faculty of Industrial Design Engineering (IDE), Delft University of Technology (TU Delft), The Netherlands

Introduction

Voxel-based additive manufacturing (AM, also known as 3D printing) is an advanced digital fabrication method of composite structures, enabled by polyjet multi-material 3D printing [1]. Definition of these composite structures consists of a grid of volumetric pixels (voxels), which represent, in this case, the compliant and stiff phases of the entire composite (Figure 1a, b). Therefore, using this approach makes it possible to deposit each phase independently and arbitrarily in space and create complex heterogeneous 3D composite structures. This approach also provides a powerful tool to implement intricate natural design paradigms (*e.g.*, functional gradient [2,3], hierarchical organization [2,4]) in the design and fabrication of bio-inspired architectured composites.

The integration of computational models with the voxel-based approach can potentially boost the search for optimized designs with superior and exceptional properties. The development of validated computational models can also enable further analysis of natural and bio-inspired materials' underlying mechanism. Towards this aim, we propose a framework to create voxel-based finite element models and present a study on bio-inspired composites' fracture behaviour.

Methods

To test the framework, we considered two types of structural designs, namely, composites with uniform "brick-and-mortar" microstructures (BM) and brick-and-mortar structures with a functional gradient (BMG). The single-edge notched specimens were additively manufactured (Objet350 Connex3 3D printer, Stratasys® Ltd.) with a voxel size of ~ 42 × 84 × 36 μm^3 and mechanically tested under tensile loading. The full-field strain was measured using digital image correlation (DIC).

We used the Extended Finite Element Method (XFEM) for the computational crack propagation simulations implemented in commercial software (Abaqus v.6.14). Every 2D computational model was generated based on a single 2D binary image (Figure 1a) and using 2D plane strain quadratic elements (CPE8). We downscaled and averaged the hard volume fraction's image resolutions value to decrease the number of elements. We assigned the result to each element (Figure 1b). We obtained the monolithic material properties from experimental data of pure soft (Agilus30™) and hard (VeroCyan™) commercial polymers designed for the used 3D printing machine.

Results and discussion

The strain distributions obtained from our computational models (XFEM) were similar to those of DIC measurements (Figure 2 c,d). We captured these strain patterns at the maximum force point of every test and simulation.

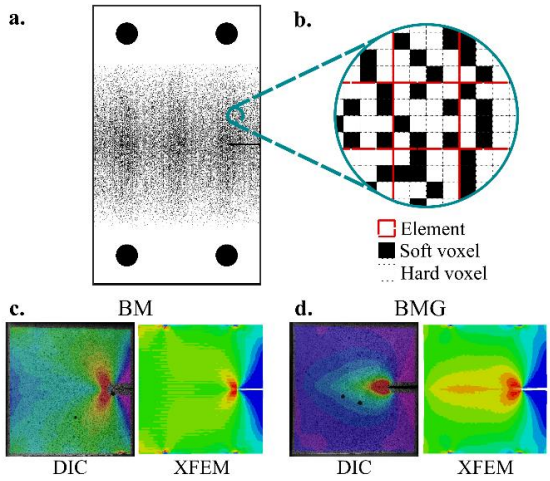

Figure 1: a) Example of a voxel-based binary image used to create single-edge notched composite specimens. b) Computational models were built from 2D elements with downscaled resolution. XFEM strain field comparison with DIC results for Brick-and-Mortar (c) and mix with gradient (d) specimens.

We observed high strain localization in the crack front for both specimen types (Figure 2c,d). The shape of the strain localization, however, was significantly different. Specimens without gradient (BM) exhibited a more concentrated butterfly-like shape in front of the crack tip. Introducing gradient to these structures changed the deformation mode and increased plastic behaviour, resulting in higher toughness. We suggest future work in developing algorithms that create 3D voxel-based models that predict plastic behaviour and crack failure. Additionally, we suggest implementing optimization algorithms to find optimum deposition of soft-hard particles in such bio-inspired structures.

References

1. E. Doubrovski et al., Computer-Aided Design, 60:3–13, 2015.
2. M. J. Mirzaali et al., Advanced Engineering Materials, 22.7:1901142, 2020.
3. Z. Liu et al., Progress in Materials Science, 88:467–498, 2017.
4. P. Fratzl and M. M. G. Guille, Hierarchically Structured Porous Materials, 29–39, 2011.

REACTION-DIFFUSION MODELS TO PREDICT HYDROGEL VISCOELASTIC PROPERTIES

Nicole Guazzelli (1), Ludovica Cacopardo (1), Giulio Iommi (1) Arti Ahluwalia (1)

1. University of Pisa, Italy

Introduction

Hydrogels viscoelastic behaviour is strongly related to liquid molecules interaction with the solid network. Despite mathematical models have been used to simulate chemical and transport phenomena in gels, (e.g. reaction, diffusion, and hindered convection), most of them lack of correlation with gel viscoelastic properties (e.g. relaxation time, τ) or do not provide experimental validations [1, 2].
Therefore, in this study, reaction-diffusion models were implemented to investigate how the presence of different dextran concentration in the aqueous phase affect liquid molecules diffusion in agarose hydrogels and how these variations can be correlated with experimental relaxation times [3].

Method

Agarose-dextran hydrogels were prepared by dissolving 0.5% w/v agarose in different dextran solutions (0, 2, 5% w/v). The viscoelastic parameters (τ, equilibrium, E_{eq}, and instantaneous E_{inst}) were derived according to the procedure described in [3].

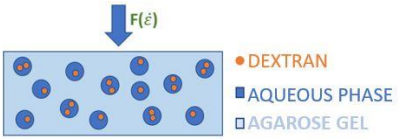

Figure 1. Schematic representation of the agarose-dextran porous system.

As shown in Fig.1, agarose gels were modelled as an homogenous porous medium and an aqueous phase; while dextran is considered as a spherical agglomerate that moves in the interstices of the gel together with the free water.
A *Reaction-Diffusion (RD) Equation* (1) was implemented in Matlab R2015 and used to describe the complessive hydrogel behaviour:

$$\frac{\partial c}{\partial t} - \nabla \cdot (D_i \nabla c) + k_r c = 0 \qquad (1)$$

where the water-dextran binding rate k_r was calculated using viscosity curves measured as a function of temperature (Brookfield viscometer).
To consider the hydrodynamic interaction between matrix fibres and diffusing macromolecules, *the Brinkman Effective medium equation* (2) was implemented to evaluate the diffusion coefficient of the different species in the system [3]:

$$D_i = \left\{1 + \left(\frac{{R_H}_i}{\kappa_i}^2\right)^{\frac{1}{2}} + \frac{1}{3}\left(\frac{{R_H}_i}{\kappa_i}^2\right)\right\}^{-1} \cdot D_{0_i} \qquad (2)$$

where D_{0_i} is the diffusion coefficient described by the Stokes-Einstein equation, R_H is the hydrodynamic radius of the specie, and κ_i is the hydrogel permeability estimated by the *Carman-Kozeny equation* [2]. A 3D finite element model (FEM) was used to estimate R_{H_i} of dextran molecules, using Comsol 5.3 and including E_{eq}, E_{inst} and τ in the material properties of the domain. The model parameters were optimised on the base of experimental diffusion curves obtained using fluorescein isothiocyanate (FITC)-conjugate dextran (Fig 2c-d).

Results

The model showed that, as the dextran concentration increases, the liquid phase diffusion time decreases (Fig.2a), reflecting the relaxation time trend shown in Fig.2b.

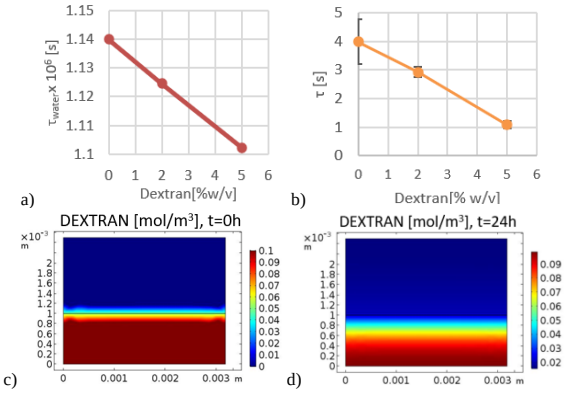

Figure 2. a) Liquid phase diffusion time; b) hydrogel relaxation time; c) dextran diffusion in the agarose hydrogel after 0 and d)24 hours.

Discussion

RD model showed the influence of the dextran in weakening the bonds between water and agarose, with a consequent decrease of the steric hindrance and a faster flow. Therefore, although liquid phase viscosity increases with increasing dextran concentration [2], it contributes to reduce the resistance to flow preventing the formation of water-agarose bonds.
Describing the interaction of liquid molecules with the solid network (which can be modulated by altering liquid phase composition and chemical affinity with respect to the polymeric chains), this model can be used to 'predict' the bulk viscoelastic behaviour of the gels. In the future, different materials can be investigated for both solid and liquid phase, providing an useful tool for the design of engineered viscoelastic hydrogels.

References

1. D. Caccavo et al., Chem. Soc. Rev., 47 : 2357-2373,2018
2. A. Pluen et al., Biophysical J. 542-552,1999
3. L. Cacopardo et al., JMBBM., 89 : 162-167, 2019

MODELLING FINITE CHAIN EXTENSIBILITY IN A DEGRADING POLYMER

Aoife Hill (1), Michel Destrade (2), William Ronan (1)

1. Biomechanics Research Centre, Biomedical Engineering, NUI Galway, Ireland; 2. School of Mathematics, Statistics and Applied Mathematics, NUI Galway, Ireland

Introduction

To utilise biodegradable polymers with optimal properties for their intended application, we must be able to predict how such properties evolve with degradation. By combining equilibrium thermodynamics with a statistical approach, the mechanical behaviour can be derived from the molecular properties. Motivated by Stepto and Taylor [1], we present a thermodynamic model of the stretching of a polymer network that considers the finite extensibility of individual polymer chains and captures the non-affine deformation of a polymer network. Departure from the typical affine deformation assumption is particularly important as degradation takes place, with shorter chains able to fully extend more easily, altering their effect on mechanical properties on further extension. We can then predict how the molecular properties deteriorate during degradation.

Methods

The elastic behaviour of a polymer network under moderate macroscopic deformation can be modelled as being due to entropy changes during straining to a good first approximation [2]. A representative polymer chain distribution is generated, i.e., chain molecular weights (Fig. 1a); two separate distributions are considered, undegraded and degraded. We determined the initial radial end-to-end distance of each chain, r_0, using a statistical approach (Fig. 1b). We assumed a spherically symmetrical sample of chains, with one end of each chain fixed at the origin. The coordinates of the free end of the chain were chosen randomly, consistent with r_0. Chains were then deformed uniaxially with stretch ratio λ in the z-direction, with incompressibility assumed. We accounted for the finite extensibility of a polymer chain, with chains stretched only until they reached their conformational maximum extension (i.e., affine behaviour is not enforced). The average Helmholtz free energy change ΔA per chain was then calculated as follows:

$$\frac{\Delta A}{NkT} = \frac{1}{N}\sum_{i=1}^{N} \ln\left\{\frac{P(r_{0,i})}{P(r_{def,i})}\right\}$$

where N is the number of chains in the network, and $P(r_{0,i})$ and $P(r_{def,i})$ are the probability densities of the ith chain initially and after deformation, respectively. Finally, we obtain the normalised stress as a function of the deformation:

$$\bar{\sigma} = 2\tau\left(\lambda - \frac{1}{\lambda^2}\right) + \left(\lambda^2 + \frac{2}{\lambda} - 3\right)\frac{\delta\tau}{\delta\lambda}$$

where τ and $\frac{\delta\tau}{\delta\lambda}$ are determined from the rate of change in free energy.

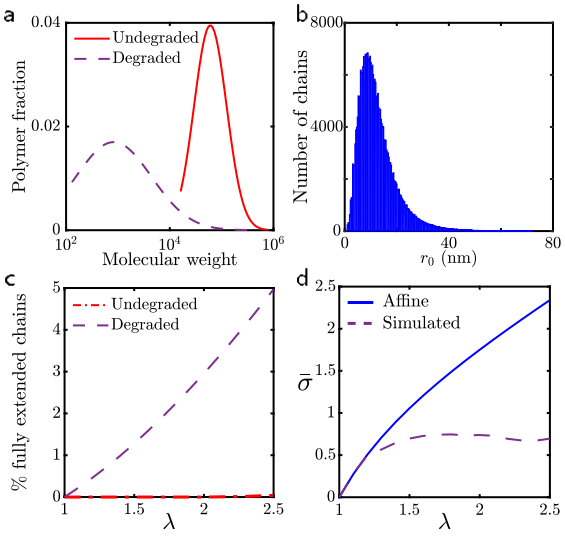

Figure 1: (a) Molecular weight distributions for non-degraded and degraded polymer. (b) Initial end-to-end distance distribution for all chains in the undegraded network. (c) Percentage of fully extended chains as network is deformed before (red) and after (purple) degradation. (d) Stress as a function of deformation for affine assumption (solid) and when the finite extensibility of polymer chains is considered (dashed).

Results and Discussion

The simulated uniaxial extension of a polymer network with finite chain extensibility captures a departure from affine behaviour. The effect of non-affine deformations increases as the system degrades, with shorter, degraded chains fully extending more quickly (Fig. 1c). Fully extended chains contribute nothing more to the change in entropy for further deformation, and the rate of change in energy declines (other contributions to ΔA are not yet considered in the model). Subsequently, predictions for the stress as a function of the deformation show a deviation from affine behaviour typical of elastomeric materials [3] (Fig. 1d). This approach provides a framework for a thermodynamically consistent model of polymer mechanical behaviour during degradation which will be coupled with macroscale models of bioresorbable devices.

References

1. Stepto et al., Macromol Symp, 93:261-268, 1995.
2. Ward, Mechanical Properties of Polymers, Wiley, 1971.
3. Treloar, Physics of Rubber Elasticity, Clarendon, 2005.

Acknowledgements

The authors gratefully acknowledge the research support provided by the Irish Research Council (GOIPG/2018/2697).

MECHANICAL PROPERTIES AND MICROSTRUCTURAL EVOLUTION OF BIODEGRADABLE POLYMERS

Ali Reza Abaei (1), Ted. J. Vaughan (1), William Ronan (1)

[1]Biomechanics Research Centre & Biomedical Engineering, School of Engineering, NUI Galway, Ireland

Introduction

Biodegradable semi-crystalline polymers, such as PLA, have shown initially promising results as a replacement for permanent implants such as vascular stents, but their detailed mechanical response is not yet fully understood or easily predicted. Here, we coupled two frameworks: (i) a micromechanical model which investigate the effect of crystallinity and the evolution of the molecular weight over degradation. (ii) implementation of physically-based model using user subroutines to predict effective modulus at each integration point by the finite element solver. [1-2]

Methods

A microscale finite element model of a semi-crystalline polymeric material, using a representative volume element (RVE) approach is created; amorphous, crystalline, and porous regions are considered (Fig. 1A). Crystalline regions are anisotropic and either randomly or preferentially oriented. Periodic boundary conditions are applied to the RVE and effective properties determined, including effective modulus $\bar{E}$. These numerical results are compared to theoretical bounds for the multiphase material. A wide parameter sweep of Mn and Xc is performed in order to establish a "map" of the mechanical behaviour (Fig. 1B). This map builds a framework to predict the modulus during degradation instead of running a simulation every time.

The "map" or database of relationship is imported into an array for use in Abaqus via a user subroutine. This array is then accessed during a coupled simulation, where values of Xc and Mn are predicted by a degradation model which considers hydrolysis, autocatalysis, and diffusion of degradation products. This degradation model is also implemented via user subroutines. The effective modulus is retrieved at each integration point in order to calculate the mechanical response of a stent during degradation.

Results

Fig 1B. shows the predicted effective modulus $\bar{E}$ for a range of crystallinity X_c and molecular weights M_n as calculated using the micromechanical RVE model. These contours of modulus can be used to predict the changes $\bar{E}$ in as the microstructure evolves during degradation. As an example, a ring of a stent is crimped and deployed in section of mock vessel and a degradation analysis is performed. Fig 1C. and Fig 1D. show the contour plots of effective modulus for degradation of a stent free surface case over 140 days.

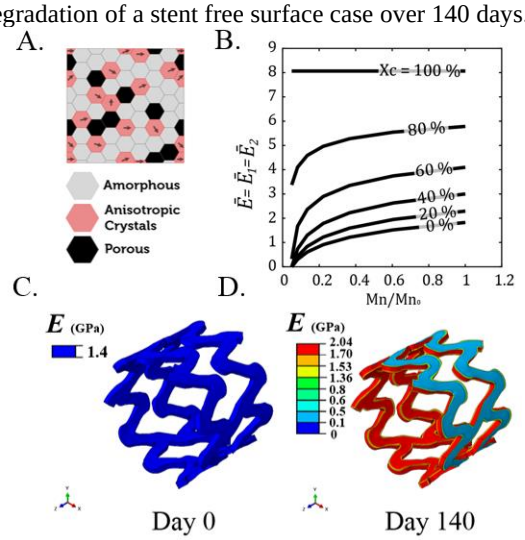

*Figure 1-**A.** 2D RVE of a semi-crystalline polymer **B.** Modulus $\bar{E}$ as a function of crystallinity Xc and normalized molecular weight (M_n/M_{n0}). **C.** and **D.** Stent contour plots showing predictions in effective modulus at beginning of degradation (day 0) and at the end of degradation (day 140).*

Discussion

The present work shows the capability of a micromechanics model to explain experimentally observed changes in modulus during degradation as related to changes in microstructure (M_n, X_c). It also shows how both mechanisms can have confounding effects: the decrease in M_n leads to a lower modulus in the amorphous phase, decreasing the overall effective modulus while the increase in X_c increase the volume fraction of the stiffer crystalline phase, leading to higher value modulus. This coupled framework can be used to investigate degradation subject to a range of factors such as heterogeneity introduced during manufacturing or the effect of neointimal growth on degradation performance.

References

1. Shine, R. et al., Journal of Medical Devices, 11(2), 2017.
2. Shirazi, R.N. et al., Journal of the Mechanical Behavior of Biomedical Materials,54, pp.48-59 ,2016.

Acknowledgements

This project has received funding from the European Union's Horizon 2020 research and innovation programme under grant agreement No 777119

CHARACTERISATION OF SCLEROSING FOAM RHEOLOGY *VIA* CLINICALLY RELEVANT PARAMETERS: A STEP TOWARDS THE OPTIMISATION OF VARICOSE VEIN SCLEROTHERAPY

A. Meghdadi (1), S. Jones (2), V. Patel (2), A. Lewis (2), T. Millar (1), D. Carugo (3)

1. Faculties of Engineering & Physical Sciences and Medicine, University of Southampton, United Kingdom
2. Biocompatibles UK Ltd, Camberley, United Kingdom
3. Department of Pharmaceutics, School of Pharmacy, UCL, London, United Kingdom

Introduction

Varicose veins are enlarged and swollen superficial veins that occur as a result of venous reflux and incompetent venous valves. One of the most common treatments for varicose veins is sclerotherapy that involves the intravenous injection of a surfactant, such as polidocanol, to damage the vascular endothelium and cause sclerosis. Given that the surfactant is prone to inactivation by blood components, it is often formulated as a foam in order to prevent mixing with blood upon injection and maximise therapeutic effects. The rheological properties of foams have been previously characterised, although they have not been correlated with clinically relevant outcomes. Most previous studies focus on two-dimensional foams and rheometric measurements. Furthermore, a number of studies have demonstrated the thixotropic behaviour of foams, suggesting hysteresis in loading/unloading curves. If the history of shearing plays a role in foam rheology, then it may be inferred that conventional rheometric measurements do not reflect the flow behaviour of sclerosing foams in physiological conditions. The aim of this study is to experimentally determine the apparent viscosity of sclerosing foams in a biomimetic setting.

Methods

Experiments consist of a technique commonly referred to as "pipe viscometry". It involves the injection of foam into a tube of known length (L) and diameter (d) flanked by two pressure sensors. Foam is injected at a constant flowrate (Q), allowing the inlet and outlet pressure curves to plateau. The pressure differential (ΔP) is used to calculate the apparent viscosity (μ) of foam at the given injection flowrate. By varying tube diameter and injection flowrate, foam viscosity can be calculated over a range of shear rates. Furthermore, pipe viscometry allows for the correction of the wall-slip phenomenon, which is a major source of error if not accounted for. The independent variables studied were foam liquid-to-gas ratio, tube diameter and foam type. Polidocanol-based (1% solution) foams were produced using the double syringe system and Tessari methods with liquid-to-gas ratios 1:3, 1:4 and 1:5. Polytetrafluoroethylene tubes of diameter 2.48, 4.48 and 9.46 mm were used, and injection flowrates were in the range 2 – 36 ml.min^{-1}.

Results

Results of the pipe viscometry experiments demonstrate a steady increase in static inlet and outlet pressures during foam injection that reach a plateau when the tube is completely filled with foam. Data obtained from experiments (which comprised different vein diameters, foam formulations, and injection flow rates) were fitted in the power law equation (Eq. 1) to obtain rheological indices (K and n). For a Tessari foam of 1:4 liquid-to-gas ratio injected into a 34 cm long tube with diameter of 2.48 cm, viscosity ranged from 0.05 to 0.27 Pa.s, corresponding to observed shear rates of 700 to 80 s^{-1}.

$$\tau_w = K\dot{\gamma}_{observed}{}^{n} \quad (1)$$

Observed shear rate ($\dot{\gamma}_{observed}$) and wall shear stress (τ_w) can be calculated from injection flowrate Q, pressure differential ΔP, pipe length L and diameter d:

$$\dot{\gamma}_{observed} = \frac{32Q}{\pi d^3} \quad (2) \qquad \tau_w = \frac{d\Delta P}{4L} \quad (3)$$

Discussion

This is the first study reporting on the rheological characterisation of sclerosing foams under conditions mimicking their end-point application. Results are in agreement with the previously observed shear-thinning behaviour of liquid foams. Furthermore, they will also be corrected for wall-slip and fitted into a non-Newtonian model to yield a more accurate rheological characterisation that can be used to more effectively predict foam's behaviour during treatment. Values of foam viscosity will be correlated with foam's efficacy in displacing blood from a vein model, which can inform the design of more efficacious foam formulations.

References

1. Bekkour, K. and Scrivener, O. (1998) 'Time-Dependent and Flow Properties of Foams', Mechanics Time-Dependent Materials.
2. Enzendorfer, C. et al. (2002) 'Pipe viscometry of foams', Journal of Rheology, 39(2), pp. 345–358.
3. Marze, S., Langevin, D. and Saint-Jalmes, A. (2008) 'Aqueous foam slip and shear regimes determined by rheometry and multiple light scattering', Journal of Rheology.
4. Weaire, D. (2008) 'The rheology of foam', Current Opinion in Colloid and Interface Science.

Acknowledgements

We hereby thank BTG plc and EPSRC for their support towards Alireza Meghdadi's PhD studentship. We are grateful to the European Society of Biomechanics and all the sponsors for supporting this congress.

A COMPUTATIONAL MODEL OF INTERACTIONS BETWEEN PARYLENE STRUCTURES AND PERIPHERAL NERVES

Pier Nicola Sergi(1), Natalia De la Oliva (2), Jaume del Valle (2), Xavier Navarro (2),Silvestro Micera (1,3)

1. Sant'Anna School of Advanced Studies, Italy; 2. Institut de Neurociències, Universitat Autònoma de Barcelona and CIBERNED, Spain; 3. Ecole Polytechnique Federale de Lausanne , Switzerland

Introduction

Neuroprostheses are advanced devices heavily relying on the ability of neural interfaces to create a stable bidirectional link with peripheral nerves [1]. However, the body responses to the surgical implantation of neural interfaces into peripheral nerves with the so called Foreign Body Reaction (FBR). Inflammation, proliferative and remodelling phases, ending with the encapsulation of the implanted device, are the main known phases of the FBR. These extremely complex chain of phenomena [2] contributes to the failure of the interface. Therefore, the knowledge of the scar tissue evolution around the implanted structure is fundamental to design strategies aimed to decrease the amount of tissue interposition and physical disconnection between nerve fibers and the interface electrode. However, this is, probably, a less explored field, because of the high number and the extreme complexity of involved processes. As a consequence, "smart paths" among so many combinations of phenomena, could be investigated to reproduce experimental results through a computational framework, accounting for the action of the main biological and biophysical phenomena.

Methods

Female Sprague-Dawley rats were used to provide experimental data [3]. The evolution in time of the capsule thickness developed around parylene-based intraneural longitudinal electrodes (see details of the experimental procedures in [3]) was then assumed to be dominated by two sets of related processes; the first phase of interaction between the nerve and parylene, and a late remodelling phase. In particular, this phase was longer than the previous one, so the mechanical characteristics of materials dominated the interaction, and, particularly, the stiffness mismatch between peripheral nerves [4,5] and parylene [3]. The evolution of the capsule thickness was theoretically predicted through a hybrid linear combination, symbolically written as follows:

$$s(t)=\kappa\Im(t)+\lambda\Omega[Y,\Psi,t] \quad (1)$$

where $\kappa,\lambda\in\Re$ were numerical constants, $\Im(t)$ was a function accounting for the contribution due to the cellular steps, while $\Omega[Y,\Psi,t]$ was a function related to the interactions between parylene and nerve tissue, whose strain energy functions were respectively Y and Ψ. In particular, the term $\Im(t)$ was computationally achieved, since it derived from a system of differential equations which does not admit a closed form solution.

Results

In Fig.1a, the evolution of Eq.(1) over time is shown. The experimental data were plotted through their mean values (circles) and standard deviation (error bars), while the solid line accounted for the evolution of the mean theoretical prediction together with the prediction bounds (dashed lines). Similarly, Fig.1b shows the volumetric expansion around an implanted structure of parylene with a circular section (∅ 10μm) after about 8 months of permanence inside peripheral nerves *in vivo*.

Discussion

The evolution of the scar capsule thickness around a hypothetical circular structure of parylene was found to be characterized by an early oscillatory expansion ending by a steady state expansion, resulting in a relative increase in volume (i.e., V(parylene+scar)/V((parylene)) of about 121 times in about 8 months. As a consequence, Eq.(1) allowed different contributions, deriving from the FBR different phases, to be split and separately investigated in order to optimize the final amount of scar tissue around implanted polymeric neural interfaces [6].

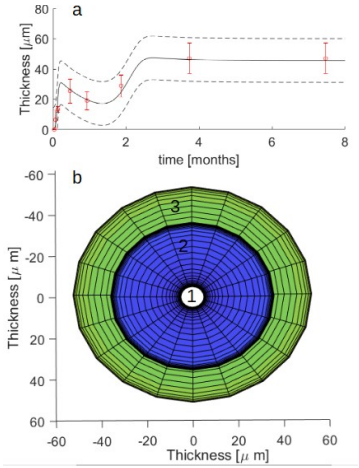

Figure 1: (a) Evolution of scar thickness over time. (b) Prediction of volumetric scar expansion: 1) Circular implanted device ∅ 10μm, 2) Early scar expansion, 3) Late scar expansion.

Acknowledgement

Authors thank NeuHeart EU project ID 824071

References

1. Raspopovic et al., Sci Transl Med 2014: 6(222): 222Ra19
2. Anderson, Semin Immunol. 2008; 20(2): 86–100
3. de la Oliva et al., Sci Rep 2018; 8: 5965
4. Giannessi et al., Med Biol Eng Comput 2018; 56:1541-51
5. Giannessi et al., Med Eng Phys 2020;76:47-55
6. Navarro et al., J Periph Nerv Syst 2005; 10: 229-258.

BIAXIAL MECHANICAL CHARACTERIZATION OF SILK-BASED MULTI-LAYERED VASCULAR GRAFT FOR SMALL VESSELS

Luca D'Andrea (1), Marta Alloisio (1), Martina Aurora Costa Angeli (1), Marco Biagiotti (2), Valentina Vincoli (2), Giuliano Freddi (2), Antonio Alessandrino (2), Pasquale Vena (1), Dario Gastaldi (1)

1. Politecnico di Milano, Italy; 2. Silk Biomaterials, Italy

Introduction

Occlusive disorders involving small diameter (less than 6 mm) peripheral arteries are continuously growing.
Scarce availability of autografts (such as saphenous vein) calls for the development of new grafts. Polyethyleneterephthalate (PET)-based grafts are widely used, but the use of this material on small arteries brings to several complications like thrombosis, or compliance mismatches. As silk-based materials meet the requirements of biocompatibility and of mechanical properties for vascular grafts, small diameter grafts obtained from silk-fibroin are here characterized mechanically [1].

Materials and Methods

Three-layers silk fibroin sheet samples have been characterized through in-situ biaxial mechanical stretching with simultaneous microscope observation of the sample surface.
To achieve mechanical properties and biocompatibility, a three layers system has been obtained by coupling two electrospun layers of silk fibroin nanofibres (typical diameter of 400 nm) to a silk fibroin textile layer [2]. The native silk fibroin fibers of the microfibers (about 12 µm of diameter) were arranged in bundles of about 300 µm of diameter.
Suitable rectangular samples have been obtained through cutting from the multi-layered silk sheets; the approximate size of the central part is 5 mm. A home-made biaxial test equipment has been used for equi-biaxial stretching of the silk sheets. The testing apparatus is equipped with four displacement actuators (50 nm resolution) and two load cells (50 N full range and 0.1% resolution). The biaxial tensile tests were performed in wet conditions. Relative displacement applied independently along the axial and circumferential directions allowed to simulate different pre-stretch conditions with simultaneous circumferential expansion. In particular, an equi-biaxial stretching was applied until 1 mm (and 3 mm) of displacement is achieved. A further expansion in circumferential direction at fixed axial stretch is also applied (Figure 1). The force-displacement slope is estimated in the equi-biaxial configuration as well as in the axially constrained configuration of the test. 7 and 5 tests have been performed for the 1mm and 3 mm pre-stretch, respectively.

Results and discussions

The force-displacement slope, which is correlated with vessel compliance, obtained in the equi-biaxial stage is higher than that obtained in the axially constrained configuration; furthermore, at constrained axial pre-stretch, the axial pre-stretch at 3 mm exhibited a circumferential force-displacement slope higher than that at 1 mm axial pre-stretch. Indeed, higher pre-stretch would induce lower compliance as a result of the micro-structural arrangement of the middle layer of silk microfibers. The graft compliance computed at 1 mm axial confinement is 3 $\frac{\%}{mmHg}$ at an equivalent internal pressure of approximately 400 mmHg. A set of tests at lower pre-stretch (equivalent to the 80 -120 mmHg regime) showed a graft compliance of 3.75 $\frac{\%}{mmHg}$ which is consistent with literature results [3].
The results of this study indicate that the circumferential compliance is dependent on the axial pre-stretch which arises upon graft implantation (Figure 2). Therefore, an extensive experimental campaign at different equivalent pressures is planned for a complete characterization study.

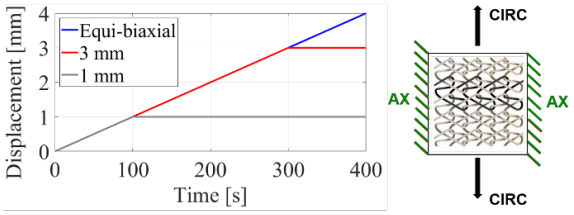

Figure 1: Loading program and sketch of test configuration

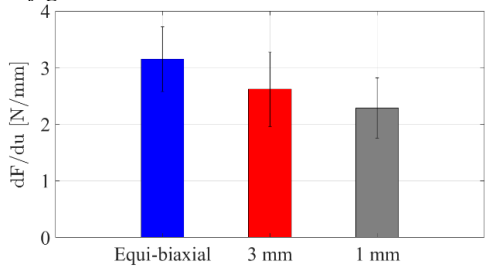

Figure 2: Force-displacement solpe in the equi-biaxial and constrained axial pre-stretch (1 mm and 3 mm).

References

1. Catto et al. Material Sciences and Engineering C, 545,101-111, 2015
2. Alessandrino et al. Frontiers in Bioengineering and Biotechnology, 7: 1-17, 2019.
3. Johnson et al. j. Tissue Sci Eng 6 151, 2015

STUDY OF THE MECHANICAL PROPERTIES OF THE PERSPECTIVE NANOCELLULOSE-BASED DURA MATER SUBSTITUTE

Anna Lipovka (1), Daniil Parsin (1), Alexei Kharchenko (2)

1. *LIH SB RAS, Russia; 2. Novosibirsk Research Institute of Traumatology and Orthopaedics n.a. Ya.L. Tsivyan, Russia;*

Introduction

Dura mater (DM) – the outer layer of three layers of membrane is a thick, dense, irregularly shaped connective tissue that surrounds the brain and spinal cord. Because of trauma, oncological processes of the brain and spinal cord, as well as in neurosurgical interventions, the dura mater can be damaged, dissected or removed to provide access to the nerve structures and under them.

In the case of a shortage of its own dura mater, a flap of biocompatible tissue (up to 100 cm^2) is required, which is necessary to restore the dura mater. The mechanical properties of such a material should be as close as possible to the properties of natural DM. Various materials are currently available to close the defects of the dura mater, however, all of them have their disadvantages.

Bacterial nanocellulose (BNC) is a good candidate for this role. It is a linear polysaccharide chain with the same chemical structure as plant cellulose. Ultrafine BNC differs from plant cellulose in high purity and degree of crystallinity, higher ability to adsorb liquid, strength of the fiber structure, and also their nanoscale [1].

Methods

Universal tensile machine INSTRON 5944 was used for uniaxial loading test of the BNC samples with different methods of preparation, as well as fresh and cadaveric dura mater tissues. Uniaxial mechanical test is considered a golden standard in the area of investigating properties of such materials. [2]

Results

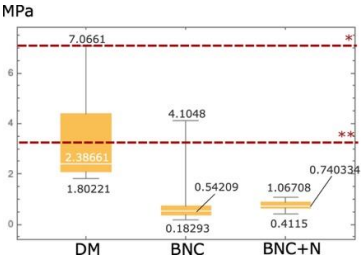

Figure 1: Boxplot of the values of the ultimate stress for DM, bacterial cellulose and bacterial cellulose with the addition of chitosan. DM stands for Dura Mater, BNC for bacterial nanocellulose, and BNC+N for bacterial nanocellulose treated with Novochizol™.

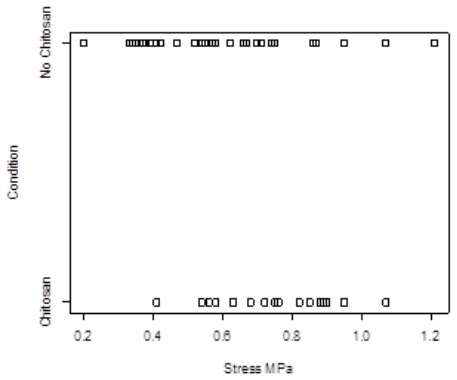

Figure 2: The difference in distribution of the ultimate stress for regular BNC and BNC with the addition of chitosan.

Discussion

With all the advantages of bacterial nanocellulose as a barrier to the human brain, the main problem during its production is the unevenness of tissue thickness, which can lead to hernias and ruptures after implantation. The aim of this work is to investigate the mechanical properties of bacterial cellulose samples made using Novochizol™ with bacterial cellulose made without it, and to assess the possibility of controlling the mechanical properties of the material by changing the thickness.

References

1. Kharchenko et al. Journal of spine surgery 16.3, 2019
2. Ogden Raymond William. *R. Soc. Lond. A* 326565–584, 1972

Acknowledgements

This work was supported by the RSF (project No.20-71-10034)

ELECTROSPINNING SMART FIBROUS SCAFFOLDS FROM SMALL PEPTIDES FOR TISSUE ENGINEERING APPLICATION

L. Sori (1), A. Pizzi (1), L. Draghi (1), A. Gautieri (2), F. Baldelli Bombelli (1), M. Soncini (2), and P. Metrangolo (1)

1. DCMIC "Giulio Natta", Politecnico di Milano, Italy; 2. Biomechanics Group-DEIB; Politecnico di Milano, Piazza L. Da Vinci 32 - 20133 Milan, Italy.

Introduction

In recent years, the development of new biomaterials with possible applications in tissue regeneration has made the engineering and medical field a fertile ground for the creation of new techniques and strategies capable of exploring the potential characteristics of new materials[1,2]. In this area, the biggest challenge is to accurately reproduce the entire architecture and the properties typical of extracellular matrix (ECM) of the native tissues replicated[3]. The electrospinning in recent years has become a particularly widespread and effective technique for obtaining scaffolds of polymeric fibers[4,5]. In this contribution we report the electrospinning of a very small, brominated peptide (7 ammino acids) highly represented in full-length resilin protein (with more than 600 amino acids). We show our preliminary results obtained electrospinning peptides as a single component and peptides in combination with other compounds (e.g., gelatin). In principle, the synergy between the two compounds should results into the emergence of new properties of the scaffold.

Methods

One of the objectives of the work aims to obtain polymeric fibers, having better performances than those offered by the full-length resilin protein. To obtain good result with electrospinning technique it is necessary to optimize several experimental parameters like solvent, concentration, flow speed, distance, voltage, temperature, and humidity. For this technique, it is necessary to apply an electric field, essential for stretching the biopolymer fibers and for solidifying the solution. The collection can take place on a mobile or fixed (metallic) collector according to the needs for subsequent studies and/or applications. For the morphological and chemical characterization of the electrospun yarn, Scanning Electron Microscopy (SEM) and Energy-dispersive X-ray spectroscopy (EDS) have been used.

Results

The first electrospinning test were carried out using the small peptide as a single component, in hexafluoroisopropanol (HFIP) as a solvent. Under this condition, the resulting scaffold was too brittle for their potential use in biomedical or tissue engineering applications. Water was also tested since aqueous solutions showed fiber formation; however, some critical issues prevented the formation of thread-like morphology. Furthermore, different peptide/gelatin mixtures have been prepared by testing the widest range of possibilities. The most encouraging results were obtained by increasing the viscosity of the solution. Solution viscosity plays an important role in determining fiber size and morphology. With a concentration of 40% *w/v* of mixed solutions we obtain stable thread-like morphology and a manipulable material suitable for the evaluation of mechanical properties.

Discussion

The results obtained with the brominated peptides as a single component, although still preliminary, are promising as it is not usual to obtain fibers through electrospinning from so low molecular weight peptides. Indeed, proteins that are commonly electrospun have weights of hundreds kDa. In all the analyzed conditions, mixing the peptide with gelatin in different ratio results in well-defined morphology (filaments). However, it is important to precisely adjust the ratio between the brominated component and the gelatin. In fact, the predominance of brominated peptides over gelatin impairs the formation of continuous fibers (Figure 1b).

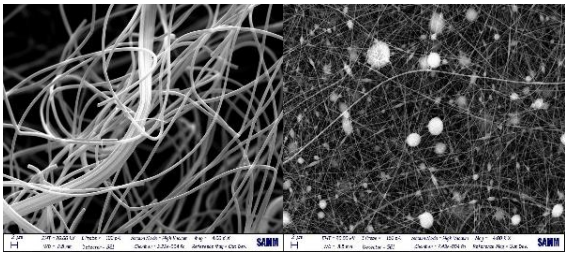

Figure 1: SEM images of electrospun of mixed solution: (a) with predominance of gelatin; (b) some beads due to a predominance of brominated peptide.

References

1. Dolcimascolo A et al, 10.5772/intechopen 83839, 2019.
2. Jiang T et al, Prog Polym Sci 46:1–24, 2015.
3. Brown T et al, Prog Polym Sci, 56:116–166, 2016.
4. Nemati S et al, Nano Convergence, 6:36, 2019.
5. Campiglio C et al, Materials, 12:2476, 2019.

Acknowledgements

Authors are thankful to the European Research Council (ERC) for funding the projects FoldHalo, no. 307108) and MINIRES, no. 789815. We are also thankful to the PoliMI PhD School for funding a multidisciplinary PhD bursary. MINIRES, no. 789815. We are also thankful to the PoliMI PhD School for funding a multidisciplinary PhD bursary.

CITRIC ACID CROSSLINKING OF METHYLCELLULOSE HYDROGELS

Lorenzo Bonetti (1), Luigi De Nardo (1,2), Fabio Variola (3), Silvia Farè (1,2)

1. Department of Chemistry, Materials and Chemical Engineering "G. Natta", Politecnico di Milano, Milan (20131), Italy; 2. National Interuniversity Consortium of Materials Science and Technology (INSTM), Florence (50121), Italy; 3. Department of Mechanical Engineering, University of Ottawa, Ottawa, ON, K1N 6N5, Canada;

Introduction

Aqueous solutions of methylcellulose (MC), a cellulose derivative obtained by partial substitution of hydroxyl groups (-OH) with methoxy ones (-OCH_3), exhibit thermo-reversible gelation around their lower critical solution temperature (LCST). In particular, MC hydrogels change from sol (T < LCST) to gel (T > LCST) state upon temperature increase [1]. MC hydrogels lend themselves to smart applications in the field of regenerative medicine, where the body temperature is exploited to activate their thermal transition [1]. However, the reduced stability in aqueous environment and unsatisfactory mechanical properties of MC gels, limit the breadth of their possible applications. The target of this work was to develop a crosslinking strategy based on citric acid (CA) for MC hydrogels, aimed at increasing their stability and mechanical performance while maintaining their smart behavior.

Methods

MC powder was dispersed (8% w/v) in a Na_2SO_4 (50 mM) solution at 55°C to obtain responsive hydrogels with a LCST ≈ 37 °C [1]. Citric acid (CA) was used as crosslinking agent, due to its low cost and toxicity [2]. Three crosslinking parameters (x_1 = CA concentration, x_2 = crosslinking time, and x_3 = crosslinking temperature, Table 1) were studied by a Design of Experiment (DOE) approach, lastly identifying optimized crosslinked MC hydrogels (MC-L, MC-M, MC-H). The optimized crosslinked hydrogels were then investigated for their physico-chemical, mechanical and *in vitro* biological properties.

CA (% w/w) x_1	T (°C) x_2	Time (min) x_3
1 - 3 - 5	165 - 177 - 190	1 - 8 - 15

Table 1: Parameters used for MC hydrogels' crosslinking.

Results

The DOE approach allowed to obtain a regression equation able to describe the swelling degree of MC hydrogels as a function of the crosslinking parameters. MC-L, MC-M, and MC-H (low, medium and high crosslinking), were selected as optimized crosslinked hydrogels and further characterized.

Swelling tests in water revealed the effectiveness of CA crosslinking in modulating the water uptake of MC hydrogels. The theoretical crosslinking density [3] increased from $(0.19 \pm 0.02)\times10^{-4}$ to $(2.58 \pm 0.65)\times10^{-4}$ mol cm^{-3} for MC-L and MC-H samples, respectively. Moreover, acid-base titrations revealed an increase in the carboxylic esters from 0.05 ± 2.74 to 42.25 ± 3.71 mmol/100 g for MC-L and MC-H samples.

Smart transition was assessed by swelling tests [4], Raman spectroscopy and rheology analyses [5], testing MC samples at different temperatures (T = 25 - 50 °C). Interestingly, MC-M hydrogels displayed increased mechanical properties (Figure 1) while preserving their LCST around 37 °C. Conversely, excessive crosslinking (MC-H) was found to cause the loss of MC hydrogels' smart behavior.

In vitro preliminary biological characterization proved the absence of any cytotoxic effect induced by CA or by the crosslinking procedure when 24- and 48h-material extracts were put in contact with L929 fibroblasts.

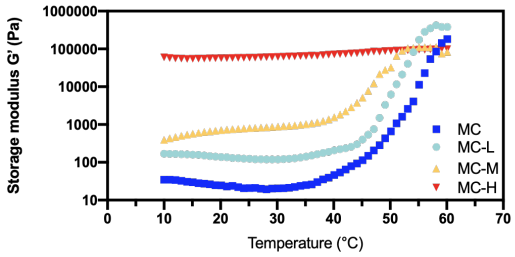

Figure 1: Representative G'/T curve obtained from rheological tests on MC samples

Discussion

The DOE approach allowed to obtain a quadratic regression model (R^2_{adj} = 0.963) able to predict and tune the swelling of MC hydrogels based on the three crosslinking parameters. Crosslinking density measurements and acid-base titrations confirmed the efficacy of CA in controlling the crosslinking degree of the hydrogels. Swelling measurements, Raman and rheological analyses were shown to be orthogonal techniques, providing information about the sol-gel transition of MC hydrogels around the LCST. A crosslinking degree of about 50 % (MC-M) was shown to increase the mechanical properties and stability of MC hydrogels, preserving their smart behavior.

Conclusions

The obtained results pave the way for the development of MC smart hydrogels with tunable properties, with potential innovative implications in the field of smart systems.

References

[1] Cochis *et al*., *Materials* (2018)
[2] Oryan *et al*., *Int. J. Biol. Macromol. (2018)*
[3] Varma *et al*., *Acta biomater. (*2014)
[4] Munoz-Pinto *et al*., *J. Biomed. Mater. Res. A* (2012)
[5] Contessi N. *et al*., Mater. Lett. (2017)

MOMENTA TRANSFERED TO DENTAL IMPLANT-BONE AND TOOTH-PDL-BONE CONSTRUCTS UNDER IMPACT LOADING

Ayda Karimi Dastgerdi (1), Alireza Yahyaiee Bavil (1), Mohammad Mehdi Dehghan (2), Saeed Farzad-Mohajeri (2), Hamid Reza Barikani (3), Gholamreza Rouhi (1)

1. Amirkabir University of Technology, Iran; 2. University of Tehran, Iran; 3. Tehran University of Medical Sciences, Iran

Introduction

During dental trauma, periodontal ligament (PDL) contributes to the stability of the tooth-PDL-bone (T-PDL-B) construct [1]. When a dental implant is inserted into the bone, the dental implant-bone (DI-B) construct will be more prone to the mechanical damage caused by impact loading, compared to the T-PDL-B construct, due to the lack of a shock-absorbing constituent. Despite the widespread presence of such traumas, the behavioural differences between these two constructs have not been thoroughly investigated to date. The main goals of this study were to: (i) identify the main differences in the mechanical behaviour of T-PDL-B and DI-B constructs under impact loading, using in-vitro tests; and (ii) develop a validated FE model to find the stress distribution within both constructs in order to discover new aspects of the existing differences between the two constructs.

Methods

First, mechanical impact tests were performed on six canine mandibles of intact (N=3) and implanted (N=3) specimens using a custom-made drop tower apparatus, from release heights of 1, 2, and 3 cm sequentially, and the transferred momenta were measured. Next, computed tomography-based finite element models were developed for both constructs, and the transferred momenta were calculated.

Results

The experimental results indicated that, for the release heights of 1, 2, and 3 cm, the linear momenta transferred to the dental implant-bone construct were 33.1, 31.0, and 27.5% greater than those of the tooth-PDL-bone construct, respectively. Results of finite element simulations were in agreement with those of the experimental tests (error < 7.5%, Table 1). Moreover, results of the FEA showed that for DI-M construct, alveolar bone experienced a high-stress concentration inside the alveolar bone cavity (max. von Mises stress of 133, 198, 283 MPa for the release heights of 1, 2, and 3 cm, respectively), while T-PDL-M resulted in significantly smaller stress intensity (max. von Mises stress of 80, 88, 110 MPa for the release heights of 1, 2, and 3 cm, respectively) (Fig. 1).

Discussion

Results of this study indicate that PDL plays a crucial role in the appearance of the behavioural differences between the T-PDL-B and DI-B constructs under impact loading. Moreover, results of this work also show that the bone in the DI-B construct is more susceptible to mechanical damage than that of a natural tooth construct. Thus, modifications to the currently used dental implants, based on the structure of a natural tooth, seem necessary.

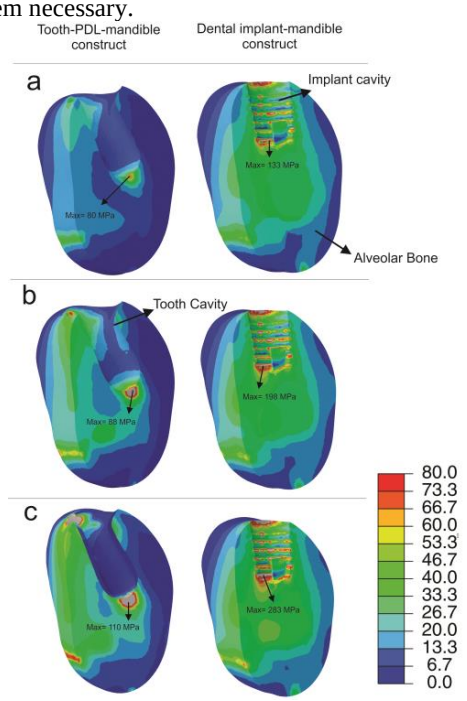

Figure 1: von Mises stress distribution in alveolar bone of T-PDL-B and DI-M constructs, resulted from impact loading simulations for the release heights of: (a) 1 cm; (b) 2 cm; and (c) 3 cm.

Release Height of impactor	T-PDL-B Construct			DI-B Construct		
	LM (Experimental-mean values) (Kg.m/s)	LM (FEM) (Kg.m/s)	Error (%)	LM (Experimental-mean values) (Kg.m/s)	LM (FEM) (Kg.m/s)	Error (%)
1 cm	2.92±0.34	2.70	7.5	4.37±0.8	4.26	2.5
2 cm	3.69±0.7	3.76	1.9	5.36±1.13	5.21	2.2
3 cm	4.80±0.7	4.68	2.5	6.62±0.93	6.23	5.9

*Table **1**. Linear momenta (LM) transferred into T-PDL-B and DI-B constructs: Comparison between results of in-vitro tests and FE models.*

References

1. Da Silva, B.R., et al., Comput Methods Biomech Biomed Engin, 2013. 16(2): 158-64.

NUMERICAL SIMULATION OF INITIAL FORCE GENERATED DURING BODILY TOOTH MOVEMENT USING ORTHODONTIC ALIGNERS

Tarek M. Elshazly (1), Ludger Keilig (1), Ahmed Ghoneima (2), Moosa Abuzayda (3), Christoph Bourauel (1)

1. Oral Technology, Bonn University, Bonn, Germany;
2. Department of Orthodontics, Hamdan Bin Mohammed College of Dental Medicine, MBRU, Dubai, UAE;
3. Department of Prosthodontics, Hamdan Bin Mohammed College of Dental Medicine, MBRU, Dubai, UAE

Introduction

Tooth movements by clear aligners are more complex compared to fixed braces [1]. The application of numerical methods, such as finite element methods (FEM), facilitates the stress analysis of orthodontic devices [2]. This study aimed to develop a 3D FE model to understand the biomechanical behaviour of clear aligners. The initial forces generated during bodily movement of several teeth were calculated.

Methods

Using the FE system Marc/Mentat, an idealised FE model consisting of three teeth was used to perform sensitivity analysis. Using Mimics software, a realistic 3D model of upper jaw was imported to design different orthodontic cases. A complete aligner with a thickness of 0.7 mm was modelled. A full model was exported to Marc/Mentat. 4-noded tetrahedral elements were used for meshing. The number of nodes and elements for each component of the model are shown in Table 1. Material parameters of all structures are shown in Table 2. The forces generated by 0.2 mm bodily movements of the teeth 21, 13, and 15 (facio-lingually, mesio-distally, and extrusion-intrusion) were calculated and compared to standard experimental measurements. A touching condition was established in contact interfaces between the aligner and the tooth surfaces, with a friction coefficient of μ=0, and interference closure -0.04.

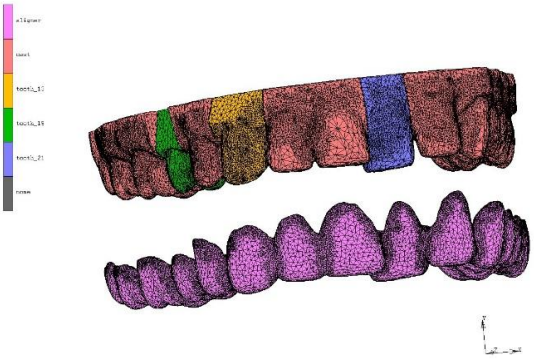

Figure 1: A realistic 3D-model of upper jaw with designed 0.7 mm clear aligner used to simulate different orthodontic movements of the teeth 21, 13, and 15.

Component	No. of Elements	No. of Nodes
Aligner	380308	92570
Cast	223637	55383
Tooth 21	13541	3450
Tooth 13	17451	4299
Tooth 15	11745	3057

Table 1: Number of nodes and elements of the Components of the finite element model.

Structure	Young's Modulus (GPa)	Poison's ratio
Aligner	2	0.3
Teeth	80	0.3

Table 2: Material parameters of all structures.

Results

The resultant forces of the three different teeth, in facio-lingual direction were ≈25 N, in mesio-distal direction were ≈25 N, while in extrusion-intrusion direction were ≈2.5 N. Decreasing the stiffness of the aligner from 2 GPa to 1 GPa results in a decrease of the forces to nearly the half.

Discussion

Although the forces generated in the numerical model is to some extent higher than the forces reported experimentally and clinically in some studies, some factors could explain this difference. Firstly absence of the PDL has a great impact on the biomechanical behaviour of the model. This will be realised in the next step. Secondly, the thickness of the experimentally investigated aligner could be reduced due to deep drawing of foil sheets compared to the one used in this numerical study. Thirdly, a realistic contact between the aligner and the teeth could not be simulated yet.

References

1. Elkholy et al, American Journal of Orthodontics and Dentofacial Orthopedics, 151:407 – 415, 2017.
2. Lee et al, Comput. Methods Biomech. Biomed. Engin., 16:1143–1149, 2013.

Acknowledgements

This work was supported by a grant (MBRU-AlMahmeed Collaborative Research Award 2019) from Mohammed Bin Rashid University of Medicine and Health Sciences (MBRU).

CORRELATION BETWEEN CONDENSING FORCE AND LATERAL STABILITY OF SCREWS

Ainara Irastorza-Landa, Sara Lehmann, Amal Saade, Peter Heuberger

Nobel Biocare Services AG, 8302 Kloten, Switzerland

Introduction

Dental implants are essentially screws which are inserted into the pre-drilled bone to replace the root of a natural tooth. Their design, i.e. shape, together with the characteristics of the threads, grooves, surfaces and/or cutting elements determine their condensing, frictional or cutting capabilities. The combination of these three parameters has a significant influence on the insertion mechanism and their mechanical stability [1]. The aim of this in vitro study is to evaluate the correlation between the lateral stability and the insertion torque as well as the condensing properties of 11 different regular screws and screw taps, which serve as simplified prototypes of dental implants.

Methods

Eight screw designs and three screw taps (Table 1) were tested in bone surrogates (solid rigid foam, 20pcf, SAWBONES®) prepared with a Ø3.2mm pre-drilled hole (based on specifications according to M4 screws).

Screw / Screw Tap	Article number	BN/FN number	Supplier
M4 stainless	291546	FN389	SFS
M4 blue galvanized	283817	N/A	SFS
Screw Tap	264210.0200	N/A	Futuro
High Performance Screw Tap	264340.0200	N/A	Futuro
Combined Screw Tap	264485.0200	N/A	Futuro
Wood	1337467	BN5948	Bossard
Forming zinc 1	2098482	BN14066	Bossard
Forming zinc 2	1373323	BN990	Bossard
Trilobular stainless	3061378	BN13278	Bossard
Trilobular zinc	1540696	BN3327	Bossard
Thread Cutting zinc	1381415	BN1015	Bossard

Table 1: Overview of the tested screws and screw taps

Three types of measurement were done with three samples per screw group and per method:

1) Torque: screw/screw taps were inserted at 40 rpm to 11.5mm into rectangular bone surrogates and the insertion torque was measured with a K6D40 six-component sensor (ME-Meßsysteme GmbH, DE).
2) Condensing Force: screws/screw taps were manually inserted to 11.5mm into previously halved bone surrogate plates. The plates were hold together with 10N preload. The condensing force, i.e. lateral force while inserting the screw, was measured with a 500N sensor dose in a Zwick machine (Zwick GmbH & Co.KG, DE).
3) Stiffness: samples from the torque measurement were laterally loaded in the same Zwick machine at the speed of 5 mm/min. The lateral stiffness was calculated by fitting the stability plots (force vs. displacement) in the load range of 10 to 15N, and normalized by the lever arm.

Results

The highest torque levels were obtained for the M4 screws, whereas the screw taps achieved the lowest (Figure 1A). Similarly, M4 screws had the highest condensing force, the screw taps had the lowest, and the other screws laid in between them. Due to their poor fixation, the screw taps could not be tested for lateral stability and the M4 screws showed the highest stability. While no correlation was found between stiffness and torque (R^2=0.14, Figure 1B), the correlation between the stiffness and condensing force was remarkable (R^2=0.79, Figure 1C).

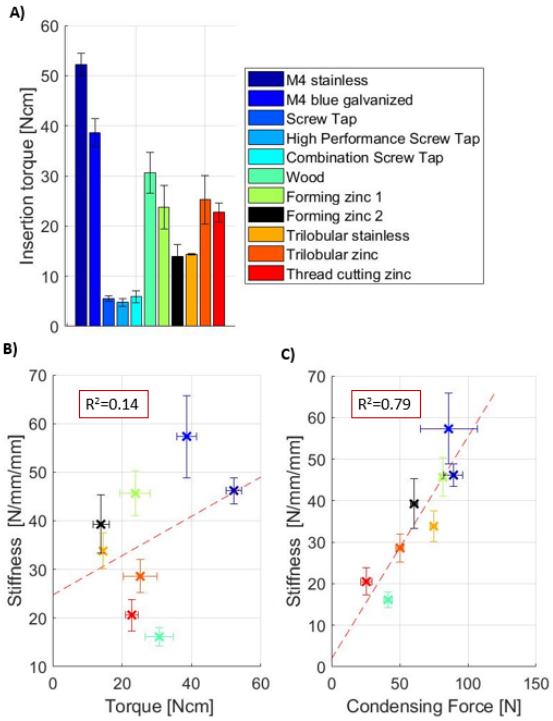

Figure 1: A) Insertion Torques of the tested screw/screw tap, B) Stiffness versus Torque, C) Stiffness versus condensing force

Discussion

These results suggest that there may be an association between stability and the condensing force that the screws exert while they are inserted. Further studies shall be performed to evaluate if this parameter could be used to predict stability depending on different design features, and investigate the application of this method in the dental implant field.

References

1. Li et al, J Mech Behav Biomed Mater, 103:103574, 2020.

IN VITRO COMPARISON OF SITE PREPARATION PARAMETERS IN RESPECT TO DENTAL ANCHORAGE AND PRIMARY STABILITY

J. Fabech (1), S. Ruch (1), A. Saade (2), P. Heuberger (2), A. Irastorza-Landa (2)

1. Zürcher Hochschule für Angewandte Wissenschaften (ZHAW), 8401 Winterthur, Switzerland;
2. Nobel Biocare Services AG, 8302 Kloten, Switzerland

Introduction

Achieving high dental implant anchorage to ensure primary stability is crucial in immediate loading protocols. However, only functional loading of the implant shows if anchorage is sufficient to ensure primary stability. Clinicians can influence stability based on the implant site preparation protocol [1]. This study evaluated the in vitro anchorage and primary stability performance of one implant design on different site preparation configurations with a biomechanical dynamic test model capable of measuring the micro movement of the dental system in bone surrogate.

Methods

One machined implant with NobelActive NP 3.5x13mm shape was welded to a load transmission hemisphere forming a rigid body (Fig.1.1) and manually inserted into bone-surrogate material 0.5 mm above bone level (solid rigid foam, 20pcf - 0.32 g/cc, SAWBONES). Sites were prepared using clinical drills with various final diameters (⌀ 2.0, 2.4/2.8, 2.8/3.2 mm) and different tip gaps (TGs), i.e. distance between the implant tip and the deepest point of the osteotomy (Fig 1.2-1.3). A TG of ~0.5mm is recommended in the manufacturer's instruction for use. Anchorage was characterized by the insertion torque (IT) and primary stability was measured using a dynamic loading test setup with two sensor units measuring movement perpendicular to (Y) and in the direction of the implant axis (Z) [1]. The test setup was based on ISO 14801 [2] with the force (F) direction at a 30° angle to the implant axis. All tests were performed by applying 50'000 cycles of sinusoidal (2 Hz), compressive load (12-120N) with a lever arm of 8 mm at 20±2 °C. The two main components Migration (MIG) and Micromotion (MM) of the movement (Fig. 1.2) were measured. The same implant was reused in all tests after cleaning the surface with ethanol.

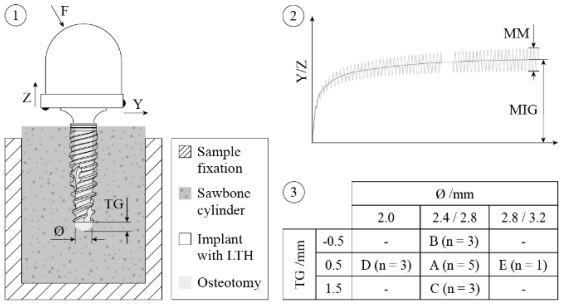

TG /mm	Ø /mm: 2.0	2.4 / 2.8	2.8 / 3.2
-0.5	-	B (n = 3)	-
0.5	D (n = 3)	A (n = 5)	E (n = 1)
1.5	-	C (n = 3)	-

Figure 1: 1. Sample sketch; 2. Measurement principle; 3. Parameter combinations & amount of repetitions (n)

The statistical analysis was done on Minitab 17 (Mann–Whitney U or Kruskal–Wallis test, α=0.05).

Results

Main effects plot for IT showed higher impact of drill diameter than of TG (Table 1): the smaller the osteotomy, the higher the IT (p=0.041, Groups A/D/E). TG variation had a lower but still significant effect (p=0.043, Groups A/B/C), particularly when the drilled depth was less than the implant length (Group B).
When loading, Group E, drilled with widest ⌀, showed unstable behavior resulting in high MIG values from the beginning. All other tests were considered stable.
Among the stable groups (A to D), main effects plot for MIG-Y&Z showed that TG has a higher effect than ⌀. When the osteotomy was prepared 1 mm deeper than recommended (Group C vs. A), MIG-Y and MIG-Z were 85% and 115% higher respectively (both p=0.0369), despite having similar IT (p=0.551). On the other hand, undersized Group D showed comparable MIG values (p=0.0369 for MIG-Y, p=0.7656 for MIG-Z) in comparison to reference Group A, even if average IT was 53% significantly higher (p=0.0369).

Table 1: Results (average±STD) at 0.32 g/cc; 12-120 N

Group	IT /Ncm	MIG-Y /µm	MIG-Z /µm
A	35.5 ± 1.2	74 ± 2	32 ± 3
B	39.0 ± 1.2	49 ± 3	22 ± 2
C	35.0 ± 0.4	137 ± 19	69 ± 6
D	54.5 ± 1.1	70 ± 2	31 ± 3
E	15.2	N.A.*	N.A.*

**Sample unstable, abortion limit >1 mm reached*

Discussion

Following the described sample preparation and loading conditions, the measurement device had the capacity to evaluate the influence of site preparation on the stability of the tested implant design. While it is well established that the osteotomy diameter has a direct effect on IT, the results of this in vitro study suggests that IT may not be an absolute predictor of stability. Increasing tip gap may have negligible effect on IT but may still jeopardize stability. Thus, controlled implant site preparation to guarantee implant anchorage may be crucial. These in vitro findings should be clinically evaluated.

References

1. Romanos et al. J Periodontal., 90(11):1320-132, 2019
2. A. Irastorza-Landa et al. Talk at 13th BSSM conference, UK (2018) www.bssm.org/2018abstracts
3. ISO 14801:2018

Acknowledgements

Funding of Nobel Biocare Services AG (Biomechanics - R18004) is gratefully acknowledged.

BIOMECHANICAL BEHAVIOR OF A TREATED MOLAR WITH CARIOUS TISSUE UNDER RESTORATION: SELECTIVE CARIES REMOVAL

Dominique Weimann (1), Anneke Morgenthal (1), Falk Schwendicke (2), Claudia Fleck (1), Hajar Razi (1)

1. *Materials Science and Engineering, Technische Universität Berlin, Germany; 2. Department of Oral Diagnostics, Digital Health and Health Services Research , Charité - Universitätsmedizin, Germany*

Abstract

Introduction. Selective caries removal (SCR) is a minimally invasive treatment for managing deeply cavitated caries lesions. During this treatment, carious tissue is removed in the periphery of the cavity, while soft dentin is left in proximity of the pulp to reduce the risk of pulp exposure and related complications such as pulp inflammation and necrosis [1]. Sealing of the residual carious tissue beneath a subsequently placed restoration deprives bacteria of nutrition so that they become inactive [1]. However, carious dentin is less mineralized and therefore less stiff than healthy dentin. This may possibly compromise restoration and tooth stability as compared to the conventional approach of "full" removal of any carious dentin (non-selective caries removal, NCR) [1].

To investigate the clinical efficiency of SCR over NCR, we compared the biomechanical behavior of a molar with SCR with an NCR treated molar by finite element modelling (FEM). Specifically, we focused on the possibility of localized stress concentrations at the interface between restoration and lesion. We further investigated the influence of different anatomical lesion sites (i.e. occlusal vs. proximal) and different lesion sizes.

Methods. We developed several 3D finite element models (Fig. 1), based on µ-CT data of a healthy permanent human third molar. Tooth models with restoration either on the occlusal or on the proximal surface were developed, where carious residual lesions with different sizes were left or fully removed, and the cavities were restored with resin composite restoration. All models were analyzed in comparison with an FE model of a healthy, non-treated molar. A vertical load of 100 N was applied onto the occlusal surface.

Results and discussion. Regardless of the lesion size, in molars with occlusal lesions, higher mean stresses were predicted along the filling-lesion interface than in all other models. In occlusal models, the smallest lesion (1 mm) induced the highest maximum stresses at the filling-lesion interface with stress peaks inside the filling (Fig. 2a). In contrast, in molar with 3 mm lesion showed one single maximum peak as expected for a typical bending configuration. We further showed using a parametric 2D model that these stress peaks are dependent on the relative size of lesion to filling (Fig. 2b) and the stress state is analogous to the presence of structural inhomogeneities within a material [2]. In conclusion, the lesion site and size are parameters affecting the filling-lesion interactions and thus the biomechanical behavior of the teeth after SCR vs. NCR.

Significance. Retaining carious lesions around the pulpal floor affects the biomechanical behaviour of the tooth-filling complex. The higher stresses in molars with occlusal lesions may affect restoration stability and longevity. Surprisingly, more extended occlusal lesions may provide a more favorable tooth performance than less extended ones.

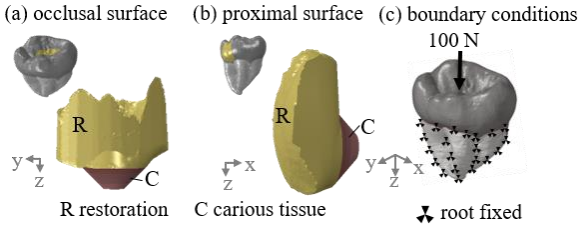

Figure 1: 3D FE models of an upper third human molar: Longitudinal sections with the composite filling and the carious carious lesion location on (a) occlusal and (b) proximal surfaces. Model boundary conditions (c).

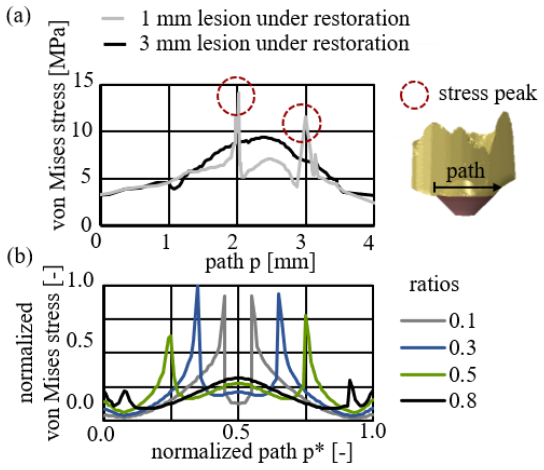

Figure 2: (a) Von Mises stress values within the filling along path p at the interface between filling and lesion. (b) Influence of the relative lesion to filling ratios on the stress distribution within the filling.

References

1. Thompson et al, J Am Dent Ass 139:705–12, 2008.
2. Weimann et al, Dent Mat 1:14,2021.

THE EFFECTS ON TEMPORO-MANDIBULAR JOINT CAUSED BY ORTHODONTIC INTER ARCH ELASTICS: A FINITE ELEMENT STUDY

Yaqiu Zhang, Ludger Keilig, Istabrak Dörsam, Christoph Bourauel

Oral Technology, University of Bonn, Germany

Introduction

Temporo-mandibular joint disorder (TMD) is a cranio-facial disease caused by the combination of diverse etiologies, such as joint structure, occlusion, dysfunction of muscle and mental factors. It mainly performances as clicking of the joint, abnormal movement of the mandible and limitation of mouth opening. TMD often happens with malocclusion, and it is also reported that TMD followed after orthodontic treatment in some cases. Inter arch elastics are a common way to apply forces during orthodontic treatment, and it causes mechanical effects on the temporo-mandibular joint (TMJ). It is expected that some adapted remodelling develops to coordinate the relation of maxilla and mandible and the respective teeth. The aim of this study was to analyse whether variations of inter arch elastics would develop harmful effects on healthy TMJ.

Method

A TMJ model with masticatory system based on Hill type actuators was established [1, 2]. The finite element model (see figures 1 and 2) is based on subjects with individual normal occlusion without temporo-mandibular joint disorders and anonymised CT and MRI scans using Mimics and MSC.Marc/Mentat software packages. Mouth opening and clenching with and without orthodontic loading was simulated and von Mises stresses and maximum principle stresses on the disc and the displacements of the condyle and the articular disc were analysed.

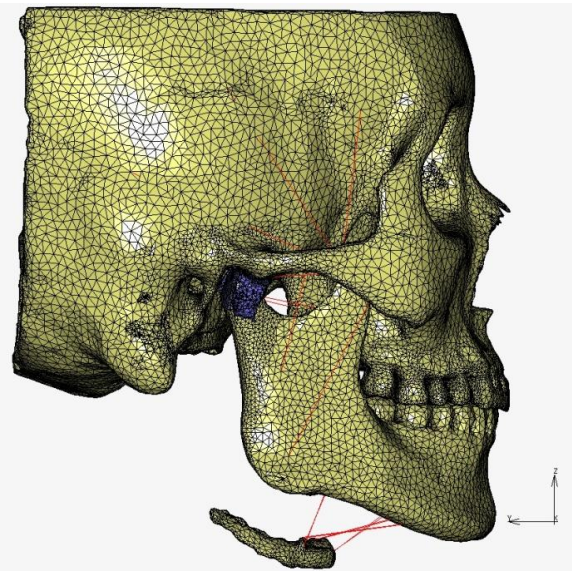

Figure 1: Left lateral view. The red lines indicate the direction of the passive muscle forces.

Results

Comparing the movement of the condyle before and after orthodontic force application, displacement of the condyle is more forward and downward with a clockwise rotation under application of class II long and short elastics, more backward and upward with counterclockwise rotation under class III long and short elastics, no apparent difference under vertical elastics, tend to the opposite side with larger anchorage under oblique elastics and tend to the side with orthodontic loading under interaction elastics.

	Von Mises Stress		Maxium Principle Stress	
	Left	Right	Left	Right
Before	1.46E-02 6.72E+00	5.08E-02 4.32E+00	-2.32E+00 4.77E+00	-3.34E+00 3.70E+00
Class II	1.89E-02 6.88E+00	4.71E-02 5.59E+00	-3.26E+00 5.63E+00	-3.82E+00 3.19E+00
Class III	2.37E-02 3.78E+00	5.19E-02 3.99E+00	-3.10E+00 4.54E+00	-2.49E+00 4.49E+00

Table 1: The stress on temporomandibular disc at the maximum opening position before and after orthodontic elastic application.

Discussion

In our study the stress on the surface of disc after orthodontic loading is in the normal biological range. Comparing with long distance elastics, the short elastics lead to more gentle stresses. It is better to choose short elastic for part of patients with TMD. Displacement of the condyle is beneficial to the corresponding orthodontic treatment.

References

[1] Hill, A.V. et al., Proc. Roy. Soc. B, 126:136-195, 1938.
[2] Van Ruijven, L. J. et al., Eur. J. Appl. Physiol, 61: 479–485, 1990.

Acknowledgements

This work was supported by a grant from China Scholarship Council.

INFLUENCE OF GEOMETRY VARIATIONS ON MICRO-MOTION AND GAP OPENING BETWEEN DENTAL IMPLANTS AND ABUTMENTS

Ludger Keilig (1,2), Martina Wylezalek (1), Helmut Stark (2) , Christoph Bourauel (1)

1. Oral Technology, Medical Faculty, University of Bonn, Germany; 2. Department of Prosthetic Dentistry, Preclinical Education and Materials Science, Medical Faculty, University of Bonn, Germany

Introduction

The interface between dental implants and abutments plays a crucial role in micro-motion and potential gap opening between the components during functional loading. Gaps opening between implant and abutment during loading might allow fluids and/or bacteria to leak into the inside of the implant/abutment complex. The influence of such effects on the long-term survival of implant-supported restorations is topic of several current papers [1,2,3].
It was the aim of our study to investigate and compare the influence of design principles in the geometry of the connection between implant and abutment on the mechanical stability and micro-mobility of the implant/abutment complex in a numerical study.

Methods

The models for this study were based on the CAD data of a commercial implant (7 mm length, 3.7 mm diameter). Several geometric properties of the existing internal connection, like internal and external diameters, wall thickness, play and insertion depth, were measured in the CAD data to be used as a basis for the following geometry variations. Then the existing internal connection was replaced by different customized connection designs. A total of eight connections, conical with 8° and 15° as well as flat, with varying length were modeled (see Fig. 1A), and four different index designs were chosen as rotation stops (see Fig. 1B). The fixation screw (taken from the original geometry) was preloaded with 200 N (representing a fixation torque of 30 Ncm) and locked in the loaded position. Then a functional load of 500 N was applied centrally on the abutment axis, 8 mm above the implant shoulders, angled in 30° to the implant axis. The outer surface of the implants was kept fixed.

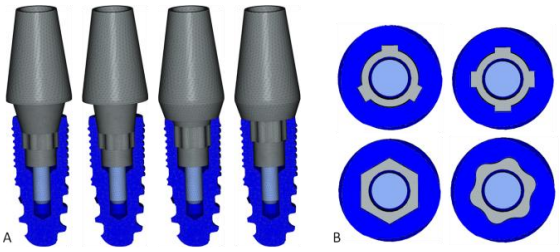

Figure 1: (A) Four of the investigated connector shapes; additionally to the shown variations the insertion depth was varied. (B) For each connector geometry four different index shapes were modeled as rotation stops.

Results

For all simulations, the following parameters were monitored: displacement and rotation of the abutment as measured at the point of force application, width of opening gaps, as well as visual inspection of the region of the implant neck. The choice between conical and flat abutment geometry showed a clearly distinct movement pattern, with an increased crown movement for the translation for conical compared to the flat connection (0.61 mm and 0.14 mm for the 'wave' index, Fig. 2). Opening of a wedge-shaped gap between implant and abutment could be observed on the outer surface of all models. The wide end of the wedge-shaped gap was located on the outer surface, with a mean width of 23 µm for all conical and 30 µm for all flat connections. The narrow end of the gap was almost closed for the conical connections, while a gap of 12 to 20 µm remained on this side for the flat connections. The shape of the index had almost no influence on the resulting movement.

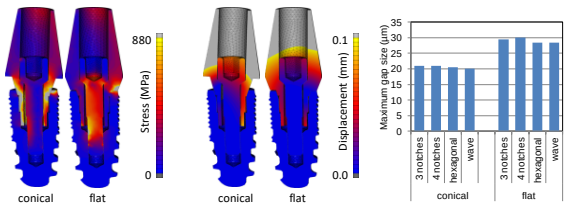

Figure 2: Stresses (left) and displacements (center) for a conical and a flat connection with a 'wave'-shaped index, and resulting gap sizes for all indices with this connection types (right).

Discussion

The design decision between conical and flat shapes had the highest influence on micro-mobility as well as on gap width. The presented method allowed investigating the shape of any opening gaps in a depth that was not possible with previous experimental in-vitro approaches. Further studies will also take the influence of the magnitude of the fixation torque into account.

References

1. Liu and Wang, Arch Oral Biol, 83:153-160, 2017.
2. Tallarico et al, J Prosthodont Res, 61:233–241, 2017.
3. Wachtel et al, J Oral Implantol 42:452–457, 2016.

EVALUATION OF PRIMARY STABILITY OF DENTAL IMPLANTS THROUGH DETERMINATION OF NEIGHBORING BONE DAMAGE

Setareh Khorshidparast (1), Pedram Akhlaghi (1), Hamidreza Barikani (2), Gholamreza Rouhi (1)

1. Amirkabir University of Technology, Iran 2. Dental Implant Research Center, Dentistry Research Institute, Tehran University of Medical Sciences, Tehran, Iran

Introduction

Dental implant primary stability (DIPS) is the initial engagement of an implant with its surrounding bone, which is a pure mechanical event [1]. DIPS can be evaluated through mechanical in-vitro tests, along with µ-CT imaging, by assessing alternation in the stiffness and ultimate load of the bone-implant structure (BIS). Through comparing the 3D µ-CT images before and after loading, derived by digital volume correlation (DVC) method, the displacement and strain field, and consequently damage in bone tissue can be quantified. The effect of damage in surrounding bone of a dental implant, and its impact on DIPS under intermittent compressive loading is not yet well understood. This study aimed at quantifying damages in bone tissue around the dental implant through applying cyclic compressive loading-unloading with an increasing amplitude, with ultimate goals of evaluation DIPS.

Methods

A trabecular bone sample was first extracted from proximal part of a bovine tibia, and the bone sample was embedded in PMMA, then a dental implant was inserted into it. Nine compressive loading-unloading cycles with an increasing amplitude, from 0.04 mm to 2.56 mm, were applied on the dental implant, according to ISO-14801 [2]. The loading step sequences, in the displacement control test with a displacement rate of 0.0024 mm/s, are as follow (in mm): 0.04 (S1), 0.08 (S2), 0.16 (S3), 0.32 (S4), 0.64 (S5) 0.96 (S6), 1.28 (S7), 1.92 (S8), and 2.56 (S9). In order to calculate the bone damages in bone surrounding the implant using DVC technique, µ-CT images were captured after each loading step. Moreover, the primary stability, for small deformations, was determined through comparing BIS's stiffness with its initial stiffness in each loading step, and for large deformations, it was made through measuring the ultimate force of the load-displacement curve. For DIPS evaluation, damage (D) parameter, which is correlated directly with the stiffness of BIS, can be found using (Eq. 1) [3]:

$$D = 1 - (S_C/S_I) \quad (1)$$

where S_C is the stiffness of the structure in current loading step and S_I is the initial stiffness of the structure.

Results

The experimental results showed that the ultimate force of BIS, i.e., 164 N, occurred approximately for the displacement of 0.96 mm, i.e., step #6 of loading (S6), and the DIPS that can be estimated by the magnitude of damage parameter, which is related to the BIS stiffness, reduced by 0.4, compared with its initial value. The values of damage parameter, which correspond to DIPS alternations for the steps which damage parameter are significant, are reported in Table 1. The difference between the maximum Tresca equivalent plastic strains, between S4 and S5, and between S5 and S6, were found to be 1.6% and 3%, respectively, which were found through comparing the µ-CT images, by using DVC technique (Fig. 1).

Displacement amplitude (mm)	0.64 (S5)	0.96 (S6)	1.28 (S7)	1.92 (S8)	2.56 (S9)
Damage parameter (D)	0.21	0.4	0.52	0.53	0.68

Table 1: Magnitude of damage parameter (D), for different displacements applied to the dental bone-implant construct in mechanical tests for S5 to S9, which correlates with the dental implant primary stability.

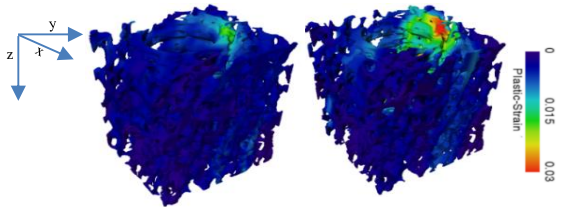

Figure 1: Tresca equivalent plastic strain distribution in neighbouring bone of the dental implant, resulted from DVC analysis between µ-CT images of: (a) S4 and S5; (b) S5 and S6 loading steps. The plastic strain correlates with the damage in bone tissue around the implant. Loading direction is aligned with y axis.

Discussion

In this study, based on the distribution of plastic strain, the damage in peri-implant bone the dental implant, caused by compressive loading-unloading cycles with an increasing amplitude, was quantified. The results showed that by increasing the damage in bone around the implant, primary stability reduces. The results of this work can be employed in design optimization of dental implants.

References

1. A. Tabassum, and et al., J Clinical Oral Implants Research, 25: 487–492, 2014.
2. B. Voumard, et al., J Mech Beh of Biomed Mat, 92: 24-32, 2019.

Acknowledgements

The authors appreciate Amirkabir University of Technology, and Dr. Phillipe Zysset from the University of Bern.

INVESTIGATION ON PRIMARY STABILITY OF DENTAL IMPLANTS IN LOADING-UNLOADONG TEST: A MICRO FINITE ELEMENT STUDY

Pedram Akhlaghi (1), Setareh Khorshidparast (1), Gholamreza Rouhi (1)

1. Amirkabir University of Technology, Iran

Introduction

Primary stability (PS) is the ability of a dental implant to sustain loads without excessive motion. Implant insertion and subsequent loading can induce some damages to the adjacent bone, which may lead to a reduction in PS. Several studies have investigated the effects of induced bone damage due to implantation, however the effects of peri-implant bone damage on PS in large deformation has not yet well understood. Accordingly, this study aimed at developing a validated micro finite element (μFE) model to assess primary stability of a dental implant, subjected to cyclic compressive loading-unloading, in term of overall stiffness of bone-implant construct, as well as peri-implant bone damage.

Method

A cylindrical spongy bone sample was core drilled from a bovine proximal tibia, and a dental implant was inserted into it. Quasi-static compressive loading-unloading mechanical test was conducted with increasing displacement amplitudes, ranging from 0.04 to 1.28mm, to find the stiffness of the bone-implant construct, according to [1]. Prior to mechanical testing, bony sample was scanned using μCT device with a resolution of 40μm. The bone-implant assembly was created through the segmented images of the bone and implant CAD geometry. Then, μFE model was generated by meshing the bone and implant with linear tetrahedral elements. Loading condition was defined according to the in-vitro test, with displacement amplitudes ranging from 0.04 to 0.64mm. The material behavior of trabecular bone was modeled based on a developed constitutive model by Ovesy et al. [2], which can mimic the failure response of trabecular bone under large deformation using nonlinear μFE. In the μFE simulation, an element got deleted as it reached to its threshold value of 24% in the plastic strain Stiffness degradation, as a result of bone damage, was modeled using element deletion technique. The value of 1-D, where D is the damage constant [3], was calculated as the ratio of the current stiffness of the bone-implant construct to the initial one. By considering the failure response of the peri-implant bone at the tissue level, a micro finite element model was developed and has been validated to explore the primary stability of dental implant for large deformations.

Results

The results showed that the μFE model can qualitatively capture the trend of the observed damage behavior from in-vitro test (Fig 1). Moreover, plastic strain distribution showed that the trabecular bone failure not only occurs in directly connected trabeculae to the implant surface, but also it can emerge in other areas which do not have direct connection with the implant's surface (Fig. 2).

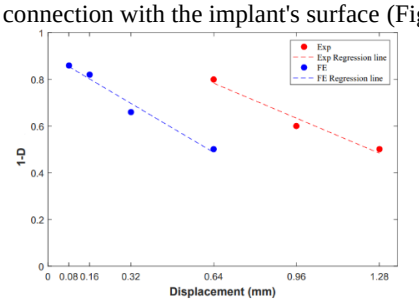

Figure 1: Relation between 1-D, where D is the damage parameter [3], and applied displacement on implant. In-vitro test (red), and μFE model (blue).

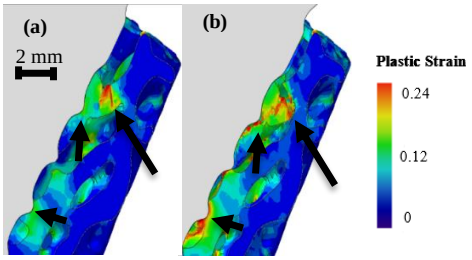

Figure 2: Plastic strain distribution in bone, due to applied displacement of: (a) 0.32, and (b) 0.64 mm to the implant. Black arrows illustrate damaged regions.

Discussion

The earlier occurrence of stiffness degradation in μFE model than the one observed in in-vitro test can be due to the employment of element deletion technique in this study. However, in in-vitro condition, the presence of broken pieces of bone, generated during implant insertion, also caused by loading after the insertion, make the structure tougher and postpone the stiffness reduction. This work can help evaluate the positive and negative aspects of different dental implant design features on the primary stability.

References

1. Voumard et al, J Mech Behav Biomed Mater, 92:24-32, 2019.
2. Ovesy et al, J Mech Behav Biomed Mater, 98:301-310, 2019.
3. Ovesy et al, Biomech. Model. Mechanobiol, 17.5:1471-1480, 2018.

Acknowledgement

The authors appreciate Amirkabir University of Technology, and Dr. Phillipe Zysset from the University of Bern.

WEAR ANALYSIS OF DIFFERENT MONOLITHIC CERAMIC MATERIALS AGAINST NATURAL TEETH

Ahmed Fouda (1, 2), Christoph Bourauel (1)

1. Oral Technology, University Hospital Bonn, Germany;
2. Department of Fixed Prosthodontics, Suez Canal University, Egypt;

Introduction

Zirconium oxide-based ceramics were introduced as metal free restorations with high flexural strength to overcome the drawbacks of the weaker glass ceramics [1]. Monolithic zirconia restorations have become a very promising alternative to glass ceramics, however, still need further investigations concerning their clinical performance [2]. The aim of this in vitro study was to evaluate and compare the wear and surface roughness of translucent cubic monolithic zirconia to glass ceramics and zirconia reinforced glass ceramics as well as the wear of opposing natural teeth.

Methods

Fifty ceramic discs were cut and grouped into 5 groups according to the material: Group 1: partially crystallised lithium disilicate (Emax CAD), Group 2: fully crystallised lithium disilicate (LiSi CAD), Group 3: zirconia reinforced lithium silicate (Celtra Duo), Group 4: super translucent zirconia (STML), Group 5: ultra-translucent zirconia (UTML). All the samples were finished according to the manufacturers' recommendations. Ceramic weights and surface roughness values (sRa) using the FRT MicroSpy of the discs were recorded before subjected to the wear test. All discs were subjected to 200.000 wear cycles against the buccal cusp of a natural premolar at a 20 N vertical force using a self-developed wear testing device. The teeth were scanned using a µCT scanner (Skyscan 1174) before and after the wear tests. Images were overlapped to determine the volumetric tooth loss (Figure 1).

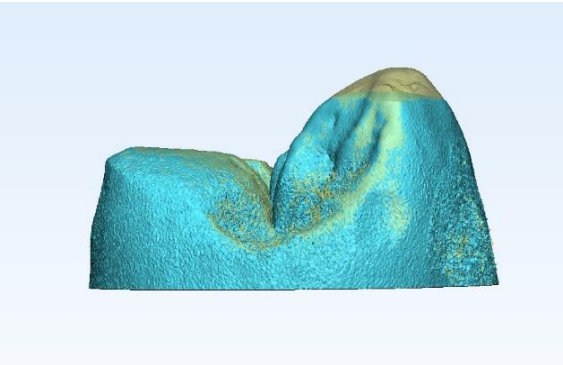

Figure 1: Matching and overlapping of the two µCT-scanned crowns (before and after the wear cycles) using 3-matic software.

Results

The weight difference for the ceramic samples (g) showed material weight loss for the LiSi (0.0026 ± 0.0002), while the UTML showed only (0.00014 ± 0.0001). Regarding the surface roughness measures (sRa in µm), the LiSi showed an average difference (2.00 ± 0.61) after 100,000 wear cycles and (1.7 ± 1.2) after 200,000 cycles, while UTML showed (0.34 ± 0.2) after 200,000 cycles. The measurement of the volumetric enamel loss (mm^3) for the LiSi was (0.41 ± 0.1, Figure 2) while for UTML was (0.16 ± 0.05).

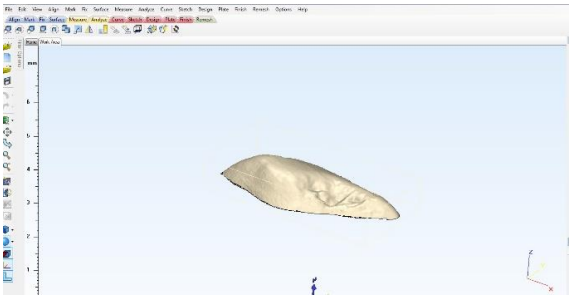

Figure 2: Visualisation of the subtraction of the worn enamel for calculation of the volumetric enamel loss.

Discussion

The wear behaviour of glass ceramics has always been discussed controversially. Some in vitro studies revealed that glass ceramic material may provide wear characteristics similar to those for enamel, while other clinical investigations of inlays showed significantly higher values for enamel wear in the antagonists [3]. Currently, the results of this study indicate that the new fully crystallised lithium disilicate (LiSi) materials can cause a degree of wear to the opposing natural dentition. Further material combinations are currently under investigation and will be finished prior to the meeting. The study involves new materials that were not tested before and the initial results are very promising.

References

1. Elie E. Daou, Open Dent J., 8: 33–42, 2014.
2. Kontonasaki E et al., Dent J (Basel), 7. pii: E90, 2019.
3. Krämer N et al, J. Dent. Res, 85:1097–100, 2006.

Acknowledgements

This work was supported by grant from the Egyptian Ministry of Higher Education, Missions Department.

IN VITRO IMPACT TESTING OF DENTAL PROSTHESIS: INFLUENCE OF CEMENT AND ABUTMENTS GEOMETRY ON RETRIEVABILITY

Andrea T. Lugas (1), Mara Terzini (1), Elisabetta M. Zanetti (2), Gianmario Schierano (3), Carlo Manzella(3), Domenico Baldi (4), Cristina Bignardi (1), Alberto L. Audenino (1)

1. PolitoBIOMed Lab, Department of Mechanical and Aerospace Engineering, Polytechnic University of Turin, Italy; 2. Department of Industrial Engineering, University of Perugia, Italy; 3. Department of Surgical Science, c.i.r. Dental School, University of Turin, Italy; 4. Division of Prosthetic Dentistry, Department of Surgical Sciences (DISC), University of Genoa, Italy

Introduction

Implant-fixed dental prosthetic reconstruction is an established treatment for edentulous patients. The prostheses can be screw- or cement-retained, and nowadays, there is no evidence of the superiority of one technique over the other [1]. Nonetheless, in some cases, the choice is forced by the patient's conditions, and a screw- or cement-retention might be needed. However, one of the main features of an implant-supported prosthesis is retrievability, which could be necessary in the case of implant complications. Ideally, the cementation should be strong enough to bear masticatory loads avoiding cement failure, and weak enough to allow easy and safe removal in case of need [2]. In this study, the retrievability of implant-fixed dental prostheses was investigated considering two of the main factors faced by dental practitioners: the abutments geometry and the luting agent.

Methods

During this study, cobalt-chrome copings were cemented on titanium abutments of different height (5 mm, 7 mm, 9 mm) and taper (0°, 2°, 4°) using three different types of luting agent (Harvard Cement, Telio CS Link, and Temp Bond). Each abutment was screwed on an implant which was in turn screwed to a piezoelectric load cell before each test. Impact stresses were performed on both single and multiple implant-supported restorations (referred to as bridges in the following) by means of different removal devices (i.e. Coronaflex and Magnetic Mallet). Up to 60 impulses were performed on both single implants and bridges until cement failure. Copings not removed within 60 impulses were considered non retrievable. The number of impulses required for removal, as well as the force trend over time during the tests, were recorded and used to compute the two indexes used for retrievability and stability evaluation: the percentage of copings removed within a determined range of impulses and the average force delivered on the implant. A Kruskal-Wallis test with Bonferroni post hoc correction was performed to investigate the statistical significance of the aforementioned factors on copings retrievability.

Results

Abutment's geometry showed a statistically significant influence on the number of impulses required for the removal of both single implant-supported prostheses and bridges (p<0.05), while the luting agent showed a less obvious evidence on impulses number. Force values were significantly influenced by cement type (p<0.05) during the test on bridges. However, the measured force resulted to be a less powerful index of retrievability compared to impulses number. Figure 1 shows the coping retrievability during tests on single implants. The codes in the abscissa axis describe the cement (H: Harvard Cement, T: Telio CS Link, and TB: Temp Bond), the height and the taper angle of the abutment.

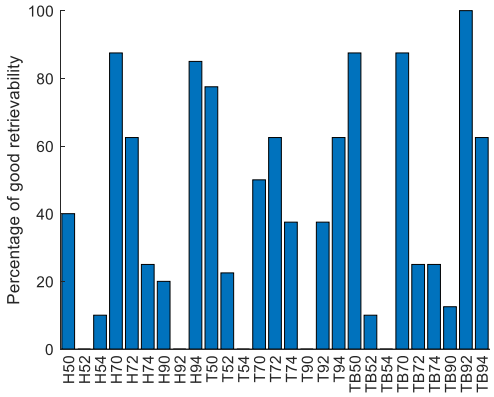

Figure 1: Percentage of good retrievability for each abutment geometry-luting agent combination.

Similar results were obtained on multiple implants supported prostheses; the bridges cemented on higher and less tapered abutments required more impulses for complete removal.

Discussion

Most of the literature data on dental prostheses retrievability is obtained through uniaxial tensile test [3]. In this study, a more clinical-like setup was exploited, obtaining comparable results regarding the relation between abutments geometry and luting agents and coping retention. The best compromise for stability and retrievability resulted to be a combination of a long, slightly tapered abutment and a temporary cement. Moreover, when dealing with impulsive stresses, the number of impulses seems to be a more reliable index, compared to the measured force.

References

1. Vigolo et al, Int. J. Oral Maxillofac. Implant, 19:260–265, 2004.
2. Breeding et al, J. Prosthet. Dent., 68:737–741, 1992.
3. Bresciano et al, Clin. Oral. Implant. Res., 16: 594-598, 2005.

MULTI-SCALE PATIENT-SPECIFIC MODELING OF THE HUMAN CORNEA

Chloe Giraudet (1,2), Patrick Le Tallec (1,2), Jean-Marc Allain (1,2)

1. LMS, CNRS, Ecole Polytechnique, Institut Polytechnique de Paris, Palaiseau, France
2. Inria, Palaiseau, France

Introduction

About 50% of the world's population will be short-sighted by 2050 [1], particularly because of the evolution of our lifestyle which increasingly exposes our eyes to artificial and screen lights on a daily basis. Laser surgery then appears as a powerful tool to help tackle this public health issue.
However, there are still gaps in the understanding of the effects of surgery on the eye so far. Indeed, during surgical interventions, the specific organization of collagen fibres is compromised by the laser and the associated effects on the mechanical behaviour of the cornea and vision recovery are not easily anticipated [2]. In addition, inter- and intra-patient variability further complicate the picture [3].

Methods

In order to better predict the effects of laser surgery on the cornea, a patient-specific model is built and implemented in a homemade finite element calculation code (MoReFEM).
Patient-specific geometry of the cornea is extracted from clinical Optical Coherence Tomography (OCT) images to construct the mesh (see figure 1). Collagen fiber images (X-rays [4] or Second Harmonic Generation microscopy [5]) are used to extract micro-structural data: the orientation of the collagen fibers. These experimental orientations are then introduced in the mechanical model of the cornea: the collagen fibers are introduced in a microsphere description of the medium and are mechanically characterized described by their 1D elastic response, while the non-collageneous components are described by a quasi-incompressible hyperelastic model. The model parameters are then identified through experimental inflation tests. Finally, the optical power is calculated for assessing the cornea ability to converge light rays in the eye, and thus ensuring its proper functioning.

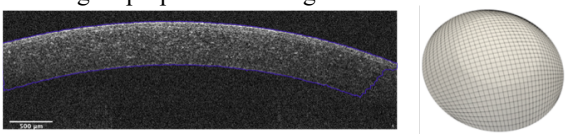

Figure 1: Left :2D – clinical OCT image of a patient cornea. Bar = 500µm. Right: Patient-specific mesh of the cornea, obtained through the OCT image.

Results

Inflation tests are done on healthy corneas and deformation fields are obtained from OCT images (see figure 2) thanks to Digital Image Correlation. Such displacements can be used to identify the numerical model parameters. The model can then be used to predict the response to cornea either to a modification of the microstructure or to pathological change of the intra-ocular pressure.

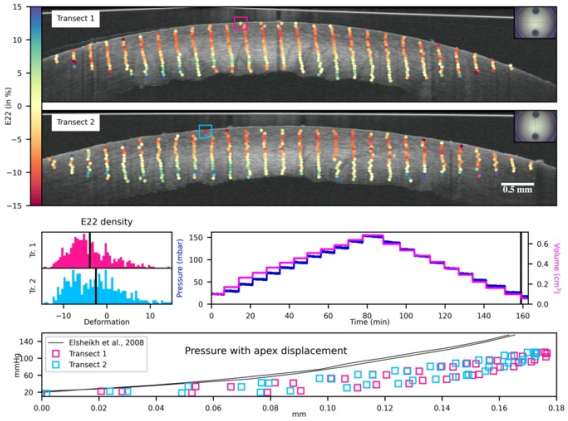

Figure 2: Up - 2D vertical deformation field in a human cornea under inflation between two different pressures steps. Bar = 500µm. Middle – Density of deformation and pressure/volume steps with time. Bottom – comparison of the apex displacement with experiment of Elsheikh's group [3].

Discussion

Today, most models are identified through the motion of the cornea apex, which is very sensitive to the quality of the boundary condition in inflation experiments. We provide a new approach using optical tomography to observe displacement fields during inflation tests. Thus, the numerical model will be better calibrated thanks to more accurate information.

References

1. Holden et al, Ophthalmology, 124:1036-1042, 2017.
2. Alastrué et al, J. Biomec. Eng., 128:150-160, 2006.
3. Elsheikh et al, Exp. Eye Res., 86:783-790, 2008.
4. Aghamohammadzadeh et al, Struct., 12: 249-256, 2004.
5. Benoit et al, J. Mec. Beh. Biomed. Mat., 60: 93-105, 2016.

Acknowledgements

We thank Mrs Pandolfi for providing the mesh.

INTRAOCULAR LENS INSERTION DURING CATARACT SURGERY

I. Cabeza (1), I. Ríos-Ruiz (1), J. Frechilla (1), B. Calvo (1,2)

1. Aragon Institute of Engineering Research (I3A), University of Zaragoza, Spain.

2. Centro de Investigación Biomédica en Red en Bioingeniería, Biomateriales y Nanomedicina (CIBER-BBN), Spain.

Introduction

Recently, small-incision cataract surgery has been developed because of the availability of innovative surgical instruments and intraocular lenses (IOLs) with advanced foldable materials. The injector has a significant meaning for the success of minimum incision cataract surgery. It has enabled a faster, more controlled, and consistent IOL insertion that reduces the risk for technical error associated with the surgery. For the syringe-type injectors, a certain degree of injection force is required, but a strong injection force might result in a higher difficulty in insertion control and an enhanced risk for IOL damage or injection-system. The resistance force for IOL insertion differs by injectors and IOL material[1]. The present study was designed to establish a numerical methodology to evaluate the resistance force of an IOL insertion system consisting of an IOL and a syringe-type injector during IOL surgery.

Methods

A FE model was developed based on commercial injector, Fig.1. Load and boundary conditions were set to replicate the experimental test. Abaqus/Explicit was used as a solver.

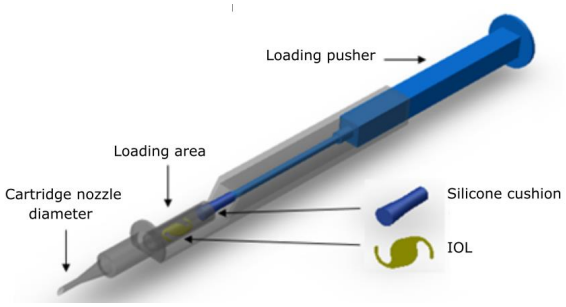

Figure 1: Syringe-type injector.

The critical features of the inserter are the plunger, the tip of the plunger, the loading area and the tip, as shown in Fig. 1. The IOL is placed in the loading area. Then, the IOL is pushed by the loading pusher through the cartridge nozzle diameter to the capsular bag. The IOL material and the silicone cushion have been fitted with a hyperelastic Ogden material model [2]. Whereas the injector has been considered as a rigid body. In use, the injector must remain relatively still while the surgeon pushes the loading pusher. The insertion velocity was chosen to be 4 mm/s, which is the fastest that would be performed in practice. The choice of the fastest delivery allows for a reduced step time and in turn less computational time. The friction of the contact applied was evaluated through a sensitivity analysis. A nonlinear pressure-overclosure relationship was used to reduce contact penetration.

Results

In a first step, the finite element model was able to calculate the force exerted in the injection of an IOL versus the displacement experienced by the loading pusher. This curve was compared accurately with experimental test data (Fig.2). The analysis yielded results that correlated well with the tests, which validated the simulations.

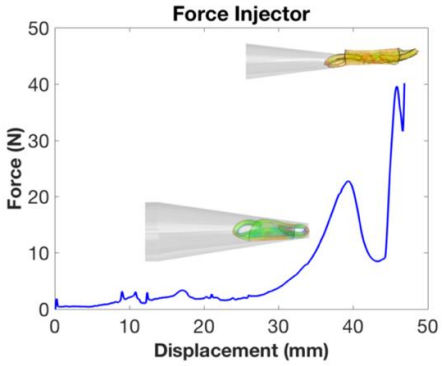

Figure 2: Experimental injection force register as the IOL is being pushed by the plunger.

In a second step, the critical features of the injector, the shape of the cartridge nozzle diameter, and the IOL material were analysed.

Discussion

The resistance force exerted by the IOL delivery system is given by the IOL and the deformable pusher. The validated FE model could be used to reduce the likelihood of failure modes. It also allows fast testing the next generation of IOLs and injectors with lower diameter incisions. Accelerating prototyping with realistic simulation provides tremendous bottom-line benefit.

References

1. Usui M and Tanaka T. J Cataract Refract Surg 2015; 41:1745–1751
2. Cabeza-Gil I et al, Ann Biomed Eng, 2020.

Acknowledgements

This work was supported by grant DPI2017-84047-R, PRE2018-084021 and DI-16-08888 from the the Spanish Ministry of Economy and Competitiveness.

ORGANIC NANOPARTICLES RESCUE VISION IN BLIND RETINAS

Guglielmo Lanzani (1,2)
1. Politecnico di Milano, Italy; 2. Istituto Italiano di Tecnologia, Italy;

Inherited retinal dystrophies and late-stage age-related macular degeneration, for which treatments remain limited, are among the most prevalent causes of legal blindness. Retinal prostheses have been developed to stimulate the inner retinal network; however, lack of sensitivity and resolution, and the need for wiring or external cameras, have limited their application. Here I report on the use of conjugated polymer nanoparticles (P3HT NPs), Figure 1, showing that they mediate light-evoked stimulation of retinal neurons and persistently rescue visual functions when subretinally injected in a rat model of retinitis pigmentosa. I will then discuss the Photophysics of the NPs and the open questions related on their functioning in vivo.

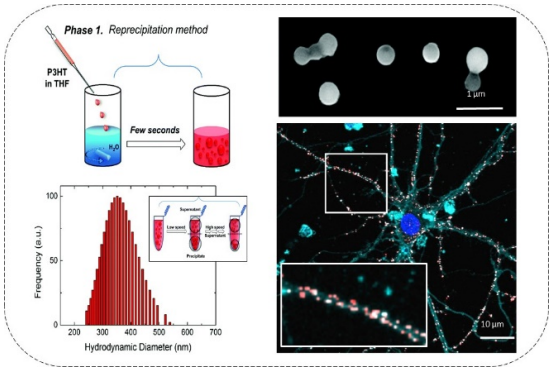

Figure 1: Left: Nanoparticles formed by nanoprecipitation adding water to the solution. Size distribution is shown below. Right: SEM nanoparticles pictures. Below a confocal image showing nanoparticles decorating the neuron membrane without getting internalized.

References

1. JF. Maya-Vetencourt et al. Nature Nanotechnology 15, 698-708, 2020

PATIENT-SPECIFIC BIOMECHANICAL MODELING OF HUMAN CORNEA: MICROSTRUCTURAL COLLAGEN DEGENERATION

Alessio Gizzi (1), Maria Laura De Bellis (2), Marcello Vasta (2), Anna Pandolfi (3)

1. University of Rome Campus Bio-Medico, Italy;
2. University of Chieti-Pescara, Italy; 3. Politecnico di Milano, Italy

Introduction

Under intraocular pressure, the cornea assumes a spherical shape by exploiting the spatial organization of the collagen network distributed in the stroma. To date, most of the numerical models of the cornea consider physiological conditions, including idealized continuum models based on anisotropic hyperelasticity or stochastic fiber distributions, patient-specific models, diagnostics, and surgery planning [1]. However, none of them has been developed with the ability to model the degenerative process leading to keratoconus. This particular pathology induces tissue thinning and geometry reshaping, hardly achievable through continuum models. We propose a multiphysics model of the collagen structure of the human cornea modeling the progressive localized reduction of the stiffness. The proposed structural model aims at identifying and predicting the development of keratoconus [2].

Methods

We model the collagen architecture based on micromechanical considerations characterized for the stroma through a simplified microstructural trusswork model. Our approach revisits the structural model of the orthogonally arranged collagen architecture of the stroma recently proposed [3], comprising two families of collagen fibers and associated fibrils. Transversal bonds supply mechanical stiffness within the fibrils of the same family (inter-crosslink bonds) and across the fibrils of the two families (intra-crosslink bonds). The representative unit cell is shown in Figure 1.

We assume that both fibrils and crosslinks' maximum and minimum stiffness correspond to the values obtained in the numerical simulations in [3]. Also, the stiffness of all truss elements is allowed to reduce according to an evolutive pathologic phenomenon,

$$\frac{\partial c}{\partial t} = D\nabla^2 c + Ac(1-c)(c-\alpha)$$

modeled as a normalized scalar field reaction-diffusion process. Here, the scalar field c represents a measure of the degeneration of the chemical bonds stabilizing the structural collagen; $D = 0.1\, mm^2/month$ is the diffusion coefficient tuned such that the resulting concentration wavefront will cover the entire surface of the cornea in fifty months; the bistable reaction term is characterized by two stable fixed points, $c = 0, 1$ and one unstable fixed point, $c = \alpha$.

Results

We present sequential quasi-static finite element analyses and associated trusswork model accounting to reduce the truss stiffness linked to the time evolution of the degradation field. Focusing on the pathology's initial stages, we identify the critical condition that corresponds to the formation of a marked conus. In particular, we can identify the loss of mechanical stability resulting in the bulging of keratoconus.

Discussion

We introduced a weakly coupled continuum-discrete model of the human cornea, modeling the time evolution of degenerative pathologies related to a loss of cohesion between collagen fibrils. A patient-specific continuum model is used to solve a reaction-diffusion problem via finite elements. The associated scalar field is linked to stiffness degeneration into the associated discrete trusswork model (representative of the structurally organized collagen). The effect of the degeneration field is to reduce selectively the stiffness of the structural components of the trusswork producing an effective predictive tool for the patho-physiology assessment of the human cornea.

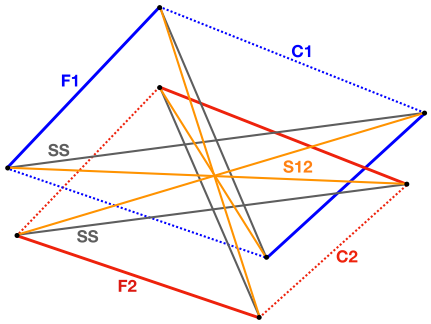

Figure 1: Structure of the unit cell: collagen fibrils F1-Fe (solid blue-red); in-plane orthogonal crosslinks C1-C2 (dashed blue-red); in-plane diagonal crosslinks SS (gray); out-of-plane diagonal crosslinks S12 (orange).

References

1. Pandolfi. Eye and Vision 7: 1-15, 2020.
2. Gizzi et al. J. Eng. Math. 2021 (In Press).
3. Pandolfi et al. Phil Trans Roy Soc A 377:20180079, 2019.

Acknowledgements

The Authors acknowledge the support of the Italian National Group of Mathematical Physics (GNFM-INdAM).

COMPUTATIONAL MODELS AND EXPERIMENTAL METHODS FOR THE HUMAN CORNEA

Anna Pandolfi (1), Federica Boschetti (1), Aram Cornaggia (2)

1. Politecnico di Milano, Italy; 2. Università degli studi di Bergamo, Italy

Introduction

Biomechanics introduces numerous numerical and experimental methods to support clinical practice in ophthalmology, with the goal of improving surgical outcomes and to develop new advanced technologies with minimum impact on clinical training. To achieve predictability is mandatory to account for all the phenomena that are of interest in the analysis and to include patient-specific features into the model.

Methods

Models of the human cornea are commonly employed to simulate refractive surgery, in order to anticipate the outcomes of interventions or to predict the long term behavior of damaging tissues. A numerical model is useful as long as it is able to capture the important physical characteristics of the system at the hand. If all the right physics are accounted for, the model will be able to predict the behavior under various conditions, although verified only through the comparison with a few particular experiments or theoretical developments. In years, we have developed an accurate model of the human cornea, accounting for patient-specific geometry and material properties, interaction between cornea and aqueous humor, anisotropy, and material degeneration.

Results

The cornea model can be used to estimate the change of corneal shape, refractive power, and stress distribution induced by laser ablation refractive surgery. Simulations aim at estimating the actual distribution of stress and strains within the cornea before and after the surgery, and at providing an indication of the increment of the engagement of the material, which is the main interest for a surgeon because in the long term it can lead to material instabilities, e.g., ectasia.

The model can be used to simulate the effects of crosslinking, a therapeutic procedure consisting in the reinforcement of the chemical bonds between collagen fibrils of the stroma, in terms of change of material stiffness on the anterior layers of the cornea.

The cornea model can also be used to simulate the quasi-static indentation with a probe, a tool derived from the contact tonometer that can be used to assess the stiffness of the cornea and to identify the constitutive properties of the material model.

Dynamic tests on the cornea, i.e., the air puff test, can be only modelled by using the model that includes the cornea and the anterior chamber filled with aqueous. The action of a contactless ocular tonometer, that uses a localized air jet to induce the oscillation of the cornea, can be modelled by applying an estimated pressure history on a small area of the central anterior cornea.

Discussion

Even though the numerical tool developed in our group is accurate and optimized, yet the biomechanical and optical behavior of a patient-specific cornea can be predicted by means of a simulation only when patient-specific geometry, material properties and IOP are known. Unfortunately, both patient-specific material properties and IOP require some important and demanding preliminary work to be correctly inserted into the model. The estimation of material properties and IOP can be done with techniques proper of inverse analysis.

The availability of in-vitro tests is fundamental to identify the material model, and this avenue has to be pursued in the preliminary characterization of the model. Nevertheless, to obtain the correct values of the material properties, the comparison between numerical predictions and experimental results must be based on in-vivo tests. The two most interesting tests are the ones that locally modify the shape of the cornea: the probe indentation tests and the dynamic contactless tonometer. While for the probe test no particular care has to be taken, since the test is very slow and conducted in quasi-static condition, the numerical model of the air puff test cannot disregard the presence of the fluid. As a matter of fact, an inverse analysis based on the air puff test conducted without fluid will overestimate the material properties of the cornea, leading to a completely unreliable model, not useful for clinical applications.

References

1. F. Boschetti et al. J. Biomech Eng, 134(3):031003, 2012
2. A. Pandolfi and F. Boschetti. Comp Methods Biomech & Biomed Eng, 18(1):64-77, 2015.
3. A. Montanino et al, ZAMM, 98:2122-2134, 2018.
4. A. Montanino et al. J Mech Behavior Biomed Mat, 94:22-31, 2019.
5. A. Pandolfi. Eye & Vision, 7:2, 2019.

Acknowledgements

These studies are based on previous research conducted in a long term collaboration with M. Angelillo, A. Gizzi, A. Montanino, and M. Vasta. We acknowledge here their contribution.

OPTIMIZED PROTOCOL FOR PULSED CORNEAL CROSSLINKING (CXL) AS A FUNCTION OF OXYGEN CONSUMPTION AND TIME

Malavika H. Nambiar (1), Maria A. Komninou (2), Theo G. Seiler (2), Beatrice E. Frueh (2), Philippe Büchler (1)

1. ARTORG Center for Biomedical Engineering Research, University of Bern, Switzerland;
2. Universitätsklinik für Augenheilkunde, Inselspital, University of Bern, Switzerland.

Introduction

Keratoconus (KC) is a pathology of the cornea characterized by weakening of the tissue biomechanical properties, which induces a progressive thinning of the cornea and poor vision. Since 2003, cross linking (CXL) is being used clinically to treat KC patients. This treatment has proven to be safe, to effectively increase corneal stiffness, and to prevent the progression of KC.
The CXL method uses ultraviolet light produced by a laser and a photosensitizer (riboflavin) to stiffen the cornea. The chemical reaction also requires enough O_2 to produce cross links. It is important to use the appropriate intensity of irradiance for a specific time to remain safe while producing as many crosslinks as possible. However, if the local concentration of O_2 drops during the laser treatment, no additional cross-links are generated.
Pulsed laser protocols have been proposed to limit this effect and allow oxygen to diffuse in between consecutive laser pulses. A deeper understanding of the amount of O_2 consumed by different laser irradiance and pulse duration is required to optimize the treatment procedure and maximize its stiffening effect.

Method

Experimental measurements were conducted on porcine corneas. The epithelium was removed, and the anterior cornea was exposed to a riboflavin solution. Experimental data was collected for different laser powers; 9mW, 18mW, and 30mW. During the experiment, the O_2 concentration was recorded at 200µm and 300µm depth from the anterior surface using an optical sensor (PreSens Precision Sensing GmbH). First measurements were performed with a constant irradiance. The laser was tuned on until the O_2 concentration reaches zero inside the cornea. At this time point, the laser was stopped and the O_2 re-diffusion in the tissue was recorded. In a second step, the O2 concentration in the cornea was recorded for a laser pulsing of 10s intervals.
A numerical model of the O_2 diffusion in the cornea was developed based on the experimental data collected using the constant laser irradiances. After its calibration, the model was used to determine the optimal pulse duration to maximize the number of cross-link per unit of time. The optimization loss function was defined as the amount of oxygen consumed by the laser during complete laser pulse (sum of the time of laser on and laser off). The numerical model was solved in 1D using MATLAB®.

Results

The model was able to reproduce the experimental data (fig. 1). When the laser is '*on*', higher laser powers increase the O_2 consumption rate. However, when the laser is turned '*off*', the O_2 re-diffusion is similar for the different irradiances. Consequently, the optimization resulted to the same time '*off*' across varying laser powers (8.5s) but a decreasing time '*on*' were identified for increasing irradiances (tab. 1).

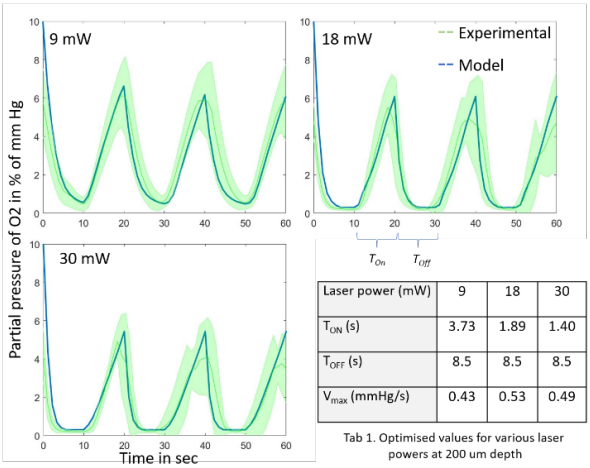

Laser power (mW)	9	18	30
T_{ON} (s)	3.73	1.89	1.40
T_{OFF} (s)	8.5	8.5	8.5
V_{max} (mmHg/s)	0.43	0.53	0.49

Tab 1. Optimised values for various laser powers at 200 um depth

Figure 1: Experimental and numerical data showing the O_2 concentration as a function of time for three laser irradiances at 200 um depth, and with 10 s pulsing. Table 1 shows the optimized reaction time and consumption rate for different laser irradiances.

Discussion

The consumption of O_2 due to the laser is directly related to cross link formation. The optimized values of laser pulsing are asymmetric (about 3 times longer *off* time than *on*), which results in a minimal O_2 concentration of more than 2%, avoiding complete depletion of O_2 inside the cornea. These optimal parameters provide the required 5.4J, in a total treatment time of around 22 minutes using a 30 mW laser irradiance. This is 30% less than the 30 minutes required by the conventional Dresden protocol. A major limitation of this study concerns its ex-vivo nature as O_2 on the posterior cornea, neglecting the O_2 regulation on the posterior side of the cornea. Additional biomechanical characterization are required to verify that the optimized parameters truly improve the mechanical stability following CXL.

COMPUTATIONAL MODELLING OF THE EYE BIOMECHANICS AFTER STRABISMUS SURGERY

Jorge Grasa (1,2), Ana Pilar Esteban (1), Begoña Calvo(1,2)

1. *Aragon Institute of Engineering Research (I3A), University of Zaragoza, Spain 2. Centro de Investigación Biomédica en Red en Bioingeniería, Biomateriales y Nanomedicina (CIBER-BBN), Spain*

Introduction

During strabismus, one of the extraocular muscles (EOM) controlling eye movements, is stronger or weaker than the others. Two surgical options may be considered: **A**ltering the attachment site on the eyeball (recession) or removing a portion of muscle and attach in the same site (resection). In this work, a thermodynamically consistent model for EOM considering the passive and active behaviour was formulated. With this model, the influence of each eye part (muscles, eye ball, orbital fat) on the eye movement was studied. Finally, the model was used to investigate dysfunctions in the EOM simulating the surgeries to reduce difficulties and risks.

Methods

The passive and active finite strain response of the muscle was simulated within the framework of continuum mechanics. A strain energy function decoupled into a volume-changing and a volume-preserving parts was used [1].

$$\Psi = \Psi_{vol}(J) + \overline{\Psi}_p(\overline{\mathbf{C}}, \mathbf{N}) + \overline{\Psi}_a(\overline{\mathbf{C}}_e, \bar{\lambda}_a, \mathbf{M}) \qquad (1)$$

Derived from the second law of thermodynamics, to account the dissipation during contraction, a new constitutive relation was obtained [2].

$$P_a - \frac{\partial \overline{\Psi}}{\partial \bar{\lambda}_a} + \left(2\overline{\mathbf{C}}_e \frac{\partial \overline{\Psi}}{\partial \overline{\mathbf{C}}_e} \overline{\mathbf{F}}_a^{-T}\right) : \frac{\partial \overline{\mathbf{F}}_a}{\partial \bar{\lambda}_a} = C\dot{\bar{\lambda}}_a \qquad (2)$$

In this expression, $\dot{\bar{\lambda}}_a$ is the contraction velocity of the muscle fibers taken as a new state variable.
A finite element mesh of the EOM, sclera and orbital fat was developed as can be observed in Figure 1.

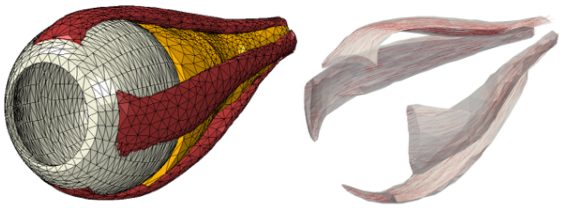

(a) (b)

Figure 1: (a) Finite element mesh of the human right sclera and superior rectus, inferior rectus, lateral rectus, medial rectus and orbital fat. (b) Muscle fiber directions of the four EOM

Results

A set of different scenarios considering a weak muscle and optimal contraction stretch were considered. In Figure 3, results of the total displacement of an active weak medial extraocular muscle are presented.

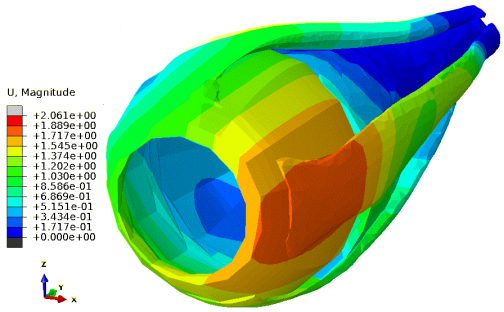

Figure 3: Displacement field under the activation of the medial extraocular muscle.

Discussion

The model is capable of reproducing the skeletal muscle contraction of the different EOM under physiological range of motion.
The effect of "weak" and "strong" muscles is reproduced by the model with noticeably effects in eye movement.
Dynamic explicit algorithm handled the high nonlinearities of the model, although techniques to increase the step time increment (mass scaling) affect active behaviour of the muscle.

References

1. B. Hernandez-Gascón et al, J Theor Biol. Vol: 335, 108-118.
2. J. Grasa et al, J Mech Behav Biomed Mater. Vol: 61, 444-454.

Acknowledgements

This work was supported by grant DPI2017-84047-R, from the Spanish Ministry of Economy and Competitiveness.

BIOMECHANICAL SIMULATION PLATFORM FOR PATIENT-SPECIFIC REFRACTIVE INTERVENTIONS

Malavika H. Nambiar (1), Harald Studer (2), Abhijit Sinha Roy (3), and Philippe Büchler (1)

1. ARTORG Center for Biomedical Engineering Research, University of Bern, Switzerland; 2. Optimo Medical AG, Switzerland. 3. Narayana Nethralaya Eye Clinic, India

Introduction

Myopia characterized by near sightedness, is one of the most common yet underestimated ocular condition affecting global health. Projections suggest nearly 50 % of the world's population will be myopic by 2050 and 10 % of the world's population will suffer from high myopia thus being at risk of associated vision impairment and blindness. Corrective surgeries such as LASIK, SMILE and PRK are becoming increasingly popular but 15 % of cases fail to provide the desired correction rates. The foremost drawback in these corrective surgeries arise in the stage of surgical planning itself. One of the explanations for this poor outcome is related to the poor biomechanical characterization of the patient's cornea during the preoperative planning. In this study, we aim at incorporating patient-specific mechanical simulations during the surgical planning of refractive interventions such as LASIK, SMILE, or PRK.

Method

In this regard, patient specific geometrical models have been developed based on Pentacam elevation maps obtained from Nethralaya Eye Clinic, India. Clinical data on patients undergoing LASIK, PRK and SMILE surgeries was collected. The unique corneal morphology and surgical parameters such as the ablation profile, the LASIK flap, or the SMILE depth have been automatically reconstructed using the software GMSH 4.6 in conjunction with Python 3.0. Since the surgical incisions are performed on the cornea under a physiological stress due to the intraocular pressure, the corneal stress-free shape was determined by performing an iterative prestressing under IOP. A Holzapfel-Gasser-Ogden hyperelastic mechanical model was implemented using an ABAQUS UMAT subroutine. The current collagen fiber distribution was modelled using a general structural tensor that accounts for two families of fibers. Both family of fibers have an orthogonal orientation in the center of the cornea and are circumferentially oriented in the corneal periphery. Besides fiber orientation, in-plane and out-of-plane fiber dispersions have considered in the model to account for the fact that the fibers are not perfectly aligned with the main direction of anisotropy. The model was validated by measuring the corneal curvature from the clinical data and ensuring that it was accurately reproduced at different steps of the modeling procedure. Simulations of the three refractive interventions were then conducted based on the pre-operative clinical data.

Results

As expected, the interventions significantly alter the corneal curvature (Fig. 2). The SMILE and PRK surgeries result in similar curvature maps. For these cases, the predicted correction matched the targeted value (Tab. 1). However, the curvature map predicted for LASIK is different due to the receding flap after removal of stoma underneath it, resulting in an underestimation of the correction by the model (Tab 1.).

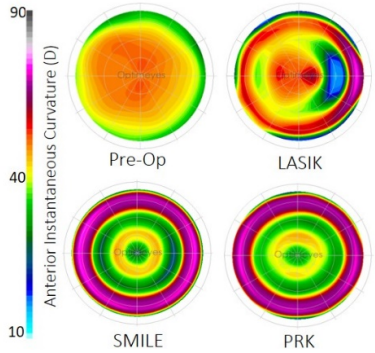

Figure 2: Curvature maps for presurgical and post-surgical intervention of a typical patient.

Condition	Spherical Equivalent
Presurgical - measured	-5 D
Presurgical - model	-5 D
Post-surgical PRK	+ 0.2 D
Post-surgical SMILE	+ 0.8 D
Post-surgical LASIK	-5.4 D

Table 1: Spherical equivalent of the patient before surgery and correction achieved post surgeries shown in Fig. 2. The ablation parameters were selected to reach a desired outcome of 0 D

Discussion

The pre-surgical models are in good agreement with the patient's corneal geometry and topography. This is established in the anterior curvature maps and the by the spherical equivalent. The surgical models correctly capture the targeted correction in spherical equivalent of the PRK and SMILE surgery models, while showing an over correction of 0.2D – 0.8D. Improvements are required to accurately model LASIK interventions. More patient specific details like biomechanical properties of the corneal tissue will be incorporated in future models. We aim to collect this data using Brillouin imaging. We will further work towards improving the mechanical model and to validate the predictions.

BIOMECHANICAL CHARACTERISTICS OF PORCINE RETINA

Beatrice Belgio (1), Sara Ragazzini (1), Paolo Arpa (2), Sara Mantero (1), Federica Boschetti (1)

1. Dept. of Chemistry, Materials, and Chemical Engineering "Giulio Natta", Politecnico di Milano, Italy;
2. Ospedale San Gerardo Monza, Italy

Introduction

The retina is a complex neurosensory tissue responsible for absorption, conversion, and transmission of visual stimuli from the external world to the brain.
In contrast to sclera and choroid, the biomechanics of the retina has been scarcely investigated. Indeed, only few studies have focused on the examination of retinal mechanical properties because of its extreme structural fragility [1], [2]. However, a better knowledge of retinal biomechanical characteristics is crucial for understanding physiology and retina-related disease mechanism, improving surgical techniques to avoid retinal detachment, developing *in silico* and *in vitro* retina models, and implementing tissue regenerative strategies.
In this study, we provide a protocol for retina isolation and we present the results of tensile tests performed on porcine retinal tissues.

Materials and Methods

Pig eyes (n=16) were obtained from a local abattoir within 1 hour post mortem. The age of the pigs was 9 months.
First, the eyeballs were cleaned from the adipose tissue and the conjunctiva (Fig. 1A) and opened at the cornea level. Then, cornea, iris, crystalline lens, and vitreous were cautiously removed in sequence. Finally, retina was gently detached from the posterior wall of the eye and maintained in PBS solution (P4417, Sigma) at 4 °C until testing (Fig. 1B).

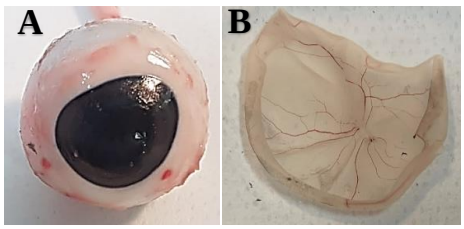

Figure 1: (A) Picture of a cleaned eyeball; (B) Isolated retina in PBS solution.

For the mechanical tests, retinal samples were clamped between the jaws of an electromechanical testing machine (Bose EnduraTEC ELF 3200). Samples were pulled until failure at a velocity of 0.1 mm/s at room temperature. From the data, we calculated the stress (Pa) as force applied/original cross-sectional area, the strain (mm/mm) as change of length/original length. The original cross section area was computed as the thickness multiplied by the initial width. The thickness was determined using optical coherence tomography (DRI OCT Triton Plus, Topcon), whilst initial width was evaluated through the ImageJ software (NIH, USA). The gap between the clamps was considered as the original length. The elastic modulus (E) was the linear portion of the stress-strain curve before the change of the slope. The yield stress (Y) was the point of change of slope in the first linear elastic region of the stress-strain curve. The failure stress was set to the maximum stress value.

Results

The average retina thickness was 0.35 mm ± 0.04 mm. Retinal samples displayed a typical tensile stress-strain curve with a narrow initial linear region followed by a wide non-linear region characterized by peaks (Fig. 2).

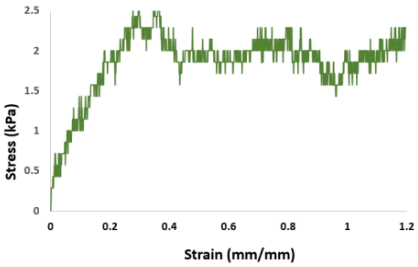

Figure 2: Tensile stress-strain curve of retinal samples.

Table 1 outlines the mean values and the SDs of the biomechanical parameters (E, Y, and failure stress).

Parameter	Mean	SD
E (kPa)	13.4	0.007
Y (kPa)	1.33	0.75
Failure stress (kPa)	2.21	0.8

Table 1: Mean and SDs of mechanical parameters

Discussion and Conclusion

Our findings show that retina exhibits both an elastic and a plastic behavior in agreement with previous studies [1], [2]. The peaks present in the non-linear region were probably due to micro-ruptures in the tissue.

References

1. G. Wollensack et al, Retina, the Journal of Retinal and Vitreous Diseases, 24:967-970, 2004.
2. K. Chen et al, Journal of Biomechanics, 2010.

Acknowledgements

We thank Dr. Fumagalli and his Fumagalli Industria Alimentari located in Como for kindly providing the pigs eyes.

OCULAR ACCOMMODATION: EXPLORING PRESBYOPIA CAUSES WITH A VALIDATED NUMERICAL MODEL

I. Cabeza-Gil[1], J. Grasa[1,2], B. Calvo[1,2]

1. Aragon Institute of Engineering Research (I3A), University of Zaragoza, Spain.2. Centro de Investigación Biomédica en Red en Bioingeniería, Biomateriales y Nanomedicina (CIBER-BBN), Spain.

Introduction

Accommodation is the ability of the eye to change its focus from distant to near objects (and viceversa). The ciliary muscle is the engine of the accommodation process. A contraction of the entire ciliary muscle moves the apex of the ciliary processes towards the lens equator and serves the primary function of releasing resting zonular tension at the lens equator to allow accommodation. With aging, there is a decline in accommodative amplitude, called presbyopia. Presbyopia is caused mainly by age-related mechanical changes in the lens according to the lenticular theory. Therefore, the aim of this research is to numerically evaluate the effect of the mechanical properties of the lens on presbyopia. To do so, a 3D finite element (FE) model coupling an optical model including the contraction of the ciliary muscle and initial stresses in the lens capsule was developed and validated according to experimental data. Then, the effect of the mechanical properties and the geometry of the lens on accommodation was analysed.

Methods

The geometries of the FE model were generated in the non-accommodated state based on recent studies [1]. The model consists of: the lens, which is composed of the nucleus, cortex and the anterior (AC) and posterior capsule (PC); the zonules, which attach the lens to the ciliary body, composed of the ciliary muscle and processes; and the sclera and cornea. All properties were based on literature [2]. The ciliary muscle contraction was simulated with an electro-chemical-mechanical model [3] and the initial stresses of the lens capsule were obtained stretching the lens from the accommodated to the non-accommodated state. The orientation of the ciliary muscle fibres was included according to literature. The effect of the age-related lens mechanical properties and geometry on accommodation was studied by a full factorial analysis. Table 1 gathers the elastic moduli levels of the factors analysed. The effect of some novel approaches as the stiffness gradient and the distribution of the capsule thickness was also studied on accommodation via sensitivity analysis.

Results

Fig.1 shows the numerical comparative between the accommodated state with an amplitude of 5.85 D against the non-accommodated state. The morphological changes of the ciliary muscle contraction and the biometric lens measurements were validated according to experimental data [4]. This validation was performed for a 29 y/o subject.

Fig. 2 shows the deformed geometry of the lens and ciliary muscle in the accommodated state.

	E (kPa)				
Factors	L1	L2	L3	L4	L5
AC	100	300	500	700	1000
PC	100	300	500	700	900
Cortex	0.75	1.50	2.25	3.00	3.75
Nucleus	0.10	0.20	0.30	0.40	0.50

Table 1: Mechanical properties for the different lens parameters of the full factorial analysis. Additionally, five age-related geometries were considered from a young to an old subject.

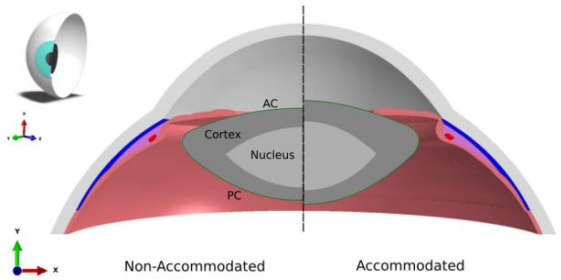

Figure 1: The deformed geometry (accommodated state) and the reference geometry (non-accommodated state) of the eye.

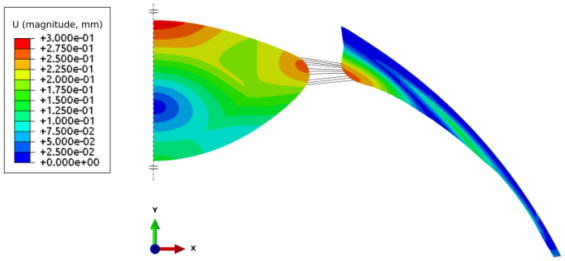

Figure 2: 2D view of the accommodated state for a 29 y/o subject.

Discussion

We simulated accurately the accommodation process, incorporating the ciliary muscle contraction and the initial stresses of the lens capsule. The full factorial analysis determined that all mechanical properties of the lens analysed have a statistical significance on accommodation. Above all, the stiffness ratio between the nucleus and cortex and the stiffness of the posterior capsule were the most influential with age, resulting in a decreasing of accommodation.

References

1. Chang et al, Biomed Opt Express, 2018
2. Krag et al, Prog Retin Eye Res, 2003
3. Grasa et al, J Mech Behav Biomed, 2016
4. Ramasubramanian et al, J Refract Surg, 2015

BROADBAND EXCITATION STIMULI FOR SPECTRAL CHARATERIZATION OF CORNEAL TISSUE

Sabine Kling (1)

1. Computer Vision Lab, ETH Zurich, Switzerland

Introduction

Corneal biomechanical properties play an essential role in the early diagnosis of degenerative corneal diseases and their follow-up after cross-linking treatment, which aims at stiffening the tissue to stop disease progression. Recently, optical coherence tomography (OCT) has been applied to measure the dynamic and quasi-static deformation behavior of corneal tissue and retrieve mechanical parameters. Previously, the measurement of shear wave propagation speed and natural frequencies has been investigated under dynamic excitation with air-pulse[1], sound[2] or a piezoelectric actuator[3]. The purpose of this study was to compare (1) different broadband waveforms for their suitability to spectrally characterize porcine cornea, and (2) the frequency and propagation analysis regarding the measurement of stiffness.

Material and Methods

A spectrometer-based OCT system (λ=878nm, $\Delta\lambda$=62.5nm) was used to record M-scans at 30 lateral locations along 5.6mm of the corneal surface. The acquisition of M-scans was synchronized with an external piezoelectric excitation source, which produced a broadband stimulus, consisting either of (i) a step, (ii) an impulse of 10ms duration, (iii) or a windowed linear chirp between 0 and 500 Hz, each at a repetition rate of 5Hz. Measurements were conducted in a freshly-enucleated porcine cornea and repeated three times with every stimulus. Phase-sensitive post-processing was applied on the raw OCT scans to compute corneal displacements. Subsequent Fourier transform of individual M-scans was applied to determine the spectral components and identify natural frequency harmonics. In an average porcine eye ball[4] with a circumference of approx. L=75mm, we expect[2] the natural frequencies to occur at

$$f_{m,n} = \frac{\lambda_{m,n} \cdot v}{L}, \qquad (1)$$

where $\lambda_{m,n}$ is the n-th root of the Bessel function of its first kind of order m. For the fundamental frequency, $\lambda_{0,1} = 2.405$. Cross-correlation of subsequent M-scans with the M-scan at the corneal apex was applied to determine the shear wave propagation speed v. The latter is directly related to the shear modulus ($\mu \propto v^2$).

Results

Step and impulse excitation stimuli produced a similar spectrogram with three dominant natural frequencies, see Figure 1. The fundamental frequency was located between 45 and 50 Hz, corresponding according to eq.1 to a shear velocity between 1.4 and 1.6 m/s and a shear modulus between 2.0 and 2.6 kPa. With chirp excitation, only one natural frequency was identified, which was close to the second peak identified with step or impulse stimuli. Shear wave propagation could be tracked with all types of stimuli and had a velocity of 2.6, 3.2 and 2.2m/s with step, impulse and chirp excitation, respectively. This corresponds to a shear modulus of 7.2, 11 and 5.1kPa.

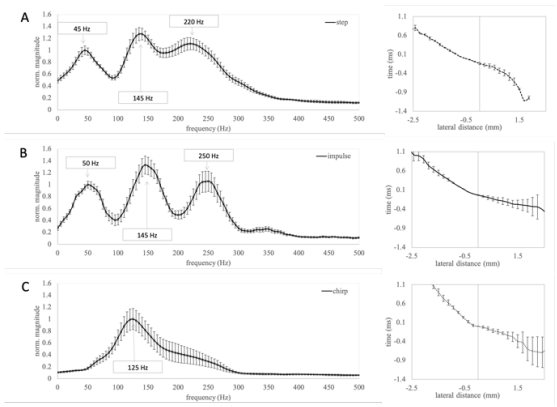

Figure 1: Spectral analysis of corneal deformation (left) and shear wave propagation (right) with different stimuli: (A) step, (B) impulse, (C) chirp.

Conclusion

Step and impulse excitation allowed to identify more natural frequencies than windowed chirp excitation, making the former more suitable for dynamic characterization. The frequency approach suggested a 2x slower shear velocity than the actual stimulus propagated, suggesting eq.1 needs further refinement.

References

1. Lan, G., Larin, K. V., Aglyamov, S. & Twa, M. D. Characterization of natural frequencies from nanoscale tissue oscillations using dynamic optical coherence elastography. *Biomed. Opt. Express* **11**, 3301–3318 (2020).
2. Akca, B. I. *et al.* Observation of sound-induced corneal vibrational modes by optical coherence tomography. *Biomed. Opt. Express* **6**, 3313–3319 (2015).
3. Ramier, A., Tavakol, B. & Yun, S.-H. Measuring mechanical wave speed, dispersion, and viscoelastic modulus of the cornea using optical coherence elastography. *Opt. Express* **27**, 16635–16649 (2019).
4. Sanchez, I., Martin, R., Ussa, F. & Fernandez-Bueno, I. The parameters of the porcine eyeball. *Graefes Arch. Clin. Exp. Ophthalmol.* **249**, 475–482 (2011).

Acknowledgements

This work was supported by the Ambizione grant PZ00P2_174113 from the Swiss National Science Foundation.

STUDY OF A MAGNESIUM-BASED DEVICE FOR OCULAR APPLICATION

M. Ferroni (1), F. De Gaetano (1), N. Bono (1), M. Zonfrillo (3), G. Sferrazza (3), G. Candiani (1), M.G. Cereda (2), F. Boschetti (1)

1. Department of Chemistry, Materials and Chemical Engineering, Politecnico di Milano, Italy; 2. Department of Biomedical and clinical science, Sacco Hospital, University of Milan, Italy; 3. Institute of Translational Pharmacology, National Council of Research, Rome, Italy

Introduction

Wet age-related macular degeneration is the main cause of vision loss in developed countries. Millions of people are treated by intravitreal injections of anti-VEGF drugs [1]. We designed a device based on magnesium able to release doses of drug and avoid the burdens of repeated injections, due to its advantageous properties. In this work we present methods and results to characterize i) corrosion rate of Mg samples subjected to ocular shear stress levels, ii) in vitro biocompatibility and iii) drug stability in presence of Mg corrosion products.

Methods

In vitro corrosion of Mg samples: Corrosion tests on pure Mg samples were done at different time steps using a custom experimental setup up to 48 hours. The experimental flux was set to recreate on the upper surface of the specimens the same shear stress field evaluated by the numerical simulations of flow inside the vitreous chamber [2],[3]. Morphology and profile of all the specimens were evaluated and compared by SEM for the evaluation of the corrosion mechanisms.
In vitro biocompatibility test: The solution used for the treatment was prepared by dissolving the sterilized magnesium in 88.3 mL of serum-free DMEM solution in order to obtain a stock solution at a concentration of 0.2 µg/ml. Murine fibroblasts (3T3-NIH) and immortalized human keratinocytes (HACAT) cell lines were used to evaluate the biocompatibility.
Cells were grown in DMEM medium supplemented with 10% FBS in a 37 °C humidified atmosphere of 5% CO2. For Trypan blue test, 150'000 cells/well were seeded in 6 wells plate. For MTT test, 25'000 cells/well were seeded in 96 wells plate. After 24h, the culture medium was removed and replaced with medium conditioned at different concentrations.
Magnesium and anti-VEGF interaction: A customized indirect ELISA protocol was developed for evaluating the interaction between anti-VEGF drug (bevacizumab) and pure magnesium. Mg samples were prepared, dry sterilized and dissolved in a volume of BSS equal to 40 mL. Half of the solution was used for the determination of Mg content by ICP-OES analytical technique. The second half of solution was used for the interaction tests and analyzed at different time periods (0-1-7-14 days).

Results

In vitro corrosion of Mg samples: SEM images of Mg samples demonstrated uniform corrosion confirmed by CLSM data acquired during the experimental corrosion. The presence of localizations was mainly due to defects related to the manufacturing process. The corrosion rates evaluated in three fluid-induced shear stress (FISS) conditions were 1.9, 2.7 and 3.4 µm/day (Figure 1).
In vitro biocompatibility: The results obtained showed that Mg extracts did not induce cell death in both cell lines. No significant toxic effects were observed at the various concentrations 24h/48h after treatment compared to untreated control.
Magnesium and anti-VEGF interaction: Changes in averaged values of bevacizumab activity in contact with magnesium are always less than or equal to 10% if compared to the control case, represented by the drug activity itself, not in contact with magnesium, at the same time points (0, 1, 7, 14 days).

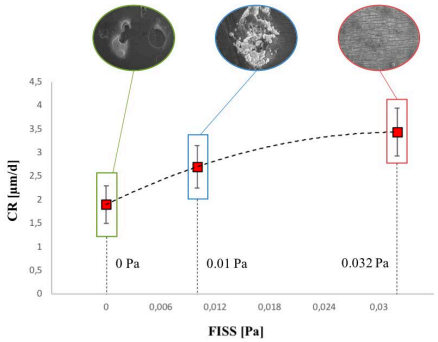

Figure 1: Trend of corrosion rate of Mg biodegradation.

Discussion

We demonstrated the feasibility of magnesium as drug carrier for the treatment of maculopathy or potentially other eye pathologies, developing a quantitative method to test whether the drug stability is affected by the presence of Mg corrosion products. Mg samples showed uniform corrosion and absence of toxic aspects. Finally, magnesium does not alter the bevacizumab stability. The Our results provide the scientific basis for continuing with the subsequent characterization in view of the clinical use of the device.

References

1. Choonara et al, J Pharm Sci, 99:2219–2239, 2010.
2. Ferroni et al, Med Eng & Ph, 86:20-28, 2020.
3. Wang et al, Acta Biomater, 10(12):5213-5223, 2014.

Acknowledgements

This study was funded by the Italian Ophthalmological Society (SOI). Mg samples were generously given by Prof. Guangyin Yuan, School of Material Science and Engineering, Shanghai Jiao Tong University, China.

DEVELOPMENT OF A NOVEL TEST BENCH FOR ASSESSING INTRAOCULAR DEVICE CORROSION AND PHARMACOKINETICS

M. Ferroni (1), F. De Gaetano (1), M. Pizzi (1), F. Inveninato (2), M. Annoni (2), F. Boschetti (1)

1. Department of Chemistry, Materials and Chemical Engineering, Politecnico di Milano, Italy; 2. Department of Mechanical Engineering, Politecnico di Milano, Italy

Introduction

To overcome the limitations associated with conventional therapy of maculopathy, which involves intravitreal injections of drugs [1], magnesium-based drug delivery devices represent a high potential solution. Nowadays, there is no standard protocol for the in vitro assessment of their corrosion mechanism in ophthalmology. In this work, we present the design process and validation of an innovative test bench, developed to predict the in vivo behavior of the device in terms of corrosion and pharmacokinetics (PK). The feasibility of the manufacturing process of prototypes used for the experimental campaign is presented as well.

Methods

Corrosion/PK test bench: Two plexiglass vitreous chambers were designed and built in 4:1 scale with respect to physiological dimensions and set in motion by brushless motors. The movements were implemented to reproduce the ocular kinematics in order to simulate the device corrosion in the eye [2],[3]. Such system was inserted in an incubator, able to maintain physiological eye conditions, i.e. temperature at 34 °C and CO_2 at 5%. The control system of the temperature is made of a thermostat associated with a heating cable, while the CO_2 control system was designed through the use of Arduino, which can change the status of a solenoid valve connected to a CO_2 cylinder, according to the output of the gas sensor. pH analysis was performed with BSS solution, used as vitreous substitute for corrosion/PK test, and Mg rods (d = 1.6 mm, h = 20 mm).

Prototype feasibility: Prototypes, consisting of concentric magnesium layers of high aspect ratio, in which the empty spaces will be loaded by the drug, can be manufactured through a mechanical microdrilling process [4]. A preliminary test was conducted on an ultraprecision five-axis micromachining center Kern EVO. The HSS-E-PM drill bit 97011 produced by HARTNER Ø350 µm was used to obtain a microhole 1.8 mm deep. The microdrilling operation was performed in dry conditions and in a single peck, imposing a feed per revolution of 15 µm and a cutting speed of 44 m/min. The workpiece consisted of a 5-mm-thick pure magnesium disk, with a diameter of 20 mm to avoid clamping issues.

Results

Corrosion/PK test bench: The setup validation proved the functioning of the motor response analyzing the effective motion of the chamber over time compared to the input functions and the capability of maintaining the ophthalmic proper conditions in terms of temperature and CO_2 control and administration. The gas concentration value and the temperature inside the vitreous chambers were maintained at a stable level of 5% and 34 °C, respectively. Then, first corrosion tests performed on magnesium rods showed the efficiency of the buffer system: pH measurements over 7 days of incubation of BSS solution underlined that the presence of CO_2 compensates for the increase in pH associated with the corrosion of magnesium (averaged $\Delta pH_{7\ days} = 0.04$).

Prototype feasibility: The preliminary microdrilling test highlighted that the process is suitable for realizing the prototypes. Through microscope inspection of the microhole, a diameter 20 µm larger than the nominal one was measured. Moreover, 10 µm high burrs were observed due to the ductile nature of magnesium. Both aspects can be minimized by optimizing process parameters and cutting conditions for the future obtaining of the 4:1 and 1:1 prototypes.

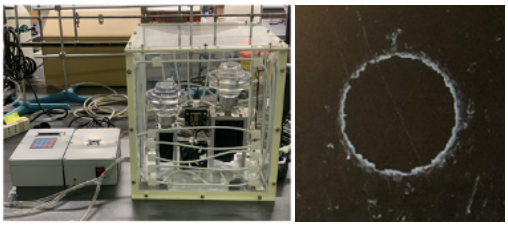

Figure 1: Test bench for in vitro tests (left) and microscope observation of the 350 µm microhole (right).

Discussion

We developed a novel test bench for the evaluation of corrosion and pharmacokinetic profiles from intraocular drug delivery devices and we proved the feasibility of the prototype manufacturing that will be used in the experimental campaign. The validation of both the movements reproduced by the motors and the control of carbon dioxide and temperature levels inside the incubator makes the test bench usable for the study of the Mg-based devices for ophthalmological applications. Process optimization of prototype manufacturing, which feasibility was proved, will be performed directly through the ongoing microdrilling tests for realizing the 4:1 and 1:1 prototypes.

References

1. Schwartz et al, Expert Opin Drug Deliv, 11:61–68, 2014.
2. Repetto et al, Phys Med Biol, 50:4729–4743, 2005.
3. Ferroni et al, Med Eng & Ph, 86:20-28, 2020.
4. Sun et al, J Eng Manuf, 234:1473-1485, 2020.

CAN CYCLIC LOADING WEAKEN THE ORIGIN OF THE OVINE PUBOVISCERAL MUSCLE?

Maria Vila Pouca(1,2), Marco Parente(1,2), Renato Natal Jorge(1,2), James Ashton-Miller(3)

1. Faculty of Engineering of University of Porto, Portugal; 2. Institute of Science and Innovation, Portugal; 3. Department of Mechanical Engineering, University of Michigan, USA

Background

Stretch-related injury of the human pubovisceral muscle during vaginal delivery has been implicated in the pathomechanics of pelvic organ prolapse. Between 13-36% of women delivered vaginally sustain this injury[1] which often involves the origin of the pubovisceral muscle [2], [3]. A characteristic of a difficult labor is repetitive pushing which would apply a cyclic stretch of the pubovisceral muscle. Molecular, cellular and ultrastructural evidence of low-cycle fatigue damage accumulation has been found at the origin of the anterior cruciate ligament after repeated sub-maximal loading[4]. So, if low-cycle material fatigue can occur at the origin of the anterior cruciate ligament, we reasoned that low-cycle fatigue could also occur at the origin of the pubovisceral muscle during labor.

The origin of the pubovisceral muscle includes the pubic bone, an aponeurosis connected to the bone, and the pubovisceral muscle connected to the aponeurosis. So, this bone-"tendon"-muscle unit has two weak links: the bone-"tendon" junction and the muscle-"tendon" junction.

Material and Methods

We tested 10 pelvises from skeletally mature female sheep. These provided 20 specimens of the bilateral origin of the pubovisceral muscle. Ultimate tensile tests of four specimens helped characterize the failure properties of the muscle-tendon-bone unit. Relaxation and fatigue tests were completed on 13 specimens at 35% and 60% of failure displacement, respectively. Relaxation tests consisted of a ramp to 35% of failure displacement and a hold for 1000 s. In the fatigue tests, 60 cycles of loading to 60% of failure displacement and unloading to 45% of failure displacement were performed. Three specimens remained as the untested controls. An ADMET eXpert 4500 500N MicroTest system with MTESTQuattro controller was the equipment used. Force-displacement curves were acquired and engineering stress-stretch curves were obtained based on the initial cross-sectional area of the specimen at the tendon-muscle junction. A histological evaluation was performed in the 13 fatigued tested specimens and in the 3 untested controls. This allowed us to verify what are the microscopic signs of fatigue damage and, more specifically, where is the damage starts within the muscle-tendon-bone unit. Tendon-bone samples and tendon-muscle samples where stained with Masson's Trichrome and viewed on a Nikon E800 light microscope.

Results

Figure 1 shows the average grip-to-grip stretch-engineering stress curve. The first cycle shows significant hysteresis due to viscoelasticity. In the subsequent cycles the fact that the stresses decrease continuously is a sign of damage in the specimen.

The histology revealed individual muscle fiber rupture and kinked muscle fibers in the muscle-tendon sections. We believe these are primary signs of fatigue damage accumulation and they were observed in the muscle, near the muscle-tendon junction.

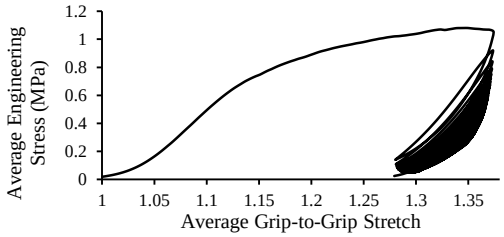

Figure 1: Grip-to-grip stretch-engineering stress curve showing the averaged result of the fatigue tests from the 13 specimens.

Conclusions

We conclude that cyclic stretch to 60% of failure strain caused fatigue damage to accumulate at the origin of the ovine pubovisceral muscle. The weakest region was the muscle near the muscle-"tendon" junction. In humans, a difficult second stage of labor lasting 3 hours would apply 60 stretch cycles to the pelvic floor muscles, so these data raise the possibility that fatigue damage could be a mechanism of pubovisceral muscle injury during human vaginal birth.

References

[1] K. L. Shek and H. P. Dietz, "Intrapartum risk factors for levator trauma," *BJOG An Int. J. Obstet. Gynaecol.*, vol. 117, no. 12, pp. 1485–1492, 2010.

[2] S. W. O'Driscoll, L. B. J. Goncalves, and P. Dietz, "The Hook Test for Distal Biceps Tendon Avulsion," *Am. J. Sports Med.*, vol. 35, no. 11, pp. 1865–1869, Nov. 2007.

[3] J. M. Miller, L. K. Low, R. Zielinski, A. R. Smith, J. O. L. Delancey, and C. Brandon, "Evaluating maternal recovery from labor and delivery: Bone and levator ani injuries," *Am. J. Obstet. Gynecol.*, vol. 213, no. 2, pp. 188.e1-188.e11, 2015.

[4] J.J. Chen *et al.*, "An Anterior Cruciate Ligament Failure Mechanism," *Am. J. Sports Med.*, vol. 47, no. 9, pp. 2067–2076, Jul. 2019.

NUMERICAL MODELLING OF A SYNTETIC MESH IMPLANT TO REPAIR THE UTEROSACRAL LIGAMENT

Elisabete Silva (1), Jorge Bessa (2), Marco Parente (1,2), Teresa Mascarenhas (3), António Fernandes (1,2)

1. LAETA, INEGI, Portugal; 2. Faculty of Engineering, University of Porto, Portugal; 3. Dep. of Obstetrics and Gynecology, CHSJ-EPE / Faculty of Medicine, University of Porto, Portugal

Introduction

In 2019, a study showed that 41-50% of women over the age of 40 are affected by pelvic organ prolapse (POP), which is a common urogenital condition [1]. Others studies showed that 11% of all women risk of undergoing POP surgery and the re-operation after surgery was about 30% [2,3]. Until, recently, surgeons relied on the use of meshes in reconstructive surgeries, but on April 16, 2019, the FDA has forbidden its use for transvaginal repair of anterior compartment POP, since its safety and effectiveness was not demonstrated in the context of patient population in a clinical trial. However, clinical trials are very expensive and can last for several years. Computer models and simulation can potentially be used in clinical trials as an alternative source of prior information.

The main aim of this study was to simulate an implant mesh to mimic the uterosacral ligament function based on pelvic computational model. For this purpose, was developed a computational model of a synthetic mesh, to repair the POP, based on existing specifications on the market.

Methods

In this work was used a pelvic cavity computational model, including the pubic bone, the pelvic organs, the pelvic floor muscles (PFM), and other supporting structures (Fig. 1) [4]. The mechanical behavior of the mesh implant (Fig. 1b)) was modeled, assuming a hyperelastic behavior, based on experimental curve that was obtained through uniaxial tensile tests performed in our laboratory (Fig. 2)).

Computational simulation of Valsalva maneuver was performed for progressive increase in intra-abdominal pressure (IAP) up to 4 kPa.

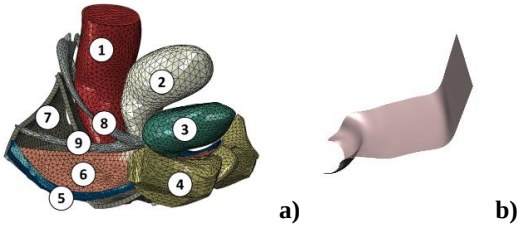

a) **b)**

Figure 1. Pelvic computational model (a) and synthetic mesh implant model (b). (1) rectum, (2) uterus, (3) bladder, (4) pubic bone rectum, (5) arcus tendineous fasciae pelvis, (6) pelvic fascia, (7) PFM, (8) uterosacral ligament (UL), (9) cardinal ligament.

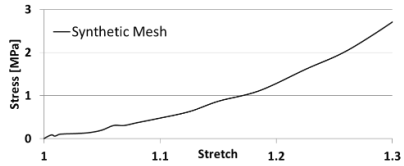

Figure 2. Experimental curve of the synthetic mesh.

Results

The maximum magnitude of displacement of the uterus for asymptomatic model was approximately 29 mm. The rupture of the UL caused an increase of 28% in this displacement. The insertion of the synthetic mesh implant caused a reduction of the displacement (23%), when compared with asymptomatic model.

Table 1. Maximum magnitude of displacement of the uterus.

Variable	Max. Mag. Disp. Uterus [mm]	Variation (%)
Asymptomatic	29.01	**…**
POP (w/o UL)	37.23	**28**
Synthetic Mesh	22.44	**23**

Note: POP (w/o UL) - pelvic organ prolapse without uterosacral ligament; Max. Mag. Disp Uterus - maximum magnitude of displacement of the uterus.

Conclusions

The obtained results show that the computational model was able to discriminate the effect of synthetic mesh implant to repair uterine prolapse when UL failure occurs. The computational models can provide powerful insights on the mechanisms underlying and predict the effects of the mesh implants in the pelvic tissues, in a relatively inexpensive, personalized, fast and safe way, without resorting to random controlled trials and animal tests.

References

1. Abhyankar P, et al. *BMC Womens Health* 2019; 1–12.
2. Segal S, et al. *Curr Bladder Dysfunct Rep* 2012; 7: 179–186.
3. Olsen A, et al. *Obs Gynecol* 1997; 89: 501–506.
4. Brandão S, et al. *J Biomech* 2015; 48: 217–223.

Acknowledgements

The authors acknowledge the funding of Project SPINMESH, through Fundo Europeu de Desenvolvimento Regional (FEDER) - POCI-01-0145-FEDER-029232.

ASSESSMENT OF SPROUTING ANGIOGENESIS IN SILICO

Ana Guerra (1), Jorge Belinha (2), Naside Mangir (3,4), Sheila MacNeil (3), Renato Natal Jorge (1,5)

1. INEGI, Portugal; 2. ISEP, Portugal; 3. Kroto Research Institute, UK; 4. Hacettepe University School of Medicine, Turkey; 5. FEUP, Portugal

Introduction

Angiogenesis, the formation of new blood vessels from the pre-existent ones, occurs throughout life in health and disease situations. This process begins in the embryonic development and remains through to adulthood, allowing the diffusion of oxygen, nutrients and metabolites. Sprouting angiogenesis is a well-defined process, being main modulated by the vascular endothelial growth factor (VEGF) [1]. This is a very complex process that often requires *in vivo* assays to study all its steps. The chicken chorioallantoic membrane (CAM) assay is one of the most used. Mathematical formulation of angiogenesis allows us to study this process using reproducible, less time-consuming, and cheaper methodologies. In this study, we developed a meshless-based model to assess the angiogenesis response for several VEGF concentrations. Furthermore, we presented a quantitative and a qualitative evaluation of angiogenesis compared with the CAM assay.

Methods

The numerical method used was the Radial Point Interpolation Method [2]. In our model, angiogenesis was simulated in a 5x5 mm^2 square domain, using a regular nodal distribution with 2601 nodes. Endothelial cells migrate according to a diffusion-reaction equation, following the VEGF gradient concentration. The CAM assay [3] was used to obtain some important parameters to implement in the model. Quantification of angiogenesis response for different VEGF concentrations (control, 50ng, 100ng) was performed *in silico* and *in vivo* and the results obtained with both methodologies were compared. Moreover, the capillary network obtained in the simulations was qualitatively compared with the one presented in CAM images.

Results

In all the simulations, we verified that endothelial cells migrate according to the VEGF gradient. To analyse the angiogenesis response we quantified the total vessel number and the total vessel length presented in the CAM images and in the simulations for all the tested VEGF concentrations. The obtained quantitative results were very similar between the two methodologies used. In both CAM assay and simulation, the treatments with VEGF increased the total vessel number [CAM assay: VEGF 50ng increased 37% (vs. control, $p < 0.01$) and VEGF 100ng increased 82% (vs. control, $p < 0.01$); Simulation: VEGF 50ng increased 25% (vs. control, $p < 0.01$) and VEGF 100ng increased 75% (vs. control, $p < 0.01$)]. The treatments with VEGF also increased the total vessel length in both methodologies used [CAM assay: VEGF 50ng increased 20% (vs. control, $p < 0.01$) and VEGF 100ng increased 36% (vs. control, $p < 0.01$); Simulation: VEGF 50ng increased 18% (vs. control, $p < 0.01$) and VEGF 100ng increased 44% (vs. control, $p < 0.01$)]. Moreover, the capillary network profile obtained in simulations showed similarities to the one obtained *in vivo* (Figure 1).

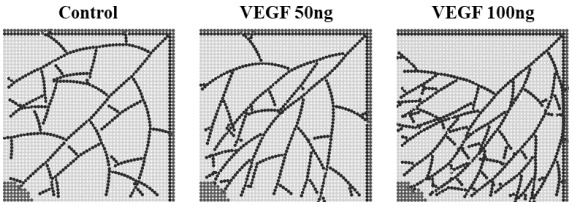

Figure 1: Capillary network obtained for the tested concentrations, using a regular nodal discretization mesh.

Discussion

Angiogenesis is as indispensable process that supports cell viability. Studying angiogenesis using only *in vivo* and *in vitro* methodologies is time consuming and very expensive. Accordingly, *in silico* methodologies arouse the interest of scientific community since they allow to simulate biological processes with different levels of complexity and to better understand the underling phenomenon. In this study, we accurately simulate the capillary network pattern presented in CAM, considering its structure and morphology. Concerning the angiogenesis quantitatively analyses, the numerical results were in agreement with experimental ones, allowing us to conclude that our model could mimic the angiogenesis response modulated by different VEGF concentrations.

References

1. Carmeliet and Jain, Nature, 473(7347):298-307, 2011.
2. Guerra et al, Int J Numer Meth Biomed Engng, 36:e3393, 2020.
3. Mangir et al, ACS Biomater Sci Eng, 5(7):3190-3200, 2015.

Acknowledgements

The authors truly acknowledge the funding provided by Ministério da Ciência, Tecnologia e Ensino Superior - Fundação para a Ciência e a Tecnologia (Portugal), under the grant SFRH/BD/133894/2017, and by projects funding MIT-EXPL/ISF/0084/2017 and LAETA (project UIDB/50022/2020).

FIBRE REORIENTATION AND STIFFNESS INFLUENCE OF A MAYLARD UTERINE SCAR DURING A VAGINAL BIRTH AFTER CAESAREAN

Daniel Fidalgo (1), Maria Vila Pouca (1), Dulce Oliveira (1), Renato Natal (1), Marco Parente (1), Kristin Myers (2), Ewelina Malanowska (3)

1. INEGI – Institute of Science and Innovation in Mechanical and Industrial Engineering / DEMec, Faculty of Engineering of University of Porto, Porto, Portugal; 2. Department of Mechanical Engineering, Massachusetts Institute of Technology, Cambridge, MA 02139, USA; 3. Department of Gynecology, Endocrinology and Gynecologic Oncology, Pomeranian Medical University, Szczecinm Poland

Introduction

Caesarean section (CS) is one of the most common surgeries worldwide [1]. CS surgery rates has been increasing worldwide, both in developed and undeveloped countries. Latin America and the Caribbean region represent the highest CS rate (40.5%), followed by Northern America, Oceania, Europe, Asia, and Africa [2]. The mechanical behaviour of a caesarean scar during a vaginal birth after caesarean (VBAC) is not well understood [3]. The aim of this study is to investigate the biomechanical Maylard fibre reorientation and stiffness influence during a VBAC through computational methods.

Methods

A biomechanical model comprising a foetus and a uterus was developed, according to Figure 1, and a chemical-mechanical constitutive model that triggers uterine contractions was used, where some of the parameters were adjusted to account for the matrix and fibre stiffness increase in the Maylard caesarean scar. Several mechanical simulations were performed to analyse different scar fibres arrangements, considering different values for the respective stiffness (Table 1).

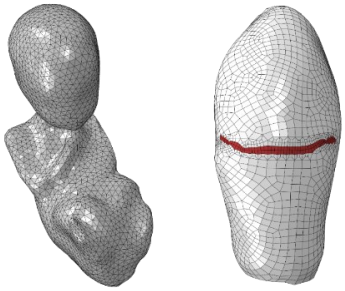

Figure 1: Biomechanical model comprising simplified geometries of a fetus and a pregnant uterus; the zone highlighted in red represents the Maylard scar.

Stiffness Parameters	Value (MPa)
C_{10} *Maylard*	0.0564
μ_{i1} *Maylard*	0.01128
μ_{i2} *Maylard*	1.88

Table 1: Matrix stiffness (C_{10} Maylard) and fibers stiffness (μ_{i1} Maylard and μ_{i2} Maylard, with i=1,2) values of the Maylard uterine scar.

Results

A random fibre distribution in the Maylard scar leads to greater maximum principal stress values than an increase of the Maylard matrix and fibres stiffness (Figure 2). Additionally, the random fibres arrangement exhibits a higher impact on the contraction pattern of the caesarean scar.

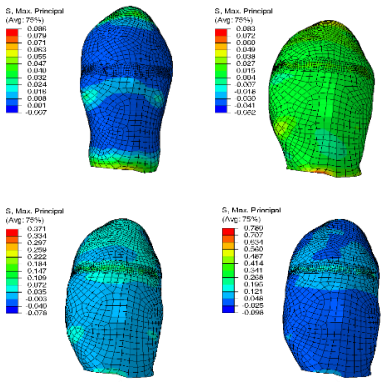

Figure 2: Maximum principal stress distribution in the uterus for the random fibers' arrangement throughout the simulation; it is evident a stress concentration in the Maylard region.

Discussion

The results revealed that a random fibre arrangement in the Maylard scar has a much higher impact on its mechanical behaviour during a VBAC than the common fibres arrangement present in the uninjured uterine tissue. An increase of the matrix scar stiffness exhibits a lower impact, while an increase of the fibre's stiffness has no significant influence.

References

1. Z. Rusavy et al, BMC Pregnancy Childbirth, 19:1-7, 2019.
2. A.P. Betrán et al, PLoS One, 11:1-12, 2016.
3. M.B. Landon et al, Obstet Gynecol., 108:12-20, 2006.

Acknowledgements

This research was supported by the LAETA, Portuguese FCT Grants 2020.05400.BD and "A TUA" UIDB/50022/2020, Individual Junior Researcher Contract 2020.01522.CEECIND, and research project NORTHE-01-0145-FEDER-030062 (SIM4SafeBirth) financed by NORTE2020, through FEDER.

BIOMECHANICS OF FETAL HEAD MOLDING DURING VAGINAL DELIVERY

Rita Moura (1), Maria Vila Pouca (2), Dulce Oliveira (2), Marco Parente (2), Teresa Mascarenhas (1), Renato Natal Jorge (2)

1. CHUSJ, FMUP, Portugal 2. INEGI-LAETA, FEUP, Portugal;

Introduction

During vaginal delivery, the fetal head molds into an elongated shape to adapt to the birth canal, a process known as fetal head molding. However, excessive molding can occur due to prolonged labor or strong contractions, leading to several disorders on the fetal head [1]. The mechanism of the molding process is mainly explained by the presence of sutures and fontanelles, and the elasticity of the skull bones, which can displace in relation to one another and overlap [2]. The sutures are dense connective tissue membranes composed of collagen fibers and, when under load, behave in a viscoelastic manner [3]. This work aims to perform a numerical study on the biomechanics of fetal head molding during the second stage of labor.

Methods

A finite element model of the pelvic floor muscles and the fetal head was used [4]. The fetal head is composed of the skin and soft tissues, the skull with sutures and fontanelles, and the brain. The sutures and fontanelles were modeled with membrane elements and characterized by a visco-hyperelastic constitutive model [5] adapted to a plane stress state. The material parameters for the sutures and fontanelles were based on a 2-month-old donor's suture [6].

The simulations were performed in Abaqus® to mimic a vertex presentation and occipito-anterior position. Three different simulations were performed to evaluate the impact of the duration of the second stage of labor on fetal head molding (20, 100 and 200 minutes for precipitous, normal, and prolonged labor, respectively). The fetal head molding was evaluated by monitoring three different diameters: suboccipito-bregmatic (SOBD), biparietal (BPD), and maxilo-vertical (MaVD) and calculating the molding index (MI) [7]:

$$MI = \frac{MaVD}{BPD \times SOBD} \quad (1)$$

Results

The variation of the MI during the vertical displacement of the fetal head for different durations of the second stage of labor is shown in figure 1. The results demonstrate that the longer the duration of this stage, the greater the molding index, which means that the deformations that the head undergoes are greater. The maximum MI corresponds to 1.88 for a prolonged labor. Table 1 presents the variation of the diameters at the end of the second stage of labor simulated for 100 minutes in comparison with literature [7].

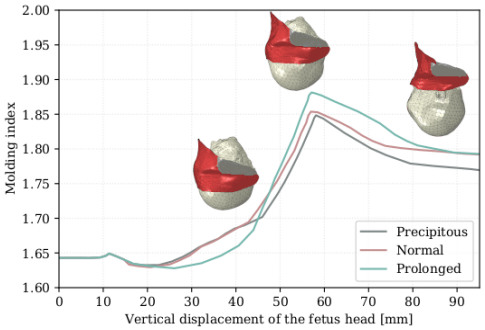

Figure 1: Variation of the molding index during the vertical displacement of the fetus for different durations.

	Variation (mm)	
Diameter	Normal	Literature [7]
SOBD	-0.81	-2.70
BPD	-4.04	-0.40
MaVD	+1.84	+2.10

Table 1: Change of diameters at the end of the simulation in comparison with literature.

Discussion

Results show that the fetal head undergoes higher deformations for prolonged labors (figure 1). These results are in accordance with the clinical study of Kriewall *et al.* [8] which reported a significant correlation between the length of the second stage of labor and the molding index. The variation of SOBD and MaVD is according to literature. The major difference is verified in the BPD which can indicate that the simulation is closer to the type of labor where an overlapping of the parietal bones is registered. A percentage of molding of 9.1% was obtained, slightly greater than the one reported in the clinical study (5.8%) [7]. The present study reflects an advance in the field of the biomechanics of childbirth. The molding process was quantified recurring to non-invasive methods, which can be a first step in the anticipation of problems that may occur during childbirth.

References

1. DeCherney et al, Current Diagnosis & Treatment Obstetrics & Gynecology, 2012.
2. Vlasyuk V. Curr. Neurol. Neurosci., 1(2), 2018.
3. Romanyk et al, Orthod Craniofac Res, 19:28–35, 2016.
4. Parente et al, Int Urogynecol J, 19: 65–71, 2008.
5. Vila Pouca et al, Int J Numer Meth Biomed Engng, 34(3):e2927, 2017.
6. Coats et al, J. Neurotrauma, 23(8):1222–1232, 2006.
7. Sorbe et al, Int. J. Gynecol. , 21(3): 205–212, 1983.
8. Kriewall TJ et al, J Perinat Med, 5(6):260–7, 1977.

BIOMECHANICAL STUDY OF DIFFERENT BIRTHING POSITIONS

Margarida Borges (1), Dulce Oliveira (2), Marco Parente (2), Teresa Mascarenhas (1), Renato Natal (2)

1. Centro Hospitalar Universitário de São João, Faculty of Medicine, University of Porto, Portugal;
2. INEGI-LAETA, Faculty of Engineering, University of Porto, Portugal

Introduction

During the second stage of labor, there are several birthing positions that can be adopted, and the outcomes may vary. These can be classified into two main groups: positions in which the weight is off the sacrum (flexible sacrum positions), allowing the coccyx to move, and positions where the weight is on the sacrum (non-flexible sacrum positions) and the coccyx movement is restricted. However, there is a limited scientific evidence to support the most ideal birthing position. To the best of our knowledge, only few studies perform a biomechanical analysis of the musculoskeletal system changes, and the pubic symphysis (PS) widening was not considered. Therefore, this work aims at contributing to a better knowledge associated with the PS widening and the biomechanics of different birthing positions.

Methods

To simulate the second stage of a vaginal delivery, a validated finite element model was used, which includes pelvic floor muscles (PFM), pelvic girdle bones and fetal head [1]. The maternal pelvic diameters were modified according to female pelvic outlet dimensions [2]. Two birthing positions were mimicked: the flexible sacrum model, in which the coccyx can move, and the non-flexible sacrum model, in which its movement is more restricted. Sacroiliac, sacrococcygeal and PS joints were modeled to study the effects induced in the PS, coccyx, sacrum, PFM and the fetus head. Additionally, a set of geometric constraints and boundary conditions were used and the vertical descent of the fetal head and its flexion/extension were imposed. The fetus model was in vertex presentation and occipitanterior position and the second stage of a birth was simulated using ABAQUS software.

Results

Despite being simulated an occipitanterior position, the bones and PFM imposed some constraints, and the predominant position was the left occipitanterior. Regarding the PS, the flexible sacrum model presented a maximum widening of 3.2 mm, while the other model had a maximum value of 6.3 mm (figure 1), but no rupture of this joint was observed [3]. The coccyx rotation was also analyzed and a notable divergence between both models was observed: the non-flexible sacrum model had a maximum rotation of 3.6°, while the flexible sacrum model had a maximum rotation of 15.7°. It is important to note that these values occurred at, approximately, the same instant of maximum PS widening. Furthermore, by analyzing the maximum principal stresses on the cortical bone of sacrum and coccyx, a greater impact was observed in the non-flexible sacrum model, but no serious injuries occurred [4]. Concerning the PFM, in the flexible sacrum model, higher stress values were observed in the left area of the levator ani, namely in the pubococcygeal muscles.

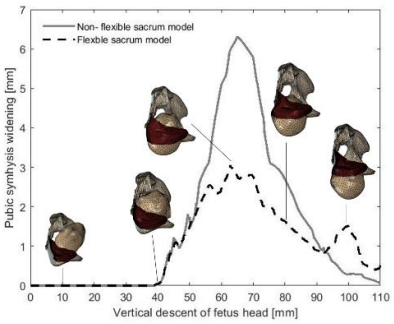

Figure 1: PS widening during fetus descent.

Discussion

The simulations performed showed that in flexible sacrum positions, a higher coccyx rotation and a lower widening of the PS occur than in positions in which the coccyx movement is restricted (non-flexible sacrum positions), but slightly higher stresses were detected in the PFM. Thus, it was verified that in non-flexible sacrum positions the presence of a surface under the mother may close the pelvis, causing a decrease in the available pelvic space. These results are consistent with the literature [1,5,6]. Regarding the clinical benefits, it was observed that different birthing positions lead to changes in the pelvic space, helping to reduce the risk of obstructed labor and the development of several disorders. More specifically, positions in which the weight is off the sacrum avoid a high effort of the PS and a high impact on the sacrum and coccyx, appearing to be more beneficial for the mother pelvis.

References

1. Parente et al, Int Urogynecol J, 19:65-71, 2008
2. Michel et al, Am J Roentgenol, 179:1063-1067, 2002
3. Hwang et al, Musculoskeletal Health in Pregnancy and Postpartum, 171-179, 2015
4. Ricci et al, J Exp Orthop ,5:33, 2018
5. Desseauve et al, Eur J Obstet Gynecol Reprod, 208:46-54, 2017
6. Reitter et al, Am J Obstet Gynecol, 211:662.e1-9, 2014

Acknowledgements

This research was supported by Portuguese FCT under research project UIDB/50022/2020 and by the project NORTE-01-0145-FEDER-030062 (SIM4SafeBirth) cofinanced by NORTE2020, through FEDER.

QUANTIFYING 3D SHAPE CHANGES TO THE DEEP AND SUPERFICIAL MUSCLES OF THE PELVIC FLOOR IN PREGNANT WOMEN

Megan R. Routzong (1), Liam C. Martin, (1), Ghazaleh Rostaminia (2), Pamela A. Moalli (3), Steven D. Abramowitch (1)

1. Department of Bioengineering, University of Pittsburgh, Pittsburgh, PA, USA; 2. Division of Urogynecology, University of Chicago, Skokie, IL, USA; 3. Department of Obstetrics, Gynecology & Reproductive Surgery, University of Pittsburgh, Pittsburgh, PA, USA

Introduction

During pregnancy, maternal pelvic organs and tissues undergo dramatic remodelling [1,2]. Evidence suggests that these hormone- and mechanically induced changes alter the shape of the maternal anatomy, purportedly to prepare the maternal pelvic soft tissues for vaginal birth [3,4]. The aim of this study was to quantify the maternal pelvic floor—including deep and superficial muscles—shape variation in pregnancy to define relationships between shape and gestational age.

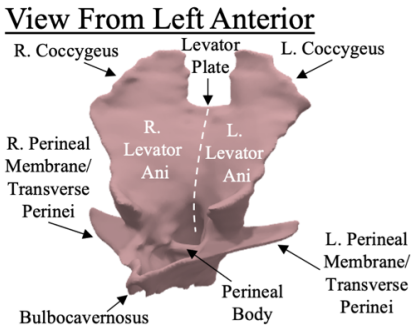

Figure 1: The geometry of the deep and superficial muscles of the pelvic floor modeled as a complex with relevant anatomy labelled.

Methods

This was a retrospective study approved by the Institutional Review Board at the University of Pittsburgh and considered exempt at Northshore University HealthSystem. Pregnant women (N= 28, age 20-49 years) who underwent pelvic MRI were included. The pelvic floor and associated muscles were segmented as one unit to reduce computational costs (Figure 1).

Corresponding shapes were imported into Mathematica™ to execute a previously established statistical shape modelling workflow [4]. This involved a Procrustes analysis; principal component (PC) analysis; and parallel analysis to determine significant modes of variation. PC scores were dependent variables in the ensuing partial correlation to determine which modes had significant associations with gestational age, while controlling for BMI and maternal age.

Results

Six significant modes of variation explained 27%, 15%, 11%, 9.1%, 5.3%, and 3.9% of the total shape variance. Mode 3 was inversely correlated with gestational age (ρ = -0.649, p = 0.022). Qualitatively, mode 3 implies that the urogenital hiatus (the opening anterior to the perineal body) widens, the superficial perineal structures bulge inferiorly-anteriorly, and the coccygeus becomes more vertical with increased gestational age (Figure 2).

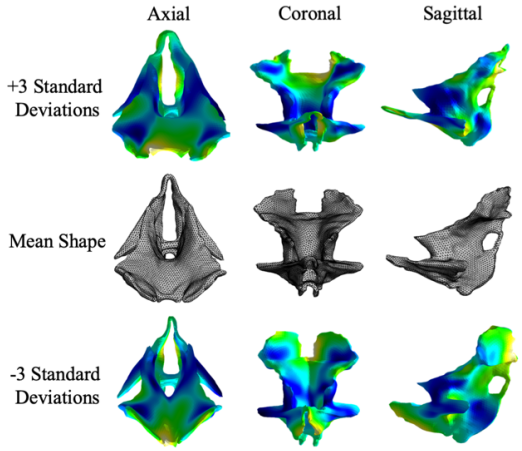

Figure 2: Visualization of mode 3. Dark to light colors signify regions with minimal to maximal variation from the mean shape.

Discussion

This unbiased, robust 3D analysis demonstrates that pregnancy influences specific aspects of maternal pelvic shape—most notably, the superficial perineal structures and coccygeus. This provides evidence that the maternal pelvic musculature noticeably remodels in pregnancy presumably to reduce the amount of stretch experienced during vaginal delivery, thereby preventing acute injury.

References

1. Alperin, M, Impact of Pregnancy and Delivery on Pelvic Floor Biomechanics, 229-238, 2016.
2. Catanzarite, T et al, Am J Obstet Gynecol, 218:512.e1-512.e9, 2018.
3. Shek, KL et al, Int Urogynecol J, 23:1561-1567, 2012.
4. Routzong, MR et al, Comput Methods Programs Biomed, 194, 2020.

Acknowledgements

We acknowledge use of the University of Pittsburgh Center for Research Computing advanced computing resources. This material is based upon work supported by the NSF GRFP under Grant #1747452.

CERVICAL REMODELING: AN INTERPLAY BETWEEN THE COLLAGEN FIBER MICROSTRUCTURE AND MICROMECHANICAL PROPERTIES

Amir Ostadi Moghaddam (1), Zixi Lin (2), Mayandi Sivaguru (1), Heidi Phillips (1), Barbara McFarlin (3), Kimani Toussaint (2), Amy Wagoner Johnson (1)

1. University of Illinois at Urbana-Champaign, USA; 2. Brown University, USA; 3. University of Illinois at Chicago, USA

Introduction

Preterm birth (PTB) affects millions annually worldwide. The current screening tools are not sensitive enough to reliably assess the risk of PTB, and etiology of premature labor remains elusive.

Cervical tissue, which connects the uterus to the vagina, has an important biomechanical role during pregnancy; it stays firm to retain the fetus, but undergoes a remodeling process that is necessary for delivery. However, early remodeling can lead to PTB.

Cervical remodeling alters the cervix microstructure and micromechanical properties, but the relationship between these changes is poorly understood. Here, we probe these properties for rat cervix using nanoindentation (NI) and second-harmonic generation microscopy (SHG), respectively, at several gestational stages. The results offer fundamental knowledge of the structure-mechanical properties relationship of the cervix and open the possibility for such techniques to be used for evaluating the risk of PTB.

Methods

Sample preparation: 15-days (n=2), 17-days (n=2), and 21-days (n=3) pregnant Sprague Dawley's rat cervices were harvested and cryosectioned (−20°C) at mid-cervix, perpendicular to the cervical canals.

SHG microscopy: Samples were imaged with a confocal microscope (Zeiss LSM 710, Oberkochen, Germany, 40x objective lens). Circular variance (CV) was used to quantitatively describe the spread of fiber orientations.

NI: A Piuma nanoindenter (Optics11, Amsterdam, Netherlands) with a spherical probe indented samples submerged in PBS along a medial-lateral line every 25 µm. Indentation modulus, E, was calculated using the Hertz model [1]. The tip radius and stiffness were 22.5 µm and 0.04 ± 0.02 N/m, respectively. The protocol for co-registering the NI and SHG data is in [2].

Statistical analysis: A one-way ANOVA with a post hoc Tukey test compared the data from different groups. Pearson's r assessed correlations.

Results

Figure 1 is a representative optomechanogram [2] of a 17-days pregnant cervix. Both local mechanical properties and microstructure vary spatially. Quantitative SHG analysis shows that as pregnancy progresses from 15 to 21 days, the collagen fibers become more disorganized, increasing CV (Figure 2A) with a positive and significant correlation (r=0.81, p=0.027), and E decreases (Figure 2B) with a negative and significant correlation (r=-0.85, p=0.016). While these trends are expected, CV and E data have not previously been co-registered and the spatially varying data have not been reported for pregnant rat tissue.

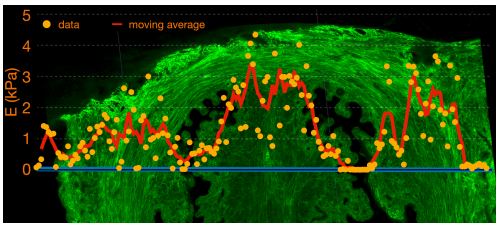

Figure 1: Representative optomechanogram of a 17-days pregnant cervix

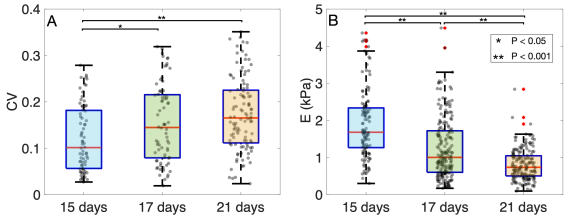

Figure 2: CV (A) and E (B) at different gestational stages

Discussion

Physiological changes during pregnancy, e.g., changes in hormone levels and tissue composition, alter the cervix microstructure and micromechanical properties to allow for natural birth. We quantified and co-registered these changes in a rat model to quantify cervical remodeling.

Evaluating the relationship between the microstructure and micromechanical properties of the cervix paves the way for assessing the risk for PTB from medical images, given that direct mechanical measurements are not often clinically feasible.

Limitations of the study are that we only quantified the tissue microstructure in 2D and did not further investigate the region-specific variations of the properties during gestation. Future studies will consider the 3D microstructure and these region-specific variations in detail.

References

1. K. L. Johnson, Cambridge University Press, 1985.
2. W. Lee et al., Scientific reports, 11, 2021.

BIOMECHANICAL INVESTIGATIONS INTO THE CERVICAL CERCLAGE

Alexa Baumer (1), Megan C. Leftwich (1), Alexis Gimovsky (2), Michael Gallagher (2)

Enter the affiliation information here ("Affiliation" style)
1. Department of Mechanical and Aerospace Engineering, The George Washington University, U.S.A., 2. School of Medicine and Health Sciences, Division of Maternal Fetal Medicine, Department of Obstetrics and Gynecology, George Washington University, U.S.A.

Introduction

Premature cervical remodeling, also called cervical insufficiency, is a medical condition in which the uterine cervix is unable to retain a pregnancy in the absence of the signs and symptoms of contractions, labor, or both during the second trimester [1]. Typically diagnosed between 18 and 22 weeks, if left untreated, it is a common cause of second trimester pregnancy loss. Once the condition is detected, part of the treatment plan could be the cervical cerclage procedure. The cervical cerclage is a purse string suture designed to close the cervix and maintain the pregnancy. There are conflicting findings on the efficacy of this procedure with most research studies focused on statistical evidence. It is our aim to understand the underlying biomechanics of when the procedure is more likely to succeed. To investigate this question, we design generalized models of the cervix and fabricate them from silicone. The models mimic physiological, softening tissue as assessed by physicians at The George Washington University Hospital. Geometric parameters such as cervical length, shape, and dilatation are varied in the models to analyze under which circumstances the cerclage mechanics best maintain integrity.

Methods

Ultrasound images were collected from the clinic and used to create a generalized model of the cervix. The synthetic cervices were fabricated out of Eco-Flex 00-30 silicone. A summary of these steps can be seen below in Fig. 1. To decide on a ratio of silicone thinner added to the mixture, we created a range of samples and relied on the qualitative analysis of physicians at The George Washington University Hospital. A group of clinicians felt each sample to assess which represented firm, healthy cervical tissue and which represented softening cervical tissue.

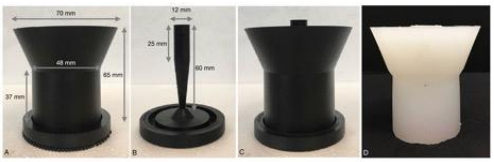

Figure 1: The generalized model of the cervix is shown in Panels C. Panels A and B depict the exterior and interior pieces of the model, both are configurable for different parameters of interest (cervical length, dilatation for example). Panel D shows the silicone cast prior to suturing.

Once the thinner percentages were agreed upon, we fabricated cervices in three groups initially: a "hard" group, a "medium" group, and a "soft" group. The synthetic models were then stitched with a McDonald cerclage by physicians. These sutured cervices were placed in capsules to constrain their motion during compression tests on the suture. Force on the stitch was increased until failure, chosen as the point when the cerclage began to tear through the synthetic tissue. In addition to the tissue stiffness parameter, we varied the length of the cervix and the inner geometry. The experimental procedure was repeated through all groups. An additional group of cervices was stitched with two different types of suture material.

Results

The first set of experiments investigating the impact of tissue stiffness on cerclage integrity revealed the firm cervices were able to withstand higher forces before failure. Investigations into the impact of cervical length revealed longer cervices were able to withstand higher forces before rupture; however, the dependence was less than that of the stiffness investigation. The group of cervices stitched with two different materials revealed Mersilene tape were able to hold a cerclage in place at significantly higher forces than the monofilament sutures.

Discussion

In investigating the biomechanics of the cervical cerclage, we can begin to understand which parameters are critically important for maintaining the suture integrity. Further, expanded studies and more physiologically accurate models of the cervix could assist clinicians in creating more effective treatment plans for patients suffering from premature cervical remodeling.

References

1. American College of Obstetricians, Gynecologists. "ACOG Practice Bulletin No. 142: Cerclage for the management of cervical insufficiency." *Obstetrics and gynecology* 123.2 Pt 1 (2014): 372-379.

Acknowledgements

We thank Dr. Scott Peterson for his assistance with analysing synthetic cervices and performing cerclages. A. Baumer is funded by The George Washington University Provost Graduate Fellowship.

MONTE CARLO SIMULATION OF PELVIC FLOOR SUPPORT BIOMECHANICAL MODEL: POPSIM

Mark T. Gordon, PhD (1), Carolyn W. Swenson, MD (2), John DeLancey, MD(2), Luyun Chen Ph.D(2,3)

1. Biomedical Engineering, California Baptist University, Riverside, CA, USA;

2. Obstetrics and Gynecology, 3. Biomedical Engineering, University of Michigan, Ann Arbor, MI, USA;

Introduction

Pelvic organ prolapse is a distressing condition in which the pelvic organs protrude through the vaginal opening (genital hiatus). The pathomechanics of prolapse is complex and involves structural and material property impairments in apical support and genital hiatus (GH) closure. Enlarged genital hiatus (GH) is present in 80% of women with prolapse and has recently emerged as a key risk factor preceding prolapse development and recurrence of prolapse after surgical treatment. It is unknown how much GH reduction is necessary to restore normal support for women with varying apical support which is difficult to quantify *in vivo*. The goal of this study is to develop a Monte Carlo simulation plug-in for a biomechanical model, POPSIM[1], to investigate the effect of variation and uncertainty of structural and material property inputs on the simulated prolapse. We demonstrate the application of this plug-in by predicting the statistical distribution of exposed vaginal length and apical tension for determined hiatus sizes while considering the random variation in apical ligament and vaginal wall geometry and material property.

Method

POP-SIM is a validated finite element biomechanical model simulation platform[1]. It consists of anatomically based FE models and a suite of Python-based tools developed to rapidly construct models with desired structural parameters representing morphological variation observed in women with and without prolapse. In this study, we developed a Monte Carlo Simulation plug-in using Python. The mean and standard deviation of the input variables and their correlations were accepted as inputs to create the joint Gaussian distribution. A random number generator then sampled this distribution and generated the input parameters for POPSIM input files together with other deterministic input parameters. In this study, resting GH size is the deterministic input while apical descent, cardinal ligament length and vaginal length and ligament material property are modelled as jointly distributed random variables with correlation between the variables measured in women with prolapse (Figure 1A). A total of 210 simulation models for seven different GH sizes were constructed. All of the models were loaded with 100 cmH_2O intra-abdominal pressure and solved using ABAQUS explicit solver. Exposed vaginal lengths and apical ligament tensions were calculated for each model at maximum pressure loading (Figure 1B).

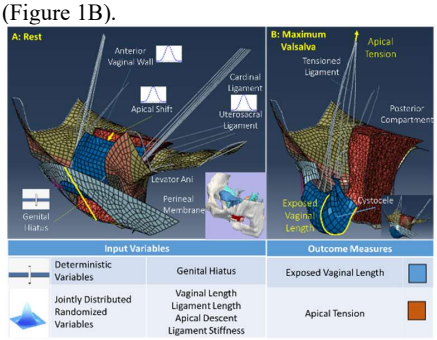

Figure 1 A: Modified input variables in the resting model. B: Output measures at simulated maximum Valsalva in a midsagittal slice.

Results

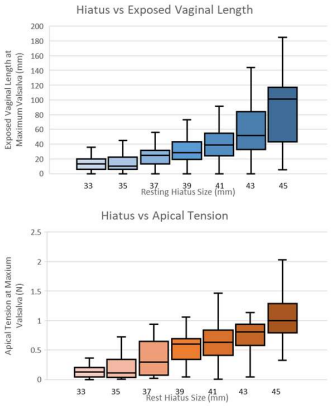

Figure 2 Simulated statistical distribution of exposed vaginal length and apical tension at Maximum Valsalva. The boxplots show the median, IQR and confident bound.

The boxplots at each resting GH size level were used to demonstrate the median, inter-quantile range (IQR), and total range of the simulation outcomes (Figure 2). The median of predicted exposed vaginal length increases non-linearly with resting GH. The IQR and overall range also increase significantly with larger resting GH size. For apical tension, the median increases linearly with GH sizes with similar IQRs.

Discussion

The Monte Carlo plug-in for POPSIM is a valuable tool providing the ability to estimate the probability distribution of outcomes considering random variation of the structure geometry and material property. Simulation results suggest that the greater probability of women with longer exposed vaginal length and larger apical tension increase with increasing of GH size.

References

1. Gordon, M.T., et al., *Development of anatomically based customizable three-dimensional finite-element model of pelvic floor support system: POP-SIM1.0.* Interface Focus, 2019. **9**(4): p. 20190022.

Acknowledgements

This work was supported by grant # R01 HD094954 from National Institution of Health of United State America.

INSIGHTS INTO PELVIC FLOOR MUSCLE BIOMECHANICS USING A NOVEL INTRA-VAGINAL PRESSURE SENSOR DEVICE (FEMFIT®)

Laura Pedofsky (1), David Budgett (1), Poul Nielsen (1,2), Hannah Orr (1), Jennifer Kruger (1)

1. Auckland Bioengineering Institute, University of Auckland, New Zealand; 2. Department of Engineering Science, University of Auckland, New Zealand

Introduction

One quarter of women will suffer from pelvic floor dysfunction such as urinary incontinence or pelvic organ prolapse (POP). Urogenital hiatus (GH) dimensions are affected by POP [1]. Vaginal pressures are likely to reflect this change due to the POP distorting the anterior and/or posterior wall of the vagina.

The use of pressure as a physiological measure to determine pathophysiology is not new, however measuring a vaginal pressure profile is a relatively new concept. The femfit® has been specifically designed to measure a profile using eight pressure sensors embedded in a soft, flexible silicone that conforms to the natural vaginal anatomy. The sensors provide independent functional measurements along the length of the vagina, capturing the three vaginal pressure zones simultaneously [2]. We propose that an intravaginal pressure sensor device (femfit®) can be used to understand the relationship between the GH, pressure and PFM dysfunction, and provide insight for diagnosis and treatment.

Real-time observation of baseline pressure and changes in pressure profiles during various activities have been measured using femfit® communicating via Bluetooth to a tablet application.

Applications and Results

The femfit® has been used in several clinical studies and found to be a valid and reliable tool to measure the vaginal profile during normal activation and relaxation of the PFM and in women pre and post surgery for POP [3-5]. It has also demonstrated utility for assessing the contribution of other muscle groups to a targeted PFM contraction [6].

To date the femfit® has been well-accepted by participants, indicating that women would be comfortable using this device in a clinical environment.

Research into the relationship between change in anatomical dimensions of the GH during PFM activation, (measured with transperineal ultrasound and the femfit® simultaneously) is underway. An ongoing clinical study will investigate the effectiveness of biofeedback provided by the femfit® to see whether it can help women effectively contract their PFM, and exercise at home. Preliminary results will be available for presentation at the conference.

Discussion

If successful, these applications could have significant impact, for postpartum women in particular. If the profile is able to reflect the anatomical status of the GH, this would provide a better understanding of PFM dysfunction biomechanics and the implications of a change in the pressure profiles.

A femfit® measured pressure profile is already shown to be useful for simultaneous measurement of the vaginal pressure zones and its use during functional activities. We believe future applications include the providing a useful objective metric to assess PFM function, quantify surgical success and/or encourage women to maintain their PFM health through home PFM exercises. The femfit® could be the standard instrument to provide quick and valuable information on the status of the GH and thus the integrity of PFM, guiding clinical treatment.

References

1. Dietz, H.P., The aetiology of prolapse. International Urogynecology Journal, 2008. 19(10): p. 1323-1329.
2. Guaderrama, N.M., et al., The vaginal pressure profile. Neurourology and Urodynamics, 2005. 24(3): p. 243-247.
3. Cacciari, L.P., et al., Reliability and validity of intravaginal pressure measurements with a new intravaginal pressure device: The FemFit®. Neurourology and Urodynamics, 2019.
4. Marriott, J., et al., Assessing vaginal pressure profiles before and after prolapse surgery using an intravaginal pressure sensor (femfit®). Int Urogynecol J, 2020.
5. Tian, T., et al., Assessing exercises recommended for women at risk of pelvic floor disorders using multivariate statistical techniques. International Urogynecology Journal, 2018. 29(10): p. 1447-1454.
6. Kruger, J., et al., Can you train the pelvic floor muscles by contracting other related muscles? Neurourology and Urodynamics, 2019. 38(2): p. 677-683.

MECHANOTRANSDUCTION IN EARLY EMBRYONIC BIOCHEMICAL / BIOMECHANICAL PATTERNING AND ANCIENT METAZOAN ENDOMESODERM EVOLUTIONARY EMERGENCE

Emmanuel Farge
Mechanics and Genetics of Embryonic Development group, CNRS, UMR168, Institut Curie, Paris, France

Bilaterians are complex organisms, characterized by the existence of a mesoderm tissue from which most of animal complex organs develop. Mesoderm emerged 570 million years ago from cnidarians that are characterized by and ectoderm and an endoderm only. The lack of conservation of biochemical signalling proteins upstream of early embryonic mesoderm differentiation across bilaterians prevents to answer the question of the signal having been at the origin evolutionary origin of mesoderm emergence and complex animals. We found the mechanical phosphorylation of the Y654 site of □-catenin at junctions by the first morphogenetic movements of embryogenesis, leading its release to the cytoplasm and nucleus, as involved and conserved in earliest mesoderm differentiation in the vertebrate zebrafish and un-vertebrate Drosophila, two species having directly diverged from the last common ancestor of bilaterians. We thus proposed mechanical activation of □-catenin signalling as having been involved in mesoderm differentiation of first bilaterian complex animals, around 600 million years ago [1].

The underlying molecular mechanism consists in the mechanical opening of the evolutionary conserved Y654-D665 major site of interaction between β-catenin and E-cadherin, favouring Y654-β-catenin phosphorylation by Src42A, which mechanotransductively impairs the interaction and leads to β-catenin release from the junctions [2]. Upstream of the first morphogenetic movement of embryogenesis, we found additional mechanotransductive cues, stimulated by mesodermal apex soft pulsations, triggering the medio-apical stabilisation of Myo-II leading to mesoderm invagination, namely to gastrulation, in drosophila embryos [3].

We are currently finding these properties as having possibly been inherited from mechanically induced evolutionary emergence of first metazoan endomesoderm, dating back to at least 700 million years ago.

Extended to tumour biology and cancer progression, we found mechanical activation of β-catenin as conserved in mice and involved in the mechanical activation of tumorigenic biochemical pathways, in the healthy epithelium compressed by the neighbouring tumour, in response to tumour growth pressure *in vivo* [4-6].

References

1. Brunet, T. et al. Evolutionary conservation of early mesoderm specification by mechanotransduction in Bilateria. Nature communications 4, doi:10.1038/ncomms3821 (2013).
2. Roper, J. C. et al. The major beta-catenin/E-cadherin junctional binding site is a primary molecular mechano-transductor of differentiation in vivo. eLife 7, doi:10.7554/eLife.33381 (2018).
3. Mitrossilis, D. et al. Mechanotransductive cascade of Myo-II-dependent mesoderm and endoderm invaginations in embryo gastrulation. Nature communications 8, 13883, doi:10.1038/ncomms13883 (2017).
4. Whitehead, J. et al. Mechanical factors activate beta-catenin-dependent oncogene expression in APC mouse colon. HFSP journal 2, 286-294, doi:10.2976/1.2955566 (2008).
5. Fernandez-Sanchez, M. E., Barbier, S. & al., e. Mechanical induction of the tumorogenic β-catenin pathway by tumour growth pressure. Nature (In press).
6. Fernandez-Sanchez, M. E., Brunet, T., Roper, J. C. & Farge, E. Mechanotransduction's Impact in Animal Development, Evolution, and Tumorigenesis. *Annu Rev Cell Dev Biol*, doi:10.1146/annurev-cellbio-102314-112441 (2015)

BIOMECHANICS OF CERVICAL FUNNELING IN HIGH-RISK PREGNANCIES

Erin Louwagie (1), Mirella Mourad (2), Chia-Ling Nhan-Chang (2), Joy Vink (2), Ron Wapner (2), Kristin Myers (1)

1. Columbia University, USA; 2. Columbia University Irving Medical Center, USA

Introduction

In 2014 there was an estimated 15 million preterm births globally, where preterm birth was the leading cause of neonatal death [1]. There is currently no accurate way to predict preterm birth (PTB), though it is believed that the biomechanical failure of reproductive tissues may be a cause [2,3]. Cervical insufficiency (CI) is the failure of cervical tissue [2]. Though there is currently no universally standard way of diagnosing CI, cervical funneling is deemed to be clinical evidence of CI and is associated with a higher risk of PTB [2,4]. Identifying the mechanisms of cervical funneling will improve understanding of PTB and identify early structural diagnostic biomarkers.

Due to the difficulty of *in vivo* pregnancy research, computational models are a suitable method to explore the mechanics of CI and cervical funneling. Previous computational research has successfully shown the cervical funnel shape progression, but has not distinguished the mechanisms through which it occurs [5]. Our goal is to ascertain the biomechanics of cervical funneling through the use of parametric patient-specific computational models of high-risk pregnancies.

Methods

Ultrasounds measurements were obtained from 5 pregnant women at high-risk for PTB at Columbia University Irving Medical Center. The parametric measurements from ultrasounds were collected as outlined in Westervelt et al., and patient-specific solid models were built [6]. Each model was built with the same weak cervical fibrous material properties to assess how anatomical differences affect loading [7, 8]. The uterus was modelled as a passive fiber composite material based on tensile tests of pregnant uterine tissue [9]. The abdominal tissue was considered to be nearly incompressible neo-Hookean. The fetal membrane was modelled as a transversely isotropic fiber-based material with a compressible Neo-Hookean ground substance based on existing literature [10]. Quarter model geometries were used to decrease computational time. The boundary conditions applied were as follows: fetal membranes sliding on the uterine wall and cervix, the uterus tied to the abdomen, the cervix sliding along the abdomen and vaginal canal, and the entire model fixed along the outside surface. A gestational intrauterine pressure of 1kPa was applied to the inner membrane surface. FEBio (v2.8.5) was used for model simulations.

Results

Cervical funneling occurs in all five of the high-risk FEA models. In the simulation, cervical funneling is initiated through thinning of the lower uterine segment, and then by compression of the cervix by the fetal membrane and the opening of the internal os. In the set of models with varied geometry and the same cervical properties, cervical stretch varied and as did location of maximum stretch.

Discussion

The computational simulations of cervical funneling can accurately capture the funnel shape in some patients (Fig. 1). Complex funnel shapes are distinctly different from their corresponding FEA model cervical funnel.

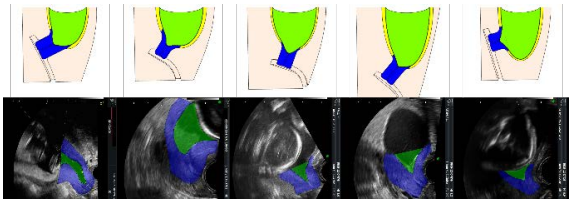

Figure 1: Visual comparison of cervical funnel in FEA model to corresponding transvaginal ultrasound.

Between the FEA models with the same weak cervical stiffness, differences are observed in cervical stretch value and location of cervical stretch showing that patient anatomy influences cervical loading. Therefore, both cervical stiffness and patient anatomy are important in understanding the mechanics of cervical funneling. This work also shows that lower uterine segment thinning could be a precursor to cervical funnel initiation and could be used as a biomechanical biomarker of PTB for earlier prediction.

References

1. Chawanpaiboon, S, et al., *The Lancet Global Health*, 7.1: e37-e46, 2019.
2. Vink, J et al., Semin Fetal Neonat Med, 21:106-112, 2016.
3. Adams Waldorf, K et al., AJOG, 213:830.e1-19, 2015.
4. Knipe, H et al., "Funneling of the internal cervical os", Radiopaedia, 2018.
5. House, M et al., Clin Anat, 26:97-104, 2013.
6. Westervelt, A et al., J Biomed Eng, 139:051004, 2017.
7. Myers et al., J Biomech, 48:1533-1540, 2015.
8. Badir et al., Prenat Diagn, 33:737-741, 2013.
9. Conrad et al., Am J Ob Gynecol, 96:1055-1059, 1966.
10. Bürzle and Mazza., J Biomech, 46:1777–1783, 2013.

Index

İgde, V., 408
Šileikytė, K., 607

A. González Ballester, M., 335
Aage, N., 534
Abaei, A., 669
Abarca-Ortega, A., 230, 239
Abayazid, F., 406
Abbasian, M., 461
Abdollahi, M., 544
Abel, R., 466
Abelin-Genevois, K., 306
Abler, D., 163, 164
Abramowitch, S., 706
Abuzayda, M., 677
Adachi, T., 217, 248, 519
Adams, R., 399
Adeli Koudehi, G., 654
Adrien, J., 53
Aerts, P., 289
Agrifoglio, M., 231
Aguirre, M., 93, 512
Ahluwalia, A., 220, 250, 667
Aikawa, E., 87
Airoldi, A., 148
Ait Ali, L., 642
Ajami, S., 474, 597, 628
Aka, I., 118
Akexopoulos, L., 620
Akhlaghi, P., 683, 684
Akyildiz, A., 62, 81, 96
Al-Dirini, R., 551
Alaña, M., 390
Alaimo, G., 640
Alamán-Diéz, P., 532
Albani, D., 215
Aldieri, A., 475, 599
Alemani, F., 410
Alessandrelli, G., 524
Alessandrino, A., 672
Ali Agha, S., 427
Alijani, H., 487
Allain, J., 687
Allard, V., 528
Allen, R., 56
Alloisio, M., 672
Alp Caridi, G., 73
Altai, Z., 453
Altundemir, S., 77
Alves, J., 630
Amin, D., 331
Amraish, N., 457
Anderson, P., 294
Andikoetxea, B., 628
André, A., 573, 629
Andrés-Esperanza, J., 552
Andrada, E., 643, 646, 647
Andrade, R., 497
Andriotis, O., 202, 203, 236
Angeli, S., 529
Anic, M., 143
Annoni, M., 699
Antinolfi, P., 421
Antognoli, G., 65
Antonini, L., 65, 122, 166, 602, 613
Antonovaite, N., 264
Antonuccio, M., 609
Apolinar, A., 214
Araújo, V., 431
Arachchi, S., 560
Arampatzis, A., 537
Arbeiter, D., 107
Arbeiter, N., 366
Arcangeli, M., 156
Arduino, A., 488
Arhiptsov, K., 418
Armando, I., 240
Armillotta, N., 421
Armour, C., 169
Arnold, D., 643
Arpa, P., 695
Arrarte Terreros, N., 63
Arsic, B., 143
Aryeetey, O., 494, 495
Asbai-Ghoudan, R., 525
Ashjaee, N., 308
Ashton-Miller, J., 700
Asimus, E., 387, 388

Assi, A., 306
Athanasiou, T., 150, 181
Athanassoulis Makris, G., 389, 452
Atkins, P., 430
Attallah, M., 126
Atttallah, M., 108
Aubin, C., 317, 348
Audenino, A., 111, 254, 344, 475, 500, 599, 686
Audige, L., 278
Auer, S., 298
Augat, P., 288, 367, 409
Auricchio, F., 103, 112, 115, 161, 640
Avadi, M., 386
Avolio, M., 255
Avril, S., 93, 168, 189, 499, 509, 512
Awadalla, M., 436
Ayensa-Jiménez, J., 621
Azadkiya, R., 440
Azari, F., 422
Aznar, I., 128
Azor, A., 400
Azzollini, N., 114, 123

Böhringer, D., 214
Büchler, P., 27, 163, 164, 692, 694
Bańczerowski, J., 662
Bańkosz, Z., 571
Baaijens, F., 245
Bacci, M., 261
Badel, P., 53, 136
Bader, R., 288, 301, 366, 445
Baggiano, A., 187
Bagherifard, S., 483
Baino, F., 240
Baker, A., 302, 405
Bakker, E., 591
Balabani, S., 157
Baldelli Bombelli, F., 211, 674
Baldi, D., 686
Baldit, A., 473
Baleani, M., 481
Ballerini, M., 253
Balocco, S., 272
Baltin, M., 300
Baltina, T., 300
Ban, F., 198
Banfi, G., 482
Barbanti-Bròdano, G., 325
Barbara, Z., 210
Barber, T., 60, 146
Barbonetti, A., 557
Bardi, F., 93
Barikani, H., 676, 683
Baron, C., 533
Barone, A., 611
Barrack, A., 562
Barrasa-Fano, J., 214
Bartholomeeusen, S., 413
Bartocci, E., 201
Baruffaldi, D., 637
Baruffaldi, F., 481, 598
Barzaghini, B., 194, 225
Bashtova, K., 438
Bassani, T., 306, 316
Basso, C., 155
Bastien, C., 407
Bastos, R., 497
Bastounis, E., 238
Battle, L., 202
Bauer, C., 583
Baumbach, S., 415
Baumer, A., 708
Baumgartner, D., 347, 395, 583, 585
Baur, L., 271
Bautista Hernandez, L., 559
Baxan, N., 324
Bayarri-Porcar, V., 269
Becker, L., 589
Beckmann, A., 330
Bednarczyk, E., 513
Bedogni, F., 165
Belgio, B., 261, 625, 635, 695
Belinha, J., 702
Belloni, M., 595
Belluzzi, E., 496
Belvedere, C., 37, 352
Benca, E., 554, 633
Benchekroun, G., 645
Bender, B., 321, 340
Benitez, R., 210
Benjumeda-Wijnhoven, I., 486
Berceli, S., 18, 51, 65, 104
Bereczki, F., 322

Bereuter, L., 658
Berg, V., 193, 204
Bergamasco, G., 111
Bermond, F., 427, 528
Bernabeu, M., 619, 656
Bernard, J., 306
Bernardo, B., 177
Bernava, G., 500
Berni, M., 349, 505
Bernini, M., 65, 166
Bershitsky, S., 193
Berti, F., 120, 122, 385, 602, 613, 627, 632
Berti, L., 558
Berti, S., 121
Bertin, A., 506
Bertozzi, F., 564, 567
Bessa, J., 701
Best, G., 266
Bezy Wendling, J., 184
Bhattacharya, P., 475, 536, 599
Bhattacharya, S., 338, 339
Białecka, M., 304
Biagiotti, M., 672
Bianchi, A., 473, 577
Bianchi, D., 78, 115
Bianchi, M., 57
Biancolini, M., 17, 171, 320
Bicer, M., 442
Biesso, G., 302
Biffi, C., 483
Biffi, E., 538
Biffo, S., 257
Bignardi, C., 111, 240, 344, 475, 686
Bini, F., 229
Birkenmaier, C., 341
Bischof, P., 583, 585
Bissacco, D., 115
Bittolo Bon, S., 636
Black, S., 151
Blaikie, P., 294
Blanch Granada, A., 90
Blauth, M., 375, 430, 459
Blazquez-Carmona, P., 664
Blickhan, R., 643
Bloom, E., 665
Blouin, S., 458
Bluestein, D., 57
Blugan, G., 323
Blunn, G., 364, 448, 476, 484, 661
Board, T., 423
Boaretti, D., 518, 603
Boeri, L., 215
Bollinger, A., 377
Bolshakov, P., 300
Bomberna, T., 652
Bona-Casas, C., 216, 530
Bonetti, L., 675
Bonfanti, M., 157
Bonicelli, A., 466, 467
Bonithon, R., 484, 661
Bonneuil, W., 657
Bono, N., 698
Boodt, N., 63, 95, 96
Boos, M., 354
Bordas, S., 506
Borges, P., 705
Borghi, A., 474, 596, 597, 628
Borgiani, E., 535
Bori, E., 373, 379, 380, 417, 421
Boriani, L., 558
Bornoff, J., 172
Borrelli, S., 344
Boschetti, F., 261, 625, 635, 691, 695, 698, 699
Bottin, F., 273
Bouchot, O., 59
Boudrieau, R., 387, 388
Boukis, A., 151
Bouleimen, A., 545
Boumpouli, M., 64
Bourauel, C., 677, 681, 682, 685
Bouten, C., 213
Bowd, J., 297
Bozkurt, S., 596
Bozzetto, M., 188
Brånemark, R., 554
Bragonzoni, L., 393, 634
Brambilla, N., 165, 167
Brandt-Wunderlich, C., 107
Branni, M., 471
Braun, B., 428
Braun, O., 477
Brayda-Bruno, M., 312
Breakey, W., 596

Brecs, I., 89
Breen, A., 342, 345
Bresci, A., 223
Bridio, S., 63, 595
Britton, M., 464
Brockett, C., 426
Brodie, R., 151
Brown, S., 281, 282, 308
Brunet, J., 53
Brunetti, C., 564
Bruno-Brayda, M., 306
Buśkiewicz, J., 304
Bucci, F., 551
Buccino, F., 482, 483
Budgett, D., 710
Bueno-Orovio, A., 36
Buist, M., 58
Burger, J., 286
Buritica, A., 659
Burke, J., 94
Burkhard, B., 378
Burkhard, F., 655, 658
Burzotta, F., 71
Bussa, F., 523
Butova, X., 204, 207

C. Marques, F., 222, 522
C. Scheuren, A., 222, 522
Cóndor, M., 214
Córcoles-Lucas, M., 230, 239
Cañadas, P., 219
Cabeza, I., 688
Cabeza-Gil, I., 696
Cabrinha, A., 432
Cacopardo, L., 220, 250, 667
Cahalane, R., 96
Caimi, A., 74, 114, 123, 135, 149, 156, 165
Caironi, M., 622
Calò, K., 16, 170
Calame, M., 477
Calcagno, A., 577
Caldiroli, A., 114, 123
Callejas, A., 508
Callens, S., 363
Calvo, B., 688, 693, 696
Camacho, D., 226
Campbell, E., 117
Camuncoli, F., 319, 557
Candiani, G., 698
Cantini, M., 251
Cantinotti, M., 642
Capelli, C., 64, 173, 631
Capellini, K., 17, 127, 185, 609, 642
Cappelletti, S., 114
Capretti, G., 502
Caravaggi, P., 37, 352, 558
Cardoso, D., 267
Cardoso, L., 86, 87
Carelli, S., 194, 225
Carlier, A., 263, 614, 617
Carlino, M., 611
Carnarius, M., 172
Carniel, E., 488, 489, 496
Carré, M., 396
Carrara, M., 231
Carriero, A., 35, 202, 485
Cartier, R., 507
Carty, C., 437
Carugo, D., 655, 670
Carvalhais, A., 582
Carvalho, V., 332
Casari, D., 451, 460, 478
Casarico, G., 537
Casarin, S., 104, 523, 524, 618
Casartelli, N., 439
Caselli, F., 13
Caspar, J., 375
Casquero, H., 216, 530
Cassanmagnago, G., 231
Cassiolas, G., 303, 505
Casteleyn, C., 654
Castellarin, G., 373
Castelvecchio, S., 138, 156
Castilho, M., 46, 80
Castro, A., 258, 260, 332
Castro-Dominguez, F., 152, 600, 601
Catani, G., 405
Catozzi, C., 253
Causa, F., 234, 244
Cava, J., 90
Cavaglià, M., 205, 206
Cavazzoni, G., 328
Cavicchio, M., 627
Cazzola, D., 292, 309

Cebeci, Ö., 429
Cecere, R., 510
Ceelen, W., 221
Celi, S., 17, 93, 121, 127, 132, 168, 171, 173, 185, 608, 609, 631, 642
Cella, U., 17, 171
Cerdá-Boluda, J., 441
Cerdà Pino, J., 530
Cereda, C., 225
Cereda, M., 698
Ceri, S., 257
Cerone, E., 121
Cerrato Casado, A., 530
Cerrato Cassado, A., 216
Cerroni, D., 653
Cerullo, G., 194, 215, 223, 256, 257, 626
Cerveri, P., 365, 523, 524, 618
Cestariolo, L., 148
Cevolini, F., 558
Chaigneau, C., 512
Chakfe, N., 182
Chambert, J., 506
Chan, W., 55, 58, 649
Chanda, S., 242
Chande, R., 312
Charles, Y., 346
Charters, P., 144
Chatelain, B., 506
Chatzizisis, I., 133
Checa, S., 412, 429
Chen, D., 157
Chen, L., 709
Cheng, C., 314
Cheng, J., 306
Cheong, V., 469, 606
Cherkasov, A., 198
Cheung, J., 327
Chevalier, Y., 341, 367
Chiastra, C., 18, 65, 71, 73, 104, 113, 133, 148, 166, 170
Chiesa, I., 636
Chirico, G., 256
Cho, H., 277
Choi, J., 277
Chouly, F., 506
Christen, P., 274, 430
Chu, W., 306
Chun, B., 361
Cibin, F., 291, 542, 543, 569, 570
Cicchetti, A., 653
Cifra, M., 191
Cifuentes de La Portilla, C., 443
Cifuentes De La-Portilla, C., 580
Cilla, M., 76, 142
Cina, A., 316
Ciniglio, A., 291, 435, 542, 543, 569, 570
Cinquepalmi, A., 558
Ciofani, G., 626
Cioffi, M., 185
Ciric, D., 331, 378
Ciriello, L., 385
Citarella, M., 138
Civet, Y., 658
Clark, J., 144
Clavica, F., 655, 658
Cmielewski, P., 436
Cochet, A., 59
Cochis, A., 240
Coelli, S., 577
Coirbay, A., 102
Coleman, R., 200
Collini, M., 256
Collins, C., 430, 459, 527, 603
Colombo, A., 65
Colombo, C., 482
Colombo, F., 18
Colombo, M., 18, 65, 104, 148, 166, 627
Colyer, S., 292
Colzy, J., 441
Compin, M., 73
Conci, C., 256, 626
Conconi, M., 265, 266, 349, 505
Condello, V., 372
Condoluci, C., 537
Condorelli, G., 231
Confavreux, C., 528
Connolly, L., 326
Contassot, D., 182
Conti, M., 103, 112, 115, 155, 161, 174, 175
Contino, M., 106
Conway, C., 162, 180
Cookson, A., 144, 172
Coombe, D., 33
Cooper-White, J., 26

Cop, C., 283
Coppadoro, L., 228, 259
Cordeiro, L., 267
Cornaggia, A., 691
Cornillie, P., 654
Cortesi, M., 545
Corti, A., 18, 65, 86, 87, 104, 220
Costa Angeli, M., 672
Costa, E., 17, 185
Costantino, M., 92, 502, 653, 658
Costanzo, F., 97
Costello, D., 162
Costi, J., 331
Cosyns, S., 221
Courtois, I., 306
Cowburn, J., 292
Crandall, D., 317
Crea, F., 71
Cristofolini, L., 318, 322, 325, 328, 333, 370, 398, 540, 665
Crivelli, D., 294
Crockett, J., 604
Cronin, D., 429
Cross, C., 526
Cruz Saldivar, M., 666
Cuevas, J., 183
Cunningham, S., 650
Curreli, C., 446, 447, 586, 588
Curt, N., 53
Cutri, E., 184

D'Andrea, L., 672
D'Souza, M., 604
Dörsam, I., 681
Dürselen, L., 372, 397, 491, 493
Déjardin, L., 387, 388
Da Roza, T., 582
Dall'Ara, E., 320, 325, 328, 463, 469, 606
Dall'ara, E., 235
Danielli, F., 127, 627
Dannhauser, D., 234, 244
Darowski, M., 445
Daunoraviciene, K., 287
Dauwe, J., 382, 590
Davey, C., 356
Davico, G., 273, 588
Davies, H., 407
Davis, S., 364
Day, G., 424, 604
De Bellis, M., 690
De Benedictis, C., 553
De Carli, F., 265, 349
De Carvalho, D., 342, 345
De Clemente, C., 233
De Gaetano, F., 92, 502, 698, 699
De la Fuente, M., 230
De la Oliva, N., 671
De Marco, F., 165
De Maria, C., 636
De Miguel, P., 62
De Nardo, L., 675
De Nisco, G., 170
De Paolis, A., 86, 87
De Pauw, T., 651
De Pieri, E., 439
De riccardis, G., 255
De Ruijter, J., 140
De Silva, C., 60
De Vecchis, M., 297
De Wildt, B., 249
Debbaut, C., 221, 652, 654
Deck, C., 346
Dede', L., 139, 179
Degli Esposti, M., 636
Dehghan, M., 676
Dehghan-Hamani, I., 282
Del Arco, A., 334, 335
Del Corso, G., 610
Del Nido, P., 156
Del Río, L., 462
Del Sarto, P., 132
Del Valle, J., 671
DeLancey, J., 709
Deliège, L., 596
Deligianni, D., 196
Della Villa, F., 563
Demertzis, S., 92
Demir, A., 632
Dendorfer, S., 274, 298, 572, 581
Denis, K., 389, 452
Denzler, J., 643
Deriu, M., 205, 206, 209, 212
Desmet, W., 389, 452
Destrade, M., 668

Destro, A., 293
Dewaele, F., 651
Dhammika, D., 560
Di Gregorio, S., 187, 462
Di Martino, A., 310
Di Martino, E., 47
di Nitto, C., 362
Di Puccio, F., 446, 447
Di Stanislao, E., 557
Diaz-Zuccarini, V., 157
Dickinson, A., 19
Diebels, S., 428, 472, 539
Diehm, N., 163, 164
Ding, K., 406
Dini, D., 511
Dixon, A., 313
Djorovic, S., 143
dM Vivanco, M., 210
Dmitriev, R., 362
Doblaré, M., 80, 621
Docaj, A., 202, 485
Domínguez, V., 431
Domanin, M., 115
Dominguez, J., 664
Donadello, M., 569
Dondossola, E., 523, 524, 618
Dong, J., 109
Dong, Z., 169
Donnaloja, F., 197, 255, 257
Donnelley, M., 436
Doubrovski, E., 666
Douglas, M., 401, 402
Doweidar, M., 232, 621
Draghi, L., 674
Drenchev, L., 387, 388
Drion, P., 458
Driscoll, H., 396
Driscoll, M., 490, 605
Droszez, A., 276, 574
Du, X., 323
Dušková, V., 616
Dubey, D., 338, 339
Dubini, G., 122, 133
Dubousset, J., 306
Duckworth, H., 400
Duda, G., 371, 589
Dueñas-Pamplona, J., 152
Dumas, R., 374
Dunaway, D., 474, 596, 597, 628
Dunlop, C., 166
Durante, S., 352
Durongbhan, P., 356
Dussan Delvasto, L., 443
Duxbury, L., 417
Dwivedi, A., 94
Dyatlova, I., 549
Dyson, C., 401, 402

Eager, D., 566, 648
Eastell, R., 475, 599
Ebenstein, D., 486
Ebermeyer, E., 306
Ebrahimzadeh, M., 587
Echeverry, J., 431
Edgar, L., 619
Eggenberger, D., 105
Eichenlaub, E., 665
Einafshar, M., 376, 420
Ekkerlein, A., 247
El-Bouri, W., 91
Elad, D., 39
Elahi, S., 218
Eliat, P., 184
Elouneg, A., 506
Elshazly, T., 677
Elson, D., 297
Eltes, P., 322, 540
Emendi, M., 57
Emig, R., 192
Engelberger, R., 163, 164
Engelhardt, L., 274
Enjalbert, R., 656
Erturk, H., 118
Escuer-Gracia, J., 124, 128
Espregueira-Mendes, J., 497
Esteban, A., 693
Estermann, S., 492
Ethier, R., 30
Eydan, B., 521

Förster-Streffleur, S., 492
Fabbri, P., 636
Fabech, J., 679
Fabry, B., 214

Faglia, A., 365
Falcinelli, C., 310, 449, 515
Famaey, N., 218, 470
Fan, Y., 82, 180
Fanciullo, C., 558
Fanizza, F., 194
Fanni, B., 17, 127, 173, 609, 631
Fantaci, B., 153
Fantazzini, A., 155
Fantozzi, S., 545
Farè, S., 675
Farge, E., 711
Farinelli, V., 319
Farzad-Mohajeri, S., 676
Faschingbauer, M., 493
Favata, A., 319
Favero, M., 496
Favier, C., 594
Favre, P., 416
Fayad, J., 540
Fedele, M., 139, 179
Fedianin, A., 300
Fels, S., 281, 308
Feng, J., 134
Fereidoonnezhad, B., 63, 88
Ferguson, S., 278, 286, 302, 323, 403, 405, 439, 503, 534
Fernández-Parra, R., 645
Fernandes, A., 630, 701
Fernandes, P., 258, 260, 332
Ferrante, B., 554
Ferraresi, C., 553
Ferrari, E., 103, 489
Ferrari, L., 658
Ferrari, M., 473
Ferrari, S., 261
Ferrarini, A., 103, 112, 161
Ferreira, J., 247
Ferretti, P., 474
Ferro, A., 344
Ferroni, M., 698, 699
Fessy, M., 374
Festa, A., 481
Ficorella, C., 624
Fidalgo, D., 703
Figliuzzi, M., 114, 123
Filipovic, N., 143
Finazzi, V., 632
Fini, M., 505
Finkemeier, C., 375
Finotello, A., 112
Fiore, G., 66, 106, 114, 123, 228, 231, 259, 622
Fiori, S., 114, 123
Fischer, M., 643, 646, 647
Fisichella, S., 181
Fiume, E., 240
Fiuza, C., 119
Flechilla, J., 688
Fleck, C., 680
Fleps, I., 302, 403, 405
Florea, L., 117
Foglieni, C., 228, 259
Fognani, R., 481
Foletto, M., 489
Follet, H., 427, 528
Fongaro, E., 489
Fonken, J., 61
Fontanella, C., 488, 489, 496
Formato, G., 175
Forte, A., 511
Fortuny Anguera, G., 514
Fortuny, G., 183
Fotiadis, D., 602, 613
Fotso Fogang, J., 488
Fouda, A., 685
Franceschelli, C., 153
Franco, W., 553
Frank, M., 494, 495, 633
Frascella, F., 637
Fraser, K., 172
Fratini, S., 634
Frattolin, J., 657
Freddi, G., 672
Freedman, B., 324
Frey, M., 342
Frey, S., 105
Friesenbichler, B., 439
Frigelli, M., 138, 156
Frigo, C., 319
Fritz, B., 394
Frueh, B., 692
Fukuyama, S., 480
Fumagalli, I., 139, 179

Fumagalli, R., 253
Funabashi, M., 342, 345
Furone, R., 576
Fusco, S., 233, 237
Fusini, L., 187

Gökgöl, C., 163, 164
Gómez-Benito, M., 238
Gabetti, S., 73, 240, 254, 500
Gachet, C., 615
Gagliani, M., 446
Gajny, L., 329
Galbusera, E., 385
Galbusera, F., 306, 312, 316, 334, 335, 627
Galili, L., 147
Gallagher, M., 708
Galli, M., 267, 537, 548, 557, 563, 564, 576, 577
Galliker, E., 403
Gallo, D., 16, 71, 73, 104, 113, 170
Gambacorta, C., 351
Gamie, Z., 386
Gantiva Díaz, M., 443
Gantner, F., 202
Gao, H., 70, 159
Garate Andikoetxea, B., 597
García, J., 152
García-Aznar, J., 15, 226, 238, 532
García-González, A., 595
García-Ortiz, J., 441
Gardegaront, M., 427
Garoffolo, G., 231
Gasbarrini, A., 325
Gasparini, I., 548
Gasparotti, E., 17, 93, 121, 127, 132, 171, 608, 631, 642
Gass, V., 541
Gastaldi, D., 481, 672
Gatta, G., 545
Gatti, A., 564
Gatti, R., 576, 577
Gaudino, M., 149
Gaul, R., 67
Gautieri, A., 38, 211, 674
Gawlitza, J., 428
Gaziano, P., 449, 515
Gefen, A., 419
Gehweiler, D., 381
Gelpi, G., 66, 106, 622
Gentile, F., 198
Genuardi, L., 71
Georgakopoulou, T., 591
Geraghty, S., 126
Gerardin, J., 90
Gerasimov, O., 300
Gerber, K., 286
Gerber, N., 286
Geris, L., 246, 263, 535
Geronzi, L., 171, 320
Geuens, T., 614
Ghajari, M., 44, 400, 406
Ghanem, I., 306
Ghasemi, M., 67
Ghidini, M., 483
Ghoneima, A., 677
Ghorbaniasl, G., 221
Ghosh, P., 109
Ghosh, R., 57
Ghouchani, A., 587
Giannitelli, S., 641
Giarmatzis, G., 284
Giese, D., 57, 74
Giezen, J., 96
Gijsen, F., 50, 63, 95, 96
Gilavary, M., 94
Gilbert, L., 638
Gilchrist, M., 470
Gill, H., 309
Gill, R., 172
Gimovsky, A., 708
Giorgi, G., 636
Giovannacci, L., 160
Giraldo, K., 580
Girardi, L., 149
Giraudet, C., 687
Giselbrecht, S., 617
Giudici, A., 75
Giurea, A., 383, 384
Giussani, A., 92
Gizzi, A., 201, 310, 611, 690
Gloria, A., 244
Godinho, M., 332
Goicolea, J., 152
Goldmann, J., 276, 574

Golse, N., 593
Gomez-Benito, M., 226
Goncalves, I., 226
Goncalves, R., 247
González Ballester, M., 334, 592
González-Ballester, M., 620
González-Bermúdez, B., 230, 239
González-Sánchez, M., 230
Gonzles Ballester, M., 600, 601
Goossens, Q., 389, 452
Goot, B., 90
Gordon, M., 709
Gori, M., 641
Gorodkov, A., 79
Gottardi, R., 255
Gotti, C., 665
Gourrier, A., 451
Gouveia, B., 258, 260
Grönquist, P., 460
Grünwald, A., 158
Grabow, N., 107
Grabski, J., 304
Gracia-Ibáñez, V., 269
Grad, S., 336
Grande, A., 211
Gras, L., 374
Grasa, J., 693, 696
Grasso, G., 209
Grawe, R., 288
Greco, F., 114, 123
Greinwald, M., 367
Gries, T., 116
Griesbach, J., 527
Griffiths, W., 606
Grimaldi, M., 618
Griskevicius, J., 287, 607
Groß-Hardt, S., 158
Groetsch, A., 451, 460, 468
Grosset, J., 499
Grossi, G., 482
Groth, C., 171
Grothe, S., 276, 574
Grupp, T., 370, 377, 383, 384, 394
Grygorowicz, M., 304
Guala, A., 16
Guan, D., 70, 159
Guazzelli, N., 220, 250, 667
Gueorguiev, B., 360, 375, 378, 381, 382, 387, 388, 425, 590
Guerra, A., 702
Guerrero, P., 226
Guidetti, I., 92
Guidetti, M., 351
Guignandon, A., 189
Guinea, G., 230
Guiotto, A., 291, 435, 542, 569, 570
Guivier-Curien, C., 533
Gunasekera, S., 60, 146
Guo, B., 169
Guo, L., 438
Gupta, A., 358
Gupta, R., 72, 83
Gusmini, M., 111
Guvenir, S., 62, 81

H Faris, I., 508
Höchner, C., 347
Hörner, M., 192
Hübner, S., 398
Hackenbroch, C., 315
Hacker, S., 372, 491
Hadjicharalambous, M., 516, 529
Hagenmeyer, N., 341
Haiat, G., 411
Halcrow, B., 426
Hall Barientos, P., 186
Hall-Barrientos, P., 56, 151
Hamady, M., 100
Hammer, P., 156
Handelshauser, M., 236
Handler, S., 90
Hanna, B., 399
Hansen, H., 81
Hansen, U., 466
Hansen, U., 324
Hardman, D., 656
Hardwicke, J., 407
Harih, G., 555
Harte, K., 504
Hartmann, M., 458
Hashemi, A., 376, 420
Haxhiademi, D., 132
He, R., 99, 101
He, Y., 104

He, Z., 54, 130
Heidsieck, C., 329
Heim, F., 182
Hejazi, S., 270
Helgason, B., 302, 403, 405, 534
Hellmuth, R., 166
Henke, P., 301
Hennige, S., 644
Hensel, B., 98
Herberg, U., 158
Herbst, Y., 556
Hernández, P., 76
Herren, C., 330
Herrero Sabartés, J., 514
Herrero, J., 183
Herrmann, S., 288, 409
Herzog, W., 270
Hess, H., 286
Hessmann, M., 375
Hettich, G., 370
Heuberger, P., 678, 679
Heyland, M., 589
Hildebrand, F., 330
Hill, A., 668
Hill, N., 48
Hirtler, L., 492, 554
Hisaund, A., 350
Ho Ba Tho, M., 499
Ho, S., 649
Hoang, C., 544
Hoang, H., 279, 295, 296
Hobusch, G., 554
Hoekstra, A., 21, 91, 615
Hoffmann, A., 321, 340
Hofmann, S., 249
Holsgrove, T., 343
Holt, C., 294, 297
Hommel, H., 371
Horgan, A., 562
Horling, L., 430
Horne, D., 386
Hossain, D., 122
Hossain, I., 566
Hraška, V., 90
Hruby, J., 404
Hu, Z., 306
Hua, J., 392
Huang, A., 543
Huber, S., 503
Hughes, A., 396
Hughes, C., 117
Humbert, L., 462
Hwang, W., 208
Hyde-Linaker, G., 186

Ianniello, A., 435
Iannuzzi, G., 523
Ieropoli, O., 111
Iervolino, F., 625, 635
Ignasiak, D., 316
Ignatius, A., 247, 372, 397, 491, 493
Immel, K., 411
Indermaur, M., 478
Ingrassia, T., 634
Innocenti, B., 373, 379, 380, 393, 417, 421, 634
Inveninato, F., 699
Ioannou, E., 516, 529
Iommi, G., 667
Ippolito, S., 139, 179
Irastorza-Landa, A., 678, 679
Isaac, G., 423
Isella, B., 122
Ishac, K., 566, 648
Islam, S., 177
Ismail, K., 572
Ito, K., 249, 359, 498, 663
Iturri, J., 210
Ivo, F., 550

J. Vaughan, T., 669
Józsa, T., 91
Jacchetti, E., 197, 215, 223, 256, 257, 626
Jacobson, N., 490
Jacquet, E., 506
Jaeger, P., 38
James, C., 438
James, G., 474, 596, 628
Jamshidi, P., 108, 126
Jang, I., 361
Jankowski, K., 454, 455
Jansen, J., 315, 336
Janssen, D., 43
Jarque-Bou, N., 269

Jarral, O., 181
Jauregui, R., 272, 575
Jaworek, M., 66, 106, 622
Jeelani, N., 474, 596, 597, 628
Joan J., C., 216
Johnson, D., 526
Johnston, L., 56
Johnston, R., 67
Joly, F., 593
Jonášová, A., 616
Jonas, R., 311
Jones, A., 423, 424, 517, 604
Jones, S., 670
Jonkers, I., 218, 279, 289, 295, 296, 578
Jorgensen, C., 219
Jovic, T., 195
Juskeniene, G., 287

Käs, J., 624
Kölby, L., 526
Künzli, S., 503
Kadirkamanathan, V., 469
Kainberger, F., 554
Kalaskar, D., 639
Kalejs, M., 89
Kališ, V., 572
Kamal, Z., 434, 531
Kameo, Y., 217, 519
Kammoun, M., 499
Kao, A., 391, 448, 476
Karagöz, Z., 614
Karakaya, C., 213
Karali, A., 448
Karam, M., 306
Karanasiou, G., 602, 613
Karimi Dastgerdi, A., 305, 676
Karkhaneh Yousefi, A., 189
Kassinos, S., 529
Kasyanov, V., 89
Kaux, J., 458
Kawchuk, G., 342, 345
Kazakidi, A., 56, 64, 151, 186, 520
Kebbach, M., 288
Keilig, L., 677, 681, 682
Kelly, A., 517
Kempf, H., 473
Kenanidis, E., 386
Kenny, D., 126
Kerckhofs, G., 102, 141, 145, 364
Kerr, G., 358
Kerskens, C., 137
Khalaf, K., 275, 314
Khamatnurova, R., 549
Khan, B., 133
Kharchenko, A., 673
Kharin, N., 300
Khir, A., 75
Khohlova, A., 204
Khokhlova, A., 207
Khonsari, R., 526
Khorshidparast, S., 683, 684
Killen, B., 279, 280
Kim, J., 248
Kim, M., 277
Kim, S., 277
King, J., 617
King, P., 162
Kislitsyn, D., 176
Kiss, B., 658
Kitchen, M., 436
Kleist, E., 288
Kling, S., 697
Klockow, A., 422
Kluess, D., 366, 445
Knobe, M., 381
Knodt, W., 192
Kobayashi, H., 230
Kobbe, P., 330
Koch, R., 375
Kochetkova, T., 477, 478
Kochurova, A., 204
Koh, I., 277
Kohl, P., 192
Komninou, M., 692
Koncar, I., 143
Konduri, P., 63
Kontomaris, S., 501
Koopman, B., 283
Kopylova, G., 193, 204
Korhonen, R., 218
Korte, J., 158
Kostenko, E., 307
Kour, R., 357
Kowal, M., 561

Kowaleski, M., 387, 388
Kozaniti, F., 196
Krüger, T., 619, 656
Krahl, L., 371
Kranioti, E., 467
Kreienbaum, K., 397
Krobot, Z., 404
Kruger, J., 710
Kuber, P., 544
Kubowitsch, S., 581
Kubyak, A., 568
Kugel, M., 493
Kuhn, G., 465
Kuianova, I., 176
Kuster, R., 347
Kuster, Y., 105
Kutzner, K., 422
Kwak, D., 277

López Besora, J., 514
López de Arancibia, A., 390
López, A., 390
López, I., 431
López, J., 183
La Barbera, L., 317, 348, 368, 385, 627
La Mattina, A., 586, 588, 598
LaDisa, J., 90
Lafuente Gracia, L., 535
Lafuente-Gracia, L., 263
Laing, A., 403
Laita, N., 80
Lalande, A., 59
Lally, C., 67, 68, 117, 126, 137, 245
Lalys, F., 184
Landreau, A., 184
Lane, B., 53
Lange, H., 366
Langi, E., 108
Langlais, T., 306
Lanzani, G., 689
LaPointe, V., 614
Larson, A., 348
Lasaygues, P., 533
Lashkarinia, S., 77
Latorre, A., 142
Lauditi, A., 165
Laurent, C., 473
Lauwers, I., 249
Lavaill, M., 358
Lazáry, Á., 322
Lazary, A., 540
Le Floc'h, S., 219
Le Roi, B., 84
Le Ruyet, A., 509
Le Tallec, P., 687
Leardini, A., 37, 352, 553, 558
Leask, R., 130, 507
Ledoux, C., 603
Ledoux, Y., 337
Lee, L., 58
Lee, M., 282
Leftwich, M., 708
Lehmann, S., 678
Lejeune, A., 506
Lekszycki, T., 513
Lennon, A., 504
Lesage, R., 246
Leszczynski, A., 346
Leunig, M., 439, 503
Leuthard, L., 278
Levi, M., 625, 635
Levillain, A., 427
Lewis, A., 670
Leyssens, L., 141
Li, X., 453
Li, Z., 157
Liebgott, H., 374
Liebig, T., 135
Liebsch, C., 398
Lihoreau, T., 506
Lim, D., 277
LIN, S., 59
Lin, Z., 707
Lind, E., 566
Linden, K., 158
Linder-Ganz, E., 372
Lindsey, D., 312
Line, P., 593
Lipovka, A., 673
List, R., 299, 439
Liu, C., 392
Liu, Y., 101, 169
Liuzzo, G., 71
Llobet Martínez-Pons, A., 575

Llop-Harillo, I., 552
Lloyd, D., 309
Lodi Rizzini, M., 71, 170
Loerakker, S., 213, 245
Lombardi, M., 57, 74, 228, 259
Long, V., 533
Longo, S., 185
Lopata, R., 61, 140, 359, 498
Lopes, J., 267
Lopez Poncelas, M., 317
Lopomo, N., 303, 505
Lories, R., 218, 289
Lozza, I., 577
Lucarno, S., 563
Lucchetti, A., 116
Lucot, Q., 506
Lugas, A., 500, 686
Lullini, G., 558
Luo, X., 70, 159
Lupton, C., 484, 661
Luraghi, G., 63, 148, 153, 174, 595

Märdian, S., 589
Müller, C., 98
Müller, P., 367
Müller, R., 222, 363, 430, 459, 465, 527, 603
Méndez, C., 152
Maas, E., 61, 140
Macchi, V., 496
MacFarlane, M., 401, 402
Mackenzie Ross, R., 144
Maclean, C., 151
MacNeil, S., 702
Madeddu, P., 231
Madekurozwa, M., 657
Maffiodo, D., 553
Mahbeer, P., 129
Mai, V., 395
Maillet, M., 499
Mainardi, A., 252
Mainardi, L., 365
Maire, E., 53
Maistrello, G., 570
Majnooni, M., 533
Majoie, C., 21, 63
Makadia, J., 133
Maknickas, A., 307
Malakoutian, M., 281, 282
Malamou, A., 501
Malanowska, E., 703
Malavolta, M., 209, 212
Maleux, G., 652
Mallikarachchi, S., 560
Malvè, M., 645
Manchester, E., 150
Mancinelli, G., 627
Mandaresu, S., 577
Mangin, P., 615
Mangini, A., 66
Mangir, N., 702
Manning, K., 97, 125, 131
Mantelli, A., 625, 635
Mantero, S., 261, 625, 635, 695
Manunza, M., 537
Manzella, C., 686
Maoz, B., 84
Marano, A., 473
Marcheggiani Muccioli, G., 634
Marchetti-Deschmann, M., 236
Marchiori, G., 303, 505
Marconi, S., 115, 640
Maremonti, M., 234, 244
Marginet i Assens, R., 272
Marie, N., 506
Marino, M., 78, 623
Marinozzi, A., 229
Marinozzi, F., 229
Mariotti, A., 608
Markert, B., 330
Marom, G., 147, 418
Maroncelli, E., 66
Marone, S., 344
Marquering, H., 63, 96
Marques, A., 584
Marques, F., 459, 518
Marras, D., 325, 333
Marret, A., 416
Marrocco-Trischitta, M., 167
Marsano, A., 252, 254
Marsilio, L., 618
Martín Sosa, E., 565
Martínez Vázquez, R., 624, 626
Martínez, M., 76, 85
Martelli, F., 231

Martelli, S., 24, 358, 436, 471, 551
Martin, L., 706
Martinelli, N., 627
Martinez, M., 80, 124, 128, 142
Martinez-Vazquez, F., 664
Martins, P., 573, 584, 629
Martorelli, M., 244
Marzorati, D., 365
Masante, B., 240
Mascarenhas, T., 701, 704, 705
Masi, A., 575
Masi, B., 394
Masmoudi, M., 438
Mason, A., 56
Masouros , S., 324
Massai, D., 240, 254, 500
Matencio, C., 659
Mathavan, N., 465
Mathiszig-Lee, J., 657
Mattar, C., 58
Mattei, L., 446, 447
Mauri, E., 641
Maurya, A., 477
Mayo Núñez, J., 565
Mazzà, C., 453
Mazzi, V., 113, 170
McCarron, A., 436
McCarthy, R., 94
McCloskey, E., 453
McCormick, C., 128
McFarlin, B., 707
McGarry, P., 49, 63, 88, 200
McGee, O., 126
McGinty, S., 124, 128
McGregor, A., 560, 594
McGuan, S., 417
McHugh, P., 31
McKenna, C., 65, 110
McLennan, S., 54, 507, 638
McLoone, M., 180
McNamara, L., 28, 162, 241
McPhee, S., 468
Meakin, J., 343
Medan, Y., 556
Meggiato, E., 435
Meghdadi, A., 670
Meier, M., 326
Melchor, J., 508
Melzner, M., 274, 572
Menary, G., 504
Mengoni, M., 313, 424, 517, 604
Menicanti, L., 138
Menze, J., 278, 286
Mercuri, M., 184
Mesiwala, A., 312
Mesnard, M., 337
Messa, L., 194, 225
Mester, J., 276, 574
Metrangolo, P., 211, 674
Metsiou, D., 196
Meyer, F., 346
Meynen, A., 413
Miceli, M., 206
Micera, S., 671
Michieletto, F., 542
Michler, J., 451, 460, 477, 478
Midei, F., 500
Mielke, F., 289
Migliavacca, F., 18, 63, 65, 71, 104, 133, 174, 182, 595, 613
Miguel, T., 550
Mihalko, W., 394
Milani, P., 74
Militskova, A., 549
Millán, C., 486
Millar, T., 670
Miller, C., 235
Minetti, A., 292
Miodownik, M., 386
Mirulla, A., 393, 634
Mirzaali, M., 666
Mischler, D., 378, 382, 590
Mitton, D., 427, 528
Moalli, P., 706
Moazen, M., 386, 392, 526
Modenese, L., 437, 442
Modrego, A., 272, 575
Moerman, K., 63
Moewis, P., 371
Mofrad, M., 45
Mojumder, J., 58
Molimard, J., 521
Molinari, L., 310
Momier, D., 533

Monaghan, M., 362
Monaldo, E., 78, 449, 515
Mondeel, M., 96
Monetti, G., 265, 349
Monfardini, E., 577
Monfort, J., 592, 600, 601
Mongrain, R., 54, 129, 130, 507, 510, 638
Monllau, J., 592, 600, 601
Monn, S., 439
Monoli, C., 548
Montanari, S., 318, 322
Montefiori, E., 453
Montino Pelagi, G., 187
Montrone, F., 254
Moore Jr, J., 181, 657
Moore, A., 657
Mora, M., 441
Morabito, A., 636
Morbidelli, D., 185
Morbiducci, U., 16, 71, 73, 113, 170, 206, 475, 500
Morgan, K., 436
Morgant, M., 59
Morganti, S., 103
Morgenthal, A., 680
Morgenthaler, V., 184
Morin, C., 136
Morita, Y., 262, 480
Morosato, F., 370
Morselli, D., 636
Moscato, F., 633
Moschini, G., 326
Mosesian, L., 562
Motalli, G., 627
Mothes, O., 643
Motoi, N., 202
Moura, R., 704
Moustakas, K., 284, 444
Mpekris, F., 227
Mslati, H., 198
Muñoz-Paniagua, J., 152
Muehlbauer, J., 271
Mueller, J., 416
Mueri, C., 416
Muhammad, F., 133
Mukhametova, E., 549
Mukherjee, S., 246
Mulier, M., 389
Mulliez, M., 377
Munafò, R., 135
Murgia, A., 291, 293, 543
Murzi, M., 642
Muscat, S., 206
Myachina, T., 204, 207
Myers, K., 703, 712
Mys, K., 360
Müller, R., 518, 522

Naaim, A., 374
Nabiev, S., 193
Nag, P., 242
Nagargoje, M., 72
Naghavi, S., 392
Najar, A., 172
Nalbach, M., 202, 203
Nambiar, M., 692, 694
Nannini, G., 149
Nappo, G., 502
Nardini, A., 626
Nasehi, R., 215
Nasello, G., 15
Natal Jorge, R., 497, 582, 700, 702, 704
Natal, R., 703, 705
Natali, A., 488
Navacchia, A., 417
Navarro, L., 136
Navarro, X., 671
Nazarian, A., 461
Neels, A., 477
Nef, C., 105
Negro, A., 215
Neidlin, M., 158, 620
Neidlinger-Wilke, C., 247, 336
Nejim, Z., 136
Nespoli, A., 627
Neto, N., 362
Netti, P., 233, 234, 237, 244
Neumann, V., 360
Neuy, T., 367
Newell, N., 560
Newell, N., 324
Nezi, L., 253
Ng, O., 60, 146
Nguyen, T., 32

Nguyen, V., 411
Ni Anaidh, A., 470
Nichols, D., 255
Nicolas, Q., 593
Nicolini, L., 330
Nicollier, C., 541
Nielsen, P., 710
Nieroda, A., 154
Nievergeld, A., 61, 140
Nikkhoo, M., 275, 314
Ninno, F., 104
Niu, C., 314
Noël, D., 219
Noailly, J., 199, 334, 335, 462, 592, 600, 601, 620, 659
Nolan, D., 245
Nostran, C., 489

O'Brien, G., 68
O'Connell, B., 162
O'Regan, D., 150
O'Reilly, D., 68, 117
O'Sullivan, E., 597
O'Regan, D., 181
Obrist, D., 69, 105, 655, 658
Occhetta, P., 252
Odino, M., 185
Oftadeh, R., 461
Ohayon, J., 142
Ohs, N., 430, 459, 527
Ojeda Granja, J., 565
Oliveira Silva, M., 355
Oliveira, C., 267
Oliveira, D., 703–705
Oliveto, S., 257
Oliviero, S., 463, 606
Ong, C., 58
Ong, J., 474, 596, 628
Orassi, V., 412
Orlov, K., 176
Orr, H., 710
Orth, M., 428, 472, 539
Ortolani, M., 558
Osellame, R., 194, 215, 223, 256, 257, 624, 626
Osouli, K., 92
Ostadi Moghaddam, A., 707
Otsuka, T., 163, 164
Ottardi, C., 368
Overbeck, J., 477
Ovesy, M., 425
Ovsianikov, A., 202
Oxland, T., 281, 282, 308
Oyekole, O., 97
Ozel, A., 644, 650
Ozolanta, I., 89

Pätzold, R., 367, 409
Püschel, K., 367
Pérez, M., 15
Pérez-Aliacar, M., 621
Pérez-González, A., 552
Pétré, M., 141
Płociński, T., 662
Pacella, M., 109
Padmos, R., 91
Pagé, I., 342, 345
Paggiosi, M., 453, 475, 599
Pahr, D., 353, 415, 450, 457, 492, 494, 495
Pai S, A., 308
Pajic-Lijakovic, I., 20
Palanca, M., 325, 328, 333, 398, 463
Palkowski, T., 399
Palladini, G., 74
Palladino, M., 435
Pallante, L., 209, 212
Palmisano, C., 319
Palumbo, M., 149
Panagiotopoulou, V., 425
Panagopoulos, A., 133
Pandini, C., 225
Pandolfi, A., 690, 691
Pane, B., 112
Panico, M., 312
Pant, S., 595
Panzetta, V., 233, 234, 237, 244
Papallo, I., 244
Pardo Ramos, D., 537
Parente, M., 497, 700, 701, 703–705
Parenti Castelli, V., 265, 349
Parker, J., 357
Parodi, V., 215, 223
Parreira, R., 267
Parrilli, A., 505

Parshin, D., 176, 568, 673
Parson, D., 436
Pase, G., 139, 179
Passini, E., 36
Passini, F., 38
Pastor, T., 381
Pastrama, M., 359, 498
Pastrav, L., 389, 452
Paszicsnyek, T., 380
Patel, V., 670
Patermoster, G., 526
Patriarca, L., 120
Paul, G., 465, 527
Pavan, D., 295, 296, 569
Pavei, G., 292
Pawlikowski, M., 154, 454, 455, 662
Payne, S., 91
Peña Fernández, M., 391, 476
Peña, E., 76, 80, 85, 124, 128, 142
Peña-Fernández, M., 644
Pederzani, E., 114, 123, 228, 259
Pedicino, D., 71
Pedofsky, L., 710
Pegolo, E., 546, 547
Pekedis, M., 612
Pekkan, K., 77, 118
Peldschus, S., 271
Pellisé, F., 334
Pennati, G., 122, 127, 148, 182, 385, 602, 613
Pereira, R., 497
Perez, M., 525, 532
Perico, F., 66, 106, 622
Perilli, E., 436, 456, 471
Perondi, S., 609
Perotto, S., 611
Perriard, Y., 658
Perrin, J., 473
Perrottoni, S., 362
Perroud, O., 473
Peruzzi, C., 460, 477, 478
Pesce, M., 42, 231, 261, 500
Pestiaux, C., 145
Petit, A., 184
Petit, C., 189
Petitjean, N., 219
Petrini, L., 120, 122, 127, 182, 602, 613, 627, 632
Pey, P., 645
Peyronnet, R., 192
Pezzotta, M., 123
Phillips, A., 442, 594
Phillips, H., 707
Piaggi, S., 220
Pianigiani, S., 369, 373, 379, 410
Piatkowska, W., 291, 293, 543, 579
Piatti, F., 57
Pica, A., 229
Pica, S., 74
Piccinini, L., 548, 557
Pickering, E., 224, 235
Piella, G., 199, 620
Piemontese, F., 545
Pieper, I., 172
Pierrat, B., 53, 509, 521
Piet, J., 289
Pietrasanta, L., 69
Pietton, R., 350
Pinoli, P., 257
Piontek, T., 304
Pires, T., 258, 260
Pirola, S., 150, 169, 181
Pirri, C., 637
Pivonka, P., 224, 235, 358
Pizzi, A., 211, 674
Pizzi, M., 699
Pizzolato, C., 309
Plánička, S., 616
Plaza, G., 230, 239
Plesec, V., 555
Pluchinotta, F., 57, 156
Pohlemann, T., 428, 472, 539
Poik, M., 203
Polak-Krasna, K., 119
Poletti, G., 122, 602, 613
Polinsky, S., 556
Polli, D., 223
Polli, R., 291, 293, 543
Polvani, G., 261
Ponnaluri, S., 125
Pontone, G., 187
Positano, V., 173, 185, 631
Possenti, L., 653

Postolka, B., 299
Powers, C., 562
Pozzuoli, A., 496
Průša, J., 191
Prahl Wittberg, L., 34
Preatoni, E., 309
Previtali, B., 632
Prouse, G., 160
Pruech, E., 372
Puente Reyna, A., 377, 394
Puerta, I., 390
Puigjaner Riba, D., 514
Puigjaner, D., 183
Putame, G., 240, 254, 344
Pyka, G., 102, 364

Quarteroni, A., 139, 160, 178, 179, 187
Quelhas Teixeira, G., 336
Quinlan, N., 180

Räber, L., 163, 164
Rösch, Y., 105
Rüggeberg, M., 460
Ríos-Ruiz, I., 85
Raanani, E., 147
Rabello, R., 567
Radhakrishnan, P., 238
Ragazzini, S., 695
Rahimi Gorji, M., 221
Raimondi, M., 194, 197, 215, 223, 225, 255–257, 362, 626
Rainbow, M., 266
Rainer, A., 641
Raistenskis, J., 287
Ramírez, J., 659
Ramachandramoorthy, R., 460
Ramajo, L., 486
Ramdat Misier, K., 596
Ramella, A., 174
Ramos, A., 337, 432, 433
Rancati, T., 653
Rapagna, S., 456
Rashedi, E., 544
Rasouligandomani, M., 334, 335
Rasponi, M., 252, 253
Rastel, D., 512
Rauch, F., 478
Ravasi, M., 148
Ravenda, S., 253
Ravens, U., 192
Rawlinson, J., 317
Razi, H., 680
Redaelli, A., 57, 74, 114, 123, 131, 135, 149, 156, 165, 167, 181, 252
Redaelli, E., 174
Regazzoni, F., 178
Reina-Romo, E., 664
Reinero, C., 645
Reinker, L., 298
Reisinger, A., 353, 457, 492
Remo, A., 241
Remus, R., 321, 340
Remuzzi, A., 114, 123, 188
Ren, M., 58
Ren, W., 82
Rendenbach, C., 412
Reni, G., 538
Rey, F., 194, 225
Rezania, V., 33
Riboldi, S., 114, 123
Ricciardi, L., 546, 547
Richards, G., 425
Riches, P., 520
Ricioppo, M., 665
Ridolfi, L., 16
Riglet, L., 374
Rigoldi, F., 197
Riley, H., 399
Rimondini, L., 240
Rinkeviciute, K., 287
Rios, I., 688
Ristori, T., 213, 245
Risvas, K., 444
Ritos, K., 151
Riva, A., 74
Rivera Tapia, E., 343
Rizzi, S., 261
Rizzo, S., 131
Roberts, B., 469, 606
Roche, E., 177, 180
Rochette, M., 184, 320
Roda-sales, A., 269
Rodrigues, J., 144
Rodriguez Florez, N., 597

Rodriguez Matas, J., 18, 63, 153, 215, 268, 595
Rodriguez, B., 36
Rodriguez-Andrade, C., 664
Rodriguez-Florez, N., 390, 474, 525, 628
Rodriguez-Palomares, J., 16
Rogati, G., 558
rojo, J., 190
Roland, M., 428, 472, 539
Roldan, A., 228
Roldo, M., 364, 661
Rolin, G., 506
Rolland, Y., 184
Romagnoni, C., 66, 106
Romanato, M., 290, 293, 543, 579
Romarowski, R., 103, 115
romita, r., 190
Ronan, W., 119, 166, 177, 668, 669
Rosa, R., 66, 106
Rosales Santana, K., 575
Rosati, R., 653
Rossdale, J., 144
Rossi, F., 282
Rossi, M., 545
Rostaminia, G., 706
Rouhi, G., 270, 305, 434, 440, 531, 587, 676, 683, 684
Routzong, M., 706
Roux, J., 528
Roy, A., 694
Royer, P., 219
Royston, T., 22, 351
Rozowsky, J., 104
Rušavý, Z., 572
Rubert, M., 527
Ruch, S., 395, 679
Rueda, D., 285
Ruffoni, D., 458
Rufin, M., 203
Ruggeri, P., 496
Ruiter, M., 231
Ruiz de Galarreta, S., 390, 525
Ruiz Wills, C., 462, 592
Rus, G., 23, 508
Russo, G., 71
Russo, M., 331
Russo, S., 532
Russow, G., 589
Rynkevic, R., 630
Rzany, A., 98

S. P. Poh, P., 525
Süß, F., 572
Sünbüloğlu, E., 408
Sérgio, B., 550
Saade, A., 678, 679
Saccu, C., 231
Sachenkov, O., 300, 549
Sacks, M., 125
Saemann, M., 445
Sahlgren, C., 213, 245
Saint-Jalmes, H., 184
Saitta, S., 135, 149, 167, 169
Sakano, N., 519
Sakellarios, A., 602
Sala, F., 624
Salaorni, F., 564
Salmasi, M., 150, 181
Salo, A., 292
Salsano, G., 112
Salurso, E., 66, 106, 622
Salvetti, M., 608
Samant, S., 133
Samsammi, S., 367, 409
Samyn, M., 90
Sanches, A., 135
Sanchez, C., 281
Sancho-Bru, J., 269
Sancisi, N., 265, 266, 349, 505
Sander, M., 445
Sanford, A., 416
Sangalli, F., 114, 123
Sanginario, A., 240
Sanno, M., 276, 574
Santare, M., 665
Santesarti, G., 623
Santos Beato, P., 639
Santos, C., 497
Santos, I., 341
Santos, J., 258, 260
Santschi, M., 503
Santuz, A., 537
Sanz-Herrera, J., 214, 664
Sanz-Pena, I., 560

Sartori, M., 283
Sas, A., 414, 422
Sasidharan, S., 181
Sasika, J., 560
Sauer, A., 383
Sauer, R., 411
Saunders, B., 387, 388
Sauvage, E., 64, 173
Savadori, P., 482
Saveljic, I., 143
Sawacha, Z., 290, 291, 293, 295, 296, 435, 542, 543, 545–547, 569, 570, 579
Scaldaferro, A., 570
Scarpolini, M., 185
Scarsoglio, S., 16
Schädli, G., 527
Schümann, K., 107
Schütz, P., 299
Schader, J., 382, 590
Schall, F., 491
Scheerlinck, T., 422
Scheys, L., 413
Schiavazzi, D., 41
Schiavi-Tritz, J., 241
Schick, S., 271
Schierano, G., 686
Schierjott, R., 370
Schievano, S., 64, 173, 474, 596, 597, 628
Schilling, C., 383, 384, 394
Schitter, G., 202, 203
Schmid, S., 326
Schmidt, W., 107
Schmidt-Bleek, K., 589
Schmitz, K., 107
Schoof, E., 357
Schopper, C., 378
Schouten, A., 283
Schuiringa, G., 663
Schwank, C., 503
Schwendicke, F., 680
Schwer, J., 274, 372, 397, 491, 493
Schwiedrzik, J., 40, 451, 460, 477, 478
Sciacca, D., 280
Scimeca, J., 533
Scolaro, M., 132
Sconfienza, L., 306
Scrofani, R., 139, 179
Seemann, R., 589
Segarra-Queralt, M., 199, 620
Segers, P., 651, 654
Seiler, T., 692
Seitz, A., 372, 397, 491, 493
Semela, M., 404
Semenova, E., 549
Sengupta, S., 100
Sensale, M., 320
Sensini, A., 665
Senteler, M., 326
Sergi, P., 671
Serino, G., 111, 500
Sermon, A., 414
Serrancolí, G., 292
Serrano-Alcalde, F., 238, 532
Sfamurri, P., 368
Sferrazza, G., 698
Sforza, C., 564, 567
Shameen, T., 86
Sharp, D., 400
Sharzehee, M., 133
Shaulian, H., 419
Shchepkin, D., 193, 204
Shemesh, M., 372
Shephard, J., 468
Shiraishi, M., 544
Si, X., 660
Sierra-Pallares, J., 152
Siewe, J., 330
Silberschmidt, V., 101, 108
Sileo, A., 254
Silva, E., 701
Silva, M., 630
Silva, P., 560
Silva-Henao, J., 353
Silvera Delgado, C., 654
Silvestros, P., 309
Simon, S., 97
Simon, U., 274
Simons, D., 509
Sin, S., 361
Singh, N., 172
Singhal, M., 83
Sironi, L., 256
Sivaguru, M., 707
Sivakumaran, D., 556

Skalli, W., 306, 329, 350
Skalski, K., 662
Smit, T., 534
Smith, E., 644
Snedeker, J., 38
Soangra, R., 544
Soares dos Santos, M., 433
Sobottke, R., 330
Soler Vizán, E., 565
Solorzano Quevedo, B., 580
Sommer, B., 583
Soncini, M., 114, 123, 197, 211, 228, 231, 259, 674
Sori, L., 211, 674
Souche, A., 188
Soulez, G., 54, 129, 130, 507
Spagnoli, A., 511
Spieker, C., 615
Spierings, J., 359
Spinella, G., 112, 155
Spinetti, G., 231
Spolaor, F., 291, 293, 435, 542, 543, 569, 570, 579
Sporer, E., 383, 384
Spronck, B., 75
Squarzoni, S., 481
Stagni, R., 540
Stanev, D., 444
Stark, H., 646, 647, 682
Stavenuiter, I., 498
Stavri, R., 466
Stefanati, M., 268
Steinman, D., 14, 170
Steinseifer, U., 158
Stella, S., 160
Stigson, H., 406
Stillavato, S., 563
Stipsitz, M., 450
Stochino, M., 103
Stock, K., 430
Stockmans, F., 360
Stoff, J., 399
Stoffel, K., 375
Stoffel, M., 330
Stok, K., 354–357
Stokes, C., 157
Stone, A., 137
Stonkus, R., 307
Storm, F., 538
Stott, B., 605
Stradins, P., 89
Straub, R., 562
Strazdins, U., 89
Street, J., 281, 282, 308
Streicher, J., 492
Stretti, E., 127
Strike, E., 89
Studer, H., 694
Sturgess, C., 407
Sturla, F., 57, 74, 138, 156, 165, 167
Styger, U., 387, 388
Stylianopoulos, T., 227
Stylianou, A., 227, 501
Suess, F., 581
Sukopp, M., 372
Suleman, K., 386
Sun, Z., 82
Suntharalingam, J., 144
Sutula, D., 506
Swapnasrita, S., 617
Swenson, C., 709
Symes, D., 162
Synek, A., 415, 554
Syntouka, I., 520
Szőke, G., 540

Tío, L., 592
Taddei, F., 303
Tait, R., 383, 384
Takamizawa, K., 52
Talaat, M., 660
Talone, B., 223
Talygin, E., 79
Tanaka, A., 368
Tanck, E., 414
Tanska, P., 218
Tao, Y., 315
Tarabini, M., 563
Tarpey, R., 177
Tassani, S., 592, 600, 601, 659
Taunt, C., 394
Tavakol, M., 479
Tavana, S., 324
Tay, T., 466

Taylor, M., 456, 471, 551, 598
Taylor, S., 392
Taylor, W., 299
Techens, C., 318, 322
Teixeira, A., 573, 629
Teixeira, G., 247
Temporiti, F., 576, 577
Terebessy, T., 540
Terzano, M., 511
Terzini, M., 344, 475, 500, 599, 686
Testa, C., 257
Testa, L., 165
Textor, D., 347
Theobald, P., 399, 401, 402
Theret, M., 282
Theriot, J., 238
Thirugnanasambandam, M., 105
Thomas, A., 231
Thomas, S., 60, 146
Thompson, J., 386
Thurner, P., 202, 203, 236
Tikhvinskii, D., 176
Timmermans, M., 452
Tio, L., 600, 601, 620
Tironi, M., 114, 123
Tits, A., 458
Toca-Herrera, J., 210, 243
Ton, A., 198
Toni, A., 369, 410
Toniolo, I., 488, 489
Torii, R., 639
Tornifoglio, B., 67, 137
Torre, M., 641
Torrente, Y., 268
Torres, J., 508
Torta, E., 73
Torun, H., 81
Touré, S., 184
Tourolle né Betts, D., 603
Tourolle, D., 363
Toussaint, K., 707
Tozzi, G., 364, 391, 448, 476, 484, 661
Trabelsi, O., 499
Traina, F., 370
Travert, C., 329
Traynor, A., 423
Treml, L., 201
Trepczynski, A., 371
Trimarchi, S., 115, 174
Tripicchio, P., 642
Trombetta, M., 641
Trommer, F., 536
Truckenmüller, R., 617
Tsimba, L., 512
Tsiridis, E., 386
Tsompou, P., 602
Tsuchiya, K., 262
Tuhtan, J., 548
Tulzer, A., 58
Tulzer, G., 58
Turkoz, R., 118
Tuset Serra, L., 514
Tuszynski, J., 33, 205

Ueki, Y., 163, 164
Uguz, A., 77
Uhl, A., 428, 539
Ulacia Flores, P., 638
Ulmer, J., 105
Unger, E., 554, 633
Urdeitx, P., 232

Vagnini, A., 576
Vairo, G., 78, 449, 515, 623
Valen-Sendstad, K., 188
Valente, G., 303
Valentini, L., 636
Valtchanov, H., 510
van Asten, J., 245
van Batenburg-Sherwood, J., 657
van Bavel, E., 591
van de Vosse, F., 61, 140
van den Bergh, J., 360
van der Have, A., 578
van der Kolk, M., 615
van der Lugt, A., 63, 95, 96
van der Wijk, A., 591
van Deursen, J., 470
van Donkelaar, C., 359, 498, 663
van Griensven, M., 614
van Hees, R., 498
van Hugten, P., 359
Van Impe, M., 654
van Lenthe, G., 360, 413, 414, 422, 458

van Lenthe, H., 376, 420
Van Oosterwyck, H., 214
Van Rossom, S., 295, 296, 578
van Sambeek, M., 61, 140
van Veen, B., 453
Van Wassenbergh, S., 289
Vandenberghe, S., 92
Vandenbulcke, S., 651
Vander Sloten, J., 470
Vanhove, C., 654
Vanneste, M., 280
Vanquickenborne, F., 413
Varcoe, R., 60, 146
Varga, P., 360, 378, 382, 387, 388, 425, 590
Variola, f., 675
Vasta, M., 690
Vaughan, T., 65, 110, 116, 119, 166, 180, 241, 464, 479, 487
Vavourakis, V., 516, 529
Vemola, A., 404
Vena, P., 302, 405, 481, 672
Vendeuvre, T., 320
Veneziani, A., 161, 611
Ventikos, Y., 526
Ventrella, D., 261
Verdonschot, n., 12
Vereecke, E., 280
Verga, R., 369
Vergani, L., 482, 483
Vergara, C., 139, 160, 179, 187
Vergara, M., 269
Vergari, C., 306, 350
Vernè, E., 240
Vernengo, A., 336
Verschueren, S., 279
Verzicco, R., 610, 623
vesentini, s., 190
Vialle, R., 306, 350
Vibert, E., 593
Viceconti, M., 273, 453, 586, 588, 598
Videira, D., 433
Vigliotti, A., 640
Vignali, E., 17, 93, 121, 132, 168, 608, 631, 642
Vignon-Clementel, I., 593
Vila Pouca, M., 700, 703, 704
Villa, T., 312, 368, 385, 627
Villegas Bermudez, D., 559
Villegas, D., 285
Vimmr, J., 616
Vinci, R., 71
Vincoli, V., 672
Viola, F., 610, 622, 623
Vismara, R., 66, 106, 622
Visone, R., 252
Visser, V., 213
Viste, A., 374
Vitullo, P., 179
Vivanco, J., 486
Vivanco, M., 243
Vogt, F., 101, 108
Vogt, M., 311
Volkova, T., 541
Volpe, D., 290, 546, 547, 579
Volpin, F., 290
Volzhaninov, D., 207
von Mentlen, R., 395
von Segesser, L., 103
Vono, R., 231
Votta, E., 74, 114, 123, 138, 156, 165, 167
Voutouri, C., 227

Wafa, H., 414
Wagoner Johnson, A., 707
Walczak, T., 304
Walker, M., 251
Walle, M., 459, 461
Wang, B., 82
Wang, K., 357, 386
Wang, L., 417
Wang, W., 578
Wang, X., 327
Wang, Y., 25, 82
Ward, S., 131
Warnecke, D., 397, 493
Warren, J., 313
Waters, S., 655
Watson, C., 131
Watson, D., 657
Wearne, L., 456
Weber, A., 210, 243, 375
Weber, W., 192
Wehrle, E., 222, 465, 518, 522
Weimann, D., 680

Weinbaum, S., 86, 87
Weinkamer, R., 458
Weinsaft, J., 149
Wenger, M., 585
Wentzel, J., 170
Wham, B., 404
Whatling, G., 297
Whelan, A., 68, 117
Whitaker, I., 195
White Zeira, A., 147
Whiting, R., 180
Wickert, K., 428, 472, 539
Widmer, L., 105
Wilcock, H., 108
Wilcox, R., 313, 423, 424, 426, 604
Wilke, H., 247, 311, 315, 336, 398
Willaert, W., 221
Willems, M., 279
Williams, D., 297
Williams, J., 342, 650
Williams, S., 423
Willie, B., 478
Willinger, R., 346
Wilmanns, N., 158, 330
Wilson, C., 297
Wilson, D., 308
Windhager, R., 554
Winiarski, S., 561, 571
Winkler, C., 158
Winkler, M., 409
Winzenrieth, R., 462
Wiputra, H., 58
Wirth, B., 278
Witte, F., 484, 661
Witter, F., 391
Woernle, C., 288
Wolf, A., 419, 556
Wolfram, U., 451, 468, 644, 650
Wong, A., 342, 345
Wu, W., 133
Wulsten, D., 589
Wyers, C., 360
Wylezalek, M., 682
Wyrwol, F., 404

Xhemali, B., 467
Xi, J., 660
Xiong, J., 157
Xu, X., 150, 169, 181
Xu, Y., 100

Yahyaiee Bavil, A., 305, 676
Yaikova, V., 549
Yamamoto, K., 262, 480
Yamamoto, S., 282
Yanguma Muñoz, N., 580
Yao, J., 604
Yap, C., 55, 58, 649
Yavuz, C., 408
Yerby, S., 312
Yeritsyan, D., 461
Yildirim, C., 118
Yilmaz, D., 465
Yokoyama, Y., 217
Yoon, H., 357
Yuan, G., 25

Závodszky, G., 91, 615
Zaccaria, A., 127, 182
Zaccone, M., 127
Zadpoor, A., 363, 666
Zaffagnini, S., 393, 505, 634
Zago, M., 537, 563, 564, 567
Zagra, L., 482
Zalaudek, M., 554
Zambrano M., L., 470
Zampato, S., 545
Zanetti, E., 686
Zanotti, G., 576
Zbiral, B., 243
Zderic, I., 375, 381, 387, 388
Zedler, M., 276
Zekonyte, J., 448
Zengerle, L., 311, 315
Zerbi, A., 502
Zgierski-Johnston, C., 192
Zhang, H., 308
Zhang, Y., 681
Zhao, F., 195, 249
Zhao, L., 99, 101, 108, 109
Zhao, S., 133
Zheng, S., 655
Zheng, Y., 55
Zhou, Q., 619

Zhu, Y., 100
Zikry, C., 507
Zimmerman, K., 406
Zimmermann, E., 478
Zinno, R., 393
Zioupos, P., 466, 467
Ziziene, J., 287
Zizzi, E., 205
Zoli, F., 665
Zomparelli, A., 558
Zonfrillo, M., 698
Zucchelli, A., 665
Zuccotti, G., 194, 225
Zumstein, M., 286
Zunino, P., 187, 653
Zysset, P., 29, 425, 450, 451, 477, 478

ADVERTISEMENTS:
SPONSORS AND EXHIBITORS AND PROJECTS CORNER

SPONSORS



Exemplar works in the sector of innovative societies and in the field of virtual simulation developing vertical tools software. We sell software products for CAE and PIDO of the best international software companies and we offer:

01 added-value services

02 courses on tools and methods proposed and developed for our clients

03 dedicated software development

We are based in Turin and we work for many Italian universities. **This is a proof of the strong relationship between Exemplar and the world of research and technological innovation.**

We are from 2010 among the Innovative Companies of Turin, we are part of the **Torino Wireless**, network, of the POLO ICT, of the **Consorzio Proplast** and of the **Aerospace District of Piedmont.**

Exemplar, with the aim of providing innovative solutions to the companies it collaborates with, **has signed software resale partnerships at an international level.**

The development of a **solid network of strategic alliances,** combined with the experience and knowledge of our professional talents, allows us to better respond to customer requests.

Registered office
Corso Vittorio Emanuele II, 161 – 10139 Torino – Italia
Phone: +39 011 435 051
Email: exemplar@exemplar.com

ESB 2021 JULY 11-14, 2021 ONLINE

26TH CONGRESS OF THE EUROPEAN SOCIETY OF BIOMECHANICS

ORGANISED BY
POLITECNICO MILANO 1863

PARAMETRIC DESIGN Ansys

› Making an in silico impact!

The healthcare community, including researchers, product developers, regulators, and clinicians, is widely embracing Computer Models & Simulation (CM&S) for:

> Fundamental Research
> Ideation & Product Design
> Regulatory Approval
> Diagnosis and Surgery Planning
> Patients follow up & Monitoring
> Digital Twin and Personal Digital Avatar

By developing and marketing an open platform of carefully verified and validated technologies and solutions, Ansys and Parametric Design bring research to the patient bed, accelerating and amplifying medical innovation.

› Come to visit our virtual booth

› ANSYS

Ansys develops and markets multiphysics engineering simulation software for product design, testing and operation.

www.ansys.com/healthcare

› PARAMETRIC DESIGN

Parametric Design is a consulting firm and a PTC, ANSYS and Onshape reseller that provides a powerful products portfolio that includes a complete range of solutions integrated in CAD / CAM / CAE/ PLM / IoT / AR and Multiphysics Simulation environments.

www.parametricdesign.com



Microscopic Characterization of Biomaterials

Linking structures, properties, processes and performances

ZEISS Portfolio

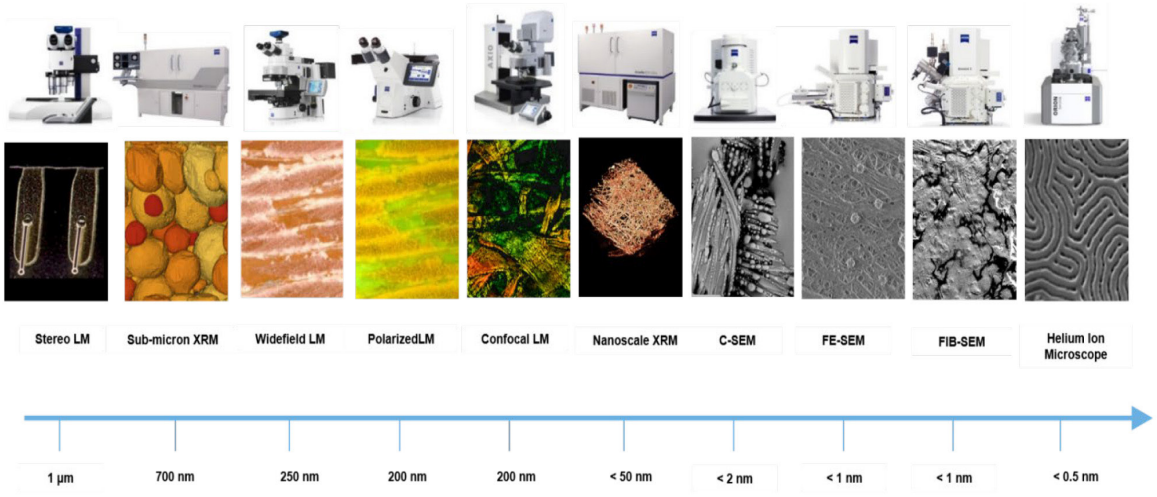

3D, multi-scale, multi-modal, in situ microscopic characterizations

Biomaterials
focus on the development of novel materials and materials for health care as well as HMI

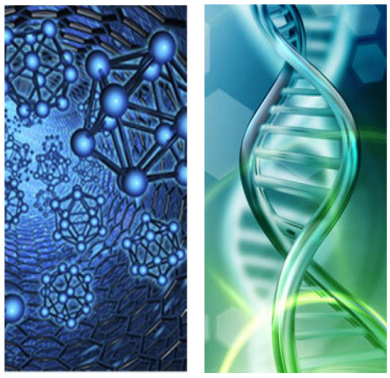

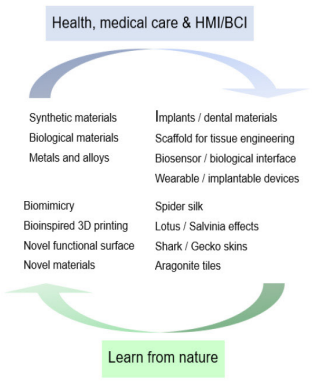

ZEISS

Seeing beyond

A PART OF THE RESEARCH COMMUNITY

Qualisys has helped to analyze and measure human movements for more than 30 years.



QUALISYS
Motion Capture Systems

Visit our Workshop Monday 12.30 CEST:
STREAMLINE YOUR RESEARCH
WITH QUALISYS MOTION CAPTURE

GPEM
Misura Conosci Migliora

cometa

www.gpem.net
www.cometasystems.com

PRODUCTS



SUPPORT & TRAINING



for your
Motion Analysis Lab

BETA
SIMULATION SOLUTIONS
Meet Reality in Biomechanics Simulation
physics on screen
www.beta-cae.com



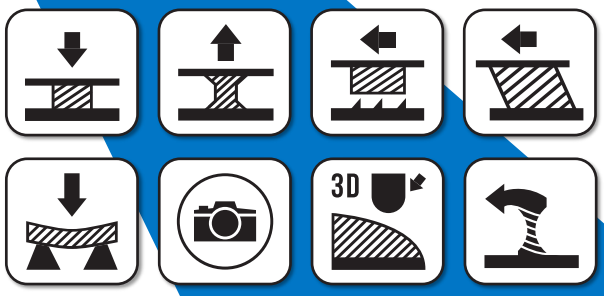

BIOMOMENTUM
MECHANICAL TESTING SOLUTIONS
FOR BIOMATERIALS AND TISSUES

Endovascular Stroke treatment and career paths in the biomedical industry.
Workshop July 13th ESB — 12:30-13:15 (CET)
CERENOVUS
NTI



materialise
innovators you can count on
The Materialise Mimics Innovation Suite was designed to make using medical image data for engineering purposes as easy and rewarding as possible. As the industry-standard medical image based engineering software and service, MIS puts you in control with the most advanced tools to support your mission to improve patient care.
www.materialise.com
Learn more

Are you interested in micro-mechanical properties:
Young's Modulus; Complex Modulus; Stress Relaxation; Creep etc



PIUMA
Tissues
Gels
(>50µm)



CHIARO
Single cells
Micro-structures
(<50µm)



PAVONE
High throughput platform
Single cells
Tissues
Hydrogels

OPTICS11 life

Visit our booth to learn more!

www.optics11life.com

OPTICS11 life

XSENSOR
Intelligent
Dynamic
Sensing

X4 Intelligent Insole System

XSENSOR's X4 Intelligent Insole system is a **plantar pressure** and **gait measurement solution** for athletic coaches and clinicians to **capture lab-quality data in the field**.

The X4 allows users to **evaluate gait**, **plantar pressure**, and **foot function** with **thin**, **flexible insole sensors** that are reliable and durable enough to accurately capture data wherever activity takes place — and without compromising natural motion.

Learn more by visiting **xsensor.com** or emailing **sales@xsensor.com**.



EXHIBITORS



PI Technologies Supporting Biomechanics and Biomedicals

Surgical robots, systems for radiotherapy, in vitro diagnostics, endoscopy, but also piezo components for ultrasound applications, pacemakers and liquid handling. All these applications can be developed thanks to PI technologies and products.
Contact our experts to find out more!

IT'S POSSIBLE
www.pionline.it



RBF Morph
the engine of the
medical digital twin

rbf
MEDITATE
spinner
next generation spine experts
EuroHPC

SAWBONES®

BIOMECHANICAL MATERIALS FOR PRECISE, REPEATABLE TESTING


BLOCKS AND SHEETS


COMPOSITE BONES

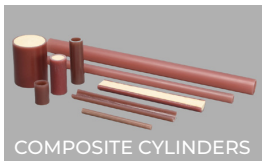
COMPOSITE CYLINDERS

www.sawbones.com
Sawbones USA
Sawbones Europe AB
(206) 463-5551
+46 (0) 40 650 70 00
info@sawbones.com
info@sawbones.se

We invite you to publish your books with Springer!
Feel free to contact publishing editor Mr. Pierpaolo Riva
(pierpaolo.riva@springer.com) and discuss your book proposals.

And browse our catalog! We are pleased to offer you a
20% conference discount, valid until September 30

Visit springer.com/shop | Use code 20DIY213



Springer

PROJECTS CORNER

CompBioMed

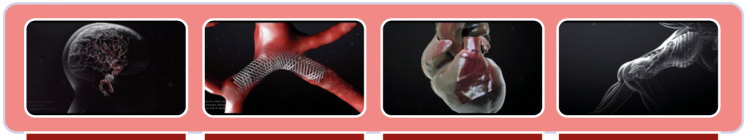

Academic Users
- Conferences, Journals, Training, Software Hub
- Promoting use and uptake of results

Industrial Users
- Training (specifically webinars), IAB, access to HPC
- Awareness through to uptake

Clinical Users
- Training (medical school courses), conferences, personal collaborations, HPC
- Awareness through to uptake

General Public
- Virtual Human film, social media, television
- Awareness only

Websites: **www.compbiomed.eu** **www.cbmc21.vfairs.com**

YouTube: **Computational Biomedicine**

Twitter: **@bio_comp**

LinkedIn **CompBioMed**

CompBioMed Conference 2021

15-17 September 2021

This project has received funding from the European Union's Horizon 2020 research and innovation programme.

INSIST

INSIST (In siliso clinical trials for treatment of acute ischemic stroke) develops simulated stroke trials, based on generation of virtual populations of stroke patients who are subjected to an ischemic stroke (module I), followed by simulation of thrombolysis, endovascular treatment and tissue progression (module II), with outcome prediction at the individual level (module III) and trial results (module IV).

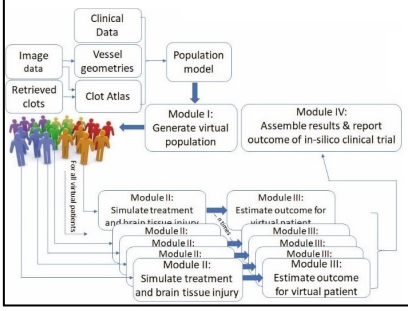

Our *in silico* trials allow targeting new devices, new pharmacotherapy and alternative decision-making in treatment.

We foresee that in silico stroke trials will lead to more effective and efficient randomized clinical trials in stroke.

https://www.linkedin.com/company/insist-h2020/

YouTube https://www.youtube.com/channel/UC_IkSzX73Hlb9tjLRfT1TZQ

Project coordinator:
Prof. Dr. Charles Majoie, MD
c.b.majoie@amsterdamumc.nl

For more information, check the 5-minute video on our website!
INSIST; www.insist-h2020.eu

This project has received funding from the European Union's Horizon 2020 research and innovation programme under grant agreement No 777072.

Amsterdam UMC, the Netherlands
University of Amsterdam, The Netherlands
Erasmus Medical Center, the Netherlands
KU Leuven, Belgium
National University of Ireland Galway, Ireland
University of Geneva, Switzerland
Politecnico di Milano, Italy
Cerenovus, Ireland
University of Oxford, United Kingdom
Lomonosov Moscow State University, Russia
Institut de Recherches Internationales Servier, France

SimInSitu

CAPVIDIA · 4RealSim · ISMETT Istituto di Ricovero e Cura a Carattere Scientifico · KU LEUVEN · Leartiker · MINES Saint-Etienne Une école de l'IMT · ARMINES · TU Graz · Panormitanae Studiorum Universitatis · XELTIS

H2020-SC1-DTH-2020-1

spinner

next generation spine experts

SPINe: Numerical and Experimental Repair strategies



Biomaterials

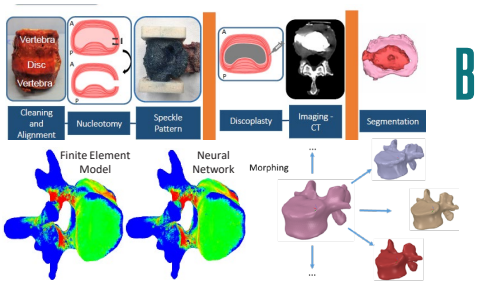

Biomechanics

in silico

This project has received funding from the European Union's Horizon 2020 research and innovation programme under the Marie Skłodowska-Curie grant agreement No 766012

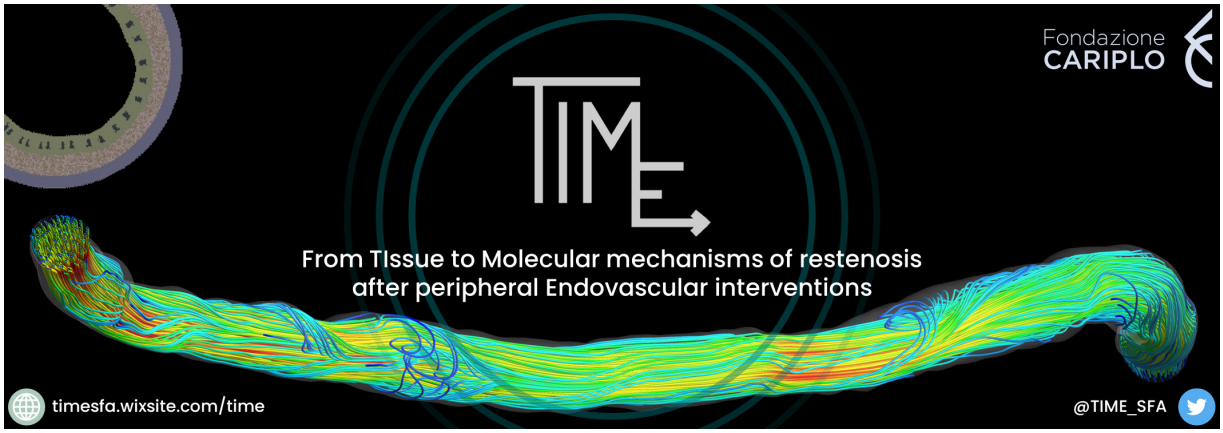
Fondazione
CARIPLO
TIME
From TIssue to Molecular mechanisms of restenosis
after peripheral Endovascular interventions
timesfa.wixsite.com/time
@TIME_SFA



Many thanks for the support

Hosting society

European Society of Biomechanics

Hosting institution

POLITECNICO MILANO 1863

POLO TERRITORIALE DI LECCO

Fondazione Politecnico di Milano